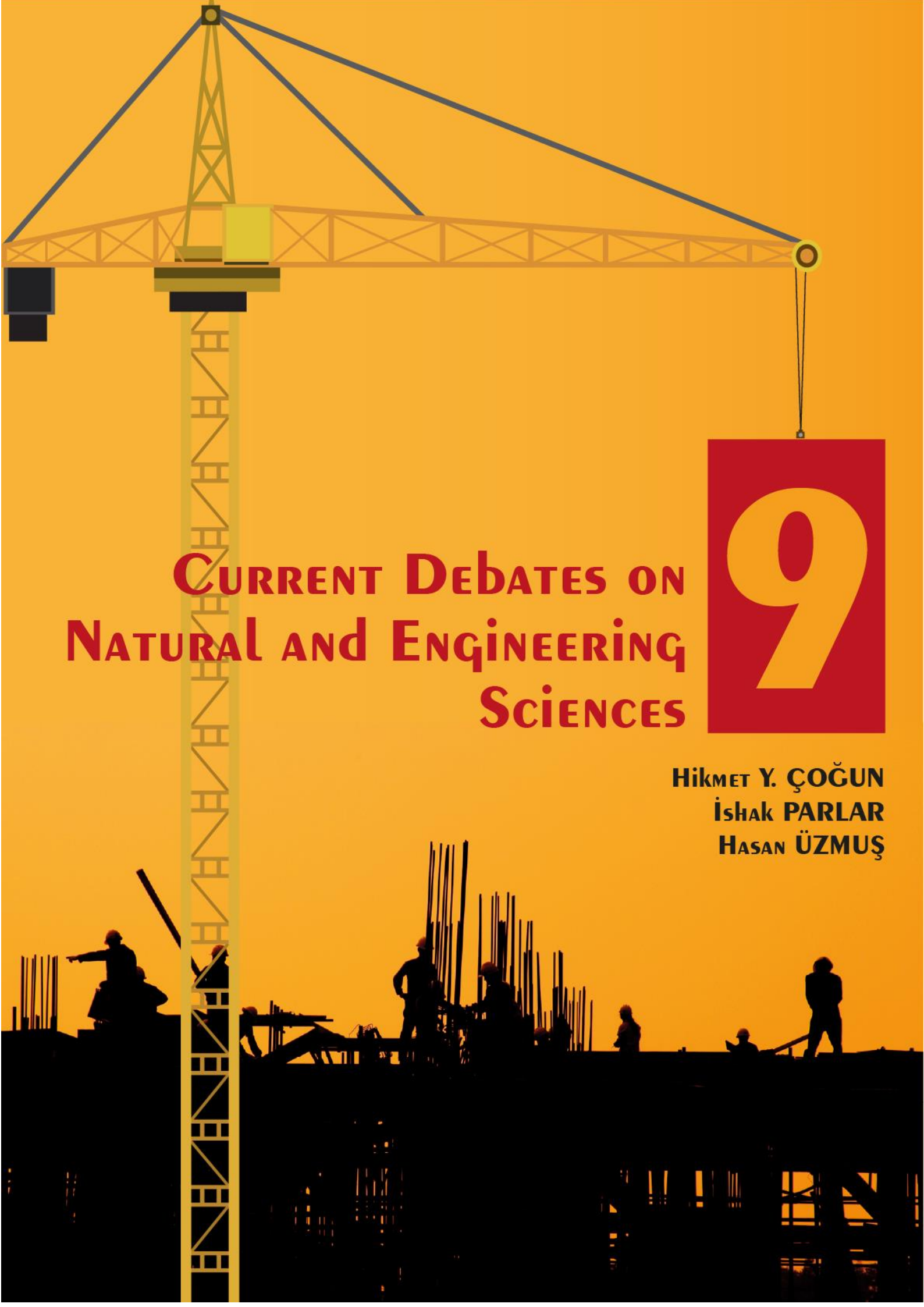

Current Debates on Natural and Engineering Sciences

9

Hikmet Y. ÇOĞUN
İshak PARLAR
Hasan ÜZMUŞ

ISBN: 978-625-6925-26-7

1st Edition

25 Haziran 2023

Current Debates on Natural and Engineering Sciences 9

Editors

Hikmet Y. ÇOĞUN

İshak PARLAR

Hasan ÜZMUŞ

Publisher

Engin DEVREZ

Bilgin Kültür Sanat Yayınları

Certificate No: 20193

Selanik Cd. No: 68/10 06640 Kızılay / Ankara

Phone: 0 (312) 419 85 67 – Fax: 0 (312) 419 85 68

www.bilginkultursanat.com

bilginkultursanat@gmail.com

Contents

A Study on Third Order Rational Difference Equation

Mehmet Emre ERDOĞAN

It is an interesting problem to find the asymptotic stability of positive solutions when approaching the equilibrium point for the difference equations. Real-life problems involving the difference equation are encountered in population biology, physics, financial and economic models, etc. The studies carried out to contribute to the theory of difference equations until today have focused on nonlinear difference equations. For example:

(Elsayed et al., 2017) investigated the global stability and the periodicity of the solutions of the recursive sequence

$$x_{n+1} = ax_n + bx_{n-1} + \frac{c + dx_{n-2}}{e + fx_{n-2}}.$$

(El-Dessoky & Al-Basyouni, 2019) deal with the global stability of the solutions, the boundedness and the periodic character of the nonlinear difference equation

$$x_{n+1} = \alpha x_n + \beta x_{n-l} + \gamma x_{n-k} + \frac{ax_n x_{n-k}}{bx_n + cx_{n-l} + dx_{n-k}}$$

(Elsayed & Alghamdi, 2019) studied the dynamics and stability behavior of the solutions of the second order nonlinear difference equation

$$x_{n+1} = ax_n + \frac{bx_n + cx_{n-1}}{d + ex_n x_{n-1}}$$

(Nirmaladevi & Karthikeyan, 2017) discussed about the periodicity of the difference equation

$$y_{n+1} = Py_n + Qy_{n-k} + Ry_{n-l} + \frac{by_{n-k}}{dy_{n-k} - ey_{n-l}}$$

(El-Moneam & Zayed, 2014) studied the boundedness and the global stability of the positive solutions of the following nonlinear difference equation

$$x_{n+1} = Ax_n + Bx_{n-k} + Cx_{n-l} + \frac{bx_n x_{n-k} x_{n-l}}{dx_{n-k} - ex_{n-l}}$$

(Elsayed & Gafel, 2022) investigated the behavior of the solutions of the following rational difference equation

$$x_{n+1} = ax_n + bx_{n-1} + \frac{cx_n + dx_{n-1}}{e + fx_{n-1}}$$

For other related studies on the subject, see (Khaliq et al., 2022; Erdogan, 2020; Ibrahim et al., 2021; Deng et al., 2020).

In this study, our aim is to examine the global asymptotic stability of the solutions of the nonlinear difference equation

$$x_{n+1} = \alpha x_{n-1} + \beta x_{n-2} + \frac{\gamma x_{n-1} + \theta x_{n-2}}{\phi + \varphi x_{n-1}} \tag{1}$$

where the initial conditions x_{-2}, x_{-1} and x_0 are real numbers and $\alpha, \beta, \gamma, \theta, \phi$ and φ are positive real numbers

Let us give some definitions and theorems that we need.

Definition 1. (Camouzis & Ladas, 2007) Let I be some interval of real numbers and let

$$f : I^3 \to I$$

be a continuously differentiable function.

Then for every set of initial conditions $x_0, x_{-1}, x_{-2} \in I$, the difference equation

$$x_{n+1} = f(x_n, x_{n-1}, x_{n-2}), \ n = 0,1,\ldots \tag{2}$$

has a unique solution $\{x_n\}_{n=-2}^{\infty}$.

A point $\bar{x} \in I$ is called an equilibrium point of (2) if

$$\bar{x} = f(\bar{x}, \bar{x}, \bar{x});$$

that is,

$$x_n = \bar{x} \text{ for } n \geq 0$$

is a solution of Eq.(2), or equivalently, $\bar{x}$ is a fixed point of f.

Definition 2. (Camouzis & Ladas, 2007) Let $\bar{x}$ be an equilibrium point of Eq.(2).

(i) The equilibrium $\bar{x}$ of Eq.(2) is called locally stable if for every $\grave{o} > 0$, there exists $\delta > 0$ such that for all $x_0, x_{-1}, x_{-2} \in I$ with $|x_0 - \bar{x}| + |x_{-1} - \bar{x}| + |x_{-2} - \bar{x}| < \delta$, we have

$|x_n - \bar{x}| < \grave{o}$ for all $n \geq -2$.

(ii) The equilibrium $\bar{x}$ of Eq.(2) is called locally asymptotically stable if it is locally stable, and if there exists $\gamma > 0$ such that for all $x_0, x_{-1}, x_{-2} \in I$ with $|x_0 - \bar{x}| + |x_{-1} - \bar{x}| + |x_{-2} - \bar{x}| < \gamma$, we have

$\lim_{n\to\infty} x_n = \bar{x}.$

(iii) The equilibrium $\bar{x}$ of Eq.(2) is called global attractor if for every $x_0, x_{-1}, x_{-2} \in I$ we have

$\lim_{n\to\infty} x_n = \bar{x}.$

(iv) The equilibrium $\bar{x}$ of Eq.(2) is called global asymptotically stable if it is locally stable and a global attractor.

(v) The equilibrium $\bar{x}$ of Eq.(2) is called unstable if it is not stable.

(vi) The equilibrium $\bar{x}$ of Eq.(2) is called source or a repeller, if there exists $r > 0$ such that for all $x_0, x_{-1}, x_{-2} \in I$ with $0 < |x_0 - \bar{x}| + |x_{-1} - \bar{x}| + |x_{-2} - \bar{x}| < r$, there exists $N \geq 1$ such that

$|x_N - \bar{x}| \geq r.$

The linearized equation of (2) about the equilibrium point $\bar{x}$ is

$$y_{n+1} = p_1 y_n + p_2 y_{n-1} + p_3 y_{n-2}, \quad n = 0,1,... \tag{3}$$

where

$$p_1 = \frac{\partial f}{\partial x_n}(\bar{x}, \bar{x}, \bar{x})$$

$$p_2 = \frac{\partial f}{\partial x_{n-1}}(\bar{x}, \bar{x}, \bar{x})$$

$$p_3 = \frac{\partial f}{\partial x_{n-2}}(\bar{x}, \bar{x}, \bar{x})$$

The characteristic equation of (3) is

$$\lambda^3 - p_1\lambda^2 - p_2\lambda - p_3 = 0 \tag{4}$$

Theorem 1. (Camouzis & Ladas, 2007) Assume that $p_i \in \mathbb{R}$, $i = 1,2,...$. Then

$$\sum_{i=1}^{3} |p_i| < 1,$$

is a sufficient condition for the asymptotic stability of (4)

Theorem 2. (Camouzis & Ladas, 2007) Let $[p,q]$ be an interval of real numbers and assume that $f : [p,q]^2 \to [p,q]$ is a continuous function satisfying the following properties:

(a) $f(x,y)$ is non-decreasing in $y \in [p,q]$ for each $x \in [p,q]$, and non-increasing in $x \in [p,q]$ for each $y \in [p,q]$;

(b) If $(m,M) \in [p,q] \times [p,q]$ is a solution of the system

$M = f(m,M)$ and $m = f(M,m)$

then $m = M$. Thus the difference equation has a unique equilibrium $\bar{x} \in [p,q]$ and every solution converges to $\bar{x}$.

Stability Analysis of Eq.(1)

In this section we investigate the stability of Equation (1) under the assumptions. The equilibrium points of Eq.(1) are obtained by

$$\bar{x} = \alpha\bar{x} + \beta\bar{x} + \frac{\gamma\bar{x} + \theta\bar{x}}{\phi + \varphi\bar{x}},$$

so the equilibrium points of Eq.(1) are $\bar{x}_1 = 0$ and $\bar{x}_2 = \frac{\gamma+\theta}{\delta\varphi} - \frac{\phi}{\varphi}$ where $\delta = 1-\alpha-\beta \neq 0$. Also if $\gamma + \theta = \delta\phi$ then $\bar{x}_1 = 0$.

Let $f : (0,\infty)^2 \to (0,\infty)$ be a function defined by

$$f(u,v) = \alpha u + \beta v + \frac{\gamma u + \theta v}{\phi + \varphi u}.$$

Then

$$\frac{\partial f(u,v)}{\partial u} = \alpha + \frac{\gamma\phi - \varphi\theta v}{(\phi + \varphi u)^2},$$
$$\frac{\partial f(u,v)}{\partial v} = \beta + \frac{\theta}{\phi + \varphi v}$$

Theorem 3. The following statement are true.

i. If $\delta > 0$ and $\gamma + \theta < \phi\delta$, then equilibrium point $\bar{x}_1 = 0$ of Eq.(1) is locally asymptotically stable.

ii. If $\delta > 0$ and $\phi\delta < \gamma + \theta$ then the equilibrium point $\bar{x}_2 = \frac{\gamma+\theta}{\delta\varphi} - \frac{\phi}{\varphi}$ of Eq.(1) is locally asymptotically stable.

iii. If $\delta < 0$ then the equilibrium points of Eq. (1) are unstable.

Proof. The linearized equation of Eq.(1) about the equilibrium point $\bar{x}_1 = 0$ is

$$y_{n+1} = \left(\alpha + \frac{\gamma}{\phi}\right) y_{n-1} + \left(\beta + \frac{\theta}{\phi}\right) y_{n-2} \tag{5}$$

The characteristic equation of (5) is

$$\lambda^3 - \left(\alpha + \frac{\gamma}{\phi}\right)\lambda - \left(\beta + \frac{\theta}{\phi}\right) = 0$$

hence the proof of (i) follows Theorem 1.

For (ii),

The characteristic equation of Eq.(1) about the equilibrium point $\bar{x}_2 = \frac{\gamma+\theta}{\delta\varphi} - \frac{\phi}{\varphi}$ is

$$\lambda^3 - \left(\alpha + \frac{\delta(\phi\delta - \theta)}{\gamma + \theta}\right)\lambda - \left(\beta + \frac{\theta\delta}{\gamma + \theta}\right) = 0.$$

By the Theorem 1, Eq.(1) is asymptotically stable on $\bar{x}_2$ if $\left|\alpha+\frac{\delta(\phi\delta-\theta)}{\gamma+\theta}\right|+\left|\beta+\frac{\theta\delta}{\gamma+\theta}\right|<1$. There are six cases about to consider.

Case (I) If $\delta>0$ and $\phi\delta\geq\theta$, the inequality occurs as

$$\alpha+\frac{\delta(\phi\delta-\theta)}{\gamma+\theta}+\beta+\frac{\theta\delta}{\gamma+\theta}<1$$

rearranging inequality we obtain

$$\phi\delta<\gamma+\theta.$$

Case (II) If $\delta>0$ and $\alpha\frac{\gamma+\theta}{\delta}+\phi\delta>\theta>\phi\delta$, the inequality occurs as before

$$\alpha+\frac{\delta(\phi\delta-\theta)}{\gamma+\theta}+\beta+\frac{\theta\delta}{\gamma+\theta}<1$$

so we find $\phi\delta<\gamma+\theta$ again.

Case (III) If $\delta>0$ and $\theta>\alpha\frac{\gamma+\theta}{\delta}+\phi\delta$, the inequality occurs as

$$-\alpha-\frac{\delta(\phi\delta-\theta)}{\gamma+\theta}+\beta+\frac{\theta\delta}{\gamma+\theta}<1.$$

This leads to

$$-2\alpha-\frac{\phi\delta^2-2\theta\delta}{\gamma+\theta}<0<\delta$$

Hence, the statement is a tautology.

Case (IV) If $\delta>0$, $\theta=\alpha\frac{\gamma+\theta}{\delta}+\phi\delta$ and $\theta>\phi\delta$, the inequality occurs as

$$\beta+\frac{\theta\delta}{\gamma+\theta}<1$$

which leads to $\gamma(\beta-1)<\alpha\theta$. If we rewrite the inequality $\delta>0$ will be

$$\begin{aligned}\delta&>0\\1-\alpha-\beta&>0\\1&>\alpha+\beta\\0&>\alpha+\beta-1\\0&>\beta-1\end{aligned}$$

so, $\gamma(\beta-1)<0<\alpha\theta$ which is tautology.

Case (V) If $\delta<0$ and $\beta+\frac{\theta\delta}{\gamma+\theta}>0$, the inequality occurs as

$$\alpha+\frac{\delta(\phi\delta-\theta)}{\gamma+\theta}+\beta+\frac{\theta\delta}{\gamma+\theta}<1$$

by rearranging inequality we conclude that $\phi\delta>\gamma+\theta$ which is contradiction to $\gamma+\theta>0$ and $\phi\delta<0$.

Case (VI) If $\delta<0$ and $\beta+\frac{\theta\delta}{\gamma+\theta}<0$, the inequality occurs as

$$\alpha+\frac{\delta(\phi\delta-\theta)}{\gamma+\theta}-\beta-\frac{\theta\delta}{\gamma+\theta}<1$$
$$-2\beta(\gamma+\theta)+\delta(\phi\delta-\theta)<\delta$$

From $\beta+\frac{\theta\delta}{\gamma+\theta}<0$, we can easily say that $\beta(\gamma+\theta)<-\theta\delta$. Thus,

$$2\theta\delta+\phi\delta^2-2\theta\delta<-2\beta(\gamma+\theta)+\delta(\phi\delta-2\theta)<\delta$$
$$\phi\delta^2<\delta$$

The inequality $\phi\delta^2<\delta$ is contradiction to $\phi\delta^2>0$ and $\delta<0$.

From Case (V) and Case (VI) δ should be positive. This completes the proof.

Theorem 4. If $(1+\alpha-\beta)\phi>\theta-\gamma$, then the equilibrium point $\bar{x}$ of Eq.(1) is global asymptotically stable

Proof. Let $M=f(m,M)$ and $m=f(M,m)$,

$$M=\alpha m+\beta M+\frac{\gamma m+\theta M}{\phi+\varphi m}$$
$$m=\alpha M+\beta m+\frac{\gamma M+\theta m}{\phi+\varphi M},$$

then

$$M(1-\beta)\phi+\varphi mM(1-\beta)=\alpha m\phi+\alpha\varphi m^2+\gamma m+\theta M$$
$$m(1-\beta)\phi+\varphi mM(1-\beta)=\alpha M\phi+\alpha\varphi M^2+\gamma M+\theta m$$

by substracting equations it gives,

$$(M-m)\left[(1-\beta)\phi+\alpha\phi+\alpha\varphi(M+m)+\gamma-\theta\right]=0$$

since $(1+\alpha-\beta)\phi>\theta-\gamma$, then $M=m$. From Theorem 2 and Definition 2 the equilibrium point $\bar{x}$ of Eq.(1) is global asymptotically stable. Thus, the proof is completed.

Theorem 5. If $\gamma+\theta<\phi\delta$ then the solutions of Eq.(1) is bounded.

Proof. Let $\{x_n\}_{n=-2}^{\infty}$. be a solution of Eq.(1). Then

$$x_{n+1} = \alpha x_{n-1} + \beta x_{n-2} + \frac{\gamma x_{n-1} + \theta x_{n-2}}{\phi + \varphi x_{n-1}}$$
$$\leq \alpha x_{n-1} + \beta x_{n-2} + \frac{\gamma x_{n-1} + \theta x_{n-2}}{\phi}$$
$$\leq \left(\alpha + \frac{\gamma}{\phi}\right) x_{n-1} + \left(\beta + \frac{\theta}{\phi}\right) x_{n-2}$$

Let $\chi = \max\{x_{n-1}, x_{n-2}\}$. So,

$$x_{n+1} \leq \left(\alpha + \frac{\gamma}{\phi} + \beta + \frac{\theta}{\phi}\right)\chi$$

since $\gamma + \theta < \phi\delta$, the inequality holds the

$$\gamma + \theta < \phi(1 - \alpha - \beta)$$
$$\alpha + \beta + \frac{\gamma + \theta}{\phi} < 1$$

which implies that $x_{n+1} < \max\{x_{n-1}, x_{n-2}\}$ for $n \geq 0$. Then

$$\lim_{n\to\infty} x_n = 0.$$

Thus the solutions of Eq. (1) are bounded. The proof is complete.

Computational Examples

Computational examples are provided in this section to show how the main results are valid. With the use of MATLAB, a graph of the solutions was created in order to better illustrate the numerical examples. These graphs are created using various starting conditions and parameter values.

- In Figure 1, the equilibrium point $\overline{x}_1$ of Eq. (1) is shown to be globally asymptotically stable under the initial conditions $x_{-2} = 3.456$, $x_{-1} = 7.879$, $x_0 = -4.57$ and the parameters $\alpha = 0.1$, $\beta = 0.2$, $\gamma = 2.24$, $\theta = 3.12$, $\phi = 9.65$ and $\varphi = 6.45$ that meet the condition $\gamma + \theta < \phi\delta$.

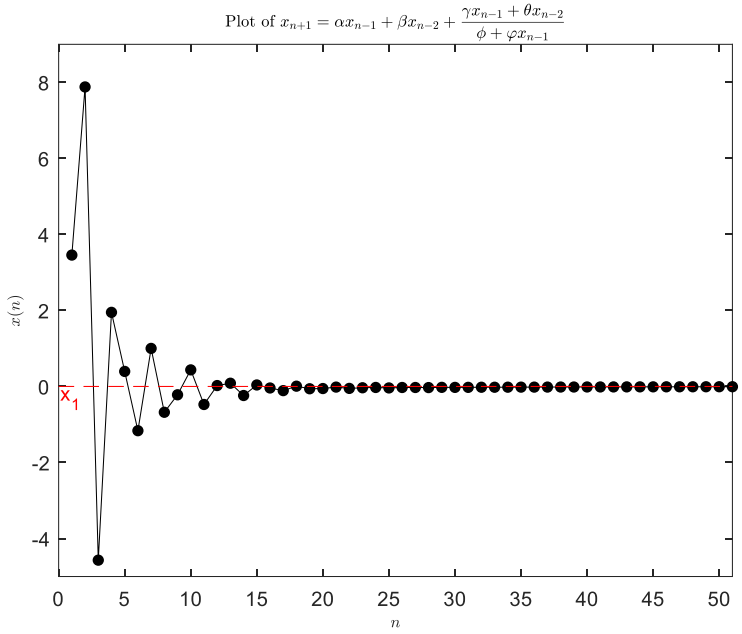

Figure 1: Stability of the solutions of Eq. (1) under the condition $\gamma + \theta < \phi\delta$.

- In Figure 2, the equilibrium point $\bar{x}_2$ of Eq. (1) is shown to be globally asymptotically stable under the initial conditions $x_{-2} = 3.456,\ x_{-1} = 7.879,\ x_0 = -4.57$ and the parameters $\alpha = 0.1,\ \beta = 0.2,\ \gamma = 5.24,\ \theta = 3.12,\ \phi = 2.65$ and $\varphi = 6.45$ that meet the condition $\gamma + \theta > \phi\delta$.

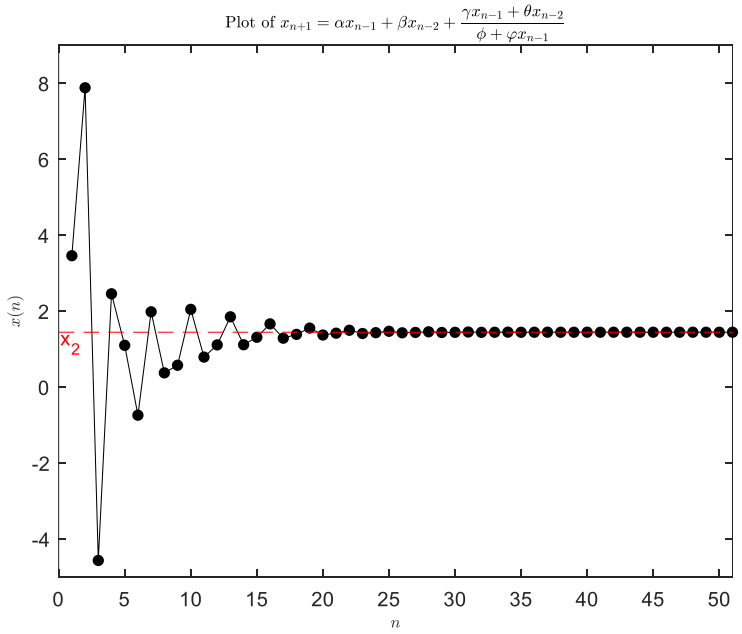

Figure 2: Stability of the solutions of Eq. (1) under the condition $\gamma + \theta > \phi\delta$.

- In Figure 3, Eq. (1) is shown to be unstable under the initial conditions $x_{-2} = 3.456,\ x_{-1} = 7.879,\ x_0 = -4.57$ and the parameters $\alpha = 0.8,\ \beta = 0.4,\ \gamma = 2.24,\ \theta = 3.12,\ \phi = 4.65$ and $\varphi = 2.45$ that meet the condition $\delta < 0$.

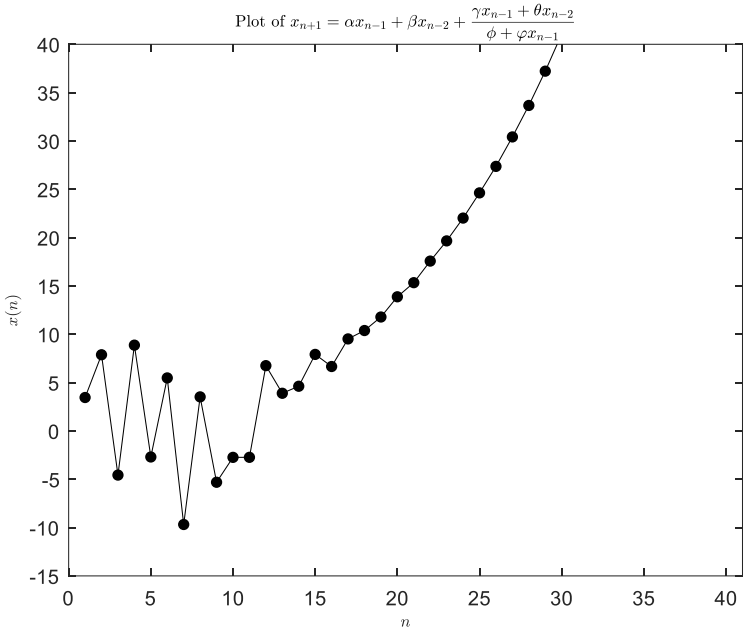

Figure 3: Unbounded solutions of Eq. (1) under the condition $\delta < 0$.

References

Camouzis, E., & Ladas, G. (2007). *Dynamics of Third-Order Rational Difference Equations with Open Problems and Conjectures.* New York: Chapman and Hall/CRC. https://doi.org/10.1201/9781584887669

El-Dessoky, M., & Al-Basyouni, K. S. (2019). On the Higher Order Difference Equation. *Journal of Computational Analysis and Applications, 27*(6), 1013-1022.

El-Moneam, M. A., & Zayed, E. M. (2014). Dynamics of the rational difference equation. *Dynamics of Continuous, Discrete and Impulsive Systems Series A: Mathematical Analysis, 21*, 317-331.

Elsayed, E. M., & Alghamdi, A. (2019). Qualitative behavior of a rational recursive sequence of second order. *Rocky Mountain Journal of Mathematics, 49*(7), 2135-2154. https://doi.org/10.1216/RMJ-2019-49-7-2135

Elsayed, E. M., & Gafel, H. S. (2022, 1 16). Dynamics And Global Stability Of Second Order Nonlinear Difference Equation. *Pan-American Journal of Mathematics, 1*, 1-16. https://doi.org/https://doi.org/10.28919/cpr-pajm/1-16

Elsayed, E. M., Alzahrani, F., & Alayachi, H. (2017, 23 7). Global Attractivity and the Periodic Nature of Third Order Rational Difference Equation. *Journal of Computational Analysis and Applications, 23*(7), 1230-1241.

Erdogan, M. E. (2020). Stability of the third order rational difference equation. *MANAS Journal of Engineering, 8*(1), 68-76.

Khaliq, A., Alam, M., & Hassan, S. (2022). Stability Chaos And Periodic Solution Of Delayed Rational Recursive. *Pan-American Journal of Mathematics, 1*, 1-15. https://doi.org/10.28919/cpr-pajm/1-15

Nirmaladevi, S., & Karthikeyan, N. (2017). Dynamics And Behavior Of Higher Order And Nonlinear Rational Difference Equation. *International Journal Of Advance Research And Innovative Ideas In Education, 3*(4), 2071-2079. https://doi.org/16.0415/IJARIIE-6261

Quantitative Analysis of the Effect of Quarantine on the Spread of COVID-19

Mehmet KOCABIYIK[1]
Mevlüde YAKIT ONGUN [2]

1.INTRODUCTION

COVID-19, short for coronavirus disease (2019), is caused by severe acute respiratory syndrome coronavirus 2 (SARS-CoV-2) (WHO,2019). The rate of spread of the virus is quite large. For this reason, its sphere of influence has expanded in a short time. Studies have been carried out to determine the dynamics of the virus. By determining the dynamics, it is aimed to intervene to reduce the spread of the virus. Mathematical models have been created for the virus spread system. Among these models, equations including the quarantine effect were also expressed.

Feng et al. (2020) examined the effects of COVID-19 on media and quarantine. Baleanu et al. (2020) took a new approach to the COVID-19 model and used the Caputo-Fabrizio derivative. They expressed the dynamics of the system of equations with the help of this derivative. Atangana (2020) created the system using novel fractal fractional derivatives. From this work, Atangana created the dynamics for the salvation of humanity before vaccination.

According to Babaei et al. (2021) developed the model system, which will be modified and used in this study. In their modeling, the authors used a type that includes quarantine data for COVID-19. The authors investigated the dynamics of this system using the Adams-Bashforth-Moulton predictor-corrector method for numerical simulations.

This model, which includes the quarantine factor from this study, has been expressed and modified with distributed order differential equations. The aim here is to use the density function of distributed order differential equations. It has been suggested to examine the different effects in a shorter time than the modeling right with the density function. Both ordinary order and fractional order differential equations can be expressed by the choice of density function. Thus, the dynamics of the system can be obtained easily with a single equation instead of several different equations.

Caputo defined distributed order differential equations in 1969 and conducted studies in 1995, including their areas of use. Afterwards, studies on this type of equations have increased due to the wide range of usage areas. Bagley and Torvik (2000) examined the solution of distributed order differential equations in their studies. Hartley and Lorenzo (2003) studied the definition of a fractional ordinal system based on continuous-order distributions.

In the early days, studies on numerical analysis were not seen in this type of equations. Recently, the increase in usage areas has led to the emergence of studies where these analyzes are also carried out. For some numerical studies and stability analysis, refer to the following resources; Diethelm and Ford (2009), Katsikadelis (2014), Li and Wu (2016), Aminikhah et al. (2013), Kocabıyık et al. (2021), Kocabıyık (2022), Kocabıyık and Ongun (2022) and Kocabıyık et al. (2022).

This study consists of four main sections. In the second section, basic definitions and concepts are given for fractional derivatives and distributed order differential equations. Also

[1] Res. Asst., Burdur Mehmet Akif Ersoy University, Department of Mathematics, Orcıd: 0000-0002- 7701-6946.
[2] Prof. Dr., Süleyman Demirel University, Department of Mathematics, Orcıd: 0000-0003-2363-9395.

in this section, the NSFD scheme and approximate Grünwald-Letnikov fractional derivative required for discretization are given. In the third section, the modified system has been discretized. Afterward, the numerical analyzes of the system are expressed with the help of graphics. In the fourth section, the conclusion part is included and the information about the obtained data is expressed.

2.BASIC DEFINITIONS AND CONCEPTS

Distributed order differential equations are a kind of general case of fractional order differential equations. For this reason, fractional differential equations are very important in terms of definition. In the first part of this chapter, different types of fractional derivatives are described. Then, with the help of these fractional derivatives, distributed order differential equations are expressed (Podlubny, 1999; Caputo, 2001).

In the second part of the chapter, the Nonstandard finite difference approach introduced by Mickens for discretization is expressed. Also in this section, the approximation method of the Grünwald-Letnikov derivative is defined for discretization (Dorciak, 1994; Mickens, 1989; Mickens, 1994; Meerschaert and Tadjeran, 2004).

2.1.Preliminary Information About Fractional Derivatives

Definition 2.1.1: (Podlubny, 1999) Let the function $h(t)$ be an integrable function in the interval $[u_1, u_2]$ with $k-1 < \alpha \leq k$ for $k \epsilon \mathbb{N}^+$. Riemann Liouville fractional derivative of order α is defined by

$$D_R^{\alpha} h(t) = \frac{1}{\Gamma(k-\alpha)} \frac{d^n}{dt^n} \int_{\alpha}^{t} \frac{h^{(k)}(v)}{(t-z)^{\alpha-k+1}} dv.$$

Definition 2.1.2: (Podlubny, 1999). Caputo fractional derivative of order α is given by

$$D_{CP}^{\alpha} h(t) = \frac{1}{\Gamma(k-\alpha)} \int_{\alpha}^{t} \frac{h^{(k)}(v)}{(t-z)^{\alpha-k+1}} dv,$$

where $\Gamma(.)$ is a Gamma function and h(t) is integrable function in the range $[u_1, u_2]\, with \;\; k \epsilon \mathbb{N}^+$ and $k-1 < \alpha \leq$ k.

Definition 2.1.3: (Podlubny, 1999) Suppose that the function $h^{(u)}$(t) is integrable function in the range $[u, t]$ and $u = 1,2,..,k+1-th$ times differentiable function. Grünwald-Letnikov fractional derivative of order α is described by

$$D_G^{\alpha} h(t) = \lim_{j \to 0} j^{-\alpha} \sum_{i=0}^{k} (-1)^i \binom{k}{i} h(t-ij).$$

Definition 2.1.4: (Caputo, 2001) The integral operator of distributed order differential equations is expressed as:

$$D_t^{d(\alpha)} h(t) = \int_{k_1}^{k_2} d(\alpha)\, D_t^{\alpha} h(t)\, d\alpha,$$

where $\alpha \epsilon (k_1, k_2)$, $\int_{k_1}^{k_2} d(\alpha) = m > 0$ and $d(\alpha)$ is as density function of distributed order differential equations. $D_t^{\alpha} h(t)$ expressed in the definition is the fractional derivative operator. So, the derivative operators above can be used here. It has been observed that different operators are used in different sources. In this study, the use of the Caputo derivative operator was preferred due to the existence of initial conditions. Distributed order derivatives are expressed as:

$$D_t^{d(\alpha)}h(t) = \sum_{i=1}^{n} \alpha^i \int_{k_1}^{k_2} d_i(\alpha)\, D_t^{i-\alpha}h(t)d\alpha + \sum_{j=0}^{n} b_j h^i(t).$$

Preliminary Information About Discretization

Definition 2.2.1: (Dorciak, 1994) Let $p_j^{\alpha} = \left(1 - \frac{1+\alpha}{j}\right) p_{j-1}^{\alpha},\ for\ j = 1,2,3, \dots,\ v = h^{-\alpha}$ and h is chosen quite small. The approximate Grünwald-Letnikov derivative formula for distributed order differential equations can be arranged as follows:

$$D_t^{\alpha}h(t) = \sum_{i=0}^{n} p_i^{\alpha} h(t_{n-r}), \quad n = 1,2,3, \dots.$$

Nonstandard finite difference (NSFD) schemes were described by Mickens. Its use for different systems of equations was also introduced by him. With this method, Mickens tried to eliminate instabilities. For this reason, he used the denominator function from his definition. It has been shown that indecisions can be removed by selecting the denominator function (Mickens, 1989; Mickens, 1994).

Definition 2.2.2: (Mickens, 1994) The NSFD scheme is defined as follows:

$$H(z) \to H(v_n), \quad v(t) \to v(t_n), \quad \frac{dv}{dt} \to \frac{v_{n+1} - v_n}{\eta}, t \to t_n,$$

where $\frac{dv}{dt} = H(\varphi, v)$ with $\varphi: parameter$ and η is a denominator function and it can be chosen as $\eta = \frac{1-e^{-ph}}{p}$.

The denominator function depends on the variable h, which is the step interval, and the variable p, which can be found with the equilibrium point, respectively. Thus, with these definitions and expressions, the NSFD scheme can be used in distributed order differential equations with the help of the Grünwald-Letnikov approximate derivative formula (Meerschaert and Tadjeran, 2004).

3.QUANTITATIVE ANALYSIS OF THE EFFECT OF QUARANTINE ON THE SPREAD OF COVID-19

The population in the equation system given in the study was expressed with seven different groups (Babaei et al., 2021):

S: People who are susceptible or exposed to the virus,

I: Infected individuals with symptoms,

N: Those who are infected with the virus but have no symptoms,

S^q: Susceptible individuals in quarantine,

Q: Infected individuals in quarantine,

H: Infected individuals in the hospital,

R: Individuals who have recovered.

The modified model of the effect of Quarantine on the Spread of COVID-19 model can be given as:

$$D_t^{u(\alpha)}S(t) = B - (cp_t\,(1-q)(1-\rho) + cp_t(1-q)\rho + cqp_t + (1-p_t)cq)\big(I(t) + t_r N(t)\big)S(t) + \lambda S^q(t) - dS(t),$$

$$D_t^{u(\alpha)}I(t) = p_t c\rho(1-q)S(t)\big(I(t) + t_r N(t)\big) - (t_1 + r_1 + a_1)I(t),$$

$$D_t^{u(\alpha)}N(t) = p_t c(1-q)(1-\rho)S(t)\big(I(t)+t_r N(t)\big) - (r_2+a_2)N(t),$$
$$D_t^{u(\alpha)}S^q(t) = (1-p_t)cqS(t)\big(I(t)+t_r N(t)\big) - (\lambda+d)S^q(t),$$
$$D_t^{u(\alpha)}Q(t) = p_t cqS(t)\big(I(t)+t_r N(t)\big) - (t_2+a_3)Q(t),$$
$$D_t^{u(\alpha)}H(t) = t_1 I(t) + t_2 Q(t) - (a_2+r_3)H(t),$$
$$D_t^{u(\alpha)}R(t) = r_1 I(t) + r_2 N(t) + r_3 H(t) - a_4 R(t),$$

where, B is the birth rate of the population. c is the contact ratio. t_r indicates the transmission rate and p_t indicates the transmission probability per contact. q indicates the rate at which susceptible individuals are quarantined. t_1 and t_2 represent the rates of passage of symptomatic infected individuals and quarantined susceptible individuals into the quarantined infected compartment, respectively. r_1, r_2, and r_3 are the recovery rates of infected persons with symptoms, infected persons without symptoms, and quarantined infected persons, respectively. d naturally denotes mortality rates. ρ is the probability of occurrence of symptoms among infected individuals.

λ indicates the rate at which quarantined uninfected persons are released into the community. a_1, a_2, a_3, and a_4 represent the rates at which virus was removed from compartments I, N, Q, and R.

If a nonstandard discretization scheme is applied to the modified distributed order model of the impact of quarantine on the spread of COVID-19, the discretized version is obtained as follows:

$$\sum_{i=1}^{l}\frac{u(\alpha_i)}{l}\sum_{j=0}^{n+1}p_j^{\alpha_i}S_{n+1-j} = B - A_1(I_n + t_r N_n)S_{n+1} + \lambda {S^q}_n - dS_{n+1},$$

$$\sum_{i=1}^{l}\frac{u(\alpha_i)}{l}\sum_{j=0}^{n+1}p_j^{\alpha_i}I_{n+1-j} = A_2(I_{n+1} + t_r N_n)S_n - (t_1+r_1+a_1)I_{n+1},$$

$$\sum_{i=1}^{l}\frac{u(\alpha_i)}{l}\sum_{j=0}^{n+1}p_j^{\alpha_i}N_{n+1-j} = A_3(I_n + t_r N_{n+1})S_n - (r_2+a_2)N_{n+1},$$

$$\sum_{i=1}^{l}\frac{u(\alpha_i)}{l}\sum_{j=0}^{n+1}p_j^{\alpha_i}{S^q}_{n+1-j} = A_4(I_n + t_r N_n)S_n - (\lambda+d){S^q}_{n+1},$$

$$\sum_{i=1}^{l}\frac{u(\alpha_i)}{l}\sum_{j=0}^{n+1}p_j^{\alpha_i}Q_{n+1-j} = A_5(I_n + t_r N_n)S_n - (t_2+a_3)Q_{n+1},$$

$$\sum_{i=1}^{l}\frac{u(\alpha_i)}{l}\sum_{j=0}^{n+1}p_j^{\alpha_i}H_{n+1-j} = t_1 I_n + t_2 Q_n - (a_2+r_3)H_{n+1},$$

$$\sum_{i=1}^{l}\frac{u(\alpha_i)}{l}\sum_{j=0}^{n+1}p_j^{\alpha_i}R_{n+1-j} = r_1 I_n + r_2 N_n + r_3 H_n - a_4 R_{n+1},$$

where A_1: $(cp_t\,(1-q)(1-\rho) + cp_t(1-q)\rho + cqp_t + (1-p_t)cq)$, A_2: $p_t c\rho(1-q)$, A_3: $p_t c(1-q)(1-\rho)$, A_4: $(1-p_t)cq$, and A_5: $p_t cq$.

The discretized system, with the Grünwald-Letnikov approximate derivative formula and the arrangement of the denominator functions described below, becomes as follows:

$$S_{n+1}\left(\sum_{i=1}^{l}\frac{u(\alpha_i)}{l}(\eta_1(h))^{-\alpha_i}+A_1(I_n+t_rN_n)+d\right)$$
$$=B+\lambda S^q{}_n-\sum_{i=1}^{l}\frac{u(\alpha_i)}{l}\left(\sum_{j=1}^{n+1}p_j^{\alpha_i}S_{n+1-j}\right),$$

$$I_{n+1}\left(\sum_{i=1}^{l}\frac{u(\alpha_i)}{l}(\eta_2(h))^{-\alpha_i}-A_2S_n+t_1+r_1+a_1\right)$$
$$=A_2t_rN_nS_n-\sum_{i=1}^{l}\frac{u(\alpha_i)}{l}\left(\sum_{j=1}^{n+1}p_j^{\alpha_i}I_{n+1-j}\right),$$

$$N_{n+1}\left(\sum_{i=1}^{l}\frac{u(\alpha_i)}{l}(\eta_3(h))^{-\alpha_i}+r_2+a_2+A_3t_rS_n\right)=A_3I_nS_n-\sum_{i=1}^{l}\frac{u(\alpha_i)}{l}\left(\sum_{j=1}^{n+1}p_j^{\alpha_i}N_{n+1-j}\right),$$

$$S^q{}_{n+1}\left(\sum_{i=1}^{l}\frac{u(\alpha_i)}{l}(\eta_4(h))^{-\alpha_i}+\lambda+d\right)=A_4(I_n+t_rN_n)S_n-\sum_{i=1}^{l}\frac{u(\alpha_i)}{l}\left(\sum_{j=1}^{n+1}p_j^{\alpha_i}S^q{}_{n+1-j}\right),$$

$$Q_{n+1}\left(\sum_{i=1}^{l}\frac{u(\alpha_i)}{l}(\eta_5(h))^{-\alpha_i}+t_2+a_3\right)=A_5(I_n+t_rN_n)S_n-\sum_{i=1}^{l}\frac{u(\alpha_i)}{l}\left(\sum_{j=1}^{n+1}p_j^{\alpha_i}Q_{n+1-j}\right),$$

$$H_{n+1}\left(\sum_{i=1}^{l}\frac{u(\alpha_i)}{l}(\eta_6(h))^{-\alpha_i}+a_2+r_3\right)=t_1I_n+t_2Q_n-\sum_{i=1}^{l}\frac{u(\alpha_i)}{l}\left(\sum_{j=1}^{n+1}p_j^{\alpha_i}H_{n+1-j}\right),$$

$$R_{n+1}\left(\sum_{i=1}^{l}\frac{u(\alpha_i)}{l}(\eta_7(h))^{-\alpha_i}+a_4\right)=r_1I_n+r_2N_n+r_3H_n-\sum_{i=1}^{l}\frac{u(\alpha_i)}{l}\left(\sum_{j=1}^{n+1}p_j^{\alpha_i}R_{n+1-j}\right),$$

where, $i=1,\dots,7$ and $0<\alpha_i<1$, $p_0^{\alpha_i}=(\eta_i(h))^{-\alpha_i}$ and denominator functions are:

$$\eta_1(h)=\frac{1-e^{dh}}{d},\eta_2(h)=\frac{1-e^{(t_1+r_1+a_1)h}}{(t_1+r_1+a_1)},\eta_3(h)=\frac{1-e^{(r_2+a_2)h}}{(r_2+a_2)},\eta_4(h)=\frac{1-e^{(\lambda+d)h}}{(\lambda+d)},$$
$$\eta_5(h)=\frac{1-e^{(t_2+a_3)h}}{(t_2+a_3)},\eta_6(h)=\frac{1-e^{(a_2+r_3)h}}{(a_2+r_3)},\eta_7(h)=\frac{1-e^{a_4h}}{a_4}.$$

Thus, the discretized version of the COVID-19 system is obtained as follows:

$$S_{n+1}=\frac{B+\lambda S^q{}_n-\sum_{i=1}^{l}\frac{u(\alpha_i)}{l}\left(\sum_{j=1}^{n+1}p_j^{\alpha_i}S_{n+1-j}\right)}{\sum_{i=1}^{l}\frac{u(\alpha_i)}{l}(\eta_1(h))^{-\alpha_i}+A_1(I_n+t_rN_n)+d},$$

$$I_{n+1}=\frac{A_2t_rN_nS_n-\sum_{i=1}^{l}\frac{u(\alpha_i)}{l}\left(\sum_{j=1}^{n+1}p_j^{\alpha_i}I_{n+1-j}\right),}{\sum_{i=1}^{l}\frac{u(\alpha_i)}{l}(\eta_2(h))^{-\alpha_i}-A_2S_n+t_1+r_1+a_1},$$

$$N_{n+1} = \frac{A_3 I_n S_n - \sum_{i=1}^{l} \frac{u(\alpha_i)}{l} \left(\sum_{j=1}^{n+1} p_j^{\alpha_i} N_{n+1-j} \right)}{\sum_{i=1}^{l} \frac{u(\alpha_i)}{l} (\eta_3(h))^{-\alpha_i} + r_2 + a_2 + A_3 t_r S_n},$$

$$S^q{}_{n+1} = \frac{A_4 (I_n + t_r N_n) S_n - \sum_{i=1}^{l} \frac{u(\alpha_i)}{l} \left(\sum_{j=1}^{n+1} p_j^{\alpha_i} S^q{}_{n+1-j} \right)}{\sum_{i=1}^{l} \frac{u(\alpha_i)}{l} (\eta_4(h))^{-\alpha_i} + \lambda + d},$$

$$Q_{n+1} = \frac{A_5 (I_n + t_r N_n) S_n - \sum_{i=1}^{l} \frac{u(\alpha_i)}{l} \left(\sum_{j=1}^{n+1} p_j^{\alpha_i} Q_{n+1-j} \right)}{\sum_{i=1}^{l} \frac{u(\alpha_i)}{l} (\eta_5(h))^{-\alpha_i} + t_2 + a_3},$$

$$H_{n+1} = \frac{t_1 I_n + t_2 Q_n - \sum_{i=1}^{l} \frac{u(\alpha_i)}{l} \left(\sum_{j=1}^{n+1} p_j^{\alpha_i} H_{n+1-j} \right)}{\sum_{i=1}^{l} \frac{u(\alpha_i)}{l} (\eta_6(h))^{-\alpha_i} + a_2 + r_3},$$

$$R_{n+1} = \frac{r_1 I_n + r_2 N_n + r_3 H_n - \sum_{i=1}^{l} \frac{u(\alpha_i)}{l} \left(\sum_{j=1}^{n+1} p_j^{\alpha_i} R_{n+1-j} \right)}{\sum_{i=1}^{l} \frac{u(\alpha_i)}{l} (\eta_7(h))^{-\alpha_i} + a_4}.$$

If the following system of equations is solved to obtain the disease-free equilibrium point:

$$S_n - \frac{B + \lambda S^q{}_n - \sum_{i=1}^{l} \frac{u(\alpha_i)}{l} \left(\sum_{j=1}^{n+1} p_j^{\alpha_i} S_n \right)}{\sum_{i=1}^{l} \frac{u(\alpha_i)}{l} (\eta_1(h))^{-\alpha_i} + A_1 (I_n + t_r N_n) + d} = 0,$$

$$I_n - \frac{A_2 t_r N_n S_n - \sum_{i=1}^{l} \frac{u(\alpha_i)}{l} \left(\sum_{j=1}^{n+1} p_j^{\alpha_i} I_n \right),}{\sum_{i=1}^{l} \frac{u(\alpha_i)}{l} (\eta_2(h))^{-\alpha_i} - A_2 S_n + t_1 + r_1 + a_1} = 0,$$

$$N_n - \frac{A_3 I_n S_n - \sum_{i=1}^{l} \frac{u(\alpha_i)}{l} \left(\sum_{j=1}^{n+1} p_j^{\alpha_i} N_n \right)}{\sum_{i=1}^{l} \frac{u(\alpha_i)}{l} \left(\eta_3(h) \right)^{-\alpha_i} + r_2 + a_2 + A_3 t_r S_n} = 0,$$

$$S^q{}_n - \frac{A_4 (I_n + t_r N_n) S_n - \sum_{i=1}^{l} \frac{u(\alpha_i)}{l} \left(\sum_{j=1}^{n+1} p_j^{\alpha_i} S^q{}_n \right)}{\sum_{i=1}^{l} \frac{u(\alpha_i)}{l} (\eta_4(h))^{-\alpha_i} + \lambda + d} = 0,$$

$$Q_n - \frac{A_5 (I_n + t_r N_n) S_n - \sum_{i=1}^{l} \frac{u(\alpha_i)}{l} \left(\sum_{j=1}^{n+1} p_j^{\alpha_i} Q_n \right)}{\sum_{i=1}^{l} \frac{u(\alpha_i)}{l} (\eta_5(h))^{-\alpha_i} + t_2 + a_3} = 0,$$

$$H_n - \frac{t_1 I_n + t_2 Q_n - \sum_{i=1}^{l} \frac{u(\alpha_i)}{l} \left(\sum_{j=1}^{n+1} p_j^{\alpha_i} H_n \right)}{\sum_{i=1}^{l} \frac{u(\alpha_i)}{l} (\eta_6(h))^{-\alpha_i} + a_2 + r_3} = 0,$$

$$R_n - \frac{r_1 I_n + r_2 N_n + r_3 H_n - \sum_{i=1}^{l} \frac{u(\alpha_i)}{l} \left(\sum_{j=1}^{n+1} p_j^{\alpha_i} R_n \right)}{\sum_{i=1}^{l} \frac{u(\alpha_i)}{l} (\eta_7(h))^{-\alpha_i} + a_4} = 0.$$

The disease-free equilibrium point is obtained as:

$$E = \left(\frac{B}{\sum_{i=1}^{l} \frac{u(\alpha_i)}{l} \left(\eta_1(h)\right)^{-\alpha_i} + d + \sum_{i=1}^{l} \frac{u(\alpha_i)}{l} \left(\sum_{j=1}^{n+1} p_j^{\alpha_i}\right)}, 0,0,0,0,0,0 \right).$$

In this part of this section, some numerical simulations are presented to better understand the dynamic behavior of the distributed order COVID-19 model including the quarantine effect. Parameter estimates and selections are described below (Babaei et al., 2021):
$B = 6931614.27, c = 14.781, t_r = 0.5944, p_t = 2.1011\ 10^{-8}, q = 1.8887\ 10^{-7},$

$t_1 = 0.13266, t_2 = 0.1259, r_1 = 0.33029, r_2 = 0.13978, r_3 = 0.11624,\ d = \frac{1}{69.5},$

$\rho = 0.86834, \lambda = \frac{1}{14},\ a_1 = 0.00723, a_2 = 1.7826\ 10^{-5}, a_3 = \frac{1}{68.5},\ a_4 = 0.0144.$

Also, let's choose the initial conditions in the form (Babaei et al., 2021):

$$S(0) = 1108100, \quad I(0) = 27.679, \quad N(0) = 53.839, \quad S^q(0) = 739,$$
$$Q(0) = 1.1642, \quad H(0) = 1, \quad R(0) = 2.$$

Some of the numerical results of the discretized system on the effects of COVID-19 are expressed in graphs below.

First of all, in Figure 1, the choice of the density function and the effect of the solution are examined. As a result of this examination, it was seen that with the appropriate density function selection, the results were consistent with their ordinary and fractional states (Babaei et al., 2021).

Figures 2 and 3 show the results of how the data changes with the selection of the density function.

In Figures 4, 5 and 6, it is aimed to examine the effects on the system of equations in different situations. For this reason, it has been shown that external effects can be easily expressed in the system with the help of the density function. At the same time, as can be seen from the figures, it has been seen that the equilibrium point can be reached by choosing the density function.

All calculations and drawings in this section are calculated with the help of MATLAB package program.

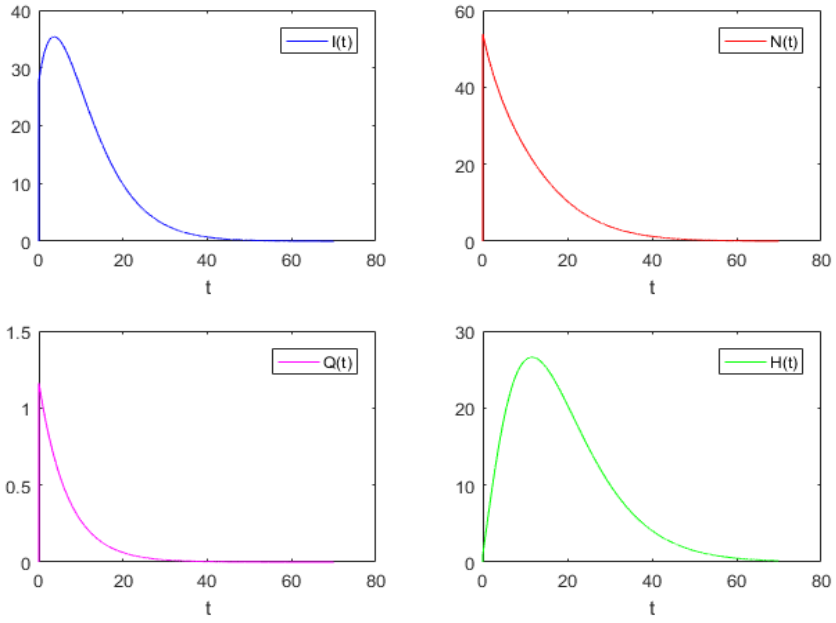

Figure 1. *Dynamics of the Effect of Quarantine on the Spread of COVID-19 for* $d(\alpha) = \Gamma(2 - 3\alpha/5)$.

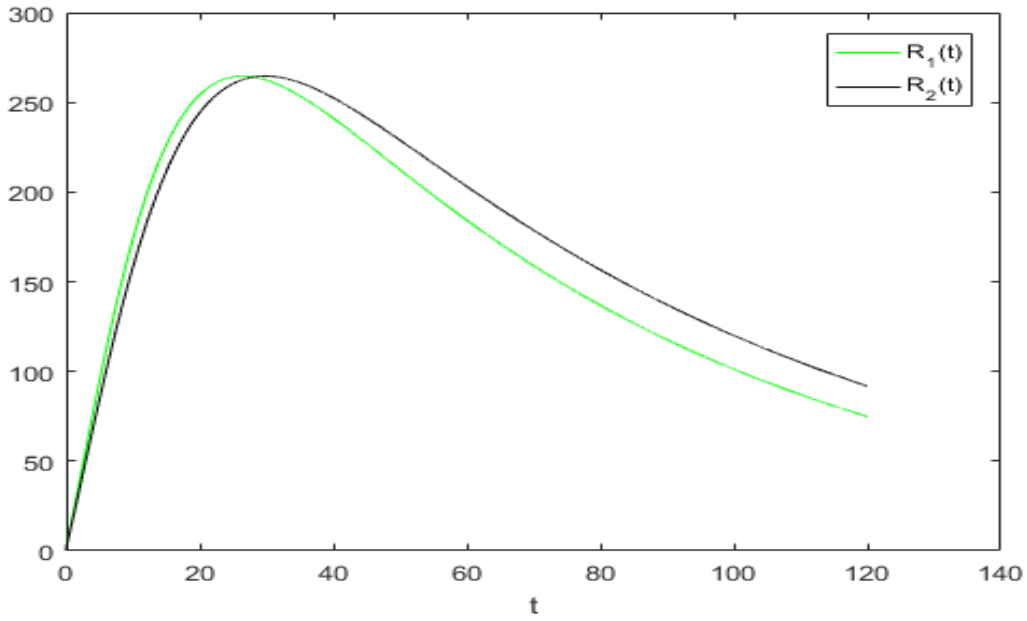

Figure 2. *Dynamics of Individuals who have recovered for different density functions* $d_1(\alpha) = \Gamma(1 + 2\alpha/7),\ and\ d_2(\alpha) = \Gamma(2 + \alpha)$.

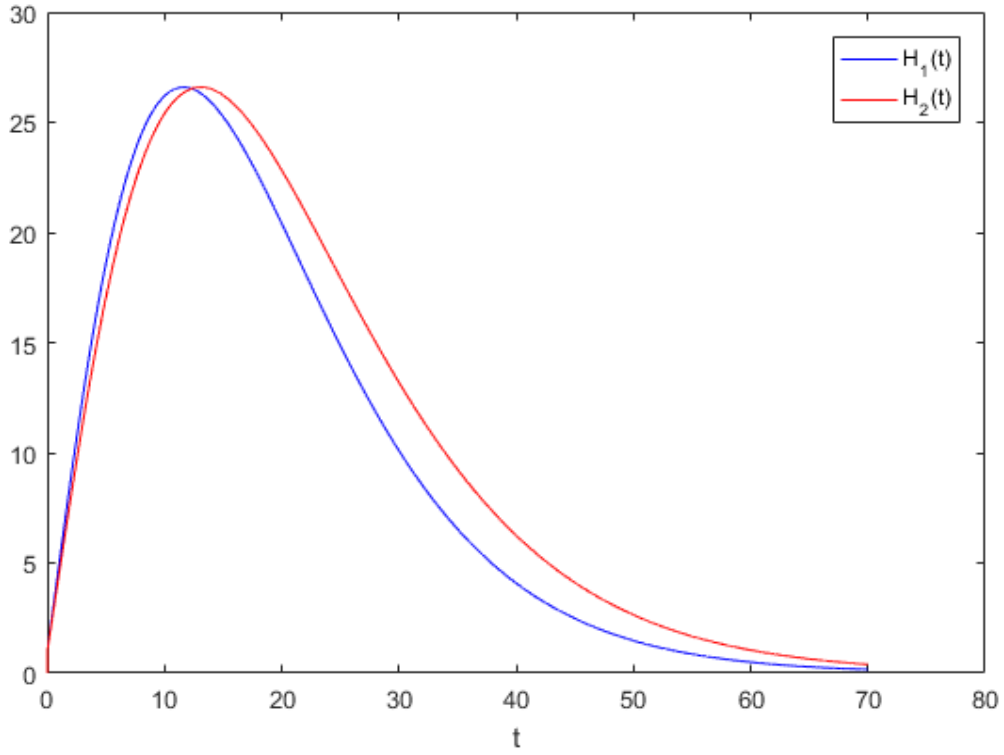

Figure 3. *Dynamics of Infected individuals in the hospital for different density functions* $d_1(\alpha) = \Gamma(2 - 3\alpha/5),\ and\ d_2(\alpha) = \Gamma(3 - \alpha)$.

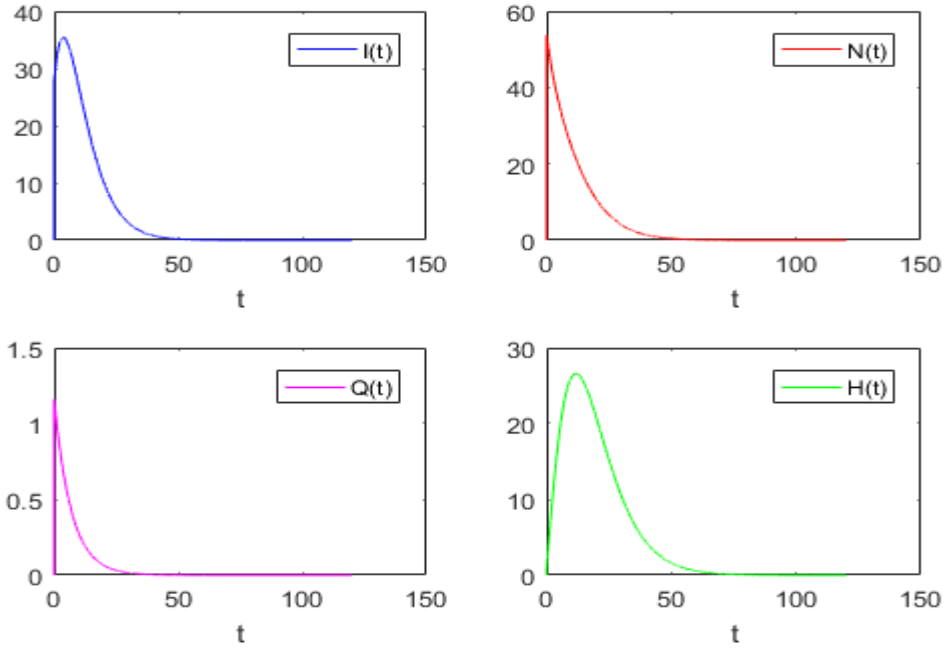

Figure 4. *Dynamics of the Effect of Quarantine on the Spread of COVID-19 for* $d(\alpha) = \Gamma(1 + 2\alpha/7)$.

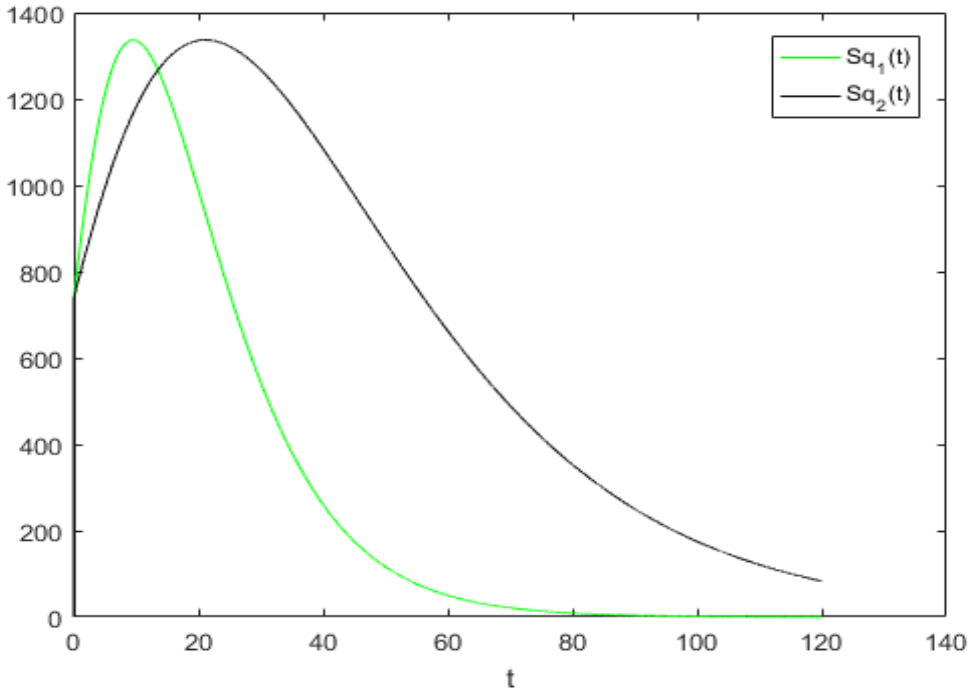

Figure 5. *Dynamics of Susceptible individuals in quarantine for different density functions* $d_1(\alpha) = \Gamma(1 + 2\alpha/7),\ and\ d_2(\alpha) = \Gamma(2 + \alpha)$.

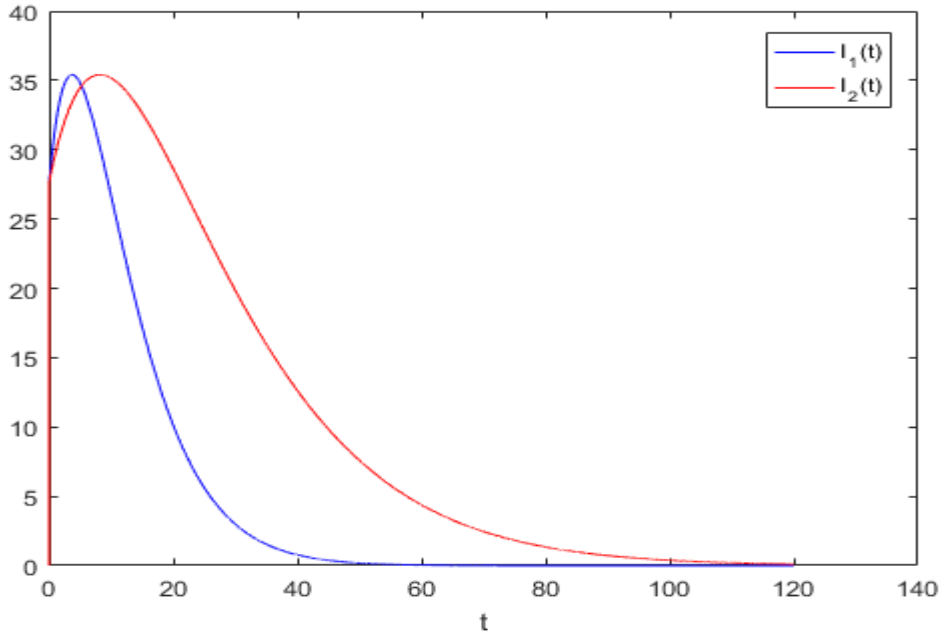

Figure 6. *Dynamics of Infected individuals with symptoms for different density functions* $d_1(\alpha) = \Gamma(1 + 2\alpha/7),\ and\ d_2(\alpha) = \Gamma(2 + \alpha)$.

4.CONCLUSION

In this study, a distributed-order coronavirus model has been created. In order to examine the effects of the disease in the quarantine situation, the quarantine factor is also included in the model. Thus, this modified equation system has been very effective in determining the dynamics of the disease. Because, the effects can be obtained quickly by choosing the density

function within the distributed order differential equations. The non-standard finite difference scheme is applied to the modified equation to determine the effects. Discretization is achieved with the help of this scheme. The Grünwald-Letnikov derivative operator is also used during discretization.

The equilibrium point was found with the discretized system. In the light of the data found, it has been seen that the use of numerical simulations and analysis of the equilibrium point in the coronavirus model of distributed order differential equations is also very effective. When the density function selection is compared with the previous study results, it is seen that the modified equation system gives very consistent results.

Thus, it has been seen that the coronavirus model can be expressed with distributed order differential equations. Consistency of the results showed that using such equations in modeling would save time in determining the dynamics. It is seen that the savings will be at a high level with the selection of the density function. In the light of the results obtained, it has been shown that the use of distributed order differential equations will contribute to the literature in modeling.

REFERENCES

Aminikhah, H., Refahi Sheikhani, A., Rezazadeh, H. (2013). Stability analysis of distributed order fractional Chen system. *The Scientific World Journal*, *2013*.

Atangana A. (2020). Modelling the spread of COVID-19 with new fractal-fractional operators: can the lockdown save mankind before vaccination? *Chaos Solitons Fractals*, 136:109860.

Bagley, R. L., Torvik, P. J. (2000). On the existence of the order domain and the solution of distributed order equations-Part I. *International Journal of Applied Mathematics*, *2*(7), 865-882.

Babaei, A., Ahmadi, M., Jafari, H., Liya, A. (2021). A mathematical model to examine the effect of quarantine on the spread of coronavirus. *Chaos, Solitons & Fractals*, *142*, 110418.

Baleanu, D., Mohammadi, H., Rezapour, S. A. (2020). fractional differential equation model for the COVID-19 transmission by using the Caputo–Fabrizio derivative. *Adv Differ Equ.*, 2020:299.

Caputo, M. (1969). Elasticita e dissipazione. Zanichelli.

Caputo, M. (1995). Mean fractional-order-derivatives differential equations and filters. Annali dell'Universita di Ferrara, 41(1), 73-84.

Caputo, M. (2001). Distributed order differential equations modelling dielectric induction and diffusion. Fractional Calculus and Applied Analysis, 4(4), 421-442.

Diethelm, K., Ford, N. J. (2009). Numerical analysis for distributed-order differential equations. *Journal of Computational and Applied Mathematics*, *225*(1), 96-104.

Dorciak L. (1994). Numerical models for simulation the fractional-order control systems, UEF-04-94, The Academy of Sciences, Institute of Experimental Physic, Kosice, Slovak Republic.

Feng L.X., Jing S.L., Hu S.K., Wang D.F., Huo H.F. (2020). Modelling the effects of media coverage and quarantine on the COVID-19 infections in the UK. *Math Bioscience Eng*, 17(4), 3618–3636.

Hartley, T. T., Lorenzo, C. F. (2003). Fractional-order system identification based on continuous order-distributions. *Signal processing*, *83*(11), 2287-2300.

Katsikadelis, J. T. (2014). Numerical solution of distributed order fractional differential equations. *Journal of Computational Physics*, *259*, 11-22.

Kocabiyik, M., Ongun, M. Y., Çetinkaya, İ.T. (2021). Standart olmayan sonlu fark metodu ile dağılımlı mertebeden SVIR modelinin nümerik analizi. *Balıkesir Üniversitesi Fen Bilimleri Enstitüsü Dergisi*, *23*(2), 577-591.

Kocabıyık, M. (2022). Nonstandard Discretization and Stability Analysis of a novel type Malaria-Ross Model . Journal of the Institute of Science and Technology , 12 (2) , 1023-1033 . DOI: 10.21597/jist.1026364

Kocabiyik, M., Ongun, M. Y., Çetinkaya, İ.T. (2022). An Application of Distributed Order Differential Equations to a HIV Infection Model, ISBN: 978-625-7799-69-0 1st Edition, 150.

Kocabiyik, M., Ongun, M. Y. (2022). Construction a distributed order smoking model and its nonstandard finite difference discretization.

Li, X. Y., Wu, B. Y. (2016). A numerical method for solving distributed order diffusion equations. *Applied Mathematics Letters*, *53*, 92-99.

Mickens, R. E. (1989). Exact solutions to a finite-difference model of a nonlinear reaction-advection equation: Implications for numerical analysis. *Numerical Methods for Partial Differential Equations*, *5*(4), 313-325.

Meerschaert, M. M., Tadjeran, C. (2004). Finite difference approximations for fractional advection–dispersion flow equations. *Journal of computational and applied mathematics*, *172*(1), 65-77.

Mickens, R. E. (1994). Nonstandard finite difference models of differential equations. World scientific.

Podlubny, I. (1999). Fractional differential equations: an introduction to fractional derivatives, fractional differential equations, to methods of their solution and some of their applications (Vol. 198). Elsevier.

World Health Organization (2019). Coronavirus disease 2019. https://www.who.int/health-topics/coronavirus

Iterations of Euler Totient Function

Emre Öztürk[1]

Introduction

In mathematics history, the prime numbers constitute very special and big area. These numbers considered of atoms of the numbers. Because, from Euclid to today, it is well-known any natural number can be represented by canonic decomposition of primes which is called the fundamental theorem of the arithmetic. Therefore, the primes play very crucial role to understand the numbers. Moreover, in "Elements" of Euclid, the finiteness of primes proved by a nice technic. Today, still his book inspires many mathematicians. After the Euclid and Pythagoras, prime numbers have been studied by many famous mathematicians, especially well-knowns are Fermat, Euler and Gauss. On the other hand, arithmetic functions in number theory played a role to understand the distribution of primes. Maybe the most well-known defined by Leonhard Euler, called today "Euler totient function" or "Euler phi function". While many of characterizations and properties of this function known but the iterations of the function still have many open questions. Like logarithm (study with small numbers instead of big numbers), study with "class" of numbers will be provide an advantage to understand the theory.

The first studies on iterations of totient function date back to 1929 by Pillai, (Pillai, 1929). Then, the first extensive study given by Shapiro, (Shapiro, 1943). His important contribution is to examine numbers by classification into the different classes and sections. Whereas he conjectured the smallest number of these classes is prime, Mills (Mills, 1943) gave a counterexample. Then by Catlin (Catlin, 1970), these numbers characterized. After Shapiro's study, many mathematicians improved his "class of numbers", for more detail, see (Bal and Bhatnagar, 2020) and (Noe, 2008).

In this study, we examine class of numbers with respect to iterations of totient function through the reference (Shapiro, 1943) and give some new identities depends on the function and the number character. **In section 4**, we use our results for apply to Fermat primes. **In the final section**, we give two procedure for calculate the iterations and classes of numbers. Moreover, in order to examine primes in class more efficiently, we consider the partition sets and give some examples.

Method

Definition 2.1 Let $n \geq 1$ is a natural number. Number of integers m that satisfy $1 \leq m \leq n$ and $(m, n) = 1$ is shown by $\phi(n)$, where ϕ is called as Euler's totient function.

Example 2.2 If we take $n = 15$, then $\phi(n) = \phi(15) = 8$. Because 1,2,4,7,8,11,13,14 are coprime with 15.

Example 2.3 For big numbers n, we can use Euler's identity. Let $n = {p_1}^{m_1} {p_2}^{m_2} \dots {p_k}^{m_k}$ where $p_1, p_2, \dots, p_k$ are distinct primes. Then, $\phi(n) = {p_1}^{m_1-1}(p_1 - 1){p_2}^{m_2-1}(p_2 - 1) \dots {p_k}^{m_k-1}(p_k - 1)$.

Therefore, we can easily calculate $\phi(10368)$. Since $10368 = 2^7 3^4$, $\phi(10368) = 2^6 \times 3^3 \times 2 = 3456$.

[1] Emre Öztürk, Dr., Turkish Court of Accounts, Data Analysis, emreozturk1471@gmail.com

Now, in accordance with (Shapiro, 1943), we give some basic concepts slightly different.

In the following discussion we shall consider a rather curious concept which arises very naturally from the iteration of the Euler ϕ function. Since $\phi(n)$ is defined as the number of positive integers, not exceeding n, which are prime to n, it follows immediately that for $n > 1, \phi(n) < n$. If we write $\phi^2(n) = \phi[\phi(n)], \phi^3(n) = \phi[\phi^2(n)], \dots, \phi^k(n) = \phi[\phi^{k-1}(n)]$, then we have

$$\phi^k(n) < \phi^{k-1}(n), \tag{2.1}$$

for $\phi^{k-1}(n) > 1$. Thus we see from Eq. (2.1) that by making k large enough we must always arrive at

$$\phi^k(n) = 1. \tag{2.2}$$

When Eq. (2.2) holds we shall say that n is of class k, and write this as $\varepsilon(n) = k$. Notice that, this definiton slightly different from definition of (Shapiro, 1943) by $\varepsilon(n) = C(n) + 1$. In fact, some authors studied properties of function ε, by different notations, for more details see [4] and [7].

Remark 2.4 From definition, $\varepsilon(1) = 0$, and $\varepsilon(2) = 1$.

Example 2.5 If we take $n = 12$ we obtain that $\phi(12) = 4, \phi^2(12) = 2, \phi^3(12) = 1$. Therefore, $\varepsilon(12) = 3$.

Iterations of Euler Totient Function

In this section, we derive some formulas for iterations of Euler totient function.

Lemma 3.1 Let m is a natural number and $n > 1$ is a positive integer. The following equation occurs:

$$\varepsilon\big(\phi^m(n)\big) = \varepsilon\big(\phi^{m+1}(n)\big) + 1.$$

Proof. Assume that $\varepsilon\big(\phi^{m+1}(n)\big) = t$. Then, by definition, t is the least natural number that satisfy $\phi^t\big(\phi^{m+1}(n)\big) = 1$. Hence,

$$\phi^t\big(\phi^{m+1}(n)\big) = \phi^{t+1}\big(\phi^m(n)\big) = 1,$$

which means

$$\varepsilon\big(\phi^m(n)\big) = t + 1. \tag{3.1}$$

From hypothesis and Eq. (3.1), it is written

$$\varepsilon\big(\phi^m(n)\big) = \varepsilon\big(\phi^{m+1}(n)\big) + 1,$$

which completes the proof.

Lemma 3.2 Let k is a natural number. Then,

$$\varepsilon(2^k) = k.$$

Proof. By straightforward calculations, we obtain

$$\begin{aligned} \phi(2^k) &= 2^{k-1} \\ \phi^2(2^k) &= 2^{k-2} \\ \phi^3(2^k) &= 2^{k-3} \\ &\vdots \end{aligned}$$

In the case of general form it is written,

$$\phi^r(2^k) = 2^{k-r}. \tag{3.2}$$

If we subs $r = k$ in Eq. (3.2) we obtain,

$$\phi^k(2^k) = 1.$$

Hence, $\varepsilon(2^k) = k$ which completes the proof.

Table 1. List of class of exponentials from 1 to 22.

1^k	2^k	3^k	4^k	5^k	6^k	7^k	8^k	9^k	10^k	11^k
0	k	$k+1$	$2k$	$2k+1$	$2k$	$2k+1$	$3k$	$2k+1$	$3k$	$3k+1$
12^k	13^k	14^k	15^k	16^k	17^k	18^k	19^k	20^k	21^k	22^k
$3k$	$3k+1$	$3k$	$3k+1$	$4k$	$4k+1$	$3k$	$3k+1$	$4k$	$3k+1$	$4k$

Theorem 3.3 Assume that n is a positive integer, and $k < \varepsilon(n)$ is an arbitrary natural number. In this case, we have

$$\varepsilon(n) = \varepsilon\left(\phi^k(n)\right) + k. \tag{3.3}$$

Proof. For proof, we use induction onto Eq. (3.3). First, assume that $k = 1$ and $\varepsilon\left(\phi(n)\right) = t$. By definition, t is the least natural number that satisfy $\phi^t\left(\phi(n)\right) = 1$. This means $\phi^{t+1}(n) = 1$ and $\varepsilon(n) = t + 1$. Hence, for $k = 1$, Eq. (3.3) holds. Assume that for $k = m$ the equation holds. We must show it is true for $k = m + 1$. From our hypothesis $\varepsilon(n) = \varepsilon\left(\phi^m(n)\right) + m$. Moreover, according to Lemma 3.1, we write $\varepsilon\left(\phi^m(n)\right) = \varepsilon\left(\phi^{m+1}(n)\right) + 1$. Then, we obtain

$$\begin{aligned} \varepsilon(n) &= \varepsilon\left(\phi^m(n)\right) + m \\ &= \varepsilon\left(\phi^{m+1}(n)\right) + 1 + m \\ &= \varepsilon\left(\phi^{m+1}(n)\right) + (m+1), \end{aligned}$$

which is intended.

Example 3.4 Let us consider $n = 2^3 3^4 5^2$ and $k = 4$ at Theorem 3.3. Then, we obtain

$$\phi(n) = 2^5 3^3 5, \phi^2(n) = 2^7 3^2, \phi^3(n) = 2^7 3, \phi^4(n) = 2^7.$$

By Lemma 3.2 and Theorem 3.3, we obtain

$$\varepsilon(n) = \varepsilon\left(\phi^4(n)\right) + 4 = \varepsilon(2^7) + 4 = 11.$$

Lemma 3.5 (Shapiro, 1943) If either x or y is odd,

$$C(xy) = C(x) + C(y),$$

and if both x and y are even

$$C(xy) = C(x) + C(y) + 1.$$

Theorem 3.6 Let m and n are coprime. Then,

$$\varepsilon(mn) = \varepsilon(m) + \varepsilon(n) - 1.$$

Proof. Since m and n are coprime, one of those numbers is odd. Assume that m is odd, then it follows from Lemma 3.5 that $C(mn) = C(m) + C(n)$. Since $\varepsilon(n) = C(n) + 1$ and $\varepsilon(m) = C(m) + 1$ we obtain,

$$\varepsilon(mn) = (\varepsilon(m) - 1 + \varepsilon(n) - 1) + 1 = \varepsilon(m) + \varepsilon(n) - 1.$$

Corollary 3.7 Let m and n are coprime. Then,

$$\varepsilon((mn)^k) = \varepsilon(m^k) + \varepsilon(n^k) - 1.$$

Theorem 3.8 Let p is odd prime. Then,

$$\varepsilon(p^k) = k\varepsilon(p) - k + 1.$$

Proof. From Lemma 3.5, we obtain $C(p^k) = kC(p)$. Hence, $\varepsilon(p^k) = C(p^k) + 1 = kC(p) + 1 = k(\varepsilon(p) - 1) + 1$, and this completes the proof.

Theorem 3.9 Let m divides n. Then,

$$\varepsilon(mn) = 2\varepsilon(m) + \varepsilon(k) + \epsilon_{k,m},$$

where

	$\epsilon_{k,m}$
$Both\ m\ and\ k\ are\ odd$	-2
$m\ is\ even\ and\ k\ is\ odd$	-1
$Both\ m\ and\ k\ are\ even$	0

and $n = mk$.

Proof. *Case 1.* Assume that n is odd.

In this case, both m and k must be odd. Then, $C(mn) = 2C(m) + C(k)$. On the other hand, $\varepsilon(mn) = C(mn) + 1 = 2C(m) + C(k) + 1$. It follows from $C(m) = \varepsilon(m) - 1$ and $C(k) = \varepsilon(k) - 1$ that

$$\varepsilon(mn) = 2\varepsilon(m) + \varepsilon(k) - 2.$$

Case 2. Assume that n is even.

Case 2.1 Let m is even and k is odd. Then, immediately we obtain $C(mn) = 2C(m) + C(k) + 1$. Since $\varepsilon(mn) = C(mn) + 1 = 2C(m) + C(k) + 2$, it follows from $C(m) = \varepsilon(m) - 1$ and $C(k) = \varepsilon(k) - 1$ that

$$\varepsilon(mn) = 2\varepsilon(m) + \varepsilon(k) - 1.$$

Case 2.2 Let both m and k are even. Then, $C(mn) = 2C(m) + C(k) + 2$. Since $\varepsilon(mn) = C(mn) + 1 = 2C(m) + C(k) + 3$, it follows from $C(m) = \varepsilon(m) - 1$ and $C(k) = \varepsilon(k) - 1$ that

$$\varepsilon(mn) = 2\varepsilon(m) + \varepsilon(k).$$

which completes the proof.

Remark 3.10 In Theorem 3.9, if we consider m is odd and k is even then, we obtain $\varepsilon(mn) = 2\varepsilon(m) + \varepsilon(k) - 2$, similarly in Case 1.

Corollary 3.11 Let m divides n. Then,

$$\varepsilon(mn) = \varepsilon(m) + \varepsilon(n) + \epsilon_{m,n},$$

where

	$\epsilon_{m,n}$
$Both\ m\ and\ n\ are\ even$	0
$m\ is\ odd\ and\ n\ is\ even$	-1
$n\ is\ odd$	-1

Theorem 3.12 Let $n = {p_1}^{m_1}{p_2}^{m_2} \dots {p_k}^{m_k}$ where $p_1 = 2, p_2 = 3, p_3 = 5, \dots, p_k$ is sequence of first k prime. Then, the following holds:

$$\varepsilon(n) = m_1 + \sum_{j=2}^{k} m_j\big(\varepsilon(p_j) - 1\big). \tag{3.3}$$

Proof. By Theorem 3.6, we obtain

$$\varepsilon(n) = \varepsilon({p_1}^{m_1}) + \varepsilon({p_2}^{m_2}) + \cdots + \varepsilon({p_k}^{m_k}) - (k-1).$$

It follows from Lemma 3.2 and Theorem 3.8

$$\varepsilon(n) = m_1 + (m_2\varepsilon(p_2) - m_2 + 1) + (m_3\varepsilon(p_3) - m_3 + 1) + \cdots + (m_k\varepsilon(p_k) - m_k + 1) - (k-1),$$

and this implies

$$\varepsilon(n) = m_1 + (m_2\varepsilon(p_2) - m_2) + (m_3\varepsilon(p_3) - m_3) + \cdots + (m_k\varepsilon(p_k) - m_k),$$

which completes the proof.

Fermat Primes

Let k is a natural number. The well-known Fermat numbers are written by $F_k = 2^{2^k} + 1$. If F_k is prime then, F_k is called a Fermat prime. While F_k is prime for $0 \leq k \leq 4$, there is no exists another prime yet. Notice that, Euler showed that F_5 is divisible by 641. After Euler, whereas many mathematicians and computers determined composite Fermat numbers but hasn't found any different Fermat prime. There is a nice project about the current investigations and search of prime divisors of the Fermat numbers at web, see (Distributed Search for Fermat Number Divisors, 2023).
Now, let us investigate the class of Fermat primes.

Theorem 4.1 Let $n = 2^{2^k} + 1$ is a Fermat prime. Then, we have

$$\varepsilon(n) = 2^k + 1.$$

Proof. Assume that $n = 2^{2^k} + 1$ is a Fermat prime, then immediately we have $\phi(n) = 2^{2^k}$. From Lemma 3.1 and Lemma 3.2, we easily obtain the intended.

Theorem 4.2 Let $n = 2^{2^k} + 1$ is a Fermat prime. Then, the following satisfies:

$$\varepsilon(n^k) = \varepsilon((n-1)^k) + 1.$$

Proof. Let $n = 2^{2^k} + 1$ is a Fermat prime. Then, the following equations can be written:

$$\begin{aligned}
\phi((2^{2^k}+1)^k) &= (2^{2^k}+1)^{k-1}2^{2^k} \\
\phi^2((2^{2^k}+1)^k) &= (2^{2^k}+1)^{k-2}2^{2^k+2^k-1} \\
\phi^3((2^{2^k}+1)^k) &= (2^{2^k}+1)^{k-3}2^{2^k+2^k+2^k-2} \\
&\vdots
\end{aligned}$$

In the general case,

$$\phi^r\left((2^{2^k}+1)^k\right) = (2^{2^k}+1)^{k-r}2^{r2^k-(r-1)}. \quad (4.1)$$

If we subs $r = k$ in Eq. (4.1), we obtain $\phi^k((2^{2^k}+1)^k) = 2^{k2^k-(k-1)}$. From Theorem 3.3, it follows

$$\varepsilon(n^k) = k2^k + 1. \quad (4.2)$$

On the other hand,

$$\varepsilon((n-1)^k) = k2^k. \quad (4.3)$$

From Eq. (4.2) and Eq. (4.3) we obtain,

$$\varepsilon(n^k) = \varepsilon((n-1)^k) + 1,$$

which completes the proof.

Corollary 4.3 If $n = 2^{2^k} + 1$ and $\varepsilon(\phi^k(n)) \neq 2^k - k + 1$, then, n is composite.

Some Procedures and Results

In this section, we give two Maple procedure in order to calculate iterations of function and classes of numbers.

Procedure 5.1 The following procedure determines values of $\phi(n), \phi^2(n), \phi^3(n), \dots, \phi^k(n)$, depends on initial number of $n = x[1]$.

```
with(numtheory):
x[1]:= "enter any positive integer":
for i from 2 to 100 do x[i]:=phi(x[i-1]) od:
L := [seq(x[i],i=2..100)]:
for k from 1 to nops(L) do
if x[k]=1 then
A:= [seq(x[i],i=2..k)]: break; end if; end do;
print(A); nops(A);
```

```
with(numtheory):
mertebe:=proc(n)
local k,x,i,A,L;
x[1]:=n;
for i from 2 to 100 do x[i]:=phi(x[i-1]);
L := [seq(x[i],i=2..100)]:od:
for k from 1 to nops(L) do
if x[k]=1 then
A:= [seq(x[i],i=2..k)]: break; end if; end do;
nops(A):end:
hesapla:=proc(f)
local j,y,C; for j from 1 to f do;y[j]:=mertebe(j);
C:=[seq(y[j],j=1..f)]:od:end:
```

Procedure 5.2 *The following procedure lists class of numbers depends on given n.*

Table 2. *Class of numbers*

Class	Number of This Class
0	1,
1	2,
2	3, 4, 6,
3	5, 7, 8, 9, 10, 12, 14, 18,
4	11, 13, 15, 16, 19, 20, 21, 22, 24, 26, 27, 28, 30, 36, 38, 42, 54,
5	17, 23, 25, 29, 31, 32, 33, 34, 35, 37, 39, 40, 43, 44, 45, 46, 48, 49, 50, 52, 56, 57, 58, 60, 62, 63, 66, 70, 72, 74, 76, 78, 81, 84, 86, 90, 98, 108, 114, 126, 162,

6	41, 47, 51, 53, 55, 59, 61, 64, 65, 67, 68, 69, 71, 73, 75, 77, 79, 80, 82, 87, 88, 91, 92, 93, 94, 95, 96, 99, 100, 102, 104, 105, 106, 109, 110, 111, 112, 116, 117, 118, 120, 122, 124, 127, 129, 130, 132, 133, 134, 135, 138, 140, 142, 144, 146, 147, 148, 150, 152, 154, 156, 158, 163, 168, 171, 172, 174, 180, 182, 186, 189, 190, 196, 198, 210, 216, 218, 222, 228, 234, 243, 252, 254, 258, 266, 270, 294, 324, 326, 342, 378, 486,
7	83, 85, 89, 97, 101, 103, 107, 113,…
8	137, 168, 179, 187, 193,…
9	257, 289, 353,…
10	641, 685, 697,…

Table 3. *Smallest number of classes*

Class	Smallest number	Primality
1	2	Prime number
2	3	Fermat prime
3	5	Fermat prime
4	11	Prime number
5	17	Fermat prime
6	41	Prime number
7	83	Prime number
8	137	Prime number
9	257	Fermat prime
10	641	Divisor of F_5
11	1097	Prime number
12	2329	17×137
13	4369	17×257

Although Shapiro conjectured that all smallest number are prime with respect to their class, Mills (Mills, 1943) gave a counterexample which shows the conjecture is not true in general. Then, in 1970, Catlin (Catlin, 1970) proved that if the smallest number in a class is odd, then it can be factored into the product of other such numbers. Hence, these numbers are characterized totally. In fact, these numbers are belonging to sequence of A007755. For more detail, see (Sloane N. J. A., 2023).

In (Shapiro, 1943), Shapiro gives the bounds for $C(n)$ by

$$\frac{logn}{log2} > C(n) \geq \frac{log\,(n/2)}{log3}.$$

Since $\varepsilon(n) = C(n) + 1$, we obtain

$$log_3(3n/2) \leq \varepsilon(n) < log_2(2n). \tag{5.1}$$

From Eq. (6.1), we obtain

$$0{,}63k - 0{,}26 \leq \lim_{n \to 2^{k-1}} \varepsilon(n) < k, \tag{5.2}$$

where $log_3 2 \cong 0{,}63$. This result leads us to consider following:

This is interesting to consider the behaviour of (odd) primes which are belongs to following sets:

$$S_1 = \{x: 2 < x < 2^2\}, S_2 = \{x: 2^2 < x < 2^3\}, S_3 = \{x: 2^3 < x < 2^4\}, \dots, S_n = \{x: 2^n < x < 2^{n+1}\}.$$

Since $3 \in S_1$ and $3 < 2^2$, we can consider $k = 3$ in Eq. (5.2). Therefore, $1{,}63 \leq \varepsilon(3) < 3$ which obviously $\varepsilon(3) = 2$.

Another example; $61 \in S_3$ and $61 < 2^6$, we can consider $k = 7$ in Eq. (5.2). Therefore, $4{,}15 \leq \varepsilon(61) < 7$, which indicates $\varepsilon(61) = 5$ or $\varepsilon(61) = 6$. In fact, $\varepsilon(61) = 6$. For big primes this interval expands. For example, the Mersenne prime $M_7 = 524287 = 2^{19} - 1 < 2^{19}$. For $k = 20$ in Eq. (5.2), we obtain

$$12{,}34 \leq \varepsilon(M_7) < 20.$$

Then, $\varepsilon(M_7) \in \{13{,}14, \ldots, 19\}$. We note that $\varepsilon(M_7) = 15$.
If we consider minimum prime in S_k, that is, $p = 2^k + \theta$, where θ is odd, depends on the θ we determine the class. For example, if $\theta = 1$, then

$$\phi(p) = 2^k,$$

which gives $\varepsilon(p) = k + 1$. Since $\varepsilon(p) < k + 2$, p has the maximum class in S_k. We note that if $2^k + 1$ is prime then, k must be a power of 2, that is p is a Fermat prime. Hence, the Fermat primes belongs to maximum class in S_k. On the other hand, the maximum prime in S_k can be written by $q = 2^{k+1} - \alpha$, where α is odd, depends on the α we determine the class. For example, if $\alpha = 1$, then $k + 1$ must be prime. Because, if $2^n - 1$ is prime then n must be prime. This implies that k is even. Here this idea can be extended. As a result, considering the primes in the partition sets $S_1, S_2, \ldots$ will be helpful for determine the classes.
Now by previous results, we finish the section with the following conjectures:

Conjecture 5.3 By Procedure 5.2, it is easy to obtain $\varepsilon(F_5) = 30$ and $\varepsilon(F_6) = 57$. Therefore, it can be conjectured that the composite F_k Fermat numbers hold

$$\varepsilon(F_k) < 2^k.$$

Conjecture 5.4 $\varepsilon(F_k)$ is divisible by 3 when F_k is composite.

References

Bal H. S., & Bhatnagar G. (2020). Prime number conjectures from the Shapiro class structure, *Integers*, (20)

Catlin P. A. (1970) Concerning the iterated φ function, *Amer. Math. Monthly*, 77, 60–61.

Distributed Search for Fermat Number Divisors. (2023). http://www.fermatsearch.org/news.html Access Date:12/03/2023

Erdos P., & Granville A., &Pomerance C., & Spiro C. (1990). On the normal behavior of the iterates of some arithmetic functions, in: Analytic Number Theory, *Proceedings of a Conference in Honor of P. T. Bateman*, Birkhauser, Boston, 165-204.

Mills W. H. (1943). Iteration of the φ function, *Amer. Math. Monthly*, 50, 547–549.

Noe T.D. (2008). Primes in classes of the iterated totient function, *Journal of Integer Sequences*, 11

Pillai S. S. (1929). On a function connected with φ (n), Bull. Amer. Math. Soc. 35(6), 837–841.

Shapiro H. (1943). An arithmetic function arising from the φ function, *Amer. Math. Monthly*, 50, 18–30.

Sloane N. J. A. (2023). *The On-Line Encyclopedia of Integer Sequences*. https://oeis.org/ Access Date: 18/04/2023

A Study on the Comparison of the Parameter Estimation Methods in the Birnbaum-Saunders Distribution

Samet KAYA[1]
Esin KÖKSAL BABACAN[2]

1. Birnbaum-Saunders Distribution

The Birnbaum-Saunders distribution (BS) is a continuous probability distribution named after Birnbaum and Saunders in 1969. This distribution is also called the fatigue life distribution. The BS distribution was first suggested to model the defect that occurred as a result of growing cracks or failures on the surfaces of metallic parts in machines. The Birnbaum-Saunders distribution is an asymmetric and positively (right) skewed distribution used to model positive data. The Birnbaum-Saunders distribution generally has two parameters: shape (α) parameter and scale (β) parameter.

Considering the random variable T following a BS distribution with shape and scale parameters, $T \sim BS(\alpha, \beta)$, the probability density function is

$$f(t|\alpha,\beta) = \frac{1}{2\sqrt{2\pi}\alpha\beta}\left[\left(\frac{\beta}{t}\right)^{\frac{1}{2}} + \left(\frac{\beta}{t}\right)^{\frac{3}{2}}\right] \exp\left\{-\frac{1}{2\alpha^2}\left(\frac{t}{\beta} + \frac{\beta}{t} - 2\right)\right\}, \quad t > 0,\ \alpha,\beta > 0 \tag{1}$$

and the distribution function is

$$F(t|\alpha,\beta) = \Phi\left(\frac{1}{\alpha}\left[\left(\frac{t}{\beta}\right)^{\frac{1}{2}} - \left(\frac{\beta}{t}\right)^{\frac{1}{2}}\right]\right), \quad t > 0,\ \alpha,\beta > 0\ . \tag{2}$$

Here, Φ is the distribution function of the standard Normal distribution. The expected value and variance of the BS distribution are

$$E(T) = \beta\left(1 + \frac{1}{2}\alpha^2\right) \qquad Var(T) = (\alpha\beta)^2\left(1 + \frac{5}{4}\alpha^2\right) \tag{3}$$

(Wang, M. et al., 2016 and Mohammadi, K. et al., 2017).

When the shape parameter (α) is constant and the scale parameter (β) takes different values, the graph of the probability density functions of the BS distribution is presented in Figure 1.

[1] Samet KAYA, Phd. Cand., The Scientific and Technological Research Council of Turkey,
[2] Esin KÖKSAL BABACAN, Assoc. Prof. Dr., Ankara University, Department of Statistics,

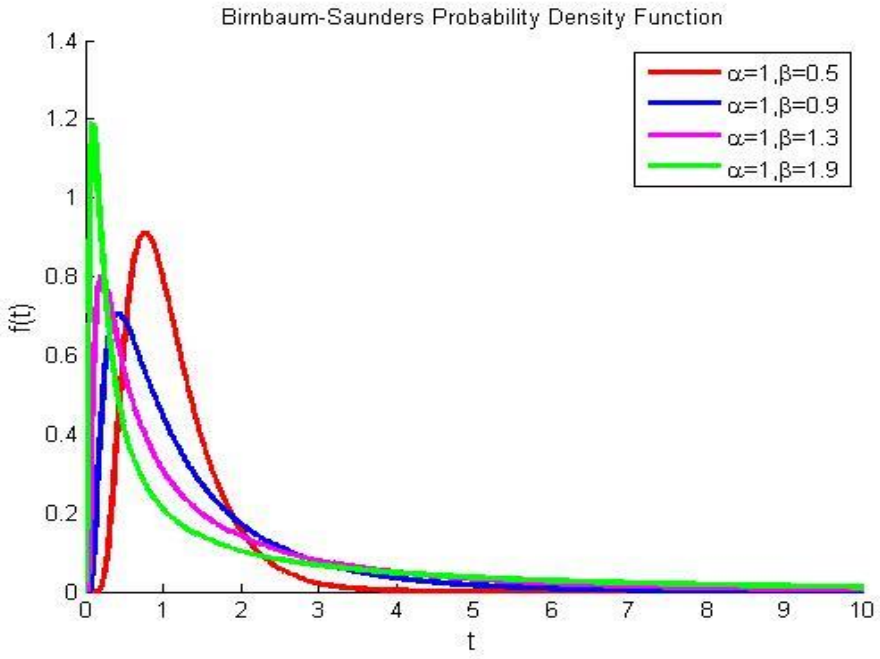

Figure 1- Probability Density Functions for different β values when the α value is constant

Likewise, when the scale parameter (β) is constant and the shape parameter (α) takes different values, the graph of the probability density functions of the Birnbaum-Saunders distribution is given in Figure 2.

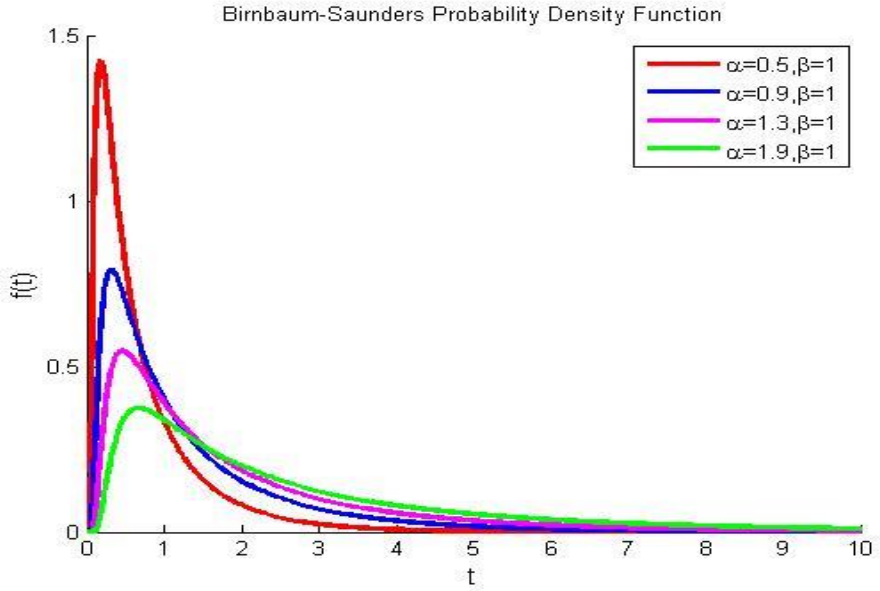

Figure 2- Probability Density Functions for different α values when the β value is constant

The BS distribution is widely used in many areas nowadays, such as water quality, agriculture, air pollution, wind velocity, business and economy, engineering sciences, environmental science, and medical science.

Regarding the BS distribution, scientific studies were conducted on the fatigue life of the 6061-T6 Aluminum coupons oscillated at 18 cycles per second by Birnbaum and Saunders (1969), the fatigue life in hours of bearings which are machine elements of a certain type

(supporting elements that decrease the friction between two machine elements in relative rotation) by Kundu et al. (2003), the tensile strength of carbon fibers in a procedure producing these fibers, which are used in fiber composite materials, by Pescim et al. (2014), the wind-related data belonging to 10 stations in the Ontario province of Canada by Mohammadi et al. (2017), the data on air pollutant concentration (SO_2) in the city of Santiago by Levia et al. (2018), and the deterioration time of a pair of disc electrodes immersed in insulating oil in an accelerated test by Sha (2018).

The rest of the paper is organized as follows. In section 2.1, maximum likelihood method is given to estimate the unknown parameters for BS Distribution. In Section 2.2, Bayesian estimation method is investigated. Section 2.2.1, estimations of the unknown BS parameters are obtained by using Lindley approximation. In Section 2.2.2, the MCMC method is explained and in subsection 2.2.2.1, the Metropolis-Hasting algorithm is given. In Section 3, a simulation study is presented to evaluate the performances of the estimators. Section 4, we use real data set to illustrate the estimation procedure developed in section 2. The last section, we make some conclusion about parameter estimation methods for BS distribution

2. Parameter Estimation in the Two-Parameter Birnbaum-Saunders Distribution

2.1 The Maximum Likelihood Method

Considering T as a random variable with a two-parameter BS distribution and $T_1, T_2, \dots, T_{\mathrm{n}}$ as an n-unit random sample taken from this distribution, the likelihood function is

$$L(\alpha,\beta|t_1,t_2,\dots,t_n)=\prod_{i=1}^{n}\left[\frac{1}{2\sqrt{2\pi}\alpha\beta}\left[\left(\frac{\beta}{t_i}\right)^{\frac{1}{2}}+\left(\frac{\beta}{t_i}\right)^{\frac{3}{2}}\right]\exp\left\{-\frac{1}{2\alpha^2}\left(\frac{t_i}{\beta}+\frac{\beta}{t_i}-2\right)\right\}\right]$$

$$=\left(\frac{1}{\sqrt{2\pi}}\right)^{n}\frac{1}{(2\alpha)^n}\frac{1}{\beta^n}\left[\prod_{i=1}^{n}\beta^{\frac{1}{2}}t_i^{-\frac{3}{2}}(t_i+\beta)\right]\exp\left\{-\frac{1}{2\alpha^2}\sum_{i=1}^{n}\left(\frac{t_i}{\beta}+\frac{\beta}{t_i}-2\right)\right\}$$

$$=\frac{1}{2^n}\frac{1}{(2\pi)^{n/2}}\frac{1}{\alpha^n}\frac{1}{\beta^{n/2}}\left[\prod_{i=1}^{n}t_i^{-\frac{3}{2}}(t_i+\beta)\right]\exp\left\{-\frac{1}{2\alpha^2}\sum_{i=1}^{n}\left(\frac{t_i}{\beta}+\frac{\beta}{t_i}-2\right)\right\} \quad (4)$$

When the logarithm of the likelihood function obtained in Equation (4) is taken,

$$LnL=-\frac{n}{2}\ln(2\pi)-n\ln(2)-n\ln(\alpha)-\frac{n}{2}\ln(\beta)-\frac{3}{2}\left(\sum_{i=1}^{n}lnt_i\right)+\sum_{i=1}^{n}ln(t_i+\beta)$$
$$-\frac{1}{2\alpha^2}\sum_{i=1}^{n}\left(\frac{t_i}{\beta}+\frac{\beta}{t_i}-2\right) \quad (5)$$

is obtained. When the partial derivative of Equation (5) is found with respect to α and equalized to zero,

$$\frac{\partial lnL}{\partial\alpha}=-\frac{n}{\alpha}+\frac{1}{\alpha^3}\left(\sum_{i=1}^{n}\left(\frac{t_i}{\beta}+\frac{\beta}{t_i}-2\right)\right)=0 \quad (6)$$

$$\alpha^2=\frac{\sum_{i=1}^{n}\left(\frac{t_i}{\beta}+\frac{\beta}{t_i}-2\right)}{n}=\frac{\sum_{i=1}^{n}t_i}{n\beta}+\frac{\beta\sum_{i=1}^{n}t_i^{-1}}{n}-2 \quad (7)$$

is obtained. Here, $s = \frac{\sum_{i=1}^{n} t_i}{n}$ and $k = \frac{\sum_{i=1}^{n} t_i^{-1}}{n}$ refer to the arithmetic and harmonic means of the sample, respectively (Mohammadi, K. et al., 2017). Accordingly, the maximum likelihood estimator of the α parameter is obtained as follows:

$$\hat{\alpha} = \left(\frac{s}{\hat{\beta}} + \frac{\hat{\beta}}{k} - 2\right)^{1/2} \tag{8}$$

To determine the maximum likelihood estimator of the β parameter, $\hat{\beta}$, the partial derivative of Equation (5) should be found with respect to β and equalized to zero. Accordingly,

$$\frac{\partial lnL}{\partial \beta} = -\frac{n}{2\beta} + \sum_{i=1}^{n} \frac{1}{(t_i+\beta)} - \frac{1}{2\alpha^2}\left(\sum_{i=1}^{n}\left(\frac{-t_i}{\beta^2} + \frac{1}{t_i}\right)\right) = 0 \tag{9}$$

To solve this equation, which is not linear according to $\hat{\beta}$, iterative methods can be used. The Newton-Raphson method is one of the commonly used methods.

2.2 The Bayesian Estimation Method

In the studies performed by Archar (1993) and Xu & Tang (2010), the Bayesian method was used in the Birnbaum-Saunders distribution, and an uninformative prior distribution was used as a prior distribution in the parameter estimation. In their studies, Archar (1993) and Wang et al. (2016) used the Inverse Gamma distribution as an informative prior distribution for α and β parameters.

In this study, inferences are made using the exponential distribution as a prior distribution for α and β parameters. Under the assumption of α and β parameters independent of each other, the prior probability density functions are built as follows:

$$\begin{aligned} \Pi_1(\alpha|\mathrm{c}) &= ce^{-c\alpha}, \quad \alpha > 0 \\ \Pi_2(\beta|\mathrm{b}) &= be^{-b\beta}, \quad \beta > 0 \end{aligned} \tag{12}$$

The likelihood function of the Birnbaum-Saunders distribution is stated as

$$L(\alpha,\beta|t_1,t_2,\dots,t_n) = \frac{1}{2^n}\frac{1}{(2\pi)^{n/2}}\frac{1}{\alpha^n}\frac{1}{\beta^{n/2}}\left[\prod_{i=1}^{n} t_i^{-\frac{3}{2}}(t_i+\beta)\right]\exp\left\{-\frac{1}{2\alpha^2}\sum_{i=1}^{n}\left(\frac{t_i}{\beta}+\frac{\beta}{t_i}-2\right)\right\} \tag{13}$$

in Equation (4). To obtain the Bayes estimator, the prior distribution is first multiplied by the likelihood function.

$$\begin{aligned} & f(\alpha,\beta,t_1,t_2,\dots,t_n) = \Pi_1(\alpha|\mathrm{c}) \times \Pi_2(\beta|\mathrm{b}) \times L(\alpha,\beta|t_1,t_2,\dots,t_n) \\ &= ce^{-c\alpha}be^{-b\beta}\,\frac{1}{2^n}\frac{1}{(2\pi)^{n/2}}\frac{1}{\alpha^n}\frac{1}{\beta^{n/2}}\left[\prod_{i=1}^{n} t_i^{-\frac{3}{2}}(t_i+\beta)\right]\exp\left\{-\frac{1}{2\alpha^2}\sum_{i=1}^{n}\left(\frac{t_i}{\beta}+\frac{\beta}{t_i}-2\right)\right\} \\ &= cbe^{-(c\alpha+b\beta)}\,\frac{1}{2^n}\frac{1}{(2\pi)^{n/2}}\frac{1}{\alpha^n}\frac{1}{\beta^{\frac{n}{2}}}\left[\prod_{i=1}^{n} t_i^{-\frac{3}{2}}(t_i+\beta)\right]\exp\left\{-\frac{1}{2\alpha^2}\sum_{i=1}^{n}\left(\frac{t_i}{\beta}+\frac{\beta}{t_i}-2\right)\right\} \end{aligned} \tag{14}$$

Then, the integral is taken with respect to both parameters, and the marginal likelihood of t is obtained.

$$\begin{aligned} & f(t_1,t_2,\dots,t_n) = \int_0^\infty\int_0^\infty f(\alpha,\beta,t_1,t_2,\dots,t_n)\,d\alpha d\beta \\ &= cb\frac{1}{2^n}\frac{1}{(2\pi)^{n/2}}\int_0^\infty\int_0^\infty \frac{1}{\alpha^n}\frac{1}{\beta^{\frac{n}{2}}}e^{-(c\alpha+b\beta)}\left[\prod_{i=1}^{n} t_i^{-\frac{3}{2}}(t_i+\beta)\right]\exp\left\{-\frac{1}{2\alpha^2}\sum_{i=1}^{n}\left(\frac{t_i}{\beta}+\frac{\beta}{t_i}-2\right)\right\}d\alpha\,d\beta \end{aligned} \tag{15}$$

In the last step, these are proportioned to each other, and the common posterior probability density function is obtained for both parameters in the following way:

$$f(\alpha,\beta|t_1,t_2,\dots,t_n) = \frac{cbe^{-(c\alpha+b\beta)}\frac{1}{2^n}\frac{1}{(2\pi)^{n/2}}\frac{1}{\alpha^n}\frac{1}{\beta^{\frac{n}{2}}}\left[\prod_{i=1}^{n}t_i^{-\frac{3}{2}}(t_i+\beta)\right]\exp\left\{-\frac{1}{2\alpha^2}\sum_{i=1}^{n}\left(\frac{t_i}{\beta}+\frac{\beta}{t_i}-2\right)\right\}}{\int_0^\infty\int_0^\infty cbe^{-(c\alpha+b\beta)}\frac{1}{2^n}\frac{1}{(2\pi)^{n/2}}\frac{1}{\alpha^n}\frac{1}{\beta^{\frac{n}{2}}}\left[\prod_{i=1}^{n}t_i^{-\frac{3}{2}}(t_i+\beta)\right]\exp\left\{-\frac{1}{2\alpha^2}\sum_{i=1}^{n}\left(\frac{t_i}{\beta}+\frac{\beta}{t_i}-2\right)\right\}d\alpha\,d\beta}$$

$$f(\alpha,\beta|t_1,t_2,\dots,t_n) = \frac{e^{-(c\alpha+b\beta)}\frac{1}{\alpha^n}\frac{1}{\beta^{\frac{n}{2}}}\left[\prod_{i=1}^{n}t_i^{-\frac{3}{2}}(t_i+\beta)\right]\exp\left\{-\frac{1}{2\alpha^2}\sum_{i=1}^{n}\left(\frac{t_i}{\beta}+\frac{\beta}{t_i}-2\right)\right\}}{\int_0^\infty\int_0^\infty e^{-(c\alpha+b\beta)}\frac{1}{\alpha^n}\frac{1}{\beta^{\frac{n}{2}}}\left[\prod_{i=1}^{n}t_i^{-\frac{3}{2}}(t_i+\beta)\right]\exp\left\{-\frac{1}{2\alpha^2}\sum_{i=1}^{n}\left(\frac{t_i}{\beta}+\frac{\beta}{t_i}-2\right)\right\}d\alpha\,d\beta} \quad (16)$$

To obtain posterior marginal probability density functions related to the parameters, the integral is taken with respect to the parameters, respectively. Thus, the marginal posterior probability density functions are obtained as

$$f_1(\alpha|t_1,t_2,\dots,t_n) = \int_0^\infty f(\alpha,\beta|t_1,t_2,\dots,t_n)\,d\beta = \int_0^\infty \frac{e^{-(c\alpha+b\beta)}\frac{1}{\alpha^n}\frac{1}{\beta^{\frac{n}{2}}}\left[\prod_{i=1}^{n}t_i^{-\frac{3}{2}}(t_i+\beta)\right]\exp\left\{-\frac{1}{2\alpha^2}\sum_{i=1}^{n}\left(\frac{t_i}{\beta}+\frac{\beta}{t_i}-2\right)\right\}}{\int_0^\infty\int_0^\infty e^{-(c\alpha+b\beta)}\frac{1}{\alpha^n}\frac{1}{\beta^{\frac{n}{2}}}\left[\prod_{i=1}^{n}t_i^{-\frac{3}{2}}(t_i+\beta)\right]\exp\left\{-\frac{1}{2\alpha^2}\sum_{i=1}^{n}\left(\frac{t_i}{\beta}+\frac{\beta}{t_i}-2\right)\right\}d\alpha\,d\beta}d\beta \quad (17)$$

and

$$f_2(\beta|t_1,t_2,\dots,t_n) = \int_0^\infty f(\alpha,\beta|t_1,t_2,\dots,t_n)\,d\alpha = \int_0^\infty \frac{e^{-(c\alpha+b\beta)}\frac{1}{\alpha^n}\frac{1}{\beta^{\frac{n}{2}}}\left[\prod_{i=1}^{n}t_i^{-\frac{3}{2}}(t_i+\beta)\right]\exp\left\{-\frac{1}{2\alpha^2}\sum_{i=1}^{n}\left(\frac{t_i}{\beta}+\frac{\beta}{t_i}-2\right)\right\}}{\int_0^\infty\int_0^\infty e^{-(c\alpha+b\beta)}\frac{1}{\alpha^n}\frac{1}{\beta^{\frac{n}{2}}}\left[\prod_{i=1}^{n}t_i^{-\frac{3}{2}}(t_i+\beta)\right]\exp\left\{-\frac{1}{2\alpha^2}\sum_{i=1}^{n}\left(\frac{t_i}{\beta}+\frac{\beta}{t_i}-2\right)\right\}d\alpha\,d\beta}d\alpha \quad (18)$$

Considering the estimators sought under the squared loss function as the expected values of these distributions, the expected values are obtained as

$$\widehat{\alpha} = E(\alpha) = \int_0^\infty\int_0^\infty \frac{e^{-(c\alpha+b\beta)}\frac{1}{\alpha^{n-1}}\frac{1}{\beta^{\frac{n}{2}}}\left[\prod_{i=1}^{n}t_i^{-\frac{3}{2}}(t_i+\beta)\right]\exp\left\{-\frac{1}{2\alpha^2}\sum_{i=1}^{n}\left(\frac{t_i}{\beta}+\frac{\beta}{t_i}-2\right)\right\}}{\int_0^\infty\int_0^\infty e^{-(c\alpha+b\beta)}\frac{1}{\alpha^n}\frac{1}{\beta^{\frac{n}{2}}}\left[\prod_{i=1}^{n}t_i^{-\frac{3}{2}}(t_i+\beta)\right]\exp\left\{-\frac{1}{2\alpha^2}\sum_{i=1}^{n}\left(\frac{t_i}{\beta}+\frac{\beta}{t_i}-2\right)\right\}d\alpha\,d\beta}d\beta\,d\alpha$$

and

$$\widehat{\beta} = E(\beta) = \int_0^\infty\int_0^\infty \frac{e^{-(c\alpha+b\beta)}\frac{1}{\alpha^n}\frac{1}{\beta^{\frac{n}{2}-1}}\left[\prod_{i=1}^{n}t_i^{-\frac{3}{2}}(t_i+\beta)\right]\exp\left\{-\frac{1}{2\alpha^2}\sum_{i=1}^{n}\left(\frac{t_i}{\beta}+\frac{\beta}{t_i}-2\right)\right\}}{\int_0^\infty\int_0^\infty e^{-(c\alpha+b\beta)}\frac{1}{\alpha^n}\frac{1}{\beta^{\frac{n}{2}}}\left[\prod_{i=1}^{n}t_i^{-\frac{3}{2}}(t_i+\beta)\right]\exp\left\{-\frac{1}{2\alpha^2}\sum_{i=1}^{n}\left(\frac{t_i}{\beta}+\frac{\beta}{t_i}-2\right)\right\}d\alpha\,d\beta}d\alpha\,d\beta \quad (19)$$

Numeric calculation methods can be used to solve such integrals. However, major errors and sample sensitivity are encountered when it is desired to obtain results using these methods. Instead, it will be more appropriate to apply the methods of the approaches developed for such cases. In this study, inferences are made using Lindley's approach. In Bayesian inference, the simulation methods developed to solve such integrals have been used in recent years. Using these methods, known as Markov chain Monte Carlo (MCMC) simulation methods, large samples are drawn from the posterior distribution, and these samples are used for inference. In this study, inferences were made using the Metropolis-Hastings algorithm, among the MCMC methods, and the results are compared with those obtained via Lindley's approach and the maximum likelihood method. To this end, Lindley's approach is first described, and the results are obtained for the BS distribution. Afterward, the Metropolis-Hastings algorithm of the MCMC methods is explained.

2.2.1. Lindley's Approach:

In general, difficulties arise in obtaining the Bayesian estimators expressed as the ratio of two integrals. The method of Lindley's approach is developed by Lindley (1980) regarding the approximate solution of the difficult integrals in multi-parameter distributions when n is large enough. When an informative prior distribution is used, the steps of Lindley's approach with regards to the BS distribution are obtained as follows.

$$g(\alpha,\beta) = ce^{-c\alpha} \times be^{-b\beta} \ , \quad log\big(g(\alpha,\beta)\big) = logc + logb - (c\alpha + b\beta)$$

$$g_1 = \frac{d\ log\big(g(\alpha,\beta)\big)}{d\alpha} = -c, \qquad g_2 = \frac{d\ ln\big(g(\alpha,\beta)\big)}{d\beta} = -b$$

The likelihood function and derivatives,

$$L(t_i,\beta,\alpha) = \frac{1}{2^n}\frac{1}{(2\pi)^{n/2}}\frac{1}{\alpha^n}\frac{1}{\beta^{n/2}}\left[\prod_{i=1}^{n} t_i^{-\frac{3}{2}}(t_i+\beta)\right]\exp\left\{-\frac{1}{2\alpha^2}\sum_{i=1}^{n}\left(\frac{t_i}{\beta}+\frac{\beta}{t_i}-2\right)\right\}$$

$$LnL = -\frac{n}{2}\ln(2\pi) - n\ln(2) - n\ln(\alpha) - \frac{n}{2}\ln(\beta) - \frac{3}{2}\left(\sum_{i=1}^{n} lnt_i\right) + \sum_{i=1}^{n} ln(t_i+\beta) - \frac{1}{2\alpha^2}\sum_{i=1}^{n}\left(\frac{t_i}{\beta}+\frac{\beta}{t_i}-2\right)$$

$$L_1 = \frac{dLnL}{d\alpha} = -\frac{n}{\alpha} + \frac{1}{\alpha^3}\left(\sum_{i=1}^{n}\left(\frac{t_i}{\beta}+\frac{\beta}{t_i}-2\right)\right)$$

$$L_{11} = \frac{d^2LnL}{d\alpha^2} = \frac{n}{\alpha^2} - \frac{3}{\alpha^4}\left(\sum_{i=1}^{n}\left(\frac{t_i}{\beta}+\frac{\beta}{t_i}-2\right)\right)$$

$$L_{111} = \frac{d^3LnL}{d\alpha^3} = -\frac{2n}{\alpha^3} + \frac{12}{\alpha^5}\left(\sum_{i=1}^{n}\left(\frac{t_i}{\beta}+\frac{\beta}{t_i}-2\right)\right)$$

$$L_2 = \frac{dLnL}{d\beta} = -\frac{n}{2\beta} + \sum_{i=1}^{n}\frac{1}{(t_i+\beta)} - \frac{1}{2\alpha^2}\left(\sum_{i=1}^{n}\left(\frac{-t_i}{\beta^2}+\frac{1}{t_i}\right)\right)$$

$$L_{22} = \frac{d^2LnL}{d\beta^2} = \frac{n}{2\beta^2} + \sum_{i=1}^{n}\frac{-1}{(t_i+\beta)^2} - \frac{1}{2\alpha^2}\left(\sum_{i=1}^{n}\left(\frac{2t_i}{\beta^3}\right)\right)$$

$$L_{222} = \frac{d^3LnL}{d\beta^3} = -\frac{n}{\beta^3} + \sum_{i=1}^{n}\frac{2(t_i+\beta)}{(t_i+\beta)^4} - \frac{1}{2\alpha^2}\left(\sum_{i=1}^{n}\left(\frac{-6t_i}{\beta^4}\right)\right)$$

$$L_{12} = L_{21} = \frac{d^2LnL}{d\alpha d\beta} = \frac{1}{\alpha^3}\left(\sum_{i=1}^{n}\left(\frac{-t_i}{\beta^2}+\frac{1}{t_i}\right)\right)$$

$$L_{211} = L_{121} = L_{112} = \frac{d^3LnL}{d\alpha^2 d\beta} = \frac{-3}{\alpha^4}\left(\sum_{i=1}^{n}\left(\frac{-t_i}{\beta^2}+\frac{1}{t_i}\right)\right)$$

$$L_{212} = L_{221} = L_{122} = \frac{d^3LnL}{d\alpha d\beta^2} = \frac{1}{\alpha^3}\left(\sum_{i=1}^{n}\left(\frac{2t_i}{\beta^3}\right)\right)$$

$$G_{ij} = \begin{bmatrix} L_{11} & L_{12} \\ L_{21} & L_{22} \end{bmatrix}^{-1}$$

$$G_{ij} = \frac{1}{\det(G_{ij})}\begin{bmatrix} L_{22} & -L_2 \\ -L_{21} & L_{11} \end{bmatrix}$$

$$= \frac{1}{\left(\frac{n}{\alpha^2} - \frac{3}{\alpha^4}\left(\sum_{i=1}^{n}\left(\frac{t_i}{\beta} + \frac{\beta}{t_i} - 2\right)\right)\right)\left(\frac{n}{2\beta^2} + \sum_{i=1}^{n}\frac{-1}{(t_i+\beta)^2} - \frac{1}{2\alpha^2}\left(\sum_{i=1}^{n}\left(\frac{2t_i}{\beta^3}\right)\right)\right) - \left(\frac{1}{\alpha^3}\left(\sum_{i=1}^{n}\left(\frac{-t_i}{\beta^2} + \frac{1}{t_i}\right)\right)\right)^2}$$

$$\begin{vmatrix} \frac{n}{2\beta^2} + \sum_{i=1}^{n}\frac{-1}{(t_i+\beta)^2} - \frac{1}{2\alpha^2}\left(\sum_{i=1}^{n}\left(\frac{2t_i}{\beta^3}\right)\right) & -\frac{1}{\alpha^3}\left(\sum_{i=1}^{n}\left(\frac{-t_i}{\beta^2} + \frac{1}{t_i}\right)\right) \\ -\frac{1}{\alpha^3}\left(\sum_{i=1}^{n}\left(\frac{-t_i}{\beta^2} + \frac{1}{t_i}\right)\right) & \frac{n}{\alpha^2} - \frac{3}{\alpha^4}\left(\sum_{i=1}^{n}\left(\frac{t_i}{\beta} + \frac{\beta}{t_i} - 2\right)\right) \end{vmatrix}$$

$$T = \left(\frac{n}{\alpha^2} - \frac{3}{\alpha^4}\left(\sum_{i=1}^{n}\left(\frac{t_i}{\beta} + \frac{\beta}{t_i} - 2\right)\right)\right)\left(-\frac{n}{2\beta^2} + \sum_{i=1}^{n}\frac{-1}{(t_i+\beta)^2} - \frac{1}{2\alpha^2}\left(\sum_{i=1}^{n}\left(\frac{2t_i}{\beta^3}\right)\right)\right) - \left(\frac{1}{\alpha^3}\left(\sum_{i=1}^{n}\left(\frac{-t_i}{\beta^2} + \frac{1}{t_i}\right)\right)\right)^2$$

$$U = \frac{n}{2\beta^2} + \sum_{i=1}^{n}\frac{-1}{(t_i+\beta)^2} - \frac{1}{2\alpha^2}\left(\sum_{i=1}^{n}\left(\frac{2t_i}{\beta^3}\right)\right)$$

$$V = -\frac{1}{\alpha^3}\left(\sum_{i=1}^{n}\left(\frac{-t_i}{\beta^2} + \frac{1}{t_i}\right)\right)$$

$$W = \frac{n}{\alpha^2} - \frac{3}{\alpha^4}\left(\sum_{i=1}^{n}\left(\frac{t_i}{\beta} + \frac{\beta}{t_i} - 2\right)\right)$$

$$G_{ij} = \begin{bmatrix} \frac{U}{T} & \frac{V}{T} \\ \frac{V}{T} & \frac{W}{T} \end{bmatrix}$$

If $\mathrm{U}(\alpha, \beta) = \alpha,\ U_1 = 1, U_2 = U_{12} = U_{21} = U_{11} = U_{22} = 0$

$$\hat{\alpha}_{BAYES} = \hat{\alpha}_{Mle} + G_{11}g_1 + G_{12}g_2 + \frac{1}{2}(L_{111}{G_{11}}^2 + 3L_{112}G_{11}G_{12} + L_{122}(G_{11}G_{22} + 2{G_{12}}^2) + L_{222}G_{12}G_{22})$$

If $\mathrm{U}(\alpha, \beta) = \beta,\ U_2 = 1, U_1 = U_{12} = U_{21} = U_{11} = U_{22} = 0$

$$\hat{\beta}_{BAYES} = \hat{\beta}_{Mle} + G_{21}g_1 + G_{22}g_2 + \frac{1}{2}\left(L_{222}{G_{22}}^2 + L_{112}(G_{11}G_{22} + 2{G_{12}}^2\right) + 3L_{122}G_{12}G_{22} + L_{111}G_{11}G_{12})$$

Here, $\hat{\alpha}_{Mle}$ and $\hat{\beta}_{Mle}$ are the maximum likelihood estimators of α and β parameters, respectively.

2.2.2 The Markov Chain Monte Carlo Methods

The most significant difficulty in the Bayesian approach is the use of integrals with high dimensions to obtain posterior distributions. In the calculation of integrals with high dimensions, the MCMC methods, which draw samples from complicated distributions using the simulation method, are first used by physicists. In recent years, they have been employed to solve many problems, particularly in the field of Bayesian statistics.

The Metropolis-Hastings algorithm and the Gibbs algorithm are the most used MCMC methods. Using these methods, samples are drawn from the relevant distribution, and then the sample means are calculated to find the expected values approximately.

2.2.2.1. The Metropolis-Hastings Algorithm

The Metropolis algorithm was generalized as a statistical simulation tool by Hastings (1970) and his student Peskun (1973, 1981) to overcome the multi-dimensionality problem brought together by the systematic Monte Carlo methods, as previously emphasized by Metropolis et al. (1953). The most important aspect distinguishing this algorithm from the Metropolis algorithm is its applicability to both symmetric and asymmetric distributions. Moreover, having asymmetric proposal distributions can be useful for increasing the convergence rate. The Metropolis-Hastings algorithm uses the probability of acceptance of

$$\alpha = \min\left(1, \frac{p(\theta^*)}{p(\theta^{t-1})}\,\frac{g(\theta^{t-1}|\theta^*)}{g(\theta^*|\theta^{t-1})}\right)$$

(Koç, 2020).

3. Application Studies

3.1 The Simulation Study

In this section, a program is written using MATLAB, and 100 trials are performed. The estimation results of the parameters of the BS distribution obtained via the maximum likelihood and Bayesian methods are compared. The sample size is selected as (n=30, 60, 90, 120, 150). When $\boldsymbol{\alpha = 2}$, $\boldsymbol{\beta = 3, 4, 5}$ is considered for each sample size, and the samples are produced through simulation.

In Lindley's approach and the Metropolis-Hastings method used in Bayesian inference, the exponential distribution is used as the prior distribution for unknown $\boldsymbol{\alpha}$ and $\boldsymbol{\beta}$ parameters. In the simulation study, the parameters of the prior distributions are selected as $\boldsymbol{c = 2}$ and $\boldsymbol{b = 2}$ while the numbers are produced.

To compare the performance of the estimation results obtained via the maximum likelihood method and Bayesian methods, the total mean squared error of both parameters is selected as a criterion. Accordingly, the selected criterion is calculated as follows:

$$\text{MSE} = \frac{(\boldsymbol{\beta}-\widehat{\boldsymbol{\beta}})^{\mathbf{2}}+(\boldsymbol{\gamma}-\widehat{\boldsymbol{\gamma}})^{\mathbf{2}}}{\boldsymbol{n}}$$

Accordingly, the simulation results are presented in the table below.

Table-1 Simulation results for α=2 and β=3,4,5

Parameter Values	n	Maximum Likelihood Method			Bayesian Method (Lindley's Approach)			Bayesian Method (MCMC)		
		$\widehat{\alpha}$	$\widehat{\beta}$	MSE	$\widehat{\alpha}$	$\widehat{\beta}$	MSE	$\widehat{\alpha}$	$\widehat{\beta}$	MSE
$\alpha=2$ $\beta=3$	30	2.033231	2.903830	0.463431	2.378851	2.995125	2.844704	2.080423	3.048188	0.489536
	60	2.088422	2.968531	0.238361	2.224810	2.992492	0.379010	2.118109	3.040453	0.252182
	90	1.998187	2.956300	0.147528	2.083621	2.965097	0.192451	2.020121	3.004934	0.152909
	120	2.030294	2.957421	0.121240	2.092607	2.963998	0.145285	2.052357	2.988867	0.124919
	150	2.012433	2.967696	0.086489	2.059872	2.972246	0.097276	2.028577	2.995835	0.089225
$\alpha=2$ $\beta=4$	30	1.999578	3.881979	0.601647	2.329217	3.885083	1.734017	2.045420	4.076068	0.653101
	60	1.982020	3.945078	0.313348	2.087386	3.948519	0.392303	2.013700	4.033043	0.330836
	90	2.050649	3.977124	0.161783	2.118436	3.978816	0.190577	2.073217	4.033412	0.167043
	120	1.964360	3.963736	0.128514	2.009450	3.964831	0.137404	1.999841	4.007540	0.133563
	150	2.031806	3.999533	0.115663	2.070249	4.000490	0.126040	2.043862	4.031660	0.122610
$\alpha=2$ $\beta=5$	30	2.065571	4.746797	0.884232	2.314588	4.750074	1.454636	2.125104	4.980367	0.901864
	60	2.063355	4.963706	0.367009	2.152887	4.495168	0.436567	2.095072	5.079223	0.394721
	90	2.016943	4.888693	0.256805	2.071258	4.889532	0.281650	2.035762	4.962406	0.250380
	120	1.995327	4.966306	0.179971	2.032211	4.966816	0.191649	2.008790	5.021907	0.190528
	150	1.996360	4.944510	0.165518	1.994605	4.944895	0.170212	1.999954	4.990478	0.170930

When the above-stated table is viewed, the estimates are observed to be quite close to the real values. The results of the Bayesian estimation obtained using the MCMC method are found to be closer to the real values compared to other estimation methods. As the number of samples increased, the mean squared error decreased for all methods. Since Lindley's approach is calculated using the maximum likelihood estimates, it gives results close to the maximum likelihood estimates, and the mean squared error is found to be quite big in small samples.

3.2 Real Data Application

In this section, an application study is carried out on the real data set, unlike the previous section. The data are taken from the article of Cooray and Ananda (2008). Kevlar 49/epoxy fibers with high strength used in fiber optic cables, plastic reinforcement and ropes are subjected to continuous pressure (at a tensile level of 90%), and their tension-failure lives are measured until their rupture. In this sense, 101 values including the rupture time of fibers are stated below.
0.01, 0.01, 0.02, 0.02, 0.02, 0.03, 0.03, 0.04, 0.05, 0.06, 0.07, 0.07,0.08, 0.09, 0.09, 0.1, 0.1, 0.11, 0.11, 0.12, 0.13, 0.18, 0.19, 0.2, 0.23, 0.24, 0.24, 0.29 , 0.34, 0.35, 0.36, 0.38, 0.4, 0.42, 0.43, 0.52, 0.54, 0.56, 0.6, 0.6, 0.63, 0.65, 0.67, 0.68, 0.72, 0.72, 0.72, 0.73, 0.79, 0.79, 0.8, 0.8, 0.83, 0.85, 0.9, 0.92, 0.95, 0.99, 1, 1.01, 1.02, 1.03, 1.05, 1.1, 1.1, 1.11, 1.15, 1.18, 1.2, 1.29, 1.31, 1.33, 1.34, 1.4, 1.43, 1.45, 1.5, 1.51, 1.52, 1.53, 1.54, 1.54, 1.55, 1.58, 1.60, 1.63, 1.64, 1.8, 1.8, 1.81, 2.02, 2.05, 2.14, 2.17, 2.33, 3.03, 3.03, 3.34, 4.2, 4.69, 7.89

The program is run for these data, and the following results are obtained.
Table-2 Parameter Estimation Results

Maximum Likelihood		Bayesian (Lindley's)		Bayesian (MCMC)	
$\widehat{\alpha}$	$\widehat{\beta}$	$\widehat{\alpha}$	$\widehat{\beta}$	$\widehat{\alpha}$	$\widehat{\beta}$
0.336199	1.843749	0.337676	1.836161	0.333175	1.870693

Concerning the results, the estimates obtained via the maximum likelihood method and the Bayesian estimates obtained using the MCMC method and Lindley's approach are close to each other. To observe the suitability of these estimation results for the model, the graphs of the probability density functions and the cumulative distribution functions of the data are presented below.

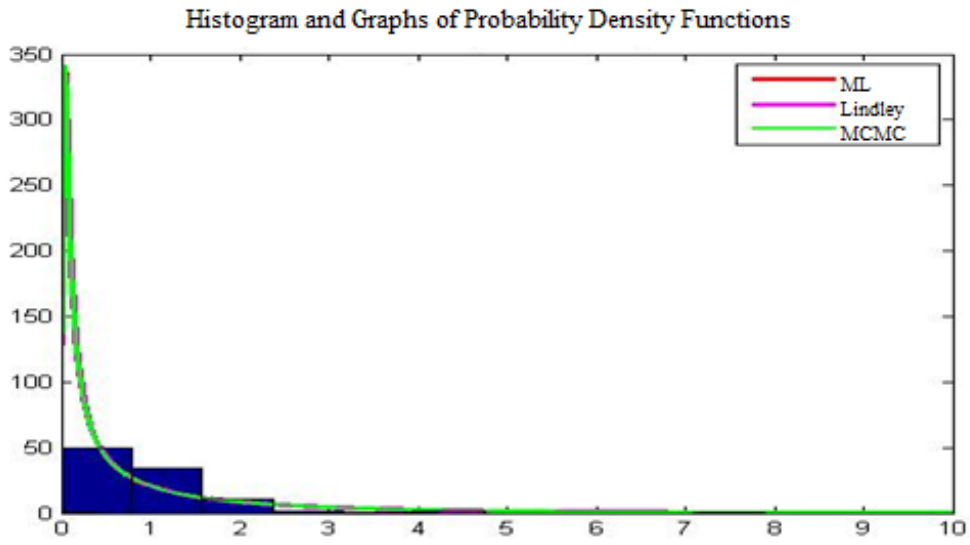

Figure-3 Histogram and Probability Density Functions Obtained with Estimates

It is observed that the graphs are in agreement with each other and with the histogram related to the data.

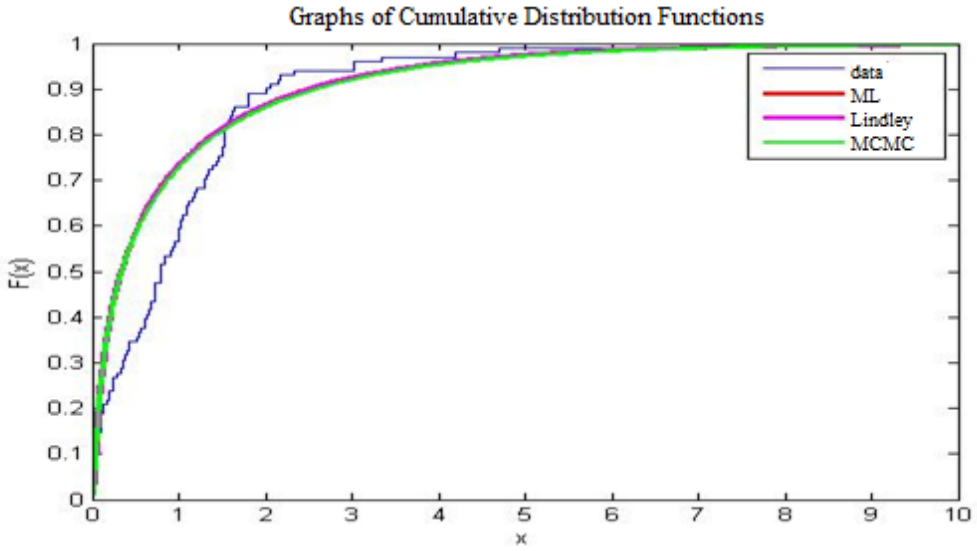

Figure-4 Empirical Distribution Function and Cumulative Distribution Functions Obtained with Estimates

In the graphs, all the three estimation methods used are observed to have produced results close to each other.

4. Conclusion

In this study, the BS distribution is first mentioned in general terms. Afterward, the maximum likelihood method and Bayesian method, which are used to estimate the parameters of the BS distribution, are explained. In Bayesian inference, the exponential distribution is used for calculations in the prior distributions related to the parameters. As a result of these calculations, the closed form of the posterior distribution could not be obtained, and therefore, the estimate values of the parameters are reached using Lindley's approach and the Metropolis-Hastings algorithms. The mean squared error criterion is employed to compare the estimation methods obtained.

In the simulation study, the program is run again and again for different sample sizes and different parameter values to make inferences. According to these estimation results, the mean squared error is observed to decrease for all the estimation methods as the number of samples increased. In Lindley's approach, the mean squared error is found big in small samples. The parameter estimation values obtained with estimators are observed to be close to the real parameter values. Since the maximum likelihood estimation is used in Lindley's approach, results are close to the maximum likelihood estimates in parameter estimations.

According to the results obtained in the real data study, parameter estimation values are close to each other. The graphs indicate that the results are compatible with the real data.

Regarding the simulation and real data, the results obtained using Lindley's and Metropolis-Hastings algorithms are similar to those obtained via the maximum likelihood method. In light of these results, it is possible to say that the Bayesian method can be used as an alternative to the maximum likelihood method.

References

Achcar, A. J., 1993. Inferences for the Birnbaum-Saunders fatigue life model using Bayesian methods. Computational Statistics & Data Analysis, 15 367-380 doi: 10.1016/0167-9473(93)90170-X

Bikramjit, B., Tiwari D., Kundu, D., Prasad, R. 2009. Is Weibull Distribution The Most Appropriate Statistical Strength Distribution for Brittle Materials. Ceramics International Journey 35 (2009), 237-246. doi: 10.1016/j.ceramint.2007.10.003

Birnbaum, W., Z., Saunders, S., C. 1969. Estimation for a Family of Life Distributions with Applications to Fatigue. Journal of Applied Probability, 6-2: 328-347 doi: 10.2307/3212004

Cooray, K., A. M. 2008. A Generalization of the Half-Normal Distribution with Applications to Lifetime Data. Communications in Statistics—Theory and Methods, 37:9, 1323-1337. doi: 10.1080/03610920701826088

Koç, Y., 2020. Weibull Dağılımının Parametrelerinin Bayesci Yöntemle Tahmini [The Estimation of the Weibull Distribution Parameters via the Bayesian Method]. Ankara Üniversitesi Fen Bilimleri Enstitüsü Yüksek Lisans Tezi

Leiva, V., Barros, M., Paula, G.A. and Sanhueza, A. 2008, Generalized Birnbaum-Saunders distributions applied to air pollutant concentration. Environmetrics, 19: 235-249. doi: 10.1002/env.861

Mohammadi, K., Alavi, O., McGowan, G. J., 2017. Use of Birnbaum-Saunders distribution for estimating wind speed and wind power probability distributions: A review. Energy Conversion and Management 143, 109–122. doi.:10.1016/j.enconman.2017.03.083

Ng., H.K.T., Kundu, D. and Balakrishnan, N. 2003. Modified moment estimation for the two-parameter Binbaum-Saunders distribution. Computational Statistics & Data Analysis. Vol:43, 283-298. doi:10.1016/S0167-9473(02)00254-2

Nwobi F. N., Ugomma. C. 2014. A Comparison of Methods for the Estimation of Weibull Distribution Parameters. Metodoloski Zvezki, Vol. 11, No. 1, 65-78.

Pescim, R., R., et al. 2014. The Kummer beta Birnbaum-Saunders: An alternative fatigue life distribution. Hacettepe Journal of Mathematics and Statistics. Vol:43(3), 473-510

Sha, N. 2018. Statistical Inference for Progressive Stress Accelerated Life Testing with Birnbaum-Saunders Distribution. Stats, 1, 189–203; doi:10.3390/stats1010014

Wang, M., Sun, X. and Park, C., 2016. Bayesian analysis of Birnbaum-Saunders distribution via the generalized ratio-of-uniform method. Comput Stat 31: 207–225. doi: 10.1007/s00180-015-0629-z

Xu, Y., et al. 2001. Optimization of sample number for Weibull function of brittle materials strength. Ceramics International Journey 27(2001) 239-241. doi:10.1016/S0272-8842(00)00056-0

Xu, A., Tang, Y., 2010. Reference analysis for Birnbaum-Saunders distribution. Computational Statistics and Data Analysis, Volume 54, Issue 1,185-192. doi:10.1016/j.csda.2009.08.004.

Rock Engineering Concept for Urban Development

Mehmet Kemal Gokay[1]

1. Introduction

In the definition of engineering, there are *"guiding instructions, orders"* that will enable the teams that make up the workforce to control their work and do it right, as well as scientifically based *"decisions"* made during the design phase of work and projects. From the first ages of history to the present, the people who provide engineering services have continued their profession by adding their own experiences to those previously transferred to them in order to fulfil their routine responsibilities in their work & projects. Experiences gained in different jobs & workplaces (in different projects) can have comprehensive features, with regional and local differences. Projects with different; purposes, boundaries, possibilities, outcomes, and working methods & workforces (chosen for relevant objectives), have shaped professions & engineering services over time with different engineering practices and decisions made by the contributing engineers. Occupations that developed in different parts of the world without being aware of each other have led to the differentiation of professions, which have developed for similar purposes, to offer outcomes (products) with different and unique experiences due to different raw material opportunities in different regions. This means that projects made to meet the different needs of people can have different solutions, and engineers can produce different solutions with different experiences. These experiences in the field of *"ground engineering"* have also manifested itself in the efforts spent in understanding (analysing) the mechanical behaviour of solid earth materials (Hudson & Harrison, 1997; Aydan, 2017; Das, 2019). When it comes to solid materials (substances); all natural solids *(rock/soil types)*, organic materials, manufactured metals and alloys, plastics, ceramics, bricks, etc. are somehow related to earth crust. Earth crust's main solid materials are rock masses and their generation and re-generation as rock formations from magma have been influenced by the interactions of climate, bioactivity, gravity, radiation, and magmatic activities in time have formed the rock/soil formations (earth's crust) around us. This rock formation mechanism is constantly being (searched) explored to find out economical potentials such as; cavities (voids, spaces) in the earth's crust, groundwater, mineral ores, energy resources (oil, natural gas, geothermal resources), etc.

When the strength of solid materials is considered, especially the strength properties of industrial products are among the most researched subjects. In other words, documentation on the mechanical behaviour of industrial products is more widely discussed due to the standards obeyed for their production. On the contrary; the analyses of the rock and soils that make up the earth's crust by measuring the strength and physical properties are limited to the studies carried out in the last 100 years. In previous years, works & projects done in/on rock and soil masses (or using these masses as materials) have emerged with the decisions and guidance of experienced, qualified people who had offered *"engineering works"*. The main concerns that come to the front in engineering fields show differences in cultures over the years with the

[1] Mehmet Kemal Gokay, Prof.Dr., Konya Technical University, Mining Engineering Department,

change of civilization. Today, in the current understanding in the field of engineering, three main concerns come to the front. It has been the basic principle to pay attention to these elements in engineering applications. These 3 concerns can be; minimizing the amount of energy used; conservation decisions & regulations regarding the environment and society; sustainability & protection measures for the raw materials used (or the earth crustal part that is in contact).

In fact, developing new technologies have created new needs and new production methods, while differentiating people and countries. With the new production methods and the cooperation of different professional groups, the engineers and the workforces in these areas have increased the communication among themselves, and new needs have enabled them to try to produce answers & solutions with different products or different possibilities. In this context, engineers have developed different methodologies to offer multiple choices and change raw material sources and products & services for sale to cope with demands in local and international markets. Concerning engineering projects *[that use the rock and soil formations as raw material sources (brick-tile-façade manufacturing activities, construction stones, soil filling materials, clay products, etc.) or as medium which supply stable spaces in/on them (like; infrastructures of cities, dams, bridges, highways, railways, airports, ports, underground and surface constructions, buildings, etc.)]* in different countries, they are being handled recently with participation from many countries through international cooperation efforts. That brings collateral knowledge and information sharing in common engineering experiences while special capabilities of companies and engineering experts have usually been kept private (patented).

One of the issues that should be emphasized at this stage is the increasing use of underground cavities opened for different purposes in the last century, in addition to underground mining activities. Although, the first settlements of humanity for the purpose of protection were caves or underground cavities. Underground spaces have continued to be opened and used for many different purposes over time. Today, the use of underground spaces has become a factor that will significantly affect modern urban planning. Digging underground comes reality with the different requirements & purposes of people; settlement spaces (underground cities), shopping malls, parking lots, transportation system tunnels, recreational (cultural & sportive) centres for social activity purposes, large or small scale commercial warehouses-depots, waste material or hazardous waste (i.e. radioactive wastes) storage volumes, etc. In the last 50 years, underground spaces have progressively started to be supplied commercially by obtaining official permissions near/under urban areas.

At this stage, the issue that should be especially emphasized is to ensure that the surface and underground usage of urban spaces should be included in official documentations (legislative data and documents compiled as “Building Information Modelling”, BIM, documentation. All the information related to urban structures regardless of its date of issue is valuable assets for the future of our settlements. It should always be remembered in BIM documentations that underground urban volumes (spaces) should be related directly to surface cadastral legislative land rights. At this point, it is important to note that underground urban spaces’ 3 Dimensional, 3D, extensions together with their surface connections should be located in/on “the lands” which have their surface/underground space usage rights. The *"living volumes"* in urban areas can be different under diverse climates, living conditions, religions, capabilities, and opportunities. Options in these habits are dependent on societies and their civilization requirements. Increase in population forces societies to handle new living structures (high buildings) including multiple living spaces. Surface land value increase in certain city

locations led also the engineers to design specially featured buildings which have more extensions in their height and depth. When we examine the surface and underground construction works, projects, in terms of stability, we observe two basic concepts emerge. The first concept includes stability of the structural elements of the buildings themselves. Their design/adjustment, and good implications (obeying engineering standards) directly influence the construction stability itself. Any malfunctions in these concerns give undesirable results, (may cause collapse of constructions). The second concept is related with structures' foundations and their behaviours. City planners, architects, civil engineers, geophysics, geotechnical and excavation engineers do their best to fulfil relevant procedures to have stable foundations. Rock/soil mechanics context in ground engineering play background (Terzaghi,.1943; Goodman, 1980; Hudson & Harrison, 1997; Gokay & Dogan, 2004; Wyllie, 2005; Atkinson, 2007; Das, 2019; Hoyos, etal., 2019; Gratchev, 2020) for the supplied decisions related with surface/underground urban spaces and their stability concerns.

2. Underground spaces in urban life

In the common construction industry, urban settlements' living volumes have been designed primarily above surface. However, there are also construction projects underground to form underground urban living spaces. Design and application efforts for underground tuff rock hotels and shopping centres in Nevsehir city (Turkey) are recent examples for this type of usage. On the contrary, the design aims have not always been the case for underground spaces. For example, the primary aims in mining activities and projects are extraction of ore bodies. In order to mine ore bodies, small/large stopes (spaces, volumes) are excavated in/on earth crust. During mining activities, it is primarily important to excavate stopes & galleries to remove required ore body parts to the ground surface with taking care of work&workplace stability (Brady & Brown, 2005) and safety. When the mining industry is under consideration, what can be the secondary usage options for abandoned mine facilities, specially surface/underground spaces.

Mining operations have been terminated after considering environmental and legal aspects. Main assets left behind are excavated volumes and groundwater (mine water) accumulated in them. Re-evaluation of them for secondary economic purposes has concerns in current market conditions. For example, Durham University (UK) has been researching currently on energy inputs from mine water to fulfil the abandoned mines through heat-pumps, (Adams, 2018). Volumes created in/on earth crust by mining operations have usually been deliberately demolished (collapsed) or backfilled after their economic usefulness. These operations usually provide stability for the other continual works at underground mines. However, there are numbers of underground mine volumes, spaces, and open mine pits which have kept their stability due to favourable surrounding rock formations. Another economic usage of these spaces have gradually emerged as "urban volumes". After performing mechanical stability *(long term)* evaluations (analyses) related to abandoned mine spaces in/on earth crust, secondary purpose usages of them re-designed as the market conditions led through. Rock mechanics knowledge and expertise play crucial roles in these evaluations. Stability of open pit slopes and underground mine spaces had usually been analysed and rock masses around these mine elements also had been measured & monitored for work & workplace safety concerns in mines. Therefore, extending the available data related to these spaces have provided valuable time dependent information for engineers during their secondary usage plans. Actually, urban surface/underground spaces should be deliberately planned for modern urban purposes, their stability issues, concerns, including static and dynamic (induced vibrations, quakes) force considerations must be evaluated deeply enough. The use of underground spaces

for urban purposes is not a new phenomenon. It is quite natural that underground spaces, *(which have been used whenever needed since the first days of humanity),* are included in urban settlement plans today. The importance of underground spaces, which are not handled other than infrastructure needs during the city planning in early periods of time for particular cities, has emerged drastically when the underground metro transportation planning started to be considered for those cities. In addition, the advantages of workplace and living volumes built on 5-10 sub-floor levels, which open & constructed towards the underground in crowded city areas, are at economical values that cannot be underestimated. With some projects implemented with the joint contributions of mining and civil engineering companies in some countries, the excavated spaces in/on rock masses (pits, quarries spaces, sublevel stopes, underground spaces, cavities etc.) left empty in the abandoned mine sites have been put into service for their secondary use after evaluating their stabilities in terms of rock mechanics. The best example is the Subtropolis underground facility which covers underground workspaces and warehouses near Kansas City, US. This abandoned but stable underground limestone mine has stopes which were excavated for limestone productions (Fig. 1). The importance of underground warehouses & tunnels with reduced risk against climatic and other dangerous interactions in the earth's crust is indispensable for today's urban settlements. It is important to note that surface/underground spaces (excavated purposely or abandoned mine spaces) in different parts of the world are presented to the Real-Estate sector for different social - cultural – economic purposes.

These spaces depicted for; *settlements, living apartments, houses, depots, hotels, shopping malls, energy production, manufacturing, large-scale factories, surface roads, rail-metro lines-stations, intercity bus stops-stations, garages, warehouses, tunnels, depots, civil-military shelter facilities, all kinds of culture-sports-social facilities etc.* should be planned in urban areas more carefully for future living standards. Special requirements of these facilities like drive-in entrances (Fig.1c) for engineered loading-hauling-transportation activities are vital and they should also be considered during city planning stages. In addition, including underground metro lines & stations, underground spaces located under "the registered surface land" have some difficulties in terms of "the land rights" concerns in some countries. Moreover, rock engineering related problems like stress & deformation redistribution due to underground spaces have produced surface deformations, subsidence, (more than the permission) which might cause dispute issues to be handled. Experiences gained in different countries have to be evaluated and used in new master-plans of urban settlements. These plans should cover all types of surface/underground settlements including 3D land ownership, rights, as well.

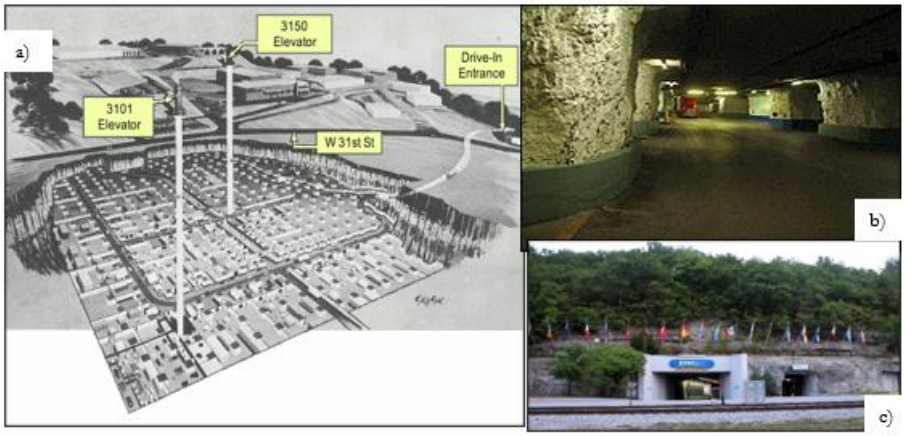

Figure 1. *a) Subtropolis, underground warehouse & storage facility at Kansas City, Missouri, US., (Historic Kansas City, 2022); b&c) Underground space & entrance view of Subtropolis facility, (Wikipedia, 2022).*

One of the examples that can be given to the reuse of surface/underground facilities in terms of urban planning is historical underground cities. Kaymakli, Ozkonak and Derinkuyu (Nevsehir, Turkey), underground cities are examples can be given here. These underground cities, which were excavated and served for different purposes in the past, have been rearranged and put into service as indispensable museums (cultural heritage and geo-sites) for tourism today (Aydan & Ulusay, 2003; Kultur portali, 2022). There are many underground spaces, cavities, excavated as underground city structures or underground shelters in many parts of the world. Mechanical behaviours of rock masses surrounding these underground spaces need to be evaluated before taking them into public service as historical museums. Alike underground mines, these museums have to be operated with official safety enforcements, which include also close observations of underground spaces' stabilities. Some of these

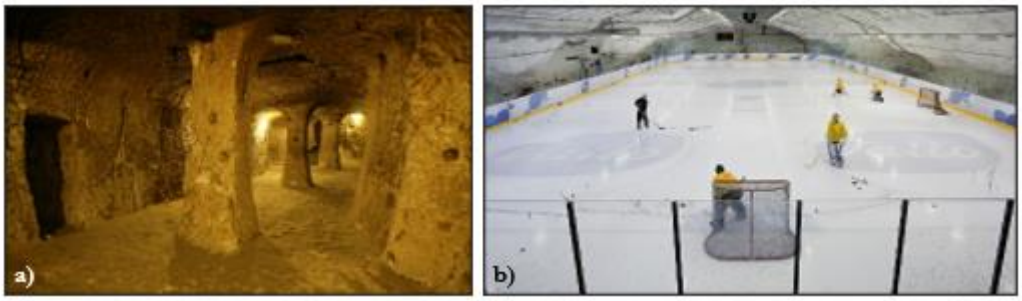

Figure 2. *Underground spaces used for urban activities; a) Underground city museum, Derinkuyu, Turkey, (Kultur portali, 2022). b) Underground ice-hockey sport facility, Helsinki, Finland, (Vähäaho, 2021).*

surface/underground spaces have places in the social-cultural heritage have been put into service as museums within the scope of the countries' socio-cultural heritage protection measures. There are also some underground space locations superimposed by current urban settlements. Actually, there are surface buildings, which have extra levels (basements) underground. But, in some cases surface structures have access passages to existing underground spaces, cavities, in surrounding rock masses. Urban areas which overlie historic underground settlements, caves, or historic mining activities might have surface structures having passages with them. Additionally, caves or excavated underground spaces have still been used in many urban localities in the world. Their usages have added advantages and generally there are common social senses, rules, formed in time for the usage of these underground spaces in those local societies, cultures. In fact, the reuse of abandoned underground mine cavities is not new. In Nottingham (UK), the basements of some houses (Bell, etal, 2009) have contact passages to warehouses, cellars, and shallow-depth galleries belonging to the mining activity that were previously exploited and abandoned underground at the same location. Similar situations can be considered for some houses in Nevsehir-Cappadocia (Turkey) region, which have contact with previously opened spaces of underground city systems. The history of underground spaces usage for urban purposes goes back to ancient times, but the idea of opening underground spaces as subway tunnels seemed like a miraculous solution for governing authorities of the populated cities. These samples, (requisites-resolutions cases) have given inspirations to city planners, architects, civil and ground engineers to design their futuristic cities together with current "carbon-zero" energy policies. Actually, engineers have recently started to design and implement more and more underground spaces in economically demanding locations.

It is important that designers and different groups of engineers should work together at all stages of urban life requirements. When the surface structures (buildings, bridges, dams, viaducts, etc.) are considered, decisions will be made about their foundation stabilities by

combining the knowledge & experience of civil and ground engineers. The stability of these structures should be analysed against static and dynamic loads (influences) so that their load carrying bodies and foundations should stay stable. It is of great importance that all engineering decisions needed in these analyses are made by people who have the authority to take responsibility in the relevant subject. The engineering branch that is missing in the decisions given is a situation that is expected to cause problems during planning or construction of the cities or their structures, buildings, or later. Apart from these facts, when examining the individual stability of constructed structures, their stabilities are also depending on the neighbouring surface/underground structures as well (Fig. 3). This reality presents the importance of urban planning. Surface structures and their social & environmental requirements may require re-evaluation to input underground spaces *(infrastructures, metro lines and their stations, cultural-sports centres, etc.)* into the city plans together with their stability interactions and land rights procedures.

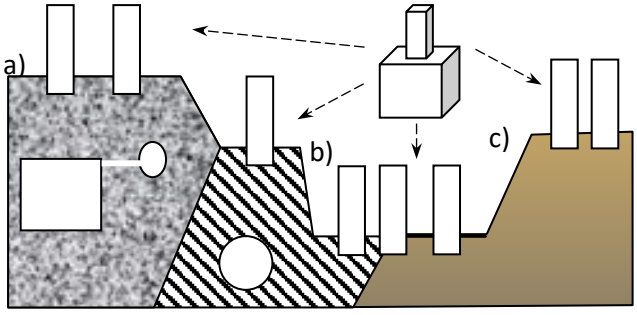

Figure 3. *Basic types of rock formations at foundations, a) Homogeneous rock mass, b) Laminated or fractures rock mass, c) Clay & Soil mass.*

As shown in Figure 3, the rock/soil masses at the foundations have vertically pressurized with their surface structures. The stresses exerted by the surface buildings on the ground, may provide deformations towards new voids, excavation, spaces to be opened next to them. These new spaces can be a new building foundation excavation *(in surface rock/soil masses)*, or an underground tunnel or cavity in the surrounding underground rock masses. It is therefore important to monitor the microscale deformations of the buildings and their foundations steadily, during & after their construction. While urban planning and urban construction rules are being put in place, it is important to set controlling teams to the locations where the planned structures are completed. These teams should measure the stresses and deformations that occur in these places on the basis of structures and their neighbourhoods. The data they collect can then be analysed regularly to monitor cities for any further instability cases. It is known that there are "Collapse prevention measurement programs" for the structures like; dams, bridges, tunnels, etc. It is important for the stability of the new futuristic cities that these types of measurement programs should be applied for urban areas. Engineering decisions to be made regarding the soil and rock engineering conditions of the foundations also include uncertainties arising from the natural properties of the earth's crust. For this reason, it is essential that the decisions about the foundation stability of the structures and the stability of the underground spaces are made by engineers who are trained in the relevant subjects, who are experts and who will take responsibilities. For these reasons, all processes and decisions should be taken in urban planning, excavation and construction activities according to available national and/or international "Engineering Standards". Eurocode 7 rules in this concern have gradually become common in Europe (EN 1997-1, 2011) which include risk assessments in designs due to the uncertain parameters. This fact is very important for earth crust (soil/rock masses) related engineering projects.

3. Underground spaces in use

The levels reached by the construction industry are presented with extreme examples made in the world. The basic requirements of the buildings constructed in urban settlements have not changed throughout history. These conditions can be listed as follows; ensuring the stability of living spaces; providing clean drinking water and food sources; safe discharge of solid-liquid-gas wastes; the suitability of safe and economical transportation manners; sustainable agricultural and industrial production areas in the immediate vicinity; existing natural-cultural-historical and sport areas; realities of socio-cultural activities. When urban developments are considered, the aims of civil engineering applications as surface structures immediately become apparent. Locations and aims of underground spaces are also important in city plans. As already mentioned before, tunnels, caves, abandoned mine spaces are apparent underground features which are already in use in different urban areas. Diamond & Kassel, (2018) provided historical perspective through; "an overview of the evolution of urban tunnels over a period of 6000 years". They focused on; "urban underground tunnels that make modern megacities possible". Galgaro etal., (2022) reported on underground food storage facilities. When it comes to storing food, the heat and humidity conditions of underground spaces are important. Because of this importance, these authors performed temperature variation analyses for the Rio Maggiore mine in Val diNon, (Trento, Italy) to evaluate reuse modelling of existing spaces. For similar abandoned mine conditions; when such a model and the other required measurement results are combined with underground space stability evaluations, reusing of the convenient underground abandoned mine (or mine sections) spaces have become economical assets to be considered. Evans, etal., (2008) have pointed out different aspects of underground spaces which should also be considered for current urbanisation and that were the aquifers and natural cavities within reservoir underground rock masses. They wrote about the secondary "use" of such spaces for new purposes. Among these uses, the purposes of “storage and disposal of different solids, liquids, gases and heat using different methods and practices” can also be considered. The modern life we live is intertwined with more underground spaces than in the old days. Successes in excavation, hauling, transportation, ventilation, lighting, groundwater discharging and other comfort technologies have increased the use of underground spaces as workplaces and/or residential areas. For instance, underground space designs supplied by Bicer (2012) and Ulusay etal., (2013) for Cappadocia (Nevsehir-Turkey) should also be examined on how underground spaces can be designed for commercial purposes. These design works include underground space plans for showrooms and restaurants in the volcanic tuff rock mass in this region. Similarly, underground cavities of different sizes (with different uses) for different purposes are already facilitated in some countries (Vähäaho, 2014; Ikavalko, etal,. 2016; Zhang,Z.,.2018; Zhang,P., 2018). The main driving aims can be listed here as; underground car parks *(protection against cold and hot weather)*; underground passages and shopping facilities *(pedestrian galleries under heavy traffic roads, protection against harsh cold/hot weather conditions)*; subway metro tunnels and stations *(protected-secure-fast underground transportation)*, underground shelters *(protection for civil-military purposes);* other cultural & sport centres *(supply protected-controlled-comforted locations)*. Thus, dealing with underground space related engineering considerations, specially rock/soil mechanics studies and models have to be main research and consideration areas also in current city plan activities.

4. Surface settlements at rock/soil slopes

The mechanical behaviours of rock/soil masses at the foundations of surface constructions have supplied signs of their load bearing capacities. For this reason, ground engineers have conducted research on the formation and mechanical behaviour differences of the earth's crust (Goodman, 1980, Gokay, 1988).). In particular, the knowledge of rock engineering, geomechanics and soil mechanics experiences gained in different engineering applications have their responses in the city planning, civil and excavation & mining engineering applications (Hoek & Bray, 1977; Singh & Goel, 2011; Hu, 2021). Earth's crust is composed of rock formations and they have numerous generation-regeneration-deposition types and include many types of defects features. Rock mass defects zones including discontinuities, weaknesses, microcavities, and chemically alteration zones have defined their whole (mass) physical properties and mechanical behaviours. It is important for city planners and civil engineers to define rock masses and alluvium depositions (soil) at particular project sites. Morphology of earth surface and rock types in particular locations force the engineers to conduct test measurements to define safe settlement locations for urban areas. The gravitational force, quakes, weather influences (wind, water, temperature), biological influences, and chemical reactions are the main factors which impact surface/underground spaces, settlements. Some of these impacts are occasional on the urban structures, however if their (i.e; quakes, tournedos, tsunamis etc.), degree of influences are in high rates (high/low weather temperatures, floods, high wind speeds, etc.) they are problematic which engineers should develop necessity prevention measures. Some impacts on engineering spaces can get harmful levels in deterioration manners (in long periods of time). Rock mass weathering types developed due to the chemical reactions, biological influences, and radiation decompositions are these types of impacts. Gravity and tectonic forces on the other hand, constantly influences all substances on the earth. These two forces actually cause most of the discontinuities in rock masses. Gravity is also the main energy source of movements of water/rock/soil masses in downward direction. Landslides, rock slope failures, avalanches, rock falling disasters with/without extreme weather conditions (heavy winds, rains and snows, floods, quakes) are main driving cases for natural disaster prevention programs. When urban residential areas are considered, negative influences of gravity should be controlled & monitored carefully. Gravity pulls might create unstable circumstances for urban hillside settlements; it may cause collapse of weak roof rocks at underground spaces, it is the main drives of sinkhole disasters, it may also cause elevation differences (subsidence) due to the collapse of underground micro/macro rock voids, compactions.

Urban settlements in/on earth or at any other planets should be realised after understanding where the minimum expected crust displacements are. These analyses contain mainly rock/soil mechanics efforts together with geophysics in ground engineering professions. Stability of the surface structures, constructions, have usually been evaluated on the bases of their internal load carrying body strengths and their foundation steadiness. Stability evaluation of the settlement locations sometimes needs exceptional awareness of one particular concept of the ground engineering, such as; landslides, ground compaction, clay mineral types in soil mass, ground liquefaction, floor heaving, rock falls, rock slope failure, induced vibrations, load bearing capacity, quake shock expectation etc. For example; slope failure like presented in Figure 4 should be expected to be predicted through its previous indications at local rock/soil masses. These kinds of local slope failures, avalanches, have their earlier signs of the earth crust deformations. The signs can be changes in 3D stress/displacement values and that could be

determined by in-situ rock/soil measurement studies. After analysing the data collected through the targeted slope locations for certain period of time, ground engineers here should

Figure 4. *Hong Kong, Po-Shan Road landslide in 1972, presenting the danger of unstable ground conditions, (Photo by Geotechnical Control Office, Hong Kong Government), (Schuster & Highland, 2007).*

feel confident to report their predictions. It should also be noted that understanding and evaluating these early slope failure symptoms require responsible ground engineering professionals who documented their measurements, analyses and reports according to rock/soil mechanics concepts which track international engineering standards also. Settlements which have rock cliffs, rock/soil hillsides, slopes, should be ready for slope failures and avalanche problems. Therefore, ground engineers employed by local authorities are better equipped to monitor (by instrumented measurements) their urban areas including slopes for early predictions of dangerous conditions. In order to observe micro scale rock/soil displacements, groundwater conditions, (charge/discharge rates), rock mass stress fields at particular locations related in-situ measurement systems *(i.e; electrical earth resistivity, micro-displacement measurements, borehole inclinometer tests, borehole dilatometer & hydraulic stress tests, groundwater depth sensors etc.)* are required to be set. It is important to evaluate collected data for reliable landslide prediction. This ground engineering decision has its risks due to uncertainties in rock/ soil data originated due to their natural features. It should not be forgotten that, when the landslide was triggered and the slope started to slide, rock/soil masses at the sliding slope moved with the settlements on them. This disastrous final fact is always tried to be predicted by responsible ground engineers by taking early precautions & measures. Rock support applications provide additional strength to inclined rock slopes in their rehabilitation projects. Rock slope considerations could be one of the project items when rehabilitating natural rock slopes or abandoned open-pit slopes. Urban areas which have included these types of slopes can also be rehabilitated to their secondary usages. Joint engineering projects supplied by designers and engineers (*joint consultancy of mining-civil-geophysics-geomechanical-mechanical-electrical etc., engineers, city planners, architects, designers, social-art-cultural heritage experts, etc.)* provide economical outputs through these natural or abandoned mine sites. Figure 5 shows how the subject can be handled in a futuristic way. In these kinds of projects, existing data related to rock/soil masses around the rehabilitation sites might have been collected during an earlier period of time by local offices, mining companies etc. Thus, these data and the other data groups measured for rock/soil masses at the beginning of rehabilitation projects can be combined to provide stable surface/underground space combinations in/on rock masses for new city settlements, plans.

Figure 5. *Urban development at rehabilitated quarry pit. Hotel construction includes futuristic design options in Shanghai, China, (Tan, etal., 2019).*

5. Ground engineering decisions in urbanisation

It is most probable that planets, satellites like the moon, meteors, etc. have their solid crust formed through rock materials. If there are engineers dealing with rocks/soils mass stabilities anywhere, they have to make stability decisions on them for mining and civil engineering purposes. Rock masses have their complex structures and they have 3D discontinuity & weakness zone distributions in them. Due to their internal uncertainty features, mechanical properties of the rock masses can not be fully determined. The rock/soil properties could be tested according to available standards through samples obtained from surface/underground positioned rock masses. When the sample locations are recorded in 3D positioning systems, the size and types of rock masses and numbers of samples can be compared geostatistical manners to reach engineering decisions on their properties. However, rock masses have not been entirely modelled yet. Thus, their statistically averaged property values have not been considered completely valid. Therefore, rock engineers who should provide engineering decisions for urban settlements for example, must supply their decision reports together with risk evaluations (i.e; Eurocode 7 procedures). As it is obvious that, there is no way to test all concrete masses used in engineering structures as a whole. Similarly it is not possible to provide properties fully representing whole rock masses out of full-scale in-situ tests. There is no way to test all rock/soil masses as a whole, located as a foundation mass under particular engineered structure either. For this reason, it is obvious that engineering evaluations should be made to cover the risks of uncertainty while providing engineering decisions for surface/underground structures and their foundation rock/soil masses. Described risks in these decisions *(risk originated due to the strength of building materials-construction elements, risk due to concrete bodies, risk due to workforce quality, risk due to foundations, etc.)* should then be considered in order to prevent engineered structures' collapses. At this point it is important to mention the following statement wrote by Elmo & Stead (2020); "Even if engineers have unlimited

resources, the natural variability of rock mass, combined with limited rock mass knowledge in the early stages of a project, will still affect the design outcome by what we do effectively not knowing rather than knowing". Therefore, it is better to understand, there should always be a risk of catastrophe in engineered structures' stabilities which are constructed in/on, rock/soil masses as a part of urban settlement projects.

6. Conclusions

The living conditions of modern life in urban settlements have gradually changed with energy requirements and cost of living. The rate of population increase and convenient manners with new technologies have pushed societies to use all possible resources around city hot-spots by considering environmental precautions. Underground metro lines&stations and underground carparks&passages roads are accepted as normal plan elements in current city plans procedures. Settlements, historic or new development areas should have several factors to be favourable by modern lifestyle as well. However, the primary concern is the stability of the city structures (buildings, infrastructures etc.) and their foundations. Abandoned city centers are not a rare case in history due to natural hazards on these features' stabilities. Rock/soil masses around the human settlements (surface/underground spaces) also have their own behaviour differences. Think about modern subway systems, including underground tunnels and stations, they are part of existing modern cities. Passageways, shopping malls, parking lots, sports and cultural centers which gradually excavated in shallow depth are suitable places for people who live in compact apartments in crowded cities. These people are used to living at surface/underground apartment levels, and they are convenient with the usage of underground spaces listed above as far as they provide added opportunities. The use of underground spaces are currently evaluated as suitable living locations for very hot/cold weather conditions. Thus, urban settlement and its elements which should provide protection for human life should also be stable as structures and foundations for a long period of time. However, it should also be known that, there is no place in/on earth's crust where ground deformations are absent. Ground engineers have a duty here to localize areas where these displacements are acceptable (tolerable) according to international standards and legislative precautions. Rock/soil mechanics concepts (Triantafyllidis, 2020; Atalar & Cinicioglu, 2023) have emerged gradually to evaluate these decisions. The basis of the mechanical behavior and stabilities of urban structures cannot be understood without evaluating global, regional and local geologic and tectonic features of rock masses. Therefore, urban settlement plans should cover primarily in-situ deformation and stress measurements to localise suitable metropolitan areas. That means, foundation areas of the city buildings and structures must be examined in wider metropolitan projectiles. Then, the local foundation area of the projected civil structure should be analysed according to local data specially collected. After that, depending on the type of civil project *(hospital, school, apartment, bridge, dam, underground spaces, depots, etc.),* at different rock and soil masses, their stability cases are considered and reported with engineering risks of threats according to current *"engineering standards*". Furthermore, it should also be borne in mind that national/international *engineering standards* have gradually been enhanced in time. So, following their procedures does not mean that the risks related to engineered structures are absent at all. Thus, supplying risk of stability concerns with engineered designs enlighten the people using those structures about the subjects. People living urban settlements, *(camps, villages, towns, cities, etc.)* should not contemplate that "engineered civil structures", are fully stable and they are 100% safe in their structure while they are using them.

References

Adams, C., Heat from abandoned mines: Developing legacy, Transactions-September 2018, North of England Institute of Mining and Mechanical Engineers, www.mininginstitute.org.uk, p4.

Atalar, C. and Cinicioglu, F., 5th International conference on new developments in soil mechanics and geotechnical engineering, (Eds.) Proceedings of ZM 2022, Lecture notes in Civil Eng. Vol305, Springer Nature, Switzerland AG, 2023, p502.

Atkinson, J., *The mechanics of soils and foundations*, Taylor&Francis Group, CRC Press, ISBN 978-0-415-36255-9, 2019, 2007, p442.

Aydan, O., *Time-dependency in rock mechanics and rock engineering*, Taylor&Francis Group, CRC Press, ISSN 2326-6872, 2017, p245.

Aydan, O. and Ulusay, R., Geotechnical and geoenvironmental characteristics of man-made underground structures in Cappadocia, Turkey, *Engineering Geology*, 69, pp245–272, 2003.

Bell, F.G., Culshaw, M.G., Forster, A. and Nathanail, C.P., The engineering geology of the Nottingham area, UK., *Engineering Geology for Tomorrow's Cities.* (Eds: Culshaw, et al.), Geological Society, London, Eng. Geology Special Publication, 22, pp1–24, 2009, doi: 10.1144/EGSP22.1 0267-9914/09.

Bicer, Z.O.P., An Example of the design and construction of rock cut places in Cappadocia: CEC, *Intercultural Understanding*, 2, pp35-44, 2012.

Brady, B.H.G. & Brown, E.T., *Rock mechanics for underground mining*. Kluwer Academic Publisher, ISBN 1-4020-2116-X. 2005, p628.

Das, B.M., *Advanced soil mechanics*, Taylor&Francis Group, CRC Press, ISBN 978-0-8153-7913-3, 2019, p712.

Diamond, R,S. and Kassel, B.G., A History of the urban underground tunnel (4000 B.C.E. - 1900 C.E.), *Journal of Transportation Technologies*, 8, pp11-43, 2018.

Elmo, D. and Stead, D., Disrupting rock engineering concepts: is there such a thing as a rock mass digital twin and are machines capable of learning rock mechanics? *Slope Stability*, p565, (Dight, PM. (ed.)), Australian Centre for Geomechanics, Perth, 2020, ISBN 978-0-9876389-7-7, doi:10.36487/ACG_repo/2025_34.

EN 1997-1, (English): Eurocode 7: Geotechnical design - Part 1: General rules [Authority: The European Union Per Regulation 305/2011, Directive 98/34/EC, Directive 2004/18/EC].

Evans, D., Highley, D., Gale, I., and Cowley, J., Underground storage, British Geological Survey, *Natural Environment Research Council, Mineral Planning Factsheet*, The Department for Communities and Local Government, DCLG-BGS Joint Mineral Programme, p22, 2008.

Galgaro, A., Santa, G.D., Cola, S., Cultrera, M., DeCarli, M., Conforti, F., Scotton, P., Viesi, D., and Fauri, M., Underground warehouses for food storage in the Dolomites (Eastern alps-Italy) and energy efficiency, *Tunnelling and Underground Space Technology*, 102, p13, 2022.

Gokay, M.K., Bearing capacity analysis of layered rock for an underground mine. *Master (MSc) thesis*, METU, Applied Science Institute, 1988, Ankara, Turkey.

Gokay, M.K. and Dogan, K., Contributions of rock mechanics in geomechanics research. 7th Regional rock Mechanics Symposium, Oct. 21-22, 2004, pp25- 33, Sivas, Turkey.

Goodman, R.E., *Introduction to Rock Mechanics*. John Willey & Sons, 1980, New York, US.

Gratchev, I., *Rock mechanics through project-based learning*, Taylor&Francis Group, CRC Press, ISBN 978-0-367-23219-1, 2020, p151.

Historic Kansas City, Downtown-Underground, www.historickansascity.org/wp-content/uploads/2013/10/down town-underground.png, Retrieved in Jan. 2022.

Hoek, E. & Bray, J.W., *Rock slope engineering*, The Institution of Mining and Metallurgy, ISBN 0-900488-36-0, 1977, p408,

Hoyos, L.R. & McCartney, J.S., *Novel issues on unsaturated soil mechanics and rock mechanics*, Proceedings of the 2cd GeoMEast international congress & exhibition on sustainable civil infrastructures, Egypt-2018, The official international congress of soil-structure interaction group in Egypt (SSIGE), ISSN 2366-3405, 2019, p227.

Hu, H., Chen, W. and Fu, J., *Rock mechanics and engineering, Prediction and control of landslides and geological disasters*, Eslevier Ltd., ISBN 978-0-12-822424-3, 2021, p407.

Hudson, J.A. & Harrison, J.P., *Engineering rock mechanics, An introduction to the principles*, Pergamon press, 1997, p443.

Ikavalko, O., Satola, I. and Hoivanen, R., *Helsinki, COST TU1206 Sub-Urban Report*, TU1206-WG1-007, (Eds:Saether, O.M. and Beylich, A.A.), March 2016, www,sub-urban.eu, p22.

Kultur portali, Derinkuyu underground city-Nevsehir, Ministry of Culture and Tourism, *Kultur portali, Gezilecek yerler*, Kultur ve Turizm Bakanligi, Turkey. Retrieved in Feb. 2022.

Schuster, R.L., and Highland, L.M., The third Hans Cloos lecture. Urban landslides: socioeconomic impacts and overview of mitigative strategies, *Bull Eng Geol Environment*, 66, pp1–27, 2007, doi:10.1007/s10064-006-0080-z.

Singh, B. & Goel, R.K., *Engineering rock mass classification, Tunneling, Foundations, and Landslides*, Elsevier Ltd., 2011, p365.

Tan, F., Jiao, Y.Y., Wang, H., Liu, Y., Tian, H., and Cheng, Y., Reclamation and reuse of abandoned quarry: A case study of Ice World & Water Park in Changsha, *Tunnelling and Underground Space technology*, 85, pp259-267, 2019.

Terzaghi, K., *Theoretical soil mechanics*, Wiley & Sons Press. 1943, p510.

Triantafyllidis, T,. Recent developments of soil mechanics and geomechanics in theory and practices, Springer, (Eds,) LNACM 91, ISSN 1613-7736, 2020, p409

Ulusay, R., Aydan, O., Genis, M., and Tano, H., Stability assessment of Avanos underground congress centre (Cappadocia, Turkey) in soft tuffs through ab integrated scheme of rock engineering methods, *Rock Mechanics and Rock Engineering*, 2013, 46, 6, pp1303-1321.

Vähäaho, I., *City of Helsinki, Helsinki urban underground spaces –Sustainable property development in Helsinki*, Real Estate Department, Geotechnical Division, Oct.2014, www.geotechnics.fi.

Vähäaho, I., *City of Helsinki, Helsinki urban underground spaces – Guidelines for visitors, (Urban Environment Brochures 2021:3,* (Ed., Vähäaho, I.), Head of Soil and Bedrock Unit, www.geotechnics.fi.

Wikipedia, SubTropolis, Kansas City, Missouri, US, www.en.wikipedia.org/wiki/ SubTropolis. Retrieved in Jan. 2022.

Wyllie, D.C., *Foundations on rock*, Taylor & Francis Group, ISBN 0-419-23210-9, 2005, p435.

Zhang, P., Japanese ways of developing urban underground recreation space, World Journal of Engineering and Technology, 2018, 6, pp504-517.

Zhang, Z., Study on urban underground streets in modern cities, American journal of Civil Engineering, 2018, 6, 2, pp60-67.

Evaluation of the Nutritional Benefits and Future Perspective of Hemp Seed Milk

Nour AWAD[1]
Mustafa MORTAŞ[2]

1. Introduction

The consumption of milk and milk products is rising quickly all across the world, and it is predicted that this trend will keep shifting in the same way going forward (Paul et al., 2019). Recently, due to milk allergies, lactose intolerance, as well a movement in consumer interest in plant-based alternatives, there has recently been a growing demand for vegan and vegetarian milk alternatives to bovine milk. This demand has contributed to a remarkable rise in the marketing of plant-based milk products such soymilk, and almond milk during the past ten years (Vanga et al., 2020). It was predicted that the global market for plant-based milk would generate US$ 13.24 billion in revenue in 2021 and to reach US$ 30.79 billion in total revenue by 2031(Besir et al., 2022). Besides, bovine milk revenues in the United States dropped 7% ($17.8 billion) in 2015 and were expected to drop a further eleven percent in 2020 (Singhal et al., 2017).

The main process for making plant-based milks involves extracting various raw materials (cereal, legume, nut, and seed) in water, which is then homogenized and thermally treated to extend shelf life and enhance stability (Besir et al., 2022). The term "milk" appears frequently in the beverage name, and they are created to mimic dairy milk in appearance. These plant-based products' nutritional value is influenced by their source, processing techniques, and fortification level (Singhal et al., 2017). Nowadays, hemp milk is viewed as an appealing substitute for dairy, soy, and nut milks since it is lactose free and has a low allergic potential due to ıts free of animal hormones and cholesterol (Wang et al., 2018). In 2018, the market for hemp seed beverages was worth over USD 185 million (Besir et al., 2022). Hemp (Cannabis sativa L.) is a herbaceous plant native to central Asia, belonging to the family *Cannabaceae*. Cannabis Sativa, which translates to "useful hemp" in Latin, is the same plant that both hemp and marijuana are derived from. The main distinction is in how much the concentration of delta-9-tetrahydrocannabinol (THC), marijuana's primary psychoactive ingredient. Compared to marijuana, which has 5% to 10% THC or higher, industrial hemp only contains 0.3% to 1.5% THC (Vahanvaty, 2009). Over the past few years, hemp and its derivatives, have gained popularity. The Plant Variety Database, which has 67 recognized variations, lists hemp as an agricultural plant species by the European Commission. France is the country that produces the most hemp seeds, accounting for over 60% of the world's total hemp output (Ignacio Alonso-Esteban et al., 2020). Hemp seeds and their food derivatives are being more widely consumed, particularly among vegans. Even though whole hemp seeds can be eaten (for example, as roasted seed snacks), they are mostly used as a raw material to make various products like hemp seed milk, flour, e**t**c. Hence, one of the most popular products derived from industrial hemp seeds is hemp seed milk. Thus, whole or dehulled hemp seeds can be used to produce hemp

[1] Doktora öğr., Ondokuz Mayıs Üniversitesi, Gıda mühendisliği bölümü, ORCID:0000-0003-3441-9080

[2] Asst. Prof, Ondokuz Mayıs Üniversitesi, Gıda mühendisliği bölümü, ORCID:0000000203167768

milk. Most of the essential nutrients are present in hemp milk, which is regarded as being very healthy. According to studies, drinking hemp milk may result in lower levels of blood triacylglycerols, cholesterol, and thyroid hormones (Wang et al., 2018).

According to the literature, hemp milk has the following characteristics: it is unsweetened and unflavored, has a thick and creamy texture, and has a nuttier flavor that is comparable to the flavor of soy milk. Additionally, hemp seed milk has a low sodium content and is free of lactose, soy, gluten, cholesterol, and trans fats (Vahanvaty, 2009). Accordingly, the objective of this study is to evaluate the chemical composition, nutritional value and biological properties of hemp seed and milk according to the recent published studies.

2. Nutritional significance

Hemp seeds have a high proportion (16–19%) of readily digested complete protein and a rich supply of oil that provides a healthy balance of the key fatty acids linoleic (C18:2, n-6, LA), and linolenic (C18:3, n-3, LNA) acids. In particular, linoleic (-6) and -linolenic (-3) acids, which are best consumed in a 2:1 to 3:1 ratio needed for healthy human nutrition, are abundant in hemp seed oil (Wang et al., 2018). As well as, the components contain stearidonic (C18:4, n-3, SDA), palmitic acid (5–8%), and gamma-linolenic acid (C18:3, n-6, GLA)(1–3%), acids wich significantly contribute to the possible therapeutic efficacy (Chich_Owska et al., 2014). Additionally, the primary components of hemp seeds include lipids (25–35%), proteins (20–25%), carbohydrates (20–30%), insoluble fiber (10–15%), vitamin E (90 mg/100 g), and minerals (sodium, phosphorus, potassium, magnesium, calcium, sulfur, iron, and zinc)(Besir et al., 2022). The literature claims that phosphorus is the most prevalent mineral element and that it is present in larger concentrations in hulled seeds (1.1 g/100 g) than in whole seeds, along with potassium, magnesium, and zinc (Alonso-Esteban et al., 2022).

In a recent published study, a comparison between the chemical composition of whole and dehulled hemp seeds has been carried out. Accordıng to the results, both protein and fat content were higher in dehulled seeds. Dehulled seeds had a protein level of 26 g/100 g on average, compared to 20.4 g/100 g for whole seeds. Whole hemp seeds had a fat level between 29.1 and 32.66 g/100 g, while dehulled seeds had a fat content closer to or even greater than 50 g/100 g (Ignacio Alonso-Esteban et al., 2022). In the same study, whole hemp seeds had an energy content of 456 to 494 kcal/100 g, whereas dehulled seeds had an energy content of 589 to 621 kcal/100 g. Their higher fat content, is what gives them their increased energy value. Moreover, there were a slight differences in the total soluble sugars. The total soluble sugar content ranged from 3.14 to 4.62 g/100 g and 3.68 and 5.65 g/100 g in whole and dehulled hemp seeds, resperctively. The most prevalent soluble sugar in whole hemp seeds was sucrose. While fructose and glucose were absent from both seed types, sucrose and raffinose was dominant in dehulled seeds (Ignacio Alonso-Esteban et al., 2022).

Hemp milk can be produced by homogenizing crushed hemp seeds in water (1:5 w/v), and then filtering the resulting milk to remove any impurities (Wang et al., 2018). According to the literature, hemp seed milk has a protein content of 0.83–4%, a fat content of 1.25–3%, and a carbohydrate content of 2.5–20%. However, the total amounts of saturated and polyunsaturated fatty acids in hemp seed milk are, respectively, 0.428% and 4.173% (Besir et al., 2022). The protein present in hemp seeds is made up of 35% albumin, and 65% of the high-quality edestin protein, which is the most important protein found in any plant source. However, hemp seeds contain all the essential amino acids, with a high quantity of sulfur-containing amino acids (methionine and cysteine), which are often scarce in vegetable proteins (Vahanvaty, 2009). On another hand, hemp secondary metabolism produces a wide range of substances, including phenolic substances (mostly flavonoids, stilbenoids, and lignanamides), terpenoids, and alkaloids (Ignacio Alonso-Esteban et al., 2022).

3. Biological activities of hemp milk

Several studies have investigated the biological activities of hemp seeds. It has been reported that hemp seeds include bioactive substances that have biological potential, such as antioxidant,and antibacterial activities. As well as, cytotoxic characteristics, inflammatory bowel disease, rheumatoid arthritis, obesity, and Alzheimer's disease, which are just a few of the chronic conditions it helps prevent (Alonso-Esteban et al., 2022 ; Paul et al., 2019). These activities attribute to their content of phenolic compounds, mainly lignanamides (N-caffeoyltyramine, grossamide, cannabisin B, cannabisin F) that constituted 79%, while the content of flavonoids was only 2.8% (Alonso-Esteban et al., 2022 ; Sławińska & Olas, 2022). Interestingly, there is evidence that hemp lignanamides have cytotoxic effects on cancer cells. At a concentration of 50 g/mL, they drastically reduced the viability of the U-87 (human glioblastoma) cell line; this effect was noticeable after 24, 48, and 72 hours of incubation(Sławińska & Olas, 2022).

On another hand, studies on hemp seeds and cardiovascular disease are ongoing. High concentrations of the amino acid arginine found in hemp seed protein, which when ingested produces nitric oxide, which relaxes blood vessels and boosts circulation (Curl et al., 2020). Low levels of C-reactive protein, a sign of inflammation linked to heart disease and chronic inflammation, have been linked to arginine. However, hemp milk includes little quantities of hemp seed per serving, and the amount of arginine in hemp milk is minimal and may not have any preventive effects against cardiovascular disease, thus more study is required (Curl et al., 2020). In a released research, the effects of treating rats with hemp milk on insulin, thyroid hormone levels, and metabolic changes were examined (Chich_Owska et al., 2014). The purpose of the study was to search at the way hemp milk consumption changed body weight, internal organs weight, insulin and thyroid hormone serum concentrations, and blood lipid indices. According to the findings, consuming hemp milk significantly lowers blood triglyceride and cholesterol levels, including total, free, and esterified cholesterol. Additionally, rats used in experiments had their thyroid hormone levels significantly decrease (Chich_Owska et al., 2014).

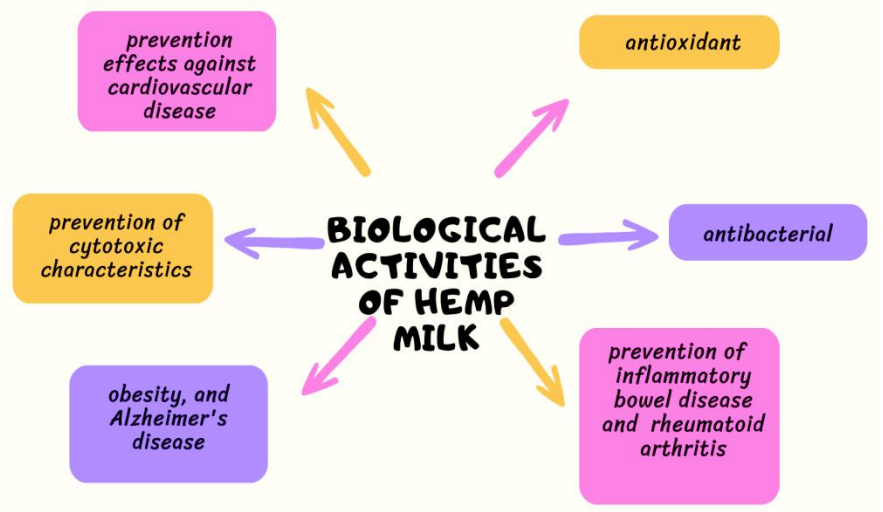

Figure 1. *Biological activities of hemp milk*

It is well known that some anti-nutrient elements in foods, including phytates and oxalates, which are contained in hemp seeds, may reduce the bioavailability of minerals. Thus, the primary type of phosphorus stored in seeds is phytic acid, which can form insoluble complexes with several cations, including calcium, magnesium, iron, and zinc (Alonso-Esteban

et al., 2022). However, during the production of hemp milk, to eliminate antinutritional elements and increase the digestibility and bioaccessibility of minerals, several physical procedures (boiling, soaking, sprouting, steam injection), chemical techniques (b-cyclo-dextrin trapping), and bioprocessing and biotechnological interventions (fermentation, enzyme processing) should be applied (Paul et al., 2019). Regarding hemp milk's phytic acid content, we couldn't find any information in the literature, and more future research is needed.

4. Comparison of hemp seed milk with other types plant milk

Bovine milk has far more of an impact than the plant-based alternatives across all criteria. Three times as much greenhouse gas emissions are produced, ten times as much land is required, two to twenty times as much freshwater is consumed, and the amount of eutrophication is noticeably higher (Ritchie, 2022). However, certain types of plant-based milk have a significant advantages over others. Either in terms of nutritional value, production cost or its impact on the environment **table 1**. In the following, there is a brief comparison between two types of plant based milk and hemp milk (Jessica Caporuscio, 2021: Ritchie, 2022).

4.1. Hemp milk Vs Soy milk

The popularity of soy milk is not surprising, considering its numerous health advantages. In terms of protein content, soy milk is about the same as dairy milk (8.25g per serving). Also it has high levels of essential monounsaturated and polyunsaturated fatty acids. Additionally, it contains plenty of fiber, phytochemicals, B vitamins, minerals (especially iron, calcium, and zinc), and unsaturated fatty acids (Paul et al., 2020). On another hand, soy milk contain isoflavones, soy compounds that may cause breast cancer in some women (Mollakhalili-Meybodi et al., 2022). As well as, high level of food allergens. Indeed, soybean is one of the "big 8" foods, which account for 90% of all food allergies caused by immunoglobulin E (Mollakhalili-Meybodi et al., 2022). According to studies, 14% of individuals who have health issues with bovine milk also have allergies to soy milk (Paul et al., 2020).

4.2. Hemp Milk VS Almond Milk

The global market for almond milk was valued at USD 5.2 billion in 2018; it is projected to increase at a CAGR of 14.3% in 2025. (*Global Industry Report, 2019-2025*). Almond milk has a considerable quantity of minerals, protein, monounsaturated fats, total dietary fiber, vitamin E, vitamin B complex, and total phenolic compounds. Additionally, almonds are also recognized as a source of anti-inflammatory, anti-tumor, and anti-hyperlipidemic chemicals (Paul et al., 2020).

However, the fatty acid content of almonds, has a significant role in the development of harmful bacteria including E. coli O157:H7 and L. monocytogenes. Although heat processing techniques can reduce infections, they can also significantly reduce nutritional value. Additionally, allergies to almonds are rather prevalent(Paul et al., 2020). On the other hand, almond milk has negative effects on the environment, particularly the water wastage. In contrast to hemp milk, which grows organically, uses very little water, and absorbs a lot of CO_2, almonds take approximately a gallon of water per almond to grow, making them less sustainable (Ritchie, 2022).

Table. 1 *A comparison of the nutritional values of 240 milliliters (ml), and the health and environmental issues related to the consumption and production of of cow, hemp, soy and almond milk.*

Parameter	Bovine milk (whole)	Hemp milk	Soy milk	Almond milk
Calories	259	60	101	29
Protein	9 g	3 g	6.0 g	1.01 g
Total fat	10.99 g	4.51 g	3.5 g	2.50 g
Sugars	31.01 g	0 g	9.0 g	0 g
Calcium	300 mg	283 mg	451 mg	451 mg
Vitamin D	0 IU	0 IU	120 IU	101 IU
Health issues	-Lacose intolerence -Allergies to protein	-antinutritional factors	- food allergens -isoflavones compound which might cause breast cancer	- pathogenic bacteria - food allergens
Environmental impact	-high greenhouse gas emissions -high land use -high freshwater use - high level of eutrophication	-less freshwater use - absorbs a lot of CO2	-lesser freshwater use and eutrophication impact than dairy and almond milk.	- high freshwater use - has lower greenhouse gas emissions and uses less land than soy and dairy

5. Conclusions and future perspectives

The interest in consuming plant-based milk is increasing day after day for several reasons, including health, environmental, ethical, and others. Hemp milk is one of the plant based milk types that has gained a lot of attention in the past few years. Today's consumer has become more aware and keen to choose the best products available, in line with his needs and interests. Therefore, interest and demand for hemp milk is expected to increase more and more in the next few years. Nutritionally, hempseed has an ideal omega-6 to omega-3 PUFA ratio, a high quantity of essential amino acids, and proteins that are easy to digest, hence, it has the potential to be used as a nutraceutical in food, as well as it has no allergens, and this increases its preference over other types of plant milk. Last but not least, the production of hemp milk is sustainable as the plant needs small amounts of water to grow and consumes large amounts of carbon dioxide, which makes it environmentally friendly.

References

Alonso-Esteban, J. I., Torija-Isasa, M. E., & Sánchez-Mata, M. de C. (2022). Mineral elements and related antinutrients, in whole and hulled hemp (Cannabis sativa L.) seeds. *Journal of Food Composition and Analysis*, *109*, 104516. https://doi.org/10.1016/J.JFCA.2022.104516

Besir, A., Awad, N., Mortas, M., & Yazici, F. (2022). A Plant-Based Milk Type: Hemp Seed Milk. *Akademik Gida*, *20*(2), 170–184. https://doi.org/10.24323/AKADEMIK-GIDA.1149875

Caporuscio, J. (2021). *Almond Milk Market Size, Share | Global Industry Report, 2019-2025*. Medical News Today. https://www.grandviewresearch.com/industry-analysis/almond-milk-market

Chich_Owska, J., Kliber, A., Koz_Owska, J., Biskupski, M., & Grygorowicz, Z. (2014). *INSULIN, THYROID HORMONE LEVELS AND METABOLIC CHANGES AFTER TREATED RATS WITH HEMP MILK*.

Curl, S., Rivero-mendoza, D., & Dahl, W. J. (2020). Plant-Based Milks : Hemp. *UF | IFAS*, 1–4.

Ignacio Alonso-Esteban, J., José González-Fernández, M., Fabrikov, D., Torija-Isasa, E., de Cortes Sánchez-Mata, M., Luis Guil-Guerrero, J., Alonso-Esteban, J. I., Torija-Isasa, E., de Sánchez-Mata, M. C., González-Fernández, M. J., Fabrikov, D., & Guil-Guerrero, J. L. (2020). Hemp (Cannabis sativa L.) Varieties: Fatty Acid Profiles and Upgrading of γ-Linolenic Acid–Containing Hemp Seed Oils. *European Journal of Lipid Science and Technology*, *122*(7), 1900445. https://doi.org/10.1002/EJLT.201900445

Ignacio Alonso-Esteban, J., Pinela, J., Ciri, A., Calhelha, R. C., Sokovi, M., CFR Ferreira, I., Barros, L., Torija-Isasa, E., & de Cortes Sánchez-Mata, M. (2022). Chemical composition and biological activities of whole and dehulled hemp (Cannabis sativa L.) seeds. *Food Chemistry*, *374*, 131754. https://doi.org/10.1016/j.foodchem.2021.131754

Jessica Caporuscio. (2021). *Almond, hemp, oat, soy, and cow's milk: Which is best?* Medical News Today; Annual Reviews Inc. https://doi.org/10.1146/ANNUREV-PUBLHEALTH-031816-044437

Mollakhalili-Meybodi, N., Arab, M., & Zare, L. (2022). Harmful compounds of soy milk: characterization and reduction strategies. *Journal of Food Science and Technology*, *59*(10), 3723–3732. https://doi.org/10.1007/S13197-021-05249-4/FIGURES/2

Paul, A. A., Kumar, S., Kumar, V., & Sharma, R. (2019). Milk Analog: Plant based alternatives to conventional milk, production, potential and health concerns. *Https://Doi.Org/10.1080/10408398.2019.1674243*, *60*(18), 3005–3023. https://doi.org/10.1080/10408398.2019.1674243

Paul, A. A., Kumar, S., Kumar, V., & Sharma, R. (2020). Milk Analog: Plant based alternatives to conventional milk, production, potential and health concerns. *Critical Reviews in Food Science and Nutrition*, *60*(18), 3005–3023. https://doi.org/10.1080/10408398.2019.1674243

Ritchie, H. (2022, December 1). *Dairy vs. plant-based milk: what are the environmental impacts?* Our Word in Data; Elsevier B.V. https://doi.org/10.1016/j.gfs.2018.08.007

Singhal, S., Baker, R. D., & Baker, S. S. (2017). A Comparison of the Nutritional Value of Cow's Milk and Nondairy Beverages. *Journal of Pediatric Gastroenterology and Nutrition*, *64*(5), 799–805. https://doi.org/10.1097/MPG.0000000000001380

Sławińska, N., & Olas, B. (2022). Selected Seeds as Sources of Bioactive Compounds with Diverse Biological Activities. *Nutrients 2023, Vol. 15, Page 187*, *15*(1), 187. https://doi.org/10.3390/NU15010187

Vahanvaty, U. S. (2009). Hemp Seed and Hemp Milk: The New Super Foods? *ICAN: Infant, Child, & Adolescent Nutrition*, *1*(4), 232–234. https://doi.org/10.1177/1941406409342121

Vanga, S. K., Wang, J., Orsat, V., & Raghavan, V. (2020). Effect of pulsed ultrasound, a green food processing technique, on the secondary structure and in-vitro digestibility of almond milk protein. *Food Research International*, *137*(March), 109523. https://doi.org/10.1016/j.foodres.2020.109523

Wang, Q., Jiang, J., & Xiong, Y. L. (2018). High pressure homogenization combined with pH shift treatment : A process to produce physically and oxidatively stable hemp milk. *Food Research International*, *106*(September 2017), 487–494. https://doi.org/10.1016/j.foodres.2018.01.021

Nitric Oxide; Does It Cancer Or Protect?

Fatma Gönül Sezgin

Introduction

Nitric oxide (NO), an endogenous gas and free radical, is an important molecule responsible for vasodilation, wound healing, tumor formation and anti-inflammation (1, 2). It is also responsible for many biological processes such as angiogenesis, cell signaling, and killing of cancerous cells (3). Its molecular weight is 30.006 g/mol and its half-life is 20-30 seconds. Endogenous NO is produced by the nitric oxide synthase enzyme (NOS) converting the amino acid L-arginine to L-citrulline (Figure 1). The oxidation of L-arginine occurs in several steps. First, Nω-hydroxy-Larginine (NOHA) is produced. This is followed by the oxidative cleavage step of the C=N bond in NOHA to NO and L-citrulline. In the next step, there is a return to L-arginine with the citrulline/arginine cycle (4). The physiological concentration of L-arginine in the human body is sufficient for sustained NO production (5) The catalytic activity of NOS (KmL-Arg 1.4 to 32.2 mmol/l) is relatively low. However, L-arginine supplementation may partially increase NO production (6). NO can also be produced without the direct action of NOS, the best example being the release of NO by interaction of NOHA with cytochrome P-450 (7).

NOS has three isoforms in the human body. Neuronal NOS (nNOS) is found in the nonadrenergic, noncholinergic nervous system (NANC), airway nerves, and epithelium, while endothelial NOS (eNOS) is mainly found in the endothelial cells of the pulmonary vasculature. Inductive NOS (iNOS) is responsible for pro- and anti-inflammatory responses. All isoforms contain a domain homologous to tetrahydrobiopterin, heme and cytochrome P450 reductase and are flavoprotein in nature. (8).

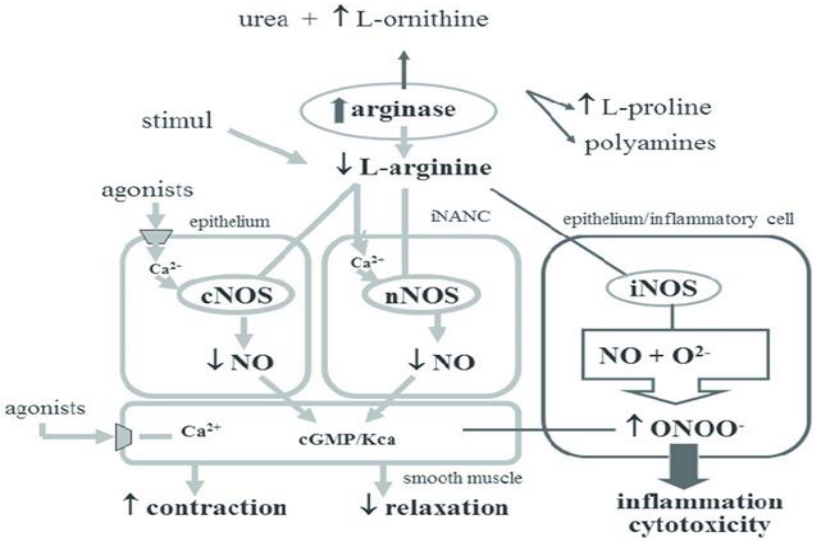

Figure 1. Nitric oxide synthesis and basic mechanisms of NO effects (24)

The difference in NOS isoforms is not only structural and positional. There are also characteristic differences in both their transcriptional and post-translational regulation (9). The activities of neuronal and endothelial NOS, which are called constitutive, depend on the amount of intracellular calcium. They are master regulators of homeostasis and produce NO at the

femto- or picomolar level (10). iNOS activity is dependent on calmodulin. Unlike other isoforms, binding to calmodulin is Cai 2+ independent. This situation causes the release of NO in higher amounts than the physiological way. NO production by iNOS can increase up to 1000 times in pathological conditions. NO, which is regulatory and protective, turns into a cytotoxic agent in this case. The very high levels of NO formed lead to smooth muscle relaxation, increasing vascular permeability and mucus secretion. As a result, it causes mucosal damage (11).

High concentrations of NO react with other reactive oxygen intermediates (ROI) such as superoxide (O2 -) oxygen to produce significant levels of reactive nitrogen species (RNT) that cause cell damage by free radical-mediated Lipid peroxidation, thiol and amine nitration, tyrosine nitration (12, 13). When the formation of these molecules cannot be suppressed, nitrosative stress occurs due to the formation of excessively reactive nitrogen. (13), this situation also creates an imbalance in redox. In the case of unbalanced redox, DNA, various proteins, carbonditrates and lipids are damaged (15), and as a result, cancer may develop (14). NO-induced genotoxicity in the cell activates the DNA repair mechanism by stimulating the G1/S, intra-S and G2/M checkpoints between cell cycle phases (16).

NO, which plays a role in many intracellular or intercellular pathways, becomes very stable and water-soluble at high concentrations in an oxygen-deprived environment. If it is at low concentrations, it can maintain its stability even in the presence of oxygen.

At low concentrations, NO can promote tumor growth in ways such as promoting angiogenesis. At high concentrations, it becomes very toxic to cancer cells and suppresses tumor growth. The potentially toxic nature of cancer cells makes NO the subject of much research in medicine (3).

NO and Cancer.

NO has a high potential in cancer treatment due to its biocompatibility and tumor cell specific cytotoxicity. However, despite this feature, clinical applications have been limited due to the variability and target specificity of available NO donors and distribution network. However, in recent years, researchers have focused on the tumor microenvironment and aimed to benefit from NO toxicity by affecting the physiological conditions there. In a study, it has been reported that NO donor is formed by using free thiol groups with which NO can be easily conjugated, and NO is produced with its correct release. As a result of the same study, it was stated that the conjugate induces cytotoxicity in tumor cells and thus inhibits metastasis (17).

Ions necessary for the body have also been evaluated as microenvironmental targets. Because ions can sometimes turn into agents that destroy cells without creating toxicity and drug resistance. The mediation of NO to Ca2+ release inspired a new study. In the study, nanoparticle NO nano donors coated with zeolitic nitro-/nitrile-imidazole framework-82 with high photoreactivity and stability and berbamine (BER) release were formed.

While these NO nano donors release NO, the released NO causes a sudden increase in Ca2+. On the other hand, BER turns off the Ca2+ excretion pumps and the amount of intracellular Ca2+ increases excessively. This induces apoptosis. Thus, cell killing with endogenous ions has taken place (18).

It has also been observed that the antitumor response of CD8+ lymphocytes is regulated by NO in an experimental strategy in which iNOS and NO are overproduced by gene transfer (19). In another study with colorectal cancer cells, it was reported that sepiapterin treatment increased the tetrahydrobiopterin:dihydrobiopterin ratio and reduced tumor growth by activating nitric oxide synthase (20). In some studies, it has been stated that tumor cells exposed to NO donors show antitumor capacity. It has been reported that the antitumor capacity mechanisms of NO are reduction of COX-2 expression and inhibition of PI3K and MAPK pathways (21, 22).

Other mechanisms showing the anticancer properties of NO have also been suggested. These are that high NO concentrations (>200 nM) can cause cell death through disruption of anti-Apoptotic mediators, p53 upregulation, cytochrome release induction, cytostasis and

cytotoxicity, and cell cycle arrest. (H) In a study investigating the ability of hyaluronic acid (HA) to scavenge nitric oxide, they showed that NO breaks down HA. It was concluded that the nitric oxide-induced degradation of HA inhibits the migration of cancer cells in the tumor environment. And the potential use of HA in different biomedical applications has been suggested.(23).

CONCLUSION

According to the results obtained from the literature review, NO may have beneficial or harmful effects for the cell depending on the environment and its concentration in that environment. The damage it causes to the cell turns into a desired situation in the fight against cancer cells. But its lack of specificity makes its controllability difficult. In addition, the evidence that NO can be used in cancer treatment is quite clear. As seen in the review, studies in recent years have focused on specific mechanisms that can create specificity. In this direction, by targeting the tumor microenvironment, key molecules that can interact with NO in this microenvironment should be well identified. Studies are needed to reveal these molecules and their tumor suppression mechanisms.

REFERENCES

Kim T., Suh J., Kim W.J., (2021) *Adv. Mater*., 33, 2008793**.**

Sung Y. C., Jin P. R., Chu L. A., Hsu F. F., Wang M. R., Chang C. C., Chiou S. J., Qiu J. T.,. Gao D. Y, Lin C. C., Chen Y. S., Hsu Y. C., Wang J., Wang F. N., Yu P. L., Chiang A. S., Wu A. Y. T, Ko J. J. S., Lai C. P. K., Lu T. T, Chen Y. C. Nat. 2019. *Nanotechnol.*, 14, 1160

Kumar A., Radzievski R., Xie J. (2018) Free Radical: Nitric Oxide in Cancer Therapy. *Int J Anal Medicinal Chem*. 1(1): 1-4.

Wu G, Morrıs SM: (1998) Arginine metabolism: nitric oxide and beyond. *Biochem J* 336: 1-17,

Sajeev C, Srıdhar N, Veeranjaneyulu A. (1998) Nitric oxide: concepts, current perspectives and future therapeutic implications. *Indian J Pharmacol* 30: 351

Su Y, Couch M, Block ER: (1997) Substrate inhibition of nitric oxide synthase in pulmonary artery endothelial cells in culture. *Nitric Oxide Biol Chem* 1: 469-475

Jia Y, Zacour M, Tolloczko B, Martin JG. (1998) Nitric oxide synthesis by tracheal smooth muscle cells by a nitric oxide synthase-independent pathway. *Am J Physiol* 275: L895-L901

Förstermann U, Sessa WC. (2012) Nitric oxide synthases: regulation and function. *Eur Heart J*. Apr;33(7):829-37, 837a-837d. doi: 10.1093/eurheartj/ehr304.

Lacza Z, Snipes JA, Zhang J, Horváth EM, Figueroa JP, Szabó C, Busija DW. (2003) Mitochondrial nitric oxide synthase is not eNOS, nNOS or iNOS. *Free Radic Biol Med* 35: 1217-1228.

Ricciardolo FLM, Sterk PJ, Gaston B, Folkerts G. (2004). Nitric oxide in health and disease of the respiratory system. *Physiol Rev* 84: 731-765,

Meurs H, Maarsingh H, Zaagsma J. (2003). Arginase and asthma: novel insights into nitric oxide homeostasis and airway hyperresponsiveness. *Trends Pharmacol Sci* 24: 450-455

Eiserich, J.P., Patel, R.P., O'Donnell, V.B. 1998. Pathophysiology of nitric oxide and related species: Free radical reactions and modification of biomolecules. *Mol. Asp. Med*., 19, 221–357.

Tamer, T. M. (2014) In Engineering of Polymers and Chemical Complexity, Volume II; Focke, W. W., Radusch, H.-J., Eds.; Apple Academic Press,

Juan, C. A.; Pérez de la Lastra, J. M.; Plou, F. J.; Pérez-Lebeña, E. (2021) The Chemistry of Reactive Oxygen Species (ROS) Revisited: Outlining Their Role in Biological Macromolecules (DNA, Lipids and Proteins) and Induced Pathologies. *Int. J. Mol. Sci.* 22, 4642.

Strzelczyk, J. K.; Wiczkowski, A. (2012) Oxidative Damage and Carcinogenesis. *Wspolczesna Onkol*., 3, 230−233

Visconti, R.; Della Monica, R.; Grieco, D. (2016) Cell cycle checkpoint in cancer: A therapeutically targetable double-edged sword. *J. Exp. Clin. Cancer Res*., 35, 153.

Kim T, Suh J, Kim J, Kim WJ. (2022) Lymph-Directed Self-Immolative Nitric Oxide Prodrug for Inhibition of Intractable Metastatic Cancer. *Adv Sci (Weinh).* Jan 5;9(8):2101935. doi: 10.1002/advs.202101935.

X. Chu, X. Jiang, Y. Liu, S. Zhai, Y. Jiang, Y. Chen, J. Wu, Y. Wang, Y. Wu, X. Tao, X. He, W. Bu. 2021. Nitric oxide modulating calcium store for Ca^{2+}-initiated cancer therapy *Adv. Funct. Mater.*, 31 p. 2008507 doi: 10.1002/adfm.202008507

Navasardyan I and Bonavida B. (2021) Regulation of t cells in cancer by nitric oxide. *Cells* 10(10): 26–55

Alam A, Smith SC, Gobalakrishnan S, McGinn M, Yakovlev VA, Rabender CS. (2023) Uncoupled nitric oxide synthase activity promotes colorectal cancer progression. *Front Oncol.* 14;13:1165326. doi: 10.3389/fonc.2023.1165326.

Bocca C, Bozzo F, Bassignana A, et al. (2010) Antiproliferative effect of a novel nitro-oxy derivative of celecoxib in human colon cancer cells: role of COX-2 and nitric oxide. *Anticancer Res* 30(7): 2659–2666.

Bechmann N, Calsina B and Susan Richter JP (2022) Therapeutic potential of nitric oxide–releasing selective estrogen receptor modulators in malignant melanoma. *J Invest Dermatol* 142(8): 2217–2227

Alsharabasy AM, Glynn S, Farràs P, Pandit A. (2022) Interactions between Nitric Oxide and Hyaluronan Implicate the Migration of Breast Cancer Cells. *Biomacromolecules*. 12;23(9):3621-3647. doi: 10.1021/acs.biomac.2c00545

Antosova, M.; Mokra, D.; Pepucha, L.; Plevkova, J.; Buday, T.; Sterusky, M.; Bencova, A. (2017) Physiology of nitric oxide in the respiratory system. *Physiol. Res*. 66, S159–S172

In Silico Identification of Possible Mutation-Prone Regions of the GRIA3 Protein

Zeynep Nur KESKİN[1]
Emre AKTAŞ[2]
Nehir ÖZDEMİR ÖZGENTÜRK[3]

1. Introduction

Schizophrenia is characterized by positive psychotic symptoms, including hallucinations and delusions, and negative symptoms including emotional limitation and social impairment (Smeland., 2020). There are three symptom groups in schizophrenia; positive, negative and cognitive (Stepnicki P., et al. 2018). It is a chronic disease triggered by the interaction of genetic, epigenetic, developmental and environmental factors that interfere with normal brain development and maturation (Millan M. et al., 2016). Although genetic linkage and association studies have targeted a large number of candidate loci and genes, no specific gene variant or gene combination is sufficient to be shown to cause schizophrenia (Jablensky A., 2022). Currently, schizophrenia cannot be diagnosed with genetic risk factors, but further genetic studies will contribute to the diagnosis of the disease (Smeland., 2020).

1.1.Schizophrenia and GRIA3 Protein

Abnormalities in the expression of iontropic glutamate receptor subunits in the temporal lobe of the brain have been detected in schizophrenia and mood disorders (Beneyto M. et al. 2007). In studies conducted with the brains of patients who died of schizophrenia, it has been reported that the expression of the AMPA receptor is abnormal, but inconsistencies exist as in other theories to schizophrenia (Yonezawa K., et al., 2022). In a comprehensive study investigating rare encoded variants in genes that carry a significant risk for schizophrenia, it was stated that NMDA receptor subunit GRIN2A and AMPA receptor GRIA3 play a role in the pathogenesis of schizophrenia together with the disorder of the glutamatergic system (Singh T., et al, 2022).

1.2. Glutamate Receptors

One of the primary excitatory neurotransmitters and the most prevalent neurotransmitter in mammalian brains is glutamate (Moghaddam B., et al, 2012). Most glutamate receptors are ionotropic receptors with ligand-gated ion channels, but a few metabotropic glutamate receptors are also found. Ionotropic glutamate receptors are divided into three subtypes; NMDA (N-methyl-D-aspartate), AMPA (α-amino-3-hydroxy-5-methylisoxaole-4-propionate), and Kainate receptors (Uno Y., et al., 2019 , García-Gaytán AC., et al., 2022). The ionotropic

[1] Yıldız Technical University, Molecular Biology and Genetics, Orcid: https://orcid.org/0009-0009-4782-3016
[2] Res. Asst., Yıldız Technical University, Molecular Biology and Genetics, Orcid: https://orcid.org/:0000-0002-9422-3402
[3] Prof. Dr., Yıldız Technical University, Molecular Biology and Genetics, Orcid: https://orcid.org/0000-0003-3809-6303

glutamate receptors in the brain play a major role in mediating fast excitatory neurotransmission (Beneyto M. et al.,2007).

1.2.1 NMDA receptors.

NMDA receptors are ligand-gated ion channels that conducts excitatory transmission through a Ca2+ permeable component in the central nervous system. It has important physiological roles such as learning, memory and synaptic flexibility (Hansen KB., et al., 2018). NMDA receptors have 7 subunits; GRIN1, GRIN2 A-D and GRIN3 A-B (García-Gaytán AC., et al., 2022).

1.2.2 AMPA receptors.

Together with the NMDA and Kainat receptors, AMPA receptors are tetrameric ion channels that mediate most of the excitatory transmission in the central nervous system. They are the main fast transmission elements in synapses (Greger IH., et al., 2017). The activity of AMPA receptors is critical not only for neuronal development and synaptic plasticity in physiological conditions, but also because it can induce neuronal death in neuropathological conditions (Guo C., et al., 2021). They are transmembrane proteins that combine as a tetrameric complex consisting of 4 subunits, GRIA 1-4 (Kamalova A., et al., 2021). Disorders of the GRIA3 protein have been associated with disorders such as intellectual developmental disorder, bipolar disorder, schizophrenia, epilepsy, autism, and spasticity (MalaCards).

1.3. Detection of Mutations

Single nucleotide polymorphisms, SNPs, are the most common genetic mutation (Ou L., et al., 2017). SNPs that change the amino acid sequence are called nonsynonymous single nucleotide polymorphisms (nsSNPs). The translation product is affected by the change in the amino acid sequence (Soremekun OS, et al., 2021). Some SNPs can cause disease, predispose a person to disease, or impact how well they respond to medicine, while others are phenotypically neutral. (Ou L., et al., 2017). Single amino acid changes are the most common cause of many diseases. Examining single point mutations of a protein is of great importance for understanding disease mechanisms (Ng PC., et al., 2006). The development of databases and web-based algorithms that calculate the probability of mutations being harmful to see the effect of these mutations on proteins has facilitated and expanded research in this area (Choudjury A., et al., 2022). In silico studies are an important method used in drug discovery and development. Such studies provide advantages in terms of cost as they replace human and animal experiments (Saldanha L., et al., 2023).

In this study, DisEMBL, I-Mutant 2.0 and PhD-SNP bioinformatics tools will be used to detect various mutation-prone regions of the AMPA receptor subunit GRIA3 protein, a protein identified in the literature that may be a possible cause of schizophrenia, and to examine the pathogenic effects of these mutations.

2.Methods & Results

The NCBI-National Center for Biotechnology, the National Center for Biotechnology Information, is a platform established to provide access to biomedical and genomic information (NCBI-National Center for Biotechnology). In order to reach the GRIA3 protein via NCBI, "Glutamate Receptor 3" was searched in "Homo sapiens" was selected from the species filter for sequence information in humans.

The code representing the protein is P42263.2 (NCBI, UniProtKB). The FASTA format is a text format representing nucleotide or peptide sequences with the code in which base pairs

or amino acids are represented by single letters (NCBI-National Center for Biotechnology). The FASTA sequence of the protein at the amino acid level obtained is as follows.

>sp|P42263.2|GRIA3_HUMAN RecName: Full=Glutamate receptor 3; Short=GluR-3; AltName: Full=AMPA-selective glutamate receptor 3; AltName: Full=GluR-C; AltName: Full=GluR-K3; AltName: Full=Glutamate receptor ionotropic, AMPA 3; Short=GluA3; Flags: Precursor

MARQKKMGQSVLRAVFFLVLGLLGHSHGGFPNTISIGGLFMRNTVQEHSAFRFAVQLYNTNQNTTEKPFHL
NYHVDHLDSSNSFSVTNAFCSQFSRGVYAIFGFYDQMSMNTLTSFCGALHTSFVTPSFPTDADVQFVIQMRPALKGA
ILSLLGHYKWEKFVYLYDTERGFSILQAIMEAAVQNNWQVTARSVGNIKDVQEFRRIIEEMDRRQEKRYLIDCEVER
INTILEQVVILGKHSRGYHYMLANLGFTDILLERVMHGGANITGFQIVNNENPMVQQFIQRWVRLDEREFPEAKNAP
LKYTSALTHDAILVIAEAFRYLRRQRVDVSRRGSAGDCLANPAVPWSQGIDIERALKMVQVQGMTGNIQFDTYGRR
TNYTIDVYEMKVSGSRKAGYWNEYERFVPFSDQQISNDSASSENRTIVVTTILESPYVMYKKNHEQLEGNERYEGY
CVDLAYEIAKHVRIKYKLSIVGDGKYGARDPETKIWNGMVGELVYGRADIAVAPLTITLVREEVIDFSKPFMSLGISI
MIKKPQKSKPGVFSFLDPLAYEIWMCIVFAYIGVSVVLFLVSRFSPYEWHLEDNNEEPRDPQSPPDPPNEFGIFNSLW
FSLGAFMQQGCDISPRSLSGRIVGGVWWFFTLIIISSYTANLAAFLTVERMVSPIESAEDLAKQTEIAYGTLDSGSTKE
FFRRSKIAVYEKMWSYMKSAEPSVFTKTTADGVARVRKSKGKFAFLLESTMNEYIEQRKPCDTMKVGGNLDSKGY
GVATPKGSALRNAVNLAVLKLNEQGLLDKLKNKWWYDKGECGSGGGDSKDKTSALSLSNVAGVFYILVGGLGLA
MMVALIEFCYKSRAESKRMKLTKNTQNFKPAPATNTQNYATYREGYNVYGTESVKI

2.1.Identification of Mutation-Prone Regions of the GRIA3 Protein

Using the amino acid sequence of GRIA3, mutation-prone regions in the GRIA3 protein were investigated by estimating the irregular/unstructured regions, then stability changes in these regions, evolutionary analysis, and SNP estimation.

2.2.Prediction of disordered/unstructured regions of the GRIA3 protein

The tool DisEMBL, was used to predict the disordered/unstructured regions in the sequence of the GRIA3 protein. With the DisEMBL tool, irregular regions can be examined for Loop and Coil, Hot-loops and Remark-465 (Linding R., et al., 2003).

Estimations were obtained by loading the amino acid sequence of the GRIA3 protein into the DisEMBL tool and converted into a table as in Table 1. In terms of loops/coils, the irregular/unstructured regions were estimated as 1-8, 390-422, 793-817. Irregular/unstructured regions in terms of hot cycles were estimated as 1-10, 409-424, 805-813. In terms of Remark-465, irregular/unstructured regions were estimated as 1-8, 412-421, 806-815. When the regions common in all results were combined, MARQKKMG between regions 1 and 8, QISNDSASSE between regions 412 and 421, and GSGGGDSK between regions 806 and 813 were determined as common. These detected regions will be used in the next stages of the study. Regions and amino acids determined to be common in the results obtained in Table 1 are highlighted in bold.

Table 1. Results of disordered/unstructured regions of the GRIA3 protein predicted by the DisEMBL tool.

Estimation tool DisEMBL	**Estimated Locations**	**Common Predicted Results**
Disordered by Loops/coils definition	**1-8**, 24-44, 59-86, 119-134, 262-278, 290-308, 329-352, 366-381, **390-422**, 442-453, 472-491, 500-507, 534-549, 575-606, 617-634, 661-668, 678-691, 707-718, 744-773, **793-817**, 852-894	**MARQKKMG: 1-8** **QISNDSASSE: 412-421** **GSGGGDSK: 806-813**
Disordered by Hot-loops definition	**1-10**, 190-200, 270-278, 298-310, 330-349, 367-378, **409-424**, 429-437, 470-489, 534-542, 678-691, 705-726, 791-800**, 805-813**, 859-882	
Disordered by Remark-465 definition	**1-8, 412-421**, 585-597, **806-815**	

2.3.Estimation of stability changes of the GRIA3 protein

The I-Mutant 2.0 tool was used to examine the effect of single point mutations on protein stability in the construct and sequence. After loading the amino acid sequence of the protein to the site, the position of the single point mutations was written and the new residue part was left blank, and the stability change of all 19 amino acid changes was obtained. The temperature in degrees Celsius was adjusted to 37 and the pH (-log[H+]) to 7.4 (Capriotti E., et al., 2005). Protein stability, which is changed by a single point mutation, is given by the score obtained from the protein's structure information and sequence information. The RI value is the Reliability Index.

Of the 475 results obtained by performing 19 single point mutations of 25 amino acids, only those with a confidence index above 8 are selected and shown in Table 2. The RI value of 35 results is 8. Of the 32 stability change analyzes with an RI value of 8 and above, 23 results showed a decrease in stability, while 9 results showed an increase in stability.

Table 2. Effect of GRIA3 mutations predicted by the I-Mutant 2.0 tool on protein stability

Estimation tool	**Variant**	**Results**	**RI**	**Variant**	**Results**	**RI**	**Variant**	**Results**	**RI**
I-Mutant	R3G	Decrease	8	I413C	Decrease	8	G808R	Decrease	8
	K5P	Increase	8	N415G	Decrease	8	G808K	Decrease	8
	K5L	Increase	8	N415A	Decrease	8	G809K	Decrease	8
	K6L	Increase	8	A418Y	Decrease	8	G809Q	Decrease	8
	K6V	Increase	8	A418K	Decrease	8	G809D	Decrease	8
	K6P	Increase	8	A418T	Decrease	8	G809R	Decrease	8
	K6F	Increase	8	A418Y	Decrease	8	G810Q	Decrease	8
	M7H	Decrease	8	E421A	Decrease	8	S812A	Decrease	8
	G8K	Decrease	8	E421K	Decrease	8	K813A	Decrease	8
	I413E	Decrease	8	E421Q	Decrease	8			

pH.:7.4, Temperature:37

2.4.Prediction of SNPs of GRIA3 protein

PhD-SNP is an optimized tool to predict whether a given single point protein mutation can be classified as a disease-associated or neutral polymorphism (Capriotti E., et al., 2006). The analysis was performed by entering the protein sequence, the location of the mutation, and the symbol of the new amino acid in the tool, replacing all 19 amino acids for 25 positions. As a result of the analysis, the disease effect of the mutation and the Relativity Index(RI) value was obtained. Disease results among the results obtained are given in Table 3.

Table 3. Disease effect of GRIA3 mutations estimated by the PhD-SNP tool

Estimation Tool	**Variant**	**Results**	**RI**	**Variant**	**Results**	**RI**	**Variant**	**Results**	**RI**
PhD -SNP	M7P	Disease	1	D416C	Disease	3	G808C	Disease	3
	M7K	Disease	1	D416H	Disease	2	G808P	Disease	1
	Q412P	Disease	4	D416K	Disease	1	G809C	Disease	2
	I413P	Disease	2	S417I	Disease	3	G810C	Disease	1
	S414P	Disease	2	S417F	Disease	0	D811V	Disease	1
	N415V	Disease	1	S417W	Disease	2	D811F	Disease	2
	N415L	Disease	2	S417K	Disease	2	D811W	Disease	1
	N415F	Disease	3	S417E	Disease	0	D811Y	Disease	5
	N415W	Disease	3	S419P	Disease	1	D811A	Disease	3
	N415T	Disease	2	G806Y	Disease	0	D811C	Disease	3

	N415Q	Disease	1	G806C	Disease	2	D811H	Disease	1
	N415R	Disease	3	S807W	Disease	0	D811R	Disease	2
	N415K	Disease	2	S807Y	Disease	2	D811Q	Disease	1
	D416Y	Disease	2	S807R	Disease	2	S812W	Disease	0
	D416P	Disease	4						

3.Discussion

The disease effect and stability changes of possible single amino acid changes of the GRIA3 protein associated with schizophrenia were investigated using bioinformatics tools such as DisEMBL, I-Mutant 2.0, and PhD-SNP. Many disease results were estimated in N415, D416, S417 and D811 reigons, highlighting these region's importance. The results obtained enabled the identification of potential variants that may cause schizophrenia. The results of this study can be supported by different in silico studies to be done later.

Acknowledgments

This project was supported by TUBITAK 2209-A University Students Research Projects Support Program.

References

Beneyto, M., Kristiansen, L., Oni-Orisan, A. et al. (2007). Abnormal glutamate receptor expression in the medial temporal lobe in schizophrenia and mood disorders. *Neuropsychopharmacol.* 32,1888–1902 doi: 10.1038/sj.npp.1301312

Capriotti E, Calabrese R, Casadio R. (2006). Predicting the insurgence of human genetic diseases associated to single point protein mutations with support vector machines and evolutionary information. *Bioinformatics*. 22, 2729-2734. doi: 10.1093/bioinformatics/btl423

Capriotti E, Fariselli P and Casadio R (2005). I-Mutant2.0: predicting stability changes upon mutation from the protein sequence or structure.,*Nucl. Acids Res*. 33: W306-W310

García-Gaytán AC, Hernández-Abrego A, Díaz-Muñoz M, Méndez I. (2022 Nov). Glutamatergic system components as potential biomarkers and therapeutic targets in cancer in non-neural organs. *Front Endocrinol (Lausanne)*. 13:1029210. doi: 10.3389/fendo.2022.1029210

Greger IH, Watson JF, Cull-Candy SG. (2017 May). Structural and functional architecture of AMPA-Type glutamate receptors and their auxiliary proteins. *Neuron*. 94(4):713-730. doi: 10.1016/j.neuron.2017.04.009

Guo C, Ma YY. (2021 Aug). Calcium permeable-AMPA receptors and excitotoxicity in neurological disorders. *Front Neural Circuits*. 15:711564. doi: 10.3389/fncir.2021.711564

Hansen KB, Yi F, Perszyk RE, Furukawa H, Wollmuth LP, Gibb AJ, Traynelis SF. (2018 Aug). Structure, function, and allosteric modulation of NMDA receptors. *J Gen Physiol*. 150(8):1081-1105. doi: 10.1085/jgp.201812032

Jablensky A. (2010). The diagnostic concept of schizophrenia: its history, evolution, and future prospects. *Dialogues Clin Neurosci*. 12(3):271-87. doi: 10.31887/DCNS.2010.12.3/ajablensky

Kamalova A, Nakagawa T. (2021 Jan). AMPA receptor structure and auxiliary subunits. *J Physiol*. 599(2):453-469. doi: 10.1113/JP278701

Linding R, Jensen LJ, Diella F, Bork P, Gibson TJ, Russell RB. (2003 Nov). Protein disorder prediction: implications for structural proteomics. *Structure*. 11(11):1453-9. doi: 10.1016/j.str.2003.10.002

Malacards. (2023 May). GRIA3. Malacards: Human Disease Database. Date of Access: 21.05.2023, URL: https://www.malacards.org/search/results/GRIA3?startPage=0

Millan MJ, Andrieux A, et al., (2016 Jul). Altering the course of schizophrenia: progress and perspectives. *Nat Rev Drug Discov*. 15(7):485-515. doi: 10.1038/nrd.2016.28

Moghaddam B, Javitt D. (2012 Jan). From revolution to evolution: the glutamate hypothesis of schizophrenia and its implication for treatment. *Neuropsychopharmacology*. 37(1):4-15. doi: 10.1038/npp.2011.181

NCBI-National Center for Biotechnology. (2023). Home Page. Date of Access: May 6, 2023, from https://www.ncbi.nlm.nih.gov/

Ng PC, Henikoff S. (2006). Predicting the effects of amino acid substitutions on protein function. *Annu Rev Genomics Hum Genet*. 7:61-80. doi: 10.1146/annurev.genom.7.080505.115630.

Ou L, Przybilla MJ, Whitley CB. (2017 Jul). Phenotype prediction for mucopolysaccharidosis type I by in silico analysis. *Orphanet J Rare Dis*. 12(1):125. doi: 10.1186/s13023-017-0678-1

Rizzato F, Rodriguez A, Biarnés X, Laio A. (2017 Oct) Predicting amino acid substitution probabilities using single nucleotide polymorphisms. *Genetics.* 207(2):643-652. doi: 10.1534/genetics.117.300078

Saldanha L, Langel Ü, Vale N. (2023 Feb). In silico studies to support vaccine development. *Pharmaceutics*. 15(2):654. doi: 10.3390/pharmaceutics15020654.

Singh T, et al. (2022 Apr). Rare coding variants in ten genes confer substantial risk for schizophrenia. *Nature*. 604(7906):509-516. doi: 10.1038/s41586-022-04556-w

Smeland, O.B., Frei, O., Dale, A.M. et al. (2020). The polygenic architecture of schizophrenia — rethinking pathogenesis and nosology. *Nat Rev Neurol* 16, 366–379. doi: 10.1038/s41582-020-0364-0

Soremekun OS, Ezenwa C, et al., (2021) Transcription-translation error: In-silico investigation of the structural and functional impact of deleterious single nucleotide polymorphisms in GULP1 gene. *Inform Med Unlocked*. 22:100503. doi: 10.1016/j.imu.2020.100503.

Stępnicki P, Kondej M, Kaczor AA.(2018 Aug). Current concepts and treatments of schizophrenia. *Molecules*. 23(8):2087. doi: 10.3390/molecules23082087

Uno Y, Coyle JT. (2019 May). Glutamate hypothesis in schizophrenia. *Psychiatry Clin Neurosci*. 73(5):204-215. doi: 10.1111/pcn.12823

Yonezawa K, Tani H, et al., (2022 May). AMPA receptors in schizophrenia: A systematic review of postmortem studies on receptor subunit expression and binding. *Schizophr Res*. 243:98-109. doi: 10.1016/j.schres.2022.02.033

Choudhury A, Mohammad T, et al., (2022 May). Comparative analysis of web-based programs for single amino acid substitutions in proteins. *PLoS One*. 17(5):e0267084. doi: 10.1371/journal.pone.0267084.

Axicon Metalens Design with Gold Aperture-Based Nanoantennas

Büşra Ersoy[1]
Ekin Aslan[2]
Erdem Aslan[3]

Introduction

By constructing an electromagnetic phase discontinuity across an interface where light undergoes a change of medium, it is possible to manipulate abnormal reflections and refractions as defined by the generalized Snell's law, and thus fully control the propagation of light(Kildishev et al., 2013; N. Yu et al., 2011):

$$\sin(\theta_t)\, n_t - \sin(\theta_i)\, n_i = \lambda_0 \nabla\Phi / 2\pi \tag{1a}$$

$$\cos(\theta_t)\sin(\psi_t)\, n_t = \lambda_0 \nabla\Phi / 2\pi \tag{1b}$$

$$\sin(\theta_r) n_i - \sin(\theta_i) n_i = \lambda_0 \nabla\Phi / 2\pi \tag{2a}$$

$$\cos(\theta_r)\sin(\psi_r)\, n_i = \lambda_0 \nabla\Phi / 2\pi \tag{2b}$$

In Equation 1a,b and Equation 2a,b, the generalized Snell's law, the angles θ_t, θ_i, and θ_r represent the in-plane refraction, incidence, and reflection angles, respectively. Furthermore, n_t and n_i represent the refractive indices of the transmitting and incident media, respectively, and λ_0 is the wavelength in free space. $\nabla\Phi$ represents the gradient of the phase discontinuity provided by the meta-atoms at the interface. The phase gradient on the incidence plane leads to in-plane reflection and refraction events, while phase gradients off the incidence plane result in out-of-plane behavior. The ψ_t and ψ_r in the equations represent the respective out-of-plane refraction and reflection angles. All of these expressions indicate that they can be achieved in a very thin layer that can provide a phase gradient across an interface (Kildishev et al., 2013).

In addition to standard reflection and refraction, phenomena such as birefringence and negative refraction can occur. These events are caused by the variation of the electromagnetic phase, denoted by Φ, across the interface, which depends on the coordinates of the interface. The specific functionality that the phase profile needs to exhibit is dictated by the desired application. The positional variation of the phase can be obtained by dividing the relevant plane into unit cells. Different nanoantenna designs can be utilized to create unit cells with distinct unit phase profiles. For instance, V-shaped nanoantennas, which have been described in the literature as cells of a gradient metasurface, can generate abrupt phase shifts from 0 to 2π for cross-polarized light due to their different geometries. To achieve full phase control, it is important for the phase shift range to be larger than the 2π phase coverage domain.

[1] Büşra Ersoy, Student, Kayseri University, Department of Electrical and Electronics Engineering, ORCID: 0000-0003-1383-3311
[2] Ekin Aslan, Assoc. Prof, Kayseri University, Department of Electrical and Electronics Engineering, ORCID: 0000-0003-0933-7796
[3] Erdem Aslan, Assoc. Prof, Erciyes University, Department of Electrical and Electronics Engineering, ORCID: 0000-0001-6829-9000

In the work of Yu et al.(N. Yu et al., 2011), it has been demonstrated that the 90° rotation of V-shaped antennas enables phase transitions in the range of 0 to π for cross-polarized incident light. This finding applies specifically to linearly polarized incoming light (Ni et al., 2012; N. Yu et al., 2013). To achieve focusing functionality, these nanoantennas can be arranged in concentric rings. This arrangement allows the nanoantennas to create abrupt phase shifts, distributing the propagating waves across the interface in a way that leads to constructive interference at a distance of f, causing the outgoing cross-polarized light to be focused at a focal distance. This results in lensing functionality being achieved(Kildishev et al., 2013; Ni et al., 2013). Indeed, these types of ultra-thin designed metalenses offer crucial designs for applications such as laser processing, high-precision position alignment, sensing, and the generation of non-diffracting Bessel beams(Aieta et al., 2012). Their unique properties and capabilities make them valuable tools in various fields where precise control and manipulation of light are required (Kildishev et al., 2013).
For flat lenses to achieve focusing, the phase change on their surface must be

$$\Phi(x,y) = \frac{2\pi}{\lambda}\ (\sqrt{(x^2+y^2)+f^2} - f) \tag{3}$$

with the surface plane being the xy −plane. In this equation, f represents the focal length, λ denotes the operating wavelength, and x and y represent the coordinates on the interface. The surface phase gradient arranged according to this equation enables focusing at a desired focal length (Aieta et al., 2012).

In plasmonic applications, noble metals such as gold (Au) and silver (Ag) are typically employed. The frequency-dependent dielectric permittivity in plasmonic materials is crucially defined by the plasma frequency ω_p. For instance, the complex and real relative permittivities are expressed as follows depending on ω_p:

$$\varepsilon_r' = 1 - \frac{\omega_p^2}{\omega^2+\gamma^2} \tag{1}$$

$$\varepsilon_r'' = 1 - \frac{\omega_p^2\gamma}{\omega(\omega^2+\gamma^2)} \tag{2}$$

Here, γ is the damping rate, which is usually in the terahertz range and specific to the material. When operating at optical frequencies ($\omega \ll \gamma$), Equation 2 can be turn into to Equation 3:

$$\varepsilon_r'' = \frac{\omega_p^2}{\omega^3} \tag{3}$$

This equation indicates that in order to reduce optical losses in plasmonic materials, it is necessary to decrease the plasma frequency or damping rate. The damping rate is temperature-dependent and is related to the scattering mechanisms of electrons in the metal (Kesim et al., 2014).

The objective of this study is to design metalenses utilizing plasmonic-based nanostructures through the creation of phase gradients. Circular aperiodic arrays of these structures are utilized. By inducing radial phase variations ranging from 0 to 2π via the resonant behavior of individual meta molecules, a distinctive metalens design with multiple focal centers is accomplished. Numerical analysis is employed to derive theoretical focusing parameters, including numerical aperture (NA) and focusing efficiency.

Method

Our study includes the design of equilateral-shaped antennas based on aperture structures, taking inspiration from the phase transition generated by antenna geometries presented in Yu

et al(N. Yu et al., 2011). The study by Yu et al. (N. Yu et al., 2011) includes the phase shifts and scattering amplitudes in cross-polarization for eight types of V-shaped nanostructures. The desired phase steps and high scattering characteristics are achieved by manipulating the arm angle and rotation difference in the meta-atoms. The unit cell images of the eight types utilized in our design are presented in Figure 1. The angles of the antennas obtained using various angles, as shown in Figure 1, are sequentially 2α = 30°,68°, 79°, and 104°. The other geometric dimensions of the employed meta-cells are as follows: arm length d = 1000 nm, arm width w = 200 nm, and interarm spacing c = 200 nm.

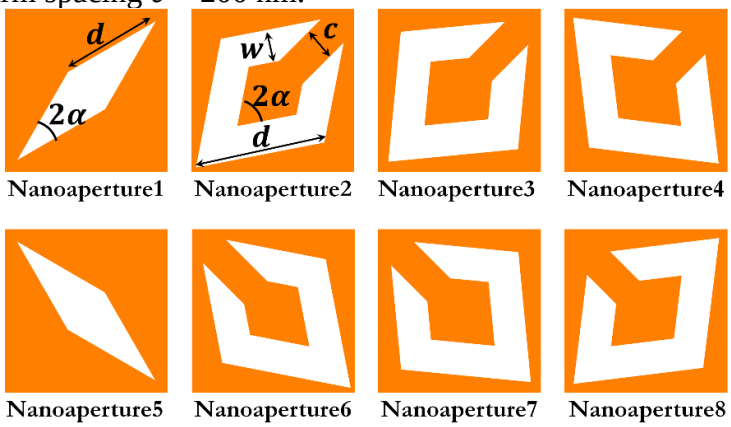

Figure 1- Top views of metacells in each arrangement.

The proposed nanostructures are designed as longitudinally opened nanoapertures on a silicon nitride (SiN) membrane coated with a subwavelength-thick layer of gold (Au). The thicknesses of the Au layer t_{Au} and the SiN membrane t_{SiN} are set to t_{Au}= 50 nm and t_{SiN}= 100 nm, respectively, for all analyses. The source wavelength is λ = 850 nm. The design of the nanostructures is accomplished through simulations using the finite-difference time-domain (FDTD) method. The analyzed structures are illuminated with vertically incident x −polarized light in the visible and near-infrared (NIR) wavelengths.

Results and Discussion

In the initial analyses, the transmittance of the structures is measured in the far field to investigate their resonant behavior, and the results are presented in Figure 2. As observed, the designed structures and their symmetries exhibit resonant behavior at 850 nm in all four angle values.

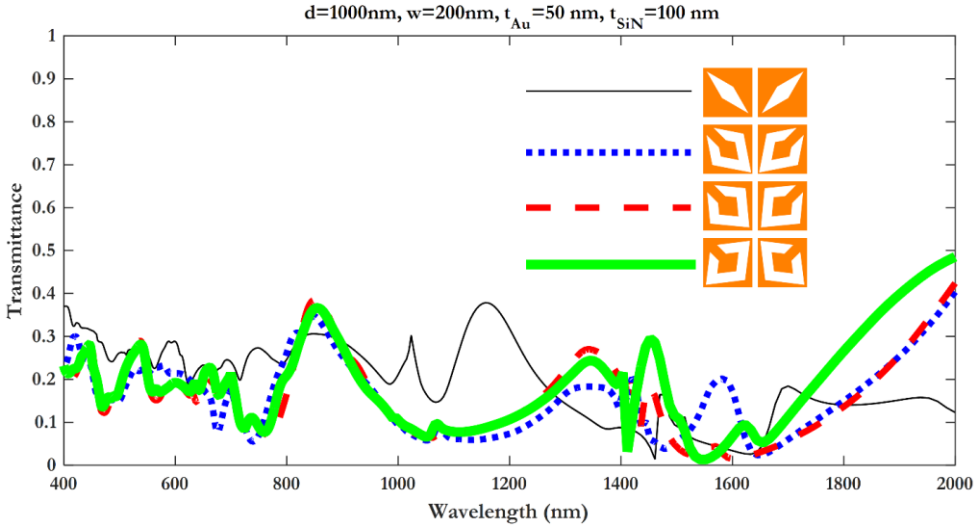

Figure 2- The transmittance analysis results of the antennas used in the arrangement.

One of the conditions for efficient focusing is the resonant behavior of the antennas used at the desired wavelength (Ding et al., 2015; Lee et al., 2011). The designed metalens consists of plasmonic nanoapertures that exhibit resonant behavior at the targeted operating wavelength, as depicted in Figure 3. The antennas are arranged in aperiodic fashion, with equal spacing, along the radial direction to achieve a uniform phase change within the range of [0,2π]. This represents a flat axicon lens approach, which results in a greater focal depth, thereby enabling long focal spots along the focusing direction. (Chang et al., 2023; Mohtashami et al., 2021). The focal performance is analyzed for the designed aperiodic arrangement, which consists of nanoapertures on a SiN membrane coated with a layer of Au.

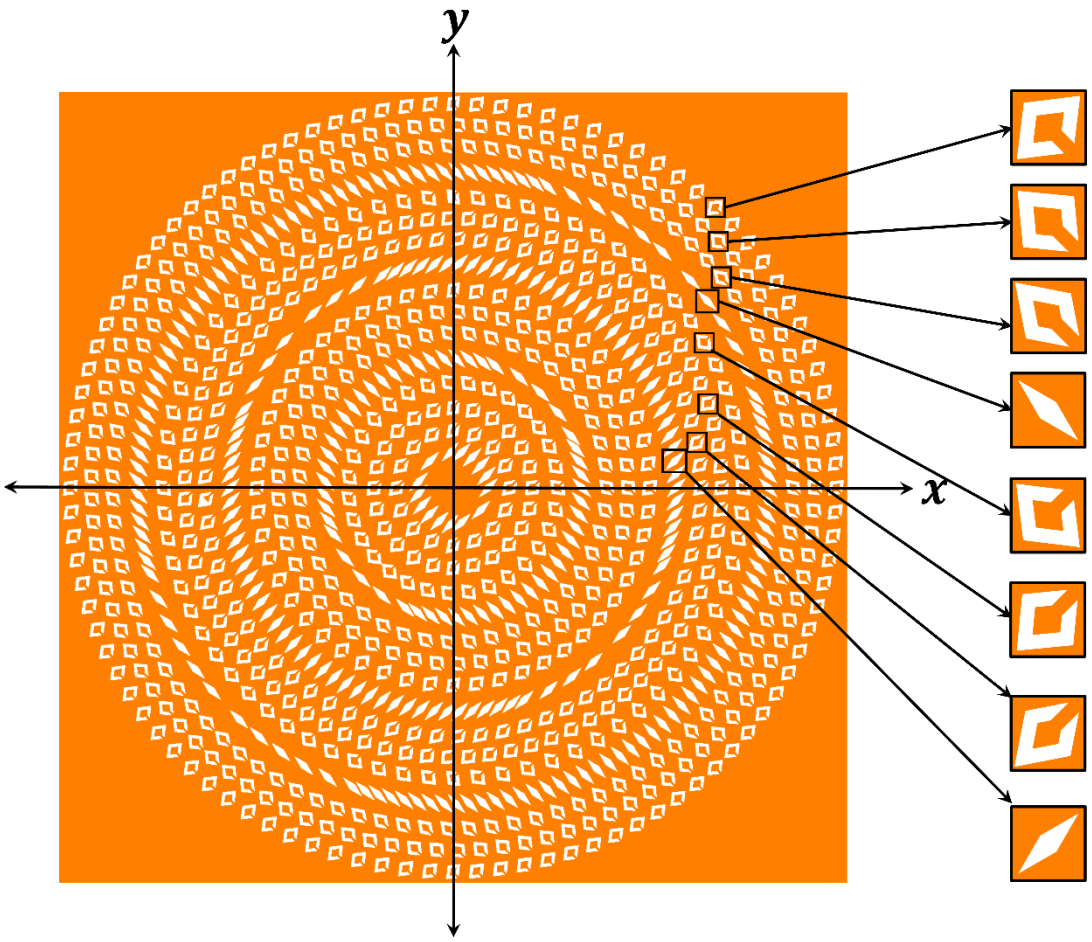

Figure 3- Top view of the antenna arrangement.

In order to demonstrate the focal points exhibited by the antenna array shown in Figure 3, two vertical monitors are placed in the $xz-$ plane and $xy-$ plane. The results obtained from the monitors are presented in Figure 4. The panels of the figure provide the normalized light intensity distributions with respect to the source in the propagation plane (Figure 4a) and perpendicular to both the propagation plane and the metalens (Figure 4b). According to this, in the designed structure, at focal distances of $f_1 = 2.88$ μm, $f_2 = 4.07$ μm, $f_3 = 8.14$ μm, $f_4 = 9.75$ μm, ve $f_5 = 16.79$ μm, multiple focal spots with a spot count of five and normalized light intensity greater than 1 have been determined. The focal distances of the identified spots are presented in Table 1.

Theoretical focusing parameters are determined through analysis by placing horizontal field monitors at the center of these identified focal spots. The light intensity distributions of each monitor at the f_1, f_2, f_3, f_4, and f_5 locations are shown in Figure 5.

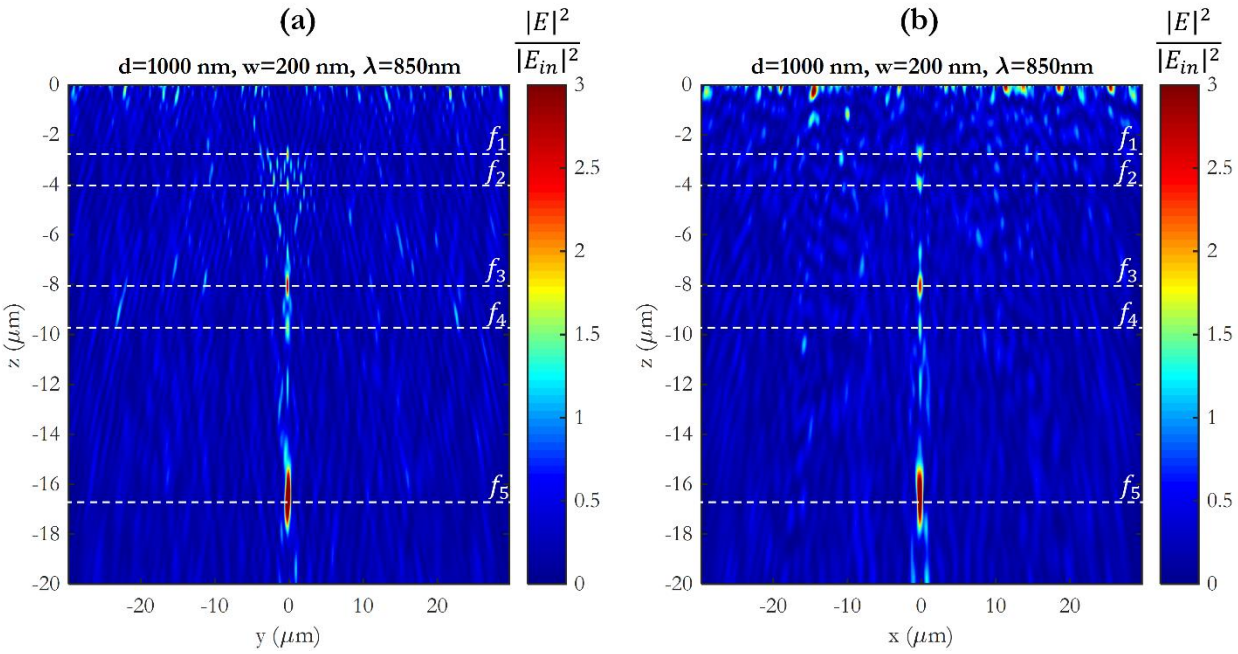

Figure 4- Light intensity distributions normalized to incident light intensity on vertical monitors.

Table 1- *Focal distance values for multiple focal points.*

Focal Spot	Focal Lenght (μm)
f_1	2.88 μm
f_2	4.07 μm
f_3	8.14 μm
f_4	9.75 μm
f_5	16.79 μm

Table 2 presents the theoretical focusing parameters of the proposed metalens, which determine its maximum resolution. These parameters are crucial factors in determining the performance of the metalens. NA is one of the focusing parameters, representing the ratio between the metalens diameter and the focal length. It plays a significant role in optical systems. NA of a metalenses expresses the resolution level determined by the design of metal or dielectric structures at the nano scale and the operating frequency. The NA is calculated using the formula $NA = n * sin\theta$, where n represents refractive index of the environment in which the metastructure is located and θ denotes the half-angle of the maximum cone of light accepted by the metalens (Aieta et al., 2012). This value determines how light will be reflected in traditional lenses, thus affecting the resolution of the lens. The second parameter to be calculated is the full width at half maximum (FWHM), which represents the width of the light intensity distribution at half of its maximum value. In microlenses, FWHM represents the distance between two points that intersect half of the light intensity, and it is calculated as $FWHM = \frac{\lambda_0}{2NA}$. This distance determines the width of the light beam and represents the midpoint of the light intensity during the transition from one point to another (Ali & Aksu, 2021; Aslan & Aslan, 2020; X. Yu et al., 2021). Another parameter we have is the depth of focus (DOF). The DOF for a regular lens with a diameter of D and a focal length of f is calculated as $DOF = 4\lambda_0 \frac{f^2}{D^2}$. It represents the distance in which objects can still be seen clearly in a region beyond the focal point (Ali & Aksu, 2021; Bayati et al., 2020). The final important parameter is the focal efficiency $\eta.\eta$ represents the proportion of light energy collected in the

optical system that is concentrated at the focal point. It is calculated by dividing the average light intensity at the focal point by the incoming average light intensity. The formulated expression is $\eta = \frac{\langle I_f \rangle}{\langle I_i \rangle}$, where η represents the calculated value as the ratio of the average light intensity at the focal point $\langle I_f \rangle$ to the incoming average light intensity $\langle I_i \rangle$ (Aslan, 2021).

Table 2- *The focusing parameter values for the proposed metalens arrangement.*

Lens Properties	Focal Points	Values
NA	f_1=2.88 µm	0.99
	f_2=4.07 µm	0.99
	f_3=8.14 µm	0.96
	f_4=9.752 µm	0.95
	f_5=16.79 µm	0.87
FWHM (µm)	f_1=2.88 µm	0,.3
	f_2=4.07 µm	0.43
	f_3=8.14 µm	0.44
	f_4=9.752 µm	0.45
	f_5=16.79 µm	0.49
DOF (µm)	f_1=2.88 µm	0.008
	f_2=4.07 µm	0.016
	f_3=8.14 µm	0.064
	f_4=9.752 µm	0.092
	f_5=16.79 µm	0.272
η (%)	f_1=2.88 µm	0.4
	f_2=4.07 µm	0.3
	f_3=8.14 µm	0.7
	f_4=9.752 µm	0.5
	f_5=16.79 µm	2

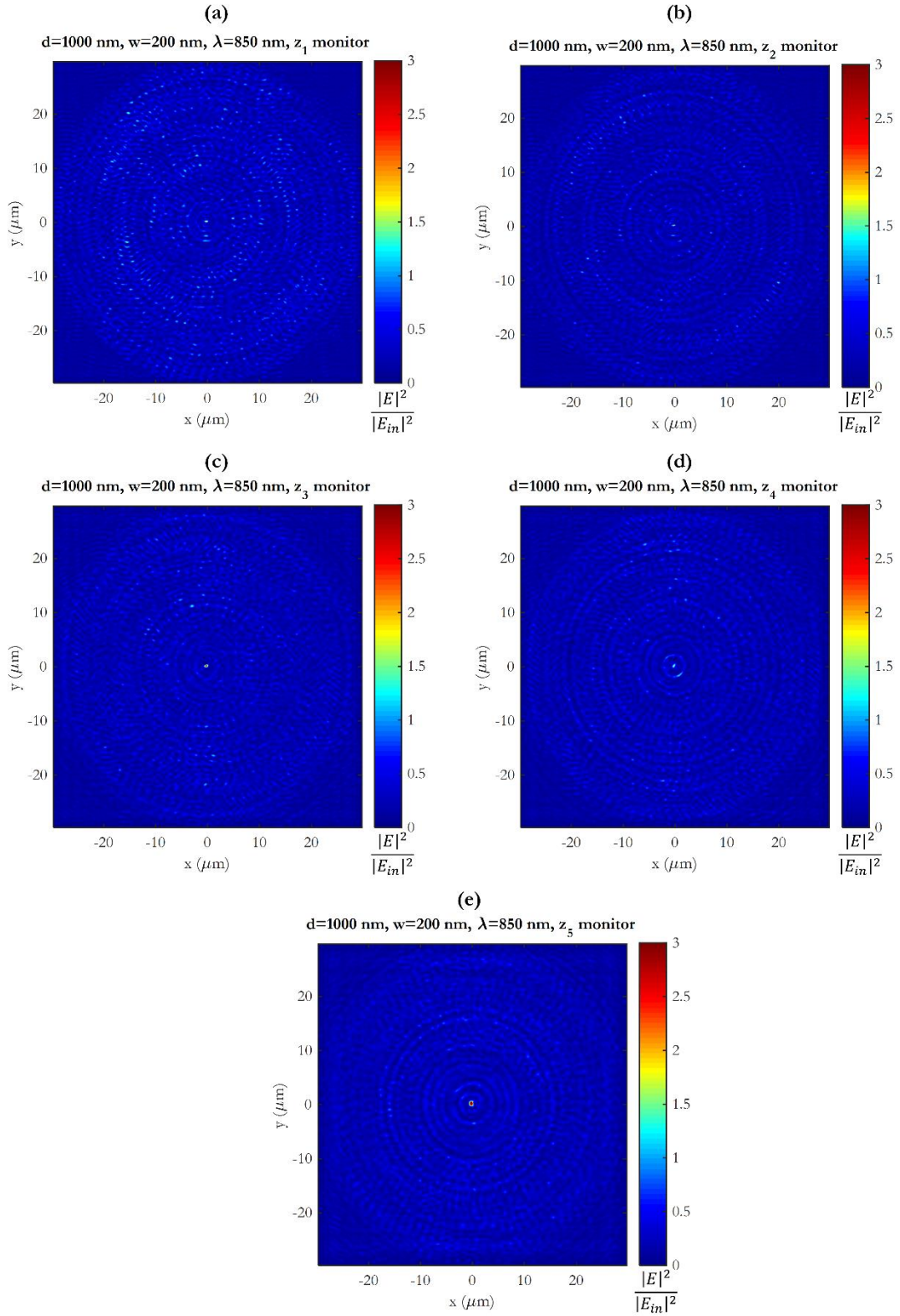

Figure 5- *Normalized light intensity distributions obtained from horizontal monitors placed at the centers of focal spots.* ***(a)*** $z = f_1$, ***(b)*** $z = f_2$, ***(c)*** $z = f_3$, ***(d)*** $z = f_4$, *and* ***(d)*** $z = f_5$.

Conclusion

Plasmonic metalenses are phase-modulated metasurfaces constituting specific phase distributions due to plasmonic nanostructures in their content. The desired phase response on the cells of plasmonic metalenses relies on various factors including the dielectric substrate and

size, shape, and rotational mode of metallic nanostructures. In the present study, we designed eight plasmonic unit cells for the metalens, enabling phase manipulation across the entire phase range necessary for achieving axicon focusing functionality. These unit cells consist of aperture-based nanoantennas embedded in a nanoscaled layer of gold film on a silicon nitride membrane with subwavelength-thickness. Simulations are conducted at a wavelength of 850 nm. The unit cells are arranged in a circular pattern at equal radial distances, forming circular phase rings that induce complete phase transition at the metalens interface. Taking into account the limitations of the analytical analiz infrastructure, our proposed plasmonic metalens design enabled the identification of multifocal points. Theoretical calculations are performed to determine key focusing parameters for each focal point, including focal length, NA, DOF, FWHM, and η.

Acknowledgement

This study acknowledges the support provided by The Scientific and Technological Research Council of Turkey (TUBITAK− Project ID: 121E518).

References

Aieta, F., Genevet, P., Kats, M. A., Yu, N., Blanchard, R., Gaburro, Z., & Capasso, F. (2012). Aberration-free ultrathin flat lenses and axicons at telecom wavelengths based on plasmonic metasurfaces. *Nano Letters*, *12*(9), 4932–4936. https://doi.org/10.1021/NL302516V/SUPPL_FILE/NL302516V_SI_001.PDF

Ali, F., & Aksu, S. (2021). A hybrid broadband metalens operating at ultraviolet frequencies. *Scientific Reports*, *11*(1), 1–8. https://doi.org/10.1038/s41598-021-81956-4

Aslan, E. (2021). Lensing for optical communication by diffraction from Peano curve-based fractal with alternative plasmonic material. *Optik*, *242*, 167072. https://doi.org/10.1016/J.IJLEO.2021.167072

Aslan, E., & Aslan, E. (2020). A Microlens by Gallium Doped Zinc Oxide-Nanoantenna. *Mühendislik Bilimleri ve Tasarım Dergisi*, *8*(3), 931–942. https://doi.org/10.21923/JESD.784056

Bayati, E., Pestourie, R., Colburn, S., Lin, Z., Johnson, S. G., & Majumdar, A. (2020). Inverse Designed Metalenses with Extended Depth of Focus. *ACS Photonics*, *7*(4), 873–878. https://doi.org/10.1021/ACSPHOTONICS.9B01703/ASSET/IMAGES/LARGE/PH9B01703_0004.JPEG

Chang, K. H., Chen, Y. C., Huang, Y. S., Hsu, W. L., Lu, G. H., Liu, C. F., Weng, C. J., Lin, Y. H., Chen, C. C., Lee, C. C., Chang, Y. C., Wang, P. H., & Wang, C. M. (2023). Axicon metalens for broadband light harvesting. *Nanophotonics*, *12*(7), 1309–1315. https://doi.org/10.1515/NANOPH-2023-0017/MACHINEREADABLECITATION/RIS

Ding, F., Wang, Z., He, S., Shalaev, V. M., & Kildishev, A. V. (2015). Broadband high-efficiency half-wave plate: A supercell-based plasmonic metasurface approach. *ACS Nano*, *9*(4), 4111–4119. https://doi.org/10.1021/ACSNANO.5B00218/SUPPL_FILE/NN5B00218_SI_001.PDF

Kesim, Y. E., Battal, E., & Okyay, A. K. (2014). Plasmonic materials based on ZnO films and their potential for developing broadband middle-infrared absorbers. *AIP Advances*, *4*(7). https://doi.org/10.1063/1.4887520/20698

Kildishev, A. V., Boltasseva, A., & Shalaev, V. M. (2013). Planar photonics with metasurfaces. *Science (New York, N.Y.)*, *339*(6125), 12320091–12320096. https://doi.org/10.1126/SCIENCE.1232009

Lee, Y., Zhang, J. X. J., & Alu, A. (2011). Efficient apertureless scanning probes using patterned plasmonic surfaces. *Optics Express*, *19*(27), 25990–25999. https://doi.org/10.1364/OE.19.025990

Mohtashami, Y., DeCrescent, R. A., Heki, L. K., Iyer, P. P., Butakov, N. A., Wong, M. S., Alhassan, A., Mitchell, W. J., Nakamura, S., DenBaars, S. P., & Schuller, J. A. (2021). Light-emitting metalenses and meta-axicons for focusing and beaming of spontaneous emission. *Nature Communications*, *12*(1), 1–7. https://doi.org/10.1038/s41467-021-23433-0

Ni, X., Emani, N. K., Kildishev, A. V., Boltasseva, A., & Shalaev, V. M. (2012). Broadband light bending with plasmonic nanoantennas. *Science*, *335*(6067), 427. https://doi.org/10.1126/SCIENCE.1214686/SUPPL_FILE/NI.SOM.PDF

Ni, X., Ishii, S., Kildishev, A. V., & Shalaev, V. M. (2013). Ultra-thin, planar, Babinet-inverted plasmonic metalenses. *Light: Science and Applications*, *2*(APRIL), e72. https://doi.org/10.1038/LSA.2013.28

Yu, N., Genevet, P., Aieta, F., Kats, M. A., Blanchard, R., Aoust, G., Tetienne, J. P., Gaburro, Z., & Capasso, F. (2013). Flat Optics: Controlling Wavefronts with Optical Antenna Metasurfaces. *IEEE Journal of Selected Topics in Quantum Electronics*, *19*(3). https://doi.org/10.1109/JSTQE.2013.2241399

Yu, N., Genevet, P., Kats, M. A., Aieta, F., Tetienne, J. P., Capasso, F., & Gaburro, Z. (2011). Light propagation with phase discontinuities: generalized laws of reflection and

refraction. *Science (New York, N.Y.)*, *334*(6054), 333–337. https://doi.org/10.1126/SCIENCE.1210713

Yu, X., Shen, Y., Dai, G., Zou, L., Zhang, T., & Deng, X. (2021). Phase-Controlled Planar Metalenses for High-Resolution Terahertz Focusing. *Photonics*, *8*(5), 143. https://doi.org/10.3390/PHOTONICS8050143

Multifocal Metalens with Titanium Nitride Aperiodic Nanoapertures for Fiber Optical Wavelengths

Büşra ERSOY[1]
Ekin ASLAN[2]
Erdem ASLAN[3]

Introduction

Plasmonic metasurfaces are nanotechnological structures that have been intensively studied and attracted significant interest in recent years. These structures are obtained by applying uniquely designed nano-scale patterns onto the surfaces of metals. Plasmonic metasurfaces enable efficient manipulation and control of electromagnetic waves called surface plasmon polaritons (SPPs). They are considered important materials and devices that offer various applications in terms of their optical, electronic, and magnetic properties (Ding et al., 2018). For instance, the manipulation of SPPs can be utilized in photonics circuits and optical communication systems to enable efficient signal transmission and processing. Moreover, plasmonic metasurfaces can play a significant role in the design of highly sensitive sensors, advanced imaging techniques, and enhanced absorptive or reflective surfaces(Kildishev et al., 2013; Yu & Capasso, 2014). Therefore, plasmonic metasurfaces offer significant potential in the development of future optoelectronic and nanophotonic devices.

Metalenses, on the other hand, have emerged as a new technology with the potential to replace traditional optical lenses. Metalenses perform focusing and imaging operations by manipulating light through nanostructures created by combining thin metal films and dielectric materials. These structures enable smaller sizes and higher resolutions compared to conventional lenses (Yu & Capasso, 2014). The potential of metalenses has sparked significant interest in various fields such as optical communications, biomedical imaging, artificial intelligence, and virtual reality (Khorasaninejad & Capasso, 2017).

In plasmonic applications, noble metals such as gold (Au) and silver (Ag) are commonly used. However, these designs are susceptible to high levels of optical losses due to a large number of free electrons and interband transitions. As a result, recent research has focused on alternative plasmonic materials such as doped silicon (Si), doped germanium (Ge), III-nitrides, and transparent conductive oxides. Most of these alternative plasmonic materials are semiconductors, and their main advantage lies in having fewer free electrons compared to metals, resulting in lower losses, particularly in the infrared (IR) wavelength range. These alternative plasmonic materials offer additional advantages over metals, including lower cost

[1] Büşra Ersoy, Student, Kayseri University, Department of Electrical and Electronics Engineering, ORCID: 0000-0003-1383-3311
[2]Ekin Aslan, Assoc. Prof, Kayseri University, Department of Electrical and Electronics Engineering, ORCID: 0000-0003-0933-7796
[3]Erdem Aslan, Assoc. Prof, Erciyes University, Department of Electrical and Electronics Engineering, ORCID: 0000-0001-6829-9000

and the ability to control plasma frequency through adjustable electron density (effective doping concentration) (Kesim, 2014).

Transition metal nitrides such as titanium nitride (TiN), zirconium nitride (ZrN), hafnium nitride (HfN), and tantalum nitride (TaN) also exhibit metallic properties and are classified as alternative plasmonic materials in the visible and IR (Naik et al., 2011). The primary advantage of these materials is their compatibility with Complementary Metal-Oxide-Semiconductor (CMOS) procedures. Additionally, they can be grown under nitrogen- or metal-rich conditions, resulting in films exhibiting metallic properties. Consequently, their plasma frequencies can be tuned.(Kesim, 2014).

The most advantageous characteristic of transition metal nitrides compared to noble metals is their non-refractory nature, which explains their thermal stability at temperatures above 2000°C. (Guler et al., 2014; Naik et al., 2013; Shaltout et al., 2016). Due to the low melting points and soft structures of traditional plasmonic metals, they can pose challenges in demanding operating conditions. As a solution, transition metal nitrides can be employed to realize nanophotonic devices that require operation at high temperatures. The optical properties of TiN are very similar to Au, exhibiting zero-crossing wavelengths in the visible range. This makes TiN plasmonic in the visible and near-infrared range.

The plasmonic properties of TiN have been experimentally demonstrated through the excitation of surface plasmon polaritons (SPPs) on TiN films in the literature. In a comparative study conducted in 2012 on the near-field distribution of TiN and Au spherical particles (Guler et al., 2012), the significance of TiN resonant nanostructures is highlighted. The local field enhancement of TiN particles is spectrally present in the important region known as the biological transparency window (650-950 nm). A lithographically fabricated array of TiN nanoparticles has been studied to demonstrate its potential for providing better heating efficiency compared to Au nanoparticles with the same geometries in the biological transparency window (Guler et al., 2013; Shaltout et al., 2016). In 2014, it is demonstrated that a TiN-based metasurface, consisting of patterned rectangular rings, achieved broad absorption in the visible and near-IR regions due to impedance matching and reduced reflection (Li et al., 2014). In this study, the effectiveness of TiN nanostructures is tested, and both absorbers exhibited high absorption when illuminated with a 5-second pulsed laser at 550 nm, compared to Au. Following laser illumination, TiN nanostructures are able to withstand high-intensity pulses where Au nanostructures failed. Beyond absorptivity, the refractory properties of TiN can provide highly efficient thermal emitters. Thermal emission from one-dimensional grating metamaterials based on TiN is investigated at working temperatures of approximately 540°C, resulting in mid-IR radiation centered around 3 μm (Liu et al., 2015). This study experimentally demonstrates that the thermal excitation of plasmon polaritons on the grating surface produces a well-collimated beam with a spatial coherence length of 32λ (angular divergence of 1.8°) and a maximum full width of 70 nm, which is quasi-monochromatic (Shaltout et al., 2016).

In this study, we are created various metamolecules by taking into account the geometric structure and angular arrangement of V-shaped metamolecules in the work of N. Yu et al., (2011) in order to generate phase gradients in the range of $[0,2\pi]$. In this context, alternative plasmonic based eight unit cells that provide phase manipulation in the full phase range are designed. The resonative behaviors of this nanoapertures in TiN layer on silicon nitride (SiN) membrane are numerically obtained. Simulations are carried out at a fiber optical wavelength

of 850 nm at which each cell is resonant. Then an aperiodic arrangement of the cells is numerically analyzed to create an interface phase profile required for the axicon focusing function. Given the constraints imposed by the technical infrastructure of the analyses, this proposed alternative plasmonic metalens design has led to the identification of multifocal points. Theoretical calculations have been employed to determine various focusing parameters for each focal point, including focal length, numerical aperture, depth of focus, focal spot width, and focal efficiency.

Method

The unit cells used to create the electromagnetic model of the proposed metasurface lens are presented in Figure 1. All analyses are performed for a operating wavelength of 850 nm. Each unit cell shares common geometric parameters, including the interior angle α of an equilateral geometry, the length d of the equilateral quadrilateral, the antenna width w, and the distance c between the open arms of the antennas. The geometric parameters for each nanoantenna in the Type 1 and Type 2 arrangements are provided in Table 1. Simulations are performed using the Finite-Difference Time-Domain (FDTD) method for the design of nanostructures. The dielectric function of TiN as an alternative plasmonic layer is obtained from (Naik et al., 2013) , which utilized the work of Boltasseva's team. The refractive index data for SiN membrane, on the other hand, is obtained from Vogt (2015). In the electromagnetic modeling of TiN, a Lorentz-Drude model is employed, which accounts for both the effects of free electrons and bound charges Drude-Lorentz parameters involve the characterization of optical properties of materials, such as refractive index, dielectric function, and dispersion behavior. These parameters are determined through the analysis of ellipsometry data, which provides information about the material's response to electromagnetic waves and plasmonic behavior. The specific values of Drude-Lorentz parameters can vary for each material and are typically reported in scientific research papers or technical literature. In the study by (Naik et al., 2013), Drude-Lorentz parameters for several alternative plasmonic materials, including TiN, are calculated. The dielectric function of the materials is approximately calculated using Equation 1 in the wavelength range of 350-2000 nm.

$$\varepsilon(\omega) = \varepsilon_b - \frac{\omega_p^2}{\omega(\omega + i\gamma_p)} + \frac{f_1\omega_1^2}{(\omega_1^2 - \omega^2 - i\omega\gamma_1)} \quad (1)$$

Here, while the second term stands for Drude model, the third one represents Lorentz oscillator.Here ε_b is the polarization response from the core electrons (background permittivity), ω_p is the plasma frequency, γ_p is the carrier relaxation rate, f_1 is the strength of the Lorentz oscillator, ω_1 the center frequency of the Lorentz oscillator, and γ_1 is the damping of the Lorentz oscillator. Thus, the optical properties of TiN (deposited at 500 °C) are taken as ε_b= 2.485, ω_p = 5.953 eV, γ_p= 0.5142 eV, f_1= 2.0376, ω_1= 3.9545 eV, γ_1=2.4852 eV (Naik et al., 2013).

The real and imaginary dielectric permittivities of TiN and similar materials, defined using the Lorentz-Drude model, are provided in Naik et al. (2011) and Naik et al. (2013). The wavelengths at which the real part of TiN's dielectric permittivity becomes negative are in the visible and infrared ranges. Therefore, TiN can be utilized as an alternative plasmonic material.

Unless otherwise specified, the thicknesses of the TiN and SiN layers are 50 nm and 100 nm, respectively.

Results and Discussion

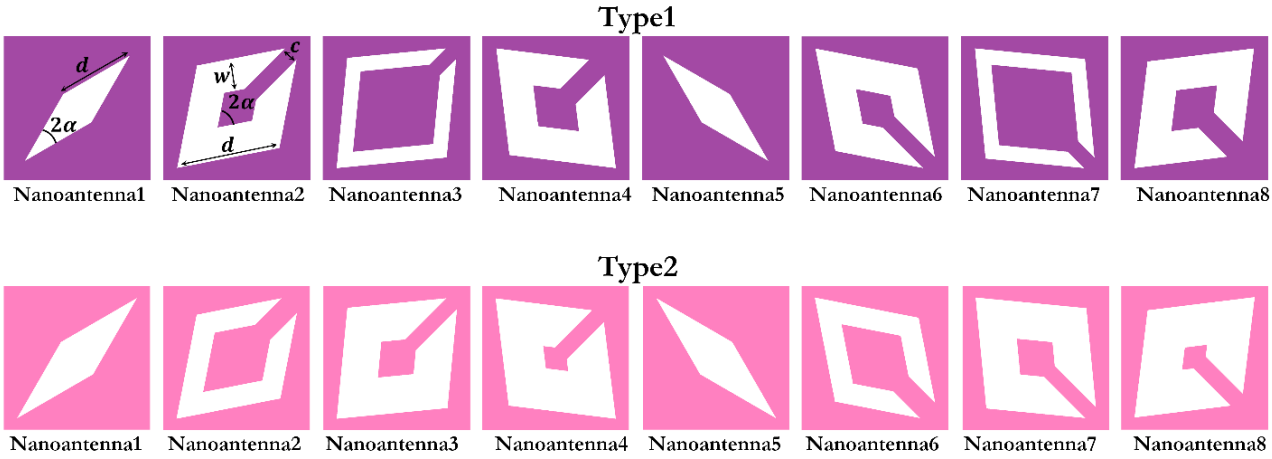

Figure 1- *Top views of metacells in each arrangement*

Table 1- *Geometrical parameters of Type1 and Type2 nanoantennas*

	Geometrical parameters	
	Type1	**Type2**
Nanoantenna1,5	d = 1000 nm, α = 15°	d = 1300 nm, α = 15°
Nanoantenna2,6	d = 1300 nm, w = 400 nm, c = 200 nm, α = 34°	d = 1000 nm, w = 200 nm, c = 200 nm, α = 34°
Nanoantenna3,7	d = 1500 nm, w = 200 nm, c = 200 nm, α = 39.5°	d = 1500 nm, w = 500 nm, c = 200 nm, α = 39.5°
Nanoantenna4,8	d = 1000 nm, w = 300 nm, c = 200 nm, α = 52°	d = 1300 nm, w = 500 nm, c = 200 nm, α = 52°

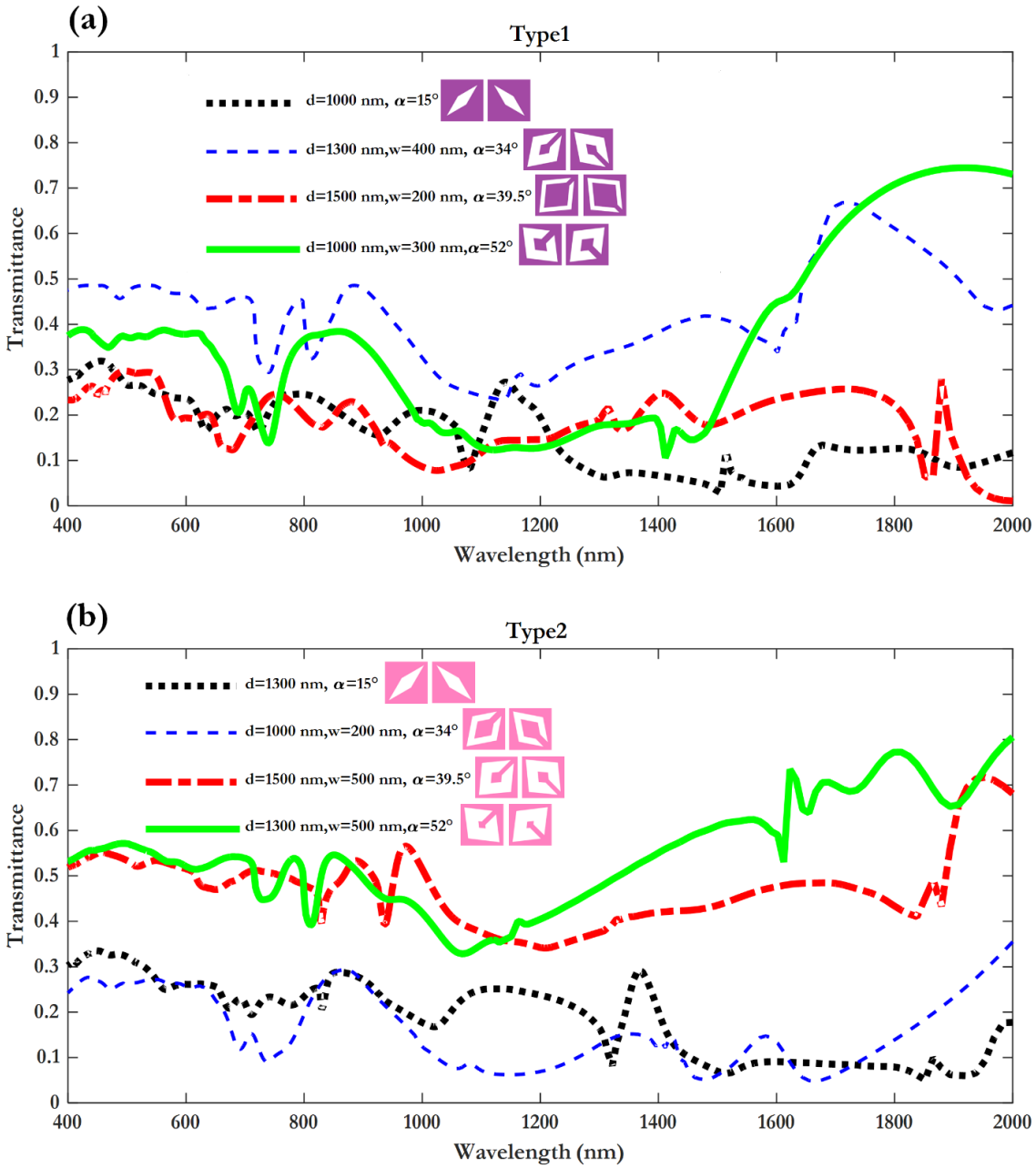

***Figure 2**. The transmittance analysis results of the antennas used in **(a)** Type1 arrangement and **(b)** Type2 arrangement.*

In the initial analyses, the transmittance of the structures is measured in the far field to investigate their resonant behavior at a wavelength of 850 nm. To determine the resonant behavior of the metamolecules, the periodic arrays of each metamolecule are analyzed. The periodicities, which are the repeating dimensions of the metamolecules in the x and y directions, were selected as P_x and P_y. The unit cell is illuminated with a plane wave of $x-$ polarized light propagating in the $z-$ direction, using a plane wave source positioned along the $z-$ axis of the system. Power meter transmittance monitors are placed to measure the power transmitted to the far-field regions of the structure. In the simulations, periodic boundary conditions along the $x-$ and $y-$ axes and perfectly matched layers along the $z-$ axis are employed. Figure 2 illustrates the transmittance monitor results for all nanocells belonging to the targeted array types. As shown in Figure 2, each unit cell exhibits resonance at a wavelength of 850 nm.

Two circular arrangements of the designed cells given in Figure 1, at equal radial distances are designed. In this way, circular phase rings in both arrangements that provide full phase transition on the metalens interface are formed. The arrangement images are provided in

Figure 3. To ensure physical interference between the cells, the distance between each arrangement trajectory is set to 100 nm, corresponding to the distance between the antennas. For better visual clarity, different colorings are presented for the Type 1 arrangement (Figure 3a) and the Type 2 arrangement (Figure 3b).

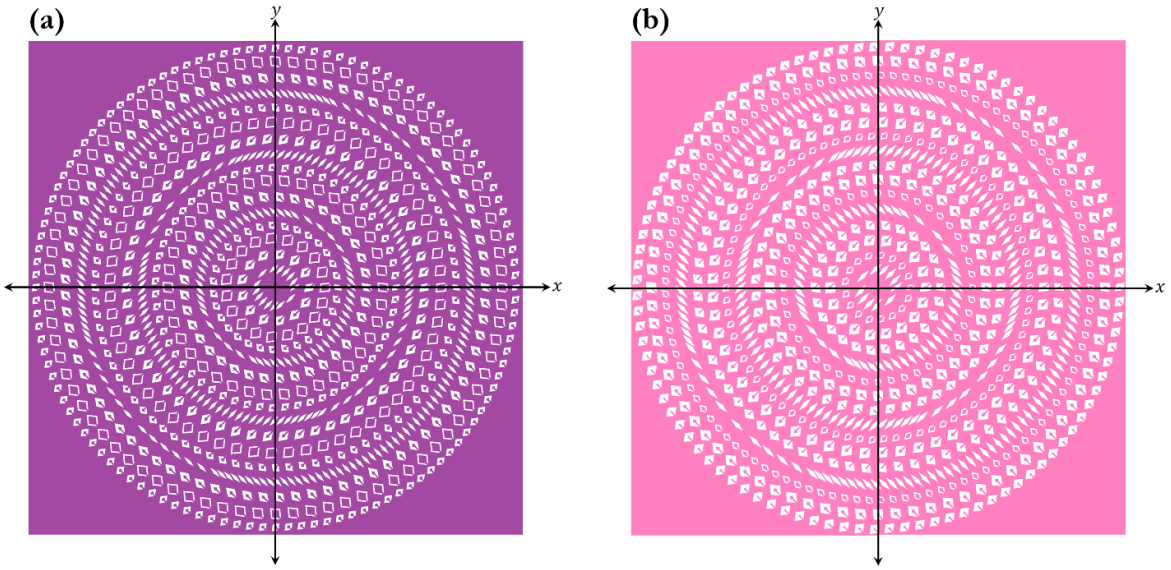

***Figure 3**- The arrangement of the antennas for **(a)** Type1 and **(b)** Type2*

In order to demonstrate the focusing performance of the structures in Figure 3, vertical monitors are placed along the $xz-$ axis. The distributions of normalized light intensity $\frac{|E|^2}{|E_{in}|^2}$, determined through the field distributions obtained from the monitors, are shown in Figure 4. The white dashed lines shown in the figure indicate the positions of the focal points determined as z_{1-10} for Type 1 and z_{1-7} for Type 2 along the $z-$axis. These analyses on the focusing performance demonstrate that both circular designs exhibit multiple focal points along the direction of light transmission. The focal distances for both designs are provided in Table 2 and Table 3. The focal points are determined as the most intense spots where the normalized light intensity exceeds 1.

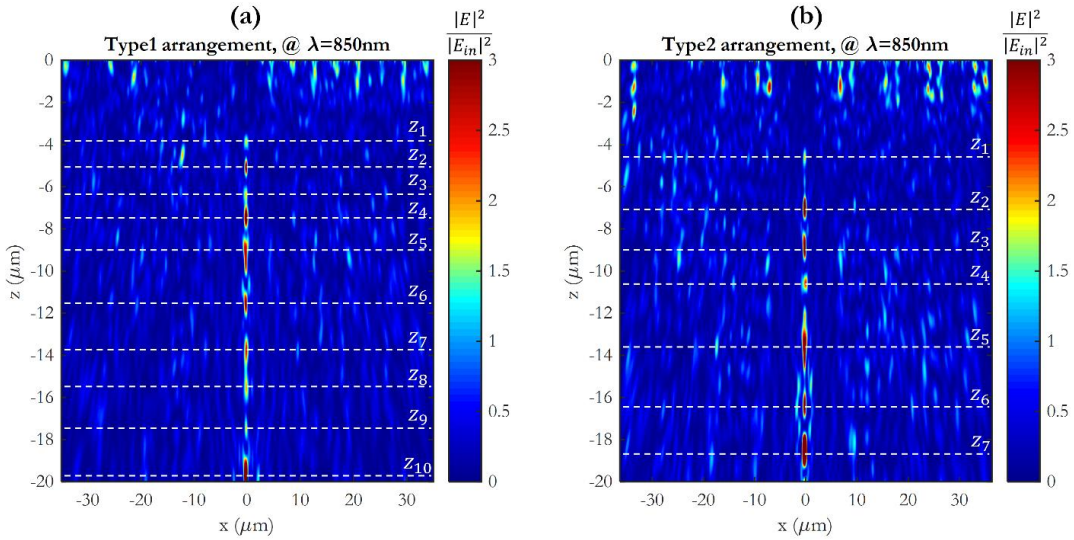

***Figure 4**- The normalized light intensity distributions along the focusing axis and polarization direction, for **(a)** Type1 and **(b)** Type2*

Table 2- *Focal lengths for Type1 arrangement*

Type1	
f_1	3.934 μm
f_2	5.15 μm
f_3	6.448 μm
f_4	7.516 μm
f_5	9.156 μm
f_6	11.6 μm
f_7	13.8 μm
f_8	15.61 μm
f_9	17.54 μm
f_{10}	19.79 μm

Table 3- *Focal lengths for Type2 arrangement*

Type2	
f_1	4.666 μm
f_2	7.082 μm
f_3	8.904 μm
f_4	10.65 μm
f_5	13.74 μm
f_6	16.45 μm
f_7	18.57 μm

To determine the other mentioned parameters related to the focusing performance, simulations are repeated by placing horizontal monitors extending along the xy −plane at the determined focal points. Through these types of analyses, the focal spot size and intensity distribution, apart from the focal distance, are intended to be determined. The normalized light intensity distributions at the focal points obtained from these monitors for Type 1 and Type 2 are shown in Figure 5 and Figure 6, respectively. Each panel in the figures represents the distribution at different focal points corresponding to the respective arrangement, and as observed, each axicon exhibits a highly narrow focal spot.

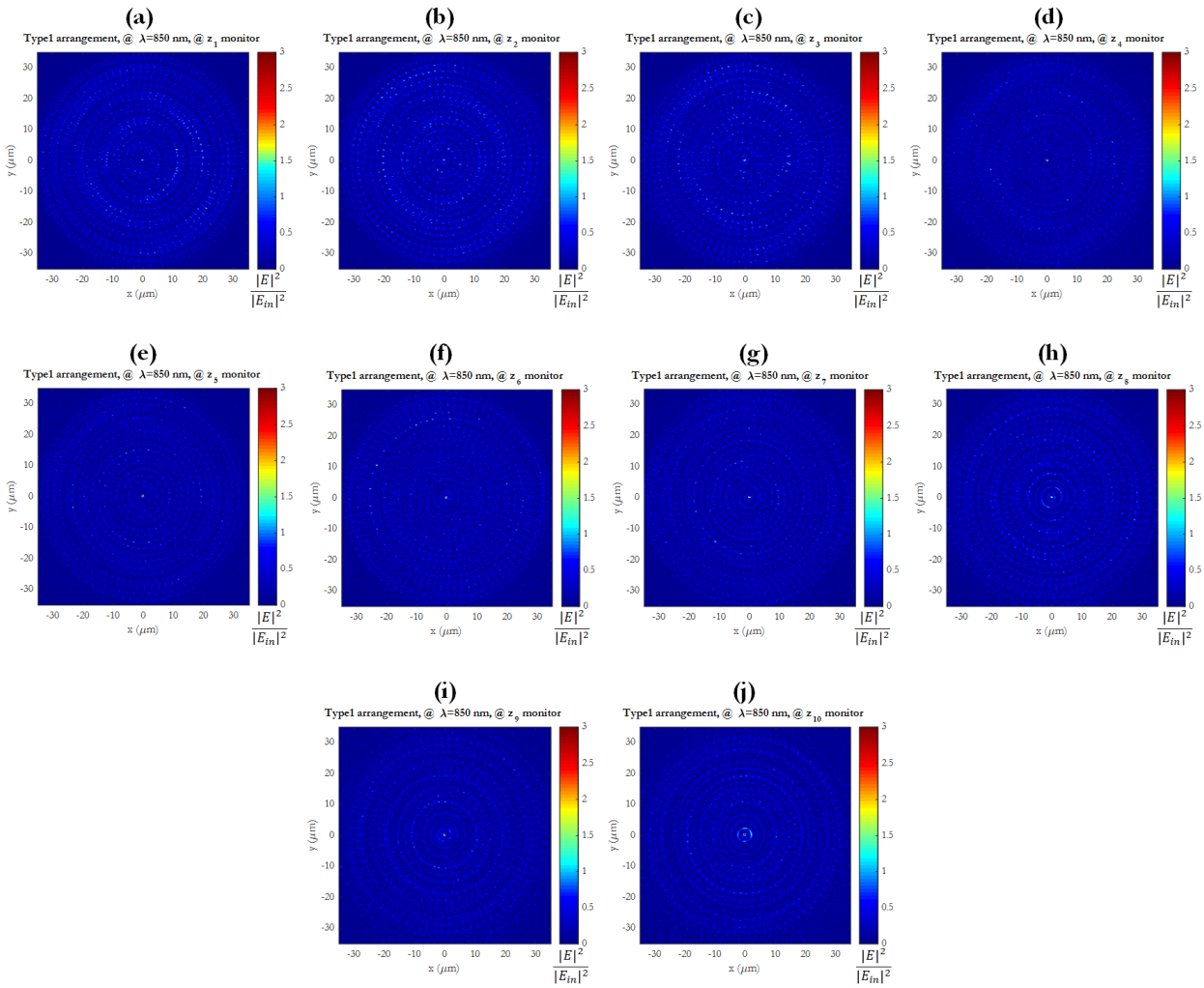

Figure 5- *The normalized light intensity distributions obtained from the focal planes for the Type1 arrangement: At* ***(a)*** $f_1 = 3.934\ \mu m$, ***(b)*** $f_2 = 5.15\ \mu m$, ***(c)*** $f_3 = 6.448\ \mu m$, ***(d)*** $f_4 = 7.516\ \mu m$, ***(e)*** $f_5 = 9.156\ \mu m$, ***(f)*** $f_6 = 11.6\ \mu m$, ***(g)*** $f_7 = 13.8\ \mu m$, ***(h)*** $f_8 = 15.61\ \mu m$, ***(i)*** $f_9 = 17.54\ \mu m$, *and* ***(j)*** $f_{10} = 19.79\ \mu m$.

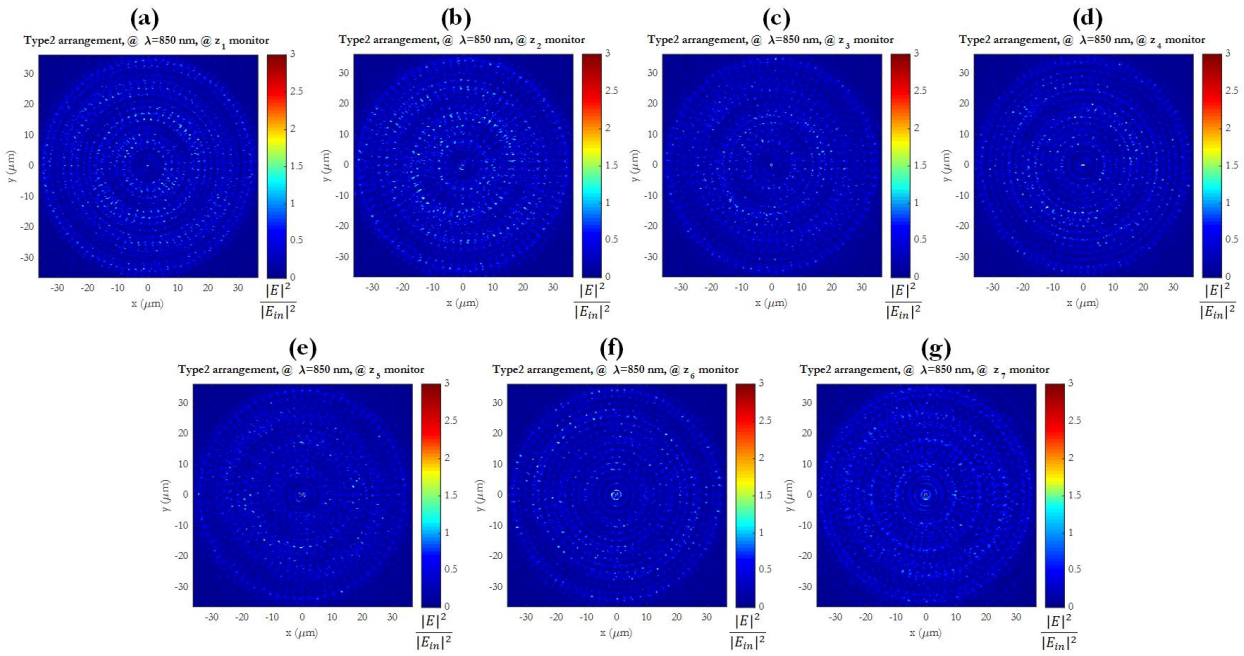

Figure 6. *The normalized light intensity distributions obtained from the focal planes for the Type2 arrangement: At* ***(a)*** $f_1 = 4.666\ \mu m$, ***(b)*** $f_2 = 7.082\ \mu m$, ***(c)*** $f_3 = 8.904\ \mu m$, ***(d)*** $f_4 = 10.65\ \mu m$, ***(e)*** $f_5 = 13.74\ \mu m$, ***(f)*** $f_6 = 16.45\ \mu m$, *and* ***(g)*** $f_7 = 18.57\ \mu m$.

The focusing parameters obtained from the simulations are described below, and the calculated values are presented in Table 4 and Table 5. The first focusing parameter is the numerical aperture (NA). NA is a parameter that determines the maximum resolution of the metalens and is calculated as follows:

$$NA = n * sin(\theta) \tag{2}$$

Here, n is the refractive index of the medium, and θ is the half-angle of the objective. This value determines how light will be refracted in the lens and influences the resolution of the lens (Aieta et al., 2012). The second parameter to be calculated is the Full Width at Half Maximum (FWHM). FWHM is the distance between two points that intersect half of the light intensity during the transition from one point to another. This distance determines the width of the light beam. FWHM is calculated as follows (Aslan & Aslan, 2020):

$$FWHM = \frac{\lambda}{2NA} \tag{3}$$

Here, λ represents the operation wavelength.

Table 4- *The focusing parameter values for the Type1 arrangement*

Lens Properties	Focusing Spot	Results
NA	f_1= 3.934μm	0.99
	f_2= 5.15 μm	0.99
	f_3=6.448 μm	0.98
	f_4=7.516 μm	0.98
	f_5=9.156 μm	0.97
	f_6=11.6 μm	0.95
	f_7=13.8 μm	0.93
	f_8=15.61 μm	0.91
	f_9=17.54 μm	0.89

	f_{10}=19.79 μm	0.87
FWHM	f_1= 3.934μm	0.43
	f_2= 5.15 μm	0.43
	f_3=6.448 μm	0.43
	f_4=7.516 μm	0.44
	f_5=9.156 μm	0.44
	f_6=11.6 μm	0.45
	f_7=13.8 μm	0.46
	f_8=15.61 μm	0.47
	f_9=17.54 μm	0.48
	f_{10}=19.79 μm	0.49
DOF	f_1= 3.934μm	0.01
	f_2= 5.15 μm	0.02
	f_3=6.448 μm	0.03
	f_4=7.516 μm	0.04
	f_5=9.156 μm	0.06
	f_6=11.6 μm	0.09
	f_7=13.8 μm	0.13
	f_8=15.61 μm	0.17
	f_9=17.54 μm	0.21
	f_{10}=19.79 μm	0.27
η(%)	f_1= 3.934μm	0.3
	f_2= 5.15 μm	0.6
	f_3=6.448 μm	0.4
	f_4=7.516 μm	0.8
	f_5=9.156 μm	0.7
	f_6=11.6 μm	0.6
	f_7=13.8 μm	0.5
	f_8=15.61 μm	0.4
	f_9=17.54 μm	0.2
	f_{10}=19.79 μm	1.5

Another important parameter is the depth of focus (DOF). DOF represents the distance over which objects can still be seen clearly beyond the focal point and is calculated as follows (Ali & Aksu, 2021):

$$DOF = 4\lambda \frac{f^2}{D^2} \tag{4}$$

Here, f represents the focal length, and D represents the diameter of the lens. (Bayati et al., 2020). The final important parameter is the focal efficiency η. Focal efficiency refers to how much of the collected light energy in the optical system is concentrated at the focal point. It is calculated by dividing the average light intensity in the focal spot by the average incident light intensity (Aslan, 2021):

$$\eta = \frac{\langle I_f \rangle}{\langle I_i \rangle} \tag{4}$$

Table 5- *The focusing parameter values for the Type2 arrangement*

Lens Properties	Focusing Spot	Results
NA	f_1=4.666 μm	0.99
	f_2=7.082 μm	0.98
	f_3=8.904 μm	0.97
	f_4=10.65 μm	0.96
	f_5=13.74 μm	0.94
	f_6=16.45 μm	0.91
	f_7=18.57 μm	0.89
FWHM	f_1=4.666 μm	0.43
	f_2=7.082 μm	0.43
	f_3=8.904 μm	0.44
	f_4=10.65 μm	0.44
	f_5=13.74 μm	0.45
	f_6=16.45 μm	0.47
	f_7=18.57 μm	0.48
DOF (μm)	f_1=4.666 μm	0.01
	f_2=7.082 μm	0.03
	f_3=8.904 μm	0.05
	f_4=10.65 μm	0.07
	f_5=13.74 μm	0.12
	f_6=16.45 μm	0.17
	f_7=18.57 μm	0.22
η(%)	f_1=4.666 μm	0.3
	f_2=7.082 μm	0.7
	f_3=8.904 μm	0.8
	f_4=10.65 μm	0.3
	f_5=13.74 μm	0.7
	f_6=16.45 μm	0.6
	f_7=18.57 μm	2.3

Conclusion

In this study including metalens designs as two different arrangements of split rhombus shaped metacells, multifocal behaviours are shown via numerical analyses. First the theoritical spectral transmittance of the cells are presented. Then, lensing performances of this flat-lens structures in two-type-arrangements are presented at a fiber optical wavelength 850 nm via ligth intensity distributions at focal points. The low efficiency values in multi-foci can be attributed to the absence of significantly high resonant transition values at 850nm. However, the sharing of light energy among multiple foci can also explain the lower focal efficiencies compared to single-focus studies in the literature. The obtained multi-foci are characterized by elongated elliptical focal spots in the direction of focusing, resembling axicon-like focal quality. This imparts light trapping capability to the metalens design.

Acknowledge

The work described in this study is supported by The Scientific and Technological Research Council of Turkey (TUBITAK− Project ID: 121E518).

References

Aieta, F., Genevet, P., Kats, M. A., Yu, N., Blanchard, R., Gaburro, Z., & Capasso, F. (2012). Aberration-free ultrathin flat lenses and axicons at telecom wavelengths based on plasmonic metasurfaces. *Nano Letters*, *12*(9), 4932–4936. https://doi.org/10.1021/NL302516V/SUPPL_FILE/NL302516V_SI_001.PDF

Ali, F., & Aksu, S. (2021). A hybrid broadband metalens operating at ultraviolet frequencies. *Scientific Reports 2021 11:1*, *11*(1), 1–8. https://doi.org/10.1038/s41598-021-81956-4

Aslan, E. (2021). Lensing for optical communication by diffraction from Peano curve-based fractal with alternative plasmonic material. *Optik*, *242*, 167072. https://doi.org/10.1016/J.IJLEO.2021.167072

Aslan, E., & Aslan, E. (2020). A Microlens by Gallium Doped Zinc Oxide-Nanoantenna. *Mühendislik Bilimleri ve Tasarım Dergisi*, *8*(3), 931–942. https://doi.org/10.21923/JESD.784056

Bayati, E., Pestourie, R., Colburn, S., Lin, Z., Johnson, S. G., & Majumdar, A. (2020). Inverse Designed Metalenses with Extended Depth of Focus. *ACS Photonics*, *7*(4), 873–878. https://doi.org/10.1021/ACSPHOTONICS.9B01703/ASSET/IMAGES/LARGE/PH9B01703_0004.JPEG

Ding, F., Yang, Y., Deshpande, R. A., & Bozhevolnyi, S. I. (2018). A review of gap-surface plasmon metasurfaces: Fundamentals and applications. *Nanophotonics*, *7*(6), 1129–1156. https://doi.org/10.1515/NANOPH-2017-0125/ASSET/GRAPHIC/J_NANOPH-2017-0125_FIG_005.JPG

Guler, U., Boltasseva, A., & Shalaev, V. M. (2014). Refractory Plasmonics. *Science*, *344*(6181), 263–264. https://doi.org/10.1126/SCIENCE.1252722

Guler, U., Naik, G. V., Boltasseva, A., Shalaev, V. M., & Kildishev, A. V. (2012). Performance analysis of nitride alternative plasmonic materials for localized surface plasmon applications. *Applied Physics B: Lasers and Optics*, *107*(2), 285–291. https://doi.org/10.1007/S00340-012-4955-3

Guler, U., Ndukaife, J. C., Naik, G. V., Nnanna, A. G. A., Kildishev, A. V., Shalaev, V. M., & Boltasseva, A. (2013). Local heating with lithographically fabricated plasmonic titanium nitride nanoparticles. *Nano Letters*, *13*(12), 6078–6083. https://doi.org/10.1021/NL4033457

Kesim, Y. E. (2014). *Ald grown zno as an alternative material for plasmonic and uncooled infrared imaging applications* [Bilkent University]. https://core.ac.uk/display/52926405?source=1&algorithmId=15&similarToDoc=52923596&similarToDocKey=CORE&recSetID=80bf561f-4d80-4a6e-beb8-58278a16672c&position=4&recommendation_type=same_repo&otherRecs=480563030,154803930,52936873,52926405,52926415

Khorasaninejad, M., & Capasso, F. (2017). Metalenses: Versatile multifunctional photonic components. *Science (New York, N.Y.)*, *358*(6367). https://doi.org/10.1126/SCIENCE.AAM8100

Kildishev, A. V., Boltasseva, A., & Shalaev, V. M. (2013). Planar photonics with metasurfaces. *Science (New York, N.Y.)*, *339*(6125), 12320091–12320096. https://doi.org/10.1126/SCIENCE.1232009

Liu, J., Guler, U., Lagutchev, A., Kildishev, A., Malis, O., Boltasseva, A., Shalaev, V. M., S Tigran, M. I., Shahbazyan, V., Springer, A., Greffet, J. J., Carminati, R., Joulain, K., Mulet, J. P., Mainguy, S., & Chen, Y. (2015). Quasi-coherent thermal emitter based on refractory plasmonic materials. *Optical Materials Express*, *5*(12), 2721–2728. https://doi.org/10.1364/OME.5.002721

Li, W., Guler, U., Kinsey, N., Naik, G. V., Boltasseva, A., Guan, J., Shalaev, V. M., & Kildishev, A. V. (2014). Refractory Plasmonics with Titanium Nitride: Broadband

Metamaterial Absorber. *Advanced Materials*, *26*(47), 7959–7965. https://doi.org/10.1002/ADMA.201401874

Naik, G. V., Kim, J., & Boltasseva, A. (2011). Oxides and nitrides as alternative plasmonic materials in the optical range. *Optical Materials Express*, *1*(6). http://arxiv.org/abs/1108.0993

Naik, G. V., Shalaev, V. M., & Boltasseva, A. (2013). Alternative plasmonic materials: beyond gold and silver. *Advanced Materials (Deerfield Beach, Fla.)*, *25*(24), 3264–3294. https://doi.org/10.1002/ADMA.201205076

Shaltout, A. M., Kinsey, N., Kim, J., Chandrasekar, R., Ndukaife, J. C., Boltasseva, A., & Shalaev, V. M. (2016). Development of Optical Metasurfaces: Emerging Concepts and New Materials. *Proceedings of the IEEE*, *104*(12), 2270–2287. https://doi.org/10.1109/JPROC.2016.2590882

Vogt, M. R. (2015). Development of physical models for the simulation of optical properties of solar cell modules [Gottfried Wilhelm Leibniz Universität Hannover]. In *Gottfried Wilhelm Leibniz Universität Hannover*. https://doi.org/10.15488/8592

Yu, N., & Capasso, F. (2014). Flat optics with designer metasurfaces. *Nature Materials 2014 13:2*, *13*(2), 139–150. https://doi.org/10.1038/nmat3839

Yu, N., Genevet, P., Kats, M. A., Aieta, F., Tetienne, J. P., Capasso, F., & Gaburro, Z. (2011). Light propagation with phase discontinuities: generalized laws of reflection and refraction. *Science (New York, N.Y.)*, *334*(6054), 333–337. https://doi.org/10.1126/SCIENCE.1210713

Using Artificial Intelligence Methods in Performance Evaluation of Sales Personnel Working in the Savings Finance Sector

Cengiz SERTKAYA[1]
Zekeriya KÖSE[2]

Introduction

The relationships that companies establish with their customers are one of the most important factors that increase the competitiveness of the company in the competitive conditions of the market. Good relations ensure growth and increase in the share obtained in the market. At the same time, as the trust and loyalty of the customers to the company increase, the loyalty between them causes the formation of permanent customer groups over time (Özdağoğlu et al., 2010). In this process, sales personnel are at the forefront of the groups that work closely with the customers.

Sales personnel are in the middle layer between the company and the customer, who can communicate directly with the customer due to their duties. New campaigns and products created by companies can be delivered to customers quickly through sales personnel. During this communication, with the question-answer method, the customer asks the questions that come to his mind directly, and due to the acceleration of the decision-making process, it is ensured that he is quickly included in the campaigns or the sale of the products.

The role of sales personnel is very important for companies working in the savings finance sector. Targets are set several times a year for the expected performance of sales personnel. Both performance targets and processes related to the course of performance are followed by customer relationship management systems (CRM) or resource planning systems (ERP) (Calixto & Ferreira, 2020). It is extremely important to determine whether the targets set will be achieved through data analysis checks carried out at intervals before the end of the year, and to take the necessary measures in order to achieve the year-end targets. Considering the different sales targets, different qualifications and the large number of sales personnel working in the company, the diversity of analysis makes the solution of the problem difficult and becomes a process that is too complex and time-consuming to be solved with human skills. In such cases, artificial intelligence-based computer systems with human-like decision-making capabilities but higher processing capacity and long-term performance are needed.

It is known that the number of studies in the literature on the prediction of the performance of sales personnel is quite low (Sohrabpour et al., 2021; Verstraete et al., 2020). It has been observed that the existing studies are generally focused on data mining processes and finding the most suitable classification model for the business structure in a way that will maximize the profitability level in the examined area (Cheriyan et al., 2019).

In a study, a probabilistic latent semantic indexing model (SPLSA), which can make an emotion-based evaluation based on customer feedback, was created for the prediction of sales performance (Yu et al., 2012).

In another study, data obtained between October 2013 and March 2014 were used for the performance analysis of 53 employees. It has been stated that the features that affect performance focus on training, bonuses and promotions.

[1] Cengiz SERTKAYA, Istanbul Topkapi University, Computer Engineering Department,
[2] Zekeriya KÖSE, Eminevim, IT Application Solutions Department,

In a study, criteria other than classical features such as weekly sales, air temperature, fuel price were used to estimate the sales performance of 99 different departments. According to the results obtained, it was stated that the long-short-term memory (LSTM) deep learning model was the most successful model.

In another study, three different regression models, namely multiple linear, elastic-net and polynomial, were created for the performance prediction of sales personnel working in Wallmart. The performance of the models was evaluated by R2 and RMSE calculations. Since the multiple linear regression model obtained 0.93 R2 and the smallest RMSE values, it was determined as the best estimation model (Chen, 2023).

In another study, decision tree (DCT), gradient reinforcement tree (GBT), k-nearest neighbor (KNN) and random forest (RF) artificial intelligence models were created to examine the number of assets that a company will have in the future from growth indicators. In the study using 1224 data, the most successful model was GBT with an accuracy value of 96.67% (Chaising et al., 2023).

In another study, sales performances for the next 5 years were estimated over the sales data collected between 2015-2017 for sales performance forecasting. Generalized linear model (GLM), decision tree and gradient strengthening tree methods from machine learning algorithms were used. The GBT model was the most successful model with an accuracy rate of 98% (Cheriyan et al., 2019).

In this study, analyzes were made on the sales data of Eminevim, which is the leader in the savings finance sector, using data mining methods, and an artificial intelligence-based model that can make forward-looking sales forecasts is proposed.

Method

In the model development processes of the study, a process such as data acquisition, preparation, analysis and model establishment was followed.

A.Data Collection

The dataset used in the study was examined by bringing together various tables from the CRM application database of the sales data of Eminevim company for the January 2021-December 2022 time interval. In the selection of the criteria to be used in the performance evaluation of the sales personnel, the literature suggests that the sources should be examined in two groups as qualitative and quantitative (Dinçer et al., 2012). While the qualitative criteria cover features such as the technical competencies of the person and the success in communication with the customer, the quantitative criteria consist of the extra-task efforts and activities he has shown, such as the trainings he received to improve himself, the customer visit plans, with the features containing numerical data on his performance in the first place. The criteria examined in this study are shown in Table 1.

Table 1 – Dataset Attributes

#	Attribute	Description
1	Education level	Education level of personnel
2	Promotion count	Total promotion count
3	Comment count	Total comment count
4	Visit count	Total visit count
5	Bonus count	Total bonus count
6	Customer count	Number of customers in portfolio
7	Training count	Total training count
8	Sales volume	Total sales volume in a month

Here, features 1-7 show the input feature, and feature 8 shows the output feature to be predicted. On the dataset, due to the data privacy policy of the institution, the sales information of some sales personnel was randomly removed from the dataset and the sales volume data, which is the output information, was anonymized by normalizing the remaining data between 0-1. Here, the formula used for the normalization process is given in Equation 1 (Aksu et al., 2019).

$$X_{nor} = \left(\frac{X_i - X_{min}}{X_{max} - X_{min}}\right) \quad (1)$$

B.Data Analysis

One of the important steps in the analysis of the collected data is to examine their distribution over time. Ensuring the correct distribution is among the important information that shows the quality and data diversity of the dataset. For this reason, the percentages of the number of data per year and quarters in the year are calculated and given in Table 2.

Table 2 – Dataset Distribution by Quarters

	Year	
Quarter	2021	2022
1	%12	%10
2	%14	%12
3	%12	%10
4	%10	%10

When the distribution of the data was examined, it was seen that a homogeneous distribution was achieved between the periods. In the next process, the analysis of the relationship levels of the input and output features planned to be used in the learning process of the models was made. This analysis method, which is called principal component analysis (PCA) in the literature, is important in order to see the connection levels and aspects of the output feature and input features (Oliveira-Esquerre et al., 2002a). For this purpose, many analysis methods are suggested in the literature (Sertkaya & Yurtay, 2018), one of the methods proposed within the scope of this study, the correlation matrix whose formula is given in Equation 2 was used (Everitt & Dunn, 2001).

$$K(X,Y) = \frac{E[(X-\mu_x)\times(Y-\mu_y)]}{\sigma_x \sigma_y} \quad (2)$$

Here, X is the input, Y is the output property, E is the expected value operator, μ_x and μ_y are the expected values, and σ_x and σ_y are the standard deviation values.

The TBA value varies between -1 and 1, decreases as it approaches 0, and increases as it approaches -1 and 1. The obtained correlation matrix results between input and output properties are given in Table 3.

Table 3 – Correlation Results

	Output
Inputs	Sales volume
Education level	-0.25
Promotion count	0.56
Comment count	0.42
Visit count	0.35
Bonus count	0.37
Customer count	0.40
Training count	-0.15

According to the TBA results, it is seen that the number of promotions, comment score, number of interviews, number of premiums and number of customers are positively related to sales volume, while education level and number of education attributes have a negative relationship. The relationship level of the number of promotions and comment score features is quite high.

PCA is also known as the feature reduction procedure (Oliveira-Esquerre et al., 2002b). This process is performed by removing the features whose PCA values are below a determined level from the dataset. In this way, training of models with fewer features can be achieved more quickly. At this stage, the features with a PCA value of 0.25 and above recommended in the literature were selected to be applied to the model in the next stage (TDS, n.d.). In this case, the number of training feature is removed from the dataset.

After the dataset was finalized, the dataset was divided into two sub-datasets, 80% training and 20% testing, in order to establish the artificial intelligence model to be developed and conduct real tests, and the dataset processes were completed.

C. Gradient Boost Tree Model

Collective learning is one of the features inherent in decision trees that combine multiple sub-learners and allow many simultaneous predictions. With this feature, the probability of finding a successful result is quite high. Gradient strengthening decision trees (GBT), on the other hand, increase the number of branches that produce successful results by improving the bad result branches produced by classical decision trees. When the results produced by the branches are brought together, the overall result of the system is formed by the combination of many successful results, and a system response is produced in which the problem is addressed and comprehended from many perspectives. Figure 1 shows the general structure of GBT trees (Shoaran et al., 2018).

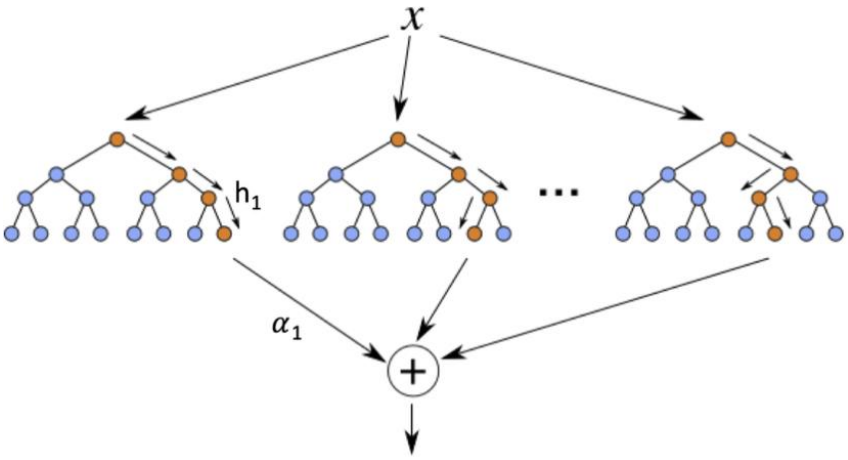

Figure 1 – General structure of GBT tree(Shoaran et al., 2018)

XGBoost library in Python language was used in the implementation of the GBT algorithm. It is extremely important to set the parameter values required for the algorithm to work efficiently (XG, n.d.). This ensures the optimization of the model, prevents memorization problems and shortens the learning time (ABG, n.d.). The values given in Table 4, which gave the best results in the simulation trials after the model was set up, were selected for the GBT model.

Table 4 – Parameter Values of GBT Model

Parameter	Value
Base score	0.5
Colsample by node	1
Colsample by tree	1
Importance type	gain
Learning rate	0.3
N estimators	500
Num parallel tree	1
Sub sample	0.8
Gamma	0

Results

As a result of the simulation of the GBT model trained to predict the performance of the sales personnel with the test data, the prediction values were obtained for each test data as shown in Figure 2.

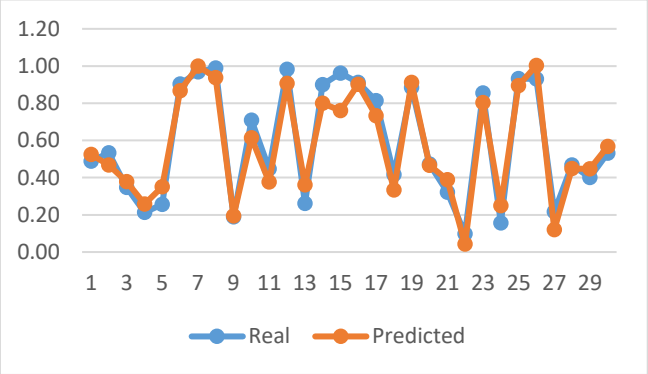

Figure 2 – Real and Predicted Values of GBT Model

As can be seen from the figure, it is understood that the actual value and the predicted values produced by the model are compatible with each other and the proposed model gives consistent results for the problem.

In order to evaluate the overall system success of the GBT model, the accuracy calculations commonly used in the literature were made according to the formula in Equation 3 (Sertkaya et al., 2023).

$$D = \left(\frac{O_i - E_{ort}}{O_i}\right) * 100 \quad (3)$$

Here, D is the accuracy value, O_i is the expected range of the predicted and true value, and E_{ort} is the mean of their differences.

After the accuracy calculation, the success of the proposed model was obtained as 92%.

Conclusion

Within the scope of this study, important criteria have been revealed to be used in the evaluation of the performance of sales personnel for companies operating in the field of savings finance. Sales are extremely important as they are among the primary needs for the growth of companies in this sector. For this purpose, the data of the years 2021 and 2022 belonging to Eminevim, which is the leader of the sector, was used. Considering the up-to-dateness of the selected data and the company's extensive branch infrastructure in Turkey, a very important dataset in terms of sampling the sector has been used within the scope of the study.

In the study, the steps applied in order to be ready for artificial intelligence models on the dataset are explained in detail.

The gradient reinforced decision tree model, which is one of the successful models in the literature on sales performance, was used in this study. It is stated with which parameters the model should be constructed for this kind of problem.

In order to measure the success of the GBT model, the accuracy values were calculated and according to the results obtained, it was shown that the proposed model is a successful model that can be used in the performance estimation of sales personnel for companies operating in the savings finance sector.

In future studies, different datasets and artificial intelligence methods can be used. Evaluations can be made by comparing the results obtained from the studies with the results of this study.

References

ABG. (n.d.). *A Beginner's guide to XGBoost. This article will have trees…. lots of… | by George Seif | Towards Data Science*. Retrieved May 24, 2023, from https://towardsdatascience.com/a-beginners-guide-to-xgboost-87f5d4c30ed7

Aksu, G., Güzeller, C. O., & Eser, M. T. (2019). The Effect of the Normalization Method Used in Different Sample Sizes on the Success of Artificial Neural Network Model. *International Journal of Assessment Tools in Education*, *6*(2), 170–192. https://doi.org/10.21449/IJATE.479404

Calixto, N., & Ferreira, J. (2020). Salespeople Performance Evaluation with Predictive Analytics in B2B. *Applied Sciences 2020, Vol. 10, Page 4036*, *10*(11), 4036. https://doi.org/10.3390/APP10114036

Chaising, S., Syukur, M., & Nithibandanseree, P. (2023). Comparison of Machine Learning Algorithms for Prediction of Total Assets. *2023 International Conference on Cyber Management and Engineering, CyMaEn 2023*, 255–259. https://doi.org/10.1109/CYMAEN57228.2023.10051085

Chen, Z. (2023). Sales Forecast of Walmart on Account of Multivariate Regression and Machine Learning Methods. *Proceedings of the International Conference on Financial Innovation, FinTech and Information Technology, FFIT 2022, October 28-30, 2022, Shenzhen, China*. https://doi.org/10.4108/EAI.28-10-2022.2328455

Cheriyan, S., Ibrahim, S., Mohanan, S., & Treesa, S. (2019). Intelligent Sales Prediction Using Machine Learning Techniques. *Proceedings - 2018 International Conference on Computing, Electronics and Communications Engineering, ICCECE 2018*, 53–58. https://doi.org/10.1109/ICCECOME.2018.8659115

Dinçer, B., Dinçer, C., Üniversitesi, G., İdari, İ., Fakültesi, B., Bölümü, İ., & Görevlisi, A. (2012). Satış Elemanı Performans Değerlemesinde Bir Öneri: Üçgensel Performans Değerleme Yöntemi. *Öneri Dergisi*, *9*(35), 163–171. https://doi.org/10.14783/OD.V9I35.1012000268

Everitt, Brian., & Dunn, Graham. (2001). *Applied multivariate data analysis*. https://www.wiley.com/en-us/Applied+Multivariate+Data+Analysis%2C+2nd+Edition-p-9780470711170

Oliveira-Esquerre, K. P., Mori, M., & Bruns, R. E. (2002a). Simulation of an industrial wastewater treatment plant using artificial neural networks and principal components analysis. *Brazilian Journal of Chemical Engineering*, *19*(4), 365–370. https://doi.org/10.1590/S0104-66322002000400002

Oliveira-Esquerre, K. P., Mori, M., & Bruns, R. E. (2002b). Simulation of an industrial wastewater treatment plant using artificial neural networks and principal components analysis. *Brazilian Journal of Chemical Engineering*, *19*(4), 365–370. https://doi.org/10.1590/S0104-66322002000400002

Özdağoğlu, A., Özdağoğlu, G., & Öz, E. (2010). Müşteri Sadakatinin Sağlanmasında Müşteri Ilişkileri Yönetiminin Önemi: Izmir'de Bir Hipermarket Araştırması. In *Atatürk Üniversitesi İktisadi ve İdari Bilimler Dergisi* (Vol. 22, Issue 1, pp. 367–388). Atatürk Üniversitesi. https://dergipark.org.tr/tr/pub/atauniiibd/issue/2693/35450

Sertkaya, C., Köse, Z., Mühendisliği Bölümü, B., Fakültesi, M., Topkapı Üniversitesi, İ., & Uygulama Çözümleri Bölümü, B. (2023). Yapay Zeka ile Tasarruf Finansmanı Sektörü Firmalarının Sosyal Medya Etkinliklerinin Tahmin Edilmesi. *International Journal of Advanced Natural Sciences and Engineering Researches*, *7*(3), 109–114. https://doi.org/10.59287/IJANSER.377

Sertkaya, C., & Yurtay, N. (2018). Artificial immune system based wastewater parameter estimation. *Turkish Journal of Electrical Engineering and Computer Sciences*, *26*(6), 3356–3366. https://doi.org/10.3906/elk-1503-206

Shoaran, M., Haghi, B. A., Taghavi, M., Farivar, M., & Emami-Neyestanak, A. (2018). Energy-efficient classification for resource-constrained biomedical applications. *IEEE Journal on Emerging and Selected Topics in Circuits and Systems*, *8*(4), 693–707. https://doi.org/10.1109/JETCAS.2018.2844733

Sohrabpour, V., Oghazi, P., Toorajipour, R., & Nazarpour, A. (2021). Export sales forecasting using artificial intelligence. *Technological Forecasting and Social Change*, *163*, 120480. https://doi.org/10.1016/J.TECHFORE.2020.120480

TDS. (n.d.). *Understanding Principal Component Analysis | by Trist'n Joseph | Towards Data Science*. Retrieved May 24, 2023, from https://towardsdatascience.com/understanding-principal-component-analysis-ddaf350a363a

Verstraete, G., Aghezzaf, E. H., & Desmet, B. (2020). A leading macroeconomic indicators' based framework to automatically generate tactical sales forecasts. *Computers & Industrial Engineering*, *139*, 106169. https://doi.org/10.1016/J.CIE.2019.106169

XG. (n.d.). *XGBoost Nasıl Çalışır? Neden İyi Performans Gösterir? - Veri Bilimi Okulu - Veri Bilimi Okulu*. Retrieved May 24, 2023, from https://www.veribilimiokulu.com/xgboost-nasil-calisir/

Yu, X., Liu, Y., Huang, X., & An, A. (2012). Mining online reviews for predicting sales performance: A case study in the movie domain. *IEEE Transactions on Knowledge and Data Engineering*, *24*(4), 720–734. https://doi.org/10.1109/TKDE.2010.269

Data Privacy In Big Data: Federated Learning

Büşra BÜYÜKTANIR [1]
Buket DOĞAN[2]

INTRODUCTION

In today's world, with internet-based evolving technologies, both the users utilizing these technologies and the objects resulting from these technologies are constantly generating data (Lee vd., 2015: 18-23). These big data produced are utilized in numerous sectors such as security, education, healthcare, research, and development, as well as the institutions and organizations associated with these sectors. Governments, institutions, and organizations that witness improvements in various aspects such as speeding up business processes, reducing costs, and providing benefits in terms of analysis and statistical significance invest more in the field of big data. Data, when in piles, become more meaningful after processing unpredictable situations. Thus, governments, institutions, and organizations utilizing meaningful data can conduct a situation analysis and make more accurate predictions for the future. The correct utilization of data in this manner leads to increased revenue and enrichment of business sectors (Atalay vd., 2017: 155-172).

On the other hand, the privacy of personal data contained within the generated data is of great importance (Zhou vd., 2015: 2147-2152). Data stored on servers or shared for processing brings along security issues in order to ensure data privacy. Countries have taken precautionary measures in the form of laws to ensure security. The General Data Protection Regulation (GDPR) and the Personal Data Protection Law (KVKK) restrict the processing of personal information by others without the individual's consent. However, relying solely on legal measures is insufficient to ensure security (Gökçay ve Arda, 2019: 218-227). Technological solutions are needed in practical terms to achieve security.

Big data is the raw material for artificial intelligence, machine learning, and deep learning (Kayaalp ve Süzen, 2018: 25-28). In recent years, these fields have been rapidly developing and still evolving (Abadi vd., 2016: 265-283). The quantity and diversity of data that influence decision-making processes are of great importance in order to produce results that are closest to the truth (Aktan, 2018: 1-22). These technological methods used to process and make data meaningful contribute to the development of applications concerning the security of personal data. Federated learning, a new-generation artificial intelligence approach, ensures data privacy and enables the generation and sharing of big data (Bagdasaryan vd., 2020: 2938-2948).

In this study, the federated learning architecture, which has been developed to ensure data privacy and security in big data, is examined. Federated learning allows the models to be trained on the data where they are generated, without the need to send the data to a central server. Instead, the models are sent to the server after training and then distributed back to each participant. In other words, the machine learning model is executed at the location where the data is generated, and the data is not transferred to another location. Processing the data where it resides eliminates concerns regarding data privacy.

[1] Büşra Büyüktanır, RA, Marmara University, Computer Engineering
[2] Buket Doğan, Assoc. Prof., Marmara University, Computer Engineering

The remainder of the study is organized as follows: Detailed explanations of big data and federated learning concepts are provided, along with a comprehensive examination of the use of federated learning for big data. Relevant studies from the literature on the subject are discussed. Finally, the obtained results are evaluated.

Big Data and Federated Learning

Big Data.

With the development of information and communication technologies, internet technologies such as social media applications, web pages, blogs, sensors, etc., provide the opportunity to collect big data. The diversity and volume of rapidly collected data have led to the emergence of the concept of big data (Sagiroglu ve Sinanc, 2013: 42-47). Big data refers to large-scale, diverse, and abundant datasets that are collected at high speed from various sources. The term "3V" is commonly used to describe the three main characteristics of big data: volume, velocity, and variety. Volume represents the size of large data sets, variety encompasses the use of different data types such as images, text, videos, and velocity denotes the rapid collection and processing of data.

Big datasets collected through internet websites, web-based applications, social media, sensors, etc. can be utilized in various fields such as banking, healthcare, education, marketing, public relations, security, logistics, agriculture, and more. Different techniques such as data mining, machine learning, artificial intelligence, and other advanced analytical technologies are employed for data collection, processing, preparation, accessibility, storage, and analysis. These techniques enable businesses, organizations, and researchers to extract valuable information from big data sets, offering a deeper understanding and a competitive advantage. They facilitate making better decisions, identifying trends, analyzing customer behavior, making predictions, discovering relationships, and developing innovative solutions.

Institutions and individuals that fail to adapt to big data find themselves at a disadvantage in the face of rapid data growth and advancing technologies. Those who can effectively harness big data, however, gain a competitive advantage by improving their business processes and conducting more efficient research, development, and implementation activities (Özdemir ve Sağıroğlu, 2018: 470-480).

Big data is utilized by following the stages of data collection, storage, cleansing, analysis, interpretation, and decision-making and implementation. Throughout these stages, ensuring the security and confidentiality of data plays a significant role. Federated learning technology has emerged to preserve data privacy in big data by safeguarding data security and confidentiality (Zhang vd., 2022: 1-8).

Federated Learning.

Federated learning is a technology developed for client-server systems (Kairouz vd., 2021: 1-210). With this technology, data is not sent from clients/users/edges to the server, but rather analyzed here. Data is not shared with clients; instead, local model training is performed. The weights of each model trained by the clients are combined and sent to the server. By combining the model weights sent to the server, a final model is created (Süzen ve Kayaalp, 2019: 297-304). Thus, by performing local model training and not sharing data, data privacy is ensured. Additionally, sending models from clients to the server instead of data reduces network traffic and communication costs, enabling fast communication with low energy consumption. Figure 1 illustrates the functioning of the federated learning architecture.

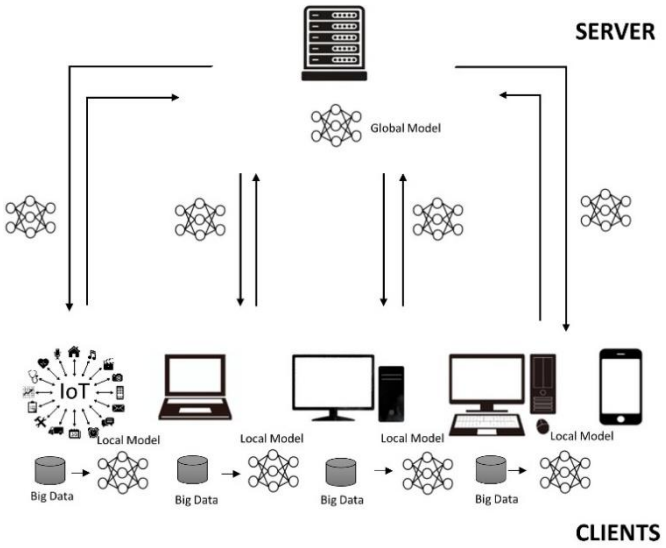

Figure 1. *The functioning of the federated learning architecture.*

When it comes to the data sources generated and utilized during model training, the federated learning method is divided into two types based on the number of clients involved: cross-device federated learning and cross-silo federated learning (Huang vd., 2022: 2206.12949).

Cross-device federated learning enables the use of smartphones, wearable devices, and similar devices as clients, where the data generated by these devices are used for model training. Since the data produced by each individual client may be limited, a large number of clients is required for successful model training. Therefore, the number of clients, i.e., users utilizing these devices, can reach millions. Mobile device applications can be given as an example.

Cross-silo federated learning is employed by data-generating organizations or companies, whereby participating clients are typically companies or institutions such as hospitals and banks. As a result, the number of clients is generally limited. This method is frequently used in cases where data is sensitive and not easily shareable among different clients.

Federated Learning Types.

Data sets in the dataset are matrices consisting of rows and columns. Each row represents a sample of data, while each column represents its attribute. Federated learning employs three different methods to solve federated learning problems: Horizontal Federated Learning, Vertical Federated Learning, and Federated Transfer Learning (Chen vd., 2020: 83-93).

Horizontal Federated Learning.

In cases where the same field is shared as an attribute among different datasets, but the examples are different, the Horizontal Federated Learning method is utilized. An application example for the Horizontal Federated Learning method is presented in Figure 2. As an illustration in the figure, patient data in three hospitals located in different geographical locations are available. There might be minimal patient overlap among the three hospitals, but the attributes in the patient data are similar. In this scenario, a horizontal federation learning model can be constructed using the patient data from the three hospitals (Li vd., 2020: 149: 106854).

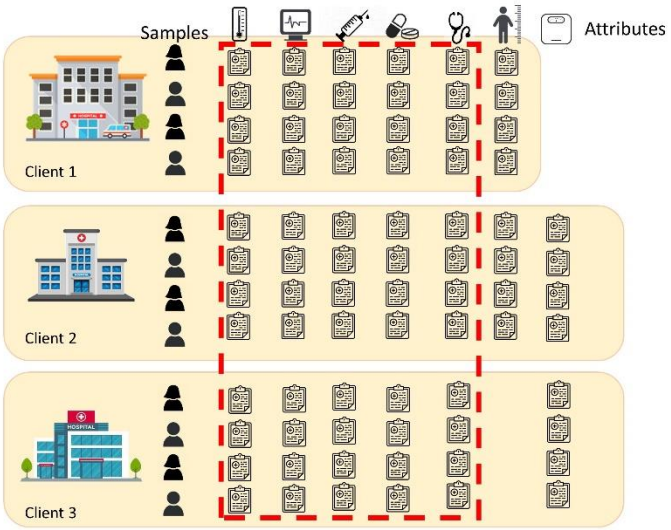

Figure 2. *Horizontal federated learning application example (Li vd., 2020: 149: 106854).*

Vertical Federated Learning.

In cases where the same examples exist in datasets but with different attribute domains, the Vertical Federated Learning method is employed (Li vd., 2020: 149: 106854). Figure 3 presents an application example of the Vertical Federated Learning method. According to the figure, there is a hospital and a health application that have the same patients. In other words, the same patients are registered at the hospital and are users of the same application. The hospital collects data obtained from patients' health check-ups, while the application records information about patients' height, weight, nutrition, and step history. Consequently, user attributes differ between the two sources. While the number of users may be small in this method, the dimensionality of the training data can be large. Therefore, the size of the dataset generated by patients is significantly large.

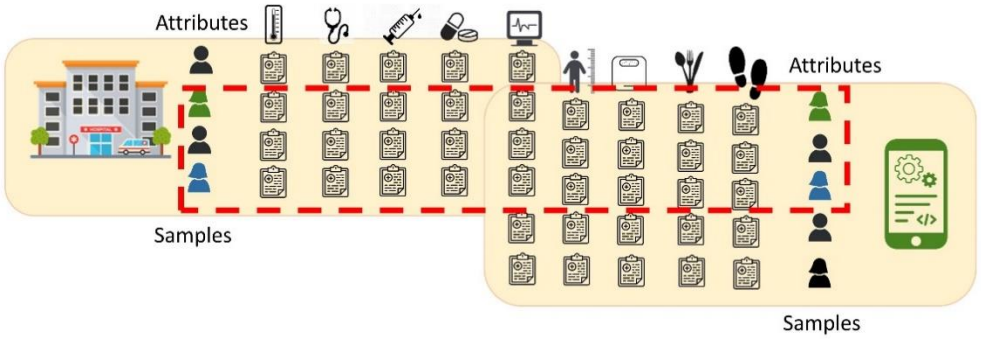

Figure 3. Vertical federated learning application example (Li vd., 2020: 149: 106854).

Federated Transfer Learning.

In cases where both the features and the samples in the datasets are different, Federated Transfer Learning method is utilized (Li vd., 2020: 149: 106854). An application example for the Federated Transfer Learning method is presented in Figure 4. In many machine learning algorithms, the development of applications assumes that the training and test data have the

same features and follow the same distribution. However, this assumption is often not valid in real-life environments. The Federated Transfer Learning method provides a solution to this problem.

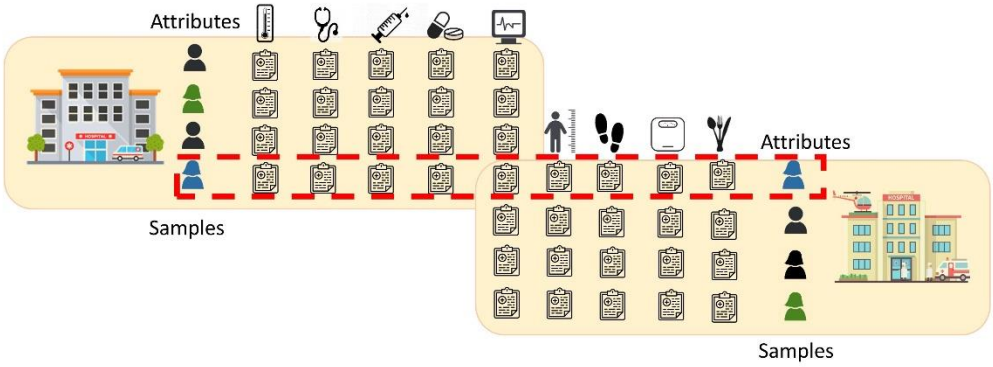

Figure 4. *Federated transfer learning application example (Li vd., 2020: 149: 106854).*

Developing Models with Federated Learning.

Federated learning starts when the clients download the training program from the server for the model to be developed. Because for the merging of models, models with common parameters must come to the server. After the training program is downloaded, each client trains the model using the data it has created locally. The information of the models trained on the clients is sent to the server periodically, usually within a certain program. Various privacy protocol techniques are used during the transfer from clients to server. Models from all clients are combined and a more advanced model is created from the latest training. After the training of the central model is complete, the updates of the enhanced model are pushed to the clients so they can use those updates as well. Figure 5 shows the steps to create a model in the federated learning architecture (Süzen ve Kayaalp, 2019: 297-304).

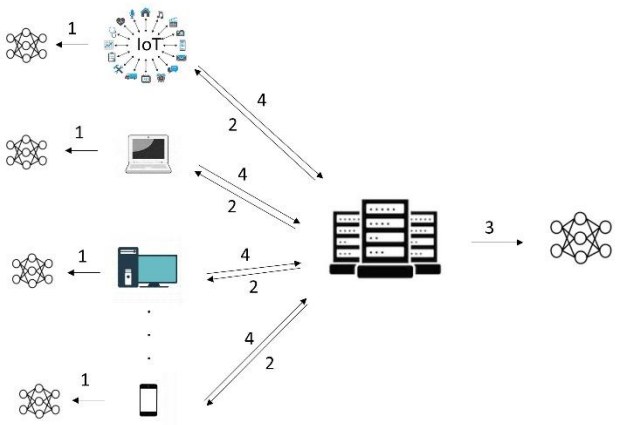

Figure 5. *Federated learning model formation.*

Privacy in Federated Learning.

In developing applications, particularly in sectors such as healthcare, education, and banking, using federated learning architecture, ensuring the privacy and security of both server-side and client-side model parameters is crucial. Although the data remains local, it is believed

that data can be reconstructed from the updates sent from the server to the client and vice versa. Therefore, various privacy algorithms are available for this purpose.

Safe Collection.

A cryptographic set that enables multiple parties on servers and clients to perform computations collectively while ensuring that the input information from clients or servers remains unknown to other parties is referred to as (Pettai ve Laud, 2015: 421-430).

Differential Privacy.

The security of data is ensured in crowded data sets through this commonly used type of privacy, where noise is added to the data and the information about its source is concealed (Choudhury vd., 2019: 1910.02578).

Homomorphic Encryption.

Homomorphic encryption is an optional encryption method used to add additional security and privacy to applications in federated learning, allowing users to perform computations on encrypted data. The results of the computations remain in encrypted form, and when decrypted, the output matches the output generated by computations performed on unencrypted data. It employs a public key for encryption and a private key for decryption (Aslett vd., 2015: 1508.06574).

Federated Learning Platforms.

In federated learning architecture, there are multiple platforms available for processing data generated from multiple edges to be used in model training. These platforms ensure the preservation of data privacy, enable the creation of a collaborative learning model and facilitate the sharing of models. The names and descriptions of the federated learning platforms most preferred by researchers in the scope of this study are presented in Table 1.

Table 1. *Federated learning platform names and descriptions*

Platform Name	Description
TensorFlow Federated (TFF)	It is an open-source federated learning platform based on TensorFlow developed by Google (Lim vd. 2020: 2031-2063).
PySyft	It is an open-source federated learning library based on PyTorch that provides data privacy developed for deep learning by OpenMined (Rodríguez-Barroso, 2020: 270-292).
Federated AI Technology Enabler (FATE)	It is an industrial-grade open-source unified learning platform developed by Webank that offers horizontal, vertical, and transfer learning methods between different organizations (Rodríguez-Barroso, 2020: 270-292).
PaddleFL (PFL)	It is an open-source federated learning framework that supports differential privacy based on PaddlePaddle, developed by the Chinese search engine Baidu for deep learning (Rodríguez-Barroso, 2020: 270-292).
IBM Federated Learning (IBM FL)	IBM Federation Learning: It is a federated learning platform developed by IBM, available in both licensed and free versions (Büyüknacar ve Canbay, 2021).

Federated Learning for Big Data.

Federated learning is utilized as a solution for the challenges encountered in the collection, storage, analysis, and privacy preservation of big data services. Figure 6 illustrates the federated learning architecture for big data services (Gadekallu vd., 2021: 2110.04160).

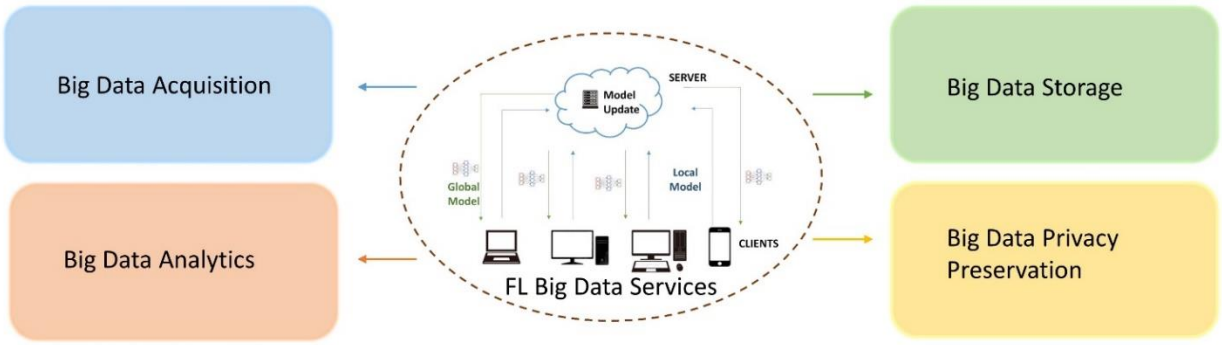

Figure 6. *Federated learning for big data services (Gadekallu vd., 2021: 2110.04160).*

Machine learning used for systems where clients and servers work together causes network traffic, communication delays, and fast energy consumption for devices due to the collection of large data generated by clients and sharing it with the server in artificial intelligence applications. In addition to these problems, sharing data compromises data security by making it accessible to attackers.

With federated learning architecture, data is not transmitted outside the area where it is generated, and model training is performed locally. This ensures data security. The size of the generated large data is larger than the size of the model trained on this data. Since a smaller-sized model is sent to the server instead of data, there is no traffic on the network, and communication delays are eliminated.

Big Data Acquisition: Instead of collecting data from each client and sharing it with the server, locally trained models with this data are shared with the server.

Big Data Storage: If the number of clients is high, storing the data sent to the server incurs additional costs. With federated learning architecture, data is not shared outside of where it is generated. The trained model is updated and circulated between the server and clients without the need for storage.

Big Data Analytics: Sending data to the server for analysis results in a long training time for the model trained on the collected large data. In the proposed approach with federated learning architecture, models are trained on clients and combined on the server. The training time on clients and the sharing time with the server are shorter than the model training time applied in traditional methods. However, sharing patient and customer information by certain institutions such as hospitals and banks raises concerns about data privacy. Not sharing such data will result in inadequate training of the model and a compromise in accuracy as it won't be exposed to different types of data.

Big Data Privacy Preservation: The main purpose of federated learning technology is to secure data privacy. By not transmitting data from clients to the server and applying methods such as homomorphic encryption and differential privacy to the models trained on clients, both data privacy and data security are ensured. The problem of data insufficiency in model training is eliminated due to the non-disclosure of personal information. Additionally, the final model obtained through the combination of models on the server is shared back with the clients. This allows continuously learning updated models to be used by clients.

Related Works.

First introduced by Google in 2016, Federated Learning (Jiang vd., 2020: 20.21: 6230) has emerged as a solution to issues such as data accessibility and privacy and has found applications in various domains such as finance, healthcare, education, smart cities, wearable devices, blockchain, and the Internet of Things (Liu vd., 2020: 2012.01973); (Yang, 2019: 1-207).

Nowadays, artificial intelligence and machine learning methods are being utilized in numerous fields. The accuracy of a model trained using these methods is directly proportional to the amount of data available. However, training models with limited data in domains where data sharing raises concerns about privacy may introduce a certain level of bias. Therefore, for collaborative frameworks involving clients and servers, data sharing among organizations and devices can be achieved through federated learning, ensuring data privacy is maintained. In the literature, studies have been conducted in the healthcare domain using federated learning architecture for tasks such as the detection of diseases like Covid-19 based on chest X-rays using deep learning algorithms (Cetinkaya vd., 2021: 429-434); (Zhang vd., 2021: 1403-1415); (Makkar vd., 2023: 1-12); (Kandati vd., 2022: 2714),autoencoder models (Huang vd., 2019: 103291), and electronic health records (Boughorbel vd., 2019: 1910.12191); (Liu vd., 2019: 283). Sharing customer information between organizations, such as banks, poses risks. Federated learning can be a good approach to mitigate this risk (Imteaj ve Amini, 2022: 200064); (Long vd., 2020: 240-254). Federated learning has also been employed in the transportation domain, as evident from studies on intelligent transportation systems (Elbir vd., 2022: 72-77) and autonomous driving (Nguyen vd., 2022: 1824-1830).

Furthermore, federated learning has been successfully applied in various areas such as identity authentication using drones (Yazdinejad vd., 2021: 102574), text recognition (Zhu vd., 2019: 1341-1345), energy prediction in smart buildings (Dasari vd., 2021: 1-6), violence prediction in simulated environments (Borger vd., 2022: 116720), network intrusion detection (Tang vd., 2022: e6812); (Doriguzzi-Corin ve Siracusa., 2022: 2205.06661), and speech recognition (Guliani vd., 2021: 3080-3084).

When examining the studies conducted and included in the literature, federated learning technology has demonstrated successful results in multiple domains, ranging from healthcare to transportation. It has been particularly utilized in research focusing on data privacy. Given that federated learning is a current technology capable of processing large datasets and generating value-added outputs, it is considered crucial for researchers to delve into this field.

Conclusion

Big data production is increasing and can be beneficial in various fields when processed correctly. However, traditional machine learning approaches are not compliant with data protection laws as they are based on centralized data collection. Therefore, innovative solutions that can preserve data privacy are needed for advancements in the field of artificial intelligence. Additionally, organizations collect and analyze data in centralized systems for their own business processes. However, this poses a risk to data security. Data privacy is of utmost importance and should be handled with great care.

Federated learning is a current technology that ensures data privacy. With this technology, the need for data centers decreases, and it enables the training of new models among similar or different institutions without data exchange through horizontal, vertical, and transfer learning types. It also complies with legal measures taken to ensure data security.

In conclusion, the volume and diversity of generated data are increasing. Ensuring the security and privacy of this data through automated systems is crucial. Federated learning technology allows data to be processed where it is generated, thereby stopping data sharing among different devices/institutions and ensuring data security and privacy. Studies in the literature indicate that this technology, which is utilized in many fields, should be implemented in numerous public institutions.

References

[1] Lee, J., Bagheri, B., & Kao, H. A. (2015). A cyber-physical systems architecture for industry 4.0-based manufacturing systems. Manufacturing letters, 3, 18-23.

[2] Atalay, M., & Çelik, E. (2017). Büyük veri analizinde yapay zekâ ve makine öğrenmesi uygulamalari-artificial intelligence and machine learning applications in big data analysis. Mehmet Akif Ersoy Üniversitesi Sosyal Bilimler Enstitüsü Dergisi, 9(22), 155-172.

[3] Zhou, K., Liu, T., & Zhou, L. (2015, August). Industry 4.0: Towards future industrial opportunities and challenges. In 2015 12th International conference on fuzzy systems and knowledge discovery (FSKD) (pp. 2147-2152). IEEE.

[4] Gökçay, B., & Arda, B. (2019). Kişisel sağlık verilerinin korunması kapsamında sağlık araştırmalarında etik bakış. Türk Kardiyoloji Derneği Arşivi, 47(3), 218-227.

[5] Kayaalp, K., & Süzen, A. A. (2018). Derin öğrenme ve Türkiye'deki uygulamaları. Yayın Yeri: IKSAD International Publishing House, Basım sayısı, 1.

[6] Abadi, M., Barham, P., Chen, J., Chen, Z., Davis, A., Dean, J., ... & Zheng, X. (2016, November). Tensorflow: a system for large-scale machine learning. In Osdi (Vol. 16, No. 2016, pp. 265-283).

[7] Aktan, E. (2018). Büyük veri: Uygulama alanları, analitiği ve güvenlik boyutu. Bilgi Yönetimi, 1(1), 1-22.

[8] Bagdasaryan, E., Veit, A., Hua, Y., Estrin, D., & Shmatikov, V. (2020, June). How to backdoor federated learning. In International Conference on Artificial Intelligence and Statistics (pp. 2938-2948). PMLR.

[9] Sagiroglu, S., & Sinanc, D. (2013, May). Big data: A review. In 2013 international conference on collaboration technologies and systems (CTS) (pp. 42-47). IEEE.

[10] Özdemir, İ., & SAĞIROĞLU, Ş. (2018). Denetimlerde büyük veri kullanımı ve üzerine bir değerlendirme. Gazi University Journal of Science Part C: Design and Technology, 6(2), 470-480.

[11] Zhang, K., Song, X., Zhang, C., & Yu, S. (2022). Challenges and future directions of secure federated learning: a survey. Frontiers of computer science, 16, 1-8.

[12] Kairouz, P., McMahan, H. B., Avent, B., Bellet, A., Bennis, M., Bhagoji, A. N., ... & Zhao, S. (2021). Advances and open problems in federated learning. Foundations and Trends® in Machine Learning, 14(1–2), 1-210.

[13] Süzen, A.A. and K. Kayaalp, Büyük Verilerde Gizlilik Tabanlı Yaklaşım: Federe Öğrenme. International Journal of 3D Printing Technologies and Digital Industry. 3(3): P. 297-304.

[14] Huang, C., Huang, J., & Liu, X. (2022). Cross-Silo Federated Learning: Challenges and Opportunities. arXiv preprint arXiv:2206.12949.

[15] Y. Chen, X. Qin, J. Wang, C. Yu, and W. Gao, "Fedhealth: A Federated Transfer Learning Framework For Wearable Healthcare," IEEE Intelligent Systems, vol. 35, no. 4, pp. 83-93, 2020.

[16] L. Li, Y. Fan, M. Tse, and K.-Y. Lin, "A Review Of Applications In Federated Learning,"

Computers & Industrial Engineering, p. 106854, 2020.

[17] Pettai, M., & Laud, P., Combining differential privacy and secure multiparty computation. In Proceedings of the 31st Annual Computer Security Applications Conference, Pages 421-430, 2015. ACM.

[18] Choudhury, O., Gkoulalas-Divanis, A., Salonidis, T., Sylla, I., Park, Y., Hsu, G., & Das, A., Differential Privacy-enabled Federated Learning for Sensitive Health Data. arXiv preprint arXiv:1910.02578. 2019.

[19] Aslett, L. J., Esperança, P. M., & Holmes, C. C., A review of homomorphic encryption and software tools for encrypted statistical machine learning. arXiv preprint arXiv:1508.06574, 2015.

[20] Lim, W. Y. B., Luong, N. C., Hoang, D. T., Jiao, Y., Liang, Y. C., Yang, Q., ... & Miao, C. (2020). Federated learning in mobile edge networks: A comprehensive survey. IEEE Communications Surveys & Tutorials, 22(3), 2031-2063.

[21] N. Rodríguez-Barroso et al., "Federated Learning and Differential Privacy: Software Tools

Analysis, The Sherpa. AI FL Framework and Methodological Guidelines For Preserving Data Privacy," Information Fusion, vol. 64, pp. 270-292, 2020.

[22] Büyüknacar, Y. C. Y. FEDERE ÖĞRENME VE VERİ MAHREMİYETİ.

[23] Gadekallu, T. R., Pham, Q. V., Huynh-The, T., Bhattacharya, S., Maddikunta, P. K. R., & Liyanage, M. (2021). Federated learning for big data: A survey on opportunities, applications, and future directions. arXiv preprint arXiv:2110.04160.

[24] Jiang, J.C., et al., Federated learning in smart city sensing: Challenges and opportunities.Sensors, 20(21): p. 6230, 2020.

[25] Liu, Y., et al., A systematic literature review on federated learning: From a model quality perspective. arXiv preprint arXiv:2012.01973, 2020.

[26] Yang, Q., et al., Federated learning. Synthesis Lectures on Artificial Intelligence and Machine Learning, 13(3): p. 1-207, 2019.

[27] Cetinkaya, A. E., Akin, M., & Sagiroglu, S. (2021, September). A communication efficient federated learning approach to multi chest diseases classification. In 2021 6th International Conference on Computer Science and Engineering (UBMK) (pp. 429-434). IEEE.

[28] Zhang, L., Shen, B., Barnawi, A., Xi, S., Kumar, N., & Wu, Y. (2021). FedDPGAN: federated differentially private generative adversarial networks framework for the detection of COVID-19 pneumonia. Information Systems Frontiers, 23(6), 1403-1415.

[29] Makkar, A., & Santosh, K. C. (2023). SecureFed: federated learning empowered medical imaging technique to analyze lung abnormalities in chest X-rays. International Journal of Machine Learning and Cybernetics, 1-12.

[30] Kandati, D. R., & Gadekallu, T. R. (2022). Genetic clustered federated learning for COVID-19 detection. Electronics, 11(17), 2714.

[31] L. Huang, A. L. Shea, H. Qian, A. Masurkar, H. Deng, and D. Liu, "Patient clustering improves efficiency of federated machine learning to predict mortality and hospital stay time using distributed electronic medical records," J. Biomed. Inform., vol. 99, no. September, p. 103291, 2019, doi: 10.1016/j.jbi.2019.103291.

[32] Boughorbel, S., Jarray, F., Venugopal, N., Moosa, S., Elhadi, H., & Makhlouf, M. (2019). Federated uncertainty-aware learning for distributed hospital ehr data. arXiv preprint arXiv:1910.12191.

[33] Liu, D., Dligach, D., & Miller, T. (2019, August). Two-stage federated phenotyping and patient representation learning. In Proceedings of the conference. Association for Computational Linguistics. Meeting (Vol. 2019, p. 283). NIH Public Access.

[34] A. Imteaj and M. H. Amini, "Leveraging asynchronous federated learning to predict customers financial distress," Intell. Syst. with Appl., vol. 14, 2022, doi: 10.1016/j.iswa.2022.200064.

[35] G. Long, "Federated Learning for Open Banking."

[36] Elbir, A. M., Soner, B., Çöleri, S., Gündüz, D., & Bennis, M. (2022, September). Federated learning in vehicular networks. In 2022 IEEE International Mediterranean Conference on Communications and Networking (MeditCom) (pp. 72-77). IEEE.

[37] Nguyen, A., Do, T., Tran, M., Nguyen, B. X., Duong, C., Phan, T., ... & Tran, Q. D. (2022, June). Deep federated learning for autonomous driving. In 2022 IEEE Intelligent Vehicles Symposium (IV) (pp. 1824-1830). IEEE.

[38] Yazdinejad, A., Parizi, R. M., Dehghantanha, A., & Karimipour, H. (2021). Federated learning for drone authentication. Ad Hoc Networks, 120, 102574.

[39] Zhu, X., Wang, J., Hong, Z., Xia, T., & Xiao, J. (2019, November). Federated learning of unsegmented chinese text recognition model. In 2019 IEEE 31st International Conference on Tools with Artificial Intelligence (ICTAI) (pp. 1341-1345). IEEE.

[40] Dasari, S. V., Mittal, K., Sasirekha, G. V. K., Bapat, J., & Das, D. (2021, April). Privacy enhanced energy prediction in smart building using federated learning. In 2021 IEEE International IOT, Electronics and Mechatronics Conference (IEMTRONICS) (pp. 1-6). IEEE.

[41] Borger, T., Mosteiro, P., Kaya, H., Rijcken, E., Salah, A. A., Scheepers, F., & Spruit, M. (2022). Federated learning for violence incident prediction in a simulated cross-institutional psychiatric setting. Expert Systems with Applications, 199, 116720.

[42] Tang, Z., Hu, H., & Xu, C. (2022). A federated learning method for network intrusion detection. Concurrency and Computation: Practice and Experience, 34(10), e6812.

[43] Doriguzzi-Corin, R., & Siracusa, D. (2022). FLAD: adaptive federated learning for DDoS attack detection. arXiv preprint arXiv:2205.06661.

[44] D. Guliani, F. Beaufays, and G. Motta, “Training Speech Recognition Models With Federated Learning: A Quality/Cost Framework,” in ICASSP 2021-2021 IEEE International Conference on Acoustics, Speech and Signal Processing (ICASSP), 2021, pp. 3080-3084: IEEE.

The Effect of Micro Fiber Type and Fiber Combination on the Elastic Modulus of Hybrid Fiber Reinforced Self-Compacting Concrete

Mahmut Başsürücü[1]
Kazım Türk[2]

Introduction

The elastic modulus, one of the most important mechanical properties of concrete, shows the capacity of concrete to resist deformation. Materials exhibit linear elastic behavior up to a certain stress value under load effects. However, if this stress value is exceeded, the materials show plastic behavior. In the design of concrete or reinforced concrete structural elements, the maximum stress value obtained within the elastic limit has a very important role in terms of structural safety and human comfort.

Currently, hybrid fiber reinforced self-compacting concrete (HFRSCC) is preferred as a novelty material for civil engineering applications. Self-compacting concrete (SCC), which was developed in Japan at the end of the 1980s, is defined as concrete that can easily spread under its weight, pass between rebar, and fill the mold without bleeding or segregation, regardless of any compaction process, even in very densely reinforced structural elements (Okamura, 1997; Ozawa et al., 1989). In the design of SCC, superplasticizer chemical admixtures, large amounts of powder materials and/or viscosity enhancers are used to prevent segregation and bleeding of the concrete during transportation and placement (Valcuende et al., 2005). On the other hand, the influence of steel fiber reinforcement on the engineering properties of concrete was first studied in the 1950s and 1960s (Hannant, 1987). Fiber combinations having different types (steel, polypropylene, glass, carbon, etc.), sizes (macro and micro), and aspect ratios are widely used today to enhance the tensile strength, toughness, and ductility properties of concrete. Fiber reinforced concrete obtained by including more than one type of fiber in concrete is called hybrid fiber reinforced concrete. The hybrid fiber idea of using macro and micro fibers together in a concrete mixture was first proposed by Rossi et al. (1987). It was stated that micro fibers controlled and bridged the growth of micro cracks and caused high tensile strength in concrete, and in the next stage, macro fibers controlled macro cracks by increasing both the ductility and load carrying capacity of structural elements (Mobasher & Li, 1996). The studies have been conducted by many authors (Banthia & Sappakittipakorn, 2007; Bassurucu & Turk, 2023; Turk et al., 2021), it has been concluded that the better performance of hybrid fiber reinforced concrete is largely due to the synergistic effect. Moreover, it was emphasized that hybrid fiber reinforcement caused important enhancements in the flexural, shear, and bond behavior of reinforced concrete structural elements compared to control without fiber reinforcement and single fiber reinforced concrete specimens (Katlav et al., 2022;

[1] Mahmut Başsürücü, Dr., Malatya Turgut Ozal University, Department of Construction Technology
[2] Kazım Türk, Prof. Dr., Inonu University, Civil Engineering

Turk et al., 2020; Turk & Bassurucu, 2021, 2022). In conclusion, the elastic modulus of reinforced concrete structural elements produced from HFRSCC has very important in terms of the design and the performance evaluation when it is considered the use of hybrid fiber reinforced composite, commonly.

In this research, the influence of fiber combination and micro fiber type on the elastic modulus values of HFRSCC mixtures was investigated experimentally and statistically. For this purpose, the elastic modulus tests of SCC mixtures with different fiber hybridizations were carried out. Besides, empirical equations were developed to predict the elastic modulus values of HFRSCC mixtures, and graphs were drawn to guide designers in determining the most appropriate micro fiber types and quantity.

Materials and Method

Materials

In this study, pozzolanic cement (CEM IV 32.5 R) manufactured by the Elazig Cimentas factory was used. Moreover, Class F fly ash waste from Isken Sugozu Thermal Power Station was added as a mineral additive to contribute to the amount of fine powder material (<0.125 mm) in the SCC mixtures. The oxide compounds of pozzolanic cement and fly ash were presented in Table 1.

Table 1. Oxide compounds of pozzolanic cement and fly ash (%).

Compound	Pozzolanic cement	Fly ash
SiO_2	29	63.04
Al_2O_3	9.5	21.63
Fe_2O_3	5.5	6.77
CaO	41	1.07
MgO	1	-
SO_3	2.86	0.10
K_2O	0.68	-
Na_2O	0.60	-
LOI	-	2.6
Specific gravity	2.95	2.3
Surface area (cm^2/g)	4380	2690

Two types of aggregates, fine (0-5 mm) and coarse (5-15 mm) were used in the production of SCC mixtures. The saturated surface dry specific gravity of fine and coarse aggregates was obtained as 2.39 and 2.68, respectively. In fresh SCC mixtures, 80% fine and 20% coarse aggregate were used of the total aggregates to obtain the highest compactness, reduce segregation and ensure homogeneous distribution of fibers in the concrete. The gradation of the total aggregate was presented in Table 2. Moreover, it was aimed to produce concrete according to SCC workability conditions without increasing the amount of mixing water in SCC mixtures by using a superplasticizer with a specific gravity of 1.08 produced by Sika Construction Chemicals.

Table 2. The gradation of total aggregate.

Sieve size (mm)	Aggregate (% passing)
16	100
8	88.7
4	78.4
2	49.3
1	30.2
0.5	18.4
0.25	10.7
0.125	7.4

As for the fiber types preferred in the study, a total of three different fiber types were used: double-hooked macro steel and two different micro types (steel and polypropylene). The properties and pictures of fibers were shown in Table 3 and Figure 1, respectively.

Table 3. The properties of fibers.

Fiber type	Length (mm)	Diameter (mm)	Aspect Ratio	Tensile Strength (MPa)	Elastic Modulus (GPa)	Density (g/cm^3)
Macro steel	60	0.90	66	1150	210	7.8
Micro steel	13	0.15	87	3000	200	7.2
Polypropylene	6	0.025	240	350	-	0.91

Figure 1. The pictures of macro and micro fibers.

SCC Mixture Proportions

In this research, a total of five self-compacting concrete mixtures were designed as the control without fiber reinforcement, single macro steel, binary hybrid (macro/micro steel and macro steel/micro polypropylene), and ternary hybrid (macro steel/micro steel/polypropylene) fiber reinforced. In all SCC mixtures, the mixture proportions were determined by trial and error method to provide the workability limits recommended by EFNARC (2005) and to prevent the balling effect of micro fibers. For the designed SCC mixtures, the water/binder ratio, pozzolanic cement, fly ash, and water components were kept constant and were determined as 0.28, 500 kg/m^3, 400 kg/m^3, and 250 kg/m^3, respectively. Moreover, fine (0-5

mm) and coarse (5-15 mm) aggregates were used as 80% and 20% of the total aggregate amount, respectively, for all SCC mixtures. On the other hand, the total steel fiber volume was selected at 1% for the single and HFRSCC mixtures while the total fiber volume was 1.25% for the SCC mixtures including micro polypropylene fiber. Besides, the amount of superplasticizer was varied between 0.5% and 1% by weight of the binder. The proportions of SCC mixtures were given in Table 4. In the naming of SCC mixtures, MACSF, MICSF, and PPF stand for macro steel, micro steel, and micro polypropylene fiber, respectively. For example, MACSF1_PPF0.25 indicates that 1% macro steel and 0.25% polypropylene fiber by volume were included in the SCC mixture.

Table 4. The proportions (kg/m^3) and fresh properties of SCC.

Components	SCC Mixtures				
	CONTROL	**MACSF 1**	**MACSF0.8-MICSF0.2**	**MACSF 1-PPF0.25**	**MACSF0.8-MICSF0.2-PPF0.25**
Pozzolanic cement	500	500	500	500	500
Fly ash	400	400	400	400	400
Fine aggregate	799	778	778	768	766
Coarse aggregate	200	194	194	192	192
Superplasticizer	4.5	5	5	8.5	9
Water	250	250	250	250	250
Macro steel fiber	-	78.5	62.8	78.5	62.8
Micro steel fiber	-	-	14.4	-	14.4
Micro polypropylene fiber	-	-	-	2.28	2.28
Slump-flow diameter (mm)	790	775	765	750	740
t_{500} (s)	4.2	5.3	5.8	6.5	6.8
J-ring value (mm)	1.7	3.3	3.4	7	8

The production of SCC mixtures consists of two stages. In the first stage, coarse aggregate, fine aggregate, macro/micro fiber, and two-thirds of the mixing water were added to the mixer and mixed for 3 minutes. In the second stage, cement, fly ash, and the remaining one-third of the mixing water with the superplasticizer were added to the mixer and mixed for 7 minutes, and thus SCC mixtures were prepared by applying a total mixing process for 10 minutes.

In addition to all these, as can be seen from Table 4, it was determined that all SCC mixtures ensured the workability conditions recommended by EFNARC (2005) except for the t_{500} values of the polypropylene fiber reinforced SCC mixtures, and thus the designed SCC mixtures had good flowability, excellent passing ability, and stability.

Preparation and Testing of SCC Specimens

In this study, the produced specimens were cured in water for 28-days to obtain the engineering properties (the compressive, the splitting tensile, the flexural tensile strength, and the elastic modulus) for all designed SCC mixtures. On the other hand, elastic modulus tests were performed on Ø100x200 mm cylindrical specimens according to ASTM C469 (2002). Finally, elastic modulus values were obtained by averaging the test results of three SCC specimens produced for each SCC mixture. For the elastic modulus tests, as seen in Figure 2(a), sulfur capping was cast so that the load to be applied to the cylindrical specimens could be uniformly distributed across the specimens of the cross-section. Moreover, before cylindrical specimens were subjected to uniaxial compressive loading, a compressometer with LVDTs was mounted on the specimen to measure horizontal and vertical deformation (Figure 2 (b)). Then,

the cylindrical specimens were placed in the press and subjected to loading. After the experiment started, the horizontal and vertical deformation values of the cylindrical specimens under loading were instantly transferred to the computer by the data acquisition system. Finally, the elastic modulus values of the SCC specimens were calculated based on 40% of the maximum stress using the method specified in the ASTM C469 (2002) standard.

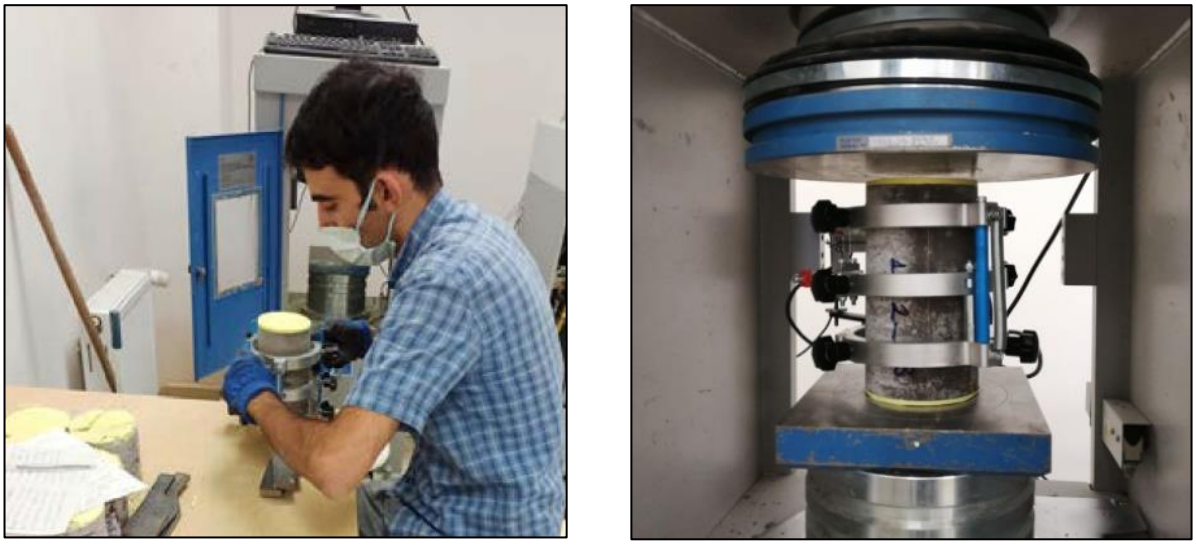

(a) **(b)**

Figure 2. The elastic modulus test for SCC specimens; (a) Compressometer installation, (b) Testing of SCC specimens.

Results and Discussion

Experimental Evaluation of Elastic Modulus Values of HFRSCC

Determining the deformations that occur in the concrete under load effects was very important in terms of building safety for the design of reinforced concrete structural elements and the evaluation of the performance of existing structures. The average elastic modulus values of non-fiber control and single/binary/ternary fiber reinforced SCC mixtures were presented in Table 5 and Figure 3. For the elastic modulus values of SCC specimens with different fiber hybridizations, the age of 28 days was preferred. Because it was emphasized in the literature that the increase in the elastic modulus values of concrete after 28 days was very low and the elastic modulus values for this curing age could be estimated by some models (Zhou et al., 1995).

As can be seen from Table 5, the elastic modulus value of the control SCC specimens without fiber was determined as 34662 MPa. Moreover, the elastic modulus values of the single macro and binary HFRSCC specimens increased with 7.02% and 7.84%, respectively, compared to the control specimens without fiber. From this here, it can be addressed that single or binary hybrid steel fiber reinforcement with a total fiber volume of 1% increased the elastic modulus value, but binary hybrid steel fiber reinforcement had a slightly more positive effect. This may be attributed to the high elastic modulus of the steel fibers the replaced by aggregates and the homogeneous distribution of fibers in the matrix for single/binary hybrid steel fiber reinforced SCC mixtures (see Figure 4(a-b)). In the study conducted by Yagmur (2020) in the literature, it was emphasized that the elastic modulus value increased for concrete containing 1% or less steel fiber by volume while the elastic modulus value decreased for concretes containing more than 1% steel fiber by volume.

Table 5. The engineering properties of SCC mixtures for 28 curing days.

SCC Mixtures	Elastic Modulus (MPa)	Compressive Strength (MPa)	Splitting Tensile Strength (MPa)	Flexural Tensile Strength (MPa)
CONTROL	34662	49.6	4.1	6.27
MACSF1	37097	48.4	5.6	10.88
MACSF0.8_MICSF0.2	37378	53.85	6.2	10.02
MACSF1_PPF0.25	34207	48.2	6.35	11.58
MACSF0.8_MICSF0.2_PPF0.25	34241	59.1	7.49	12.45

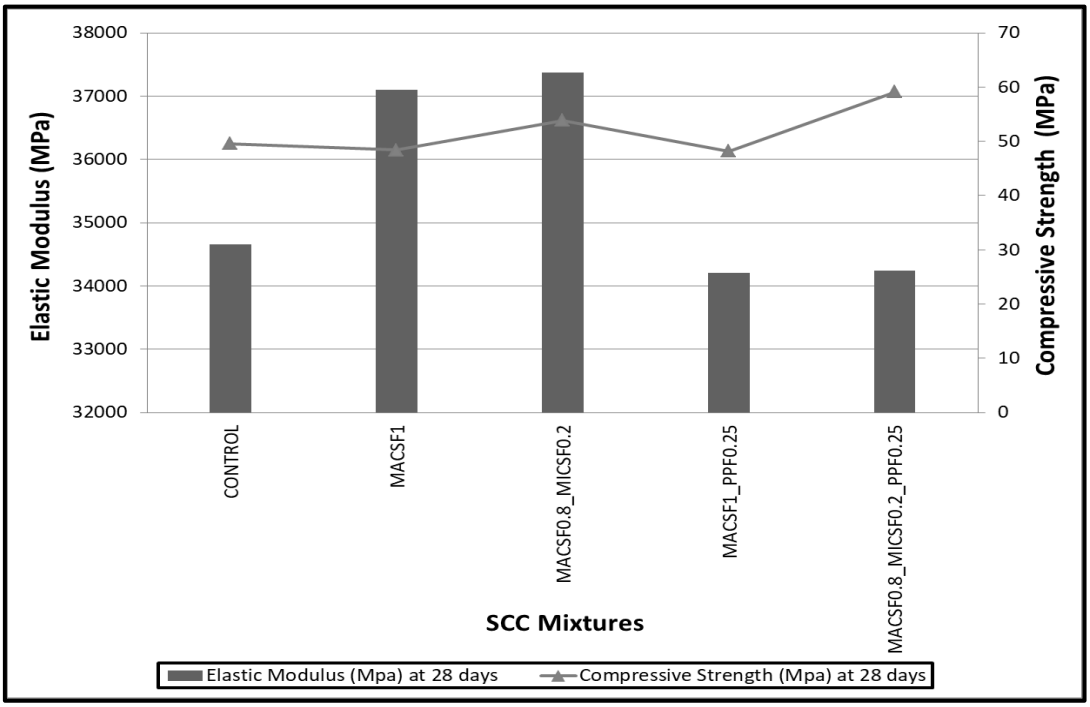

Figure 3. The elastic modulus and compressive strength values of SCC mixtures.

(a) MACSF1

(b) MACSF0.8_MICSF0.2

(c) MACSF1_PPF0.25 (d) MACSF0.8_MICSF0.2_PPF0.25

Figure 4. Fiber distribution pictures of single/hybrid fiber reinforced SCC specimens.

On the other hand, it was determined that the elastic modulus values of the binary HFRSCC specimens containing polypropylene fiber decreased with 7.79% compared to the specimens containing only 1% macro steel fiber. Moreover, it was found that the elastic modulus value of ternary HFRSCC specimens reduced with 8.39% compared to the binary hybrid steel fiber reinforced specimens. In conclusion, it can be stated that polypropylene fiber reinforcement as micro fiber in HFRSCC mixtures negatively affected the elastic modulus values. The decrease in elastic modulus of HFRSCC samples containing polypropylene fibers may be attributed to the low elastic modulus of polypropylene fibers compared to steel fibers and the inhomogeneous distribution of the fibers in the matrix due to negative influence of polypropylene fiber on the workability ((see Table 4 and Figure 4(c-d)). In the studies performed in the literature (Singh & Rai, 2021; Topçu et al., 2017), it was emphasized that polypropylene fiber reinforcement had a negative effect on the elastic modulus of the concrete.

In addition to all these, it can be said that macro and micro fibers bridged the cracks formed in the specimens under the effect of axial compressive load during the test and prevented the propagation of cracks up to a certain load level. Therefore, it was thought that the integrity of the HFRSCC specimens was maintained for a longer time compared to the control specimens without fiber, allowing the specimens to carry more load (Figure (5)).

Figure 5. Pictures of SCC specimens after elastic modulus test.

Statistical Evaluation of Experimental Results

The elastic modulus values of binary and ternary HFRSCC was predicted with the help of multiple linear regression analysis (MLR). In the statistical analysis, the variables were the volume fractions of macro, micro steel, and polypropylene fibers. The summary outputs of the statistical analysis using the elastic modulus values were shown in Table 6. It was obtained from this analysis that R^2 values of elastic modulus were 0.998. From this here, it can be concluded that there was a good correlation between the test results and the predicted values obtained. Besides, as can be seen from Table 7, it was determined that the efficient ratio values of the elastic modulus values obtained by MLR analysis were approximately 1.

Table 6. The summary output of MLR analysis for the elastic modulus.

	Coefficients	Standard Error	t stat	P-value
Intercept	34662	123.5	280.66	0.002
MACSF	249675	16337.51	15.28	0.042
MICSF	328425	57596.57	5.7	0.111
PPF	-1205400	49400	-24.4	0.026

Table 7. The experimental and predicted values for the elastic modulus.

SCC Mixtures	Test	Predicted	EM_T/EM_{Pr}
CONTROL	34662	34662	1.000
MACSF1	37097	37159	0.998
MACSF0.8_MICSF0.2	37378	37316	1.002
MACSF1_PPF0.25	34207	34145	1.002
MACSF0.8_MICSF0.2_PPF0.25	34241	34303	0.998

On the other hand, the graph was drawn based on MLR analysis considering three different variables (the volume fraction of macro, micro steel, and polypropylene fiber). Also, the graph will be guide for designers to obtain the most suitable micro fiber type and the volume fraction of fiber (Figure (6)).

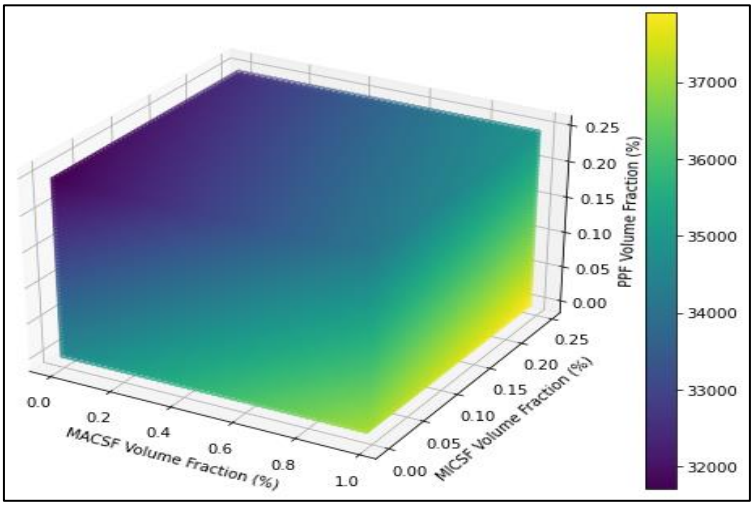

Figure 6. The influence of total fiber amount and micro fiber types on elastic modulus values for binary and ternary HFRSCC.

In addition to all these, the empirical equation was developed to estimate the elastic modulus values of hybrid fiber reinforced SCC specimens (Equation 1). In this equation, the effect of fiber reinforcement on the elasticity modulus was determined based on the fiber reinforcement index and the flexural tensile strength of fiber reinforced concrete. In many studies in the literature, fiber reinforcement index was used to interpret the performance of fiber reinforced concrete elements (Harajli et al., 1995; Turk et al., 2021). As can be seen from Figure 7, there was a high correlation between the normalized elastic modulus and fiber reinforcement index.

$$EM = (1287.4\left(\frac{V_f L_f}{d_f}\right)^2 - 3732.9\left(\frac{V_f L_f}{d_f}\right) + 5519.7)f_{tf} \quad (1)$$

where, EM was the elastic modulus value of fiber reinforced SCC specimens, V_f was the fiber volume fraction (%), L_f was the fiber length (mm), d_f was the fiber diameter (mm) and f_{tf} was the flexural tensile strength of SCC (MPa).

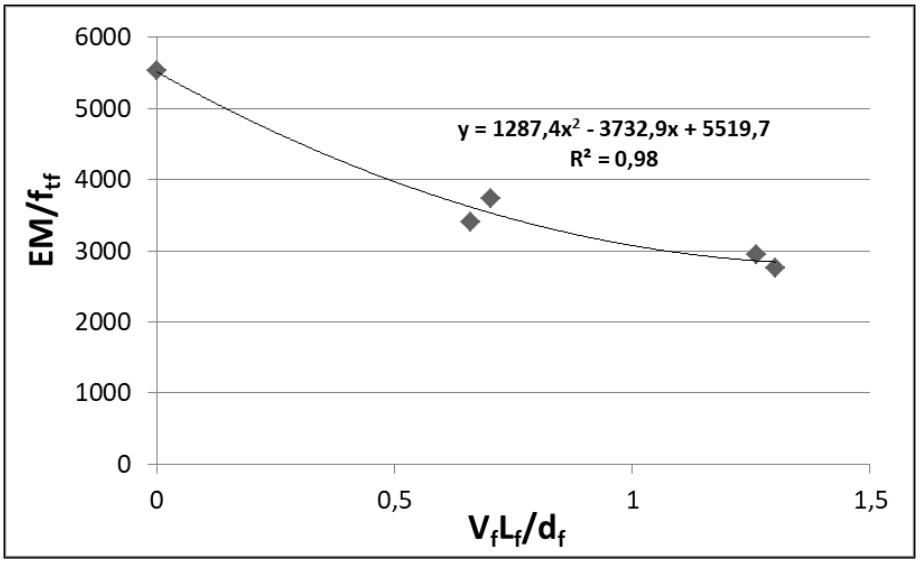

Figure 7. The variation of normalized elastic modulus and fiber reinforcement index.

Conclusions

In this research, the influence of fiber combination and micro fiber type on the elastic modulus values of HFRSCC mixtures was investigated experimentally and statistically. The conclusions can be drawn as follows:

- The single or binary hybrid steel fiber reinforcement with a total fiber volume of 1% increased the elastic modulus value compared to control test specimens without fiber.
- A total of 1% binary blends of hybrid steel fiber increased the elastic modulus more than single steel fiber reinforcement.
- The inclusion of polypropylene fiber as micro fiber to HFRSCC mixtures negatively influenced the elastic modulus values.

- The use of micro steel fiber together with macro steel fiber as hybrid had a more positive effect on the elastic modulus values compared to micro polypropylene fiber.
- The empirical equation was developed to predict the elastic modulus values of HFRSCC mixtures.
- The graph drawn will guide for designers to use the most suitable micro fiber type and volume fraction of fibers in production of HFRSCC mixtures.

Acknowledgement

The financial support for this study was provided by Scientific Research Projects Committee of Inonu University, Türkiye (Project No: FDK-2019-1974). Their support was gratefully acknowledged.

References

ASTM C469-02. (2002). Standard Test Method for Static Modulus of Elasticity and Poisson's Ratio of Concrete in Compression. In *ASTM Standard Book* (Vol. 04).

Banthia, N., & Sappakittipakorn, M. (2007). Toughness enhancement in steel fiber reinforced concrete through fiber hybridization. *Cement and Concrete Research*, *37*(9), 1366–1372. https://doi.org/10.1016/j.cemconres.2007.05.005

Bassurucu, M., & Turk, K. (2023). An experimental and statistical investigation on the fresh and hardened properties of HFR-SCC: the effect of micro fibre type and fibre hybridization. *European Journal of Environmental and Civil Engineering*, *27*(1), 263–287. https://doi.org/10.1080/19648189.2022.2042396

EFNARC. (2005). The European Guidelines for Self-Compacting Concrete. *The European Guidelines for Self Compacting Concrete*.

Hannant, D. (1987). *Fiber Cements and Fiber Concrete*. Wiley.

Harajli, M. H., Maalouf, D., & Khatib, H. (1995). Effect of fibers on the punching shear strength of slab-column connections. *Cement and Concrete Composites*, *17*(2), 161–170. https://doi.org/10.1016/0958-9465(94)00031-S

Katlav, M., Turk, K., & Turgut, P. (2022). Research into effect of hybrid steel fibers on the V-shaped RC folded plate thickness. *Structures*, *44*(August), 665–679. https://doi.org/10.1016/j.istruc.2022.08.046

Mobasher, B., & Li, C. Y. (1996). Mechanical properties of hybrid cement-based composites. *ACI Materials Journal*, *93*(3), 284–292. https://doi.org/10.14359/9813

Okamura, H. (1997). Self-Compacting High-Performance Concrete. *Concrete International*, *19*(7).

Ozawa, K., Maekawa, K., Kunishima, M., & Okamura, H. (1989). Development of high performance concrete based on the durability design of concrete structures. *Proceeding of the Second East - Asia and Pacific Conference on Structural Engineering and Construction (EASEC - 2)*, *1*, 445–450.

Rossi, P., Acker, P., & Malier, Y. (1987). Effect of steel fibres at two different stages: The material and the structure. *Materials and Structures*, *20*(6), 436–439. https://doi.org/10.1007/BF02472494

Singh, N. K., & Rai, B. (2021). Assessment of synergetic effect on microscopic and mechanical properties of steel-polypropylene hybrid fiber reinforced concrete. *Structural Concrete*, *22*(1), 516–534. https://doi.org/10.1002/suco.201900166

Topçu, İ. B., Enes Demirel, O., & Uygunoğlu, T. (2017). Polipropilen Lif Katkılı Harçların Fiziksel ve Mekanik Özelikleri. *Journal of Polytechnic*, *20*(1), 91–96.

Turk, K., & Bassurucu, M. (2021). Bond strength of full-scale beams with blended short and long steel fiber. *Pamukkale University Journal of Engineering Sciences*, *27*(3), 274–280. https://doi.org/10.5505/pajes.2020.34846

Turk, K., & Bassurucu, M. (2022). An investigation on the effect of hybrid fiber reinforced on the flexural behavior of RC beams having different lap-spliced lengths. *Structural Concrete*, *January*, 1–13. https://doi.org/10.1002/suco.202200106

Turk, K., Bassurucu, M., & Bitkin, R. E. (2021). Workability, strength and flexural toughness properties of hybrid steel fiber reinforced SCC with high-volume fiber. *Construction and Building Materials*, *266*, 120944. https://doi.org/10.1016/j.conbuildmat.2020.120944

Turk, K., Kina, C., & Oztekin, E. (2020). Effect of macro and micro fiber volume on the flexural performance of hybrid fiber reinforced SCC. *Advances in Concrete Construction*, *10*(3), 257–269. https://doi.org/10.12989/acc.2020.10.3.257

Valcuende, M., Parra, C., & Benlloch, J. (2005). Permeability, porosity and compressive strength of self-compacting concretes. *Mater Construcc*, *55*(280), 17–25.

Yağmur, E. (2020). Elastic Modulus Prediction for Fiber-Reinforced Concretes. *Pamukkale University Journal of Engineering Sciences*, *26*(6), 1098–1109. https://doi.org/10.5505/pajes.2019.34017

Zhou, F. P., Lydon, F. D., & Barr, B. I. G. (1995). Effect of coarse aggregate on elastic modulus and compressive strength of high performance concrete. *Cement and Concrete Research*, *25*(1), 177–186. https://doi.org/10.1016/0008-8846(94)00125-I

GIS Analysis for Topographic Effects of Landfill: A Case Study of Istanbul-Odayeri Landfill

Hüseyin YURTSEVEN[1]
Mehmet Can SARIKAP[2]
Miraç Nur CİNER[3]
Emine ELMASLAR ÖZBAŞ[4]
H. Kurtuluş ÖZCAN[5]
Sinan GÜNEYSU[6]
Atakan ÖNGEN[7]
Serdar AYDIN[8]

INTRODUCTION

A significant amount of municipal solid waste (MSW) is produced globally as a result of modern life. Because it directly affects people, especially those who live in cities, MSW is a significant source of pollution if it is not properly disposed of. MSW is made up of a variety of different material categories. Along with changes in people's consumption habits, the amount of organic materials, plastics, glass, and similar components in solid waste is increasing (Ozcan, 2016). As a result, appropriate MSW disposal has become critical for reasons such as conservation of natural resources, pollution prevention, energy savings, and economic concerns.

In a hierarchical system, waste prevention and reducing waste generation at the source are given the highest priority. The recommended technology application should follow prevention and avoidance principles, with the goal of minimizing negative consequences on energy, the environment, and human health. Furthermore, the technology selected may differ depending on the geographical location of the implementation region (Güvenç, 2016).

The final option in waste management hierarchy is proper MSW disposal. Sanitary landfills receive a major part of solid waste. Because of the economic benefits, the disposal of solid waste in sanitary landfills is the most often utilized approach among various alternative waste disposal methods such as incineration and composting. The process of disposing of solid waste in large, impermeable areas, compacting it, and covering it in order to make a natural biological reactor is known as sanitary landfilling (Tchobanoglous et al, 1993). To qualify as

[1] Assoc. Prof. Dr., Istanbul University-Cerrahpaşa, Surveying and Cadastre Department, Orcıd: 0000-0003-2469-9365
[2] Lec., Istanbul University-Cerrahpaşa, Project and Technology Office, Orcıd: 0000-0002-5044-1184
[3] Res. Asst., Istanbul University-Cerrahpaşa, Environmental Engineering Department, Orcıd: 0000-0002-9920-928X
[4] Assoc. Prof. Dr., Istanbul University-Cerrahpaşa, Environmental Engineering Department, Orcıd: 0000-0001-9065-6684
[5] Prof. Dr., Istanbul University-Cerrahpaşa, Environmental Engineering Department, Orcıd: 0000-0002-9810-3985
[6] Assoc. Prof. Dr., Istanbul University-Cerrahpaşa, Environmental Engineering Department, Orcıd: 0000-0002-4875-101X
[7] Assoc. Prof. Dr., Istanbul University-Cerrahpaşa, Environmental Engineering Department, Orcıd: 0000-0002-9043-7382
[8] Prof. Dr., Istanbul University-Cerrahpaşa, Environmental Engineering Department, Orcıd: 0000-0002-0626-5224

sanitary landfilling, the essential procedures must be followed for the collection, removal, and treatment/utilization of the produced leachate and landfill gas.

The selection of a landfill site is the most important stage in MSW management. The examination of places with the lowest cost and minimal environmental impact is critical in site selection (Kuru et al, 2021). The selection of sanitary landfill sites includes taking into account a number of factors, which may be divided into two categories: non-environmental factors and environmental ones. Non-environmental variables such as present land usage, economic concerns or limits, legal procedures, and so on are examples of non-environmental factors. Environmental factors, on the other hand, include waste type and characterization, permeability of the site soil (geological factors), depth of the groundwater table from the soil surface (hydrological factors), and meteorological factors such as annual precipitation (Beskese et al, 2015). Considerations are given to factors such as the impact on air transportation safety, distance to specially protected areas with specific purposes such as forest areas, afforestation areas, wildlife and vegetation conservation, the condition of groundwater and surface water sources, as well as their protection zones, groundwater levels, and groundwater flow directions, in the selection of a sanitary landfill site. Topographic, geological, geomorphological, geotechnical, and hydrogeological conditions of the site, risks of flooding, landslides, avalanches, erosion, and high seismic activity, prevailing wind direction and precipitation patterns, and the status of natural or cultural heritage are also considered (MEU 2014). To make the most of the volume and space available, there are a number of methods to manage MSW within the landfill area. These methods vary depending on the topography (presence of slopes, bumps or hole) of the landfill site, the characteristics of the soil, the kind of soil cover used to cover the waste, the equipment available for landfilling operations, and the operational characteristics differs to the landfill site.

The purpose of this study is to examine how the Odayeri landfill site and its surroundings, where Istanbul's MSW is stored, have changed spatially over time using GIS-enabled satellite images.

MATERİALS AND METHODS

Study Area

Istanbul is a city located between the continents of Europe and Asia, between the longitudes of 28º 10' and 29º 55' East and the latitudes of 41º 33' and 40º 28' North. The city is bounded in Europe by Çatalca and in Asia by Kocaeli, with the Marmara Sea and Bursa to the south, Tekirdağ to the southwest, and Kırklareli to the northwest. Istanbul is Turkey's most populated metropolis, with a population of over 16 million people living on an area of approximately 5.750 km^2 (TURKSTAT 2022).

Istanbul and its surroundings are made up of the Thrace and Kocaeli plateaus. The sea surrounds these plateaus from the north and south, and the Istanbul Strait separates them. While Istanbul and its surrounding areas do not have a single dominating regional climatic type, there are numerous climate types that differ from one another due to differences in terrain, elevation, relative position, aspect, and flora. Istanbul's climate is unique in that it is affected by both the Black Sea and the continental climate of the Balkans and Anatolia. Marmara climate prevails throughout the city. Except for the Black Sea shore, this climatic type affects the whole Marmara area. In July, the average temperature is between 23°C and 24°C. The average temperature in January, the coldest month, is around 3-5°C. There are no significant

temperature changes in Istanbul between summer and winter, or between day and night. The most rain falls throughout the winter. The yearly precipitation averages 500 mm to 700 mm, with snowfall being typical. When compared to the Mediterranean climate, freezing occurrences are more often (Apak and Ubay, 2007).

Maquis is the most frequent plant species found in Istanbul's area. These plants have adapted to a hot, dry summer. The slopes, however, are not naked due to features of the climate. The Belgrade Forest, located 20 kilometers north of the city, is the most substantial forested region visible in certain areas. The Belgrade Forest is home to several diverse species, the most common of which are oak trees (Yaltırık, 1966).

In Istanbul province, there are no significant rivers. The Riva River is the major river and the main source of water on the Kocaeli Peninsula. The two most important streams that pour into the Bosphorus are the Küçüksu and Göksu. Other significant rivers that run into the Golden Horn are the Kağıthane and Alibey streams, Sazlıdere stream, which flows into Küçükçekmece Lake, Karasu stream, which flows into Büyükçekmece Lake, and Trança stream, which flows into Terkos Lake. These are Istanbul's major waterways. The province has three small but significant lakes, all of which are located on the European side. Terkos Lake, which is separated from the sea, has freshwater. The Terkos basin is an important supply of water for the city. Because of its proximity to the Marmara Sea, Küçükçekmece Lake (11 km^2) and Büyükçekmece Lake (16 km^2) contain saltwater.

Landfill Site

Landfilling is the last option for disposing of MSW. Like in many major cities, solid waste management has been a major priority for Istanbul's authorities.

Since 1995, MSW from Istanbul's European side has been stored in the Odayeri Landfill Site. The 125-hectare dispose of site is located in a gently sloping valley and is covered with layers of clay, sand, gravel, and coal in certain areas (Akkaya et al., 2011). The Odayeri Sanitary Landfill Site, which opened in 1995, is located near Kemerburgaz (Figure 1). The landfill site no longer accepts organic waste as of January 1, 2018. MSW on the European side of Istanbul’s has been placed in the Odayeri Sanitary Landfill for the past 23 years. According to the Turkish Statistical Institute's Environmental Status Report issued in 2020, the average daily MSW amount per capita is 1.13 kg (TURKSTAT 2020).

Currently, MSW that does not include organic substance is being placed in Class II landfill areas. The average daily waste volume in the Odayeri sanitary landfill is 11154 tons (Korkutan et al., 2018).

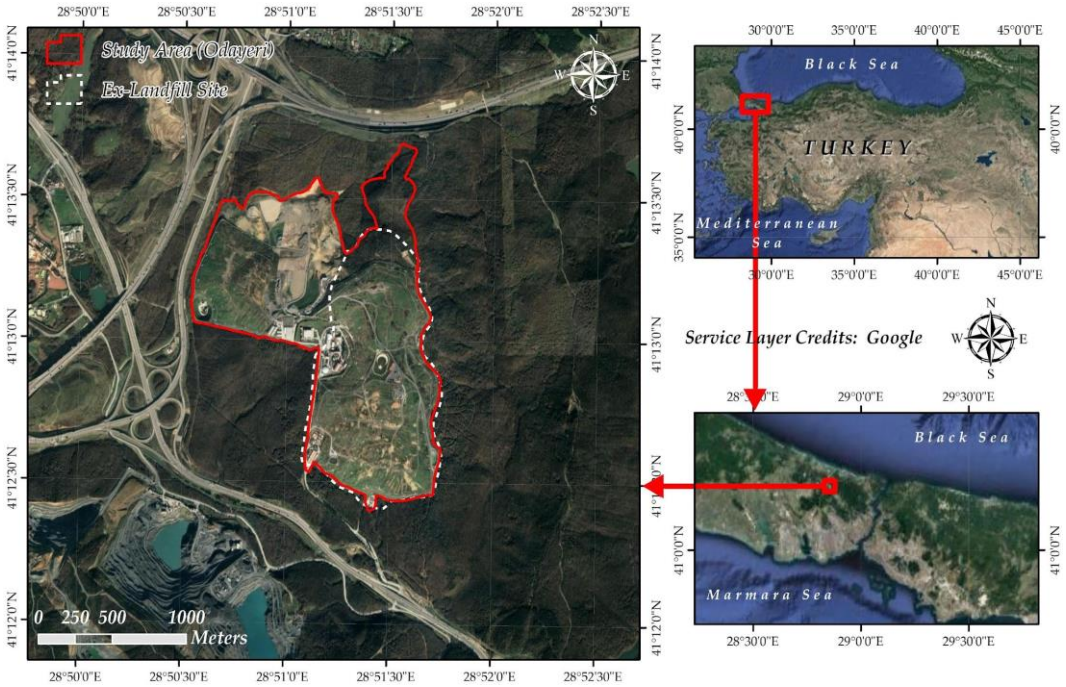

Figure 1. Location of Odayeri Landfill Site

MSW, which do not have a uniform property, are classified into three types. The first group includes organic components that can be separated, such as food waste, fruit and vegetable waste, and garden waste (grass, leaves, and so on); the second group includes flammable materials that decompose slowly or cannot decompose, such as paper, cardboard, textiles, plastics, and other synthetics; and the third group includes inert components, such as stone, sand, glass, and metals. The variety and quantity of MSW increase as the population of the community grows. The changes in Istanbul's MSW composition throughout time are shown in Table 1. Improvements in living conditions, scientific and technological advancements, and the development of modern packing materials all have a significant influence on both the volume of MSW produced per person and the composition of the MSW. This trend may also be seen in Table 1's changing MSW composition over time.

Tablo 1. Changes in the composition of Istanbul's MSW throughout time

Parameter	CH2M Hill, (1992) (%weight)	Arıkan, (1996) (%weight)	Özkaya, (2004) (%weight)	Yıldız et al, (2013) (%weight)
Ash	15	13,2	9	0,63
Organic Matter	45	48	44	54,09
Paper	14,5	8,4	8	15,57
Plastic	9,5	11	5	2,62
Glass	3,8	4,6	6	3,03
Textile	5,6	2,9	5	3,42
Metal	2,2	2,3	6	1,12
Other substances	4,4	6,3	9	2,03
Diaper	-	3,2	8	5,45

GIS Analysis of Landfill Site

The current part of the study looked at the impact of MSW storage activities on the surrounding surface and environment in the organized landfill region of Odayeri. Assessments

were performed for this purpose based on data accessible since the site's inception in 1995. In this context, spatial changes on orthophoto data (Table 2) and satellite images for the years 1996, 2002, 2005, 2010, 2013, 2014, 2017, 2018, 2021 and 2022 were made through the Geographic Information System (GIS).

Table 2. Imagery Data

Year	Data
1996	Orthophoto
2002	Hi-Resolution Satellite Imagery
2005	Hi-Resolution Satellite Imagery
2010	Hi-Resolution Satellite Imagery
2013	Orthophoto
2014	Hi-Resolution Satellite Imagery
2017	Hi-Resolution Satellite Imagery
2018	Hi-Resolution Satellite Imagery
2021	Hi-Resolution Satellite Imagery
2022	Hi-Resolution Satellite Imagery

The data on plant types provided by the General Directorate of Forestry in 2003 were utilized at the stage of identifying changes in land use caused by spatial changes. When these statistics are examined, it is discovered that places within the existing limits of the Odayeri Landfill Site consist of stone pine stands, mixed broadleaf (mainly oak) stands, oak-hornbeam mixed stands, glades, open-pit mines, and lakes.

Evaluations were carried out utilizing digital elevation models (DEM) to identify the fillings carried out in the region. Digital elevation models (DEMs) are recognized as crucial data sources for environmental modeling (Hutchinson et al., 2011; Wilson and Fotheringham, 2008). In this study, we utilized DEMs generated from two specific sources. The Shuttle Radar Topography Mission (SRTM) DEM is the first source. The photogrammetrically produced National Topographic DEM is the second source.

The National Aeronautics and Space Administration (NASA), the National Geospatial-Intelligence Agency (NGA) of the United States Department of Defense (DOD), the German Aerospace Center (DLR), and the Italian Space Agency (ASI) collaborated on the Shuttle Radar Topography Mission (SRTM) in 2000. It is worth noting that the SRTM data only includes topographic information from the year 2000. Until 2015, the highest resolution SRTM data was confined to the area of the United States. However, on September 23, 2014, the US government stated its intention to make the highest resolution SRTM data (1 arc second, or 30 meters) available globally by late 2015 (JPL NASA, 2014). As a result, SRTM data with a resolution of 1 arc second, or about 30 meters, was used for this investigation.

Topographic Digital Elevation Models (Topo-DEMs) with a 5-meter grid interval are produced nationally by the General Directorate of Mapping (GDM), which serves as the National Mapping Agency of Turkey. These Topo-DEMs are generated using automatic matching techniques and rely on 30-centimeter resolution stereo aerial photographs. They provide comprehensive coverage of the terrain, capturing intricate details such as human-made structures and vegetation. The Topo-DEM was produced in the year 2013 (GDM, 2023). Thus, the aim was to calculate the topographic changes and volumetric differences between the years 2000 (SRTM-DEM) and 2013 (Topo-DEM). All processing and analysis of the entire dataset were performed using the ArcGIS Desktop 10.8 GIS software (ArcGIS Desktop, 2023).

RESULTS

In the methods of creating orthophoto data from various sources, high-resolution satellite imagery, DEM data, and vector forest stand data spatially assessable in geographic information system (GIS) databases were carried out within the scope of the study. In this context, coordinate transformations were used to collect data from various sources into a single database, and coordinate and projection transformations were performed using the World Geodetic System 1984 (WGS84) and Universal Transverse Mercator (UTM) Zone 35 North (EPSG: 32635).

The major goal after compiling the data was to determine spatial changes in the Odayeri Landfill Site by digitizing the boundaries of each year using the appropriate photographs. Following that, the boundary data for each year were analyzed in conjunction with the forest stand data to discover changes in land use cover. Since it was available, the General Directorate of Forestry's oldest available forest stand data from 2003 was used at this stage. These data were utilized in the overlay analysis to determine changes in land use cover. These figures are based on forest inventory data collected using photogrammetric and ground surveys. Because there was no digital (vector) data accessible prior to 2003, an assessment was carried out using the oldest known aerial photograph from 1970. As shown in Figure 2, the evaluation found that there was no activity on the site at the time.

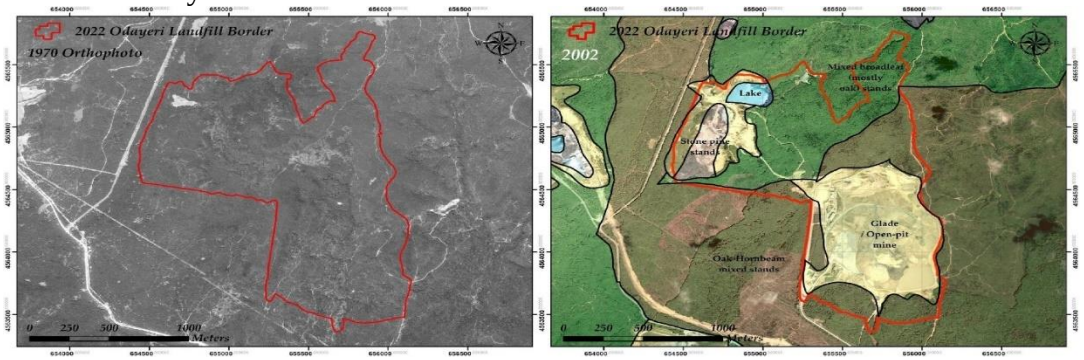

Figure 2. Condition of Odayeri Landfill in 1970 (Left), Stand Types Data (Right)

As previously stated, the Odayeri Landfill Site began operations in 1995. Spatial extents from 1996 to the present have been established using photos from the developed database. The results of the overlay analysis with forest stand data are shown in Figure 3, Figure 4, and Table 3.

Table 3. Land cover changes throughout time

	1996	**2002**	**2005**	**2010**	**2013**	**2014**	**2017**	**2018**	**2021**	**2022**
Stone pine stands	0	0.357	0.357	0.357	0.357	3.687	10.452	10.452	10.452	10.452
Mixed broadleaf (mostly oak) stands	0	0.825	4.183	6.206	7.302	19.270	25.656	34.725	50.399	62.048
Oak-Hornbeam mixed stands	0.035	2.197	9.176	40.294	42.301	43.093	43.390	43.390	47.591	47.751
Glade / Open-pit mine	30.627	73.719	75.186	76.505	76.505	78.553	91.563	91.697	91.697	91.697
Lake	0	0	0	0	0	0	4.383	4.385	4.385	4.385
Total Area (ha)	30.662	77.098	88.903	123.362	126.464	144.602	175.444	184.649	204.523	216.332

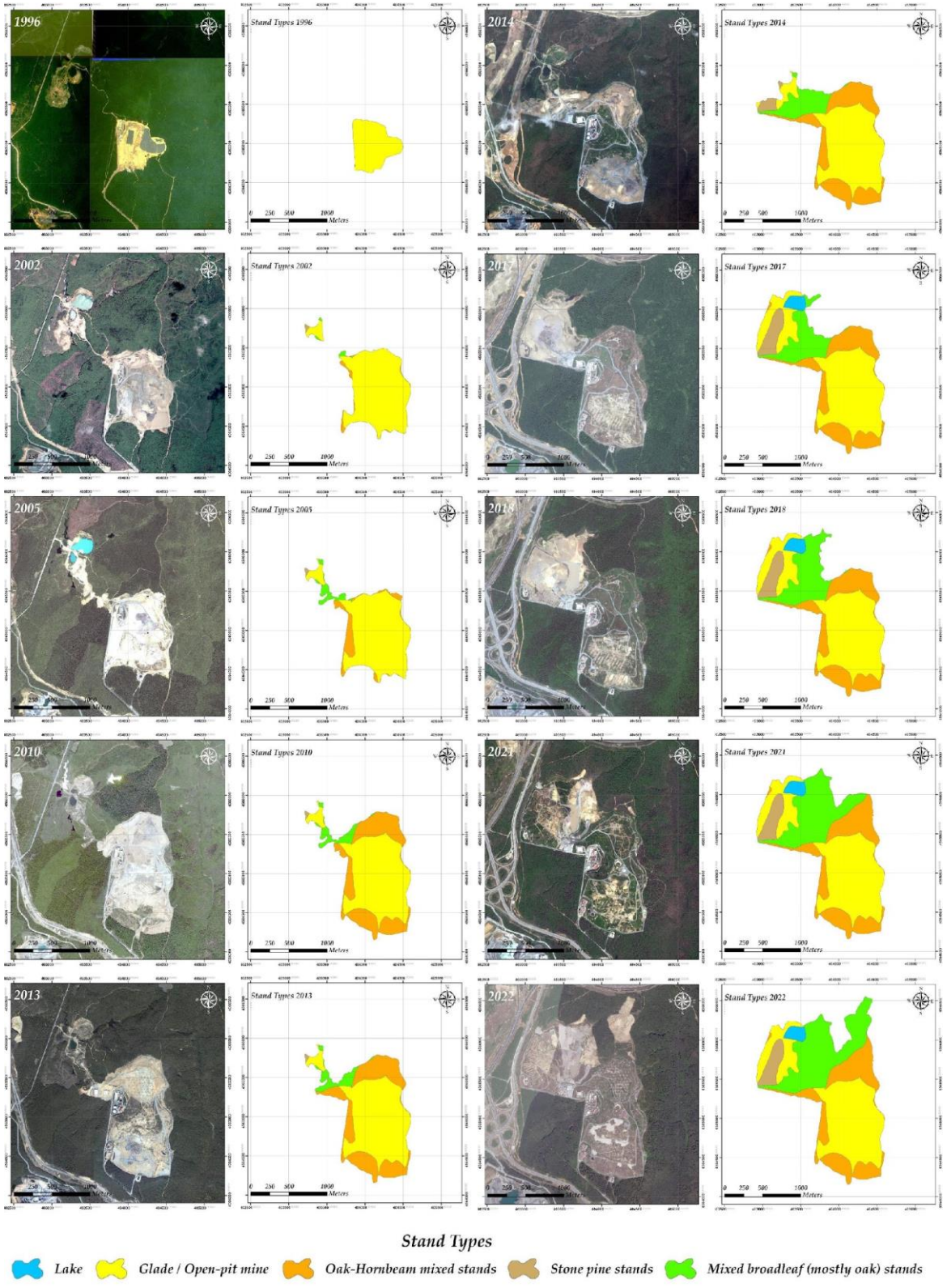

Figure 3. Situation of Odayeri Landfill in 1996, 2002, 2005, 2010, 2013, 2014, 2017, 2018, 2021 and 2022 and the stands it cover.

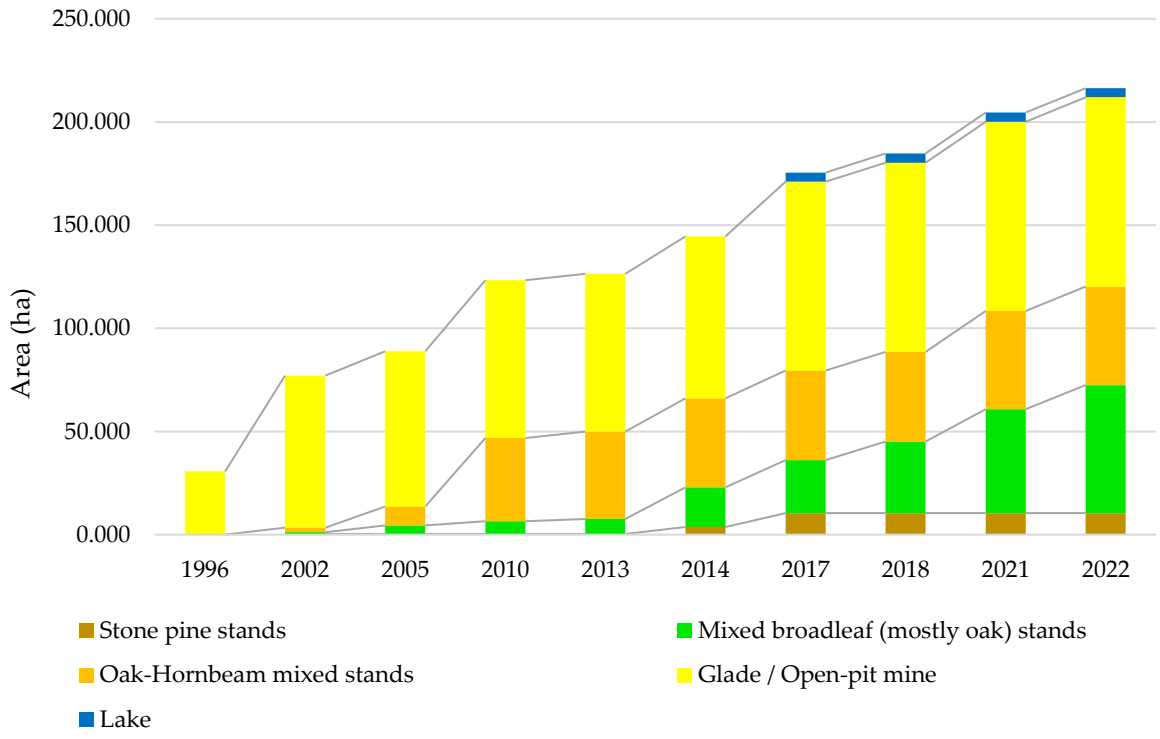

Figure 4. Temporal changes in land cover

Storage activities were carried out in an area of roughly 30 hectares in the Odayeri Landfill Site during the first year after its formation in 1995 until 1996. A linear trend has been detected when assessing spatial variations over time (Figure 5). Within this framework, it has been determined that forest areas provide spatial improvements based on needs.

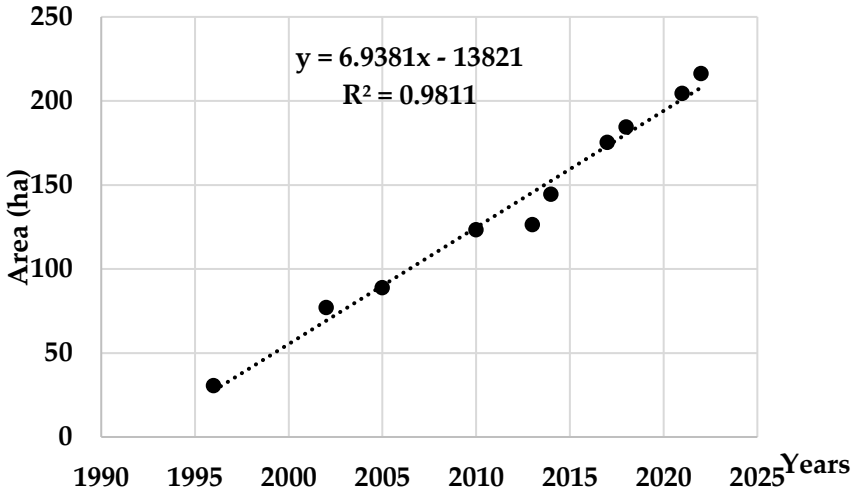

Figure 5. Total area change trend

Another study conducted in the study area focuses on determining the topographic changes. In this stage, the 2000 SRTM-DEM and 2013 Topo-DEM (Turkish GDM-DEM) data were used. The aim was to identify the topographic changes in the area that were closed off for storage by reaching the storage threshold boundary in the southern part of the study area (Figure 1. Ex-Landfill Area). In line with this objective, the changes occurring in the three-dimensional aspect were initially identified. By subtracting one terrain model from the other in a GIS environment, a Difference Surface Model was obtained. The analysis revealed differences of

up to 65 meters between the two terrain models. Additionally, excavations of up to 12 meters were identified within this area (Figure 6). At this stage, it was determined that the removal of trees from the area during soil preparation in the forest area was the cause of this difference.

DEM data was used to assess the volumetric changes occurring in the landfill site. A total storage volume of roughly 24 million cubic meters was accomplished within the closed-off storage region, which has a breadth of around 120 hectares, according to analyses conducted in a GIS environment. Volumetric losses were recorded at this stage in locations where excavation occurred or where the forest cover was removed due to the aforementioned topographical adjustments in the landfill site (Figure 6) (Table 4).

Table 4. Volumetric difference in landfill area

	Volume (m^3)	Area (m^2)
Net Gain	-24,397,192.4	1,073,433.0
Unchanged	0.0	0.0
Net Loss	449,709.6	151,631.8
Total	-23,947,482.8	1,225,064.8

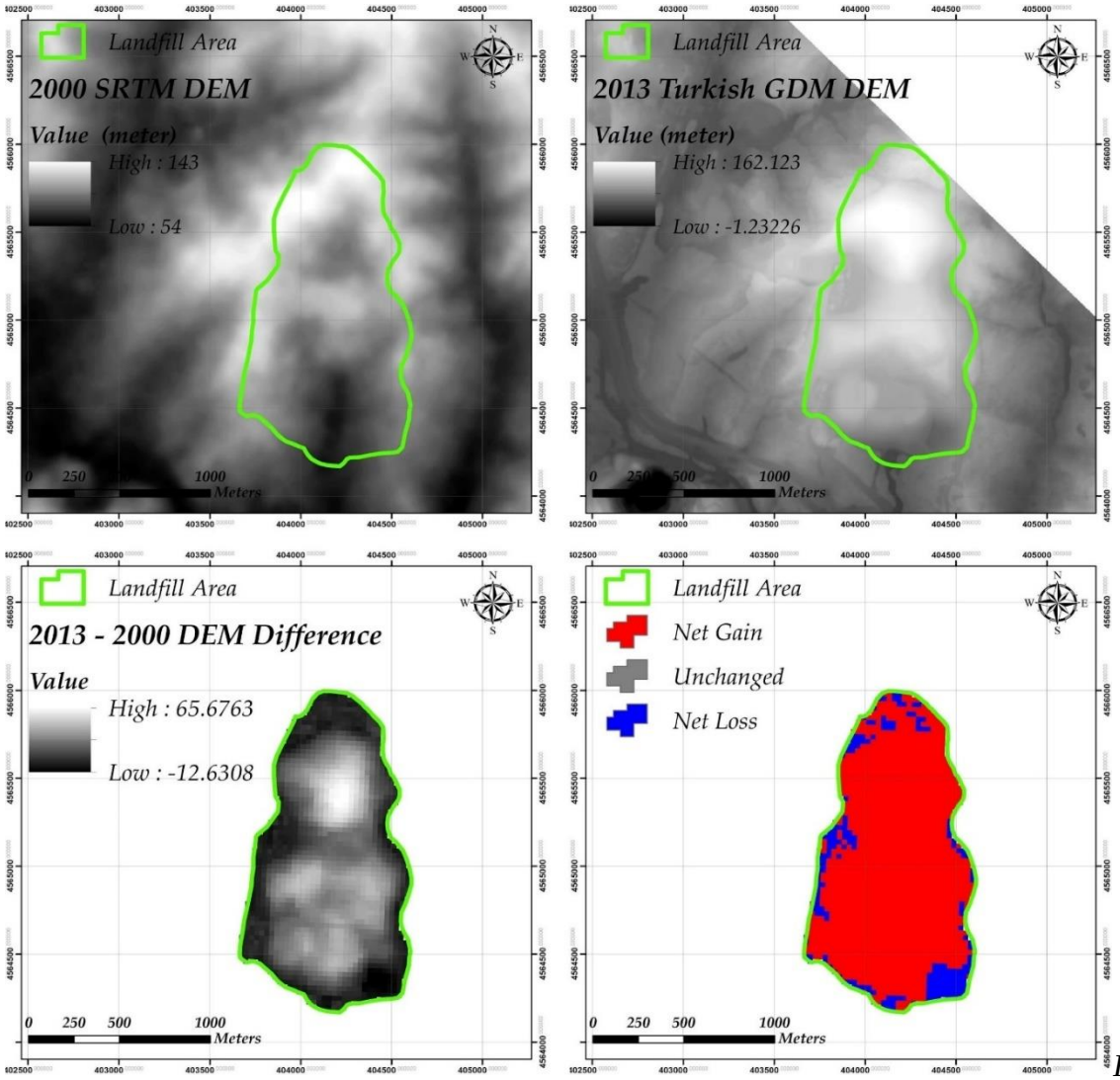

Figure 6. 2000 SRTM-DEM, 2013 Topo-DEM (Turkish GDM-DEM), 2013-2000 DEM Difference Map, 2013-2000 Cut-Fill Map

CONCLUSİONS

The final stage in the management of MSW, known as landfilling, ensures the minimization of environmental impacts caused by MSW. Sanitary landfilling is an integral part of every waste management system. Due to the fact that processes such as biological treatment and incineration themselves generate waste by-products, the disposal of a certain amount of waste in a sanitary landfill sites is always necessary in all cases. Due to its economic advantages; landfilling, also known as "sanitary landfilling," is frequently preferred for the disposal of MSW. Sanitary landfilling is the most widely used MSW disposal method globally due to its low cost of disposal and operational convenience.

The storage of MSW in sanitary landfills is a long-term activity. Landfill areas are typically designed to provide service for an average of 25 years. Therefore, during the waste disposal process, certain changes occur in the topography and vegetation of the landfill area and its surrounding environment. It is crucial to have a good understanding of the land conditions and land use in the areas where landfill sites are established. Agricultural land classifications and the current land use of the area play a significant role in site selection. In this study, the aim was to determine the topographic changes caused by MSW disposal activities in the Odayeri Sanitary Landfill Site located in Istanbul, Turkey.

According to the findings of the study, it was determined that storage was conducted in an area of approximately 120 ha. When examining the spatial changes over the years, a linear change is observed. During the storage period, it was observed that there were spatial gains from forest areas, depending on the needs. To determine the topographic changes in the area, changes occurring in the third dimension were identified. Based on the results obtained from the Difference Surface Model, variations of up to 65 m were found between the two land models. Additionally, it was determined that excavations of up to 12 m, believed to be due to surface leveling during the preparation stage of the landfill area, were carried out within this region (Figure 6).

The construction and operation technology implemented in a modern sanitary landfill site ensures the protection of public health and the environment. In this respect, important considerations include the appropriate design of the landfill site and the effective implementation of post-closure monitoring. These measures are essential to guarantee the long-term effectiveness and safety of the landfill, as well as to minimize potential risks to the surrounding environment and public health. The re-vegetation of closed sanitary landfill sites is carried out with the aim of adapting the surrounding environment to the site, ensuring public acceptance, and minimizing erosion on slopes. Additionally, the utilization of closed landfill areas for purposes such as parks, golf courses, or grass skiing areas is also common. Therefore, it is expected that the changes in land use structure occurring during the operation of sanitary landfill site will not be permanent.

REFERENCES

Akkaya, E., Demir, A., & Varank, G. (2011). Characterisation of Odayeri Sanitary Landfill Leachate. *Sigma*, *3*, 238-251.

Apak, G., & Ubay, B. (2007). Türkiye iklim değişikliği birinci ulusal bildirimi. *Republic of Turkey Ministry of Environment and Forestry*. Ankara, Turkey. *(In Turkish)*

ArcGIS Desktop, (2023). Date of access: 02.05.2023, Available: http://desktop.arcgis.com/

Arikan, O.A. (1996). *İstanbul katı atıklarının karakterizasyonu ve havasız kompostlaşabilirliği üzerine bir çalışma*, Yüksek Lisans Tezi, İstanbul Teknik Üniversitesi / Fen Bilimleri Enstitüsü, Istanbul. *(In Turkish)*

Beskese, A., Demir, H.H., Ozcan, H.K., & Okten, H.E. (2015). Landfill site selection using fuzzy AHP and fuzzy TOPSIS: a case study for Istanbul, *Environmental Earth Science*, *73*, 3513-3521.Doi: 10.1007/s12665-014-3635-5

CH2M Hill International Ltd.-Antel Arıtma A.Ş. (1992). İstanbul anakenti katı atık yönetimi etüdü projesi raporu. İstanbul/ Turkey. *(In Turkish)*

GDM (General Directorate of Mapping), (2023). Date of access: 02.05.2023, Available: https://www.harita.gov.tr.

Güvenç, L. (2016). *Kartal belediyesi sınırları içerisinde oluşan ambalaj atıklarının belirlenmesi ve ekonomik analizi*, Yüksek Lisans Tezi. İstanbul Üniversitesi Fen Bilimleri Enstitüsü, İstanbul. *(In Turkish)*

Hutchinson, M. F., Xu, T. & Stein, J. A. (2011). Recent progress in the ANUDEM elevation gridding procedure. *Geomorphometry*, 19-22.

Korkutan, M., Doğru, A. Ö., & Göksel, C. (2018). Impact analysis of sanitary landfill based odour in Istanbul using GIS. *International Journal of Environment and Geoinformatics*, *5*(2), 169-177. Doi: https://doi.org/10.30897/ijegeo.421545

Kuru, A., Tok, E., Agdas, G.M., Demir, H.H., Ozcan, H.K., & Demir, G. (2021). GIS and multicriteria decision analysis for landfill site selection in Edirne Province, Turkey. *Journal of the Institute of Science and Technology*, *11*(2): 969-981. Doi: 10.21597/jist.792249

MEU (Republic of Turkey Ministry of Environment and Urbanisation), (2014). Düzenli depolama tesisleri saha yönetimi ve işletme kılavuzu. Ankara, Turkey. *(In Turkish)*

Ozcan, H. K., Guvenc, S. Y., Guvenc, L., & Demir, G. (2016). Municipal solid waste characterization according to different income levels: A case study. *Sustainability*, *8*(10), 1044. Doi: 10.3390/su8101044

Özkaya, B. (2004). *Katı atık depo sahalarında sızıntı suyu geri devrinin atıkların ayrışması ve sızıntı suyu üzerindeki etkilerinin incelenmesi*, Doktora Tezi, Yıldız Teknik Üniversitesi Fen Bilimleri Enstitüsü, Istanbul. *(In Turkish)*

Tchobanoglous, G., Theisen, H., & Vigil, S. (1993). *Integrated solid waste management-engineering principles and management issues*. McGraw-Hill, Inc. ISNB 0070632375.

TURKSTAT (Turkish Statistical Institute), (2020). Atık istatistikleri. Newsletter; Number: 37198. Ankara, Turkey. *(In Turkish)*

TURKSTAT (Turkish Statistical Institute), (2022). Adrese dayalı nüfus kayıt sistemi sonuçları. Ankara, Turkey. *(In Turkish)*

Wilson, J. P., & Fotheringham, A. S. (Eds.). (2008). *The handbook of geographic information science*. Blackwell Pub.

Yaltırak., F. (1966). Belgrad Ormanı vejetasyonunun floristik analizi ve ana mescere tiplerinin kompozisyonu üzerinde arastırmalar. *General Directorate of Forestry Publication*. *(In Turkish)*

Yildiz, S., Yaman, C., Demir, G., Ozcan, H. K., Coban, A., Okten, H. E., Sezer, K., & Goren, S. (2013). Characterization of municipal solid waste in Istanbul, Turkey. *Environmental Progress Sustainable Energy*, *32*(3), 734-739. Doi: https://doi.org/10.1002/ep.11640

Comparison of K-means and Fuzzy C-means Clustering Algorithms on Water Quality Parameters: Case Study of Ergene Basin for 17 Stations

Gülay ARSLAN ÇENE[1]
Coşkun PARİM[2]
Erhan ÇENE[3]

Introduction

Surface water quality plays a critical role in safeguarding human health and ecological systems, particularly in urban areas where rivers and tributaries pass through industrial, domestic/sewage, and agricultural areas, posing significant challenges (Qadir et al., 2008). The deterioration of surface water quality is influenced by various anthropogenic factors, such as urbanization, industrial and agricultural practices, chemical spills, dam construction, as well as natural processes like erosion and climatic conditions. These factors contribute to the presence of macro pollutants and micropollutants, which include complex organic compounds and nutrients, leading to environmental consequences such as oxygen depletion and algal blooms in aquatic ecosystems (Emadian et al., 2020).

To effectively control and manage water pollution, it is necessary to evaluate multiple limnological parameters in streams and rivers, as they are particularly vulnerable to pollution (Singh et al., 2005 and Köse et al., 2014). However, accurately determining the specific contribution of each factor to water quality remains uncertain, highlighting the need to reduce this uncertainty by examining temporal and spatial variations in water quality and identifying hidden sources of pollution (Zhang Y et al., 2009). This knowledge is crucial for guiding decision-making processes and prioritizing actions aimed at improving water quality (Wang et al., 2008; Zhang Q et al., 2009).

Previous research has shown that deterministic water quality models based on simulations often yield inaccurate results, as they fail to capture the intricate nature of water quality influenced by multiple factors and struggle to address imperfections and uncertainties in the underlying data. In contrast, multivariate statistical methods have frequently been utilized in the existing literature to assess surface water quality, offering a more comprehensive approach (Orak et al., 2020; İşçen et al., 2009; Bilgin and Konanç, 2016).

In 1988, the Water Pollution Control Regulation was published, establishing a framework for comprehensive water quality management. This regulation implemented a classification system for surface waters, dividing them into four classes based on their quality levels. The classification system aims to assess and monitor the pollution status of surface waters. The four classes are defined as follows: (Akın and Akın 2007)

Class I: High Quality Water: This class represents surface waters with excellent water quality, indicating minimal pollution and high ecological integrity. Class I waters are considered pristine and suitable for various purposes, including drinking water supply and conservation of aquatic ecosystems.

[1]Research Assistant, Marmara University, Departmant of Environmental Engineering, Orcıd: 0000-0003-1983-266X
[2] Research Assistant PhD., Yildiz Technical University, Departmant of Statistics, Orcıd: 0000-0002-6412-1325
[3] Assistant Professor, Yildiz Technical University, Departmant of Statistics, Orcıd: 0000-0001-5336-6004

Class II: Slightly Polluted Water: Class II waters indicate a slightly higher level of pollution compared to Class I. Although they may exhibit slight impairments in water quality, they are still relatively clean and suitable for most water uses, including recreational activities and irrigation.

Class III: Polluted Water: Class III waters denote a higher degree of pollution compared to the previous classes. These waters may exhibit noticeable impairments in quality, potentially resulting from various pollution sources such as industrial discharges or agricultural runoff. Special attention and management practices are required to mitigate pollution in Class III waters.

Class IV: Highly Polluted Water: Class IV represents surface waters with a significantly high level of pollution. These waters exhibit severe impairments in quality and may pose risks to both human health and the environment. Class IV waters typically require intensive pollution control measures and restoration efforts to improve their quality.

The Ergene River, situated in the European part of Turkey, serves as a crucial water source for 1.7 million people in the region, catering to recreational, industrial, and agricultural needs. However, due to intense industrial and agricultural activities and inadequate regulations regarding wastewater discharge quality in Turkey, the Ergene River has become one of the most polluted rivers in both Turkey and Europe. Moreover, as the Ergene River converges with the Maritsa River, an international transboundary river that flows into the Aegean Sea, the water quality of the Ergene River carries international significance. Currently, macro pollutant levels in the Ergene River are regularly monitored. This study aims to assess the status of macro pollutants in the Ergene River, examine the impact of seasonal variations on macro pollutant concentrations, and evaluate the compliance of macro pollutant levels with surface water quality standards established by the European Union and Turkey. The study is based on a dataset comprising 15 water-related variables from 17 water stations within the period of 1985-2013.

This study aims to employ k-means and fuzzy c-means cluster analysis on water stations on the Ergene basin and compare the results with the water quality classification of Water Pollution Control Regulation.

Methodology

Mean and standard deviation, for each parameter among each station is reported (Table 2). To reveal the similarities and differences among water stations k-means cluster analysis and fuzzy c-means cluster analysis are employed (Landau, Leese, Stahl, & Everitt, 2011). In addition, multidimensional scaling maps the variables on a two-dimensional coordinate system according to their similarities and differences (Kruskal, 1964) and can be used to support CA (Kruskal, 1977). MDS and CA are employed to visualize the performance metrics of water quality indicators and how they spread through a two-dimensional space. Two MDS maps are used in this study, one for k-means cluster analysis results and one for fuzzy c-means cluster analysis results. All the statistical analyses are performed with the R programming language (R Core Team, 2022).

k-means cluster analysis

K-means cluster analysis is a widely used method for partitioning data into k clusters based on similarity metrics such as Euclidean distance or cosine similarity (MacQueen, 1967). The algorithm works by iteratively assigning each data point to one of k clusters based on the similarity between the data point and the centroid of each cluster. The centroid of each cluster is calculated as the mean of the data points in that cluster, and the similarity between a data point and a cluster centroid is often measured by the squared Euclidean distance between the two.

The k-means algorithm can be formalized as follows:

1. Initialize k cluster centroids randomly.
2. Assign each data point to the nearest cluster centroid.
3. Recalculate the centroids of each cluster as the average of the data points in that cluster.
4. Repeat steps 2 and 3 until convergence is reached.

The resulting clusters can be used to identify patterns in the data and to gain insights into the relationships between variables. A drawback of k-means is that it can be sensitive to the initial random initialization of the cluster centroids and can converge to suboptimal solutions. Several variants of k-means have been proposed to address this issue (Arthur & Vassilvitskii, 2007).

Fuzzy c-means cluster analysis

Fuzzy c-means (FCM) is a generalization of k-means that allows for overlapping clusters and degrees of membership. In FCM, each data point is assigned a degree of membership in each cluster, rather than being assigned to a single cluster. The algorithm works by iteratively updating the degrees of membership of each data point based on the distance to each cluster centroid and a fuzziness parameter that controls the degree of overlap between clusters. The cluster centroids are then updated based on the weighted average of the data points, where the weights are the degrees of membership.

The FCM algorithm can be formalized as follows:

1. Initialize k cluster centroids randomly.
2. Calculate the degree of membership of each data point to each cluster.
3. Update the cluster centroids based on the weighted average of the data points, where the weights are the degrees of membership.
4. Repeat steps 2 and 3 until convergence is reached.

FCM can handle noisy data and outliers better than k-means and can be used in applications such as image segmentation and pattern recognition (Bezdek et al., 1981).

Multidimensional Scaling

Multidimensional scaling (MDS) is a technique used to visualize the similarities and differences between objects or observations in high-dimensional space. MDS works by reducing the dimensionality of the data while preserving the pairwise distances between the objects. The result is a two- or three-dimensional representation of the data that allows for easy visualization and interpretation.

MDS can be formalized as follows:

Given a dissimilarity matrix D of size n x n, where n is the number of objects, the goal of MDS is to find a set of points X in m-dimensional space (usually m = 2 or 3) such that the pairwise Euclidean distances between the points approximate the dissimilarity matrix D:

$$d_{ij} = \|x_i - x_j\|_2$$

for all $i, j = 1,2, \ldots, n$

The solution to this problem can be obtained by optimizing an objective function such as stress or Kruskal's stress (Kruskal, 1964).

MDS can be used to explore relationships between variables, to identify patterns in the data, and to identify outliers or unusual observations. MDS is a useful technique for exploratory data analysis and can help to generate hypotheses for further investigation.

Data

The Ergene River Basin, located in northwestern Turkey, is an important water resource for the region, providing water for irrigation, drinking, and industrial purposes. The basin covers an area of approximately 10,000 km² and is home to over two million people. However, due to the high level of pollution in the Ergene River, the quality of the water has been deteriorating, leading to serious environmental and health problems. According to a study conducted by Dokmeci, A. H. (2017), the Ergene River is contaminated with heavy metals, organic pollutants, and pathogens, posing a threat to both human health and the ecosystem. Therefore, protecting and restoring the water quality in the Ergene River Basin is crucial for ensuring the sustainable use of this vital resource for the region. Thus, investigating similarities and differences among water stations inside the Ergene Basin has great importance.

The Ergene Basin dataset consists of 15 water related variables from 17 water stations within the period of 1985-2013. The study area is denoted in Figure 1.

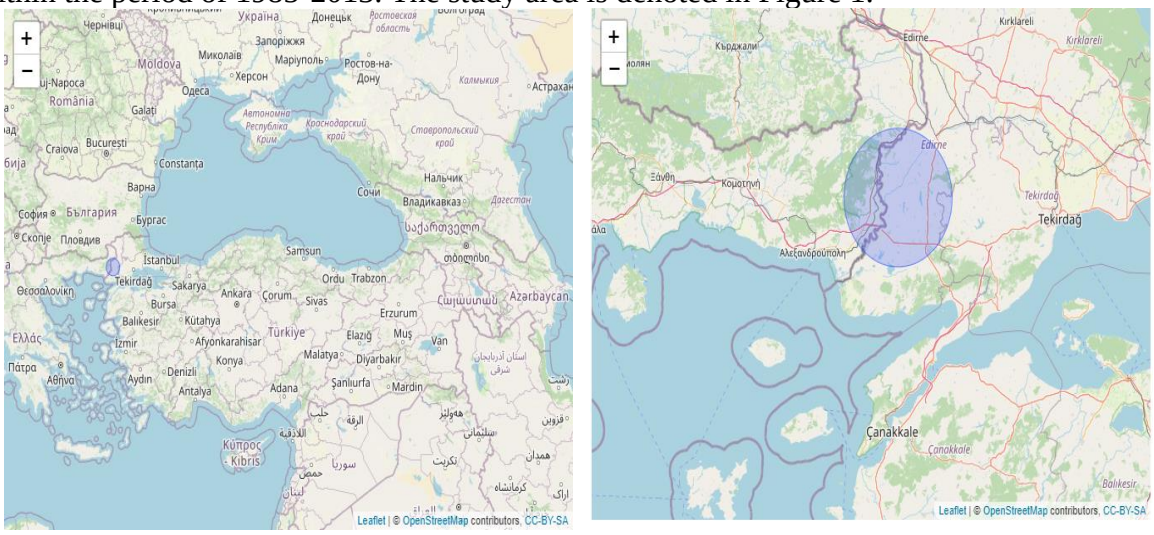

Figure 1: *The study area Ergene Basin, Turkiye*

The water parameters are in yearly format so for each station there are 420 observations and in the entire dataset there are 7140 observations. The list of the stations and variables is given in Table 1.

Table 1. Description of Stations and water quality parameters

Station	Station No	Station Name	Parameter	Description
S1	01-11-00-001	MERIC NEHRI KAPIKULE	**BOD5**	Biochemical oxygen demand
S2	01-11-00-002	TUNCA NEHRI SU AKACAGI	**Cl-**	Chloride
S3	01-11-00-003	ARDA NEHRI ESKI DEMIRYOLU KOPRUSU	**DO**	Dissolved oxygen
S4	01-11-00-008	MERIC NEHRI ESKIKOY	**EC**	Escherichia coli
S5	01-11-00-009	MERIC NEHRI IPSALA	**Al**	Aluminum
S6	01-11-00-013	ERGENE NEHRI CORLU KOPRUSU	**NH4-N**	Ammonium–nitrogen
S7	01-11-00-014	ERGENE NEHRI INANLI	**NO2-N**	Nitrite–nitrogen
S8	01-11-00-015	ERGENE NEHRI LULEBURGAZ	**NO3-N**	Nitrate–nitrogen
S9	01-11-00-016	ERGENE NEHRI ALPULLU	**o-PO4**	Orthophosphate
S10	01-11-00-017	ERGENE NEHRI UZUNKOPRU	**pH**	Potential of Hydrogen
S11	01-11-00-018	SAZLIDERE OLMUK GIRISI	**pV**	Photovoltaics
S12	01-11-00-019	SAZLIDERE OLMUK CIKISI	**SS**	Suspended Solid
S13	01-11-00-022	GALA GOLU CIKISI	**T**	Temperature
S14	01-11-00-023	MERIC NEHRI FERREKUPURU	**TDS**	Total Dissolved Solid
S15	01-11-00-024	MERIC NEHRI EDIRNE CIKISI BOSNA	**Turb**	Turbidity
S16	01-11-00-025	MERIC NEHRI_KARASAZ SU ALMA AGZI		
S17	01-11-01-020	SULOGLU DERESI SULOGLU BARAJI		

Water quality parameters are important measures of the health and safety of water sources, which can be affected by various natural and human-induced factors. Biochemical Oxygen Demand (BOD5) is a measure of the amount of oxygen required by microorganisms to decompose organic matter in water. High BOD5 levels indicate high levels of organic pollution, which can cause a decrease in dissolved oxygen (DO) levels, leading to the death of aquatic organisms. Chloride (Cl-) is an important indicator of salinity in water, which can affect the taste, quality, and suitability of water for different uses. High chloride levels can be harmful to aquatic life and can cause corrosion in pipelines and other infrastructure.

Dissolved oxygen (DO) is a measure of the amount of oxygen present in water and is essential for the survival of aquatic organisms. Low DO levels can lead to the death of fish and other aquatic organisms, as well as contribute to the growth of harmful algal blooms. Escherichia coli (EC) is a bacterium found in the intestines of humans and animals, and its presence in water can indicate fecal contamination, which can pose a significant risk to human health. Aluminum (Al) is a toxic metal that can cause a range of health effects in humans and aquatic organisms, including neurological damage and respiratory problems.

Ammonium-nitrogen (NH4-N), Nitrite-nitrogen (NO2-N), Nitrate-nitrogen (NO3-N), and Orthophosphate (o-PO4) are important indicators of nutrient pollution in water, which can lead to the growth of harmful algae and other aquatic plants, deplete dissolved oxygen, and cause fish kills. The potential of Hydrogen (pH) is a measure of the acidity or basicity of water, which can affect the solubility and toxicity of different substances in water. Photovoltaics (pV) is a measure of the light intensity in water, which can affect the growth and reproduction of aquatic organisms. Suspended solids (SS) and Turbidity (Turb) are measures of the amount of particulate matter in water, which can affect the clarity, taste, and quality of water, as well as affect aquatic habitats.

Water quality parameters are essential tools for monitoring and managing the health and safety of water sources. Understanding the effects of different water quality parameters, such as BOD5, Cl-, DO, EC, Al, NH4-N, NO2-N, NO3-N, o-PO4, pH, pV, SS, and Turb, can help identify potential water quality issues and implement appropriate management strategies to protect and improve water quality.

The averages and standard deviations of water quality parameters for each observation point (station) are given in Table 2. Among stations, the average BOD5 values varies from 2.38 to 77.91, the average CL- values varies from 17.16 to 727.98, the average DO values varies from 2.94 to 10.29, the average EC values varies from 332.28 to 4455.74, the average Al values varies from 107.05 to 865.92, the average NH4-N values varies from 0.13 to 15.37, the average NO2-N values varies from 0.01 to 0.37, the average NO3-N values varies from 0.37 to 3.88, the average O-PO4 values varies from 0.1 to 8.83, the average pH values varies from 7.29 to 8.43, the average pV values varies from 2.06 to 56.4, the average SS values varies from 29.52 to 301.57, the average T values varies 15.03 to 17.97, the average TDS values varies from 245.94 to 2523.93, and the average Turb values varies from 24.86 to 449.87.

Table 2. Averages and standard deviations of water quality parameters in observation points.

Station	BOD_5	Cl^-	DO	EC	Al
S1: 01-11-00-001	4.32 (1.79)	25.70 (8.66)	9.59 (1.38)	600.21 (97.93)	165.50 (21.32)
S2: 01-11-00-002	4.49 (2.04)	51.61 (16.63)	10.29 (1.64)	837.85 (602.03)	241.62 (27.09)
S3: 01-11-00-003	2.38 (1.76)	17.16 (6.73)	10.09 (1.47)	332.28 (38.44)	107.05 (14.70)
S4: 01-11-00-008	4.34 (1.33)	27.62 (5.83)	9.35 (1.34)	539.67 (64.47)	156.21 (21.68)
S5: 01-11-00-009	5.67 (2.50)	55.50 (18.08)	9.82 (1.74)	660.12 (106.33)	181.50 (37.06)
S6: 01-11-00-013	8.54 (7.81)	78.08 (26.38)	8.52 (2.46)	715.39 (164.04)	187.65 (32.34)
S7: 01-11-00-014	55.31 (34.94)	618.58 (376.46)	3.52 (2.46)	3062.97(1515.61)	469.79 (145.59)
S8: 01-11-00-015	54.97 (35.29)	475.56 (252.23)	2.94 (2.41)	4455.74 (9590.90)	490.94 (146.38)
S9: 01-11-00-016	54.08 (29.35)	424.75 (232.64)	3.22 (2.24)	2394.71 (1023.98)	485.64 (121.30)
S10: 01-11-00-017	32.39 (18.27)	295.92 (174.23)	3.82 (2.06)	1848.89 (829.60)	865.92 (2563.77)
S11: 01-11-00-018	5.43 (4.59)	166.39 (433.84)	8.18 (1.90)	833.84 (92.97)	285.90 (26.93)

S12: 01-11-00-019	77.91 (79.68)	82.61 (8.28)	3.38 (1.34)	1081.50 (149.18)	432.81 (123.28)
S13: 01-11-00-022	5.70 (2.59)	727.98 (922.49)	9.12 (1.34)	3857.04 (6736.50)	245.98 (64.29)
S14: 01-11-00-023	5.45 (1.48)	238.14 (568.08)	9.65 (1.57)	1083.25 (1203.49)	180.06 (29.61)
S15: 01-11-00-024	4.81 (1.25)	31.57 (8.03)	9.75 (1.30)	1085.36 (2676.61)	172.44 (18.22)
S16: 01-11-00-025	9.85 (6.11)	113.02 (48.51)	8.26 (1.61)	954.58 (246.75)	239.10 (59.13)
S17: 01-11-01-020	3.57 (1.92)	30.71 (6.70)	10.09 (1.63)	597.72 (1177.50)	132.85 (71.19)
Station	**NH_4-N**	**NO_2-N**	**NO_3-N**	**O-PO_4**	**pH**
S1: 01-11-00-001	1.00 (1.25)	0.02 (0.02)	2.83 (1.98)	1.35 (0.88)	7.92 (0.28)
S2: 01-11-00-002	0.68 (0.57)	0.04 (0.05)	2.11 (1.15)	1.55 (1.11)	8.17 (0.26)
S3: 01-11-00-003	0.13 (0.10)	0.01 (0.01)	0.94 (0.94)	0.13 (0.10)	8.01 (0.24)
S4: 01-11-00-008	0.50 (0.45)	0.01 (0.02)	1.80 (1.04)	1.06 (0.68)	7.90 (0.25)
S5: 01-11-00-009	0.80 (0.27)	0.03 (0.08)	1.52 (0.90)	0.97 (0.40)	7.93 (0.24)
S6: 01-11-00-013	1.19 (1.14)	0.09 (0.23)	1.98 (2.05)	2.34 (1.59)	7.72 (0.24)
S7: 01-11-00-014	15.37 (11.65)	0.04 (0.05)	0.46 (0.41)	8.83 (21.09)	7.71 (0.20)
S8: 01-11-00-015	10.78 (5.46)	0.04 (0.03)	0.73 (1.35)	4.67 (1.98)	7.80 (0.22)
S9: 01-11-00-016	10.93 (4.81)	0.08 (0.16)	0.57 (0.50)	4.26 (1.94)	7.76 (0.35)
S10: 01-11-00-017	7.23 (4.18)	0.34 (1.61)	1.16 (2.14)	3.31 (1.68)	7.83 (0.27)
S11: 01-11-00-018	0.50 (0.29)	0.10 (0.06)	3.88 (2.82)	0.61 (0.37)	7.93 (0.19)
S12: 01-11-00-019	6.10 (5.89)	0.13 (0.28)	0.87 (0.68)	0.36 (0.27)	7.29 (0.21)
S13: 01-11-00-022	0.68 (0.21)	0.03 (0.07)	0.37 (0.56)	0.28 (0.18)	8.43 (1.95)
S14: 01-11-00-023	0.75 (0.37)	0.03 (0.07)	1.77 (1.19)	1.02 (0.46)	7.93 (0.26)
S15: 01-11-00-024	0.95 (0.92)	0.02 (0.02)	2.18 (1.57)	1.33 (0.86)	8.00 (0.26)
S16: 01-11-00-025	1.84 (0.99)	0.37 (1.62)	1.35 (1.37)	1.29 (0.50)	7.84 (0.25)
S17: 01-11-01-020	0.35 (0.14)	0.01 (0.01)	0.82 (1.07)	0.10 (0.07)	8.29 (0.31)
Station	**pV**	**SS**	**T**	**TDS**	**Turb**
S1: 01-11-00-001	3.57 (1.12)	61.76 (34.06)	16.60 (3.37)	399.92 (76.76)	56.13 (34.39)
S2: 01-11-00-002	3.79 (0.91)	67.88 (68.37)	16.98 (3.20)	466.01 (72.52)	47.65 (27.13)
S3: 01-11-00-003	2.06 (0.52)	29.52 (19.60)	15.68 (3.72)	278.67 (364.50)	24.86 (21.44)
S4: 01-11-00-008	3.44 (0.63)	59.06 (27.67)	16.40 (3.52)	366.39 (60.22)	49.70 (25.43)
S5: 01-11-00-009	3.95 (0.48)	75.18 (43.92)	17.78 (3.31)	444.28 (66.43)	75.13 (69.51)
S6: 01-11-00-013	4.33 (2.75)	81.28 (66.24)	17.05 (3.85)	459.50 (101.52)	89.55 (83.27)
S7: 01-11-00-014	35.77 (15.15)	174.00 (88.30)	17.75 (4.26)	2192.21 (1438.90)	152.15 (84.97)
S8: 01-11-00-015	32.79 (19.86)	111.38 (83.46)	17.33 (4.09)	1837.40 (1006.43)	112.79 (98.69)
S9: 01-11-00-016	30.32 (15.34)	301.57 (274.03)	17.96 (3.56)	1530.11 (673.24)	323.70 (322.75)
S10: 01-11-00-017	17.78 (9.31)	182.93 (220.51)	17.45 (3.48)	1169.02 (535.32)	214.73 (327.79)
S11: 01-11-00-018	2.86 (0.82)	43.27 (27.12)	15.03 (3.86)	535.54 (86.41)	35.34 (23.07)
S12: 01-11-00-019	56.40 (59.02)	262.75 (270.34)	16.56 (3.06)	986.33 (753.63)	449.87 (622.92)
S13: 01-11-00-022	6.59 (0.95)	67.68 (45.18)	17.09 (2.87)	2523.93 (4021.10)	52.96 (36.58)
S14: 01-11-00-023	4.08 (0.58)	67.67 (47.45)	17.50 (3.07)	812.34 (1179.22)	62.26 (66.04)
S15: 01-11-00-024	3.65 (0.73)	57.43 (23.71)	16.44 (3.46)	570.35 (991.11)	54.70 (29.32)
S16: 01-11-00-025	5.583 (1.17)	68.52 (30.42)	16.87 (2.91)	622.99 (170.90)	67.16 (53.39)
S17: 01-11-01-020	4.45 (0.76)	48.14 (83.85)	17.97 (3.74)	245.94 (32.28)	27.44 (16.22)

Results

Two cluster analysis methods are conducted among water stations: K-means clustering and Fuzzy c-means clustering. Both clustering methods suggest using 4 clusters. Based on the clustering results cluster 1 is named as Slightly Polluted Water Cluster, cluster 2 is named as High-Quality Water Cluster, cluster 3 is named as Highly Polluted Water Cluster, and cluster 4 is named as Polluted Water Cluster. The center of the clusters is provided in Table 3.

Table 3. Centers of Clusters based on K-means and Fuzzy C-means Clustering.

K-Means Clustering						Fuzzy C-means Clusters					
Cluster	**BOD_5**	**Cl^-**	**DO**	**EC**	**Al**	**Cluster**	**BOD_5**	**Cl^-**	**DO**	**EC**	**Al**
1	5.82	140.82	9.56	1102.87	188.11	**1**	4.69	132.56	10.07	1128.54	182.91
2	6.73	98.93	8.83	723.38	214.77	**2**	6.45	135.95	9.27	808.34	210.45
3	52.60	458.31	2.64	3020.92	598.56	**3**	69.54	506.89	2.20	3414.14	693.37
4	86.27	123.59	3.99	1214.66	444.58	**4**	23.85	152.69	5.06	1129.16	278.78
Cluster	**NH_4-N**	**NO_2-N**	**NO_3-N**	**o-PO_4**	**pH**	**Cluster**	**NH_4-N**	**NO_2-N**	**NO_3-N**	**o-PO_4**	**pH**
1	0.99	0.06	1.54	1.14	7.98	**1**	0.89	0.07	1.62	1.15	8.00
2	0.64	0.07	2.17	0.71	8.03	**2**	0.60	0.06	1.99	0.69	8.07
3	10.84	0.13	0.93	5.07	7.73	**3**	13.54	0.16	0.73	5.44	7.70
4	9.91	0.12	0.67	1.67	7.36	**4**	3.43	0.05	1.32	2.01	7.70
Cluster	**pV**	**SS**	**T**	**TDS**	**Turb**	**Cluster**	**pV**	**SS**	**T**	**TDS**	**Turb**
1	4.52	72.72	14.95	697.28	68.63	**1**	3.97	75.62	14.58	706.43	73.18
2	4.35	44.55	21.46	484.22	30.59	**2**	4.31	44.18	20.93	545.98	31.69
3	29.53	125.58	18.38	1729.00	116.96	**3**	46.26	224.40	18.88	2021.20	278.47
4	72.81	642.67	15.09	1151.27	990.73	**4**	12.28	123.04	15.97	718.03	135.35

The center of the clusters can be used to identify the characteristics of stations. For the k-means clustering results, the center of the first cluster has the lowest BOD5, Al, NO2-N, T average, has the second lowest EC, NH4-N, o-PO4, pV, SS, TDS and Turb average, has the second highest Cl-, NO3-N and pH average, and the highest DO average. The center of the second cluster has the lowest Cl-, EC, NH4-N, o-PO4, pV, SS, TDS and Turb average, has the second lowest BOD5, Al, and NO2-N, has the second highest DO average, and the highest NO3-N, pH and T average. The center of the third cluster has the lowest DO average, has the second lowest NO3-N, pH average, has the second highest BOD5, pV, SS, T and Turb average, and has the highest Cl-, EC, Al, NH4-N, NO2-N, o-PO4 and TDS average. The center of the fourth cluster has the lowest NO3-N and pH average, has the second lowest Cl-, DO and T average, has the second highest EC, Al, NH4-N, NO2-N, o-PO4 and TDS average, and has the highest BOD5, pV, SS and Turb average.

For the fuzzy c-means clustering results, the center of the first cluster has the lowest BOD5, Cl-, Al, pV and T average, has the second lowest EC, NH4-N, o-PO4, SS, TDS and Turb average, has the second highest NO2-N, NO3-N and pH average, and the highest DO average. The center of the second cluster has the lowest EC, NH4-N, o-PO4, SS, TDS and Turb average, has the second lowest BOD5, Cl-, Al, NO2-N, and pV average, has the second highest DO average, and the highest NO3-N, pH and T average. The center of the third cluster has the lowest DO, NO3-N, and pH average, has the second highest T average, and has the highest BOD5, Cl-, EC, Al, NH4-N, NO2-N, o-PO4, pV, SS, TDS and Turb average. The center of the fourth cluster has the lowest NO2-N and pH average, has the second lowest, DO, NO3-N and T average, has the second highest BOD5, Cl-, EC, Al, NH4-N, o-PO4, pV, SS, TDS and Turb average.

Figure 2 and Figure 3 visualize the k-means clustering results and fuzzy c-means clustering results of water quality classes for each station-year combination.

	Stations																
Year	S1	S2	S3	S4	S5	S6	S7	S8	S9	S10	S11	S12	S13	S14	S15	S16	S17
1985	1	1	1	1	1	1	1	1	4	1	1	4	1	1	1	1	1
1986	1	1	1	1	1	1	1	1	4	1	1	4	1	2	1	1	2
1987	1	1	1	1	1	1	1	1	4	1	1	4	1	1	1	1	1
1988	1	1	1	1	1	1	1	1	4	4	1	4	1	1	1	1	1
1989	1	1	1	1	1	1	1	1	1	1	1	4	1	1	1	1	1
1990	1	1	1	1	1	1	3	3	4	3	1	4	1	1	1	1	1
1991	1	1	1	1	1	1	3	1	4	4	1	4	1	1	1	1	1
1992	1	1	1	1	1	1	3	3	4	3	1	4	1	1	1	1	1
1993	1	1	1	1	1	1	3	3	4	3	1	4	1	1	1	1	1
1994	1	1	1	1	1	1	3	3	3	3	1	4	1	1	1	1	1

1995	1	1	1	1	1	1	3	3	3	3	1	4	1	1	1	1	1
1996	1	1	1	1	1	1	3	3	3	3	1	3	1	1	1	1	2
1997	1	1	1	1	1	1	3	3	3	3	1	3	1	1	1	1	1
1998	2	1	1	1	1	1	3	3	3	3	1	3	1	2	1	1	1
1999	1	1	1	1	1	1	3	3	3	3	1	1	1	1	1	1	1
2000	1	1	1	1	1	1	3	3	3	3	1	1	1	1	1	1	1
2001	1	1	1	1	2	2	3	3	3	3	1	3	1	2	1	2	2
2002	1	1	1	1	1	2	3	3	3	3	1	3	1	1	1	1	2
2003	1	1	1	1	2	1	3	3	3	3	1	1	1	1	1	1	1
2004	1	1	1	1	2	1	3	3	3	3	1	3	1	1	1	1	1
2005	1	1	1	1	3	3	3	3	3	3	3	3	1	1	1	3	2
2006	2	2	1	1	2	3	3	3	3	3	3	3	2	2	2	3	2
2007	2	1	1	2	2	2	3	3	3	3	2	3	1	2	2	2	2
2008	2	2	2	2	2	3	3	3	3	3	2	3	2	2	1	2	2
2009	1	1	1	1	2	1	3	3	3	3	1	1	1	2	1	2	2
2010	2	2	2	2	2	2	3	3	3	3	2	3	2	2	2	2	2
2011	2	2	2	2	2	2	3	3	3	3	2	3	2	2	2	2	2
2012	2	2	2	2	2	2	3	3	3	3	2	3	2	2	2	2	2
2013	2	2	2	2	2	2	3	3	3	3	2	2	2	2	2	2	2

Figure 2*. Water quality classes with K-means clustering*

According to Figure 2, the analysis of water quality clusters acquired by k-means clustering across stations and years reveals intriguing variations and notable trends. Several stations exhibit consistent water quality characteristics throughout the study period. For instance, stations S1 to S6 consistently belong to the Slightly Polluted Water Cluster until the 2000s. However, a significant shift occurs during subsequent years, as these stations transition to the High-Quality Water Cluster. This change suggests notable improvements in water quality in these locations, possibly attributed to effective pollution control measures or natural processes that have positively influenced the aquatic ecosystems.

Other stations, such as S7 to S10, consistently fall into the Highly Polluted Water Cluster, indicating persistent pollution challenges throughout the study period. This highlights the need for targeted pollution control strategies and continuous monitoring to address the underlying sources of contamination in these areas.

Furthermore, stations S11 to S13 demonstrate interesting changes over time. These stations initially exhibit mixed water quality clusters, with occasional presence in the Slightly Polluted Water Cluster and the Polluted Water Cluster. However, starting from the early 2000s, these stations consistently belong to the High-Quality Water Cluster. This transformation reflects substantial improvements in water quality in these particular locations, indicating the effectiveness of pollution reduction efforts or changes in environmental factors that positively influenced water conditions.

	Stations																
Year	S1	S2	S3	S4	S5	S6	S7	S8	S9	S10	S11	S12	S13	S14	S15	S16	S17
1985	1	1	1	1	1	1	1	1	4	4	1	3	2	1	1	1	1
1986	1	1	1	1	1	1	1	1	4	4	1	3	1	2	1	2	2
1987	1	1	1	1	1	1	4	4	4	1	1	3	1	1	1	1	1
1988	1	1	1	1	1	1	4	4	1	4	1	3	1	1	1	1	1
1989	1	1	1	1	1	1	4	4	4	4	1	3	1	1	1	2	1
1990	1	1	1	1	1	1	3	4	3	4	1	3	1	1	1	1	1
1991	1	1	1	1	1	1	3	4	4	4	1	3	1	1	1	1	1
1992	1	1	1	1	1	1	3	4	3	4	1	3	1	1	1	1	1
1993	1	1	1	1	1	1	3	4	3	4	1	3	1	1	1	1	1
1994	1	1	1	1	1	1	3	3	3	3	1	3	1	1	1	1	1
1995	1	1	1	1	1	1	3	3	3	4	1	3	1	1	1	1	1
1996	1	1	1	1	1	1	3	3	3	4	1	4	1	1	1	1	2

1997	1	1	1	1	1	1	3	3	3	4	1	3	1	1	1	1	1
1998	2	1	1	1	2	1	4	4	4	4	1	4	2	2	1	4	1
1999	1	1	1	1	1	1	4	3	4	4	1	4	2	1	1	1	1
2000	1	1	1	1	1	1	4	3	3	4	1	4	1	1	1	4	1
2001	2	2	1	2	2	2	3	3	3	3	2	4	2	2	2	4	2
2002	1	1	1	1	1	2	3	3	3	3	1	4	1	1	1	1	2
2003	1	1	2	1	2	1	3	3	3	4	1	4	1	1	1	1	2
2004	1	1	1	1	2	4	3	3	3	3	4	4	4	2	1	4	4
2005	4	4	4	4	4	4	3	3	3	3	4	4	4	4	4	4	4
2006	4	4	4	4	4	4	3	3	3	3	4	4	4	4	4	4	2
2007	2	2	2	2	2	2	3	3	3	3	4	4	2	2	2	2	2
2008	2	2	2	2	2	4	3	3	3	3	4	4	2	2	2	2	2
2009	2	1	2	2	2	1	3	3	3	3	4	4	2	2	1	2	2
2010	2	2	2	2	2	2	3	3	3	3	2	4	2	2	2	2	2
2011	2	2	2	2	2	2	3	3	3	3	2	3	2	2	2	2	2
2012	2	2	2	2	2	2	3	3	3	3	2	3	2	2	2	2	2
2013	2	2	2	2	2	2	3	3	3	3	2	2	2	2	2	2	2

Figure 3. *Water quality classes with fuzzy C-means clustering.*

The analysis of the water quality clusters across stations and years in the fuzzy C-means clustering reveals interesting patterns and notable changes. Stations S1 to S6, which were initially classified as belonging to the Slightly Polluted Water Cluster until the 2000s, show a remarkable improvement in water quality. Starting from the 2000s, these stations consistently transition to the High-Quality Water Cluster, indicating successful efforts to mitigate pollution and enhance water conditions in these areas.

Stations S7 to S10, on the other hand, persistently fall within the Highly Polluted Water Cluster throughout the study period, indicating ongoing pollution challenges in these locations. These stations require focused interventions and continued monitoring to address the sources of contamination and improve water quality.

Furthermore, stations S11 to S13 demonstrate interesting dynamics over time. Initially showing mixed water quality clusters, with occasional presence in the Slightly Polluted Water Cluster and the Polluted Water Cluster, these stations experience a positive shift in the early 2000s. They consistently join the High-Quality Water Cluster, suggesting significant improvements in water quality. These changes may be attributed to pollution reduction measures, changes in land use practices, or other environmental factors that positively impacted water conditions in these specific locations.

Overall, the analysis highlights both positive and persistent challenges in water quality across the studied stations. The shift of several stations to the High-Quality Water Cluster indicates successful pollution control efforts, while the presence of highly polluted water in other stations underscores the need for targeted interventions. Understanding these patterns and trends is crucial for effective water management strategies, continuous monitoring, and ongoing efforts to protect and improve the health of the aquatic ecosystems in the region.

MDS is also used to visualize both the k-means cluster analysis (Figure 4) and fuzzy c-means cluster analysis in a two-dimensional graph (Figure 5). The graphs also visualize the findings of Figure 2 and Figure 3 with a different approach.

MDS visualization for the k-means cluster analysis reveals how year and station combination behave (Figure 4). For cluster 1 which is labeled as Slightly Polluted Water we can identify most of the station year combinations belong to pre 2000s with stations S1 to S6, S11, S13, S14 and S15 noteworthy. For the cluster 2 which is labeled as High-Quality Water mostly contains stations from post 2000s with stations S1, S4, S5, S11, S13, S14 and S17. For the cluster 3 which is labeled as Highly Polluted Water contains both pre 2000 and post 2000 era. This cluster mostly contains stations S7, S8, S9, and S10. For the cluster 4 labeled as Polluted Water Cluster contains stations S9, S10 and S12 for the years period before 1995.

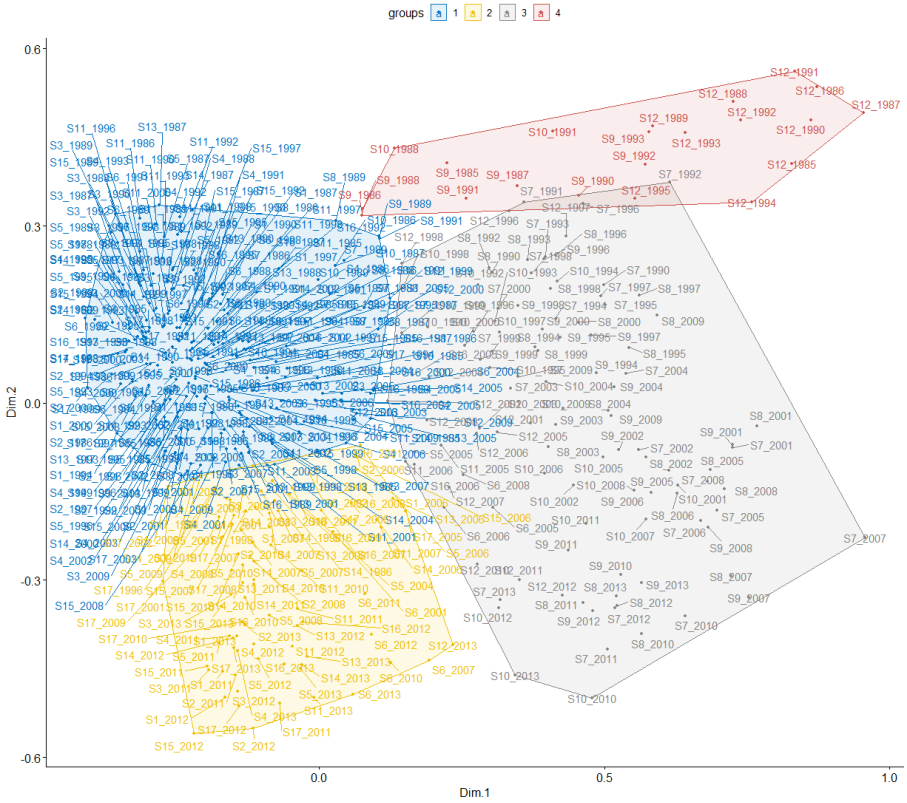

Figure 4. *MDS maps for K-means clustering.*

MDS visualization for the fuzzy c-means cluster analysis reveals how year and station combination behave (Figure 5). For cluster 1 which is labeled as Slightly Polluted Water we can identify most of the station year combinations belong to pre 2000s with stations S1 to S6, S11, S13, S14, S15, S16 and S17 noteworthy. For the cluster 2 which is labeled as High-Quality Water mostly contains stations from post 2000s with stations S1 to S6 and S13 to S17. For the cluster 3 which is labeled as Highly Polluted Water contains both pre 2000 and post 2000 era. This cluster mostly contains stations S7, S8, S9, S10 and S12. For the cluster 4 labeled as Polluted Water Cluster contains S7, S8, S9, S10 for the years period before 2000 and S11 and S12 after 2004.

Discussion and Conclusion

River water quality assessment plays a crucial role in monitoring and managing freshwater resources. Clustering analysis techniques, such as k-means and fuzzy clustering, offer valuable insights by grouping river segments or monitoring locations based on shared characteristics. This study aims to compare the effectiveness and applicability of k-means and fuzzy clustering methods in analyzing river water quality data.

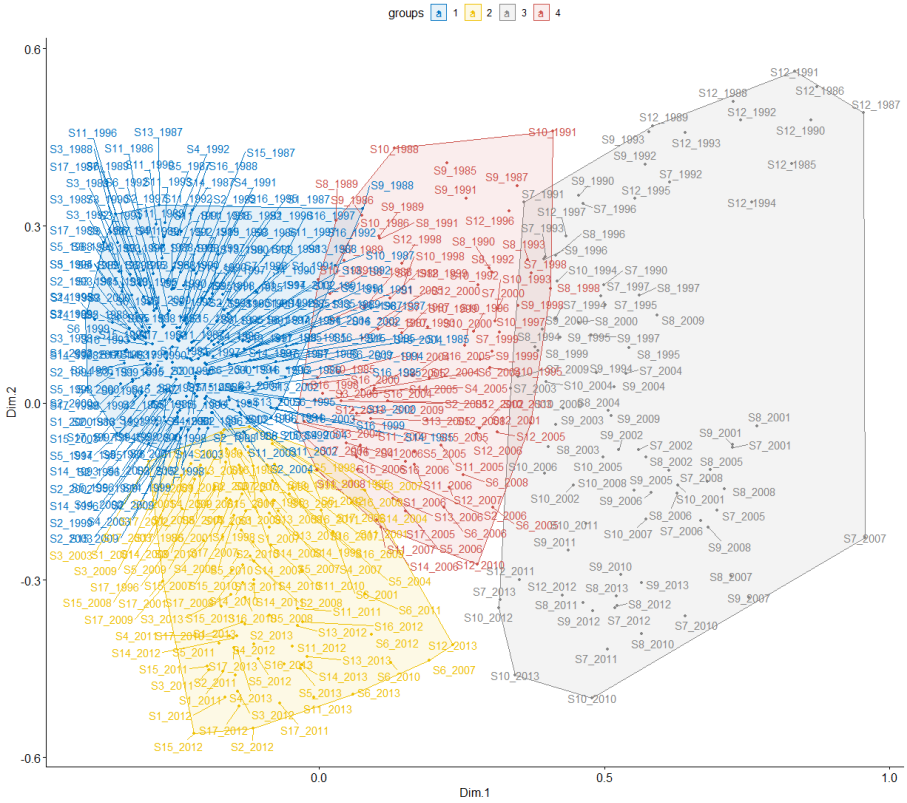

Figure 5. *MDS maps for Fuzzy C-means clustering.*

Through a comparative analysis of the two clustering methods, we provide insights into their strengths and limitations for river water quality assessment. We discuss the implications of each method's outcomes for decision-making, water resource management, and the identification of pollution sources as well as their comparison with Water Pollution Control Regulations.

The classification system outlined in the Water Pollution Control Regulation serves as a crucial tool for assessing and managing water quality across different regions. It provides a basis for developing appropriate pollution control strategies, monitoring programs, and environmental policies to safeguard water resources and promote sustainable water management practices.

This study contributes to the advancement of clustering techniques in the field of river water quality analysis and provides a foundation for further research and refinement of these methods. It underscores the importance of selecting appropriate clustering algorithms based on the specific objectives and characteristics of the water quality dataset.

Table 3 presents the physicochemical and microbiological water quality data obtained from multiple stations located within the Ergene River Basin, spanning the years 1983 to 2013. The data within the table encompass a diverse set of parameters that pertain to the physical, chemical, and biological attributes of water samples collected from distinct monitoring stations within the basin over the specified time.

The analysis of aluminum as an inorganic pollution parameter indicates that it serves as an indicator of Class IV water quality, and its measured values significantly exceed the threshold limit (>1).

In basin waters, Biological Oxygen Demand (BOD) values are generally observed to be significantly high. BOD serves as an important indicator of biological activity and organic matter content in aquatic systems. When comparing the BOD5 (Biological Oxygen Demand over 5 days) values according to the Turkish Standards Institute's regulations, it was observed that the first and second K-means cluster models corresponded to Class II water quality, while

the third and fourth K-means cluster models corresponded to Class IV water quality. Similarly, using the Fuzzy C-means cluster model, it was determined that the first and second Fuzzy C-means models corresponded to Class II water quality, while the third and fourth Fuzzy C-means models corresponded to Class IV water quality. These results indicate variations in water quality within the studied area based on BOD5 levels, as defined by the respective classification criteria.

Dissolved oxygen serves as a crucial parameter for monitoring changes in water quality. In accordance with the Water Pollution Control Regulation, the first and second K-means cluster models classify the water as Class I in terms of quality, while the third K-means cluster model indicates Class IV water quality based on the dissolved oxygen threshold value. Similarly, the fourth K-means cluster model is associated with Class II water quality. Notably, the findings obtained from the Fuzzy C-means cluster model analysis corroborated the water quality classifications derived from the dissolved oxygen values, demonstrating concurrence between the clustering approaches.

Significant regional variations have been observed in the electrical conductivity (EC) values detected in the waters, and based on the Water Pollution Control Regulation, it has been determined that the EC values identified in the first and fourth cluster models correspond to Class III water quality, the EC values in the second cluster model correspond to Class II water quality, and the third cluster model represents Class IV water quality (Turkish Regulations, 2015). Additionally, it has been found that the range of 150-500 μS/cm specified for electrical conductivity in the protocol on standards for aquatic products and the protection of surface water sources against pollution is exceeded throughout almost the entire basin (Uslu and Türkman, 1987).

The nitrate levels measured in the basin stations have been determined to comply with the Class I water quality standards set by the Water Pollution Control Regulation. Regarding nitrite concentrations, the first K-means cluster model corresponds to Class I threshold, the second K-means cluster model corresponds to Class II, the third K-means cluster model corresponds to Class IV, and the fourth K-means cluster model corresponds to Class III threshold. Similarly, when comparing nitrite values using the Fuzzy C-means cluster model, it has been established that the first Fuzzy C-means model corresponds to Class III threshold, the second and fourth Fuzzy C-means models correspond to Class II, and the third Fuzzy C-means model corresponds to Class IV water quality (Turkish Regulations, 2015). These findings provide scientific evidence of the nitrate and nitrite levels in accordance with the water quality classifications established by the respective clustering methods and regulatory guidelines.

Nitrite is an intermediate product in the biological oxidation process that converts ammonium to nitrate, and it can reach high levels, particularly in oxygen-deficient environments and in waters contaminated with organic matter (Egemen and Sunlu, 1996). According to the drinking water standards reported by the World Health Organization, the nitrite value in water is expected to not exceed the limit of 0.2 mg/L (WHO, 2011).

According to the Surface Water Quality Regulation (SWQR) in our country, the orthophosphate phosphorus value is reported as <0.05 mg/L for Class I waters and 0.65 mg/L for Class IV waters. Considering these criteria, both models indicate Class IV water quality. This observation aligns with the regulations set by the SWQR and confirms the classification of the water samples according to their orthophosphate phosphorus levels.

The geological composition of the region is a significant factor influencing the pH of water, and natural waters typically exhibit a slightly alkaline nature due to their carbonate and bicarbonate content. The optimal pH range for aquatic organisms is 6.5 to 8.5, while fish generally thrive within a range of 6.4 to 8.6 (Tanyolaç, 2009). Deviations from these pH ranges can have adverse effects on the survival of aquatic organisms as they move further away from the acceptable intervals. In the Ergene River Basin, the stations demonstrate a mildly alkaline character in terms of pH. According to the Water Pollution Control Regulation, all stations within the basin possess Class 1-2 water quality based on their pH values. Furthermore, it has

been determined that the pH values of the waters do not exceed the range of 6.5 to 9.5, as specified in the Turkish Standards Institute's regulation for water intended for human consumption (TS266, 2005).

Total dissolved solids (TDS) primarily comprise inorganic minerals and organic substances, including a wide range of salts (Miranda and Krishnakumar, 2015). High TDS concentration in water can result in aesthetic issues such as discoloration, unpleasant taste, or precipitation (Sibanda et al., 2014). The levels of TDS, in a general sense, serve as an indicator of the overall pollutant load. According to the Water Quality Control Regulation, when comparing TDS values, the first and fourth K-means cluster models represent Class II water quality, while the second K-means cluster model represents Class I, and the third K-means cluster model represents Class III. Similar results were observed when evaluating the same values using the Fuzzy C-means cluster model. Specifically, the first, second, and fourth Fuzzy C-means models correspond to Class II water quality, the third Fuzzy C-means model corresponds to Class II, and the third Fuzzy C-means model corresponds to Class III (Turkish Regulations, 2015).

Suspended solids (SS) are natural pollutants and cause turbidity in the river water (Mahvi & Razazi, 2005). The excess amount of SS in water can also be an indicator of land erosion in the river catchment.

High turbidity levels limit the amount of light able to penetrate the water’s surface. This affects plant growth by reducing their ability to photosynthesis. Reduced plant growth leads to decreased amounts of oxygen in the water and the loss of vital habitat for aquatic animals. Fine particles settle on surfaces, smothering plants, rocks, logs and fish eggs and larvae. Fish can also suffer from clogged gills. The turbidity level results in the Ergene Basin vary between 30.59 and 990.73 NTU, indicating a high degree of turbidity in the water.

The importance of assessing water quality accurately has been amplified due to the diminishing availability of water resources on both national and global scales, coupled with the rapid growth of the world population (Evsahibioğlu et al., 2010). Anthropogenic activities have further exacerbated the deterioration of water quality, underscoring the significance of employing various methods, including mathematical modeling, statistical techniques, and soft computing methods, to evaluate water quality (Bilgin and Konanç, 2016). Based on the surface water data obtained in our study, it has been determined that the Ergene River, which is significantly exposed to industrial pollution, exerts considerable pressures on the ecosystem. The data obtained from statistical analyses clearly demonstrate the adverse effects of environmental and industrial pollution on the system.

References

Akın, M., & Akın, G. (2007). Suyun önemi, Türkiye'de Su Potansiyeli, Su Havzaları ve Su Kirliliği, Ankara ˘ Üniversitesi Dil ve Tarih-Coğrafya Fakültesi Dergisi.

Arthur, D., & Vassilvitskii, S. (2007, January). K-means++ the advantages of careful seeding. In Proceedings of the eighteenth annual ACM-SIAM symposium on Discrete algorithms (pp. 1027-1035).

Bezdek, J. C., Coray, C., Gunderson, R., & Watson, J. (1981). Detection and characterization of cluster substructure i. linear structure: Fuzzy c-lines. SIAM Journal on Applied Mathematics, 40(2), 339-357.

Bilgin, A., & Konanç, M U. (2016). Evaluation of surface water quality and heavy metal pollution of Coruh River basin Turkey by multivariate statistical methods. Environmental Earth Sciences, 75(12), 1029. https://doi.org/10.1007/s12665-016-5821-0.

Dokmeci, A. H. (2017). Evaluation of heavy metal pollution in the Ergene River Basin from a public health perspective. Turkish Journal of Public Health, 15(3), 212.

EC (European Communities), (2006). EC of the European Parliament and of the council of 6 September 2006 on the quality of fresh waters needing protection or improvement in order to support fish life. Directive 2006/44

Egemen Ö, Sunlu U. (1996). Su kalitesi. İzmir: Ege Üniversitesi Su Ürünleri Fakültesi Yayınları Yayın No:14. Ege Üniversitesi Basımevi 153s.

Emadian S.M Sefiloglu F.O., Akmehmet Balcioglu I., Tezel. (2020). Identification of core micropollutants of Ergene River and their categorization based on spatiotemporal distribution. Science of the Total Environment

Evsahibioğlu, A N, Çakmak, B, & Aküzüm, A. (2010). Su Yönetimi, Su Kullanım Stratejileri ve Sınırı Aşan Sular. TMMOB Ziraat Mühendisleri Odası Türkiye Ziraat Mühendisliği VII. Teknik Kongresi, 1, 119–134.

İşçen, C F, Altın, A, Şenoğlu, B, & Yavuz, H S. (2009). Evaluation of surface water quality characteristics by using multivariate statistical techniques: a case study of the Euphrates river basin, Turkey. Environmental Monitoring and Assessment, 151 (1), 259–264. https://doi.org/10.1007/s10661-008-0267-9.

Köse, E., Tokatlı, C., Çiçek, A. (2014). Monitoring Stream Water Quality: A Statistical Evaluation. Polish Journal of Environmental Studies, 23 (5): 1637-1647.

Kruskal, J. (1977). The relationship between multidimensional scaling and clustering. In Classification and clustering (pp. 17-44). Academic Press.

Kruskal, J. B. (1964). Multidimensional scaling by optimizing goodness of fit to a nonmetric hypothesis. Psychometrika, 29(1), 1-27.

Landau, S., Leese, M., Stahl, D., & Everitt, B. S. (2011). Cluster analysis. John Wiley & Sons.

MacQueen, J. (1967, June). Classification and analysis of multivariate observations. In 5th Berkeley Symp. Math. Statist. Probability (pp. 281-297). Los Angeles LA USA: University of California.

Mahvi A.H., Razazi M. (2005) Application of polyelectrolyte in turbidity removal from surface water, Am. J. Appl. Sci. 2, 397

Miranda, J. & Krishnakumar, G. (2015) Microalgal diversity in relation to the physicochemical parameters of some Industrial sites in Mangalore, South India. Environ Monit Assess 187(11)

Orak E., Akkoyunlu A., Can Z.S. (2020). Assessment of water quality classes using self-organizing map and fuzzy C-means clustering methods in Ergene River, Turkey. Springer

Qadir, A., Malik, R.N., Husain, S.Z. (2008). Spatio-temporal variations in water quality of Nullah Aik-tributary of the river Chenab, Pakistan. Environ. Monit. Assess. 140, 43e59.

R Core Team (2022). R: A language and environment for statistical computing. R Foundation for Statistical Computing, Vienna, Austria. URL https://www.R-project.org/.

Sibanda T, Chigor VN, Koba S, Obi CL, Okoh AI (2014) Characterisation of the physicochemical qualities of a typical ruralbased river: ecological and public health implications. Int J Environ Sci Technol 11(6):1771–1780

Singh K. P., Malık A., Sınha S. (2005). Water Quality Assessment and Apportionment of Pollution Sources of Gomti River (India) Using Multivariate Statistical Techniques - A Case Study. Anal Chim Acta, 538; 355–374.

Tanyolaç J. (2009). Limnoloji. Ankara: Hatiboğlu Yayınevi 294s.

Tokatlı C., Çiçek A., Emiroğlu Öç., Köse E. (2019). Water Quality Monitoring of Meriç, Tunca and Ergene Rivers (Edirne, Turkey) in Rainy Season. Research Journal of Biology Sciences, 1308-0261, 12(1): 13-17, 2019

Turkish Water Pollution Control Regulation Regulations (2015) Su kirliliği kontrolü yönetmeliği (SKKY). Yayımlandığı Resmi Gazete: Tarih 15 Nisan Çarşamba 2015, Sayı :259327 https://www.resmigazete.gov.tr/eskiler/2015/04/20150415-18.htm

Uslu, O., Türkman, A. (1987). Su Kirliliği ve Kontrolü. T.C. Başbakanlık Çevre Genel Müdürlüğü Yayınları, Eğitim Dizisi I, Ankara.

Wang, J.Y., Da, L.J., Song, K., Li, B.L. (2008). Temporal variations of surface water quality in urban, suburban and rural areas during rapid urbanization in Shanghai, China. Environ. Pollut. 152, 387e393

WHO (World Health Organization). (2011). Guidelines for drinking-water quality. World Health Organization Library Cataloguing-in-Publication Data, NLM classification: WA 675.

Zhang, Q., Li, Z.W., Zeng, G.M., Li, J.B., Fang, Y., Yuan, Q.S., Wang, Y.M., Ye, F.Y. (2009). Assessment of surface water quality using multivariate statistical techniques in red soil hilly region: a case study of Xiangjiang watershed, China. Environ. Monit. Assess. 152, 123e131.

Zhang, Y., Guo, F., Meng, W., Wang, X.Q. (2009). Water quality assessment and source identification of Daliao river basin using multivariate statistical methods. Environ. Monit. Assess. 152, 105e121.

Effects of Na-Humate and Ca-Humate Application on Cold Hardiness of Wheat and Corn

Vedat BEDİRHANOĞLU[1]
Metin TURAN[2]
Adem GÜNEŞ[3]
Müdahir ÖZGÜL[4]

Introduction

This study was carried out to determine the effects of Na-humate and Ca-humate applications on the cold resistance of wheat and corn plants. Wheat and corn are strategic plants that rank first both in the world and our country in terms of cultivation area and production among the cultivated plants used in human nutrition, and they play an essential role as the basic energy and protein source of people. Wheat and corn yields in our country show significant differences depending on seasonal and year-to-year differences in climatic conditions, especially cold damage. Changes in the temperature regime due to global climate changes, especially low temperatures and cold damage, can affect the region and cause significant yield losses in these plants. Therefore, effective fertilizer formulations should be used to reduce yield and quality losses caused by low temperature and cold stress in wheat and corn, important income sources for farmers in that region.

Humic substances are chemically stable, dark colored, and have a high molecular weight structure, contains 44-58% Carbon, 42-46% Oxygen, 6-8% Hydrogen, and 0.5-4% Nitrogen (Larcher, 2003). Humic substances are divided into three groups humic acid, fulvic acid, and humin according to their solubility in acids and bases (Sparks, 2003:82). Humic acid has a large molecular weight and takes a long time to break down. Therefore, humic acids are generally used as soil promoters (Chen and Avnimelech, 1986:161-186; Yılmaz, 2007:74).

Humic substances increase soil fertility by affecting the physical, chemical, and biological properties of soils. It has been reported that humic compounds have a positive effect on plant, root, and shoot development growth through several mechanisms, increase the availability of nutrients in the soil, and provide resistance against different stress conditions (Nardi et al. 2002:1527-1536). The cation exchange power of humic substances is considerably higher than that of clay minerals, so they significantly increase the CECs of soils (Stevenson, 1994:367-372). Due to this feature, all the necessary metals in the soil can chelate with humic acids.

[1] Dr. Vedat BEDİRHANOĞLU, International Agricultural Research and Training Center, Orcıd: 0000-0003-4642-715X
[2] Prof. Dr. Metin TURAN, Yeditepe University, Agricultural Trade and Management, Orcıd: 0000-0002-4849-7680
[3] Doç. Dr. Adem GÜNEŞ, Erciyes University, Soil Science And Plant Nutrition, Orcıd: 0000-0003-0411-6134
[4] Prof. Dr. Müdahir ÖZGÜL, Atatürk University, Soil Science And Plant Nutrition, Orcıd: 0000-0002-5855-0086

Humic substances bond with calcium carbonate forming weak, soluble calcium humates. Calcium protects plant tissues against freeze-thaw stress and prevents cold damage by reducing the outflow of substances from the plant cell. Accumulating calcium in cell vacuoles plays an important role in maintaining anion-cation balance (Kacar and Katkat, 2009a:351-374). Sodium plays an important role in enzyme activities, reduces the freezing point of plant sap, and reduces cold damage in winter and early spring (Kacar and Katkat, 2009b:593-602).

This study aimed to reduce the effects of cold damage caused by unexpected temperature changes by applying Ca-humate and Na-humate fertilizer formulations.

Materials and Methods

The experiment was carried out on the farm of Atatürk University Agricultural Management Directorate in Erzurum. The trial was conducted at the field with 2 plants (Wheat, Corn), 3 different fertilizer applications (Control, Ca-Humat, Na-Humat), 5 different application levels (0, 1, 3, 9, 12 kg/ha), 3 replications as a factorial experiment under complete randomized design. Before the applications, soil samples were collected from each plot, and physical, chemical, and biological analyzes were performed. Ca-humate and Na-humate were applied to the plants with soil and foliar at the beginning of the growth period, in the middle of the growing period, and during the ripening period.

The pH of the soil samples was measured potentiometrically in a 1:2.5 soil-water suspension with a Glass Electrode pH meter (McLean, 1982). The lime content of the soils was determined volumetrically by using Scheibler Klasimeter (Nelson and Sommer 1982). The organic matter contents of the soils were determined by the Smith-Weldon method (Nelson and Sommer, 1982). Nitrogen content of soil samples was determined using Dumas Nitrogen Analyzer. Phosphorus contents of soils were determined with an ICP-OES Inductively Coupled Plasma spectrophotometer (Perkin-Elmer, Optima 2100 DV, ICP/OES, Shelton, CT 064844794, USA) (Olsen and Sommer, 1982).

At the end of the experiment, cold damage on the leaves of the plants was determined by the electrical conduction technique (Griffith et al. 1992). In order to determine the cell permeability, the plant leaves were thoroughly washed with distilled water, and shaken in 10 ml of deionized water at 25^{o}C for 24 hours, and the electrical conductivity (EC_1) of the solution was measured. Afterward, the samples were left in an autoclave at 120^{o}C for 20 minutes. The samples were removed from the autoclave and the electrical conductivity (EC_2) values were measured again when the temperature dropped to 25^{o}C. From the obtained electrical conductivity values; cell permeability was determined from the formula (%)=(EC_1/EC_2)x100 (Lutts et al. 1996). Analysis of variance and multiple comparison tests were performed on the results obtained from the experiment (SPSS, 2004).

Results and Discussion

Wheat

The Effect of Applications on the Chemical Properties of Soils

The effects of Na and Ca-humate treatments on some chemical properties of wheat-planted soils were evaluated (Table 1). pH level increased from 7.60 to 7.85 and 7.65, respectively, due to increasing amounts of Na and Ca-humate applications. Stevenson (1994), found that the accumulation of humic substances in soils contributes to the increase of pH. The lime contents of the soils did not change significantly depending on the increasing levels of Na and Ca-humate applications ($p<0.01$).

Table 1 - *Some chemical analysis results of Na and Ca-humate applied to wheat-planted soils*

Treatments		pH (1:2,5)	$CaCO_3$	Organic Matter (%)	N mg/kg	P
	Initially	**7 .60**	**0.55**	**1.40**	**7.35**	**4.26**
Na-Humat (kg/ha)	**0**	7.65c	0.52	1.36c	6.80c	3.36c
	1	7.68bc	0.54	1.42b	7.10b	3.45c
	3	7.72b	0.56	1.38c	6.75c	3.65bc
	9	7.70b	0.53	1.40b	7.00b	3.85b
	12	7.85a	0.55	1.48a	7.40a	4.02a
Ca-Humat (kg/ha)	**0**	7.64	0.53	1.34	6.65d	3.42a
	1	7.72	0.55	1.36	7.40ab	3.35ab
	3	7.68	0.51	1.38	7.54a	3.22b
	9	7.71	0.56	1.40	7.36b	3.14b
	12	7.65	0.58	1.36	7.28c	3.01c

The organic matter content of the soils increased depending on the Na and Ca-humate applications. The highest amount of organic matter was obtained with Na-humate application at the level of 12 kg/ha, and with Ca-humate application at the level of 9 kg/ha. The amount of N was 6.80 and 6.65 mg/kg in the control groups and increased with increasing Na and Ca-humate application doses. The amount of N available to the plant reached the highest value at 12 kg/ha Na-humate level and 3 kg/ha Ca-humate application level with 7.40 and 7.54 mg/kg, respectively. The amount of available P to the plant in the soil generally increased with Na-humate application and reached 4.02 mg/kg with 12 kg/ha Na-humate application. The amount of P decreased in general with Ca-humate application and reduced to the lowest value (3.01 mg/kg) with 12 kg/ha Ca-humate application (Table 1). David et al. (1994) reported that applying humic acid compounds obtained from different sources to the tomato plant increases the uptake of plant nutrients, especially for N and P.

The Effect of Applications on the Yield and Yield Parameters of Wheat

Spike weight, average grain yield, and cell permeability values of the wheat plant significantly increased depending on the increasing Na and Ca-humate applications ($p<0.01$). Spike weight and average grain yield reached the highest levels with 9 kg/ha Na and Ca-humate applications. With 9 kg/ha Na and Ca-humate applications, the spike weight increased by 23.29% and 28.74%, respectively, while the average grain yield increased by 24.40% and 28.89%, respectively, compared to the control group (Table 2). Nardi et al. (2002) found that humic compounds increase plant nutrient availability and have a positive effect on plant growth in their study of different plants.

Table 2 - *The Effect of Na and Ca-humat on the Yield and Yield Parameters of Wheat*

Treatments		Spike Weight	Average Grain Yield	Cell Permeability
		kg/ha		%
Na-Humat (kg/ha)	0	28.563e	22.035d	15.62d
	1	29.653d	24.123c	16.55c
	3	32.460b	25.689b	20.32b
	9	35.214a	27.411a	22.14a
	12	30.569c	25.236b	16.98c
Ca-Humat (kg/ha)	0	29.251e	22.236e	16.11d
	1	30.562d	25.163d	16.88d
	3	34.026b	27.015b	19.52b
	9	37.659a	28.659a	20.16a
	12	32.514c	26.511c	18.63c

Cell permeability increased depending on Na and Cahumate applications. While cell permeability was 15.62% to 16.11% in the control group, it reached the highest value in 9 kg/ha Na and Ca-humate applications. With 9 kg/ha Na and Ca-humate applications, it was determined that there was an increase of 41.74% and 25.14%, respectively, compared to the control group (Table 2). Waldrighi et al. (1996) determined in their study that humic acid increased the uptake of plant nutrients by increasing cell permeability.

As a result of Na and Ca-humate applications, the spike weight and average grain yield values of the wheat plant were subjected to regression analysis. As a result of the analysis, the spike weight reached the optimum value at the application doses of 6.5 kg/ha and 6.8 kg/ha, depending on the Na and Ca-humate application, respectively. The average grain yield was obtained with 7.2 kg/ha Na-humate and 7.4 kg/ha Ca-humate application doses (Figure 1).

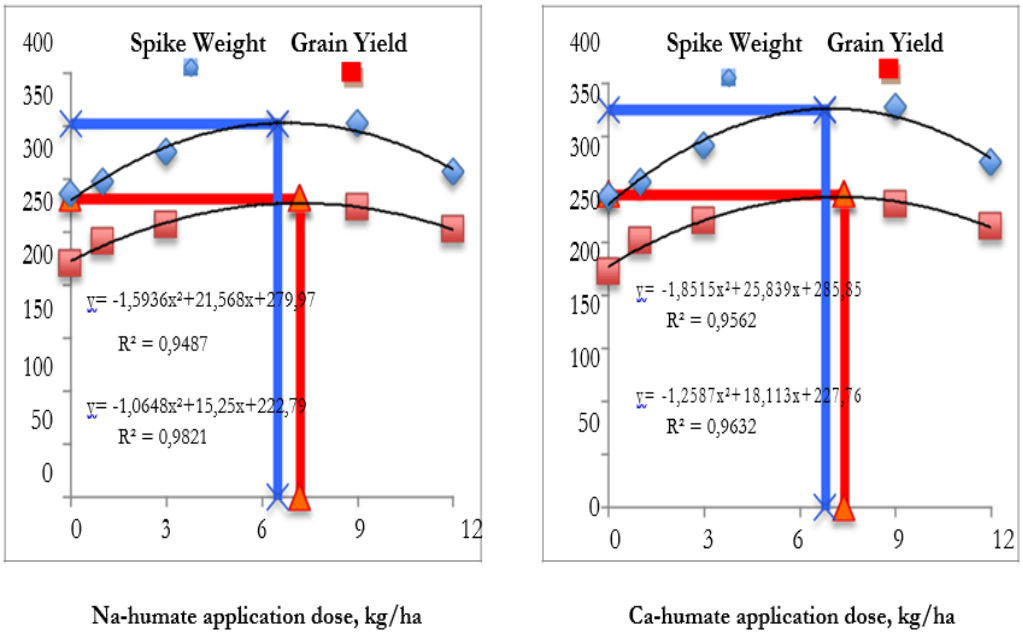

Figure 1. *Changes in spike weight and average grain yield of the wheat plants depending on Na and Ca-humate applications.*

The Effect of Applications on the Cold Resistance of Wheat

As a result of the statistical analysis, it was determined that the effects of Na and Ca-humate applications on the cold damage rate of the plant were very significant ($p<0.05$).

While the cold damage rate at 0 °C was 52.16% in the control group, it decreased to 34.26% at the highest Na-humate application dose (12 kg/ha). The cold damage rate decreased by 34.32% at 12 kg/ha Na-humate application dose compared to the control. While the cold damage rate was 60.07% in the control group at -5 °C, it decreased to 42.76% at the highest Na-humate application dose of 12 kg/ha. Cold damage rate decreased by 28.82% at 12 kg/ha application dose compared to the control. While the cold damage rate was 73.91% in the control group at -10 °C, it decreased to 53.19% at the highest Na-humate application dose of 12 kg/ha. The cold damage rate decreased by 28.03% at 12 kg/ha application dose compared to the control. While the cold damage rate was 85.46% in the control group at -15 °C, it decreased to 65.35% at the highest Na-humate application dose of 12 kg/ha. The cold damage rate decreased by 23.53% at 12 kg/ha application dose compared to the control. While the cold damage rate was 92.27% in the control group at -20 °C, it decreased to 69.88% at the highest Na-humate application dose of 12 kg/ha. The cold damage rate decreased by 24.27% at 12 kg/ha application dose compared to the control (Table 3).

Tablo 3 - *The effect of Na and Ca-humate applications on the cold damage rate of wheat plants.*

Treatments		Cold Damage Rate (%)				
		0 °C	**-5 °C**	**-10 °C**	**-15 °C**	**-20 °C**
Na-Humat (kg/ha)	0	52.16a	60.07b	73.91a	85.46a	92.27a
	1	48.69b	62.18a	70.42b	81.73b	89.97b
	3	41.25c	55.86c	66.11c	75.73c	79.78c
	9	38.59d	50.06d	62.52d	71.52d	72.36d
	12	34.26e	42.76e	53.19e	65.35e	69.88e
Ca-Humat (kg/ha)	0	54.15a	62.53a	72.11a	86.41a	93.22a
	1	52.36a	60.25ab	65.59b	80.19b	86.52b
	3	45.26b	58.41b	62.33c	72.17c	72.15c
	9	40.11c	55.12c	59.23d	68.53d	71.11c
	12	36.59d	45.36d	52.17e	62.11e	67.48d

While the cold damage rate at 0 °C was 54.15% in the control group, it decreased to 36.59% at the highest Ca-humate application dose of 12 kg/ha. The cold damage rate decreased by 33.17% at 12 kg/ha application dose compared to the control. While the cold damage rate was 62.53% in the control group at -5 °C, it decreased to 45.36% at the highest Ca-humate application dose of 12 kg/ha. The cold damage rate decreased by 27.46% at 12 kg/ha application dose compared to the control. While the cold damage rate was 72.11% in the control group at -10 °C, it decreased to 52.17% at the highest Ca-humate application dose of 12 kg/ha. The cold damage rate decreased by 27.65% at 12 kg/ha application dose compared to the control. While the cold damage rate was 86.41% in the control group at -15 °C, it decreased to 62.11% at the highest Ca-humate application dose of 12 kg/ha. The cold damage rate decreased by 28.12% at 12 kg/ha application dose compared to the control. While the cold damage rate was 93.22% in the control group at -20 °C, it decreased to 67.48% at the highest Ca-humate application dose of 12 kg/ha. The cold damage rate decreased by 27.61% at 12 kg/ha application dose compared to the control (Table 3). Nardi et al. (2002) reported that humic compounds provide resistance against different stress conditions.

Corn

The Effect of Applications on the Chemical Properties of Soils

The effects of different levels of Na and Ca-humate applications on some chemical properties of the corn-planted soils were evaluated (Table 4). While the initial soil pH was 7.53, depending on the increasing Na and Ca-Humate application doses, the pH value reached 7.63 and 7.59, respectively. While the lime content of the soils did not show a significant change depending on the application of Na-humate, a significant increase was determined due to the application of Ca-humate compared to the control group ($p<0.01$).

Table 4 -*Some chemical analysis results of Na and Ca-humate applied to corn-planted soils*

Treatments		pH	$CaCO_3$	Organic Matter	N	P
		(1:2,5)		(%)	mg/kg	
	Initial	**7.53**	**0.60**	**1.25**	**8.12**	**3.26**
Na-Humat (kg/ha)	**0**	7.51d	0.58	1.22	7.52	3.02d
	1	7.54c	0.62	1.26	7.41	3.11d
	3	7.59b	0.58	1.25	7.40	3.24c
	9	7.52d	0.61	1.22	7.35	3.36b
	12	7.63a	0.62	1.24	7.38	3.59a
Ca-Humat (kg/ha)	**0**	7.52	0.59c	1.20	7.48c	3.00a
	1	7.55	0.62bc	1.21	7.51c	2.96a
	3	7.56	0.64b	1.18	7.62b	2.95a
	9	7.59	0.66a	1.16	7.60b	2.86b
	12	7.55	0.67a	1.19	7.85a	2.75c

The organic matter content of the soils did not show a statistically significant change depending on the applied Na and Ca-humate application. The highest amount of organic matter was obtained from the 1 kg/ha dose of Na and Ca-Humate applications. While the amount of N in the soil decreased depending on the increasing Na-humate application doses, it increased due to the increasing Ca-humate application doses. At the highest Ca-Humat application dose, the amount of N reached 7.85 mg/kg. The amount of P available to the plant in the soil generally increased with Na-humate application and reached 3.59 mg/kg with 12 kg/ha Na-humate application. However, the amount of P in the soil decreased with increasing Ca-humate application doses (Table 4). Brannon and Sommers (1985) determined that humic substances physically increase the structure and water-holding capacity of the soil, biologically increase the usefulness of inorganic plant nutrients, and beneficial to soil microorganisms effective in plant growth.

The Effect of Applications on the Yield and Yield Parameters of Corn

The effects of Na and Ca-humate applications on yield and yield parameters of corn plant were evaluated. Yield and cell permeability values of corn plants increased due to increasing Na and Ca-humate applications, and this increase was found to be statistically significant ($p<0.01$).

The highest corn yield was obtained at 9 kg/ha levels of Na and Ca-humate applications. It was determined that with 9 kg/ha Na and C-humate applications, there was an increase of 33.68% and 33.76%, respectively, compared to the control group. Ayaş et al. (2005) determined that increasing amounts of humic acid applied to the spinach plant increased the total yield, nitrogen, and phosphorus content of the plant. While the cell permeability reached the highest value (17.11%) at the level of 9 kg/ha of Na-humate application, it reached the highest value (15.86%) at the level of 3 kg/ha of Ca-humate application (Table 5). Chen and Avaid (1990) reported that humic acids increase cell permeability and positively affect plant growth.

Table 5 - *The Effect of Na and Ca-humat on the Yield and Cell Permeability of Corn*

Treatments		Plant Weight	Cell Permeability
		kg/ha	%
Na-Humat (kg/ha)	0	521.1c	15.26c
	1	632.6b	15.63c
	3	685.1a	16.24b
	9	696.6a	17.11a
	12	625.8b	16.59b
Ca-Humat (kg/ha)	0	532.6d	14.15b
	1	645.1c	15.24a
	3	692.5b	15.86a
	9	712.4a	15.42a
	12	652.8c	15.11a

As a result of Na and Ca-humate applications, the plant weight values of the corn were subjected to regression analysis. As a result of the analysis, the optimum plant weight was determined with 6.5 kg/ha Na-humate and 6.8 kg/ha Ca-humate application doses (Figure 2).

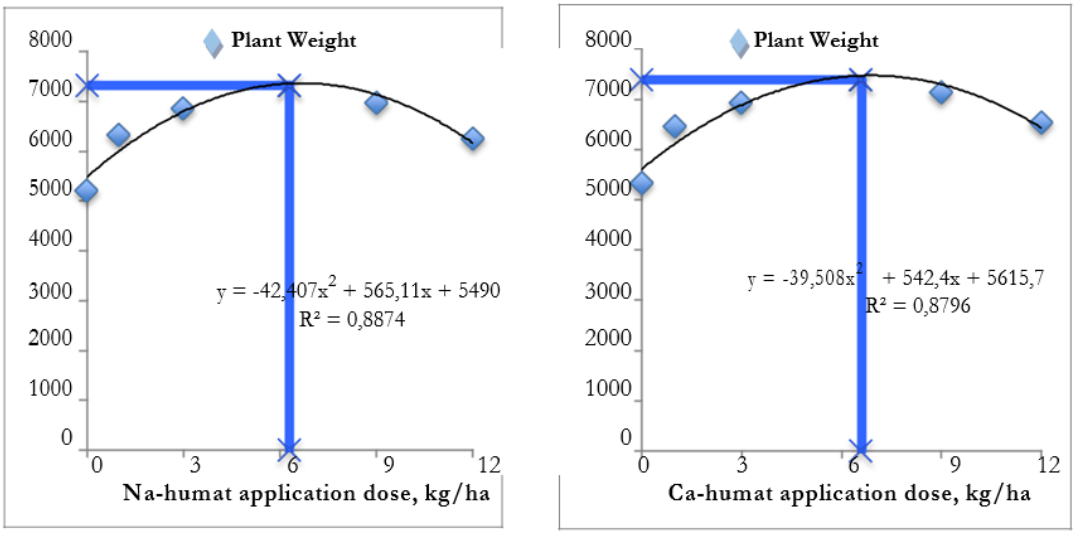

Figure 2. *Changes in plant weight of the corn depending on Na and Ca-humate applications.*

The Effect of Applications on the Cold Resistance of Corn

The effects of applying different doses of Na and Ca-humate to corn plants on the cold damage rate were evaluated. As a result of the statistical analysis, it was determined that the effects of Na and Ca-humate applications on the cold damage rate of the plant were very important ($p<0.05$).

While the cold damage rate at 0°C was 60.12% in the control group, it decreased to 44.29% at the highest Na-humate application dose (12 kg/ha). Cold damage rate decreased by 26.33% at 12 kg/ha application dose compared to the control. While the cold damage rate was 68.52% in the control group at -5°C, it decreased to 47.53% at the highest Na-humate application dose (12 kg/ha). Cold damage rate decreased by 30.63% at 12 kg/ha application dose compared to the control. While the cold damage rate was 73.63% in the control group at -10°C, it decreased to 58.63% at the highest Na-humate application dose (12 kg/ha). The cold

damage rate decreased by 19.83% at 12 kg/ha application dose compared to the control. While the cold damage rate was 96.53% in the control group at -15ºC, it decreased to 80.06% at the highest Na-humate application dose (12 kg/ha). Cold damage rate decreased by 17.09% at 12 kg/ha application dose compared to the control. While the cold damage rate was 98.66% in the control group at -20ºC, it decreased to 85.62% at the highest Na-humate application dose (12 kg/ha). The cold damage rate was decreased by 13.22 % at 12 kg/ha application dose compared to the control (Table 6).

Table 6 – *The effect of Na and Ca-humate applications on the cold damage rate of corn plants.*

Treatments		Cold Damage Rate (%)				
		0⁰C	**-5⁰C**	**-10⁰C**	**-15⁰C**	**-20⁰C**
Na-Humat (kg/ha)	0	60.12a	68.52a	75.63a	96.53a	98.66a
	1	56.23b	62.13b	71.42b	91.52b	94.52b
	3	51.24c	57.42c	65.25c	88.53c	92.11c
	9	46.53d	51.22d	61.22d	83.17d	90.24d
	12	44.29e	47.53e	58.63e	80.06e	85.62e
Ca-Humat (kg/ha)	0	61.25a	67.52a	72.45a	95.68a	98.11a
	1	58.41b	64.59b	70.15b	92.36b	95.42b
	3	52.36c	55.28c	66.26c	89.52c	94.16b
	9	50.14d	54.11c	58.42d	85.46d	92.33c
	12	46.59e	49.53d	54.26e	82.11e	88.71d

While the cold damage rate at 0ºC was 61.25% in the control group, it decreased to 46.59% at the highest Ca-Humat application dose (12 kg/ha). Cold damage rate decreased by 23.93% at 12 kg/ha application dose compared to the control. While the cold damage rate was 67.52% in the control group at -5ºC, it decreased to 49.53% at the highest Ca-Humat application dose (12 kg/ha). The cold damage rate decreased by 26.21% at 12 kg/ha application dose compared to the control. While the cold damage rate was 72.45% in the control group at -10ºC, it decreased to 54.26% at the highest Ca-Humate application dose (12 kg/ha). The cold damage rate decreased by 25.11% at 12 kg/ha application dose compared to the control. While the cold damage rate was 95.68% in the control group at -15ºC, it decreased to 82.11% at the highest Ca-Humat application dose (12 kg/ha). The cold damage rate decreased by 14.18% at 12 kg/ha application dose compared to the control. While the cold damage rate was 98.11% in the control group at -20ºC, it decreased to 88.71% at the highest Ca-Humate application dose (12 kg/ha). The cold damage rate decreased by 9.58% at 12 kg/ha application dose compared to the control (Table 6). Kutlu and Gülmezoğlu (2019) stated in their study that humic acid increases the tolerance of the oat plant in winter conditions and can be considered as a useful application against cold stress.

Conclusion

In this study, the effects of Na and Ca-humate applications on some yield components and cold resistance of wheat and corn plants were evaluated.

According to the results, as reported by previous researchers, it was determined that Na and Ca-humate applications improved the physical and chemical properties of the soil, and increased the uptake of plant nutrients. Depending on the increasing Na and Ca-humate

applications, some yield parameters and cell permeability values of wheat and corn plants increased compared to the control groups, and this increase was found to be statistically significant ($p<0.01$). When the cold damage rate of the plants was evaluated, it was determined that the effects of Na and Ca-humate applications on the cold damage rate were very important in wheat and corn plants ($p<0.05$). The results showed that applying Na and Ca-humat can reduce cold damage rates in wheat and corn plants in cold regions.

Acknowledgements

The study was supported by the Scientific Research Projects of Atatürk University. Project number: 2012-276.

References

Ayaş, H., Gülser, F. (2005). The effects of sulphur and humic acid on yield components and micronutrient contents of spinach (Spinacia oleracea var. Spinoza). Journal of Biological Science. Vol.5, number 6. 801-804.

Brannon, C. A., & Sommers, L. E. (1985). Preparation and characterization of model humic polymers containing organic phosphorus. Soil Biology and Biochemistry, 17(2), 213-219.

Chen, Y., Avnimelech, Y. (1986). The Role of Organic Matter in Modern Agricultur. Martinus Nijhoff Publisers, Dordrecht, 80.

Chen, Y., Aviad, T. (1990). Effects of humic substances on plant growth. Humic substances in soil and crop sciences: Selected readings, 161-186.

David, P.P., Nelson, P.V., Sanders, D.C. (1994). Humic Acid Improves Growth of Tomato Seedling in Solution Culture. Journal of Plant Nutrition (USA), 17(1), 173-184.

Griffith, M., Ala, P., Yang, D.S.C., Hon, W., Moffat, B. (1992). Antifreeze protein produced endogenously in winter rye leaves. Plant Physiol. 100, p: 593-596.

Kacar, B. Katkat, V, K. (2009a). Bitki Besleme. Nobel Bilim ve Araştırma Merkezi Yayınları No: 49, 351-374 s, Ankara.

Kacar, B. Katkat, V, K. (2009b). Bitki Besleme. Nobel Bilim ve Araştırma Merkezi Yayınları No: 49, 593-602 s, Ankara.

Kutlu, İ., Gülmezoğlu, N. (2019). Effects of humic acid and zinc applications on yield and agronomic features of oat genotypes sown in winter or spring. ICOFAAS 2019, 62.

Larcher, W. (2003). Physiological Plant Ecology: Ecophysiology and Stress Physiology ofFunctional Groups, 4th. Edition, Springer, New York.

Lutts S., Kinet JM., Bouharmont J. (1996). NaCl-induced senescence in leaves of rice (*Oryza sativa* L.) cultivars differing in salinity resistance. Annals of Botany 78: 389-398.

McLean, E. O. (1982). Soil pH and Lime Requirement. Methods of Soil Analysis Part2. Chemical and Microbiological Properties Second Edition. Agronamy. No: 9 Part 1. Edition P: 199-224

Nardi, S., Pizzeghello, D., Muscolo, A., Vianello, A. (2002). Physiological effects of humic substances on higher plants. Soil Biology and Biochemistry, 34(11), 1527-1536.

Nelson, D. W., Sommers L. E. (1982). Organic Matter. Methods of Soil Analysis Part 2. Chemical and Microbiological Properties Second Edition. Agronamy. No: 9 Part 2. Edition P: 574-579.

Olsen, S.R., Sommers, L.E. (1982). Phosphorus. Methaods of Soil Analysis Part 2. Chemical and Microbiological Properties Second Edition. Agronomy No: 9 Part 2. Edition P: 403-427.

Sparks, D. L. (2003). Environmental Soil Chemistry, Second Edition, Academic Press, San Diego, 82.

SPSS. (2004). SPSS Inc. SPSS® 13.0 Base User's Guide, Prentice Hall. Stevenson, F. J., 1994. Humus Chemistry: Genesis, Composition, Reactions, 2nd. Edition, John Wiley and Sons, Inc, New York 285.

Stevenson, F. J. (1994). Humus chemistry: genesis, composition, reactions. John Wiley & Sons. Page: 367-372

Yılmaz, C. (2007). Hümik ve Fülvik Asit. Hasad Bitkisel Üretim. Ocak, 260, 74.

Waldigri, M., Pera, A., Agnolucci, M., Frassinetti, S., Lunardi, D., Vallini, G. (1996). Effects of compost-derived humic acids on vegetable biomass production and microbial growth within a plant (Cichorium intybus) soil system: a comparative study. Agriculture, Ecosystems and Environment, 58, (2-3), 133-144.

Strucutral Design and Optimization of Bearingless Helicopter Rotor System

Mert Mustafa Tekin[1]
Vahit Mermertaş[2]

1. Introduction

The importance of vertical take-off and landing (VTOL) aircrafts are getting more popular day by day. The biggest member of the VTOL industry is helicopters which is leading that industry for a long time. New developments and advances in the material science, vibration and acoustics, flight dynamics and control, battery and fuel technology are creating a new era for the future designs of these aircrafts, especially the rotor system and blades.

The importance of rotor blades for helicopters cannot be overstated. Designing these blades requires considering factors such as manufacturability, reliability, accessibility, cost-effectiveness, performance and ease of installation. Moreover, rotor blade design entails a joint optimization problem that involves various elements, including aerodynamics, aeroelasticity, flight dynamics and control, structural design, vibration, acoustics, and material science.

Composite materials are a popular choice for solving these issues because of their exceptional fatigue resistance, low weight, high strength, and modulus. Furthermore, composite structures offer the added benefit of being able to be tailored to specific requirements, which is made possible by the anisotropic nature of composite materials. This means that designers can deliberately adjust the strength of the structure in particular directions as desired. This is an enormous advantage for designing such complex structures. Moreover, Mangalgiri indicates that the usage of composite materials reduces the weight of the aircrafts 30% in total (Mangalgiri, 1990: 657-654).

The use of composite materials in the rotor system can be optimized by utilizing finite element modelling software during the design phase. Moreover, computer aided design software can be employed to generate a detailed design of this intricate system in a digital environment. Additionally, multibody dynamic solvers contribute while extracting loads and creating kinematic and dynamic relations. In this study, the advantage of these three continuous engineering loops will be used to design and optimize a tail rotor system effectively.

The most prevalent rotor configuration globally is the single rotor type system, which consists of a main rotor and a tail rotor. The main rotor is placed horizontally, and the tail rotor is placed vertically with respect to the ground. According to Newton's third law and the gyroscopic effect theory, the main rotor produces torque, and the fuselage creates counter-torque during operation. This counter-torque is offset by the tail rotor blades, which produce anti-torque (Johnson, 2013: 271-274). In this study, it is concentrated to develop a comprehensive design for a single rotor configuration tail rotor system.

[1] Mert Mustafa Tekin, Master's Degree Student, Istanbul Technical University, Department of Mechanical Engineering
[2] Vahit Mermertaş, Prof. Dr., Istanbul Technical University, Department of Mechanical Engineering, ORCID: 0000-0001-9441-1502

Determining the suitable rotor type is a significant step following the establishment of the rotor configuration for a helicopter. The four most common rotor types for single rotor configuration are articulated, semi-articulated, hingeless, and bearingless rotors which are widely using in helicopter industry. Articulated rotors feature flap, lag, and pitch hinges to minimize root moments on the rotor blade, resulting in greater flexibility in rotor blade design. Though, this approach also leads to increased rotor hub complexity, maintenance costs, and the requirement for multipart bearings in the system, known as elastomeric bearings or tension links (Johnson, 2013: 273).

Semi articulated rotors comprise feathering and tethering hinge and generally two-sided rotor blades are installed directly to the rotor hub from the blade root region. The hub flaps in relative to the rotor shaft axis, resulting in the complete blade structure flapping according to the rotor hub's position. A pre-cone angle is often comprised in the hub to lessen solid coning loads. Nonetheless, without lag hinges, the blade's in-plane loads must be accommodated by the root structure (Johnson, 2013: 273-274). Semi articulates systems are cost effective and easy to design systems so, it is preferred most of the civil and small-scale helicopters (mostly 1-4 seated helicopters). However, it is inefficient to use in large scale helicopters because of the excessive loads and more complex design relative to the small-scale ones.

Unlike other articulated and semi articulated rotors, hingeless rotor system doesn't have flap or lag hinges, and the rotor blades attach directly to the hub system using only a feathering hinge. The rotor blade design must consider the high moments at the blade root due to the lack of flap and lag hinges. Structural stiffness is less substantial than centrifugal stiffening, leading to mode shapes resembling rigid body rotations (Johnson, 2013: 273-274). Without flap and lag hinges, the rotor system exhibits flap-lag coupling, meaning deflection in one motion affects deflection in the other motion. Hingeless rotor design is an intermediate design step through to the bearingless rotor system. Some of the helicopter models are used that system and saw the advantages of not using any complex hinges and bearings in the rotor system directly.

The design of bearingless rotor systems eliminates the need for flap, lag, and pitch hinges, and instead, the rotor blades are directly attached to the hub. The rotor blades provide the necessary flap, lag, and pitch movements through deflection (Bramwell, 2000: 277-288). With fewer parts in the rotor hub, the system has lower parasite drag, low weight, increased aerodynamic performance, less noise and is easier to maintain. Additionally, the absence of complex bearings and dampers helps to reduce costs.

One of the biggest advantages of the bearingless rotor system is reduced maintenance operations. Aircrafts have to be inspected after a certain flight hour or if the part is primary structure, sometimes it has to be inspected for after every flight. In this study, developed bearingless rotor reduces the number of primary structures and therefore that saves time for a certain inspection after flight. Moreover, the maintenance cost is lower compared to the other types of rotor systems because of the simplicity of the system in terms of design. To conclude, bearingless rotor concepts have the lowest direct operating cost among the all-rotor systems. Not only the direct operating cost, also the manufacturing cost of bearingless rotor systems is quite favourable when the mass and number of components is compared with the other rotor systems (Emmerling, et al., 2019: 3).

Moreover, the reliability of the bearingless rotor system is higher compared to the other rotor systems since there are fewer dynamic parts in the system. This reduces the risk of failure for overall rotor system and increases the reliability. Briefly, bearingless rotor systems mostly

face less incidents during operation when compared to the other rotor systems (Emmerling et al., 2019: 3).

Another big advantage of bearingless rotors is the degradation of noise and vibration during the flight. One of the reasons is coming from that the system has fewer rotating parts compared to the other systems. Moreover, bearingless rotor systems have more rationalised design; the aerodynamic design reduces the amount of turbulence and that leads to less noise generation. Finally, the bearingless rotor system have a stiffer structure compared to the other systems. Increased stiffness helps to reduce noise levels in the structure because of the mitigated deflection levels. Moreover, with the development of active control systems, the pitch, flap and lag motions can be more controlled and allows to avoid in range of high pitch-flap or flap-lag couplings. This also has an effect on reducing noise in overall.

The purpose of this study is to evaluate the advantages of a bearingless tail rotor system through the use of numerical methods and modern technology, as well as to perform an extensive weight optimization on the rotor blade components to reduce the overall weight of the rotor system as well as helicopter.

2. Literature Review

There were lots of studies about bearingless rotor systems that are starting from mid-1970's which also coincides with the developments in composite materials and these advances directly influences the aviation and automotive industries.

Klöppel et al. investigates the bearingless tail rotor concept including the noise generation, weight, reliability, manoeuvrability, structural design and power efficiency aspects. Results shows that articulated rotors provide higher stability and dynamic properties while bearingless rotors requires significantly less power compared to the articulated rotors (Klöppel et al., 1983).

Narayana et al. investigates the four bladed stiff in plane bearingless tail rotor and dynamic validation of that structure. This study mostly covers in the aerodynamic and design parameters. As the parameters; mass distribution, flap, lag and torsional stiffness parameters are extracted for the baseline design. Moreover, Campbell diagrams and stability charts have been extracted to investigate the stability performance. Finally, structural and dynamic parameters are tested in a whirl tower test which is a quite important step to understand the behaviour of the bearingless rotor at those times (Narayana et al., 1998)

Kim et al. developed a bearingless main rotor system and performed some structural test in a whirl tower with KARI (Korea Aerospace Research Institute). The structural design comprises four bladed soft in plane rotor blade without any hinges and bearings. This is an important improvement in terms of proving the bearingless rotor concept could accommodates higher loads unlike the tail rotor system. Crucial form flexbeam and hollow shape torque tube is designed for that study. As a result of that study, it is mandatory to have a quite simplified lead-lag damper (which will call as snubber later) and it is proved that that kind of hingeless and bearingless system can be applicable for the main rotor system with high accuracy on predicting dynamic and static loads (Kim et al., 2014)

Ichihashi et al. released an article which overviews the design, fabrication and testing of composite bearingless rotor system. The aim of the study is to increase the manoeuvrability and stability which is mentioned as a con compared to articulated rotors. Moreover, it is also aimed to reduce the parts that are used in the rotor hub design to decrease parasite drag at root

region. Finally, Ichihashi et al. proved that with flight test that stability and manoeuvrability of the bearingless rotors could be improved and these parameters are not blockers for development of that concept (Ichihashi et al., 1992).

Cheney is tried to develop a bearingless rotor concept even more less complex and cost effective. In this study, Cheney used all of the advantages of the composite materials and tailoring capabilities. The required low torsional stiffness of the rotor blade to reduce control loads is provided by tailoring capabilities of composite materials. Additionally, Cheney performed coupon and material fatigue tests, analytical results of a full-scale model and wind tunnel test results of scaled rotor blade model. Moreover, after these tests, the inertial and stiffness data are extracted and optimized including Campbell diagram. Finally, stability and manoeuvrability concerns are eliminated with performing stable operation up to 180 knots in the wind tunnel tests (Cheney, 1976).

3. Design and Modelling of Bearingless Tail Rotor Components

The design study can be segmented into rotor hub and rotor blade design. Rotor hub design involves rotor hub, pitch link and swashplate assembly whereas rotor blade design includes flexbeam, torque tube, snubber, skins, sandwich structure, and inner stiffeners, such as epoxy moulding compounds and other aerospace grade structural inner foam materials.

The rotor hub is a critical structural component responsible for bearing the various loads and moments generated by the engine and the helicopter's operation. As the rotor blades are attached directly to the hub plate with cantilever beam conditions, the hub must be robust enough to withstand the centrifugal force generated during operation. Typically, materials that require high strength are produced through machining or forging, as welding can weaken the material. The hub plate for most helicopter designs is forged to ensure that grain boundaries are oriented along the material's length, improving strength. In this study, Ti 6Al 4V has been chosen as the rotor hub material.

As an integral part of the rotor hub assembly, the pitch link serves to transmit pitch input from the pilot's controls to each rotor blade. This link is directly connected to the torque tube and the rotor blade, any failure of this component can result in serious consequences can be called as catastrophic. Consequently, the pitch link is designed with durability and strength concerns during the design. For the purposes of this study, the pitch link will be treated as a 2D rigid element in order to simplify some of the calculations since it is not considered for an optimization design space component.

Swashplate assembly is a crucial component that facilitates the transfer of pilot inputs to the rotor blades via spherical bearing motion. It is comprised of two distinct parts: a non-rotating swashplate that is connected to the rotor mast via a spherical bearing and can tilt in multiple directions, and a rotating swashplate that rotates at the same speed as the tail rotor system. The non-rotating swashplate is linked to the rotating swashplate via ball bearings. In this study, the most common swashplate assembly will be used and not targeted to optimize it further.

Before starting rotor blade design, it is quite important to understand the concept; especially the cross-section model of the rotor blades. Hodges proposed a comprehensive study for composite rotor blade modelling (Hodges, 1990: 561-565) and as many of the conventional helicopter rotor blades take that study as basis for cross section modelling, it is also considered as the baseline cross-section of the rotor blade.

One of the most structural part of the rotor blade is called flexbeam. Flexbeam is a flexible structural member that connects directly to the rotor hub plate in bearingless rotor systems, enabling flap, lead, and pitch movements (Brynes et al., 1994a). Flexbeam is generally made from either GFRP or CFRP materials, which provide advantages such as easy maintenance and manufacturing, reduced weight and complexity, and increased fatigue life and damage tolerance. It is attached to the hub plate with four bolts at the root section and is covered by a torque tube structure and snubber bearings at the same section. In this study, a rectangular shaped flexbeam is designed considering simplification of manufacturing and design operations.

The torque tube is an essential component that ensures equal distribution of the pitch link input among the rotor blade. It must bear high torsional stiffness to prevent any deformation during the transfer of torque. The connection between the flexbeam and torque tube is made through four bolts at the 50% rotor radius, along with snubber bearings mounted at the root area. The pitch link is connected to the swashplate crosshead at one end and the pitch lever, which is linked to the root of the torque tube, at the other. Whenever the swashplate assembly receives a control input, it directly affects the torque tube, resulting in a torsional motion that is transferred from the root section with the help of the snubber bearing and bolted joint section at the 50% blade span. Finally, the flexbeam and torque tube work together to produce a combined torsional movement that reproduces the necessary pitch input to the rotor blade. They not only accommodate torsional motion as well as flap and lag motions together (Brynes et al., 1994a).

The snubber bearing is positioned at the root of the blade and connects the flexbeam and torque tube, using a snubber retainer and film adhesives. It comprises of elastomer and metal shims to provide stiffness in different directions, as well as upper and lower plates for interfacing with the flexbeam and torque tube. The snubber provides two main functions: it transfers control inputs between the rotor blade and other components, and it centres the flexbeam with respect to the torque tube while eliminating relative torsional motion differences. Additionally, the snubber provides a path for current in the incident of a lightning strike. Essentially, snubber bearings are similar to elastomeric bearings that exists in articulated rotors, with the main difference being the loads they experience during flight (Brynes et al., 1992).

Skin assembly is divided into three main structures; hexagon honeycomb, upper and lower skin. The assembly is responsible for providing torsional stiffness and creating the airfoil shape. To meet weight and strength requirements, the blade skins are constructed using [45°/0°/-45°] fiberglass lay-up to increase torsional stiffness of skins lay-ups. Hexagonal honeycomb structure fills the gap between the skins, providing out-of-plane stiffness, damage tolerance, and structural integrity. Skins could be manufactured by hand lay-up method with the help of a tool and hexagon honeycombs mostly machined with the help of 5 axis milling machines. Once constructed, the skin and honeycomb structures are bonded together to create the aerodynamically functional region of the rotor blade. Afterwards, these parts are secondarily bonded and forms the skin assembly.

As a results, an overview of the baseline design for a bearingless tail rotor system could be seen in Figure 1.

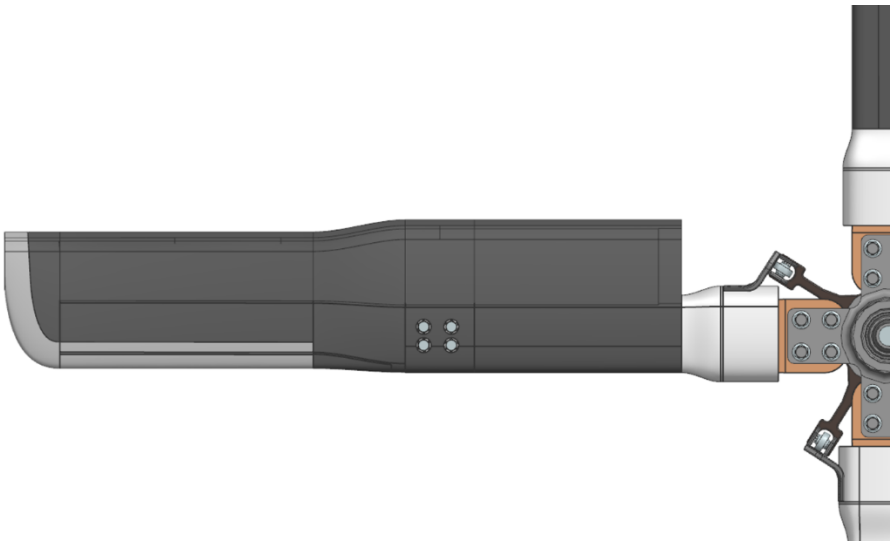

Figure 1. *Overview of the bearingless tail rotor system.*

4. Preparation of Baseline Design of Flexbeam

As mentioned previously, flexbeam is the most important component since it accommodates many principal loads as well as increases the motion spectrum of the entire rotor blade. Moreover, there is no standard design principle is available such as torque tube. The external shape and ply configuration is significantly specific to the designed helicopter model. Therefore, it is quite important to perform an initial sizing for a baseline design before starting optimization process.

In this step, it is aimed to divide flexbeam into several regions in order to assign specific capabilities to each region to accommodate load and motion spectrum in overall. This separation is based on tailoring capabilities of the composite materials, as known as anisotropy. It is aimed to take advantage of that tailoring capability and reflect it to the current design approach. The design of a flexbeam necessitates dividing it into three primary groups and two subgroups, which are known as HAR (Hub Attachment Region), ITR (Inboard Transition Region), PR (Pitch Region), OTR (Outboard Transition Region), and BAR (Blade Attachment Region), respectively (Brynes et al., 1994a).

HAR is responsible for creating an interface for attaching the rotor blade to the rotor hub. After performing some non-linear static analyses for bearing and bypass stresses acting on the holes, it is obtained that the interface should be provided with the help of four bolts in two rows, in total. The HAR is the most heavily loaded region in terms of forces and moments, and it has four Ø28 mm holes that necessitate an increase in the number of plies, particularly off-axis plies, to support bearing loads (Brynes et al., 1994b). During the design, transition fit tolerance range has been selected for hub interface holes in order to provide proper load transfer between flexbeam and rotor hub. The width and thickness of the HAR are uniform along the region as no flexibility is needed based on the design principle of the flexbeam (Brynes et al., 1994a).

ITR region is primarily designed to enhance the structure's flap-bending capacity by properly tapering the width and thickness to handle the flapwise and lagwise moments. Basically, ITR section is divided into two sub regions named as ITR-1 and ITR-2. ITR-1 is characterized by a thickness taper, while ITR-2 features both width and thickness tapering and a necessary width transition across the HAR. Both ITR-1 and ITR-2 utilize a combination of

(UD) unidirectional and off-axis ply configuration. The optimal length of the transition region should be determined based on two factors: the length of the transition region and composite drop-off design principles. During the development of that study, it is aimed to determine and finalize the proper length and width of ITR region to be able to ensure required motion of flap, lead and lag will be achieved (Brynes et al., 1994a).

The main function of the PR is to bear the torsional stresses across the length of the rotor blade. The pitch region plays a crucial role in managing torsional loads, minimizing control input loads, ensuring necessary edgewise buckling stability, and establishing the chordwise frequency of the rotor blade. The edgewise stiffness of the flexbeam is an important factor because it affects the first chordwise frequency of the structure, which is controlled by the PR. Therefore, proper checks should be done during sizing of PR in order to avoid ground resonance issue. Moreover, the outcomes of ground resonance for an articulated rotor system are investigated and validated by many researches that have been made in the past (Eckert, 2007). Therefore, it is quite significant to understand the dynamics of that phenomenon and take actions accordingly. Tuning the first chordwise frequency between 1.5-1.9 cycles/rev is a vital consideration in bearingless tail rotor applications, as it can avoid the requirement for a lag damper and prevent load amplification at the resonant harmonic frequencies of the rotor blade assembly. To avoid aeroelastic instability and load amplification, it is typically necessary to tune the first chordwise frequency between harmonic frequencies, like 1.0, 2.0, or 3.0 cycles/rev (Brynes et al., 1994a).

OTR is basically a transition region between PR and BAR and the only important parameter while designing is to follow the drop off ratio rules in order to avoid any excessive stress concentration at that region. Moreover, it is quite important to extend the PR as could as possible since it leads to reducing of the control loads. However, that extension leads to shortening of ITR and OTR or increasing the total length of the flexbeam. Extension is not an option since it is already finalized at the begging of the study while finalizing rotor radius. Besides, shortening ITR and OTR leads to excessive stresses and strains due to sudden transaction between thicker and thinner regions. For that reason, the optimum value should be calculated between these three regions during design step (Brynes et al., 1994a).

BAR is responsible for creating the required interface between the rotor blade and the flexbeam to ensure proper functioning of the rotor system. Designing of BAR quite critical since it is obviously a transfer region of most dominant load, which is centrifugal load (Brynes et al., 1994a). Double shear connection using two rows of four fasteners is employed in this region to ensure a secure connection between the flexbeam and rotor blade. As a result, Ø20 fastener holes with transition fit tolerance feature is selected. The width and thickness of BAR are consistent throughout the region, and its ply configuration is similar to that of HAR. Nonetheless, HAR is thicker as it is exposed to higher moments than BAR. In Figure 2., the regions of flexbeam could be seen.

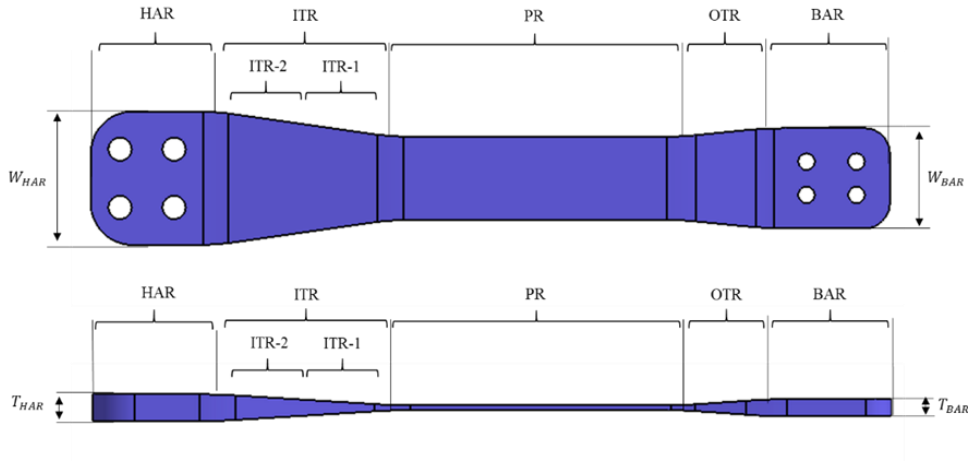

Figure 2. *Definitions of flexbeam regions.*

5. Structural Optimization Method

After finalization of the baseline design for the tail rotor system and blade components, optimization step could be performed. In this optimization, a three-stage special method for composite structures is used. Free-size optimization is the first step of the optimization process and it will be followed by size and shuffling optimizations, respectively.

Free sizing optimization is primarily focused on optimizing composite structures. The aim is to generate design ideas that explore all the possibilities of a composite structure while considering both the structure and the material. To accomplish this, a super-ply concept is implemented where each fiber orientation is assigned a free thickness super-ply. The approach of free-size optimization is distinct from topology optimization in that it doesn't strive to achieve a specific thickness. Rather, it allows thickness to vary between T0 and T for each element within a shell cross-section, as displayed in Figure 3.

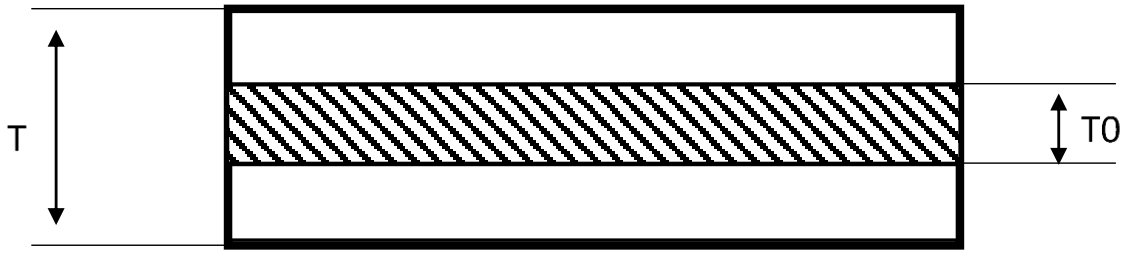

Figure 3. *Minimum and maximum laminate thickness constrain in free size optimization.*

In the design phase of free-sizing, SMEAR option is usually preferred to cancel out the impact of stacking sequence unless the super-ply laminate model follows the stacking preference. Moreover, free-sizing optimization comes with extra manufacturing restrictions. Generally, composite laminates go through a curing process after being stacked, and it has to adhere to certain manufacturing standards to avoid undesirable consequences (Goelke, 2021: 97).

The free size optimization process also provides valuable insights into the load paths within the structure. User could clearly visualize the load flow and could comment on it in post optimization step. This is quite significant since initially there was no idea about the load flow about the design because of complexity of the component interfaces. Although any orientation

can be utilized during the design, common orientations like 0°, ±45 and 90° are recommended to be more practical in terms of availability in markets and lay-up simplicity.

The process of sizing optimization involves adjusting the thickness of each layer within the laminate to achieve optimal results. Sizing optimization allows to check ply continuity across the zones and these zones could be tracked automatically, without the need for manual tracking of numerous zones. Moreover, sizing optimization also involves the refinement of adjusting manufacturable ply thicknesses instead of using super-plies anymore (Goelke, 2021: 98). This stage could be seen in Figure 4.

Free size and sizing optimization are the fundamental steps to perform a proper composite optimization. After these steps, designer will understand the behaviour of the structure that have different ply configurations. This provides visibility and allows designer to check and re-design the baseline design if needed. Additionally, sizing optimization allows to involve the manufacturing constraints to the optimization process to have more realistic results. Even though some manual adjustments are required in size optimization step, it is quite acceptable since the necessary manual operations have minor effect on the optimization process time. Moreover, during the modelling of the structure with using FEM and CAD software, it is quite important to use simplified and adjustable (parametric) features to reduce the time required to finalize the optimization process.

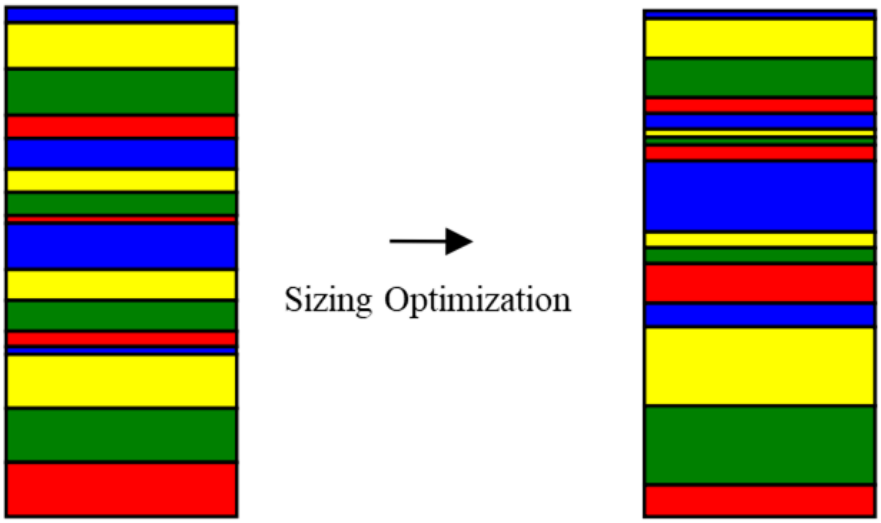

Figure 4. *Graphical representation of sizing optimization (Goelke, 2021: 98).*

Size optimization addresses the question of the exact number of plies needed for each ply outline to meet strength and manufacturing engineering requirements. Mathematical optimization algorithms are employed to optimize the ply thickness, size, and orientation of the structure iteratively, taking into account a variety of engineering constraints, including buckling strength, maximum stresses, composite strains, and deflections (Goelke, 2021: 98).

The free size optimization output model could be directly used as sizing optimization input. This could be done with adding FSTOSZ control card output to the free size optimization step and analysis could be run with that. This allows designer to transfer all required and pre-defined engineering and manufacturing constraints to the new analysis step which is sizing optimization (Goelke, 2021: 112).

Shuffling optimization is a stage in the optimization process of composite design that answers the question of finding feasible stacking sequences that meet the final manufacturing

requirements, taking into account various factors. This information consists of the part's dimensions, the outlines of the plies that create the sections of unchanging thickness, and the specific quantity of plies for each outline. The precise disposition of these plies to meet the manufacturing engineering requirements is yet to be determined and requires the use of composite shuffling optimization (Goelke, 2021: 99).

Shuffling optimization can be performed using the input data obtained from the size optimization phase. Similar to the transition from free-size to size optimization, output parameters from size optimization could be directly transferrable with using SZTOSH control card (Goelke, 2021: 116).

The DSHUFFLE bulk data card includes a MAXSUCC continuation line, which determines the maximum number of plies that can be successively stacked for a specific orientation. A characteristic cover stacking sequence is [-45/0/45/90], and it can be frequent as many times as needed. The plies on the top and bottom shells of the laminate are determined using the cover stacking sequence, which can be established by utilizing the COVER continuation line on the DSHUFFLE bulk data card. Moreover, the plies located in the centre of the laminate can be specified using a core stacking sequence that can be repeated as needed. A core stacking sequence, which establishes the plies on the middle surface of the laminate, can be defined using the DSHUFFLE bulk data card. This sequence can be repeated as many times as necessary and is set using the CORE continuation line (Goelke, 2021: 118). For an overview of the shuffling optimization process, see Figure 5.

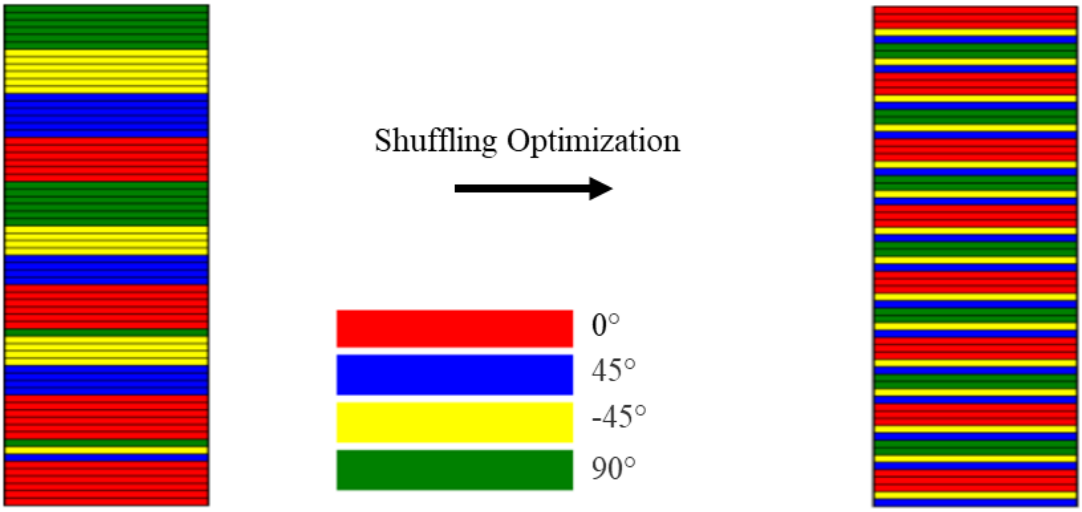

Figure 5: *Graphical representation of shuffling optimization (Goelke, 2021: 118).*

6. Validation of Flexbeam and Torque Tube Baseline Designs

Optimization of rotor blade is concentrated on two main primary components; flexbeam and torque tube. These two parts are selected because they are primary structures for bearingless tail rotor blade design and as weight, they have the biggest pie on weight percentage. It is aimed to first validate the strength of the baseline designs under centrifugal force since this is the most dominant force compared to the flight loads.

The baseline flexbeam design is generated with the help of patents (Brynes et al., 1994a & Brynes et al., 1994b). Optimization process will be constrained by the values obtained from the required motion envelope. The composite strains experienced by the flexbeam will also be

used as another constraint. In the end, the optimized flexbeam should operate properly under the constrains that is given at the beginning. The optimization's objective is to create a flexbeam design that can accommodate the necessary motions while minimizing mass and maximizing stiffness. In order to reduce complexity, the thickness and ply orientation is kept as simple as possible for both flexbeam and torque tube components. Basically, this leads to a flexbeam which has constant thickness along the spanwise and chordwise directions. As a result, the baseline design for the flexbeam can be seen in Figure 6.

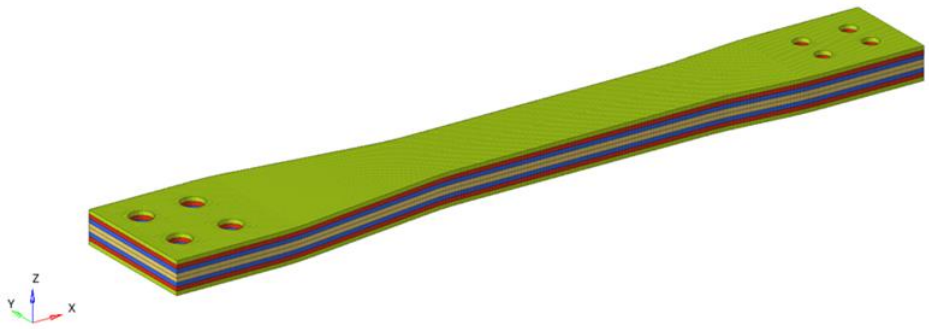

Figure 6. *Baseline design of flexbeam.*

The purpose of the non-linear static analysis with using only centrifugal load is to investigate the behaviour of the flexbeam under most dominant load and also to understand some of its modal characteristics. The laminate is constructed from plies with orientations of 0°, ±45°, and 90°, with each ply having a total thickness of 10mm. Carbon/Epoxy material is selected because of high strength and lower density features. The predominant function of the 0° plies in the laminate is to support the centrifugal load. The +45°/-45° plies are employed to resist in-plane shear forces, while the 90° plies are used to resist transverse loads during operation. After the free size optimization is finalized, the percentage of ply orientations that is required for the flexbeam to withstand flight loads will be determined. Finally, the baseline laminate complies with composite guidelines and is symmetrically balanced, as presented in Figure 7.

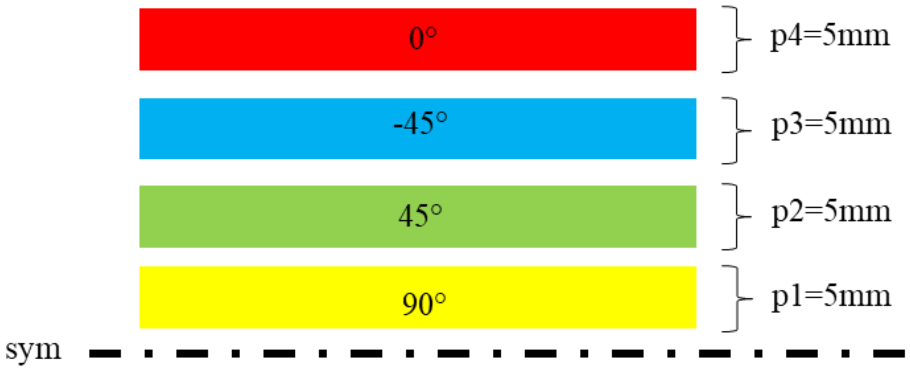

Figure 7. *Baseline ply configuration for flexbeam.*

Two subcases will be carried out during the optimization process: the first subcase entails applying centrifugal force and observing the structure's response under high axial load, while the second subcase involves performing modal analysis to understand the component's modal behaviour. The flexbeam's root region holes are clamped, and force is applied to the tip region holes. Note that other inertial loads are extracted by applying a RESTRAT analysis in NASTRAN solver and importing these SOL103 and SOL106 outputs to ADAM's Multibody

Dynamic Solver software (Xiaocheng, 1999: 2-5). Moreover, the effect of centrifugal stiffening is included during the modal analysis. To make the analysis easier, the calculated centrifugal force is multiplied by a safety factor of 1.5 and distributed equally among four equivalent holes. The analysis setup employs a total of 11,201 nodes and 10,740 quad shell elements, with the Tsai-Wu method chosen as the failure criteria.

The Rigid Body Element (RBE) method is employed for the fixed and force application points in the analysis. RBEs act as a Multi-Point Constraint (MPC) that can connect multiple nodes to one node or vice versa. The two most frequently utilized RBE types are RBE2 and RBE3, which will be used extensively in this study. By linking an independent node to numerous dependent nodes without any degrees of freedom in relation to each other, the RBE2 method introduces extra stiffness to the component, which can result in slightly different outcomes than anticipated. For example, due to the additional rigidity, the modes of the structure may have shifted upwards. Nonetheless, the RBE2 method can be valuable in describing fixed joints because the nodes at these joints are practically rigid to each other.

RBE3 is different from RBE2 in that the reference node is a dependent node and the linked nodes are independent. This allows for relative motion between the independent nodes, which makes load and moment applications more accurate by avoiding additional stiffness generation. The loads or moments applied are distributed among the independent nodes according to their weighting factor. In the flexbeam analysis, RBE2 is used at the clamped end and RBE3 is used at the force application locations.

The first step of the analysis is to perform a linear static analysis with only the centrifugal load, as mentioned previously. The baseline design uses 0°, ±45°, and 90° plies equally, and it is necessary to ensure that the design can tolerate the centrifugal load. A basic approach is used for the analysis; if flexbeam could accommodate centrifugal load with the baseline design, it could be said that flexbeam could also could accommodate other loads because for the baseline design it is intended to create a quasi-isotropic structure.

The decision to perform a non-linear static analysis only is based on the belief that the deflections in the spanwise direction will be negligible however the load-deflection relationship will be non-linear. Furthermore, performing a non-linear static analysis enables a better understanding of the component's behaviour under loads, as the load is incrementally applied and the component has enough time to reach equilibrium. Figure 8 indicates the deflections, composite strains and stresses, respectively.

Additionally, modal analysis is carried out to assess the risk of ground resonance effects and determine the natural frequencies of the structure. The first three modes are examined to identify any critical frequencies that may coincide with the landing gear frequencies and cause resonance issues. This analysis must be performed and confirmed at this stage of the design development otherwise could cause some issues at the latest stages of design. After optimization, it is important to ensure that the natural frequencies of the rotor blade are not significantly altered. Therefore, modal analysis is a crucial step to avoid any unexpected resonance problems. Figure 9 represents the results of the modal analysis.

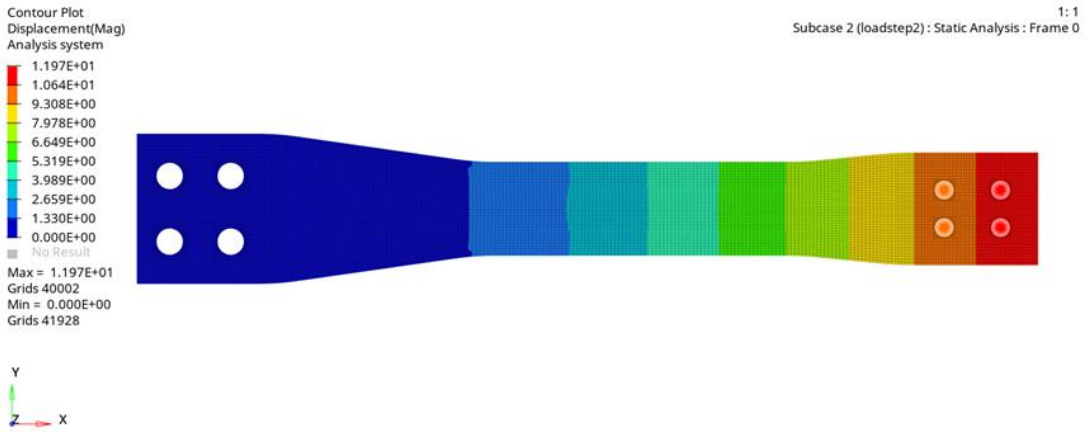

(a) Displacements.

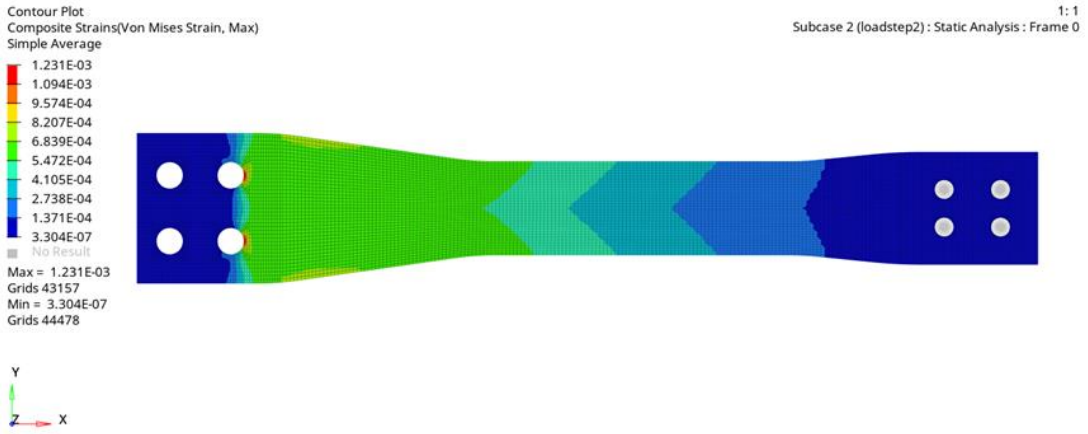

(b) Composite strains.

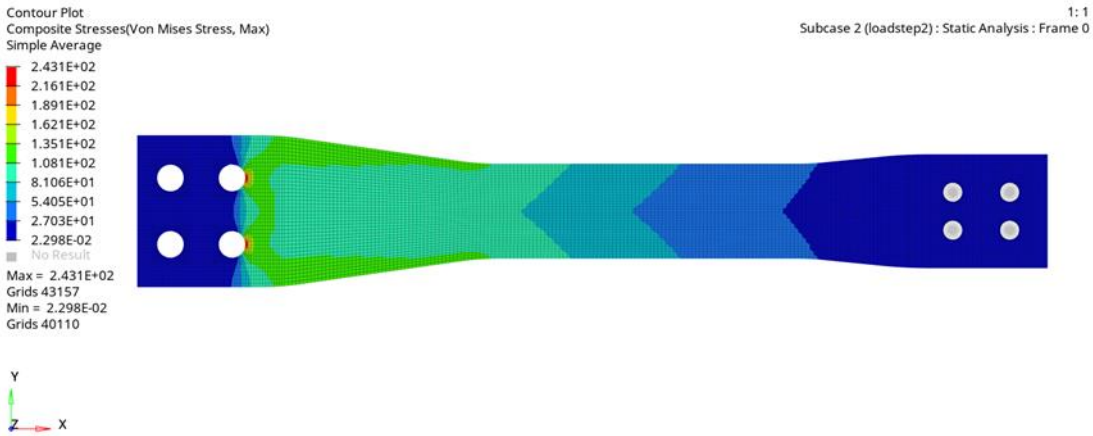

(c) Composite stresses.

Figure 8. *Displacements, strains and stresses on baseline flexbeam under centrifugal load.*

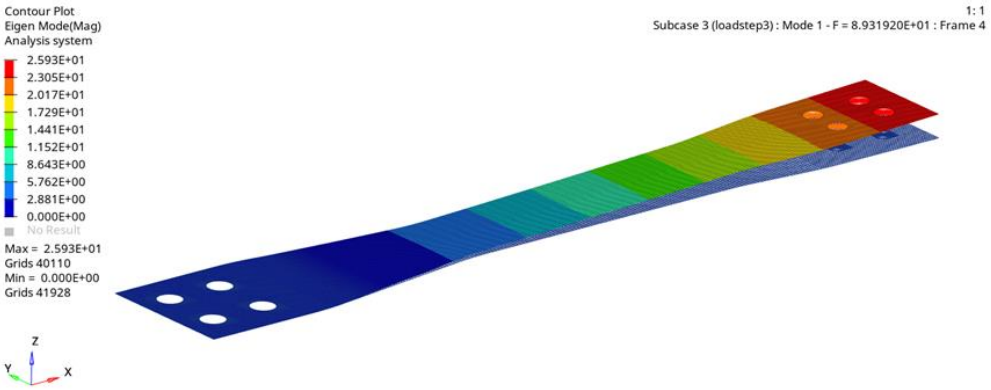

(a) First mode.

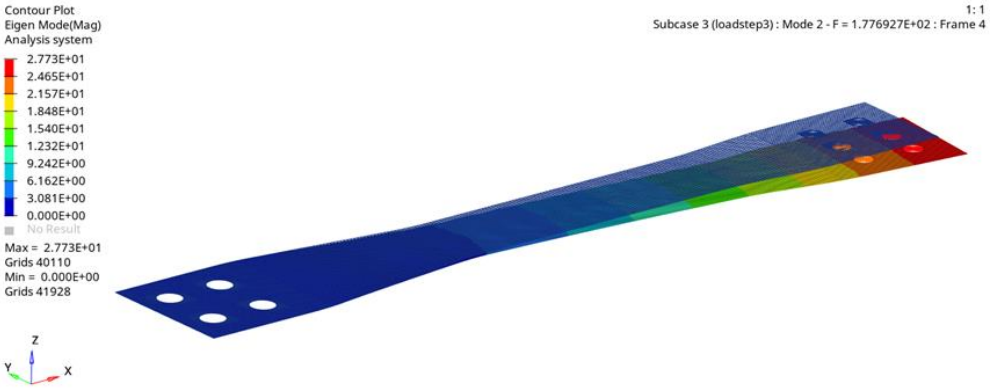

(b) Second mode.

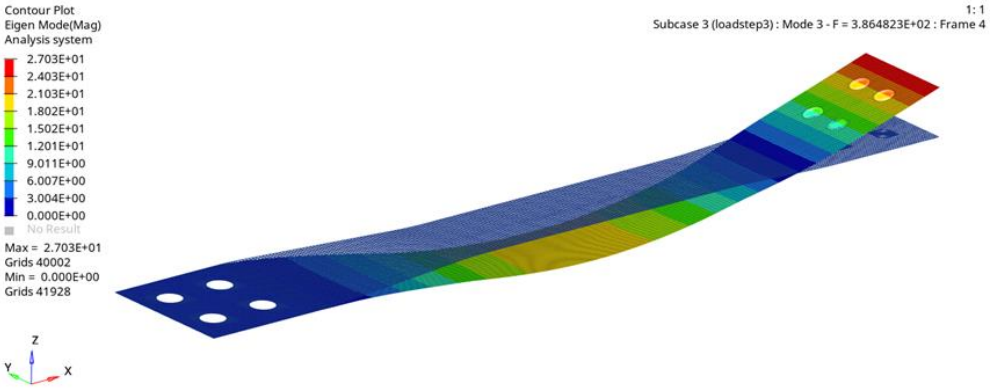

(c) Third mode.

Figure 9. *First three modes of baseline flexbeam with centrifugal load.*

Moreover, a very similar approach will be performed for also another primary structure which is torque tube. The torque tube plays a crucial role in the bearingless rotor system by ensuring that the pitch is distributed equally across the entire length of the rotor blade. It is typically a hollow, cylindrical, or elliptical structure that runs nearly the entire length of the blade tip. Additionally, the pitch input provided by the pilot is initially transmitted to the swashplate assembly and then to the pitch link, pitch lever, and torque tube, respectively. Finally, torque tube provides a bridge between flexbeam and the other rotor blade components. Flapwise and lagwise movements are primarily controlled by the flexbeam, whereas the torque tube is responsible for managing torsional (pitch) loads. The design aims to maximize

compliance and minimize weight while maintaining torsional stiffness. Figure 10 shows the baseline design of the torque tube.

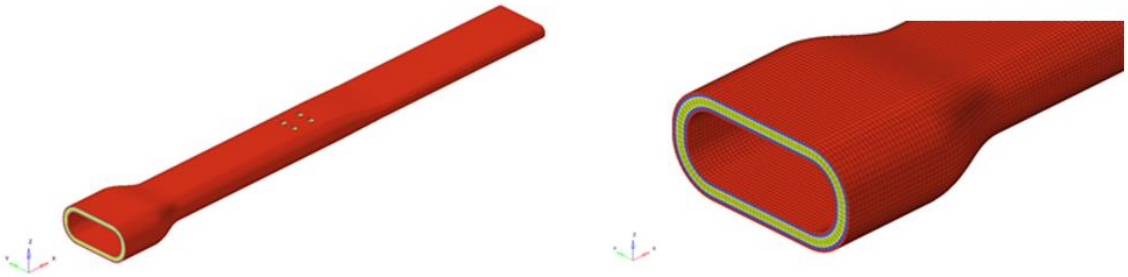

Figure 10. *Baseline torque tube design.*

Torque tube is connected to the flexbeam at two locations, specifically the snubber attachment area (STA300) and the bolted joint connection (STA950 and STA1010). Both the torque tube and the flexbeam are dynamic components that are interconnected, so the analysis of the torque tube is carried out with the flexbeam, and the fasteners are also taken into account. The boundary conditions can be seen in Figure 11.

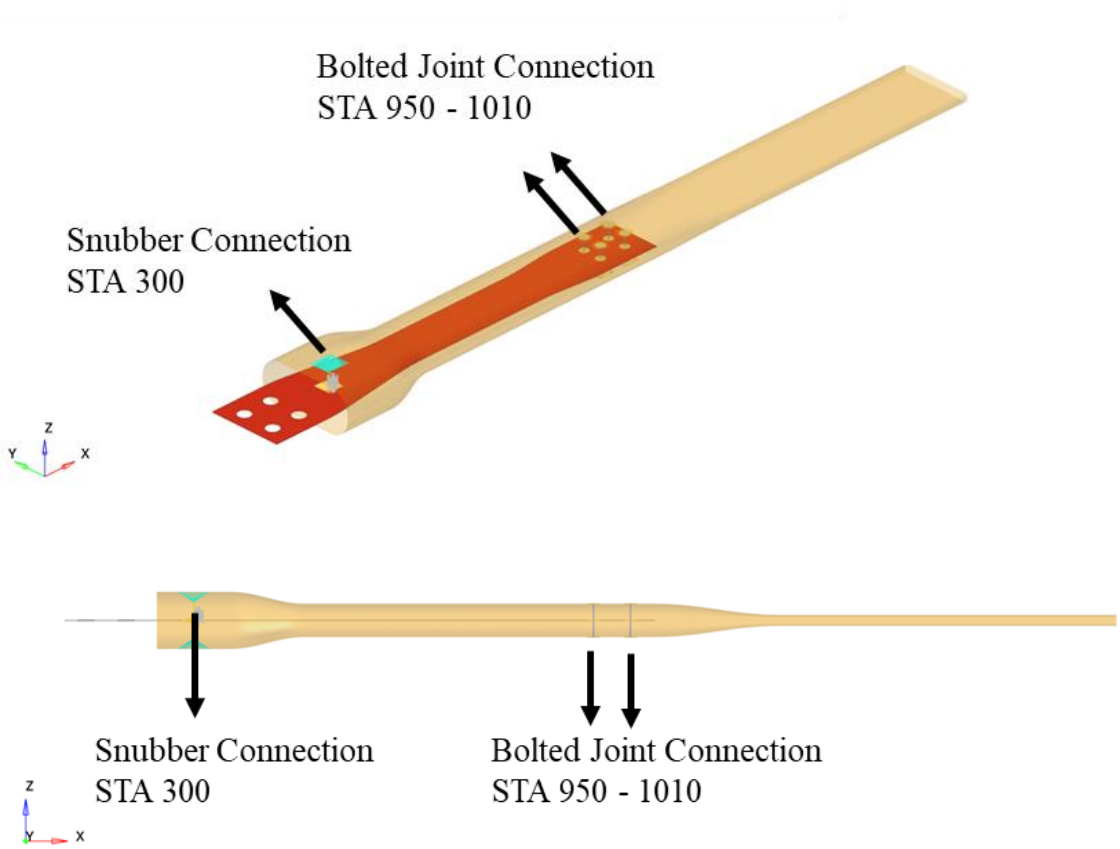

Figure 11. *Boundary conditions of torque tube.*

Definition of torque tube boundary conditions for the inward (root) section starts with definition of contact area with the snubber. For that definition, RBE3 is the best coupling element to describe the relative motion between these two components. Once the contact nodes for flexbeam and torque tube are determined, they are connected to form a dependent node.

Consequently, two dependent nodes have created and these two dependent nodes is connected with CBUSH element type which allows to define stiffness and damping values for each direction. This flexibility of defining antistrophic stiffness values for snubber is the crucial point, otherwise the proper contact between flexbeam and torque tube could not be defined successfully. As in Figure 12, the snubber is modelled as a spring-damper model. Additionally, in the bolted joint region between STA950 and STA1010, fasteners are represented using CBAR element type. CBEAM element type enables the fastener to be depicted with particular stiffness and strength values. Structural steel S450 is chosen as the bolt material based on EN1993-1-1 §3.2.6 standards.

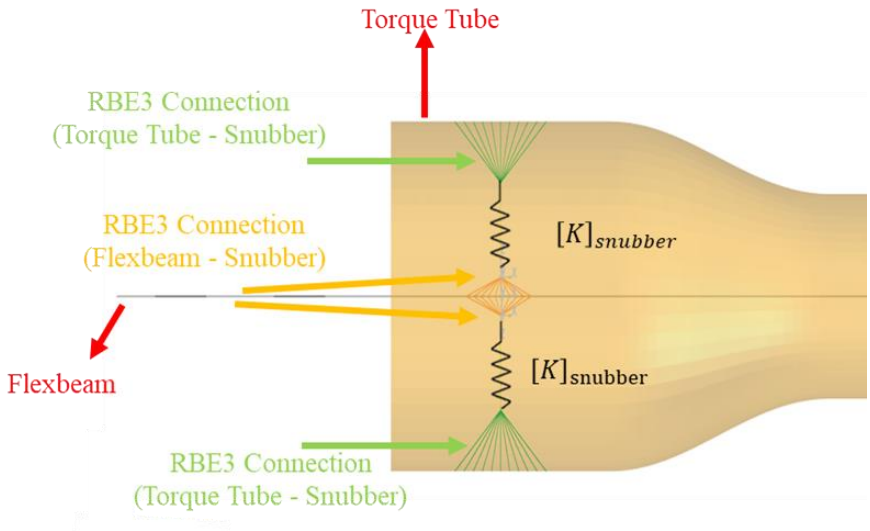

Figure 12. *Root side connection of torque tube.*

Because of the nature of the design, the fasteners are placed perpendicular to their principal axis. This leads to an excessive shear and bending moments on the both root and blade fasteners. As a result, that non-proper positioning leads to enlarging of the root and blade fasteners than it is calculated. For the fasteners that will be used to connect flexbeam and torque tube, Ø20 mm fasteners are planned to use for both flexbeam and torque tube with a transition fit characteristic. In order to evenly distribute the load to separate nodes located in holes, the RBE3 connection type has been chosen over RBE2 as it does not cause any additional stiffness to the structure. The RBE3 method facilitates the clear observation of shear stresses and strains that are present in bolted joints. Therefore, a four-bolt connection, as shown in Figure 13, is used to connect the flexbeam and torque tube at the bolted joint region.

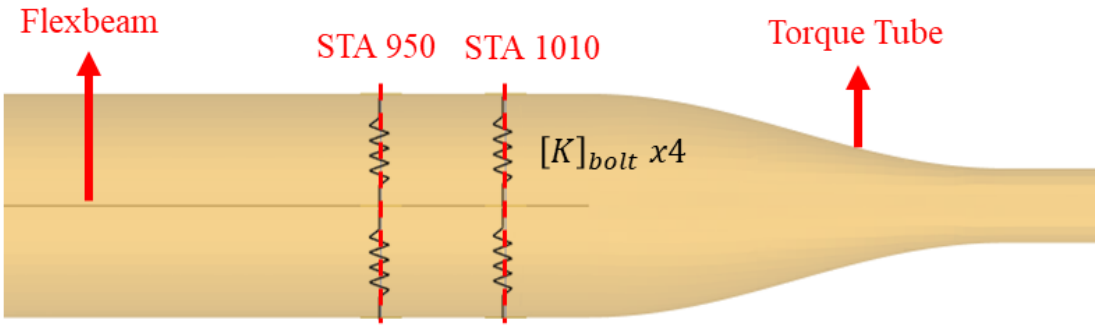

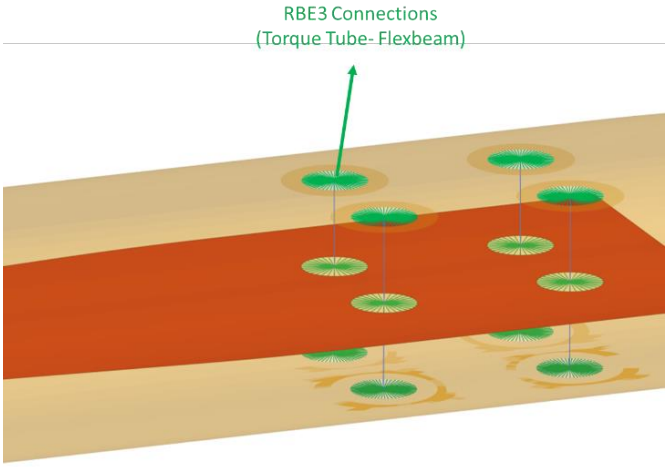

Figure 13. *Torque tube – flexbeam connection at STA 950 and STA 1010.*

The same stack up and orientation are employed for the super ply concept with flexbeam in the baseline design of torque tube, with the only difference being varying thicknesses. The laminate includes plies with orientations of 0°, ±45°, and 90°, and each ply has a total thickness of 5 mm, as shown in Figure 14.

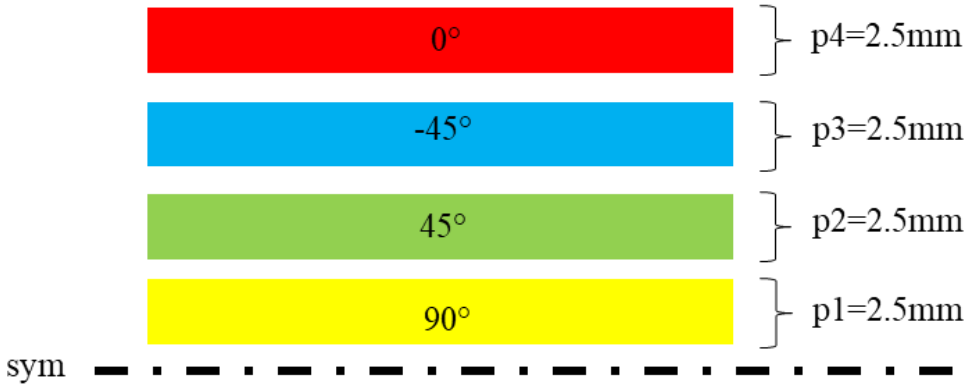

Figure 14. *Baseline ply configuration of torque tube.*

The analysis and optimization phases will incorporate a balance and symmetry condition as a constraint. As a result, the final laminate, much like the one utilized in the flexbeam, will be symmetric and balanced. Furthermore, aerospace standards specify specific drop-off ratios and maximum numbers of successive plies. In this study, these values remain the same as in the flexbeam design, with a drop-off ratio of 1:20 in the main load direction and 1:10 in the perpendicular direction, and a maximum successive number of plies for each orientation set to 2. Finally, Carbon-Epoxy material is nominated for torque tube design.

Following the analysis setup, the initial analysis for the baseline design was executed. Figure 15 briefly indicates the displacements of the flexbeam, torque tube, and snubber, respectively.

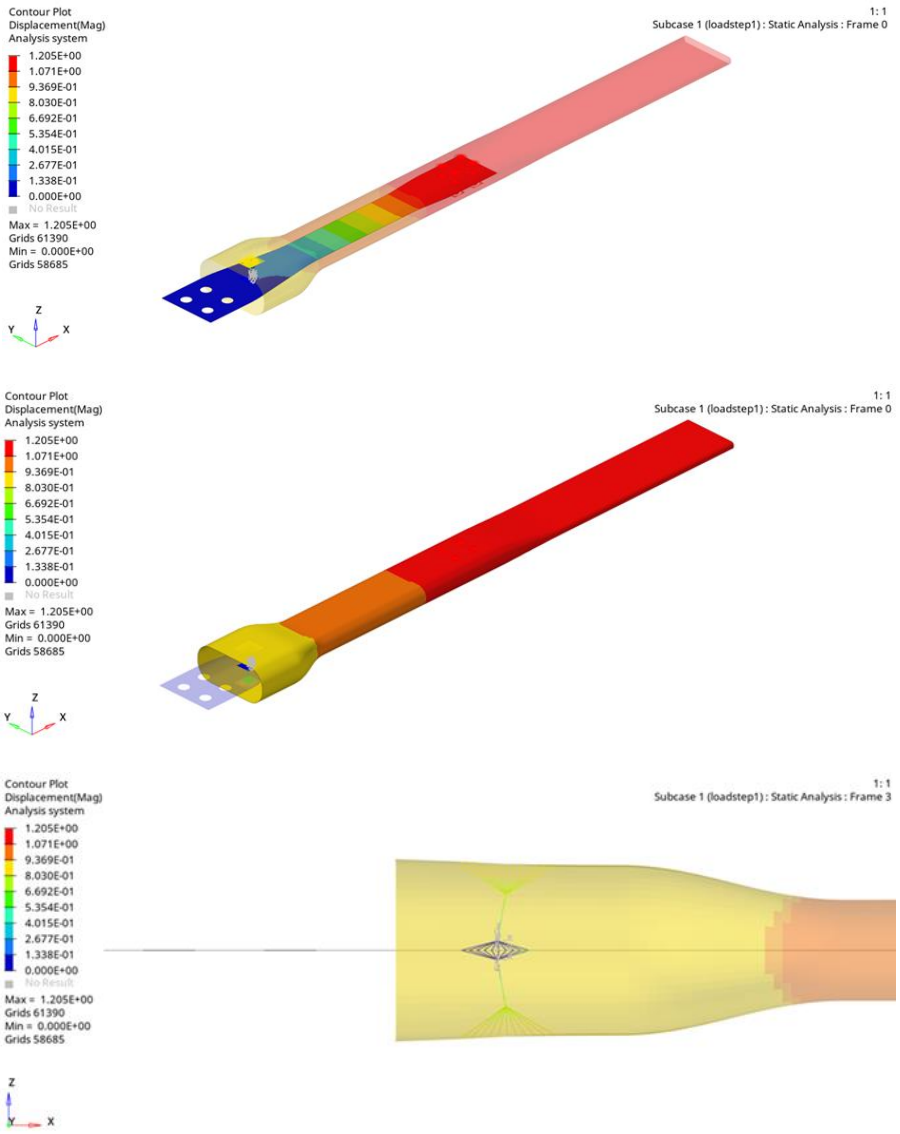

Figure 15. *Displacements of flexbeam, torque tube and snubber components under centrifugal load, respectively.*

Additionally, the stresses and strains were analysed after the initial assessment, as illustrated in Figure 16. The root region, which is the most critical region in terms of strength, showed no indications of strain or stress issues.

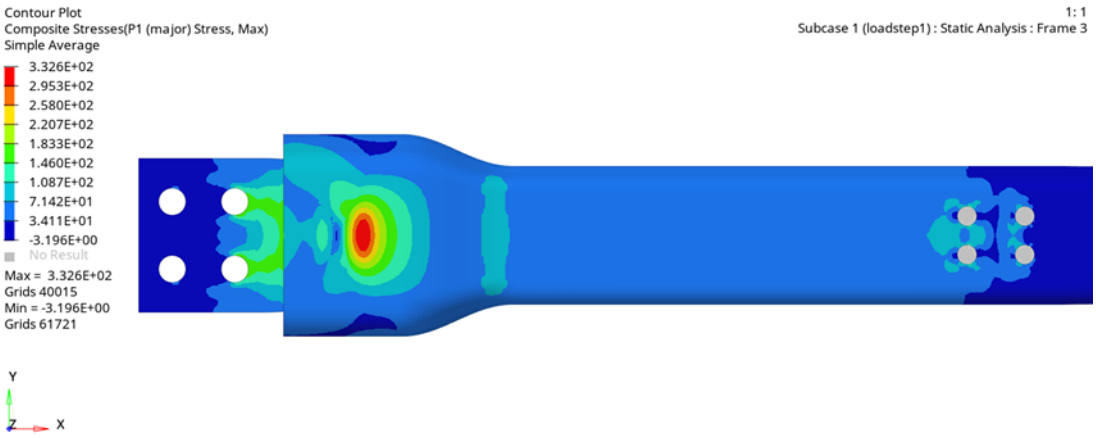

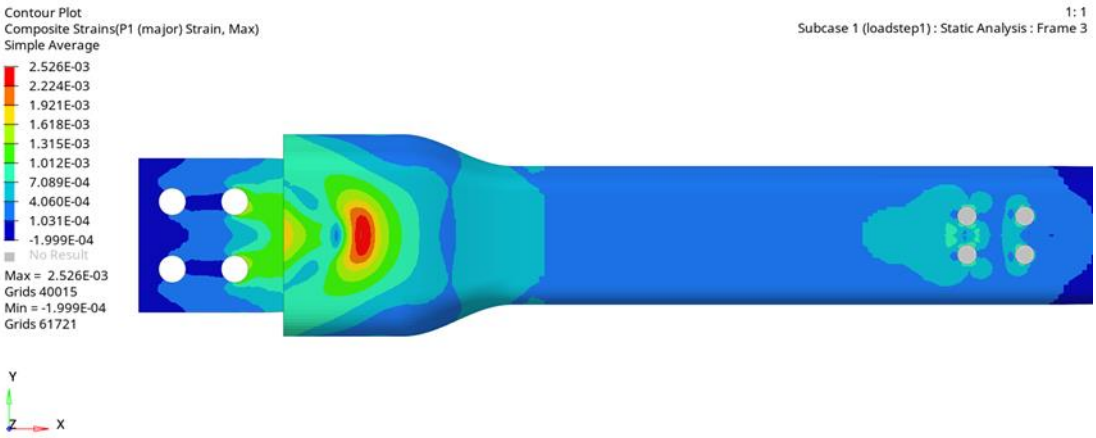

Figure 16. *Stress and strain levels on torque tube root under centrifugal load.*

7. Structural Optimization of Flexbeam and Torque Tube

The optimization will follow the sequential steps; free size, size and shuffling optimization. For all optimization steps, entire flexbeam and torque tube model will give as design space to the solver. For flexbeam, as a design constrain, the minimum laminate thickness is given as 10 mm as well as maximum values is 40 mm. Performing a non-linear static analysis to the baseline design gives much information about what should be the thickness range is. Moreover, the balance, symmetry, and the drop off ratio is given as inputs.

The optimization process aims to minimize mass, compliance, and keep the static displacement in range in the z direction (flapwise direction). It is essential to keep the tip deflection of the flexbeam between 45-50 mm in the flapwise direction and is considered an engineering constraint in the optimization process as a design constraint at the beginning.

It is essential to monitor the iterations, outputs, and deviations from objectives at the beginning of each optimization step. Analysing each iteration step in detail from the output text file is vital since it provides valuable information about the optimization's direction for the structure and what might cause the optimization to fail. The mass and compliance outputs were thoroughly investigated in this study by analysing the output text file. Moreover, the effect of the manufacturing constraints on the engineering parameters was assessed and controlled, as presented in Figure 17.

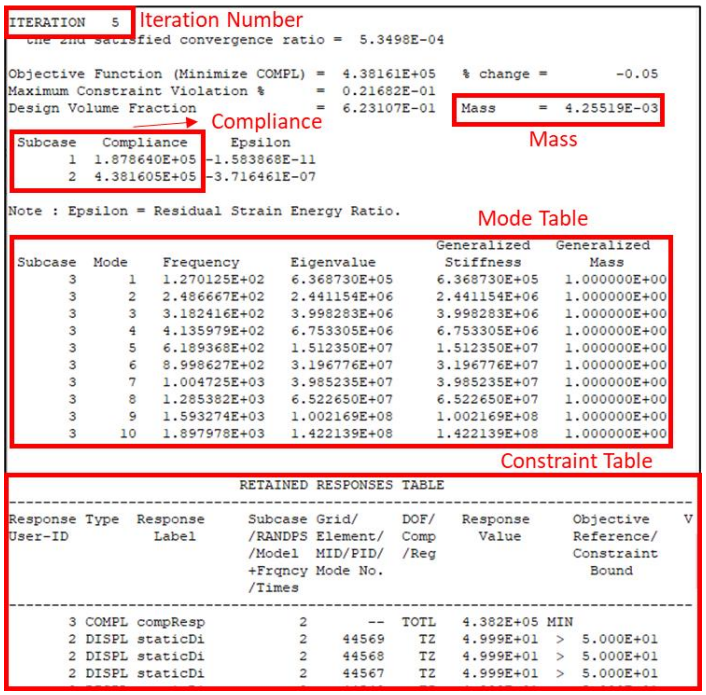

Figure 17. *Flexbeam optimization parameters control panel.*

In Figure 18, the thickness distribution of 0°-90° and ±45° plies can be observed after the free size optimization.

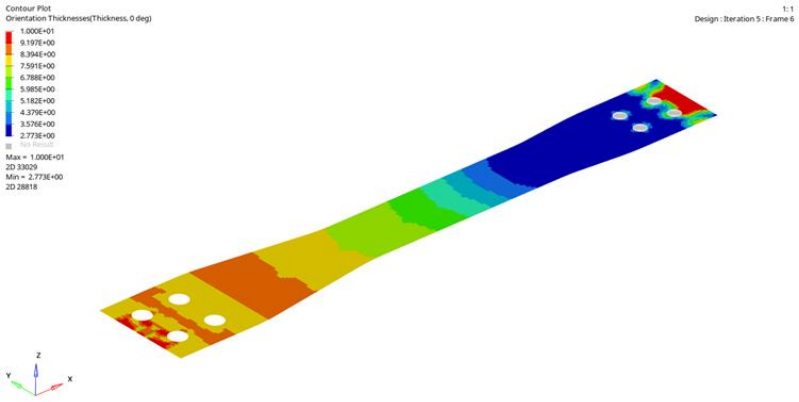

(a) 0°-90° superply thickness output.

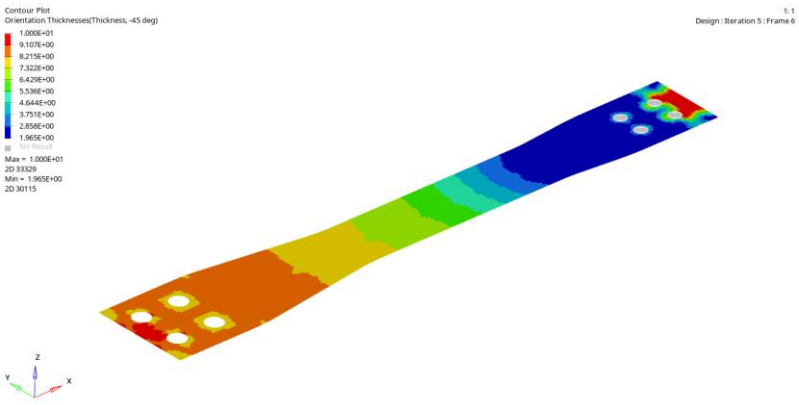

(b) ±45° superply thickness output.

Figure 18. *Flexbeam laminate and ply thickness output from free size optimization.*

One of the most important outcomes of performing size optimization is to understand the load paths, as mentioned before. It is quite significant that the HAR, ITR, PR, OTR and BAR regions are shaped automatically (without giving any additional constraints) as mentioned before. This is a milestone for the optimization since it clearly indicates that the boundary conditions, manufacturing and engineering constraints are applied correctly. As it is predicted previously, the thicknesses of HAR and BAR regions are quite thicker than the other flexbeam regions. In Figure 18, the thicknesses of the 0° - 90° and -45° - +45° plies are not separated each other because this is a symmetric and balanced laminate and it is enough to only indicate one of them. Moreover, during the optimization, the software identifies the reason for optimization failure if a feasible design cannot be reached due to engineering or manufacturing constraints, making it straightforward to resolve during the analysis.

Both 0° and 45° plies have thickest regions of 10 mm and thinnest regions of 2.773 mm and 1.965 mm, respectively. Currently, the optimization loop does not include constraints for manufacturable or cured ply thickness, but this information will be incorporated in the size optimization step. The output of the free size optimization is presented in Figure 19.

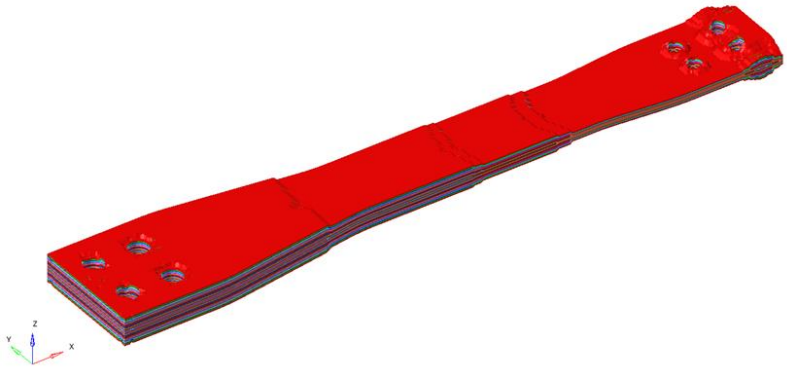

Figure 19. *Output of the free size optimization for flexbeam.*

As stated earlier, the free size optimization typically does not produce designs that are easy to manufacture. Nonetheless, this stage is critical for understanding the function and load distribution. The plies identified by the free size optimization presented in Figure 19 will be refined through size optimization and with the help of manual modifications.

Figure 20 indicates that the ply shapes is to reorganized and adjusted to address practical manufacturability concerns. To achieve this, some modifications to the FEM are necessary, consisting of adding or subtracting elements from the 2D FEM model. This process must be performed for each ply generated during the size optimization step and according to experience it gives more accurate results to perform in manually.

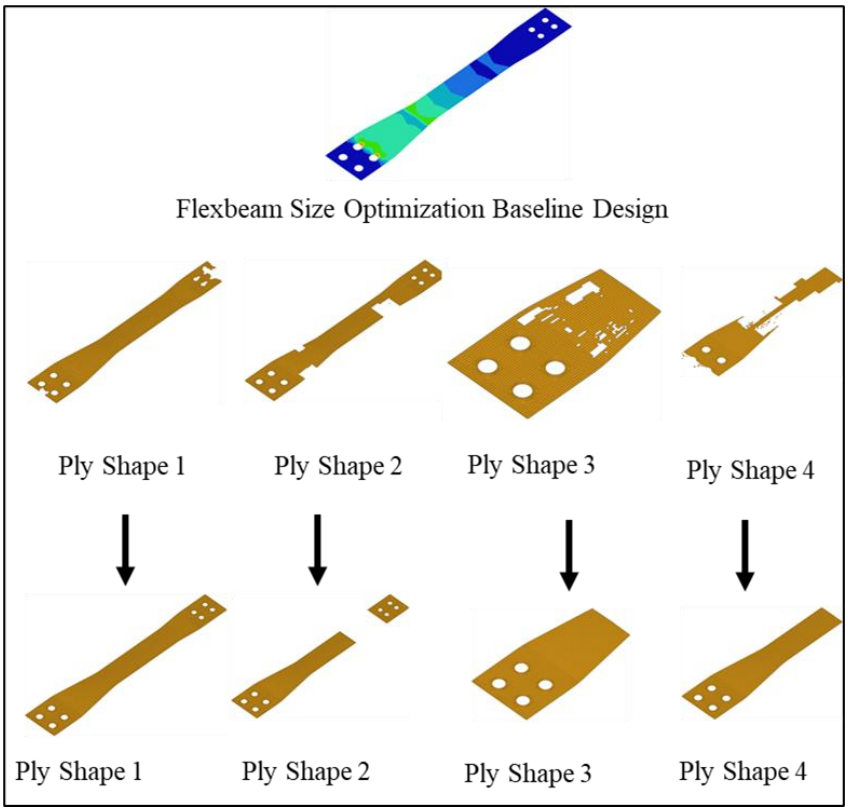

Figure 20. *Edition of flexbeam ply shapes manually.*

The weight of the flexbeam was lowered from 8.474 kg to 4.255 kg in this step, demonstrating that the baseline structure was over-engineered as a laminate. Other important point of discussion is that during the optimization, the structure's compliance hardly changes; it was initially 438160 mm/N and increased to 586160 mm/N. This suggests that the weight of the structure was nearly halved while the stiffness remained in range. After obtaining the all results from free size optimization, this information could be transferred to the sizing optimization. An easy and swift way to perform this is to using FSTOSZ control card. All information from free size optimization could be transferred to the sizing optimization with adding that control card to the output card section. Afterwards, a new analysis window could be opened and the free sizing results solver deck could be directly imported to the new sizing optimization study.

One notable aspect of the free size optimization phase is the discrepancy in the number of plies between the two stages. As explained earlier, the baseline design only had four plies, but after free size optimization, the number of plies increased to 16. The variation results from the solver dividing all the superplies into four subgroups. This segmentation leads to more distinct ply quantities after the sizing optimization process, where the manufacturable ply thicknesses are set. Additionally, the solver incorporates one design variable for each ply, which represents the design space. In summary, there are 16 design variables for 16 plies.

Furthermore, the menu depicted in Figure 21 enables the user to specify the manufacturable ply thickness for each ply. Additionally, the thickness assigned to each ply by the solver is visible in this menu. The menu also allows to show the pre assigned thickness that is coming from free size optimization, basically user able to see the thickness of each superply generated by free size optimization. During this phase, alterations can be made to the design space, ply shapes, ply orientation, and base material. Nonetheless, these parameters are maintained the same as in the free size optimization in this study. Lastly, the manufacturable

ply thickness parameter is set to 0.5 mm for all optimizations that is performed in this study. The industrial ply thicknesses are varying between 0.1 mm to 0.25 mm (there could be exceptions), however, using such thin ply thicknesses in the optimization loop extending the process time, consumes more CPU memory and slows down the procedure. To overcome that issue, a simple approach will be used: 0.5 mm single ply would also mean two times 0.25 mm ply and five times 0.1 mm ply. If any practical reasons could require some changes in the optimizations, this will be handled by using that "multiples" approach.

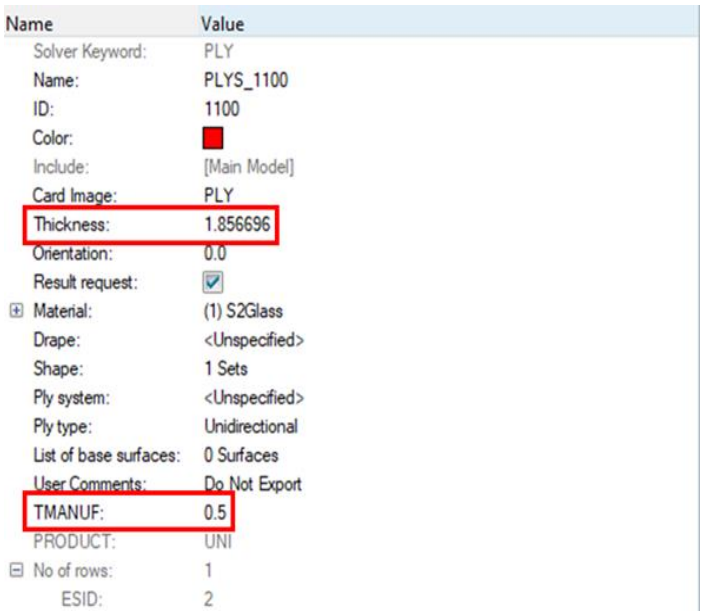

Figure 21. *Manufacturable ply thickness input to the flexbeam size optimization.*

The ply shapes and thickness distribution along the flexbeam can be observed in Figure 22 after all parameters are defined and some plies are modified manually for practicality.

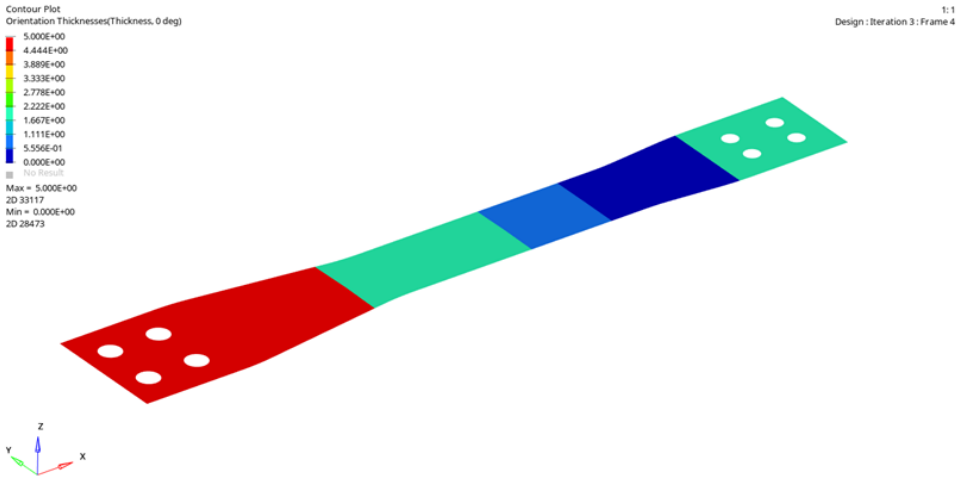

(a) 0° and 90° ply thickness distributions

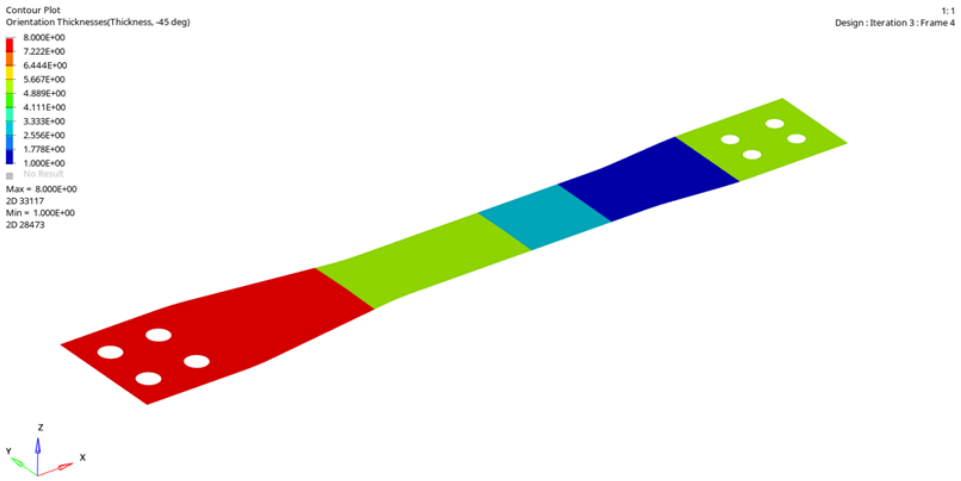

(b) 45° and -45° ply thickness distributions

Figure 22. *Ply thickness distributions after sizing optimization of flexbeam*

The 3D shape of the flexbeam after sizing optimization is depicted in Figure 23. The weight of the structure decreases from 4.255 kg to 3.375 kg in this phase. Furthermore, the compliance increases from 586160 mm/N to 626639 mm/N. The structure experiences a slight softening after the sizing optimization, but this is advantageous in terms of the engineering targets for the flapwise and torsion wise directions. Also, a weight reduction of around 20% is accomplished in this stage, which is highly beneficial for the overall weight of the rotor blade.

As performed during the transition between free-size to sizing optimization, there is one control card that could transfer all the information of results coming from sizing optimization. SZTOSH control card will perform this transfer and the output of the sizing optimization could be imported as a solver deck directly to the new shuffling optimization step.

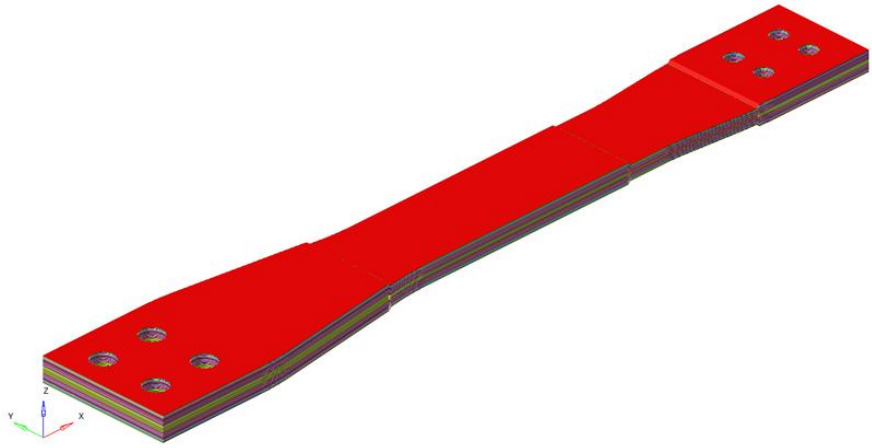

Figure 23. *Output shape of flexbeam after sizing optimization*

The shuffling optimization environment demonstrates that the number of plies has been altered again after importing the size optimization solver deck. The user can manage this parameter by imposing a manufacturing thickness constraint. As shown in Figure 24, the number of plies is changed from 16 to 30. This is an outcome of the solver has applied 0.5 mm manufacturable thickness constrain to all superplies.

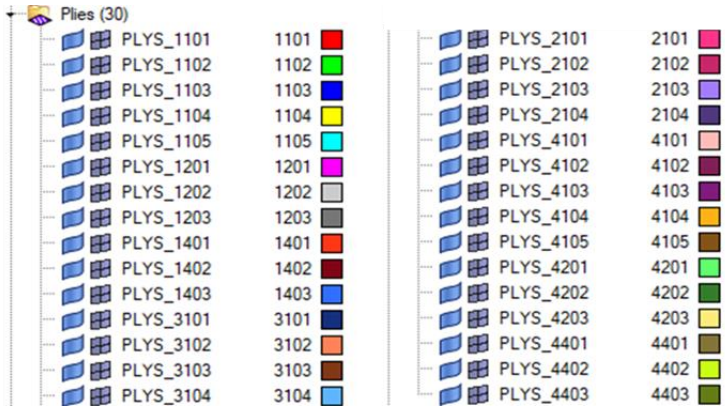

Figure 24. *New ply configuration after sizing optimization.*

This step also includes placing limitations on the maximum successive ply and the pairing of 45° and -45° ply. During this optimization phase, the maximum successive plies for each orientation are restricted to 2. Besides, another parameter is defined for using 45° and -45° plies as the outermost covers since it would enhance the damage tolerance of the structure. The setting of these parameters is demonstrated in Figure 25 and 26

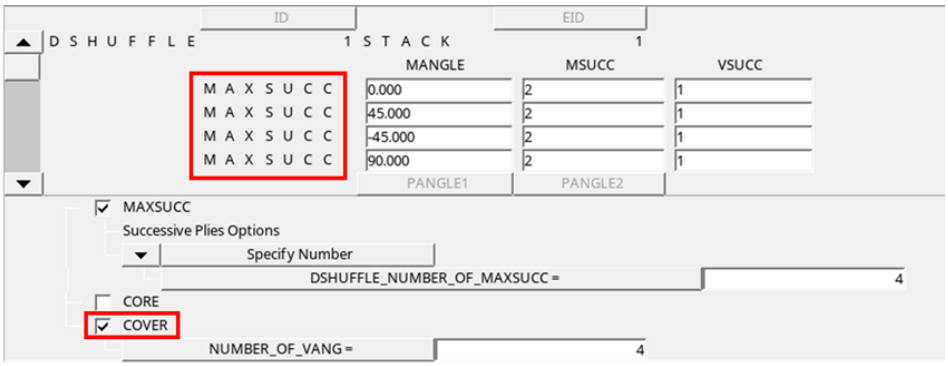

Figure 25. *Setting of maximum successive plies and cover ply for each orientation.*

Figure 26. *Setting of pairing for 45° and -45° plies as design constraint.*

With the shuffling optimization setup complete, the solver can initiate the optimization process that comprises shuffling optimization and non-linear analysis, yielding results as depicted in Figure 27.

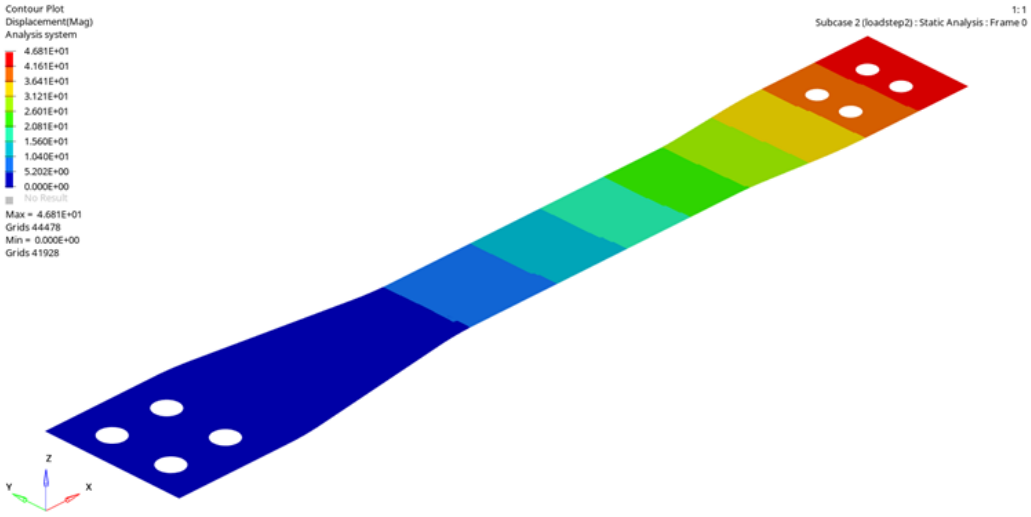

(a) Displacements.

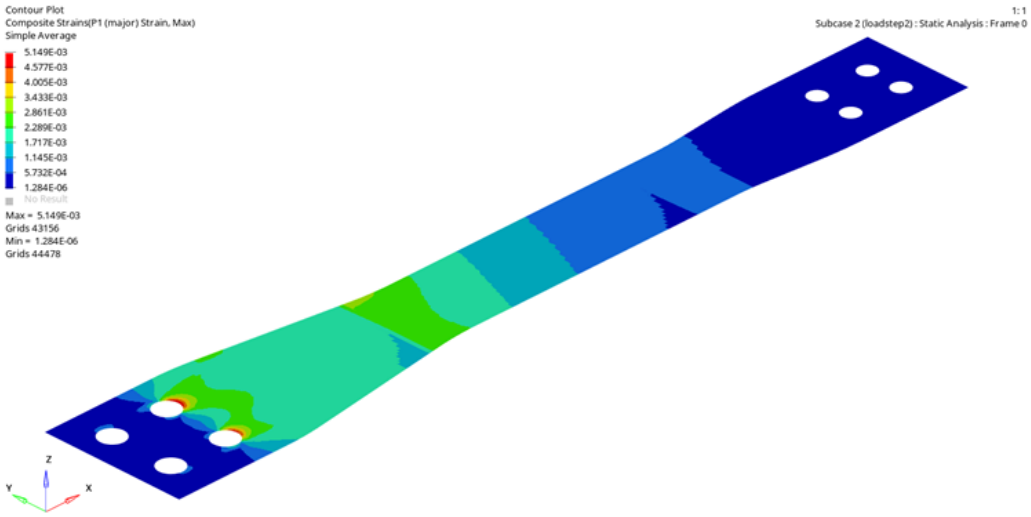

(b) Composite strains.

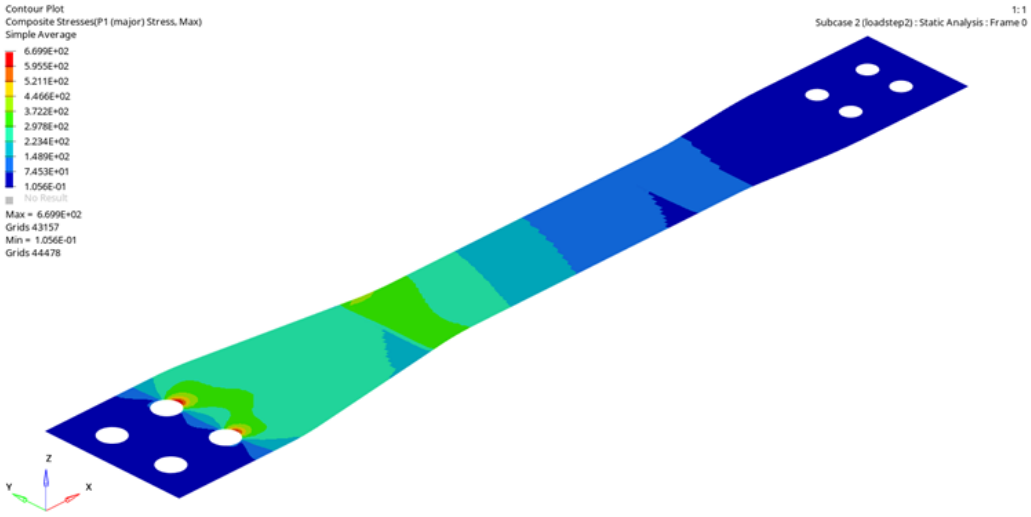

(c) Composite stresses.

Figure 27. *Displacements, composite strains and stresses after shuffling optimization of flexbeam*

Eventually, the mass is reduced from 3.375 kg to 3.36 kg during this step. The compliance has remained almost the same at 645256 mm/N. Thus, the structure has become softer to some extent, but this doesn't significantly impact its behaviour since the difference is negligible. Following all of the optimization steps, the final flexbeam structure is presented in Figures 28 and 29.

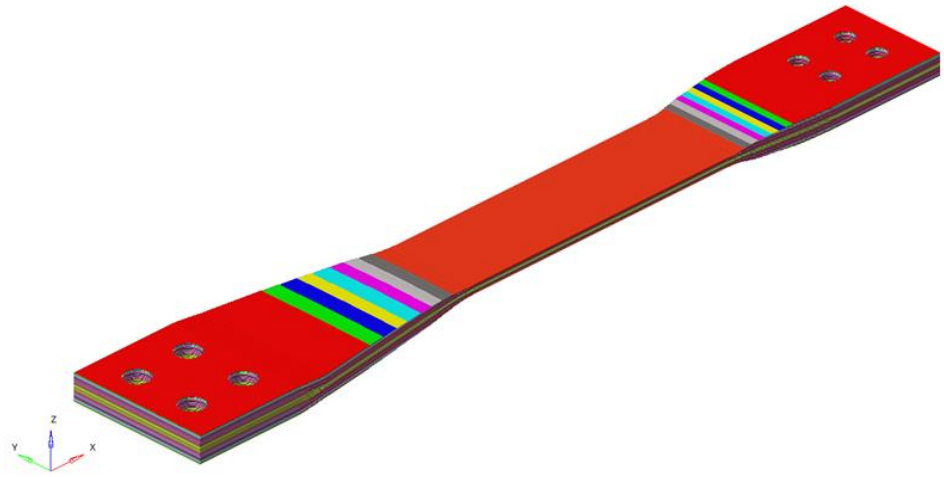

Figure 28. Final flexbeam structure after optimization.

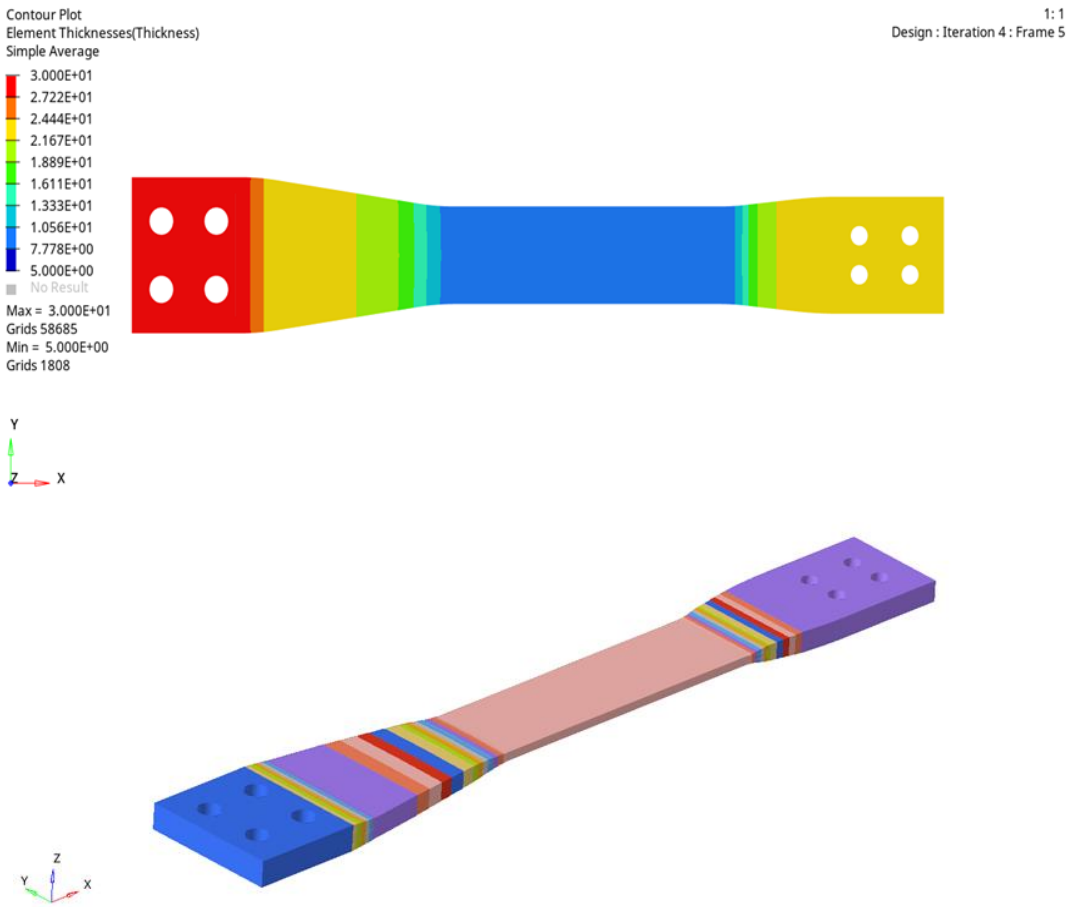

Figure 29. *Thickness distribution of flexbeam after optimization.*

In addition, the drop-off regions play a vital role in preventing any structural failures. It is crucial to verify that the constraints are being applied correctly during each shuffling

optimization step. Figure 30 confirms that the drop-off constraints have been accurately implemented in the spanwise direction.

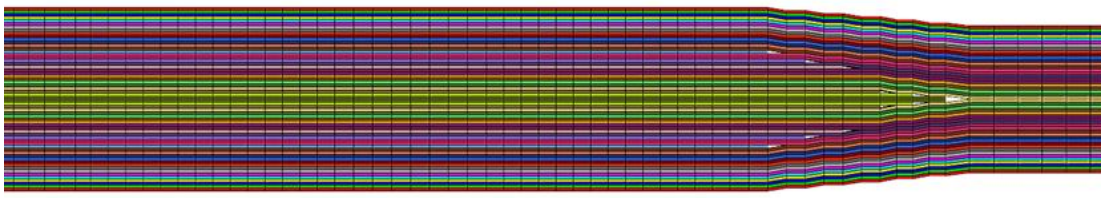

(a) Transition from HAR to ITR-2

(b) Transition from ITR to PR

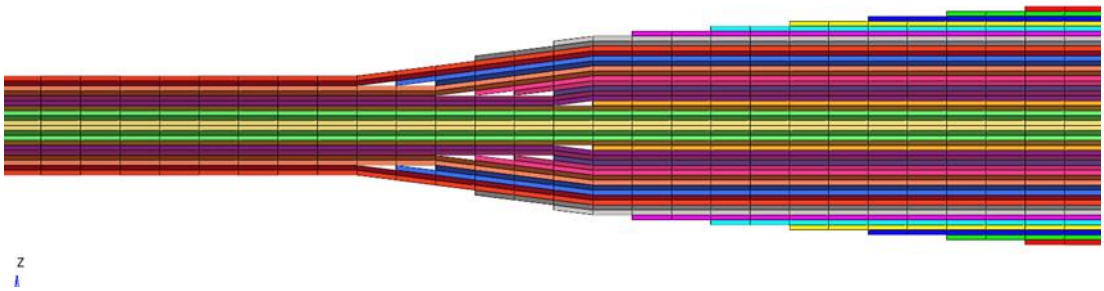

(c) Transition from PR to OTR and BAR

Figure 30. *The transition regions among the flexbeam after shuffling optimization*

As did in flexbeam optimization, similar steps will be followed also in torque tube optimization. The same steps that are followed with flexbeam is not extensively explained in that section in order to prevent any repetition. It is aimed to show the milestones that is specific to the torque tube design.

The torque tube's element and orientation thicknesses are depicted in Figure 31 after the free sizing optimization stage. The figure reveals that the maximum laminate thickness is 15.84 mm, whereas the lowest laminate thickness is 5 mm. The snubber region, particularly in the root area, has a significantly greater thickness than the functional portion of the torque tube, as anticipated. Furthermore, the bolted joint area has an insufficient thickness since it was not specified as a design space parameter for the solver. This decision was made to avoid a significant increase in solving time, and it will be analysed during the size optimization phase.

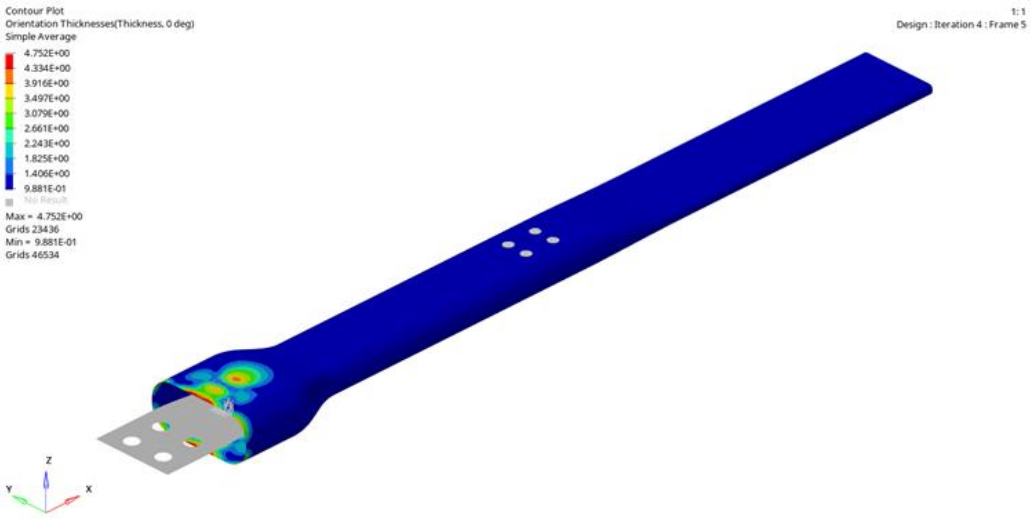

(a) 0° - 90° superply thickness output.

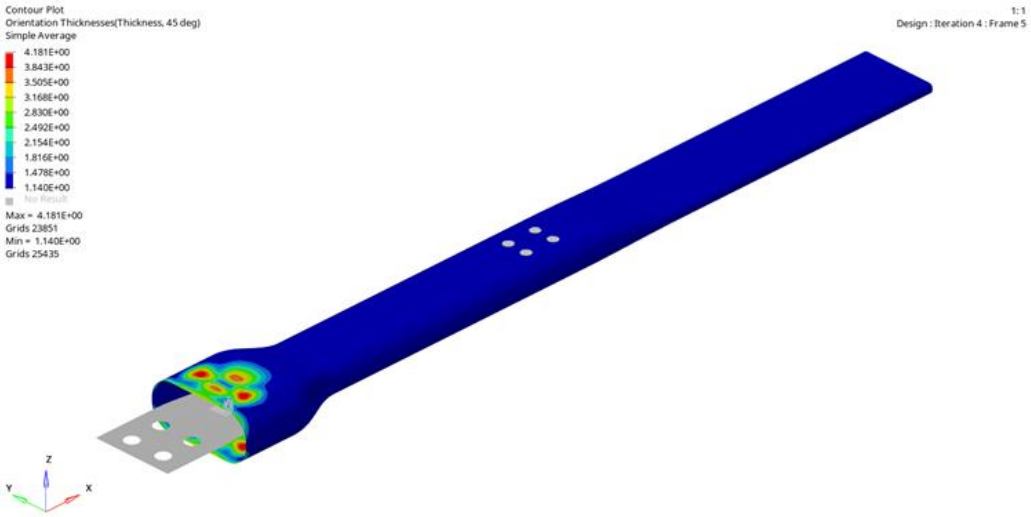

(b) ±45° superply thickness output.

Figure 31. *Torque Tube laminate and ply thickness output from free size optimization*

As indicated in flexbeam section, the number of 0° and 90° plies are equal to each other as well as +45° and -45° plies. After successfully passing the centrifugal load safety check, it was determined that the 45° and -45° plies are more influential than the 0° and 90° plies in improving the torque tube's torsional stiffness. The thickness of the 0° and 90° plies fluctuates between 4.752 mm and 0.988 mm, whereas the thickness of the 45° and -45° plies ranges from 4.181 mm to 1.140 mm. After performing the free size optimization, the overall shape and thickness distribution is shown in Figure 32.

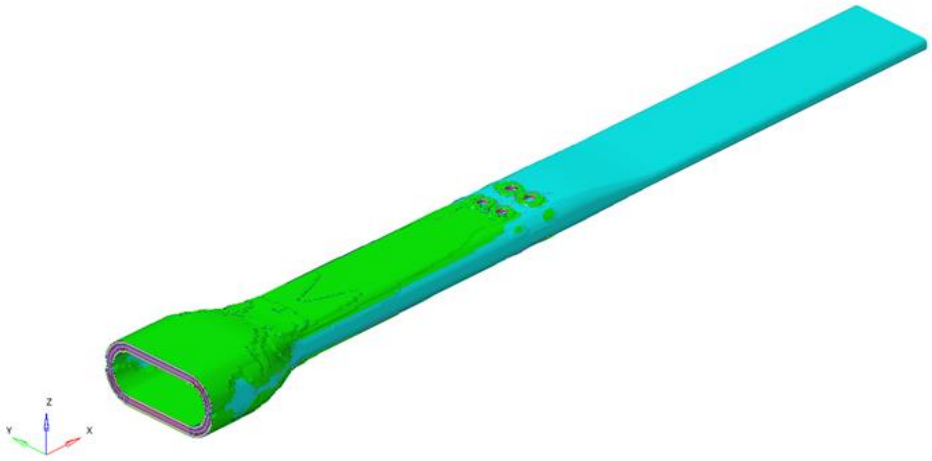

Figure 32. *Output of the free size optimization for torque tube.*

Based on the outcomes of the free size optimization, modifications were made to the shapes of certain plies, similar to the flexbeam optimization. This procedure was implemented for all the plies generated during the free size optimization, and a few of the changes are illustrated in Figure 33.

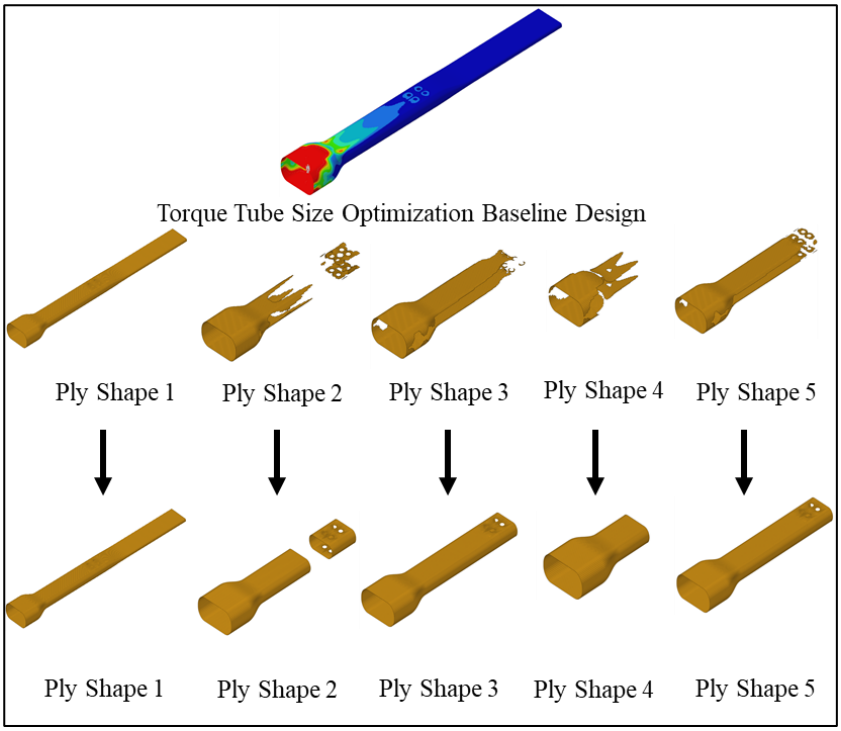

Figure 33. *Edition of torque tube ply shapes manually.*

The weight of the flexbeam was reduced from 17.41 kg to 7.627 kg after the free size optimization. Since a significant amount of material was removed from the structure, the compliance of the torque tube increased from 259634 mm/N to 502905 mm/N. However, even the stiffness of the structure is decreased, it remains still in the safe zone. Moreover, this is also another proof that the baseline design is overdesigned at the beginning, this was also proven with non-linear static analysis for baseline design. As did in flexbeam optimization, the transition between free size and size optimizations is possible with using FSTOSZ output control card. After performing size optimization with using the same design and manufacturing constrains that is used in flexbeam optimization, the results could be seen in Figure 34.

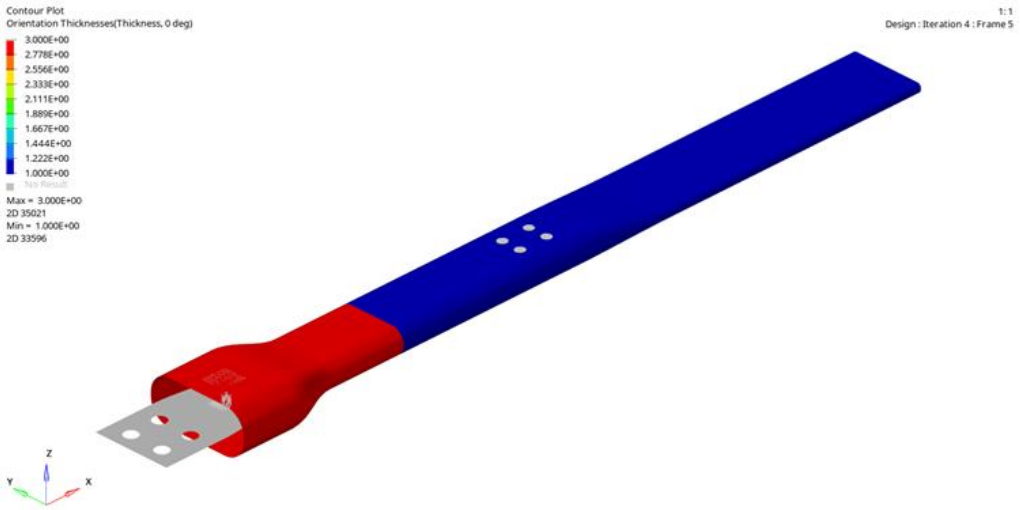

(a) 0° and 90° ply thickness distributions

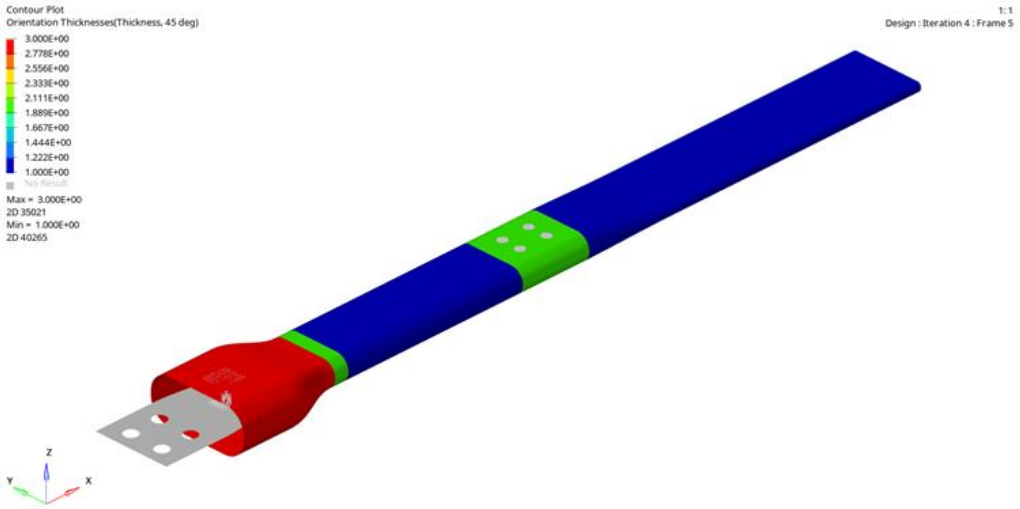

(b) 45° and -45° ply thickness distributions

Figure 34. *Ply thickness distributions after sizing optimization of torque tube.*

The weight of the torque tube decreased from 7.627 kg to 4.719 kg after the sizing optimization. Additionally, there was no significant stiffness alteration in the component, with a previous value of 502905 mm/N and a current value of 545233 mm/N. The final shape of the torque tube after the size optimization can be viewed in Figure 35.

Figure 35. *Output shape of torque tube after sizing optimization.*

The last checkpoint of the optimization process is again shuffling optimization. The shuffling optimization setup commences with the arrangement of successive plies and pairing plies. Once the shuffling optimization is complete, the solver automatically performs a non-linear static analysis of the torque tube, and the constraints are examined to ensure they meet the desired levels. The results of the shuffling optimization can be seen in Figure 36.

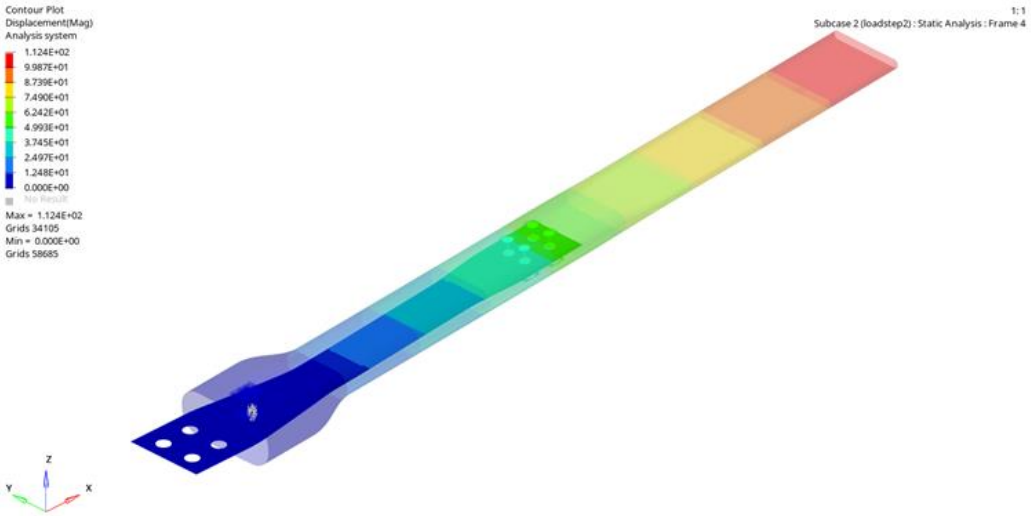

(a) Displacements.

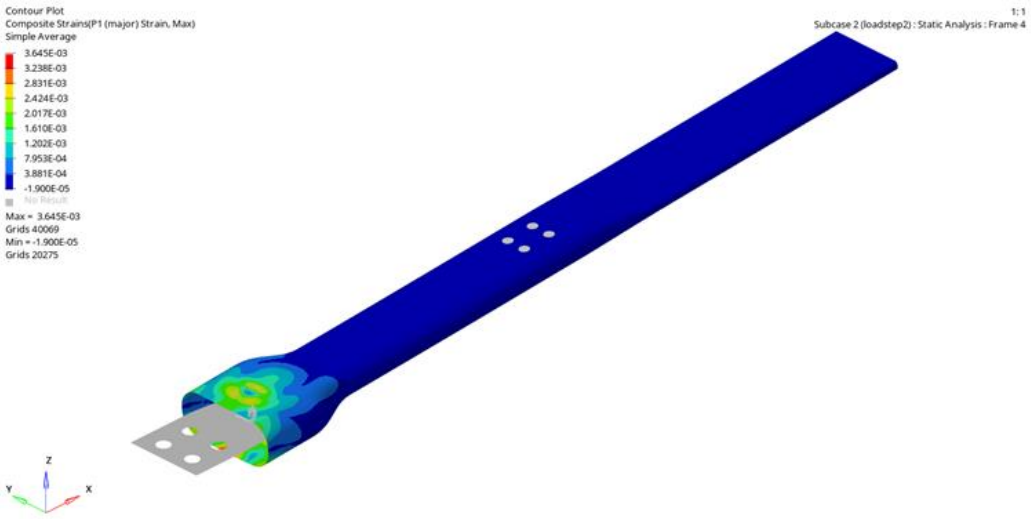

(b) Composite strains.

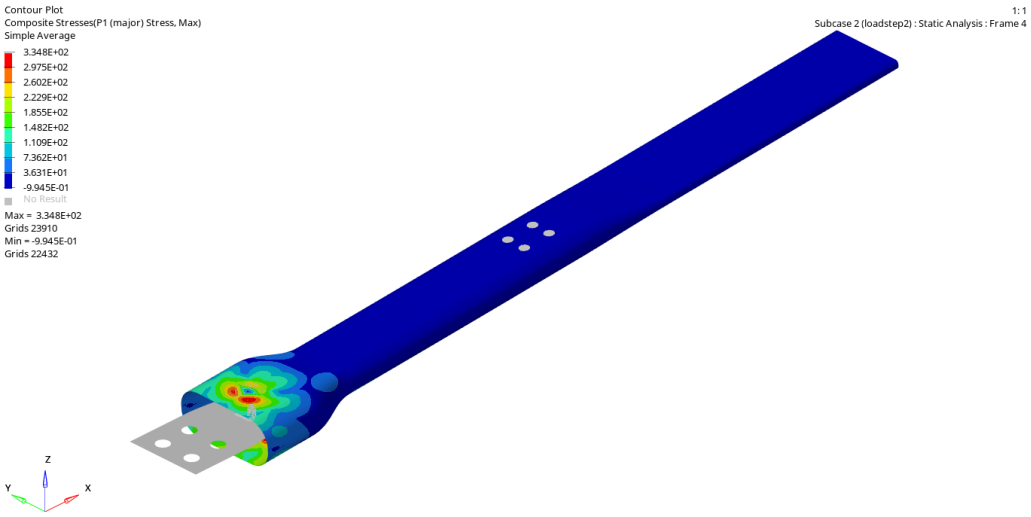

(c) Composite stresses.

Figure 36. *Displacements, composite strains and stresses after shuffling optimization of torque tube.*

The final weight of the torque tube structure is 4.802 kg after completion of the optimization. Although there is a minor weight increase in the structure due to the shuffling optimization constraints, it can be observed that most of the constraints have been satisfied. Additionally, the compliance has decreased from 545233 mm/N to 501270 mm/N. The final ply configuration for the root region, bolted joint region, and functional region are depicted in Figure 37, 38, and 39, respectively.

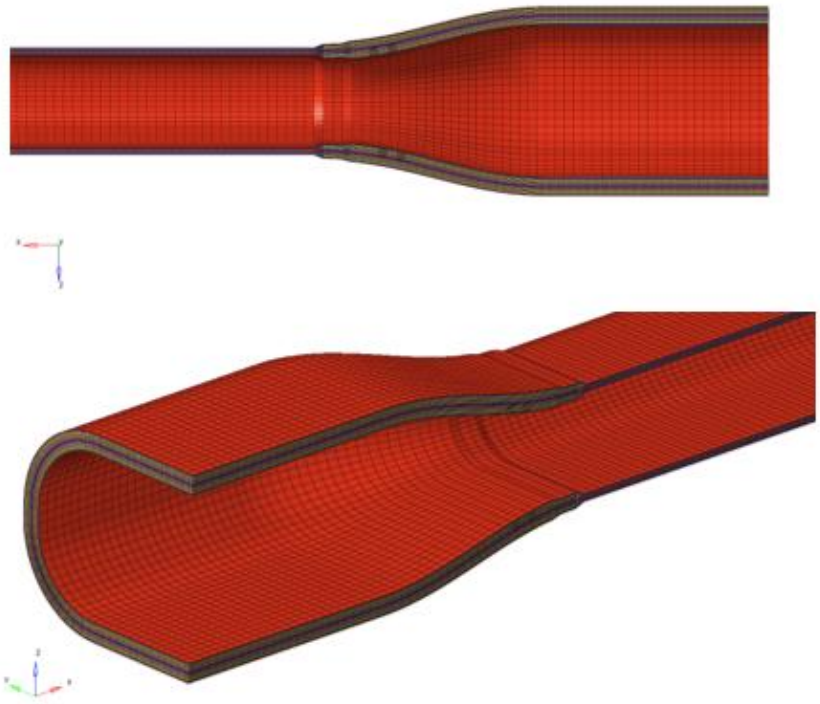

Figure 37. *Root region of optimized torque tube.*

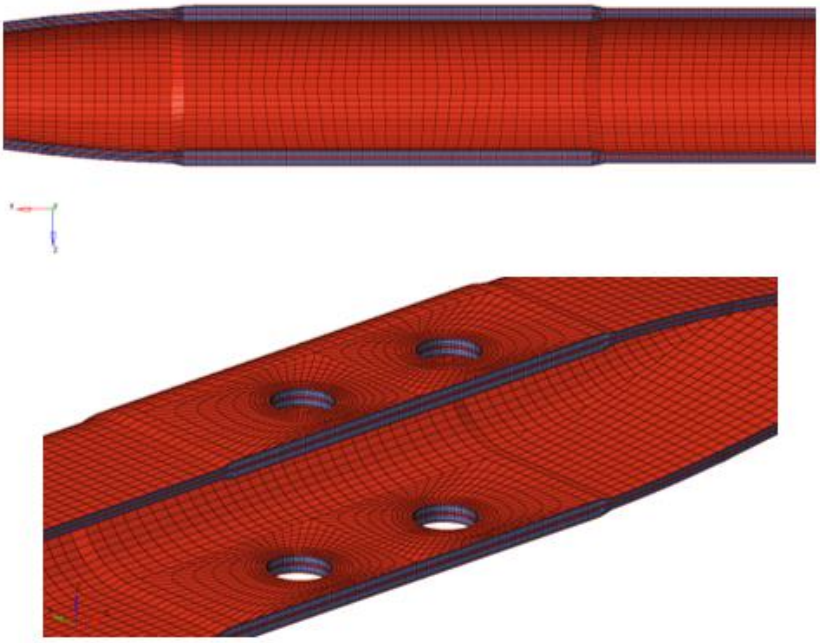

Figure 38. *Bolted joint region of optimized torque tube.*

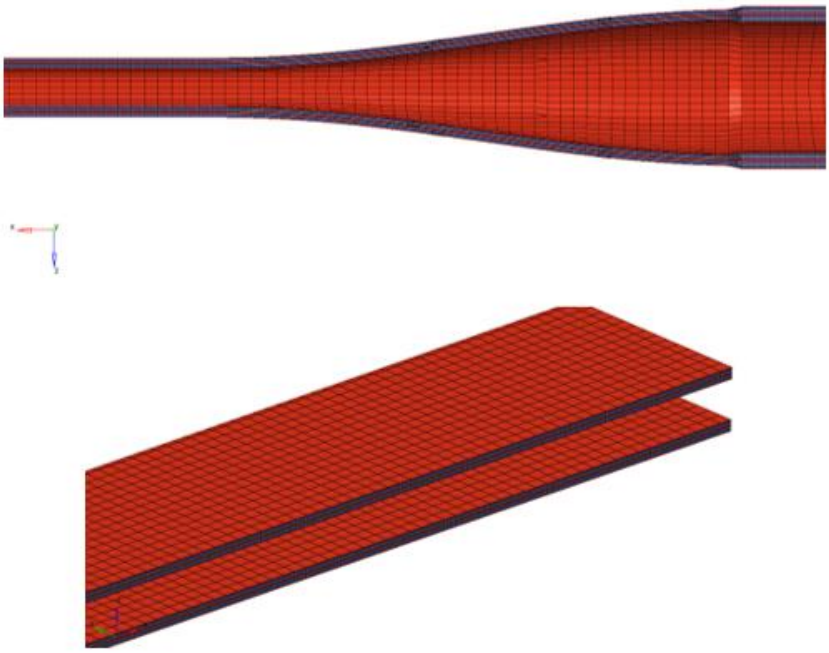

Figure 39. *Functional region of optimized torque tube.*

8. Conclusion

In this study, a comprehensive design and optimization process is performed for a bearingless tail rotor system considering the loads, stability and safety. Briefly, bearingless rotor system eliminates the usage of bearings, hinges and attachment links that are using in conventional articulated rotor systems.

With the optimization process, the overall weight of the entire bearingless rotor system is also reduced within a certain value. Three different optimization steps (free-size, size and shuffling) are performed for two primary structures which is flexbeam and torque tube. Both components are the heaviest components of the entire rotor structure, therefore these two components are targeted to optimize. After optimization, weight reduction of 60.35% for flexbeam and 72.43% for torque tube is achieved. Note that these are the weight reduction percentages compared to the baseline design and final design. The weight reduction comparison could also be performed after the free-size optimization to see efficiency of the further steps. This step is also required since the baseline design is prepared for an overdesign structure and comparing the weight reduction starting from baseline design could not be informative as intended. For flexbeam and torque tube, these values are 18% and 37%, respectively. In overall, including the weight savings from optimization and elimination of bearings, hinges and attachment links, the overall rotor structure becomes 23.08% lighter compared to the conventional articulated rotor systems.

Finally, bearingless rotor system development is closely following the advances on material science since usage of advanced materials allows to develop bearingless system. Therefore, with the developments of material science, the utilization of bearingless rotor systems in helicopters will find an enormous place in the future. Moreover, development of bearingless rotor systems influences also two trending industries; e-VTOL (Electrical Vertical Take-off and Landing) and VTOL (Vertical Take-off and Landing) because of the cost effectiveness and simplicity of the system in terms of design.

References

Bramwell, A. R. S., Done, G., Balmford, D., (2001). *Bramwell's helicopter dynamics*. Butterworth-Heinemann.

Brynes, F.E., D'Anna F.P. (1992). Flexbeam helicopter rotor with improved snubber-vibration damper between the torque tube and the flexible spar member. (Patent No. US005092738A). U.S. Patent and Trademark Office, 1-12.

Brynes, F.E., Federici, F.D., Schmaling, D.N. (1994a). Optimized composite Flexbeam for helicopter tail rotors (Patent No. US005690474A). U.S. Patent and Trademark Office, 1-19.

Brynes, F.E., Schmaling, D.N. (1994b). Spar-to-hub joint for a flexbeam helicopter rotor (Patent No. US005286167A). U.S. Patent and Trademark Office, 1-16.

Cheney Jr., M.C. (1976). Results of preliminary studies of a bearingless helicopter rotor concept. United Aircraft Research Laboratories, Connecticut, USA, 1-11.

Eckert, B. (2007). *Analytical and a numerical ground resonance analysis of a conventionally articulated main rotor helicopter* (Published Master's Thesis). Stellenbosch University, Stellenbosch, South Africa.

Emmerling, S., Kuntze-Fechner, G. The H145 bearingless main rotor – earnings of the H135 heritage. *45th European Rotorcraft Forum,* Warsaw, Poland, 1-13.

Goelke M. (2021). *Introduction to practical aspects of composites with Altair Optistruct*. Altair Engineering, Inc.

Hodges, D. H. (1990). A review of composite rotor blade modeling. *AIAA Journal, 28(3),* 561-565.

Ichihashi, T., Bandoh, S. (1992). Design, fabrication and testing of the composite bearingless rotor system for rotary-wing aircraft. *18th European Rotorcraft Forum,* Avignon, France, 1-14.

Johnson, W. (2013). *Rotorcraft aeromechanics*. Cambridge University Press.

Kim., D., Kim., S. (2014). The overview of KARI bearingless main rotor hub system. Korea Aerospace Research Institute (KARI), Daejeon, Korea, 1-12.

Klöppel, V., Huber, H., Enenkl, B. (1983). Development of bearingless tail rotors. Messerschmitt-Bölkow-Blohm GmbH, Munich, Germany, 1-14.

Mangalgiri, P. D. (1999). Composite materials for aerospace applications. *Bulletin of Materials Science, 22(3),* 657-664.

Narayana, K.S., Pranesh, B., Maiti, N.K. (1998), Dynamic validation of a stiff-in-plane bearingless tail rotor of advanced light helicopter. *24th European Rotorcraft Forum*, Marseilles, France, 1-10.

Xiaocheng, X. (1999). Random response analysis of pre-stressed structures using MSC/NASTRAN. *MSC Aerospace Users' Conference Proceedings*, 1-5.

Investigation of the Effect of Process and Design Parameters on the Mechanical Properties of PETG Materials Produced by Fused Deposition Modeling

Cem GÜDÜR[1]
Türker TÜRKOĞLU[2]
İlker EREN[3]

Additive Manufacturing (Additive Manufacturing) is a method of producing the desired part by adding layers on top of each other (Özer, 2020; Sezer, Eren, & Börklü, 2016). Today, there are many additive manufacturing methods and FDM (Fused Deposition Modelling) Method is one of them (Kaygusuz & Özerinç, 2018; Sezer et al., 2016). FDM 3D printers are the most widely used 3D printers due to their low cost, fast printing and easy accessibility (Evlen, 2019; Kamer, Yaykaşlı, Kaya, & Akay, 2022). It is possible to produce models with complex structures with FDM 3D Printers. FDM Technology is rapidly becoming widespread in many fields such as automotive, aerospace and aviation, biomedical engineering, and architectural structures (Kamer et al., 2022; Kaygusuz & Özerinç, 2018). In the FDM, thermoplastic materials called filaments wrapped around the spool are used. PLA (Polylactic Acid), ABS (Acrylonitrile Butadiene Styrene), PET-G (Polyethylene Terephthalate Glycol), PC (Polycarbonate) materials are used as filaments in FDM Technology. When the market research and literature review is conducted, it is seen that the filament diameters also vary (1.75 mm, 2.85 mm) (Başçı & Yamaoglu, 2021; Evlen, 2019). The filament to be used in the FDM Method is first placed in the extrusion head. Here, the filament, which liquefies with the help of a heater, easily passes through the nozzle and starts to form the first layer. After the filament passes through the nozzle, it cools and solidifies. When the layer is completed, the table part goes down as much as the layer thickness. This process continues until the desired part is formed. After the part is completed, it is separated from the table part and the support parts, if any, are cleaned and the part is finalized (Cano-Vicent et al., 2021).

In this study, PETG materials were successfully produced by FDM method under different design and manufacturing parameters. The effects of lattice structures and production parameters on the tensile test results were analysed. As a result of the findings, it was determined that both lattice designs and manufacturing parameters have a significant effect on mechanical properties.

Material and Method

In this study, samples in accordance with ISO 527 Standard were produced with PETG filament with a diameter of 1.75 mm. The PETG filament used is a filament compatible with FDM (Fused Deposition Modelling) Method. Ender 3 Pro was used as a 3D printer in the production of the samples and all samples were printed on the same printer. Ultimaker Cura

[1] Postgraduate Researcher, Balikesir University, Department of Mechanical Engineering
[2] Assistant Professor, Balikesir University, Department of Mechanical Engineering
[3] Assistant Professor, Balikesir University, Department of Mechanical Engineering

was used as the slicer programme in the production of the samples. Some parameters were kept constant for all samples in Ultimaker Cura Programme. Layer height (0.2 mm), nozzle (0.4 mm), table temperature (70 °C), support Status (Off), cooling fan (On), flow (100%) are the parameters kept constant in the Ultimaker Cura programme and these parameters are shown in Table 1.

After all adjustments were completed in the Ultimaker Cura Slicer Programme, G codes were created in the Ultimaker Cura Programme, transferred to the 3D Printer and printed. The printed samples were subjected to tensile test in ZwickRoell Z250 device. The tensile test was performed at a speed of 5 mm/s. All specimens were processed in the same tensile machine and at the same speed. The tensile machine used and the specimen produced are shown in the Figure 1.

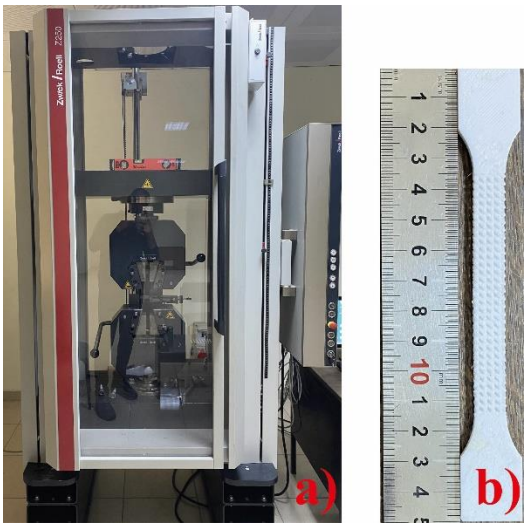

Figure 1. a) Tensile test machine b)Sample

Table 1. Fixed production conditions

Layer Height	0.2 mm
Nozzle	0.4 mm
Table Temperature	70 °C
Support Status	Off
Cooling Fan	On
Flow	100 %

Results and discussion

The sample numbers created for the experimental designs of PETG materials in the study are given in Table 2. Each factor consists of three levels. Lattice designs were differentiated as gyroid, lidinoid and schwarz. The production temperature varies between 230-240-250 °C and the production speed varies between 40-50-60 mm/s. All samples with different design and production parameters produced by the additive manufacturing process were manufactured according to the order specified in Table 2. The parameters selected in the study were found to be effective on the tensile strength determined as output.

***Table 2** Production parameters for PETG material*

Sample No.	Latis Structure	Temperature (°C)	Speed (mm/s)
1	Lidinoid	230	40
2	Schwarz	230	40
3	Lidinoid	250	40
4	Schwarz	250	40
5	Lidinoid	230	60
6	Schwarz	230	60
7	Lidinoid	250	60
8	Schwarz	250	60
9	Lidinoid	240	50
10	Schwarz	240	50
11	Diamond	230	50
12	Diamond	250	50
13	Diamond	240	40
14	Diamond	240	60
15	Diamond	240	50

Figure 2 shows the tensile test results of the specimens produced in the study. Data were collected on a graphical stress-strain scale. As a result of the comparison between the PETG samples produced by FDM, it was determined that the lattice design played a dominant role on the mechanical properties. While maximum tensile strength value was obtained in schwarz lattice design, minimum tensile strength value was determined in diamond lattice design. TPMS structures are diversified through their mathematical formulations and maximum properties can be obtained at optimum input values. Due to their exceptional properties, they have recently been applied in many fields. It is also known that the lattice structures are renowned for their excellent strength-to-weight ratio and capacity for absorbing energy. Inadequate design may result in serious engineering failures like crack growth. It is crucial to identify the ideal parameters before applying lattice structure. The lattice thickness values of the designs selected in the study were determined as 1 mm.

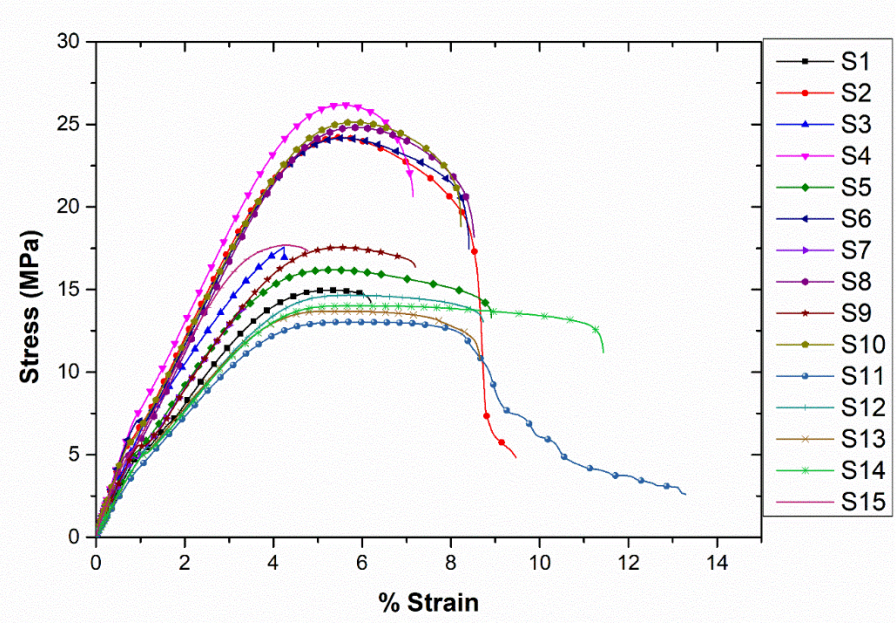

Figure 2 Tensile strength test data

It was determined that lattice design as well as production temperature and production speed were effective on the tensile test results of the specimens produced from PETG material under different design and production parameters

Maximum tensile strength of specimens produced by FDM with schwarz lattice design, 250 °C (S4), which was produced at a production temperature of 240 °C and a production speed of 40 mm/s. In the tensile strength comparison, the second place was taken by specimen S10 (lattice design: schwarz, production temperature: 240 °C, production speed: 40 mm/s), while the third place was obtained from specimen S8 with schwarz lattice design, produced at a production temperature of 250 °C and a production speed of 60 mm/s. It can be seen that the schwarz structure is present in all of the combinations that give the maximum tensile strength.

The minimum tensile strength value obtained in the study was obtained from sample S11 with diamond lattice design, 230 °C production temperature and 50 mm/s production speed. This sample was followed by sample S13 (lattice design: diamond, production temperature: 240 °C, production speed: 40 mm/s) and sample S7 (lattice design: diamond, production temperature: 250 °C, production speed: 60 mm/s). It was found that the lowest tensile strength values of the specimens produced by FDM method were obtained from the specimens produced using diamond lattice design. Higher temperatures are believed to improve layer cohesion and, as a result, increase the mechanical properties of materials. The maximum tensile strength value was obtained at a production temperature of 250 °C. In accordance with the literature, the positive effect of relatively high temperatures on tensile strength was also reported in the study of Pang et al. (Pang, Lai, Ismail, & Yap, 2022).

Conclusions

In this study, PETG materials were successfully produced by FDM method under the specified production parameters. No manufacturing defects were detected in post-production visual inspections. Weight reduction was achieved by applying lattice structures in the sample design. The production parameters with the highest tensile strength were determined as schwarz lattice design, 250 °C production temperature and 40 mm/s production speed. It was reported that the highest tensile strength values were obtained with the Schwarz lattice structure. It was observed that the production temperature was effective on the tensile strength and 250 °C represents the production temperature at which the maximum tensile strength was obtained.

References

Başçı, G., & Yamaoglu, R. (2021). Yeni Nesi Üretim Teknolojisi: FDM ile Eklemeli İmalat. *INTERNATIONAL JOURNAL OF 3D PRINTING TECHNOLOGIES AND DIGITAL INDUSTRY*, 5(2), 339–352. Retrieved from https://doi.org/10.46519/ij3dptdi.838281

Cano-Vicent, A., Tambuwala, M. M., Hassan, S. S., Barh, D., Aljabali, A. A. A., Birkett, M., … Serrano-Aroca, Á. (2021). Fused deposition modelling: Current status, methodology, applications and future prospects. *Additive Manufacturing*, 47(August). Retrieved from https://doi.org/10.1016/j.addma.2021.102378

Evlen, H. (2019). Doluluk Oranının 3B Yazıcıda Üretilen TPU ve TPE Numunelerinin Mekanik Özellikleri Üzerine Etkilerinin İncelenmesi Investigation of the Effect of Infill Rate on Mechanical Properties of TPU and TPE Specimens Produced in 3D Printer. *DEUFMD*, 21(63), 793–804. Retrieved from https://doi.org/10.21205/deufmd.2019216310

Kamer, M. S., Yaykaşlı, H., Kaya, A., & Akay, O. E. (2022). Comparison of mechanical properties of tensile test specimens produced with ABS and PLA material at different printing speeds in 3D printer 3B yazıcıda farklı yazdırma hızlarında ABS ve PLA malzeme ile üretilen çekme test numunelerinin mekanik özellikleri. *Journal of the Faculty of Engineering and Architecture of Gazi University*, 3, 1197–1211. Retrieved from https://doi.org/10.17341/gazimmfd.961981

Kaygusuz, B., & Özerinç, S. (2018). 3 Boyutlu Yazıcı ile Üretilen PLA Bazlı Yapıların Mekanik Özelliklerinin İncelenmesi. *MAKİNA TASARIM VE İMALAT DERGİSİ*, 16(1), 1–6.

Özer, G. (2020). Eklemeli üretim teknoloj ileri üzerine bir derleme. *Nigde Omer Halisdemir University Journal of Engineering Sciences*, 9(1), 606–621. Retrieved from https://doi.org/10.28948/ngumuh.626011

Pang, R., Lai, M. K., Ismail, K. I., & Yap, T. C. (2022). The Effect of Printing Temperature on Bonding Quality and Tensile Properties of Fused Deposition Modelling 3d-Printed Parts. *IOP Conference Series: Materials Science and Engineering*, 1257(1), 012031. Retrieved from https://doi.org/10.1088/1757-899x/1257/1/012031

Sezer, K., Eren, O., & Börklü, R. (2016). Carbon Fiber Reinforced ABS Filament Manufacturing and Investigation of Mechanical Properties and Investigation of Mechanical Properties. In *1. 3B BASKI TEKNOLOJİLERİ ULUSLARARASI SEMPOZYUMU (3B-BTS2016)* (p. 12).

Investigation of Enhancing Energy Absorption in Aerospace Applications through Gradient Lattice Structures

Erkan TUR[1]

Introduction

The significance of energy absorption in aerospace contexts is of utmost importance and cannot be overemphasized. The research focus on the development of materials and structures with superior energy absorption properties has become crucial due to the increasing demands for safety, efficiency, and performance. The present article offers a comprehensive exploration of the augmentation of energy absorption in aerospace contexts through the utilization of gradient lattice structures. Over the course of numerous decades, the aerospace sector has been at the forefront of investigating novel materials and structures in order to satisfy progressively rigorous safety and performance standards. The process of energy absorption holds significant importance in various situations such as crashworthiness and debris impact, as it serves as a crucial protective mechanism. The utilization of materials and structures with efficient energy absorption capabilities can significantly impact the outcome of a situation, potentially preventing catastrophic failure and enabling controlled damage mitigation. affecting not only structural integrity but also passenger safety and survivability (Suresh, 2001). The present materials utilized in aerospace applications, for instance, aluminum and carbon-fiber composites, have conferred considerable enhancements in performance, however, their capacity to absorb energy is restricted. In order to address these constraints and achieve improved energy absorption, the industrial sector has initiated an investigation into novel categories of material configurations. Among these, gradient lattice structures have exhibited significant promise. Functionally graded lattice structures, commonly referred to as gradient lattice structures, exhibit micro-architectures that vary spatially, resulting in mechanical properties that are superior to those of uniform lattice structures. These objects are designed with a continuous variation in both structural and material properties, which facilitates a more effective distribution of stress, resulting in heightened energy absorption. The efficacy of gradient lattice structures is derived from their distinctive characteristic of customizing material dispersion within the structure, thereby enabling them to efficiently regulate energy absorption. The aforementioned characteristic renders them exceedingly appropriate for aerospace applications wherein weight efficiency is of utmost importance, and energy absorption prerequisites can exhibit substantial variations throughout the structure (Rahman et. al., 2021).

This study aims to delve deeper into the aforementioned potential. The objective of our investigation is to establish a thorough comprehension of the techniques employed to manipulate and optimize the characteristics of gradient lattice structures in order to achieve maximum energy absorption in aerospace contexts. The objective of our study is not solely to establish the efficacy of gradient lattice structures, but also to furnish pragmatic recommendations for their design and implementation in the aerospace sector. The study conducted by Xu and colleagues in 2022. The present study employs a combination of theoretical and experimental approaches, complemented by sophisticated computational simulations, to enhance our comprehension of the energy absorption potential of gradient lattice structures. This study explores the material science aspects of these structures, including their

[1] Erkan Tur, Middle East Technical University, Department of Natural and Applied Sciences, Orcid: 0000-0002-3764-2184

mechanical properties, and evaluates the influence of various design parameters on their energy absorption capacity. The research endeavors to offer a novel viewpoint on the augmentation of energy absorption in aerospace contexts. Through the utilization of gradient lattice structures, we anticipate a forthcoming era in which aerospace structures can endure severe circumstances and collisions with improved durability and security. The present article commences by providing an overview of the existing knowledge regarding energy absorption in aerospace contexts, as well as the constraints of current materials and structures. Subsequently, a comprehensive exposition of gradient lattice structures is presented, encompassing their distinctive characteristics and elucidating their potential as a viable option for augmenting energy absorption. Subsequently, we explicate the methodology employed in our inquiry, succeeded by the exposition and discourse of our discoveries. Ultimately, our study culminates in the presentation of our findings and subsequent recommendations for potential avenues of inquiry. The escalating requirements for aerospace performance and safety have intensified the necessity for structures that possess exceptional energy absorption properties. The study of gradient lattice structures presents a viable solution for addressing this requirement, with the potential to transform the landscape of aerospace design and engineering. We extend an invitation to participate in our endeavor to investigate and discover resolutions that surpass the existing limitations in aerospace implementations.

Methodology

The present investigation utilized a comprehensive computational approach, employing the ABAQUS Finite Element Analysis (FEA) software, to examine the energy absorption capacity of gradient lattice structures in the context of aerospace applications. The investigation of the distinctive characteristics of said structures and their influence on energy absorption was conducted via meticulous computational modeling, facilitating the attainment of a comprehensive comprehension of their performance across diverse scenarios (Xiao and Song, 2018).

Uniform Lattice Structures:

Homogeneous lattice structures, commonly referred to as uniform lattice structures, are composed of a recurring pattern of a solitary unit cell throughout the entirety of the structure. The structures exhibit uniform characteristics across their entirety, indicating that each unit cell within the structure possesses identical material properties and geometry. The entities in question may exhibit either a two-dimensional or three-dimensional nature, and their geometric arrangement may manifest in a diverse array of forms, such as cubic, tetrahedral, and octahedral, among other possibilities. The utilization of these structures has been extensive across diverse applications owing to their lightweight properties and their capacity to endure various forms of loading. Hollow structures are highly desirable in weight-sensitive fields like aerospace due to their superior stiffness-to-weight and strength-to-weight ratios when compared to solid structures. Uniform lattice structures exhibit certain limitations with respect to their energy absorption capabilities, particularly when subjected to non-uniform stress distributions or high-impact scenarios. (Seharing et. al., 2020).

Gradient Lattice Structures:

Functionally graded lattice structures, commonly referred to as gradient lattice structures, exhibit distinct characteristics from uniform lattice structures due to their spatially varying properties throughout the structure. It is possible to regulate the diversity of characteristics to conform to a specific gradient profile, such as linear, exponential, or sinusoidal. This regulation may encompass modifications in the geometry of the unit cells, the material properties, or both.

The implementation of functional grading in properties enables gradient lattice structures to exhibit superior stress distribution management capabilities in comparison to their uniform lattice structure counterparts. Structures can be engineered to effectively manage stress distribution by strategically directing it towards regions with greater strength or away from critical areas. This approach can result in superior structural performance and increased capacity for energy absorption. The ability to customize the distribution of materials within the structure enables gradient lattice structures to effectively conform to particular loading circumstances. Moreover, the utilization of functional grading renders gradient lattice structures highly advantageous for aerospace applications, wherein the energy absorption prerequisites can exhibit substantial variations across the structure. Efficient energy absorption and dissipation are essential in various applications, especially in situations that involve crashworthiness and debris impact. The complexity of designing and manufacturing gradient lattice structures is comparatively higher than that of uniform lattice structures, owing to the presence of spatially varying properties (Bai et. al., 2020)

To summarize, although uniform and gradient lattice structures possess their respective merits, gradient lattice structures exhibit superior capabilities in managing stress distribution and energy absorption, rendering them highly promising for advanced applications such as aerospace.

Modeling and Simulation of Gradient Lattice Structures:

The first step in our methodology involved creating detailed 3D models of the gradient lattice structures using ABAQUS/CAE. (Alaña et. al., 2021) Our models incorporated functionally graded micro-architectures, allowing for continuous variation in structural and material properties. As the lattice design, FCC was considered as unit cell. The lattice structures were designed with different gradient profiles, such as linear, exponential, and sinusoidal, varying in properties like density and modulus (Al-Qrimli et. al., 2015).

Figure 1 – FCC Unit Cell

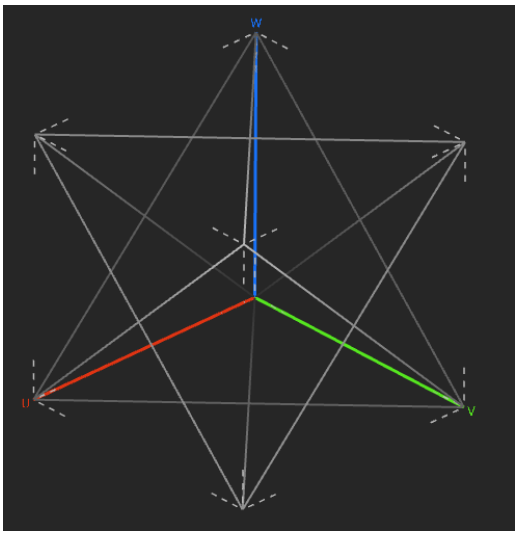

Table 1 – Strut size and cell sizes

Cubic Unit Cell Size, μm	Strut Dimensions			
	Diameter	Strut Angles	Strut Length	Strut Design
24.8 x 24.8 x 24.8	5 μm	45^o	17.54 μm	FCC

Figure 2 – All Direct and All Principal Conditions

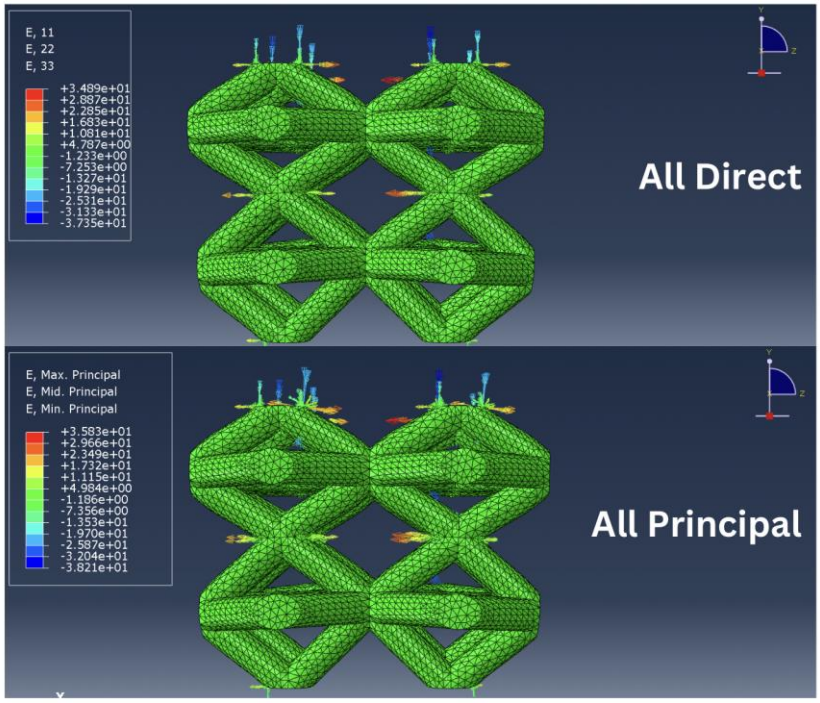

Material properties for the models were defined based on the aerospace-grade materials used in the industry. We made use of user-defined material subroutines in ABAQUS (UMAT and VUMAT) for defining the functionally graded material properties (Alwattar et. al., 2019).

Zable 2 – Materials Properties

Material	Plastic Properties		Elastic Properties	
	Young's Modulus E (GPa)	Tensile Yield Strength (MPa)	Poisson Ratio, v	Plastic Strain, ε_p
ABS	0.862	33.33	0.35	0.045

Load Application and Boundary Conditions:

In order to replicate real-life aerospace scenarios, our models were exposed to diverse loading and boundary conditions, with a particular emphasis on compressive forces. The load application was developed with the purpose of emulating various scenarios that a structure could potentially face in an aerospace environment, including but not limited to, collision, debris impact, and high-velocity projectile impact. The aforementioned procedure facilitated the evaluation of the energy absorption properties of the lattice structures across a wide range of circumstances.

Analysis Type:

The FEA simulations were run using static structural (ABAQUS/Standard) solvers, depending upon the nature of loading conditions. The static analysis provided insights into the deformation and stress distribution under slow, quasi-static loadings.

Energy Absorption Calculation:

The energy absorption of the lattice structures was calculated by integrating the area under the stress-strain curve obtained from the simulation results. We made use of ABAQUS' capability to track the energy quantities (like internal, kinetic, and strain energy) throughout the simulation. This facilitated the calculation of energy absorption and understanding the energy distribution within the lattice structure. In SI unit system, total energy absorption (tea), is calculated in kilojoules, Specific energy absorption has the unit kJ/kg and volumetric energy absorption unit is kg/m^3 (Al-Qrimli et. al., 2015).

Table 3 – Energy Absorption Equations

Total Energy Absorption	Specific Energy Absorption	Volumetric Energy Absorption
$tea = \int P_{av} \equiv P_{av} * (d_f - d_i)$	$sea = \frac{tea}{mass}$	$vea = \frac{tea}{volume}$

Parameter Study:

In addition, our research encompassed a comprehensive examination of parameters. The study involved the manipulation of crucial design parameters, including the unit cell configuration, gradient distribution, strut width, and material characteristics. This study facilitated comprehension of the impact of said parameters on the energy absorption capacities of gradient lattice structures. Through the utilization of ABAQUS software, our research conducted a thorough and meticulous evaluation of the viability of gradient lattice structures in augmenting energy absorption within the realm of aerospace. The utilization of numerical simulations has facilitated the resolution of fabrication and testing constraints, thereby providing an opportunity to assess the efficacy of complex gradient lattice structures that would have been arduous to produce or experimentally examine.

Results and Discussion

The study employed a thorough methodology that utilized the ABAQUS Finite Element Analysis software to investigate the energy absorption capacity of gradient lattice structures in the context of aerospace applications. The findings of the study were enlightening. The simulation outcomes obtained from ABAQUS demonstrated significant dissimilarities in energy dissipation capabilities between gradient lattice configurations and their uniform equivalents. The energy absorption capabilities of gradient lattice structures were found to be consistently superior under different loading and boundary conditions.

The stress distribution in gradient lattice structures was found to be more homogeneous than that in uniform lattice structures under quasi-static loading. Consequently, there was an increase in energy dissipation effectiveness and improved deformation control, leading to a corresponding enhancement in energy absorption. The simulations conducted indicated that lattice structures with gradients exhibited enhanced energy absorption capabilities. The deformation modes exhibited by the object were distinct and capable of efficiently absorbing compressive energy, indicating potential for averting disastrous outcomes in the event of such scenarios, particularly under varying flight loads. The investigation of parameters revealed the impact of the configuration of the unit cell, the gradient profile, and the thickness of the strut on the capacity for energy absorption. The utilization of an exponential gradient profile in the design of the face centered cubic unit cell resulted in the highest level of energy absorption

when compared to the uniform FCC model variants that were subjected to testing. The aforementioned results hold significant value in the context of developing and enhancing gradient lattice configurations intended for employment in the aerospace sector.

Figure 3 – Stress Strain Graphs for Simulation Results

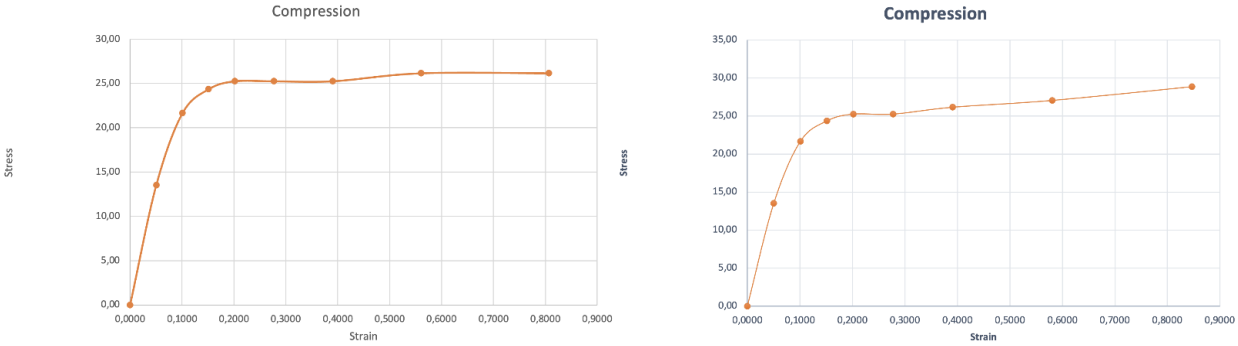

Figure 4 – AC Yield Results

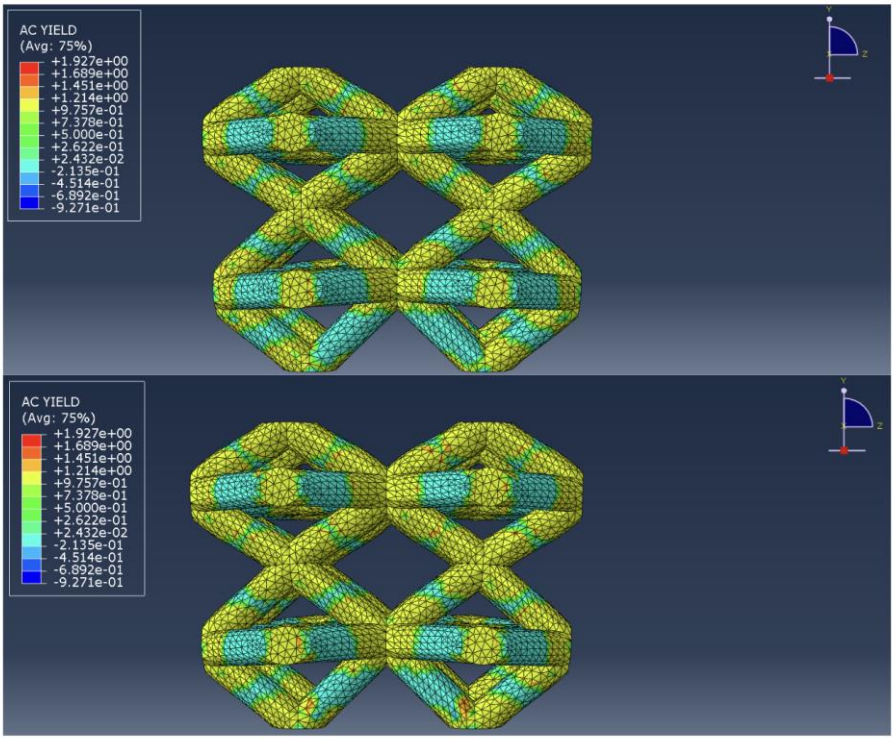

Figure 5 – Results for Tresca Criterion (Stress)

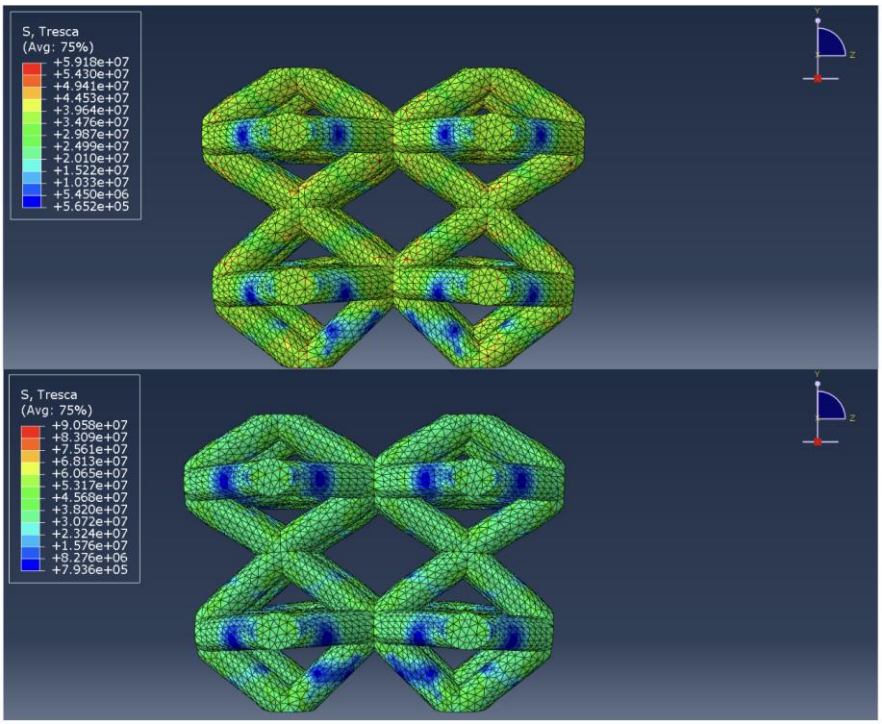

Figure 6 – Results for von Mises (Stress)

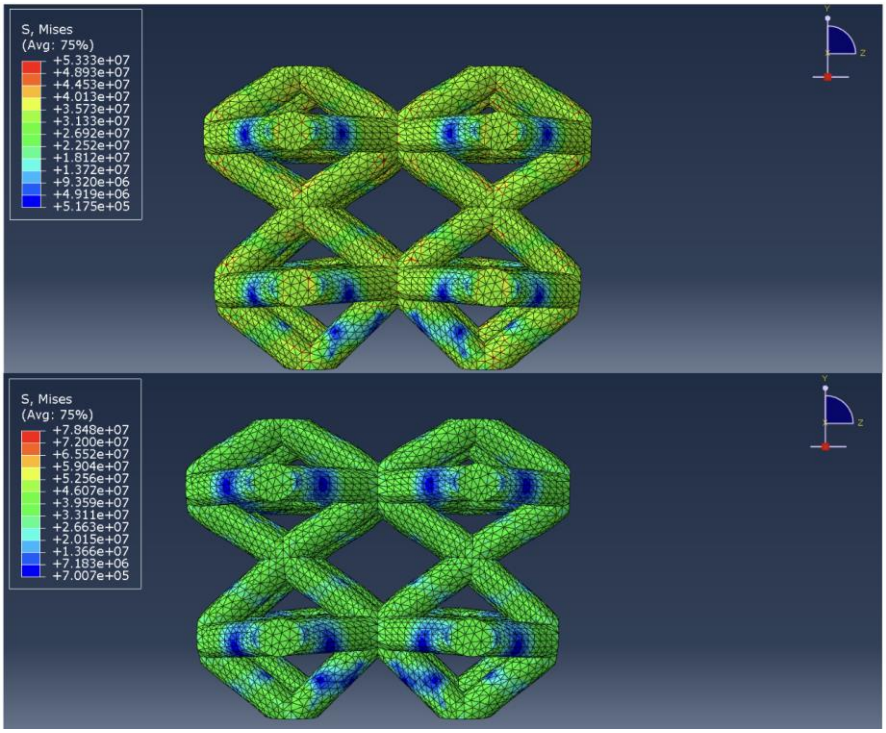

Figure 7 – Results of Resultant Displacement, by Magnitude

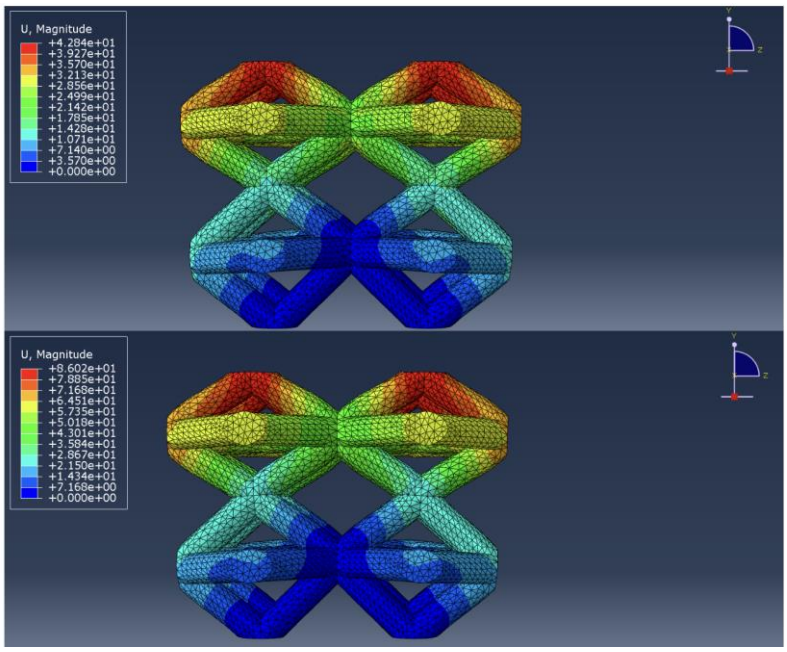

The study employed a thorough methodology that utilized the ABAQUS Finite Element Analysis software to investigate the energy absorption capacity of gradient lattice structures in the field of aerospace. The findings were enlightening. The simulation outcomes obtained from ABAQUS demonstrated significant dissimilarities in energy absorption between gradient lattice structures and their uniform equivalents. The energy absorption capabilities of gradient lattice structures were found to be consistently superior under different loading and boundary conditions.

The enhanced capacity of gradient lattice structures to absorb energy can be ascribed to their micro-architecture that is functionally graded. This distinctive characteristic facilitates a heightened efficacy in the dispersion of stress, resulting in proficient dissipation of energy and improved management of deformation. In addition, the capacity of materials to absorb energy can be enhanced by tailoring the distribution of material within their structure. This provides them with a competitive advantage over uniform lattice structures. The simulations conducted on high-speed impacts were highly informative, demonstrating the efficacy of gradient lattice structures in efficiently absorbing impact energy. This attribute holds significant importance in the aerospace industry. The capacity of these structures to withstand extreme loading conditions highlights their potential to augment safety protocols in aerospace contexts. The conducted parameter study yielded significant findings regarding the optimization of energy absorption through the manipulation of design parameters. The aforementioned results can be utilized to direct the formation and enhancement of gradient lattice configurations in the context of aerospace implementations, thereby facilitating the creation of aerospace structures that are both more secure and more effective.

In brief, the outcomes of our study furnish convincing proof endorsing the utilization of gradient lattice configurations in aerospace sectors to augment energy absorption. The study highlights the superior energy absorption capabilities of gradient lattice structures compared to conventional uniform lattice structures, thereby advocating for their integration into forthcoming aerospace design and manufacturing methodologies. Nevertheless, additional investigation is required to thoroughly examine their capabilities and to establish feasible techniques for their integration in practical aerospace scenarios.

REFERENCES

Al-Qrimli, H. F. A., Khalid, K. S., & Mahdi, F. A. (2015). The effect of cone angle on composite tubes subjected to axial loading. British Journal of Applied Science and Technology, 7(4), 351-363.

Alaña, M., Cutolo, A., Ruiz de Galarreta, S., & Van Hooreweder, B. (2021). Influence of relative density on quasi-static and fatigue failure of lattice structures in Ti6Al4V produced by laser powder bed fusion. Scientific Reports, 11(1), 19314.

Alwattar, T. A., & Mian, A. (2019). Development of an elastic material model for BCC lattice cell structures using finite element analysis and neural networks approaches. Journal of composites science, 3(2), 33.

Bai, L., Gong, C., Chen, X., Sun, Y., Xin, L., Pu, H., ... & Luo, J. (2020). Mechanical properties and energy absorption capabilities of functionally graded lattice structures: Experiments and simulations. International Journal of Mechanical Sciences, 182, 105735.

Rahman, H., Yarali, E., Zolfagharian, A., Serjouei, A., & Bodaghi, M. (2021). Energy absorption and mechanical performance of functionally graded soft–hard lattice structures. Materials, 14(6), 1366.

Seharing, A., Azman, A. H., & Abdullah, S. (2020). A review on integration of lightweight gradient lattice structures in additive manufacturing parts. Advances in Mechanical Engineering, 12(6), 1687814020916951.

Suresh, S. (2001). Graded Materials for Resistance to Contact Deformation and Damage. Science, 292(5526), 2447-2451.

Xiao, L., & Song, W. (2018). Additively-manufactured functionally graded Ti-6Al-4V lattice structures with high strength under static and dynamic loading: Experiments. International Journal of Impact Engineering, 111, 255-272.

Xu, Z., Razavi, S. M. J., & Ayatollahi, M. R. (2022). 00019 Functionally Graded Lattice Structures: Fabrication Methods, Mechanical Properties, Failure Mechanisms and Applications. International Journal of Impact Engineering, 125, 163-172.

Underground Spaces: Ownership and Responsibility Dilemma

Mehmet Kemal Gokay[1]

1. Introduction

In societies which have common agricultural and urbanisation activities over earth crust have come rarely across problems related with man-made underground activities other than the natural ones. Earthquakes, landslides, sudden sinkhole formations, ground compactions, ground displacements, climate related disasters like floods, frost, hurricane are usually main concerns for their land related insurances. Landowners in the world have experiences of negative influences (disasters) due to; natural rock cliff failures (rock falls, rock slope failures); soil slope avalanches (landslides); subsidence due to underground mining operations and civil purpose tunnelling; ground displacement due to surface/underground space excavations; cave, metro tunnels & underground space collapses; failures/subsidence due to oil and natural gas extractions through underground rock porosities. New approaches in the energy sector which are related to Carbon-Zero policies have re-introduced exploration of geothermal resources. Decreasing energy requirements in modern urban life have also been supplied through subways and underground settlements (car parks, shopping centres, pedestrian passageways, hotels, living spaces, depots, shelters, machine rooms, etc.). Thus, the earth crust supplying resources for human civilisation through mining activities has re-evaluated for its underground micro/macro spaces (natural/manmade) to obtain efficient opportunities.

Underground spaces have been in use in different human requirements in different design opportunities. New opportunities on the other hand push underground spaces gradually into modern urban life style. Subway (metro) lines and stations are currently used in many crowded cities by millions of people. In addition, re-discovering subterranean urban living options as marketable (sometimes unavoidable) options, yet again, is an important step in the urbanisation history. Usage of caves, excavation of ancient underground cities (like Derinkuyu, Kaymakli in Turkey), actually have supplied valuable information for engineers (rock, civil, mining, geomechanical) and architectures for their design & stability features. That early ancient urban life, together with their living conditions and regulations related with underground and surface urban structures had steadily been explored by archaeologists. Modern urban cities have diverse city-plans which have been improved by using earlier experiences gained through man-made structures in/on earth crust. Government bodies in countries have reputations to document man-used lands and structures for taxations (& responsibilities) through history. These land ownerships defined and written with boundaries through history are totally two dimensional, 2D, but covers sky and sub ground of that lands as well, (i.e.; “Latin Maxim” approach).

Earth surfaces in urban areas have progressively mapped, documented and registered (legal ownership paper) to citizens in some countries. There are also countries whose citizens

[1] Mehmet Kemal Gokay, Prof.Dr., Konya Technical University, Mining Engineering Department.

do not have land ownership rights as well. Increasing use of underground spaces have introduced new conditions for land ownership procedures. Because this should require introducing three dimensional, 3D, ownership procedures. Some countries have described their ownership procedures (legislations, rules, acts, etc.) for subterranean and sky layers, below/over surface lands. However, due to economic and social issues, earth crust related economic resources (minerals, oils, natural gasses and thermal energy) in/on earth crust have mostly been regulated in all countries for their legal meticulous extractions. Land ownership descriptions for underground spaces differ from these legal earth resource extraction rights and they are only related to subterranean space usage for urbanisation requirements. Most countries which have detailed surface land ownership descriptions (land-rights) and earth resources descriptions & rights (mining, oil, natural gases, and geothermal laws and rights) do not currently have descriptive ownership rules for subterranean spaces. Thus, metro lines, stations, caves, underground depots etc. have tried to be regulated with existing laws & regulation systematized lands and earth resources rights. The dilemmas among these right owners have increasingly become more complex after attempts to define subterranean space ownership rights.

2. Surface land ownership and underground space (land) registrations

Ownership of goods and properties in human history has developed gradually up to modern times. In early times, prehistoric hunters might have their own hunting tools. Early communities might have then organised to cover their hunting localities. When agricultural activities had gradually started and the population was forced to share available suitable agricultural fields, ownership phenomena might have started to be considered on land and irrigation water sources. Human societies have then organised and provided rules for the use of agricultural land according to their cultural and governing traditions. Human history has different social governing activities on ownership of land and life-stokes. When human societies have provided government bodies to organise their activities to live together, they might have explored some kind of taxation procedures as well. Land ownerships have especially main concerns for central and local governments to secure some of their food supply and tax incomes. Therefore, rules controlling land ownerships and related taxation of land & foods, (provided through those lands), might have been the main source of incomes of early national government bodies. Following Latin maxim, words for instance, describe the land ownership rule in Roman Empire times; ***Cuius est solum, eius est usque ad coelum etad inferos*** (whoever's is the soil, it is theirs all the way to Heaven and all the way to Hell), (Wikipedia, 2023). This is the principle of property law for the countries followed basic Roman Law principle. This statement in Latin is also called as “the ad coelom” doctrine. In some countries, certain limitations have already been attached to this approach to form restricted practises of the Latin Maxim rule. First, land related rights are divided into sky rights above the land and subsurface rights (mostly related with earth resources) below the land. Land owners have rights to control immediate layers below and above their lands. But nobody can have rights to restrict flight over their land boundaries. Similarly, nobody can construct surface structures which have overhanging parts over neighbouring parcels. As it is stated before, (Wikipedia, 2023). *“early versions of the maxim have been traced to the 13th-century Italian jurist Accursius, and is said to date in common law to the time of Edward-I (of England). It was more recently promulgated, in broadform (air above and ground below) by William Blackstone in his influential treatise Commentarieson the Laws of England (1766)”.* However, certain natural resources related with earth crust under certain land surfaces have gradually been evaluated differently in time in

different societies. Rights of natural mineral, energy and groundwater resources below the land are especially kept in state hands in some countries, like Turkey for instance. Mineral resource rights in/on earth crust might be defined, in some countries, completely different then surface land/property ownerships. These rights *"are often owned permanently by the state and are leased from it for a fixed time period",* (Wikipedia, 2023).

After developing different aviation vehicles in time starting from balloon, property rights above the land surface had been problematic. Government bodies of societies have then supplied additional rules to describe limitations of land ownership right (just) above it. Limitations and related rights just above the lands have then been handled differently by states to organise the common well-being of their society. Passage routes of planes and other civil aviation vehicles have then been controlled according to the national state-rights gained from land owners by supplying related national laws. In urban areas for example, building a skyscraper have their own precaution described in city plans. It should be borne in mind that high towers obstruct winds and city views plus their shades of influence on neighbouring lands and buildings. In addition, in case of any earthquake or other types of natural incidents which cause diminishing the stability of high-rise surface structures, and might cause collapsing of them over neighbouring lands/buildings. Government bodies and related city planners should know these dangers and be well informed about the results of aftermath analyses of any earthquake (like what happened in Turkey in February 2023).

Similarly, land ownership rights below the earth's surface have been restricted after realising the opportunity of natural resources in different manners in different countries. Likewise, laws provided by different states to regulate mineral, ore, oil, natural gases, geothermal and groundwater have put extra restrictions on land ownership described in the Latin maxim "the ad coelom". Beside the main differences on land ownership between socialist, communist and capitalist countries; there are further different applications among the socialist-capitalist world as well. Natural resources are usually accepted as national treasures for countries and their inputs through mining, oil, natural gas, geothermal and groundwater handling industries have then been well regulated and they have been provided different taxation rates and fees according to government policies.

In the last century, after excavation of tunnels for highways and railways (including subways, metros), underground spaces supplied for public transportation have become valuable assets in countries, especially in urban areas. In addition, after subterranean spaces *(caves, passageways, shopping centres, carparks, machine halls, shelters, large scale depots, sports and social activity etc.)* use have gradually become alternative (sometimes necessary) urban areas for modern life style, their usages also have gradually been increased. For the current cases, there are no common approaches for the ownership and liability of the subterranean (underground) spaces in urban areas. Land ownership rights and their limitations above the land have been regulated somehow but, what about the land ownership rights below the surface. As the metro tunnel networks have progressively got complex structure and surface land owners have restricted themselves from certain activities which disturb underground tunnel structures with their vibrations, land ownerships, earth resources rights and subterranean space usages have interlocked into deep discussions. The question is who has the ownership rights below the land. According to Latin Maxim rules, land ownership has the right to control above and below the land. However, like earlier natural resources (mining, oil, natural gases rights) pre-

descriptions and following state controls over them besides land ownership rights, current underground spaces and their usages have gradually been regulated to organise their ownerships, liabilities and responsibilities through central governments of societies. Countries have different levels of awareness of this concept, and some of them already have legislation acts (law) for their underground spaces besides their natural resources laws. Baker, (1991), pointed that as urban life structures extend their up & down limits, therefore new legal conditions need to be defined. He noted Thomas's study, (1979), who wrote the following statements about "the ad coelom" doctrine; *"the exact origin of this maxim eludes legal historians, but it was cited at least as early as the year 1250 and was later common in Jewish, French, Germanic, and Roman law. The maxim first appeared in a recorded English case in 1586".* Baker also stressed the points about the countries which have *"centrally planned economies and ownership of resources, private land ownership is either nonexistent or very restricted*". At this point the study given by Ball, (1930), which was about ownership rights above the land surface, needs to be mentioned. About the underground land rights concept, Jalil & Arshad, (2020), supplied the following lines; "*when use of land is changed from horizontal to vertical, there is a need for the traditional legal framework governing the changes to be legislated".* That means, land & property ownership registration procedures should be transferred from 2D to 3D by introducing related background legislative acts/codes. Therefore, it is very important for societies to clarify rights and responsibilities of the "underground spaces" which can be defined outside of underground mineral & natural resources rights.

Barker (1991) stated the survey was conducted by the International Tunnelling Association (ITA) among its members to point to "legal and administrative issues in underground spaces". The results of this study pointed to four main application differences. He wrote about them as; *"First, the surface owner owns to the limit of the earth. Second, the surface owner owns as far as a reasonable interest. Third, the surface owner owns only to a limited depth beneath the land (as little as 6 metres). Fourth, private landownership is almost non-existent and, hence, the underground is also publicly owned".* Description of land ownership rights for the cases of underground spaces were also presented by Admiraal & Cornaro, (2016), in three approaches; First one is "effective landownership". This land right, *"can be limited to a specific depth beneath the surface. Japan and Singapore have taken this route and limit space beyond the limit and deem it to be owned by the State and it may be used for public purposes",* (Admiraal and Cornaro, 2016; Kishii, 2016; Zhou and Zhao, 2016). The second approach *"is to acquire land based on a legal mandate through compulsory purchase, eminent domain, resumption, or expropriation. This usually requires compensation".* The third one, *"is an easement, a private agreement between two parties to access land*".

Defining separate living spaces, flats, (and their rights) at high-rise apartments, "*skyscrapers*", above the land surface might push to define similar living spaces (and their rights) for "*earthscrapers*" below the land surface-datum. Land ownerships and their usages have some concerns on responsibilities of "enjoyments" of neighbouring land parcels. Thus, urban life settlement plans are realised with the organisation of the city structures (types, locations, sizes, orientations, height etc.) to not restricted others' access to sunshine, view, wind etc. rights. When the stabilities of foundations are considered for city buildings, their interactions should also be analysed carefully before proofing any further constructions, pilings and excavations for their foundations. Stresses transferring through surface structure

foundations influence the rock/soil masses under them in 3D manners. These stress-states might cause 3D deformation problems, if the land owners who plan a construction without thinking (getting information) about the existing neighbouring structures and their foundation features. Similar stress-deformation features have already become undesirable cases for subterranean spaces and surface land & property owners. There are no foundations or underground spaces which can be designed without thinking about the other adjacent spaces and foundations around. Thus, underground space(s) below the defined surface land parcels should not be designed & excavated individually without taking into consideration its stress-deformation influencing fields. This field can be considered in 3D around the subterranean spaces and it has effective thicknesses, "wi", starting from the space walls, (*Kirsch-Solution* define "wi" at least equal *(can be bigger than)* to space's diameter, (Kirsch, 1898; Xu etal., 2019).

Actually underground space influences surrounding rock masses with decreasing 3D induced-stress rates starting from its volumetric peripheries. Thus, surface land owners who would like to have subterranean spaces under their surface lands should be regulated to limit their underground spaces' induced effects on other's subterranean spaces and surface structures. This could be handled only by organising rock engineering considerations in city plans in 3D manners. The concept should clearly be defined and described through Legislative Acts to control stabilities of structures *(including adjacent spaces, structures, foundations etc.)* in/on earth crust by defining ownerships & responsibilities in/on earth crust (rock/soil masses). It should also be borne in mind that underground spaces gradually influence surface buildings in time and it may cause subsidence related influences on surface urban structures which nobody would like to be faced with.

2.1. Underground space rights in Turkey

In Turkey, registration of land ownership has taken place in the Cadastral system approach since 1924. The system was re-organised in 2008 as The Cadastral Law (with National Law code: 3402). This law facilitated all related regulations and included 3D cadastral bases to include subterranean spaces. However, providing 2D cadastral systems have gradually been compiled for all parts of the country but Aydin reported in 2008 that, 3D cadastre system approach in Turkey has some legal gaps in practices. According to him, "*3D cadastre is mentioned about, people only understand xyz cadastral coordinates instead of thinking about how to use the above surface and underground space*". He supplied a statement also that, "*In particular new cadastral databases with 3D coordinates have been produced by the private sector using Turkish National Fundamental GPS Network standards"* since 2005, (Aydin, 2008). New approaches in land ownerships however, have provided innovative opportunities beneath the earth surface in crowded urban areas. Then, subterranean spaces excavated together with surface constructions, (below the registered land ownerships) need documentation as well. Underground facilities which have not been considered in official ownership documentations before are main dispute areas among land ownership holders. Registering all the spaces engineered in/on earth crust should then be realized after their 3D localization *(with definite xyz-coordinates*).

The urban spaces in/on earth crust must then be defined with their physical boundaries (*2D/3D area/volume descriptions*) and related connections (passages) to each other. In addition, land and property ownerships of surface lands and subterranean spaces *(together with their 3D positions)* need to be defined clearly by new rules to eliminate further disputes and unrequired

circumstances. For instance, surface land ownership holders in cities have to be careful about their land & property rights' limitations with respect to the subterranean tunnel spaces (if there is any). Metro lines in urban areas have their 3D plans in detail but, due to the lock of 3D land registration of the metro tunnels & stations in some countries, individual surface land ownership holders might have not officially warned yet, about the subterranean tunnel(s) and related subterranean layers' ownership-parcels below their lands. This fact sometimes causes physical influences, for instance, ground engineering related drilling for a planned surface structure was intersected subterranean metro tunnel and caused an accident in Istanbul, Turkey, (Haberler, 2006).

Subterranean tunnels & spaces naturally cause a new order of stress-deformation pattern around them which might also cause subsidence at ground surface. Since there are shades in 3D modelling of the cities, metro tunnels, metro stations, underground passageways excavated (opened) under the private lands might end up disputes with "land ownership rights" holders in near future in Turkey. Surface land and property ownership and related responsibilities including taxation have been well documented due to their income characteristics for local and central governments. In Turkey, land ownerships can be agricultural or urban types which have separate taxation rates. If urban land has surface structures, (constructions, houses, apartments etc.) they can be taxed according to their property types and areas. Some houses and apartments have basements and they are also included in this property ownership rights and taxation procedures. Living spaces which are located just below the surface land ownership and fully connected to adjacent surface structures are included in these concepts. However, ownerships of subway tunnels which were excavated underground and passing below through many surface land parcels have needed new acts and evaluation to settle ownership rights, responsibilities, taxations etc. This type of adjustment will further regulate urban subterranean spaces *(may include porosity spaces, ancient subways, underground city spaces, natural caves, etc.)* for advanced conditions in Turkey.

2.2. Underground space rights in England

In England, usage of subterranean space for urban purposes has reached certain limits that land and surface property owners have wondered if there are any negative impacts of underground urban purpose excavations on their lands and lifestyle. Garrett wrote in a daily newspaper as an article to note the increase in usage of underground spaces in recent years and asked a question that *"So how to keep track of what's down there?"* (Garrett, 2018). Underground metro maps of crowded cities are very complex, and tunnels elongated among underground metro stations and infrastructures of urban areas of cities are well mapped to obtain problem-free public transportation and functional infrastructures. This operation requires 3D mapping of the underground tunnels, stations, depots with their position referenced to 2D surface mapping locations. If there are already laws limiting land ownership rights below the surface land locations, surface land ownership and underground space ownership had already been categorised in law together with their liability and responsibilities. If there is no legislative law for similar conditions, disputes have already been taken to the courts for compensation. Garrett mentioned an example from Melbourne, Australia, about a tunnel excavation; "*the government is currently preparing to bore underneath 260 properties, including more than 100 homes, to build a road tunnel. Homeowners received a letter explaining that their "sub-stratum" land was being sequestered, without compensation".*

According to Grecksch, (2021), governing efforts needed to handle underground spaces are complex in character due to "conflicting objectives and regulatory frameworks". The author defined the key objective here as; conceptualising and implementation of "new approaches for underground space governance, taking into account its diverse uses and various stakeholders' claims". Grecksch, pointed Riddall's, (2003), note about land ownership as, "*in English law there is no such thing as absolute ownership of land. Instead, all land is held from the Crown by tenure*". Thus, minerals, oils, gas and coal extractions from underground can only be possible by licensing in the UK, (Morgan, 2013). At this point, it is required to present Gravells's, (2010), observation that, *"the cases support in principle that the owner of land owns any natural or man-made structure below the surface of the land"*. Despite *"Latin maxim"* rules, there are cases discordant with this property right approach. According to Gray & Gray, (2009), "*the maxim has limited definitional value and has virtually become worthless in contemporary law*". Air right above "the land" is the example for the cases. In the UK, the Infrastructure Act of 2015 described *"a new land access regime to use deep-level land below 300 metres",* (Admiraal & Cornaro, 2016), for rock fracturing attempt to produce oil and natural gasses by using vertical and adjoining horizontal (inclined) drillings through underground rock masses. After evaluating underground spaces, following three facts were provided by Grecksch, (2021), to summarise these spaces' legal conditions for the UK. Firstly, underground resources (*minerals, oils, groundwater, or planning regulations for private houses, etc.)* are already wisely regulated in the UK. However, regulation is fragmented and it does not cover all subterranean spaces *"as an entity*". Secondly, governing concerns of subterranean spaces usages should be performed by facilitating experiences learned from rock fracturing. These experiences should also be evaluated as valuable assets in geothermal and carbon capture & storage activities. Thirdly, *"there is an interdependence and an interplay between the themes identified, (property rights, regulation, groundwater, fracking, nuclear waste storage), requiring a coordinated, interdisciplinary, and integral approach".*

Volchko etal., (2020), wrote about spatial planning and they mentioned "subsurface data collection" which have been started in the UK and the Netherlands to assist this planning process. They also noted that the British Geological Survey had collaborated with Glasgow City Council to develop the "Assessing Subsurface Knowledge", ASK, network. ASK was basically introduced *"for collecting and making accessible environmental and engineering geoscience data",* (Whitbread etal., 2016; Von der Tann etal., 2018). Data collection related to subsurface have accumulated through industry & national stakeholders in the UK by donation (voluntarily). The related data and procedures resulted in recognition of "*the environmental and economic value of the subsurface and reflects the importance of the subsurface environment for the health, wealth and growth of the city",* (Dick etal., 2019).

2.3. Underground space rights in Singapore

Singapore subterranean space use history can be briefly provided through the facts pointed by Seng, (2022). Singapore has limited land resources then some urban facilities have been positioned in rock masses. Use of underground spaces started with the British Fort Canning Hill military shelter in early 1936. Seng reviewed underground facilities in Singapore and mentioned; the first subterranean car park for 150 vehicles linked to the basement of a department store through an underground walkway; the Singapore metro system called MRT is 67 km in length *(including 19 km of underground tunnels)* in 2022. Seng noted also that by 2022, 10% of Singapore's roads (approximately 22 km in 2027) will be underground. Singapore has subterranean pedestrian passageway & shopping mall facilities as well *(City Link Mall: opened in 2000, 350 m in length, 6,039 m^2 of subterranean retail spaces), (Marina Bay Link*

Mall: opened in 2010, 16,630 m^2 subterranean spaces), (Seng, 2022). Getting effective and economic progress in subterranean urban works (other than mining activities) is an important step for Singapore. Defining ownerships for subterranean spaces might also have a positive impact on these progresses. This fact was pointed like; "*the State Lands Act and Land Acquisition Act were amended in 2015 to facilitate the use and development of underground space by clarifying the extent of underground ownership and the introduction of strata powers for the acquisition of a specific stratum of space",* (Seng, 2022; MLS, 2015).

The Singapore government approved the Master Plan in Nov. 2019 which includes more green areas. The plan covers usage of subterranean spaces as well. Singapore Land Authority and Singapore-ETH Centre have started a collaborative project in 2017 to digitise underground usages in Singapore. The aim in this project is to work on *"how underground space can be used more efficiently and effectively"* in Singapore. Schrotter & Van Son, (2019) stated that digital surface and underground land usage plan is helpful for people in Singapore (specially for; building owners, developers, and city planners), by supplying a truthful, digital representation of the physical world below. Requirements of subterranean spaces and surface land ownership rights have shown interactions because surface land owners have rights also for their land's sub terrain for civil usages. Therefore, The Republic of Singapore issued a law, (State Lands (Amendment) Act 2015), on March 13th 2015 to regulate this new circumstances. This Act supplied descriptions of underground rights in the case of natural resource reserve features and "Easement of subjacent support" features as well. In this Act statement, "*Amendment of section 3B-b*" stated that; "*if no such depth is specified, subterranean space to -30.000 metres from the Singapore Height Datum.", (SSO, 2023).* This means the mentioned Act in Singapore here put limitations to surface land ownership rights for their land's underground extension.

2.4. Underground space rights in Malaysia

When urban city life forces new development in Malaysia, clarification of land ownership rights has been comprehended for the surface lands and subterranean spaces. Zaini etal., (2013) reviewed the similarities of surface land ownership rights in countries which *"extended downward but limited depending on the circumstances"*. As they noted, development of the surface and subterranean spaces have their dilemmas and ended up to complex, legal court issue considerations. These features cause some drives, (solutions), in some countries "*to help in overcoming issues in underground land"*. Zaini etal., (2013) stated that Malaysia reviewed the National Land Code 1965 (NLC 1965) for legalisation actions of underground spaces and the amendment to NLC 1965 was realised (*printed on Feb. 22cd 1990)* by inserting *"Part Five (A) to enable the State Authority to dispose underground land and gives the State Authority a clear power to dispose underground land for new cases of land disposal"*. Earlier NLC 1965 rules has ownership descriptions about the term "land" which covers; *"not only the surface of the earth and all things that formed the surface, but it also includes land under the surface of the earth and all substances therein, all the plants and other natural produce either above or below the surface of the earth", "There are exceptions to the rights, as for example, the mineral belongs to the state and not to the landowner".* Definition of *"underground land"* which *"refers to a space that is situated below the ground level"* was added to NLC 1965 with Section 92A. This section presented *"the meaning of adjoining underground land, stratum and underground land as follows: a) Adjoining underground land means underground land adjoining a stratum above, below and on the sides of the stratum; b)*

Stratum means a cubic layer of underground land; and c) Underground land means land which lies below the surface of the earth". Then, the Federal Department of Lands and Mines (JKPTG) issued a Director General of Lands and Mines (Federal) Circular No. 1/2008 which defines "stratum" on the disposal of the underground land. According to this circular, "stratum" is "*the underground land which has been identified for the purpose of disposal as an independent use and not related with the above usage*", (Zaini etal., 2013).

2.5. Underground space rights in some European countries

Underground space use has been taken into consideration in a strategic manner in the Netherlands. Edelenbos etal., (1998) supplied brief facts related to underground spaces. They mentioned Netherlands efforts on the national "Strategic Study on the Utilization of Underground Space". The study was initiated by *the National Physical Planning Service, RPD) of the Ministry of Housing, Spatial Planning and the Environment (Netherlands).* Related works here had been performed by *Centre for Underground Construction, COB)* and *Delft University of Technology (TUD)*. These efforts result in a new strategy and then *"The Netherlands is the first country in the world to publish a national planning strategy for the subsurface (Government of the Netherlands, 2018). This takes place in a larger framework of the Environment and Planning Act, an ambitious piece of legislation combining fifteen separate environmental acts into one*", (Volchko etal., 2020). Sustainable use of subsurface potentials, including subterranean spaces, were arranged in the Netherlands *(Dutch government, provinces, municipalities, water authorities)* in 2016. The procedures of "Covenant 2016" include *"different subsurface functions and uses, e.g. cables and pipes, natural resources and geothermal energy"*. Furthermore, Campbell etal., (2017) reported that a national "Subsurface Policy Strategy", STRONG, has been developed in the Netherlands *"to promote sustainable use of the subsurface"*. These authors noted also that, underground register system, *Basisregistratie Ondergrond* (BRO), was established in the Netherlands in 2015 *"to consolidate geological and exploration data as well as data about mining activities and the associated structural assets".* Campbell etal., (2017) noted also that contributions to BRO are mandatory. One of the current studies on subsurface land ownerships is the one supplied by Ramlakhan, etal., (2021). In this work they stressed that, *"two dimensional (2D) Land Administration Systems (LASs) do not adequately represent 3D underground objects. It is not easy to identify the owners of these objects and the relations between objects below and above the surface are not explicitly provided"*. They wrote also that "*a 3D LAS can however facilitate a better understanding, as well as a more efficient registration and clear visualisation of the Rights, Restrictions and Responsibilities (RRRs) of the 3D underground objects".* They wrote about their BIM/IFC models *(standardized workflow to model the legal spaces)* which include *"3D underground objects according to the LADM in 3D LASs"*. Subsurface land ownership variances among countries (including Europe) were tabulated by Volchko etal., (2020), to point to three different procedures. These countries have already realized the significance of legal engagements for underground land ownership. Countries in the first procedure group put depth limitation "to address private ownership of the subsurface" (i.e.; Singapore). Second group "uses rights to the subsurface by private landowners" (i.e.; Japan, Finland and Norway), Third group defines "ownership of such underground resources as minerals, oil and gas by the state" (i.e.; Denmark and the Netherlands). In these groups; 1st and 2cd group procedures aimed to facilitate "*the use of physical space underground in the public interest",* (Kishii, 2016; Vahaaho, 2016; Zhou and Zhao, 2016). However, 3rd group members acted "*to protect property rights of the state (or the Crown) to underground resources"*. In Finland, special regulations

related to subterranean-planning are supplied by "§56, The Land Use and Building Act of Finland" and this Act has control actions over subsurface usage plans, (Volchko, etal., 2020).

Karabin, etal., (2020) worked on the land & property ownerships (rights) related to subway tunnels in Austria, Bulgaria, Czech Republic, Croatia, Greece, Poland, Slovenia, and Sweden. They presented vitality concerns in "appropriate property rights to construct and exploit tunnels". They supplied model studies to define 3D property (cadastre) rights through available underground metro design works. They also marked limitations in actual property rights in 3D manners, and they wrote a brief history of the metro line constructions in the listed EU countries. Land ownership rights have mostly been documented in 2D systems for these countries *(besides, like Bulgaria, private land ownerships and their documentation were started after the governmental system change).* However, subsurface spaces such as metro tunnels and stations had already been in use for them which required positioning with respect to earth surface positions. Ownership rights defined for surface lands and subterranean spaces then have to be resolved according to applicable legislations in these countries. Karabin, etal., (2020) wrote for the Czech Republic for instance that Prague has the only city with metro lines in this country, and *"in practice, many underground constructions are not registered in the cadastre. Currently, underground constructions are only registered when some part(s) of the construction is located above the ground".* Similar case was reported by Perperidou, etal., (2021) for Piraeus metro station (Greece) together with 3D subsurface property rights of transportation infrastructures. They also provided that Greek surface land owners did not obtain any compensation due the metro lines deeply passing under their surface lands. They added that *"the current Greek cadastral system is two-dimensional and there are no records for underground transportation networks".* However, the requirement of "Urban Underground Space", UUS, pushed 3D modelling of the transportation tunnels. They noted also that UUS documentation is required particularly in heavily populated Greek cities".

3. Surface disturbances during and after underground space excavation

Underground spaces are not a new phenomenon in civilisation, ancient urbanisations cover even underground city organisations like in Nevsehir (Turkey). However, after subway transportation systems prove themselves efficient in crowded cities, subway tunnels and stations are common locations people are passing through in their everyday urban life. Locations of underground spaces in 3D coordinate systems are the new focus of the governing bodies in addition to their available 2D land registration & ownership documentations. There are already conflicts among holders of 2D land ownerships due to surface lands' border disputes, surface construction features, vegetation, crops, etc. These land owners might also have conflicts due to underground mining, oil, natural gas, and geothermal operations. The economic interest cases among surface land ownership rights and earth resources *(in/on earth crust)* have been clearly defined by legislative Acts/Codes in most of the countries. But there could still be dilemmas when these rights are overlapped in/on earth crust. Subterranean spaces which are already available and subterranean spaces currently under planning have introduced new concepts in documentations and ownership rights. These re-discovered use of underground spaces have similar conflicts/dilemmas in future, if there is no legislative rule to define their ownership situations in 3D positioning systems. These facts have already been recognised by some countries and they have provided the legislative Acts/Codes which usually divide land ownership rights into layered ownership starting from the centre of the earth up to high sky. These rules on the other hand are diminishing the land ownership definition defined by Latin Maxim in "the ad coelom" doctrine. Description of spaces which are used by private or public purposes in planned urban settlements should be defined by their volumetric positions.

According to these volumetric coordinates, they can be on earth surface or underground, *(in other words they can be in/on rock/soil masses)*. Governing bodies have gradually evaluated ownership procedures in 3D systems and they have tried to provide legislative procedures in taxation & responsibilities. They have also supplied procedures to overcome conflict among the ownership dilemmas among surface and underground land owners. The 3D stresses-deformations related conflicts which have been interacted among underground mining right owners and surface land owners are expected to act among underground and surface land owners as well.

Rock/soil mechanic concepts and rules are going to be the main decision background for ground engineering decisions. Man-made structures in/on earth crust need excavation for their foundations/subterranean spaces. These excavation works, foundations, and subterranean spaces created in rock masses have influenced the rock masses surrounding themselves. Stresses/deformations are redistributed to form induced stress fields which affect neighbouring man-made structures in/on earth crust. Thus, engineered structures should then be positioned in/on earth crust (at related surface/underground parcels) according to pre-calculated and evaluated urban plans (in 3D). Without such a plan, just excavating subterranean spaces and metro lines without estimating future problems (due to surface/underground land ownership rights disputes and more importantly their induced stresses-deformations influences) cause civil paradoxes in modern urban settlements.

Influence of surface vibration sources on underground spaces or visa-versa cases, are current disputes cases in different parts of the world. In Turkey, for example, the underground irrigation tunnel management office provided their opposition against a travertine ore mining rights holder to inherit their mining operations above the tunnel, *(height difference between planned mine and tunnel is about 450-500m).* One of the concerning/disputed points might be the danger of rock vibrations expected around the tunnel structures. Similar disputes will be forwarded in future for urban structures which are just over the metro tunnels in crowded cities. Thus, neighbouring urban spaces in/on rock masses should definitely be designed (and then excavated) according to 3D city planning which should be based on rock/soil mechanics concepts. Thus, rock engineering designs for; surface structures' foundations, and underground tunnels must vitally include; site characterisation, preliminary plans, rock mechanics laboratory and field tests, rock masses' mechanical behaviours, rock mass characterisations and classifications, rock engineering decisions for designed subterranean space dimensions, their stabilities & supports, risk evaluations for their safe usage. Supplying rules for 3D land ownerships for taxation purposes or defining rights for responsibilities are not totally enough for getting safe & stable urban structures and cities. Engineers in subterranean space design concepts should keep their focus on 3D rock mass stabilities when urban settlements in/on earth crust are under consideration.

4. Conclusions

Digging the basement (in several apartment layers) in crowded cities have been new urban planning considerations in crowded cities where land values are high enough. If there is demand for underground spaces for depot, car parks or living places, there will always be engineering and consulting companies trying to supply these spaces. Some cities already have complex subway lines and stations. Besides, some roads are positioned below the earth surface to eliminate crowded city traffic. Actually usage of underground spaces is not new in characters. This started as early as human history through caves, underground cities etc. Evaluation of 3D land ownership registry brings new dilemmas among the uses of surface areas and underground

spaces. Subterranean spaces have 3D positions in the earth crust *(mostly in rock masses)* which are below certain land parcels of the earth surface. Surface land ownership rights in most of the countries have earlier been defined with "Latin Maxim" rules except earth resource rights. Some countries have already diminished this concept by limiting land ownership access in sky and the underground by defining different layers. Surface land ownership has rights to use immediately adjacent sky and subterranean layers. But their rights cannot be applicable after the described layered thicknesses in legislative Acts/Codes. Beside these facts, in some countries there are no land ownership rights, all the lands belong to States. Currently, 2D surface land ownership documentations (in cadastral parcel papers) have gradually been computerised and recorded in 2D software models. However, increases in the use of subterranean spaces have gradually forced the governing bodies to produce 3D digital registry systems for 3D land ownerships. On the other hand, while government bodies define 3D land ownerships in layered methods, *(or any other methods which will be introduced)*, they should judiciously consider earlier 2D land ownership rights which hold "Latin maxim" rights. Introducing (mandatory) layered 3D land ownerships without supplying proper acknowledgements to the earlier surface land ownership holders might not be the motivation which modern countries follow. Besides ownership issues, induced stress-deformation fields' influences among 3D neighbouring parcels are also very important in city plans. That means, influences of manmade structures planned in/on rock masses should be well documented with their risk of stabilities through "adequate" ground engineers, (Gokay, 2023). Subterranean spaces and tunnels might push some limitation procedures for the planned surface structures by considering ground vibrations they may cause. Similar precautions could also be applicable for the stabilities of surface structures due to subterranean space originated vibrations. Thus city plans and related excavations and structures in/on earth crust should definitely be in order of planning actions. Otherwise urban life of people will unavoidably approach endless dilemmas caused by these structures' 3D positioning disputes and their instabilities cases. In the next decades, underground settlement issues will be concerned with new legislative acts covering land ownerships in 3D *(but covering earlier surface land rights and rock/soil mechanical concepts to supply risk assessments of stabilities)* for the part of earth crust (rock/soil masses) in use.

References

Admiraal, H. and Cornaro, A., Why underground space should be included in urban planning policy and How this will enhance an urban underground future, *Tunnelling and Underground Space Technology*, 2016, 55, pp214–20.

Aydin, C.C., Usage of underground space for 3D cadastre purposes and related problems in Turkey, *Sensors*, 2008, 8, pp6972-6983.

Ball, S.S., Division into Horizontal Strata of the Landspace above the Surface, *The Yale Law Journal*, 39, 5, March 1930, pp616-658, www.jstor.org/stable/789808.

Barker, M., Legal and administrative issues in underground space use: a preliminary survey of ITA member nations. *Tunneling and Underground Space Technology*, 1991, 6, 2, pp191–209.

Campbell, D., De Beer, J., Mielby, S., Van Campenhout, I., Van der Meulen, M., Erikkson, I., Ganerod, G., Lawrence, D., Bacic, M., Donald, A., Radu Gogui, C., Jelenek, J., Geoscientists and urban decision-makers: European COST Sub-Urban Action (TU1206). *Procedia Eng*. 2017, 209, pp4–11.

Dick, G., Eriksson, I., De Beer, J., Bonsor, H., Van Der Lugt, P., Planning the city of tomorrow: bridging the gap between urban planners and subsurface specialists. *Earth Environ. Sci. Trans. R. Soc. Edinb*. 2019, 108, 2-3, pp327–335.

Edelenbos, J., Monnikhof, R., Haasnoot, J., Van der Hoeven, F., Horvat, E., and Van der Krogt, R., Strategic study on the utilisation of underground space in the Netherlands, *Tunnelling and Underground Space Technology*, 1998, 13, 2, pp159-165.

Garrett, B.L., Who owns the space under cities? The attempt to map the earth beneath us. *The Guardian newspaper*, July 10th, 2018.

Gokay, M.K., Engineering required to have safe structures in/on the earth crust and Eurocode 7, *Konya Journal of Engineering Sciences*, Accepted paper, 2023, 11, 2. pp312-323.

Government of the Netherlands, *Spatial planning strategy for the subsurface, Summary*, (Den Haag, Ministry of Infrastructure and Water Management), 2018.

Gravells, N.P., *Land Law: Text and Materials*, 4th edition, 2010, Sweet & Maxwell, London, UK.

Gray, K.J. and Gray, S.F., *Elements of Land Law*, 5th edition, 2009, Oxford Univ. Press, Oxford, UK.

Grecksch, K., Out of sight-out of regulation? Underground space governance in the UK, *Journal of the British Academy*, 2021, 9, 10, pp43-68.

Haberler., Istanbul: Metro hattinda meydana gelen sondaj kazasi (Drilling accident at Istanbul Metro line), (in Turkish), Aug. 10th 2006, *Haberler.com*, Ihlas haber ajansi, Turkey.

Infrastructure Act 2015, webpage, www.legislation.gov.uk/ukpga/2015/7/contents/enacted.

Jalil, N.I.A. and Arshad, A.H.M., Right of access on underground land development: Guidance from Singapore and Australia, *International Journal of Law, Government and Communication, IJLGC*, 5, 21, Dec. 2020, pp267-276.

Karabin, M., Kitsakis, D., Koeva, M., Navratil, G., Paasch, J.M., Paulsson, J., Vučić, N., Janečka, K., and Lisec, A., Layer approach to ownership in 3D cadastre in the case of underground tunnels, *Land Use Policy*, 2020, 98, 104464.

Kirsch, E.G., Die Theorie der Elastizität und die Bedürfnisse der Festigkeitslehre. *Zeitschrift des Vereines deutscher Ingenieure*, 1898, 42, pp797–807.

Kishii, T., Utilization of underground space in Japan, *Tunnelling and Underground Space Technology*, 2016, 55, pp320–23.

MLS, Ministry of Law Singapore, "Legislative Changes to Facilitate Future Planning and Development of Underground Space,", 12 Feb. 2015, Webpage, www.mlaw.gov.sg/news/

press-releases/legislative-changes-planning-development-underground-space, Retrieved date; Feb. 2023.
Morgan, J., Digging Deep: Property Rights in Subterranean Space and the Carbon Capture and Storage, *International Comparative Law Quarterly*, 2013, 62, 4, pp813–37.
Thomas, W., Ownership of subterranean space. *Underground Spaces*, 1979, 3, 4, pp155-163.
Perperidou, D.G., Sigizis, K., and Chotza, A., 3D Underground property rights of transportation infrastructures: Case study of Piraeus Metro Station, Greece, *Sustainability*, 2021, 132, 3162.
Ramlakhan, R.J.K., Kalogianni, E., and Van Oosterom, P.J.M., Modelling 3D underground legal spaces in 3D Land Administration Systems, *Proceedings of the 7th International FIG Workshop on 3D Cadastres (Virtual/online event)*, (Eds.; Kalogianni, etal.), International Federation of Surveyors (FIG), 2021, pp37-52.
Riddall, J.G., *Land Law*, 7th edition, 2003, London, Lexis Nexis, UK.
Schrotter, G. and Van Son, R., Digital Underground: Towards a Reliable Map of Subsurface Utilities in Singapore (Singapore: Digital Underground, 2019), Singapore-ETH Centre, Webpage, https://sec.ethz.ch/research/digital-underground.html., Retrieved date; Feb. 2023.
Seng, L.T., Subterranean Singapore: A deep dive into manmade tunnels and caverns underground in the city state, Biblioasia, National Library Singapore, Singapore Government Agency Website, July 2022, Retrieved date; Feb. 2023, p36.
SSO, Singapore Statutes Online, "State Lands (Amendment) Act 2015, (No 11 of 2015)", A Singapore Government Agency webpage, 2015, Retrieved date; Feb. 2023.
Xu, M.F., Wu, S.C., Gao, Y.T., Ma, J., and Wu, Q.L., Analytical elastic stress solution and plastic zone estimation for a pressure-relief circular tunnel using complex variable methods, *Tunneling and Underground Space Technology*, 2019, 84, pp381-398.
Vahaaho, I., An introduction to the development for urban underground space in Helsinki. *Tunnelling and Underground Space Technology*, 2016, 55, pp324–328.
Vahaaho, I., Urban Underground Space - Sustainable Property Development in Helsinki. Urban Environment Publications, 2018:11. City of Helsinki, Urban Environment Division, Soil and Bedrock Unit GEO, Helsinki.
Volchko, Y., Norrman, J., Ericsson, L.O., Nilsson, K.L., Markstedt, A., Oberg, M., Mossmark, F., Bobylev, N., and Tengborg, P., Subsurface planning: Towards a common understanding of the subsurface as a multifunctional resource, *Land Use Policy*, 2020, 90:104316.
Von der Tann, L., Metje, N., Admiraal, H., and Collins, B., The hidden role of the subsurface for cities. *Proc. Inst. Civil Eng.: Civil Eng.* 2018, 171, 6, pp31–37.
Whitbread, K., Dick, G., and Campbell, D., Glasgow. TU1206 COST Sub-Urban WG1 Report. British geological Survey, 2016, Glasgow City Council, UK.
Wikipedia, Cuius est solum, eius est usque ad coelum etad inferos, Wikipedia, The Free Encyclopaedia, Retrieved date; Dec. 2023.
Zaini, F., Hussin, K., Suratman, R., and Rasid, K.A., Review of the underground land ownership in Malaysia, Jurnal Pentadbrian Tanah, 3, 1, 2013, pp39-52, ISSN 2231-9190.
Zhou, Y. and Zhao, J., Assessment and planning of underground space use in Singapore', *Tunnelling and Underground Space Technology*, 2016, 55, pp249–56.

.

Variation of Spatial Coherence Factor for Quantitative Differential Phase Contrast Microscopy

Nur Efşan KÖKSAL GÜLTEKİN[1]
Esra ŞENGÜN ERMEYDAN[2]
İlyas ÇANKAYA[3]

INTRODUCTION

Quantitative phase imaging (QPI) is a label-free imaging method to measure phase delay of light passing through a thin samples in vitro. Label-free imaging methods offer a variety of advantages since they do not need contrast agents (i.e. dyes or fluorophores), which cause to the photo-bleaching and photo-toxicity in live biological specimens. Traditional methods such as differential interference contrast (DIC) and Zernike phase contrast (PhC) can only capture intensity, however; QPI provides the quantitative phase information of a specimen. Phase information cover an optical thickness and composition of cell. It can be also used to detect genetic diseases, infectious diseases and cancer. Some of substantial methods in QPI includes digital holographic microscopy (DHM), transport of intensity imaging (TIE), Fourier Ptychography Microscopy (FPM) and differential phase contrast (DPC) microscopy. The main idea of all QPI methods is to extract the phase map from a specimen (Lee et al., 2018; Lin, Huang, & Luo, 2018; Tian & Waller, 2015).

Differential phase contrast (DPC) is another label free phase imaging method that use multiple images with an asymmetric half-circle illumination patterns. At least two-axis (4 images) intensity measurements in opposite direction are required to avoid missing frequencies. The missing frequencies produce artifacts of phase reconstructions because phase transfer function is not circularly symmetric using only 4 images. DPC images can be used to obtain phase map quantitatively. When compared to the other QPI methods, using DPC for quantitative phase imaging is both experimentally straightforward to implement and provides resistance to speckle noise and 2× better lateral resolution (H. H. Chen, Lin, & Luo, 2018; M. Chen, Phillips, & Waller, 2018; Kellman, Chen, Phillips, Lustig, & Waller, 2018).

In this study, the objective is to retrieve phase delay without the requirement of any complicated setups. The effect of variation in spatial coherence factor for quantitative differential phase contrast microscopy is presented in simulation.

METHOD AND METHODOLOGY

Assuming there is neither defocusing nor spherical aberration, a thin object with a two-dimensional (2D) object transmission function can be defined using weak object approximation (J. Li et al., 2017),

$$o(r) = e^{-\mu(r)+i\phi(r)} \approx 1 - \mu(r) + i\phi(r) \quad (1)$$

[1]Research Assistant, Ankara Yıldırım Beyazıt University, Electrical and Electronics Engineering, Orcıd: 0000-0002-6046-8014
[2]Assistant Prof. Dr, Ankara Yıldırım Beyazıt University, Electrical and Electronics Engineering, Orcıd: 0000-0002-5953-4301
[3]Prof. Dr, Ankara Yıldırım Beyazıt University, Electrical and Electronics Engineering, Orcıd: 0000-0002-6072-3097

where r = (x, y) is the spatial coordinates, μ and ϕ are the absorption and the phase of the objects, respectively. The detected image intensity at the camera (I_{rc}) of total illumination is (Tian & Waller, 2015),

$$I_{rc} = \iint \left| \iint \left[\iint o(r) q\,(r)\, e^{i2\pi r.u''} dr \right] P(u'')\, e^{-i2\pi u''.r_c}\, d^2u'' \right|^2 d^2u' \qquad (2)$$

where u = (u_x, u_y) is the spatial frequency coordinates, u'' is the pupil plane coordinates, u' is the source plane coordinates, rc is the camera plane coordinates, $q\,(r) = \sqrt{S(u')} e^{i2\pi u'.r}$ is the total illumination of each single point Light-Emitting-Diode (LED) source, and $P(u'')$ is the pupil function (low-pass filter) in the Fourier space (Y. J. Chen, Lin, Vyas, Young, & Luo, 2022),

$$\tilde{I}(u) = I_o + H_{abs}(u)\, \tilde{\mu}(u) + H_{ph}(u)\, \tilde{\phi}(u) \qquad (3)$$

where ($\tilde{.}$) represents the Fourier transform, I_o is the background term, $H_{abs}(u)$ is the absorption transfer function, and $H_{ph}(u)$ is the phase transfer function, defining as following formulas (Vyas, Li, Lin, Yeh, & Luo, 2022),

$$I_o = \iint S(u') |P(u')|^2 \; d^2u' \qquad (4)$$

$$H_{abs}(u) = -\left[\iint S(u')\, P^*(u')\; P(u'+u) + \iint S(u')\, P^*(u')\; P(u'-u) \right] \qquad (5)$$

$$H_{ph}(u) = i\left[\iint S(u')\, P^*(u')\; P(u'+u) - \iint S(u')\, P^*(u')\; P(u'-u) \right] \qquad (6)$$

where $(*)$ represents the complex conjugates of a function.

In the aberration-free systems, the background terms and absorption transfer function are removed because these terms are symmetric; $I_o = 0$ and $H_{abs}(u)\, \tilde{\mu}(u) = 0$. Hence, only phase transfer function is retained because of antisymmetric,

$$\tilde{I}(u) = H_{ph}(u)\, \tilde{\phi}(u) \qquad (7)$$

This transfer function is used to solve the phase retrieval inverse problem. Quantitative phase can be recovered by deconvolving the DPC image using the calculated phase transfer function by the following least square problem (A. C. Li et al., 2021),

$$min \sum_j \left| \tilde{I}_{DPC,j}(u) - H_j(u)\, \tilde{\phi}(u) \right|^2 + \alpha \left| \tilde{\phi}(u) \right|^2 \qquad (8)$$

where j is the index of DPC intensity measurements, and α is the Tikhonov regularization term, which is $5x10^{-3}$ in this study. For reconstruction $\phi(r)$, the solution of this inverse problem is associated with Tikhonov regularization term to avoid noise amplification in inverse step using following formula (A. C. Li et al., 2021),

$$\phi_{tik}(r) = \Im^{-1}\left\{\frac{\sum_j \left|H_j^*(u)\,\tilde{I}_{DPC,j}(u)\right|}{\sum_j \left|H_j(u)\right|^2 + \alpha}\right\} \tag{9}$$

where $\Im^{-1}$ is the inverse Fourier transform.

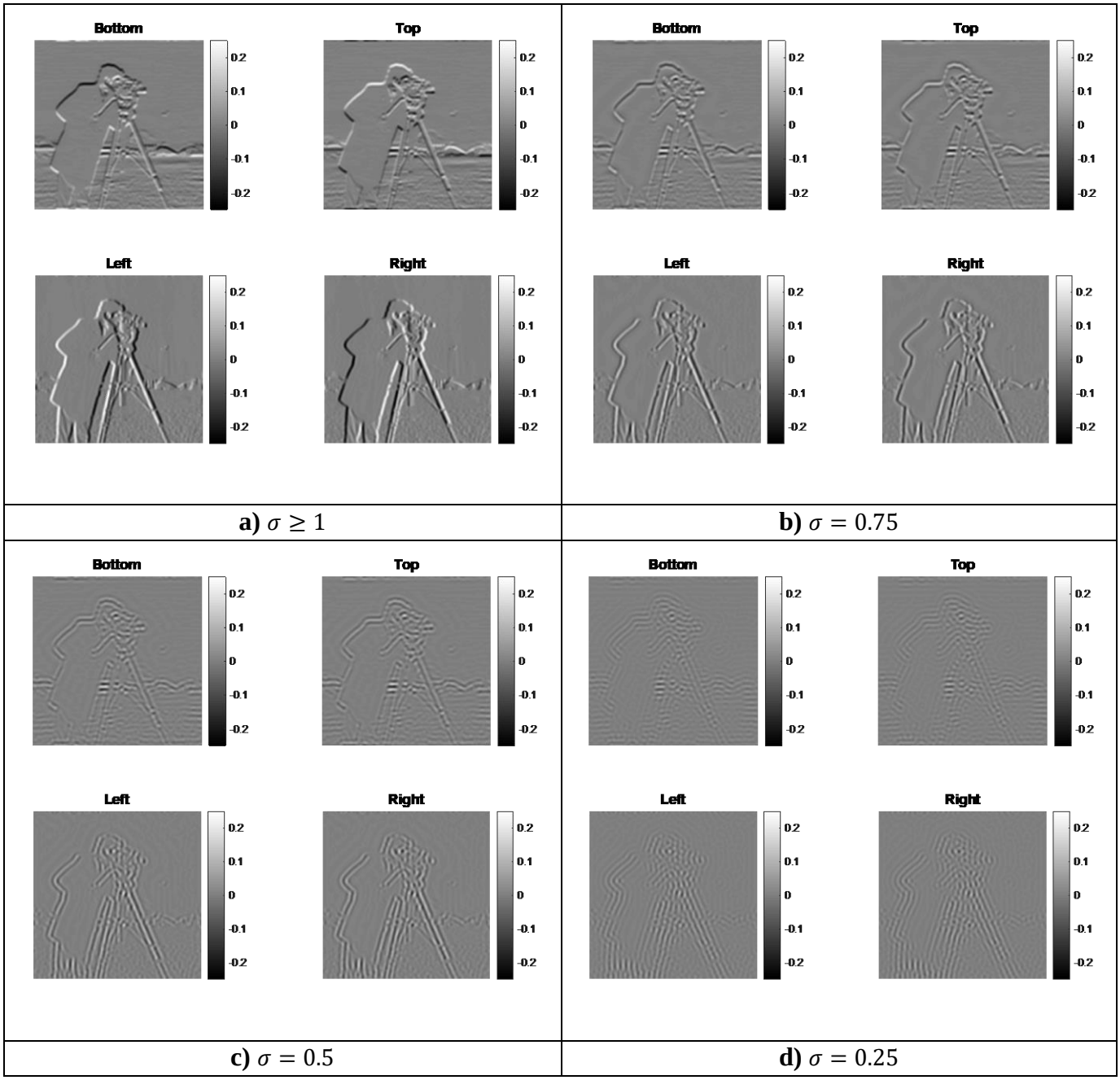

a) $\sigma \geq 1$ **b)** $\sigma = 0.75$

c) $\sigma = 0.5$ **d)** $\sigma = 0.25$

Figure 1. Simulated I_{DPC} images using top-bottom and left-right illumination pattern

The original object field is considered to have a unity intensity and 2D images. All the ground-truth images have the size of 256 × 256 pixels in the range of [0, 1] radians. It is set that the wavelength λ to 514 nm, magnification to 40x, and NA to 0.4. All applications are implemented in MATLAB R2017b (The MathWorks, Inc., Natick, MA) on a computer with CPU E5-1650 v3 @ 3.50GHz (Intel(R) Xeon(R)) and 16 GB of RAM. It is illustrated that the utility of variation of spatial coherence parameter by performing simulated configurations. The spatial coherence factor (σ) is generally defined as (Streibl, 1985),

$$\sigma = \frac{NA_{ill}}{NA_{obj}} \tag{10}$$

where NA_{ill} and NA_{obj} are the numerical aperture of illumination and objective, respectively.

RESULTS AND DISCUSSIONS

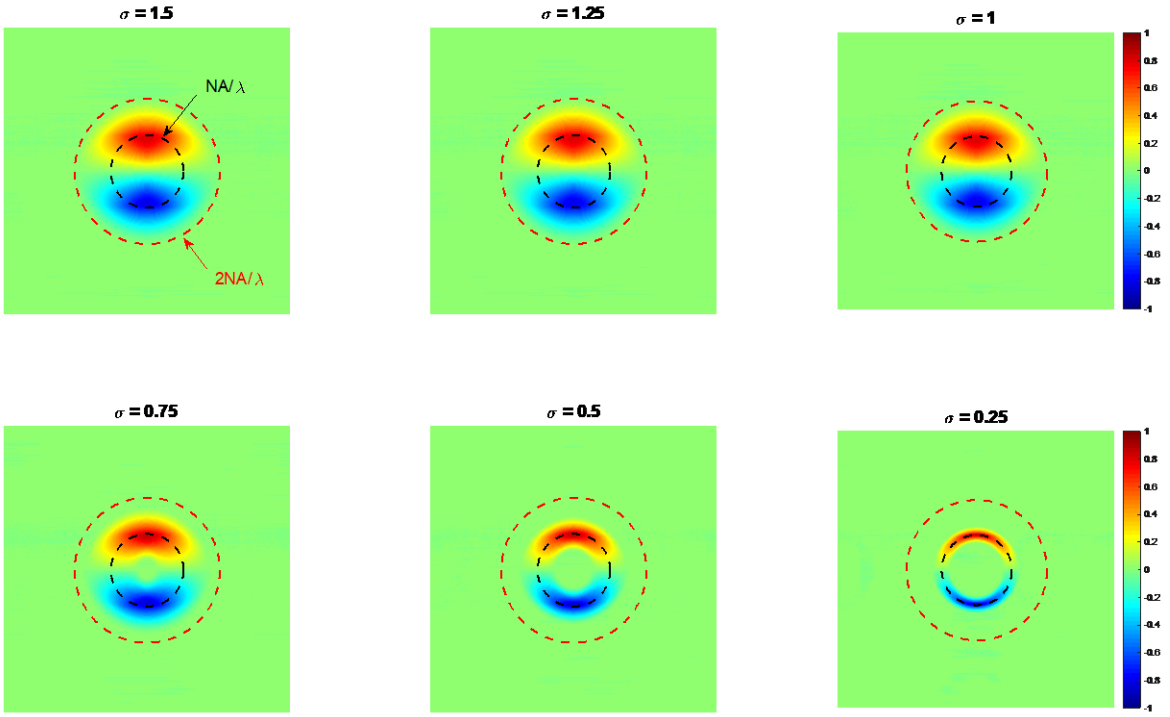

Figure 2. The phase-transfer function for half-circle source

Figure 1 shows the simulated I_{DPC} images using top-bottom and left-right illumination pattern with different sigma values. Highly coherent illumination condition ($\sigma \leq 0.5$) as demonstrated in Figure 1c and d includes the important artifacts. The increase in σ diminishes the coherent artifacts and also allows widely spatial frequencies for recovery. When σ is close to 1, the I_{DPC} provides detailed edge features. $\sigma < 1$ results in attenuated phase contrast compared to $\sigma \geq 1$. Hence, the phase information of DPC images is partly missing in the low spatial frequency. The illumination with $\sigma \geq 1$ shown in Figure 1a does not increase the resolution since it's at the incoherent resolution limit. That is, the missing phase information of DPC images cannot be observed, but produce high contrast image. As the spatial coherence factor increases, the range of spatial frequencies gathered by the microscope system is

increased. The very small spatial coherence generates the noise and degrades the images quality in microscope applications. Therefore, researchers can design optical microscope systems by taking the sigma values into consideration. As a result, NA_{ill} should be larger than NA_{obj} to obtain high contrast phase imaging and high-accuracy (Barone-Nugent, Barty, & Nugent, 2002; Lee et al., 2018; Tian & Waller, 2015; Tian, Wang, & Waller, 2014).

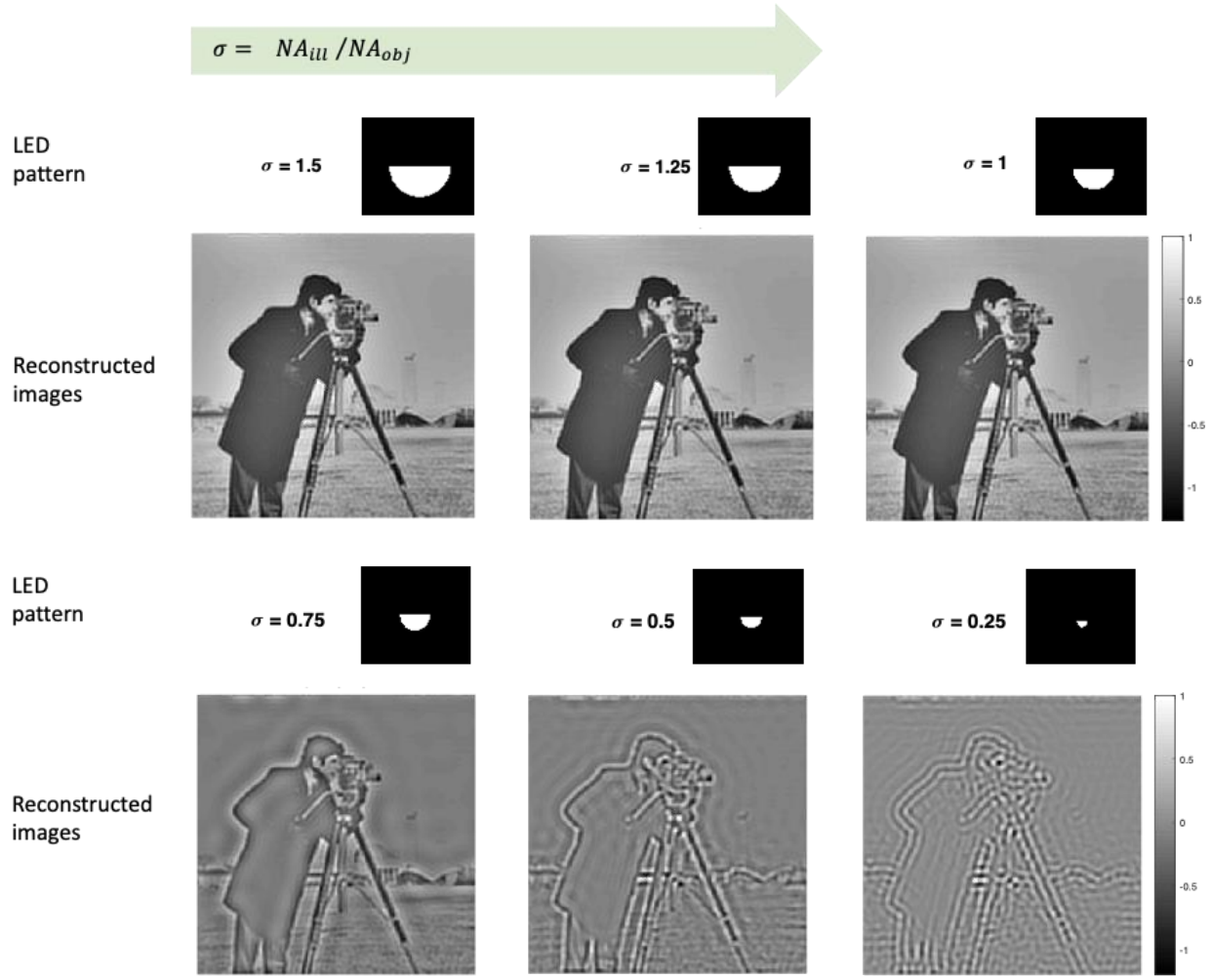

Figure 3. The phase-reconstructed images with different sigma values

Figure 2 shows the phase-transfer function for a half-circle source with different sigma values. In the case of $\sigma \geq 1$, the phase-transfer function also overlap because of the resolution limit. When $\sigma \ll 1$, low-frequencies ($(1-\sigma)NA_{obj}/\lambda$) and high-frequencies ($(1+\sigma)NA_{obj}/\lambda$) are cut-off and a small amount of frequency is mapped. (Tian & Waller, 2015).

Figure 3 demonstrates the phase-reconstructed images with different sigma values. In the case of $\sigma \geq 1$, the PTF does not change, hence the simulated IDPC and phase-reconstructed images does not change. As σ decreases, the quality of the phase-reconstructed images decreases. Figures 3 are also compatible with Figure 1 and 2.

CONCLUSION

In this study, the spatial coherence factor is investigated in the quantitative differential phase contrast microscopy using theoretical WOTF model based simulations. The spatial

coherence factor is highly effective in reconstructed phase images. While the differential phase contrast images and reconstructed phase images do not have any changes for $\sigma \geq 1$ having high contrast and accuracy, there are highly coherence conditions producing more artifacts and low contrast images for $\sigma < 1$. Besides, the reconstructed images get better when $\sigma \geq 1$, therefore using $\sigma \geq 1$ more preferable in designing the optical microscope systems. Besides, as a continuation of this work, the single-shot quantitative differential phase contrast microscopy will be simulated with different illumination patterns.

ACKNOWLEDGEMENTS

This work is supported by BAP of the Ankara Yıldırım Beyazıt University (under Project Number AYBU-2018-BAP-4981).

REFERENCES

Barone-Nugent, E. D., Barty, A., & Nugent, K. A. (2002). Quantitative phase-amplitude microscopy I: optical microscopy. *J Microsc, 206*(Pt 3), 194-203.

Chen, H. H., Lin, Y. Z., & Luo, Y. (2018). Isotropic differential phase contrast microscopy for quantitative phase bio-imaging. *J Biophotonics, 11*(8), e201700364.

Chen, M., Phillips, Z. F., & Waller, L. (2018). Quantitative differential phase contrast (DPC) microscopy with computational aberration correction. *Opt Express, 26*(25), 32888-32899.

Chen, Y. J., Lin, Y. Z., Vyas, S., Young, T. H., & Luo, Y. (2022). Time-lapse imaging using dual-color coded quantitative differential phase contrast microscopy. *J Biomed Opt, 27*(5).

Kellman, M., Chen, M., Phillips, Z. F., Lustig, M., & Waller, L. (2018). Motion-resolved quantitative phase imaging. *Biomed Opt Express, 9*(11), 5456-5466.

Lee, W., Choi, J. H., Ryu, S., Jung, D., Song, J., Lee, J. S., et al. (2018). Color-coded LED microscopy for quantitative phase imaging: Implementation and application to sperm motility analysis. *Methods, 136*, 66-74.

Li, A. C., Vyas, S., Lin, Y. H., Huang, Y. Y., Huang, H. M., & Luo, Y. (2021). Patch-Based U-Net Model for Isotropic Quantitative Differential Phase Contrast Imaging. *IEEE Trans Med Imaging, 40*(11), 3229-3237.

Li, J., Chen, Q., Zhang, J., Zhang, Y., Lu, L., & Zuo, C. (2017). Efficient quantitative phase microscopy using programmable annular LED illumination. *Biomed Opt Express, 8*(10), 4687-4705.

Lin, Y. Z., Huang, K. Y., & Luo, Y. (2018). Quantitative differential phase contrast imaging at high resolution with radially asymmetric illumination. *Opt Lett, 43*(12), 2973-2976.

Nguyen, T. L., Pradeep, S., Judson-Torres, R. L., Reed, J., Teitell, M. A., & Zangle, T. A. (2022). Quantitative Phase Imaging: Recent Advances and Expanding Potential in Biomedicine. *ACS Nano*.

Streibl, N. (1985). Three-dimensional imaging by a microscope. *Optical Society of America, 2*(2).

Tian, L., & Waller, L. (2015). Quantitative differential phase contrast imaging in an LED array microscope. *Opt Express, 23*(9), 11394-11403.

Tian, L., Wang, J., & Waller, L. (2014). 3D differential phase-contrast microscopy with computational illumination using an LED array. *Opt Lett, 39*(5), 1326-1329.

Vyas, S., Li, A.-C., Lin, Y.-H., Yeh, J. A., & Luo, Y. (2022). Isotropic quantitative differential phase contrast imaging techniques: a review. *Journal of Physics D: Applied Physics, 55*(18).

Sedımentary Features Of The Uzunçarşıdere Formatıon (Paleocene-Lower Eocene) Around Lezgi (Ankara, Türkiye)

Ali Müjdat Özkan[1]
Ayla Bozdağ

Introduction

Offering a wide spread in the study area; The unit, which consists of conglomerate, sandstone, mudstone, clayey limestone marl, and andesitic lava spread, took its name from Uzunçarşı Creek in the south of Orhaniye Village. Gökten et al. (1988) first defined and named this unit under the name of Uzunçarşıdere Formation. In this study, the unit was studied under the name of Uzunçarşıdere Formation.

The formation crops out in the study area, on the slopes of Uzunçarşı Creek, Lülük Hill, Yayla Hill, Asmalı Hill, east of Güvenç Village, Lezgi Village, and its surroundings, Tabyebayır Hill and Deveboynu Hill (Figure 1).

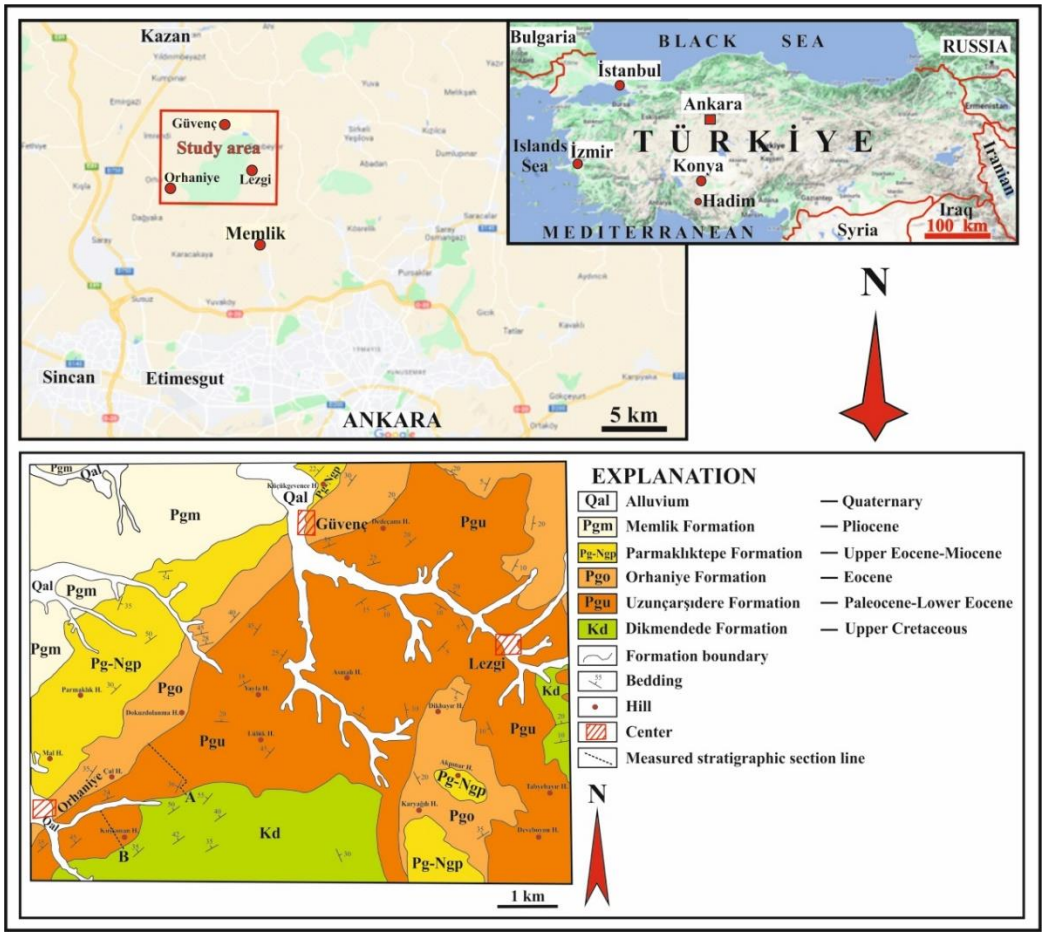

Figure 1. Location (GoogleMaps) and geological map of the study area (modified from Özkan and Ayaz, 2004)

[1] Assoc. Prof. Dr., Konya Technical University,

Sedimentary Characteristics of Uzunçarşıdere Formation

The Uzunçarşıdere Formation is predominantly composed of yellow, red, and gray colored conglomerate, green, red, gray colored sandstone, red, green, purple mudstone, yellow, beige limestone, and beige marls.

Conglomerates, which are generally observed at the base of the formation, are grain-supported, polygenic, poorly sorted, medium-tight calcite cemented. The pebbles of the polygenic conglomerate are composed of gray-colored limestone, white and gray-colored chert, burgundy-colored phyllite, green metasandstone, and black gabbro pebbles. The maximum grain diameter of the conglomerate is 40 cm and its matrix is sand. Normal grading, reverse grading, and imbricated structure are observed at some levels within the conglomerates (Figures 2, 3, 4). Sandstones overlie the conglomerates with a gradual transition. Conglomerates and sandstones continue for several hundred meters laterally.

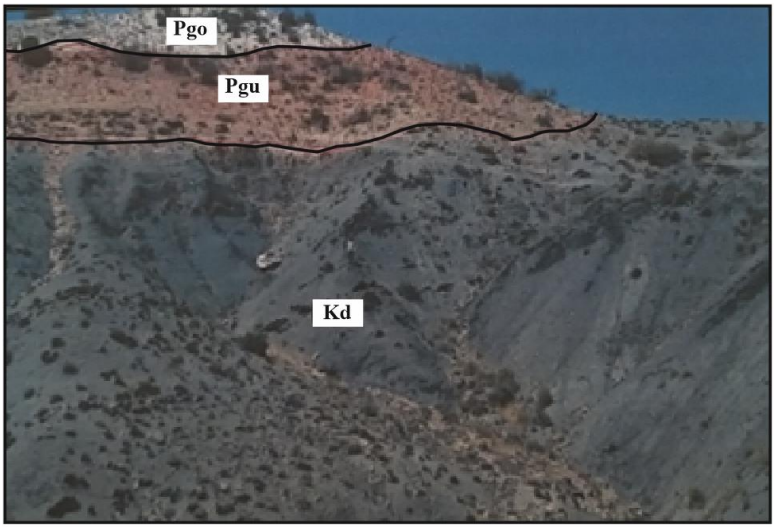

Figure 2. Boundary relationship of Dikmendede (Kd), Uzunçarşıdere (Pgu) and Orhaniye (Pgo) formations (looking northeast from the northeast hillside of Kuşkonan Tepe)

Figure 3. Normal grading was observed in the conglomerates of the Uzunçarşıdere Formation (west of Lezgi). Scale (hammer length: 28 cm)

Sandstones with medium-fine-grained and widespread cross-bedding also contain tuffite units at some levels. The succession first passes to yellow and red colored mudstones towards the top, followed by white-colored lacustrine limestones that show little laterally spread. At the

top, the unit ends with an alternation of cream-colored limestone and marl containing gray and white colored chert bands (Figures 5, 6, 7).

Figure 4. Reverse gradation observed in the conglomerates of the Uzunçarşıdere Formation (north of Asmalı Tepe). Scale (hammer length: 28 cm)

Figure 5. The imbricate structure observed in the conglomerates of the Uzunçarşıdere Formation (west of Lezgi). Scale (hammer length: 28 cm)

Figure 6. Convoluted lamination observed in the sandstones of the Uzunçarşıdere Formation (northeast of Kayaönü Dere). Scale (pencil length: 14 cm)

Figure 7. The cherty (Ch) limestone (Ls) observed in the Uzunçarşıdere Formation (east of Dedeçamı Tepe). Scale (hammer length: 28 cm)

The Uzunçarşıdere Formation also includes an andesitic lava deposit south of Orhaniye Village. This lava bed, which is less widespread laterally, is brown, gray in color, and massive (Figure 8).

Figure 8. Yellowish gray colored mudstone (Ms), sandstone (Ss), and red-colored sandstone alternation and gray-colored andesitic lava (Al) spread observed in Uzunçarşıdere Formation (looking northwest from the north of Dam Dere)

To the south of Güvenç Village, the Uzunçarşıdere Formation shows a green-colored sandstone-shale alternation (Figure 9).

In the sandstone samples taken from the Uzunçarşıdere Formation, 10-30% monocrystalline quartz, 0-10% polycrystalline quartz, 1-10% feldspar, 5-25% rock particles, 1-4% mica, 1-3% heavy mineral, 20-40% sparry calcite cement, 1-50% iron oxide cement, 3-10% clay matrix were observed. Sandstones are named litarenite according to Folk's (1968) classification.

Monocrystalline quartzes are mostly flat extinction and slightly wavy extinction. Quartz grains are mostly angular and less often round in shape. Polycrystalline quartzes are mostly in the form of semi-round and less angular grains. Feldspar minerals are mostly composed of plagioclase and lesser orthoclase. Plagioclases are generally albite twinned and exhibit semi-

angular and angular shapes. Orthoclases are generally wavy extinction and are observed as semi-round and round. The rock particles in our samples are mostly composed of carbonate and chert grains, with lesser volcanic and metamorphic grains. Mica minerals are mostly muscovite and less biotite. Muscovites are in the form of highly birefringent and platy crystals and exhibit unidirectional cleavage. Biotite is observed as brown and plate-like crystals. Generally, opaque minerals and epidotes were observed as heavy minerals. In our samples, mostly drase sparry calcite and amorphous iron cement, and very little clay cement were encountered.

Figure 9. Sandstone (Ss)-shale (Sh) alternation observed in the Uzunçarşıdere Formation. A dark brown color is observed in the sandstones due to oxidation at the lower levels, while a yellowish color is observed at the upper levels (South of Güvenç Village)

Another component of the Uzunçarşıdere Formation includes marl, 40-50% carbonate particles, 50% clay, 2-4% intraclast, and 1-2% extraclasts. Grain-supported carbonate particles in the clay matrix and a few quartz and plagioclase particles were observed in marls. In some levels of the marls, lamination consisting of intercalation of bioclastic fragments and clay is also observed (Figure 10).

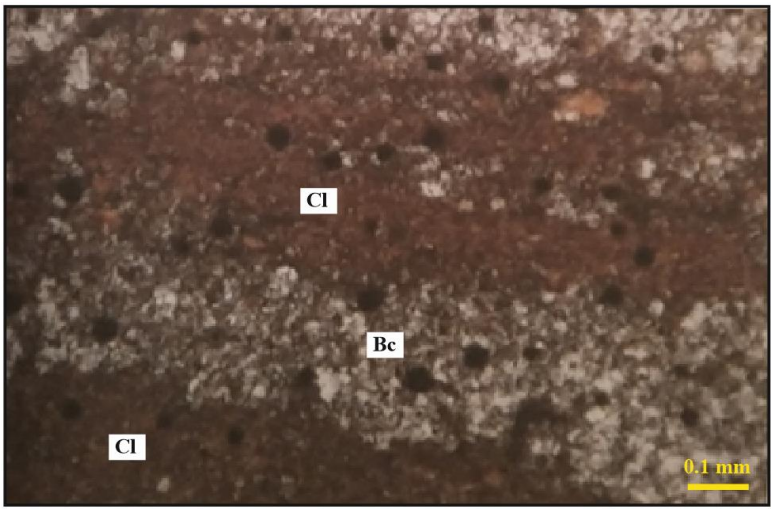

Figure 10. Lamination consisting of an alternation of bioclasts (Bc) and clay (Cl) observed in marls of the Uzunçarşıdere Formation (PPL)

Another component of the Uzunçarşıdere Formation consists of limestones, 35% intraclast, 4-6% pellet, 7-9% micritic matrix, and 50-52% sparry calcite cement (Figure 11). Limestone was named packstone according to Dunham's (1962) classification.

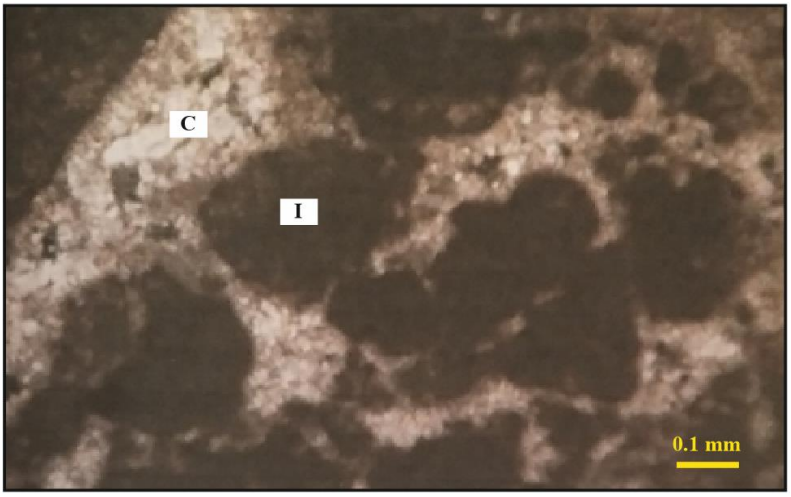

Figure 11. Sparicalcite drase cement (C) and intraclasts (I) observed in the limestones of the Uzunçarşıdere Formation (PPL)

The type section of the Uzunçarşıdere Formation was measured from approximately 2 km east of the Orhaniye Village to the northeast of Çal Tepe in the northwest direction (Figures 1 and 12; Özkan and Ayaz, 2004). A reference section from the Uzunçarşıdere Formation was taken from the southeast of the Orhaniye Village, from the south of Kuşkonan Tepe, to the northwest (Figures 1 and 12).

While the Uzunçarşıdere Formation overlies the Dikmendede Formation (Upper Cretaceous) with an angular unconformity from the bottom, it is overlain by the Parmaklıktepe Formation (Paleocene-Lower Eocene) conformably (Figure 2). While the thickness of the Uzunçarşıdere Formation is 260 m according to the type section, it was expressed as 500 m by Ocakoğlu (1998).

In this study, no fossils that could give an age from the formation were found. Gökten et al. (1988) found ostracod shell sections in the lacustrine limestones of the Uzunçarşıdere Formation and stated that the clayey parts of the formation were sterile in terms of spores and pollen. Gökten et al. (1988) evaluated the age of the Uzunçarşıdere Formation as probably Paleocene-Lower Eocene based on stratigraphic relationships. In this study, the age of the Uzunçarşıdere Formation was determined by Gökten et al. (1988), it was considered as Paleocene-Lower Eocene.

The Uzunçarşıdere Formation was developed in a braided stream and lacustrine environment as a depositional environment.

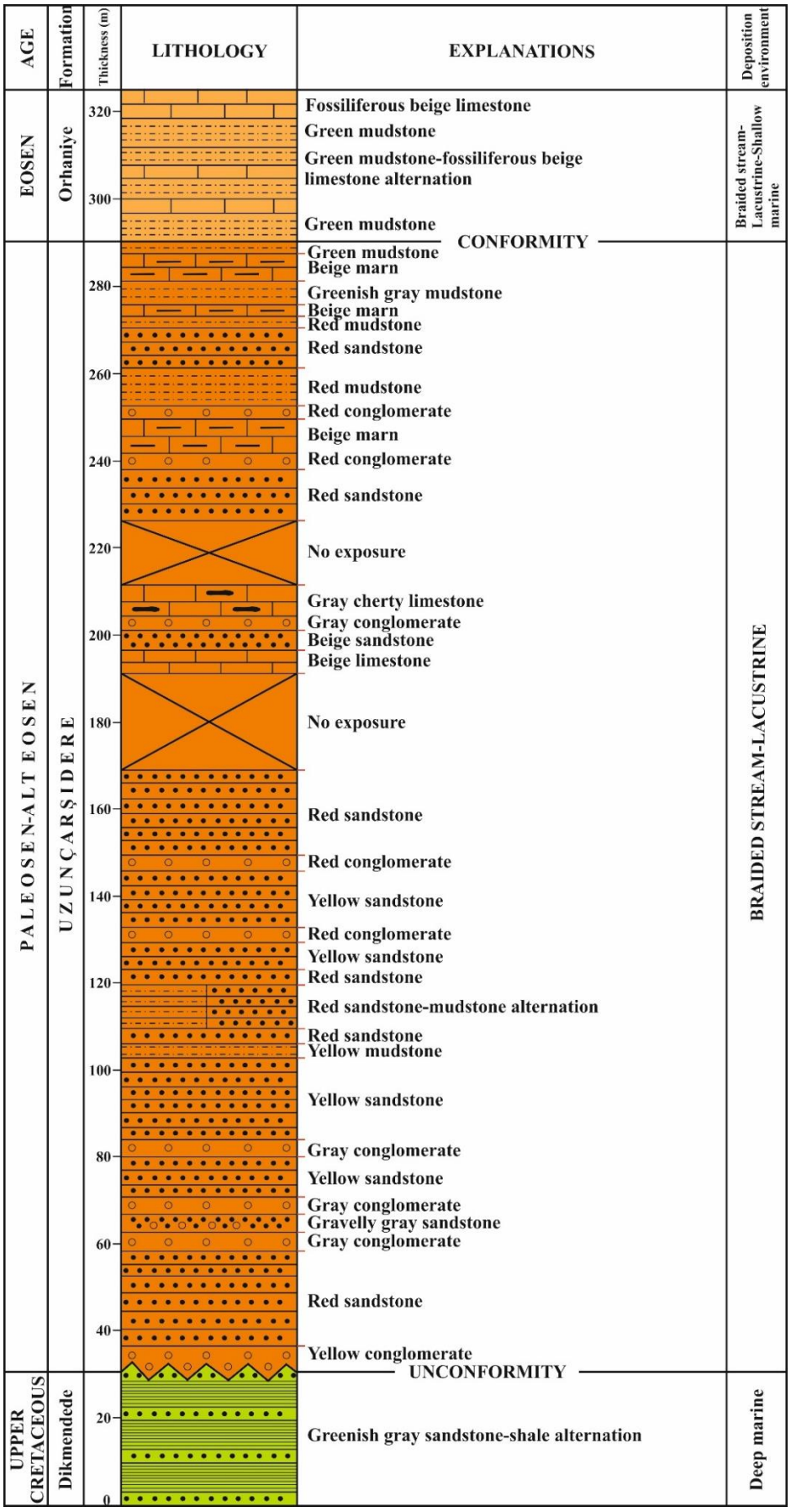

Figure 12. Uzunçarşıdere Formation type section (modified from Özkan and Ayaz, 2004)

REFERENCES

Dunham, R. J. (1962). Classification of carbonate rocks according to depositional texture. *Mem. Am. Assoc. Pet. Geol. 1,* 108-121.

Folk, R. L. (1968). Petrology of sedimentary rocks. Austin: Hemphill's.

GoogleMaps: https://www.google.com/maps/@40.079773,32.794561,12.21z

Gökten, E., Kazancı, N. and Acar, Ş. (1988). Ankara kuzeybatısında (Bağlım-Kazan arası) Geç Kretase-Pliyosen serilerinin stratigrafisi ve tektoniği. *MTA Dergisi, 108,* 69-81.

Ocakoğlu, F. (1998). Orhaniye bölgesi (Ankara kuzeyi) Üst Kretase-Eosen istifinin kil stratigrafisi: eski ortamsal ve iklimsel koşullarla ilişkin ip uçları. *Türkiye Jeoloji Bülteni, 41* (2), 31-40.

Özkan, A. M. and Ayaz, A. (2004). Güvenç-Memlik (Kazan-Ankara) yöresinin sedimantolojisi. *Selçuk Üniversitesi Bilimsel Araştırmalar Projesi*, Proje no: 2003/024.

Petrographıc Features of The Hacıalabaz Formatıon (Upper Jurassıc) Lımestones North Of Hadım (Konya, Türkiye)

Ali Müjdat ÖZKAN[1],
Salih DİNÇ[2]

Introduction

This study, it was aimed to determine the sedimentary petrographic properties of the Late Jurassic Hacıalabaz Formation limestones located in the north of Hadim (Konya, Türkiye) district (Figure 1). A detailed stratigraphic study in the study area was made by Turan (1990), but the carbonates defined as Hacıalabaz limestone were not studied in detail.

The unit, which consists of dolostone, calcitic dolostone, dolomitic limestone, and limestone, was first described by Demirkol (1981) in the Sultan Mountains region under the name "Hacıalabaz limestone". Later, the unit was defined and named “Ovacık limestone” by Turan (1990) in and around the study area. However, Turan (1997) named this unit "Hacıalabaz limestone", adhering to the naming principle later on. Özkan and Dinç (2008) defined and examined the unit under the name of Hacıalabaz Formation, as they saw it at the formation level.

The formation, which starts with gray, dark gray, medium-thick bedded, sugar-textured dolomitic limestones containing micritic intermediate levels at the base, passes into gray-colored, medium-bedded limestones towards the top. At higher levels, it continues with dark gray colored, medium-thick bedded, brecciated limestone, and dolomitized intermediate levels at some levels. While the dolomitic levels are composed of euhedral or subhedral dolomite crystals, it has been observed that the limestones are mudstone, wackestone, packstone, and crystalline limestone from bottom to top.

The Hacıalabaz Formation, which overlies the Late Cambrian-Early Ordovician-aged Seydişehir Formation from below with angular unconformity, is overlain by the Late Cretaceous-aged Saytepe Formation with an angular unconformity. According to the 3 measured stratigraphic sections taken from the study area, the Hacıalabaz Formation starts with limestone in some areas and dolostone in some areas at the base (Figure 2). The unit continues upward as limestone-dolomitic limestone-calcitic dolostone and dolostone (Figure 2).

The Hacıalabaz Formation was transgressively developed in a shelf environment that started with carbonate deposition on the Seydişehir Formation.

[1] Assoc. Prof. Dr., Konya Technical University,
[2] Assist. Prof. Dr., Batman University,

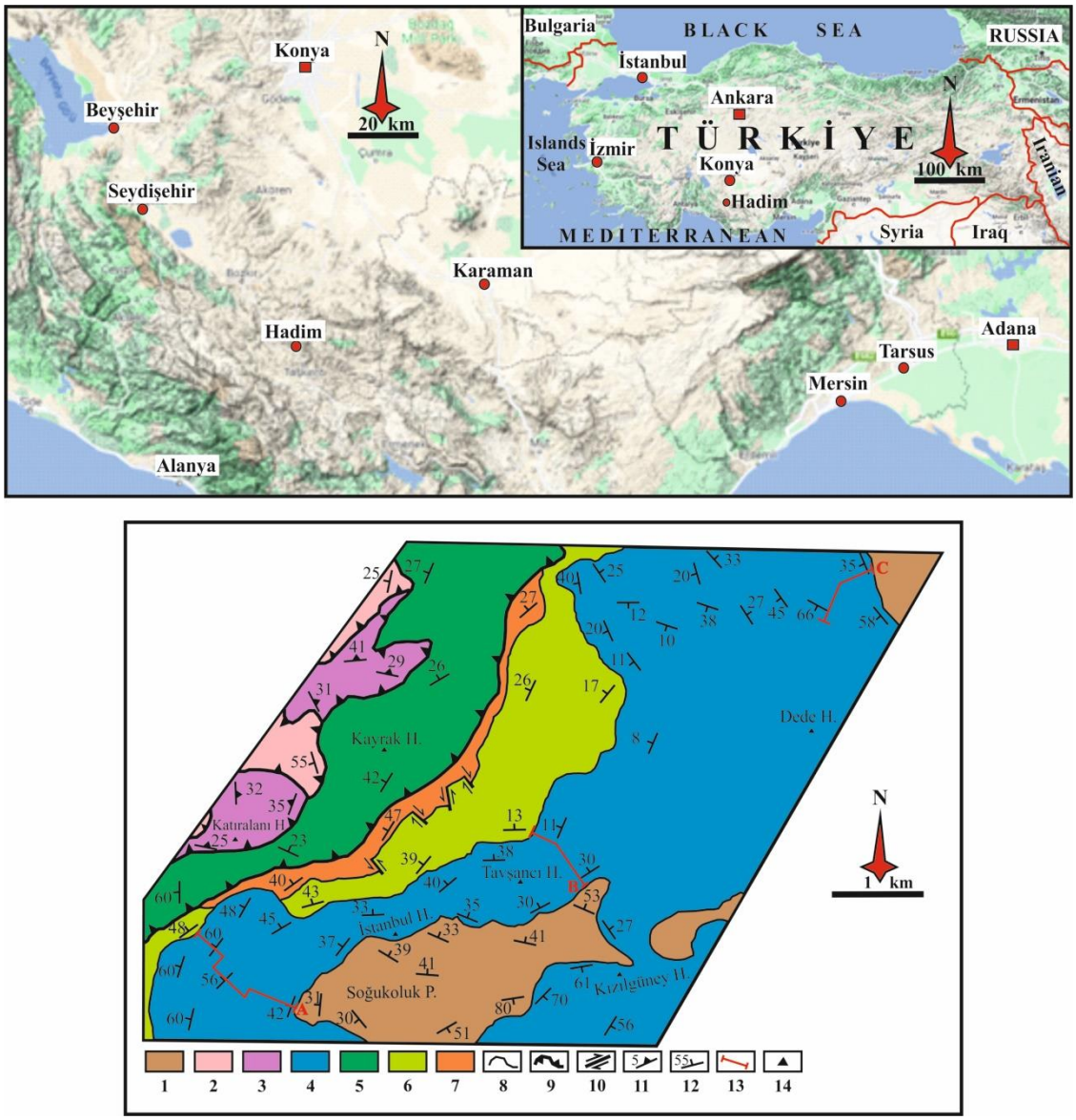

Figure 1. Location (https://www.google.com/maps/@37.5369627,39.5182898,5z/data=!5m1!1e4) and geological map of the study area (modified from Turan, 1990).

1) Seydişehir Formation (Upper Cambrian-Lower Ordovician), 2) Kahtepe Formation (Upper Permian), 3) Zindancık Complex (Triassic), 4) Hacıalabaz Formation (Upper Jurassic), 5) Taşkent Melange (Upper Cretaceous), 6) Saytepe Formation (Upper Cretaceous), 7) Çobanağacık Formation (Lutetian), 8) formation boundary, 9) thrust fault, 10) strike-slip fault, 11) cleavage, 12) bedding, 13) measured stratigraphic section line, 14) hill

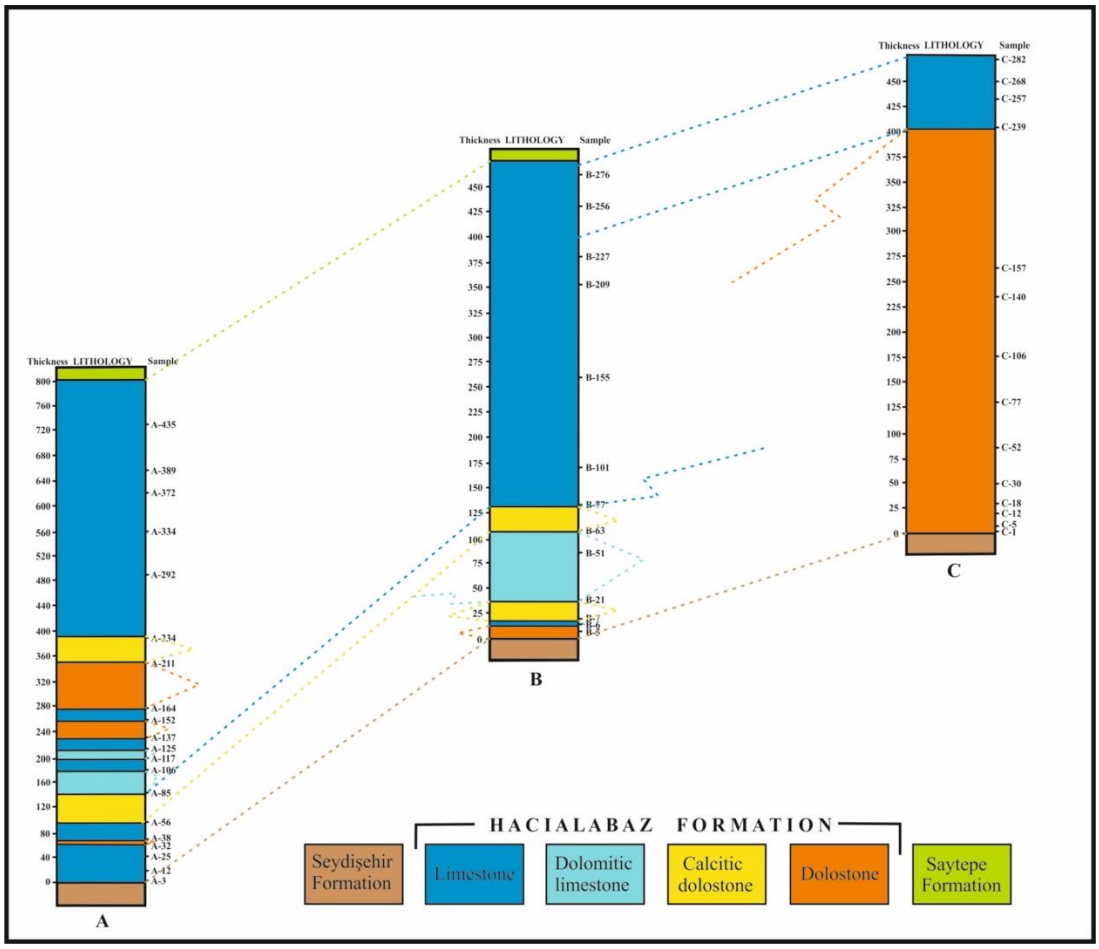

Figure 2. Correlation of measured stratigraphy sections taken from the study area (modified from Özkan and Dinç, 2008)

Results

Petrographic Properties of İstanbultepe Measured Stratigraphy Section (A) Samples

Twenty samples were taken from the measured stratigraphic section taken from the southwest of Istanbul Tepe (Figure 2). 15 of these samples are limestone (2 samples of dolomitic limestone), and 5 of them are dolostone (2 samples of calcitic dolostone). According to Dunham (1962), the limestones begin as mudstone at the base. It transitions upwards to wackestone and continues with mudstone. A thin layer of dolostone (according to Compton, 1962) is located on the mudstone. Packstone, calcitic dolostone, dolomitic limestone, and mudstone overlie the dolostone. Above, dolomitic limestone, packstone, dolostone, wackestone, dolostone, calcitic dolostone, and packstone are found. At the top are mudstone, wackestone, crystalline limestone, and mudstone (Figure 2).

In sample A-3, 3% fossil and 97% micrite were observed and the rock was named as mudstone (Table 1). In mudstones, where high porosity (Figure 3a) and breccia (Figure 3b, c) are observed in places, iron oxide veins were also observed (Figure 3a, b, c).

12% fossil, 81% micrite, and 7% sparry were observed in the A-12 sample (Table 1). Sparrytes are found in the form of void-filling cement, and micrites are found in the form of a matrix (Figure 3d, e). As the fossils are seen as a whole, they are mostly seen as bio-molds (Figure 3d), and green algae (especially *Clypeina* sp.) molds and fossils are common (Figure

3d). Small void porosity and crack porosity were observed in this sample (Figure 3e). Fine veins with iron oxide are also common in this sample (Figure 3e).

Sample A-25 consists entirely (100%) of micrite (Table 1; Figure 3f). A high porosity rate was observed in this sample (Figure 3f).

Sample A-38 contains 37% fossil, 7% pellet, 52% micrite, and 4% sparry (Table 1). Fossils can generally be whole or can be observed as bio-molds (Figure 3g, h, j). Some molds contain the development of dolomite rhombohedra (Figure 3j). Calcite-filled veins, micro-faulting (Figure 3g), and sparry calcite-filled stylolite (Figure 3j) were also observed in this sample.

The wackestone feature was also observed in this sample (Figure 3g). 40% fossil and 60% micrite are found in the A-85 sample, which exhibits wackestone-packstone (Figure 3k, m, n) characteristics (Table 1). Fossils are whole and in the form of bioclasts, dolomites are in the form of disseminated rhombs (Figure 3k, m, n). Sparry calcite veins (Figure 3m, n) and iron oxide stylolites (Figure 3k, m) were observed in this sample.

18% fossil, %5 intraclast, 70% micrite, and 12% sparry were observed in the A-117 sample (Table 1). In this wackestone sample, mostly green algae (especially *Clypeina*; Figure 4b) and fewer bioclasts (Figure 4a, b) are found. In this sample, sparry calcitic veins, sparry calcitic and iron oxide-filled stylolites (Figure 4a, b), and dolomitization along the stylolites (Figure 4a, b) are also observed.

In the packstone sample A-125, there are 38% fossils and 62% micrite (Table 1), and the fossils are observed as whole and as bioclasts (Figure 4c, d). In this sample, iron oxide-filled veins (Figure 4d), stylolites (Figure 4c, d), and crack porosity (Figure 4d) are also found.

20% fossil, 72% micrite, and 8% sparry calcite were observed in wackestone sample A-152 (Table 1). Fossils in this sample are found in the form of whole, bio-mold, and bioclasts (Figure 4e), while sparry calcite-filled stylolites and veins are also observed (Figure 4e).

In the packstone sample A-234, 43% fossils, 7% intraclasts, 10% pellets, and 40% micrite were observed (Table 1; Figure 4f, g). In this sample, mostly green algae (especially *Clypeina*) and fewer foraminiferal fossils and bioclasts are found (Figure 4f, g). The sample also contains sparry calcitic veins and iron oxide-filled stylolites (Figure 4f).

12% fossil, 8% intraclast, 20% pellet, 40% micrite, and 20% sparry calcite were observed in the packstone A-292 sample (Table 1). The fossils in this sample are in the form of unidentified bioclasts. Sparry calcites are in the form of void-filling cement (Figure 4h), porosities are bird's eye and/or fenestra, some of them are empty and some of them are sparry calcite-filled (Figure 4j). Sparry calcite-filled stylolites (Figure 4j) were also observed in this sample.

3% fossil, 2% intraclast, 3% pellet, 89% micrite, and 3% sparry calcite were observed in the mudstone A-334 sample (Table 1). Fossils in this sample are foraminifera and bioclasts (Figure 4k). The porosities are bird's eye and/or fenestra shaped, most of them are empty, and some of them are sparry calcite-filled (Figure 4k). This sample also contains iron oxide-filled veins and stylolites.

15% fossil, 5% intraclast, 75% micrite, and 5% sparry calcite were observed in the wackestone sample A-372 (Table 1). In this sample, in which the brecciated zone (Figure 4m) is also seen, the fossils are mostly in the form of bio-mold (Figure 4m), and thin stylolites with iron oxide (Figure 4m).

6% fossil, 82% micrite, and 12% sparry calcite were observed in the mudstone A-435 sample (Table 1). Fossils in this sample are mostly in the form of bio-mold (Figure 4n). In this

sample sparry calcite veins (Figure 4n), iron oxide-filled thin stylolites (Figure 4n), and stylolitic porosity was also observed.

Table 1. Microscopic properties of samples taken from İstanbultepe measured stratigraphy section

Sample	Calcite %	Dolomite %	Fossil %	Intraclast %	Ooid %	Pellet %	Spar %	Micrite %	Rock name
A-435	100	-	6	-	-	-	12	82	Mudstone
A-389	40	60	-	17	-	-	21	62	Calcitic dolostone
A-372	100	-	15	5	-	-	5	75	Wackestone
A-334	100	-	3	2	-	3	3	89	Mudstone
A-292	100	-	12	8	-	20	20	40	Packstone
A-234	100	-	43	7	-	10	-	40	Packstone
A-211	46	54	6	-	-	-	54	40	Calcitic dolostone
A-164	8	92	-	-	-	-	100	-	Dolostone
A-152	100	-	20	-	-	-	8	72	Wackestone
A-137	4	96	-	-	-	-	100	-	Dolostone
A-125	100	-	38	-	-	-	-	62	Packstone
A-117	80	20	18	5	-	-	12	65	Dolomitic limestone
A-106	100	-	-	-	-	-	10	90	Mudstone
A-85	87	13	40	-	-	-	-	60	Dolomitic limestone
A-56	20	80	-	-	-	-	30	70	Calcitic dolostone
A-38	100	-	37	-	-	7	4	52	Packstone
A-32	3	97	-	-	-	-	92	8	Dolostone
A-25	100	-	-	-	-	-	-	100	Mudstone
A-12	100	-	12	-	-	-	7	81	Wackestone
A-3	100	-	3	-	-	-	-	97	Mudstone

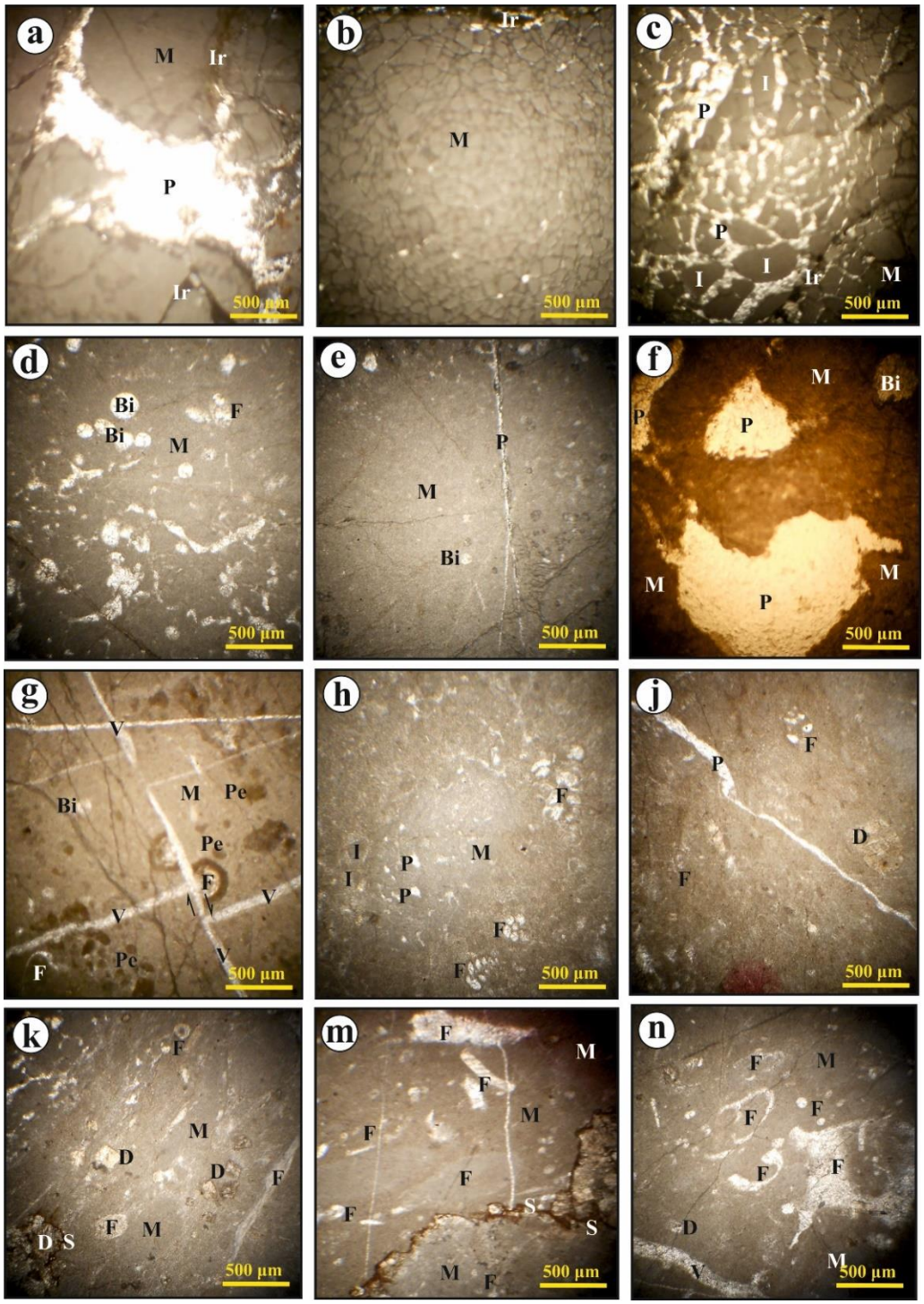

Figure 3. Microphotographs of samples taken from İstanbultepe measured stratigraphy section.

a) Mudstone, micrite (M), porosity (P), iron-oxide veins (Ir) (sample no: A-3), b) brecciated mudstone (sample no: A-3), c) brecciated mudstone, I: intraclast (sample no: A-3), d) wackestone, F: fossil, Bi: bio-mold, (sample no: A-12), e) wackestone (sample no: A-12), f) high-porosity mudstone (sample no: A-25), g) packstone, micrite, fossil, pellet (Pe), sparry calcite vein, arrows: micro-fault (sample no: A-38), h) packstone, micrite, I: intraclast, fossil, porosity (sample no: A-38), j) packstone, micrite, Crack porosity (P), fossil, D: dolomite (sample no: A-38), k) dolomitic limestone (wackestone feature), micrite, fossil, dolomite, stylolite (S) (sample no: A-85), m) dolomitic limestone

(wackestone feature) (sample no: A-85), n) dolomitic limestone (wackestone feature) (sample no: A-85) (All photos were taken in the PPL)

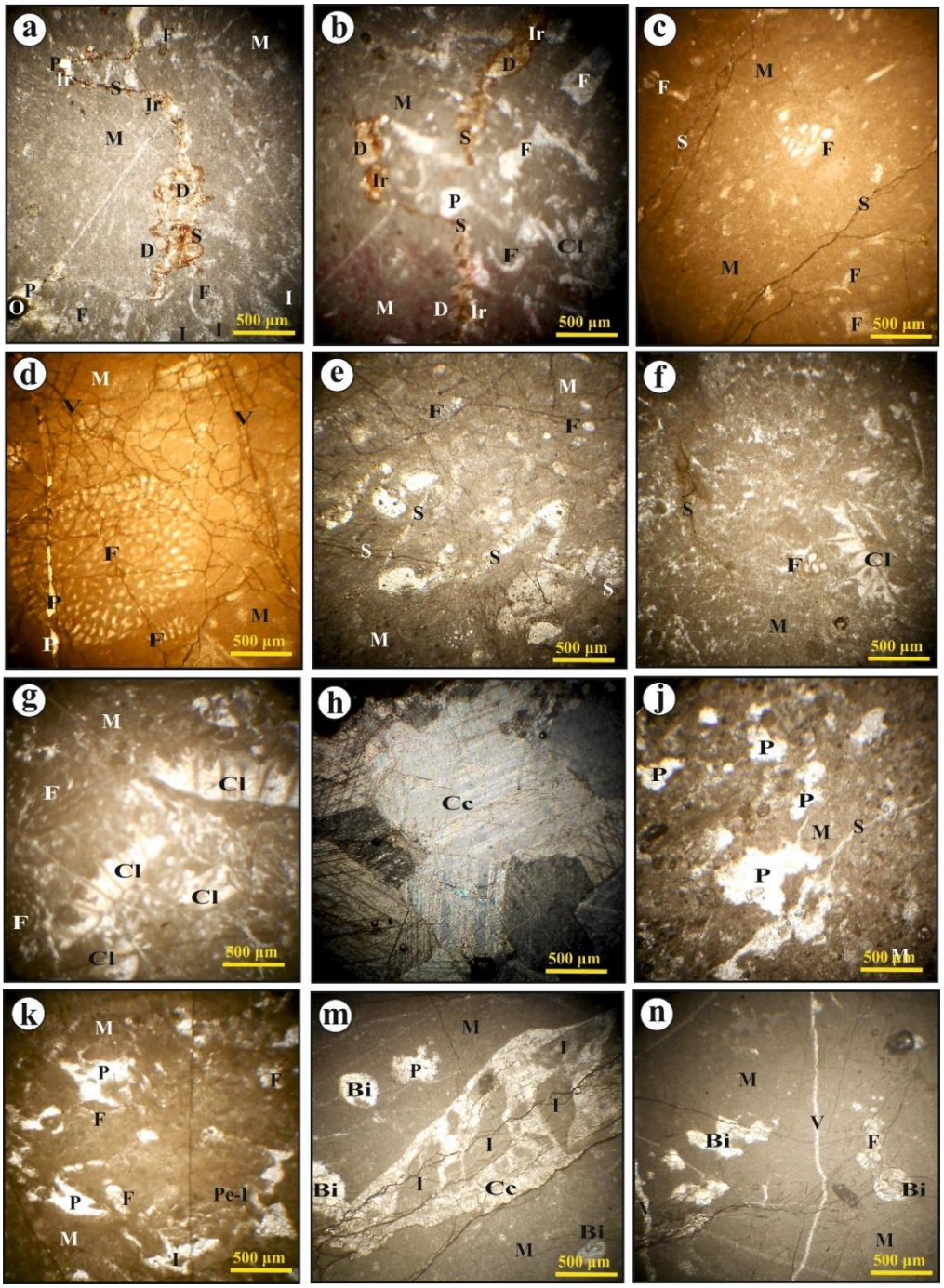

Figure 4. Microphotographs of samples taken from İstanbultepe measured stratigraphy section.

a) Dolomitic limestone (wackestone feature), micrite (M), fossil (F), opaque minerals (O), dolomite (D), stylolite (S) (Sample no: A-117), b) dolomitic limestone (wackestone feature), micrite, fossil, Clypeina (Cl), dolomite, stylolite, iron-oxide (Ir) (Sample no: A-117), c) packstone, micrite, fossil, stylolite (Sample no: A-125), d) packstone, micrite, crack porosity, fossil, vein (Sample no: A-125), e) wackestone, micrite, fossil, stylolite (Sample no: A-152), f) packstone, micrite, fossil, stylolite, Clypeina (Cl) (Sample no: A-234), g) packstone, micrite, fossil, stylolite, Clypeina (Cl) (Sample no: A-234), h) packstone, sparry calcite-cement (Cc) (Sample no: A-292), j) packstone, micrite,

stylolite, porosity (Sample no: A-292), k) mudstone, micrite, fossil, porosity, pellet-intraclast (Pe-I), intraclast (I) (Sample no: A-334), m) wackestone, micrite, bio-mold (Bi), sparry calcite-cement (Cc), porosity (Sample no: A-372), n) mudstone, micrite, bio-mold, fossil, vein (V) (Sample no: A-435) (All photos were taken in the PPL, except h [XPL])

Petrographic Properties of Tavşancıtepe Measured Stratigraphic Section (B) Samples

Thirteen samples were taken from the measured stratigraphic section taken from the southeast of Tavşancı Tepe (Table 2). 10 of these samples are limestone (2 samples of dolomitic limestone), 3 of them are dolostone (2 samples of calcitic dolostone). Carbonates begin as dolostone at the base. According to Dunham (1962), it transitions to mudstone towards the top and continues with calcitic dolostone and dolomitic limestone. Calcitic dolostone, packstone, and wackestone overlie the dolomitic limestone. Wakestone is located at the top (Table 2).

4% fossil, 81% micrite, and 15% sparry calcite were observed in the mudstone B-6 sample (Table 2). The foraminiferal fossils in this sample are whole, and the spar calcite cement developed as a void filling.

10% fossil and 90% micrite were observed in the B-21 sample, which is dolomitic limestone (Table 2). In this example, the fossils are mostly foraminifera and all fossils are in the form of bio-molds and bioclasts (Figure 5a, b, d). The dolomites are in the form of disseminated rhombs (Figure 5a, b, c, d) and stylolitic dolomites (Figure 5b).

8% fossil and 92% micrite were observed in the B-51 sample, which is dolomitic limestone (Table 2). Fossils in this sample are mostly green algae (probably *Clypeina*) and less commonly foraminifera (Figure 5e, f). Dolomites are generally composed of euhedral and less commonly subhedral crystals (Figure 5e, f).

36% fossil and 64% micrite were observed in the packstone B-77 sample (Table 2). Fossils are in the form of green algae, foraminifera, and bioclasts (Figure 5g, h, j, k). In this sample, sparry calcite-filled veins and stylolites are also present (Figure 5h, j).

In the packstone, B-101 sample, 42% fossil, and 58% micrite were observed (Table 2). The fossils are mostly composed of all foraminifera, with fewer bioclasts and green algae (Figure 5m, n).

22% fossil, 43% micrite, and 35% sparry calcite cement were observed in the wackestone sample B-155 (Table 2). Fossils are in the form of whole foraminifera, bioclast, and micritized crinoid discs (Figure 6a). Allochems were bonded with sparry calcite cement and micritic matrix (Figure 6a).

40% fossil, 5% intraclast, 55% micrite, and 3% sparry calcite were observed in the packstone B-209 sample (Table 2). Fossils are in the form of green algae (especially *Clypeina*), foraminifera, and bioclasts (Figure 6b, c, d). In this sample, there are sparry calcite veins (Figure 6b), sparry calcite-filled stylolites (Figure 6d), and void-fill sparry calcite cement (Figure 6c).

In the packstone, B-227 sample, 25% fossil, 20% pellet, 50% micrite, and 5% sparry calcite were observed (Table 2). Fossils are mostly in the form of foraminifera and bioclasts (Figure 6e, f, g, h), sparry calcite cement cavity filling (Figure 6f, g, h), and fossil infill (Figure 6e). In this sample, the alizarin red-s staining technique was used in the section of Figure 6g and it was seen that it was entirely composed of calcite.

18% fossil, 13% intraclast, 7% pellet, 50% micrite, and 12% sparry calcite were observed in the packstone B-256 sample (Table 2). Fossils are in the form of green algae, foraminifera (Figure 6j, k, m), and some fossils show a geopetal structure (Figure 6j). In this sample, iron

oxide-replaced sparry calcitic veins (Figure 6k), sparry calcite, and iron oxide-filled stylolites (Figure 6m) were also observed.

7% fossil, 26% intraclast, 8% pellet, 31% micrite, and 28% sparry calcite were observed in the packstone B-276 sample (Table 2). The fossils in this sample could not be identified, but they were estimated to consist of ostracods and foraminifera (Figure 6n).

Table 2. Microscopic properties of samples taken from Tavşancıtepe measured stratigraphy section

Sample	Calcite %	Dolomite %	Fossil %	Intraklast %	Ooid %	Pellet %	Spar %	Micrite %	Rock name
B-276	100	-	7	26	-	8	28	31	Packstone
B-256	100	-	18	13	-	7	12	50	Packstone
B-227	100	-	25	-	-	20	5	50	Packstone
B-209	100	-	40	5	-	-	3	52	Packstone
B-155	100	-	22	-	-	-	35	43	Wackestone
B-101	100	-	42	-	-	-	-	58	Packstone
B-77	100	-	36	-	-	-	-	64	Packstone
B-63	37	63	-	-	-	-	57	43	Calcitic dolostone
B-51	70	30	8	-	-	-	-	92	Dolomitic limestone
B-21	75	25	10	-	-	-	-	90	Dolomitic limestone
B-7	49	51	5	-	-	-	87	8	Calcitic dolostone
B-6	97	3	4	-	-	-	15	81	Mudstone
B-5	9	91	-	-	-	-	90	10	Dolostone

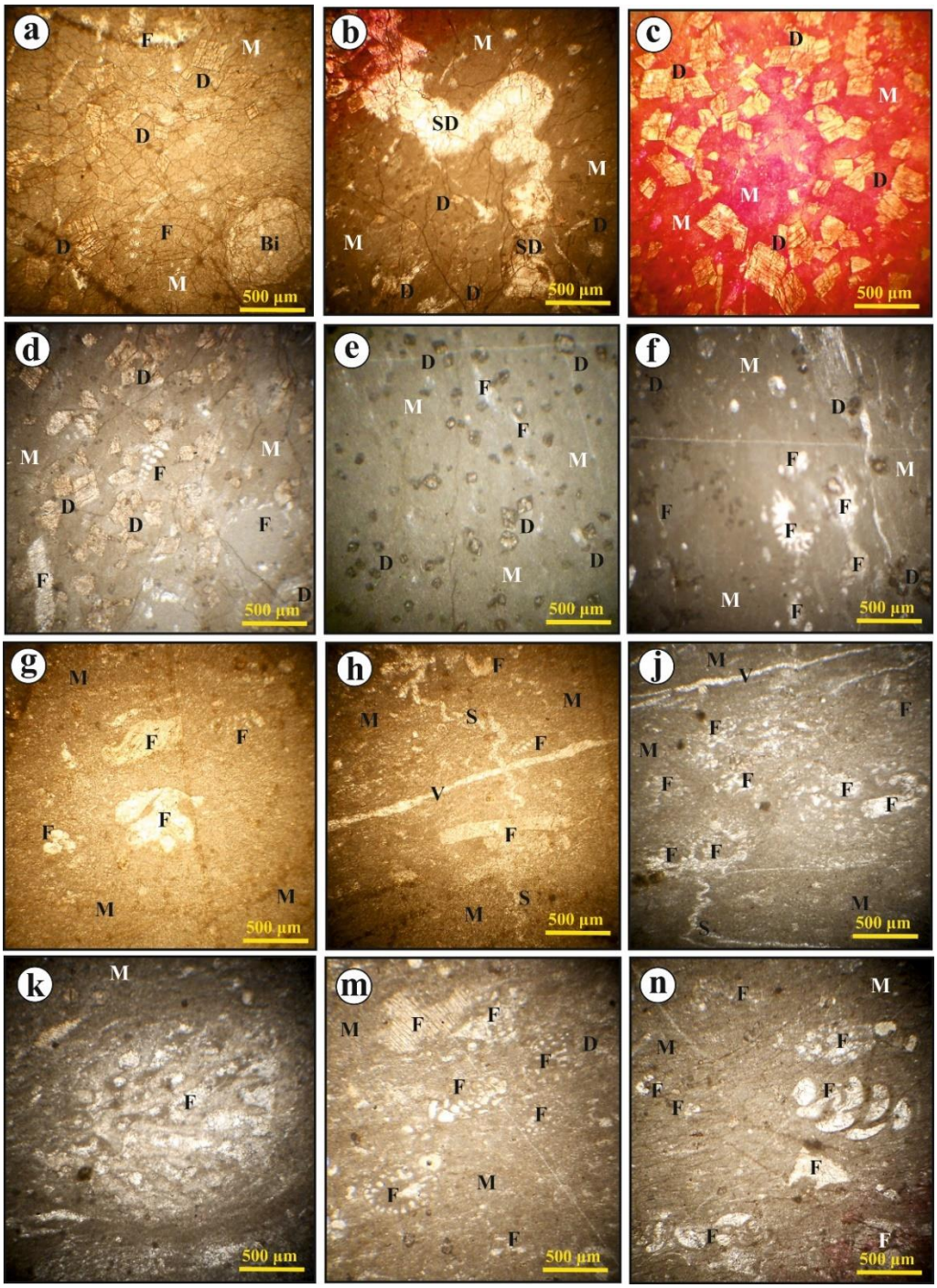

Figure 5. Microphotographs of samples taken from Tavşancıtepe measured stratigraphy section.

a) Dolomitic limestone, micrite (M), fossil (F), bio-mold (Bi), dolomite rhombs (D) (Sample no: B-21), b) dolomitic limestone, micrite, dolomite, stylolitic dolomite (SD), alizarin red-s (upper left corner) (Sample no: B-21), c) dolomitic limestone, micrite, dolomite rhombs (D), alizarin red-s (the whole section is painted) (Sample no: B-21), d) dolomitic limestone, micrite, fossil, dolomite, (Sample no: B-21), e) dolomitic limestone, micrite, fossil, dolomite (Sample no: B-51), f) dolomitic limestone, micrite, fossil, dolomite (Sample no: B-51), g) packstone, micrite, fossil (Sample no: B-77), h) packstone, micrite, fossil, stylolite (S), vein (V) (Sample no: B-77), j) packstone, micrite, fossil, stylolite, vein (Sample no: B-77), k) packstone, micrite, fossil (Sample no: B-77),

m) packstone, micrite, fossil, dolomite (Sample no: B-101), n) packstone, micrite, fossil (Sample no: B-101) (All photos were taken in the PPL)

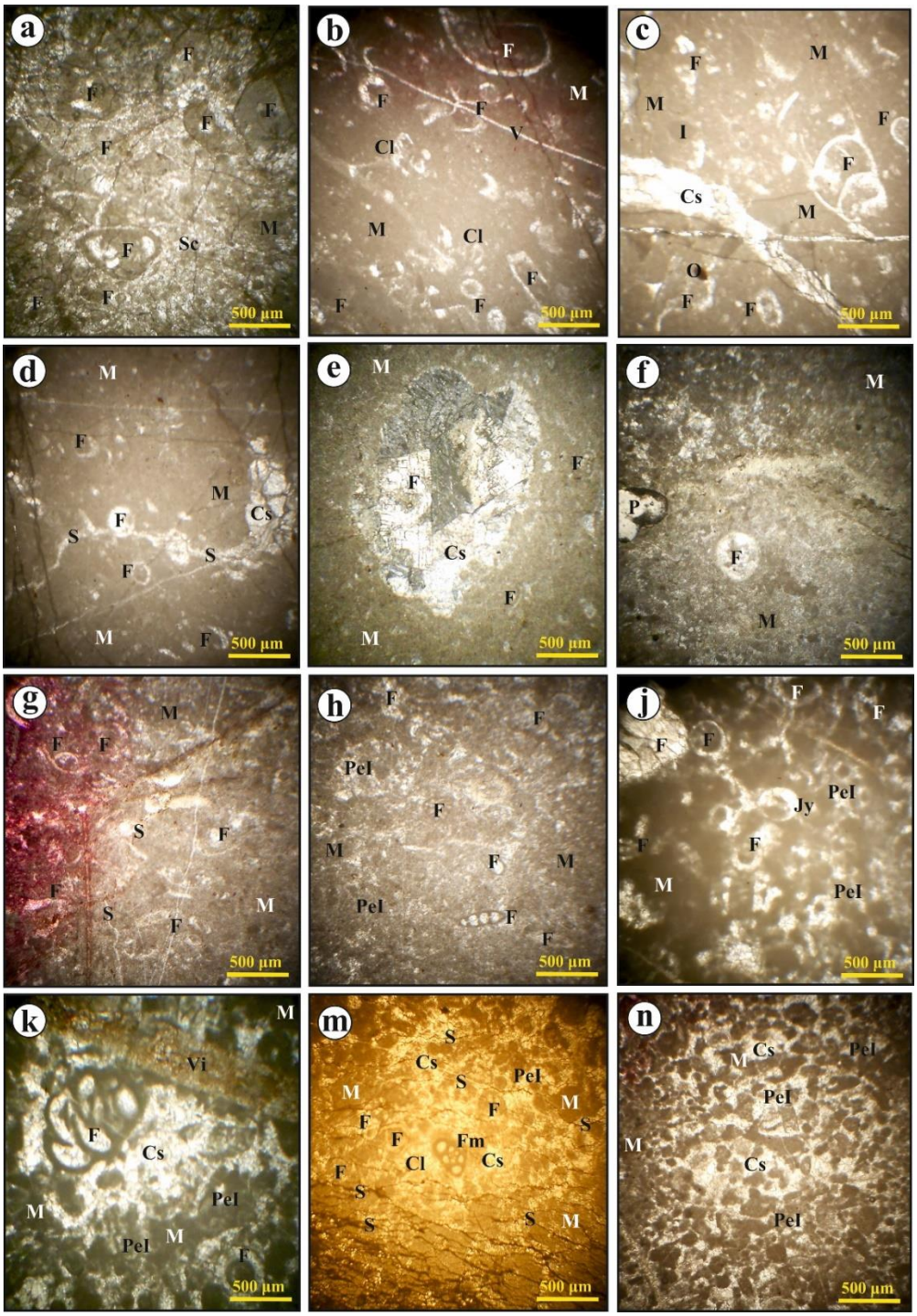

Figure 6. Microphotographs of samples taken from Tavşancıtepe measured stratigraphy section.

a) Wackestone, micrite (M), fossil (F), sparry calcite-cement (Sc) (Sample no: B-155), b) packstone, micrite, fossil, Clypeina (Cl), vein (V) (Sample no: B-209), c) packstone, micrite, fossil, intraclast (I), opaque minerals (O), sparry calcite-cement (Cs) (Sample no: B-209), d) packstone, micrite, fossil, stylolite (S), sparry calcite-cement (Cs) (Sample no: B-209), e) packstone, micrite, fossil, sparry calcite-cement (Cs) (Sample

no: B-227), f) packstone, micrite, fossil, vuggy porosity (P) (Sample no: B-227), g) packstone, micrite, fossil, stylolite (S) (Sample no: B-227), h) packstone, micrite, fossil, pellet-intraclast (PeI) (Sample no: B-227), j) packstone, micrite, fossil, pellet-intraclast, geopetal structure (Jy) (Sample no: B-256), k) packstone, micrite, fossil, pellet-intraclast, iron oxide-filled vein (Vi) (Sample no: B-256), m) packstone, micrite, fossil, pellet-intraclast, Clypeina, miliolid (Fm), stylolite, sparry calcite-cement (Cs) (Sample no: B-256), n) packstone, micrite, fossil, pellet-intraclast, sparry calcite-cement (Cs) (Sample no: B-276) (All photos were taken in the PPL, except e [XPL])

Petrographic Properties of Dedetepe Measured Stratigraphic Section (C) Samples

14 samples were taken from the measured stratigraphic section taken from the northeast of Dede Tepe. 10 of these samples are limestone (2 samples of dolomitic limestone), and 3 of them are dolostone (2 samples of calcitic dolostone). In the measured stratigraphic section of Dedetepe, the units begin with dolostone at the base and continue with calcitic dolostone after a thin mudstone. It transitions to dolomitic limestone towards the top and continues with calcitic dolostone. At the top, there is packstone and wackestone, while at the top there is packstone.

8% dolosparite and 92% micrite were observed in the mudstone sample C-239 (Table 3). The dolomites in this sample are disseminated, anhedral, and micro-spar in size. In this sample, in which no allochem is observed, there is only the micritic matrix as orthochem.

30% fossil, 9% intraclast, and 61% micrite were observed in the packstone sample C-257 (Table 3). The fossils are whole, bio-mold, and bioclasts and could not be identified, but were thought to be foraminifera and ostracod (Figure 7a, b, c, d, e). This sample has stylolitic porosity (Figure 7a) and void porosity (Figure 7d). In addition, sparry calcite-filled and iron oxide-filled stylolites (Figure 7a, b, c, d, e) and sparry calcite-filled veins (Figure 7b) were also observed in this sample.

47% fossils and 53% micrites were observed in the C-268 sample, which has packstone characteristics (Table 3). The fossils are in the form of whole, bio-mold, and bioclast (Figure 7f, g, h, j, k) and consist mostly of green algae (especially *Clypeina*; Figure 7h, j, k) and lesser foraminifera (Figure 7h). Iron oxide-filled stylolites (Figure 7f, g, h, j, k) are common in this sample. In addition, geopetal structure (Figure 7j, k) is observed in some fossils in this sample.

20% fossils, 14% intraclast, 5% pellets, and 61% micrites were observed in the packstone sample C-282 (Table 3). Fossils are in the form of whole, bio-mold, and bioclasts (Figure 7m, n), mostly composed of foraminifera. In this sample, sparry calcite-filled veins (Figure 7m, n) and iron oxide-filled intersecting stylolites (Figure 7m, n) are also present.

Table 3. Microscopic properties of samples taken from Dedetepe measured stratigraphy section

Sample	Calcite %	Dolomite %	Fossil %	Intraklast %	Ooid %	Pellet %	Spar %	Micrite %	Rock name
C-282	100	-	20	14	-	5	-	61	Packstone
C-268	100	-	47	-	-	-	-	53	Packstone
C-257	100	-	30	9	-	-	-	61	Packstone
C-239	92	8	-	-	-	-	8	92	Mudstone
C-157	-	1000	-	-	-	-	96	4	Dolostone
C-140	-	100	-	-	-	-	100	-	Dolostone
C-106	1	99	-	-	-	-	95	5	Dolostone

C-77	-	100	-	-	-	-	100	-	Dolostone
C-52	5	95	-	-	-	-	97	3	Dolostone
C-30	-	100	2	-	-	-	100	-	Dolostone
C-18	-	100	-	-	-	-	100	-	Dolostone
C-12	-	100	-	-	-	-	100	-	Dolostone
C-5	-	100	-	-	-	-	92	8	Dolostone
C-1	-	100	5	-	-	-	95	-	Dolostone

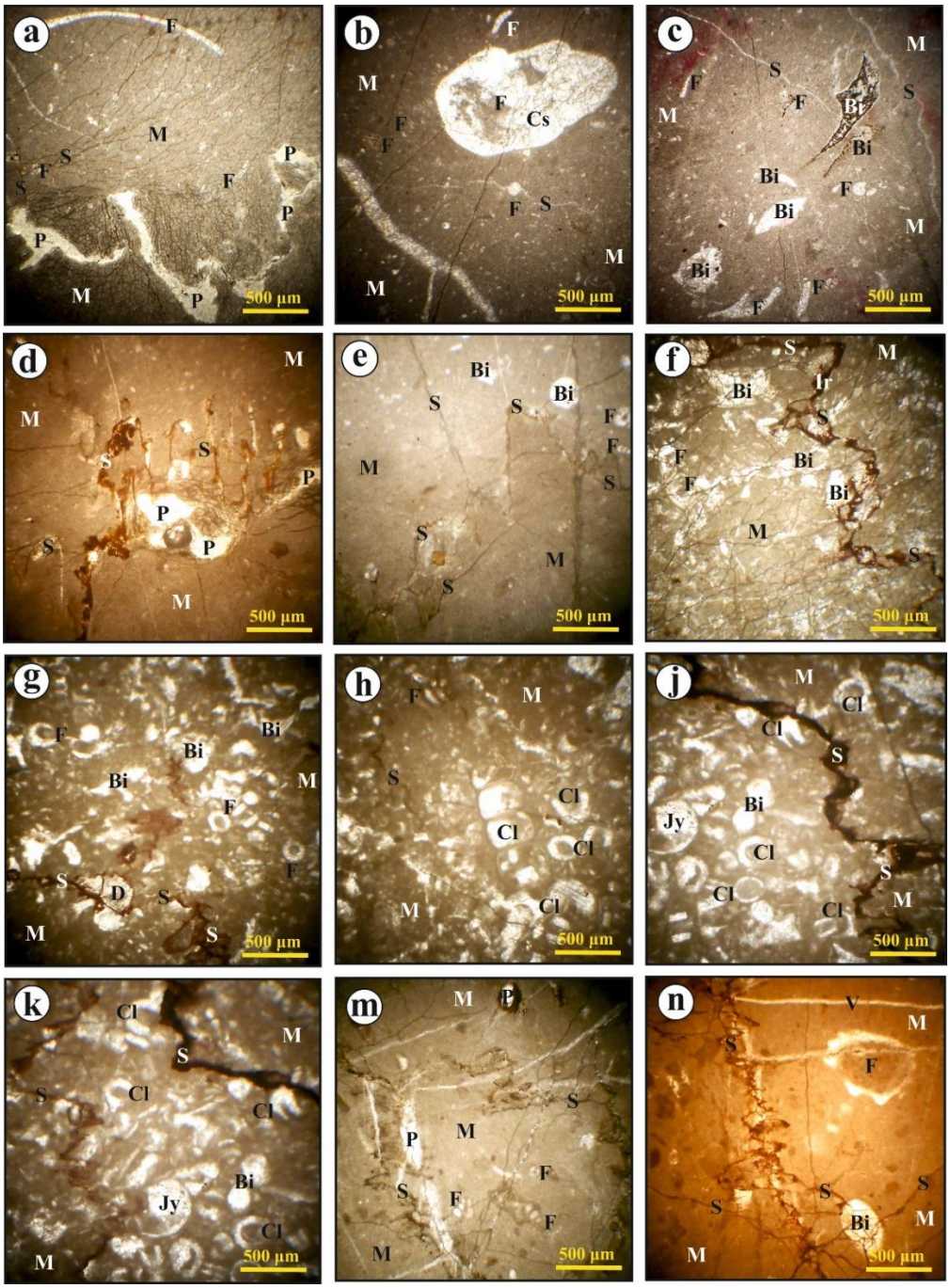

Figure 7. Microphotographs of samples taken from the Dedetepe measured stratigraphy section.

a) Packstone, micrite (M), Fossil (F), stylolite (S), porosity (P) (Sample no: C-257), b) Packstone, micrite, Fossil, stylolite, sparry calcite-cement (Cs), vein (Sample no: C-257), c) Packstone, micrite, fossil, stylolite, bio-mold (Bi), iron oxide (Ir) (Sample no: C-257), d) Packstone, micrite, iron oxide filled stylolite, porosity (Sample no: C-257), e) Packstone, micrite, fossil, stylolite, bio-mold, (Sample no: C-257), f) Packstone, micrite, fossil, iron oxide filled stylolite, bio-mold, iron oxide (Sample no: C-268), g) Packstone, micrite, fossil, iron oxide filled stylolite, bio-mold, dolomite (D) (Sample no: C-268), h) Packstone, micrite, fossil, stylolite, Clypeina (Cl) (Sample no: C-268), j) Packstone, micrite, bio-mold, iron oxide filled stylolite, Clypeina, geopetal structure (Jy) (Sample no: C-268), k) Packstone, micrite, bio-mold, iron oxide filled stylolite, Clypeina, geopetal structure (Sample no: C-268), m) Packstone, micrite, fossil, iron oxide filled stylolite, porosity (Sample no: C-282), n) Packstone, micrite, fossil, bio-mold, iron oxide filled stylolite, vein (V) (Sample no: C-282) (All photos were taken in the PPL)

REFERENCES

Compton, R. R. (1962) Manual of Field Geology. New York: *John Wiley & Sons, Inc*.

Demirkol, C. (1981). Sultandağ kuzeybatısının jeolojisi ve Beyşehir-Hoyran Napı ile ilişkileri, Tübitak Temel Bilimler Araştırma Grubu, Proje no: TBAG-382, 56 s. (unpublished).

Dunham, R. J. (1962). Classification of Carbonate Rocks According to Depositional Texture. *Am. Assoc. Pet. Geol*., *1*, 108-121.

GoogleMaps: https://www.google.com/maps/@37.5369627,39.5182898,5z/data=!5m1!1e4

Özkan, A. M. and Dinç, S. (2008). Hadim (Konya) dolayındaki karbonat kayaçların (Üst Jurasik) sedimentolojisi, *Selçuk Üniversitesi Bilimsel Araştırma Projesi*, Proje no: 05401032.

Turan, A. (1990). Toroslar′da Hadim (Konya) ve güneybatısının jeolojisi, stratigrafisi ve tektonik gelişimi; *Selçuk Üni. Fen Bil. Enst*., Doktora Tezi, 229 s. (unpublished).

Turan, A. (1997). Bağbaşı ve Korualan kasabaları (Hadim-Konya) arasındaki otokton ve allokton birliklerin stratigrafisi; *S.Ü. Müh.-Mim. Fak. Derg*., 12 (1), 46-62.

Microbial Chondroitin

Esra ULKE[1]
Sebnem ERENLER[2]

Bacterial Capsular Polysaccharide (CPS)

Cell surface polysaccharides are complex carbohydrates produced by various bacterial species (Willis and Whitfield, 2013). They are classified into three categories according to their type of binding to the cell surface and behaviors: Lipopolysaccharides (LPSs), capsular polysaccharides (CPSs), and O-antigens, which are part of exopolysaccharides (EPSs). LPSs are formed by an oligosaccharide core and a lipidic component (lipid-A) that binds strongly to O-antigens on the outer cell membrane of Gram-negative bacteria. CPS is covalently bound to phospholipids or lipid-A molecules in the cell membrane. Still, they can also be released due to an imbalance of the phosphodiester bond between the polysaccharide and the phospholipid membrane junction. EPSs generally form an amorphous layer around the cell, are not covalently attached to the cell surface, and are therefore released in their environment (Schiraldi et al., 2010; Willis and Whitfield, 2013; Cress et al., 2014).

Bacterial pathogens have developed complex physiological stimuli to find a suitable site in the host organism and allow it to settle there. The infectivity of a pathogenic microorganism consists of two components: its ability to enter the host organism and spread and multiply. The cellular components required for one or more of these processes are called "Virulence Factors." Gram-negative pathogens include important surface and extracellular components, including flagella (and associated) chemotaxis proteins, fimbrial adhesins, secreted proteins, LPSs, and capsules (Willis and Whitfield, 2013; Cress et al., 2014).

The bacterial capsule is an extracellular structure seen with a microscope as a significant layer surrounding the cell. In some *E. coli* isolates this layer is about 100-400 nm in diameter and is formed by glycan chains longer than 200 sugars. The capsules are found in *E. coli, Neisseria meningitidis, Actinobacillus pleuropneumonia, Sinorhizobium meliloti* species, and important Gram-positive pathogens such as *Staphylococcus aureus* and *Streptococcus pneumonia* (Cress et al., 2014).

Bacterial pathogens carrying capsular polysaccharides identical to mammalian glycans have additional protection against the host's immune response. The increase in antibiotic resistance in bacteria and the inadequacy of common therapeutic approaches against bacterial infections, especially against organisms with multidrug resistance, point to a post-antibiotic era shortly. The first line of defense for most bacterial pathogens consists of a physical and immunological barrier known as the capsule, consisting of a diffuse viscous carbohydrate layer covalently attached to the cell wall in Gram-positive bacteria or lipids of the outer membrane in many Gram-negative bacteria (Willis and Whitfield, 2013). Bacterial capsular polysaccharides are a distinct class of high molecular weight polysaccharides that contribute to the virulence of many human pathogens by concealing cell surface components that may induce a host immune response in the gut, lung, urinary tract, and other host tissues. Such non-

[1] Ph.D.
[2] Associate Professor, Malatya Turgut Ozal University

immunogenic layers render pathogens insensitive to specific immune reactions, effectively increasing the residence time in host tissues and enabling pathological population densities to be achieved (Cress et al., 2014).

CPSs are key virulence factors that confer protective effects on their transporters against various environmental pressures, including against the immune system during the infection of animal hosts. Because of the large number of encapsulated pathogens, the capsules are generally thought to be formed by pathogenic bacteria. However, non-pathogenic and commensal bacteria also can form capsules (Dasgupta and Kasper, 2010). In Gram-negative bacteria, capsular polysaccharides bind to the outer membrane, usually at the reductive end, through covalently bonded lipids placed on the bilayer membrane. This property provides a water-saturated layer of high molecular weight polysaccharides that protects against drying out in the face of complex environmental conditions, blocks infection caused by most bacteriophages, and physically restricts the entry of cell surface antigens, preventing phagocytosis and other host immune responses. Figure 1 shows the cell wall of a typical Gram (-) bacterium (Anonymous, 2019). This polysaccharide layer is the rational target of broad-spectrum therapeutic compounds aimed at replacing antibiotic therapy of microbial infections or complementing treatment since the loss of the capsule exposes bacteria to the normal immune response that comes into play with the activation of the complement system (Cress et al., 2014).

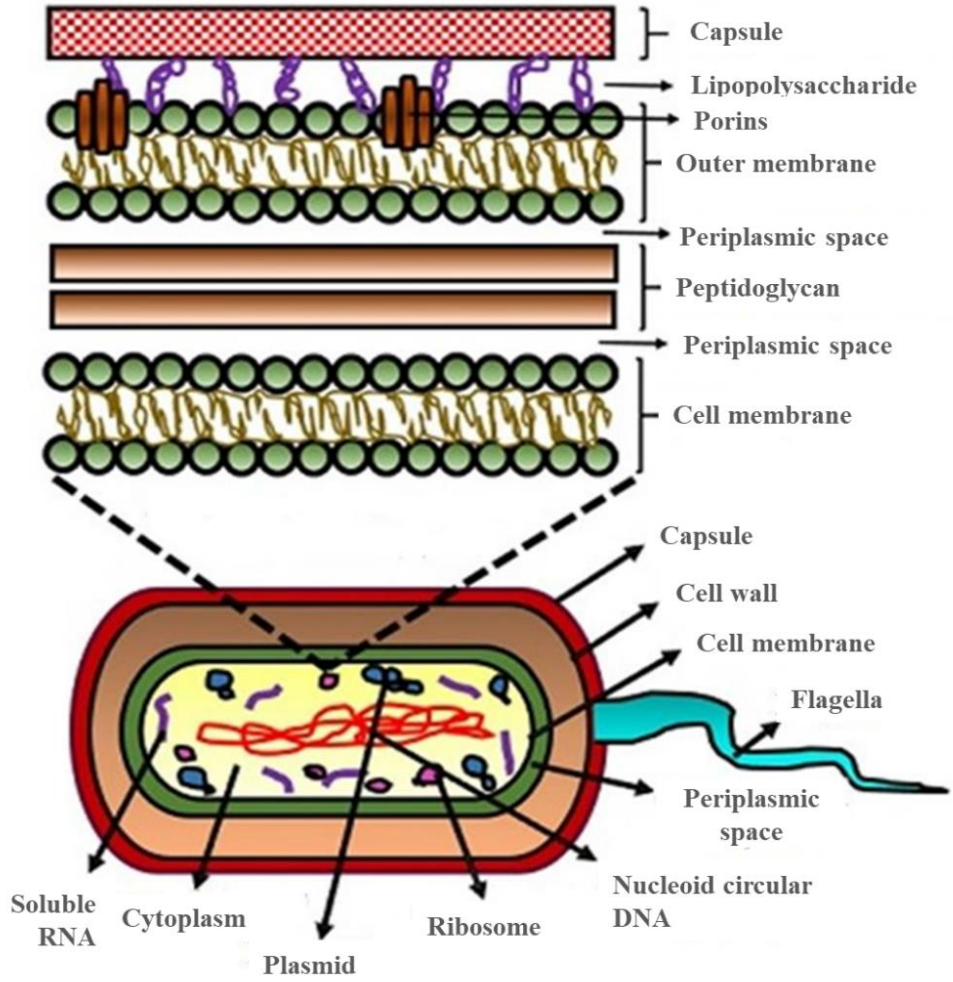

Figure 1. Schematic representation of the layers forming the bacterial cell wall of a typical Gram-negative bacterium (Anonymous, 2019)

Since Gram-positive bacteria do not have an outer cell membrane, the peptidoglycan layer is thicker than Gram-negative bacteria. Lipoteichoic acids bind the inner layers of peptidoglycan to a glycolipid extending from the cytoplasmic membrane. In contrast, teichoic

acids associated with the cell wall bind the outer layers to MurNAc (N-Acetylmuramic acid) residues through covalent bonds. CPS synthesized by Gram-positive bacteria attaches to the inner membrane, oligopeptide crosslinkers in the peptidoglycan or GlcNAc (N-Acetylglucosamine) residues in the peptidoglycan lattice (Cress et al., 2014). In some cases, the capsule consists of GAG-like polymers. This similarity between microbial CPS and eukaryotic extracellular matrix components makes these molecules interesting for biotechnological applications (Schiraldi et al., 2010). One of these applications is acquiring a CS precursor from cultures of *E. coli* strains that biosynthesize the K4 capsule. This similarity has made possible biotechnological applications aimed at improving the biosynthesis of K4 CPS by directing the metabolism of *E. coli*.

The Bacterial Capsular Polysaccharide of *E. coli*

E. coli strains that produce capsules have been recognized as encapsulated Gram-negative bacterial models and have been extensively researched. Capsular antigens of *E. coli* are acidic polysaccharides that differ in oligosaccharidic composition, branching, and charge density (Schiraldi et al., 2010). These are classified into four groups based on serological characteristics, genetic and biosynthesis criteria. Group I and IV CPS structures are found in enteropathogenic (EPEC), enterotoxigenic (ETEC), and enterohemorrhagic (EHEC) strains of *E. coli*. Uronic acid sugars are common in Group I CPS repeat units, while the presence of acetamido sugars characterizes Group IV CPS repeat units. Despite this apparent structural difference between group I and IV CPSs, they are polymerized and similarly transported to the cell surface. While Group II and III *E. coli* CPSs are generally produced in strains associated with extraintestinal infections (ExPEC), all known *E. coli* CPSs, identical in structure to animal glycans, belong to Group II. Unlike Group I and IV CPSs, the repeat units of Group II and III CPSs have a wide structural variety. They are also entirely polymerized in the cytoplasm and transported outside the cell along the cell wall (Cress et al., 2014). Group II capsular polysaccharides are very interesting regarding their structural properties and richness. *E. coli* K4 and K5 strains express capsular polysaccharides with a structure similar to non-sulfated chondroitin and heparosan (Schiraldi et al., 2010).

Gram-negative bacteria produce capsular polysaccharides by one of two standard coupling systems: Wzy-bound or ATP-binding cassette (ABC) transporter-dependent metabolic pathways (Cuthbertson et al., 2009; Cuthbertson et al., 2010). Capsular K antigens of *E. coli* have provided effective models for these metabolic pathways. *E. coli* capsule systems are divided into four groups based on the fusion system, the organization of critical genes, and regulatory properties. The Wzy-linked path is mainly used for group 1 and 4 capsules found in isolates that cause gastrointestinal disease (Whitfield, 2006). This pathway involves synthesizing polyprenol-bound CPS repeat units in the cytoplasm. These are then reversed across the inner membrane by a Wzx protein and polymerized into full-length CPS by a Wzy protein. After being exported in a particular pathway, CPS chains are added to a capsule structure on the cell surface. However, how they adhere to the cell surface is still being determined, and the process is probably multifactorial (Bushell et al., 2013). On the other hand, capsules belonging to Groups 2 and 3 require a fusion system connected to an ABC transporter. One of the characteristic features of CPS combined with the ABC transporter-dependent pathway is the presence of a phospholipid at the reduction end of the polysaccharide chain (Willis and Whitfield, 2013). The in vivo synthetic mechanism involves different catalytic activities responsible for the supply of UDP (Uridine diphosphate)-sugar precursors, the assembly of the polysaccharide chain, and their transport through the periplasm and cell membrane. In particular, glycosyltransferases in the cytoplasm advance the newly formed chain by adding residues to the irreducible end. The proteins involved in the biosynthesis, polymerization, and transport of capsules are encoded by genes called cps. In particular, the genetic organization of the group II cps locus has been studied extensively (Schiraldi et al.,

2010). CPS is synthesized in the cytoplasm and transferred across the inner membrane through an ABC-transporter system consisting of the nucleotide-binding domain (NBD) polypeptides (KpsT in the *E. coli* nomenclature) and integral membrane polypeptide (KpsM). The completion of the transport from the periplasm to the cell surface requires two different characteristic components: a member of the polysaccharide co-polymerase (PCP-3) family (KpsE) and an outer membrane polysaccharide (OPX) protein (KpsD). The protein KpsD assumes the role of the transporter of the chain across the outer membrane. It is thought that these proteins form a protein complex that enables synthesis and translocation from the cytoplasm to the cell surface in a coordinated process that is suggested to be similar to the movement of drug flow pumps consisting of three parts (Figure 2) (Willis and Whitfield, 2013). The presence of homologs of kpsTMED genes functions as a distinctive feature of genetic loci that direct the production of ABC transporter-dependent CPS (Willis and Whitfield, 2013).

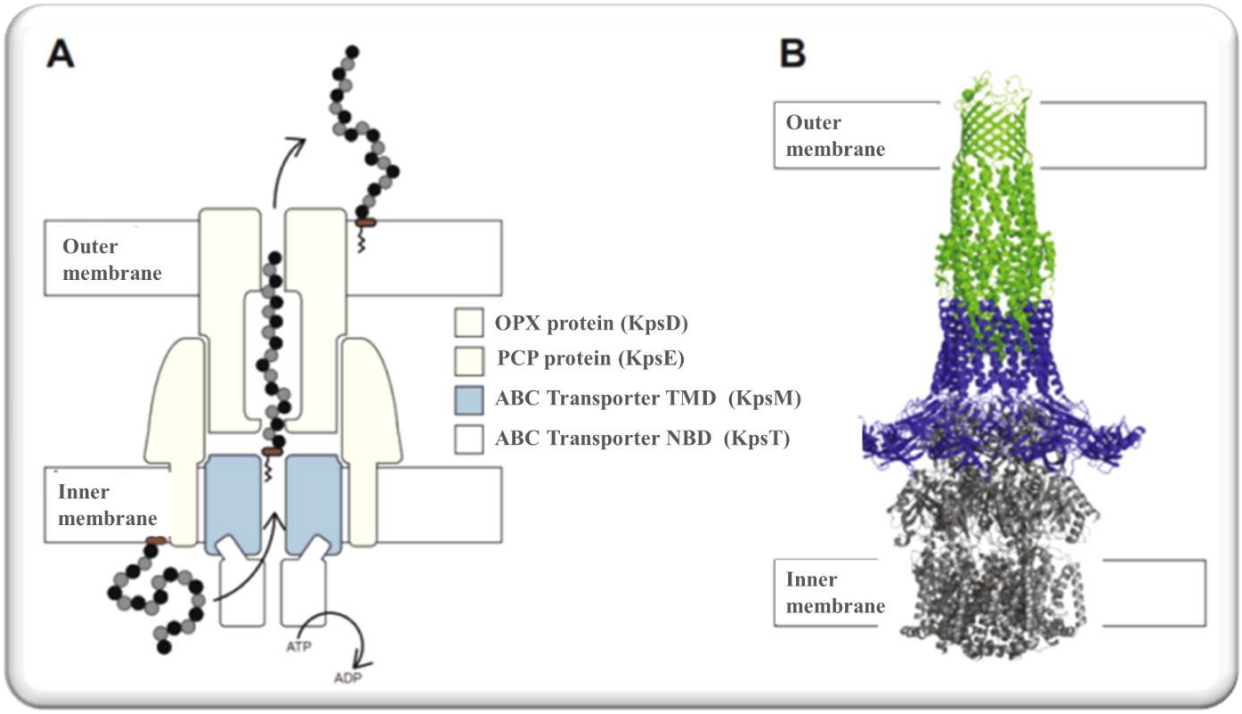

Figure 2. CPS transmission model via the ABC transporter-dependent pathway (Willis and Whitfield, 2013)

The majority of *E. coli* CPS sequence variation occurs within the N-terminal region, which is the region where the N-acetyl hexosamine glycosyltransferase domain is located. As a result of experiments with hybrid enzymes, a region of 44 amino acids was found near the middle of this region; this region controls the specificity of UDP-GlcNAc. In the chondroitin derivative produced by *E. coli* K4, the CPS backbone is modified by β-fructose in the C3 of GLCA. While the KfoC enzyme synthesizes the chondroitin backbone, an unidentified enzyme fructosylates the polymer. *E. coli* K4 CS is the only polymerase associated with an ABC transporter-dependent pathway whose structure has been determined (Figure 3) (Willis and Whitfield, 2013). It consists of two almost identical glycosyltransferase domains; the N terminal region contains GalNAc-transferase activity, while the C terminal region has GlcA-transferase activity. The N-terminal GlcNAc transferase domain, which comes first, is a long and primarily irregular region surrounding the GlcA domain (Figure 4) (Willis and Whitfield, 2013). For the polymerization activity, the interaction between the two parts is essential. Deleting 107 amino acids from the N-terminal end decomposes polymerization; the resulting protein can transfer a single GIgNAc or GlcA residue to a suitable acceptor in vitro but cannot polymerize. There is a significant hydrophobic interaction here; one is at the N-terminal region,

and the other is at the extreme C-terminal end of the protein. Without this interaction, the substrate can no longer bind the GlcA active site, and polymerization cannot occur, possibly due to a conformation change of the substrate-binding pocket (Willis and Whitfield, 2013). This interaction coordinates the activity of the two transferases, but it is not yet clear how this occurs.

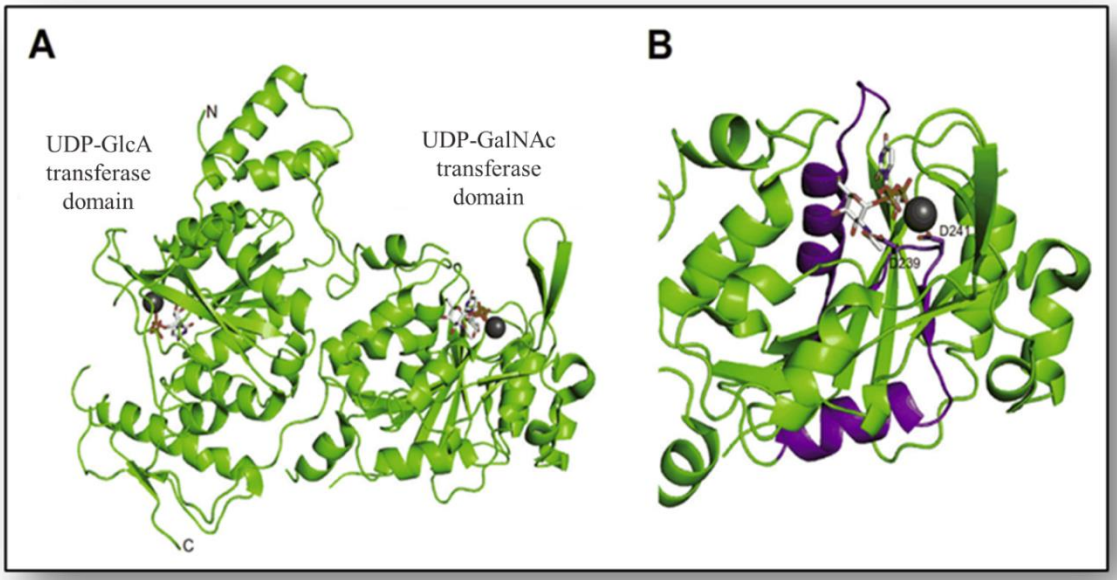

Figure 3. The crystal structure of E. coli K4 chondroitin synthase with UDP-GLCNAC (Willis and Whitfield, 2013)

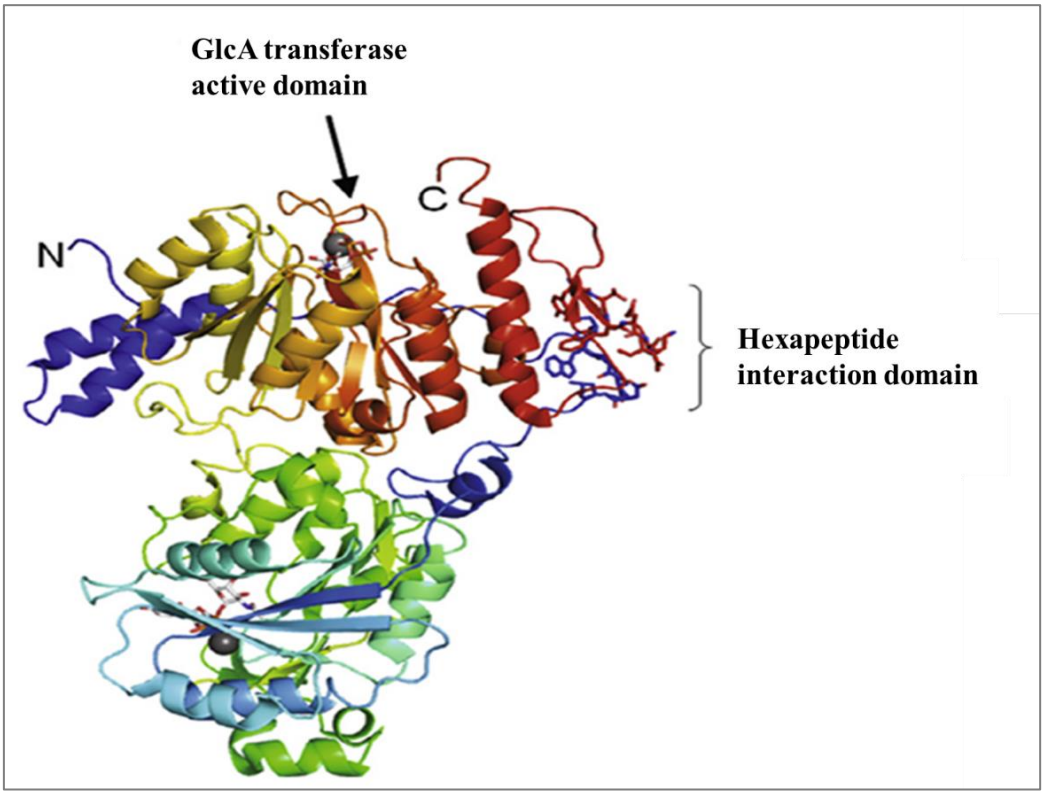

Figure 4. The crystal structure that shows the interaction between N- and C-terminal hexapeptides (shown with rods) of E. coli K4 chondroitin synthase (Willis and Whitfield, 2013)

E. coli K4 produces a capsule with protective properties. The transmission electron microscope image of *E. coli* K4 is shown in Figure 5 (Schiraldi et al., 2010). The pgm and galU endogenous genes are involved in the biosynthesis of UDP-glucose, a critical intermediate in carbohydrate metabolism and the biochemical precursor of UDP-glucuronic acid. For capsule biosynthesis, UDP-glucuronic acid is used together with UDP-N-acetylgalactosamine as a sugar donor (Cress et al., 2014).

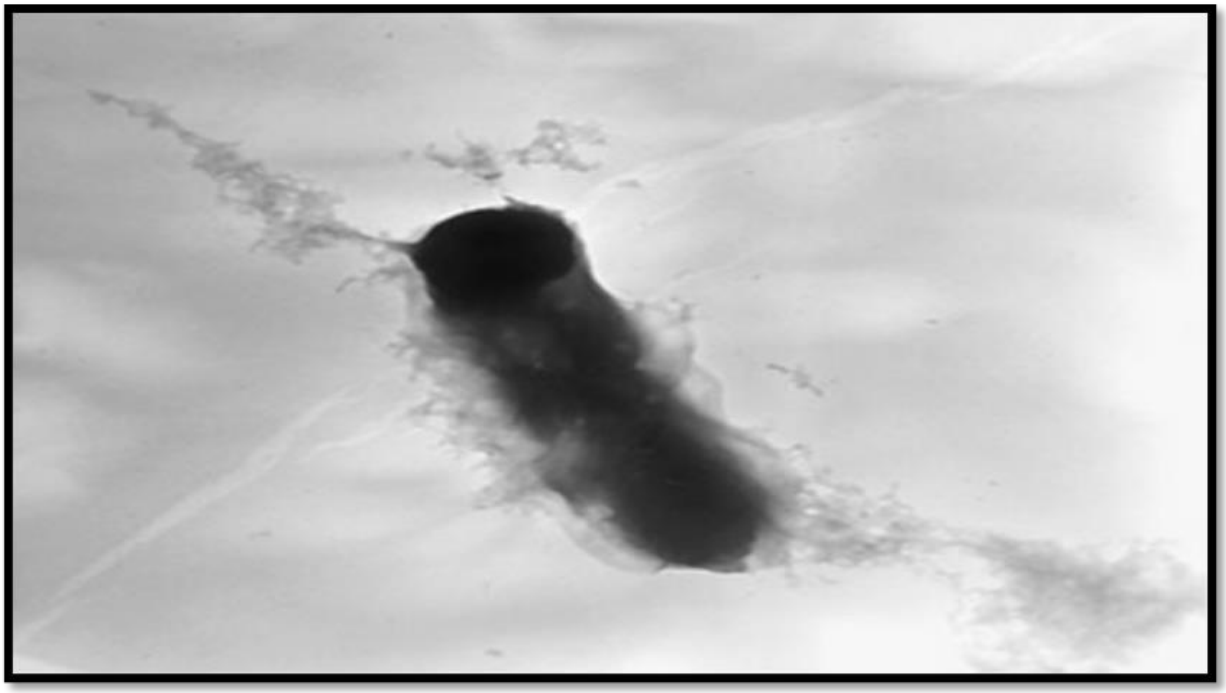

Figure 5. Transmission electron microscopy of E. coli K4 (magnification: 28,000 ×) (Cress et al., 2014)

CS and K4 CPS are composed of alternative glucuronic acid (GlcA) and N-acetyl-D-galactosamine (GalNAc) β-bonded residues, and the difference between the two polymers is the absence of sulfate groups at various positions in the microbial molecule and the presence of acid-unstable fructose at C3 of GLCA (Cress et al., 2014).

The biosynthesis of the K4 polysaccharide is controlled by a triplet, of which two regions (1 and 3) are protected between group II *E. coli* strains. These regions are responsible for the transport and release of CPS. Region 2, which is the central region, is directly involved in the synthesis of serotype-specific polysaccharides and encodes enzymes responsible for the final stage in the biosynthesis of UDP- sugar precursors and necessary for the collection and fructosylation of the polymer and probably form a biosynthetic complex on the cytosolic side of the inner cell membrane (Figure 6(a)) (Cress et al., 2014). Region 2 of *E. coli* K4, is 14 Kb long; this region contains seven genes (*kfoA-G*) and an insertion sequence IS2; these genes encode enzymes that combine and directly synthesize polysaccharides, such as chondroitin (Schiraldi et al., 2010). The function of *kfoB, kfoD,* and *kfoG* is still unknown. It has been suggested in most of the studies that they are not directly involved in the production of capsular polysaccharides. The *kfoA* gene encodes the enzyme UDP-GlcNAc 4–epimerase, which is responsible for the epimerization of UDP GlcNAc to UDP-GALNAC. The *kfoF* gene encodes the enzyme UDP-glucose dehydrogenase, which is involved in the redox reaction in which NAD^+ is reduced to NADH, and UDP-glucose is oxidized to UDP-GLCA. The *kfoC* gene encodes a chondroitin polymerase that works bidirectionally to transfer both Glca and GalNAc residues to the non-reducing end of an oligosaccharide/polysaccharide acceptor. The *kfoE* gene is thought to encode the fructosyltransferase responsible for adding a fructose group to GlcA with the 3-position. This reaction is estimated to occur during the biosynthesis of the

chondroitin backbone or after the synthesis is completed (He et al., 2015). A detailed biosynthetic pathway of *E. coli* K4 CPS is shown in Figure 7 (Zhang et al., 2018). Accordingly, when glycerol was a substrate, fructose-6-phosphate was the first widespread precursor in synthesizing chondroitin and chondroitin-like polysaccharides. Fru-6-P is converted into glucosamine-6-phosphate and glucose-6-phosphate by GlcN (Glucosamine)-6-P synthase (GLMs) and phosphoglucose isomerase (Pgi), respectively. GlcN-6-P is then converted into UDP-GalNAc by GlcN synthase (GlmM), UDP-N-acetylglucosamine pyrophosphorylase (GlmU) and UDP-glucose-4-epimerase (KfoA). In contrast, Glc-6-P is converted to UDP-GlcA by phosphoglucomutase (Pgm), UTP-glucose-1-phosphate uridityltransferase (GalU) and UDP- glucose by dehydrogenase (KfoF). Finally, chondroitin is formed by UDP-GalNAc and UDP-GlcA chondroitin polymerase (KfoC) (Zhang et al., 2018).

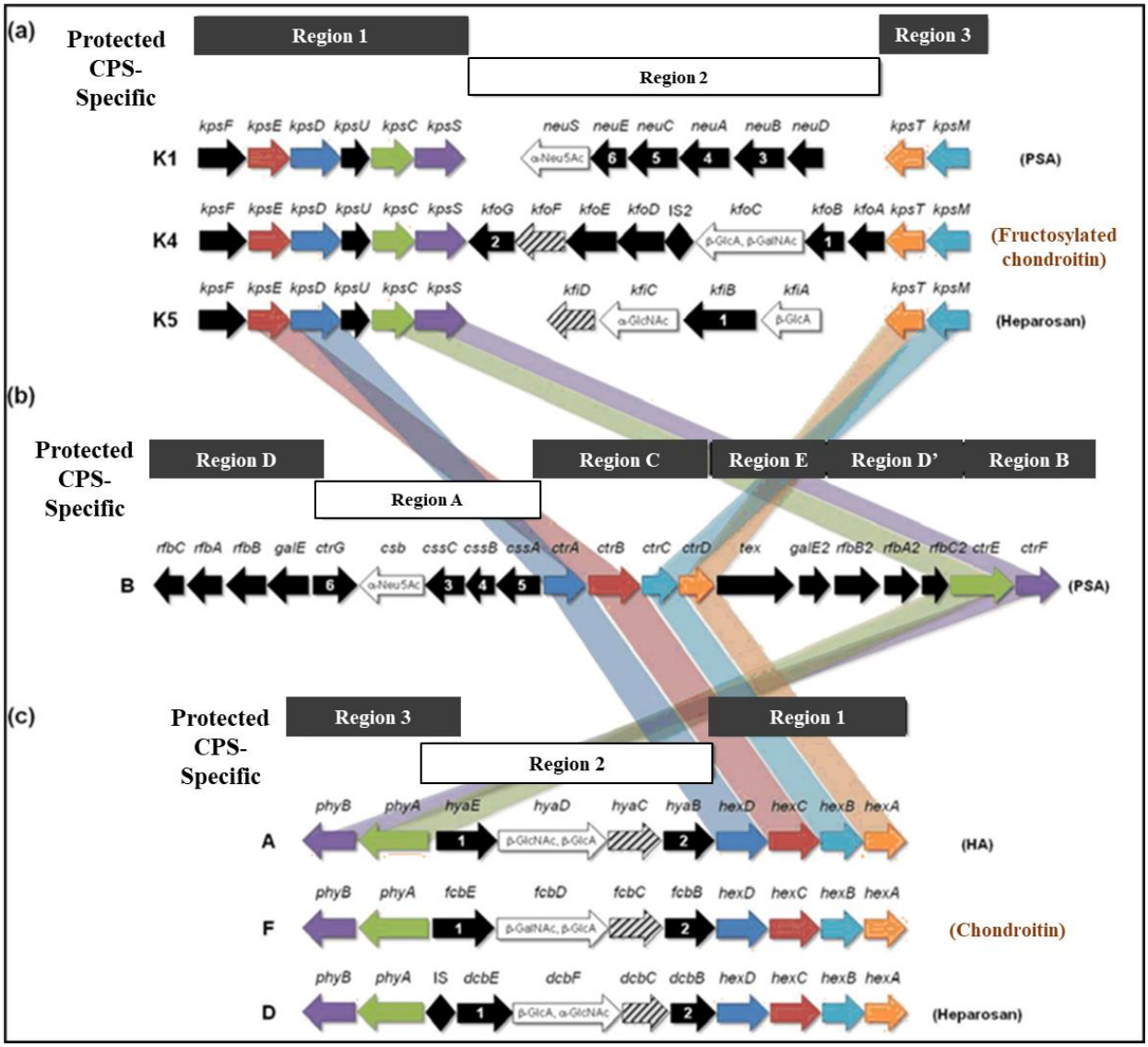

Figure 6. CPS gene locus junction pathways in Gram-negative bacteria expressing ABC-transporter-dependent CPS (Cress et al., 2014)

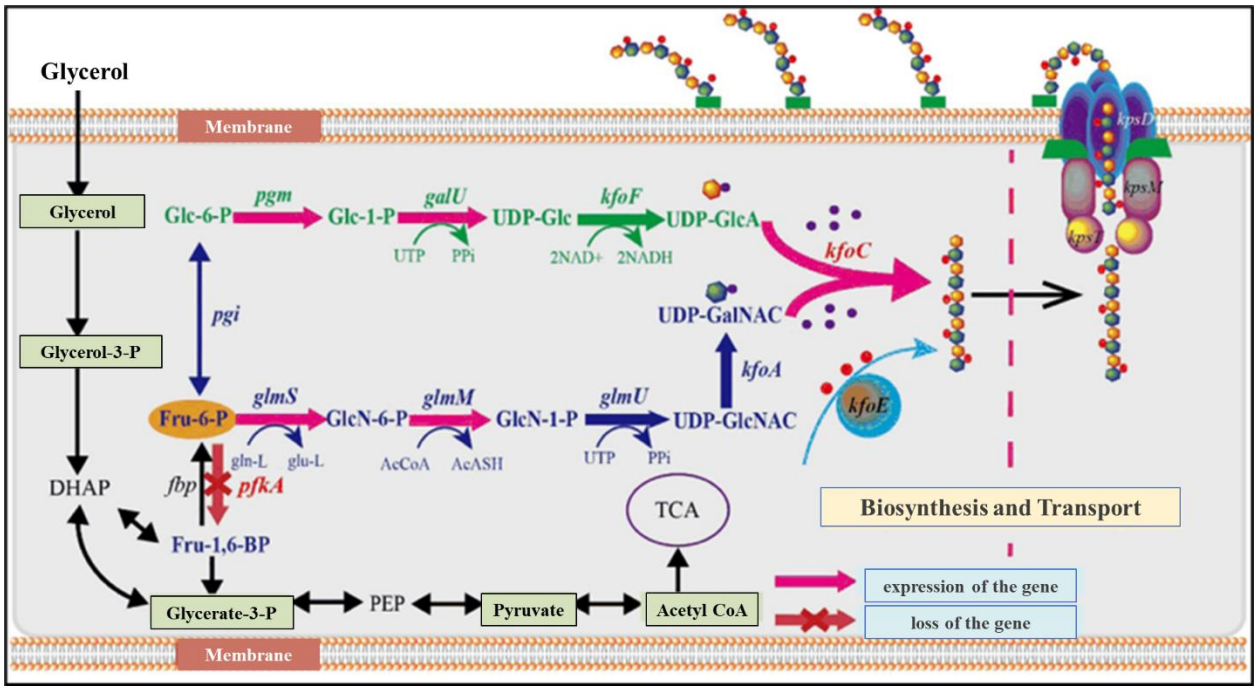

Figure 7. Capsular polysaccharide synthesis in E. coli K4 (Zhang et al., 2018)

Microbial Production of Chondroitin Sulfate

CS's current extraction and purification procedures are complex and expensive methods with disadvantages such as risks of viral contamination, low product yield, severe pollution levels caused by many organic chemicals and protein residues, and unstable product quality. To overcome these problems, different strategies have been proposed for the biotechnological production of CS or CS-like products in recent years. Research activities on this subject are mainly carried out with two basic operations:

1. by enzymatic reaction
2. by microbial production (Shi et al., 2014).

Microorganisms That Produce Chondroitin Sulfate

In nature, some bacteria and fungi can produce CS or CS-like compounds. The structural similarity of microbial capsular polysaccharides to these biomolecules makes these bacteria ideal candidates as a non-animal source of glycosaminoglycan derivatives. As potential strains of industrial production, they must meet the following prerequisites:

(1) They must be safe (2) They must be able to make efficient use of easily accessible raw sugar materials (3) Their fermentation periods must be short (4) They must have a defined genetic infrastructure (5) They must be able to efficiently synthesize a large number of CS or its analogs (Shi et al., 2014).

Example bacteria include *Actinobacteria* (e.g., *Corynebacterium, Microbacterium, Micrococcus, Monascus,* and *Streptomycetes*), *Proteobacteria* (e.g., *Escherichia*), and *Firmicutes* (e.g., *Bacillus* and *Lactobacillus*). For this method, the appropriate bacteria must be well-known in the technique and readily available from a commercial supplier, food product, or natural sources such as soil (Jolly et al., 2010). elevant research so far has focused chiefly on *Pasteurella multocida, E. coli,* and *Bacillus subtilis* (Shi et al., 2014). The CS-producing bacteria are given in Table 1 (Jolly et al., 2010).

Table 1. Bacteria that produce CS (Jolly et al., 2010)

Bacterial Species	**Chondroitin Sulfate (ng/ml)**
Bacillus cereus	8.6
Bacillus circulans	11.7
Bacillus coagulans	8.5
Bacillus licheniformis	9.0
Bacillus megalerium	8.8
Bacillus subtilis	8.9
Lactobacillus acidophilus	8.9
Corynebacterium glulamicum	80.8
Microbacterium arborescens	8.0
Micrococcus varians	8.7
Monascus purpureus	10.1
Streptomyces olivochromogenes	8.3
Streptomyces rubiginosus	8.0
Escherichia coli	8.8

Example fungi: Deuteromycota (e.g., Aspergillus), Ascomycota (e.g., Endomycopsis, Hansenula, Hasegawaea, Penicilhum, Pichia, Monascus, Candida, Debaryomyces, Eurotium, Galaktomycetes, Geotrichum, Saccharomyces, Trichoderma, Kluveromyces), Schizosaccharomyces, Talaromyces Torulopsis, Yamadazyma, Yarrowia, and Zygosaccharomyces), Zygomycota (e.g., types of Mucor, Mortierella, Rhizomucor, and Rhizopus), Basidiomycota (e.g., genus Cryptococcus, Dipodascus ve Trichosporon). Suitable fungi for this process are well-known microorganisms in the industry and are easy to access from a commercial supplier, food product, or natural sources such as soil (Jolly et al., 2010).

Various microorganisms can be cultured for the production of CS or CS-like compounds. Some applied systems use natural microorganisms that are not genetically engineered, while others use recombinantly transformed microorganisms to produce CS or CS-like compounds (Jolly et al., 2010).

REFERENCES

Anonymous. (2019). https://biologyreader.com/difference between gram and gram negative bacteria.html (Online Access on 11 May, 2023)

Bushell, S. R., Mainprize, I. L., Wear, M. A., Lou, H., Whitfield, C., & Naismith, J. H. (2013). Wzi is an outer membrane lectin that underpins group 1 capsule assembly in *Escherichia coli*. *Structure (London, England : 1993)*, *21*(5), 844–853. https://doi.org/10.1016/j.str.2013.03.010

Cress, B. F., Englaender, J. A., He, W., Kasper, D., Linhardt, R. J., & Koffas, M. A. (2014). Masquerading microbial pathogens: capsular polysaccharides mimic host-tissue molecules. *FEMS microbiology reviews*, *38*(4), 660–697. https://doi.org/10.1111/1574-6976.12056

Cuthbertson, L., Kos, V., & Whitfield, C. (2010). ABC transporters involved in export of cell surface glycoconjugates. *Microbiology and molecular biology reviews: MMBR*, *74*(3), 341–362. https://doi.org/10.1128/MMBR.00009-10

Cuthbertson, L., Mainprize, I. L., Naismith, J. H., & Whitfield, C. (2009). Pivotal roles of the outer membrane polysaccharide export and polysaccharide copolymerase protein families in export of extracellular polysaccharides in gram-negative bacteria. *Microbiology and molecular biology reviews: MMBR*, *73*(1), 155–177. https://doi.org/10.1128/MMBR.00024-08

Dasgupta, S., & Kasper, D. L. (2010). Novel tools for modulating immune responses in the host-polysaccharides from the capsule of commensal bacteria. *Advances in immunology*, *106*, 61–91. https://doi.org/10.1016/S0065-2776(10)06003-7

He, W., Fu, L., Li, G., Andrew Jones, J., Linhardt, R. J., & Koffas, M. (2015). Production of chondroitin in metabolically engineered *E. coli*. *Metabolic engineering*, *27*, 92–100. https://doi.org/10.1016/j.ymben.2014.11.003

Jolly J.F. et al.(2010). Microbial-derived chondroitin sulfate, US Patent 2010/0063001 A1, Mar. 11, 2010.

Schiraldi, C., Cimini, D., & De Rosa, M. (2010). Production of chondroitin sulfate and chondroitin. *Applied microbiology and biotechnology*, *87*(4), 1209–1220. https://doi.org/10.1007/s00253-010-2677-1

Shi, Y.-g., Meng, Y.-c., Li, J.-r., Chen, J., Liu, Y.-h. and Bai, X. (2014), Chondroitin sulfate: extraction, purification, microbial and chemical synthesis. *J. Chem. Technol. Biotechnol.*, *89*, 1445-1465. https://doi.org/10.1002/jctb.4454

Whitfield C. (2006). Biosynthesis and assembly of capsular polysaccharides in Escherichia coli. *Annual review of biochemistry*, *75*, 39–68. https://doi.org/10.1146/annurev.biochem.75.103004.142545

Willis, L. M., & Whitfield, C. (2013). Structure, biosynthesis, and function of bacterial capsular polysaccharides synthesized by ABC transporter-dependent pathways. *Carbohydrate research*, *378*, 35–44. https://doi.org/10.1016/j.carres.2013.05.007

Zhang, Q., Yao, R., Chen, X., Liu, L., Xu, S., Chen, J., & Wu, J. (2018). Enhancing fructosylated chondroitin production in *Escherichia coli* K4 by balancing the UDP-precursors. *Metabolic engineering*, *47*, 314–322. https://doi.org/10.1016/j.ymben.2018.04.006

Barrıers And Strategıes For Adaptıng To Clımate Change In Sheep Farms: The Case Of Konya Provınce

Cennet OĞUZ
Aysun YENER ÖĞÜR
Aykut ÖRS
Yusuf ÇELİK

Introduction

Climate is an important factor of agricultural productivity. Given the fundamental role of agriculture in human nutrition and well-being, there are concerns for the future. **Climate change can seriously affect agricultural production and thus food security (food availability).** Climate change is one of the biggest environmental problems facing humanity today, and its effects are seen not only in certain regions but all over the world (Adams et al., 1990; Swart, 2008). Global climate change, and especially global warming, has been the most thematic issue on the world's and Turkey's agenda after 2007. **Agriculture is an area of activity that causes climate change as much as it is affected by climate change.** Climate change affects not only plant production but also animal production. The impact of climate change on animal production differs from year to year and increases every year (Descheemaeker et al., 2018). Small cattle breeding plays a very important socio-economic role in animal production (Brahmi et al. 2012). Small cattle breeding is important in terms of meat, milk, fertilizer, wool and leather production (Thornton, 2010). Considering the natural and economic conditions and agricultural structure of Turkey, it can be said that some regions are more suitable for small cattle breeding (Kaymakçı and Engindeniz 2010; Semerci and Çelik 2016). Ovine breeding has a very important place especially in arid or semi-arid regions (Sejian et al., 2017). According to FAO (2015), the global demand for animal products is projected to double by 2050 due to the rising standard of living and population pressure. Because, in parallel with the increase in population and income in the world, the demands for animal food are increasing (Lemaire et al., 2019; Khan and Sameen, 2018; Godfray and Garnett, 2014; Speedy, 2003; Steinfeld, 2003). Therefore, climate change is emerging as one of the biggest threats to the animal food supply. Because **reducing the negative effects of climate change will only be possible by adapting to these effects. Because, to the extent that the producer has knowledge about climate change and its effects, it will endeavor to reduce the negative effects.** Turkey is in a semi-arid climate zone, and the Konya region, which ranks 20th in terms of provincial development, is one of the driest provinces in Turkey. For this reason, Konya was chosen as the research area. Konya province constitutes 5% of the agricultural production value of Turkey, 5.08% of the number of small cattle and 5.88% of the number of sheep (1.432,705 head). In the study, it was aimed to measure the perceptions of the sheep farmers about the awareness of climate change, adaptation and to measure barriers to compliance and perceptions of strategy. As a matter of fact, in all national climate change notifications, climate change strategy document and climate change action plan, it is emphasized that the effects of climate change on agriculture should be determined at the national, regional and local level.

Material And Method

The main material of the research was the primary data collected from the sheep farms of Konya through a questionnaire. Domestic and foreign literature was also used to determine the criteria for measuring the climate change perception and adaptation levels of farmers. In the preparation of the survey forms applied to the enterprises, the survey forms used in various researches were also used, taking into account the subject of the research and the characteristics of the agricultural enterprises in the region. The data collected in the research belong to the production period of 2021, and the survey was conducted in December, January and February. As the study area, Konya province constitutes 5% of the agricultural production value of Turkey, 5.08% of the number of small cattle and 5.88% of the number of sheep (1.432,705 head). In the study, the records of the Konya Province Sheep and Goat Breeders' Association were used to determine the population. Accordingly, there are a total of 9228 sheep breeding enterprises in Konya. The main framework of the research is the districts of Karapınar, Ereğli, Cihanbeyli, Meram, Karatay, and Çumra, which have the highest number of sheep in the province and account for 54.92% of all the sheep in Konya province. According to the formula below, 151 businesses were surveyed as part of the study using Neyman's " stratified sampling method".

$$n = \frac{[\sum(N_h S_h)]^2}{N^2 D^2 + \sum[N_h (S_h)^2]}$$

$D^2 = d / z$

In the formula;

n: number of samples,

N: total unit number belonging to the sampling frame,

Nh: the number of enterprises in the hth layer (frequency),

Sh: standard deviation of the hth layer,

d: Allowable margin of error from the main population average,

z: refers to the z value in the standard normal distribution table according to the error rates. (Yamane, 1967).

In determining the level of knowledge and application level of farmers about adaptation/adaptation to climate change, a 5-point Likert-type scale was used and the data were interpreted by creating tables and graphs according to weighted averages and importance level index. The Likert scale is the most appropriate technique used to measure attitudes and behavior patterns. The answer option with the highest average is the most preferred option and weighted averages are calculated (Oğuz and Karakayacı, 2017).

W = weight of rating X = number of answers of the answer option

$$\text{Weighted average} = \frac{X1.W1 + X2.W2 + \cdots .. + Xn.Wn}{\text{Total Sample Size}}$$

In addition, the importance index was calculated according to the formula below to measure the climate change perceptions and attitudes of sheep farms.

$$Severity\ Index = \frac{\sum_{i=1}^{5}(pi*qi)}{\sum_{i=1}^{5}(pi)*qi} * 100$$

İ=1,2,3,4,5

Moreover, p1, p2, p3, p4, p5 represent the corresponding answer frequencies, q1, q2, q3, q4, q5 represent the answer frequency (Majid and Mc Caffer 1997; Masud et. al., 2017). The valuation arrangement is as follows:

q1= Strongly Disagree 0.00 < SI < 12.5

q2= Disagree 12.5 <SI < 37.5

q3 =I partially agree38 <SI < 62.5

q4= Agree 63 <SI < 87.5

q5=Strongly Agree 88 <SI <100

To reveal and analyse the knowledge, perception, and attitudes of farmers toward climate change, the following categories have been created:

1: Perception of farmers' vulnerability to climate change
2: Farmers' attitudes towards climate change vulnerability
3: Barriers and developed strategies for farmers to adapt to climate change

Research Findings and Discussion

Perception of farmers' vulnerability to climate change.

The climate change awareness status of the sheep farms in the research area is given in Table 1. According to the table, 69.54% of the sheep farms have heard of the concept of climate change, and 11.43% of these enterprises are in the first group, 53.33% are in the second group, and 35.24% are in the third group. 30.46% of farmers have not heard of the concept of climate change before. The farmers who have not heard of the concept of climate change, are 21.74% in the first group, 50% in the second group and 28.26% in the third group.

Table 1. The sheep farms' knowledge of climate change

Farm size group (Head)	Number of people who have heard about climate change		Those who haven't heard		Total	
	Number	Ratio (%)	Number	Ratio (%)	Number	Ratio (%)
1-100 (1st Group)	12,00	11,43	10.00	21.74	22,00	14.57
101-250 (2nd Group)	56,00	53,33	23,00	50.00	79	52.32
251 - + (3rd Group)	37,00	35,24	13,00	28.26	50	33.11
Total	105,00	100,00	46,00	100.00	151	100.00
Ratio	69.54		30.46		100.00	

When the rates of hearing about climate change within the group are calculated: In the first group, the rate of those who heard is 54.55%, while the rate of those who did not hear is 45.45%; it is 70.89% vs. 29.11% in the second group and 74.00% vs. 26.00% in the third group. Farmers' perception of vulnerability to climate change and the index of severity are given in Table 2.

According to the five-point Likert scale, the importance indexes of the perceptions of the sheep farms that climate change is a serious problem vary between 28.80% and 96.20%. While 96.20% of the farmers in the first group stated that climate change is a serious problem on a global scale, they stated that the share of people in this change is high, negative results will be experienced more in the long run and it will be more effective on agricultural enterprises.

Table 2. Farmers' perception of susceptibility to climate change and its severity Index

Factors	5	%	4	%	3	%	2	%	1	%	Average	Severity Index %
It is a significant issue on a global level.	92	85,19	14	12,96	1	0,93	0	0,00	1	0,93	4,81	96.20
Humans have a high share in climate change.	74	68,52	24	22,22	5	4,63	2	1,85	3	2,78	4,52	90.40
It will have negative consequences in the long run.	79	73,15	23	21,30	6	5,56	0	0,00	0	0,00	4,68	93.60
It will directly affect the farms.	71	65,74	27	25,00	7	6,48	1	0,93	2	1,85	4,52	90.40
It will affect cities more than rural areas.	41	37,96	13	12,04	19	17,59	13	12,04	22	20,37	3,35	67.00
I haven't noticed their effects yet, but I believe they will be observable in the next 50 years.	37	34,26	9	8,33	16	14,81	22	20,37	24	22,22	3,12	62.40
It will not affect Turkey, but rather regions such as Africa and the Middle East.	31	28,70	17	15,74	16	14,81	15	13,89	29	26,85	3,06	61.20
It will affect future generations and will have no impact on current generations.	19	17,59	8	7,41	20	18,52	15	13,89	46	42,59	2,44	48.80
My standard of living will improve due to climate change.	2	1,85	1	0,93	8	7,41	21	19,44	76	70,37	1,44	28.80

While 67% of the farmers in the second group predicted that cities would be more impacted by climate change, 62.40% noted that they had not yet noticed the effects, which may not become apparent for another 50 years, and 61.20% predicted that Turkey would not experience such effects, but mostly Africa and the Middle East countries will. There are also those who do not believe that there is climate change, but 28.80% of the farmers state that climate change will improve their quality of life and standard.

Farmers' attitudes towards climate change vulnerability

In the research area, the attitudes of farmers towards climate change vulnerability and the importance index are calculated and given in Table 3. According to this, the severity indexes of farmers in environmental issues vary between 63.40% and 95.40%.

Table 3. Attitudes of farmers towards climate change vulnerability

Farmers' adaptation	5	%	4	%	3	%	2	%	1	%	Average	Severity Index %
Switching to a green farming method doesn't require me to make much of a change in my current activities.	24	22,22	18	16,67	34	31,48	16	14,81	16	14,81	3,17	63.40
In adopting environmental methods, it is important that I lead rather than follow.	37	34,26	14	12,96	29	26,85	10	9,26	18	16,67	3,39	67.80
I'm planting more trees.	45	41,67	17	15,74	20	18,52	8	7,41	18	16,67	3,58	77.00
It is very important for other farmers to consider their greenhouse gas emissions.	47	43,52	22	20,37	20	18,52	7	6,48	12	11,11	3,79	75.80
I know how to use the resources such as land, water, pasture, workforce and technology more efficiently.	41	37,96	24	22,22	29	26,85	12	11,11	2	1,85	3,83	76.60
I would like to try different technologies and/or systems to reduce greenhouse gas emissions in my business.	55	50,93	19	17,59	20	18,52	8	7,41	6	5,56	4,01	80.20
Other family members think I should grow as environmentally friendly as possible.	58	53,70	25	23,15	21	19,44	2	1,85	2	1,85	4,25	85.00
I want to farm as environmentally friendly as possible.	65	60,19	31	28,70	7	6,48	3	2,78	2	1,85	4,43	88.60
As a farmer, I take responsibility for protecting or improving the environment for future generations.	66	61,11	27	25,00	14	12,96	0	0,00	1	0,93	4,45	89.00
Reducing the pollution caused by my livestock is important to me.	66	61,11	33	30,56	5	4,63	1	0,93	3	2,78	4,46	89.20
Awareness training and demonstrations should be organized for climate change.	71	65,74	24	22,22	11	10,19	2	1,85	0	0,00	4,52	90.40

Businesses should share their efforts and adaptation to climate change with their environment.	67	62,04	34	31,48	6	5,56	0	0,00	1	0,93	4,54	90.80
It is important to me to leave the land as good or better as I took it.	71	65,74	31	28,70	6	5,56	0	0,00	0	0,00	4,60	92.20
Encouraging wildlife, planting trees, and protecting the water supply are important to me.	81	75,00	15	13,89	10	9,26	2	1,85	0	0,00	4,62	92.40
Everyone must work together to adapt to climate change.	82	75,93	19	17,59	7	6,48	0	0,00	0	0,00	4,69	93.80
I think it's important to adapt to climate change.	85	78,70	18	16,67	5	4,63	0	0,00	0	0,00	4,74	94.80
Climate change will pose more of a threat to farming in the next 10 years	88	81,48	17	15,74	2	1,85	0	0,00	1	0,93	4,77	95.40
Climate change will lead to reduced yields due to disease and pests.	90	83,33	13	12,04	4	3,70	0	0,00	1	0,93	4,77	95.40

While 95.40% of farmers believe that diseases and dangerous insects will cause lower yields as a result of climate change, 95.40% believe that the threat from climate change will increase over the course of the next 10 years. 94.80% of respondents say it's critical to adapt, and 93.80% say all parties involved should cooperate to do so. 92.40% of people agree that protecting water resources and planting trees are essential for preserving the environment. 90.40% of them mention the importance of organizing climate change awareness trainings and demonstrations and state that it is important to leave a cleaner environment and soil water resources for future generations.

Identifying barriers to adaptation to climate change in sheep farms

There are significant barriers to the implementation of climate change adaptation strategies. In the context of agriculture, there are several factors that hinder farmers' ability to cope with climate change, such as social, technological, economic, institutional, informational, and natural barriers. These factors help to explain the gap between the widely accepted need for compliance and the general lack of action. However, farmers' understanding of these barriers is currently limited (Gifford et al., 2011). Barriers to climate change adaptation need to be better understood, as these barriers constrain the adaptation process and reduce the adaptation capacity of farmers.

In the research area, the importance index of the barriers in front of the farmers' adaptation to climate change has been calculated and given in Table 4. According to the importance index of the barriers to adaptation to climate change, the percentages in the table are as follows: very costly inputs 96.20%, irrigation water problem 93.20%, not having sufficient cash financing 90.60%, limited farm sizes 82.20%, low soil fertility % 77.20, difficulty in accessing agricultural extension staff 71.60%, insufficient agricultural workforce 70.60%, marketing

problems of agricultural products 67.20%, difficulty in accessing credit opportunities 67%, access to agricultural subsidies 66.40%, difficulty in accessing meteorological data 62%.

Table 4. Farmers' perspectives on the barriers to climate change adaptation

Factors	5	%	4	%	3	%	2	%	1	%	Average	Severity Index %
Difficulties in accessing timely weather information	43	39,81	11	10,19	8	7,41	6	5,56	40	37,04	3,10	62.00
Difficulties in accessing agricultural subsidies	31	28,70	21	19,44	27	25,00	10	9,26	19	17,59	3,32	66.40
Difficulties in accessing credit facilities	30	27,78	29	26,85	17	15,74	13	12,04	19	17,59	3,35	67.00
Marketing woes	42	38,89	17	15,74	13	12,04	10	9,26	26	24,07	3,36	67.20
Insufficient agricultural workers	54	50,00	5	4,63	16	14,81	10	9,26	23	21,30	3,53	70.60
Limited access to agricultural extension experts	40	37,04	17	15,74	26	24,07	16	14,81	9	8,33	3,58	71.60
Poor soil fertility	52	48,15	17	15,74	18	16,67	14	12,96	7	6,48	3,86	77.20
Limited farm sizes	59	54,63	23	21,30	14	12,96	3	2,78	9	8,33	4,11	82.20
Inability to have sufficient cash financing	75	69,44	25	23,15	2	1,85	2	1,85	4	3,70	4,53	90.60
Irrigation water shortage	92	85,19	4	3,70	7	6,48	1	0,93	4	3,70	4,66	93.20
High cost of farm inputs	96	88,89	8	7,41	1	0,93	1	0,93	2	1,85	4,81	96.20

(1=Strongly disagree, 2=Disagree, 3=Partly agree, 4=Agree, 5=Strongly agree.)

To minimize the negative impacts of climate change, a clear understanding of climate change issues can help create positive attitudes towards tackling the negative impacts of climate change (Bardsley and Rogers, 2011). Alternatively, this understanding could lead to adaptation practices that minimize the harmful effects of climate change. Numerous studies have shown that understanding is significantly associated with positive attitudes (Masud et.al., 2015; Zsoka et al., 2013). Perceptions and attitudes of farmers towards climate change are indispensable for the implementation of appropriate strategies against adaptation barriers. The changes (strategies) they have made in their production systems for adaptation/adaptation to climate change are asked to the farmers who are aware of climate change, and these responses are listed in Table 5.

According to the calculated importance index, the fact that 81.80% of the regional farmers have abandoned stubble burning is a great strategic approach. 70.60% of them changed

their irrigation methods, 70% of them started small cattle breeding and afforestation. 61.20% of them went to product diversification during rotation and 60.02% of them changed their seed type. Half of the farmers have done soil conservation work and reduced the use of fertilizers and pesticides. 46.80% of the farmers changed the planting date, which is one of the important indicators of climate change. According to the study by Erkan et al. conducted in the area in 2009, none of the farmers made any changes in their production systems due to the increase in temperature or climate changes. However, at this point, farmers are developing different strategies and showing more sensitive behaviours according to changing climatic conditions.

Table 5. Adaptation strategies of farmers to climate change

Factors	5	%	4	%	3	%	2	%	1	%	Average	Severity Index %
I changed the planting date.	13	12,15	12	11,21	19	17,76	17	15,89	46	42,99	2,34	46.80
I reduced my pesticide use.	14	13,08	13	12,15	22	20,56	17	15,89	41	38,32	2,46	49.20
I cut back on fertilizer use.	20	18,69	11	10,28	17	15,89	26	24,30	33	30,84	2,62	52.40
I've protected the soil (erosion, flood, etc.)	15	14,02	20	18,69	24	22,43	8	7,48	40	37,38	2,64	52.80
I altered the planting techniques.	23	21,50	13	12,15	21	19,63	7	6,54	43	40,19	2,68	53.60
I changed the product variant	18	16,82	24	22,43	17	15,89	11	10,28	37	34,58	2,77	55.44
I switched seed varieties.	30	28,04	16	14,95	18	16,82	11	10,28	32	29,91	3,01	60.02
I diversified the product during the planting shift.	31	28,97	20	18,69	14	13,08	8	7,48	34	31,78	3,06	61.20
I planted trees	48	44,86	11	10,28	18	16,82	6	5,61	24	22,43	3,50	70.00
I started sheep farming	56	52,34	6	5,61	10	9,35	5	4,67	30	28,04	3,50	70.00
I changed irrigation methods	49	45,79	13	12,15	14	13,08	8	7,48	23	21,50	3,53	70.60
I stopped burning stubble	72	67,29	6	5,61	12	11,21	1	0,93	16	14,95	4,09	81.80

(1=Strongly disagree, 2=Disagree, 3=Partly agree, 4=Agree, 5=Strongly agree.)

Conclusion And Recommendations

Farmers in the study area of Konya expressed their perceptions and vulnerabilities on climate variability such as increasing temperature, changing precipitation patterns and increasing drought. Local farmers are aware that climate change is a serious problem affecting Konya's agricultural sector and they emphasized that the government, NGOs and universities should work together to ensure appropriate adaptation/adaptation to reduce vulnerability to climate change. Regional farmers cited various barriers to adaptation, such as high cost of production inputs, unpredictable weather conditions, insufficient water resources, uncertainty of weather information, inadequate agricultural extension studies, insufficient financing opportunities and agricultural subsidies. It shows that most of the farmers apply advanced irrigation system, different planting dates, use of organic fertilizers, good agricultural practices and crop diversification to adapt to climate change.

Farmers, especially in developing countries such as Turkey, should adapt to climate change in order to reduce the negative effects of climate change and reap the benefits of adaptation. It is necessary to develop and implement appropriate strategies in order to improve the understanding of farmers to adapt to climate change and to counteract the negative effects of climate change. This can only be achieved through climate awareness training activities, skills development and capacity building. These programs are important not only for farmers, but also because government officials provide appropriate technical support to farmers. As a result, policymakers should develop and implement appropriate adaptation/transformation strategies that will reduce the adverse effects of climate change, such as enhancing technological irrigation and weather forecasting, lowering the cost of production inputs, ensuring the availability of agricultural support and subsidies, increasing access to agricultural markets, and providing access to information.

Acknowledgement

This article has been prepared by using the Tübitak Project entitled " Determination of Typology of Sheep Enterprises in the Scope of Climate Change Perception and Adaptation, and Comparison of Resource Use Efficiency by Types of Enterprises". This study was supported the Scientific and Technological Research Institution of Turkey (TUBITAK) project numbered 121K885. We would like to thank TUBITAK for their financial support to this project.

Reference

Adams, R. M., Rosenzweig, C., Peart, R. M., Ritchie, J. T., Mc. Carl, B. A., Glyer, J. D. & Allen Jr, L. H. (1990). Global climate change and US agriculture. *Nature*, *345*(6272), 219.

Bardslay, D.K. & Rogers, G.P. (2011). Prioritizing engagement for sustainable adaptation to climate change: an example from natural resource management in South Australia. Soc. Nat. Resour. 24, 1-17.

Brahmi, A., Khaldi, R., Jaouad, M., Hicheri, A., Touati, I., Rkhissi, A. & Khaldi, G. (2012). Impacts of climate change on the small ruminants farming systems in north western Tunisia and adaptation tools. *New Approaches for Grassland Research in a Context of Climate and Socio-Economic Changes*, 427-431.

Descheemaeker, K., Zijlstra, M., Masikati, P., Crespo, O. & Tui, S. H. K. (2018). Effects of climate change and adaptation on the livestock component of mixed farming systems: A modelling study from semi-arid Zimbabwe. *Agricultural Systems*, *159*, 282-295.

Gifford, R., Kornos, C. & Mclntyre, A. (2011). "Behavioral dimensions of climate change: drivers, responses, bariers, and interventions. Wiley Interdiscip. Rev. Vlim. Change 2 (6), 801-807.

Godfray, H. C. J. & Garnett, T. (2014). Food security and sustainable intensification. *Philosophical transactions of the Royal Society B: biological sciences*, *369*(1639), 20120273.

Kaymakçı, M. & Engindeniz, S. (2010). Türkiye'de keçi yetiştiriciliği: sorunlar ve çözümler. Ulusal Keçicilik Kongresi 24-26 Haziran 2010, Bildiriler Kitabı, Çanakkale, 1-25.

Khan, M. I. & Sameen, A. (2018). Animal sourced foods for developing economies: preservation, nutrition, and safety. CRC Press.

Lemaire, G., Giroud, B., Bathily, B., Lecomte, P. & Corniaux, C. (2019). Toward ıntegrated crop-livestock systems in west africa: a project for dairy production along senegal river. In Agroecosystem Diversity (pp. 275-285). Academic Press.

Majid, M. Z. & McCaffer. R. (1997). "Assessment of work performance of maintenance contractors in saudi arabia" Journal of Management in Engineering. Volume 13, Issue 5, Pages 91.

Masud, M. M., Al-Amin, A. Q., Akhtar, R., Kari, F., Afroz, R., Rahman, M. S., & Rahman, M. (2015). Valuing climate protection by offsetting carbon emissions: rethinking environmental governance. *Journal of Cleaner Production*, *89*, 41-49.

Masud, M. M., Azam, M. N., Mohiuddin, M., Banna, H., Akhtar, R., Alam, A. F. & Begum, H. (2017). Adaptation barriers and strategies towards climate change: Challenges in the agricultural sector. *Journal of cleaner production*, *156*, 698-706.

Oğuz, C. & Karakayacı, Z. (2017). Tarım Ekonomisinde Araştırma ve Örnekleme Metodolojisi. Atlas Akademi, ISBN: 978-605-827852-3 1. Basım Konya.

Sejian, V., Kumar, D., Gaughan, J. B. & Naqvi, S. M. (2017). Effect of multiple environmental stressors on the adaptive capability of Malpura rams based on physiological responses in a semi-arid tropical environment. *Journal of Veterinary Behavior*, *17*, 6-13

Semerci, A. & Çelik, A. D. (2016). Türkiye'de küçükbaş hayvan yetiştiriciliğinin genel durumu. *Mustafa Kemal Üniversitesi Ziraat Fakültesi Dergisi*, *21*(2).

Speedy, A. W. (2003). Global production and consumption of animal source foods. *The Journal of nutrition*, *133*(11), 4048S-4053S.

Steinfeld, H. (2003). Economic constraints on production and consumption of animal source foods for nutrition in developing countries. *The Journal of nutrition*, *133*(11), 4054S-4061S.

Swart, R. (2008). Impacts of Europe's changing climate-2008 indicator-based assessment, European Environment Agency (EEA).

Thornton, P. K. (2010). Livestock production: recent trends, future prospects. *Philosophical Transactions of the Royal Society B: Biological Sciences, 365*(1554), 2853-2867.

Yamane, T. (1967) Elementary Sampling Theory.

Zsoka, A., Szerenyi, Z. M. Szechy, A. & Kocssis, T. (2013). Greening due to environmental education? Environmental knowlodge, attitudes, consumer behaviour and everyday pro-environmental activities of Hungarian high school and university students. J. Clean. Prod. 48. 126-138.

Hydrogen Production Via Nabh$_4$ Hydrolysis With Nanocatalysts: A Review

Deniz UZUNOĞLU DOĞRUYOL[1]
Ayla ÖZER[2]

Introduction

Hydrogen energy emerges as an important alternative in solving the economic, environmental, and social problems resulting from the use of fossil-based fuels to meet the energy needs of societies. Thus, several methods have been reported for the production of hydrogen. Among the reported methods, hydrogen production via $NaBH_4$ hydrolysis has attracted much attention since early 2000s due to its high theoretical hydrogen storage capacity (10.8 %) and relatively safe operation over against other chemical hydrides. Herein, developing a suitable catalyst is a crucial factor that is required to enhance the slow reaction rate of $NaBH_4$ hydrolysis. Therefore, this review has focused on nanocatalysts utilized in hydrogen production via $NaBH_4$ hydrolysis. In this content, the comparison of hydrogen energy with the other energy resources has been firstly evaluated, and then the main problem of hydrogen energy storage has been presented. After that, $NaBH_4$ hydrolysis and the catalyst types used in the hydrolysis have been discussed in detail. Due to the superior properties, especially the reported metal-based and carbon-based nanocatalysts used for hydrogen production via $NaBH_4$ hydrolysis have been reviewed and the advantages/disadvantages of them have been discussed. Lastly, the challenges and some solution suggestions for hydrogen production via $NaBH_4$ hydrolysis with nanocatalysts have been revealed to assist in the production of retainable and clean hydrogen energy.

Energy Resources

Energy, which is of vital importance for the survival of living things, is one of the indispensable elements for people and states. It has a strategic importance in many areas such as heating, defense, transportation, lighting, and communication. For these reasons, the energy dependence for humanity will never end. Increasing energy production and use cause environmental problems such as air pollution, global warming, and climate changes to directly affect people's lives. The main reason is that most of the energy needed today is met from fossil fuels. It is known that fossil fuels will run out in a very short time as their reserves are limited. Therefore, renewable energy sources such as hydrogen energy should be used.

The currently used energy sources are classified according to their use and convertibility, and the classification is shown in Schema 1. Accordingly, while energy resources are classified as renewable and non-renewable energy sources according to their use, they are divided into primary and secondary energy sources in regard to their convertibility. Non-renewable energy resources, namely fossil sources and core sources, are predicted to be depleted in a short time. Renewable energy sources, on the other hand, can renew themselves at the same rate as the energy taken from the energy source or faster than the depletion rate of the source. Primary energy sources such as coal, oil, natural gas, hydraulic, nuclear, wave-tide, biomass, wind and solar are the forms of energy that have not undergone any change or transformation. Electricity, diesel, gasoline, hydrogen, diesel, secondary coal, coke, petroleum coke, liquefied petroleum

[1] Dr., Mersin University
[2] Prof. Dr., Mersin University

gas (LPG), and air gas are the types of energy acquired by converting primary energy (Koç & Şenel, 2013).

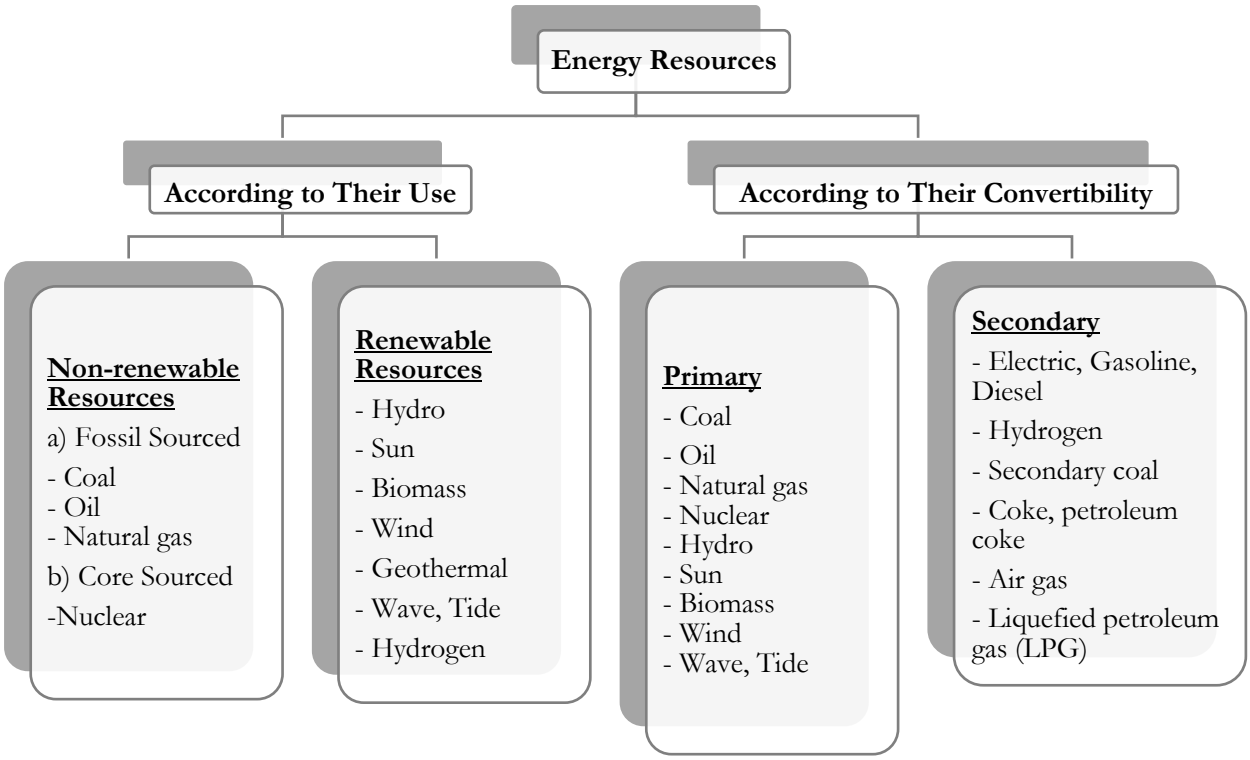

Schema 1. Classification of energy resources

According to 2019 data, the distribution of energy consumption in the world by fuel types is presented in Schema 2. It is clearly seen that the consumption is mostly covered by fossil resources (66.3%). With the increasing world population and developing technology, the need for energy is constantly increasing. For example, while the annual energy consumption was 194 EJ in 1973, this amount reached 418 EJ in 2019. Accordingly, the amount of needed energy has naturally increased due to the increase in the world population (IEA, 2019; Kilci, 2017).

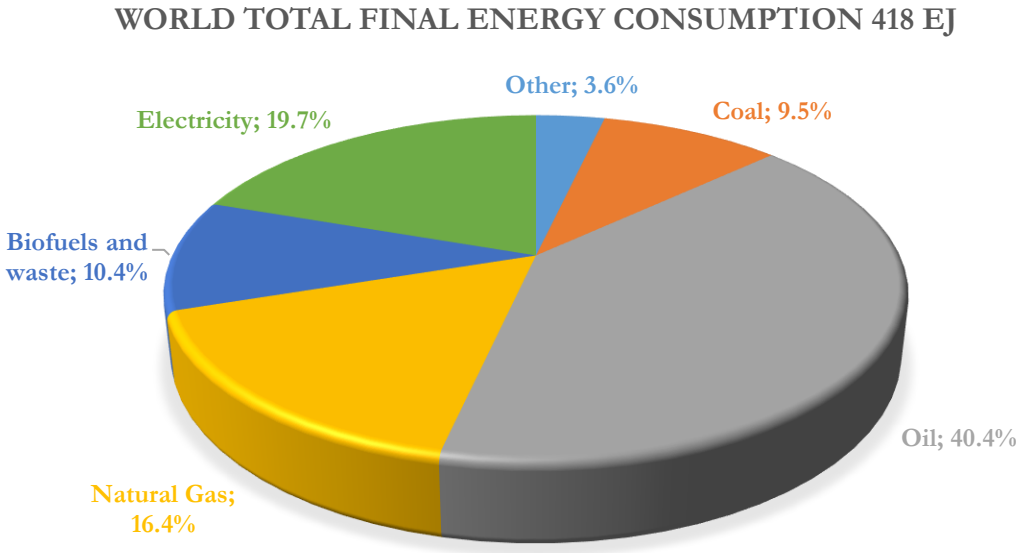

Schema 2. Share of world total final consumption by source, 2019

The change in the world's energy demand (Million tons of oil equivalent-Mtoe) by years is given in Table 1. Accordingly, it is predicted that global energy consumption will increase by 21.5% from 2015 to 2035 and energy demand will increase from 13776 Mtoe to 16748 Mtoe. In addition, it is seen that the highest average annual growth rate belongs to other renewable energy sources. It is estimated that between 2020-2035, fossil fuels will continue to meet the majority of energy consumption. In 2035, the share of fossil fuels in energy production is estimated to decrease from 81.3% to 73.7% compared to 2008; however, even then, fossil fuels will continue to be the dominant energy source. However, fossil fuels both have very limited reserves and are a great source of CO_2 gas for greenhouse gases, as they form CO_2 and H_2O when carbon-containing fossil fuels are burned. As long as dependence on fossil fuels continues, greenhouse gas levels will continue to rise and the world will continue to warm. Therefore, according to many scientists, the biggest problem of the 21st century is global warming. In order to solve this problem, it is of great importance to switch to alternative energy sources. As a renewable energy source, hydrogen can be preferred as a good alternative for future energy systems. Since only water is produced as the final product as a result of the combustion or consumption of hydrogen in the fuel cell, hydrogen can be produced from renewable sources and used in high efficiency fuel cells or engines in order to significantly reduce global warming and environmental pollution, which are the disadvantages of using fossil fuels. Hydrogen can be produced using various methods without emitting pollutants and greenhouse gases, and as the technology progresses, it is aimed that the production cost will reach levels that can compete with other sources(Kilci, 2017; Ruhe, 2019; World Energy Council, 2019).

Table 1. Change of world energy demand (Million tons of oil equivalent-Mtoe) by years

Fuel type	**1980**	**2008**	**2015**	**2020**	**2030**	**2035**	**2008-2035 Average annual growth rate**
Coal	1792	3315	3892	3966	3984	3934	0.6 %
Oil	3107	4059	4252	4346	4550	4662	0.5 %
Gas	1234	2596	2919	3132	3550	3748	1.4 %
Nuclear	186	712	818	968	1178	1273	2.2 %
Hydro-energy	148	276	331	376	450	476	2.0 %
Bio-energy	749	1225	1385	1501	1780	1957	1.7 %
Other renewable energy	12	89	178	268	521	699	7.9 %
Total	**7229**	**12271**	**13776**	**14556**	**16014**	**16748**	**1.2%**

Hydrogen Energy

There are many areas where hydrogen can be used as a fuel. These usage areas vary according to the way hydrogen is burned. The usage areas of hydrogen according to its combustion type are summarized in Table 2. Accordingly, when compared with other fuels, it can be said that hydrogen can be used safely and effectively in many areas. For example, the use of coal in automobiles or airplanes is not practically suitable while hydrogen can be used almost everywhere. It can easily be used instead of natural gas in heaters, ovens, and water heaters for heating purposes in houses (Şenaktaş, 2005).

Table 2. Usage areas of hydrogen according to its combustion type

Type of Combustion	Usage areas
Flaming combustion	Internal combustion engines, gas turbines, jet engines, rocket engines, heating, cooking areas
Conversion directly to steam	Steam turbines, steam propulsion, industrial steam, steam heating
Catalytic combustion (flameless combustion)	Cooking areas, water heating, space (ambient heating), absorption cooling

The ability to use hydrogen as an environmentally friendly fuel instead of petroleum products with limited reserves in vehicles with internal combustion engines such as buses, trucks, automobiles, tractors, and agricultural machinery has become the focus of attention of companies that manufacture vehicles in recent years. In particular, the fuels used in internal combustion engines are required to have the following properties;

- It should be easily transported and stored anywhere,
- It can be used in many places such as industry, house, vehicle,
- It should have a high calorific value per unit mass,
- It should be clean, light, and economical.
- It should be easily converted into heat, electrical, and mechanical energy.
- It should be able to produce energy with high efficiency.

Although the above properties are desired under ideal conditions, there is no fuel that has all these properties among the fuels currently used. However, it can be said that hydrogen is an ideal fuel that contains most of these features.

Figure 1 shows the energy contents per mass of various combustible materials. Accordingly, 1.0 kg of hydrogen has the same energy as 2.56 kg of methane or 3.0 kg of natural gas or 3.1 kg of gasoline. Accordingly, one of the most important superior features of hydrogen-fueled vehicles compared to vehicles using other fuels is that their engine efficiency is quite high. Another important feature is that the combustion product is only water vapor. It can be said that there may be only a small amount of carbon monoxide and hydrocarbons from petroleum products used to lubricate cylinders and nitrogen oxides from high temperature as waste products. It is possible to reduce the amount of nitrogen oxides caused by high temperatures by reducing the combustion temperature by sending some of the wastewater vapor back to the cylinder. Therefore, gas emissions from hydrogen-fueled engines are negligibly low compared to fossil-fueled vehicles.

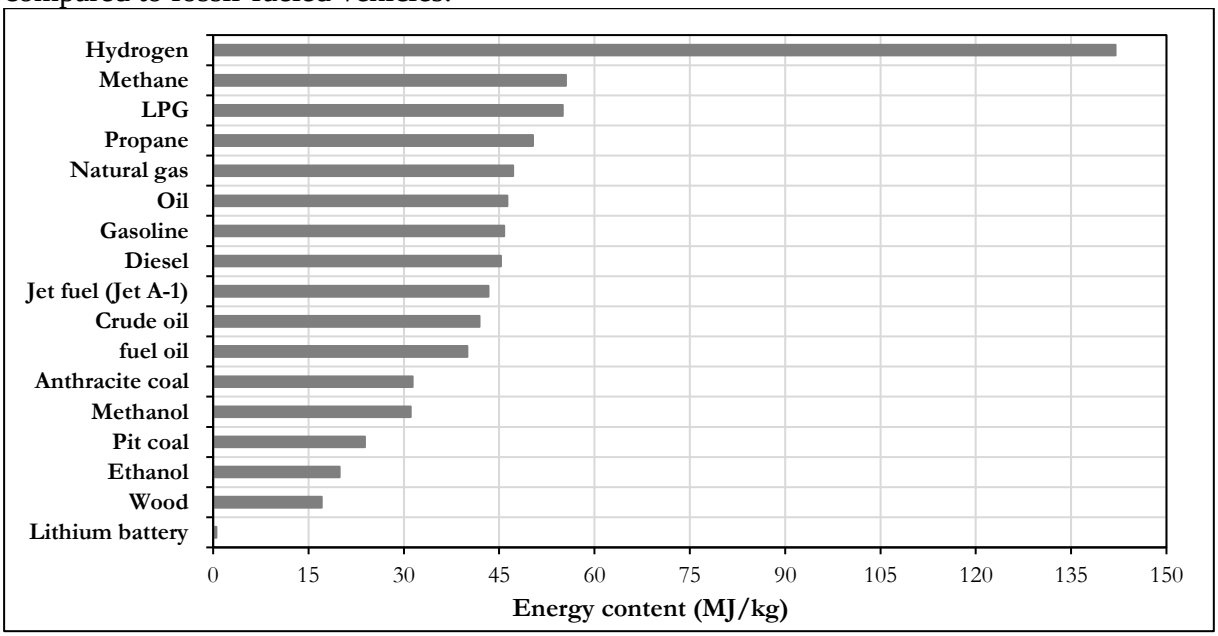

Figure 1. Energy content per unit mass of various combustible materials

The comparison of the properties of gasoline and methane used in internal combustion engines with hydrogen is presented in Table 3. One of the most important properties of hydrogen is its usability in liquid and gaseous forms. Gaseous hydrogen is about 14 times lighter than the same volume of air while it was 10 times lighter than gaseous fuels used in internal combustion engines such as methane. The most important advantage of using hydrogen as a fuel in engines is that the ignition limits extend to very wide fuel mixture ratios. It is known that hydrogen can ignite when it is present in the air at rates of 4.0-75% by volume. While this value is 1.0-7.6% for gasoline-air mixture, it is between 5.3-15% for methane-air mixture. Accordingly, hydrogen-air mixtures have wider flammability limits compared to other specified fuels. The flame temperature of hydrogen in air is higher than methane and very close to gasoline. When the lower calorific values are compared, it is seen that the lower calorific value of hydrogen on a mass basis is higher than that of gasoline and methane. However, when the lower calorific value of hydrogen is considered in terms of volume, it is lower than other fuels. In addition, since hydrogen is a carbon-free fuel, only water is released when it is burned, and therefore, emission gas (carbon dioxide, NO_x, SO_x, hydrofluoride carbons, perfluorocarbons, sulfurhexafluoride, etc.) is not emitted to the environment as in the combustion of fossil fuels; therefore, the use of hydrogen as a fuel does not cause the kind of pollution caused by fossil fuels. The toxicity of the fuel and its combustion products are, in decreasing order, gasoline, methane, and hydrogen. The safety assessment made according to factors such as the toxicity of fuel and combustion products, diffusion coefficient in air, flame spread, ignition energy in air, and explosion energy shows that the safety factors of gasoline, methane, and hydrogen are 0.53, 0.80, and 1.00, respectively. Accordingly, it can be said that hydrogen is the safest fuel comparison to gasoline and methane (Finegold et al., 1973; Şenaktaş, 2005).

Table 3. Comparison of hydrogen, gasoline, and methane fuel properties

Property	**Gasoline**	**Methane**	**Hydrogen**
Density (kg/m^3)	4.40	0.65	0.089
Diffusion in air (cm^2/s)	0.05	0.16	0.61
Specific heat (J/g.K)	1.20	2.22	14.89
Ignition limit in air (% by volume)	1.0-7.6	5.3-15	4.0-75
Ignition energy in air (mJ)	0.24	0.29	0.02
Ignition temperature (°C)	228-471	540	585
Flame temperature in air (°C)	2197	1875	2045
Flame spread (emissivity, %)	34-42	25-33	17-25
Explosion energy (g TNT/kJ)	0.25	0.19	0.17
Lower calorific value (kJ/g)	44.15	50.04	119.95
Lower calorific value (MJ/L)	32.70	31.8	8.69

Hydrogen can also be used in direct electricity generation with the help of fuel cells and electrochemical cycle, without being under the limiting effect of the Carnot cycle. Thus, it is possible to use the electricity produced by converting hydrogen into electricity in fuel cells, in houses and industries. It is also possible to power the vehicle by transmitting the electricity produced in hydrogen fuel cells to electric motors. There are no harmful gas emissions to the air, including water vapor, in vehicles where hydrogen is used as a source of electricity generation instead of burning it. Whether it is internal combustion or fuel cell, the main problem in vehicles where hydrogen will be used as fuel is safe storage (Boran, 2011).

Storage of Hydrogen

Hydrogen can be stored by various physical or chemical methods like compressed gas in high-pressure tanks, liquefied in insulated tanks, in carbon nanotubes, and adsorbed on metal or chemical hydrides. Each storage method has its own advantages and disadvantages. The advantages and disadvantages of these methods are listed below (Boran, 2011):

Compressed gas storage: Most prototype vehicles using fuel cells use hydrogen that is compressed and stored in high-pressure tanks. Hydrogen is fed to the fuel cell from the compressed gas tanks by suitable control units. Considering the lower volumetric calorific values (Table 3), an automobile can consume an average of 65 L (47 kg) of gasoline, which corresponds to 17 kg of hydrogen as energy. In other words, in order to provide the same energy, larger volume tanks are required for hydrogen fuel. However, the biggest problem in storing hydrogen gas in compressed form in steel cylinders is the weight of the steel cylinders. According to regulations, the pressure and temperature of filling hydrogen into tanks are limited to 87.5 MPa and 85°C. Even at this high-pressure value, the best possible energy equivalent for hydrogen is 4.4 MJ/L, which is about 14% of the energy equivalent (31.6 MJ/L) of the same amount of gasoline. Considering the weight of the entire system (weights of steel storage tanks), high-pressure tanks may contain 3.5-4.5% hydrogen by weight. Therefore, the portability of such high-pressure tanks is quite limited. Buses and other large vehicles have the physical size required by compressed tanks, but this will be difficult to provide in cars and other small portable devices. One of the other problems is that hydrogen creates a physical hazard because it is a flammable and explosive gas under high pressure, and in addition, leakage problems may occur due to hydrogen being a low molecular weight gas (Boran, 2011).

Liquefied storage: Since the volume occupied by hydrogen in the gas phase is large, liquefied storage of hydrogen emerges as a good alternative in order to reduce this volume. Storing of hydrogen by liquefaction is the method that can be stored in the largest volume compared to other methods. The density of liquid hydrogen at atmospheric pressure (0.1 MPa) is 70.9 g/L, while the density of compressed hydrogen (70 MPa, 288 K) is 40 g/L; therefore, since liquefied storage can be done at lower pressures than storage as compressed gas, it is safer and more advantageous to store hydrogen in liquefied form than in high-pressure tanks. This storage method is generally recommended to be used in situations where the storage volume is limited, such as space studies. However, an energy requirement is also required for the liquefaction of hydrogen. This energy needed is 1/3 of the energy of liquid hydrogen. However, since the distance between hydrogen molecules is large even in the liquid state, hydrogen (70.9 g/L) has a considerably lower density than water (1000 g/L). The energy equivalent of this low-density hydrogen is only 27% of the energy equivalent of gasoline. In addition to providing a low energy equivalent, another problem in the storage of hydrogen by liquefaction is that the hydrogen passes into the gas phase by taking heat from the outside and increases the pressure of the storage tank. In order to prevent this pressure increase, it is necessary to evacuate this gaseous phase (Boran, 2011).

Storage in nanotubes: Hydrogen can be stored physically or chemically in carbon nanotubes. In the physical system, storage occurs with weak Van der Waals bonds, and the stored hydrogen can be recovered and the same amount of hydrogen can be stored back into carbon nanotubes. In the chemical system, storage is provided by the formation of covalent bonds, but this method is not preferred because the recovery of the stored hydrogen is possible at only high temperatures. Studies in the literature have indicated that it is possible to store 4-14% hydrogen in carbon nanotubes. This method can be likened to compressed gas storage, but unlike this method, the pressurized storage tank is filled with carbon nanotubes. Apart from the weight of the tank itself, although graphite also adds weight, more hydrogen can be stored in carbon nanotubes at the same pressure and tank size (Kilci, 2017).

Storage in metal hydrides: Some metals and alloys have the ability to absorb hydrogen at normal pressure and temperature. At the end of this absorption process, hydrogen and hydride compounds containing one or more elements are formed. In the storage method with the metal hydride system, hydrogen is stored in the space between metal atoms. This storage method takes place in six stages given below (Kilci, 2017):

- **i.** Molecular hydrogen gas and metal encounter each other.
- **ii.** Hydrogen molecules begin to physically bond with the metal surface at normal temperature and pressure.

iii. Hydrogen molecules split into atoms and form chemical bonds with atoms on the metal surface.
iv. Hydrogen atoms begin to move between spaces in the metal.
v. Hydrogen atoms continue to diffuse through the spaces in the metal until there is no space left.
vi. Hydrogen atoms fill all the spaces in the metal and hydride formation is complete.

Metal hydrides are inherently stable and so do not require much energy for storage; however, it is necessary to give heat for the recovery of hydrogen stored in metal hydrides, which is an energy expenditure. Metal hydrides are generally made of metals such as Pd, Mg, Ta, special compounds such as $ZrMn_2$, $LaNi_5$, Mg_2Ni, or multi-phase alloys such as TiNi-Ti_2Ni, Mg-Mg_2Ni. The advantages and disadvantages of metal hydride systems are listed below:

Advantages:

- Temperature and pressure required for storage are low.
- Various preparation methods are available.
- It is possible to store repeatedly.
- The resulting hydrogen is quite pure.
- There is no evaporation loss as in liquefied hydrogen storage tanks, so it is safe.

Disadvantages:

- It has low storage capacity per unit mass.
- It can be used for short distances in vehicles due to its low storage capacity.
- The time required for storage is long.

Storage in chemical hydrides: Complex chemical hydrides can be used as hydrogen sources. This method has more hydrogen storage capacity by weight compared to many storage methods. In metal hydrides, hydrogen atoms settle into spaces in the metal, while in complex hydrides, BH_4^- ions are ionically bonded to the metallic cation. The biggest advantage of the storage method in chemical hydrides is not only the storage of hydrogen but also its production when necessary. However, the fact that the hydrogen production reaction is not completely reversible and so, the material cannot be easily recycled is a situation that limits the use of this method. In aluminum-containing hydrides (alanates) such as $NaAlH_4$, $LiAlH_4$, $Mg(AlH_4)_2$, $KAlH_4$, $Ca(AlH_4)_2$, hydrogen storage is carried out in the solid form as in metal hydrides. Boron-containing complex hydrides such as $NaBH_4$, KBH_4, LiH, and NaH provide advantages because they can be used in liquid conditions (Boran, 2011).

Table 4 shows the energy capacities of hydrogen storage methods. Except for gaseous and liquefied storage methods, among some complex hydrides and materials listed in Table 4, $NaBH_4$ has the highest hydrogen content as a hydrogen source. Accordingly, some advantages and disadvantages of the use of $NaBH_4$ are listed below (Yaşar, 2013):

Advantages:

- It is easily accessible.
- It has a high hydrogen storage capacity by mass and volume.
- It provides faster, reliable, and controlled hydrogen production with suitable catalysts.
- There are no reaction by-products harmful to the environment.
- Reaction by-products (BO_2^- ion) are recyclable.
- There is no risk of ignition of the reaction solution.
- The hydrogen production reaction is exothermic and therefore there is no need for any heat transfer from the outside to the environment.

Disadvantages:

- $NaBO_2$, one of the reaction by-products, forms a crystalline structure with water molecules and accumulates in the reaction medium, and may adversely affect hydrogen gas production.

- The availability of hydrogen gas produced by $NaBH_4$ hydrolysis in vehicles and other applications is limited.

Table 4. Energy capacities of hydrogen storage methods

Storage method	Hydrogen content (by mass %)	Energy density	
		MJ/kg	MJ/L
Gas phase (35 MPa)	100	141.9	3.35
Gas phase (70 MPa)	100	141.9	5.63
Liquefied (-253 ºC)	100	141.9	10.27
MgH_2	7.65	9.92	14.32
Mg_2NiH_4	3.60	4.48	11.49
$TiFeH_{1.95}$	1.95	2.47	13.56
$LaNi_5H_{6.7}$	1.50	1.94	12.77
$NaAlH_4$	7.40	-	8.25
$NaBH_4$ (solid)	10.6	-	-
$NaBH_4$ (20% solution)	4.40	44	-
$NaBH_4$ (35% solution)	7.70	77	-
Nanotube	1-10	-	-
Gasoline	-	46.94	34.77
Diesel	-	45.60	38.19
Natural gas		50.84	0.03905
Methanol	-	22.69	5.9-8.9

Hydrogen Production Methods

The methods used in the current hydrogen production is shown in Schema 3. Accordingly, global raw hydrogen production is carried out almost exclusively by methods using fossil resources. However, this situation will continue to depend on fossil resources and therefore will cause air pollution (Singh & Dutta, 2018).

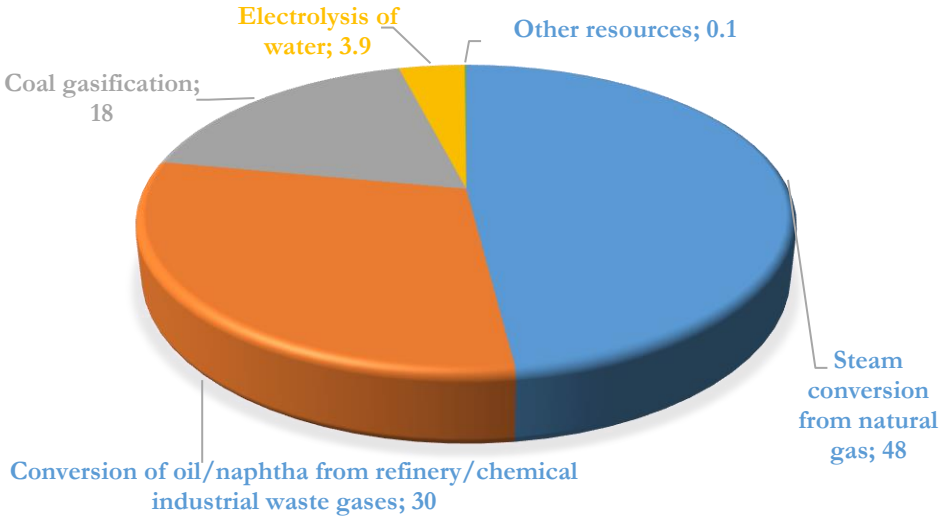

Schema 3. Methods used in current hydrogen production

Hydrogen production methods can theoretically be divided into three main parts as thermochemical processes, production from water and biological processes as shown in Schema 4 and these methods are briefly explained following parts (Chandrasekhar et al., 2015; Ji & Wang, 2021):

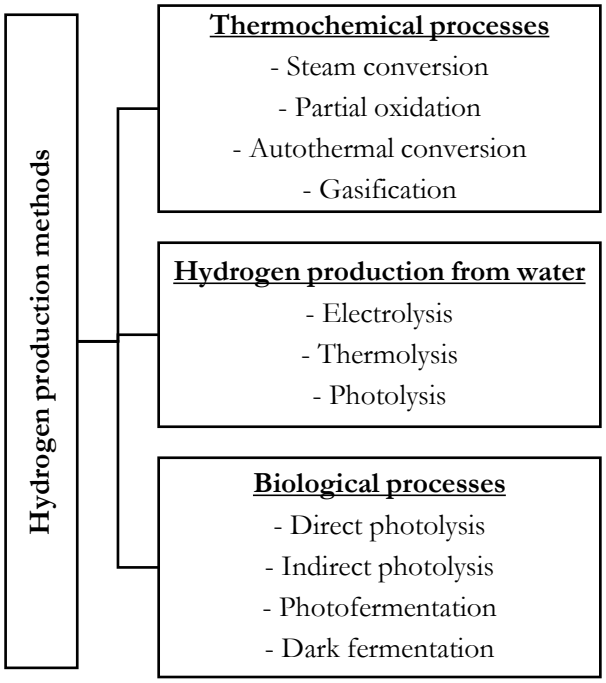

Schema 4. Detailed hydrogen production methods

Thermochemical processes: Nowadays, hydrogen is produced mostly from sources such as fossil fuels and biomass by thermochemical methods such as steam transformation, partial oxidation, autothermal transformation and gasification.

i. *Steam conversion method:* The most frequently used method in the production of hydrogen by thermochemical processes is the steam conversion method and the hydrogen production efficiency is in the range of 74-85%. This method is based on the catalytic conversion of gas mixtures containing hydrocarbons such as methane, ethane, propane, butane, pentane into CO_2 and H_2 together with steam at high temperature (850-900 ºC) and high pressure (2.0-3.5 MPa). If the raw material mixture used contains sulfur, the mixture is passed through the desulphurization process before the reaction process in order to prevent deterioration of the catalyst structure. The general units of the vapor conversion process are desulphurization, reformer, water gas diverting reactor, CO_2 absorber-H_2 separator.

ii. *Partial oxidation method:* This method is based on the partial combustion of hydrocarbon-containing fossil fuels at 1300-1500 ºC with water vapor and limited amounts of oxygen in a closed combustion chamber. In this method, the hydrogen production efficiency is about 70% and no catalyst is needed as in the steam conversion method. Therefore, this method can allow the use of even low-quality fossil fuels containing sulfur, as it does not require a catalyst. However, despite the advantage that this method does not require a desulphurization process, the use of 95-99% pure oxygen in the method increases the cost. In processes that use air instead of oxygen, an additional process is required in which the hydrogen produced is purified from nitrogen and other gases by using a palladium membrane.

iii. *Autothermal conversion:* This method is a combination of vapor conversion and partial oxidation methods. Accordingly, the heat required for hydrogen production by steam conversion is provided from oxidation, which is an exothermic reaction, and the hydrogen production efficiency is increased by using the steam conversion method. As can be understood from here; steam and oxygen (or air) are fed together to the converter so that oxidation and conversion reactions take place simultaneously.

iv. *Gasification method:* In this method, raw materials such as coal (especially coals with low combustion heat), fuel oils containing high sulfur, biomass, and wastes (hazardous wastes, domestic wastes, and so on) are treated with steam at high pressure (1-33 bar) and high temperature (500-1400 ºC) in a low oxygen environment, and as a result of this reaction, syngas containing hydrogen, methane, carbon dioxide, carbon monoxide and nitrogen is obtained. This synthesis gas obtained can be used to generate electricity by sending it directly to a turbine, or it can be used to produce chemicals such as hydrogen and fertilizers after some processes. At the end of the gasification process, the non-gasified materials are taken from the bottom of the gasifier as slag and this slag can be used as an additive in the construction industry.

Hydrogen production from water: In recent years, due to the limited fossil fuel resources and their damage to the environment, it is directed to hydrogen production from renewable and environmentally friendly sources. At this point; hydrogen production methods from water such as electrolysis, thermolysis, and photolysis become prominent. These methods used in hydrogen production, whose source is renewable, provide very clean production.

i. *Electrolysis:* In this method, hydrogen is produced by the decomposition of water into hydrogen and oxygen via electrochemical reaction. The electrolysis process consists of an anode and a cathode electrode, a power source and an electrolyte. Here, when a direct current is applied between the anode and the cathode, the water in the electrolyte decomposes into hydrogen at the cathode and oxygen at the anode. Since pure water has a high electrical resistance (100 ohms/cm), a large amount of current is required to carry out the electrolysis process. This causes the electrolysis process to be very expensive and has a share of only 4% in hydrogen production, as shown in Schema 3. The voltage required for the electrolysis of water is 1.24 volts at 25 °C and 1.0 atm pressure, and the minimum amount of energy required for the electrolysis of 1.0 mole of water is 65.3 Wh, while the minimum amount of energy required to produce 1.0 m^3 of hydrogen is 4.8 kWh. Accordingly, the efficiency of the electrolysis process is approximately 70%. In order to reduce the cost of this method, it is necessary to reduce the electrical resistance of the water, in other words, to increase the conductivity. For this purpose, the water temperature can be increased to 700-1000 °C or compounds such as salt and potassium hydroxide can be added to the electrolyte or nickel-plated steel electrodes can be used.

ii. *Thermolysis:* The breakdown of a substance into simpler molecules or atoms as a result of exposure to high temperature is called thermolysis (thermal decomposition). Hydrogen production by the thermolysis method is carried out by heating the water up to 1400 °C and decomposing it into hydrogen and oxygen atoms. The higher the thermolysis temperature, the faster the decomposition rate. After the water vapor decomposes, the gases formed are separated from each other with the help of a ceramic membrane. Hydrogen production by thermolysis is costly due to the high temperature requirement and the need for materials resistant to these temperatures. Therefore, some chemicals such as sulfur and iodine can be used for thermal decomposition of water at low temperatures. Accordingly, the following reactions are carried out.

$2H_2O + SO_2 + I_2 \rightarrow 2HI + H_2SO_4$ (exothermic) (1)

$H_2SO_4 \rightarrow SO_2 + H_2O + 1/2O_2$ (endothermic) (2)

$2HI \rightarrow I_2 + H_2$ (endothermic) (3)

According to Equation (1), the H_2SO_4 and HI products required for the process are firstly produced by an exothermic reaction. Then, as seen in Equation (2), the produced H_2SO_4 decomposes into its components at approximately 900 °C, and at

the end of this reaction, oxygen gas is formed as a product. Finally, the HI produced by the reaction in Equation (1) is separated into its components at approximately 400 °C according to Equation (3) and hydrogen gas is taken as a product.

iii. *Photolysis:* This method is based on the decomposition of water into hydrogen and oxygen atoms with sunlight absorbed by a photocatalyst cell. The photocatalyst cell in the process consists of a photo-electrochemical cell and semiconductor electrodes, and this cell starts to work when the sun's rays fall on the semiconductor electrode; then, the energy produced by the cell causes the water to electrochemically decompose. In this respect, this method is similar to the hydrogen production method by electrolysis, but studies indicate that the photolysis method is more efficient.

Biological processes: Although fossil fuels are not used in methods such as electrolysis, thermolysis and photolysis, the use of water as a resource may cause water shortages in the world in the long run. Therefore, the use of biological resources and wastes in hydrogen production is a better alternative than other methods. In addition, in processes where biological resources and wastes are used, less energy is required as it can operate at room temperature and pressure, and therefore, these methods are more preferred because the process cost is lower than other methods. The basis of these methods is the degradation of biomass or waste by some bacteria or algae by hydrogenase and nitrogenase enzymes.

i. *Direct photolysis:* In this method, water molecules are directly separated into hydrogen and oxygen as a result of the photosynthesis processes of plants and algae with solar energy. The produced hydrogen ions are converted to hydrogen gas by the hydrogenase enzyme.

ii. *Indirect photolysis:* In this method, hydrogen is produced in two stages. In the first stage, carbohydrates and oxygen are produced by the combination of water, carbon dioxide and solar energy ($6H_2O + 6CO_2 +$ "sunlight" $\rightarrow C_6H_{12}O_6 + 6O_2$). In the second stage, hydrogen is produced from the produced carbohydrate through the nitrogenase and hydrogenase enzymes of *Cyanobacteria* ($C_6H_{12}O_6 + 12H_2O +$ "light" $\rightarrow 12H_2 + 6CO_2$).

iii. *Photofermentation:* In this method, hydrogen gas can be produced by photofermentative bacteria with nitrogenase enzyme by using organic acids, water, and sunlight in cases where the amount of nitrogen is low ($CH_3COOH + 2H_2O +$ "light" $\rightarrow 4H_2 + 2CO_2$).

iv. *Dark fermentation:* In this method, hydrogen can be produced in a dark environment using carbohydrate-rich anaerobic bacteria (*Enterobacter, Bacillus, Clostridium*) ($C_6H_{12}O_6 + 2H_2O \rightarrow 2CH_3COOH + 2CO_2 + 4H_2$).

Hydrogen Production via $NaBH_4$ Hydrolysis

Unlike the methods mentioned above; Schlesinger and Brown (1953) (Schlesinger et al., 1953) reported that $NaBH_4$ can be used in the production of $H_{2(g)}$ as well as hydrogen storage. Ideally, $NaBH_4$ gives the following exothermic hydrolysis reaction with water:

$$NaBH_{4(aq)} + 2H_2O_{(l)} \rightarrow 4\ H_{2(g)} + NaBO_{2(aq)} \qquad \Delta H = -300\ kJ/mol\text{-}NaBH_4 \quad (4)$$

The conversion of the exothermic hydrolysis reaction of $NaBH_4$ is only 7-8% and this reaction rate is so slowly in absence of catalyst. A suitable catalyst significantly accelerates the rate of $NaBH_4$ hydrolysis to produce hydrogen.

The actual hydrolysis reaction of $NaBH_4$ in water is given by Equation (5) as the hydrolysis of $NaBH_4$ is highly affected by the amount of water in the medium which is another hydrogen source for the hydrolysis.

$$NaBH_{4(aq)} + (2 + x)H_2O_{(l)} \rightarrow NaBO_2.xH_2O_{(s)} + 4H_{2(g)} \quad (5)$$

where x is the excess hydration factor, which may be a value of 2 or 4 depending on the reaction conditions. Accordingly, at least 4.0 moles of water H_2O are required for every mole of $NaBH_4$. This is thought to be due to two reasons; *(i)* very fast hydration of sodium metaborate ($NaBO_2$) and *(ii)* low solubility of $NaBH_4$ (55 g for every 100 g of H_2O at 25 ^oC).

$NaBH_4$ hydrolysis reactions occur as Equations (6) and (7) depending on the water amount.

$$NaBH_{4(aq)} + 6H_2O_{(l)} \rightarrow 4H_{2(g)} + NaBO_2 \cdot 4H_2O \text{ (or } NaB(OH)_4 \cdot 2H_2O)_{(s)} \quad \Delta H = -272.4 kJ/mol\ NaBH_4 \quad (6)$$

$$NaBH_{4(aq)} + 4H_2O_{(l)} \rightarrow 4H_{2(g)} + NaBO_2 \cdot 2H_2O \text{ (or } NaB(OH)_4)_{(s)} \quad \Delta H = -250.1 kJ/mol\ NaBH_4 \quad (7)$$

Accordingly, 1.0 mole of $B(OH)_4^-$ forms with the hydrolysis of 1.0 mole of BH_4^-. It means that BO_2^- ions surround 2.0 moles of free H_2O resulting in reducing of H_2O reactivity. Hence, it can be concluded that hydrogen production is highly dependent on the amount of water and thus the amount of $NaBH_4$ when especially high concentrated $NaBH_4$ solutions are used for the hydrolysis reaction. However, there are some studies showing that the hydrogen production would be affected by even low concentrated $NaBH_4$ concentration. This case could be hitched on to the catalyst structure and/or amount because $NaBH_4$ hydrolysis is affected by both of them. Therefore, synthesis of suitable catalysts is of great importance for hydrogen industry in order to advance the hydrolysis of $NaBH_4$ (B. H. Liu & Li, 2009).

Catalysts types for the hydrogen production via $NaBH_4$ hydrolysis and their advantages and disadvantages are summarized in Schema 5 (B. H. Liu & Li, 2009). In brief, $NaBH_4$ hydrolysis can occur in presence of homogenous catalysts including acid and metal-complex, or heterogeneous catalysts including metal-based and metal-free. Although homogeneous catalysts are inexpensive and widely available, and their all catalytic sites are available for the reaction, they have various disadvantages such as reactor corrosion, difficult separation, difficult reaction rate control, and no reusability. Acid catalysts are consumed during the reaction thus they are one-use catalysts, which increases the process cost. Most of the metal-complex catalysts should be in-situ reduced during the $NaBH_4$ hydrolysis reaction before working as effective catalysts, which causes loss of time and the formation of undesirable by-products. Unlike homogeneous catalysts, heterogeneous catalysts could be easily separated, recovered, and reused as well as have better catalytic activity in the $NaBH_4$ hydrolysis reaction.

In order to further improve catalytic activity, metal or carbon species among the heterogeneous catalysts are frequently downsized to nanoparticles to maximize the ratio of surface atoms, which intensely rises the number of active sites on the nanoparticle surfaces and their interaction with different molecules. Therefore, in recent years, heterogeneous nanocatalysts have attracted much attention for hydrogen production because of their superior properties like very high catalytic activity and stability.

Metal-based nanomaterials are divided into two groups of precious (Au, Ag, Pt, Pd, Rh, Ru, Ir) and non-precious (Co, Cu, Ni, Ti, Mo, Ce, Zr, Y, Yb) metal nanocatalysts. Precious metal nanocatalysts are not preferred to be used in industrial applications due to their high cost and shortage although they exhibit high catalytic activity, stability, and tolerance against deactivation. For this reason, the precious metal nanocatalysts are generally supported on non-precious metals or metal-free materials. Another reason of this supporting process is the easily agglomeration of the nanocatalysts. The nanocatalysts tend to aggregate to form larger species, causing the decline of the catalytic activity, due to the high surface energy caused by large ratio of surface atoms. Therefore, various supporting materials such as metallic oxides (e.g., Al_2O_3, TiO_2, SiO_2, Co_3O_4), foam materials (e.g., Ni foam, Co foam), carbon-based materials (e.g., multiwalled carbon nanotube, graphene, activated carbon, porous carbon, mesoporous graphitic carbon), chitin, zeolitic imidazolate frameworks, metal-organic frameworks, polypyrrole are utilized in order to prevent the agglomeration of the nanocatalysts, provide higher stability and lower tendency to oxidation, resulting to increase the hydrogen gas production efficiency.

On the other hand, it is well known that the physicochemical properties like size, shape, composition, and structure of the nanocatalysts considerably affect the hydrogen gas production efficiency. These properties could be tuned by altering some reaction conditions (e.g., temperature, pressure, time, stirring), initiators, solvents, reducing agents, surfactants, and stabilizers. Hence, nanocatalysts in a variety of sizes, shapes (spheres, cubes, sheets, tubes, rods, wires, fibers, plates, octahedrons, etc.), compositions (e.g., Co, Au, Pt, Ag, Ru, Pd, etc.), and architectures (alloys, core-shell, composites, hollow, etc.) have been investigated for the hydrogen production processes.

Additionally, some heterogenous nanocatalysts are treated with acids during the synthesis process for the hydrogen production via $NaBH_4$ hydrolysis. Its' purpose is to combine the superior properties of both homogenous and heterogenous catalysts in order to raise the efficiency of the synergistic catalysts by bridging the gap between them, i.e., connecting the two areas (Fiorio et al., 2022).

Consequently, it can be understood that it is important for the hydrogen production via $NaBH_4$ hydrolysis to synthesize effective nanocatalysts with high catalytic activity, stability, and selectivity by optimizing of their properties via the methods mentioned above. Hence, a literature survey has been conducted related to various metal-based nanocatalysts used for the hydrogen production via $NaBH_4$ hydrolysis, and the results are summarized in Table 5.

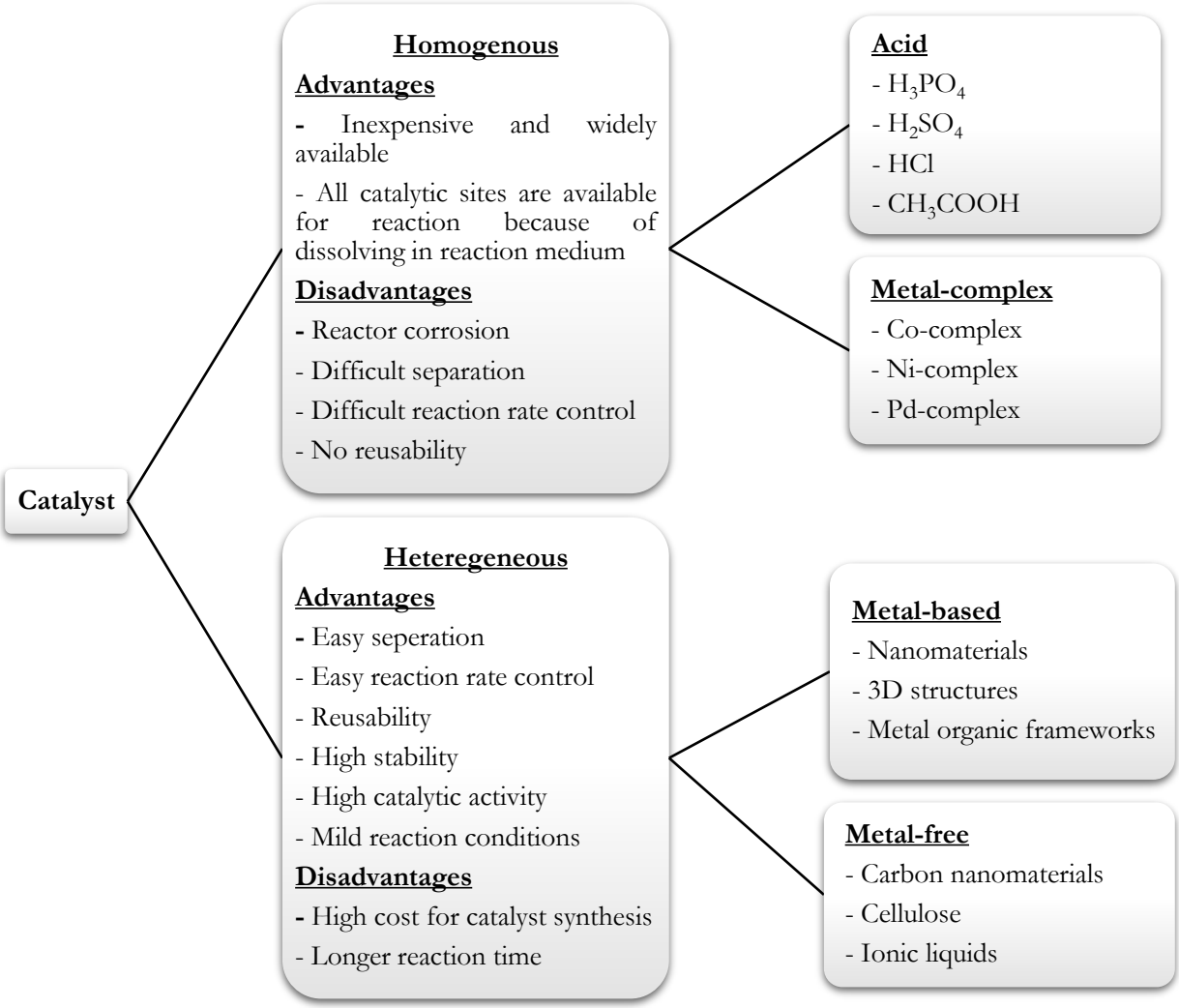

Schema 5. Catalysts types for the hydrogen production via $NaBH_4$ hydrolysis and their advantages and disadvantages

Table 5. The catalytic activities of various metal-based nanocatalysts used for the hydrogen production via $NaBH_4$ hydrolysis

Catalyst	Size (nm)	Activation energy (kJ/mole)	Temperature (˚C)	Activity (mL H_2/g.min)	Reference
Ruthenium based supported multiwalled carbon nanotube tungsten nanoalloy (3% RuW/MWCNT)	6.5	16.327	30	95841.4	(Avcı Hansu, 2022)
Ruthenium nanosheets (RuNSs) decorated cobalt foam	RuNSs: 100-200	30.18	30	92310	(J. Zhang et al., 2022)
Carbon nanotube (CNT) supported bimetallic RuMo nanoparticles (RuMo(80-20)/CNT)	3.12	35.11	30	82758.43	(Avci Hansu et al., 2020)
Ultrafine Ru nanoparticles (RuNPs) on a TiO_2 nanospheres (TiO_2 NSs)-Ti_3C_2 support	RuNPs: 2 TiO_2 NSs: 200	50.96	30	60000	(T. Li et al., 2022)

Ru nanoparticles (RuNPs) on magadiite	RuNPs: 1.2	54.5	25	59276 ± 500	(H. Liu et al., 2021)
Ultrasmall Ru nanoparticles (RuNPs) supported on chitin nanofibers (ChNFs)	RuNPs: 2.4 ChNFs: 10-100	39.16	30	55290	(J. Zhang et al., 2020)
CeO_2 supported Ni (II)-Schiff Base complex	200	20.587	50	43392	(Kilinc & Sahin, 2021)
Co nanoparticles (CoNPs)@ zeolitic imidazolate frameworks-8	CoNPs: 2.1	62.9	30	19400	(Luo et al., 2019)
Cotton stalk activated carbon-supported Co–Ce–B nanoparticles	10	48.22	25	16420	(X. Zhang et al., 2019)
Carbon nanotubes (CNTs)-promoted Co-B	CNTs: 10-20	23.5	25	12000	(Shi et al., 2019)
Cobalt nanoparticles (CoNPs) supported on bagasse-derived porous carbon	CoNPs: 50	31.25	25	11086.4	(Bu et al., 2021)
Co–W–B nanoparticles on polypyrrole	31.7	49.18	30	9920	(Baydaroglu et al., 2022)
Boron-Cobalt-Nickel-Yttrium nanocatalysts	20	28.1	40	9700	(Kord et al., 2022)
Ru nanoparticles (RuNPs) decorated P-vacancy-rich CoP ($Ru_{9.8}$/r-CoP)	RuNPs: 2.52	45.3	25	9783.3	(S. Zhou et al., 2021)
Triton stabilized NiB nanoparticles	30-50	58.91	65	8970	(Elçiçek et al., 2021)
Ru-clusters decorated core-shell metal-organic framework (Ru/CoO_x@NPC)	500	54.2	25	8019.5	(Dou et al., 2021)
Metal-organic frameworks derived CuO nanoparticles (CuO NPs)@C	CuO NPs: 10-30	-	25	7240	(Kassem et al., 2019)
Ru nanoparticles supported on Co_3O_4	19.9	28.26	25	6514	(Bozkurt et al., 2019)
CoMnPt/TiO_2	3-4	34.19	22	6250	(Çakanyildirim & Gürü, 2022)
Fe-Doped CoP nanoarray	100	39.6	25	6060	(Tang et al., 2017)
CoMnPt/Al_2O_3	3-4	40.02	22	5600	(Çakanyildirim & Gürü, 2022)
CoB supported on nano-sepiolite clay treated with phosphoric acid	2.4	21.4	30	5025	(Selvitepe et al., 2019)
Chitosan-mediated Co-Ce-B nanoparticles	100	33.1	30	4760	(Zou et al., 2018)
Pt nanoparticles supported on Co_3O_4	3.2	43.52	25	4713	(Bozkurt et al., 2019)
Pitaya pulp structural cobalt (Co/CoO_x NPs)-	Co/CoO_x NPs: 5-10	38.16	25	3998	(L. Wang et al., 2019)

based carbon nanocatalyst					
Ternary NiCoP urchin like 3D nanostructure supported on nickel foam	12-30	38.3	25	3986	(Pornea et al., 2019)
Ruthenium nanoparticles supported on zeolitic imidazolate frameworks-67	41.6	36.2	30	3875	(Tuan & Lin, 2018)
Nitrogen-doped mesoporous graphitic carbon encapsulated cobalt nanoparticles (Co@NMGC)	4.5-8	35.2	25	3575	(J. Li et al., 2020)
Monolithically integrated NiCoP nanosheet array on Ti mesh	700	52.68	30	3016.79	(K. Li et al., 2017)
PVP-protected Au/Ni bimetallic nanoparticles ($Au_{50}Ni_{50}$ BNPs)	2.7	30.3	30	2597	(X. Wang et al., 2014)
Co-P nanoparticles supported on dandelion-like CNTs-Ni foam composite carrier	80	49.94	25	2430	(F. Wang et al., 2018)
Polyacrylonitrile nanofiber composite membranes loaded with silver nanoparticles (Ag@PNCMs)	250-500	52.13	25	2269	(Z. Li et al., 2021)
Pd nanoparticles supported on Co_3O_4	12.2	65.82	25	2109	(Bozkurt et al., 2019)
$Co_{0.45}W_{0.55}$ nanocomposite from zeolitic imidazolate frameworks-67	23	55.56	25	1770	(J. Zhou et al., 2022)
Cobalt nanoparticles supported on magnetic coreshell structured carbon (Co/Fe_3O_4 NPs@C)	Fe_3O_4 NPs: 200-500	49.2	25	1403	(Chen et al., 2018)
Engineered nano-foam of tri-metallic (FeCuCo) oxide	20-40	16.3	25	1380	(Patil et al., 2021)
Nanostructured urchin-like $CuCo_2O_4$ spinel catalyst	25.5	22	30	1370	(Patil et al., 2020)
Titanate nanotube supported Co nanoparticles (CoNPs)	CoNPs: 2-7	29.68	30	1040	(R. Li et al., 2022)
$NiCo_2O_4$ hollow spherical nanoparticles	93.17	52.211	25	1000	(Jadhav et al., 2017)
Cobalt nanorods (CoNRs) anchored on a $Ti_4N_3T_x$ MXene composite	CoNRs: 100	44.23	30	526	(T. Li et al., 2021)

Ni–Ru nanocomposite (Ni–Ru/50WX8)	<100 nm	52.73	35	400	(C. H. Liu et al., 2009)
PdPt bimetallic nanoparticles	10-25	13.93	25	372.52	(Aygun et al., 2022)
Silver-platinum bimetallic nanoparticles (N@Pt-Ag BNPs)	5.6	16.07	25	367.01	(Lin et al., 2022)
NiB/$NiFe_2O_4$ NPs	$NiFe_2O_4$ NPs: 30-40	72.52	25	299.88	(Liang et al., 2017)
Biosynthesized Ag–Pt bimetallic nanoparticles using propolis extract	11.35±7	25.61	25	294.78	(Tiri et al., 2022)
Fe_2O_3 nanoparticles coupled with modified MWCNTs (Fe_2O_3@OMWCNTs)	22	15.92	25	195.4	(Prasad et al., 2019)
Iron-doped Ni_5P_4 ultrathin nanoporous nanosheets (Fe-doped Ni_5P_4)	0.875	53.41	25	175	(Ma et al., 2019)
Ni/TiO_2 nanoparticles	70-162	25.11	60	110.87	(Dönmez & Ayas, 2021)
Silver nanoparticle (AgNPs)/multi-walled carbon nanotube composite (AgMWCNT)	AgNPs: 20 MWCNT: 30	44.45	30	17.4	(Huff et al., 2017)
Platinum nanoparticles	2-4	39.2	30	1.30	(Huff et al., 2021)

It has been determined from the latest papers summarized in Table 5 that among the precious metal nanocatalysts, especially Ru nanoparticles, which are very small in size and synthesized in composite form, exhibit very high catalytic activity for the hydrogen production via $NaBH_4$ hydrolysis. It can be said that the very small size of Ru nanoparticles provides to minimize internal diffusion resistance, resulting in obtaining higher hydrogen production efficiency. Among the non-precious metal nanocatalysts, cobalt-based nanocatalysts have much higher catalytic activity for the hydrogen production via $NaBH_4$ hydrolysis. On the other hand, the cobalt-based nanocatalysts have generally magnetic structures, providing simply separation from the environment via external magnet and also being important for recyclability. Furthermore, it has been known that nickel cannot exhibit catalytic property in the hydrolysis of $NaBH_4$; however, it greatly increases the efficiency of hydrogen production via $NaBH_4$ hydrolysis. Thus, nickel is generally combined with Ru, Co, Fe, or a metalloid atom (such as B or P) due to the shift in electronic states of the active metals.

Although a lot of the works related to $NaBH_4$ hydrolysis using metal-based nanocatalysts have been reported in the literature, it is noticed that there are a few works that used metal-free nanocatalysts in $NaBH_4$ hydrolysis. The metal-free nanocatalysts have generally great potential in hydrogen production via $NaBH_4$ methanolysis. Among the metal-free nanocatalysts used for hydrogen production via $NaBH_4$ hydrolysis, carbon-based nanomaterials have higher catalytic activity. Santra et al. (2017) (Santra et al., 2017) synthesized positively charged functionalized carbon nanodots (CNDs) with a variety of different effective surface areas (ESAs) and applied for the hydrogen production via $NaBH_4$ hydrolysis. The CNDs were positively charged via microwave treatment of citric acid monohydrate and urea. CNDs synthesized with a reaction time of 2.5, 3.5 and 4.5 min were marked as sample A, B, and C, respectively. TEM images of

the CNDs revealed that the average diameters of samples A, B and C were found to be 2.5, 3.5, and 15.6 nm, respectively. The catalytic activity followed the order of B > A > C, which was directly related to the ESA of the samples. It was found that sample B showed the highest hydrolysis activity that of 1066 mL H_2/g.min at 20 ˚C with an activation energy of 22.01 kJ/mole. Also, it was observed that all of the samples exhibited good reusability and 100% conversion even after the 10^{th} cycle. In the work of Nabid et al. (2016) (Nabid et al., 2016), boron and nitrogen co-doped carbon-based dots (CDs) with the size of approximately 10 nm were used as catalyst in the hydrogen production via $NaBH_4$ hydrolysis. The aim of the co-doping one with lower (B:2.04) and one with higher (N:3.04) electronegativity than that of C (2.55) was to tune the electronic properties and so to improve the catalytic activity of CDs. The catalytic activity of boron and nitrogen co-doped CDs was determined as 74.6 mL H_2/g.min at 25 ˚C while the single-doped CDs had lower catalytic activity proving the synergistic coupling effects of two heteroatoms. Also, it was found that the catalyst could be reused for five circles with slight decrease in catalytic activity. Fangaj and Ceyhan (2020) (Fangaj & Ceyhan, 2020) investigated the applicability of apricot kernel shell waste treated with phosphoric acid as a green metal-free catalyst ($GAKS_{cat}$) for hydrogen generation from hydrolysis of $NaBH_4$. The average particle size of $GAKS_{cat}$ was calculated from TEM images as 1.989 nm, which was compatible with the average particle size of 1.44 nm calculated by the XRD Debye-Scherrer equation. The results indicated that the optimum H_3PO_4 percentage was found as 15%. $GAKS_{cat}$ treated with 15% H_3PO_4 exhibited the catalytic activity of 20199 mL H_2/g.min at 30 ˚C with an activation energy of 30.23 kJ/mole for hydrogen generation from hydrolysis of $NaBH_4$. A quite high catalytic activity was obtained with the catalyst without adding any noble metals (Ru, Pt, Pd) or support materials (polymers, resins).

It can be deduced that although metal-free nanocatalysts can be thought as alternatives in terms of minimizing or replacing high-cost and scarce precious-metal nanocatalysts, much higher catalytic activities could be obtained without the need for high activation energies by metal-based nanocatalysts especially containing Ru and/or Co.

Challenges and Solution Suggestions

Hydrogen production processes via $NaBH_4$ hydrolysis, whether with metal-based or metal-free nanocatalysts, have some challenges such as mist elimination, crystallization of borates, temperature control, catalyst stability, and so on. These challenges are summarized below (B. H. Liu & Li, 2009).

- Mist elimination: In the hydrogen production processes via $NaBH_4$ hydrolysis, it is wanted to obtain pure hydrogen gas because of being the only gas product of hydrogen. However, in the $NaBH_4$ hydrolysis reaction, the mist contains solution components such as $NaBO_2$, $NaBH_4$, NaOH, and H_2O could reveal with the produced hydrogen. In systems where hydrogen will be used as fuel, it is recommended to separate the hydrogen gas from these alkaline impurities with a gas-liquid separation system, as mist formation will be an undesirable situation that will reduce the efficiency. However, a simple gas-liquid separation system is not easy to implement, especially when hydrogen gas is produced at high rates and high temperatures. Therefore, mist elimination is still one of crucial limitations in the hydrogen production processes via $NaBH_4$ hydrolysis.
- Crystallization of borates: The main aim of $NaBH_4$ hydrolysis process is to raise the amount of produced hydrogen gas in order to enhance the energy density of the hydrogen production system. For this, high concentrations of $NaBH_4$ are required; however, this causes the crystallization of borates after hydrogen production. In this situation, the crystalized borates would consume H_2O to form hydrated borates that could precipitate on catalysts and/or in pipelines of the system resulting in decrease of hydrogen production rate particularly when using heterogeneous catalysts. Anhydrous borates can

form only under extreme temperature or pressure conditions, which are restrictive for practical and economical applications. The precipitation of hydrated borates on catalysts may damage the structure of the catalyst or the precipitation of hydrated borates in pipelines may prevent the flow of hydrogen gas through the pipelines. The deterioration of the catalyst structure can be prevented with the use of homogeneous catalysts if a solution can be found to the problem of how to control the hydrolysis reaction. Another solution suggestion might be to increase the amount of water used in the system simultaneously with the $NaBH_4$ concentration. However, since water management is also a limiting factor in such systems, recycling the water used in the system can be suggested as an alternative to this limitation.

- Temperature control: The hydrogen production via $NaBH_4$ hydrolysis is an exothermic reaction. Therefore, it is very important to control the temperature of $NaBH_4$ hydrolysis reaction in terms of the mist emission and borate crystallization. Because, although low reaction temperatures reduce the mist emission, it causes the utilization of lower H_2O due to the formation of $NaB(OH)_4 \cdot 2H_2O$. Higher reaction temperatures could enhance the H_2O utilization but exasperate the mist emission. Hence, the thermal management is still a crucial problem to be solved in the hydrogen production processes via $NaBH_4$ hydrolysis.
- Catalyst stability: It is desired to continue to utilize the catalyst without losing its activity throughout the $NaBH_4$ hydrolysis reaction. However, agglomeration of catalyst particles, surface oxidation of catalyst, and catalyst component dissolution in alkaline $NaBH_4$ solutions of the catalyst are the main reasons for deteriorating the catalyst structure that directly affects the hydrolysis reaction. In order to overcome such problems, the use of support materials is a good alternative, thus preventing deterioration of the catalyst and ensuring long-term and recyclable use.

Conclusions

Scopus database was employed to acquire the required data for the study. According to the Scopus database search results (Figure 2), 74 articles have been published about hydrogen production via $NaBH_4$ hydrolysis with nanocatalysts out of 891 articles about hydrogen production via $NaBH_4$ hydrolysis since 1993. Over the last 30 years, the studies on the synthesis and characterization of catalyst for hydrogen production via $NaBH_4$ hydrolysis have increased rapidly. The reported studies showed that an effective catalyst applied for hydrogen production via $NaBH_4$ hydrolysis should possess three properties of high hydrogen production efficiency, low activation energy, and long-term stability. The researchers have started to study nanocatalysts due to their large surface areas and high catalytic activities since 2007 as seen in Figure 2. However, aggregation is the main problem for the nanocatalysts to further maintain the large surface area and thus the high catalytic activity and stability. Although several materials such as metallic oxides, foams, carbon-based materials, chitin, zeolitic imidazolate frameworks, metal-organic frameworks, polypyrrole have been used for forming alloy, supported materials, or films in order to overcome this problem, more practicable and effective strategies have to be benefitted to meet the practical requirements for applications. On the other hand, although there have been several studies on hydrogen production via $NaBH_4$ hydrolysis with nanocatalysts, its practical application has not been evaluated yet. In this respect, it is important to develop small-sized, lightweight, and low-pressure portable hydrogen generators that could produce hydrogen gas via $NaBH_4$ hydrolysis with the synthesized nanocatalysts.

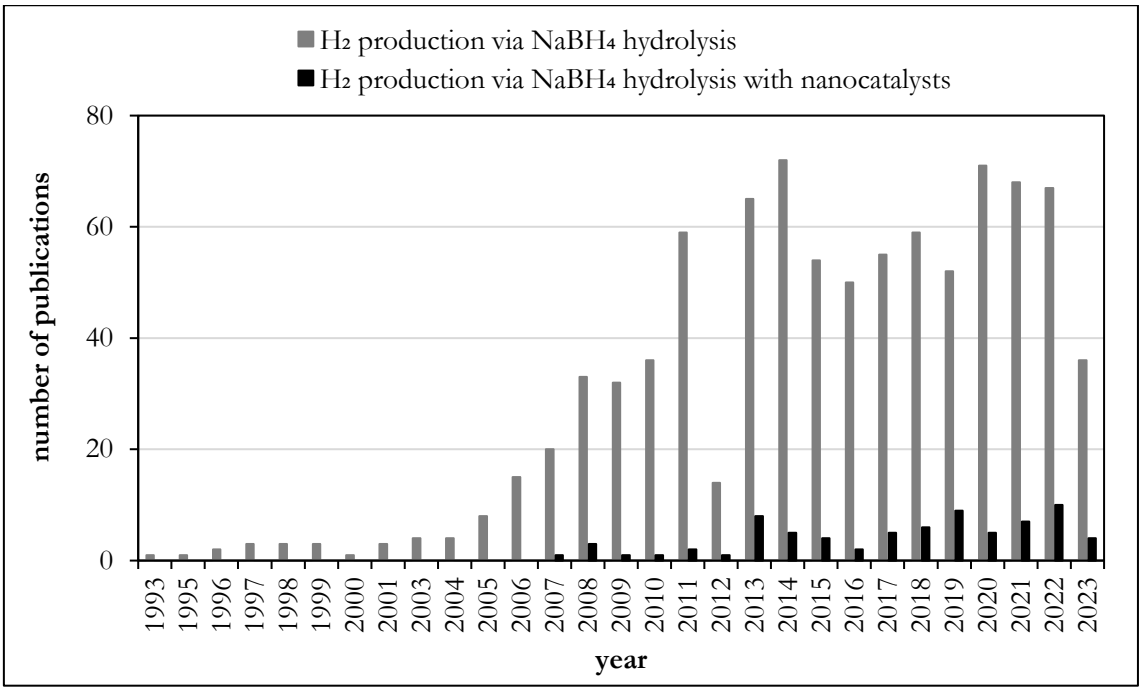

Figure 2. Number of publications in the last 30 years in Scopus using the keywords 'Hydrogen production' and 'NaBH4 hydrolysis' and/or 'nanocatalyst'

References

Avci Hansu, T., Sahin, O., Caglar, A., & Kivrak, H. (2020). A remarkable Mo doped Ru catalyst for hydrogen generation from sodium borohydride: the effect of Mo addition and estimation of kinetic parameters. *Reaction Kinetics, Mechanisms and Catalysis*, *131*(2), 661–676. https://doi.org/10.1007/s11144-020-01884-8

Avcı Hansu, T. (2022). A novel and active ruthenium based supported multiwalled carbon nanotube tungsten nanoalloy catalyst for sodium borohydride hydrolysis. *International Journal of Hydrogen Energy*, *8*, 4–13. https://doi.org/10.1016/j.ijhydene.2022.04.269

Aygun, A., Gulbagca, F., Altuner, E. E., Bekmezci, M., Gur, T., Karimi-Maleh, H., Karimi, F., Vasseghian, Y., & Sen, F. (2022). Highly active PdPt bimetallic nanoparticles synthesized by one-step bioreduction method: Characterizations, anticancer, antibacterial activities and evaluation of their catalytic effect for hydrogen generation. *International Journal of Hydrogen Energy*, *48*(17), 6666–6679. https://doi.org/10.1016/j.ijhydene.2021.12.144

Baydaroglu, F. O., Özdemir, E., & Gürek, A. G. (2022). Polypyrrole supported Co–W–B nanoparticles as an efficient catalyst for improved hydrogen generation from hydrolysis of sodium borohydride. *International Journal of Hydrogen Energy*, *47*(16), 9643–9652. https://doi.org/10.1016/j.ijhydene.2022.01.052

Boran, A. (2011). *Design of Prototype Reactor For Hydrogen Production From Sodium Borohydride* (Issue September). Middle East Technical University, Graduate School of Natural and Applied Sciences, Master Thesis.

Bozkurt, G., Özer, A., & Yurtcan, A. B. (2019). Development of effective catalysts for hydrogen generation from sodium borohydride: Ru, Pt, Pd nanoparticles supported on Co3O4. *Energy*, *180*, 702–713. https://doi.org/10.1016/j.energy.2019.04.196

Bu, Y., Liu, J., Chu, H., Wei, S., Yin, Q., Kang, L., Luo, X., Sun, L., Xu, F., Huang, P., Rosei, F., Pimerzin, A. A., Seifert, H. J., Du, Y., & Wang, J. (2021). Catalytic hydrogen evolution of nabh4 hydrolysis by cobalt nanoparticles supported on bagasse-derived porous carbon. *Nanomaterials*, *11*(12), 1–15. https://doi.org/10.3390/nano11123259

Çakanyildirim, Ç., & Gürü, M. (2022). NaBH4hydrolysis performance and kinetic evaluation of synthetic Co-Mn-Pt catalyst prepared with different supports. *Journal of the Faculty of Engineering and Architecture of Gazi University*, *37*(1), 423–437. https://doi.org/10.17341/gazimmfd.877826

Chandrasekhar, K., Lee, Y. J., & Lee, D. W. (2015). Biohydrogen production: Strategies to improve process efficiency through microbial routes. *International Journal of Molecular Sciences*, *16*(4), 8266–8293. https://doi.org/10.3390/ijms16048266

Chen, B., Chen, S., Bandal, H. A., Appiah-Ntiamoah, R., Jadhav, A. R., & Kim, H. (2018). Cobalt nanoparticles supported on magnetic core-shell structured carbon as a highly efficient catalyst for hydrogen generation from NaBH4 hydrolysis. *International Journal of Hydrogen Energy*, *43*(19), 9296–9306. https://doi.org/10.1016/j.ijhydene.2018.03.193

Dönmez, F., & Ayas, N. (2021). Synthesis of Ni/TiO2 catalyst by sol-gel method for hydrogen production from sodium borohydride. *International Journal of Hydrogen Energy*, *46*(57), 29314–29322. https://doi.org/10.1016/j.ijhydene.2020.11.233

Dou, S., Zhang, W., Yang, Y., Zhou, S., Rao, X., Yan, P., Isimjan, T. T., & Yang, X. (2021). Shaggy-like Ru-clusters decorated core-shell metal-organic framework-derived CoOx@NPC as high-efficiency catalyst for NaBH4 hydrolysis. *International Journal of Hydrogen Energy*, *46*(11), 7772–7781. https://doi.org/10.1016/j.ijhydene.2020.12.011

Elçiçek, H., Erol, M., & Özdemir, O. K. (2021). Preparation of highly efficient NiB catalyst via triton-stabilized for alkaline NaBH4 hydrolysis reaction. *International Journal of Energy Research*, *45*(10), 14644–14657.

Fangaj, E., & Ceyhan, A. A. (2020). Apricot Kernel shell waste treated with phosphoric acid used as a green, metal-free catalyst for hydrogen generation from hydrolysis of sodium

borohydride. *International Journal of Hydrogen Energy*, *45*(35), 17104–17117. https://doi.org/10.1016/j.ijhydene.2020.04.133

Finegold, J. G., Lynch, F. E., Baker, N. R., Takahashi, R., & Bush, A. F. (1973). The UCLA hydrogen car: Design, construction, and performance. *SAE Technical Papers*, *82*, 1626–1637. https://doi.org/10.4271/730507

Fiorio, J. L., Gothe, M. L., Kohlrausch, E. C., Zardo, M. L., Tanaka, A. A., de Lima, R. B., da Silva, A. G. M., Garcia, M. A. S., Vidinha, P., & Machado, G. (2022). Nanoengineering of Catalysts for Enhanced Hydrogen Production. *Hydrogen*, *3*(2), 218–254. https://doi.org/10.3390/hydrogen3020014

Huff, C., Biehler, E., Quach, Q., Long, J. M., & Abdel-Fattah, T. M. (2021). Synthesis of highly dispersive platinum nanoparticles and their application in a hydrogen generation reaction. *Colloids and Surfaces A: Physicochemical and Engineering Aspects*, *610*(October 2020), 125734. https://doi.org/10.1016/j.colsurfa.2020.125734

Huff, C., Long, J. M., Aboulatta, A., Heyman, A., & Abdel-Fattah, T. M. (2017). Silver Nanoparticle/Multi-Walled Carbon Nanotube Composite as Catalyst for Hydrogen Production. *ECS Journal of Solid State Science and Technology*, *6*(10), M115–M118. https://doi.org/10.1149/2.0051710jss

IEA, I. E. A. (2019). World Energy Outlook 2019 – Analysis - IEA. In *World Energy Outlook 2019* (p. 1). https://www.iea.org/reports/world-energy-outlook-2019

Jadhav, A. R., Bandal, H. A., & Kim, H. (2017). NiCo2O4 hollow sphere as an efficient catalyst for hydrogen generation by NaBH4 hydrolysis. *Materials Letters*, *198*, 50–53. https://doi.org/10.1016/j.matlet.2017.03.161

Ji, M., & Wang, J. (2021). Review and comparison of various hydrogen production methods based on costs and life cycle impact assessment indicators. *International Journal of Hydrogen Energy*, *46*(78), 38612–38635. https://doi.org/10.1016/j.ijhydene.2021.09.142

Kassem, A. A., Abdelhamid, H. N., Fouad, D. M., & Ibrahim, S. A. (2019). Metal-organic frameworks (MOFs) and MOFs-derived CuO@C for hydrogen generation from sodium borohydride. *International Journal of Hydrogen Energy*, *44*(59), 31230–31238. https://doi.org/10.1016/j.ijhydene.2019.10.047

Kilci, E. (2017). *Experimental Study of Availability of Using Of CO2 Coming From Exhaust In Hydrogen Production Technology Of NaBH4*. Ankara Yildirim Beyazit University, Graduate School of Natural and Applied Sciences, Master Thesis.

Kilinc, D., & Sahin, O. (2021). Highly active and stable CeO2 supported nickel-complex catalyst in hydrogen generation. *International Journal of Hydrogen Energy*, *46*(1), 499–507. https://doi.org/10.1016/j.ijhydene.2020.09.201

Koç, E., & Şenel, M. C. (2013). The State of Energy in World and Turkey - General Evaluation. *Muhendis ve Makina*, *54*(639), 32–44.

Kord, S., Fathirad, F., Afzali, D., & Fayazi, M. (2022). Boron-Cobalt-Nickel-Yttrium nanocatalysts for hydrogen production from the hydrolysis of alkaline sodium borohydride solution. *Inorganic Chemistry Communications*, *136*(October 2021), 109130. https://doi.org/10.1016/j.inoche.2021.109130

Li, J., Hong, X., Wang, Y., Luo, Y., Huang, P., Li, B., Zhang, K., Zou, Y., Sun, L., Xu, F., Rosei, F., Verevkin, S. P., & Pimerzin, A. A. (2020). Encapsulated cobalt nanoparticles as a recoverable catalyst for the hydrolysis of sodium borohydride. *Energy Storage Materials*, *27*(November 2019), 187–197. https://doi.org/10.1016/j.ensm.2020.01.011

Li, K., Ma, M., Xie, L., Yao, Y., Kong, R., Du, G., Asiri, A. M., & Sun, X. (2017). Monolithically integrated NiCoP nanosheet array on Ti mesh: An efficient and reusable catalyst in NaBH4 alkaline media toward on-demand hydrogen generation. *International Journal of Hydrogen Energy*, *42*(30), 19028–19034. https://doi.org/10.1016/j.ijhydene.2017.06.092

Li, R., Zhang, F., Zhang, J., & Dong, H. (2022). Catalytic hydrolysis of NaBH4 over titanate nanotube supported Co for hydrogen production. *International Journal of Hydrogen Energy*, *47*(8), 5260–5268. https://doi.org/10.1016/j.ijhydene.2021.11.143

Li, T., Xiang, C., Chu, H., Xu, F., Sun, L., Zou, Y., & Zhang, J. (2022). Catalytic effect of highly dispersed ultrafine Ru nanoparticles on a TiO2-Ti3C2 support: Hydrolysis of sodium borohydride for H2 generation. *Journal of Alloys and Compounds*, *906*, 164380. https://doi.org/10.1016/j.jallcom.2022.164380

Li, T., Xiang, C., Zou, Y., Xu, F., & Sun, L. (2021). Synthesis of highly stable cobalt nanorods anchored on a Ti4N3Tx MXene composite for the hydrolysis of sodium borohydride. *Journal of Alloys and Compounds*, *885*, 160991. https://doi.org/10.1016/j.jallcom.2021.160991

Li, Z., Xu, Y., Guo, Q., Li, Y., Ma, X., Li, B., Zhu, H., & Yuan, C. G. (2021). Preparation of Ag@PNCMs nanocomposite as an effective catalyst for hydrogen generation from hydrolysis of sodium borohydride. *Materials Letters*, *297*, 129828. https://doi.org/10.1016/j.matlet.2021.129828

Liang, Z., Li, Q., Li, F., Zhao, S., & Xia, X. (2017). Hydrogen generation from hydrolysis of NaBH4 based on high stable NiB/NiFe2O4 catalyst. *International Journal of Hydrogen Energy*, *42*(7), 3971–3980. https://doi.org/10.1016/j.ijhydene.2016.10.115

Lin, J., Gulbagca, F., Aygun, A., Elhouda Tiri, R. N., Xia, C., Van Le, Q., Gur, T., Sen, F., & Vasseghian, Y. (2022). Phyto-mediated synthesis of nanoparticles and their applications on hydrogen generation on NaBH4, biological activities and photodegradation on azo dyes: Development of machine learning model. *Food and Chemical Toxicology*, *163*(March), 112972. https://doi.org/10.1016/j.fct.2022.112972

Liu, B. H., & Li, Z. P. (2009). A review: Hydrogen generation from borohydride hydrolysis reaction. *Journal of Power Sources*, *187*(2), 527–534. https://doi.org/10.1016/j.jpowsour.2008.11.032

Liu, C. H., Chen, B. H., Hsueh, C. L., Ku, J. R., Jeng, M. S., & Tsau, F. (2009). Hydrogen generation from hydrolysis of sodium borohydride using Ni-Ru nanocomposite as catalysts. *International Journal of Hydrogen Energy*, *34*(5), 2153–2163. https://doi.org/10.1016/j.ijhydene.2008.12.059

Liu, H., Ning, H., Peng, S., Yu, Y., Ran, C., Chen, Y., Ma, J., & Xie, J. (2021). Surface tailored Ru catalyst on magadiite for efficient hydrogen generation. *Colloids and Surfaces A: Physicochemical and Engineering Aspects*, *631*(September), 127627. https://doi.org/10.1016/j.colsurfa.2021.127627

Luo, C., Fu, F., Yang, X., Wei, J., Wang, C., Zhu, J., Huang, D., Astruc, D., & Zhao, P. (2019). Highly Efficient and Selective Co@ZIF-8 Nanocatalyst for Hydrogen Release from Sodium Borohydride Hydrolysis. *ChemCatChem*, *11*(6), 1643–1649. https://doi.org/10.1002/cctc.201900051

Ma, T., Qiu, Y., Zhang, Y., Ji, X., & Hu, P. A. (2019). Iron-Doped Ni5P4 Ultrathin Nanoporous Nanosheets for Water Splitting and On-Demand Hydrogen Release via NaBH4 Hydrolysis. *ACS Applied Nano Materials*, *2*(5), 3091–3099. https://doi.org/10.1021/acsanm.9b00441

Nabid, M. R., Bide, Y., & Fereidouni, N. (2016). Boron and nitrogen co-doped carbon dots as a metal-free catalyst for hydrogen generation from sodium borohydride. *New Journal of Chemistry*, *40*(10), 8823–8828. https://doi.org/10.1039/c6nj01650b

Patil, K. N., Prasad, D., Bhagyashree, Manoorkar, V. K., Nabgan, W., Nagaraja, B. M., & Jadhav, A. H. (2021). Engineered nano-foam of tri-metallic (FeCuCo) oxide catalyst for enhanced hydrogen generation via NaBH4 hydrolysis. *Chemosphere*, *281*(May), 130988. https://doi.org/10.1016/j.chemosphere.2021.130988

Patil, K. N., Prasad, D., Bhanushali, J. T., Kim, H., Atar, A. B., Nagaraja, B. M., & Jadhav, A. H. (2020). Sustainable Hydrogen Generation by Catalytic Hydrolysis of NaBH4 Using Tailored Nanostructured Urchin-like CuCo2O4 Spinel Catalyst. *Catalysis Letters*, *150*(2), 586–604. https://doi.org/10.1007/s10562-019-03025-w

Pornea, A. M., Abebe, M. W., & Kim, H. (2019). Ternary NiCoP urchin like 3D nanostructure supported on nickel foam as a catalyst for hydrogen generation of alkaline

NaBH4. *Chemical Physics*, *516*(May 2018), 152–159. https://doi.org/10.1016/j.chemphys.2018.08.044

Prasad, D., Patil, K. N., Sandhya, N., Chaitra, C. R., Bhanushali, J. T., Samal, A. K., Keri, R. S., Jadhav, A. H., & Nagaraja, B. M. (2019). Highly efficient hydrogen production by hydrolysis of NaBH4 using eminently competent recyclable Fe2O3 decorated oxidized MWCNTs robust catalyst. *Applied Surface Science*, *489*(May), 538–551. https://doi.org/10.1016/j.apsusc.2019.06.041

Ruhe, C. H. W. (2019). Statistical Review of World Energy. *The Journal of the American Medical Association*, *225*(3), 299–306. https://doi.org/10.1001/jama.1973.03220300055017

Santra, S., Das, D., Das, N. S., & Nanda, K. K. (2017). An efficient on-board metal-free nanocatalyst for controlled room temperature hydrogen production. *Chemical Science*, *8*(4), 2994–3001. https://doi.org/10.1039/C7SC00162B

Schlesinger, H. I., Brown, H. C., Finholt, A. E., Gilbreath, J. R., Hoekstra, H. R., & Hyde, E. K. (1953). Sodium Borohydride, Its Hydrolysis and its Use as a Reducing Agent and in the Generation of Hydrogen. *Journal of the American Chemical Society*, *75*(1), 215–219. https://doi.org/10.1021/ja01097a057

Selvitepe, N., Balbay, A., & Saka, C. (2019). Optimisation of sepiolite clay with phosphoric acid treatment as support material for CoB catalyst and application to produce hydrogen from the NaBH4 hydrolysis. *International Journal of Hydrogen Energy*, *44*(31), 16387–16399. https://doi.org/10.1016/j.ijhydene.2019.04.254

Şenaktaş, B. (2005). Hydrogen Energy, Production & Application. In *Pamukkale University, Graduate School of Natural and Applied Sciences, Master Thesis*. Pamukkale University, Graduate School of Natural and Applied Sciences, Master Thesis.

Shi, L., Chen, Z., Jian, Z., Guo, F., & Gao, C. (2019). Carbon nanotubes-promoted Co–B catalysts for rapid hydrogen generation via NaBH4 hydrolysis. *International Journal of Hydrogen Energy*, *44*(36), 19868–19877. https://doi.org/10.1016/j.ijhydene.2019.05.206

Singh, R., & Dutta, S. (2018). A review on H2 production through photocatalytic reactions using TiO2/TiO2-assisted catalysts. *Fuel*, *220*(January), 607–620. https://doi.org/10.1016/j.fuel.2018.02.068

Tang, C., Zhang, R., Lu, W., He, L., Jiang, X., Asiri, A. M., & Sun, X. (2017). Fe-Doped CoP Nanoarray: A Monolithic Multifunctional Catalyst for Highly Efficient Hydrogen Generation. *Advanced Materials*, *29*(2), 1–6. https://doi.org/10.1002/adma.201602441

Tiri, R. N. E., Gulbagca, F., Aygun, A., Cherif, A., & Sen, F. (2022). Biosynthesis of Ag–Pt bimetallic nanoparticles using propolis extract: Antibacterial effects and catalytic activity on NaBH4 hydrolysis. *Environmental Research*, *206*(September 2021), 112622. https://doi.org/10.1016/j.envres.2021.112622

Tuan, D. D., & Lin, K. Y. A. (2018). Ruthenium supported on ZIF-67 as an enhanced catalyst for hydrogen generation from hydrolysis of sodium borohydride. *Chemical Engineering Journal*, *351*(June), 48–55. https://doi.org/10.1016/j.cej.2018.06.082

Wang, F., Zhang, Y., Wang, Y., Luo, Y., Chen, Y., & Zhu, H. (2018). Co-P nanoparticles supported on dandelion-like CNTs-Ni foam composite carrier as a novel catalyst for hydrogen generation from NaBH4 methanolysis. *International Journal of Hydrogen Energy*, *43*(18), 8805–8814. https://doi.org/10.1016/j.ijhydene.2018.03.140

Wang, L., Liu, Y., Ashraf, S., Jiang, J., Han, G., Gao, J., Wu, X., & Li, B. (2019). Pitaya pulp structural cobalt–carbon composite for efficient hydrogen generation from borohydride hydrolysis. *Journal of Alloys and Compounds*, *808*, 151774. https://doi.org/10.1016/j.jallcom.2019.151774

Wang, X., Sun, S., Huang, Z., Zhang, H., & Zhang, S. (2014). Preparation and catalytic activity of PVP-protected Au/Ni bimetallic nanoparticles for hydrogen generation from hydrolysis of basic NaBH4 solution. *International Journal of Hydrogen Energy*, *39*(2), 905–916. https://doi.org/10.1016/j.ijhydene.2013.10.122

World Energy Council. (2019). World Energy Scenarios 2019: Exploring Innovation Pathways to 2040. *World Energy Council*, 1–148. https://www.worldenergy.org/publications/entry/world-energy-scenarios-2019-european-regional-perspectives

Yaşar, A. Ö. (2013). *Preparation of Metal Nanoparticles Within Smart Hydrogel and Its Composites and Their Use in Hydrogen Production*. Çanakkale Onsekiz Mart University, Graduate School of Natural and Applied Sciences, Master of Science Thesis in.

Zhang, J., Li, Y., Yang, L., Zhang, F., Li, R., & Dong, H. (2022). Ruthenium Nanosheets Decorated Cobalt Foam for Controllable Hydrogen Production from Sodium Borohydride Hydrolysis. *Catalysis Letters*, *152*(5), 1386–1391. https://doi.org/10.1007/s10562-021-03730-5

Zhang, J., Lin, F., Yang, L., He, Z., Huang, X., Zhang, D., & Dong, H. (2020). Ultrasmall Ru nanoparticles supported on chitin nanofibers for hydrogen production from NaBH4 hydrolysis. *Chinese Chemical Letters*, *31*(7), 2019–2022. https://doi.org/10.1016/j.cclet.2019.11.042

Zhang, X., Li, C., Qu, J., Guo, Q., & Huang, K. (2019). Cotton stalk activated carbon-supported Co–Ce–B nanoparticles as efficient catalysts for hydrogen generation through hydrolysis of sodium borohydride. *Carbon Resources Conversion*, *2*(3), 225–232. https://doi.org/10.1016/j.crcon.2019.11.001

Zhou, J., Yan, J., Meng, X., Chen, W., Guo, J., & Liu, X. (2022). Co0.45W0.55 Nanocomposite from ZIF-67: An Efficient and Heterogeneous Catalyst for H2 Generation Upon NaBH4 Hydrolysis. *Catalysis Letters*, *152*(2), 610–618. https://doi.org/10.1007/s10562-021-03661-1

Zhou, S., Yang, Y., Zhang, W., Rao, X., Yan, P., Isimjan, T. T., & Yang, X. (2021). Structure-regulated Ru particles decorated P-vacancy-rich CoP as a highly active and durable catalyst for NaBH4 hydrolysis. *Journal of Colloid and Interface Science*, *591*, 221–228. https://doi.org/10.1016/j.jcis.2021.02.009

Zou, Y., Yin, Y., Gao, Y., Xiang, C., Chu, H., Qiu, S., Yan, E., Xu, F., & Sun, L. (2018). Chitosan-mediated Co–Ce–B nanoparticles for catalyzing the hydrolysis of sodium borohydride. *International Journal of Hydrogen Energy*, *43*(10), 4912–4921. https://doi.org/10.1016/j.ijhydene.2018.01.125

Isolated Three-Phase Voltage And Current Measuring Circuit Design And Implementation

Erdem İLTEN[1]

Introduction

In electrical power systems, particularly in industrial and commercial settings, the distribution of electrical power is commonly achieved using three-phase systems. Three-phase power offers numerous advantages such as higher power capacity, efficient transmission, and balanced loads. To effectively monitor and control these systems, accurate measurement of voltage and current is essential (Altomonte *et al.*, 2021). Three-phase voltage and current measuring refers to the process of quantifying the electrical characteristics of a three-phase power system. It involves the measurement of voltage and current across all three phases to ensure proper functioning and optimal performance of the system. By accurately measuring these parameters, engineers and technicians can analyze power consumption, assess system efficiency, detect faults, and make informed decisions regarding power management (Arote *et al.*, 2016). In a three-phase system, three voltage waveforms and three current waveforms are present, each with a phase shift of 120 degrees from one another (Saadat, 2009). This arrangement allows for a continuous and smooth power flow, minimizing energy losses and ensuring stable operation of electrical machinery. Measuring the voltage and current in all three phases provides a comprehensive view of the system's behavior and helps identify any imbalances or abnormalities (Sharma and Saini, 2015). Various instruments and devices are utilized to measure three-phase voltage and current accurately. Voltage is typically measured using voltmeters or multimeters, while current is measured using ammeters or current clamps. These instruments provide real-time readings and can be used for both single-phase and three-phase measurements. Additionally, specialized power quality analyzers can provide more detailed information about power factor, harmonic distortion, and other parameters affecting the system's performance. Accurate measurement of three-phase voltage and current is crucial for maintaining system stability, optimizing energy usage, and ensuring the safety of electrical equipment and personnel (Grigoras and Neagu, 2019). By carefully monitoring these electrical parameters, engineers can detect potential issues, perform preventive maintenance, and troubleshoot problems promptly.

In various electrical and electronic applications, it is often necessary to measure voltage and current accurately while maintaining the safety of both the measurement equipment and the personnel involved. Isolated voltage and current measuring techniques provide a solution to this challenge by providing electrical isolation between the measured circuit and the measuring instruments (Villani *et al.*, 2016). Isolated voltage and current measuring involves the use of isolation devices or techniques to separate the measured circuit from the measurement equipment, thereby creating a barrier that prevents direct electrical contact (Koziy *et al.*, 2013). This isolation is crucial in situations where the measured circuit operates at high voltages, carries high currents, or involves hazardous environments. The primary purpose of isolating the voltage and current measurements is to ensure the safety of the measuring instruments and the individuals performing the measurements. By using isolation techniques, the risk of electrical

[1] Asst. Prof. Dr., Balikesir University Electrical-Electronics Engineering

shocks, equipment damage, and potential accidents is minimized. It allows measurements to be taken without the need for direct physical contact with the measured circuit, reducing the chances of electrically induced injury or equipment malfunction. Isolated voltage and current measuring is particularly essential in power systems, industrial control systems, and high-voltage applications. In these scenarios, precise measurement of electrical parameters is vital for system monitoring, control, and protection. Isolation ensures that the measurement equipment and the personnel are shielded from the high voltage or high current levels present in the circuit, maintaining a safe working environment. There are various methods employed to achieve isolation in voltage and current measuring. Optical isolation, transformer-based isolation, and digital isolation are commonly used techniques. Optical isolation relies on optocouplers or optical isolators that use light to transmit signals across the isolation barrier. Transformer-based isolation utilizes transformers to electrically separate the input and output sides of the measuring circuit. Digital isolation employs digital techniques such as capacitive or magnetic coupling to achieve isolation. Isolated voltage and current measuring instruments, such as isolated multimeters, isolated oscilloscopes, and isolated current probes, are specifically designed for safe and accurate measurements in isolated environments. These instruments incorporate isolation techniques within their circuitry to ensure the integrity of the measurements while maintaining the required safety standards.

This chapter is organized as follows: Circuit Design is given in second section. In third section, experimental realization of the designed card is explained, and the results are given. Finally, the conclusion is the last section.

Circuit Design

±12 Vdc source for feeding op-amp circuits and +5 Vdc power supplies required for DC offset are designed as in Figure 1. 220 Vac input voltage (J7) is reduced to 2x15 Vac by using with centre tapped transformer (TR1). Diode bridge (BR1) is used to rectify the AC voltage to DC. ±12 Vdc symmetrical power supply in Figure 1 is made by using 7812 and 7912 integrated circuits. Last of all, +5 Vdc output is obtained with 7805 integrated circuit from +12 Vdc (Ilten, 2022a).

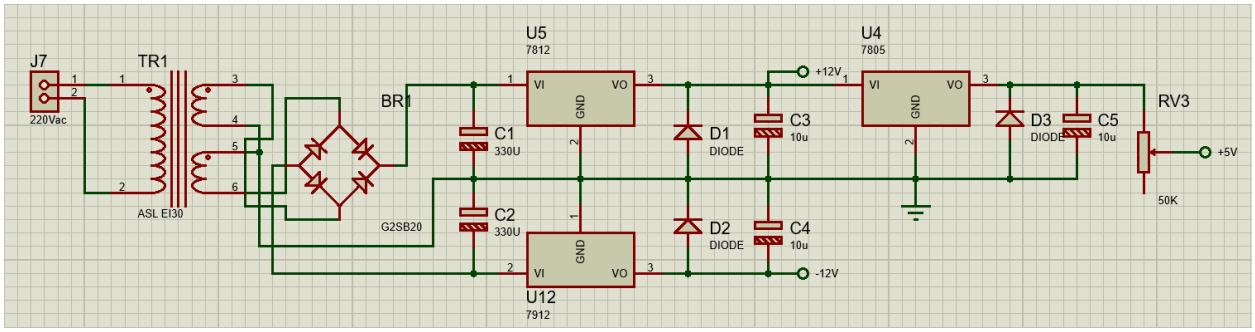

Figure 1. +12 V_{dc}, -12 V_{dc} and +5 V_{dc} power supplies

Circuit diagrams of isolated voltage and current transducers are given in Figure 2. J1 and J4 connectors show the source input and output of the line to be measured. The designed card will be connected in series between the grid and the plant. U1, U2 and U3 in Figure 2 are LEM-LA55P current transducers are shown in Figure 3 (LEM, 2014a). They provide the measurement of phase currents with hall-effect. Thanks to the Hall-effect, they provide isolation between the grid and the measuring circuit. R37, R38 and R39 resistors are connected to the output of the current transducers. The values of these resistors have been calculated to ensure that the output signal is at the desired amplitude. Q1, Q2 and Q3 components in Figure 2 are

LEM-LV25P voltage transducers are shown in Figure 4 (LEM, 2014b). They provide the measurement of phase voltages with hall-effect. Thanks to the Hall-effect, they provide isolation between the grid and the measuring circuit. Resistors R1, R2 and R3 are connected in series to the input of voltage transducers. The values of these resistors are determined by the amplitude of the source voltage. R37, R38 and R39 resistors are connected to the output of the voltage transducers. The values of these resistors have been calculated to ensure that the output signal is at the desired amplitude.

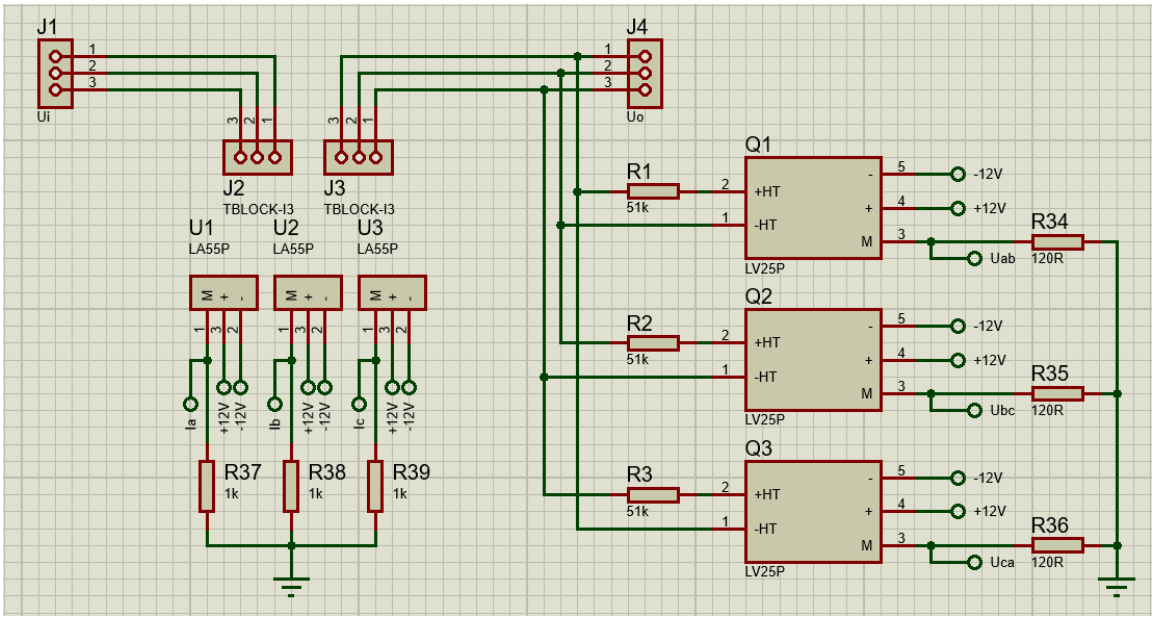

Figure 2. Isolated voltage and current transducers

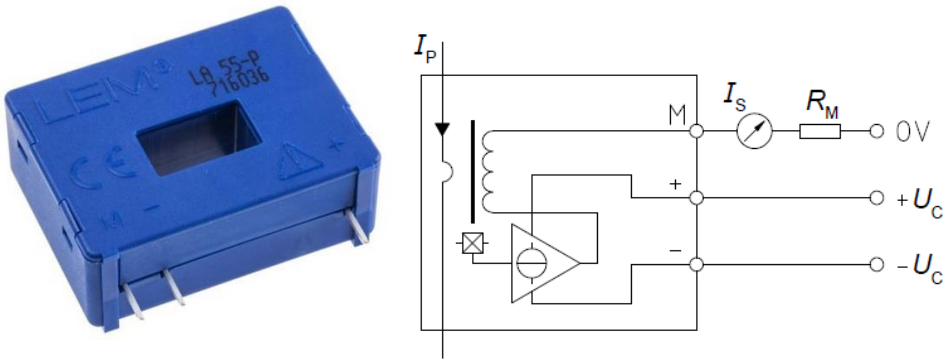

Figure 3. LEM-LA55P current transducer and its connection

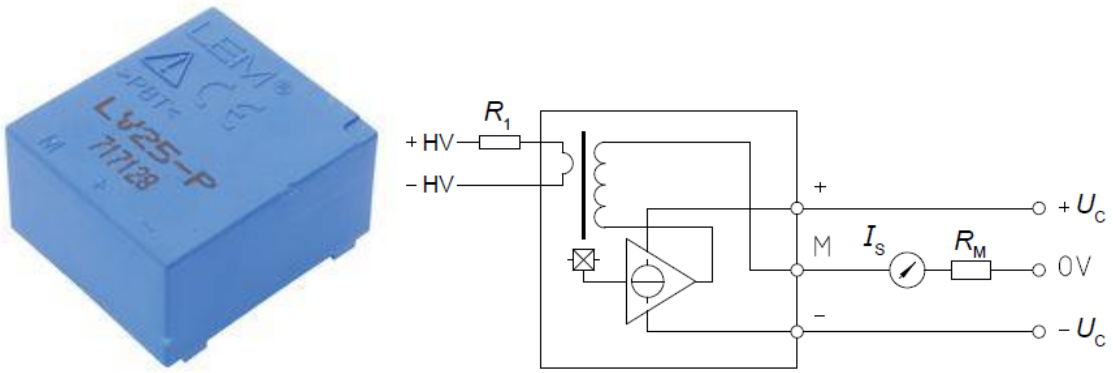

Figure 4. LEM-LV25P voltage transducer and its connection

The op-amp circuits in Figure 5 are designed to reduce the levels of phase currents and voltages. AD820 integrated circuit is used as op-amp. AD820 and its circuit diagram are given in Figure 6 (Analog_Devices, 2011). The upper 3 circuits are used for phase voltages U_a, U_b and U_c, and the lower 3 circuits are used for phase currents I_a, I_b and I_c. These circuits are used to scale the signals measured from the grid to the range of 0-3.3 V (Ilten, 2022b; Ilten *et al.*, 2022). The transfer functions of the op-amp circuits in Figure 5 are given in equation (1).

$$
\begin{aligned}
U_{ab1} &= \frac{11}{30}(U_{ab}+5) \;\;,\;\; I_{a1} = \frac{11}{30}(I_a+5) \\
U_{bc1} &= \frac{11}{30}(U_{bc}+5) \;\;,\;\; I_{b1} = \frac{11}{30}(I_b+5) \\
U_{ca1} &= \frac{11}{30}(U_{ca}+5) \;\;,\;\; I_{c1} = \frac{11}{30}(I_c+5)
\end{aligned}
\tag{1}
$$

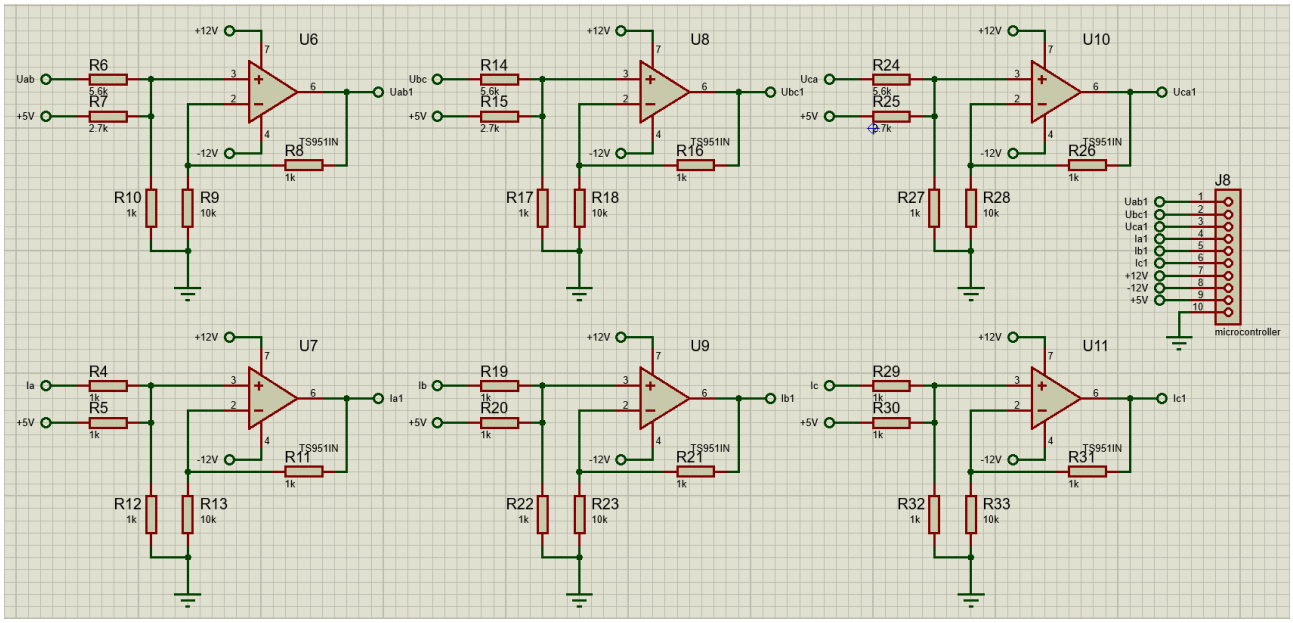

Figure 5. Voltage and current amplitude scaling circuits

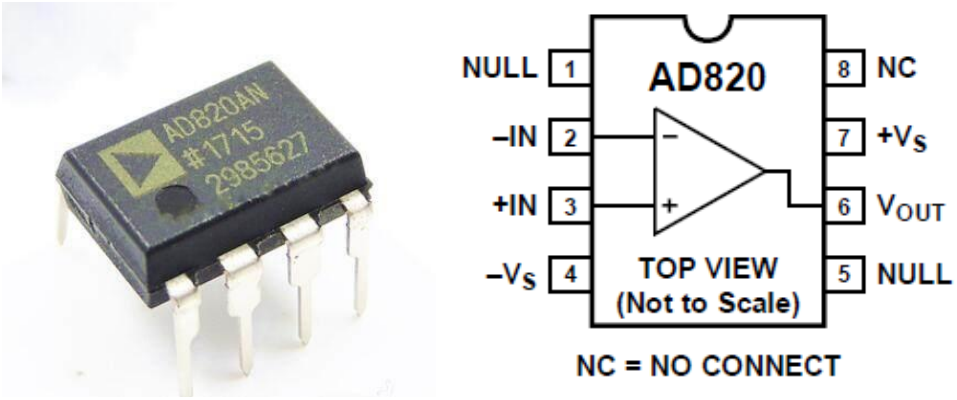

Figure 6. AD820 and its circuit diagram

The PCB schematic of the designed measuring circuit is drawn for 200x100mm FR4 board. The PCB is given in Figure 7. The 220 V_{ac} 50 Hz supply required by the card is provided through the J7 connector. The board is connected to the grid in series via J1 and J4 connectors. Scaled phase currents and voltages can be measured via J8 connector.

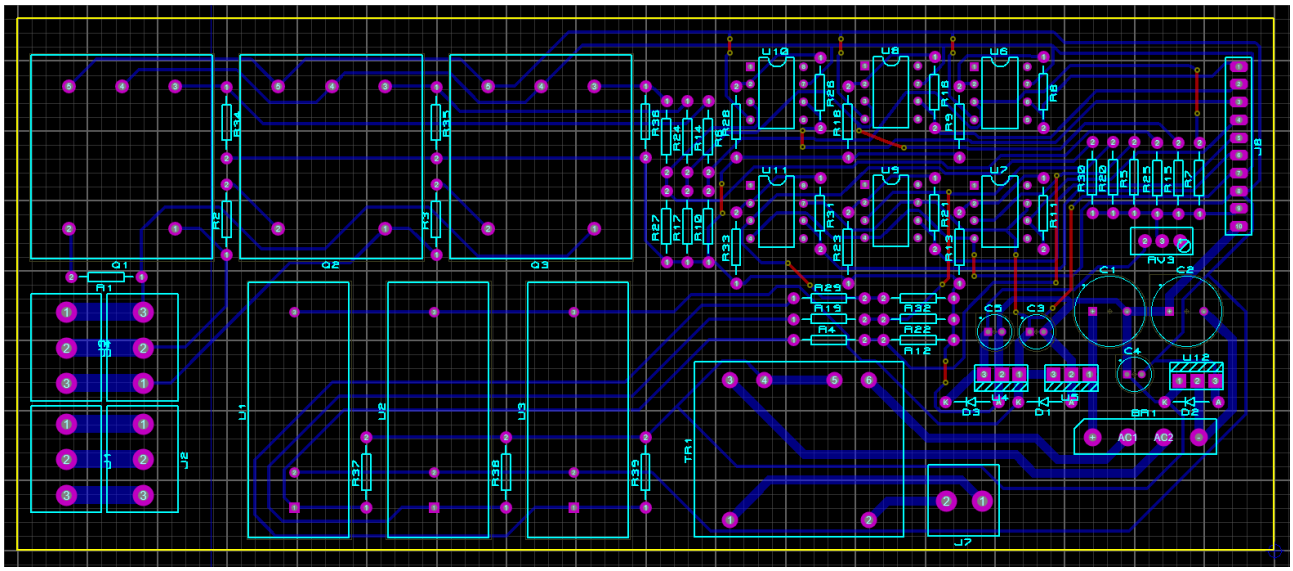

Figure 7. Designed PCB schematic

The 3D model of the designed card is presented in Figure 8. Examining the 3D model before proceeding to card production is important to prevent possible errors. When Figure 8 is examined, there is no overlap between the components. There is no obstacle to the physical production of the design.

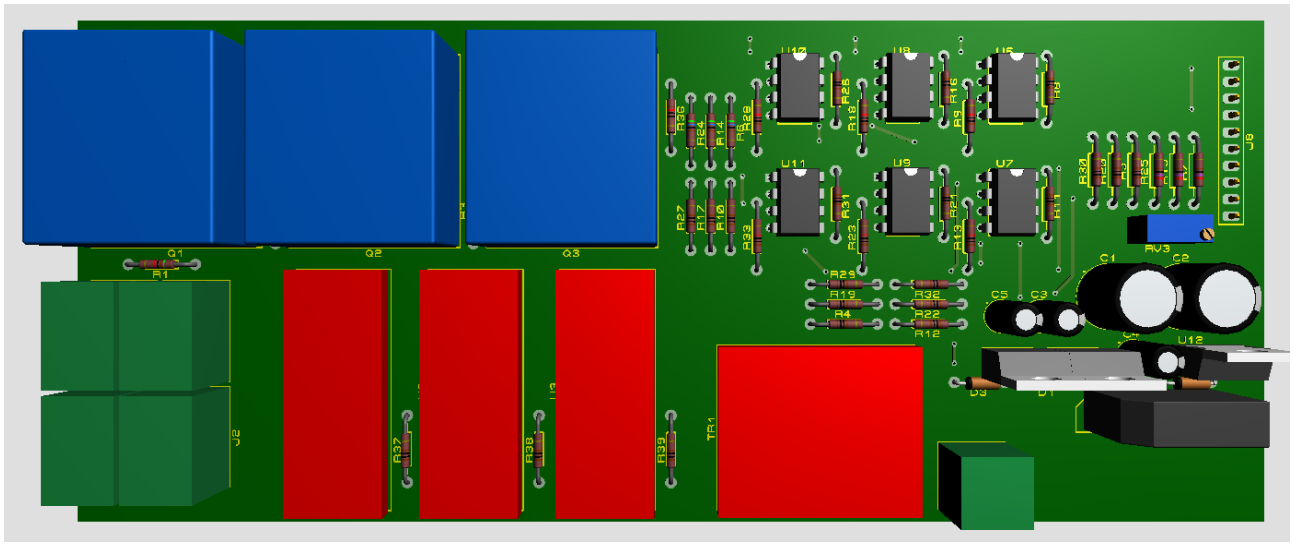

Figure 8. 3D model of the designed PCB

The image of the produced PCB is given in Figure 9. The designed PCB is engraved on the 3018 Pro CNC. Then, components are manually placed and soldered. After the production is completed, the testing process of the card begins.

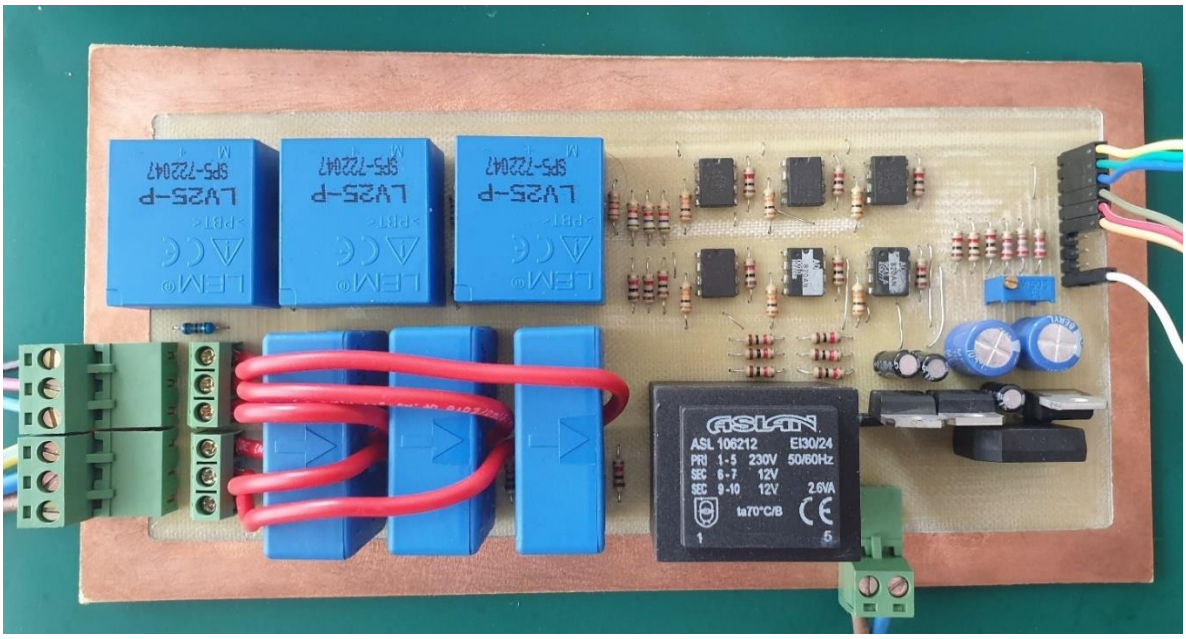

Figure 9. Produced PCB

Experiments

The experimental setup is given in Figure 10. The designed card is tested on between 3 phase induction motor and inverter circuit (Demirtas *et al.*, 2019; Ilten, 2022c; Ilten and Demirtas, 2016). The inverter in Figure 10 is driven by the TI F28335 Control Card. TI F28335 Control Card is presented in Figure 11. Inverter circuit is driven by 6 pulse width modulation (PWM) signals are generated by F28335. Algorithm generating PWM signals for F28335 was written in Matlab/Simulink program and downloaded to control card via USB emulator. The prepared Simulink block diagram for 3-phase sinusoidal PWM generation is illustrated in Figure 12. The scaled signals at the output of the designed card are measured with 100 MHz 1 GSa/s digital oscilloscope. The measured phase voltages and currents are presented in Figures 13 and 14 respectively.

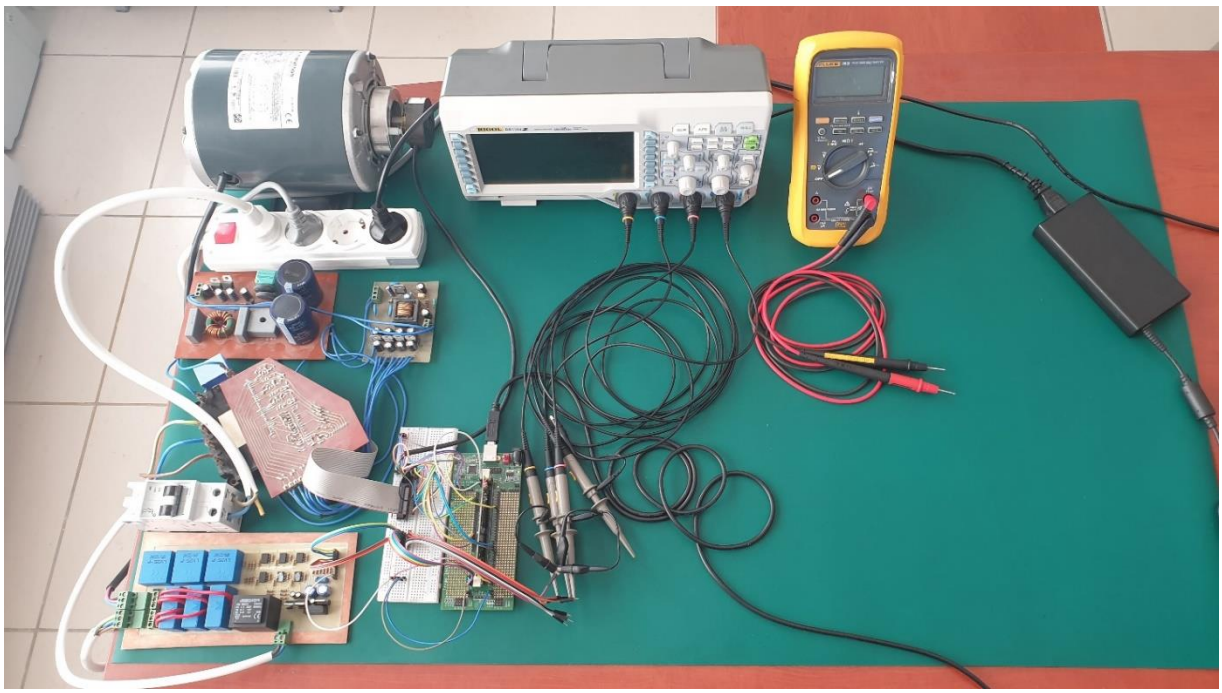

Figure 10. Experimental setup

Figure 11. TI F28335 Control Card

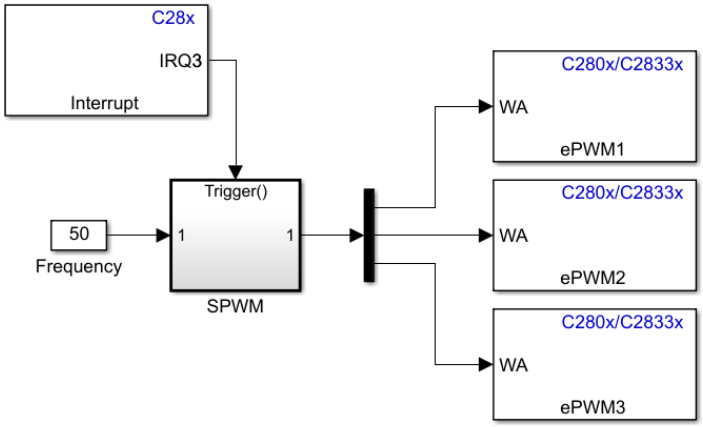

Figure 12. Simulink block diagram for 3-phase sinusoidal PWM generation

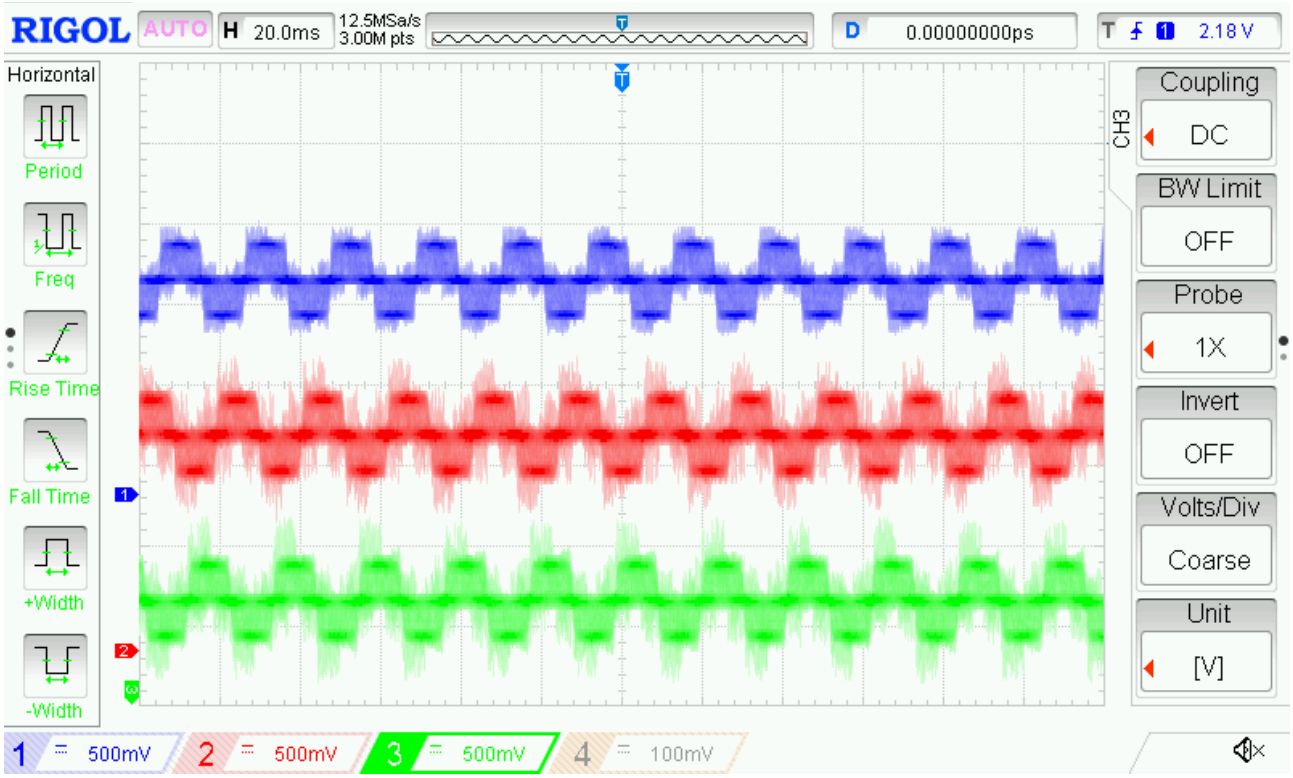

Figure 13. Scaled phase voltages

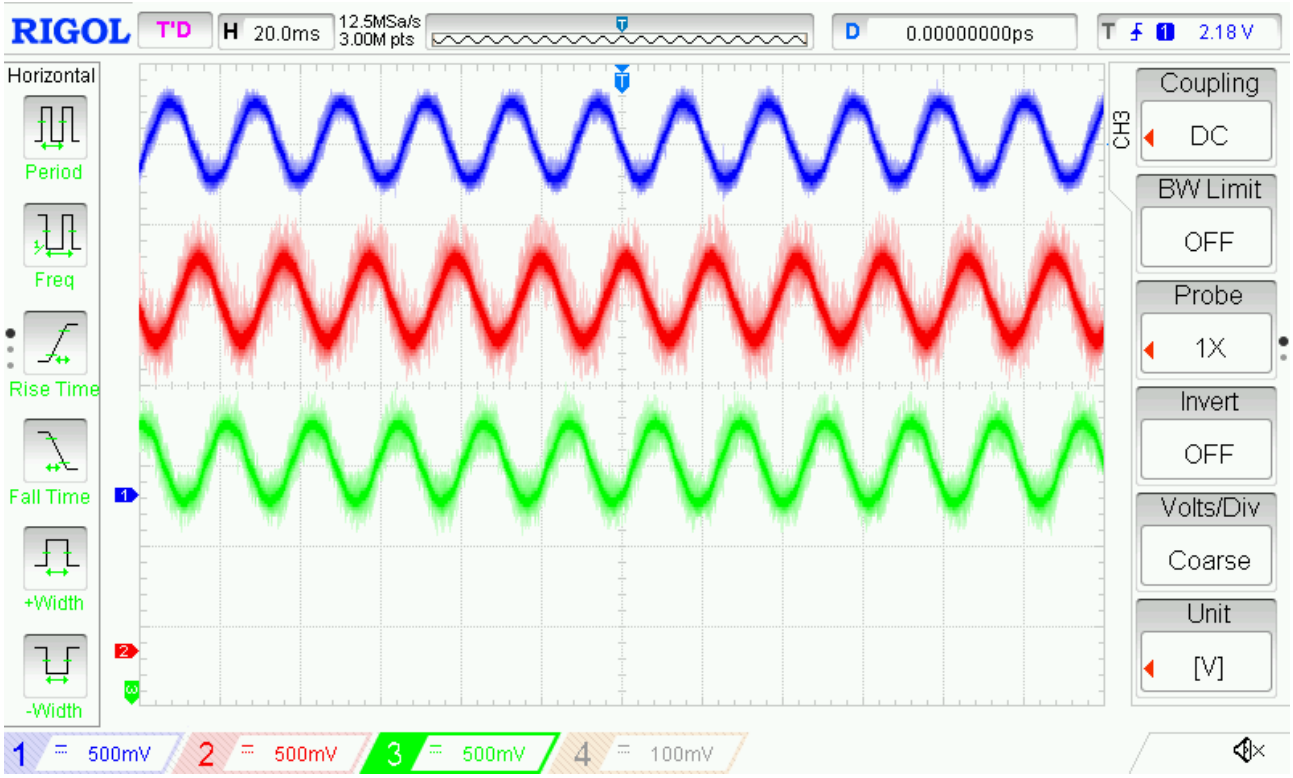

Figure 14. Scaled phase currents

The reason why the voltages in Figure 13 are not seen as smooth sinuses is because no filter is used at the output of the inverter circuit. When the Figures 13 and 14 are examined, it is seen that the amplitudes of phase voltages and currents have been successfully scaled.

Conclusion

In this study, a circuit is designed, produced, and tested to measure phase currents and voltages in 3-phase systems. Thanks to the hall-effect sensors used in the designed circuit, the measurement circuit and the power circuit are completely isolated from each other. In this way, any malfunction in the power circuit is prevented from damaging the measuring circuit. It is seen in the experimental results that the designed circuit can measure successfully even in systems containing harmonics. The value of each phase current and voltage is scaled instantly with high accuracy.

REFERENCES

Altomonte, A., Arena, F., Riccio, M. and Irace, A. (2021), "A New Three-Phase Smart Meter for Cloud Connection: Network Architecture and Performances", *Engineering Proceedings*, MDPI, Vol. 10 No. 1, p. 46.

Analog_Devices. (2011), *AD820 Datasheet*.

Arote, S., Mulay, G.N. and Khaparde, A. (2016), "Design and implementation of smart three phase energy meter", *2016 International Conference on Smart Grid and Clean Energy Technologies (ICSGCE)*, IEEE, pp. 44–49.

Demirtas, M., Ilten, E. and Calgan, H. (2019), "Pareto-Based Multi-objective Optimization for Fractional Order PIλ Speed Control of Induction Motor by Using Elman Neural Network", *Arabian Journal for Science and Engineering*, Springer, Vol. 44 No. 3, pp. 2165–2175.

Grigoras, G. and Neagu, B.-C. (2019), "Smart Meter Data-based three-stage algorithm to calculate power and energy losses in low voltage distribution networks", *Energies*, MDPI, Vol. 12 No. 15, p. 3008.

Ilten, E. (2022a), "Measuring and Control Circuit Design and Implementation for Sensorless Control of Induction Motor", *3rd International Conference on Applied Engineering and Natural Sciences*, Konya, Turkey, pp. 1903–1906.

Ilten, E. (2022b), "Conformable fractional order controller design and optimization for sensorless control of induction motor", *COMPEL-The International Journal for Computation and Mathematics in Electrical and Electronic Engineering*, Emerald Publishing Limited.

Ilten, E. (2022c), "Induction Motor Speed Controller Interface Design Via Simulink External Mode", *II. International Joint Conference on Engineering, Science and Artificial Intelligence*, pp. 59–63.

Ilten, E., Calgan, H. and Demirtas, M. (2022), "Design of induction motor speed observer based on long short-term memory", *Neural Computing and Applications*, Springer, Vol. 34 No. 21, pp. 18703–18723.

Ilten, E. and Demirtas, M. (2016), "Off-line tuning of fractional order PIλ Controller by using response surface method for induction motor speed control", *Journal of Control Engineering and Applied Informatics*, Vol. 18 No. 2, pp. 20–27.

Koziy, K., Gou, B. and Aslakson, J. (2013), "A low-cost power-quality meter with series arc-fault detection capability for smart grid", *IEEE Transactions on Power Delivery*, IEEE, Vol. 28 No. 3, pp. 1584–1591.

LEM. (2014a), *Current Transducer LA 55-P Datasheet*.

LEM. (2014b), *Voltage Transducer LV 25-P/SP5 Datasheet*.

Saadat, H. (2009), "Power system analysis,(2nd)", *McGraw-Hill Higher Education*.

Sharma, K. and Saini, L.M. (2015), "Performance analysis of smart metering for smart grid: An overview", *Renewable and Sustainable Energy Reviews*, Elsevier, Vol. 49, pp. 720–735.

Villani, C., Benatti, S., Brunelli, D. and Benini, L. (2016), "A contactless three-phase autonomous power meter", *2016 IEEE SENSORS*, IEEE, pp. 1–3.

A Research; The Changes On Lıvıng Spaces Affected By Lıvıng Standards

Gamze DEMİRCİ [1]
Burçin Cem ARABACIOĞLU[2]
Burcu Köse KHIDIROV[3]

Introduction

From ancient times, human beings have designed spaces which they can be protected when fulfilling their routines. These spaces varied according to different geographies, cultures and societies; furthermore they are formed with so many factors such as fast population increase, wars, migrations, natural factors and economic reasons. Most people have moved from their native places to different ones and adapted there. Therefore, living spaces have shaped, and differentiated; as they have stood as a representation of society, reflecting the values, successes, and eventual downfall of civilizations over time. The wide variety of those available today in terms of design and architecture is a reflection of the huge shift in how the general population live.

Especially regions which located on passageways and economic centres, have exposed to dense human mobility throughout history. Living spaces of those have undergone a severe change in terms of operational, functional, aesthetical etc. ways. These kind of different living spaces subsist in separate parts of today's world. As the needs increase or differentiate, it has become inevitable that the living spaces is insufficient, unable to respond to requests, and therefore changing the space and seeking new alternatives. In some regions, living spaces are supposed to be larger for the household to gather and socialize, when on the contrary- in some (the ones in metropoles, mega cities etc.) living spaces have only enough space to allow basic and limited activities. New gated community projects built in this kind of regions are designed in different dimensions for different users, as a high rise buildings. They have generally a main living space for many daily activities. These houses in city centres are quite smaller compared to the traditional ones in rural areas.

The most important factor that causes the change and transformation of living spaces is the life standards that change over time. The purpose this study is to examine the changes of living spaces against living standards. Different house types from different regions are chosen as examples and their changes in outgoing process are studied.

1. Changing Value of Houses

Definition of house is a place that a person sleeps, stays except working time or a place which is an institutional home, apartment likely place, dwelling, and residence [1]. Emerging of shelters which are accepted as first houses is as old as history of humanity.

Throughout human history, space design originated from social needs. Spaces, which have evolved as the answer to these needs that have changed and developed since the first man, are classified according to their functions[2]. Because space design, arising out of social requirements, is rapidly developing in response to changing needs [3].

[1] Research Assistant, Mimar Sinan Fine Art University
[2] Proffesor Dr. Mimar Sinan Fine Art University
[3] PhD. Student, Mimar Sinan Fine Art University

The term “shelter,” which is often used to define housing, has a strong connection to the ultimate purpose of housing throughout the world. The mental image of a shelter is a safe, secure place that provides both privacy and protection from the elements and the temperature extremes of the outside world [4]. A house is defined as a space in which users are located, and a "place" where subject and object interact. Thus, housing includes dimensions that carry the need for shelter beyond what is seen. The reflection of the lifestyle on the space contributes to its transformation into a living place.

Throughout history; houses interpersonal communication have been a like a bond that preserves the integrity of communication, interaction, time, space and meaning between people [5]. It indicates not only the lifestyle, culture and preference of the family, group or community to which it belongs, but also the essence of its user. It is an image of the individual's personality and perspective of the world with its form, material and equipment. Use gives a space meaning and at the same time guides how it is used. This cycle describes how the house would benefit and what it means to occupants.

First hominids that appeared about 4.5 million years ago in Africa, did not need any shelter because of convenient climatic conditions. First human beings who embraced huntsmen and collector life style, refuged to caves or tree holes to be secure against wild animals in nature and other people. Human, who biologically is the less adaptive living creature to the environment, built shelters to avoid different climate conditions of where they settled. It’s possible to come across with this basic planned, one-roomed houses almost all over the world [6].

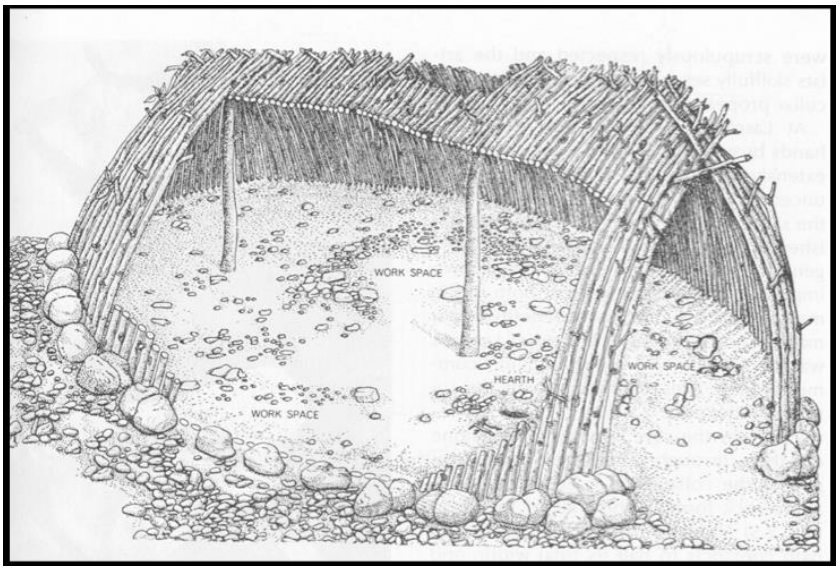

Fig.1. Terra Amata, homo erectus settlement, Nice, France

Although they had learnt to build shelters to protect themselves from nature conditions, because of their huntsmen and collector life style, they could not built permanent houses. When they had started agricultural activities, they also had started to build permanent shelters which they stay longer (See Fig. 1). These first human beings who had begun to settled life, started social relationships as well, so that shelters which was only for protective reasons before, had become social spaces as well [7].

Fig.2. Çatalhöyük, Konya, Turkey

Human beings have continued their biological evolution during their life time which lasts millions of years. Our civilization is shaped with the collection of experiences and pursuits of human who developed by his technologies, abilities and mind power. During this period cultural components that formed the society has started to change. Referring to the fact that space designers, like all other designers, take the standards into account while making their designs, Arabacıoğlu mentions that they sometimes set out from standards in their designs[8]. In durations human were canalized to new pursuits, components of culture from social relationships to economy, from architecture to technology were totally changed and a new system is arranged. In Fig. 2 Çatalhöyük, which was a quite large settlement nine thousand years ago in Central Anatolia. This kind of hill towns inhabited roughly two thousand years uninterrupted. Especially wideness of Neolithic settlement, its population, strong art and culture traditions were quite remarkable. Eight thousand people were supposed to be lived in the settlement. Main difference of Çatalhöyük from other Neolithic settlements is its exposing to an urban phase rather than a rural one. Residents of Çatalhöyük that was one of the oldest settlements of the world, were one of the first agriculturist communities. From the remnants that can be seen today, it is understood that houses were built adjacent to each other so that the walls were used mutual element; and there were narrow corridors reached to courtyard. These courtyards were used as a place providing light and fresh air, and a storage for litter as well. These houses with courtyards constitutes neighbourhoods; and these neighbourhoods forms the Çatalhöyük City.

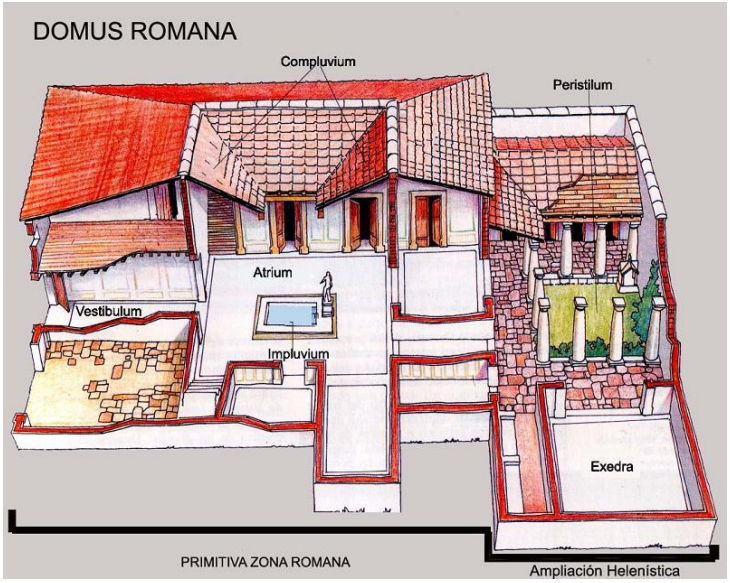

Fig.3. Domus example, Rome

Ancient Roman Civilization became a huge empire around Mediterranean from a small agriculture city in Italian Peninsula in B.C. 10th century. In cities of Roman Civilization in cities, besides houses, roads, bridges, water arches, tunnels, infrastructure and large-scaled constructions were built. In Fig. 3 private houses called Domus from Roman Civilization are seen. Daily life was spent in square or rectangular planned atriums. Atriums which used for chatting and resting, reached from the streets though corridors. The space between atrium and these corridors were an open living space.

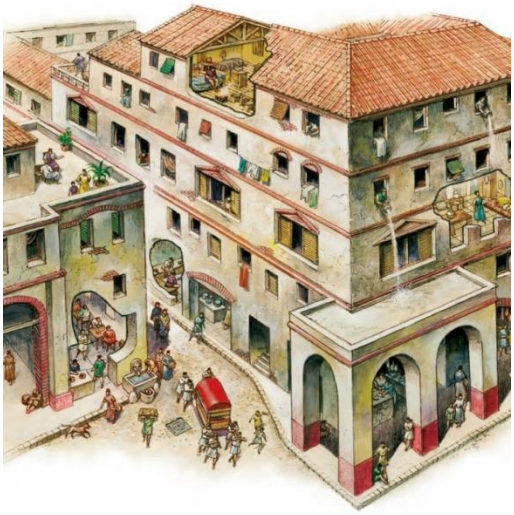

Fig. 4. Insulae example, Rome

After production revolution or Neolithic Revolution which people were settled down, most significant order change was definitely Industrial Revolution. In industrial revolution regarding dense population increase, diversification of social classes and change in production ways, urbanization and understanding of house reached to a totally different stage. During industrial revolution there had been developments in areas such as transportation, textile, agriculture and mining. Together with each development there had been some changes in social life and cities which was the centre of social life.

In the Western world, one of the primary forces driving the change of housing was the Industrial Revolution. This significant circumstance force people who lived and produced in villages to move to big cities to work in factories. Together with migrations from rural to urban

areas had made need of sheltering to turn into “need of sheltering in limited spaces”. Because of the increase in urban population boundaries of cities started to get larger and larger [9]. With embracing factory system there had been a crucial change on the society. Especially around factories, there were housings built by factory owners to reside the workers.

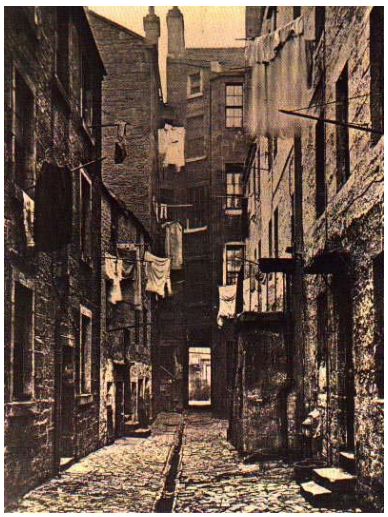

Fig.5. An Industrial Settlement

Settlements around factories spread to the all-world through industrialization which became race of strategic cities. Accumulation after life chaos towards cities, squeezed people in those buildings by snatching them from large settlements they came. Extreme population in cities forced people to use the lands vertically. Intensive working conditions and metropole life had affected people’s daily needs as well. These intense industrialization sprawled to the world through production of materials that allow vertical growth and spread.

Fig.6 Hashima Island, Japan

One of the most particular examples reflecting the impacts of the industrial revolution on houses is Hashima Island in Japan. Coal was first discovered on the island around 1810, and the island was continuously inhabited from 1887 to 1974 as a seabed coal mining facility [10]. In 1916, Japan's first large reinforced concrete building was built on the island to accommodate the workers. Over the next 55 years, more buildings were constructed, including apartment blocks, a school, kindergarten, hospital, town hall, and a community centre, a club house, cinema, communal bath, swimming pool, rooftop gardens, shops, and a game saloon were built for the miners and their families. Buildings had nine storeys highest and one of the most advanced concrete buildings in the world of its time.

Just after Bolshevik revolution in 1917, in USSR communal homes (in progressive years called communal or commune houses) are constructed. These houses had functions both for providing shelter to the population in crowded cities and for punishing the bourgeoisie who had a fancy life. Cruel colonization strategy in the country actually had an effect like transforming the country from an under-developed agriculture country to an industrialized society; on the other hand employment blow out in city's industry, developed faster than building of needed houses. Most parts of the city's population had no chance rather than staying highly dense crowded commune apartments or sheds.

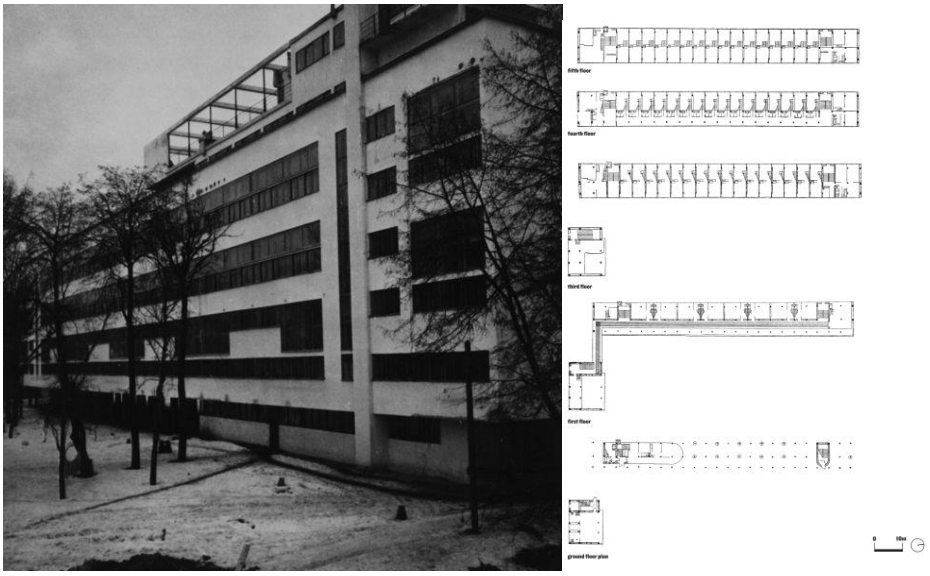

Fig 7. Narkomfin building, Russia

Narkomfin Building is another peculiar example which indicates the inevitable results of industrialization. It is a block of flats in the central district of Moscow, conceived as a transitional type of experimental house [11]. It is also a renowned piece of constructivist architecture and avant-garde house design; still in use after a renovation in 2019. Houses flourished in Soviet Union during 1920-1930 were abstract and austere, and aimed to reflect modern industrial society and urban space, while rejecting decorative stylization in favour of the industrial assemblage of materials [12]. Designs combined enhanced technology and engineering with an openly social purpose. Therefore, the concept of a transitional type of dwelling was developed. This concept combines, in the same building, several apartment types, differing in the level of privacy, ranging from three- and two-room apartments for families with children to one-room apartments and dormitories for singles and childless couples. The sense of community was fostered by joint use of circulation areas, and communal spaces and facilities, such as dining halls, kitchens and bathrooms, to encourage residents accustomed to old, family-based, lifestyles, to transition to collective modes of living [13]. The general program of Russian constructivist house units works as a response to its social mission, with the building divided horizontally into two parts. Whereas the lower levels include large flats for families, the upper floors featured one-room apartments that encouraged more collectivised living; and the adjacent communal block -owns a gym, a kitchen and dining halls- served to facilitate a smooth transition to higher social forms of housekeeping. The interior design of the flats are also contemplated thoughtfully. Low bedroom ceilings are made tolerable by the double height of main living spaces, large windows allow interior to reunite with nature.

Although it was divided into several competing factions, the movement produced many forerunning projects and finished buildings, before falling out of preference around mid-1930s. It has left marked influences on later developments in architecture.

Fig 9. Housing in Hong Kong.

After 2. World War, concept of houses have continued to dwindle. According to Lucas, term of small came into our lives during 1950s and subsequent 50 years everything got smaller [14]. In 1960s this understanding in many daily objects and products, gradually gained significance in technology and architecture as well, so that small housings caught on. Currently, this kind of housings especially built in metropoles as vertical buildings with small scales. Because of limited spaces and spaces' getting more valuable, the houses are used for many activities together such as sleeping, resting, eating and working in one single space.

Intensifying of urbanization in developing countries in last years affected city plans and architecture as well. Population living in cities is dramatically increasing day by day. This intense urbanization came with many economic, social and cultural problems. Excessive population density emerges when the number of living creatures in an area exceeds that area's ecological capacity [15].When migrations from rural areas to big cities are out of control, it causes urban sprawl and increase in concrete mass.

Fig. 10 Housing in Hong Kong

Hong Kong is one of the most exemplary place about density. Housing in Hong Kong varies by location and income. More than seven million people live on approximately one thousand km² of land that making it one of the densest places in the world [16]. Most common way of housing in Hong Kong is public housing, as around half of the residents live in public housing estates and other tower blocks with some form of subsidy. Public housings can be traced back to the 1950's, since huge masses of people migrates into Hong Kong because of political issues on the mainland China. In response to this drastic increase, Hong Kong Government commenced a programme of mass public housing, providing affordable homes for low income citizens [17].

2. Living Spaces of Houses vs. Living Spaces Changed by Houses

In one sense using interior spaces had emerged with human's sheltering and protection needs. In prehistoric times people fulfil their heating, sleeping, eating and storage needs in caves and rock holes with primal but practical arrangements. To understand the importance of living spaces in houses first of all it is needed to examine the developments of living spaces in history.

When human beings who were living in caves realized that sources were difficult to reach, they tried to find ways to get and produce them artificially. Change of climate, heating the earth up encouraged people producing goods. Together with start of agriculture and animal breeding human beings had moved from caves to plain lands and changed their life styles. Besides difficulty of living together, brought about social life to organize. Building need is a natural result of sheltering together will of human whose number increased gradually. During this period buildings were out of materials which were easy to find in nature and easy to collect. After the change started with agricultural activities circular shelter plans got longer and shaped more rectangular in time. In living spaces there were sets for sitting, sleeping, and stoves seen on the walls or ground.

People had started to fulfil his sheltering need only with one space, gradually changing social and cultural factors, shaped with life conditions and needs, and generate new living spaces. These living spaces are quite crucial because they generally are the spaces that people spend their time most. When the meaning of a living space change, dimensions of these spaces get bigger or smaller as well.

For the construction of first housing examples local materials were used. Change of these local materials from one region to another, and change of construction technique of each material, caused emerge of different housing types in different geographical regions. First housing types which had circular or square forms were quite simple and modest constructions although they were different on shape and they were formed with only one roomed plans. Each development in engineering and each architectural style had changed the face of houses in time as well.

In ancient Greek, life was organized in housing units that arranged through compose of social environment came with social life. During this period more roomed buildings took the place of one or two roomed buildings.

In ancient Rome, house of rich and noble people's houses formed by different parts like living room, bedroom or eating room. After Roman Empire's collapse in A.D. V. Century, in feudalism period, nobles chose to live in castles surrounded by trenches. These castles formed by different units such as eating halls, living rooms, bedrooms as well.

By Industrial Revolution, using machines for production caused lots of fast changes to start. New production areas generates new roads to distribute the products, and new housings for producer's sheltering and socializing needs. In this point of urbanization, there had been changes in existing house spaces. Two main reasons of seeing the effects of urbanization in housings first were transferring to nuclear family and production areas in houses had lost their old function. Streets in settlement plans and rooms in house scale started to standardization like industrial products. This situation made almost all regions to look similar to each other and

architectural identity had been lost. The biggest change in living spaces definitely had lived between 18th and 19th centuries, because of the significant developments on production, mining and transportation, during industrial revolution which socioeconomic and cultural conditions changed.

The living room used to be located in the back of the house and was mainly used privately or restricted to family use. Through the 1970s, the living room became a social area, and moved near the entryway of the home [18]. The trend of living areas being social areas is still alive and thriving today, even more so than it once was. Living rooms are no longer set apart from other rooms by walls, and often have large windows to integrate with outside. With cars becoming more readily available and more affordable, people could afford to live further away from work as they didn't need to rely on public transportation to get themselves to and from work. This continued until the 1990s.

Fig. 11 Interiors of Housings in Hong Kong

More people started moving into the cities, communities started to demand more housing and facilities. Today, the most important factor affecting and shaping houses and living spaces, besides culture, is economic opportunities and the population density of the city. Houses are now expanding vertically as cities grows.

Houses with one main living space –called micro apartments- for different uses are a very typical representative of Hong Kong and China cities. Especially Hong Kong, which has extremely high cost of housing, adapted some policies to place occupants in a very limited piece of land. In 1962, the government proposed small house policy for low-income residents. Even though life in this houses is not suitable for humanitarian conditions, today many people try to live in such spaces. In these small houses, all functions are gathered in the living area. Some of them have shared kitchen, bathroom and toilet areas throughout the building or block. Although it seems positive at first that living spaces are a place that gathers and socializes those who share the house, such small houses with single spaces may not be good for both psychological and physical health of the users.

3. Conclusion

This study examined outgoing story of living spaces throughout the history. In prehistoric eras, from the first shelters built to solve one of human's main needs-sheltering- till today, house and term of house had developed and changed as human beings change. Accommodation need of dense population that accelerated drastically with industrial revolution, house and urban planning studies tried to fulfil easiest and most healthy way so that communal housing term had emerged. These houses provided suitable living spaces for different type of users; as well as proposing social facilities. Therefore, this housing system was far beyond just being a place to live; it was a new way of thinking. As population increase continued to rise, housing started to become a problem. Separate housings with one or two storeys that can be in old cities often, had changed into high-rise buildings which aimed to fulfil more people's problem of sheltering.

While buildings got higher, spaces inside became much smaller for occupants, but for a cheaper price.

Rising buildings with economic growth, increase in the value of city terrains, evaluating high buildings as a political enterprise goal, need of constructing monumental buildings that symbolize the power of big companies, imprison people in a rushed system.

Human beings who disclaimed their living areas on rural and could not spare time and space to himself due to intensive working conditions, actually have returned to his starting point of living spaces over time. People started living in one space, then moved to larger houses with different rooms; after they built multi-storey buildings. At the last point of the population, they had to take refuge in the high-rise buildings and their tiny, usually single-room houses. Thus, humanity has returned to its first living space.

REFERENCES

[1] Turkish Dictionary (1988) Turkish Historical Society Printing House, Ankara, Turkey.

[2] Demirci, G. (2017) The Affects Of Indoor Ski Centres on Behavior of Riders By Space Perception, Master Thesis, Mimar Sinan Fine Arts University, İnstitute Of Science,İstanbul, Turkiye (In Turkish)

[3] Demirci, G., Arabacıoğlu, B. A. (2017) "Space Perception - Indoor Ski Center and Athlete in the User Behavior Relationship", Research on Science and Art in 21th Century Turkey, Chapter 258, Ankara, Turkiye

[4] U.S. Deprt. of Housing and Urban Development (2006) Healthy Housing Reference Manual. (Retr. 21.10.2020) https://www.cdc.gov/nceh/publications/books/housing/housing_ref_manual_2012.pdf

[5] Salija, K., Muhayyang, M., Rasyid, M. A. (2018) Interpersonal Communication: A Social Harmony Approach. Badan Penerbit UNM, Gunung Sari, Indonesia.

[6] Nuttgens, P. (1997) The Story of Architecture. Hong Kong: Phaidon Press Limited.

[7] Morris-Kay, G. M.. (2009) The Evolution of Human Artistic Creativity. Journal of Anatomy, Volume 216 (2) p. 158-176.

[8] Arabacıoğlu, B. C. (2007). Mimarlıkta Mekân Analizi İçin Bulanık Çıkarım Sistemi Temelli Bir Model Önerisi. 512-513.

[9] Deane, P. (1979) The First Industrial Revolution. Cambridge University Press, Cambridge, UK.

[10] Sakamoto, D., Gotoh, K. (2005) The Heritage of Gunkanjima: Fading Symbol of Modernization Period. Nagasaki Shimbunsya, p. 34.

[11] Movilla Vega, D. (2020). "Housing and Revolution: From the Dom-Kommuna to the Transitional Type of Experimental House (1926–30)". Architectural Histories 8.

[12] "Constructivism". Tate Modern. Retr. 09.04.2020. https://www.tate.org.uk/art/art-terms/c/constructivism

[13] Vronskaya, A. (2017) Making Sense of Narkomfin. The Architectural Review. https://www.architectural-review.com/essays/making-sense-of-narkomfin

[14] Lucas, R. (2004) The Industrial Revolution: Past and Future, 2003 Annual Report Essay.
https://www.minneapolisfed.org/publications/the-region/the-industrial-revolution-past-and-future

[15] Sherbin, A., Carr, D., Cassels, S., Jiang, L. (2007) Population and E.nvironment. US National Library of Medicine National Institutes of Health. Annu Rev Environ Resour. 2007; 32: 345–373.

[16] Rosario, L. (1995) Hong Kong - Long Way From A Home: Housing Programme Can't Keep Up with Demand. Far Eastern Economic Review. Vol. 31. p. 1 – via The Hang Seng University of Hong Kong Library.

[17] Choi, B. (1975) Housing Means More Than a Roof. South China Morning Post. (Retr. 07.02.2007) https://lib.hku.hk/hkulauth/

[18] How Houses Have Changed Over Time (2017) Garden State Home Loans Inc. https://www.gardenstateloans.com/houses-changed-time/

An Optimal Fractional-Order Pi Controller Design For Active Power Filter

Metin DEMİRTAŞ[1]
Haris CALGAN[2]

Introduction

In modern life, the use of electrical energy needs power electronic devices and microelectronic technology to transfer the power needed by the load from the source to the load (Sis & Akça, 2020). Power electronics circuits consist of switching elements to control the flow of power transferred from the source to the load. They are widely used in industrial applications such as adjustable motor speed drives, uninterruptible power supplies, and computers. The power electronic circuits cause power quality problems in electrical power systems during energy consumption. Modern switching devices have nonlinear load characteristics. These loads draw non-sinusoidal currents from the grid and they are an important part of the power system (Demirtas et al., 2022). They cause non-linear conditions on the grid and decrease the power quality and distortion of the sine wave. In addition, they increase the power losses on the line and some devices like transformers. They act as a source that generates harmonics affecting sensitive devices. The harmonics produced by nonlinear load cause voltage distortions at the point common coupling (PCC) as shown in Figure 4. The linear and nonlinear loads are connected to this point as shown in Figure 5.

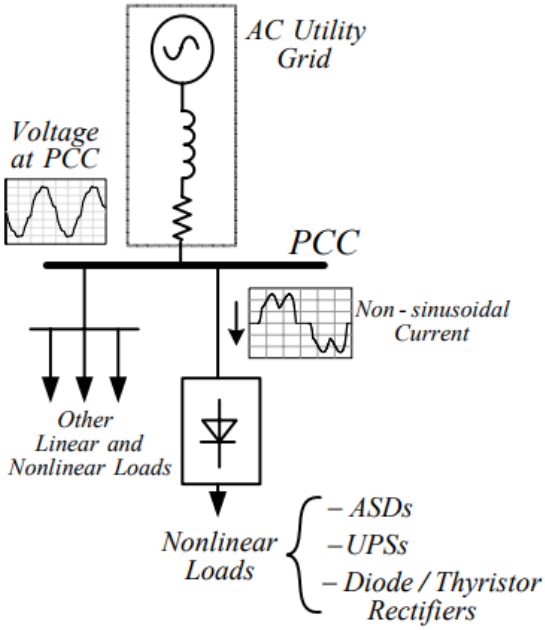

Figure 4. Explanation of the point of common coupling

[1] Prof. Dr., Balikesir University, Department of Electrical-Electronics Engineering, 10145, Balikesir.
[2] Dr. , Balikesir University, Department of Electrical-Electronics Engineering, 10145, Balikesir.

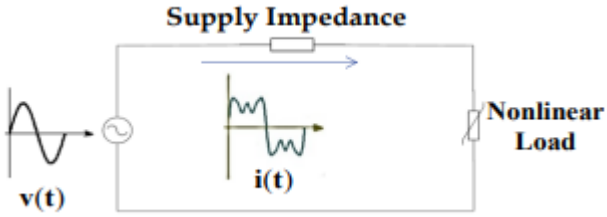

Figure 5. Distorted source current due to nonlinear load

There are three different filter types, which are passive, active and hybrid filters, to eliminate the harmonics. Passive filters are preferred to eliminate certain harmonics on the lines (Calgan, 2023). Active filters are designed to cancel the harmonics as soon as possible if the harmonics occur on the line. International harmonic standards are defined by EN61000-3-4 and IEEE 519-1992 as given in Table 3. These standards are used as a measurement to eliminate the harmonics. Total Harmonic Distortion (THD) term explains the harmonic contents of current and voltage waveforms as follows (Çalgan et al., 2020):

$$THD_I = \frac{\sqrt{\sum_{n=2}^{nmax} I_n^2}}{I_1} \tag{6}$$

where I_n and I_1 rms value of the current harmonic components and fundamental current component, respectively. n is the harmonic component number. Similarly, the THD for voltage is written as below:

$$THD_v = \frac{\sqrt{\sum_{n=2}^{nmax} V_n^2}}{V_1} \tag{7}$$

where V_n and V_1 rms value of the current harmonic components and fundamental current component, respectively.

Table 3. IEEE 519 harmonic current limits

$V_n \leq 69\,\text{kV}$						
I_{SC}/I_L	h<11	$11 \leq h < 17$	$17 \leq h < 23$	$23 \leq h < 35$	$35 \leq h$	*TDD*
<20	4.0	2.0	1.5	0.6	0.3	5.0
20-50	7.0	3.5	2.5	1.0	0.5	8.0
50-100	10.0	4.5	4.0	1.5	0.7	12.0
100-1000	12.0	5.5	5.0	2.0	1.0	15.0
>1000	15.0	7.0	6.0	2.5	1.4	20.0
$69\,\text{kV} < V_n \leq 161\,\text{kV}$						
<20*	2.0	1.0	0.75	0.3	0.15	2.5
20-50	3.5	1.75	1.25	0.5	0.25	4.0
50-100	5.0	2.25	2.0	0.75	0.35	6.0
100-1000	6.0	2.75	2.5	1.0	0.5	7.5
>1000	7.5	3.5	3.0	1.25	0.7	10.0
$V_n > 161\,\text{kV}$						
<50	2.0	1.0	0.75	0.3	0.15	2.5
≥50	3.0	1.50	1.15	0.45	0.22	3.75

Another subject about the filters is to design a controller to drive the switching elements in the filter circuits. Controllers to be used in active power filters (APFs) should be designed to control the entire system. Obtaining the reference signal, balancing the capacitor voltage, and generating the gate trigger signals are performed at this stage. The control techniques are based on open-loop and closed-loop control systems to improve power quality to eliminate the harmonics on the line. The control process can be made in the frequency domain based on Fourier analysis of corrupted voltage or current. Frequency domain analysis is suitable for three-phase and single-phase power systems. The control algorithms are based on the instantaneous derivation of commands in form of polluted current or voltage (Ilten, 2022).

There are a lot of studies about passive filters, active filters, hybrid filters, and controllers in the literature. Amlak Abaza and Ragab A. El-Sehiemy studied active power filters for harmonics elimination and power factor correction. They designed a shunt active power filter (SAPF) for single-phase as simulation using Proteus program and hardware by using Arduino to improve power quality. To generate gating switching signals, a hysteresis band current controller is designed for SAPF switches. THD value is obtained lower than 5% (Abaza et al., 2022). Ahmet Teke and Lütfü Sarıbulut studied the converter topologies and control strategies of APF to review the studies in the literature (SARIBULUT et al., 2011). Belqasem Aljafari and Kanagavel Rameshkumar presented a single-phase SAPF by using predictive current control technique based on a cost function model. The reference current is obtained by using PI control over the DC-link capacitor voltage. This method is compared with conventional MPCC, predictive PWM, and hysteresis control methods (Aljafari et al., 2022). Abdallah El Ghaly and Mohamad Tarnini offered the SAPF consisting of a reference signal extraction module for a three-phase system. They obtain the reference signal extraction based on designed filter-less time-domain method . The method is faster than the PQ method in response of system (El Ghaly et al., 2022). Alok K. Mishra and Prakash K. Ray studied a hybrid SAPF with adaptive fuzzy control for improving power quality. PI controller is used to obtain the reference current and to regulate the dc capacitor voltage. The adaptive fuzzy hysteresis current controller is designed to adjust switching signals (Mishra et al., 2021). Campanhol et. al, explained an application with a SAPF to harmonic mitigation, reactive power compensation, and power factor correction in three-phase four-wire power systems. Sinusoidal reference currents are obtained using a matrix that enables linear conversion from a two-phase system to a three-phase fixed reference frame system. Thus, the compensating reference current values are obtained by subtracting the sinusoidal reference currents from the measured load currents (Garcia Campanhol et al., 2014). S. Ozdemir and M. Demirtas presented a paper about harmonic estimation using support vector machines for power systems. Discrete Fourier Transform (DFT) and Fast Fourier Transform (FFT) are employed for analysis the real system results and model outputs are compared to verify the accuracy of method. The obtained results show that the method is very good for the estimation of total harmonic values (Ozdemir et al., 2016). Yousef Asadi and Mohsen Eskandari designed a stabile SAPF in Distorted Weak Grids by using Adaptive Neural Network (ANN) for harmonic elimination. The adaptive linear neuron is used to calculate the reference currents. To separate the harmonic from the main component to mitigate harmonics in signals for the phase-locked loop, another study presented a robust synchronous filter (Asadi et al., 2022). Gunduz and Demirtas presented an adaptive fuzzy fractional-order PI (FOPI) controller for a parallel active filter (Gunduz et al., n.d.). They employed variable nonlinear loads and evaluate the effectiveness of designed controller in case of load alteration. They compared the results with classical PI controller and reported that THD is decreased more with the FOPI controller.

In this chapter, an optimal Fractional Order Proportional Integral (FOPI) controller for an active power filter is designed by utilizing particle swarm optimization (PSO). Simulink program is employed to carry out simulation studies. Performance of FOPI controller is compared with classical PI controller. Therefore, this paper includes 5 sections. The filter structures and controller scheme are presented in Section 2. PI and FOPI controller are designed

and their parameters are optimized in the next section. Simulation results are given in Section 4. Section 5 is conclusion.

Filter Structures

It has become inevitable to use filter circuits used for the elimination of harmonics in power systems. The main problem with nonlinear loads generating harmonics is overheating. In particular, operating temperatures of generators and transformers may cause the insulation material of their windings to deteriorate or even burn. To solve this problem, a harmonic filter for each nonlinear load connected to the power system can be designed. The determination of filter structure constitutes the first step of filter design. Passive, active, and hybrid configurations are different types of harmonic filters**.**

Passive Filters

The traditional method to eliminate the harmonics is the passive filter (parallel or series) design. These filters have low cost, simple structure, and high efficiency (Calgan, 2023). For this reason, they are preferred by customers instead of the other filters. Although passive filters are simple to design and operate, they do not always respond to the dynamics of the power system. The size of these filters is very heavy and quite bulky due to the presence of capacitors, inductance, and resistance elements as shown in Figure 6.

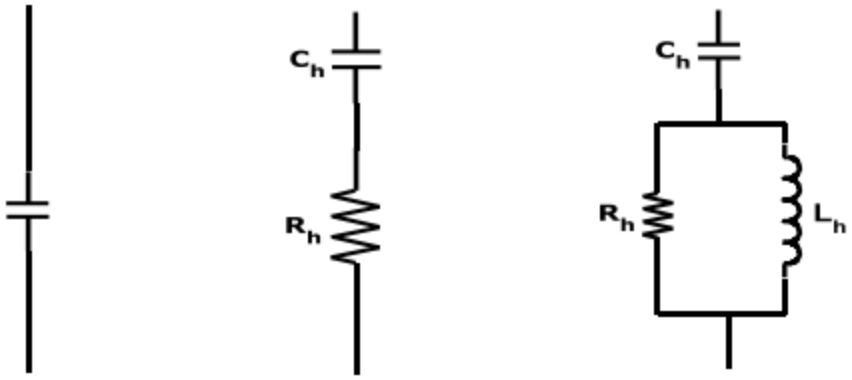

a. First order filter *b. Second order filter* *c. Third order filter*

Figure 6. Passive filters

Active Filters

In power electronics, the advances and developments in modern control methods have played a vital role in the industrial applications of active filters. The main aim of active filters is injecting opposite signals that have the same amplitude and frequency as the harmonics produced by nonlinear load. Active power filters (APF) are smaller than passive power filters when compared to each other in view of physical size. These filters are the effective solution method to increase the power quality. Shunt active filter circuits are widely used in active filter applications on the power system. The topology of shunt active power filter is illustrated in Figure 7. They have controllable voltage or current sources. On the other hand, series active passive filters isolate the harmonics between the nonlinear loads and sources.

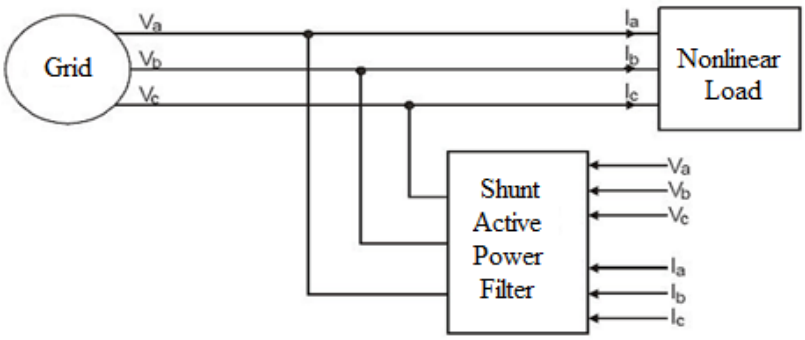

Figure 7. Shunt active power filter topology

Hybrid Filters

Hybrid filters consist of a series of passive filters and an active power filter as demonstrated in Figure 8. There are different configurations in order to boost the efficiency of filter. Hybrid power filter is designed to suppress the disadvantages of APF and passive filters. It combines the good aspects of both passive and active filters and provides very good performance and cost-effective solutions. But it is difficult to design a hybrid filter according to the passive filter. The harmonic filtering process is shared between the two filters. The APF eliminates the lower-order harmonics while the power filters cancel the higher-order harmonics. APF can be designed for single-phase and three-phase power systems.

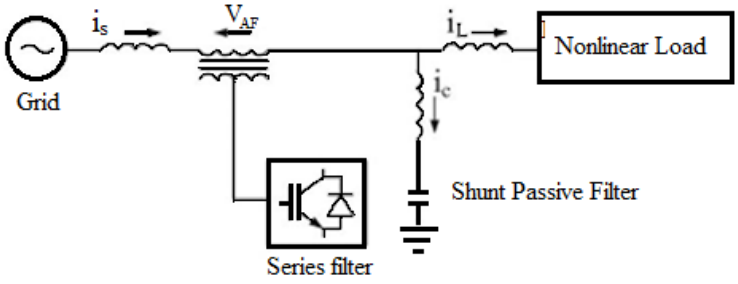

Figure 8. Hybrid active power filter topology

Controller Design for Active Filter Circuits

Active power filters have different circuit topologies and control systems. In this study, the system model includes a single-phase voltage source, a nonlinear load, a voltage source Pulse Width Modulation (PWM) converter, control circuit for triggering. Single-phase APF circuit is built in MATLAB/Simulink. FOPID controller is preferred to generate the PWM signals in the APF circuit. Control and power circuit topology of APF is given in Figure 9.

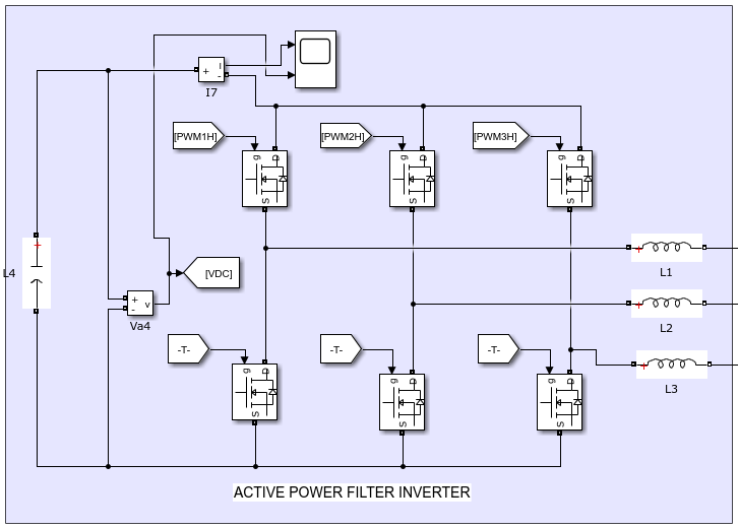

a. Power circuit

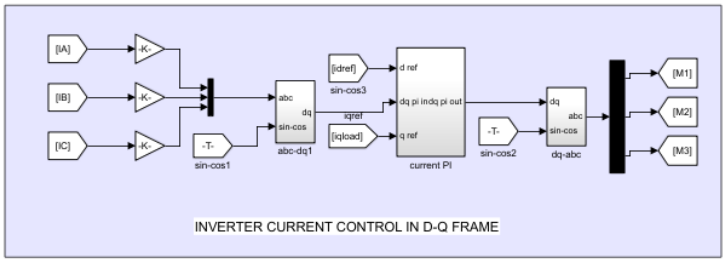

b. Control circuit

Figure 9. Control and power circuit topology of APF

PI Controller

Arjun Baliyan and Majid Jamil presented a hybrid series APF to increase the power quality by using intelligent PI Controller. The gain values of controller is obtained by using PSO technique to increase the steady state response of the power system (Baliyan et al., 2021). Hadi et. al, presented a review paper that declares a SAPF in which different control techniques such as PI, PID, adaptive neuro-fuzzy, model predictive control, and PSO-based PID are applied to the three-phase system (Hadi et al., 2022). Ghania Boudechiche and Mustapha Sarra studied a SAPF to improve the power quality for balanced and unbalanced conditions on solar system using direct power control command which is combination of FOPID and fuzzy maximum power point tracking (Boudechiche et al., 2021). General explanation of PID controller is given as follows (Çalgan et al., 2018):

$$u(t) = K_p e(t) + K_i \int_0^t e(t)\,dt + K_d \frac{de(t)}{dt} \tag{8}$$

Fractional-order PI Controller

Kashani et. al, designed Optimal Cascade Non-Integer Controller to improve the performance of the three-phase SAPF. FOPI-FOPD cascade controller is used to reduce the total current harmonics. THD value of source current is obtained less than 2%. Non-dominated sorting genetic algorithm is employed for optimization of controller coefficients (Nikkhah Kashani et al., 2022). Monika Sharma Bharat Singh Rajpurohit designed a FOPID controller to improve the power quality of smart power systems. A genetic algorithm is used to obtain the

best coefficients of controller (Sharma & Rajpurohit, 2022). The typical fractional-order controller can be represented in time domain as fallows(Demirtas et al., 2019):

$$u(t) = K_p e(t) + K_i D^{-\lambda} e(t) + K_d D^{\mu} e(t) \tag{9}$$

where e(t) is the error signal, K_p, K_i, and K_d are proportional, integral, derivative coefficients of PID controller, respectively. λ and μ are the fractional order of integration and differentiation. They are positive real number and change between zero and 1. The transfer function of FOPID controller can be written as below (Ilten & Demirtas, 2016):

$$G_c(s) = K_p + \frac{K_i}{s^{\lambda}} + K_d s^{\mu} \tag{10}$$

Algorithm for Optimization of Controller Coefficients

Youcef Bekakr and Laid Zellouma presented Grey Wolf Optimizer (GWO) and Ant Lion Optimizer(ALO) algorithm based predictive direct power control of three-phase (3-phase) SAPF to decrease DC-link voltage variation and maximum overshoot by means of MATLAB/Simulink. Performance evaluation is made for PI, PI-GWO, and PI-ALO. THD values is minimized using the PI controller gains obtained by the ALO algorithm (Bekakra et al., 2021). M.T Benchouiaa and I.Ghadbanea designed and implemented PI and sliding mode controllers for a three-phase SAPF. There is no overshoot and the settling time is very small the DC voltage regulation when sliding mode control is used (Benchouia et al., 2014). Nima Khosravi and Hamid Reza Abdolmohammad presented a switched power filter compensators to reduce the harmonics in micro-grids using PID controller. The best gains of controller are obtained using artificial bee colony, PSO, harmonic search, and differential evolution. The best result is obtained by using differential evolution algorithm (Khosravi et al., 2021). In this chapter, optimization of FOPID controller is occurred by using PSO algorithm. Matlab/Simulink model of APF is taken into account and minimization of THD_I value is aimed (Farswan, 2023). For this purpose max and min values of tuning parameters as well as fitness function (*FF*) are determined as follows:

$$\underset{fp \in \Omega}{Min}\ FF(fp)$$

$$subject\ to: \Omega \begin{cases} 0.1 \le K_p \le 5 \\ 0.1 \le K_i \le 5 \\ 0.1 \le K_d \le 5 \\ 0.1 \le \lambda \le 0.99 \\ 0.1 \le \mu \le 0.99 \end{cases} \tag{11}$$

Regarding these constraints, classical PSO algorithm of Matlab/Simulink program is used in this study with options such as function tolerance $1e^{-6}$, min neighbours fraction 0.25, self-adjustment weight 1.49, initial swarm span 2000, social adjustment weight 1.49, swarm size [100,300].

Results and Discussion

In this study, the performance of APF created in the Matlab/Simulink environment is compared with the designed controllers. The purpose of the parallel active filter is to increase the energy quality by filtering the harmonic current drawn by the load connected to the network with three-phase rectifier. The proposed nonlinear load at PCC is shown in Figure 10. As illustrated in the figure, R-C load is at the output of rectifier as a nonlinear load. Additionally, R-L load is connected to PCC. This system can be easily installed by using the Power System

Blockset in Matlab/Simulink. The values of R-C and R-L loads are 100 Ω, $100e^{-6}$ F, 160 Ω and 0.5 H, respectively. The circuit parameters of the network, load and filter are given in Table 4.

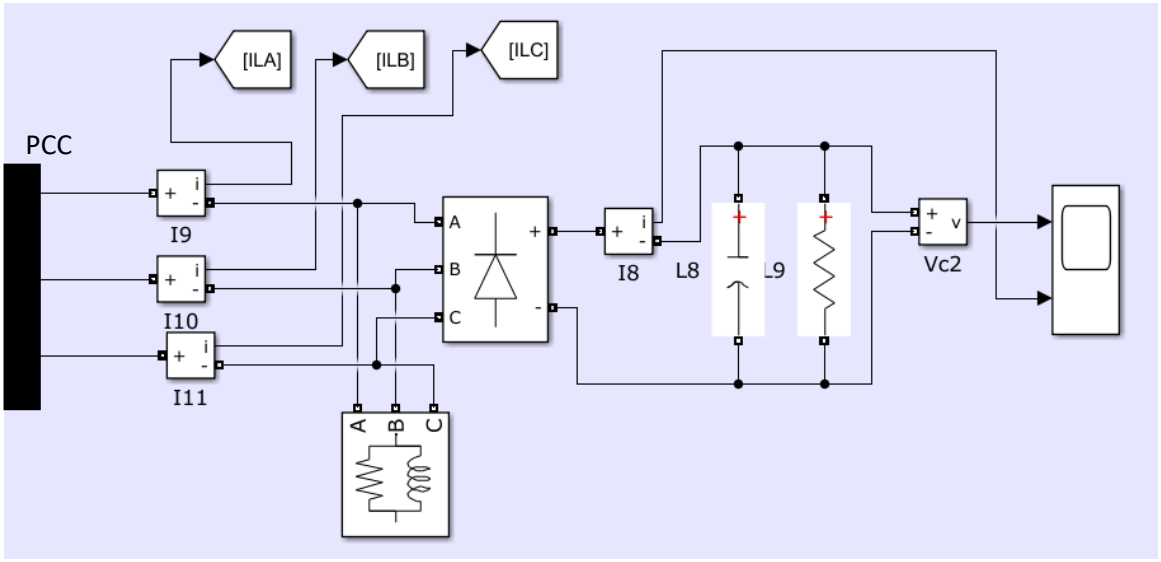

Figure 10. The nonlinear load connected to PCC

Table 4. Circuit Parameters

Parameter	Symbol	Value
Supply voltage	V_s	400 V
Supply frequency	f	50 Hz
Supply impedance	(R_s, L_s)	0.14 Ω, 0.1 H
Filter inductance	L_f	2.5 mH
DC capacitor	C_{dc}	1 mF
Reference DC voltage	V_{dc}(ref)	800 V

With the chosen nonlinear load values, the system is run on Matlab/Simulink program without any power filter. Total simulation time and integration step are taken as 0.4 and $1e^{-3}$ s, respectively. Ode23tb solver is used in the simulation. At the end of the simulation, current drawn by grid is kept by scope and saved to be used in Fast Fourier Transform (FFT). Matlab/Simulink Powergui block is employed for FFT analysis. Figure 11 shows the magnitude and THD value of current drawn by the nonlinear load. As seen from the figure, THD_I is calculated as 32.45% which considerably high value.

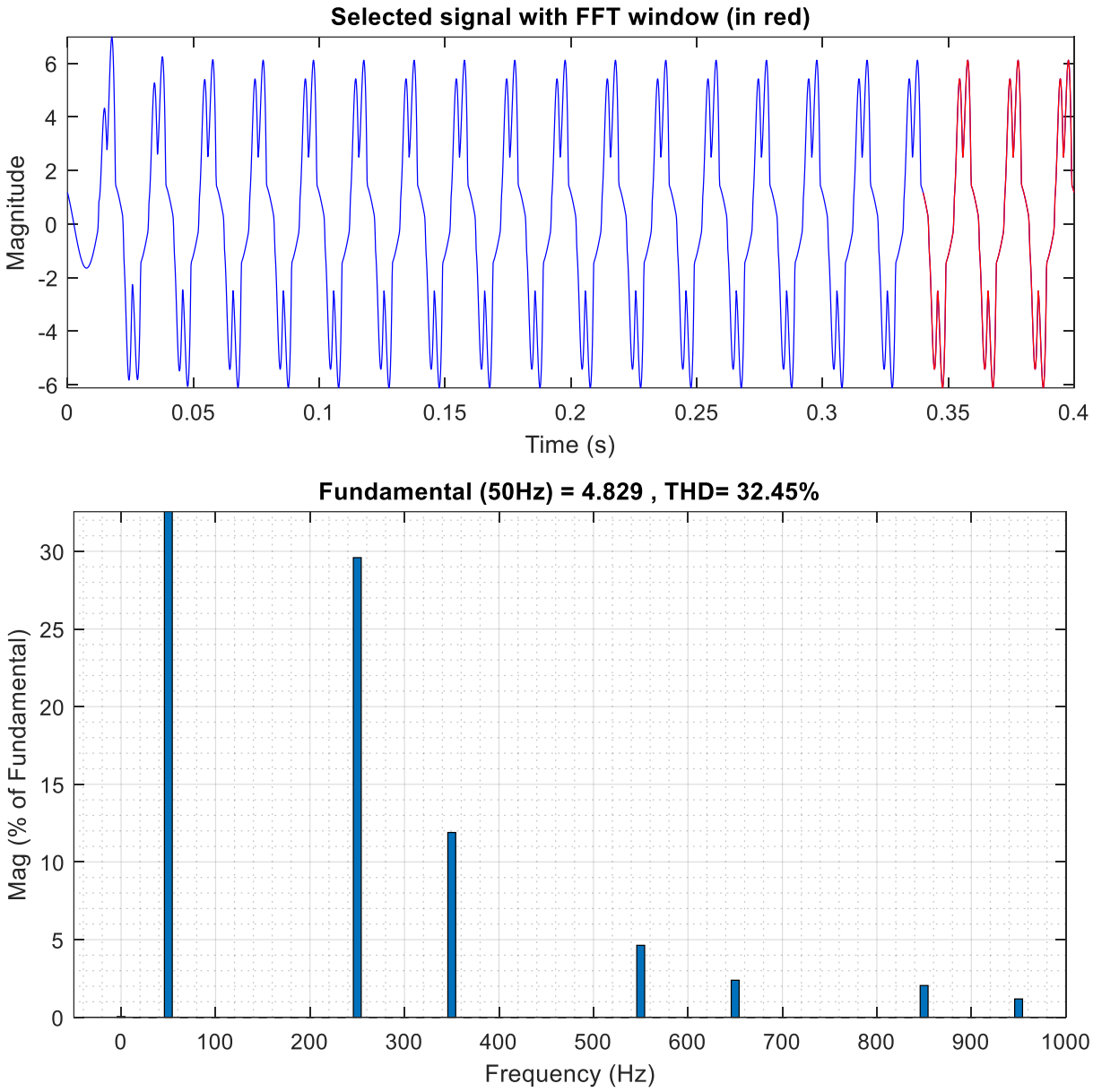

Figure 11. THD_I measurement without APF

In this study, instantaneous power (p-q) theory is used to determine reference d-q currents of power filter. The application area of this theory is only 3-phase systems. Three-phase current and voltage are converted from a-b-c coordinates to α-β coordinates and then instantaneous power components are obtained. This transformation from the three-phase structure to the two-phase structure is called the Clarke transform. Later, the instantaneous active and reactive power components drawn by the load from the network are defined by the expressions 'p' and 'q'. However, these powers include alternating current and direct current components. If both the harmonics and the reactive power drawn by the load are required to be compensated, only $\bar{p}$ will be the desired power component of the p-q theory. If harmonics are wanted to be mitigated, the powers of $\tilde{p}$ ve $\tilde{q}$ should be provided with the filter. Figure 12 shows the extracting of reference d and q current by using instantaneous power theory. Figure 13 demonstrates the method of adjusting the triggering angles of inverter in order to track reference d and q currents. With a pulse generator or a hysteresis controller these triggering angles are converted to sequent pulses to control the inverter current.

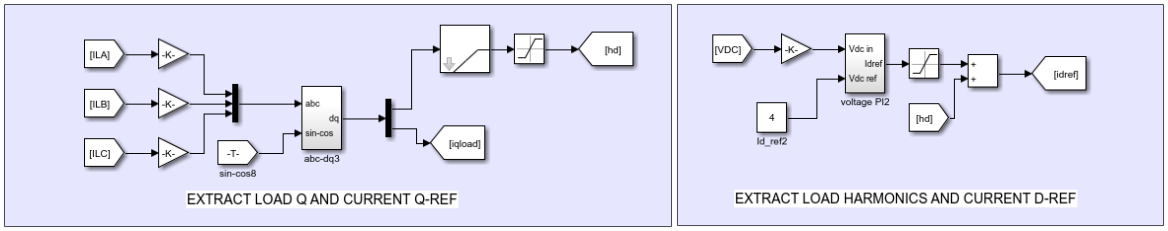

Figure 12. Extracting reference currents

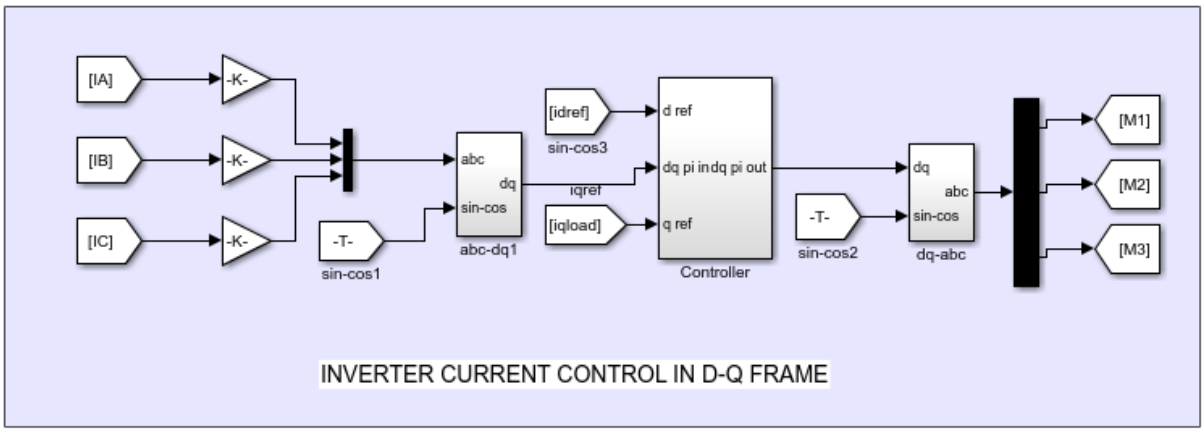

Figure 13. Control scheme of inverter

After creating the general scheme of APF, the proposed controller shown in Figure 13 is optimized with PSO algorithm as mentioned in Section 3.3. Two different controllers, namely PI and FOPI, are employed and their performances are compared in terms of harmonic mitigation. Additionally, controller block in the figure contains two separate controllers for d and q components of current. K_{p1}, K_{p2}, K_{i1}, K_{i2} are determined as 0.1, 2.09, 0.1, 5, respectively in the optimization process of PI controller. On the other hand, K_{p1}, K_{p2}, K_{i1}, K_{i2}, λ_1, and λ_2 are determined as 0.1, 2.85, 0.1, 3.33, 0.97 and 0.64, respectively. Both of the controllers are employed in the system separately and currents are obtained. The current drawn from the source and its FFT analysis are given in Figure 14. Compared to current harmonics given in Figure 13, PI filter gives good results and decreases the THD_I to 4.74%. On the other hand, FOPI controller performs better result in terms of eliminating THD_I value. THD_I is measured as 4.61% with FOPI controller. It is obvious that both controllers work fine and keep the THD_I value within the limits of IEEE-519 standard. But, FOPI controller is more flexible than PI control via its more tuning parameters to be optimized.

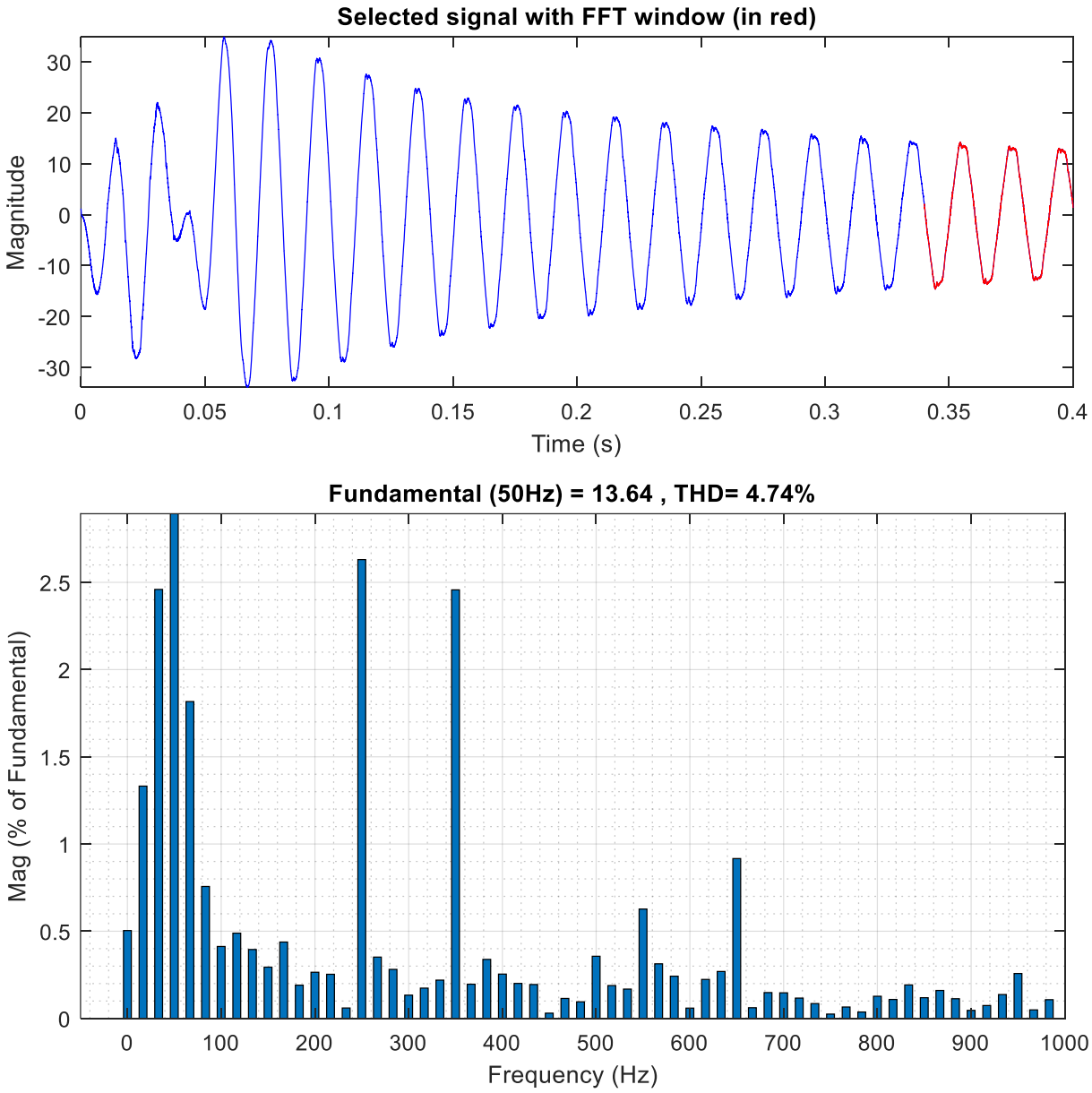

Figure 14. FFT analysis with PI controller

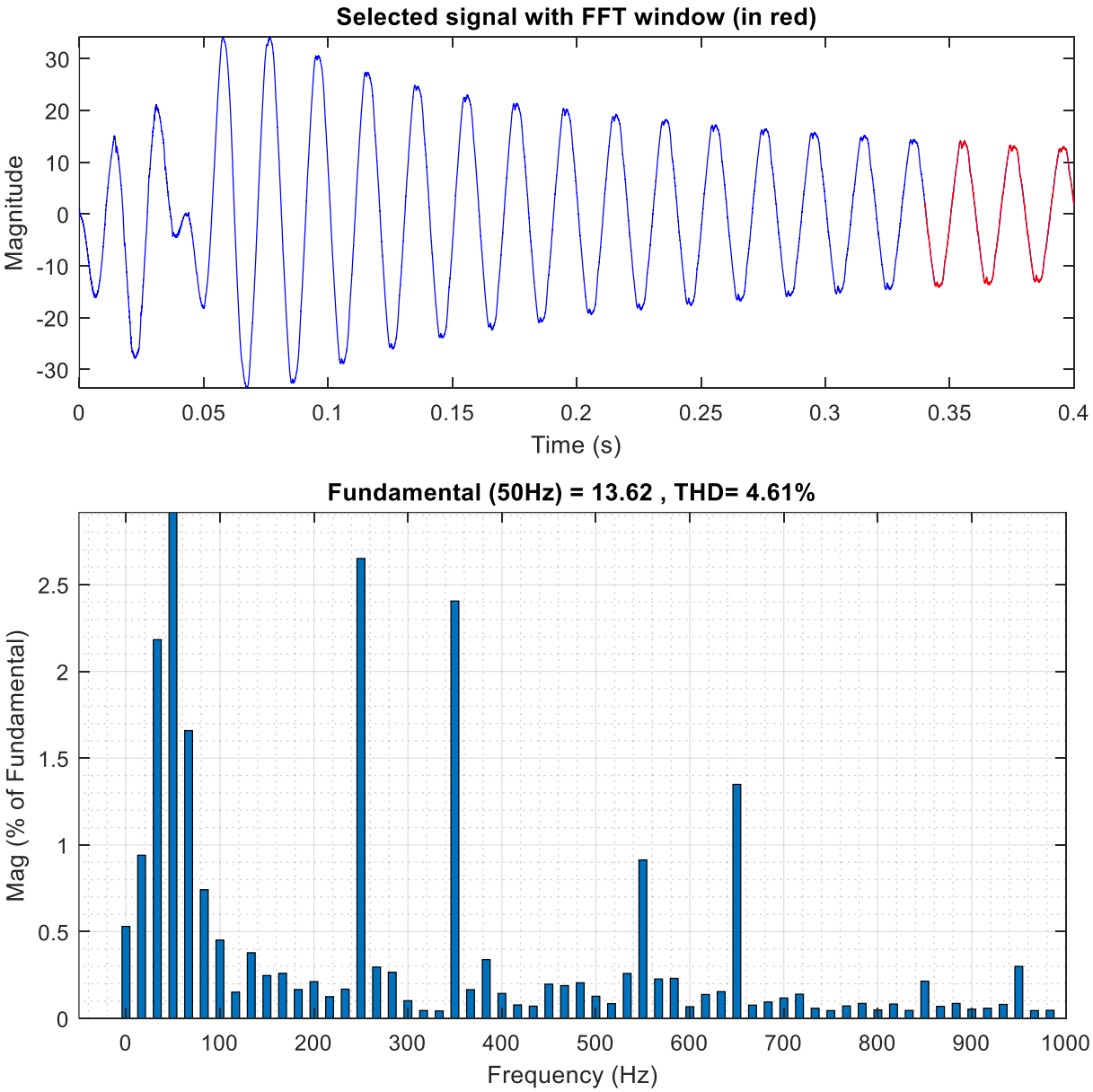

Figure 15. FFT analysis with FOPI controller

Conclusion

In the future, the power quality problem in power systems will be a very serious problem as a result of the rapid increase in electric vehicles. The best solution to improve power quality in power systems is to use an APF, which reduces harmonics and provides reactive power compensation. This study present two controllers, namely PI and FOPI, are employed to eliminate THD_I value in a system with nonlinear load. The results of simulations performed in the Matlab/Simulink environment show the efficiency and robustness of the controllers. Both the controllers can keep the THD_I of current within the limits specified by the IEEE-519 standard and exhibit the desired dynamic behavior. They remained below the limits specified by IEEE St. 519. Compared with classical PI controller, FOPI shows a better reduction in harmonic distortion rate.

References

Abaza, A., El-Sehiemy, R. A., Said, M., Ghoniem, R. M., & Barakat, A. F. (2022). Implementation of an Electronically Based Active Power Filter Associated with a Digital Controller for Harmonics Elimination and Power Factor Correction. *Electronics*, *11*(14), 2205.

Aljafari, B., Rameshkumar, K., Indragandhi, V., & Ramachandran, S. (2022). A Novel Single-Phase Shunt Active Power Filter with a Cost Function Based Model Predictive Current Control Technique. *Energies*, *15*(13), 4531.

Asadi, Y., Eskandari, M., Mansouri, M., Chaharmahali, S., Moradi, M. H., & Tahriri, M. S. (2022). Adaptive Neural Network for a Stabilizing Shunt Active Power Filter in Distorted Weak Grids. *Applied Sciences*, *12*(16), 8060.

Baliyan, A., Jamil, M., Rizwan, M., Alsaidan, I., & Alaraj, M. (2021). An intelligent PI Controller-based hybrid Series active power filter for power quality improvement. *Mathematical Problems in Engineering*, *2021*, 1–10.

Bekakra, Y., Zellouma, L., & Malik, O. (2021). Improved predictive direct power control of shunt active power filter using GWO and ALO–Simulation and experimental study. *Ain Shams Engineering Journal*, *12*(4), 3859–3877.

Benchouia, M. T., Ghadbane, I., Golea, A., Srairi, K., & Benbouzid, M. H. (2014). Design and implementation of sliding mode and PI controllers based control for three phase shunt active power filter. *Energy Procedia*, *50*, 504–511.

Boudechiche, G., Sarra, M., Aissa, O., & Lashab, A. (2021). Intelligent solar shunt active power filter based on direct power control strategy. *Artificial Intelligence and Renewables Towards an Energy Transition 4*, 467–477.

Calgan, H. (2023). Optimal C-type Filter Design for Wireless Power Transfer System by using Support Vector Machines. *An International Journal of Optimization and Control: Theories & Applications (IJOCTA)*, *13*(2). https://doi.org/10.11121/ijocta.2023.1354

Çalgan, H., Ilten, E., & Demirtas, M. (2020). Thyristor controlled reactor-based voltage and frequency regulation of a three-phase self-excited induction generator feeding unbalanced load. *International Transactions on Electrical Energy Systems*, e12387.

Çalgan, H., Yaman, R., İlten, E., & Demirtaş, M. (2018). Fırçasız DA motorunun hız kontrolünde PI katsayılarının Pareto tabanlı çok amaçlı optimizasyonu. *Balıkesir Üniversitesi Fen Bilimleri Enstitüsü Dergisi*.

Demirtas, M., Calgan, H., & Ilten, E. (2022). Elektrikli Araçlar için Şebekeden bağımsız Kablosuz Şarj İstasyonu Tasarımı. In *Mühendislikte Araştırma ve Değerlendirmeler* (pp. 241–266). Gece Kitaplığı.

Demirtas, M., Ilten, E., & Calgan, H. (2019). Pareto-Based Multi-objective Optimization for Fractional Order PIλ Speed Control of Induction Motor by Using Elman Neural Network. *Arabian Journal for Science and Engineering*, *44*(3), 2165–2175.

El Ghaly, A., Tarnini, M., Moubayed, N., & Chahine, K. (2022). A Filter-Less Time-Domain Method for Reference Signal Extraction in Shunt Active Power Filters. *Energies*, *15*(15), 5568.

Farswan, R. (2023). *Three phase active power filter*. MATLAB Central File Exchange. https://www.mathworks.com/matlabcentral/fileexchange/72735-three-phase-active-power-filter

Garcia Campanhol, L. B., Oliveira da Silva, S. A., & Goedtel, A. (2014). Application of shunt active power filter for harmonic reduction and reactive power compensation in three-phase four-wire systems. *IET Power Electronics*, *7*(11), 2825–2836.

Gunduz, H., Demirtas, M., Ilten, E., & Calgan, H. (n.d.). Paralel Aktif Güç Filtresi için Bulanık Uyarlamalı Kesirli PI Denetleyici Tasarımı. *Düzce Üniversitesi Bilim ve Teknoloji Dergisi*, *8*(3), 1975–1994.

Hadi, A. M., Thjeel, E. M., & Nahar, A. K. (2022). A review of control technique applied in shunt active power filter (SAPF). *Engineering and Technology Journal*, *40*(8), 140–149.

Ilten, E. (2022). Conformable fractional order controller design and optimization for sensorless control of induction motor. *COMPEL-The International Journal for Computation and Mathematics in Electrical and Electronic Engineering*.

Ilten, E., & Demirtas, M. (2016). Off-Line Tuning of Fractional Order PIλ Controller by Using Response Surface Method for Induction Motor Speed Control. *Journal of Control Engineering and Applied Informatics*, *18*(2), 20–27.

Khosravi, N., Abdolmohammadi, H. R., Bagheri, S., & Miveh, M. R. (2021). A novel control approach for harmonic compensation using switched power filter compensators in micro-grids. *IET Renewable Power Generation*, *15*(16), 3989–4005.

Mishra, A. K., Ray, P. K., Mallick, R. K., Mohanty, A., & Das, S. R. (2021). Adaptive fuzzy controlled hybrid shunt active power filter for power quality enhancement. *Neural Computing and Applications*, *33*, 1435–1452.

Nikkhah Kashani, H., Rouhi Ardeshiri, R., Gheisarnejad, M., & Khooban, M.-H. (2022). Optimal Cascade Non-Integer Controller for Shunt Active Power Filter: Real-Time Implementation. *Designs*, *6*(2), 32.

Ozdemir, S., Demirtas, M., & Aydin, S. (2016). Harmonic Estimation Based Support Vector Machine For Typical Power Systems. *Neural Network World*, *233*, 252.

Sarıbulut, L., Ahmet, T., Meral, M., & Tumay, M. (2011). Active power filter: review of converter topologies and control strategies. *Gazi University Journal of Science*, *24*(2), 283–289.

Sharma, M., & Rajpurohit, B. S. (2022). Experimental analysis of fractional order PIλDμ controller for improvement of power quality in smart grid environment. *Energy Conversion and Economics*, *3*(2), 85–93.

Sis, S. A., & Akça, H. (2020). Maximizing the efficiency of wireless power transfer systems with an optimal duty cycle operation. *AEU-International Journal of Electronics and Communications*, *116*, 153081.

New Approaches To Some Matrix Equation Solutions

Hasan KELEŞ[1]

Introduction

In this section, the solutions of equations $AX = B, XC = D$ and $EXF = G$ or $Af(X) = B$, $g(X)C = D$ and $Eh(X)F = G$ are investigated, where $A, B, C, D, E, F, G \in M_n(\square)$ and f, g, h are functions matrices. More solutions of these are explored in articles in different ways. The focus is on solutions resulting from line and column co-divisors. In addition, the relationship between simplification and extension in rational matrices resulting from matrix multiplication and this solution is examined. Some new equations arising from these equations are solved. New theorems and examples are given about the difference between co-divisors and the solutions of these equations. Although there are many studies on this subject, the method here of the study is different and some new gains are expected for the literature.

The linear equation systems are known to be used for the first time in geometric coordinates in 1637 by the European Ren'e Descartes. In the new geometric structure of the age, lines and planes are defined by lines, and thus solutions are sought. These solutions are cross-sections of definitions. The subject of linear equation systems has found many application areas and produced solutions until today. Also they can find many application areas, especially in economics, chemistry, computer and engineering sciences.
Our study here is based on Gaussian reduction method and determinant calculation.
Let us start with the line co-divisor definition, for which we gave the definition for the first time.

The set of all regular matrices of order $n \in \square^+$ over a field F is denoted by

$$M_n(F) = \left\{ \left[a_{ij} \right]_n \middle| a_{ij} \in F, n \in \square^+ \right\}$$

The concept of determinate and Gaussian reduction method are frequently used in the study.

The transpose of $A \in M_n(F)$ is denoted by A^T.

Let us start with the row co-divisor definition that I gave in a study in 2022.

Definition 1. Let A and B be two regular square matrices of order n. The determinant of the new matrix obtained by writing the i^{th} ith row of the matrix A on the j^{th} row of the matrix B is called the row co-divisor row on the matrix B of matrix A. It is denoted by $\underset{ij}{AB}$. Their number is n^2. The matrix row co-divisors is $\left[\left(\underset{ij}{AB} \right)_{ij} \right]$.

[1] Lecturer, Karadeniz Technical University, e-mail: hasankeles@ktu.edu.tr

Example 2. Let $A=\begin{bmatrix}1 & 3\\ 2 & 5\end{bmatrix}$, $B=\begin{bmatrix}2 & 1\\ 4 & 7\end{bmatrix}\in M_2(\square)$. Matrix of the row co-divisors on the matrix B of the matrix A is $\left[\left(\underset{ij}{AB}\right)_{ij}\right]$.

$$\underset{11}{AB}=\begin{vmatrix}1 & 3\\ 4 & 7\end{vmatrix}=-5,\ \underset{12}{AB}=\begin{vmatrix}2 & 1\\ 1 & 3\end{vmatrix}=5.\ \underset{21}{AB}=\begin{vmatrix}2 & 5\\ 4 & 7\end{vmatrix}=-6,\ \underset{22}{AB}=\begin{vmatrix}2 & 1\\ 2 & 5\end{vmatrix}=8.$$

$$\left[\left(\underset{ij}{AB}\right)_{ij}\right]=\begin{bmatrix}-5 & 5\\ -6 & 8\end{bmatrix}.$$

Likewise, the matrix of co-dividing rows of the matrix B over the matrix A is the matrix $\left[\left(\underset{ij}{BA}\right)_{ij}\right]$.

$$\underset{11}{BA}=\begin{vmatrix}2 & 1\\ 2 & 5\end{vmatrix}=8,\ \underset{12}{BA}=\begin{vmatrix}1 & 3\\ 2 & 1\end{vmatrix}=-5.\ \underset{21}{BA}=\begin{vmatrix}4 & 7\\ 2 & 5\end{vmatrix}=6,\ \underset{22}{BA}=\begin{vmatrix}1 & 3\\ 4 & 7\end{vmatrix}=-5.$$

$$\left[\left(\underset{ij}{AB}\right)_{ij}\right]=\begin{bmatrix}8 & -5\\ 6 & -5\end{bmatrix}.$$

For the two matrices satisfying the above conditions, the matrix division is also given by $\frac{A}{B}:=\frac{1}{|B|}\left[\left({}_{B}^{A}i_j\right)_{ji}\right]$ and at the same time, the solution of the equation $AX=B$ is $X=\frac{B}{A}$. Volodymyr P. Shchedryk gave the following theorem. It is determined that this theorem is given with column division. The proof is given in my papers.

Volodymyr P. Shchedryk gave the following proved theorem in 2020. It is been determined that this theorem has to do with column division. Its proof was given in my study called " Different Approaches on the Matrix Division and Generalization of Cramer's Rule".

Theorem 3. ***Let*** F ***be a commutative elementary divisor domain. If*** $BX=A$ ***is a solvable matrix equation over*** F***, where*** $A,\ X,\ B\in M_n(\mathrm{F})$ ***then a left g.c.d. and a left l.c.m. of solutions of this equation are also solutions of*** $BX=A$**.**

The solution of the equation $BX=A$ is $X=\left[x_{ij}\right]=\left[\frac{\left({}_{A}^{B}i_j\right)ji}{|B|}\right]$ in terms of column co-divisors and $X=\frac{A}{B}$ according to the division operation.

Solutions of The Equations $XA=B$ **and** $AX=B$

In the first part of this section, similar properties of the transpose according to the multiplication operation are examined. Secondly, it is investigated whether the transpose provides some of its properties compared with the division operation.

If $A, B \in M_n(F)$ then

$$\left(\frac{A}{B}\right)^T \neq \frac{A^T}{B^T}.$$

Example 1. Let $A = \begin{bmatrix} 1 & 3 \\ 2 & 5 \end{bmatrix}$, $B = \begin{bmatrix} 2 & 1 \\ 4 & 7 \end{bmatrix} \in M_2(\square)$, then

$$\left(\frac{A}{B}\right)^T = \begin{bmatrix} \frac{1}{2} & 0 \\ \frac{8}{5} & -\frac{1}{5} \end{bmatrix},$$

$$A^T = \begin{bmatrix} 1 & 2 \\ 3 & 5 \end{bmatrix} \text{ and } B^T = \begin{bmatrix} 2 & 4 \\ 1 & 7 \end{bmatrix}$$

$$\frac{A^T}{B^T} = \begin{bmatrix} -\frac{1}{2} & -\frac{3}{5} \\ \frac{1}{2} & \frac{4}{5} \end{bmatrix}.$$

As a result,

$$\begin{bmatrix} \frac{1}{2} & 0 \\ \frac{8}{5} & -\frac{1}{5} \end{bmatrix} \neq \begin{bmatrix} -\frac{1}{2} & -\frac{3}{5} \\ \frac{1}{2} & \frac{4}{5} \end{bmatrix}.$$

Lemma 2. Let $A \in M_n(\square)$. Then,

$$\left(\frac{I_n}{A}\right)^T = \frac{I_n}{A^T}.$$

Proof. Let a regular matrix $A = \left[a_{ij}\right]_n$ be given.

$$\left(\frac{I_2}{A}\right) A^T = I_n,\ A^T \left[\frac{I_n}{A^T}\right] = I_n,$$

$$\frac{I_2}{A} == \left(A^{-1}\right)^T = \left(\frac{I_n}{A}\right)^T,$$

$$\left(\frac{I_n}{A}\right)^T = \frac{I_n}{A^T}.$$

The following lemma is given which simply explains the relationship between the row co-divisors matrix and the transpose.
The following Lemma 3 is given which simply explains the relationship between the row co-divisors matrix and the transpose.

Lemma 3. Let $A, B \in M_n(F)$. Then,

$$\frac{1}{|A|}\left[\left(\underset{ij}{AB}\right)_{ij}\right] = \left(\frac{B^T}{A^T}\right)^T.$$

Proof. If $A, B \in M_n(F)$ then $\underset{ij}{AB} = \underset{A^T}{B^T} i_j$. Because, the row co-divisors of B on the matrix A are the same as the column co-divisors of matrix B^T on the matrix A^T.

$$\left(\underset{ij}{AB}\right)_{ij} = \left(\underset{A^T}{B^T} i_j\right)_{ij}$$

$$\frac{1}{|A|}\left[\left(\underset{ij}{AB}\right)_{ij}\right] = \frac{1}{|A^T|}\left[\left(\underset{A^T}{B^T} i_j\right)_{ji}\right]^T = \left(\frac{B^T}{A^T}\right)^T.$$

Lemma 4. Let $A, B \in M_n(F)$. Then,

$$\frac{B}{A} = \left(\frac{B^T}{A^T}\right)^T.$$

Proof. If $A, B \in M_n(F)$ then $\underset{ij}{AB} = \underset{A^T}{B^T} i_j$. Because, the row co-divisors of B on the matrix A are the same as the column co-divisors of matrix B^T on the matrix A^T.

$$\frac{B}{A} = \frac{1}{|A|}\left[\left(\underset{ij}{AB}\right)_{ij}\right] = \frac{1}{|A^T|}\left[\left(\underset{A^T}{B^T} i_j\right)_{ji}\right]^T = \left(\frac{B^T}{A^T}\right)^T.$$

Proposition 5. Let $A, B \in M_n(F)$. Then, the solution of the linear matrix equation $XA = B$ is

$$X = \left(\frac{B^T}{A^T}\right)^T.$$

Proof. The solution of the equation $AX = B$ is $X = \frac{B}{A}$ for all $A, X, B \in M_n(F)$.

$$(XA)^T = B^T \Leftrightarrow A^T X^T = B^T,$$

$$X^T = \frac{1}{|A^T|}\left[\left(\underset{ij}{B^T A^T}\right)_{ij}\right] \Rightarrow X = \frac{1}{|A^T|}\left[\left(\underset{ij}{B^T A^T}\right)_{ji}\right]^T$$

$$X = \left(\frac{B^T}{A^T}\right)^T.$$

Proposition 6. Let $A, B \in M_n(F)$. Then the solution of the two equations $XA = B$ and $A^T X = B^T$ is same.

Proof. The proof of this Proposotion 6 is obvious from Lemma 4 and Proposotion 5.

Proposition 7. Let $A, B \in M_n(F)$. If one of the factors of the matrix A is BA_1 and one of the factors of matrix B is AB_1, then

i. The rational matrix $\frac{A}{B}$ is equal to matrix A_1.

ii. The rational matrix $\frac{A}{B}$ is equal to matrix $\frac{I_n}{B_1}$.

Proof.

i. If the matrix A is written in terms of B as $A = BA_1$, then

$$\frac{A}{B} = \frac{BA_1}{B} = A_1.$$

ii. If the matrix B is written in terms of A as $B = AB_1$, then

$$\frac{A}{B} = \frac{A}{AB_1} = \frac{I_n}{B_1}.$$

Note. In the solution of equations $AX = B$ and $YC = D$, it should be noted that if $B = 0$ and $D = 0$, the equation will also be satisfied when $X \neq 0$ and $Y \neq 0$. In shortly, for X, A and zero-dividing matrices Y, C, D the equation solution is still provided. Therefore, if the solution of the equation $AX = 0$ is obtained by multiplying the inverse of the matrix A, it turns out that the solution matrix X is the matrix [0], which means that the matrices A and X are zero dividing matrices. The situation is also valid for the equation $AX = B$. Going to the operational result in the solution of the equations given above may create a contradiction. The operations used are valid whether they are multiplication or division. Therefore, going with the definitions of row co-divisors or column co-divisors avoids conflict. Because in operational solution, if $B = 0$ then either $A = 0$ or $X = 0$. The validity of the division operation is satisfied for regular square matrices.

Theorem 8. Let $A, B, X \in M_n(F)$ and X unknowns matrix. Then, in the solution of the equation $AX = B$, there are regular matrices $A = B_2 A_3$, $B = B_2 B_3$, such as B_2, A_3 and B_3, and the rational matrix $\frac{B_3}{A_3}$ is the solution of the equation $AX = B$. This solution is equal to the rational matrix $\frac{B}{A}$.

Proof. Since the solution of $AX = B$ is the rational matrix $\frac{B}{A}$, where any factor of matrix B is matrix B_2

$$B = B_2 B_3,$$

Likewise, matrix A in terms of this B_2 matrix multiplier.

$$A = B_2 A_3$$

can be written as

therefore

$$X = \frac{B}{A} = \frac{B_3}{A_3}.$$

Example 9. For the given $A = \begin{bmatrix} 1 & 3 \\ 2 & 5 \end{bmatrix}$, $B = \begin{bmatrix} 2 & 1 \\ 4 & 7 \end{bmatrix}$ matrices, the solution of the equation $AX = B$ is $X = \frac{B}{A}$. If $B_2 = \begin{bmatrix} 3 & 3 \\ 1 & 2 \end{bmatrix}$ is selected $B = B_2 \underbrace{\begin{bmatrix} -\frac{8}{3} & -\frac{19}{3} \\ \frac{10}{3} & \frac{20}{3} \end{bmatrix}}_{B_3}$. Likewise,

$A = B_2 \underbrace{\begin{bmatrix} -\frac{4}{3} & -3 \\ \frac{5}{3} & 4 \end{bmatrix}}_{A_3}$.

Like this

$$X = \frac{B}{A} = \frac{B_2 B_3}{B_2 A_3} = \frac{B_3}{A_3}.$$

Theorem 10. Let $A, B \in M_n(F)$. Then the solutions of the equation $AX - YA = B - C$ are $X = A_1 A + B_1 - C_1$ and $Y = AA_2 - (B_1 - C_1)$, where $A_1, A_2, B_1, C_1 \in M_n(F)$.

Proof.

$$AX - YA = A(B_1 - C_1) \wedge Y = AA_1$$

$$A(X - A_1 A) = A(B_1 - C_1)$$

$$X - A_1 A = B_1 - C_1$$

$$X = A_1 A + B_1 - C_1.$$

And

$$AX - YA = (B_1 - C_1) A \wedge X = A_1 A$$

$$(AA_2 - Y)A = (B_1 - C_1)A$$

$$AA_2 - Y = B_1 - C_1$$

$$Y = AA_2 - (B_1 - C_1).$$

Comparison of Matrix Equations

Any regular matrix of the same order is written as a factor of any other matrix as follows:

$$X \mid A \Leftrightarrow A = XX_1, \text{ where } X_1 \in M_n(\square).$$

The theorem given that some equations is solved by the factors of a regular matrix.

Theorem 1. Let $A, B \in M_n(F)$. For any $n \in \square^+$ the followings hold.

i. The solution of the equations $AX = B$ and $X^n X_n X = B$ is same, where $X_1 = \frac{A}{X}, X_n = \frac{X_{n-1}}{X}$.

ii. The solution of the equations $YC = D$ and $Y^{n+1} Y_n = D$ is same, where $Y_1 = \frac{D}{Y}, Y_n = \frac{Y_{n-1}}{Y}$.

Proof. Let $AX = B$ be a linear equation of matrices. Let us give the proof by the induction method.

i. The solution of the linear equation $AX = B$ is $X = \frac{B}{A}$. It is true for $n = 1$, because;

$$XX_1X = B \Rightarrow X\frac{A}{X}X = B \Rightarrow AX = X$$

It is $X = \frac{B}{A}$.

Assume that it is true for n. The solution equation $X^n X_n X = B$ is

$$X = \frac{B}{A}.$$

$$X^{n+1} X_{n+1} X = B \Rightarrow X^n X \frac{X_n}{X} X = X^n X_n X = B$$

$$X = \frac{B}{A}.$$

ii. The solution of the linear equation $YC = D$ is $Y = \left(\frac{D^T}{C^T}\right)^T$. It is true for $n = 1$, because;

$$Y^2 Y_1 = D \Rightarrow Y^2 \frac{C}{Y} = D \Rightarrow YC = D.$$

It is $Y=\left(\frac{D^T}{C^T}\right)^T$.

Assume that it is true for n . The solution equation $Y^{n+1}Y_n=D$ is $Y=\left(\frac{D^T}{C^T}\right)^T$.

$$Y^{n+2}Y_{n+1}=D\Rightarrow Y^{n+1}YY_{n+1}=D$$

$$Y^{n+1}Y\frac{Y_n}{Y}=Y^{n+1}Y_n=D\Rightarrow Y=\left(\frac{D^T}{C^T}\right)^T .$$

Example 2. Let $A=\begin{bmatrix}1 & 3\\ 2 & 5\end{bmatrix}$, $B=\begin{bmatrix}-6 & -6\\ 19 & 28\end{bmatrix}\in M_2(\square)$. Then the solution of the equation $AX=B$ is

$$X=\frac{B}{A}=\begin{bmatrix}2 & 16\\ 0 & -5\end{bmatrix}.$$

i. The solution of the linear equation $XX_1X=B$ is $\begin{bmatrix}2 & 16\\ 0 & -5\end{bmatrix}$, where $X_1=\frac{A}{X}=\begin{bmatrix}\frac{37}{10} & \frac{19}{2}\\ -\frac{2}{5} & -1\end{bmatrix}$

.

ii. The solution of the quadratic equation $X^2X_2X=B$ is $\begin{bmatrix}2 & 16\\ 0 & -5\end{bmatrix}$, where $X_2=\frac{X_1}{X}=\begin{bmatrix}\frac{121}{100} & \frac{63}{20}\\ \frac{2}{25} & \frac{1}{5}\end{bmatrix}$.

iii. The solution of the equation $X^4X_4X=B$ of degree 4 is $\begin{bmatrix}2 & 16\\ 0 & -5\end{bmatrix}$, where $X_4=\frac{X_3}{X}=\begin{bmatrix}\frac{34091}{10000} & \frac{1767}{2000}\\ \frac{2}{625} & \frac{1}{125}\end{bmatrix}$.

iv. The solution of the equation $X^nX_nX=B$ of degree n is also $\begin{bmatrix}2 & 16\\ 0 & -5\end{bmatrix}$, by continuing the iterative process.

Example 3. Let $C=\begin{bmatrix}1 & 3\\ 2 & 5\end{bmatrix}$, $D=\begin{bmatrix}34 & 86\\ -1 & 525\end{bmatrix}\in M_2(\square)$. Then the solution of the equation $YC=D$ is

$$Y=\left(\frac{D^T}{C^T}\right)^T=\begin{bmatrix}2 & 16\\ 0 & -5\end{bmatrix}\in M_2(\square).$$

i. The solution of the linear equation $Y^5Y_4=D$ of degree 5 is $Y=\begin{bmatrix}2 & 16\\ 0 & -5\end{bmatrix}$, where $Y_4=\begin{bmatrix}\frac{34091}{10000} & \frac{1767}{2000}\\ \frac{2}{625} & \frac{1}{125}\end{bmatrix}$.

ii. The solution of the quadratic equation $Y^{n+1}Y_n=D$ of degree $n+1$ is $\begin{bmatrix}2 & 16\\ 0 & -5\end{bmatrix}$, calculated by continuing the iterative process.

Results

Although the coefficient matrices of the equations $AX=B$ and $XA=B$ are the same, they have different solutions. These solutions are correlated in terms of some operational properties of the coefficient matrices. In addition to the solutions in the literature, new equations arising from new definitions are provided and brought to the literature.

References

Rafael B,, Maria T. G., Isabel G. and José A. S., (2015). The Hadamard Product of a Nonsingular General H-Matrix and Its Inverse Transpose Is Diagonally Dominant, Hindawi Publishing Corporation Journal of Applied Mathematics Volume, Article ID 264680, 6 pages.

Keles, H**., (2010).** The Rational Matrices, **New Trends in Nanotechnology and Nonlinear Dynamical Systems, Ankara,** paper58.

Keleş, H., (2018). On Matrix Division and Rational Matrices, Soi: 1.1/im doi: 10.15863/im, International Scientific Journal Intelligent Mathematics, 1(7).

Keleş, H., (2015). Lineer Cebire Giriş-I-, Bordo yayınları, Trabzon, Turkiye.

Keleş, H., (2015). Different Approaches on the Matrix Division and Generalization of Cramer's Rule, Journal of Scientific and Engineering Research, 2017, 4(3):105-108.

Keleş, H., (2022). On The Relationship Between Transpose and Division, 8. International İstanbul scıentific Research Congress March 12-13, pages 719-722, İstanbul, Turkiye.

Keleş, H., (2022). On Results Divisibility and Multipliers of Regular Matrices of Order *nth,* 8. International İstanbul Scientific Research Congress March 12-13, pages 712-718, İstanbul, Türkiye.

Volodymyr, P. S., (2020). A Greatest Common Divisor and a Least Common Multiple of Solutions of A Linear Matrix Equation, Pidstryhach Institute for Applied Problems of Mechanics and Mathematics, National Academy of Sciences of Ukraine, 16 October,. MATH. GM.

Porter, D. A., (1976). Solvability of the Matric Equation $AX = B$, Linear Algebra and Its Applzcatzons, 13, 177-164.

New Magnetıc Nanocatalysts Dıscovered For The Synthesıs Of Coumarın And Its Derıvatıves Sınce 2022

Hasniye YAŞA[1]
Hülya ÇELİK ONAR[2]

In order to limit or completely avoid the usage and manufacture of hazardous compounds, and to make chemical synthesis activities more environmentally friendly, "green chemistry" is described as product design and chemical reaction processes (Scheme 1). In short, the field of chemistry known as "green chemistry" is focused on creating chemical products with the least amount of dangerous substances. Preferring green solvents, such as ionic liquids, solvent-free methods, fluorous processes, and supercritical fluids, is the most appropriate course of action. The use of heterogeneous catalysts in a chemical reaction is the green synthesis strategy that is gaining popularity among academics. To improve the circumstances for organic reactions, their efficiency, and their effects on the environment, an ideal catalyst needs to be designed and synthesize (Kumar & et al., 2022a).

Scheme 1. Green Chemistry

Advancing nanotechnology is reflected in the production of several nano-level catalysts for various uses. One of the most important factors in how well the nanomaterials interact with the substrates is their capacity to be easily manipulated into the desired shape and size with a high surface area to volume ratio. Currently, a wide range of catalysts (nanocatalysts) are

[1] Assoc.Prof. Hasniye YAŞA İstanbul University-Cerrahpaşa, hasniye@iuc.edu.tr
[2] Assoc.Prof. Hülya ÇELİK ONAR, İstanbul University-Cerrahpaşa, hcelik@iuc.edu.tr

utilized in organic reactions to manufacture significant compounds with a reusability, high yield and selectivity in reduction, hydrogenation, oxidation, condensation, C-C coupling, cyclization, and other processes (Gebre, 2023). There are numerous uses for magnetic nanoparticles in the fields of medicine (Hashemi-Moghaddam & et al., 2016), sensing (Jiang & et al., 2016), and catalysis (Rostamnia & et al., 2015; Rostamnia & Doustkhah, 2015). They may also have additional active catalytic species inside of them (Allaedini, Tasirin & Aminayi, 2015). These substances are simple to isolate from the media using an external magnet because of their magnetic characteristics. A magnetic field tracks and regulates them during drug delivery. They are simple to utilize and recycle in catalysis (Gawande, Branco & Varma, 2013; Gawande, Luque & Zboril, 2014). Due to its usefulness in a variety of sectors, including biomedicine, biomaterials, sensors, photonics, imaging, and catalysis, as well as their exceptional physicochemical features, nanomaterials have demonstrated an important role in modern advancements. Nanomaterials have been used to address environmental problems because they offer a quasi-homogeneous catalytic system that combines heterogeneous and homogeneous catalytic capabilities (Scheme 2) (Kumar & et al., 2022b).

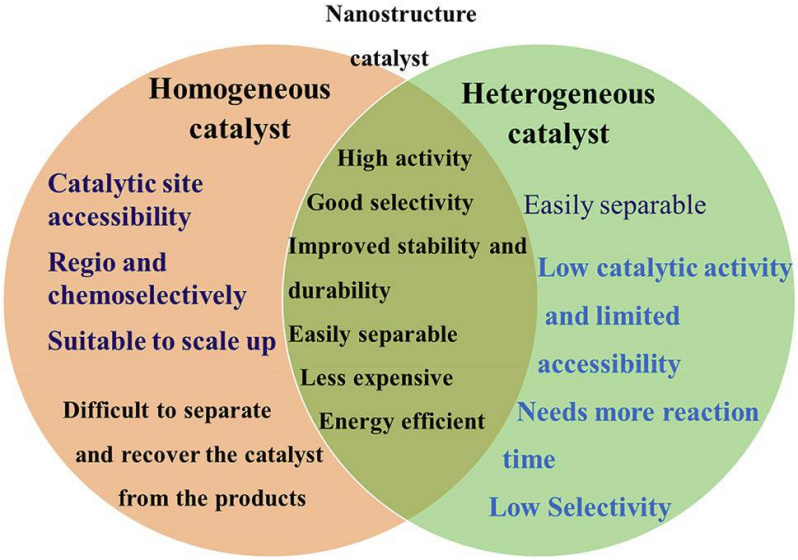

Scheme 2. Distinctive Properties of Homogeneous, Heterogeneous and Nanocatalysts

Particles having dimensions and tolerances of 1–100 nanometers are known as nanoparticles (nm). However, the word "nanoparticles" is also sometimes used to refer to bigger particles (between 100 and 500 nm), fibers, and tubes that are 100 nm in diameter and they have distinctly different physicochemical properties from microparticles or macroparticles, such as colloidal qualities (Nahar & Sarker, 2017; Khan, Saeed & Khan, 2019). Depending on their overall shape, nanoparticles can be 0D, 1D, 2D, or 3D in nature. They can also be divided into the following categories: organic nanoparticles, magnetic nanoparticles, lipid-based nanoparticles, hybrid nanoparticles, metal nanoparticles, semiconductor nanoparticles, ceramic nanoparticles, polymeric nanoparticles, and carbon-based nanoparticles (Khan, Saeed & Khan, 2019). Recently, nanoparticles have been employed in medicine, especially for the administration of targeted, controlled-release drugs (Nahar & Sarker, 2017). Nanoparticles can be utilized as efficient transport and delivery systems since they can enter cells more quickly than bigger microparticles. For instance, medications can be attached to the surface of nanoparticles or incorporated into their matrix for use in medicine. Nanoparticles, which are small and have a large surface area, can improve the solubility and stability of medicinal compounds, enhance drug penetration, facilitate drug absorption and persistence in target tissues, shield drugs from early cellular deterioration, improve bioavailability, show significant

differences in uptake efficiency between target and normal cells and extend the time spent in the bloodstream.

Coumarins (2H-1-benzopyran-2-ones), which have a benzene structure fused to a pyran structure, are present in various plants and It is a significant heterocyclic group with biological and medicinal activities including anticancer, antithrombotic, antifungal, antibacterial, anticoagulant, antioxidant, cytotoxicity, and enzyme inhibitor. Many methods, including Wittig, Reformatsky, Pechmann, Knoevenagel, and Perkin processes, have been used in the past to synthesis coumarins (Scheme 3). In the Pechmann reaction have been used several catalysts, for example, mineral acids like $ClSO_3H$, CF_3COOH, H_3PO_4, H_2SO_4, $HClO_4$, HCl, oxalic acid, p-toluenesulfonic (PTSA), and Lewis acids such as $BiCl_3$, $FeCl_3$, $Cu(ClO_4)_2$, $ZnCl_2$, mesoporous zirconium phosphate, $TiCl_4$, $BaCl_2$, $AlCl_3$, $ZrCl_4$, $SnCl_4$, $SnCl_2.H_2O$, $Sm(NO_3)_3$, $BF_3.H_2O$, $InCl_3$ (Verdoliva, Saviano & De Luca, 2019; Rao & et al., 2012; Karami & Kiani, 2011; Nagana , Nayak & Peddinti, 2014). In the Knoevenagel method, pyridine, piperidine, weak acids or additional organic bases are used as catalysts (Tariq, Ali & Khalid, 2012; Loncaric, Susjenka & Molnar, 2020). However, there are some downsides to the disclosed methods, including challenges in extracting the catalyst from the reaction mixture, the use of a toxic catalyst, challenging reaction conditions, a nonreusable catalyst, and extended reaction times (Adimule & et al., 2021). Magnetic nanoparticles have been synthesized recently and employed in a variety of sectors such as drug delivery and biotechnology, consisting of pure metals (Fe, Co, and Ni), metal oxides (Fe_3O_4 and γ-Fe_2O_3), ferrites (MFe_2O_4, M = Cu, Ni, Mn, Mg, etc.), and metal alloys (FePt,CoPt) (Laurent & et al., 2008; Lu, Salbas & Schuth, 2007; Lyer & et al., 2015; Hepel, 2020; Bruschi & de Toledo, 2019; Bilal & et al., 2019).

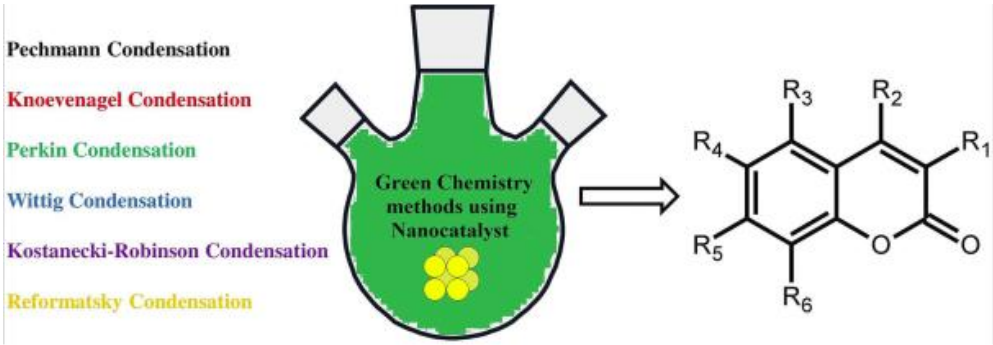

Scheme 3. Coumarin Synthesis Methods

So far, in the synthesis of coumarin, biscoumarin and coumarin or biscoumarin-attached compounds, $MgFe_2O_4$, Fe_3O_4, $Fe_3O_4@SiO_2@PrSO_3H$, $Fe_3O_4@SiO_2@Et\text{-}PhSO_3H$, $Fe_3O_4@SiO_2$-imidazole, Fe_3O_4-DABCO, $Fe_3O_4@Boehmite\text{-}NH_2\text{-}Co^{II}$(HAp-AgNPs, $Fe_3O_4@SiO_2@(CH_2)_3$semicarbazide-SO_3H/HCl, $[Fe_3O_4@SiO_2@(CH_2)_3\text{-}Im\text{-}SO_3H]Cl$, Fe_3O_4@ABM-TUD, HAP/Fe_3O_4, $CuFe_2O_4@SiO_2$@AAPTMS@Ni(II), $CuFe_2O_4@SiO_2$ @AAPTMS@Cu(II), Fe_3O_4@sulfosalicylic acid and etc. magnetic nanocatalysts were used (Zeinali & et al., 2023).

The current work involves the synthesis of pyrano[3,2-c]chromens, pyrano[2,3-c] pyrazoles, and benzyl pyrazolyl coumarins using a magnetic polymer-based nanocatalyst (SMPSMA@Fe_3O_4) (Figure 1). The results showed yields of 85-94%, 85-94%, and 92-96%, respectively. The simplicity of the magnetic separation, the ease of product isolation, and the catalyst's reusability with minimal activity loss are the main advantages of the current approach. Simple reaction conditions are also present (Ghorbanipour & et al., 2023).

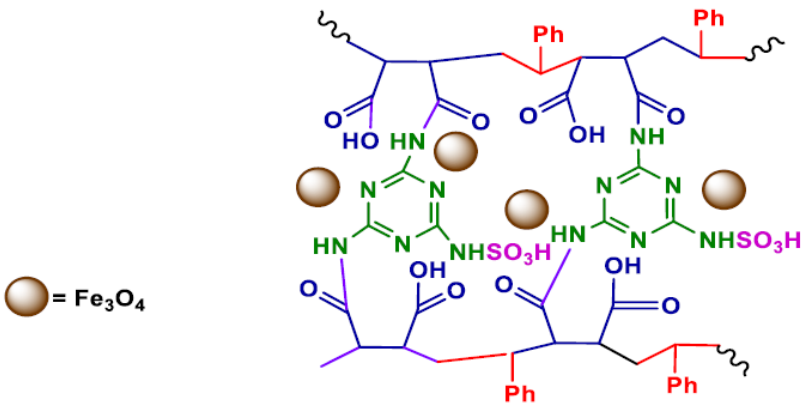

Figure 1. SMPSMA@Fe_3O_4 nanocatalyst

The other work produced a brand-new, reusable catalyst called SPION@CS-IL by adding superparamagnetic iron oxide nanoparticles to the chitosan-functionalized ionic liquid (Figure 2). Pyrido[2,3-d] pyrimidine-dione derivatives were synthesized from 4-hydroxy coumarin using it. Use of water as solvent, rapid reaction rates, little catalyst loading, five times recyclability of the nanocatalyst and good yields are the most outstanding advantages of the method (Sayahi & et al., 2023).

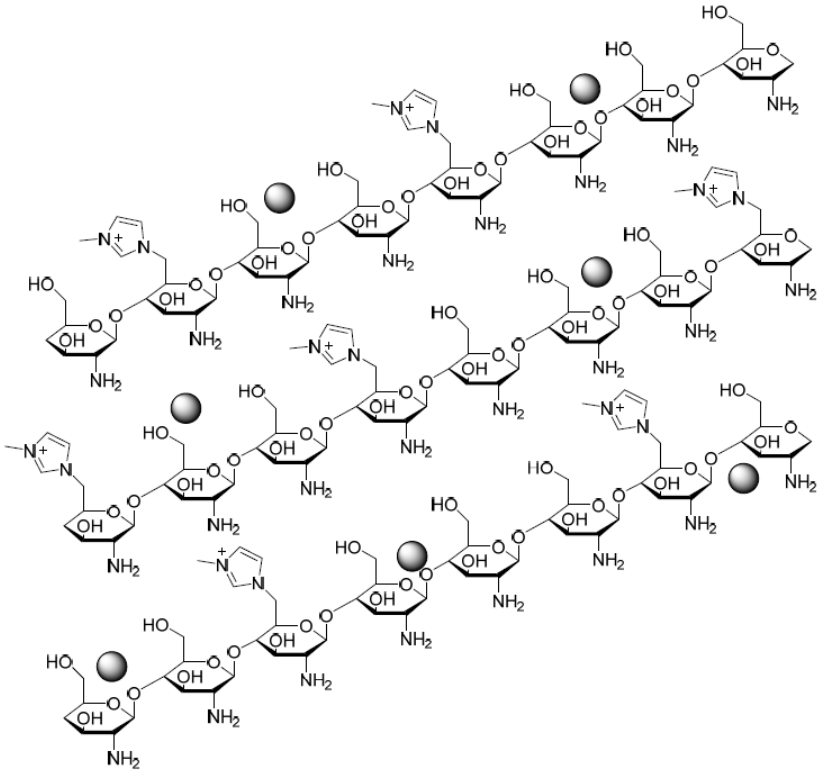

Figure 2. SPION@CS-IL nanocatalyst

In another study, the Fe_3O_4@C@PrS-SO_3H magnetic nanocatalyst was synthesized, its structure was elucidated and it was successfully used in the synthesis of mono- and disubstitue simple coumarin derivatives and yields of 83-98% were obtained. (Figure 3) (Bonab, Soleimani-Amiri & Mirza, 2023).

Figure 3. Fe_3O_4@C@PrS-SO_3H magnetic nanocatalyst

In this study, copper ions were coordinated to L-cysteine functionalized magnetic nanoparticles to create an eco-friendly nanocatalyst (Fe_3O_4-Cys-Cu). The obtained new magnetic nanocatalyst has been successfully used in the synthesis of coumarin-linked triazoles with yield of 92-96% (Figure 4) (Kumari & et al., 2022).

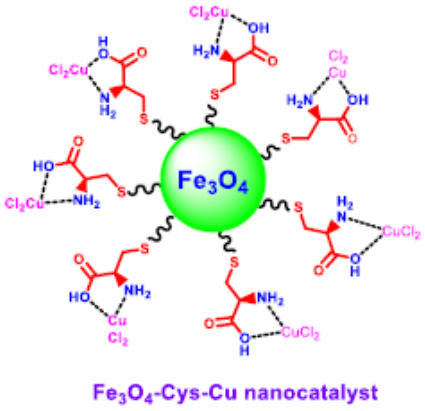

Figure 3. Fe_3O_4-Cys-Cu magnetic nanocatalyst

In a different work, it was shown that the recently developed magnetic nanocatalyst ($HFe(SO_4)_2.4H_2O$-Chitosan) served as a powerful catalyst for the environmentally responsible synthesis of coumarin derivatives at both 100 °C and 70 °C utilizing ultrasonically aided Pechmann condensation. High product yields (96-97%), short response times (10-15 min), and mild reaction conditions were obtained by both processes (Figure 4)(Zarei, Soleimani-Amiri & Azizi, 2022).

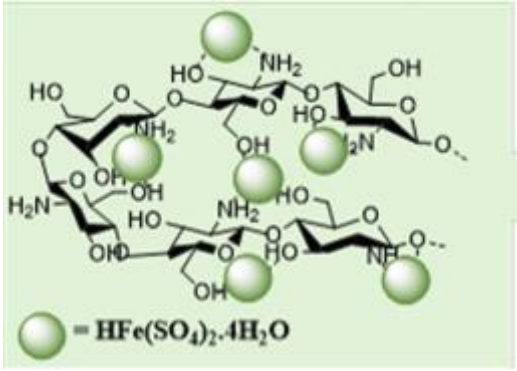

Figure 4. $HFe(SO_4)_2.4H_2O$-Chitosan magnetic nanocatalyst

In this study, a heterogeneous catalyst made of reduced graphene oxide that has been functionalized with piperazine and embellished with Fe_3O_4 nanoparticles (Fe_3O_4@rGO-NH) is synthesized and characterized. The catalyst was then employed as an effective and simple to separate heterogeneous catalyst for the solvent-free Pechmann reaction synthesis of certain coumarins (Figure 5) (Rezaei-Seresht, Gazkoh & Maleki, 2023).

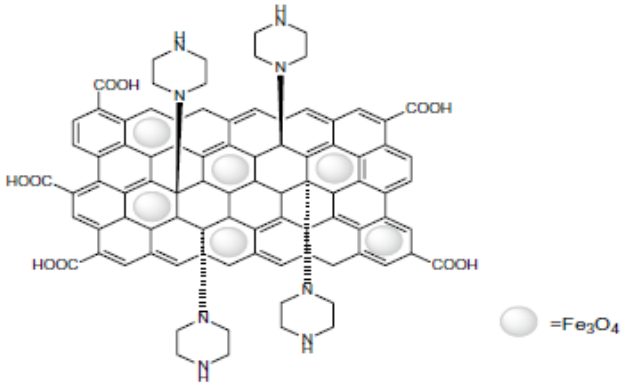

Figure 5. Fe_3O_4@rGO-NH magnetic nanocatalyst

In the present study, a novel one-pot multi-component sequentially cross-linked L-glutamic acid based on multi-walled carbon nanotubes that have been functionalized by magnetic carboxylic acid (Fe_3O_4/f-MWCNT-CS-Glu) nanocomposite was developed, and nickel II nanoparticles were then trapped within this matrix to produce Fe_3O_4/f-MWCNT-CS-Glu/Ni^{II}. Biscoumarins were synthesized using this nanoparticle with good to excellent yields, acceptable cycle rates (TONs), cycle frequencies (TOFs), usage of a solvent-free reaction media or water as a solvent, satisfactory reaction rates, appropriate recoverability and satisfactory reusability obtained (Figure 6) (Galehban, Zeynizadeh & Mousav, 2022a).

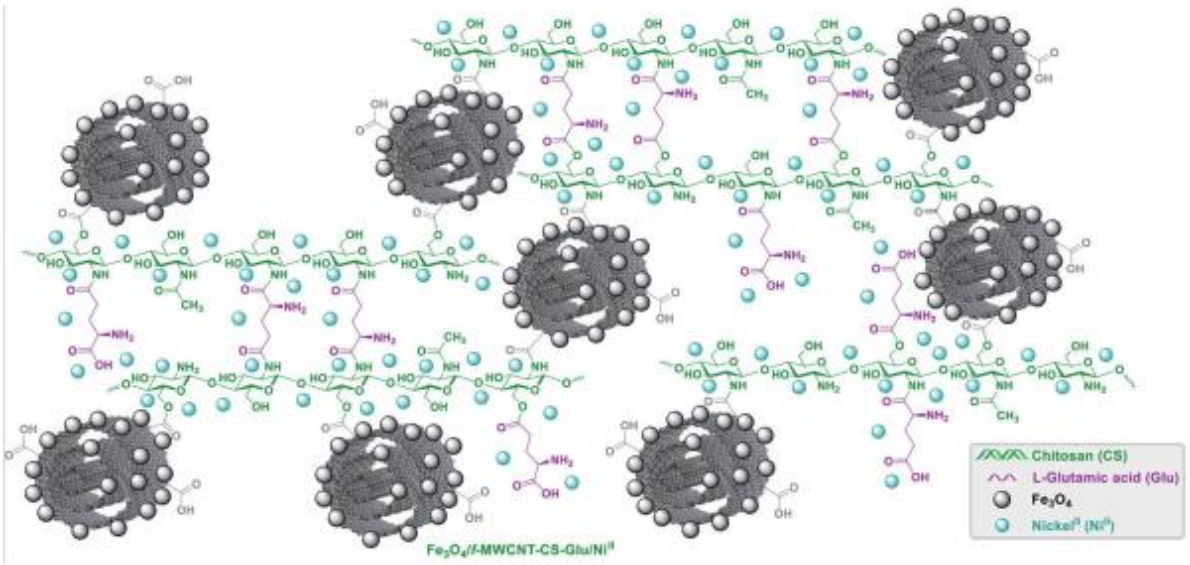

Figure 6. Fe_3O_4/f-MWCNT-CS-Glu magnetic nanocatalyst

In this research, Fe_3O_4@SiO_2@KCC-1@MPTMS@Cu^{II} magnetic nanocatalyst was prepared and some coumarin derivatives were obtained successfully. The best result with 97% efficiency in 20 minutes shows the success of the catalyst. (Figure 7) (Galehban, Zeynizadeh & Mousav, 2022b).

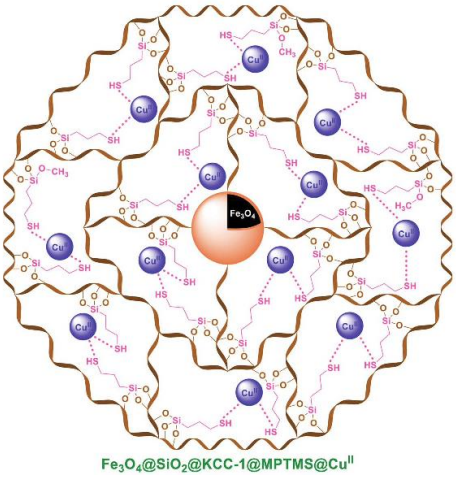

Figure 7. Fe_3O_4@SiO_2@KCC-1@MPTMS@Cu^{II} magnetic nanocatalyst

In another study by Jokar et al, platinum nanocatalyst was synthesized and successfully used in the synthesis of biscoumarin derivatives (Figure 8). The best results in the reactions performed in the presence of this catalyst were achieved with 98% yield in the presence of Ethanol in 5 minutes. (Jokar, Naeimi & Bidhendi, 2022).

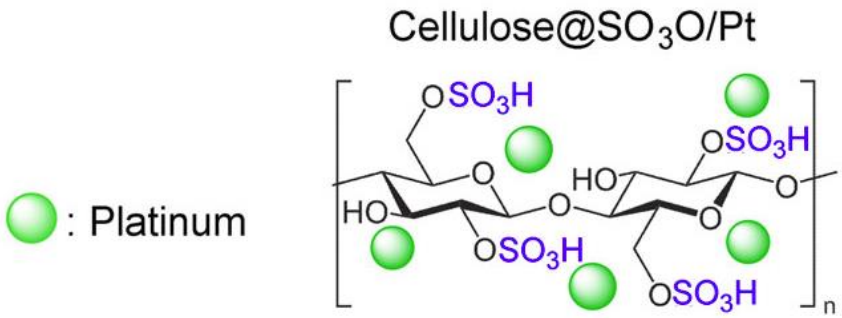

Figure 8. Cellulose sulfate chitosan@Pt nanocatalyst

In a different work, $NiFe_2O_4$ magnetic nanoparticles with MCM-41 coatings were created, and their surfaces were then modified with PWA and sulfate. In the presence of this nanocatalyst, the synthesis of 7-hydroxy-4-methyl coumarin was carried out with a yield of 78.32%. Also, the produced magnetic nanoparticles were discovered to be readily recoverable and reused numerous times (El-Yazeed, Hayes & Ahmed, 2022).

The number of nanocatalysts with numerous benefits continues to increase day by day.

KAYNAKÇA

Adimule, V. Yallur, B.C. Bhowmik, D. & Gowda, A.H.J. (2021) Morphology, structural and photoluminescence properties of shaping triple semiconductor YxCoO:ZrO2 nanostructures. *J Mater Sci Mater Electron*. *32*, 12164–12181. https://doi.org/10.1007/s10854-021-05845-2.

Allaedini, G. Tasirin, S. M. & Aminayi, P. (2015) Magnetic properties of cobalt ferrite synthesized by hydrothermal method. *Int Nano Lett . 5*, 183–186.

Bilal, M. Mehmood, S. Rasheed, T. & Iqbal, H.M.N. (2019) Bio-catalysis and biomedical perspectives of magnetic nanoparticles as versatile carriers. *Magnetochemistry*. *5*, 42-61. https://doi.org/10.3390/magnetochemistry5030042.

Bonab, M.F. Soleimani-Amiri, S. & Mirza, B. (2023) Fe_3O_4@C@PrS-SO_3H: A Novel Efficient

Magnetically Recoverable Heterogeneous Catalyst in the Ultrasound-Assisted Synthesis of Coumarin Derivatives, *Polycyclic Aromatic Compounds*. *43* (2), 1628-1643. https://doi.org/10.1080/10406638.2022.2032768.

Bruschi, M.L. & de Toledo, L.D.A.S. (2019) Pharmaceutical Applications of Iron-Oxide Magnetic Nanoparticles. *Magnetochem*. *5*, 50-68. https://doi.org/10.3390/magnetochemistry5030050.

El-Yazeed, W.S.A. Hayes, O.R. & Ahmed, A.I. (2022) Novel green sulfated phosphotungstic acid supported on MCM-41-coated $NiFe_2O_4$ MNPs for xanthene and coumarin synthesis. *Journal of Sol-Gel Science and Technology*. 1-17. https://doi.org/10.1007/s10971-022-05966-y.

Galehban, M.H. Zeynizadeh, B. & Mousav, H. (2022a) Ni^{II} NPs entrapped within a matrix of L-glutamic acid cross-linked chitosan supported on magnetic carboxylic acid-functionalized multi-walled carbon nanotube: a new and efficient multi-task catalytic system for the green one-pot synthesis of diverse heterocyclic frameworks. *RSC Adv*. *12*, 16454-16478. https://doi.org/10.1039/d1ra08454b.

Galehban, M.H. Zeynizadeh, B. & Mousav, H. (2022b) Diverse and efficient catalytic applications of new cockscomb flower-like Fe_3O_4@SiO_2@KCC1@MPTMS@Cu^{II} mesoporous nanocomposite in the environmentally benign reduction and reductive acetylation of nitroarenes and one-pot synthesis of some coumarin compounds. RSC Adv. 12: 11164-11189. https://doi.org/10.1039/d1ra08763k.

Gawande, M.B. Branco, P.S. & Varma, R.S. (2013) Nano-magnetite(Fe_3O_4) as a support for recyclable catalysts in the development of sustainable methodologies. *Chem Soc Rev*. *42*, 3371–3393.

Gawande, M.B. Luque, R. & Zboril, R. (2014) The rise of magnetically recyclable nanocatalysts. *ChemCatChem. 6*, 3312–3313. https://doi.org/10.1002/cctc.201402663.

Gebre, S.H. (2023) Recent developments of supported and magnetic nanocatalysts for organic transformations: an up-to-date review. *Applied Nanoscience. 13*, 15–63. https://doi.org/10.1007/s13204-021-01888-3.

Ghorbanipour, F. Nezhad, S.M. Pourmousavi, S.A. Zare, E.N. & Heidari, G. (2023) Superparamagnetic polymer nanocomposite as a catalyst for the synthesis of pyrano[3,2-c]chromene, pyrano[2,3-c]pyrazole, and benzylpyrazolyl coumarin. *Inorganic Chemistry Communications. 147*, 110271-110286. https://doi.org/10.1016/j.inoche.2022.110271.

Hashemi-Moghaddam, H. Kazemi-Bagsangani, S. Jamili, M. & Zavareh, S. (2016) Evaluation of magnetic nanoparticles coated by 5-fluorouracil imprinted polymer for controlled drug delivery in mouse breast cancer model. *Int J Pharm*. *497*, 228–238. https://doi.org/10.1016/j.ijpharm.2015.11.040.

Hepel, M. (2020) Magnetic Nanoparticles for Nanomedicine. *Magnetochem. 6*, 3-19. https://doi.org/10.3390/magnetochemistry6010003.

Jiang, H. Jiang, D. Shao, J. & Sun, X. (2016) Magnetic molecularly imprinted polymer nanoparticles based electrochemical sensor for the measurement of Gram-negative bacterial quorum signaling molecules (N-acyl-homoserine-lactones). *Biosens Bioelectron*.*75*, 411–419. https://doi.org/10.1016/j.bios.2015.07.045.

Jokar, M. Naeimi, H. & Bidhendi, G.N. (2022) Design and Preparation of Platinum Anchored on Cellulose as Heterogeneous Nanocatalyst for Synthesis of Bis-Coumarin Derivatives. *Polycyclic Aromatic Compounds*. *42 (*8), 4994-5005. https://doi.org/10.1080/10406638.2021.1922468.

Karami, B. & Kiani M. K (2011) $ZrOCl_2.8H_2O/SiO_2$: An efficient and recyclable catalyst for the preparation of coumarin derivatives by Pechmann condensation reaction. *Catalysis Communications*. *14*(1), 62–67. https://doi.org/10.1016/j.catcom.2011.07.002.

Khan, I. Saeed, K. & Khan, I. (2019) Nanoparticles: Properties, applications and toxicities. *Arabian J. Chem. 12*, 908–931. https://doi.org/10.1016/j.arabjc.2017.05.011.

Kumar, S. Saroha, B. Kumar, G. Lathwal, E. Kumar, S. Parshad, B. Kumari, M. Kumar, N. Mphahlele-Makgwane, M.M. & Makgwane, P.R. (2022a) Recent Developments in Nanocatalyzed Green Synthetic Protocols of Biologically Potent Diverse O-Heterocycles—A Review. *Catalysts 12*, 657-700. https://doi.org/10.3390/catal12060657.

Kumar, P. Tomar, V. Kumar, D. Kumar Joshi, R. & Nemiwal, M. (2022b) Magnetically active iron oxide nanoparticles for catalysis of organic transformations: A review. *Tetrahedron*. 106–107: 132641-132670.

Kumari, M. Yadav, P. Jain, Y. Laddha, H. & Gupta, R. (2022) Preparation of Fe_3O_4-Cys-Cu magnetic nanocatalyst for expedient synthesis of tripodal C3 symmetric chromofluorogenic receptor for sensing of fluoride ion selectively: An experimental and computational slant. *Materials Chemistry and Physics*. *288*, 126360-126371. https://doi.org/10.1016/j.matchemphys.2022.126360.

Laurent, S. Forge, D. Roch, A. Robic, C. & Vander Elst, L. (2008) Magnetic iron oxide nanoparticles: synthesis, stabilization, vectorization, physicochemical characterizations, and biological applications. Chem Rev. 108, 2064–2110. https://doi.org/10.1021/cr068445e.

Loncaric, M. Susjenka, M. & Molnar, M. (2020) An Extensive Study of Coumarin Synthesis via Knoevenagel Condensation in Choline Chloride Based Deep Eutectic Solvents. *Curr Org Synth. 17*(2), 98–108. https://doi.org/10.2174/1570179417666200116155704.

Lu, A.H. Salbas, E.L. & Schuth, F. (2007) Magnetic Nanoparticles: Synthesis, Protection,Functionalization, and Application. *Angew Chem*.: *46*, 1222–1244. https://doi.org/10.1002/anie.200602866.

Lyer, S. Singh, R. Tietze, R. & Alexio, C. (2015) Magnetic nanoparticles for magnetic drug targeting. *Biomed Eng. 60* (5), 465–475. https://doi.org/10.1515/bmt-2015-0049.

Naganaboina, R.T. Nayak, A. & Peddinti, R.K. (2014) Trifluoroacetic acid-promoted Michael addition–cyclization reactions of vinylogous carbamates. *Org Biomol Chem*. *12*, 3366–3370. https://doi.org/10.1039/C4OB00437J.

Nahar, L. & Sarker, S.D. (2017) Importance of nanotechnology in drug delivery. *J. Pharm. Res. 1*, 000130.

Rao, P. Konda, S. Iqbal, J. & Oruganti, S. (2012) InCl3 catalyzed three-component synthesis of a-benzylamino coumarins and diketones*Tetrahedron Lett*. *53*, 5314–5317. https://doi.org/10.1016/j.tetlet.2012.07.098.

Rezaei-Seresht, E. Gazkoh, F.T. & Maleki, B. (2023) Solvent-free Pechmann synthesis of coumarins catalyzed by magnetic heterogeneous catalyst Fe_3O_4@rGO-NH. *Carbon Letters*. *33*, 115–124. https://doi.org/10.1007/s42823-022-00408-9.

Rostamnia, S. & Doustkhah, E. (2015) Synthesis of water-dispersed magnetic nanoparticles (H_2O-DMNPs) of β-cyclodextrin modified Fe_3O_4 and its catalytic application in

Kabachnik-Fields multicomponent reaction. *J Magn Magn Mater. 386*, 111–116. https://doi.org/10.1016/j.jmmm.2015.03.064.

Rostamnia, S. Zeynizadeh, B. Doustkhah, E. Baghban, A. & Aghbash, K.O. (2015) The use of κ-carrageenan/Fe_3O_4 nanocomposite as a nanomagnetic catalyst for clean synthesis of rhodanines. *Catal Commun. 68*, 77–83. https://doi.org/10.1016/j.catcom.2015.05.002.

Sayahi, M.H. Sepahdar, A. Bazrafkan, F. Dehghani, F. Mahdavi, M. & Bahadorikhalili, S. (2023) Ionic Liquid Modified SPION@Chitosan as a Novel and Reusable Superparamagnetic Catalyst for Green One-Pot Synthesis of Pyrido[2,3-d]pyrimidine-dione Derivatives in Water. *Catalysts*. *3*, 290-304. https://doi.org/10.3390/catal13020290.

Tariq, M. Ali, S. & Khalid, N. (2012) Activity of homogeneous and heterogeneous catalysts, spectroscopic and chromatographic characterization of biodiesel: A review. *Renew Sustain Energy Rev. 16*, 6303–6316. https://doi.org/10.1016/j.rser.2012.07.005.

Verdoliva, V. Saviano, M. & De Luca, S. (2019) Zeolites as Acid/Basic Solid Catalysts: Recent Synthetic Developments. *Catalysts. 9* (3), 248-268. https://doi.org/10.3390/catal9030248.

Zarei, F. Soleimani-Amiri, S. & Azizi, Z. (2022) Heterogeneously Catalyzed Pechmann Condensation Employing the $HFe(SO_4)_2.4H_2O$-Chitosan Nano-Composite: Ultrasound-Accelerated Green Synthesis of Coumarins. *Polycyclic Aromatic Compounds*. *42* (9), 6072-6089. https://doi.org/10.1080/10406638.2021.1973520.

Zeinali, S. Fekri, L.Z. Nikpassand, M. & Varma, R.J. (2023) Greener Syntheses of Coumarin Derivatives Using Magnetic Nanocatalysts: Recent Advances. *Topics in Current Chemistry*. *38 (*1), 1-71. https://doi.org/10.1007/s41061-022-00407-4.

Multi-Directonal Natural Gas Compressor Station Application And Planning Of Distribution Line

Merdin DANIŞMAZ[1]
Ersin GÖK[2]

Introduction

In the evolving world, where the energy demand in the world is increasing rapidly, countries are making investments to reach clean, cheap, and alternative energy sources. Due to the diversification of supply sources due to energy policies, variability of energy prices, long-term agreements, export capacities of countries, geographical distances, natural gas drilling works, etc., appropriate piping installation at compressor stations that can operate at alternative directions, pressures and capacities that will provide gas imports from different countries in certain quantities and for certain periods. development was required. In this study, considering the geographical location of the compressor stations needed in the natural gas transmission system during the project design phase, a versatile collector design has been made that will allow it to operate at alternative pressures and flow rates. Thus, the compressor station located at the intersection of the transmission lines on four different routes will be able to serve. This station also provides the possibility of routing the transmission lines separated in different directions at variable flow rates.

One of the main purposes is to direct the flow in compressor stations established for the distribution, transmission, and storage of natural gas. In this chapter, first section is a review of the most relevant research studies carried out to solve the problems of natural gas transportation through pipe main distribution line systems and present the collector application that allows the development of the versatile compressor station. In the second part, there will be a multi - directional collector design. The literature review reveals the pipeline system group in three main sections: base stations and collector systems. Global trends in natural gas may differ slightly among reports provided by specific international agencies. However, the conclusion of the research is that natural gas consumption, production, reserves, and dependencies will continue to increase steadily for the foreseeable future. This increase in expectations results in the need for more advanced optimization methods that can manage larger and more complex projects both in the national and international arena. The efficient and effective transportation of natural gas from production areas to consumption areas requires a comprehensive and detailed transportation system. Such a system consists of a complex network of pipelines, compressor stations, regulators, valves, and city distribution lines, among other components. The natural gas produced from a particular well often must travel long distances to reach the point of use. This could mean larger and more demanding pipeline systems. If there is no immediate use of the transported natural gas, it can be put into storage facilities to be used when needed. It can be complicated for countries that buy natural gas from neighboring countries in different directions or enter the country from different remote points to establish an internal distribution and station line. In this study, we aim to initiate a new discussion and application ideas through a new collector application for the optimization of natural gas transmission and distribution lines.

[1] Assist. Prof., Kırşehir Ahi Evran Universityr
[2] Mechanical Eng., BOTAŞ

Natural gas has continuously increased its importance in the last century and has taken its place among the main energy sources for the future. Its various benefits include low greenhouse gas emissions and relatively low capital costs. As a result, it has become the reason why it is preferred among other energy sources in many sectors, especially for new power generation facilities. Global indicators of natural gas reserve levels reveal the role natural gas will play in supporting growth in markets through to 2041 (Borraz-Sánchez, 2015). According to these indicators, it also explains the increasing role of natural gas in its importance.

Worldwide natural gas demand is increasing by 1.7% each year and this demand is expected to increase by approximately 50% in the next two decades. The share of industry and energy sectors in the increase in natural gas demand is the main share. In the transportation sector, this increase shows a small volume, but rapid growth compared to other sectors. It has been observed that the transition from coal to natural gas as an energy source in China, the industrial investments in the Middle East and Africa, which have especially large gas resources, and the development of the country's economies have been effective in the increase in the demand for natural gas. With the increase in the production of China and Russia, 50% of the global gas production sector is carried out by the United States (USA), Qatar and Iran. However, it has been observed that the growth rate of natural gas demand depends on the rate of establishment of infrastructures (BP Energy , 2019). Natural gas and electricity demand in Turkey is expected to increase by 8% every year. Natural gas imports constitute more than 70% of Turkey's total annual imports. While creating Turkey's energy policies, it was aimed not to be dependent on any country for more than 40% in energy imports and to diversify the supply sources (Erdogdu, 2010). It is observed that Turkey's quest to reach economic, sustainable, and quality supply sources continues. In addition, Turkey's geopolitical position, being close to supply sources and being in the energy corridor offers the opportunity to cooperate with the European Union (EU) (Öztürk M, 2011). The potential increase in natural gas supply indicates that decisions must be made at strategic, geopolitical, and operational levels in the process of building and expanding new natural gas networks.

Natural gas is delivered to consumers by going through the stages of exploration, extraction, production, transmission, storage, and distribution. The high-pressure gas taken from the supply sources during the transmission stage is transported to long distances, pipelines and compressor stations and distribution centers via the large-diameter pipeline system. Many countries are developing natural gas transmission lines and installing compressor stations to meet the increasing demand for natural gas in an efficient and cost-effective manner. The high investment costs of compressor stations, which are one of the important parts of the transmission system, show that future-oriented design and planning should be done about compressor stations (Üster & Dilaveroğlu, 2014). Optimization studies have been carried out on transmission systems that will minimize these high costs and provide the required natural gas flow. One of the first optimization studies of the natural gas pipeline system, which includes compressors designed for serial operation, was made by Larson and (Wong PJ, 1968). In the study, optimum suction, and discharge pressures of a fixed number of compressor stations were calculated using the dynamic programming solution technique (Wong PJ, 1968). Edgar, in his study in 1978, developed an algorithm that can simultaneously determine the locations, numbers, capacities of the required compressor stations, the diameters and lengths of the pipes between the compressor stations, and a compressor station operating conditions that will maximize profit and minimize cost (Edgar, 1978). In his study, El-Shiekh made the optimization of steel transmission pipelines with different diameters and compression ratio of 1–1.5, carrying 150-550 million standard cubic feet of natural gas per day, using lingo software (El-Shiekh, 2013). Okoro used the Weymouth equation in pipeline capacity calculations (Okoro, 2018). He argued that in the literature research, the specific gravity and compressibility factor of the gas are accepted as constant, and this gives false results. However, 10% of the gas flow capacity is due to these neglected values, so the non-negligible effect of the specific gravity

and compressibility factor has been revealed. Gas from different sources feeding the transmission lines is likely to have different specific gravity. Some scientists experimentally investigated the maximum flow and pressure changes by taking the specific gravity of the gas at the junction of the pipelines and the average of the specific gravity of the incoming gases (Borraz-Sánchez, 2015), as well as accepting it as a constant temperature and constant system. On the other hand, Egbe conducted a study on the optimization of a natural gas pipeline network design based on minimization of installation costs (Jerome G.Egbe, 2016).In this study, using the advanced cost estimation computer program, he compared the installation costs of different natural gas pipeline networks with the construction capital and concluded that the critical parameter is the diameter of the pipes. By establishing a relationship between the diameter of the pipes and the number of compressor stations, he proved that the installation costs of the network decreased.

The world's focus is on reducing the greenhouse gases in the atmosphere and limiting the increase in global warming. Technological research and development continue in every field in order to reduce emissions, limit and control them. Tavakkoli investigated the heat losses of natural gas compressor stations in the USA in a study (Sakineh Tavakkoli, 2016). He determined that about two-thirds of the fuel energy used in the compressor station is lost as waste heat with hot flue gases. Parameters such as thermodynamic analysis, load factor, and U.S. The Energy Information Administration (EIA) has obtained the amount of waste heat and the regional distribution of CO_2 with the data received. He calculated that 47000 tons of CO_2 emissions per day can be reduced with the recovery of waste heat ((Michael Hendryxa, 2020). The increase in energy demand has led to an increase in the need for natural gas and an increase in natural gas infrastructure and facilities. In his study, Hendryxa investigated the effects of emissions from compressor stations on humanity. In the study, it was found that volatile compounds including 1,3-butadiene from volatile organic compounds emerged in emissions (VOC) from compressor stations, acetaldehyde, benzene, ethylbenzene, formaldehyde, propylene dichloride, styrene and vinyl chloride were carcinogenic to humans and cardiovascular, respiratory, neurological It has been shown to impair reproductive, chromosomal, or immune system functionality. Therefore, the death rate is increasing (Michael Hendryxa, 2020).

In the literature, it is observed that new methods are being investigated to recover the waste heat in compressor stations. (L. Branchini, 2019) conducted a feasibility study of an Organic Rankine Cycle application for the recovery of waste heat generated in compressor stations. For this, he added Rankine cycles to turbines in a natural gas compressor station and created a detailed technical, economic, and environmental analysis of the new system over a 7-year period. As another way to combat environmental pollution, it has been proposed to increase the operating efficiency of gas turbines in natural gas compressor stations. In other words, it is aimed to reduce fuel consumption and thus emissions, reduce maintenance costs and increase the capacity of the station by optimizing the natural gas turbines in the compressor stations (Kurz, 2019). Trigeneration is also a method of utilizing the energy contained in the exhaust gases resulting from the combustion of natural gas. He conducted the feasibility study of a trigeneration system that can reduce the energy requirement of a compressor station by approximately 30% and thus also reduce CO_2 emissions ((Paolo Silva, 2017).

It is observed that the global natural gas demand has increased in parallel in Turkey. Uninterrupted supply, increasing pipelines, ongoing drilling works, international agreements show that investments in natural gas transmission systems will continue rapidly. Within the scope of this thesis, the collector application, which can meet the versatile supply-demand needs for the compressor stations needed in the natural gas transmission system and allow it to operate in a versatile, alternative pressure and flow rate, considering its geographical location, has been evaluated.

Natural Gas Processing and Pipeline

Natural gas was discovered in the USA by the indigenous people in the first half of the 17th century. It started with its use in street lighting and the first well was drilled in New York in 1821 for natural gas production. Thanks to the technological developments in the 1960s, the use of natural gas began to become widespread. Between the 1930s and 1960s, its use in lighting systems and engines, as well as the developments in the industrial revolution, made natural gas a strategic and economic energy source. With the environmental effects and technological developments, the use of natural gas has become more used than oil over time. The fact that natural gas is an important alternative energy source was fully accepted with the oil crisis that started in the 1970s. Since these years, the adventure of national and international reserves, processing, transmission, transportation, and storage of natural gas has begun. Increase in the use of natural gas; It has gained momentum due to the development of compressor, pipelines and welding technologies that provide transmission from production wells to the end consumer (Pala, 2003).

Natural gas, oil and coal are formed from fossil fuels because of the chemical interaction of animal and plant wastes, which are organic substances between the layers of the earth, within millions of years, with the effect of temperature and pressure in an oxygen-free environment. Natural gas is a colorless, odorless, and lighter-than-air hydrocarbon consisting of flammable gases. It contains flammable gases such as methane, ethane, propane, butane, pentane, nitrogen, and carbon dioxide as a mixture.

As seen in Table 1, natural gas liquefies at -162 ºC and turns into a solid at -182.5 ºC. The density of natural gas under 15 ºC temperature and 1 atm pressure is 0.71 kg/Sm3. In order for natural gas to burn, it must mix between 5-15% with air. If the mixing ratio is above or below this range, natural gas will not burn. The best combustion mixture is 9% natural gas and 91% air. The self-ignition temperature (ignition temperature) of natural gas in air varies between 580 and 650 ºC, depending on the mixture. Natural gas burns with a blue flame now of complete combustion and the theoretical combustion temperature is 1960ºC. The maximum combustion speed of natural gas in air is 0.43 m/s (Türkel, 2015).

Table 5. Chemical Properties of Natural Gas (Türkel, 2015)

Chemical Properties of Natural Gas		
Boiling point @1 atm	-162	ºC
Critical Point (Temperature-Pressure)	-83	ºC
	45,39	atm
Density (Gaz@1 atm, 15ºC)	0,71	kg./Sm^3
Density (Liquid)	0,46	kg./lt.
Auto-ignition temperature	580	ºC
Lower heating value	8250	kcal/Sm^3
Higher heating value	9155	kcal/Sm^3

The natural gas transmission system is a set of systems where gas or liquids are transported over long distances through pipelines, extending to the final distribution points. The natural gas transmission system consists of pipes of different diameters, compressor stations, storage facilities and facilities up to distribution stations. The pipes are generally located buried underground and consist of steel pipes with a polypropylene coating on the outer surface to protect against corrosion and electrically insulated with cathodic protection. Transmission

pipelines generally consist of pipes made of high carbon steel alloys along the projected route. Pipes are produced and tested in accordance with the American Petroleum Institute (API) standards. In general, pipes in the X60 standard are used in the API-5L system. API 5L specification provides pipe standards suitable for use in the transportation of gas, water and oil in the natural gas and oil industries. API 5L covers seamless and welded steel pipes. KSI (Kip Square Inch) equals 6.894 N/mm^2 and KIP is used in API standards tables (PM International Suppliers, 2023). Although it is an advantage to transmit the gas without chemical and physical changes in pipeline transportation, the initial investment amount that varies according to the length and diameter of the pipeline is seen as a disadvantage.

The whole of the systems that distribute the natural gas transported at high pressure in the main transmission pipeline to the final consumption points by taking the natural gas through the distribution network with pipes of different diameters and making pressure adjustments is called natural gas distribution. The natural gas distribution process is shown in Figure 1. During distribution, industrial facilities, factories, power generation plants and other consumers receive the gas they need from distribution companies. It is the responsibility of the distribution companies to ensure the pressure, temperature and flow rate in the contracted amounts determined in the contracts signed with industrial facilities and electricity generation plants, to invoice them, to ensure the safety, maintenance, and regular functioning of the network. There are three main pipelines along the transport route. These are the collection system, the intercity pipeline transmission system, and the distribution system. Unlike transmission systems, which consist of long and large diameter pipelines operating at high pressure levels, collection and distribution systems consist of low pressure and small diameter pipelines. If the natural gas from the well in which it is discovered has a high sulfur and carbon dioxide content (sour gas), a special acid gas collection pipeline must be installed to transport the raw gas from the wellhead to the processing plant (DL Katz: D. Cornell, 1959) (Speight, 2006).

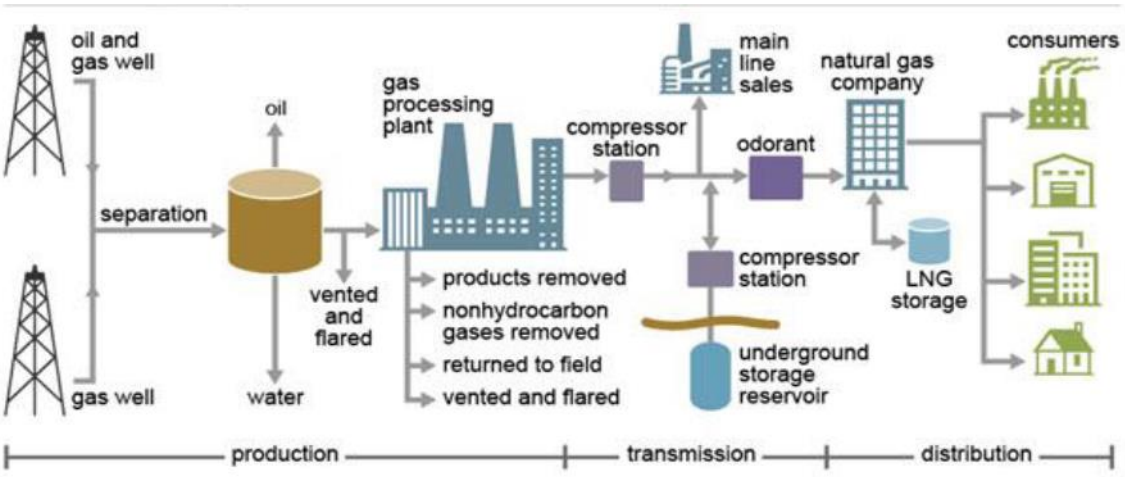

Figure 16. Natural Gas Production, Transmission and Distribution Scheme (EIA, 2022)

Natural gas transportation is a very important activity carried out by the gas industry, where gas must be transported from one place to another. Several types of transport vehicles can be applied to transport gas, but it is well known that pipelines represent the most economical way to transport large volumes of natural gas. In addition, metallurgical advances, and the emergence of welding techniques, coupled with the exponential growth of pipeline networks in recent years all over the world, have made gas transportation through pipelines more economically attractive. Gas transportation sectoral applications are constantly changing and are being improved according to new technologies. As a result, application models and needs are changing. This situation has created a gas marketing competition that varies from country to country. It should be noted that the size of a gas distribution network system can

vary greatly from one country to another. Therefore, when financial, political, or environmental problems arise, gas transport operators look for different alternatives to fulfill this task. Current technology for steady-state gas transmission network problems can be exploited to efficiently address large gas systems, for example, by applying grid reduction and decoupling techniques or hybrid heuristics (Menon E. , 2005).

There are three main types of pipelines, mainly collection systems, transmission systems, and distribution systems, ranging from 4 inches to 48 inches (10-1220 mm) in diameter along shipping lines, and these lines are often buried underground. Collection pipeline systems collect raw natural gas from production wells. Transmission pipeline systems travel thousands of kilometers worldwide to bring natural gas from pretreatment plants or storage facilities to distribution systems. Distribution pipeline systems are located in residential areas or organized industrial zones and provide the delivery of natural gas to homes and workplaces. The main differences between these pipeline systems are the variations in their maximum and minimum flow pressures as well as their physical properties such as diameter, hardness, and material. For example, collection and transmission lines are made of steel pipe, and distribution lines are made of steel or modern plastic pipes (polyethylene pipe).

Pressure Reducing and Measuring Stations (RMS)

Pressure reducing and measuring stations are the building blocks of the natural gas distribution system. The natural gas coming from the transmission lines at 50-100 bar high pressure is brought to the pressure and temperature required by the customer and is created to meet the demand amount. Solid and liquid particles that may damage the equipment at the consumption points are filtered and chemical odorization is applied to facilitate the detection of gas leaks. Station types and operating pressures are shown in Figure 2.

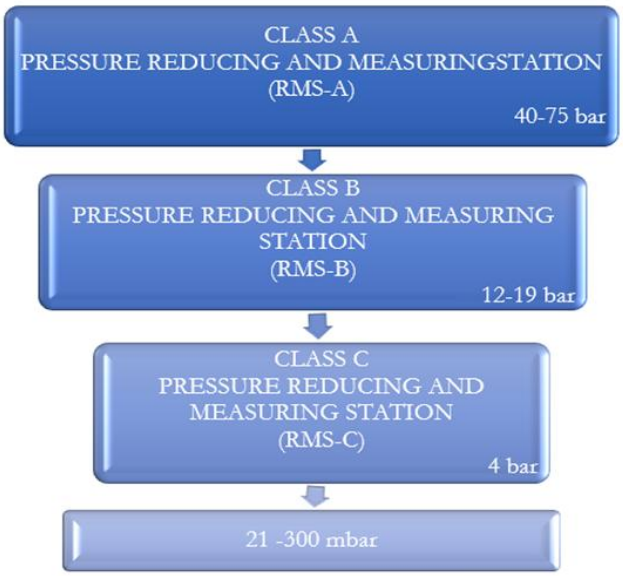

Figure 17. Pressure Levels Chart for Pressure Reducing Stations

In order to prevent the gas temperature from falling below zero as a result of the "Joule-Thomson" effect in the pressure reduction process and damaging the equipment, the gas must be heated before regulation. Heating systems are installed according to their consumption capacity. Consumption amounts are billed by measuring with flow meters. Measurement systems are established to meet current and future demands in an uninterrupted and secure manner. There are 3 types of pressure reducing station, A, B and C type. A-type pressure reduction and measurement stations, also called RMS-A, are the stations where the pressure of the high-pressure natural gas coming from the transmission line is first reduced and measured. RMS-A stations, known as city entrance stations, consist of systems that reduce the incoming gas at 40-75 bar high pressure to 12-19 bar. There are main and backup lines at the stations to

meet the entire gas demand. To ensure uninterrupted gas supply in line with the changing demand at the stations, backup and by-pass lines are ready. The installation and operating activities of the stations must be carried out in accordance with the standards of national and international institutions. Figure 3 shows an example of the pressure relief and metering station diagram.

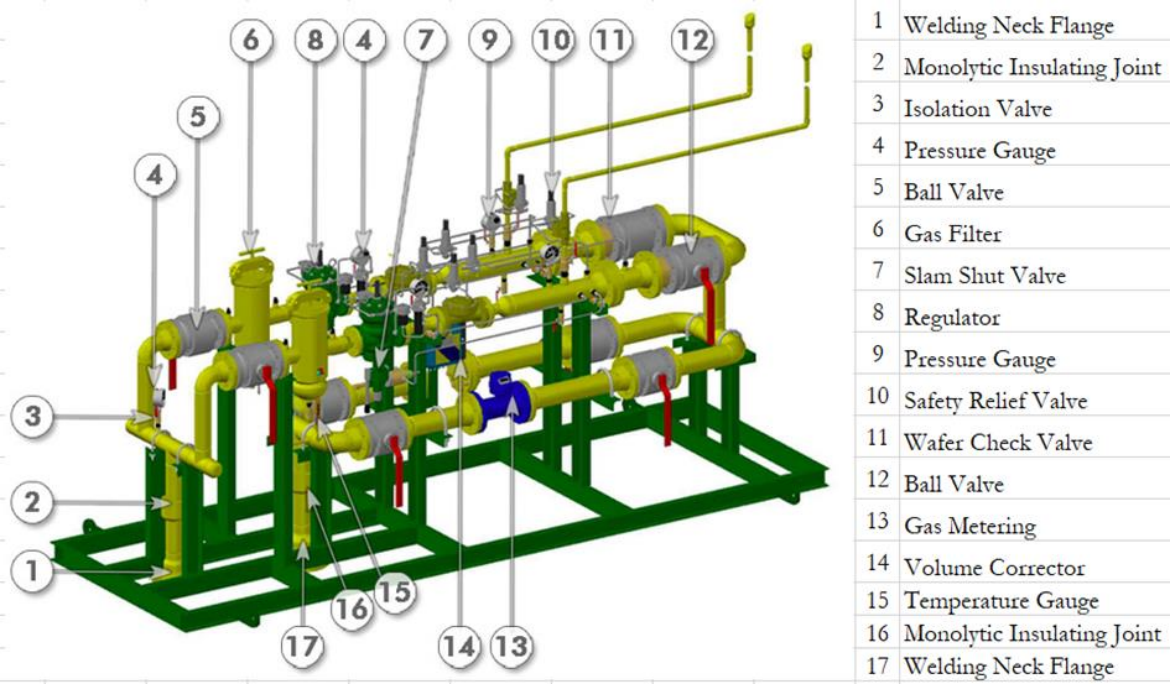

Figure 18. Pressure Reducing and Measuring Station Collector ((Penawaran, 2023)

Natural gas is first separated from solid and liquid particles by passing through filters. Installation and redundancy are provided as two lines. After the filters, it is heated by entering the heat exchangers. It is necessary to heat before sudden pressure and drop. The gas coming out of the heater exchanger system enters the pressure reduction section and the gas reduced to the demand pressure exits the main and backup lines and enters the measurement system. It is then sent to the consumption points where the measurement is made. In addition, there are ball valves used intermittently between systems to cut off the gas in the system. There are manometers installed to see the pressure of the gas passing through different stages, thermocouples, or resistance thermometers to measure and monitor the temperature and pressure relief valves to ensure system safety and evacuate the gas. At these stations.

- Fragrance,
- Calculating the average calorific value by analyzing the gas
- Gas flow measurement,
- Pre-entry filtering of city network,
- Pressure adjustment according to need,
- Automatic cut-off of gas in emergency situations,
- All data is collected, monitored, and managed with the SCADA system.

Type B station, on the other hand, is the station that reduces the 2nd stage pressure of the gas coming from the A type station in the city and is also called the zone regulator. In type B stations, the gas entering at a pressure of 12-19 bar is reduced to 4 bars, and the gas coming through steel pipes is switched to polyethylene pipes after the B type station. C-type pressure reducing station is the system that provides the last stage pressure reduction in the distribution lines. It adjusts the output of the gas entering at 4 bars in the pressure range of 19-300 mbar according to the need (Winrow, 2011).

Compressor Stations

Gas compressors are machines that pressurize a certain volume of gas by reducing its volume. It is preferred in many applications such as chemical plants, refineries, gas production and injection from gas wells. Centrifugal and positive displacement reciprocating compressors are generally used in natural gas pressurization plants. Piston compressors have a constant volume and high compression ratio. Centrifugal compressors, on the other hand, create the centrifugal effect caused by the rotation of the compressor wheel, which converts kinetic energy into pressure energy of the gas. Centrifugal compressors are mostly preferred in gas transmission system due to their compact structure. Low installation costs and low maintenance costs, and the ability to operate at high speeds are among the most important advantages. The general structure of the cascade centrifugal compressor is comprised of the rotor, stator, shaft bearing and sealing elements. The station piping is connected to the compressor inlet and outlet flange. The compressor is operated by determining the number of compressors according to the gas demand. Centrifugal compressors are generally powered by gas turbines or electric motors. Compressor manufacturers manufacture multi-stage compressors designed for gas turbine power and capable of operating at different speeds. Piston compressors, on the other hand, are in the category of positive displacement compressors and cover a larger area than centrifugal compressors, but their efficiency and pressurization range are higher. Piston compressors provide pressures up to 30,000 psi and the ability to operate from low powers up to 20,000 hp. They are designed as single or multi-stage and the compression ratio is limited to 4 at each stage. The power required for the compressor is obtained from the technical documents determined by the compressor manufacturers.

Compressor stations, typically consisting of several compressor units connected in series or in parallel, play a very important role in the natural gas industry. The compressor unit consists of a unit used to increase the pressure of the natural gas by reducing its volume. It provides the necessary thrust or reinforcement to keep the natural gas moving along the line. In other words, compressor stations are strategic facilities established on pipelines that regulate gas pressure and flow. It ensures the transmission of gas from the production point to the end consumer by pressurizing it. Pressure losses and variable costs according to the pipeline diameter determine the points where the compressor stations will be installed on the boat line. Depending on the station's basic operating parameters, there are pre-prepared compressor molds (Okay, 2019). Thanks to this design and set-up molds, fast installation of stations and ease of maintenance and repair are provided. A standard type of station structure is given in Figure 4.

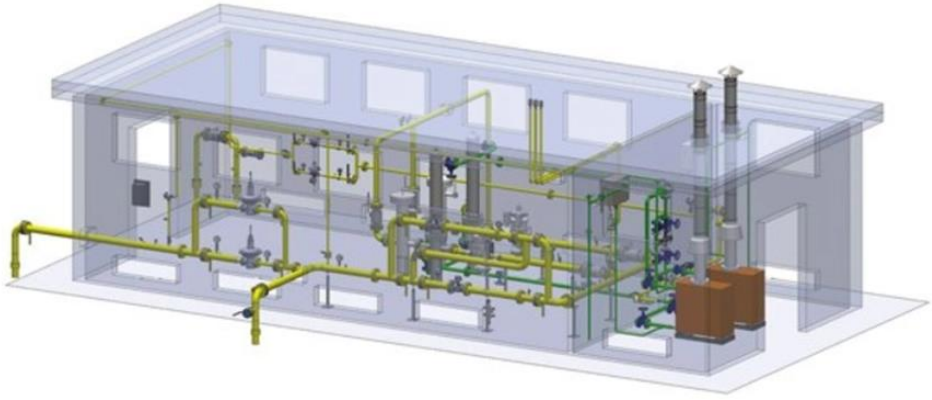

Figure 19. Standard Compressor Structure

Compressor stations, which are of great importance to the gas transport industry, are strategically installed along the gas transmission lines to provide sufficient energy for the natural gas to be delivered to different points. To express in numerical values; A natural gas compressor station is a comprehensive mechanical facility that takes natural gas at pressures ranging from 13 bar to 40 bar and compresses it up to 69 bar and 95 bar. To better understand

these pressure scales, let's take an example of the pressures in vehicle tires. Typical vehicle tires contain air at roughly 2-2.5 bar pressure (Speight, 2006). As a result of pressurization, the natural gas flow overcomes frictional losses and conserves the energy necessary to continue moving from the conveying line to another compressor station or end users.

There are several types of compressor units in the natural gas industry. Among the most found are compressors whose operating principle is characterized by centrifugal dynamic movements or positive back and forth displacements. The second type with reciprocating motion is the compressor, in which the compression element uses a piston that moves back and forth in a cylinder (Cleveland, 2007). Many mechanical, electrical, construction and automation project applications are carried out in the design and installation of compressor stations. Compressor power and numbers suitable for the amount of gas to be transported in the transmission line are determined, and the pipe installations are manufactured in accordance with the technical specifications such as diameter, thickness, pressure resistance according to the station power and capacity. An example of an industrial natural gas compressor station is shown in Figure 5.

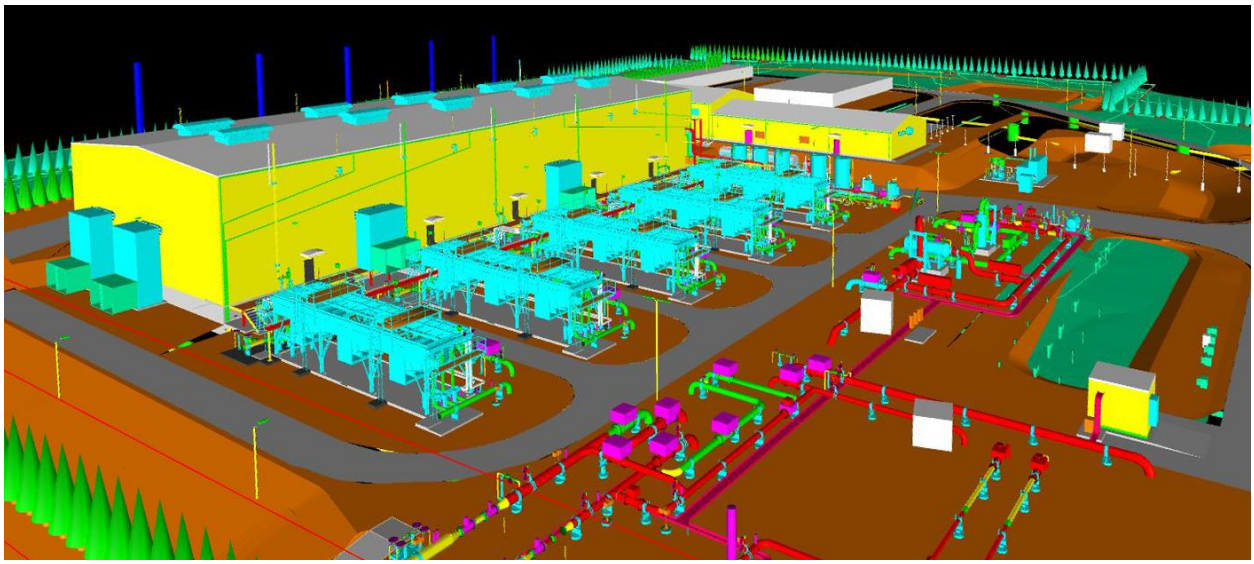

Figure 20. An Industrial Natural Gas Compressor Station (Malone, 20223)

The station generally consists of filters, gas compressors, gas turbines, pigging and pigging facilities, measurement systems, cooling units, heating boiler systems, industrial valves, electronic measurement, monitoring, and control systems.

Connection of Standard Compressor Station to Pipelines (Collector Structure)

As it is known from fluid mechanics, pipelines experience pressure loss due to friction during transmission. At the same time, the gas coming to the compressor station inlet changes direction as it passes through the piping inside the station. It loses pressure as it flows through valves, fittings, filters, and meters. When the operating conditions of the compressor stations are examined, the transmission direction is designed towards the consumption points in the supply sources. In the compressor station, the most important issue is handled as pressure. The gas coming from the transmission line A shown in Figure 6 to the compressor inlet with the inlet pressure P_s; It loses pressure while passing through pipes, elbows, valves, and instruments. Compressing is done in the compressor and P_d flows towards the B transmission

line with the outlet pressure. The inlet and outlet pressure relationship are determined from the following equations (Cengel, 2014).

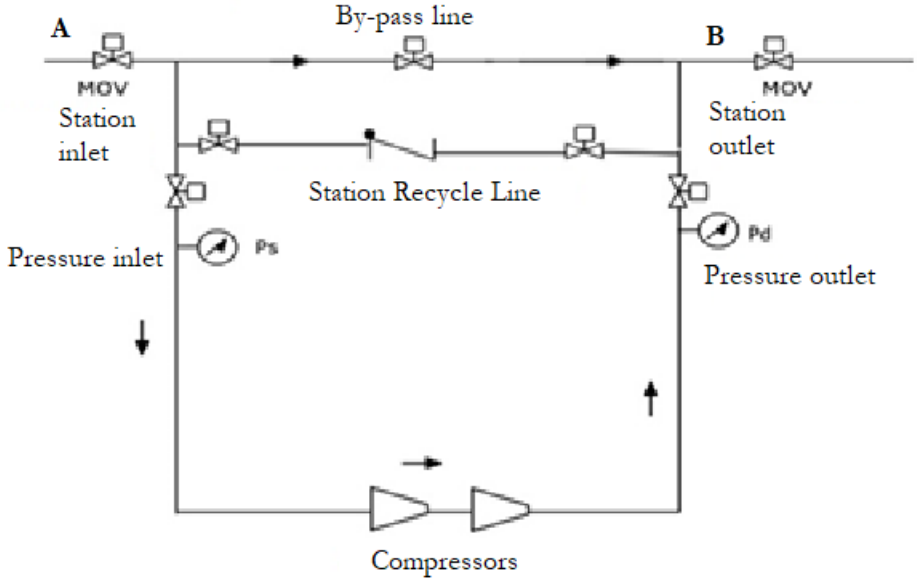

Figure 21. Compressor Station Gas Flow (Menon E. , 2005)

$$P_s = P_1 - \Delta P_s \quad (1)$$

$$P_2 = P_d - \Delta P_d \quad (2)$$

$$r = \frac{P_d}{P_s} \quad (3)$$

Here, r is the compressor compression ratio. The local belts experienced in the piping vary according to the geometric shapes of the valves, elbows, filters, and Reynold number (Re) that make up the line. All these calculations are calculated by the energy balance Bernoulli method. H_C represents the power gained by the compressor, h_L is the head loss between different pressurized points, V velocity, g gravity. The total head loss h_L at the pipeline transmission moment is equal to the sum of the continuous and local losses. Losses in the flow; It varies depending on whether it is laminar or turbulent, the geometric shape of the pipe and the roughness values of the material. It can be called permanent losses.

$$Re = \frac{\rho V D}{\mu} \quad (4)$$

$$P_1 + \frac{1}{2}\rho\upsilon_1^2 + \rho g z_1 = P_2 + \frac{1}{2}\rho\upsilon_2^2 + \rho g z_2 \quad (5)$$

$$Z_1 + \frac{P_1}{\gamma} + \frac{V_1^2}{2g} + H_C = Z_2 + \frac{P_2}{\gamma} + \frac{V_2^2}{2g} + h_L \quad (6)$$

$$h_L = h_{L_{yerel}} + h_{L_{sürekli}} \quad (7)$$

The state of flow through a pipe generally provides the conditions for continuous flow. In flows where the mass flow rate does not change, the energy balance is expressed by the conservation of energy equation given below.

$$\dot{W} - \dot{Q} = \dot{m} c_p \Delta\left(T_{çıkış} - T_{giriş}\right) \quad (8)$$

The mathematical model for pipe flow is developed based on the performance values of the compressors, the equations for the gas flow in the pipes, and the principles of conservation of mass. The mathematical formulation and types of equations included in the main simulation equations depend on pipeline configurations, the nature of the gas (natural gas or another gas) and internal corrosion. The pipe flow equation is one of the main equations used for flow modeling and simulation. Derived based on the principle of flow analysis of gas in pipes. The

flow of gas through the pipes varies depending on various factors such as the properties of the gas, the friction factor, and the geometry of the pipes. The relationship between the upstream pressure, downstream pressure, and flow of the gas in the pipes has been expressed in the literature with various equations. In this study, the general flow equation is used to explain the relationship between the pressure difference in the pipes and the gas flow, as it is frequently applied in the gas industry.

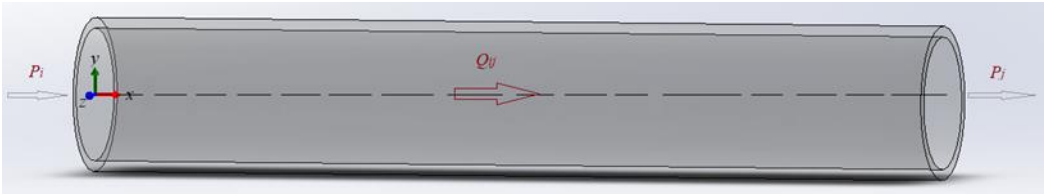

Figure 22. Pipe flow

For a pipeline element, the inlet and outlet pressure P_i, the downstream pressure P_j, and the flow through the pipe Q_{ij} can be expressed as in Equation 9 for single-phase flow.

$$P_i^2 - P_j^2 = K_{ij} Q_{ij}^2 \tag{9}$$

This equation is a functional form of unknown parameters in the flow. Here, K_{ij} is defined as in equation 10 as a coefficient that changes depending on the dimensions of the parameters in the flow equations.

$$K_{ij} = 4{,}3599 \times 10^8 \frac{fGZT}{D^5} \left(\frac{P_n}{T_n}\right)^2 L \tag{10}$$

Here, f, G, Z and T represent the Darcy friction factor, gas weight, compressibility of the gas and temperature of the fluid, respectively (Menon E. , 2005).

Many researchers have demonstrated empirical calculations as a function of pipe internal diameter and internal roughness in turbulent flow. In addition, the friction factor for different types of flow can be found from the Moody diagram (Figure 8). For turbulent flow in straight smooth pipes f (friction factor) is minimum. Although the friction force is not zero, it varies depending on the Reynolds number. For rough pipes, it depends on the relative roughness and Reynolds number. The roughness value used in the calculations assumes the material as new. The increase in the rough surface in the used pipes and fittings depending on the working conditions causes the losses and friction factor to increase.

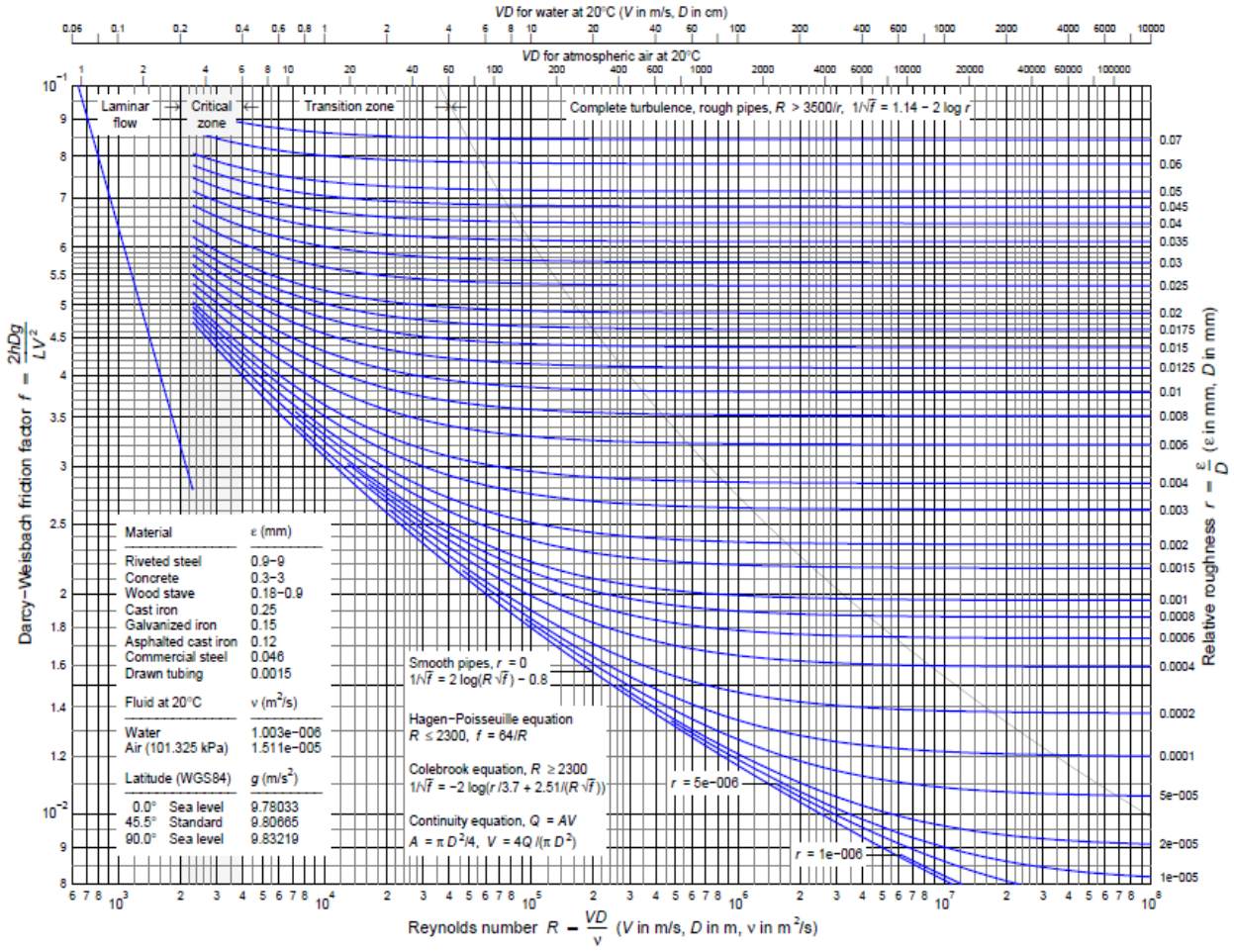

Figure 23. Moddy Diagram (Chaurette, 2023)

In high pressure, turbulent high flow rate and large diameter pipeline plants, the Weymouth equation is generally used for calculation (Menon E. S., 2015). Weymouth equation (equation 11) was used in the calculations within the scope of this study.

$$Q = 3{,}7435\ x\ 10^{-3}\ x\ E\ x \left(\frac{T_b}{P_b}\right) x \left[\frac{(P_1^2 - P_2^2)}{GxT_f xL_e xZ}\right]^{0.5} x\ D^{2.667} \qquad (11)$$

Q: Flow rate standard m3/day (SCMD)
E: Pipeline efficiency 1 or less decimal
T_b: Temperature (K)
P_b: Atmospheric Pressure (kPa)
P_1: Gas inlet pressure to the system (kPa)
P_2: Gas outlet pressure from the system (kPa)
G: Specific Gravity (1 for air)
T_f: Average gas flow temperature (K)
L_e: Equivalent length of the fittings, km (bars, tees, valves, etc.)
Z: Compressibility coefficient (dimensionless)
D: Pipe inner diameter (mm)

Modeling and Simulation

Standard Collector Model and Flow Analysis

Compressor facilities are installed on the main transmission lines, in the determined areas. Gas enters the compressor station by making station inlet, outlet and By-pass valves and piping to the main transmission line. Gas entering through pipes passes through valves, filters, gas cooling units, measuring equipment and compressor units, and is reconnected to the main transmission line. The blue piping shown in Figure 9 shows the inlet line of the gas from the main transmission line to the compressor station, and the red piping shows the outlet line where the pressurized gas from the compressor station is reconnected to the main transmission line. By-pass valve system is also added to the main transmission line. By-pass valve is generally chosen as a ball valve. It is the equipment that is used openly in cases where the gas continues the normal flow of the main transmission line without entering the compressor facility. In addition, it is one of the important equipment that ensures the continuation of gas flow in the main transmission line in emergency and dangerous situations that may occur in the facility. The blue piping shown in Figure 9 represents the line from the main transmission line to the compressor inlet, and the red piping represents the compressor outlet and pressurized flow. Compressors will continue to pressurize without changing the operating regime. The installation of pipelines and facilities and the selection and calculation of installation equipment are made according to ASME B31.8 (Gas Transmission and Distribution Pipe Network Systems Standard). The effects of the selected equipment on the total head loss are calculated as equivalent length (ASME, 2004).

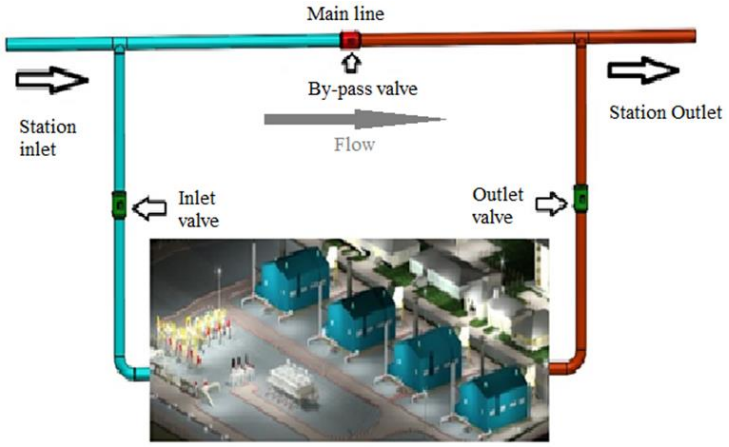

Figure 24. Connection from Transmission Line to Compressor Station

The diagram in Figure 10 represents the lines followed by the standard gas before and after the pressurization process. Gas with flow rate Q, entering the system with P_s pressure, T temperature, suffers a pressure loss as it passes through 1st and 2nd stage filtering, valves, and other connection parts to the compressor inlet via pipes. The flow, which is pressurized according to the compressor pressurization ratio, reaches the pipeline again by passing through the pressure safety system, measuring systems, valves, and other connection parts with P_d pressure.

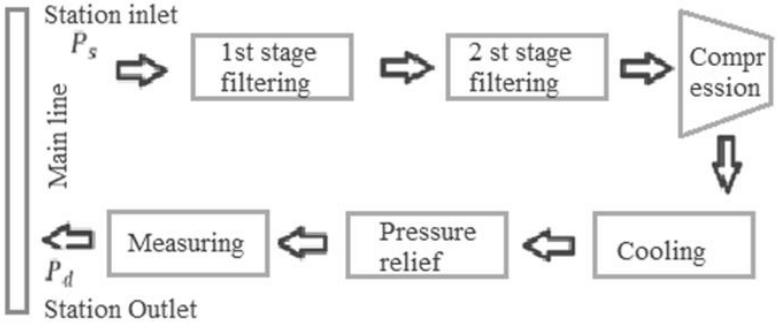

Figure 25. Schematic for Compressor Gas Flow

The gas flow chart in a standard compressor station was named *B0* operating system in this study and is shown in Table 2. It is the system in which the gas flowing from the eastern transmission lines to the western transmission lines is pressurized in the compressor and flow is ensured. It starts by taking the position of the By-pass valve in the main transmission line to the closed position and directing the gas to the inlet piping. The gas flowing to the station inlet piping flows towards the process equipment in the compressor plant and reaches the compressor unit by turning the station inlet valve to the open position. The operation continues by controlling and monitoring the pressure, temperature and flow rate of the gas pressurized in the compressor unit. The flow continues into the main transmission line piping in the open position of the station outlet valve.

Table 6. Standard Compressor Station Gas Flow

FROM	LINE OPTION	TO
East	*B0* →	West

The installation of pipelines and facilities and the selection and calculation of installation equipment are made according to ASME B31.8 (Gas Transmission and Distribution Pipe Network Systems Standard). The effects of the selected equipment on the total head loss are calculated as equivalent length. The equivalent length is expressed as the ratio of the pipe valve and fittings used in Table 3 according to the D diameter to the length L.

Table 7. Equivalent Lengths for High Pressure Piping (Menon E. S., 2015)

EQUIPMENT	L/D
Gate Valve	8
Globe Valve	340
Angle Valve	55
Ball Valve	3
Check valve with lift control	600
Standard elbow, 90^0	30
Standard elbow, 45^0	16
Standard elbow long bend, 90^0	16
Standart Tee	20

Pipeline friction losses, losses caused by instruments and pipe connection equipment represent the total pressure loss. In determining the inlet and outlet pressure losses, the losses

of the devices and fixtures used in addition to the pipe length losses are also included in the calculation on the basis of equivalent pipe length. This proportional evaluation, which is determined according to the line pressure load and pipe diameter, is considered in the design and projecting of the station inlet and outlet collectors. An example of such a calculation is given in Table 4. Note that for the inlet, the collector pressure is 40 bar. On the other hand, for the outlet, the collector pressure is 60 bar. Apart from this basic evaluation, detailed gain-loss calculations are also made. Pressure, temperature, and velocity changes were analyzed during the flow of gas from the natural gas pipelines in the compressor station. The piping system and other instruments through which the gas flow passes cause pressure loss. The effects of other instruments such as filters, measuring equipment, cooling units on pressure loss have been determined by their manufacturers. These values are included in the calculations considering the working conditions of the designed system. Figure 8 shows the pressure drop analysis of the piping of a gas compressor station in the pipelines. The pressure in the piping continues to decrease until the compressor inlet. The gas, whose pressure and temperature increases by being compressed in the compressor, loses pressure again in the outlet line of the station. Pressure loss values are extremely important for the efficiency of the system. It shows that the compressor inlet pressure will be low due to the losses occurring before the compressor in the system, which is accepted as station inlet pressure of 40 bar, compressor outlet pressure of 60 bar and pressurization ratio of 1.5. Although the output is accepted as 60 bars in the calculation made according to the pressurization rate, it is a lower value. However, the desired 60 bar outlet pressure is compensated by compressor configurations.

Table 8. Pressure Loss over Equivalent Lengths (Standart Collector)

INPUT (FEED) LINE [40 bar]				*OUTPUT (DISTRIBUTION) LINE [60 bar]*			
Pipe Piece	Equivalent length ratio [L/D]	Amount (Number)	Total Length [m]	Pipe Piece	Equivalent length ratio [L/D]	Amount (Number)	Total Length [m]
40” Pipe line (D=1,01 m)							
Elbow 90º	30	1	30.3	Dirsek 90º	30	2	60.6
Elbow 45º	16	2	32.30	Dirsek 45º	16	1	16.15
Pipe	1	5	5	Pipe	1	20	20
36” Pipe line (D=0,9144 m)							
Elbow 90º	30	6	164.5	Elbow 90º	30	2	54.83
Tee	20	4	73,15	Elbow 45º	16	1	14.63
Ball valve	3	5	13.7	Check valve	60	1	54.86
Pipe	1	20	20	Pipe	1	40	40
32” Pipe line (D=0,8128 m)							
Elbow 90º	30	2	48.75	Elbow 90º	30	4	97.50
Tee	20	2	32.57	Elbow 45º	16	5	65.02
Ball valve	3	2	4.88	Check valve	60	1	48.76
Pipe	1	30	30	Pipe	1	30	30
Total equivalent length		*455.15*		Total equivalent length		*502.35*	
Total pressure loss (40 bar)		*0,077 bar*		Total pressure loss (40 bar)		*0,1617 bar*	

Pressure, temperature, and velocity changes were analyzed during the flow of gas from the natural gas pipelines in the compressor station. The piping system and other instruments through which the gas flow passes cause pressure loss. The effects of other instruments such as filters, measuring equipment, cooling units on pressure loss have been determined by their manufacturers. These values are included in the calculations considering the working conditions of the designed system. Figure 8 shows the pressure drop analysis of the piping of a gas compressor station in the pipelines. The pressure in the piping continues to decrease until the compressor inlet. The gas, whose pressure and temperature increases by being compressed in the compressor, loses pressure again in the outlet line of the station. Pressure loss values are extremely important for the efficiency of the system. It shows that the compressor inlet pressure will be low due to the losses occurring before the compressor in the system, which is accepted as station inlet pressure of 40 bar, compressor outlet pressure of 60 bar and pressurization ratio of 1.5. Although the output is accepted as 60 bars in the calculation made according to the pressurization rate, it is a lower value. However, the desired 60 bar outlet pressure is compensated by compressor configurations.

Pressure, velocity and temperature changes in standard collector and piping applications are calculated according to the equipment used and pipe lengths, thus creating a standard suitable for practical applications. Within the scope of the study, considering these standards, the installation and components in the compressor inlet and outlet lines were designed according to the equivalent pipe lengths in the SolidWorks program, and analyzes were made with the flow-simulation application. Licensed SolidWorks software belonging to Ahi Evran University was used in these analyzes. The velocity, temperature, and pressure (velocity, inlet pressure, temperature) input conditions from the collector and piping starting point were defined in the program. For the parts where the flow ends, the existing output conditions (dynamic pressure) in the application were entered into the system. Finite element analysis was carried out in accordance with the in-pipe flow conditions. By making more precise cellular meshing on the pipe walls, precise calculation of the wall effect was achieved. In ambient conditions, summer and winter temperature conditions and standard atmospheric conditions were applied. As a result of iterations, flow trajectories for pressure, velocity and temperature were simulated (Inc., 2012). Most of the natural gas pipelines continue under the ground. For this reason, the pipes are less affected by the outdoor temperature. Stations, on the other hand, consist of installations that are installed in areas where pipelines pass and above ground and that do not have pipe insulation. In the temperature change and the flow rate distribution of the gas in parallel with the pressure drop of the gas emerging from the underground to the surface and entering the station is shown in Figure 11.

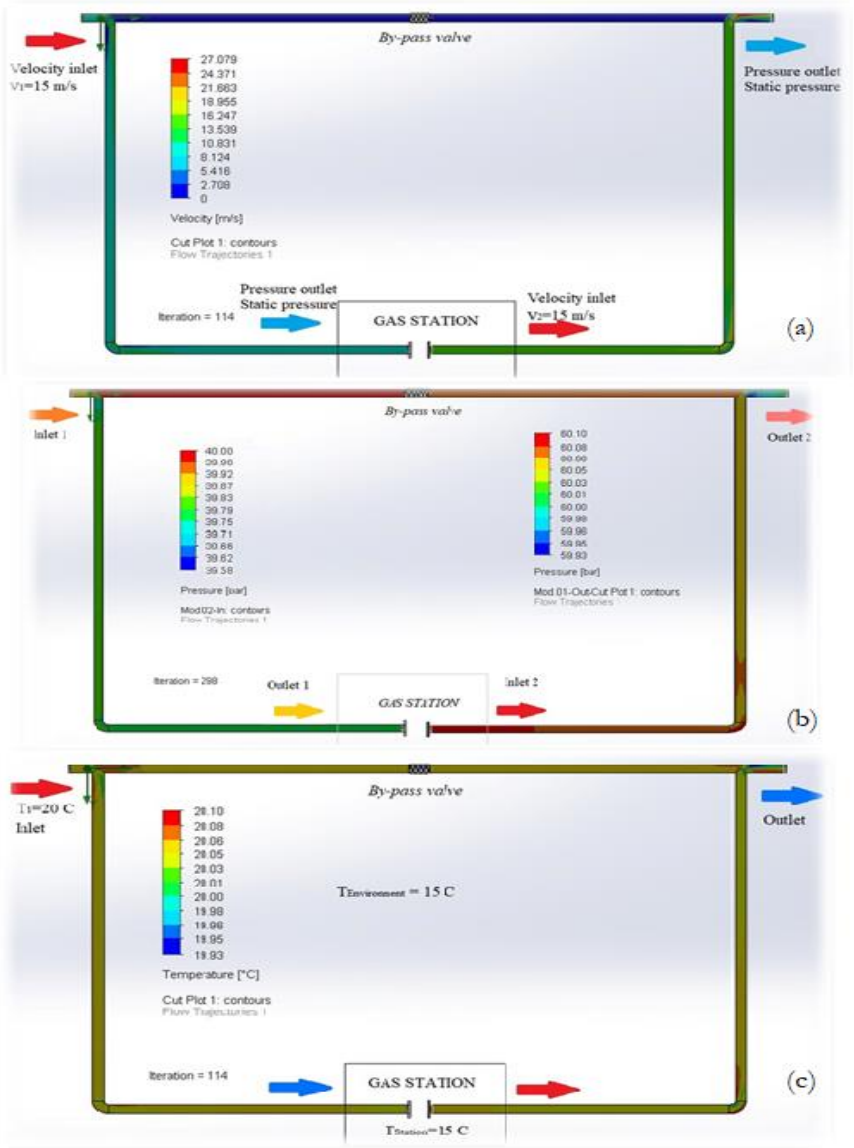

Figure 26. Contours of a) speed b) pressure and) temperature for standart collector

The Designed Collector Model and Operation

The designed collector: refers to the model formed from pipes, fittings, flow control valves, measuring instruments. The main piping, called the inlet and outlet collector, was created, and combined with the piping of four different transmission lines. The piping of each transmission line consists of a flow control valve, pressure-temperature measurement transmitters, ultrasonic meters providing flow measurement, ball valve at the connection point to the inlet collector, and bypass lines and connection parts. Again, connection piping to the outlet collector was formed from ball valves, bypass lines, check valves, temperature and pressure measuring instruments. Backflow was prevented by positioning check valves on four different piping connected to the inlet collector. It is assumed that the inlet collector is connected to the compressor station inlet pipeline and the outlet collector is connected to the compressor station's outlet pipeline. The general view of the model designed in the SolidWorks program is shown in Figure 12.

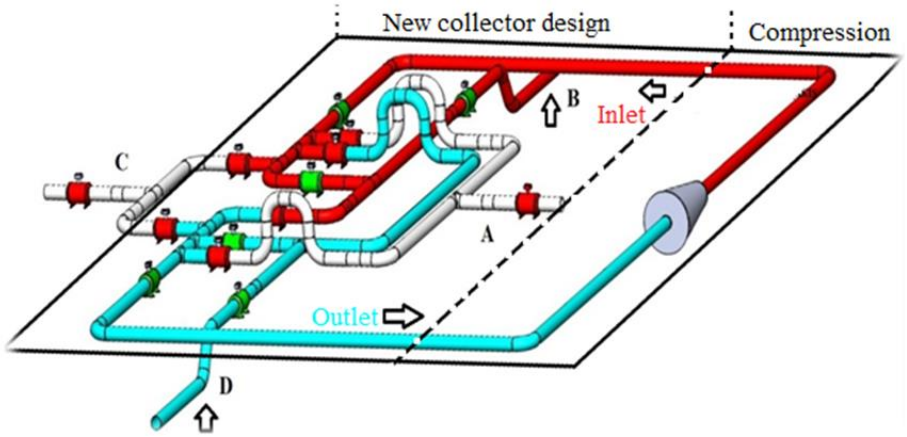

Figure 27. General View of Collector Design and Compressor Connection Line

The piping of each transmission line consists of a flow control valve, pressure-temperature measurement transmitters, ultrasonic meters providing flow measurement, ball valve at the connection point to the inlet collector, and bypass lines and connection parts. Again, connection piping to the outlet collector is made up of ball valves, bypass lines, check valves, temperature and pressure measuring instruments. Check valves are positioned on four different piping connected to the inlet collector and reverse flow will be prevented. It is assumed that the inlet collector will be connected to the compressor station inlet pipeline, and the outlet collector to the compressor station's outlet pipeline. Initial and boundary conditions are defined, with flow velocity at the inlet and static pressure conditions at the outlet. The new type of collector designed to meet all flow conditions is given in Figures 13 and for SolidWorks Piping in Figure 14.

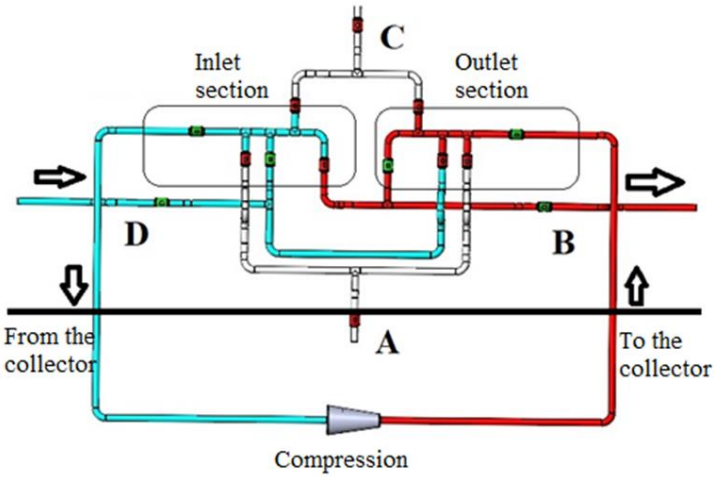

Figure 28 New Type Collector Schematic

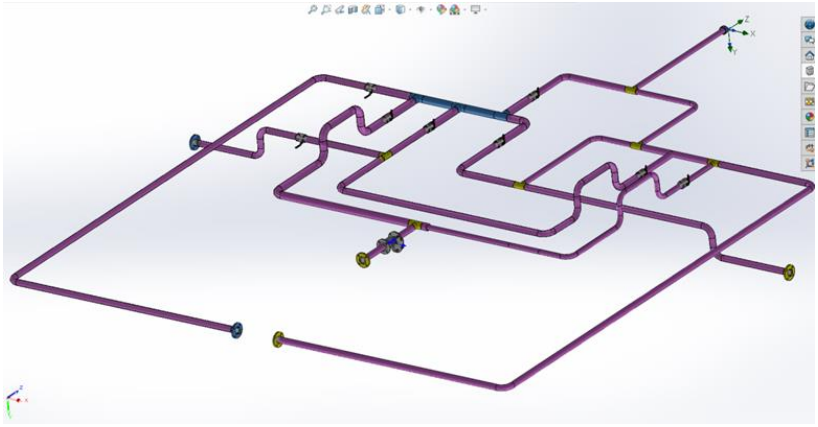

Figure 29. Collector Design and Compressor Connection Line (Top View)

By defining the calculation area for the whole system, it is aimed to consider the effect of ambient conditions on the flow parameters together with the internal flow analysis. Local meshing and the most precise global meshing possible are used for precise analysis of the wall effect under in-pipe flow conditions. Computational domain boundaries and meshing application are given in Figure 16.

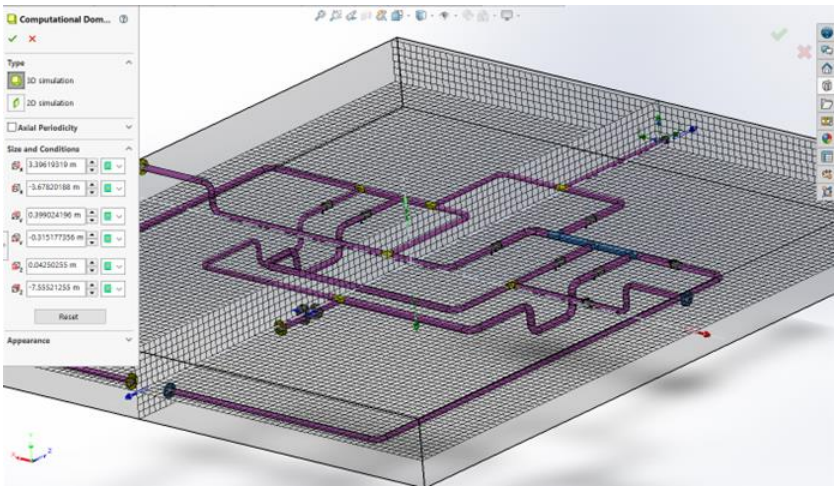

Figure 30. Meshing

In accordance with the alternative orientations of the natural gas, the inner surface of the inner cover defined to the inlet area was chosen as the inlet cross-sectional area. This region represents the first flow region where the solid surface and the fluid region come into contact. Input definition is increased for natural gas entering the collector from more than one point. It is generally seen in the analysis that the East and South lines are determined as gas entry points. The same evaluation was made for the exit conditions. Flow rate definition has been made for these points where the natural gas supplied from the remote transmission lines enters the station for the first time. The change of system parameters can be seen for different input speed conditions. It is possible to define additional thermodynamic parameters in the inlet conditions of natural gas in this section. For example, 40 bar inlet pressure condition is also defined for this system. At the points where the natural gas leaves the station, environmental pressure conditions are defined. These points are also defined to the system for each flow condition. Besides the East, West, North and South exits where gas supply is required, it is possible to deliver natural gas to more than one point.

The collector flow chart, which is connected to four different transmission lines, to the existing compressor plant shown in Figure 16 is shown. Natural gas entering the inlet collector in the pipeline with P_1 pressure loses pressure and enters the compressor with P_s pressure. After

pressurization, the gas leaving the compressor station with the P_d pressure loses pressure in the outlet collector in an alternative direction and moves towards the natural gas pipelines with the P_2 pressure. The location, working conditions, capacities, etc. of the compressor stations. many variables determine the amount of flow in transmission lines. Investment may be necessary when the capacity of the pipe diameters is sufficient, but the gas needs to be supplied from alternative sources for different reasons.

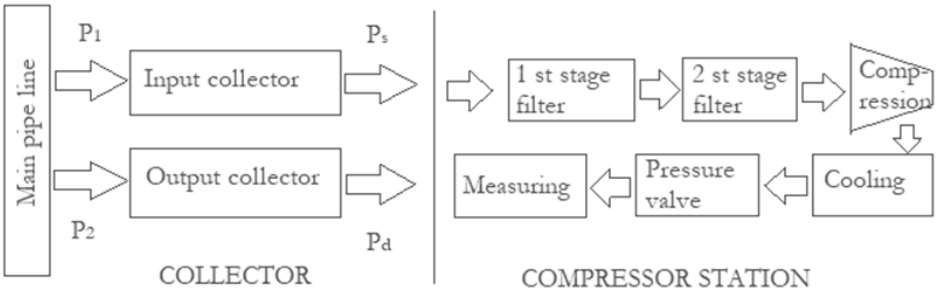

Figure 31. Collector-Station Connection Diagram

The collector operating conditions must be open to the transmission line to which at least one flow must be sent to the inlet collector from at least one transmission line, and at least one flow like the state inlet collector for flow input and output. The collector operating conditions must be open to the transmission line, where at least one flow must be sent to the inlet collector from at least one transmission line, and at least one flow similar to the state inlet collector for flow input and output. Within the scope of this study, the alternatives in which the gas taken from the east, north and south transmission lines with different scenarios are pressurized to the west transmission lines are numbered *B1, B2, B3, B4, B5,* and *B6*. The pressurization alternatives of the gas taken from the western, northern, and southern transmission lines with different scenarios to the eastern transmission lines are numbered as *D1, D2, D3, D4, and D5*. These are shown in detail in Table 5.

Table 9. Line Routing Diagram at The Compressor Station

FROM	LINE OPTION	TO
East	B1	West
East + South	B2	
East + North	B3	
East + North + South	B4	
East	B5	West + South
North + South	B6	West
West	D1	East
South	D2	
North	D3	
North + South	D4	East + West
West + North	D5	East

The flow control system is the system in which the gas coming to the compressor inlet from the pressurization process D transmission lines of the existing compressor facility is pressurized and sent to the B transmission lines. The working system of the already established and working

stations is like this. Sending the flow to the B transmission lines starts with the introduction of gas to the compressor inlet by opening the valve in the installation connected to the collector inlet from the D transmission line in the designed collector. After pressurization, the gas reaching the outlet collector starts to flow in the B direction. The flow control valve in the D and B transmission lines, the data coming from the measurement systems are monitored and controlled in the SCADA system. In the designed model, Pipes, valves, fittings (elbow, tee, check valve) have been added up to the compressor inlet. Flow control model is shown in Figure 17.

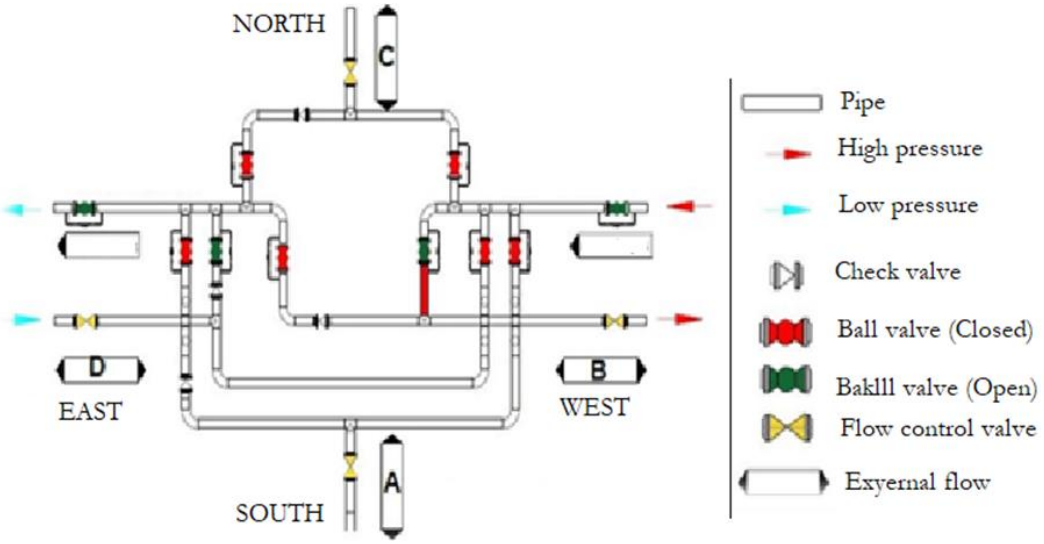

Figure 32. Alternative Working Diagram

Gas in different transmission lines and at different pressures will enter the compressor station by passing through the designed collector system. Filtering, pressurization, metering, etc. After the process stages, the compressor station will be connected to the outlet collector from the outlet line. The number, characteristics and dimensions of the installation equipment that affect the pressure loss as the gas in the transmission line passes over the inlet and outlet collectors have been determined on the design drawings. The effect of the equipment used on the pressure loss is calculated according to the equivalent length L/D ratio in Table 3 and shown in Table 6 as the total length. As can be seen in the table, with other system equipment, the 36-inch piping designed for the inlet line is determined as 648 m and 152 m for the outlet line. Pressure loss calculation according to equivalent lengths for B1 line is given in Table 6.

Table 10. Pressure Loss over Equivalent Lengths (Designed Collector-B1)

INPUT (FEED) LINE [40 bar]				*OUTPUT (DISTRIBUTION) LINE [60 bar]*			
Pipe Piece	Equivalent length ratio [L/D]	Amount (Number)	Total Length [m]	Pipe Piece	Equivalent length ratio [L/D]	Amount (Number)	Total Length [m]
36" Pipe line (D=0,9144 m)							
Tee	20	3	54.8	Elbow 90º	30	1	27.4
Ball valve	3	3	8.2	Tee	20	4	73.1
Check valve	600	1	548.4	Ball valve	3	2	5.48
Pipe	1	36.6	36.6	Pipe	1	46.4	46.4
Total equivalent length		*648*		Total equivalent length			*152*
Total pressure loss		*0,1364 bar*		Total pressure loss			*0,025 bar*

(40 bar)		(40 bar)	

In the designed collector system, independent analyzes of the inlet line, the outlet line and the total pressure loss of the system were made. By ignoring the pressure losses inside the compressor station, only the pressure loss arising from the pipes, fittings and other equipment in the designed system has been calculated. The variation according to the outdoor temperature and different inlet pressures in the transmission lines has been analyzed and shown on the graph. Compressor pressurization ratio was accepted as 1.5. The pressure loss that occurs when the gas coming from the pipeline to the collector inlet line passes through the pipes and connections made up to the compressor station inlet has been calculated. The effect on the decrease is calculated and given in Figure 18.

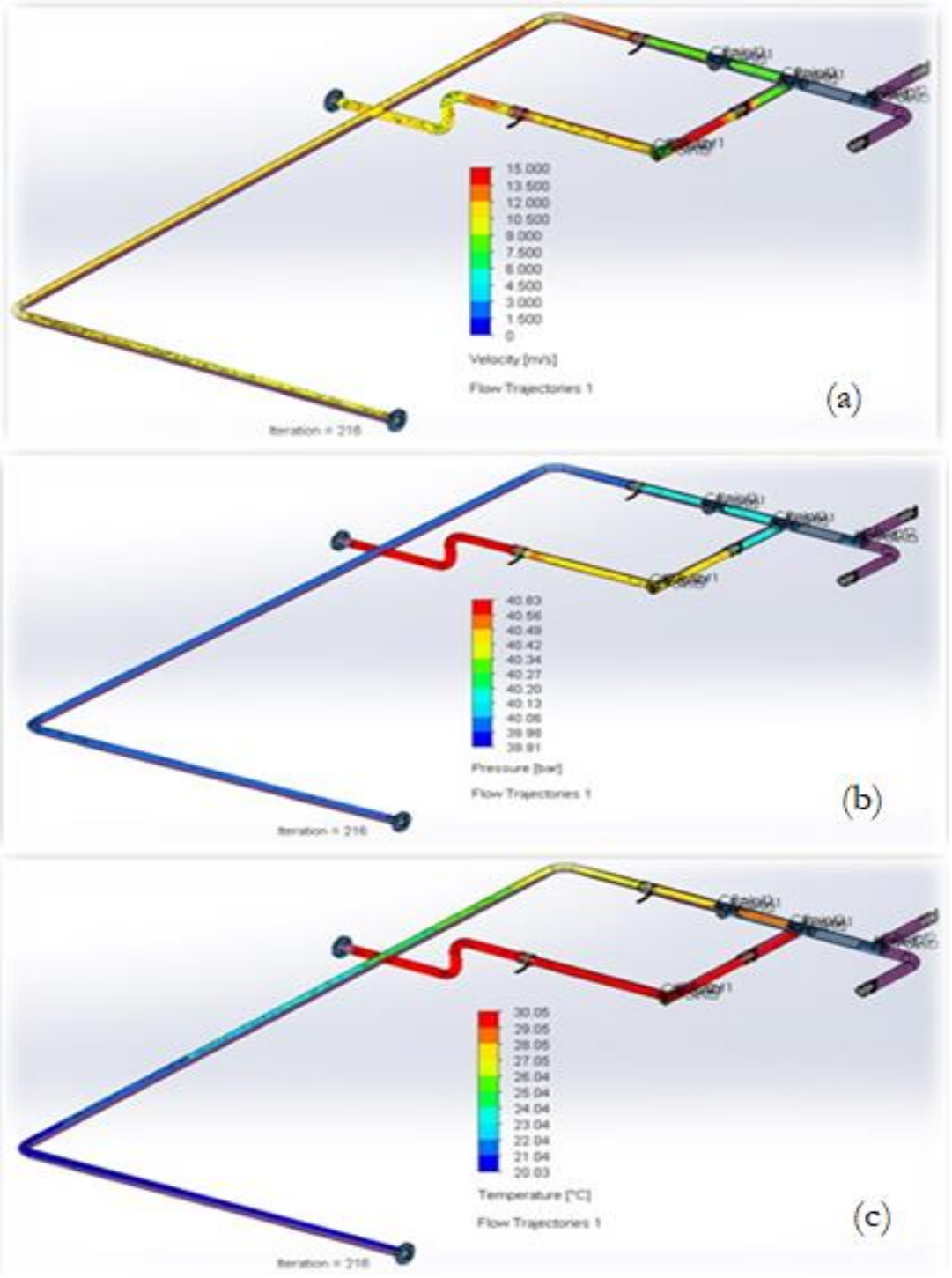

Figure 33. Contours of a) speed b) pressure and) temperature for alternative collector

The speed, pressure, and temperature counters for the B1 line are given below. These contours reveal the effects of decreasing pipe length as expected. It is expected to obtain similar flow counters for all lines. It is also not included here.

Table 11. Equivalent length and pressure drops for line alternatives

	INLET LINE (40 bar)		OUTLET LINE (60 bar)	
Line	Total equivalent length (m)	Total pressure loss (bar)	Total equivalent length (m)	Total pressure loss (bar)
B0	455,15	0,077	502,35	0,1617
B1	648	0,1364	152	0,025
B2	1376	0,288	152	0,025
B3	1276	0,245	152	0,025
B4	2216	0,448	152	0,025
B5	664	0,141	338	0,052
B6	1330	0,272	152	0,025
D1	885	0,176	313	0,048
D2	661	0,140	289	0,041
D3	689	0,146	289	0,041
D4	1420	0,286	386	0,061
D5	1343	0,282	289	0,041

The values given in the Table 7 are obtained from the calculation made for 40-60 stationary compressor pressurization. Pressure losses at the compressor inlet are achieved by proportionally changing the compression ratio. In most station applications, the compression ratio is variable. In cases where 1.5 bar compression is not sufficient, the compressor automatically compresses to provide the desired inlet and outlet pressure.

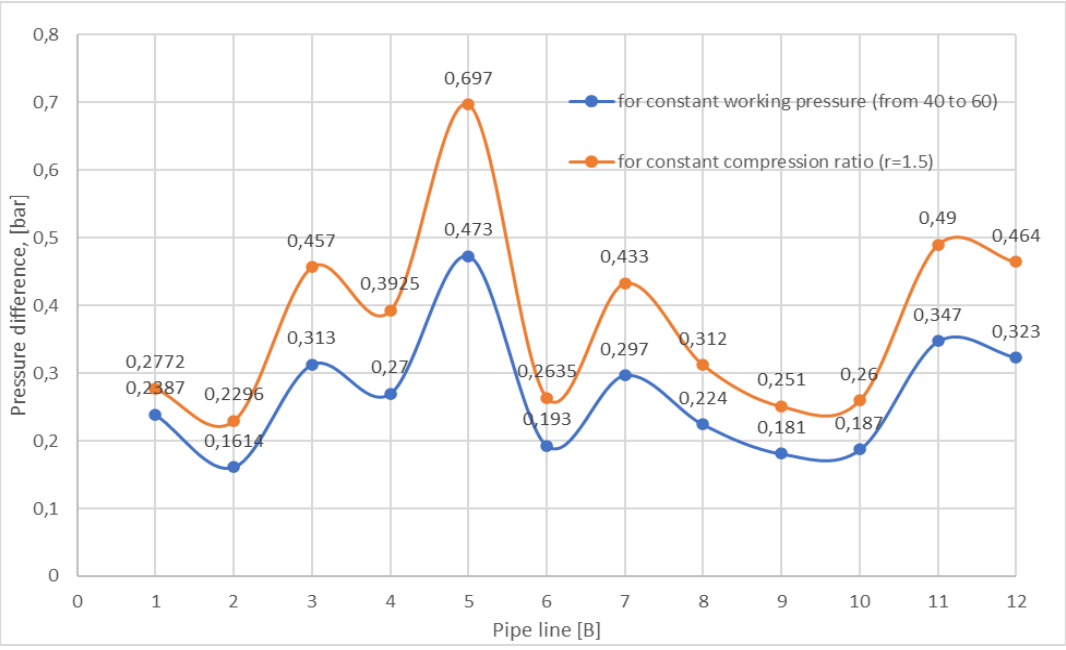

Figure 34. Pressure Loss Changes for Compressor Station

In the compressor unit (compressor + collector) with a compression ratio of 1.5, the pressure at the compressor inlet will be lower than 40 bar due to the pressure loss in the inlet collector. Therefore, the pressure at the compressor outlet is lower than 60 bar. The pressure losses in the inlet and outlet collector need to be recalculated. The evaluation of the calculations made under constant compression ratio and constant pressure conditions is given in Figure 21. The total losses in the input and output collectors are the highest for line 5. In both cases, the pressure losses vary similarly according to the line number.

Conclusion

It is estimated that the use of natural gas will continue to increase soon. It is one of the widely used energy sources in our country. They are pressurization facilities that have critical importance in delivering them to the final consumption points. The necessity of designing these facilities in a way that can respond to future demands is a matter of debate. In changing market conditions, the transmission direction and capacity of the gas may change. Depending on these developments, a collector model has been proposed for the new facilities to be established.

In the collector design, four pipelines and gas sources in each line are specified. Different flow scenarios were created and examined. The design dimensions were determined in accordance with ASME and API standards and the design was completed in the SolidWorks program. In cases where the pressure, speed, temperature, and flow parameters are variable, the flow is monitored, and improvements are made in the installation connection parts. The design dimensions were determined and examined in parts. The pressure losses and temperature changes of the gas coming directly to the compressor plant and the gas that is pressurized through the collector installation and sent back to the transmission line are investigated. While the compressor compression ratio, gas flow rate, and pipe diameters were considered constant, the maximum pressure loss in the inlet and outlet lines of the flow was determined as 0.57 bar in the 1.3 operation alternative, and the lowest loss was determined as 0.18 bar in the 1.0 alternative. There will be lower pressure losses in designs made considering the effects on pressure loss. By examining the effect of ambient temperatures between -150C and 350C; It was concluded that the temperature increase has a positive effect on the pressure loss. Within the scope of future plans in pressurization facilities located in transmission lines:

- Installation of storage facilities
- Installation of LNG facilities
- Changing market conditions (price)
- Malfunctions
- Emergencies, (explosion, fire)
- Natural disasters (landslide, earthquake, etc.)
- Drilling works new reserves
- Energy policies
- Wars
- Epidemics
- The effect of climate change on seasons, etc.

The reasons directly and indirectly affect the transportation of natural gas from production areas to consumption areas. The suitability of the pressurization facilities to be installed in the transmission system to operate in alternative directions and capacities will respond quickly to ordinary or unusual gas flow profiles in the transmission lines.

REFERENCES

ASME. (2004). *Gas Transmission and Distribution Piping Systems, ASME 831.8-2003.* Neew York: The American Society of Mechanical Engineers.

Borraz-Sánchez, R. Z.-M. (2015). Optimization problems in natural gas transportation systems: A state-of-the-art review. *Applied Energy*, s. Volume 147, Pages 536-555.

BP Energy . (2019). *Natural gas grows strongly, with broad-based demand low-cost supplies and increasing global availability.* BP Energy Outlook 2019 edition.

Cengel, Y. A. (2014). *Heat and Mass Transfer: Fundamentals and Applications.* New York: McGraw-Hill Education (Asia); 5. Edition.

Chaurette, J. (2023, May). *Index of /php_pages/friction*. Pump Fundamentals: Web page, https://www.pumpfundamentals.com/php_pages/friction/moody.pdf page

Conrado Borraz-Sanchez, D. H. (2011). Optimization methods for pipeline transportation of natural gas with variable specific gravity and compressibility. *Springer*.

DL Katz: D. Cornell, :. K. (1959). *Handbook of natural gas engineering.* New York: McGraw-Hill.

Edgar, T. F. (1978). Optimal Design of Gas Transmission Networks. New Orleans: society of petroleum engineers journal.

EIA. (2022, December). *Natural gas explained*. U.S. Energy Information Administration-EIA: https://www.eia.gov/energyexplained/natural-gas/ page

El-Shiekh, T. M. (2013). The Optimal Design of Natural Gas Transmission Pipelines. Cairo: Taylor & Francis.

Erdogdu, E. (2010). Natural gas demand in Turkey. *Elsevıer, Applied Energy, 87*(1), 211-219.

Inc., S. (2012). *Solidworks Flow Simulation Tutorial* . www.TechnicalBooksPDF.com.

Jerome G.Egbe, S. I. (2016). Design Approach for Trans –Sahara Gas Pipeline Transmission. Nijerya: IJOER.

Kurz, R. (2019). Optimization of compressor stations. San Diego: GPPS Journal.

L. Branchini, L. B. (2019). Feasibility of ORC application in natural gas compressor stations. Bologna: Elsevıer.

Malone, J. (20223). *Gas Compressor Station.* Sargent & Lundy: Web page https://sargentlundy.com/projects/sargent-lundy-gas-compressor-station-project/ page

Menon, E. (2005). *Gas pipeline hydraulics.* Boca Raton: CRC Press.

Menon, E. S. (2015). *Transmission pipeline calculations and simulations manual, .* Elsevier inc.,.

Michael Hendryxa, J. L. (2020). Natural gas pipeline compressor stations: VOC emissions and mortality rates. Indıana: Elsevıer.

Okay, O. (2019). *Endüstriyel Bir Doğal Gaz Kompresör İstasyonu İçin SCADA Sisteminin Geliştirilmesi.* Kahramanmaraş: Master Thesis.

Okoro, E. E. (2018). Estimation of Flow Capacity in Pipelines Based on the IntrinsicVariation of the Volumetric Properties of the Natural GasMixtureEstimation of Flow Capacity in Pipelines Based on the IntrinsicVariation of the Volumetric Properties of the Natural Gas Mixture. *Petroleum & Petrochemical Engineering Journal*.

Öztürk M, Y. Y. (2011). A bridge between east and west: Turkey's natural gas policy. *Renew Sustain Energy Rev*, 86-94.

Pala, C. (2003, 9 13). 21. yy Dünya Enerji Dengesinde Petrol ve Doğalgazın Yeri ve Önemi. *Uluslararası Stratejik Araştırmalar Dergisi*, 13-20.

Paolo Silva, A. B. (2017). Trigenerative solution for natural gas compressor stations. Milano: Elsevıer.

Penawaran, M. (2023, Ocak). *Lebıh Darı 20 Tahun Kamı Sudah Berpengalaman Dalam Industrı Gas Bumı Dı Indonesıa*. PT. Angka Teknik Sepadan: http://www.angka.co.id/ adresinden alındı

PM International Suppliers, L. (2023, May). *API 5L X Grades*. https://www.api5lx.com/api5lx-grades/ adresinden alındı

Sakineh Tavakkoli, O. R. (2016). Systems-Level Analysis of Waste Heat Recovery Opportunities from Natural Gas Compressor Stations in the United States. Pennsylvania: Acs Sustaınable Chemestry And Engıneerıng.

Speight, S. M. (2006). *Handbook of natural gas transmission and processing.* Houston: Gulf Professional Publishing.

Türkel, V. (2015). *Doğalgaz Dağıtımında Tasarım İmalat ve Yönetim.* İstanbul: İGDAŞ.

Üster, H., & Dilaveroğlu, Ş. (2014). Optimization for design and operation of natural gas transmission. *Applied Energy, 133*, 56-69.

Winrow, G. (2011). Turkey: An Emerging Energy Transit State and Possible Energy. *İnternational Spectacor*, 79-91.

Wong PJ, L. R. (1968). Optimization of tree structured natural gas transmission. *Journal of Mathematical Analysis and Applications*, 613–26.

Characterization Of Ancient Mortars: The Case Of The Harem Buildings In Topkapi Palace

Özlem GÖKÇE KOCABAY[1]
Osman İSMAİL[2]

Introduction

Later the conquest of Istanbul, Topkapi Palace did a service for approximately 400 years from the fifteenth century and has been employed as a museum after the proclamation of the republic. Topkapi Palace is one of the most important Ottoman buildings in Ottoman Architecture. In the studies carried out in 1924, the collection of Harem buildings, which were isolated from the other parts of the palace with high walls, showing a multi-storey-graded structuring and extending from the Baltacılar Ward to the Elephant Garden; 25 corridors, 1 tower, 1 kitchen, 2 baths, 2 toilets, 2 laundries, 1 lavatory, 1 hospital, 2 mosques, 1 crypt, 1 treasury, 2 wards, 10 hall-saloons, 115 rooms and 15 apartments were defined and described by giving door numbers (Beşinci, 2023).

Cultural heritage structures have a unique place in the urban landscaping. In addition to harbouring, these structures contain in itself the local cultural and historical properties which describe societies. For this reason, increasing their useful lifetime holds many advantages that also spill over into the environment, contributing to economical and social progress (Foster, 2020).

At the present time several historical structures in many countries require a big restoration. The causes that lead to this circumstance are very wide, they are outcomes of: human activity, natural disasters, naturel ageing (Kareeva & Glazkova, 2017).

Today, cultural heritage authorities and civil engineers attach importance to the use of compatible materials for repair work which must fulfil the functional necessaries on their qualities, durableness, performance, and at the same time comply with the building standards (Pavlík et al., 2019).

A number of new interventions performed with cement based mortars reveal that these materials are incompatible with the ancient materials. Cement mortars promote the degradation of substrates induced by salt crystallization processes by the reason of its contents on alkaline ions and exhibit mechanical properties considerably different from the old masonries (Almeida, Faria & Pinto, 2008).

Aerial lime has been widely used as binder for preparing mortar in masonry buildings over the centuries. Aerial lime is fundamentally consisted of CaO and, in some instances, it can contain also considerable contents of MgO. For aerial lime mortar, carbonation has crucial structural results by the reason of the directly effect on physical and mechanical properties. Generally, carbonation leads to an increasement of density and strength, as gradationally modifying the pore structure of the mortar. Mentioned processing can continue decades or even centuries in thick elements. Therefore, the transformation of calcium hydroxide into carbonate is generally characterised as a long duration processing. Additionally, as $CaCO_3$ crystals precipitate, the size of pores is decreased, thereby inhibiting the accessing of CO_2 to interior parts of the material (Oliveira et al., 2017).

[1] Dr., T.R. Ministry of Culture and Tourism
[2] Assoc. Prof. Dr., Department of Chemical Engineering, Yildiz Technical University

In a study, as a preliminary work for restoration of the architectural heritage of the Meknes region (renders for the Historic City of Meknes and bedding mortars for Volubilis), it was investigated that the probability of brick waste recycling and its employ in aerial lime based mortars so as to enhance their qualities, particularly that natural hydraulic lime is insufficient in Morocco (Aalil et al., 2019).

In another study it has been studied that the practicability of a fluid catalytic cracking catalyst residue (FC3R) as an alternating sustained pozzolanic additive in aerial lime mortars (Arizzi & Cultrone, 2018). In a study carried out the mechanical and microstructure progresses of common aerial lime and sticky-rice mortars by accelerated laboratory tests was investigated (Zhang et al., 2020). It was stated that the purpose of a work conducted in the literature is to compare data from an analysis of historical mortar samples with data measured in a laboratory mortar (Frankeová & Koudelková, 2020). Various binder mixs have been generated and their mechanical qualities were compared with the qualities of similar conservation/restoration binders obtained from literature (Dimou et al., 2022).

There are very few analyzes with regards to ancient mortars of Harem buildings in the Topkapi Palace in literature, within this context the study targets to make contribution to the subject. First of all samples were described by visual examination. Samples were analysed by simple spot tests to determine protein, fat and water-soluble salt content. The $CaCO_3$ loss was detected by calcination test. The qualifications and ratios of aggregates of acid-treated mortars were specified by stereomicroscope. Thin sections were prepared from the ancient mortar samples and in-depth petrographic research was performed by a polarizing microscope to qualify the aggregate types.

Materials and method

Materials

35.5% hydrochloric acid (HCl), concentrate hydrogen peroxide (H_2O_2), para dimethylaminobenzaldehyde were bought from Sigma-Aldrich. Nitric acid (HNO_3), silver nitrate ($AgNO_3$) (technical-grade), barium chloride ($BaCl_2$), diphenylamine, concentrate sulfuric acid (H_2SO_4), copper sulphate ($CuSO_4$), concentrate ammonia (NH_3) solution were procured from Merck. Epoxy resin and hardener set was provided from RAKU-TOOL.

Visual examination

Sample 1: It is a solid mortar sample taken from the Room of the Master of the Stables (Seyis Odası), with white masses visible from place to place, bone-pink color, medium amount, small size, brick colored aggregates, and small pores up to 1 mm size. Photographs of the sample 1 are given in Figure 1.

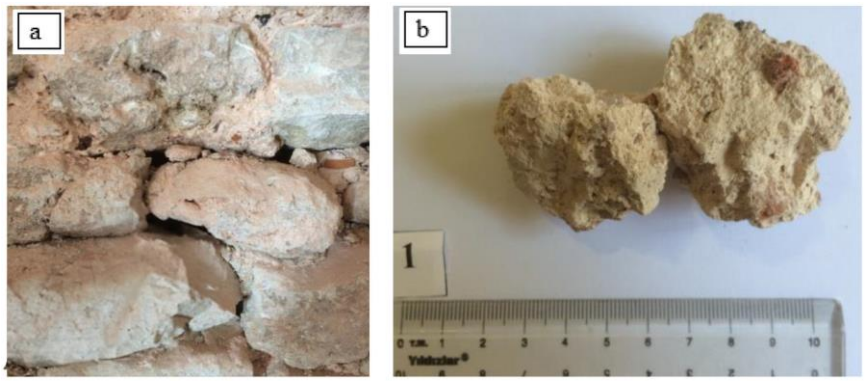

*Figure 1. The location of the sample taken from the Room of the Master of the Stables (Seyis Odası) on the work **(a)**, Visual examination in the laboratory **(b)***

Sample 2: It is a sample of medium strength mortar taken from the Music School (Meşkhane), in bone-pink color, with medium amount, small size, brick colored aggregates,

medium amount of pores up to 0.5 mm in size and white masses from place to place, with gray colored pollution on the surface. Photographs of the sample 2 are given in Figure 2.

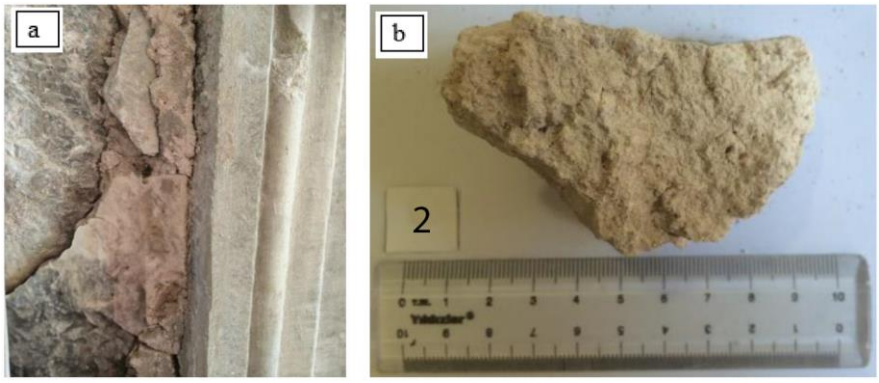

*Figure 2. The location of the sample taken from the Music School (Meşkhane) on the work **(a)**, Visual examination in the laboratory **(b)***

Sample 3: It is a solid jointing mortar sample taken from the Dressing Room, in cream-pink color, with medium amount of large sized brick and gray colored aggregates, medium amount of pores up to 1 mm in size and white masses from place to place. Photographs of the sample 3 are given in Figure 3.

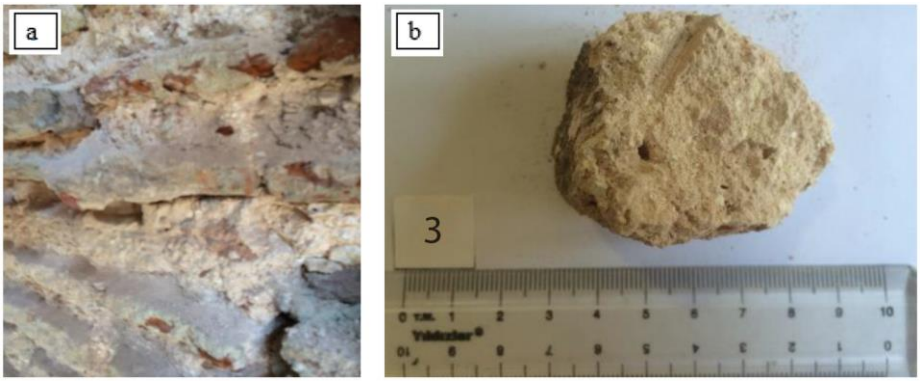

*Figure 3. The location of the sample taken from the Dressing Room on the work **(a)**, Visual examination in the laboratory **(b)***

Sample 4: It is a medium strength jointing mortar sample taken from the Hospital Toilet, in cream-pink color, with medium amount of large sized brick and gray colored aggregates, medium amount of pores up to 0.5 mm in size and white masses from place to place. Photographs of the sample 4 are given in Figure 4.

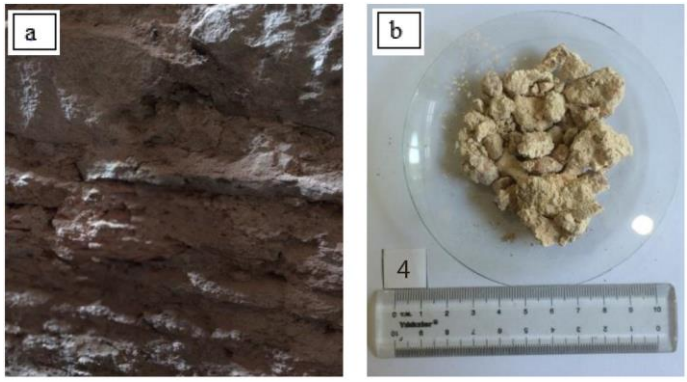

*Figure 4. The location of the sample taken from the Hospital Toilet on the work **(a)**, Visual examination in the laboratory **(b)***

Sample 5: It is a very solid jointing mortar sample taken from the Horse Ramp, in pink color, with medium amount of medium sized, brick colored aggregates, in small quantities pores up to 0.5 mm in size and white masses from place to place. Photographs of the sample 5 are given in Figure 5.

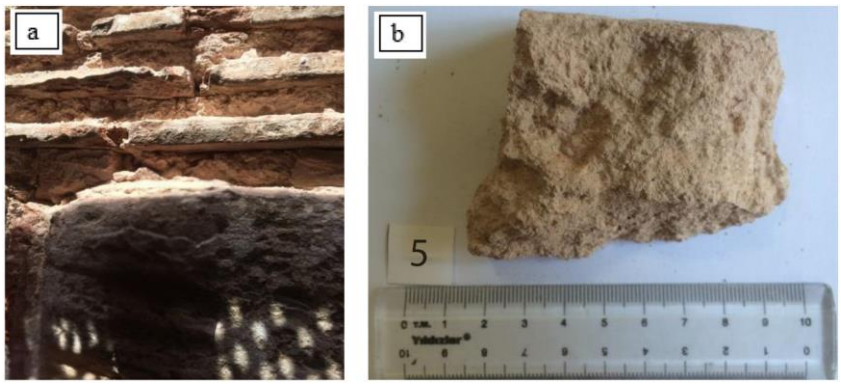

*Figure 5. The location of the sample taken from the Horse Ramp on the work **(a)**, Visual examination in the laboratory **(b)***

Sample 6: It is a sample of medium strength jointing mortar taken from the turning part of the Horse Ramp, in cream-pink color, with medium amount of large sized brick and gray colored aggregates, medium amount of pores up to 1 mm in size and white masses from place to place. It has gray colored pollution on it. Photographs of the sample 6 are given in Figure 6.

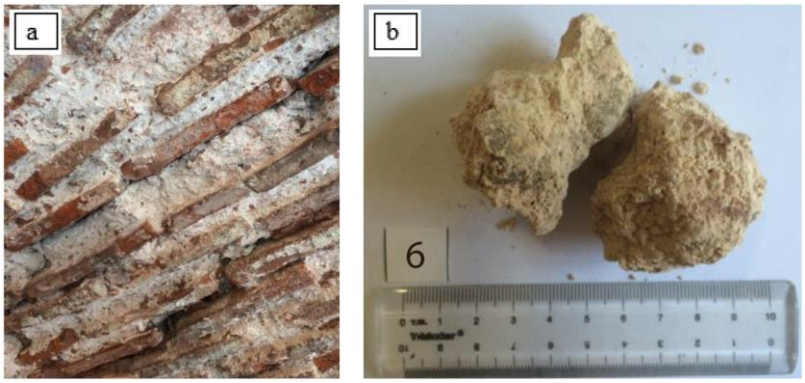

*Figure 6. The location of the sample taken from the turning part of the Horse Ramp on the work **(a)**, Visual examination in the laboratory **(b)***

Sample 7: It is a sample of medium strength jointing mortar taken from the Outer Wall of the Courtyard, in pink color, with medium amount of large sized brick and gray colored aggregates, with medium amount of pores up to 1 mm and white masses from place to place. Photographs of the sample 7 are given in Figure 7.

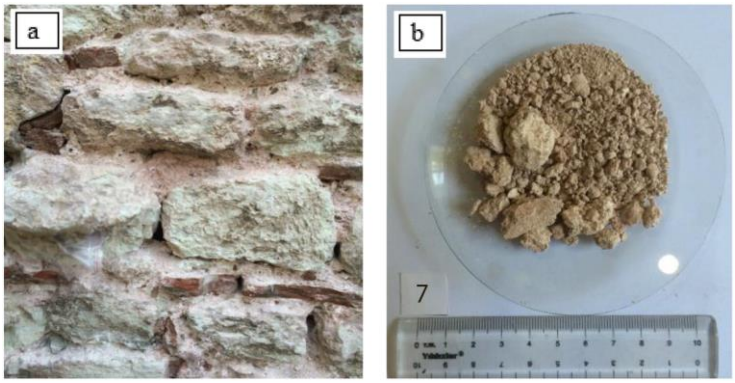

*Figure 7. The location of the sample taken from the Outer Wall of the Courtyard on the work **(a)**, Visual examination in the laboratory **(b)***

Sample 8: It is a weak mortar sample taken from the Courtyard Portico Vault, in pinkish-white color. Photographs of the sample 8 are given in Figure 8.

Figure 8. Visual examination of the sample taken from the Courtyard Portico Vault in the laboratory

Salt, protein and fat tests

Water-soluble salt tests

Firstly the mortar samples are powderized, after that 1 g of powder sample is taken and a mixture is prepared with 100 mL distilled water (Millipore, elix 10). The conductivity of the mixture, which was stirred with a glass stirrer at prespecified time intervals and kept for 48 h, was measured by a conductometer (WTW pH/cond 340i SET PORTABLE). Spot tests are then performed to determine the existence of water-soluble chloride (Cl^-), nitrate (NO_3^-), sulfate (SO_4^{2-}) salts.

Protein and fat analyzes

Protein and fat tests are performed to specify whether protein and/or fat-based materials are employed in the practises to the mortar and to identify the characteristics of the binder to be used in the conservation-restoration work.

Acid loss test

The dried beaker was tared (KERN, PFB 600-2M model) with an accuracy of 0.01 g and mentioned weight was recorded (W_0). Immediately after, nearly 20-30 g of mortar sample was put in the beaker and the weight was recorded (W_1) and the sample was dehydrated in an oven (Memmert, UM100) at 105ºC. Following the sample was cooled in the desiccator, it was weighed once again and its weight (W_2) was recorded. Later the weighing was finished off, about 25 mL of 10% hydrochloric acid (HCl) was added on the mortar sample and it was hold at the fume cupboard. This mixture is stirred by a glass stirrer at periodic intervals and HCl was put on it, and this processing was proceeded till the sample did not react with HCl. The upper solution was removed and the sample was neutralised with distilled water. Then, the remaining sample at the beaker was dehydrated at 105ºC for 4 h. The W_3 amount was specified by weighing the dry sample cooled in desiccator; moisture% and acid loss% were estimated using the following equation.

Calculation of per cent moisture:

$$\text{Moisture\%} = \frac{W_1 - W_2}{W_1 - W_0} \times 100 \qquad (1)$$

where;

W_0: Weight of dried beaker

W_1: W_0 + Sample

W_2: W_0 + Dried Sample

Calculation of per cent acid loss:

$$\text{Remainder\%}=\frac{W_3-W_0}{W_1-W_0}\times 100 \quad (2)$$

$$\text{Loss\%}=100-\text{Remainder\%} \quad (3)$$

where;

W_0: Weight of dried beaker

W_1: W_0 + Sample

W_3: W_0 + Dried sample remaining after acid loss

Sieve analysis

Following acid loss, the sample was firstly dehydrated at 105ºC till constant weight and thereafter cooled in a desiccator. Subsequently weighing, the samples were kept for sieve analysis. Afterwards the sieve analysis was performed, the weight was taken and the samples were packeted one by one in terms of sizes of aggregates and hold for microscope examination.

Calcination analysis

The per cent of contents such as moisture, molecular water, organic matter and calcium carbonate ($CaCO_3$) in the material were specified with the loss on ignition (calcination) analysis carried out on the powdered mortar samples by benefitting from the weight change at increasing temperatures.

Following taking the tare (W_d) of the dehydrated porcelain crucibles, nearly 1 g of powder mortar sample was weighed (SARTORIUS, CP224S model) and the weight value (W_0) was recorded. The mortar samples were hold in an oven at 105ºC for 4 h. The porcelain crucibles, that were removed from the oven and cooled in the desiccator, were weighed and their weight (W_1) was recorded, the realised weight loss was in connection with the moisture involved in the sample. Following this processing; the mortar samples were kept in the muffle furnace (Protherm, PLF 110/10) at 550ºC for half-hour. The mortar samples put in the desiccator were weighed afterwards cooling and the weighing data (W_2) were recorded. Mortar samples were kept in a muffle furnace at 1050ºC for 5 min. Following cooling, it was weighed (W_3) and the data were recorded. To compare and check obtained analysis conclusions, two experiments were carried out for every mortar sample. Using the results of calcination analysis, the quantity of moisture, molecular water and organic materials in the mortar sample, along with the quantity of carbon dioxide (CO_2) moved away the mortar sample and thereby the quantity of calcium carbonate ($CaCO_3$) were specified.

Estimating per cent moisture:

$$\text{Moisture\%}=\frac{W_0-W_1}{W_1-W_d}\times 100 \quad (4)$$

where:

W_d: Weight of dried crucible

W_0: W_d + Mortar sample

W_1: Weight of mortar sample dehydrated at 105°C

Calculating of molecular water and organic matter contents of the mortar sample:

$$\%=\frac{W_1-W_2}{W_1-W_d}\times 100 \qquad (5)$$

where:

W_d: Weight of dried crucible

W_1: Weight of mortar sample dehydrated at 105°C

W_2: Weight of mortar sample dried at 550ºC

Calculating of the quantity of $CaCO_3$ contained in the mortar sample:

$$CaCO_{3(s)} \xrightarrow{1050°C} CaO_{(s)}+CO_{2(g)} \qquad (6)$$

At 1050ºC, the calcium carbonate ($CaCO_3$) included in the mortar sample decomposed and gaseous carbon dioxide (CO_2) was moved away its constitution. The quantity of carbon dioxide (CO_2) was specified using the difference in the weight of the mortar sample, and the quantity of $CaCO_3$ in the mortar sample was estimated using these conclusions and the molar weights of the compounds in the reaction. The quantity of $CaCO_3$ in the mortar sample was calculated using the mole weights and weighing data in accordance with the above reaction, with the below ratio:

where;

$CaCO_3$ mole weight: 100 $g.mole^{-1}$

CO_2 mole weight: 44 $g.mole^{-1}$

W_d: Weight of dried crucible, g

W_0: W_d + Dried mortar sample weight, g

W_3: Weight of sample dried at 1050ºC, g;

If 44 g of CO_2 was contained in 100 g of $CaCO_3$,

How many g of $CaCO_3$ contain (W_0- W_3) g of CO_2

$$CaCO_3\%=\frac{\left[\left(W_0-W_3\right)\times 100\right]/44}{W_0-W_d}\times 100 \qquad (7)$$

Petrographical analysis

Thick section analysis

About 2x2 cm mortar sample was put in the mold along with the epoxy and accelerator mix.

Thin section analysis

The thin section is a part of mortar sample (0.030-0.005) mm thick and covered with a lamella, placed on a lame.

Results and discussion

Water-soluble salt and protein and fat analysis results

The experiments were carried out and the data obtained are shown in Table 1.

Table 1. Total water-soluble salt and protein and fat test results

Sample number	Cl^-	$SO_4^=$	NO_3^-	Conductivity (µs)	Salt%	Protein	Fat
1	±	-	-	82	0.5	+	-
2	±	-	-	95	0.5	+	-
3	++	-	++	603	3.4	-	-
4	++	-	+	244	1.4	-	-
5	±	-	+	162	0.9	-	-
6	+++	-	++	847	4.7	-	-
7	++	-	++	348	1.9	-	-
8	+	-	-	178	1.0	-	-

Very high content (++++), high content (+++), medium content (++), low content (+), extremely low content (±).

Calcination, acid treatment and sieve analysis

The results of calcination analysis of mortar samples at 105±5ºC (moisture), 550±5ºC (organic) and 1050±5ºC ($CaCO_3$), and the ratio of silicate aggregates which did not react and remained intact following acid treatment process and the size distribution of silicate aggregates are given in Table 2.

Table 2. Calcination, acid treatment and sieve analysis of mortar samples

Sample Number	Calcination (%)			In acid (%)		Sieve Remaining (%, µ)					
	105˚C	**550˚C**	**1050˚C**	**Loss**	**Remaining**	**2500**	**1000**	**600**	**250**	**125**	**<125**
1	1.73	4.26	59.04	71.24	28.76	11.87	35.21	5.45	5.84	12.06	29.57
2	1.07	5.05	59.13	69.39	30.61	7.19	32.46	12.28	14.04	18.25	15.79
3	5.63	7.93	53.03	62.31	37.69	38.04	20.47	6.64	12.45	9.13	13.28
4	2.83	6.36	66.04	62.13	37.87	62.91	10.58	1.51	1.79	7.69	15.52
5	1.05	3.48	25.52	32.49	67.51	0.00	13.25	11.81	46.31	16.45	12.19
6	6.53	6.59	58.15	65.86	34.14	38.39	28.38	5.92	5.61	5.77	15.93
7	2.95	6.43	44.64	62.51	37.49	0.00	30.18	9.33	10.70	24.69	25.10
8	1.32	4.92	67.84	76.72	23.28	0.00	10.73	33.33	15.75	21.00	19.18

Visual analysis of silicate aggregates

Sample 1: The aggregates of 125-1000 µ size remaining after treatment with acid of the sample are generally brick-colored. The aggregates of the sample are generally angular and under 6 mm sieve.

Sample 2: The aggregates of 125-1000 µ size remaining after the acid treatment of the sample are generally brick-colored, and the rest are white and black. The aggregates of the sample are generally angular and under 6 mm sieve.

Sample 3: The aggregates of 125-1000 µ size remaining after the acid treatment of the sample are generally brick-colored, while the rest are white and black. The aggregates of the sample are angular and under 8 mm sieve.

Sample 4: The aggregates of 125-1000 µ size remaining after the acid treatment of the sample are generally brick-colored, and the rest are white and yellow. The aggregates of the sample are angular, approximately 55-60% of them are 8-10 mm in size, the rest is under 6 mm sieve.

Sample 5: The aggregates of 125-1000 μ size remaining after the acid treatment of the sample are generally brick-colored. The aggregates of the sample are angular and under 4 mm sieve.

Sample 6: The aggregates of 125-1000 μ size remaining after the acid treatment of the sample are generally brick-colored. The aggregates of the sample are angular, approximately 30-35% of them are 8-10 mm in size, the rest is under 6 mm sieve.

Sample 7: The aggregates of 125-1000 μ size remaining after the acid treatment of the sample are generally brick-colored, and the rest are white and black. The aggregates of the sample are angular and under 6 mm sieve.

Sample 8: The aggregates of 125-1000 μ size remaining after the acid treatment of the sample are generally brick-colored. The aggregates of the sample are angular and under 7 mm sieve.

Petrographical analysis results

Thick section analysis

Sample 1: The remainder of the sample, which has a binding area is approximately 35 to 40%, is aggregate and freely dispersed minerals. Binder/binder and binder/aggregate phases of the sample are in good condition and have small pores up to 0.5 mm in size. Mentioned finding demonstrates that the mortar was considerably homogeneous during its production. A thick section photograph of sample 1 is given in Figure 9.

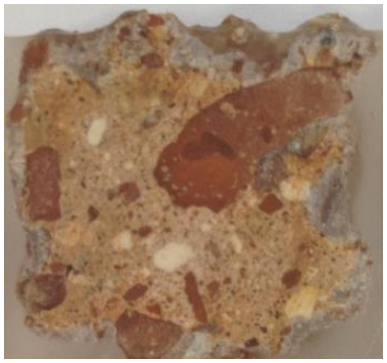

Figure 9. Thick section photograph of Sample 1

Sample 2: The remainder of the sample, which has a binding area is approximately 35 to 40%, is aggregate and freely dispersed minerals. Binder/binder and binder/aggregate phases of the sample are in good condition and have small pores up to 0.5 mm in size. A thick section photograph of sample 2 is given in Figure 10.

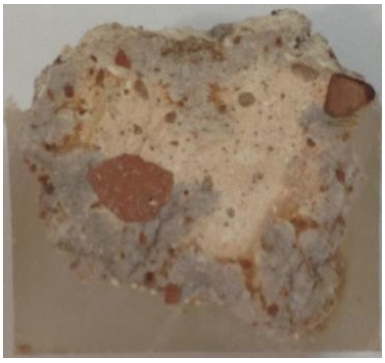

Figure 10. Thick section photograph of Sample 2

Sample 3: The remainder of the sample, which has a binding area is approximately 35 to 40%, is aggregate and freely dispersed minerals. The sample with a small amount of pores up to 0.5 mm in size has a good binder/binder phase and a relatively good binder/aggregate phase. A thick section photograph of sample 3 is given in Figure 11.

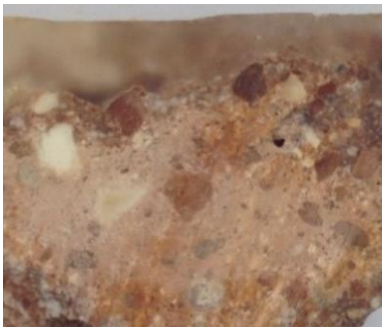

Figure 11. Thick section photograph of Sample 3

Sample 4: The remainder of the sample, which has a binding area is approximately 35 to 40%, is aggregate and freely dispersed minerals. Binder/binder and binder/aggregate phases of the sample are in good condition and have small pores up to 0.5 mm in size. A thick section photograph of sample 4 is given in Figure 12.

Figure 12. Thick section photograph of Sample 4

Sample 5: The remainder of the sample, which has a binding area is approximately 30 to 35%, is aggregate and freely dispersed minerals. Binder/binder and binder/aggregate phases of the sample are in good condition and have small pores up to 0.5 mm in size. A thick section photograph of sample 5 is given in Figure 13.

Figure 13. Thick section photograph of Sample 5

Sample 6: The remainder of the sample, which has a binding area is approximately 35 to 40%, is aggregate and freely dispersed minerals. Binder/binder and binder/aggregate phases of the sample are in good condition and have small pores up to 0.5 mm in size. A thick section photograph of sample 6 is given in Figure 14.

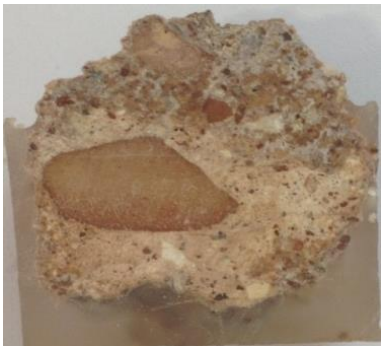

Figure 14. Thick section photograph of Sample 6

Sample 7: The remainder of the sample, which has a binding area is approximately 30 to 35%, is aggregate and freely dispersed minerals. The binder/binder and binder/aggregate phases of the sample, which has a medium amount of pores up to 0.5 mm in size, are in good condition. A thick section photograph of sample 7 is given in Figure 15.

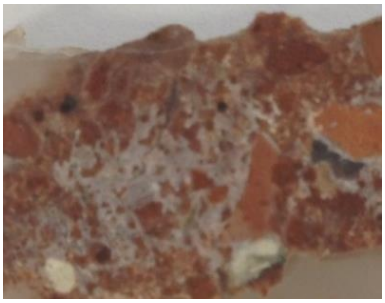

Figure 15. Thick section photograph of Sample 7

Sample 8: The remainder of the sample, which has a binding area is approximately 35 to 40%, is aggregate and freely dispersed minerals. Binder/binder and binder/aggregate phases of the sample are in relatively good condition and have small pores up to 0.5 mm in size. A thick section photograph of sample 8 is given in Figure 16.

Figure 16. Thick section photograph of Sample 8

Thin section analysis

Within the context of the thin section analysis, aggregate and mineral types in the samples 1, 4, 6, 7 and 8 were examined. Whole mortar samples had nearly similar contents and their contents are given in Table 3. In addition, whole mortar samples had same properties in respect to aggregate and mineral content. Sample 8 had the least amount of aggregate. Mortar samples 4 and 6 had contained less freely dispersed minerals than 7 and 8. Brick fragments and quartz mineral were the main components in the whole mortar samples. Whole mortar samples had included sandstone and feldspar mineral. In general, feldspar minerals were of the potassium feldspar (K-feldspar) character. Besides these, limestone, fossil shell, opaque minerals and lime lumps were detected in some of the mortar samples. The properties of the cement render and

mortar used for stone repair and/or substitution, as well as the efflorescence from the lower part of the Myszkowskis chapel façade were investigated. The cement mortar included round quartz grains, rock fragments, and feldspars in very fine-grained masses of calcite and gypsum, furthermore including remains of cement clinker (Marszałek, Dudek & Gaweł, 2020).

Table 3. Aggregate types in mortar samples

Sample Number	Type							
	Brick fragment	**Sandstone**	**Limestone**	**Quartz**	**Feldspar**	**Opaque mineral**	**Fossil shell**	**Lime lump**
1	+	+	+	+	+	+	-	+
4	+	+	+	+	+	+	-	+
6	+	+	+	+	+	+	-	+
7	+	+	+	+	+	-	-	+
8	+	+	-	+	+	+	-	+

Figure 17 displays the general view of the thin section of sample 1 under a polarizing microscope.

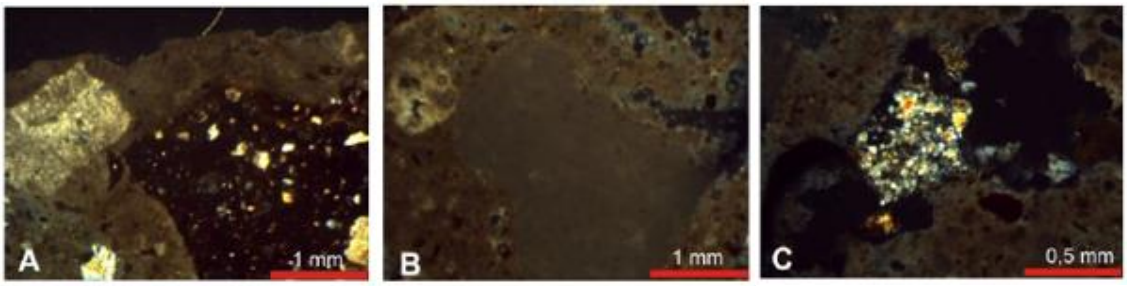

Figure 17. *General view of the thin section of sample 1 under a polarizing microscope. A. Brick fragment and limestone fragment (double nicol) found in sample 1. B. Lime lump (double nicol) found in sample 1. C. Sandstone fragment (double nicol) found in sample 1*

Content of the ancient mortars

Sample 1: The binder of the bone-pink colored solid mortar sample taken from the Room of the Master of the Stables (Seyis Odası) is 35-40% aerial lime (lime putty). It has been determined that the historical decorative lime plasters of Ellora caves, which date back to the 6–11th century A.D are comprised of weakly dolomitic lime binder (aerial lime) (Singh, Kumar & Waghmare, 2015). It is thought that the negligible amount of chlorine ($C\ell^-$) salt detected in the fat-free sample is caused by environmental pollution, and the protein is caused by the residuals of insects and similar biological livings. It has been expressed that the salty phases which stand for a number of the simultaneous reasons of mechanics and chemical deterioration in the host materials are fundamentally nitrates, carbonates and chlorides (Torrielli et al., 2016).

Sample 2: The binder of the bone-pink colored medium strength mortar sample taken from the Music School (Meşkhane) is 35-40% aerial lime (lime putty). The study related to the characterization of Cathedral mortars from Evora indicated that two kinds of aerial binders were used, dolomitic and calcitic limes, the first mentioned being dominant. It has been stated that the mortars were unlike in the aggregate content and, in some instances, crushed bricks were used as an addition agent (Adriano et al., 2009). It is thought that the protein detected in the fat-free sample is caused by the residuals of insects and similar biological livings. It has been expressed that several natural additives for example egg, milk, curds, whey, and blood involve a great quantity of proteins (Krizkova et al., 2014).

Sample 3: The binder of the cream-pink colored solid jointing mortar sample taken from the Dressing Room is 35-40% aerial lime (lime putty). Mortars taken from various masonry structures of the National Palace of Sintra (Portugal), constructed in different centuries, were researched. All analyzed mortars were lime based with calcium carbonate as main component of binder. Mortars had greatly diverse b:a ratios (1:1.2 to 1:4.4) (Ferreira Pinto, Sena da Fonseca & Vaz Silva, 2021). The aggregates were in siliceous structure. It is thought that the medium amount of chlorine ($C\ell^-$) salt detected in the fat and protein-free sample is caused by environmental pollution, and the medium amount of nitrate (NO_3^-) salt is caused by the wastes of insects and similar biological livings. It has been stated that a very-high content of nitrates was identified in the mortar samples of the North wall, attributed to the more intensive biological degradation on this side, the transportation of fertilizers through increasing moisture into the masonries, as well as the existence of an underground ossuary at close proximity to the north wall of the church (Apostolopoulou et al., 2017).

Sample 4: The binder of the cream-pink colored, medium strength jointing mortar sample taken from the Hospital Toilet is 35-40% aerial lime (lime putty). In a study, the compositional and textural characteristics of bedding mortars from rubble stone masonries of a historical building, built between 13th and 17th centuries and during different construction periods (National Palace of Sintra, Portugal) were examined. The binders are predominantly comprised of calcite originating in aerial lime carbonation and indications of low hydraulicity were observed in certain mortars. The aggregates are comprised of angular and sub-angular particles corresponding to minerals and mineral agglomerates from granitic rocks. The binder:aggregate (b:a) ratio by mass of mortars varies considerably, from 1:1.2 to 1:4.4, while the aggregates gradations have certain differences fundamentally regarding the content of coarser particles. Hierarchical clustering analysis let creating groups of mortars having similar textural characteristics. For this reason, three repair mortars possessing various textural characteristics were suggested: for interior walls, exterior walls/interior leaves and exterior walls/exterior leaves (Sena da Fonseca, Ferreira Pinto & Vaz Silva, 2020). It is thought that the small amount of nitrate (NO_3^-) salt detected in the fat and protein-free sample is caused by the wastes of insects and similar biological livings. It has been stated that the presence of nitrate salts at high levels in the walls is consistent with their high solubility (Nunes, Skružná & Válek, 2018).

Sample 5: The binder of the pink colored, very solid jointing mortar sample taken from the Horse Ramp is between 50-100 doses probably an early period cement-reinforced 20-25% lime hybrid mortar. It has been stated that the large quantity of cement reduce ductility and permeability of mortar, leading to damages to preserved constructions (Vasovic et al., 2021).

Sample 6: The binder of the cream-pink colored, medium strength jointing mortar sample taken from the turning part of the Horse Ramp is 35-40% aerial lime (lime putty). The mortar samples chosen from Ramappa Temple (Proposed UNESCO World Heritage), designated Site A and from two more Sites B and C (Kakatiya Dynasty Fort Temples) were analyzed. By X-ray diffraction analysis (XRD), existence of calcite and quartz mineral phases were recognized. This demonstrates binder either in the form of hydrated lime or slaked lime used along with siliceous aggregates for mortars (Degloorkar & Pancharathi, 2020). It is thought that the plenty amount of chlorine ($C\ell^-$) salt detected in the fat and protein-free sample is caused by the environmental pollution, and the medium amount of nitrate (NO_3^-) salt is caused by the wastes of insects and similar biological livings. It has been expressed that in case of destructive effects of the environment such as seawater, air-pollution, use of polluted materials, anionic salt crystals, namely chlorides, sulfates and nitrates, will form, and therefore, types of damage such as mortar decomposition, deeper cracks and draping of the mortar will occur (Arıoglu & Acun, 2006).

Sample 7: The binder of the pink colored, medium strength jointing mortar sample taken from the Outer Wall of the Courtyard is between 50-100 doses probably an early period cement-

reinforced 20-25% lime hybrid mortar. Several studies with regard to conservation practices in historic constructions indicates that lime-cement mortars should be avoided and lime-pozzolan mortars should be use alternatively (Pacheco-Torgal, Faria & Jalali, 2012). It is thought that the medium amount of chlorine ($C\ell^-$) salt detected in the fat and protein-free sample is caused by the cement binder, and the medium amount of nitrate (NO_3^-) salt is caused by the wastes of insects and similar biological livings. Porous construction materials, for instance mortar is prone to the penetration of moisture and degradation from salt crystallization. Increasing moisture takes place when ground moisture is drawn into mortar and masonry surfaces by capillary movement. Above ground level, water evaporates from the wall and the solution becomes more and more concentrated while still being subject to capillary rise. As the solution becomes saturated in the course of transportation much more evaporation will result in crystallisation and immobilisation of the salt (Lopez-Arce et al., 2009).

Sample 8: The binder of the pinkish-white colored, weak mortar sample taken from the Courtyard Portico Vault is 30-35% aerial lime (lime putty). Historical mortars at Alamparai fort with valley conical arch, Tamilnadu, India were analyzed. Binder (air lime): aggregate (river sand) (1:3) were used primarily with the organic additives of kadukkai and jaggery with the dosage of 12.5% to enhance the properties of the restoration mortar (Santhanam & Ramadoss, 2022). The small amount of chlorine ($C\ell^-$) salt detected in the fat and protein-free sample is thought to be caused by environmental pollution. It has been stated that chloride ions dissolved in water may form hydrochloric acid (HCl) or hypochlorous acid (HClO) which may also dissolve mortars components (Veiga & Silva, 2019).

Grouping of ancient mortars according to analysis results

The samples taken from the walls within the scope of "Istanbul Topkapi Palace Harem Buildings Restoration Work" can be classified into 4 groups according to the results of the analysis:

The binder of mortar sample 8, which is classified as the 1st group, is 30-35% aerial lime (lime putty). In Sample 8, under 7 mm sieve brick fragments were used as aggregate.

The binder of samples 4 and 6, classified as the 2nd group, is 35-40% aerial lime (lime putty). In sample 4, 55-60%, in sample 6, 30-35%, 8-10 mm brick gravel was added, and under 6 mm sieve brick fragments were used.

The binder of samples 1, 2 and 3, which are classified as the 3rd group, is 35-40% aerial lime (lime putty). Under 6 mm sieve brick fragments were used in samples 1 and 2, and under 8 mm sieve brick fragments were used in sample 3.

Binders of samples 5 and 7, which are classified as group 4 and contain brick fragments similar to group 3, are between 50-100 doses probably an early period cement (late 19th century, early 20th century) reinforced 20-25% lime hybrid mortar, in sample 5, under 4 mm sieve brick fragments, and in sample 7, under 6 mm sieve brick fragments were used.

Recommended formulas for repair mortars

For sample 8, it would be appropriate to use the following mixture:

1 part of hydrated and aged aerial lime (lime putty) (50% ± 2 aqueous),

2 part of limestone fracture and dust,

1 part of brick fragments and dust.

If the places where this group will be used has the characteristics of plaster, it would be appropriate to use under 5 mm sieve aggregates (brick fragments and limestone fracture and dust), and if has the characteristics of mortar, 25% of these aggregates should be used as brick gravel in sizes ranging from 7-10 mm.

In areas where Group 2 samples (samples 4 and 6) are present, the following repair mortar mix will be appropriate:

1 part of hydrated and aged aerial lime (lime putty) (50% ± 2 aqueous),

1 part of limestone fracture and dust,

1.5 parts of brick fragments and dust.

In the areas to be used as plaster, the aggregate size should be under 6 mm sieve, and in the areas to be used as mortar, 1 part of the aggregates should be 8-10 mm brick gravel, and 2 parts should be under 6 mm sieve brick fragments and dust.

In areas with samples in group 3 (for samples numbered 1, 2 and 3) it would be appropriate to use the following repair mortar mix:

1 part of hydrated and aged aerial lime (lime putty) (50% ± 2 aqueous),

1.5 parts of under 6 mm sieve limestone fracture and dust,

1.5 parts of under 6 mm sieve brick fragments and dust.

Conclusions

To follow the international charters telling that architectural heritage should be restored with traditional materials compatible to the original material – it must be known comprehensive knowledge in regard to the authentic material.

The mortar samples analyzed in this study and collected from the structures of Harem Buildings in Istanbul Topkapi Palace can be divided into four groups. The first, second and third groups comprises original (or likely-to-be) layer that are made only by aerial lime (lime putty). Finally, the fourth group of samples encompasses cases where a mixture of cement and lime binder is applied as a formulation.

Aggregates comprise of brick, sandstone, limestone, quartz, feldspars, opaque minerals, fossil shell and lime lump.

Concerning the distribution of chlorine, sulfate and nitrate salts in ancient mortars very small concentrations were detected in the samples collected.

Organic additives were partially added to the ancient mortars.

The exploitation of the results presented in this work can ensure the longevity of historical buildings.

Acknowledgements

The authors would like to commemorate colleagues and institution director at the Ministry of Culture and Tourism, Istanbul Restoration and Conservation Central and Regional Laboratory Directorate for their valuable contribution. The authors would like to thank the Assoc. Prof. Dr. Ahmet Güleç as overall scientific supervisor. The authors would like to thank the to the geologists in the petrographic laboratory for their petrographic analysis.

References

Aalil, I., Badreddine, D., Beck, K., Brunetaud, X., Cherkaoui, K., Chaaba, A., & Al-Mukhtar, M. (2019). Valorization of crushed bricks in lime-based mortars. *Construction and Building Materials, 226,* 555-563. Doi: 10.1016/j.conbuildmat.2019.07.265

Adriano, P., Santos Silva, A., Veiga, R., Mirão, J., & Candeias, A. E. (2009). Microscopic characterisation of old mortars from the Santa Maria Church in Évora. *Materials Characterization, 60* (7), 610-620. Doi: 10.1016/j.matchar.2008.11.008

Almeida, N. G. D., Faria, P., & Pinto, A. P. F. (2008). Lime mortars with rice husk ash for ancient masonry. *HMC08 - 1st Historical Mortars Conference: Characterization, Diagnosis, Conservation, Repair and Compatibility, LNEC*, 24-26 Sept 2008, Lisbon.

Apostolopoulou, M., Aggelakopoulou, E., Siouta, L., Bakolas, A., Douvika, M., Asteris, P. G., & Moropoulou, A. (2017). A methodological approach for the selection of compatible and performable restoration mortars in seismic hazard areas. *Construction and Building Materials, 155*, 1-14. Doi: 10.1016/j.conbuildmat.2017.07.210

Arıoglu, N., & Acun, S. (2006). A research about a method for restoration of traditional lime mortars and plasters: A staging system approach. *Building and Environment, 41*, 1223-1230. Doi: 10.1016/j.buildenv.2005.05.015

Arizzi, A., & Cultrone, G. (2018). Comparing the pozzolanic activity of aerial lime mortars made with metakaolin and fluid catalytic cracking catalyst residue: A petrographic and physical-mechanical study. *Construction and Building Materials, 184*, 382-390. Doi: 10.1016/j.conbuildmat.2018.07.002

Beşinci, B. B. (2023). Topkapı Sarayı Koğuş Yapıları, Yüksek Lisans Tezi, Yıldız Teknik Üniversitesi Fen Bilimleri Enstitüsü.

Degloorkar, N. K., & Pancharathi, R. K. (2020). Investigation of microstructure characterization of mortars from 800 years old heritage structures in Southern part of India. *Journal of Archaeological Science: Reports, 34,* 102634. Doi: 10.1016/j.jasrep.2020.102634

Dimou, A. E., Metaxa, Z. S., Kourkoulis, S. K., Karatasios, I., & Alexopoulos, N. D. (2022). Tailoring the binder matrix of lime-based binders for restoration interventions with regard to mechanical compatibility. *Construction and Building Materials, 315,* 125717. Doi: 10.1016/j.conbuildmat.2021.125717

Ferreira Pinto, A. P., Sena da Fonseca, B., & Vaz Silva, D. (2021). The role of aggregate and binder content in the physical and mechanical properties of mortars from historical rubble stone masonry walls of the National Palace of Sintra. *Construction and Building Materials, 268,* 121080. Doi: 10.1016/j.conbuildmat.2020.121080

Foster, G. (2020). Circular economy strategies for adaptive reuse of cultural heritage buildings to reduce environmental impacts. *Resources, Conservation and Recycling, 152,* 104507. Doi: 10.1016/j.resconrec.2019.104507

Frankeová, D., & Koudelková, V. (2020). Influence of ageing conditions on the mineralogical micro-character of natural hydraulic lime mortars. *Construction and Building Materials, 264,* 120205. Doi: 10.1016/j.conbuildmat.2020.120205

Kareeva, D., & Glazkova, V. (2017). Reconstruction and restoration of historical buildings of transport infrastructure. *IOP Conference Series: Earth and Environmental Science, Volume 90, Energy Management of Municipal Transportation Facilities and Transport - EMMFT 2017*, 10–13 Apr 2017, Far Eastern State Transport University, Russian Federation.

Krizkova, M. C., Kuckova, S. H., Santrucek, J., & Hynek, R. (2014). Peptide mass mapping as an effective tool for historical mortar analysis. *Construction and Building Materials, 50,* 219-225. Doi: 10.1016/j.conbuildmat.2013.09.059

Lopez-Arce, P., Doehne, E., Greenshields, J., Benavente, D., & Young, D. (2009). Treatment of rising damp and salt decay: The historic masonry buildings of Adelaide, South Australia. *Materials and Structures, 42,* 827-848. Doi: 10.1617/s11527-008-9427-1

Marszałek, M., Dudek, K., & Gaweł, A. (2020). Cement render and mortar and their damages due to salt crystallization in the Holy Trinity Church, Dominicans Monastery in Cracow, Poland. *Minerals, 10* (7), 641. Doi: 10.3390/min10070641

Nunes, C., Skružná, O., & Válek, J. (2018). Study of nitrate contaminated samples from a historic building with the hygroscopic moisture content method: Contribution of laboratory data to interpret results practical significance. *Journal of Cultural Heritage, 30*, 57-69. Doi: 10.1016/j.culher.2017.09.013

Oliveira, M. A., Azenha, M., Lourenço, P. B., Meneghini, A., Guimarães, E. T., Castro, F., & Soares, D. (2017). Experimental analysis of the carbonation and humidity diffusion processes in aerial lime mortar. *Construction and Building Materials, 148*, 38-48. Doi: 10.1016/j.conbuildmat.2017.04.120

Pacheco-Torgal, F., Faria, J., & Jalali, S. (2012). Some considerations about the use of lime–cement mortars for building conservation purposes in Portugal: A reprehensible option or a lesser evil?. *Construction and Building Materials, 30*, 488-494. Doi: 10.1016/j.conbuildmat.2011.12.003

Pavlík, Z., Pokorný, J., Pavlíková, M., Zemanová, L., Záleská, M., Vyšvařil, M., & Žižlavský, T. (2019). Mortars with crushed lava granulate for repair of damp historical buildings. *Materials, 12* (21), 3557. Doi: 10.3390/ma12213557

Santhanam, K., & Ramadoss, R. (2022). Conservation & restoration of historic mortars at Alamparai fort with valley conical arch, Tamilnadu, India. *Construction and Building Materials, 339*, 127619. Doi: 10.1016/j.conbuildmat.2022.127619

Sena da Fonseca, B., Ferreira Pinto, A. P., & Vaz Silva, D. (2020). Compositional and textural characterization of historical bedding mortars from rubble stone masonries: Contribution for the design of compatible repair mortars. *Construction and Building Materials, 247*, 118627. Doi: 10.1016/j.conbuildmat.2020.118627

Singh, M., Kumar, S. V., Waghmare, S. A. (2015). Characterization of 6–11th century A.D decorative lime plasters of rock cut caves of Ellora. *Construction and Building Materials, 98*, 156-170. Doi: 10.1016/j.conbuildmat.2015.08.039

Torrielli, G., Gaggero, L., Caratto, V., & Ferretti, M. (2016). Innovative method and apparatus for deep cleaning of soluble salts from mortars and lithic materials. *Energy Procedia, 97*, 523-530. Doi: 10.1016/j.egypro.2016.10.066

Vasovic, D., Terzovic, J., Kontic, A., Okrajnov-Bajic, R., & Sekularac, N. (2021). The influence of water/binder ratio on the mechanical properties of lime-based mortars with white portland cement. *Crystals, 11* (8), 958. Doi: 10.3390/cryst11080958

Veiga, M. D. R., & Silva, A. S. (2019). Long-term performance and durability of masonry structures. *Mortars* (pp. 169-208). Elsevier Ltd.

Zhang, Q., Li, B., Zeng, Q., Deng, J., Wang, J., & Yan, D. (2020). Erosion of aerial lime and sticky rice mortars by cyclic wetting–drying and dilute sulfate acid actions. *Advances in Cement Research, 32* (8), 343-357. Doi: 10.1680/jadcr.18.00103

Web Scraping and Machine Learning Techniques to Prediction of Secondhand Car Prices

Pınar CİHAN[1]
Enes CERRAHOĞLU[2]

Introduction

Automobiles are the second most purchased (or desired) asset after real estate. According to the research, it has been determined that the sales volume of second-hand cars in some countries is higher than the first-hand sales volume (Asilkan and Irmak, 2009).

According to the report of the Turkish Statistical Institute (TurkStat) dated January 26, 2022, when the number of vehicles registered to traffic is examined, it is seen that the number of cars is considerably higher than other vehicles (Tuik, 2021). The number of registered vehicles between December 2019 and December 2021 is given in Figure 1.

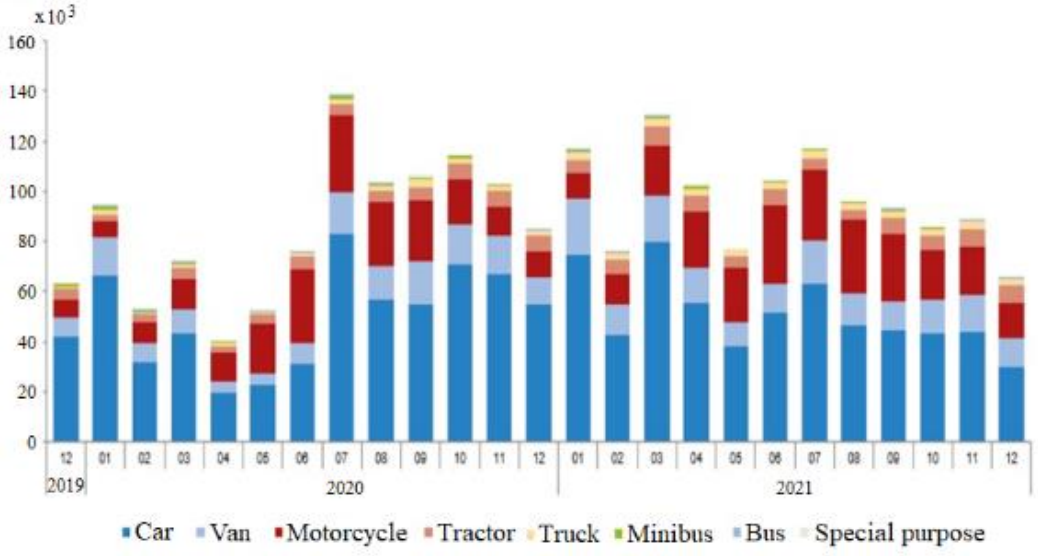

Figure 1. Number of registered vehicles (December 2019-December 2021)

In addition, when the number of motor land vehicles transferred in the TurkStat report is examined (Table 1), it is seen that cars are transferred more than other vehicles (Tuik, 2021).

Table 1. Number of handed-over motor land vehicles.

Year	Car	Minibus	Bus	Van	Truck	Motorcycle	Special purpose	Tractor
2020	6.477,155	81.898	5.312	1.486,762	07.439	510.743	12.002	293.629
2021	6.015,043	81.237	50.856	1.455,536	210.680	564.192	15.242	322.827

[1] Assoc. Prof., Tekirdağ Namık Kemal University
[2] Student, Tekirdağ Namık Kemal University

As is known, pricing is a complicated issue for both vehicle manufacturers and buyers/sellers. Developing a learning model based on the technical characteristics of the cars will allow both groups to price the cars easily (İşeri and Karlık, 2009).

In recent years, machine learning has given very successful results in many areas. Time series estimation (Cihan, 2022; Cihan, 2021), classification (Namlı et al, 2019), heuristic methods (Cihan and Özger, 2019), and regression (Cihan, 2022a; Cihan et al., 2019; Cihan et al., 2021) studies can be given as examples. Machine learning allows learning from data and making predictions by generalizing the learned information. Machine learning can be basically divided into supervised learning (classification/regression problems) and unsupervised learning (clustering problems). While the output of the available data is known in supervised learning, the outputs are not available in unsupervised learning. Compared to classical methods such as linear regression, machine learning methods are much more complex and can find meaningful outputs from large data. From this point of view, our study, it is aimed to make a used car price prediction using various information of cars.

The fact that there are too many vehicle sales advertisements on the websites directs the customers to the advertisement sites instead of the dealers. In this way, people can post advertisements for their cars from where they live, or they can examine the advertisements of the car they want to buy. Services such as not paying any commission when purchasing from websites, and free vehicle sales advertisements increase the demand for purchase/sale transactions from these websites.

Collecting data from websites and extracting the collected data is called web scraping. There is a lot of data on the websites. With web scraping, distributed data is collected properly and automatically. For this, the html code of the website to which data will be collected must be examined and a code block suitable for the site must be written. In this study, car features and prices were collected from websites that sell second-hand vehicles with web scraping and transferred to excel. Python Selenium was used for web scraping in the study. The aim of this study is to predict the prices of used cars based on car features. For this purpose, Python Selenium was used to create an up-to-date dataset. The estimation performances of the Decision Tree (DT), Gradient Boosting (GB), Linear Regression (LR), and Random Forest (RF) methods were compared according to the R^2 and MAE metrics. After determining the most successful method for estimation performance, the success of this method was tested with the independent test dataset.

Literature Review

Namlı et al. (2019), used artificial neural networks (ANN), Support Vector Machines (SVM), and linear regression methods to estimate the prices of used trucks. The dataset used in the study was taken from two different databases in 2013. The average dataset of 13000 vehicles was reduced to 1500 to facilitate analysis. The dataset consists of brand, brand group, type, model year, km, number of damages, condition of tires, air conditioning and price features. The metrics R^2, MAE, root absolute error (RAE), root relative square error (RRSE), root mean squared error (RMSE) and mean absolute percentage error (MAPE) were used to compare the success of machine learning methods. The findings obtained from the study showed that the SVM method was the most successful method with an accuracy rate of approximately 96% when 90% of the dataset was used for training and 10% for testing.

Narayana et al. (2021), aimed to estimate automobile prices between 2008 and 2009 using data from 2005-2007. In the study, systematically collected data for 3 years from about 40 websites that publish used car advertisements in various European countries were used. The raw data obtained were made suitable for analysis with various computer techniques and analysis methods. The dataset used includes the brand, model, model detail, case type, number of doors, and engine power features. Time series analysis and artificial neural network methods

were used for modeling. The estimation performances of these methods were compared according to MAE, MAPE, and RMSE criteria. In the study, 70%-30%, 80%-20%, and 90%-10% rates were tried for the training and test sets, respectively, and it was observed that the most successful results were obtained at the rates of 90%-10%. Artificial neural networks have made more successful predictions, with MAE, MAPE, and RMSE as 249.879, 1.502, and 315.837, respectively. As a result of the study, it has been reported that artificial neural networks give more successful results than time series estimation methods in used car price predictions.

Ecer (2013), aimed to make a second-hand vehicle price estimation with hedonic model and artificial neural network models by using automobile advertisements on websites in Turkey. In the study, a dataset of 640 cars from different brands and models was used randomly. The dataset includes km, engine power, engine volume, number of airbags, number of sensors, number of painted parts, number of changed parts, color, fuel type, body type, traction, air conditioning, gear, and seat type features. The hedonic model was preferred both for the purpose of revealing the determinants of used car prices and for achieving the purpose of price estimation, while the multi-layer perceptron was preferred especially for the purpose of price estimation. The prediction performances of the models were compared using MSE and RMSE criteria. In the study, the hedonic model was used to show how the characteristics of second-hand cars affect the price, and it was seen that the features that affect the price the most are brand, model, engine power, km, age, fuel type and traction type. Since hedonic functions have the potential to be nonlinear, ANN was used as an alternative to the hedonic model in the study and used car prices were estimated. The MSE and RMSE values for the hedonic model were 0.018 and 0.134, respectively, while these values were 0.006 and 0.078 for the multilayer perceptron model, respectively. According to the prediction performance results of the models, it has been reported that ANN makes better predictions than the hedonic model.

Daştan (2016) aimed to determine the factors affecting second-hand car prices in Turkey by using the hedonic price model. The dataset of the study consists of 1000 data obtained in October 2016. According to the results obtained from the study, make and model, age, traction, mileage, gear, fuel type, torque, width, fuel tank volume, ABS, hardtop, panoramic glass roof, rear window defroster, power steering, start/stop, color, net weight, height, number of painted parts, aux, lane change assist, driver airbag, roof airbag, bi-Xenon headlights, electric windshields, auto-dimming rearview mirror, heated steering wheel, backup camera, acceleration, length, replacement part It has been determined that the number of ABS, immobilizer, xenon headlight, fog light, headlight washer, sunroof, cooled glove box, and front view camera variables affect the price of the car. In this study, firstly, the relationships between the variables that are thought to be effective in second-hand car prices and second-hand car prices were investigated with the Pearson Chi-Square test. Then, three functional forms, linear, semi-logarithmic, and logarithmic, were analyzed by the least squares method in order to predict the hedonic model. The performances of these models were compared using the R^2 metric. As a result of the study, it was decided that the most successful model was the semi-logarithmic model.

İşeri ve Karlık (2009), used artificial neural networks to create a pricing model for automobiles. The dataset used in the study was taken from the Laboratory of Artificial Intelligence and Computer Science website. The dataset contains 159 samples and 16 properties of each sample (wheelbase, length, width, height, weight, engine displacement, cylinder bore, stroke size, compression ratio, horsepower, urban fuel consumption, extra-urban fuel consumption, and rpm number). 60% of the samples in the dataset were used for training, 20% for cross-validation, and the remaining 20% for testing. Levenberg-Marquardt method, one of the backpropagation methods, was used in the study. Model performance was evaluated according to R^2 and MSE metrics. When the network is trained for 900 epochs with the Levenberg-Marquardt backpropagation function, the MSE value is 3.42329e−3, for training

1.67505e−2 for validation, and 1.66757e−2 for testing. In addition, the R^2 was found to be approximately 0.89.

Web Scraping and Machine Learning

Web Scraper

In this study, data was collected from the web portal arabam.com, one of the most used car buying/selling websites in Turkey. Selenium library, which can also work with Python programming language, was used for Web Scraper. Selenium is an open source, flexible library used to extract data from websites [15]. The code block of the libraries used to collect the data from the web portal and transfer it to the excel environment is given in Figure 2.

```
from selenium import webdriver
from time import sleep
import pandas as pd
import matplotlib.pyplot as plt
import seaborn as sns
from selenium.webdriver.support.ui import WebDriverWait
from selenium.webdriver.common.by import By
from selenium.webdriver.support import expected_conditions as EC
from selenium.webdriver.common.keys import Keys
import openpyxl
```

Figure 2. Code block for web scraper libraries

With the web scraper, 10.702 car features were collected for 10 different brands (Audi, BMW, Fiat, Ford, Hyundai, Mercedes-Benz, Renault, Skoda, Toyota, and Volkswagen) in January 2023. These features are advertisement number, date of advertisement, brand, series, model, year, km, gear, fuel, case type, engine volume, engine power, traction, and price. The code block part developed for this process is presented in Figure 3.

```
driver = webdriver.Chrome(executable_path="D:/chromedriver.exe")

brand = "volkswagen"

sleep(1)

cars = []
for x in range(1, 1000, 1):
    driver.get("https://www.arabam.com/ikinci-el/otomobil/%s?take=50&page=%s" % (brand, x))
    table_id = driver.find_element(By.ID, 'main-listing')
    rows = table_id.find_elements(By.TAG_NAME, "tr")
    for row in rows:
        if(row.get_attribute('id') != None and str(row.get_attribute('id')) !=  ""):
            sleep(1)
            driver.execute_script("window.open('%s', '_blank')" % row.find_elements(By.TAG_NAME, "td")[0].find_elements(By.TAG_NAME, "a")[0].get_attribute('href'))
            driver.switch_to.window(driver.window_handles[1])
            sleep(1)
            car = Car()

            try:
                car.ilan_no = driver.find_element(By.XPATH, '//*[@id="js-hook-for-observer-detail"]/div[2]/ul/li[1]/span[2]').text.strip()
                car.ilan_tarihi = driver.find_element(By.XPATH, '//*[@id="js-hook-for-observer-detail"]/div[2]/ul/li[2]/span[2]').text.strip()
                car.marka = driver.find_element(By.XPATH, '//*[@id="js-hook-for-observer-detail"]/div[2]/ul/li[3]/span[2]').text.strip()
                car.seri = driver.find_element(By.XPATH, '//*[@id="js-hook-for-observer-detail"]/div[2]/ul/li[4]/span[2]').text.strip()
                car.model = driver.find_element(By.XPATH, '//*[@id="js-hook-for-observer-detail"]/div[2]/ul/li[5]/span[2]').text.strip()
                car.yil = driver.find_element(By.XPATH, '//*[@id="js-hook-for-observer-detail"]/div[2]/ul/li[6]/span[2]').text.strip()
                car.km = driver.find_element(By.XPATH, '//*[@id="js-hook-for-observer-detail"]/div[2]/ul/li[7]/span[2]').text.strip()
                car.vites = driver.find_element(By.XPATH, '//*[@id="js-hook-for-observer-detail"]/div[2]/ul/li[8]/span[2]').text.strip()
                car.yakit = driver.find_element(By.XPATH, '//*[@id="js-hook-for-observer-detail"]/div[2]/ul/li[9]/span[2]').text.strip()
                car.kasa_tipi = driver.find_element(By.XPATH, '//*[@id="js-hook-for-observer-detail"]/div[2]/ul/li[10]/span[2]').text.strip()
                car.motor_hacmi = driver.find_element(By.XPATH, '//*[@id="js-hook-for-observer-detail"]/div[2]/ul/li[11]/span[2]').text.strip()
                car.motor_gücü = driver.find_element(By.XPATH, '//*[@id="js-hook-for-observer-detail"]/div[2]/ul/li[12]/span[2]').text.strip()
                car.çekiş = driver.find_element(By.XPATH, '//*[@id="js-hook-for-observer-detail"]/div[2]/ul/li[13]/span[2]').text.strip()
                car.fiyat = driver.find_element(By.XPATH, '//*[@id="js-hook-for-observer-detail"]/div[2]/div[1]/div/span').text.split("TL")[0].strip()
            except:
                pass

            cars.append(car)
            print("Number of cars: ", len(cars))
            driver.close()
            driver.switch_to.window(driver.window_handles[0])
    sleep(1)
driver.close()
df = pd.DataFrame([x.as_dict() for x in cars])
df.to_excel('%s.xlsx' % (brand))
```

Figure 3. Python code snippet for scraping car information from the web portal

The advertisement information, which was taken one by one with Selenium, was transferred to the excel environment using the code block in Figure 4.

```
[ ]  # df.to_excel('dataset.xlsx')

     def append_df_to_excel(df, excel_path):
         df_excel = pd.read_excel(excel_path)
         result = pd.concat([df_excel, df], ignore_index=True)
         result.to_excel(excel_path, index=False)

     append_df_to_excel(df, 'dataset.xlsx')
```

Figure 4. Collection of scraped data in excel environment

In order for the obtained dataset to be used in model development, conversion processes were applied to the characteristics of brand, series, fuel type, gear type, case type, engine power, and these are as follows.

Brand:

Audi = 1 | BMW = 2 | Fiat = 3 | Ford = 4 | Hyundai = 5 | Mercedes Benz = 6 | Renault = 7 | Skoda = 8 | Toyota = 9 | Volkswagen = 10

Series:

Audi A1 = 1 | A3 = 2 | A4 = 3| Volkswagen Arteon = 901 | Golf = 902 | Polo = 903 etc.)

Fuel type:

Gasoline = 1 | Diesel = 2 | LPG & Gasoline = 3 | Hybrid = 4 | Electric = 5

Gear type:

Manual = 1 | Semiautomatic = 2 | Automatic = 3

Car type:

Sedan = 1 | Station Wagon = 2 | Hatchback/5 = 3 | Cabrio = 4 | Coupe = 5 | Hatchback/3 = 6 | MPV = 7 | Roadster = 8

Motor Power (hp) and Engine Capacity (cc): if the engine power and engine volume information are specified with a range, the average of the range was taken.

After preprocessing steps were applied to the raw dataset, the number of samples in the dataset was reduced to 10596 and the number of features was reduced to 10 (brand, series, year, km, gear, fuel, body type, engine volume, engine power, price).

In the study, the dataset was divided into three parts 80% (for training) and -20% (for testing) to predict car prices. In addition, 10 advertisement information for each brand, a total of 100 advertisement information was used as an independent test dataset. In this way, the prediction performance of the developed model will be verified. In the study, after the Decision Tree, Gradient Boosting, Linear Regression, and Random Forest methods were trained with the training dataset, their prediction performance was measured with the test set. These methods are briefly explained below and the Python codes of each model are presented.

Decision Tree

Decision Tree is used for both classification and regression in machine learning. When used for regression, they are called regression trees. This model analyzes the variables in the data and creates the decision tree diagram according to the data. It separates the data into different categories by choosing the feature that can make the best discrimination at each node. The mean of the data at the end nodes is used as the predictive value for that node (Quinlan,

1986). The decision tree is frequently used because it is an easy-to-understand and easy-to-implement method, but there may be a risk of overfitting according to the data. One of the methods developed in this study for used car prediction is the decision tree. The Python code of the decision tree method is presented in Figure 6. After 20% of the dataset was reserved for testing, the training process of the decision tree was carried out. By giving test data to the learning model, the predicted prices of the cars and their actual prices were compared and the MAE and R^2 metrics were measured. The decision tree code block fragment used in the study is presented in Figure 5.

```
X_train, X_test, y_train, y_test = train_test_split(features, target, test_size=0.2)
model = DecisionTreeRegressor()
model.fit(X_train, y_train)
y_pred = model.predict(X_test)
mae = mean_absolute_error(y_test, y_pred)
print("Mean Absolute Error:", mae)
accuracy = model.score(X_test, y_test)
print("Accuracy:", accuracy)
```

Figure 5. Python code block for Decision Tree

Gradient Boosting

Another regression method used in machine learning is the Gradient Boosting model. This model aims to make predictions on the data by combining many small tree models. Each tree model aims to correct the prediction errors of previous tree models. Gradient boosting is a method in which new models are created that calculates the error in the previous model and then the residuals are added to make the final estimate (Touzani et al., 2018). Gradient Boosting heavily considers the outcome of each tree model to provide the best prediction performance. This method can offer high accuracy on the data, but the model may become overly specialized. The Python code of the Gradient Boosting method is given in Figure 6.

```
X_train, X_test, y_train, y_test = train_test_split(features, target, test_size=0.2)
model = GradientBoostingRegressor(n_estimators=49, random_state=49)
model.fit(X_train, y_train)
y_pred = model.predict(X_test)
mae = mean_absolute_error(y_test, y_pred)
print("Mean Absolute Error:", mae)
accuracy = model.score(X_test, y_test)
print("Accuracy:", accuracy)
```

Figure 6. Python code block for Gradient Boosting

Linear Regression

One of the regression methods developed for prediction in the study is the Linear Regression model. This model uses a line slope to determine the relationship between data. The model aims to find a line slope that best reflects the relationship between data points. This line expresses the slope as an equation that describes the relationship between the data. Linear Regression offers a simple and fast estimation of the data, but estimation errors may occur if the relationship between the data is not properly linear. The Python code of this method is given in Figure 7.

```
X_train, X_test, y_train, y_test = train_test_split(features, target, test_size=0.2)
model = LinearRegression()
model.fit(X_train, y_train)
y_pred = model.predict(X_test)
mae = mean_absolute_error(y_test, y_pred)
print("Mean Absolute Error:", mae)
accuracy = model.score(X_test, y_test)
print("Accuracy:", accuracy)
```

Figure 7. Python code block for Linear Regression

Random Forest

Random Forest is an ensemble learning method and is a machine learning model that is often preferred in solving problems due to its success. This model aims to make predictions on the data by combining many decision trees. Each tree model is trained on randomly selected features and the results are averaged to make predictions. This method aims to predict more accurately on the data and also reduces the risk of data overfitting. The Python code used in the study of this method is given in Figure 8.

```
X_train, X_test, y_train, y_test = train_test_split(X.values, y.values, test_size=0.2, random_state=7)
model = RandomForestRegressor(n_estimators=49, random_state=49)
model.fit(X_train, y_train)

y_pred = model.predict(X_test)
accuracy = model.score(X_test, y_test)
print("Accuracy:", accuracy)
```

Figure 8. Python code block for Random Forest

Comparison of Model Performances

To evaluate the prediction performance of machine learning regression models, it is measured how much the predicted value and the actual value overlap. In this study, R^2 and MAE metrics were used to compare the prediction accuracy of the models. R^2 and MAE are calculated as in Equation 1 and Equation 2, respectively (Cihan et al., 2021).

$$R^2 = 1 - \frac{\sum_i (a_i - p_i)^2}{\sum_i (a_i - \bar{a})^2} \quad (1)$$

$$MAE = \frac{1}{n}\sum_{i=1}^{n} a_i - p_i \quad (2)$$

Here, n is the number of data, a is the actual value, p is the predicted value, and $\bar{a}$ is the actual value mean.

Results

After the dataset obtained by the web scraper was brought into a format in which machine learning regression methods can be applied, second-hand car price estimation was made with Decision tree, Gradient Boosting, Linear Regression, and Random Forest methods. The prediction performances of these methods were compared with the MAE and R^2 statistics. The MAE and R^2 results of four different machine learning regression methods developed for used vehicle price estimation are given in Table 2.

Table 2. Comparison of the prediction performances of the methods.

Method	**MAE (TL)**	**R^2**
Decision Tree	72.032	0.9170
Gradient Boosting	107.978	0.9311
Linear Regression	337.968	0.5155
Random Forest	55.154	0.9780

When the models whose training process was completed were tested with 20% of the dataset, the random forest method made the most successful predictions with approximately 98% accuracy and 55.154 MAE values. While the random forest method is followed by gradient boosting with an accuracy of 93%, it is seen that the estimation error of the linear regression method is quite high.

Car prices were predicted with 100 independent test datasets using the RF method, which makes the most successful predictions, and some of the results are given in Table 3.

Table 3. Prediction results for the independent test dataset of the RF method.

#	Brand	Series	Year	Km	Gear Type	Fuel Type	Case Type	Engine Capacity	Engine Power	Actual Price (TL)	Predict Price (TL)
1	Audi	A6	2020	87.000	Semiautomatic	Diesel	Sedan	1968	204	2.750.000	2.839.994
2	BMW	3 Serisi	2012	284.000	Automatic	Gasoline	Sedan	1997	184	647.000	606.602
3	Fiat	Tipo	1998	257.500	Manual	LPG & Gasoline	Hatchback/5	1372	70	123.750	118.799
4	Ford	Focus	2008	150.303	Manual	Diesel	Sedan	1560	110	300.000	311.732
5	Hyundai	Accent Blue	2013	75.500	Automatic	Diesel	Sedan	1582	128	430.000	428.851
6	Mercedes - Benz	C	2010	197.000	Automatic	Gasoline	Sedan	1597	156	730.000	647.688
7	Renault	Megane	2017	190.000	Semiautomatic	Diesel	Sedan	1461	110	500.000	525.832
8	Skoda	Favorit	1993	254.000	Manual	LPG & Gasoline	Hatchback/5	1289	57	72.000	69.464
9	Toyota	Corolla	2006	372.000	Manual	LPG & Gasoline	MPV	1598	110	225.000	235.694
. . .	. . .	. . .	. . .	. . .	. . .	. . .	. . .	. . .	. . .	. . .	. . .
100	Volkswagen	Golf	2010	153.000	Manual	Gasoline	Hatchback	1390	122	409.500	395.566
									AVG.	**512737.5**	**518747.3**

As seen in Table 3, brand, series, year, km, gear type, fuel type, case type, engine capacity, and engine power of the cars were given as input to the RF model, and the car price was predicted by the RF model. It is seen that the actual price average of 100 cars and the predicted price averages are quite close to each other.

Discussion and Conclusion

The automotive industry represents a globally significant market with a thriving secondhand car sector in Turkey. In this context, sellers aim to achieve profitable sales, whereas buyers seek high-performance-to-price ratios, resulting in a constantly fluctuating market. To address this challenge, this study aims to collect current data from second-hand vehicle sales websites through web scraping and utilize machine learning techniques to predict car prices based on their features. The study collected up-to-date data using Python Selenium from the website with the highest number of advertisements in Turkey. The study employed various prediction models, such as decision tree (DT), gradient boosting (GB), linear regression (LR), and random forest (RF).

Developing a successful prediction model based on the technical properties of cars is critical for both used car buyers and sellers, as it can assist in determining a fair price for a vehicle. The objective of this study is to estimate the price of cars based on their features using

machine learning methods. Up-to-date data was collected from a web portal using web scraping techniques. The initial dataset consisted of 10,702 advertisements from 10 different brands, including 14 features. After preprocessing, the dataset was reduced to 10,596 data points, with 10 attributes remaining (brand, series, year, km, gear type, fuel type, case type, engine capacity, engine power, and price). This dataset was utilized for training, testing, and independent testing. When comparing the price prediction performances of different models, R2 value and MAE statistics were used. The Random Forest (RF) method was identified as the most successful model, with an accuracy of 98%, while linear regression exhibited an accuracy of approximately 52%. The prediction performance of the RF model was further validated using an independent test dataset. The average predicted price of the RF model was 518,747 TL, while the average selling price for the independent test dataset was 512,737 TL. The results of this study demonstrate that up-to-date data collected with a web scraper can be successfully used to price cars with the RF method.

REFERENCES

Asilkan, Ö., Irmak, S. (2009). İkinci El Otomobillerin Gelecekteki Fiyatlarının Yapay Sinir Ağları İle Tahmin Edilmesi. Süleyman Demirel Üniversitesi İktisadi ve İdari Bilimler Fakültesi Dergisi, 14(2), 375-391.

Cihan, P. & Özger, Z.B. (2019). A new heuristic approach for treating missing value: ABCIMP. Elektronika ir Elektrotechnika, 25(6). DOI: 10.5755/j01.eie.25.6.24826

Cihan, P. (2021). Forecasting fully vaccinated people against COVID-19 and examining future vaccination rate for herd immunity in the US, Asia, Europe, Africa, South America, and the World. Applied Soft Computing, 111, 107708. DOI: 10.1016/j.asoc.2021.107708

Cihan, P. (2022). Impact of the COVID-19 lockdowns on electricity and natural gas consumption in the different industrial zones and forecasting consumption amounts: Turkey case study. International Journal of Electrical Power & Energy Systems, 134, 107369. DOI: 10.1016/j.ijepes.2021.107369

Cihan, P. (2022a). The machine learning approach for predicting the number of intensive care, intubated patients and death: The COVID-19 pandemic in Turkey. Sigma Journal of Engineering and Natural Sciences, 40(1), 85-94. DOI: 10.14744/sigma.2022.00007

Cihan, P., Gökçe, E., Atakişi, O., Kirmizigül, A. H. & Erdoğan, H. M. 2021. Prediction of immunoglobulin G in lambs with artificial intelligence methods. Kafkas Universitesi Veteriner Fakultesi Dergisi, 27(1). DOI: 10.9775/kvfd.2020.24642

Cihan, P., Ozel, H. & Ozcan, H. K. (2021). Modeling of atmospheric particulate matters via artificial intelligence methods. Environmental Monitoring and Assessment, 193, 1-15. DOI: 10.1007/s10661-021-09091-1

Daştan, H. (2016). Türkiye'de ikinci el otomobil fiyatlarini etkileyen faktörlerin hedonik fiyat modeli ile belirlenmesi, Gazi Üniversitesi İktisadi ve İdari Bilimler Fakültesi Dergisi, 18(1), 303-327.

Ecer, F. (2013). Türkiye'de 2. El Otomobil Fiyatlarının Tahmini ve Fiyat Belirleyicilerinin Tespiti, Anadolu Üniversitesi Sosyal Bilimler Dergisi, Cilt: 13, Sayı: 4.

İşeri, A. & Karlık, B. (2009). An artificial neural networks approach on automobile pricing. Expert Systems with Applications, 36(2), 2155-2160.

Namlı, E., Ünlü, R. & Gül, E. (2019). Fiyat Tahminlemesinde Makine Öğrenmesi Teknikleri ve Doğrusal Regresyon Yöntemlerinin Kıyaslanması; Türkiye'de Satılan İkinci El Araç Fiyatlarının Tahminlenmesine Yönelik Bir Vaka Çalışması. Konya Mühendislik Bilimleri Dergisi, 7(4), 806-821. DOI: 10.36306/konjes.654952

Narayana, C. V., Likhitha, C. L., Bademiya, S., & Kusumanjali, K. (2021). Machine Learning Techniques To Predict The Price Of Used Cars: Predictive Analytics in Retail Business. In 2021 Second International Conference on Electronics and Sustainable Communication Systems (ICESC) (pp. 1680-1687). IEEE.

Rai, B. K., Verma, R. & Tiwari, S. (2021). Using open source intelligence as a tool for reliable web searching. SN Computer Science, 2(5). DOI: 402. 10.1007/s42979-021-00777-4

Touzani, S., Granderson, J., & Fernandes, S. (2018). Gradient boosting machine for modeling the energy consumption of commercial buildings. Energy and Buildings, 158, 1533-1543.

TUİK (2021). Motor Vehicles. 20/02/2023 tarihinde https://data.tuik.gov.tr/Bulten/Index?p=Motorlu-Kara-Tasitlari-Aralik-2021-45703 adresinden ulaşılmıştır).

Post-Earthquake Rapıd Damage Determınatıon From Satellıte Photos Usıng Image Processıng Technıques: Case Study On Hatay Antakya

Taner ÇARKIT[1]

1. Introduction

Since the formation of the world, many different types of disasters have occurred throughout history and continue to do so. This also applies to Turkey, which is at the crossing point of the continents and is affected by continental movements. Many factors such as Turkey's geographical location, global warming and people reveal the risk of natural disasters. Disaster management and crisis management in disaster situations require knowledge from engineering science and many different disciplines. One of the important points among this information requirement is to reach up-to-date and correct information as soon as possible and to monitor information changes continuously. To meet this need, it is important to analyze the images obtained from satellites, which is one of the possibilities offered by today's technologies, in terms of spectral, temporal and spatial analysis and transfer them to the methods.

It is of great importance to reach accurate and up-to-date information in a short time in the studies to be carried out before, during and after the disaster. After the disaster, it is possible to determine the dimensions of the disaster and to determine the situation with remote sensing data in coordination. Especially, time series created from satellite images are important in instant damage assessment studies before and after the disaster (ITU, 2023a). It becomes possible to determine the changes that occur in the regions by examining the temporal changes with the selection of appropriate data and image processing methods (Alzubade & et al., 2021). In addition, roads closed due to destruction, areas where earthquake tents are set up, places where container cities are established, and fractures on the surface for fault line tracking can also be determined.

There are two important bottlenecks in the use of satellite photographs in image processing applications. The first bottleneck is the presence of climatic cloudiness covering a wide area in the region and the inaccessibility of usable data due to unsuitable weather conditions. The second factor is the suitability of using the same image after confirmation by different satellites to increase accuracy. On the other hand, different methods such as radar technology are also used to determine the deformations caused by earthquake effects (Ertren & Rossi, 2019).

In the current literature, studies dealing with similar and different methods related to this paper can be summarized as follows: In the study of Nagy (Nagy, 1972), data and images obtained from satellites have been processed and used for the determination of earth resources such as mines, oil, forests, and water. The methods that can be applied to derive geographic information from motion images of the Earth through image processing methods have been determined by using satellite data in the general research conducted by Tholey (Tholey, 2000). In Kusakabe et al.'s study (Kusakabe & Sanada, 2004), the data obtained with the help of remote sensing sensors have been analyzed with image processing technology and it has been aimed to detect rapid damage after an earthquake. The ability of digital aerial images to detect various damages caused by earthquakes has been emphasized in Yamazaki et al.'s paper (Yamazaki,

[1] Dr., Kırklareli University

Suzuki & Maruyama, 2008). The images of before and after the earthquake have been subjected to both pixel-based classification and object-based classification. The wreckage of collapsed buildings has been identified using digital image processing. In Singh et al.'s investigation (Singh & Verma, 2015), damage detection has been aimed by analyzing satellite images before and after the earthquake with image processing techniques. In the study by Joshi et al. (Joshi & et al., 2017), a different study has been was intended apart from the usual analysis of before and after images of earthquake and tsunami events. For the cases where pre-earthquake data have not available, only post-earthquake data have been processed for damage assessment. Image segmentation and image classification methods were used in the study. In Korkmaz et al.'s research (Korkmaz & Abualkibash, 2018), damage detection has been aimed by processing images based on comparison before and after the earthquake. In Aali et al.'s study (Aali, Sharifi & Malian, 2019), satellite images have been used to efficiently determine the size and extent of damaged areas after a devastating event such as an earthquake. The pre- and post-event images have been classified using a neural network and a support vector machine. The urbanization rate has been examined by using 92 satellite images obtained for the same region over a 3-year period in Erten et al.' analysis (Ertren & Rossi, 2019). In Alzubade et al.'s research (Alzubade & et al., 2021), the effects of events as a result of climate change on the environment have been analyzed. The effects of observed climate variability on land use and land cover have been investigated by remote sensing methods. In the research process, Pearson correlation analysis and regression coefficient, which are two different statistical analysis methods, have been used in addition to the methods specific to the study areas. In Kocaaslan et al.'s paper (Kocaaslan, Musaoglu & Karamzadeh, 2021), satellite images have been analyzed with image processing methods to perform regional drought analysis. Takhtkeshha et al.'s study (Takhtkeshha, Mohammadzadeh & Salehi, 2023), a new method based on deep learning has been proposed for rapid building damage detection after an earthquake. One-epoch convolutional autoencoder is used to extract deep features from non-deep features. Extreme gradient boosting (XGB), decision trees algorithm, adaBoost-and a basic deep learning algorithm (multi-layer perceptron), k-nearest neighbors, support vector machine, random forest, gradient boosting are implemented to obtain building damage maps. In Rao et al.'s work (Rao & et al., 2023), a framework is presented for the assessment of damage caused by earthquakes in remote sensing data and other additional datasets using machine learning algorithms. Surface level changes have been determined by comparing the images before and after the earthquake. Classification methods have been used for the analysis of damaged buildings. The model has been able to successfully identify more than 50% or almost half of the damaged buildings while using the binary classification for three of the four earthquakes studied.

In this paper, the data obtained from the satellite images of the earthquake region have been scanned and transferred to image processing methods for the purpose of contributing to disaster and crisis management in a technological sense. One of the main aims of this study is to provide information support for rapid reaction after an earthquake. In the images, completely destroyed or heavily damaged buildings have been detected. By determining the collapsed or tilted buildings, the damage rate of the region in general has been determined.

2. Earthquake Technical Information of the Region

The statistical values of the earthquakes that occurred in Turkey from the beginning of the 2000s to March 2023 are shown in Fig. 1 (AFAD, 2023b). As can be seen from the graph, the number of earthquakes in the first three months of 2023 is abnormally higher than in other years. On the other hand, when the statistical data specific to the earthquake region are investigated, 224 earthquakes with a magnitude of over 4.0 moment magnitude (Mw), the largest of which were 6.0 Mw, have occurred from 1900 to 6 February 2023. In addition, there are 75 historical period earthquake records for the region before 1900 (AFAD, 2023a).

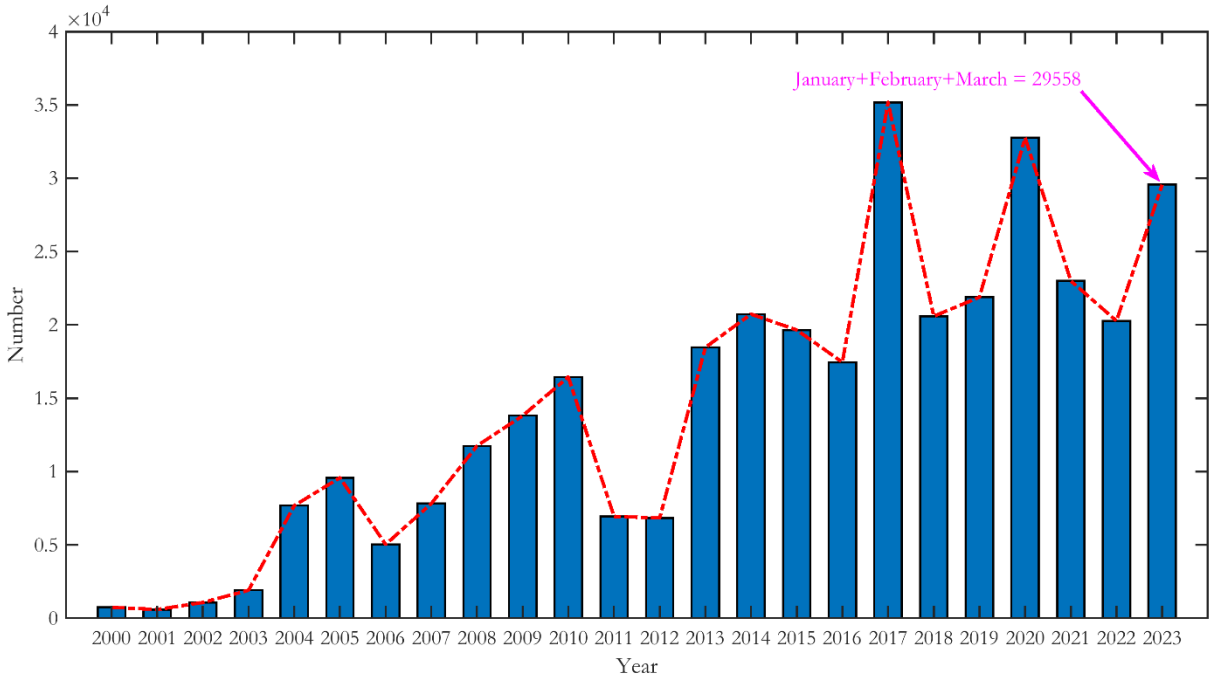

Figure 1. *Earthquake statistics after 2000*

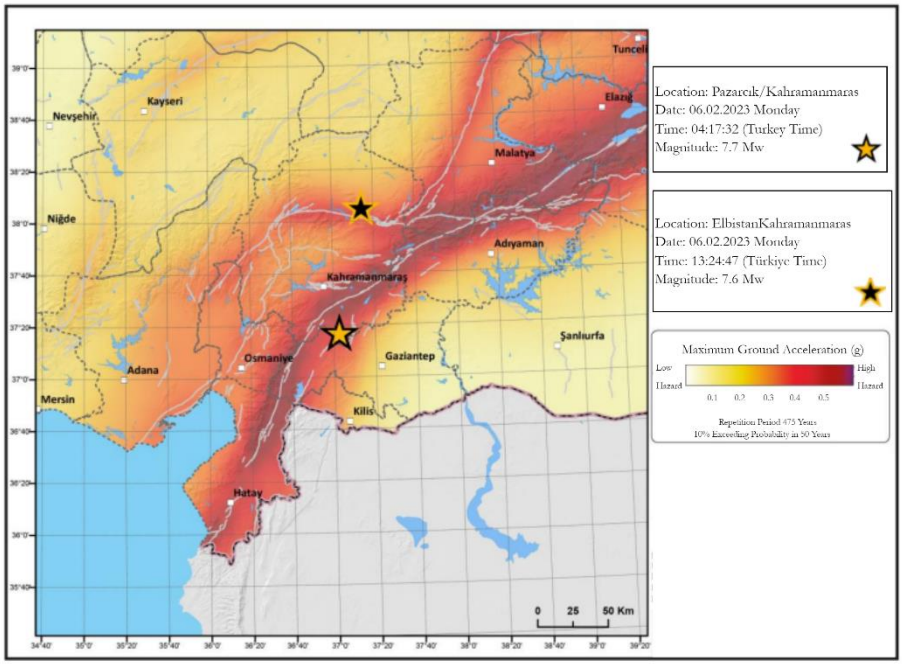

Figure 2. *Earthquake hazard of the region according to Türkiye Earthquake Hazard Map*

According to the Turkey Earthquake Hazard Map, the earthquake hazard of the region is shown in Fig. 2 (AFAD, 2023c). The yellow stars correspond to the epicenters of the 7.7 Mw and 7.6 Mw earthquakes occurred on 6 February 2023 (BOUN, 2023). The provinces affected by the earthquake in Turkey are shown in Fig. 3 (ITU, 2023b). The starting points of both earthquakes affecting Hatay Antakya, which is located in the risky area for the earthquake event and examined by this study, can be seen in the fault extension of the region (AFAD, 2023a). The mentioned earthquakes have been felt in a wide geography including Lebanon, Cyprus, Iraq, Israel, Jordan, Iran, and Egypt as well as Turkey and Syria. Two major earthquakes caused damage in an area of approximately 350.000 km^2. These earthquakes affected 14 million people, 16% of Turkey's population (Url-1, 2023).

Figure 3. *Provinces affected by the earthquake in Turkey*

In line with this information, the effects of the earthquake (The epicenter of the earthquake, which has teken place on 6 February 2023 at 04:17 and 13:24 Turkish time, is Pazarcık and Elbistan districts of Kahramanmaraş province. The magnitude of the earthquake was 7.7-7.8 Mw and 7.6-7.7 Mw (AFAD, 2023d)), which has been recorded the literature in terms of size, damage rate, and impact area on the Antakya/Hatay have been examined. This natural event has caused many reinforced concrete buildings to collapse and become debris. Many parameters are effective in the destruction of destroyed buildings. The most prominent ones are (ITU, 2023a):

- Age of buildings,
- Low bearing capacity of the floors on which the foundations sit,
- Inadequate quality of materials used in construction,
- Insufficient dimensions and reinforcement amounts of columns and beams,
- The structural elements have not been constructed in accordance with the regulations in force in the years they were built,
- Other construction defects,
- Issues such as different floor levels of buildings constructed in adjacent order are seen as the most obvious causes of demolition.

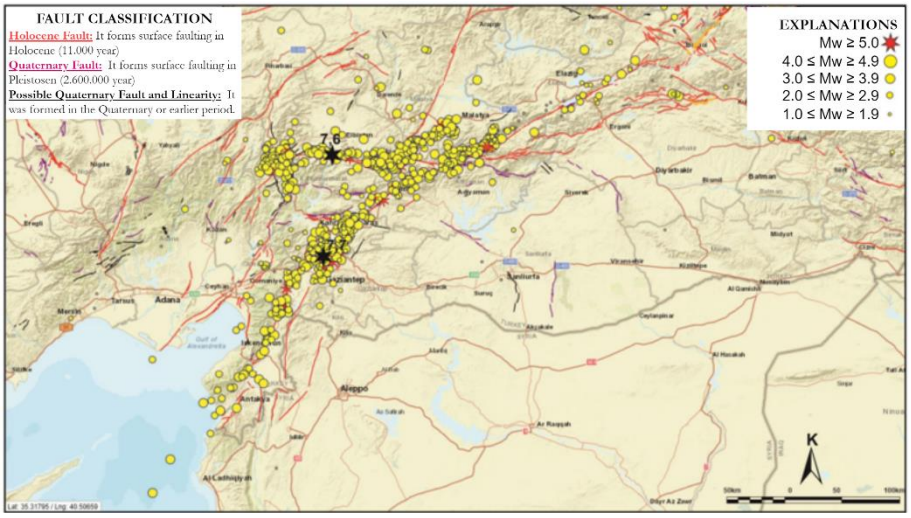

Figure 4. *Aftershocks (Emre & et al., 2013; AFAD, 2023e)*

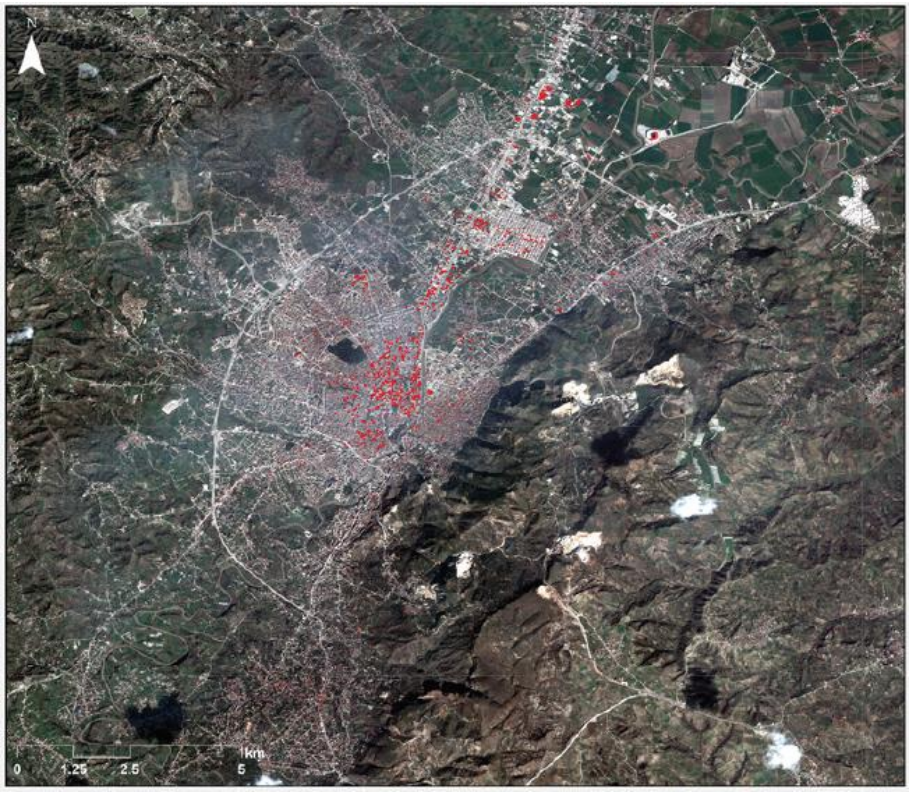

Figure 5. *Map showing the completely destroyed structures in and around the central district of Hatay according to the first determinations (Red: Destroyed structures)*

During these earthquakes, which damaged a large area, after 6 February 2023, more than 3000 aftershocks occurred in the region as seen in Fig. 4 (MTA, 2023). On the other hand, more than 11000 aftershocks have occurred in the region to date (Url-2, 2023). As of 16 February 2023, after the disaster, preliminary damage has been determined in 481865 buildings within the scope of damage assessment studies carried out by Ministry of Environment, Urbanisation and Climate Change throughout the regions affected by the earthquake. Among these damaged structures, there are 61722 buildings that have been demolished or are about to be demolished, and their ratio in the overall number is 12.8%. 13917 of the damaged structures have been determined as moderately damaged and its rate has been 2.8%. Considering the heavily damaged and moderately damaged structures, the rate of buildings that have been uninhabitable after earthquakes is 15.6%. Within the scope of the examinations carried out by the official institution, it has been determined that 121515 buildings, corresponding to 25.2%, have slightly been damaged. In addition, the rate of undamaged structures is 47.5%, corresponding to 229023 structures.

68116 buildings have been examined to determine the situation throughout Hatay. 29188 buildings have been undamaged (provincial-wide rate 42.8%), 17212 buildings have slightly been damaged (provincial-wide rate 25.2%), 2827 buildings have moderately been damaged (provincial-wide rate 4.1%), 15248 buildings have heavily been damaged or completely destroyed (provincial-wide rate 22.3%) in Hatay. On the other hand, the number of collapsed buildings determined from the existing satellite images for the center of Hatay and its surroundings as of the same date has been determined as 1760 (ITU, 2023b). In Antakya, which is the district of Hatay that has most affected by the earthquake, 5382 buildings have been examined. 2619 buildings, corresponding to 48.6% of this number, have been determined to be demolished immediately, heavily damaged or demolished (Url-3, 2023). According to the rapid preliminary investigation reports submitted by some institutions, the map showing the completely destroyed structures in and around the central district of Hatay according to the first determinations is given in Fig. 5. In figure, collapsed buildings are shown in red. In addition,

the collapsed building density can be seen in Fig. 6 (ITU, 2023a). If the color change in the density map is taken into account, the number of destroyed buildings increases as they approach the district center.

3. Image Processing

Digital images consist of the interaction of energy by transferring it to a hardware in a measurable way. Digital image processing (DIP) studies are a broad subject. Image processing technology can be used with many different algorithms or different disciplines to become more effective depending on where it is used. In the 1960s and later, at the Jet Propulsion Laboratory, Massachusetts Institute of Technology, Bell Laboratories, Maryland University, and several other places many topics (Satellite image, medical imaging, image transmission over telephone wires, video transmission over telephone cables, character recognition and image enhancement applications…etc.) in the DIP field have been developed.

DIP applications in the field of image processing have expanded their usage area frequently and at low cost, thanks to the fast computers and signal processors that have found use with the developing technology after the 2000s. DIP, which can be considered as a sub-field of digital signal processing, has many advantages over analog image processing. DIP allows wide use of algorithms to be applied to the input information. In addition, DIP can get rid of problems such as noise and signal distortion throughout the process. The mentioned noise and distortions can be eliminated by applying different filtering methods on the image(Dincer, 2009).

In this study, satellite images have been used to determine the damage of 7.7-7.8 Mw and 7.6-7.7 Mw earthquakes in Pazarcık and Elbistan/Kahramanmaras province in Antakya region of Hatay. The satellite image (597x600x3) of the pre-earthquake and post-earthquake, which is used for damage assessment in this study, is shown in Fig. 7. The difference image obtained by superimposing both images is also in the same image. The figure shows the unfiltered state of destruction rates between 0-100 (0: solid, 100: completely destroyed). The slightest difference in this image, aid vehicles, aid tents, and containers are considered demolition. Therefore, data above a certain damage value or above a certain pixel density should be taken as destruction.

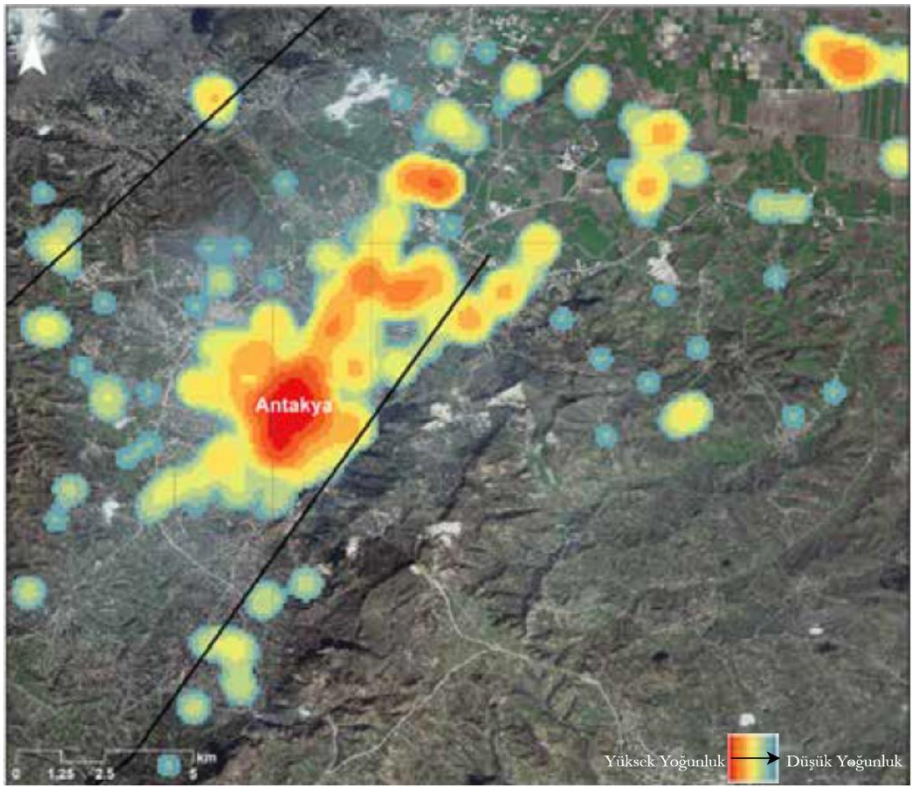

Figure 6. *Density of collapsed buildings in and around the center of Hatay*

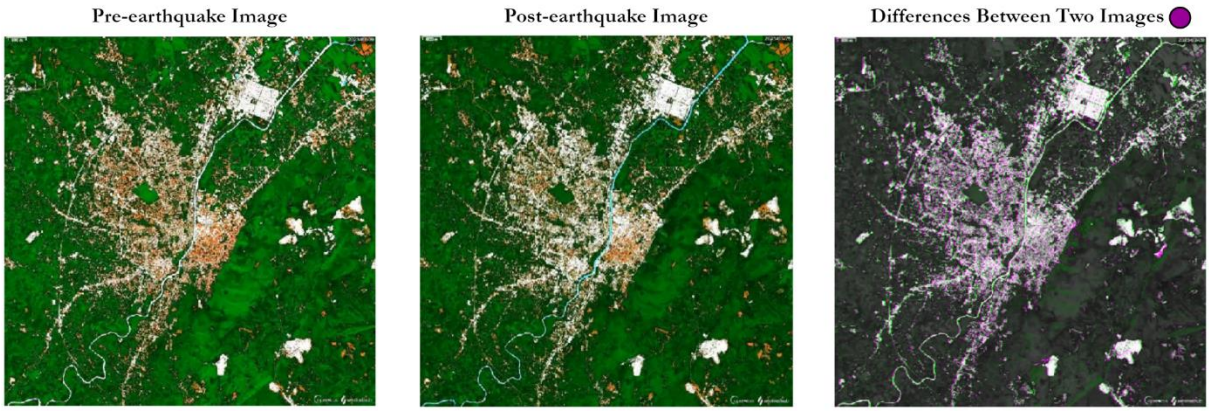

Figure 7. *Satellite image before and after the earthquake*

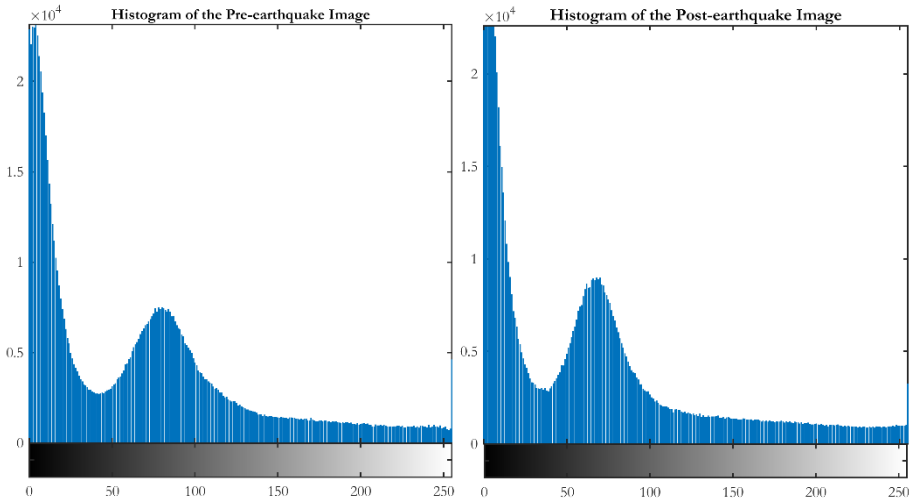

Figure 8. *Pixel density (histogram) graph of the satellite image before and after the earthquake*

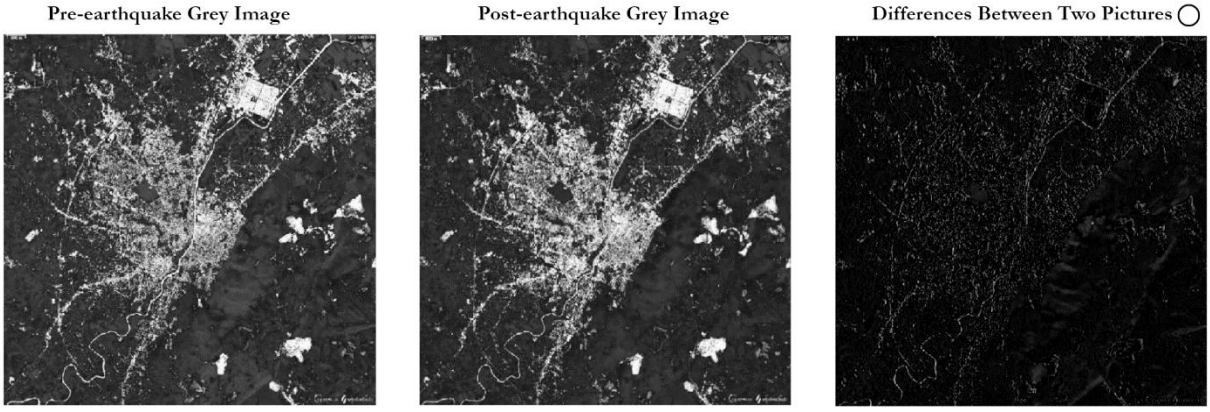

Figure 9. *Black and white image before and after the earthquake*

The data expressing the pixel density graph (histogram) of the images of both dates are given in Fig. 8. Pixel densities have been collected below 150 because the region has green-dominated vegetation and because of the satellite support that provides the data. The black and white (gray) version of the images given in Fig. 7 is given in Fig. 9. The unfiltered difference between the gray images of both dates can also be seen in Fig. 9. Similar to the difference image in Fig. 7, data above a certain damage value should be taken as destruction. Or, the presence of edge detection support for the detection of debris boundaries of collapsed structures are

developments that will increase accuracy. The pixel density of the presented gray image is concentrated in the 50s as seen in the histogram graph in Fig. 10.

The graphic version of the original gray colored satellite image (597x600x1) of the pre-earthquake and post-earthquake dates is given in Fig. 11. As can be seen, the data difference between both dates is presented in Fig. 12. This situation represents destroyed buildings. In the image in Fig. 13, the difference obtained after the intervention to increase the clarity on the image can also be seen.

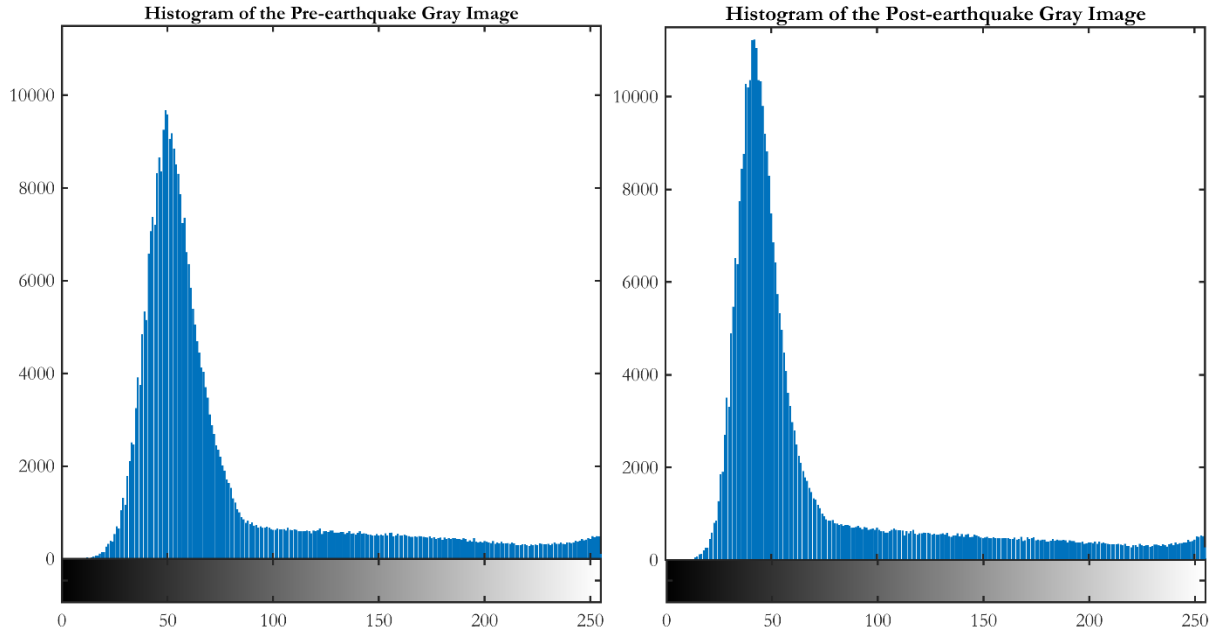

Şekil 10. *Deprem öncesi ve sonrası görüntünün gri görüntünün histogram verisi*

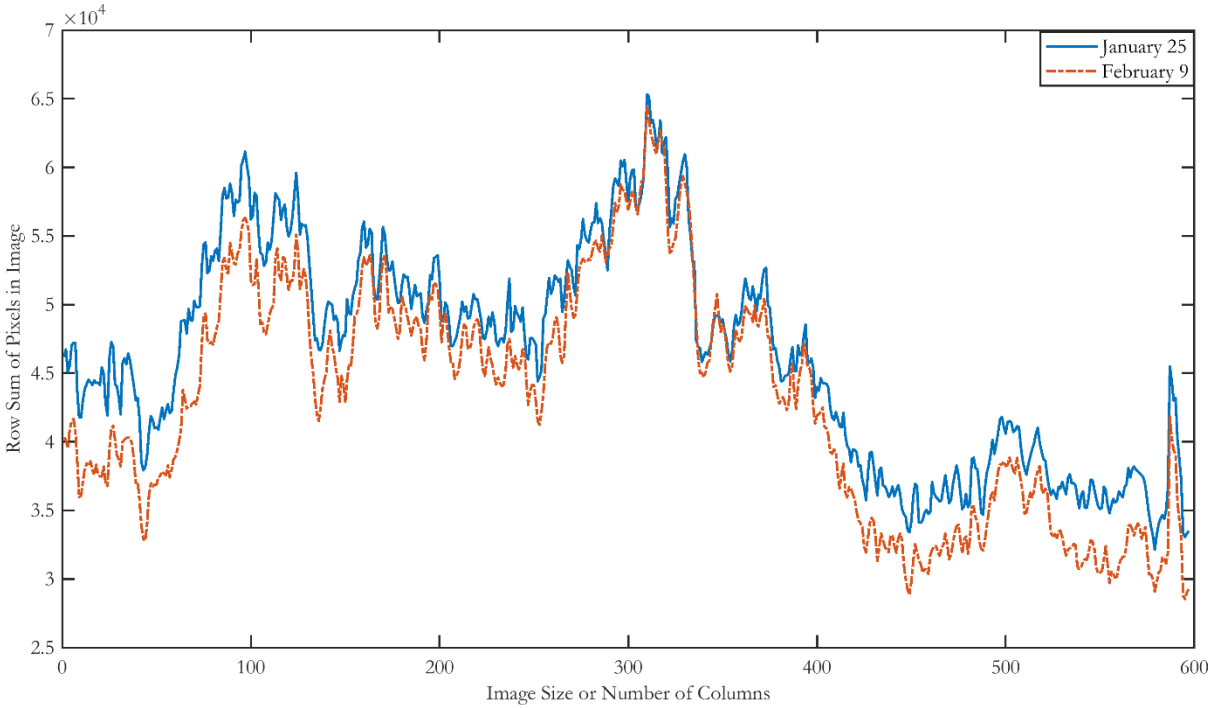

Figure 11. *Gray images*

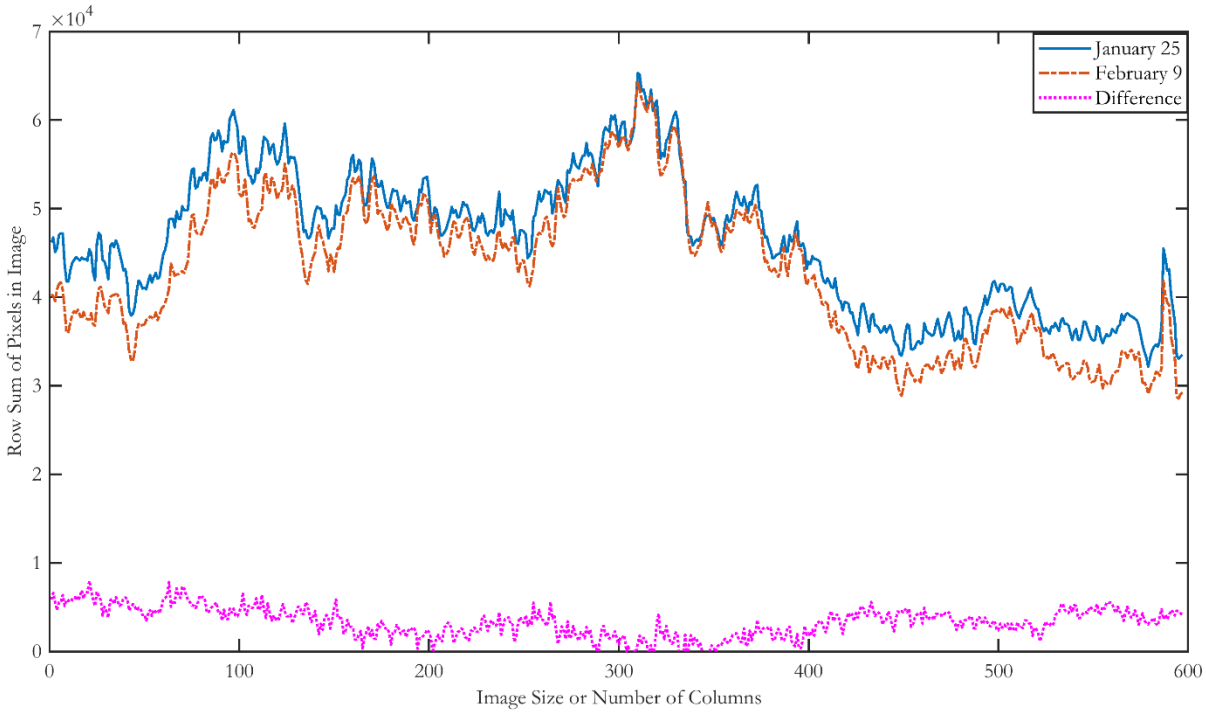

Figure 12. *The difference between gray images and*

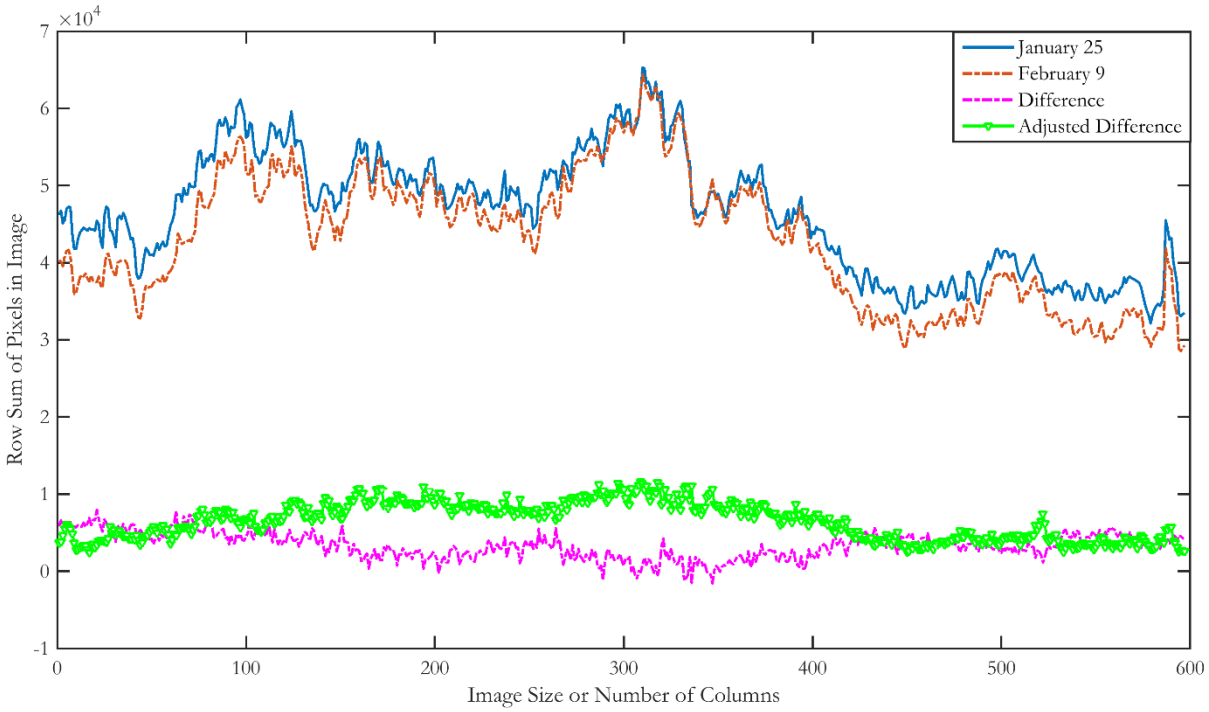

Figure 13. *The main images in gray color and the difference of the adjusted state*

According to real data, the rate of buildings that will be demolished urgently, heavily damaged or demolished is 48.6%. In this case, the proportion of completely collapsed and tilted buildings is less than this value. According to the situation reported in the satellite image given in Fig. 5, the rate of collapsed buildings was determined as 32%. In the study, the damage rate obtained from only the gray image without pixel limitation and filtering is approximately 20%. On the other hand, the damage rate including the structures damaged by 60% or more is 55%. The damage rate, including structures damaged by 70% or more, was determined as 21%.

4. Conclusion and Discussion

In the process when rapid information is needed right after disasters, many institutions/organizations or researchers need to work to produce the same information from these data. This situation causes loss of labor and time. It is important to analyze the natural events that recorded the world literature and affect Turkey in every aspect with technological methods. Satellite images that can be used in this direction are available in a short time after disasters. It is also possible to perform change analyzes if images of pre-disaster and post-disaster dates are available. By quickly generating information from these data, the locations of events such as collapsed buildings, closed roads, fire, the places they affect, and the open areas required for assembly areas can be determined.

In some earthquake zones, building boundaries cannot be determined due to the complete collapse of buildings built close to each other. In addition, although the images of the vehicles that came to the earthquake area for aid purposes in the first time have been neglected according to their density values, in some cases the vehicles are also considered as damaged buildings. To prevent this situation, the studies should be supported by building edge detection methods and image processing algorithms. Subsequently, these studies made from satellite imagery can be detailed and accuracy analyzes can be made. Accurate analyzes help direct aid teams and equipment to the right places quickly. This situation constitutes a very critical issue for human life.

References

Aali, H., Sharifi, A., Malian, A. (2019). Earthquake damage detection using satellite images (Case study: Sarpol-Zahab earthquake). International Archives of the Photogrammetry, Remote Sensing and Spatial Information Sciences, 42: 1-6.

AFAD (Disaster and Emergency Management Presidency), (2023). Preliminary evaluation report. (Access Date: 27 March 2023, https://deprem.afad.gov.tr/assets/pdf/Kahramanmaras%20%20Depremleri_%20On%20Degerlendirme%20Raporu.pdf).

AFAD, Republic of Turkey earthquake statistics. (Access Date: 27 March 2023, https://deprem.afad.gov.tr/event-statistics).

AFAD, Turkey earthquake hazard map. (Access Date: 27 March 2023, https://tdth.afad.gov.tr/TDTH/main.xhtml).

AFAD, Republic of Turkey earthquake information support system. (Access Date: 29 March 2023, https://deprem.afad.gov.tr/assets/pdf/deprem-bilgi-destek-sistemi.pdf).

AFAD, Republic of Turkey for strong ground motion records. (Access Date: 29 March 2023, https://tadas.afad.gov.tr/).

Alzubade, M., Ozcan, O., Musaoglu, N., Turkes, M. (2021). Observed impacts of climate variability on LULC in the Mesopotamia region. Computers, Materials and Continua, 67(2):2255-2269.

BOUN (Boğaziçi University), (Access Date: 27 March 2023, https://eqe.boun.edu.tr/sites/eqe.boun.edu.tr/files/kahramanmaras-gaziantep_earthquake_06-02-2023_04.17-bogazici_university_earthquake_engineering_department_v6.pdf).

Dinçer, S. (2009). Drawing two dimensional images using digital image processing algorithms by the help of MATLAB and a microcontroller. Istanbul Technical University, Master Thesis, p. 69.

Emre, O., Duman, TY., Ozalp, S., Elmacı, H., Olgun, S., Şaroğlu, F. (2013). Açıklamalı Türkiye diri fay haritası, ölçek 1:1.250.000. Maden Tetkik ve Arama Genel Müdürlüğü, Özel Yayın Serisi, 30, Ankara, Türkiye.

Ertren, E., Rossi, C. (2019). The worsening impacts of land reclamation assessed with Sentinel-1: The Rize (Turkey) test case. International Journal of Applied Earth Observation and Geoinformation 74: 57-64.

ITU (Istanbul Technical University). Preliminary Evaluation Report. (Access Date: 27 March 2023, https://haberler.itu.edu.tr/docs/default-source/default-document-library/2023_itu_deprem_on_raporu.pdf?sfvrsn=77afe59e_4.pdf).

ITU. Final Report. (Access Date: 29 March 2023, https://haberler.itu.edu.tr/docs/default-source/default-document-library/2023_itu_deprem_son_raporu_.pdf?sfvrsn=35e6665b_2).

Joshi, AR., Tarte, I., Suresh S., Koolagudi SG. (2017). Damage identification and assessment using image processing on post-disaster satellite imagery. IEEE Global Humanitarian Technology Conference.

Kocaaslan, S., Musaoglu, N., Karamzadeh, S. (2021). Evaluating drought events by time-frequency analysis: A case study in aegean region of Turkey. IEEE Access, 9:125032-123041.

Korkmaz, KA., Abualkibash, M. (2018). Earthquake damage detection using before and after earthquake satellite images. IEEE International Conference on Electro/Information Technology, 615-619.

Kusakabe, T., Sanada, A. (2004). Application of image processing to detect infrastructure damage caused by earthquakes. 36th Joint Meeting of US-Japan Panel on Wind and Seismic Effects, 267-275.

MTA (Mineral Research & Exploration General Directorate). (Access Date: 29 March 2023, https://www.mta.gov.tr/v3.0/sayfalar/bilgi-merkezi/deprem/pdf/Deprem_Bilgi_Notu_2023-02-06_Pazarcik-Kahramanmaras_2.pdf).

Nagy, G. (1972). Digital image-processing activities in remote sensing for earth resources. Proceedings of the IEEE, 60(10):1177-1200.

Rao, A., Jungkyo, J., Vitor, S., Giuseppe, M., Yun, SH. (2023). Earthquake building damage detection based on synthetic-aperture-radar imagery and machine learning. Natural Hazards and Earth System Sciences, 23:789-807.

Singh, RP., Verma, T. (2015). Damage detection caused by natural disaster using image processing technique. International Journal on Recent and Innovation Trends in Computing and Communication, 3(4):2287-2291.

Takhtkeshha, N., Mohammadzadeh, A., Salehi, B. (2023). A rapid self-supervised deep-learning-based method for post-earthquake damage detection using UAV data (Case study: Sarpol-e Zahab, Iran). Remote Sensing, 15(1):123.

Tholey, N. (2000). Digital processing of earth observation images. Surveys in Geophysics, 21:209-222.

URL-1. (Access Date: 27 March 2023, https://tr.wikipedia.org/wiki/2023_Kahramanmara%C5 % 9F_depremleri).

URl-2. 2023 Turkey-Syria Earthquake. (Access Date: 27 March 2023, https://disasterphilant hropy.org/disasters/2023-turkey-syria-earthquake/?gclid=Cj0KCQjww4-hBh CtARIsAC9gR3Yp-bIT7WxlRNpHr-pbK0sepnGiR_vpQ6-NeX7krTprEswevoz35BMaAv MnEA Lw_wcB).

URL-3. Türkiye Gazetesi. (Access Date: 13 February 2023, https://www.turkiyegazetesi.com.tr /f otogaleri/antak yayi-dumduz-eden-aluvyon-etkisi-uzmanlar-acikladi-deprem-esnasinda-sivilasiyor-32943).

Yamazaki, F., Suzuki, D., Maruyama, Y., (2008). Detection of damages due to earthquakes using digital aerial images. 6th International Workshop on Remote Sensing for Disaster Applications.

Benefıts Of Blockchaın Technology In Identıfyıng Infectıous Dıseases In Healthcare And Innovatıon

Yeliz DURGUN

Introduction

Blockchain technology has been gaining importance as a potential disruptive force in many industries in recent years Shah and Jani (2018). One of the areas where blockchain has the potential to make a significant impact is healthcare. The use of blockchain in healthcare will create solutions for various applications in healthcare Kumar et al. (2018) . Blockchain technology will shed light on the creation of new solutions, especially in the management of data such as clinical trial data management, supply chain management, electronic medical records Reda, Kanga, Fatima, and Azouazi (2020) . Clinical trials will be a crucial part of the process of developing and testing new drugs and treatments.The management of EMR is an important area of focus for blockchain application in healthcare. EMRs are a critical component of modern healthcare, as they contain important information about a patient's medical history and treatment. However, EMRs are often stored in centralized systems, which can make them vulnerable to data breaches and other security threats.Blockchain technology provides a decentralized platform for storing and sharing EMRs that can improve the security and accessibility of this important data. However, data collected during clinical trials is often complex and sensitive, and there is a risk of data fraud or error. Blockchain technology can provide a secure and transparent platform for storing and sharing clinical trial data, improving the integrity and accuracy of data, and helping to prevent fraud. In addition, blockchain technology has the potential to improve supply chain management in the healthcare industry Popov et al. (2022b) . The medical supplies and equipment supply chain is often complex with many different parties involved in the manufacture, distribution and delivery of these products. By using blockchain to track the movement of these products, healthcare organizations can increase efficiency, reduce the risk of fraud and ensure patients receive the highest quality products.

Overall, the use of blockchain technology in healthcare has the potential to improve the safety, efficiency and transparency of various healthcare processes.This article describes the various applications of blockchain in healthcare and the potential benefits and challenges of implementing these solutions.

Digital health and Blockchain

A digital health platform is a database in which a person's health information is kept digitally. As can be seen in Figure 1, the medical examinations and tests in the health institutions of the person, the drugs he has taken, the insurance agencies to which he is affiliated, the payments made by the patient for these, and the information about the services received from the research centers are recorded in the blockchain network.This technology includes information such as the person's health history, medications taken, medical examinations and tests performed.A digital health platform was created to collect a person's health information in one place and make this information accessible.This platform helps to understand the health status of the person Popov et al. (2022a) .And it helps doctors learn about treatment options. Digital health platforms are usually created and managed by a health care provider.However, sometimes people can create their own digital health platforms.Blockchain technology can be

used to provide security and reliability for digital health platforms M. T. Alam and Raza (2021) .This technology is a method that prevents a data from being changed.Therefore, when the data of a person's digital health platform is stored on the blockchain network, the security and accuracy of this data is further enhanced.Also, the blockchain network can be used to restrict a person's access to their health data.In this way, data can only be viewed and protected by authorized persons.The use of the blockchain network in digital health platforms also enables faster and more efficient sharing of data. For example, when a doctor wants to access a patient's digital health platform, the doctor's access to that profile will be much faster if that platform is stored on the blockchain network. This helps doctors treat their patients more effectively.

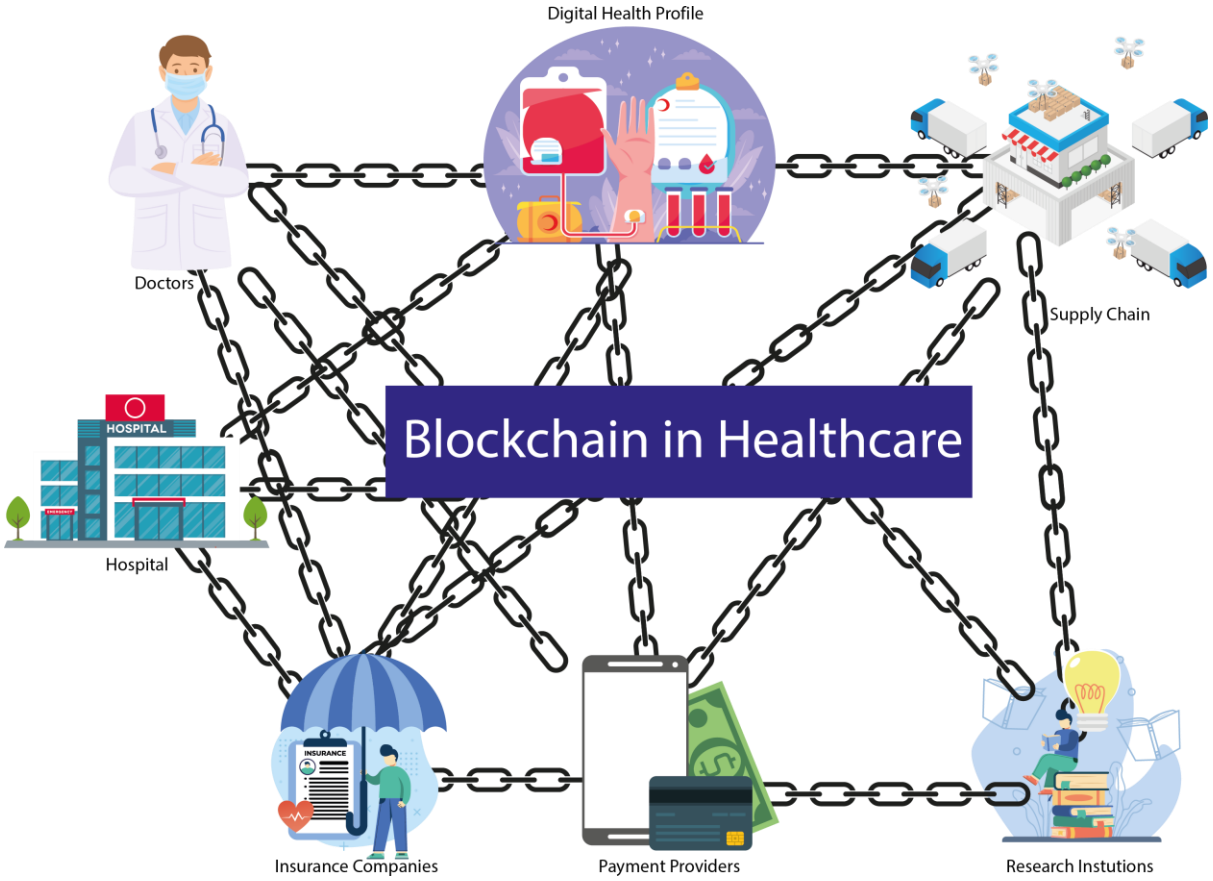

Figure 1. Blockchainin Healthcare

Why should we choose blockchain in the field of health?

Trust and traceability are the two key promises of blockchain out-of-the-box, solving the general problem of trust at all public, federated and organizational levels Katuwal, Pandey, Hennessey, and Lamichhane (2018) .However, these features are not always enough to provide a complete solution, so we often see blockchain paired with strong cryptographic protocols such as zero-knowledge proofs Tomaz, Nascimento, Hafid, and Souza (2020) .This mapping ensures trust, traceability, security and control, which are fundamental building blocks for critical solutions in a variety of industries, including healthcare and supply chain.Data saved on the blockchain cannot be changed or deleted without leaving a trace Li et al. (2018a) . This immutability and traceability of data is a critical requirement for any healthcare system.

Therefore, the benefits of blockchain seem close. Here,

- Secure storage and integrity protection
- Confidentiality and ownership of data
- Information sharing
- Traceability and accountability of data

While each of these concerns can be addressed individually with the proper use of cryptography and privacy-preserving technologies, the main concerns in such solutions have always been the prevailing trust model.In such solutions, blockchain as a trusted decentralized ledger technology can act as a trust-binding glue.

Benefits Of Blockchain Technology To The Field Of Microbiology

Blockchain technology has the potential to revolutionize the field of microbiology by providing a secure and transparent platform for tracking and sharing data Golosova and Romanovs (2018) .This technology has the ability to create immutable records, ensuring that data cannot be altered or tampered with. Additionally, blockchain technology can facilitate secure sharing of data between various parties, such as researchers, hospitals, and laboratories, while maintaining the privacy and confidentiality of sensitive information Li et al. (2018b)

.One potential application of blockchain technology in microbiology is in the tracking and management of infectious diseases. By creating a centralized and secure platform for tracking the spread of diseases, public health agencies can more effectively respond to outbreaks and prevent the spread of infections. Similarly, blockchain technology can be used to track and verify the authenticity of diagnostic tests and treatments, helping to ensure that patients receive the highest quality care Koshechkin, Lebedev, Radzievsky, Seepold, and Martinez (2021) .

Another area where blockchain technology can be beneficial in microbiology is in the tracking of research studies and clinical trials. By creating a secure and transparent record of study results, researchers can more easily share their findings with others in the field, leading to more rapid advances in the field. Additionally, the use of blockchain technology can help to reduce the risk of fraud or misconduct in research, as any changes to the data can be easily detected. Overall, the use of blockchain technology has the potential to significantly improve the accuracy, efficiency, and transparency of research and data management in the field of microbiology Mohammadipanah and Sajedi (2021) . By providing a secure and reliable platform for storing and sharing data, blockchain technology has the potential to revolutionize the way that research is conducted and data is analyzed in this field.

Innovations That Blockchain Technology Will Bring In The Detection Of Infectious Diseases

Blockchain technology has the potential to revolutionize the way infectious diseases are detected and tracked. By creating a decentralized, transparent, and secure database, blockchain can facilitate the exchange of information among healthcare providers, public health agencies, and other relevant stakeholders in real-time. This can help speed up the detection and response to outbreaks, as well as improve disease surveillance and management Ahmad et al. (2021) .

One key innovation that blockchain brings to the detection of infectious diseases is the ability to securely and efficiently share data T. Alam (2020) . With traditional centralized databases, the exchange of information can be slow and prone to errors, as it often requires multiple intermediaries and manual processes. In contrast, blockchain allows for the creation of a single, shared database that can be accessed and updated by authorized parties in real-time. This can improve the accuracy and timeliness of data, enabling more effective and efficient decision-making.Another innovation is the use of smart contracts to automate and streamline processes related to disease detection and management Khatoon (2020) . Smart contracts are self-executing contracts with the terms of the agreement between buyer and seller being directly written into lines of code. They can be used to automatically trigger actions based on pre-defined conditions, such as the reporting of a new case of an infectious disease. This can help to reduce the burden on healthcare providers and public health gencies, allowing them to focus on more pressing tasks.In addition, blockchain can improve the traceability of infectious diseases by providing a secure and transparent record of the movement of people and goods

Zhu, Hu, Zhang, and Li (2021) . This can help to identify the sources of outbreaks and track the spread of diseases, enabling more targeted and effective interventions.Overall, the innovations brought by blockchain technology have the potential to significantly improve the detection and management of infectious diseases. By facilitating the exchange of information, automating processes, and improving traceability, blockchain can help to ensure a more efficient and effective response to outbreaks, ultimately leading to better outcomes for individuals and communities.

Results

In the classical methods used in health services, there are various problems such as accessing patient information, collecting information from patients and storing this information. Wearable devices etc. Patient data obtained from instant follow-up devices facilitated obtaining both personal and social information and facilitated diagnosis by experts by accessing this information easily.However, situations such as the security, distribution and centrality of the information produced here also create problems.The decentralized, secure distribution and storage of the information produced as a result of the use of blockchain technology in the healthcare industry by combining it with IoT, the fact that there is access to information without intermediaries, and that the information owner can share their information with any expert shows how great the contributions of blockchain technology to healthcare services can be.Blockchain technology has the potential to revolutionize the field of microbiology in a number of ways.Blockchain technology allows for the secure and transparent tracking of data, ensuring that it cannot be tampered with or altered without detection. This is especially important in the field of microbiology, where data integrity is critical for ensuring the accuracy and reliability of research findings. Blockchain technology can facilitate the sharing of data and research findings among different institutions and researchers, enabling greater collaboration and speeding up the pace of scientific discovery.

Blockchain technology allows for the transparent tracking of data and results, which can help to increase trust and confidence in research findings and reduce the risk of fraud or misconduct. Blockchain technology could help to streamline the research process by automating certain tasks and reducing the need for manual record-keeping and data entry.Overall, the use of blockchain technology in microbiology could help to improve the accuracy and reliability of research findings, facilitate collaboration and data sharing, and increase transparency and traceability in the field.

Blockchain technology has the potential to bring a number of innovations to the detection and management of infectious diseases. These innovations include:

By creating a decentralized, transparent, and secure database, blockchain can facilitate the exchange of information among healthcare providers, public health agencies, and other relevant stakeholders in real-time. This can improve the accuracy and timeliness of data, enabling more effective and efficient decision-making. The use of smart contracts can automate and streamline processes related to disease detection and management. This can help to reduce the burden on healthcare providers and public health agencies, allowing them to focus on more pressing tasks.Improved traceability: Blockchain can improve the traceability of infectious diseases by providing a secure and transparent record of the movement of people and goods. This can help to identify the sources of outbreaks and track the spread of diseases, enabling more targeted and effective interventions.Overall, the innovations brought by blockchain technology have the potential to significantly improve the detection and management of infectious diseases. By facilitating the exchange of information, automating processes, and improving traceability, blockchain can help to ensure a more efficient and effective response to outbreaks, ultimately leading to better outcomes for individuals and communities.

REFERENCES

Ahmad, R. W., Salah, K., Jayaraman, R., Yaqoob, I., Ellahham, S., & Omar, M. (2021). The role of blockchain technology in telehealth and telemedicine. *International journal of medical informatics*, *148*, 104399.

Alam, M. T., & Raza, K. (2021). *Blockchain technology in healthcare: making digital healthcare reliable, more accurate, and revolutionary.* Elsevier.

Alam, T. (2020). Internet of things and blockchain-based framework for coronavirus (covid-19) disease.

Golosova, J., & Romanovs, A. (2018). The advantages and disadvantages of the blockchain technology. In *2018 IEEE 6th workshop on advances in information, electronic and electrical engineering (AIEEE)* (p. 1-6).

Katuwal, G. J., Pandey, S., Hennessey, M., & Lamichhane, B. (2018). Applications of blockchain in healthcare: current landscape & challenges. *arXiv preprint arXiv:1812.02776*.

Khatoon, A. (2020). A blockchain-based smart contract system for healthcare management.

Electronics, *9*(1), 94.

Koshechkin, K., Lebedev, G., Radzievsky, G., Seepold, R., & Martinez, N. M. (2021).

Blockchain technology projects to provide telemedical services: Systematic review.

Journal of medical internet research, *23*(8), e17475.

Kumar, T., Ramani, V., Ahmad, I., Braeken, A., Harjula, E., & Ylianttila, M. (2018).

Blockchain utilization in healthcare: Key requirements and challenges. In *2018 IEEE 20th International conference on e-health networking, applications and services (Healthcom)* (p. 1-7).

Li, H., Zhu, L., Shen, M., Gao, F., Tao, X., & Liu, S. (2018a). Blockchain-based data preservation system for medical data. *Journal of medical systems*, *42*(8), 1-13.

Li, H., Zhu, L., Shen, M., Gao, F., Tao, X., & Liu, S. (2018b). Blockchain-based data preservation system for medical data. *Journal of medical systems*, *42*(8), 1-13.

Mohammadipanah, F., & Sajedi, H. (2021). Potential of blockchain approach on development and security of microbial databases. *Biological Procedures Online*, *23*(1), 1-8.

Popov, V. V., Kudryavtseva, E. V., Katiyar, N. K., Shishkin, A., Stepanov, S. I., & Goel, S. (2022a). Industry 4.0 and Digitalisation in Healthcare. *Materials*, *15*(6), 2140.

Popov, V. V., Kudryavtseva, E. V., Katiyar, N. K., Shishkin, A., Stepanov, S. I., & Goel, S. (2022b). *Industry 4.0 and Digitalisation in Healthcare. Materials 2022, 15, 2140.* s Note: MDPI stays neutral with regard to jurisdictional claims in published ….

Reda, M., Kanga, D. B., Fatima, T., & Azouazi, M. (2020). Blockchain in health supply chain management: State of art challenges and opportunities. *Procedia Computer Science*, *175*, 706-709.

Shah, T., & Jani, S. (2018). Applications of blockchain technology in banking & finance.

Parul CUniversity, Vadodara, India.

Tomaz, A. E. B., Nascimento, J. C. D., Hafid, A. S., & Souza, J. N. D. (2020). Preserving privacy in mobile health systems using non-interactive zero-knowledge proof and blockchain. *IEEE access*, *8*, 204441-204458.

Zhu, P., Hu, J., Zhang, Y., & Li, X. (2021). Enhancing traceability of infectious diseases: A Blockchain-based approach. *Information Processing & Management*, *58*(4), 102570.

A Comparison of the Sensitivity of Artificial Neural Networks(ANN), Support Vector Machines(SVM), and Decision Trees (DT)for Landsat-8Data Analysis

Hüseyin YAŞAR
A. Hüsnü ERONAT

Giriş

Remote sensing and image processing have become essential tools for analyzing and understanding the Earth's surface and its various features. With the increasing availability of remote sensing data, there is a growing need for accurate and efficient methods for classifying, segmenting, and detecting objects in these images. To address this challenge, learning techniques such as artificial neural networks, support vector machines, and decision trees have been widely used in remote sensing and image processing. In this context, the present study aims to evaluate the performance of these machine learning algorithms in classifying multi-spectral images obtained from the LANDSAT 8+ETM scan of Urla semi-island in the city of Izmir, Turkey. The accuracy and sensitivity of these algorithms are evaluated using a confusion matrix to ensure their effectiveness for remote sensing and image processing tasks.

Artificial neural networks (ANNs) play an important role in remote sensing and image processing. Remote sensing involves the analysis of data collected through sensors to detect objects, features, and conditions. ANNs are a popular tool for understanding and classifying these data. Image processing, on the other hand, involves the detection and recognition of objects and features in images. ANNs have been successfully used in image classification, segmentation, and object detection tasks. For example, ANNs have been used to classify land cover from remotely sensed imagery (Almeida et al., 2019), and to detect objects in satellite imagery (Wang et al., 2018). ANNs have also been used in combination with other techniques, such as fuzzy logic and genetic algorithms, to improve the accuracy of remote sensing and image processing tasks (Liu et al., 2020).

Support vector machines (SVMs) have been widely used in remote sensing for classification and regression tasks. SVMs are particularly well-suited for handling high-dimensional data, such as remotely sensed imagery, and have been shown to outperform other classification algorithms in many studies (Mountrakis et al., 2011). SVMs have also been used for change detection in remote sensing data (Ravanelli and Napoli, 2016), and for feature extraction and selection in hyperspectral image analysis (Li et al., 2018). SVMs have been compared with other machine learning algorithms, such as artificial neural networks and decision trees, and have been shown to have advantages in terms of accuracy and computational efficiency (Yang et al., 2017).

Decision trees are a popular machine learning technique that has been widely used in remote sensing for classification and feature selection tasks. Decision trees are particularly useful for handling high-dimensional data, such as remotely sensed imagery, and have been shown to achieve high classification accuracy in many studies (Pal and Mather, 2003). Decision

trees have also been used in combination with other techniques, such as fuzzy logic and wavelet transform, to improve the accuracy of remote sensing classifications (Jia et al., 2017). One advantage of decision trees is their ability to perform feature selection, which can improve classification accuracy and reduce computational complexity. Feature selection can be performed using various criteria, such as information gain, gain ratio, and Gini index, and can help identify the most important features for a given classification task (Qi and Kerr, 2019). Decision trees have also been used for object-based image analysis, which involves segmenting an image into meaningful objects and classifying them based on their spectral and spatial characteristics (Blaschke et al., 2014). Object-based image analysis has been shown to be particularly useful for analyzing high-resolution imagery, such as that obtained from unmanned aerial vehicles (UAVs) and satellites.

Study Area

Located in the western region of Izmir province, Urla is a charming district distinguished by its rugged topography and undulating hills. To the northeast of the district, mountain ranges parallel to the coast ascend to altitudes of 600-700 meters, where a vast plain extends to the southeast. From a geological perspective, the district is characterized by a diverse assemblage of sedimentary rocks that originate from the Neogene and Quaternary periods, in addition to volcanic tuffs and basalts. The region also hosts deposits of limestone, shale, and sandstone (Güner, 2014).

Figure 1 Urla image taken by LANDSAT 8

The area selected for study in Figure 1 is situated in the predominantly rural district of Urla, located in the western part of Izmir. The district is known for its rugged terrain and rolling hills, and its economy is primarily driven by agriculture and tourism. Olive groves, vineyards, vegetable fields, and citrus orchards abound in this region, which is also replete with historic structures and ancient ruins such as Klazomenai, Erythrai, and Teos Ancient Cities. Notwithstanding its limited urbanization, the district center is home to bustling markets and administrative centers. The district's pristine beaches and holiday resorts are popular tourist destinations during the summer months and add to the area's appeal.

Material andMethod

The LANDSAT-8 satellite, which constitutes a part of the aforementioned program, was launched on February 11, 2013, with the aim of facilitating Earth observation. This satellite is the eighth of its series and the seventh to have been successfully deployed into orbit (Leberl, 2006). The development and engineering of the mission systems, as well as the acquisition of the launch vehicle, were under the purview of the National Aeronautics and Space Administration (NASA), while the ground systems were developed by the United States Geological Survey (USGS), which also continues to oversee ongoing mission operations.

The selection of spectral bands plays a pivotal role in the image classification process since it influences the discriminative power of the algorithm in capturing class-specific reflectance values. Therefore, selecting and combining bands that provide the clearest representation of the target classes is crucial. In this study, we employed Landsat-8 OLI images obtained from channels 1 to 7. Radiometric and geometric corrections were applied to improve the accuracy of the images. Additionally, the water section was masked to enhance sensitivity and reduce processing time (Tulbure, M. G., & Georgieva, O., 2015).

Determination of Training Areas

In this study, unsupervised classification was conducted for image processing. The maximum number of classes present in the region was determined. Subsequently, areas with high vegetation density were explored, and their coordinates were recorded. Further explorations were carried out in the study area to investigate the land cover structure.

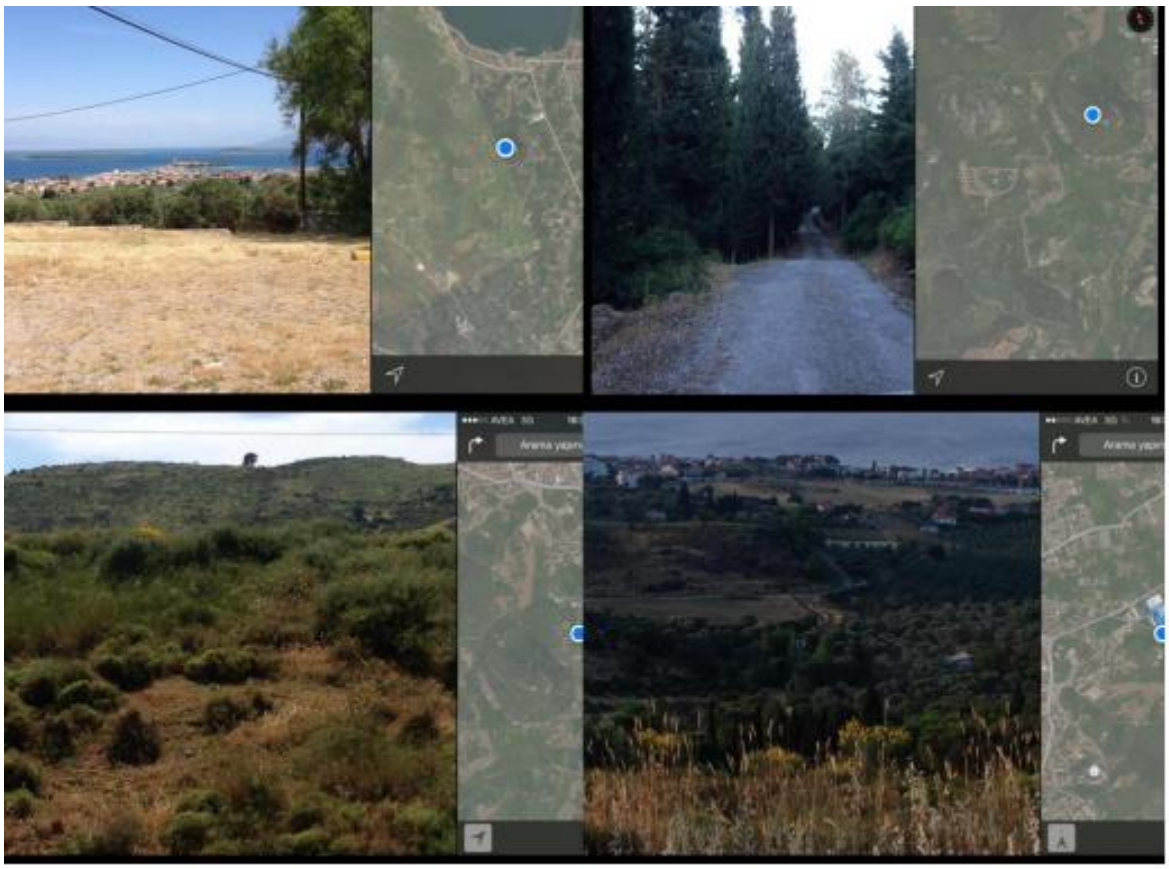

Figure 2 The areas where in-situ studies have been made by designating their locations with the help of GPS for the land covers which cannot be detected and for the true colors in satellite imaging

Moderate resolution satellite imagery and in-situ studies were utilized to validate the selection of class labels in Figure 2. This ensured the accuracy of the assigned class labels. Geometric correction during in-situ studies was aided by a GPS device with a sensitivity of 2m. Figure 2 illustrates the locations of the in-situ studies.

Calculation The Complex Matrix

The aim of this operation is to evaluate the accuracy of image processing algorithms in a classification study by examining their performance using actual data. The primary contribution of this operation is to assess the effectiveness of the algorithms employed. The overall accuracy is computed as the sum of pixels classified correctly, divided by the total number of pixels, where the true class of the pixels is determined by the ground truth image or ground truth ROIs. The confusion matrix table displays the number of pixels classified correctly into their corresponding ground truth class, which are located along the diagonal of the matrix. Additionally, the Kappa coefficient, which measures the agreement between the classification and ground truth pixels, is calculated. A Kappa value of 1 indicates perfect agreement, while a value of 0 implies no agreement (Jensen, 1986).

$$\kappa = \frac{N\sum_{i=1}^{n} m_{i,i} - \sum_{i=1}^{n}(G_i C_i)}{N^2 - \sum_{i=1}^{n}(G_i C_i)} \quad (1)$$

Where:

- i is the class number,

-N is the total number of classified pixels that are being compared to ground truth,

- $m_{i,i}$ is the number of pixels belonging to the ground truth class i, that have also been classified with a class i (i.e., values found along the diagonal of the confusion matrix),

- C_i is the total number of classified pixels belonging to class i,

-G_i is the total number of ground truth pixels belonging to class i,

Confusion matrix table shows the class distribution in percent for each ground truth class. The values are calculated by dividing the pixel counts in each ground truth column by the total number of pixels in a given ground truth class. Errors of commission represent pixels that are labeled as belonging to the class of interest but actually belong to another class. The errors of commission are shown in the rows of the confusion matrix. Errors of omission represent pixels that belong to the ground truth class but are incorrectly classified into another class by the classification technique. The errors of omission are shown in the columns of the confusion matrix. Producer accuracy is a measure indicating the accuracy of the classifier in labeling an image pixel into Class A given that the ground truth is Class A. User accuracy is a measure indicating the accuracy of labeling a pixel as Class A given that the classifier has labeled the pixel into Class A.

Processing the Images by Support Vector Machines

Linear kernel function is a function of support vector machines. In this study, this function has been utilized during image processing. After determined training area, their images were processed first with the help of SVM algorithm. Functions such as linear kernel, polynomial kernel, radial floored kernel and sigmoid kernel were used made use of while the images are processed in this algorithm. Linear kernel function is part of SVM. Linear kernel function can mathematically be defined as follows:

$$K(X_i, X_J) = x_j^T x_j \quad (2)$$

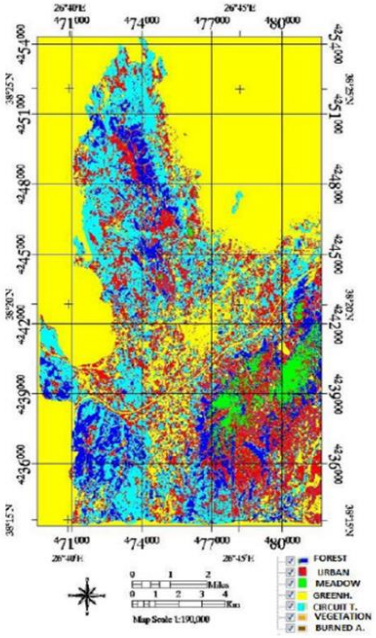

Figure 3 Linear kernel function

The analysis of the processed image through linear kernel functions is shown given in Figure 3. The sensitivity of the algorithm used has been tested by the help of the data on Table 1 which were obtained by help of complex matrix. In mathematical terms, the Linear kernel function takes two data points and computes their dot product, which represents their similarity. If the dot product is greater than a threshold value, the two data points are classified as being in the same class, otherwise they are classified as being in different classes.

Linear kernel function is particularly useful when the data points are linearly separable, meaning they can be separated by a straight line. However, it may not be as effective when the data is non-linearly separable, in which case non-linear kernel functions can be used.

Table 1 Confusion matrix data obtained through Linear Kernal Function

CLASS	PROD. ACC.(PERCENT)	USER ACC.(PERCENT)	PROD. ACC.(PİXEL)	USER ACC.(PİXEL)
FOREST	99.30	95.09	426/429	426/448
URBAN	91.84	99.26	135/147	135/136
MEADOW	87.50	98.82	84/96	84/85
GREENHOUSE	69.17	71.21	92/133	92/129
CİTRUS TREES	80.73	80.00	88/109	88/110
VEGETATION	72.46	72.46	50/69	50/69
BURNED AREA	81.58	75.61	62/76	62/82

Table1 general accuracy of 87.4797% when complex matrix data have been examined. When examined in a more detailed way, the accuracy in the classification of forest areas is high. Controversially, this has no effective role in the exploration of greenhouse areas.

Artificial Neural Networks (ANN)

Another algorithm, which is used in image processing is artificial neural networks. The parameter values which are used in processing images are training threshold contribution: 0.9, training rate: 0.2, training momentum: 0.9, training RMS:0.1. Training Threshold Contribution: Determines the size of the contribution of the internal weight with respect to the activation level of the node. It is used to adjust the changes to a node's internal weight. The training algorithm interactively adjusts the weights between nodes and optionally the node thresholds to minimize the error between the output layer and the desired response. Setting the training threshold contribution to zero does not adjust the node's internal weights. Adjustments of the nodes internal weights could lead to better classifications but too many weights could also lead to poor generalizations.

Training Rate, the training rate determines the magnitude of the adjustment of the weights. A higher rate will speed up the training, but will also increase the risk of oscillations or non-convergence of the training result. Training momentum, entering a momentum rate greater than zero allows you to set a higher training rate without oscillations. A higher momentum rate trains with larger steps than a lower momentum rate. Its effect is to encourage weight changes along the current direction. Training root meen square (RMS), in the training RMS exit criteria field, enter the RMS error value at which the training should stop. If the RMS error, which is shown in the plot during training, falls below the entered value, the training will stop, even if the number of iterations has not been met. The classification will stop, even if the number of iterations has not been met. The classification will then be executed.

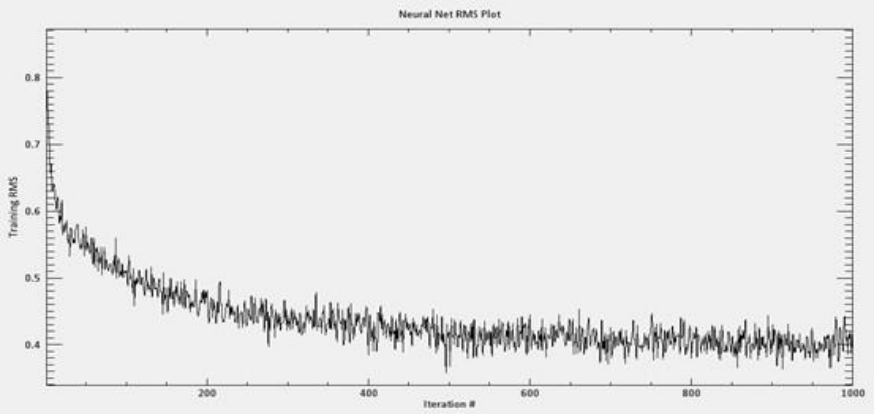

Figure 4 RMS curve obtained with 1000 iteration

Table 2 Confusion matrix data obtained through artificial neural network

CLASS	PROD. ACC.(PERCENT)	USER ACC.(PERCENT)	PROD. ACC.(PİXEL)	USER ACC.(PİXEL)
FOREST	98.83	97.25	424/429	424/450
URBAN	94.56	94.50	139/147	139/129
MEADOW	91.67	98.88	88/96	88/86
GREENHOUSE	69.92	73.81	93/133	93/126
CİTRUS TREES	81.65	85.44	89/109	89/104
VEGETATION	78.57	61.97	48/69	48/58
BURNED AREA	90.79	55.68	69/76	69/99

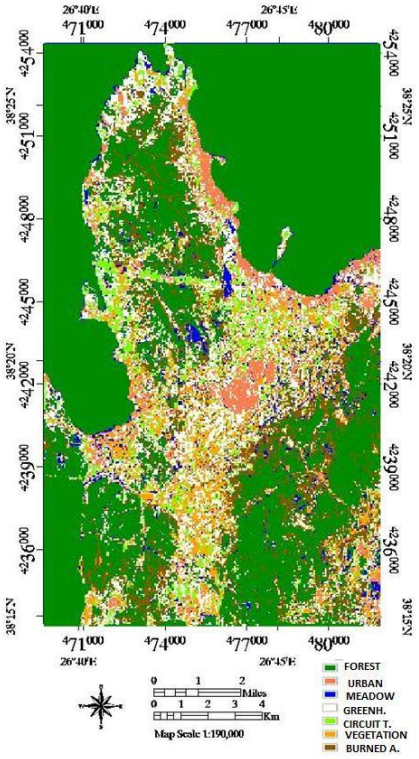

Figure 5 View classified through artificial neural

Sea was masked from the classification. One of the artificial colors in the classification is automatically appointed to the masked area, which is sepin figure 5 rate, because of masking. The reason for masking the sea section is to prevent spectral perturbation. Therefore, the sensitivity of the classification has been increased. It can be seen that the general accuracy is 89.90% when Table 2 is examined. This value is quite operative for the classification accuracy. It gives results with high accuracy in the detection of meadow areas, urban regions, coniferous areas and burned regions.

Decision Trees (DT)

The basic parameter is the parameter of reflection in the formation of decision trees as in all classification studies. Statistical data base is obtained for each band of multi-spectral image according to this parameter. Proportioning is done according to this data. Critical points for classification are mediated by taking these proportions as a base. Classes are appointed according to these critical points. The spectral values of the multispectral image are used in

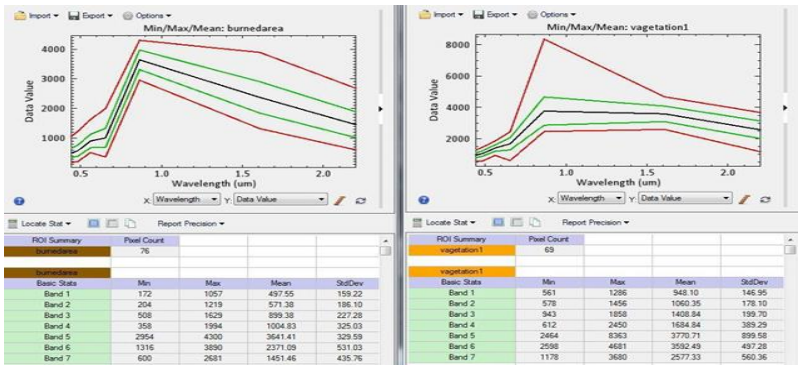

Figure 6 The spectral values of burned areas and vegetation regions

Figures 6, 7, and 8

The ratio of band 5 and band 4 is taken into consideration to explore the burned areas when statistical averages are taken in Figure 6. It is emphasized that ratio must be higher than 3. Besides, it is emphasized that this ratio is lower than 3 after taking the ratios of band 6 and band 4. The knot, which represents burned areas, has been determined by taking this emphasis into consideration. It has been emphasized that the ratio of band 7 to band 1 is more than 2.5 as a value when statistical averages are taken to explore the operative areas. It has also been emphasized that the ratio of band 6 to band 4 is less than 2.2. Therefore, a mediating knot has been formed to explore the effective areas when all these stresses are combined.

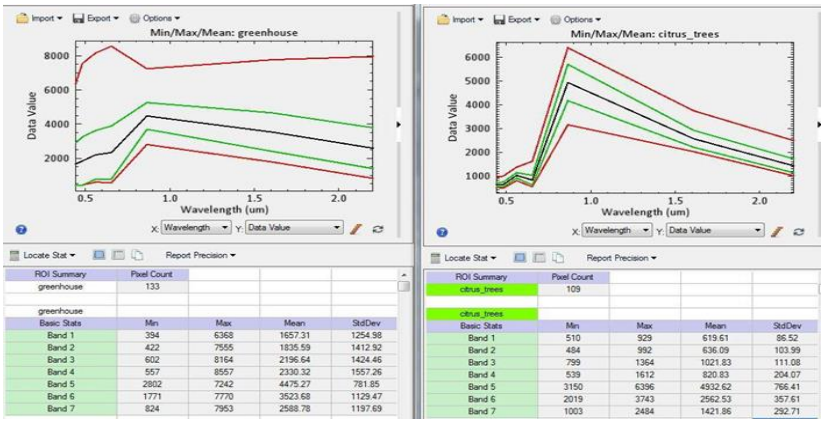

Figure 7 The spectral values of greenhouse and citrus trees

It has been shown that the ideal band ratio to mediate greenhouse areas is band 6 and band 4 when spectral values in Figure 7 are investigated. It has been stressed that this ratio is less than 1.6 the ratio of band 7 to band 1 which is less than 2.5 and the ratio of band 4 to band 3 which is smaller than 0.9 have all been determined and it has been emphasized that these values are ideal in the designation of citrus trees when the spectral values in Figure 3.12 are taken into

consideration. It has been determined that the ideal band ratio for the meadow areas is that of band 7 to band 1 when Figure 8 is examined.

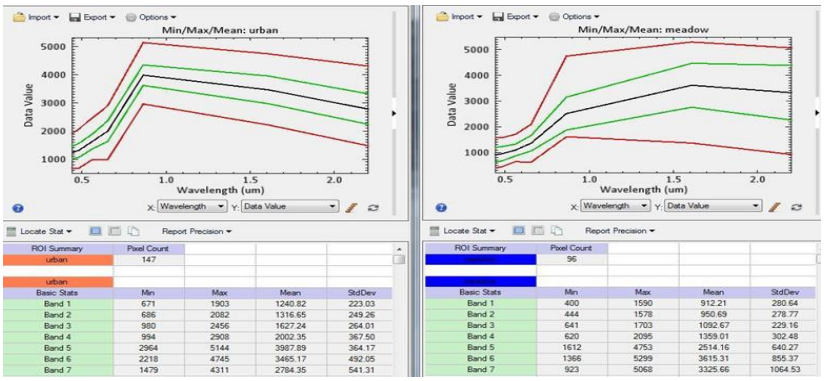

Figure 8 The spectral values of urban and meadow

Table 3 Confusion matrix data obtained through artificial neural network

CLASS	PROD. ACC.(PERCENT)	USER ACC.(PERCENT)	PROD. ACC.(PİXEL)	USER ACC.(PİXEL)
FOREST	98.20	93.78	422/429	422/450
URBAN	73.15	84.50	109/147	109/129
MEADOW	82.38	94.19	81/96	81/86
GREENHOUSE	61.90	66.94	81/133	81/121
CİTRUS TREES	82.90	75.44	86/109	86/114
VEGETATION	64.77	61.97	44/69	44/71
BURNED AREA	61.47	55.68	49/76	49/88

As seen in Table 3, general accuracy is 82%. Although decision tree algorithm is has got high accuracy for forest and meadow areas but not sufficient enough for other classes. As seen in Table 3.8, general accuracy is 82%. Although decision tree algorithm is has got high accuracy for forest and meadow areas but not sufficient enough for other classes.

CONCLUSION

The analysis of classified images of Urla semi-island using various algorithms highlighted the diversity in their performance across different classes and terrains. Although no single algorithm was found to be suitable for accurately classifying all classes, the results showed that SVM, ANN, and decision trees were effective in identifying urban, meadow, and vegetation areas, respectively. Furthermore, the use of thermal camera images was found to enhance the reliability of classification in greenhouse areas. Despite some limitations, this study

provides valuable insights for the classification and identification of specific areas within Urla semi-island, which can be useful for various applications such as land-use planning, environmental monitoring, and biodiversity conservation. Further research could focus on the refinement and integration of algorithms to improve their accuracy and applicability in various contexts.

References:

Almeida, C. M., Vieira, C. M., & Fonseca, L. M. (2019). A Comparison of Artificial Neural Networks and Decision Trees for Land Cover Classification of a Complex Mediterranean Landscape. Remote Sensing, 11(6), 703.

Blaschke, T., Lang, S., Hay, G. J., & Schmidtlein, S. (2014). Object-based image analysis: still a hot topic. Remote Sensing, 6(11), 11182-11205.

Güner, M. (2014). The Geomorphological Evolution of the Urla Peninsula, Western Turkey. Journal of Geography, Environment and Earth Science International, 1(2), 35-46.

Jia, P., Zhang, J., Cheng, G., & Zhang, L. (2017). Remote sensing image classification based on a decision tree algorithm using optimized object-based features. International Journal of Remote Sensing, 38(7), 1859-1883.

Leberl, F. W., & Baltsavias, E. P. (Eds.). (2006). Image and signal processing for remote sensing XII: Proceedings of SPIE, Europto Series. Bellingham, WA: SPIE.

Li, W., Gong, P., Wu, C., & Hu, T. (2018). Support vector machines for hyperspectral remote sensing classification: a review. ISPRS Journal of Photogrammetry and Remote Sensing, 150, 83-107.

Liu, Q., Chen, Y., & Zhang, H. (2020). A hybrid intelligent model for remotely sensed image classification using fuzzy logic and artificial neural networks. Journal of Applied Remote Sensing, 14(1), 016502.

Mountrakis, G., Im, J., & Ogole, C. (2011). Support vector machines in remote sensing: A review. ISPRS Journal of Photogrammetry and Remote Sensing, 66(3), 247-259.

Pal, M., & Mather, P. M. (2003). An assessment of the effectiveness of decision tree methods for land cover classification. Remote Sensing of Environment, 86(4), 554-565.

Tulbure, M. G., & Georgieva, O. (2015). Accuracy assessment in image classification: A review. In R. B. Nagarajan, V. K. Govindan, & T. R. Lakshmi (Eds.), Machine learning and data mining in pattern recognition (pp. 149-166). Cham: Springer. doi: 10.1007/978-3-319-24042-1_8

Qi, J., & Kerr, J. T. (2019). Automated selection of spectral bands for classification of multispectral remote sensing data using decision trees. International Journal of Remote Sensing, 40(16), 6261-6284.

Ravanelli, R., & Napoli, C. (2016). Change detection in remote sensing images using support vector machines. Journal of Applied Remote Sensing, 10(3), 036006.

Wang, Y., Mao, S., & Zhu, S. (2018). Object detection in remote sensing images based on convolutional neural networks. Remote Sensing, 10(10), 1606.

Yang, C., Everitt, J. H., & Bradford, J. M. (2017). Comparison of support vector machine, artificial neural network, and CART algorithms for the land-cover classification using limited training data points. ISPRS Journal of Photogrammetry and Remote Sensing, 124, 78-86.

Spatial and Temporal Dynamics of Marine Litter on Southeast Black Sea Beaches

Koray ÖZŞEKER[1]
Bilal ONMAZ [2]

Introduction

All kinds of materials that have lost their function that people throw directly into the seas or indirectly deliver to the coasts and beaches are called marine litter (Bettencourt et al. 2021). According to a more detailed definition, they are defined as all kinds of human-made, non-use wastes that are left to marine ecosystems either by land transport such as rivers, sewage, wind or directly (Okuku et al. 2021). Marine litter is classified into many types and subcategories according to the United Nations Environment Program (UNEP) and the Convention for the protection of the Marine Environment of the Northeast Atlantic (OSPAR) (Ospar 2010). Marine litter can generally be classified as plastic, metal, glass, textile, rubber, and materials of hygienic origin. In these main categories, they are examined in 42 subclasses. One of the most important features of marine litter is that it stays in marine ecosystems for a very long time without undergoing chemical and physical deterioration (Mghili et al. 2023). For this reason, they pose a danger to marine ecosystems and habitats for many years. Marine litter not only provides a bad appearance in the seas, but also negatively affects the sustainability of marine and coastal ecosystems. They damage coral reefs, benthic habitats and marine mammals(Ribeiro et al. 2021). As a result of eating these wastes by some sea creatures, mistaking them for food, unfortunately, death occurs due to lack of breath. The issue of marine litter is also common on the beaches where people go to rest and relax (Terzi et al. 2020; Özşeker et al. 2022; Erüz et al. 2022). Marine litter should be considered as a major global problem, as it negatively affects not only living populations but also our living spaces and socio-economic conditions. The most common type of marine litter in marine and ocean ecosystems is plastics (Mazarrasa et al. 2019; Simeonova and Chuturkova 2019; Valderrama-herrera et al. 2023). Plastics are the most important components of modern life. It facilitates people's quality of life. In addition to these, there are many more benefits. However, as a result of their unconscious and excessive use, they become a great threat to the surrounding ecosystems. They do not disappear from nature even in thousands of years. The damage caused by such wastes causes great falsification in the ecological balance of the world. While there is such a great danger, it is still seen that 5 million tons of garbage is thrown into the seas and oceans every year (Gonçalves et al. 2020; Okuku et al. 2021). For this reason, it is feared that the amount of garbage thrown into ocean ecosystems will reach 250 million tons, especially with plastic waste, by 2025. Most people want to spend their lives by the sea. They want to benefit from the relaxing feature of the sea and its air. In addition, coastal areas are the most important source of getting rid of our stress, resting the body and being fit. For this reason, we have to ensure the sustainability of coastal areas and beach ecosystems. Based on all this information, in this study, it is aimed to investigate the spatial and temporal dynamics of marine litter in coastal areas (beaches) that are gradually decreasing in our region.

[1] Assoc. Prof. Dr., Karadeniz Technical University, Institute of Marine Science and Technology, Orcıd: 0000-0002-7044-1843
[2] MSc Student, Karadeniz Technical University, Faculty of Marine Science, Orcıd: 0009-0003-7913-7279

Material and Method

In this study, the most intensively used beaches of Giresun, Trabzon and Rize provinces in the Eastern Black Sea region were determined as the research area (Figure 1). Marine litter sampling was carried out on seasonally in 2022. Marine litter was separated and recorded as qualitatively and quantitatively in areas ranging from 50 to 120 m^2 determined for each station. The separated marine litter is categorized under 8 main headings: plastic, metal, textile, glass, paper, sanitary, medical, and wood. In addition, the collected marine litter was evaluated in 42 subclasses determined under these main headings, according to the OSPAR (Ospar 2010) directive.

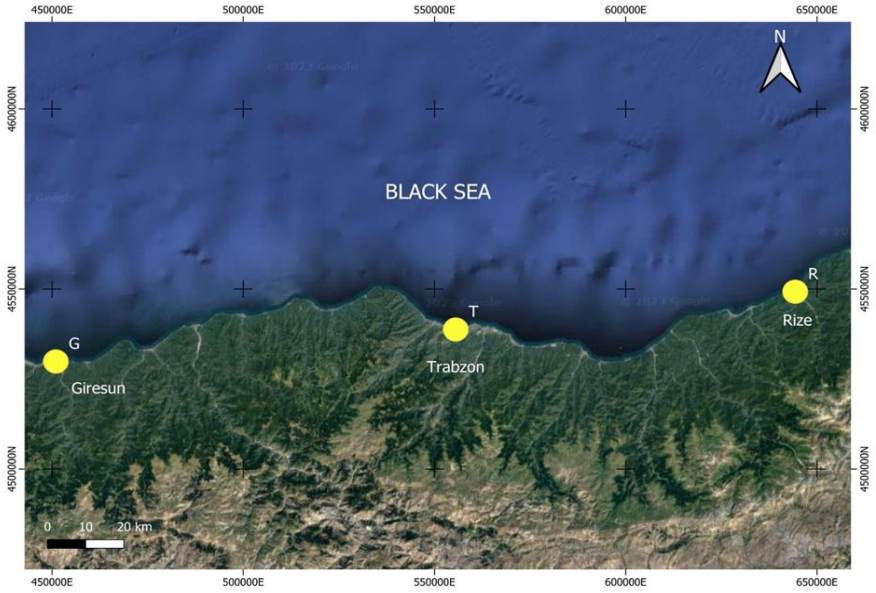

Figure 1. The map of study area

In order to determine the abundance of marine litter per square meter, the separated samples were counted and weighed in the field. In order to contribute to the environment, the wastes collected from the stations were eliminate of in the nearest rubbish container. Kolmogorow-Smirnov test, one of the most important normal distribution tests, was used to determine the normal distribution of the data. Benferroni test, one of the post hoc tests, was used to reveal the difference between stations. Temporal and spatial visual and statistical differences were determined according to Nonmetric multidimensional scaling (NMDS) and ANOSIM tests (Oksanen et al. 2020). Principal component analysis (PCA) was used to determine the extent to which marine litter derivatives in the subcategory differ.

Result and Discussion

A total of 4261 marine litter material with a unified weight of 48.761 kg were gathered from the three beaches. Each type of garbage material was put in place at all the stations during the all-seasons survey time. The plenty of litter materials diverse among the stations. The highest densities in symbol and mass were saved at station T (beach of Trabzon province) (summer; 14.53 items/m^2; 630 g/m^2) and (winter; 3.21 items/m^2; 475 g/m^2), respectively. (Figure 2).

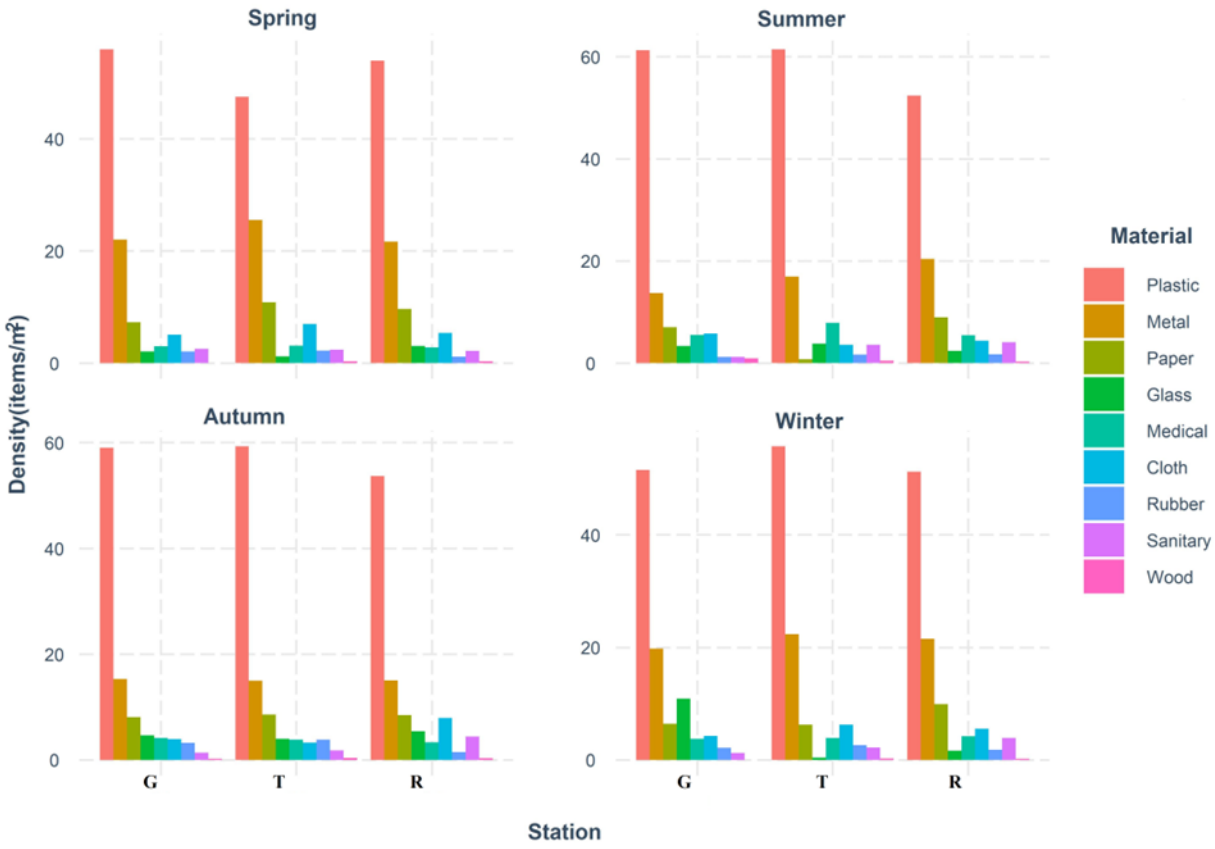

Figure 2. Spatial and temporal distribution of marine litter

The mean plenty by symbol and mass was the maximum in summer (station of T); Also, there was notable dissimilarity infertility between the years both by symbol (ANOVA, F (4,30) = 1.13, $p < 0.03$) and mass (Kolmogrov-Simirnov, $\chi 2(4) = 2.8\ 1$, $p < 0.05$). The mean prosperity by the station was remarkably higher at T, R, and G by symbol (ANOVA, F (6,28) = 7.43, $p < 0.05$) and mass (K–S test, $\chi 2(6) = 24.1$, $p < 0.05$) (Figure 3).

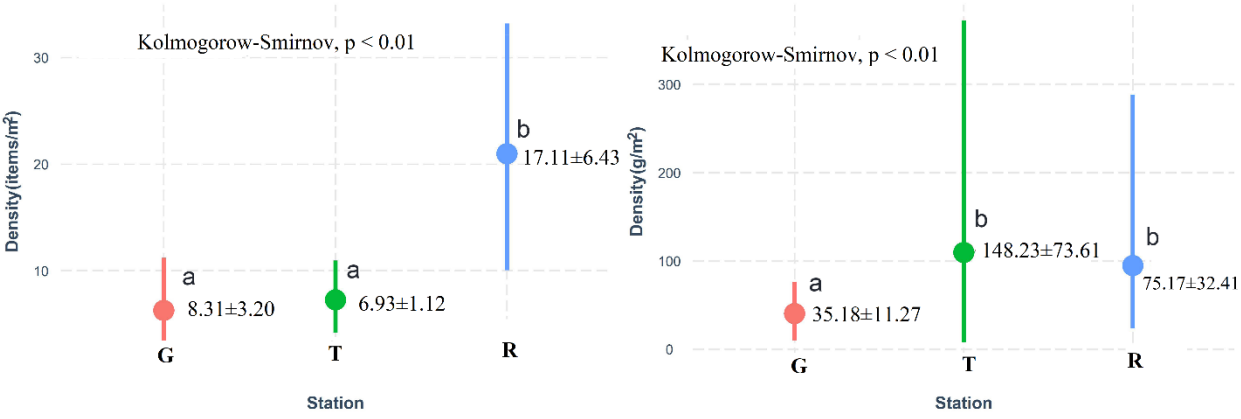

Figure 3. According to number and weight of marine litter assessment as a statistical

Marine litter in the research area was evaluated in 8 main classes and 42 sub-categories belonging to these classes. According to this evaluation, when the abundance of marine litter per unit area is examined, it is seen that the order is plastic>metal>paper>glass>medical>cloth>rubber>sanitary>wood (Figure 4).

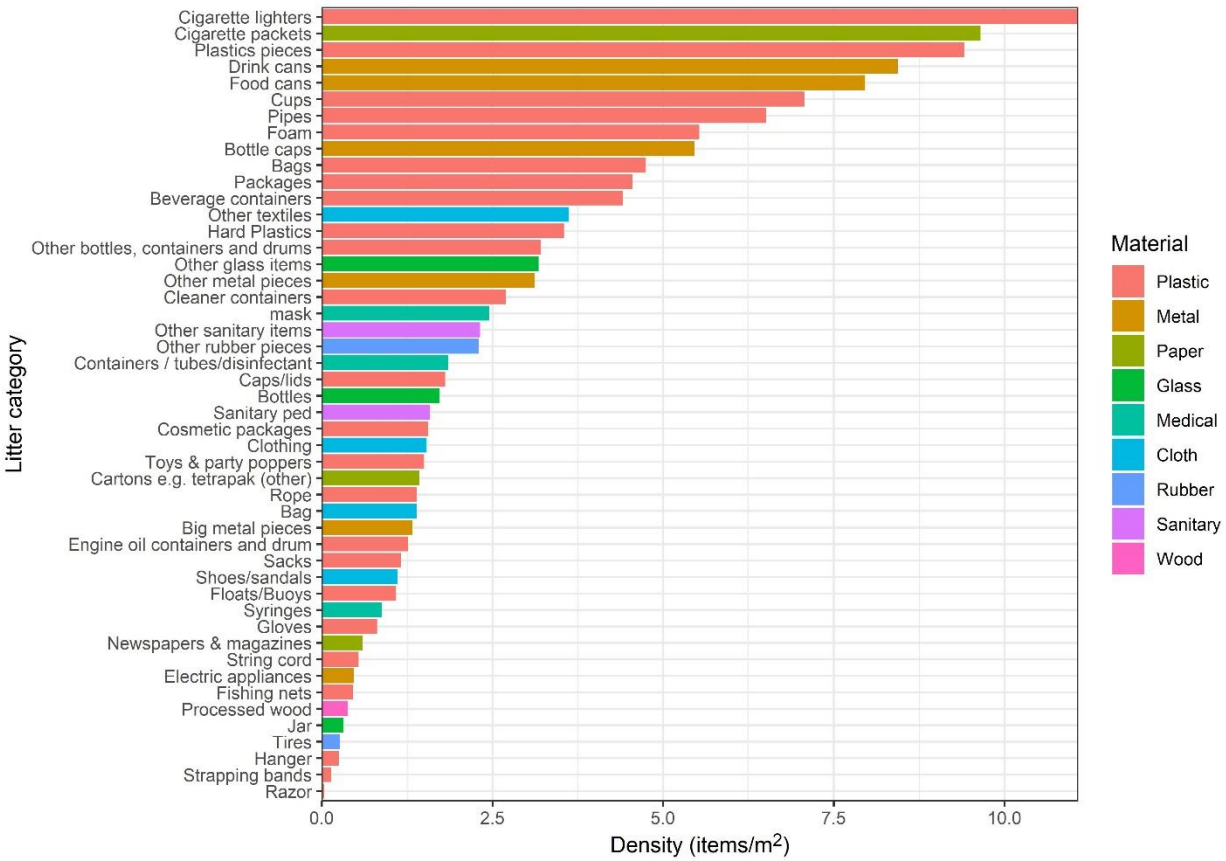

Figure 4. Classification of marine litter by subcategories

This ranking is similar to other studies conducted in the region (Terzi et al. 2020, 2022; Erüz et al. 2022). It is particularly noteworthy that plastic is reported as the most concentrated marine litter derivative. In addition, the increase in medical and sanitary derivatives increased after the Covid-19 pandemic period, but it is similar to other studies. River transport (30.40%), human activities (28.61%), poor disposal (20.75%) and other factors (20.24%) constitute the main source of marine litter on the beaches identified in Giresun, Trabzon and Rize provinces. The x and y axes determined according to principal component analysis (PCA) constitute 95.2% of the total variance. According to these variances, high differentiation between summer and winter seasons draws attention (Figure 5). The decomposition in this visual graph is due to the increase in plastic, metal, glass and medical-derived marine litter in the summer.

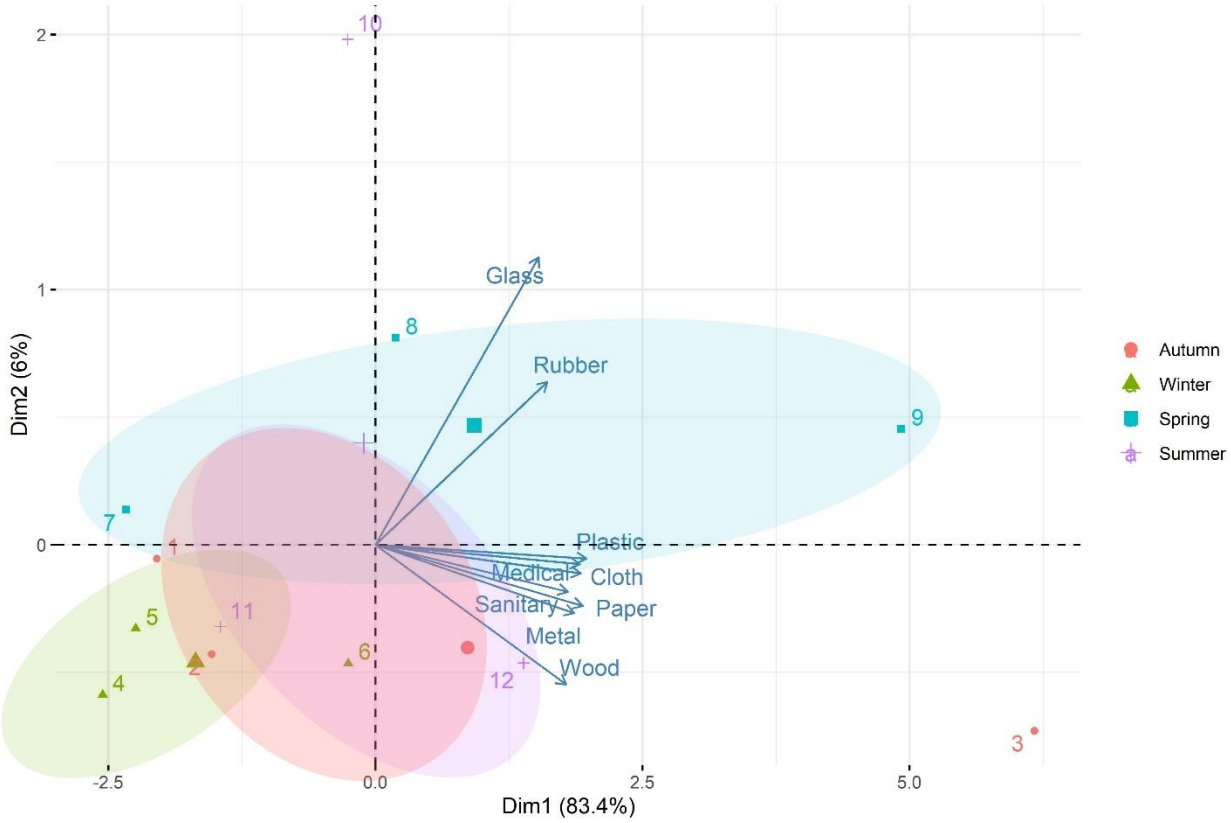

Figure 5. Seasonal variation in marine litter according to PCA analysis

Many studies have been conducted on the spatial and temporal distribution of marine litter in the Black Sea coastal ecosystems(Topçu et al. 2013; Stanev and Ricker 2019; Simeonova and Chuturkova 2019; Chuturkova and Simeonova 2021; Erüz et al. 2022). In summary, it has been reported that the most common marine litter derivative in all of these studies is plastic. In addition, a high increase was observed in marine litter from sanitary and medical sources after 2019-2020.

Conclusion

The spatial and temporal distribution of seasonal marine litter was determined in 2022 on the beaches determined in the provinces of Giresun, Trabzon and Rize, located on the southeastern Black Sea coast. In addition, possible sources were revealed. Plastic was determined as the best extensive and abundant marine litter derivative in the research area. Human activities and river transport are the most important sources of marine litter. Unfortunately, we still see the environmental effects of the Covid-19 pandemic as medical waste. Depending on the intensity of human activities, the summer season was determined to be different from other seasons in terms of marine litter abundance. These studied beaches are an example to understand the current litter problem and threat for the future of the shore ecosystems of the Black Sea. Raising awareness and training of citizens for garbage pollution in local areas should be more effective. We can responsibly take advantage of all the possibilities offered by plastics by disposing of them correctly or sending them for recycling after use. It would also be a good measure to limit the manufacture and use of plastic products, especially sacks, and plastic bottles. Recognition and training programs should be implemented to increase awareness on waste recycling and nature protection. Practices such as individual liability and objective penal sanctions, on-site disposal, waste reduction and recycling should definitely be implemented. In particular, the production and disposal of hygienic products that

are difficult to disperse in nature, such as masks, disinfectant boxes, child and patient diapers, should be controlled.

References

Bettencourt S, Costa S, Caeiro S (2021) Marine litter: A review of educative interventions. Mar Pollut Bull 168:. https://doi.org/10.1016/j.marpolbul.2021.112446

Chuturkova R, Simeonova A (2021) Sources of marine litter along the Bulgarian Black Sea coast: Identification, scoring and contribution. Mar Pollut Bull 173:113119. https://doi.org/10.1016/J.MARPOLBUL.2021.113119

Erüz C, Terzi Y, Öztürk RÇ, Karakoç FT, Özşeker K, Şahin A, Ismail NP (2022) Spatial pattern and characteristics of the benthic marine litter in the southern Black Sea shelf. Mar Pollut Bull 175:113322. https://doi.org/10.1016/J.MARPOLBUL.2022.113322

Gonçalves G, Andriolo U, Pinto L, Duarte D (2020) Mapping marine litter with Unmanned Aerial Systems: A showcase comparison among manual image screening and machine learning techniques. Mar Pollut Bull 155:111158. https://doi.org/10.1016/j.marpolbul.2020.111158

Mazarrasa I, Puente A, Núñez P, García A, Abascal AJ, Juanes JA (2019) Assessing the risk of marine litter accumulation in estuarine habitats. Mar Pollut Bull 144:117–128. https://doi.org/10.1016/j.marpolbul.2019.04.060

Mghili B, De-la-Torre GE, Aksissou M (2023) Assessing the potential for the introduction and spread of alien species with marine litter. Mar Pollut Bull 191:114913. https://doi.org/10.1016/j.marpolbul.2023.114913

Oksanen J, Blanchet FG, Friendly M, Kindt R, Legendre P, McGlinn D, Minchin PR, O'Hara RB, Simpson GL, Solymos P, Stevens MHH, Szoecs E, Wagner H (2020) vegan: Community Ecology Package

Okuku EO, Kiteresi L, Owato G, Otieno K, Omire J, Kombo MM, Mwalugha C, Mbuche M, Gwada B, Wanjeri V, Nelson A, Chepkemboi P, Achieng Q, Ndwiga J (2021) Temporal trends of marine litter in a tropical recreational beach: A case study of Mkomani beach, Kenya. Mar Pollut Bull 167:112273. https://doi.org/10.1016/j.marpolbul.2021.112273

Ospar (2010) Marine Litter | OSPAR Commission. https://www.ospar.org/work-areas/eiha/marine-litter. Accessed 7 Sep 2021

Özşeker K, Terzi Y, Erüz C (2022) Solid waste composition and COVID-19-induced changes in an inland water ecosystem in Turkey. Environ Sci Pollut Res 29:54596–54605. https://doi.org/10.1007/s11356-022-19750-6

Ribeiro V V., Pinto MAS, Mesquita RKB, Moreira LB, Costa MF, Castro ÍB (2021) Marine litter on a highly urbanized beach at Southeast Brazil: A contribution to the development of litter monitoring programs. Mar Pollut Bull 163:. https://doi.org/10.1016/j.marpolbul.2021.111978

Simeonova A, Chuturkova R (2019) Marine litter accumulation along the Bulgarian Black Sea coast: Categories and predominance. Waste Manag 84:182–193. https://doi.org/10.1016/J.WASMAN.2018.11.001

Stanev E V., Ricker M (2019) The Fate of Marine Litter in Semi-Enclosed Seas: A Case Study of the Black Sea. Front Mar Sci 6:1–16. https://doi.org/10.3389/fmars.2019.00660

Terzi Y, Erüz C, Özşeker K (2020) Marine litter composition and sources on coasts of south-eastern Black Sea: A long-term case study. Waste Manag 105:. https://doi.org/10.1016/j.wasman.2020.01.032

Terzi Y, Gedik K, Eryaşar AR, Öztürk RÇ, Şahin A, Yılmaz F (2022) Microplastic contamination and characteristics spatially vary in the southern Black Sea beach sediment and sea surface water. Mar Pollut Bull 174:113228. https://doi.org/10.1016/J.MARPOLBUL.2021.113228

Topçu EN, Tonay AM, Dede A, Öztürk AA, Öztürk B (2013) Origin and abundance of marine litter along sandy beaches of the Turkish Western Black Sea Coast. Mar Environ Res 85:21–28. https://doi.org/10.1016/j.marenvres.2012.12.006

Valderrama-herrera M, Amada S, Calvo-mac C, Celi-v RG, Chumpitaz-levano VL, Flores-miranda WE, Lopez-tirado ZMT, Molina-alvarez M, Rubio-cheon DN, L ADF, Trucios-castro M, Fern MD, Ramos W, Pretell V, Castro IB, Ribeiro VV, Dioses-salinas DC, De-la-torre GE (2023) Rajids ovipositing on marine litter : A potential threat to their survival. Mar pol 191:. https://doi.org/10.1016/j.marpolbul.2023.114941

Method Validation for the Sensitive and Simultaneous Detection of Fifty-Five Volatile Organic Compounds (VOCs) with Human Health Hazards in Environmental Waters

Barış GÜZEL[1]

1.Introduction

The ever-increasing impact of climate change has made it essential to utilize existing water resources with the highest efficiency. In order to maintain the ecological balance and ensure the continuity of human life, water resources should be used in the most rational way to meet current and future needs (Karaman and Gökalp, 2010). For this reason, the utilization and sustainable management of water resources have been the main agenda item of the countries. However, the uncontrolled and rapid increase in human population, urbanization, and industrialization activities in the world and in our country constitute an obstacle to the efficient use of water resources. Many harmful pollutants are released into the environment during or as a result of these activities (Botwe et al., 2017; Özdemir, 2021). Substances generated as a result of industrial activities and the disposal and storage of their wastes, industrial gases, and chemicals used to prevent crop loss in agricultural activities are important environmental pollutants, especially in terms of posing serious threats to human health. Today, volatile organic compounds (VOCs), polycyclic aromatic hydrocarbons, polychlorinated biphenyls, polybrominated diphenyl ethers, polychlorinated dibenzo-p-dioxins/furans, phthalates, phenols, organochlorine/phosphorus pesticides, perfluorinated and polyfluorinated alkyl substances, and heavy metals are the most studied pollutant groups in the environment (Aravind Kumar et al., 2022; Başar et al., 2017; Güzel et al., 2022).

VOCs are defined as organic substances consisting of carbon chains with boiling points between 40 °C and 260 °C and having a high vapor pressure at room temperature (ASTM, 1989; Huybrechts et al., 2005; Riddick et al., 1985; WHO, 1987). Due to their physical features and chemical structures, VOCs quickly penetrate into the aquatic environment. In particular, water solubility, boiling point, vapor pressure, log Kow, and density values are the most important properties that determine the diffusion of these substances into the aquatic environment and their long-term presence in the relevant media. Henry's constant is significant because it provides information about a substance's concentration and potential for volatility in a state of chemical equilibrium in water (Güzel et al. 2018a). Table 1 lists the log K_{ow} values for fifty-five VOCs along with their water solubility, boiling temperature, Henry constant, density, and vapor pressure. Their persistence causes them to have poisonous, mutagenic, and carcinogenic impacts on people and aquatic life. According to some studies on found nasal tumors and irritation of human skin and eyes brought on by exposure to VOCs the International Agency for Research on Cancer (IARC) has classified naphthalene as a material that may be carcinogenic to humans (Liu et al., 2021; Weber et al., 2022). The release of VOCs is regularly monitored and restricted around the world with the help of national and international lists such as the Food and Environmental Protection Act (FEPA/1985), European Union (EU) Water Framework Directive (2000/60/EC), Prevention and Control (PPC) Regulations, Türkiye Regulation Concerning Water Intended for Human Consumption (Official Gazette: 17.02.2005.

[1] Barış Güzel, Kıdemli Uzman Araştırmacı/Dr., TUBITAK Marmara Research Center, Climate Change and Sustainability Vice Presidency, Water Management and Treatment Technologies Research Group

Number: 25730), Türkiye Surface Water Quality Regulation and the United Kingdom (UK) Surface Waters (dangerous substances) Regulations (SI 1997/2560).

A wide variety of methods are available for measuring VOCs in water in analytical chemistry. However, many of them are not preferred due to various analytical difficulties (use of solvents, etc.) and not being economical in terms of time and cost (Jakubowska et al., 2005; Ketola et al., 2002; Tor and Aydin, 2006). Solid phase micro-extraction, purge-trap (PT), headspace, gas/liquid chromatography (GC/LC), mass spectrometry (MS), and multi-instrument combinations, unlike other techniques, are often the mainstays of VOC measurement technology. These techniques are more sensitive and offer lower detection limits for VOCs (Chen et al., 2014; Demeestere et al., 2007; Gu et al., 2010; Safarova et al., 2004; Yu et al., 2003).

This study was to aim for precise, accurate, and simultaneous measurements of the fifty-five VOCs that pose a high toxicity threat to human and environmental health, taking into account the scope of various national and international regulations such as the Water Framework Directive and the Surface Water Quality Regulation.

Table 1. *Some physical, and chemical properties of fifty-five VOCs (ATSDR 1997; EPA 2002; Tsuchiya, 2010; Alonso et al., 2011; Güzel et al., 2018a; Güzel et al., 2018b; Güzel and Canlı, 2020a)*

Compound	Cas no	Chemical Formula	Water Solubility (mg/L) (25 °C)	Boiling point (°C)	Vapor Pressure (mm Hg)	Density (g/cm^3)	Log K_{ow}	Henry Constant ($atm.m^3/mol$)
Vinyl Chloride	75-01-4	C_2H_3Cl	1100	-13	290 (25°C)	0.91	1.46	$2.78x10^{-2}$
Dichloromethane	75-09-2	CH_2Cl_2	13200	40	58.4 (25°C)	1.33	1.25	$2.19x10^{-3}$
1,1-Dichloroethane	75-34-3	$C_2H_4Cl_2$	8600	57	180.0 (20°C)	1.24	1.48	$5.62x10^{-3}$
Bromochloromethane	74-97-5	CH_2BrCl	9	68	142.0 (25°C)	1.93	1.41	$1.46x10^{-3}$
Trichloromethane	67-66-3	$CHCl_3$	7950	61	158.3 (20°C)	1.48	1.97	$3.67x10^{-3}$
1,2-Dichloroethane	107-06-2	$C_2H_4Cl_2$	8600	84	61.0 (20°C)	1.25	1.48	$9.79x10^{-4}$
2,2-Dichloropropane	594-20-7	$C_3H_6Cl_2$	2800	96	53.3 (25°C)	1.16	1.98	$2.82x10^{-3}$
Benzene	71-43-2	C_6H_6	1790	80	95.2 (25°C)	0.88	2.13	$5.55x10^{-3}$
Trichloroethene	79-01-6	C_2HCl_3	1280	87	58.0 (20°C)	1.46	2.61	$1.00x10^{-2}$
1,2-Dichloropropane	78-87-5	$C_3H_6Cl_2$	2800	96	53.3 (25°C)	1.16	1.98	$2.82x10^{-3}$
Dibromomethane	74-95-3	CH_2Br_2	12	97	44.4 (25°C)	2.50	1.70	$8.22x10^{-4}$
Bromodichloromethane	75-27-4	$CHBrCl_2$	3968	90	50.1 (20°C)	1.90	2.00	$1.60x10^{-3}$
Cis-1,3-Dichloropropene	10061-01-5	$C_3H_4Cl_2$	2700	104	28.0 (25°C)	1.22	2.06	$2.70x10^{-3}$
Trans-1,3-Dichloropropene	10061-01-6	$C_3H_4Cl_2$	2800	112	34.0 (25°C)	1.22	2.03	$8.70x10^{-4}$
Toluene	108-88-3	$C_6H_5CH_3$	526	111	28.4 (25°C)	0.87	2.73	$6.64x10^{-3}$
1,1,2-Trichloroethane	79-00-5	$C_2H_3Cl_3$	4590	113	23.0 (25°C)	1.44	1.89	$8.24x10^{-4}$
1,1,1-Trichloroethane	71-55-6	$C_2H_3Cl_3$	1290	74	124.0 (25°C)	1.31	2.49	$1.63x10^{-2}$
1,3-Dichloropropane	142-28-9	$C_3H_6Cl_2$	2750	120	18.2 (25°C)	1.19	2.00	$7.96x10^{-4}$
Dibromochloromethane	124-48-1	$CHBr_2Cl$	2700	120	5.5 (25°C)	2.38	2.16	$7.83x10^{-4}$

Tetrachloroethene	127-18-4	C_2Cl_4	206	121	12.8 (20°C)	1.62	3.40	$1.84x10^{-2}$
1,2-Dibromoethane	106-93-4	$C_2H_4Br_2$	3910	131	11.2 (25°C)	2.18	1.96	$6.50x10^{-4}$
Chlorobenzene	108-90-7	C_6H_5Cl	499	132	12.0 (25°C)	1.11	2.84	$3.11x10^{-3}$
Tetrachloromethane	56-23-5	CCl_4	793	77	91.3 (20°C)	1.59	2.83	3.04x10-^{2}
1,1,1,2-Tetrachloroethane	630-20-6	$C_2H_2Cl_4$	1070	131	12.0 (25°C)	1.54	2.66	$2.50x10^{-3}$
Ethylbenzene	100-41-4	C_8H_{10}	169	136	6.8 (20°C)	0.90	3.15	$7.88x10^{-3}$
P_M_Xylene	106-42-3; 108-38-3	C_8H_{10}	165	138-139	8.8 (25°C)	0.86	3.15	$6.90x10^{-4}$
Styrene	100-42-5	C_8H_{10}	178	145	4.5 (20°C)	0.91	3.12	$5.18x10^{-4}$
O-Xylene	95-47-6	C_6H_8	300	144	6.7 (25°C)	0.88	2.95	$2.75x10^{-5}$
Tribromomethane	75-25-2	$CHBr_3$	3100	149	5.3 (20°C)	2.89	2.40	$5.35x10^{-4}$
1,1,2,2-Tetrachloroethane	79-34-5	$C_2H_2Cl_4$	2830	147	5.7 (25°C)	1.59	2.39	$4.20x10^{-4}$
Isopropylbenzene	98-82-8	C_9H_{12}	50	151	4.5 (25°C)	0.86	3.66	$1.15x10^{-3}$
1,1-Dichloropropene	563-58-6	$C_3H_4Cl_2$	2700	77	24.0 (25°C)	1.19	2.53	$2.60x10^{-5}$
1,2,3-Trichloropropane	96-18-4	$C_3H_5Cl_3$	1750	158	3.7 (25°C)	1.39	2.27	$3.43x10^{-4}$
4-bromofluorobenzene (IS)	460-004	C_6H_4BrF	140	152	4.1 (25°C)	1.50	3.02	$5.30x10^{-3}$
Bromobenzene	108-86-1	C_6H_5Br	410	156	4.2 (25°C)	1.49	2.99	$6.50x10^{-3}$
2-Chlorotoluene	95-49-8	C_7H_7Cl	5	159	3.4 (25°C)	1.08	3.42	$3.57x10^{-3}$
N-Propylbenzene	103-65-1	C_9H_{12}	23	159	3.4 (25°C)	0.86	3.69	$1.05x10^{-3}$
4-Chlorotoluene	109-43-4	C_7H_7Cl	2	162	2.8 (20°C)	1.07	3.33	$4.30x10^{-3}$
1,3,5-Trimethylbenzene	108-67-8	C_9H_{12}	48	165	1.9 (20°C)	0.86	3.42	$8.77x10^{-4}$
Tert-Butylbenzene	98-06-6	$C_{10}H_{14}$	30	169	2.2 (25°C)	0.87	4.11	$1.32x10^{-2}$
1,2,4-Trimethylbenzene	95-63-6	C_9H_{12}	57	168	7.0 (44°C)	0.88	3.78	$6.16 x10^{-3}$
1,3-Dichlorobenzene	541-73-1	$C_6H_4Cl_2$	125	173	3.4 (38°C)	1.29	3.53	$3.10x10^{-3}$
Sec-Butylbenzene	135-98-8	$C_{10}H_{14}$	18	174	1.8 (25°C)	0.86	4.57	$1.80x10^{-2}$
1,4-Dichlorobenzene	106-46-7	$C_6H_4Cl_2$	79	174	2.2 (25°C)	1.25	3.44	$2.43x10^{-3}$
P-Isopropyltoluene	99-87-6	$C_{10}H_{14}$	23	177	1.5 (25°C)	0.86	4.10	$1.10x10^{-2}$
1,2-Dichlorobenzene	95-50-1	$C_6H_4Cl_2$	156	180	1.7 (25°C)	1.30	3.38	$1.90x10^{-3}$
N-Butylbenzene	104-51-8	$C_{10}H_{14}$	12	183	0.9 (20°C)	1.06	1.06	$1.60x10^{-2}$
1,2-Dibromo-3-chloropropane	96-12-8	$C_3H_5Br_2Cl$	1200	165	0.8 (25°C)	2.08	2.96	*$1.47x10^{-4}$*
1,3,5-Trichlorobenzene	108-70-3	$C_6H_3Cl_3$	6	208	1.4 (25°C)	1.46	4.19	$1.89x10^{-4}$
1,2,4-Trichlorobenzene	120-82-1	$C_6H_3Cl_3$	49	214	10.0 (78°C)	1.45	4.02	$1.42x10^{-3}$
Naphthalene	91-20-3	$C_{10}H_8$	30	218	0.1 (25°C)	1.16	4.05	$1.25x10^{-3}$
Hexachlorobutadiene	87-68-3	C_4Cl_6	31	215	0.2 (25°C)	1.56	3.30	$4.83x10^{-4}$
1,2,3-Trichlorobenzene	87-61-3	$C_6H_3Cl_3$	3.20	218	1.0 (25°C)	1.45	4.78	$8.15x10^{-3}$
1-methylnaphthalene	90-12-0	$C_{11}H_{10}$	26	244	0.07 (25°C)	1.02	3.87	$5.14x10^{-4}$
1-chloronaphthalene	90-13-1	$C_{10}H_7Cl$	17	259	0.03 (25°C)	1.19	4.00	$3.55x10^{-4}$
2-chloronaphthalene	91-58-7	$C_{10}H_7Cl$	12	255	0.01 (25°C)	1.14	3.90	$3.20x10^{-4}$

IS:Internal Standard

2.Materials and Methods

2.1.Reagents and Chemicals

VOC standard solution, which contains 60 different chemicals (200 mg/L each in methanol), was supplied from High Pourity Standards Co., Inc. (North Charleston, USA) in 2 ml amber glass bulb. Standard solutions of 1,2,3-trichlorobenzene, 1-methylnaphthalene, 1-methylnaphthalene, 1-chloronaphthalene, and 2-chloronaphthalene in methanol (GC gradient grade) greater than 99.8% were purchased as single ampoules by Dr. Ehrenstrofer (Augsburg,

Germany). 4-Bromofluorobenzene (25 mg/mL in methanol), the internal standard (IS) for the analysis, was purchased from Absolute Standards Co., Inc. (Hamden, USA). The highest purity grade of methanol was given by Merck (Darmstadt, Germany), and the water as blank was purified using the Milli-Q Plus system (EMD Millipore, Billerica, MA).

Moreover, 200 mg/L of stock VOC solution and 100 mg/L of additional single standards were combined to create stock standard solutions with concentrations of 1 mg/L and 10 mg/L. These solutions were kept in 1.5 mL vials and protected in a freezer (- 20 °C). Due to their stability, they should be prepared again once a month. By diluting stock standard solutions in the ultra-pure water, standard solutions were prepared for the linearity and other tests.

2.2.Water Samples

Within the scope of the study, surface water, seawater and wastewater samples were examined as environmental water samples. 250 mL glass bottles were used to collect the seawater samples, which were taken 1500 meters from the Fener port in the Black Sea region (Rumelifeneri, Saryer, Istanbul). Surface water samples were collected in 250 mL glass bottles from Terkos, Alibey, Büyükçekmece, Papuçdere, Kazandere dam lakes and the rivers connected to these lakes. Sampling in dam lakes was carried out with the help of Zodiac boat. From the Istanbul Water and Sewerage Administration (ISKI) wastewater treatment facility in Kadıköy, samples of wastewater were collected in 500 mL bottles. Until their measurements, all of the samples were safeguarded and kept at a temperature of less than 5 °C. The processing and preservation of water samples were done in accordance with the relevant ISO standard (ISO, 2012). The sample underwent a stability test as follows: Following sampling, each sample was kept in an atmosphere of approximately 5 °C for 48 hours before being tested. No substantial difference or divergence from the results was discovered.

2.3.Analytical Instrumentation

2.3.1.PT Analytical Condition

The PT system is the instrumental system consisting of an OI analytical Eclipse Model 4660 sample concentrator (College Station, TX, USA) fitted with an OI analytical 4552 water/soil autosampler for collecting relevant VOCs from water samples. The collection of VOCs in the PT system gradually occurs as follows: A sample of water was added to the 50 ml sample container so that no air remains. It was then transferred to the purge unit for 25 ml sample extraction process by means of autosampler. IS (20 µL from IS with a concentration of 2.5 mg/L) was added to the sample via the injector before the extraction process to see possible pre-treatment based analyt losses. Using just pure helium gas (purge gas), water sample was purged to completely extract all of the volatile analytes. Analytes were sent to the trap unit after the purging process (the trapping material is Purge Trap K VOCARB 3000). As a result, the captured analytes in the trap were moved to the GC column for separation by high temperature desorption. The details of the work program of the PT where the extraction and enrichment of VOCs before their analysis by GC-MS are presented in Table 2.

Table 2. *The working conditions of PT for fifty-five VOCs*

Parameters	Conditions
Purge gas flow rate	50 mL/min
Purge time	12 min
Trap initial temperature	30 °C
Dry purge time	8 min
Desorb preheat-trap temperature	200 °C
Desorb time	3 min
Desorb-trap temperature	200 °C
Bake time	7 min
Bake-trap temperature	260 °C

2.3.2.GC-MS Condition

For the purpose of determining the related VOCs, an Agilent Technologies 6890N network GC system (Avondale, USA) in conjunction with a 5975C inert mass spectrometer with a triple detector (MSD) was used. To ensure effective chromatographic separation of each VOC purged out of the water samples, a fused silica capillary column (DB-5MS) was employed. Details of the GC program and MS analytical conditions for the determination of fifty-five VOCs are detailed in Table 3. In this study, the peak appearances of some VOCs in the GC-MS chromatogram of 5 μg/L standard solution are also shown in Figure 1.

Table 3. *GC program and MS analytical condition for the determination of fifty-five VOCs*

Compound	Retention time (min)	Target ion (m/z)	Quantified ion-1 (m/z)	Quantified ion-2 (m/z)
Vinyl Chloride	4.45	62	27	64
Dichloromethane	5.28	84	86	51
1,1-Dichloroethane	5.87	63	65	83
Bromochloromethane	6.51	130	128	132
Trichloromethane	6.61	83	85	87
1,2-Dichloroethane	7.28	62	64	63
2,2-Dichloropropane	7.42	78	77	79
Benzene	7.48	78	77	79
Trichloroethene	8.55	130	95	97
1,2-Dichloropropane	8.65	63	62	65
Dibromomethane	8.70	174	93	95
Bromodichloromethane	8.97	83	85	129
Cis-1,3-Dichloropropene	9.84	75	77	110
Trans-1,3-Dichloropropene	10.77	75	77	110
Toluene	10.78	91	92	93
1,1,2-Trichloroethane	11.14	97	83	99
1,1,1-Trichloroethane	11.14	97	61	99
1,3-Dichloropropane	11.44	76	78	63
Dibromochloromethane	12.01	129	127	131
Tetrachloroethene	12.14	166	164	168
1,2-Dibromoethane	12.34	107	109	121
Chlorobenzene	13.58	112	77	114
Tetrachloromethane	13.80	117	119	121
1,1,1,2-Tetrachloroethane	13.80	131	133	117
Ethylbenzene	14.07	91	106	77
p_m_Xylene	14.41	91	106	77
Styrene	15.10	104	103	78
o-Xylene	15.15	91	106	77
Tribromomethane	15.19	173	171	175
1,1,2,2-Tetrachloroethane	16.00	83	85	95

Isopropylbenzene	16.15	105	120	103
1,1-Dichloropropene	16.21	75	110	112
1,2,3-Trichloropropane	16.21	110	75	112
IS-4-bromofluorobenzene	16.28	95	174	176
Bromobenzene	16.47	83	85	95
2-Chlorotoluene	17.07	77	156	158
n-Propylbenzene	17.11	91	120	
4-Chlorotoluene	17.29	91	125,9	89
1,3,5-Trimethylbenzene	17.58	105	120	119
tert-Butylbenzene	18.28	119	91	134
1,2,4-Trimethylbenzene	18.36	105	120	119
1,3-Dichlorobenzene	18.77	146	148	111
sec-Butylbenzene	18.82	105	134	106
1,4-Dichlorobenzene	19.04	146	148	111
p-Isopropyltoluene	19.25	119	134	91
1,2-Dichlorobenzene	19.60	146	148	111
n-Butylbenzene	20.13	91	92	134
1,2-Dibromo-3-chloropropane	21.14	157	75	155
1,3,5-Trichlorobenzene	22.31	180	182	184
1,2,4-Trichlorobenzene	23.49	180	182	184
Naphthalene	23.80	128	129	51
Hexachlorobutadiene	24.26	225	223	
1,2,3-Trichlorobenzene	24.34	180	182	184
1-methylnaphthalene	26.82	142	141	115
1-chloronaphthalene	28.31	162	127	
2-chloronaphthalene	28.39	162	127	

Instrument	Agilent 6890N Headspace GC Single Quadropole MS		
Carrier Gas	Helium	**MS Temperature**	250 °C
Carrier Gas Flow	1.0 mL/min	**Quad Temperature**	170 °C
Column Type	DB-5MS	**Electron Energy**	70 eV
Column Length	60 m	**Split Ratio**	1:20
Column Inner Diameter	0.25 mm	**Split Liner**	4.0 mm
Film Thickness	0.25 μm	**Injector Temperature**	200 °C
Detector Type	MS	**Transfer Temperature**	325 °C

Oven Temperature Program	**Ratio (°C/min)**	**Temperature (°C)**	**Hold Time (min.)**
Initial		40	2
	7	200	0.01
	15	280	3

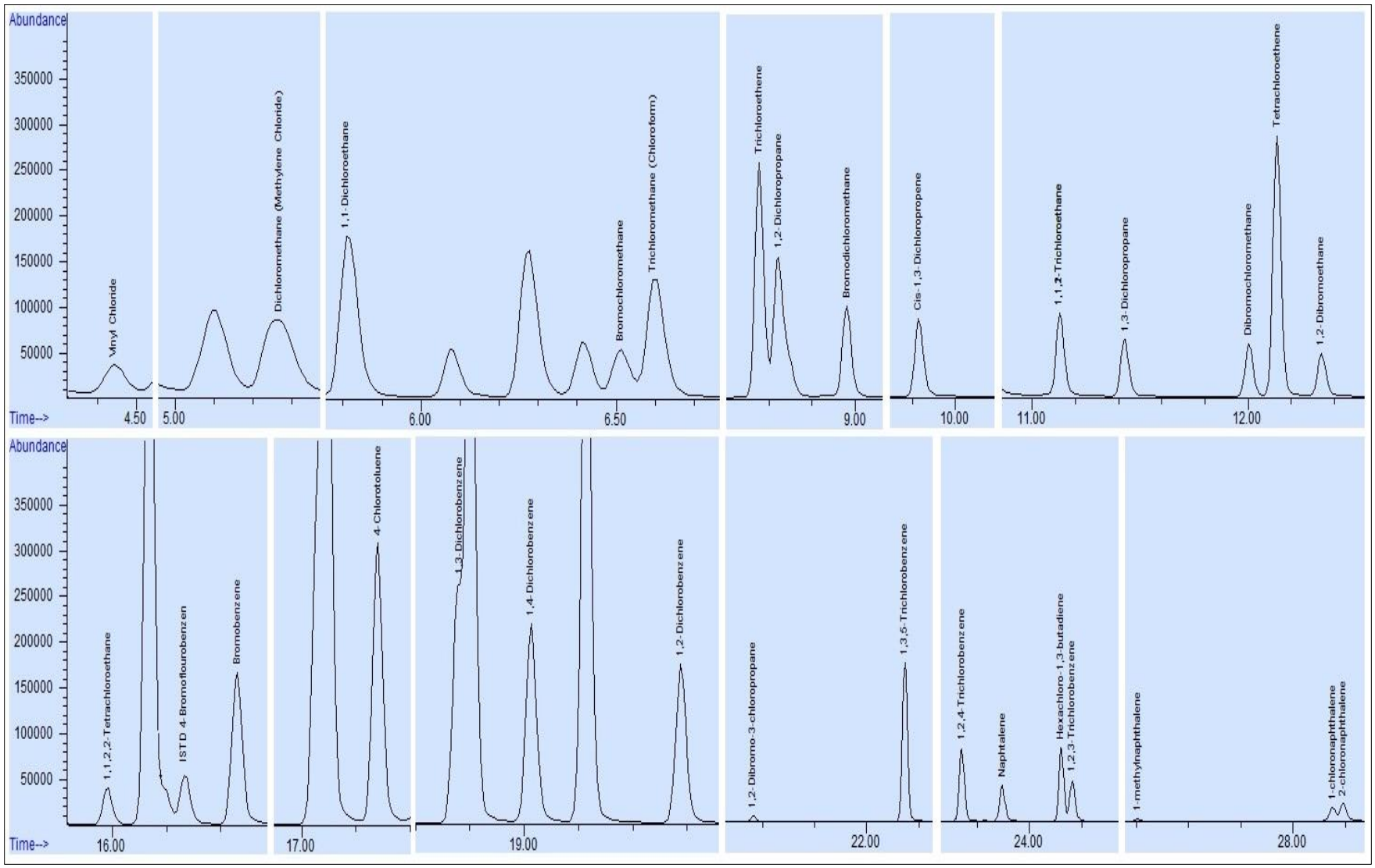

Figure 1. *GC-MS chromatogram of some VOCs in 5 µg/L standard solution*

3.Results and Discussion

According to decisions of international commissions in the related guidelines EURACHEM Guideline (EURACHEM/CITAC, 2014) and Guidelines for Standard Method Performance Requirements (AOAC, 2016)), the performance of this method was assessed in terms of the following parameters: Selectivity, linearity, the limit of detection (LOD) and quantification (LOQ), trueness, accuracy, and precision. High purity water was used as a control sample.

3.1.Selectivity

Selectivity is the ability of a method to identify and quantify the analyte when there are other components present as interference (Kaiser and Ritts, 2006; Taverniers et al., 2004). The selectivity study was carried out by binary analysis of six purified water samples used as blank samples. At the conclusion of the analysis, the peaks of undesired substances were not found in the chromatograms close to the retention time of the target analytes in this study. Also, these VOCs did not have significant background contamination, which raised the LOD in blank samples.

3.2.Linearity

The capacity of analytical procedures to give results that are directly proportional to the analyte concentration range in samples while maintaining the necessary concentration levels is defined as the linearity of an analytical/calibration curve. The fact that the linear regression with correlation coefficient is higher than 0.99 and the deviation in the calibration line is less than 25% for all individual calibration points indicates that this graph exhibits adequate and sufficient linearity (Ferreira et al., 2016; Güzel and Canlı, 2020a). The data of coefficient correlation, calibration curve equation, and linear dynamic range of each VOC are presented in Table 2. Analytical curves consisting of fifty-five different VOCs, at nine concentrations (0.15; 0.25; 0.50; 1.00; 2.00; 5.00; 10.00; 20.00 and 40.00 μg/L), were prepared by plotting the peak area versus the relative concentration for each analyte. As seen in the results in Table 2, the analytical curve linearity among working concentrations is considered to be excellent since the correlation coefficients for all VOCs ranged from 0.9975 to 0.9999. The linear dynamic range varies between 0.15-40.00 μg/L, excluding dichloromethane (2.00-40.00 μg/L) and p_m_xylene (0.30-80.00 μg/L). In some VOCs, and especially BTEXs, their calibration curves in this study have more preferable linearity in that it starts from lower concentration levels than that curves in previous studies (Cavalcante et al., 2010; Dongqiang et al., 2006; Serrano and Gallego, 2004).

Table 2. *Linearity and LOD-LOQ results of fifty-five VOCs*

Compound	Coefficient correlation (r^2)	Calibration curve equation (y = ax + b)	Linear dynamic range (µg/L)	LOD (µg/L)	LOQ (µg/L)
Vinyl Chloride	0.9994	y = 1091.9x - 52.181	0.15-40.00	0.053	0.177
Dichloromethane	0.9991	y = 18054x + 213661	2.00-40.00	0.019	0.062
1,1-Dichloroethane	0.9998	y = 32546x - 500.11	0.15-40.00	0.014	0.048
Bromochloromethane	0.9997	y = 6932.3x - 1367.7	0.15-40.00	0.089	0.295
Trichloromethane	0.9998	y = 34184x - 5046.6	0.15-40.00	0.017	0.058
1,2-Dichloroethane	0.9996	y = 13031x - 2191.5	0.15-40.00	0.046	0.153
2,2-Dichloropropane	0.9996	y = 78210x - 9356	0.15-40.00	0.007	0.023
Benzene	0.9997	y = 75303x + 9609.7	0.15-40.00	0.007	0.022
Trichloroethene	0.9990	y = 24918x - 6931.5	0.15-40.00	0.025	0.084
1,2-Dichloropropane	0.9994	y = 17715x - 5402.6	0.15-40.00	0.034	0.114
Dibromomethane	0.9997	y = 5096.2x - 989.32	0.15-40.00	0.091	0.304
Bromodichloromethane	0.9988	y = 20290x - 8183.6	0.15-40.00	0.034	0.115
Cis-1,3-Dichloropropene	0.9980	y = 20845x - 11303	0.15-40.00	0.035	0.115
Trans-1,3-Dichloropropene	0.9983	y = 13607x - 6599	0.15-40.00	0.054	0.180
Toluene	0.9996	y = 97609x + 97944	0.15-40.00	0.006	0.020
1,1,2-Trichloroethane	0.9994	y = 7871.2x - 2298.8	0.15-40.00	0.093	0.311
1,1,1-Trichloroethane	0.9996	y = 7848.4x - 2323.8	0.15-40.00	0.078	0.260
1,3-Dichloropropane	0.9992	y = 13868x - 4638.1	0.15-40.00	0.050	0.166
Dibromochloromethane	0.9983	y = 10346x - 5086.4	0.15-40.00	0.023	0.077
Tetrachloroethene	0.9999	y = 22962x - 363.87	0.15-40.00	0.027	0.091
1,2-Dibromoethane	0.9993	y = 7195.2x - 2377.4	0.15-40.00	0.057	0.191
Chlorobenzene	0.9998	y = 56836x - 9373.6	0.15-40.00	0.013	0.042
Tetrachloromethane	0.9993	y = 12673x - 3735.9	0.15-40.00	0.060	0.199
1,1,1,2-Tetrachloroethane	0.9993	y = 17912x - 5135	0.15-40.00	0.043	0.142
Ethylbenzene	0.9999	y = 121781x + 6841.1	0.15-40.00	0.005	0.017
p_m_Xylene	0.9997	y = 44856x - 9081.3	0.30-80.00	0.006	0.021
Styrene (Vinylbenzene)	0.9999	y = 57766x - 10087	0.15-40.00	0.012	0.042
o-Xylene	0.9998	y = 93040x - 2895.5	0.15-40.00	0.007	0.023
Tribromomethane	0.9989	y = 4559.6x - 1681.6	0.15-40.00	0.038	0.125
1,1,2,2-Tetrachloroethane	0.9995	y = 8716.6x - 2753.5	0.15-40.00	0.089	0.296
Isopropylbenzene	0.9996	y = 133550x + 18469	0.15-40.00	0.005	0.015
1,1-Dichloropropene	0.9996	y = 6288.4x - 1283.5	0.15-40.00	0.067	0.225
1,2,3-Trichloropropane	0.9994	y = 1939.5x + 48.924	0.15-40.00	0.079	0.264
Bromobenzene	0.9998	y = 32093x - 4265.7	0.15-40.00	0.021	0.069
2-Chlorotoluene	0.9995	y = 234416x + 43747	0.15-40.00	0.002	0.008
n-Propylbenzene	0.9998	y = 236680x + 35492	0.15-40.00	0.009	0.029
4-Chlorotoluene	0.9975	y = 83214x - 4209.9	0.15-40.00	0.008	0.027
1,3,5-Trimethylbenzene	0.9999	y = 112267x + 11792	0.15-40.00	0.006	0.019
tert-Butylbenzene	0.9998	y = 101816x + 9052.8	0.15-40.00	0.006	0.021
1,2,4-Trimethylbenzene	0.9998	y = 107730x + 14524	0.15-40.00	0.006	0.020
1,3-Dichlorobenzene	0.9996	y = 44536x - 5264.9	0.15-40.00	0.017	0.058
sec-Butylbenzene	0.9991	y = 139329x + 34232	0.15-40.00	0.004	0.014
1,4-Dichlorobenzene	0.9996	y = 39184x - 2500.3	0.15-40.00	0.019	0.064
p-Isopropyltoluene	0.9995	y = 121223x + 20969	0.15-40.00	0.005	0.017
1,2-Dichlorobenzene	0.9999	y = 31839x - 3378.3	0.15-40.00	0.025	0.082
n-Butylbenzene	0.9994	y = 116459x + 15745	0.15-40.00	0.005	0.017
1,2-Dibromo-3-chloropropane	0.9979	y = 1035.8x - 520.69	0.15-40.00	0.034	0.114
1,3,5-Trichlorobenzene	0.9999	y = 31299x + 168.14	0.15-40.00	0.003	0.010
1,2,4-Trichlorobenzene	0.9999	y = 17134x - 2202.7	0.15-40.00	0.002	0.008
Naphthalene	0.9997	y = 17499x - 5484.5	0.15-40.00	0.045	0.149
Hexachlorobutadiene	0.9994	y = 16910x + 2436.6	0.15-40.00	0.042	0.140
1,2,3-Trichlorobenzene	0.9997	y = 9467.3x - 894.31	0.15-40.00	0.011	0.037
1-methylnaphthalene	0.9986	y = 127253x + 28701	0.50-40.00	0.107	0.356
1-chloronaphthalene	0.9977	y = 638814x + 92514	1.00-40.00	0.105	0.350
2-chloronaphthalene	0.9997	y = 734633x - 133804	1.00-40.00	0.093	0.311

3.3.LOD and LOQ

LOD is expressed as the lowest amount of analyte that can be identified, although not precisely determined. The smallest concentration of an analyte that can be quantitatively detected with sufficient precision (repeatability and reproducibility) and accuracy is known as

LOQ (Budiman and Zuas, 2017). The calculated values of LODs and LOQs of each compound are schedule in Table 2. For related VOCs, LODs were computed as three times the signal-to-noise ratio, with values between 0.002-0.107 µg/L, while LOQs were calculated as ten times the signal-to-noise ratio, with values between 0.008 µg/L and 0.356 µg/L. Among the fifty-five VOCs, 1,2,4-trichlorobenzene, 2-chlorotoluene and sec-butylbenzene had the lowest LOD and LOQ values. 1-methylnaphthalene, 1-chloronaphthalene and 2-chloronaphthalene had the highest LOD and LOQ values, as well. The LODs presented in this study are significantly lower than those reported other studies in the literature (Cavalcante et al., 2010; Fernández et al., 2016; Golfinopoulos et al., 2001; Kistemann et al., 2008; Liu et al., 2009; Menéndez et al., 2000; Serrano and Gallego, 2004; Serrano et al., 2007; Tabani et al., 2016) for water samples. Other studies with the same or comparable LOD levels include those by Antoniou et al. (2006), Behzadi and Mirzaei (2016), Dongqiang et al. (2006), Huybrechts et al. (2005), and Ridgway et al. (2007).

3.4.The Accuracy of the Method

The accuracy of the measurement results of an analytical method is understood by the closeness of the measured value of the relevant analyte to the determined/known value. This situation is revealed by the recovery values calculated for each analyte. The recovery of each VOC in this study was determined with nine successive measurements by spiking standard solution at two different concentrations of 1.00 µg/L, and 2.00 µg/L. The recoveries of fifty-five VOCs were calculated from the mean of measurements performed at these concentrations. Details about the mean recoveries and corresponding relative standard deviations (RSDs) for each VOC are shown in Table 2. Mean recovery of fifty-five VOCs varied from 86.83% to 94.93% (RSD: 3.31%-6.35%). The recovery results of three water matrices for VOCs were satisfactory and compatible with the analytical method performance requirements in the related guidelines (AOAC, 2016; EURACHEM/CITAC, 2014). In the literature, similar results has also been reported for accuracy from Demeestere et al. (2007), Kolb and Ettre (2006), Golfinopoulos et al. (2001), and Huybrechts et al. (2005).

3.5.The Precision of the Method

Intra-day (repeatability) and inter-day (reproducibility) studies were carried out to determine the precision level of this analytical method. Intra-day precision can be defined as the degree of closeness of the results of multiple measurements of the same sample under the same analytical conditions during a short time interval. On the other hand, inter-day precision can be explained as the measurement study performed by a single person on different days using the same equipment in the same sample (AOAC, 2016; Budiman and Zuas, 2017; 2014; Güzel and Canlı, 2020a). While inter-day precision was investigated with seven repetitive measurement studies performed by the same person on different days at a concentration of 5.00 µg/L, intra-day precision was examined with nine serial measurements by spiking standard solution at two different concentrations of 2.00 µg/L, and 5.00 µg/L, respectively. Table 2 exhibits the measured concentration of each analyte, recovery (%), and RSD (%) values obtained at the end of the studies of intra-day and inter-day precisions. Intra-day recovery values at the concentration of 2.00 µg/L ranged from 85.41% to 98.61% (RSD: 1.62%-7.73%), whereas these values at the concentration of 5.00 µg/L were between 87.51% and 92.65% (RSD: 3.33%-6.68%). Intra-day recovery values as a result of measurements made as described above were changed from 83.23% to 99.25% (RSD: 1.96%-9.21%), as well. The results of intraday and interday precision, expressed as recovery and RSD, in Table 2 indicate that there is no significant alteration between measurements. In addition, the recovery and RSD values have successfully met the criteria (Recovery: 80%-110%; RSD: <20%) specified in the

analytical method validation guidelines (AOAC, 2016; EURACHEM/CITAC, 2014) and are sufficient for the simultaneous measurement of fifty-five VOCs. Finally, the results are comparable to similar studies (Antoniou et al., 2006; Behzadi and Mirzaei, 2016; Dongqiang et al., 2006; Kistemann et al., 2008; Liu et al., 2009) in the literature.

3.6.Trueness

The applicability of a method is clearly understood by evaluating the precision and trueness before working on the real sample. From this point of view, trueness alludes to how near the mean of normal results (obtained from the method) of a series of studies is to the real value (EURACHEM/CITAC 2014). The trueness of fifty-one analytes in this study was verified by an inter-laboratory test with code WP319 Water pollution for wastewater issued by ERA-A Waters Company. The results of relevant inter-laboratory trials determined with the PT-GC/MS system are displayed in Table 4. As a result of the test, the method for twenty-four analytes was successful with a z-score between -1.450 and 1.810. In addition, the results for twenty-seven analytes were presented as less than reporting value and were obtained as satisfactory. Meanwhile, it was investigated whether false positive results were given for similar analytes. Since 1,3,5-trichlorobenzene, 1-methylnaphthalene, 1-chloronaphthalene, and 2-chloronaphthalene were not included in the test, no z-score was obtained. The z score calculations are presented in detail in the studies in the literature (Camino-Sánchez et al., 2013; Güzel and Canlı, 2020b).

Table 3. *Accuracy and precision (intra-day and inter-day) results of fifty-five VOCs*

Compound	Accuracy		Precision											
			Intra-day (repeatability)						Inter-day (reproducibility)					
			2 µg/L (n = 9)			5 µg/L (n = 9)			Day 1 (5 µg/L (n =7))			Day 2 (5 µg/L (n =7))		
	Mean Recovery (%)	Mean RSD (%)	Measured Conc. (µg/L)	Recovery (%)	RSD (%)	Measured Conc. (µg/L)	Recovery (%)	RSD (%)	Measured Conc. (µg/L)	Recovery (%)	RSD (%)	Measured Conc. (µg/L)	Recovery (%)	RSD (%)
Vinyl Chloride	87.6	5.73	1.73	86.6	6.65	4.43	88.7	4.81	4.21	84.2	5.33	4.51	90.2	6.87
Dichloromethane	91.4	5.09	1.86	93.1	3.88	4.48	89.7	6.31	4.68	93.6	5.91	4.54	90.7	6.57
1.1-Dichloroethane	88.9	4.89	1.78	89.0	5.68	4.44	88.8	4.11	4.40	88.1	8.48	4.46	89.3	4.19
Bromochloromethane	90.7	5.55	1.80	90.2	6.55	4.56	91.3	4.55	4.63	92.6	7.33	4.65	93.0	2.71
Trichloromethane	90.7	5.11	1.85	92.6	5.77	4.44	88.9	4.45	4.72	94.3	4.35	4.47	89.5	4.73
1.2-Dichloroethane	92.4	5.26	1.89	94.4	5.57	4.52	90.5	4.95	4.72	94.4	6.56	4.53	90.6	5.33
2.2-Dichloropropane	91.8	5.44	1.87	93.7	6.07	4.49	89.9	4.80	4.67	93.4	7.83	4.58	91.7	2.30
Benzene	89.4	4.44	1.82	91.0	4.70	4.39	87.8	4.17	4.59	91.8	6.22	4.40	88.1	2.85
Trichloroethene	91.7	5.57	1.83	91.6	6.12	4.58	91.7	5.02	4.51	90.2	5.45	4.66	93.3	4.57
1.2-Dichloropropane	88.7	4.68	1.74	87.2	5.83	4.51	90.2	3.53	4.38	87.7	8.70	4.54	90.8	2.47
Dibromomethane	88.5	6.05	1.75	87.4	6.00	4.48	89.6	6.11	4.35	87.0	6.89	4.50	90.1	6.24
Bromodichloromethane	90.4	4.58	1.84	91.8	4.31	4.45	89.1	4.85	4.57	91.3	4.20	4.48	89.6	5.51
Cis-1.3-Dichloropropene	89.0	5.75	1.77	88.3	7.73	4.48	89.6	3.77	4.55	90.9	9.21	4.48	89.6	8.17
Trans-1.3-Dichloropropene	89.2	4.68	1.75	87.7	4.41	4.54	90.8	4.95	4.40	88.0	6.97	4.60	92.0	4.19
Toluene	91.8	4.96	1.84	91.9	6.24	4.59	91.8	3.68	4.61	92.2	6.89	4.65	93.0	2.40
1.1.2-Trichloroethane	87.3	5.55	1.73	86.5	6.59	4.41	88.1	4.50	4.28	85.6	7.26	4.37	87.4	4.14
1.1.1-Trichloroethane	89.3	5.25	1.79	89.3	6.19	4.47	89.4	4.32	4.38	87.6	6.61	4.49	89.8	3.65
1.3-Dichloropropane	92.3	3.42	1.89	94.5	2.69	4.51	90.2	4.14	4.68	93.7	2.65	4.50	90.0	4.47
Dibromochloromethane	90.3	3.87	1.84	91.9	4.40	4.44	88.8	3.33	4.62	92.4	6.04	4.48	89.5	2.97
Tetrachloroethene	91.7	5.50	1.89	94.3	6.20	4.45	89.0	4.80	4.78	95.6	8.16	4.52	90.3	3.90
1.2-Dibromoethane	88.6	4.99	1.76	87.9	5.25	4.46	89.3	4.73	4.46	89.3	7.10	4.49	89.8	3.76
Chlorobenzene	89.9	4.36	1.78	88.8	5.03	4.55	91.0	3.69	4.40	88.1	6.39	4.58	91.6	2.32
Tetrachloromethane	92.2	4.58	1.89	94.7	5.00	4.49	89.8	4.16	4.70	94.0	6.39	4.48	89.6	3.78
1.1.1.2-Tetrachloroethane	90.3	4.42	1.80	90.2	3.83	4.52	90.4	5.01	4.50	90.0	6.16	4.53	90.6	5.07
Ethylbenzene	91.4	4.61	1.84	92.2	4.88	4.53	90.7	4.35	4.69	93.8	4.63	4.58	91.6	3.94
P_M_Xylene*	90.6	4.55	3.74	93.6	5.25	8.76	87.6	3.86	9.52	95.2	7.39	8.85	88.5	3.27
Styrene (Vinylbenzene)	88.4	4.42	1.71	85.5	4.83	4.56	91.2	4.02	4.16	83.2	3.88	4.60	92.1	3.75
O-Xylene	94.1	3.56	1.95	97.3	2.21	4.55	91.0	4.91	4.90	97.9	3.29	4.63	92.6	4.21
Tribromomethane	93.4	3.31	1.92	96.2	3.24	4.53	90.5	3.37	4.84	96.9	4.49	4.56	91.1	4.03
1.1.2.2-Tetrachloroethane	90.0	4.95	1.77	88.3	5.31	4.58	91.6	4.60	4.39	87.8	7.74	4.56	91.1	5.19
Isopropylbenzene	91.5	6.35	1.86	92.8	6.03	4.51	90.2	6.68	4.79	95.7	6.16	4.52	90.3	7.28

1.1-Dichloropropene	91.4	3.58	1.84	91.8	2.06	4.55	91.0	5.09	4.62	92.5	2.95	4.60	91.9	2.83
1.2.3-Trichloropropane	87.7	3.35	1.71	85.4	2.83	4.50	90.1	3.87	4.31	86.1	3.55	4.49	89.8	3.08
Bromobenzene	90.8	4.60	1.86	93.1	4.34	4.43	88.5	4.85	4.70	94.0	5.12	4.47	89.4	4.41
2-Chlorotoluene	89.7	4.94	1.79	89.5	5.22	4.50	90.0	4.67	4.59	91.7	5.05	4.47	89.5	4.68
n-Propylbenzene	92.0	4.83	1.87	93.5	6.09	4.52	90.5	3.58	4.67	93.3	6.38	4.54	90.7	3.06
4-Chlorotoluene	91.7	5.26	1.86	93.1	6.70	4.51	90.2	3.82	4.72	94.5	8.24	4.53	90.7	3.85
1.3.5-Trimethylbenzene	93.6	3.84	1.93	96.3	3.17	4.54	90.8	4.51	4.87	97.5	2.18	4.56	91.3	4.10
Tert-Butylbenzene	91.2	4.54	1.86	92.9	3.41	4.47	89.5	5.68	4.66	93.3	5.03	4.52	90.5	4.95
1.2.4-Trimethylbenzene	93.9	5.20	1.95	97.6	4.47	4.51	90.1	5.94	4.96	99.2	2.64	4.50	89.9	6.54
1.3-Dichlorobenzene	93.1	5.43	1.91	95.6	4.89	4.53	90.7	5.97	4.80	95.9	7.37	4.60	92.0	5.46
Sec-Butylbenzene	91.0	5.26	1.83	91.5	4.12	4.53	90.6	6.40	4.61	92.3	4.77	4.60	91.9	6.64
1.4-Dichlorobenzene	93.2	5.70	1.93	96.3	5.56	4.51	90.2	5.85	4.94	98.9	2.68	4.61	92.3	4.28
4-isopropyltoluene	91.8	4.02	1.86	93.1	3.78	4.52	90.4	4.26	4.72	94.5	5.39	4.53	90.6	3.91
1.2-Dichlorobenzene	94.9	3.52	1.96	98.0	1.62	4.59	91.8	5.41	4.95	98.9	3.71	4.67	93.5	4.21
n-butylbenzene	92.0	3.81	1.88	93.9	3.52	4.50	90.1	4.09	4.73	94.6	4.27	4.52	90.4	3.03
1.2-Dibromo-3-chloropropane	89.3	4.33	1.78	88.8	3.69	4.49	89.8	4.97	4.41	88.3	3.89	4.50	90.1	4.75
1.3.5-Trichlorobenzene	92.8	4.97	1.91	95.5	3.50	4.50	90.1	6.44	4.84	96.8	3.52	4.51	90.3	7.58
1.2.4-Trichlorobenzene	94.6	3.54	1.97	98.6	2.43	4.53	90.7	4.65	4.95	99.0	2.55	4.55	91.0	4.44
Naphtalene	94.1	5.08	1.91	95.6	3.90	4.63	92.7	6.26	4.77	95.4	4.74	4.75	95.1	3.70
Hexachloro-1.3-butadiene	93.5	3.42	1.90	94.9	3.05	4.60	92.1	3.79	4.79	95.8	4.46	4.65	92.9	2.85
1.2.3-Trichlorobenzene	94.6	4.56	1.94	97.0	3.58	4.61	92.2	5.53	4.86	97.2	2.15	4.70	94.0	4.71
1-methylnaphthalene	88.4	4.10	1.73	86.3	3.83	4.53	90.5	4.36	4.28	85.5	1.96	4.59	91.8	2.94
1-chloronaphthalene	86.8	4.00	1.71	85.7	4.01	4.40	88.0	3.99	4.32	86.4	4.39	4.45	89.1	2.59
2-chloronaphthalene	87.2	5.12	1.74	86.9	5.86	4.38	87.5	4.37	4.31	86.2	7.17	4.39	87.7	4.41

*p&m-xylene was measured for 4 µg/L and 10 µg/L of VOC solutions

Table 4. *Inter-laboratory test results for fifty-five VOCs*

Compound	Reported value (µg/L)	Assigned value (µg/L)	SDPA (µg/L)	z-score*	Evaluation
Dichloromethane	19.8	18.1	2.48	0.833	Satisfactory
Vinyl Chloride	<8.00	<8.00	-	-	Satisfactory
1,1-Dichloroethane	25.9	21.2	2.60	1.810	Satisfactory
Bromochloromethane	<3.50	<3.50	-	-	Satisfactory
Trichloromethane	72.2	60.9	9.03	1.260	Satisfactory
1,2-Dichloroethane	<10.6	<10.6	-	-	Satisfactory
2,2-Dichloropropane	<2.50	<2.50	-	-	Satisfactory
Benzene	16.1	14.3	2.09	0.825	Satisfactory
Trichloroethene	41.7	39.2	8.84	0.282	Satisfactory
1,2-Dichloropropane	35.9	31.2	3.61	1.721	Satisfactory
Dibromomethane	<6.50	<6.50	-	-	Satisfactory
Bromodichloromethane	<6.00	<6.00	-	-	Satisfactory
Cis-1,3-Dichloropropene	15.8	15.4	2.17	0.219	Satisfactory
Trans-1,3-Dichloropropene	46.1	44.7	7.12	0.219	Satisfactory
Toluene	124.7	114.0	12.5	0.851	Satisfactory
1,1,2-Trichloroethane	< 10.5	< 10.5	-	-	Satisfactory
1,1,1-Trichloroethane	19.9	19.6	4.17	0.190	Satisfactory
1,3-Dichloropropane	<3.50	<3.50	-	-	Satisfactory
Dibromochloromethane	65.0	71.9	10.7	-0.653	Satisfactory
Tetrachloroethene	84.5	80.7	16.9	0.222	Satisfactory
1,2-Dibromoethane	41.8	35.7	5.88	0.587	Satisfactory
Chlorobenzene	76.2	62.7	8.81	1.641	Satisfactory
Tetrachloromethane	<7.70	<7.70	-	-	Satisfactory
1,1,1,2-Tetrachloroethane	<9.80	<9.80	-	-	Satisfactory
Ethylbenzene	<7.00	<7.00	-	-	Satisfactory
P-M-Xylene	45.5	44.1	6.78	0.216	Satisfactory
Styrene	41.3	35.2	5.96	0.583	Satisfactory
o-Xylene	70.0	59.2	7.84	1.380	Satisfactory
Tribromomethane	<6.00	<6.00	-	-	Satisfactory
1,1,2,2-Tetrachloroethane	<9.80	<9.80	-	-	Satisfactory
Isopropylbenzene	<3.20	<3.20	-	-	Satisfactory
1,1-Dichloropropene	<3.10	<3.10	-	-	Satisfactory
1,2,3-Trichloropropane	<4.10	<4.10	-	-	Satisfactory
Bromobenzene	<3.40	<3.40	-	-	Satisfactory
2-Chlorotoluene	<3.20	<3.20	-	-	Satisfactory
n-Propylbenzene	<3.30	<3.30	-	-	Satisfactory
4-Chlorotoluene	<3.30	<3.30	-	-	Satisfactory
1,3,5-Trimethylbenzene	22.8	21.1	3.86	0.435	Satisfactory
Tert-Butylbenzene	<3.00	<3.00	-	-	Satisfactory
1,2,4-Trimethylbenzene	74.1	73.4	5.27	0.127	Satisfactory
1,3-Dichlorobenzene	22.1	21.0	4.54	0.244	Satisfactory
Sec-Butylbenzene	<3.20	<3.20	-	-	Satisfactory
1,4-Dichlorobenzene	13.1	12.2	2.05	0.444	Satisfactory
4-isopropyltoluene	<3.20	<3.20	-	-	Satisfactory
1,2-Dichlorobenzene	33.8	32.8	4.46	0.233	Satisfactory
n-butylbenzene	<3.00	<3.00	-	-	Satisfactory
1,2-Dibromo-3-chloropropane	<9.00	<9.00	-	-	Satisfactory
1,3,5-Trichlorobenzene	-	-	-	-	-
1,2,4-Trichlorobenzene	81.8	103.0	14.4	-1.450	Satisfactory
Naphthalene	75.3	59.8	8.98	1.730	Satisfactory
Hexachloro-1,3-butadiene	<4.30	<4.30	-	-	Satisfactory
1,2,3-Trichlorobenzene	<2.90	<2.90	-	-	Satisfactory
1-methylnaphthalene	-	-	-	-	-
1-chloronaphthalene	-	-	-	-	-
2-chloronaphthalene	-	-	-	-	-

SDPA: Standard Deviation for Proficiency Assessment

*z score less than or equal to 2.0 calls satisfactory; z score greater than 2.0 and less than 3.0 is warning or questionable; and z score greater than or equal to 3.0 refers to unsatisfactory.

3.7.Application to Real Samples

The proposed method was practiced to the qualification/quantification of the presence of fifty-five VOCs in different environmental samples such as seawater (seventy-eight samples), surface water (one hundred twenty five samples). and wastewater (twenty-nine samples). These samples were preconcentrated by PT system and submitted to GC-MS analysis. They were filtered with the help of a 0.45 μm polytetrafluoroethylene (PTFE) syringe filter to prevent clogging of the purging unit against suspended solids Before transferring them to the PT system. Identification of each analyte in the real samples was obtained from a comparison of retention times and MS spectra with the standard solution of VOCs. Furthermore, the peaks of each analyte in the total ion chromatograms of real samples were examined in detail. The chromatograms of blank samples did not contain any interfering compounds. In Table 5, VOCs and their concentrations detected in seawater, surface water and wastewater samples are presented. Sixteen seawater, twenty-three surface water, and twenty-nine wastewater samples had at least one positive result. Eleven analytes in seawater, twenty nine analytes in surface water and twelve analytes in wasteawater were found in different amounts. The highest concentrations were trichloromethane (1.11 μg/L) and 1.2-dichloroethane (0.31 μg/L) in seawater, dichloromethane (2.01 μg/L) and p-m-xylene (0.94 μg/L) in surface water, trichloromethane (6.68 μg/L) and dichloromethane (5.64 μg/L) in wastewater. Dibromomethane, cis-1.3-dichloropropene, trans-1.3-dichloropropene, 1.3-dichloropropane, 1.2-dibromoethane, chlorobenzene, 2-chlorotoluene, 4-chlorotoluene, and sec-butylbenzene were not detected in these environmental water matrices.

Table 5. *Detected VOCs and their concentrations in the environmental waters*

Compound	Seawater (μg/L)	Surface water (μg/L)	Wastewater (μg/L)
Vinyl Chloride	<0.15	<0.15	0.21-0.76
Dichloromethane	<2	<2-2.01	2.17-5.64
1.1-Dichloroethane	<0.15-0.17	0.16-0.24	0.80-5.70
Bromochloromethane	<0.15	<0.15-0.22	0.25-0.98
Trichloromethane	0.41-1.11	0.19-0.68	0.94-6.68
1.2-Dichloroethane	0.18-0.31	0.15-0.41	0.78-3.14
2.2-Dichloropropane	<0.15	<0.15	0.16-0.44
Benzene	<0.15	0.18-0.22	0.26-6.49
Trichloroethene	<0.15-0.21	0.16-0.54	<0.15-0.78
1.2-Dichloropropane	<0.15	<0.15	0.19-0.33
Dibromomethane	<0.15	<0.15	<0.15
Bromodichloromethane	<0.15	0.22-0.39	0.45-1.68
Cis-1.3-Dichloropropene	<0.15	<0.15	<0.15
Trans-1.3-Dichloropropene	<0.15	<0.15	<0.15
Toluene	<0.15	<0.15	0.45-4.84
1.1.2-Trichloroethane	<0.15-0.18	<0.15-0.26	<0.15
1.1.1-Trichloroethane	<0.15-0.16	<0.15-0.24	<0.15
1.3-Dichloropropane	<0.15	<0.15	<0.15
Dibromochloromethane	0.15-0.28	0.16-0.35	0.45-0.61
Tetrachloroethene	0.16-0.28	0.17-0.28	<0.15
1.2-Dibromoethane	<0.15	<0.15	<0.15
Chlorobenzene	<0.15	<0.15	<0.15
Tetrachloromethane	<0.15-0.24	0.18-0.44	0.38-1.18
1.1.1.2-Tetrachloroethane	<0.15-0.18	<0.15-0.34	0.28-0.78
Ethylbenzene	<0.15	0.18-0.21	0.19-2.17
P_M_Xylene	<0.30	0.34-0.94	0.44-4.46
Styrene	<0.15	0.16-0.28	0.44-0.56
O-Xylene	<0.15	0.19-0.41	0.25-0.86
Tribromomethane	<0.15	<0.15	0.19-0.84
1.1.2.2-Tetrachloroethane	<0.15	<0.15-0.62	0.24-0.94
Isopropylbenzene	<0.15	0.18-0.32	0.24-1.65
1.1-Dichloropropene	<0.15	<0.15	<0.15-0.21

1.2.3-Trichloropropane	<0.15	<0.15	0.17-0.45
Bromobenzene	<0.15	<0.15	<0.15-0.48
2-Chlorotoluene	<0.15	<0.15	<0.15
N-Propylbenzene	<0.15	<0.15-0.24	0.15-2.17
4-Chlorotoluene	<0.15	<0.15	<0.15
1.3.5-Trimethylbenzene	<0.15	0.16-0.22	0.18-0.90
Tert-Butylbenzene	<0.15	<0.15	<0.15-0.29
1.2.4-Trimethylbenzene	<0.15	<0.15-0.21	0.38-1.79
1.3-Dichlorobenzene	<0.15	<0.15-0.18	0.21-2.98
Sec-Butylbenzene	<0.15	<0.15	<0.15
1.4-Dichlorobenzene	<0.15	<0.15-0.22	0.22-1.77
P-Isopropyltoluene	<0.15	<0.15	<0.15-0.22
1.2-Dichlorobenzene	<0.15	<0.15-0.19	0.28-3.16
N-Butylbenzene	<0.15	<0.15	0.34-0.88
1.2-Dibromo-3-chloropropane	<0.15	<0.15	<0.15-0.18
1.3.5-Trichlorobenzene	<0.15	<0.15-0.21	0.15-0.96
1.2.4-Trichlorobenzene	<0.15	0.15-0.19	0.19-0.81
Naphthalene	0.21-0.30	0.17-0.38	0.16-1.71
Hexachlorobutadiene	<0.15	<0.15	<0.15-0.18
1.2.3-Trichlorobenzene	<0.15	<0.15	0.15-1.28
1-methylnaphthalene	<0.50	<0.50	0.78-2.16
1-chloronaphthalene	<1	<1	1.18-4.44
2-chloronaphthalene	<1	<1	1.04-2.18

4.Conclusions

This paper presents studies that validate the proposed analytical method for the precise, accurate, and simultaneous determination of fifty-five VOCs that are highly toxic to human health and the environment. This takes into account a range of various national and international regulations like the Water Framework Directive and the Surface Water Quality Regulation. The proposed method is well suited to the green chemistry approach, as it has a simple solvent-free sample preparation procedure and in the PT system, VOCs are absorbed onto the porous solid sorbent with the aid of a stream of gas from the water sample. The analytical performance of this method was appraised in terms of selectivity, linearity, the LOD-LOQ, trueness, accuracy, and precision parameters. It showed a high sensitivity for each VOC with respect to LODs (between 0.002 μg/L and 0.107 μg/L) and LOQs (ranging from 0.008 μg/L to 0.356 μg/L). Calibration curves have fairly good linearity with correlation coefficients ranging from 0.9975 to 0.9999 for all VOCs at nine concentrations from 0.15 μg/L to 40.00 μg/L. This method has great accuracy (recovery ranges from 86.83% to 94.93%) and good precision (intra-day and inter-day studies, RSD is less than 10% in all cases). In addition, except for 1,3,5-trichlorobenzene, 1-methylnaphthalene, 1-chloronaphthalene, and 2-chloronaphthalene, satisfactory results were obtained within the criteria determined in the interlaboratory test in the wastewater matrix for all other VOCs. It has been clarified by the relative analytical method validation guidelines and previous literature studies that the gas chromatographic method validation results have sufficient consistency, precision, and accuracy. The applicability of the method has been tested on a significant number of real samples and successful results have been obtained.

Acknowledgements

This research was supported from the Hazardous Waste Analysis Project situated in TUBITAK MAM. The author would like to thank Hüseyin Demir for his assistance in the laboratory.

References

Alonso. M.. Cerdan. L.. Godayol A.. Antico. E.. Sanchez. J.M. (2011). Headspace needle-trap analysis of priority volatile organic compounds from aqueous samples: application to the analysis of natural and wastewaters. J. Chromatogr. A. 1218. 8131–9.

Antoniou. C.V.. Koukouraki. E.E.. Diamadopoulos. E. (2006). Determination of chlorinated volatile organic compounds in water and municipal wastewater using headspace-solid phase microextraction-gas chromatography. J. Chromatogr.. A 1132 (2006) 310.

ASTM. (1989). The ASTM Standard Practice for Determining Volatile Organic Compounds (VOC) Contents of Paints and Related Coating (D3960). American Society for Testing and Materials. Philadelphia. USA.

ATSDR. (1997). Agency for Toxic Substances and Registry. Atlanta: U.S. Public Health Service. U.S. Department of Health and Human Service.

Basar. H.. Güzel. B.. Ozer-Erdogan. P.. Tolun. L. (2017). Determination of the environmental effects of Turkey's marine dredged materials before beneficial use: commercial ports & fishery harbours. J. Fac. Eng. Archit. Gaz. 32 (4). 1063–1076.

Behzadi. M.. Mirzaei. M. (2016). Poly(o-anisidine)/graphene oxide nanosheets composite as a coating for the headspace solid-phase microextraction of benzene, toluene, ethylbenzene and xylenes. J. Chromatogr. A. 1443. 35–40.

Botwe. B.O.. Kelderman. P.. Nyarko. E.. Lens. P.N.L. (2017). Assessment of DDT. HCH and PAH contamination and associated ecotoxicological risks in surface sediments of coastal Tema harbour (Ghana). Mar. Pollut. Bull. 115. 480–488.

Budiman. H.. Zuas. O. (2017). Trace measurement of CO, CH_4, and CO_2 in high purity gases by GC-FID-methanizer: Method validation and uncertainty estimation. Sci. Study & Res. 18(3). 259-274.

Camino-Sánchez. F.J.. Zafra-Gómez. A.. Ruiz-García. J.. Vílchez. J.L. (2013). Screening and quantification of 65 organic pollutants in drinking water by stir bar sorptive extraction-gas chromatography-triple quadrupole mass spectrometry. Food Anal. Methods. 6. 854-867.

Cavalcante. R.M.. Andrade. M.V.F.. de Marins. R.V.. Oliveira. L.D.M. (2010). Development of a headspace-gas chromatography (HS-GC-PID-FID) method for the determination of VOCs in environmental aqueous matrices: optimization. verification and elimination of matrix effect and VOC distribution on the Fortaleza coast, Brazil. Microchem. J. 96(2). 337-34.

Chen. E.X.. Yang. H.. Zhang. J. (2014). Zeolitic imidazolate framework as formaldehyde gas sensor. Inorg. Chem. 53. 5411–5413.

Demeestere. K.. Dewulf. J.. Witte. B.. Van Langenhove. H. (2007). Sample preparation for the analysis of volatile organic compounds in air and water matrices. J. Chromatogr. A. 1153. 130.

Dongqiang. H.. Wanyun. M.. Dieyan. C. (2006). Determination of biodegradation products from benzene, toluene, ethylbenzene and xylenes in seawater by purge and trap gas chromatography. Chin. J. Anal. Chem. 34. 1361.

Dongqiang. H.. Wanyun. M.. Dieyan. C. (2006). Determination of biodegradation products from benzene, toluene, ethylbenzene and xylenes in seawater by purge and trap gas chromatography. Chin. J. Anal. Chem. 34 (2006) 1361.

EPA. (2002). Volatile Organic Compounds in Water, Soil, Soil Gas, and Air by Direct Sampling Ion Trap Mass Spectrometry (DSITMS). USA: U.S. Public Health Service. U.S. Department of Health and Human Service.

Fernández. E.. Vidal. L.. Canals. A. (2016). Zeolite/iron oxide composite as sorbent for magnetic solid-phase extraction of benzene. toluene. ethylbenzene and xylenes from water samples prior to gas chromatography-mass spectrometry. J. Chromatogr. A. 1458. 18–24.

Ferreira. J.A.. Ferreira. J.M.S.. Talamini V. Facco. J.F.. Rizzetti. T.M.. Prestes. O.D.. Adaime. M.B.. Zanella. R.. Bottoli. C.B.G. (2016). Determination of pesticides in coconut (Cocos nucifera Linn.) water and pulp using modified QuEChERS and LC-MS/MS. Food Chem. 213. 616-624.

Golfinopoulos. S.K.. Lekkas. TD.. Nikolaou. A.D. (2001). Comparison of methods for determination of volatile organic compounds in drinking water. Chemosphere. 45. 275.

Gu. Z.Y.. Wang. G.. Yan. X.P. (2010). MOF-5 metal-organic framework as sorbent for in-field sampling and preconcentration in combination with thermal desorption GC/MS for determination of atmospheric formaldehyde. Anal. Chem. 82. 1365–1370.

Güzel. B.. Canli. O.. Öktem. O.E. (2018a). Volatile organic compounds in waters and their health effects. Anadolu Uni. J. Sci. and Tech. C - Life Sci. and Biotech. 7(2). 277–90.

Güzel. B.. Canli. O.. Öktem. O.E. (2018b). Gas chromatography method validation study for sensitive and accurate determination of volatile aromatic hydrocarbons (VAHs) in water. Cumhuriyet Sci. J. 39(4). 970-982.

Güzel. B.. Canli. O. (2020a). Applicability of purge and trap gas chromatography- mass spectrometry method for sensitive analytical detection of naphthalene and its derivatives in waters. J. Mass Spectrom. 55. e4672. 1-10.

Güzel. B.. Canli. O. (2020b). Method validation and measurement uncertainty of possible thirty volatile organic compounds (VOCs) presented in the polyethylene present in bottled drinking waters sold in Turkey. J. Sci. & Tech. 11 (44). 1-17.

Güzel. B.. Canli. O.. Celebi. A.. (2022). Characterization, source and risk assessments of sediment contaminants (PCDD/Fs. DL-PCBs. PAHs. PCBs. OCPs. Metals) in the urban water supply area. Appl. Geochem. 143. 105394. 1-10.

Huybrechts. T.. Dewulf. J.. Moerman. O.. Van Langenhove. H. (2000) Evaluation of purge-and- trap-high-resolution gas chromatography-mass spectrometry for the determination of 27 volatile organic compounds in marine water at the ng l^{-1} concentration level. J. Chromatogr. A. 893. 367

Huybrechts. T.. Dewulf. J.. Van Langenhove. H. (2005). Priority volatile organic compounds in surface waters of the southern North Sea. Environ. Pollut. 133. 255.

ISO. (2012). Water Quality-Sampling—Part 3: Preservation and Handling of Water Samples. International Organization for Standardization (ISO) 5667-3: 2012(E). Geneva. Switzerland. https://www.iso.org/standard/ 53569.html. Accessed October 2012.

Jakubowska. N.. Polkowska. Ż.. Namieśnik. J. Przyjazny. A.(2005). Analytical application and environmental liquid sample preparation. Crit. Rev. Anal. Chem. 35. 217-235.

Kaiser. H.J.. Ritts. B. (2006). Validation of Analytical Methods Used in Cleaning Validation. Analytical Methods Validation. Institute of Validation Technology. 15-30.

Karaman. S. Gökalp. Z. (2010). Impacts of global warming and climate change over water resources. J. Agric. Sci. Res. 3 (1). 59-66. (in Turkish)

Ketola. R.A.. Kotiaho. T.. Cisper. M.E.. Allen. T.M. (2002). Environmental applications of membrane introduction mass spectrometry. J. Mass Spectr. 37. 457.

Kistemann. T.. Hundhausen. J.. Herbst. S.. Claben. T.. Farber. H. (2008). Assessment of a groundwater contamination with vinyl chloride (VC) and precursor volatile organic compounds (VOC) by use of a geographical information system (GIS). Int. J. Hyg. Environ. Health. 211. 308.

Kolb. B.. Ettre. L.S. (2006). Static Headspace Gas Chromatography. Theory and Practice.2nd ed. John Wiley & Sons. Hoboken. New Jersey.

Kumar. J.A.. Krithiga. T.. Sathish. S.. Renita. A.A.. Prabu. D.. Lokesh. S.. Geetha. R.. Namasivayam. S.K.R.. Sillanpaa. M. (2022). Persistent organic pollutants in water resources: Fate. occurrence. characterization and risk analysis. Sci. Total Environ. 831. 154808.

Liu. H.W.. Liu. Y.T.. Wu. B.Z.. Nian. H.C.. Chen. H.J.. Chiu. K.H.. Lo. J.G. (2009). Process sampling module coupled with purge and trap-GC-FID for in situ auto-monitoring of volatile organic compounds in wastewater. Talanta. 80. 903

Liu. M.D.. Wu. T.. Zhao. X.Y.. Zan. F.Y.. Yang. G.. Miao. Y.Q. (2021). Cyanobacteria blooms potentially enhance volatile organic compound (VOC) emissions from a eutrophic lake: Field and experimental evidence. Environ. Res. 202. 111664–111671.

Menéndez. J.C.F.. Sánchez. M.L.F.. Uría. J.E.S.. Martínez. E.F.. Sanz-Medel. A. (2000). Static headspace. solid-phase microextraction and headspace solid-phase microextraction for BTEX determination in aqueous samples by gas chromatography. Anal. Chim. Acta. 415. 9.

Özdemir. A. (2021). Evaluation of climate change impacts on runoff and sediment at the basin scale: Yuvacık dam lake basin. Int. J. Geo-Eng. 45. 129–153.

Riddick. J.A.. Bunger. W.B.. Sakano. T.K. (1985). Techniques of Chemistry. Volume II. Organic Solvents. John Wiley and Sons. New York. 1985.

Ridgway. K.. Lalljie. S.P.D.. Smith. R.M. (2007). Use of in-tube sorptive extraction techniques for determination of benzene. toluene. ethylbenzene and xylenes in soft drinks. J. Chromatogr. A. 1174. 20.

Safarova. V.I.. Sapelnikova. S.V.. Djazhenko. E.V.. Teplova. G.I.. Shajdulina. G.F.. Kudasheva. F.K. (2004). Gas chromatography-mass spectrometry with headspace for the analysis of volatile organic compounds in waste water. J. Chromatogr. B. 800. 325.

Serrano. A.. Gallego. M. (2004). Direct screening and confirmation of benzene. toluene. ethylbenzene and xylenes in water. J. Chromatogr. A. 1045. 181.

Serrano. A.. Gallego. M.. Silva. M. (2007). Rapid determination of total trihalomethanes index in drinking water. Anal. Chem. 79. 2997.

Tabani. H.. Khodaei. K.. Movahed. S.K.. Moghaddam. A.Z.. Zare. F.D.. Mirzaei. S. (2016). Evaluation of three dimensional high nitrogen doped graphene as an efficient sorbent for the preconcentration of BTEX compounds in environmental samples. RSC Adv. 6. 7198–7211.

Tavernier. I.. De Loose. M.. Van Bockstaele. E. (2004). Trends in quality in analytical laboratory. II. Analytical method validation and quality assurance. Trends Anal. Chem. 23(8). 535-552.

Tor. A.. Aydin. M.E.. (2006). Application of liquid-phase microextraction to the analysis of trihalomethanes in water. Anal. Chim. Acta. 575. 138.

Tsuchiya. Y. (2010). Organical Chemicals as Contaminants of Water Bodies and Drinking Water. Water Quality and Standards. Volume II.

Weber. I.C.. Ruedi. P.. Sot. P.. Guntner. A.T.. Pratsinis. S.E. (2022). Handheld device for selective benzene sensing over toluene and xylene. Adv. Sci. 9 (4). 2103853.

WHO. (1987). Indoor air quality: Organic Pollutants. Report on a WHO Meeting. World Health Organization. Berlin.

Yu. P.H.. Cauglin. C.. Wempe. K.L.. Gubisne-Haberle. D. (2003). A novel sensitive high-performance liquid chromatography/electrochemical procedure for measuring formaldehyde produced from oxidative deamination of methylamine and in biological samples. Anal. Biochem. 318. 285–290.

On Spherıcal Fuzzy Bıtopologıcal Spaces

Taha Yasin ÖZTÜRK[1]

Giriş

Fuzzy mathematics departs from standard mathematics, most notably in set theory. Fuzzy mathematics, which was invented only a few years ago, is full of innovative concepts. It is widely used in vehicles and traffic control systems, where logic circuits manage anti-lock brakes, electrical systems, and other operations. This is a more specialized version of the term "crisp set." It can determine whether to say yes or no, which corresponds to the numbers 1 and 0. Several of the topics described in this paper were foreseen thirty years ago by an American philosopher named Black [5]. [5] created a theory utilizing "fuzzy sets," which are essentially sets with "imperfect" boundaries, as its basic building elements. Zadeh's [29] seminal work from 1965 offers a critical point about the genesis of modern concepts about ambiguity and was an immediate extension of the crisp set concept. In 1983, Atanassov [2, 3, 4] proposed the concept of intuitionistic fuzzy sets (IFS) and intuitionistic fuzzy numbers (IFN). Yager suggested "Pythagorean fuzzy sets (PFS)" [20] and later "q-rung orthopair fuzzy sets (q-ROFS)" [21]. Molodtsov invented soft sets (SS) and SS theory [12]. By adding another grade to FS, Smarandache [18] proposed a new model termed neutrosophic sets. Smarandache [19] extended the soft set to the hypersoft set. Cuong [6] suggested picture fuzzy sets (PiFS). The most recent expansion of fuzzy sets is spherical fuzzy sets (SFSs), which were recently developed by Kutlu Gündogdu and Kahraman [10]; in these, the squared sum of the hesitancy-neutral degree, membership degree, and non-membership degree does not exceed 1. Using Archimedean t-norm and t-conorms, Ashraf et al. [1] and Mahmood et al. [11] proposed spherical fuzzy sets with specific operating rules and aggregation processes. Yolcu [22] introduced bipolar spherical fuzzy soft topology and its applications. SFS covers a larger region than picture fuzzy set (PFS). Feng et al. [8] suggested new q-rung orthopair fuzzy set score functions for use in decision analysis. Deveci et al. suggested autonomous cars based on q-ROFs for personal mobility in the metaverse [7]. Riaz et al. [17] described a supply chain management application of bipolar fuzzy soft sets (BFSSs). Yolcu et.al investigated theoretical studies and applications in decision-making based on these set structures and its extensions can be seen at [13, 14, 15, 22-28].

Bitopological structures, which are more general than topological spaces, are developed on spherical fuzzy sets in this work. The essential arguments are stated and their fundamental properties are described, which are pairwise spherical fuzzy open set, pairwise spherical fuzzy closed set, pairwise spherical fuzzy closure, and pairwise spherical fuzzy interior. The relationships between these notions and their analogues in spherical fuzzy topological spaces are discussed, and several examples are shown.

Preliminaries

In this section, we will give some preliminary information for the present study.

[1] Prof. Dr., Kafkas University

Definition 1 *[10] Let S be a initial universe. A spherical fuzzy set U in S,* $U = \{s, \theta_U(s), \pi_U(s), \rho_U(s) : s \in S\}$, *where* $\theta_U, \pi_U, \rho_U : U \to 0,1]$ *is the positive, neutral and negative membership degrees of* $s \in U$ *respectively with the condition* $0 \le \theta_U(s) + \pi_U(s) + \rho_U(s) \le 1$. *All spherical fuzzy sets on the universe S denoted by $SF(S)$.*

Definition 2 *[1] Let U and V be spherical fuzzy sets on the universe S. Then:*

i) $\theta_U(s) \le \theta_V(s), \pi_U(s) \le \pi_V(s)$ and $\rho_U(s) \ge \rho_V(s)$ for all $s \in S$ iff $U \subseteq V$.

ii) $U \subseteq V$ and $V \subseteq U$ iff $U = V$.

iii) U is called spherical fuzzy universal set, denoted by 1_S, if $\theta_U(s) = 1, \pi_U(s) = 0$ and $\rho_U(s) = 0$ for all $s \in S$.

iv) U is called spherical fuzzy empty set, denoted by 0_S, if $\theta_U(s) = 0, \pi_U(s) = 0$ and $\rho_U(s) = 1$ for all $s \in S$.

v) The spherical fuzzy complement of U defined by $U^c = \{\langle s, \rho_U(s), \pi_U(s), \theta_U(s)\rangle : s \in S\}$. Clearly, the neutrosophic complements of 1_S and 0_S are defined:

$$(1_S)^c = \langle s, 0, 0, 1\rangle = 0_S,$$

$$(0_S)^c = \langle s, 1, 0, 0\rangle = 1_S.$$

Definition 3 *[9] Let U and V be spherical fuzzy sets on the universe S. Then:*

i) $U \cup V = T = \{s, \theta_T(s), \pi_T(s), \rho_T(s) : s \in S\}$ where

$$\theta_T(s) = \max\{\theta_U(s), \theta_V(s)\}$$

$$\pi_T(s) = \begin{cases} & \left(\max\{\theta_U(s), \theta_V(s)\}\right)^2 + \\ \max\{\pi_U(s), \pi_V(s)\} \quad \textit{if} & \left(\max\{\pi_U(s), \pi_V(s)\}\right)^2 + \ , \\ & \left(\min\{\rho_U(s), \rho_U(s)\}\right)^2 \le 1 \\ \min\{\rho_U(s), \rho_U(s)\} \quad \textit{if} & \textit{otherwise} \end{cases}$$

$$\psi_S(\kappa) = \min\{\psi_U(\kappa), \psi_V(\kappa)\}$$

ii) $U \cap V = T = \{s, \theta_T(s), \pi_T(s), \rho_T(s) : s \in S\}$ where

$$\theta_T(s) = \min\{\theta_U(s), \theta_V(s)\}$$

$$\pi_T(s) = \begin{cases} \max\{\pi_U(s), \pi_V(s)\} \quad \textit{if} & \theta_U(s) \text{or} \theta_V(s) = 1, \\ \min\{\rho_U(s), \rho_U(s)\} \quad \textit{if} & \textit{otherwise} \end{cases}$$

$$\psi_S(\kappa) = \max\{\psi_U(\kappa), \psi_V(\kappa)\}$$

Definition 4 *[16] Let S be a non empty set and $\tau^U \subseteq SF(S)$. Then τ^U is said to be a spherical fuzzy topology on S, if*

i) $1_S, 0_S \in \tau^U$

ii) If $U, V \in \tau$, then $U \cap V \in \tau$,

iii) If $U_i \in \tau \ \ \forall i \in I$, an index set, then $\underset{i \in I}{\cup} U_i \in \tau$.

Then $\left(S, \tau_1^{sp}\right)$ is called spherical fuzzy topological space, members of τ_1^{sp} are known as spherical fuzzy open sets and their complements are spherical fuzzy closed sets.

Definition 5 *[16] For a spherical fuzzy set U over S, the spherical fuzzy interior and the spherical fuzzy closure of U are defined as: $int^{sp}(U) = \cup\left\{G : G \subseteq U, G \in \tau_1^{sp}\right\}$ and $cl^{sp}(U) = \cap\left\{\rho : U \subseteq \rho, \rho^c \in \tau_1^{sp}\right\}$.*

Definition 6 *Let S be a non empty set. If θ, π, ρ be real standard or non standard subsets of $]^-0,1^+[$, then the neutrosophic set $s_{\theta,\pi,\rho}$ is called a spherical fuzzy point in given by*

$$s_{\theta,\pi,\rho}(y) = \begin{cases} (\theta, \pi, \rho), & \text{if } s = y \\ (0,0,1), & \text{if } s \neq y \end{cases}$$

for $y \in S$ is called the support of $s_{\theta,\pi,\rho}$.

It is clear that every spherical fuzzy set is the union of its spherical fuzzy points.

Spherical Fuzzy Bitopological Spaces

Definition 7: *Let $\left(S, \tau_1^{sp}\right)$ and $\left(S, \tau_2^{sp}\right)$ be the two different Spherical fuzzy topologies on S. Then $\left(S, \tau_1^{sp}, \tau_2^{sp}\right)$ is called a spherical fuzzy bitopological space.*

Definition 8: *Let $\left(S, \tau_1^{sp}, \tau_2^{sp}\right)$ be a spherical fuzzy bitopological space. A spherical fuzzy set $U = \left\{\left\langle s, \theta_U(s), \pi_U(s), \rho_U(s)\right\rangle : s \in S\right\}$ over S is said to be a pairwise spherical fuzzy open set in $\left(S, \tau_1^{sp}, \tau_2^{sp}\right)$ if there exist a spherical fuzzy open set $U_1 = \left\{\left\langle s, \theta_{U_1}(s), \pi_{U_1}(s), \rho_{U_1}(s)\right\rangle : s \in S\right\}$ in τ_1^{sp} and a spherical fuzzy open set $U_2 = \left\{\left\langle s, \theta_{U_2}(s), \pi_{U_2}(s), \rho_{U_2}(s)\right\rangle : s \in S\right\}$ in τ_2^{sp} such that $U = U_1 \cup U_2$.*

Definition 9: *Let $\left(S, \tau_1^{sp}, \tau_2^{sp}\right)$ be a spherical fuzzy bitopological space. A spherical fuzzy set U over S is said to be a pairwise spherical fuzzy closed set in $\left(S, \tau_1^{sp}, \tau_2^{sp}\right)$ if its spherical fuzzy*

copmlement is a pairwise spherical fuzzy open set in $\left(S,\tau_1^{sp},\tau_2^{sp}\right)$. *Obviously, a spherical fuzzy set* $C=\left\{\left\langle s,\theta_C(s),\pi_C(s),\rho_C(s)\right\rangle : s\in S\right\}$ *over* S *is a pairwise spherical fuzzy closed set in* $\left(S,\tau_1^{sp},\tau_2^{sp}\right)$ *if there exist a spherical fuzzy closed set* $C_1=\left\{\left\langle s,\theta_{C_1}(s),\pi_{C_1}(s),\rho_{C_1}(s)\right\rangle : s\in S\right\}$ *in* $\left(\tau_1^{sp}\right)^c$ *and a spherical fuzzy closed set* $C_2=\left\{\left\langle s,\theta_{C_2}(s),\pi_{C_2}(s),\rho_{C_2}(s)\right\rangle : s\in S\right\}$ *in* $\left(\tau_2^{sp}\right)^c$ *such that* $C=C_1\cap C_2$, *where*

$$\left(\tau_i^{sp}\right)^c=\left\{U^c\in SF(S):U\in\tau_i^{sp}\right\},i=1,2.$$

The family of all pairwise spherical fuzzy open (closed) sets in $\left(S,\tau_1^{sp},\tau_2^{sp}\right)$ is denoted by $PSO\left(S,\tau_1^{sp},\tau_2^{sp}\right)$ $\left[PSC\left(S,\tau_1^{sp},\tau_2^{sp}\right)\right]$, respectively.

Example 1: *Let* $S=\{a,b,c\}$. *We consider that following spherical fuzzy set over* S.

$$U_1=\left\{\left\langle a,0.2,0.3,0.3\right\rangle,\left\langle b,0.6,0.5,0.3\right\rangle,\left\langle c,0.3,0.6,0.5\right\rangle\right\},$$

$$U_2=\left\{\left\langle a,0.5,0.6,0.6\right\rangle,\left\langle b,0.5,0.3,0.4\right\rangle,\left\langle c,0.2,0.7,0.4\right\rangle\right\},$$

$$U_3=\left\{\left\langle a,0.2,0.3,0.6\right\rangle,\left\langle b,0.5,0.3,0.4\right\rangle,\left\langle c,0.2,0.6,0.5\right\rangle\right\},$$

$$U_4=\left\{\left\langle a,0.5,0.6,0.3\right\rangle,\left\langle b,0.6,0.5,0.3\right\rangle,\left\langle c,0.3,0.7,0.4\right\rangle\right\}$$

and

$$V_1=\left\{\left\langle a,0.2,0.2,0.3\right\rangle,\left\langle b,0.5,0.2,0.4\right\rangle,\left\langle c,0.2,0.5,0.6\right\rangle\right\},$$

$$V_2=\left\{\left\langle a,0.6,0.6,0.3\right\rangle,\left\langle b,0.6,0.4,0.4\right\rangle,\left\langle c,0.3,0.7,0.3\right\rangle\right\}.$$

Then $\left(S,\tau_1^{sp},\tau_2^{sp}\right)$ is a spherical fuzzy bitopological space, where

$$\tau_1^{sp}=\left\{0_S,1_S,U_1,U_2,U_3,U_4\right\},$$

$$\tau_2^{sp}=\left\{0_S,1_S,V_1,V_2\right\}.$$

Obviously,

$$\tau_{1,2}^{sp}=\tau_1^{sp}\cup\tau_2^{sp}\cup\left\{U_1\cup V_2,U_2\cup V_1,U_3\cup V_1,U_4\cup V_2\right\}$$

because the spherical fuzzy sets $U_1 \cup V_1$, $U_2 \cup V_1$,$U_3 \cup V_1$ and $U_4 \cup V_2$ not belong to either τ_1^{sp} nor τ_2^{sp} .

Theorem 1: *Let* $\left(S, \tau_1^{sp}, \tau_2^{sp}\right)$ *be a spherical fuzzy bitopological space. Then,*

i) 0_S and 1_S are pairwise spherical fuzzy open sets and pairwise spherical fuzzy closed sets.

ii) An arbitrary spherical fuzzy union of pairwise spherical fuzzy open sets is a pairwise spherical fuzzy open set.

iii) An arbitrary spherical fuzzy intersection of pairwise spherical fuzzy closed sets is a pairwise spherical fuzzy closed set.

Proof. **i.** Since $0_S \in \tau_1^{sp}$, τ_2^{sp} and $0_S \cup 0_S = 0_S$, then 0_S is a pairwise spherical fuzzy open set. Similarly, 1_S is a pairwise spherical fuzzy open set.

2. Let $\left\{\left(U_i\right) : i \in \pi\right\} \subseteq PSO\left(S, \tau_1^{sp}, \tau_2^{sp}\right)$. Then U_i is a pairwise spherical fuzzy open set for all $i \in \pi$, therefore there exist $U_i^1 \in \tau_1^{sp}$ and $U_i^2 \in \tau_2^{sp}$ such that $U_i = U_i^1 \cup U_i^2$ for all $i \in \pi$ which implies that

$$\underset{i\in\pi}{\cup} U_i = \underset{i\in\pi}{\cup}\left[U_i^1 \cup U_i^2\right] = \left[\underset{i\in\pi}{\cup} U_i^1\right] \cup \left[\underset{i\in\pi}{\cup} U_i^2\right].$$

Now, since τ_1^{sp} and τ_2^{sp} are spherical fuzzy topologies, then $\left[\underset{i\in\pi}{\cup} U_i^1\right] \in \tau_1^{sp}$ and $\left[\underset{i\in\pi}{\cup} U_i^2\right] \in \tau_2^{sp}$. Therefore, $\underset{i\in\pi}{\cup} U_i$ is a pairwise spherical fuzzy open set.

3. It is immediate from the Definition 9, Proposition ??.

Corollary 1 *Let* $\left(S, \tau_1^{sp}, \tau_2^{sp}\right)$ *be a spherical fuzzy bitopological space. Then, the family of all pairwise spherical fuzzy open sets is a supra spherical fuzzy topology on S. This supra spherical fuzzy topology we denoted by* $\tau_{1,2}^{sp}$.

Remark 1 *The Example 1 show that:*

1. $\tau_{1,2}^{sp}$ is not spherical fuzzy topology in general.

2. The finite spherical fuzzy intersection of pairwise spherical fuzzy open sets need not be a pairwise spherical fuzzy open set.

3. The arbitrary spherical fuzzy union of pairwise spherical fuzzy closed sets need not be a pairwise spherical fuzzy closed set.

Theorem 2: *Let* $\left(S,\tau_1^{sp},\tau_2^{sp}\right)$ *be a spherical fuzzy bitopological space. Then,*

1. Every $\tau_i^{sp}-$open spherical fuzzy set is a pairwise spherical fuzzy open set $i=1,2$, i.e., $\tau_1^{sp}\cup\tau_2^{sp}\subseteq\tau_{1,2}^{sp}$.

2. Every $\tau_i^{sp}-$closed spherical fuzzy set is a pairwise spherical fuzzy closed set $i=1,2$, i.e., $\left(\tau_1^{sp}\right)^c\cup\left(\tau_2^{sp}\right)^c\subseteq\left(\tau_{1,2}^{sp}\right)^c$.

3. If $\tau_1^{sp}\subseteq\tau_2^{sp}$, then $\tau_{1,2}^{sp}=\tau_2^{sp}$ and $\left(\tau_{1,2}^{sp}\right)^c=\left(\tau_2^{sp}\right)^c$.

Proof. Straightforward.

Definition 10: *Let* $\left(S,\tau_1^{sp},\tau_2^{sp}\right)$ *be a spherical fuzzy bitopological space and* $U\in SF(S)$. *The pairwise spherical fuzzy closure of* U, *denoted by* $cl_p^{sp}(U)$, *is the spherical fuzzy intersection of all pairwise spherical fuzzy closed super sets of* U, *i.e.,*

$$cl_p^{sp}(U)=\cap\left\{C\in\left(\tau_{1,2}^{sp}\right)^c:U\subseteq C\right\}.$$

It is clear that $cl_p^{sp}(U)$ is the smallest pairwise spherical fuzzy closed set containing U.

Example 2: *Let* $\left(S,\tau_1^{sp},\tau_2^{sp}\right)$ *be the same as in Example 1. and*

$H=\left\{\langle a,0.5,0.5,0.6\rangle,\langle b,0.3,0.3,0.6\rangle,\langle c,0.3,0.7,0.3\rangle\right\}$ be a spherical fuzzy set over S.

Now, we need to determine pairwise spherical fuzzy closed sets in $\left(S,\tau_1^{sp},\tau_2^{sp}\right)$ to find $cl_p^{sp}(G)$. Then, $0_S,1_S$,

$$U_1^c=\left\{\langle a,0.3,0.3,0.2\rangle,\langle b,0.3,0.5,0.6\rangle,\langle c,0.5,0.6,0.3\rangle\right\},$$

$$U_2^c=\left\{\langle a,0.6,0.6,0.5\rangle,\langle b,0.4,0.3,0.5\rangle,\langle c,0.4,0.7,0.2\rangle\right\},$$

$$U_3^c=\left\{\langle a,0.6,0.3,0.2\rangle,\langle b,0.4,0.3,0.5\rangle,\langle c,0.5,0.6,0.2\rangle\right\},$$

$$U_4^c=\left\{\langle a,0.3,0.6,0.5\rangle,\langle b,0.3,0.5,0.6\rangle,\langle c,0.4,0.7,0.3\rangle\right\}$$

$$V_1^c = \{\langle a, 0.3, 0.2, 0.2\rangle, \langle b, 0.4, 0.2, 0.5\rangle, \langle c, 0.6, 0.5, 0.2\rangle\},$$

$$V_2^c = \{\langle a, 0.3, 0.6, 0.6\rangle, \langle b, 0.4, 0.4, 0.6\rangle, \langle c, 0.3, 0.7, 0.3\rangle\}.$$

and

$$(U_1 \cup V_2)^c = \{\langle a, 0.3, 0.6, 0.6\rangle, \langle b, 0.3, 0.5, 0.6\rangle, \langle c, 0.3, 0.7, 0.3\rangle\}$$

$$(U_2 \cup V_1)^c = \{\langle a, 0.3, 0.6, 0.5\rangle, \langle b, 0.4, 0.3, 0.5\rangle, \langle c, 0.4, 0.7, 0.2\rangle\}$$

$$(U_3 \cup V_1)^c = \{\langle a, 0.3, 0.3, 0.2\rangle, \langle b, 0.4, 0.3, 0.5\rangle, \langle c, 0.5, 0.6, 0.2\rangle\}$$

$$(U_4 \cup V_2)^c = \{\langle a, 0.3, 0.6, 0.6\rangle, \langle b, 0.3, 0.5, 0.6\rangle, \langle c, 0.3, 0.7, 0.3\rangle\}$$

In here, the pairwise spherical fuzzy closed sets which contains H are U_2^c and 1_S it follows that $cl_p^{sp}(H) = U_2^c \cap 1_S$. Therefore, $cl_p^{sp}(H) = U_2^c$.

Theorem 3: *Let* $\left(S, \tau_1^{sp}, \tau_2^{sp}\right)$ *be a spherical fuzzy bitopological space and* U, $V \in SF(S)$. *Then,*

1. $cl_p^{sp}(0_S) = 0_S$ and $cl_p^{sp}(1_S) = 1_S$.
2. $U \subseteq cl_p^{sp}(U)$.
3. U is a pairwise spherical fuzzy closed set iff $cl_p^{sp}(U) = U$.
4. $U \subseteq V \Rightarrow cl_p^{sp}(U) \subseteq cl_p^{sp}(V)$.
5. $cl_p^{sp}(U) \cup cl_p^{sp}(V) \subseteq cl_p^{sp}(U \cup V)$.
6. $cl_p^{sp}\left[cl_p^{sp}(U)\right] = cl_p^{sp}(U)$, i.e., $cl_p^{sp}(U)$ is a pairwise spherical fuzzy closed set.

Proof. Straightforward.

Theorem 4: *Let* $\left(S, \tau_1^{sp}, \tau_2^{sp}\right)$ *be a spherical fuzzy bitopological space and* $U \in SF(S)$. *Then,*

$$s_{\theta,\pi,\rho} \in cl_p^{sp}(U) \Leftrightarrow U_{s_{\theta,\pi,\rho}} \cap U \neq 0_S, \forall U_{s_{\theta,\pi,\rho}} \in \tau_{1,2}^{sp}\left(s_{\theta,\pi,\rho}\right),$$

where $U_{s_{\theta,\pi,\rho}}$ is any pairwise spherical fuzzy open set contains $s_{\theta,\pi,\rho}$ and $\tau_{1,2}^{sp}\left(s_{\theta,\pi,\rho}\right)$ is the family of all pairwise spherical fuzzy open sets contains $s_{\theta,\pi,\rho}$.

Proof. Let $s_{\theta,\pi,\rho} \in cl_p^{sp}(U)$ and suppose that there exists $U_{s_{\theta,\pi,\rho}} \in \tau_{1,2}^{sp}\left(s_{\theta,\pi,\rho}\right)$ such that $U_{s_{\theta,\pi,\rho}} \cap U = 0_S$. Then $U \subseteq \left(U_{s_{\theta,\pi,\rho}}\right)^c$, thus $cl_p^{sp}(U) \subseteq cl_p^{sp}\left(U_{s_{\theta,\pi,\rho}}\right)^c = \left(U_{s_{\theta,\pi,\rho}}\right)^c$ which implies $cl_p^{sp}(U) \cap U_{s_{\theta,\pi,\rho}} = 0_S$, a contradiction.

Conversely, assume that $s_{\theta,\pi,\rho} \notin cl_p^{sp}(U)$, then $s_{\theta,\pi,\rho} \in \left[cl_p^{sp}(U)\right]^c$. Thus, $\left[cl_p^{sp}(U)\right]^c \in \tau_{1,2}^{sp}\left(s_{\theta,\pi,\rho}\right)$, so, by hypothesis, $\left[cl_p^{sp}(U)\right]^c \cap U \neq 0_S$, a contradiction.

Theorem 5: *Let* $\left(S, \tau_1^{sp}, \tau_2^{sp}\right)$ *be a spherical fuzzy bitopological space. A spherical fuzzy set* U *over* S *is a pairwise spherical fuzzy closed set iff* $U = cl_{\tau_1^{sp}}^{sp}(U) \cap cl_{\tau_2^{sp}}^{sp}(U)$.

Proof. Suppose that U is a pairwise spherical fuzzy closed set and $s_{\theta,\pi,\rho} \notin U$. Then, $s_{\theta,\pi,\rho} \notin cl_p^{sp}(U)$. Thus, [by Theorem 4], there exists $U_{s_{\theta,\pi,\rho}} \in \tau_{1,2}^{sp}\left(s_{\theta,\pi,\rho}\right)$ such that $U_{s_{\theta,\pi,\rho}} \cap U = 0_S$. Since $U_{s_{\theta,\pi,\rho}} \in \tau_{1,2}^{sp}\left(s_{\theta,\pi,\rho}\right)$, then there exists $V_1 \in \tau_1^{sp}$ and $V_2 \in \tau_2^{sp}$ such that $U_{s_{\theta,\pi,\rho}} = V_1 \cup V_2$. Hence, $\left(V_1 \cup V_2\right) \cap U = 0_S$ it follows that $V_1 \cap U = 0_S$ and $V_2 \cap U = 0_S$. Since $s_{\theta,\pi,\rho} \in U_{s_{\theta,\pi,\rho}}$, then $s_{\theta,\pi,\rho} \in V_1$ or $s_{\theta,\pi,\rho} \in V_2$ implies, $s_{\theta,\pi,\rho} \notin cl_{\tau_1^{sp}}^{sp}(U)$ or $s_{\theta,\pi,\rho} \notin cl_{\tau_2^{sp}}^{sp}(U)$. Therefore, $s_{\theta,\pi,\rho} \notin cl_{\tau_1^{sp}}^{sp}(U) \cap cl_{\tau_2^{sp}}^{sp}(U)$. Thus, $cl_{\tau_1^{sp}}^{sp}(U) \cap cl_{\tau_2^{sp}}^{sp}(U) \subseteq U$. On the other hand, we have $U \subseteq cl_{\tau_1^{sp}}^{sp}(U) \cap cl_{\tau_2^{sp}}^{sp}(U)$. Hence, $U = cl_{\tau_1^{sp}}^{sp}(U) \cap cl_{\tau_2^{sp}}^{sp}(U)$.

Conversely, suppose that $U = cl_{\tau_1^{sp}}^{sp}(U) \cap cl_{\tau_2^{sp}}^{sp}(U)$. Since, $cl_{\tau_1^{sp}}^{sp}(U)$ is a spherical fuzzy closed set in $\left(S, \tau_1^{sp}\right)$ and $cl_{\tau_2^{sp}}^{sp}(U)$ is a spherical fuzzy closed set in $\left(S, \tau_2^{sp}\right)$, then,[by Definition 9], $cl_{\tau_1^{sp}}^{sp}(U) \cap cl_{\tau_2^{sp}}^{sp}(U)$ is a pairwise spherical fuzzy closed set in $\left(S, \tau_1^{sp}, \tau_2^{sp}\right)$, so U is a pairwise spherical fuzzy closed set.

Corollary 2 *Let* $\left(S, \tau_1^{sp}, \tau_2^{sp}\right)$ *be a spherical fuzzy bitopological space. Then,*

$$cl_p^{sp}(U) = cl_{\tau_1^{sp}}^{sp}(U) \cap cl_{\tau_2^{sp}}^{sp}(U), \forall U \in SF(S).$$

Definition 11: *An operator* $\Psi : SF(S) \to SF(S)$ *is called a spherical fuzzy supra closure operator if it satisfies the following conditions for all* U, $V \in SF(S)$.

1. $\Psi(0_S) = 0_S$,

2. $U \subseteq \Psi(U)$,

3. $\Psi(U) \cup \Psi(V) \subseteq \Psi(U \cup V)$

4. $\Psi(\Psi(U)) = \Psi(U)$.

Theorem 6 *Let* $(S, \tau_1^{sp}, \tau_2^{sp})$ *be a spherical fuzzy bitopological space. Then, the operator* $cl_p^{sp} : SF(S) \to SF(S)$ *which defined by*

$$cl_p^{sp}(U) = cl_{\tau_1^{sp}}^{sp}(U) \cap cl_{\tau_2^{sp}}^{sp}(U)$$

is spherical fuzzy supra closure operator and it is induced, a unique spherical fuzzy supra topology given by $\{U \in SF(S) : cl_p^{sp}(U^c) = U^c\}$ which is precisely $\tau_{1,2}^{sp}$.

Proof. Straightforward.

Definition 12 *Let* $(S, \tau_1^{sp}, \tau_2^{sp})$ *be a spherical fuzzy bitopological space and* $U \in SF(S)$. *The pairwise spherical fuzzy interior of* U, *denoted by* $int_p^{sp}(U)$, *is the spherical fuzzy union of all pairwise spherical fuzzy open subsets of* U, *i.e.,*

$$int_p^{sp}(U) = \cup\{V \in \tau_{1,2}^{sp} : V \subseteq U\}.$$

Obviously, $int_p^{sp}(U)$ is the biggest pairwise spherical fuzzy open set contained in U.

Example 3 *Let* $(S, \tau_1^{sp}, \tau_2^{sp})$ *be the same as in Example 1 and*

$G = \{\langle a, 0.3, 0.3, 0.1\rangle, \langle b, 0.6, 0.5, 0.2\rangle, \langle c, 0.4, 0.6, 0.3\rangle\}$ be a spherical fuzzy set over S. Then the pairwise spherical fuzzy open sets which containing in G are U_1, U_3, V_1, $U_3 \cup V_1$ and 0_S. Therefore,

$$int_p^{sp}(G) = U_1 \cup U_3 \cup V_1 \cup (U_3 \cup V_1) \cup 0_S$$

$$= U_1.$$

Theorem 7 *Let* $(S, \tau_1^{sp}, \tau_2^{sp})$ *be a spherical fuzzy bitopological space and* $U, V \in SF(S)$. *Then,*

1. $int_p^{sp}(0_S) = 0_S$ and $int_p^{sp}(1_S) = 1_S$,

2. $int_p^{sp}(U) \subseteq U$,

3. U is a pairwise spherical fuzzy open set iff $int_p^{sp}(U) = U$,

4. $U \subseteq V \Rightarrow int_p^{sp}(U) \subseteq int_p^{sp}(V)$,

5. $int_p^{sp}(U \cap V) \subseteq int_p^{sp}(U) \cap int_p^{sp}(V)$,

6. $int_p^{sp}\left[int_p^{sp}(U)\right] = int_p^{sp}(U)$.

Proof. Starightforward.

Theorem 8 *Let* $\left(S, \tau_1^{sp}, \tau_2^{sp}\right)$ *be a spherical fuzzy bitopological space and* $U \in SF(S)$. *Then,*

$$s_{\theta,\pi,\rho} \in int_p^{sp}(U) \Leftrightarrow \exists U_{s_{\theta,\pi,\rho}} \in \tau_{1,2}^{sp}\left(s_{\theta,\pi,\rho}\right) \text{such that} U_{s_{\theta,\pi,\rho}} \subseteq U.$$

Proof. Starightforward.

Theorem 9 *Let* $\left(S, \tau_1^{sp}, \tau_2^{sp}\right)$ *be a spherical fuzzy bitopological space. A spherical fuzzy set* U *over* S *is a pairwise spherical fuzzy open set iff* $U = int_{\tau_1^{sp}}^{sp}(U) \cup int_{\tau_2^{sp}}^{sp}(U)$.

Proof. Let U be a pairwise spherical fuzzy open set. Since, $int_{\tau_i}^{sp}(U) \subseteq U$, $i = 1,2$, then $int_{\tau_1^{sp}}^{sp}(U) \cup int_{\tau_2^{sp}}^{sp}(U) \subseteq U$. Now, let $s_{\theta,\pi,\rho} \in U$. Then, there exists $U_{s_{\theta,\pi,\rho}}^1 \in \tau_1^{sp}$ such that $U_{s_{\theta,\pi,\rho}}^1 \subseteq U$ or there exists $U_{s_{\theta,\pi,\rho}}^2 \in \tau_2^{sp}$ such that $U_{s_{\theta,\pi,\rho}}^2 \subseteq U$, thus $s_{\theta,\pi,\rho} \in int_{\tau_1^{sp}}^{sp}(U)$ or $s_{\theta,\pi,\rho} \in int_{\tau_2^{sp}}^{sp}(U)$. Hence, $s_{\theta,\pi,\rho} \in int_{\tau_1^{sp}}^{sp}(U) \cup int_{\tau_2^{sp}}^{sp}(U)$. Therefore, $U = int_{\tau_1^{sp}}^{sp}(U) \cup int_{\tau_2^{sp}}^{sp}(U)$

Coversely, since $int_{\tau_1^{sp}}^{sp}(U)$ is a spherical fuzzy open set in $\left(S, \tau_1^{sp}\right)$ and $int_{\tau_2^{sp}}^{sp}(U)$ is a spherical fuzzy open set in $\left(S, \tau_2^{sp}\right)$, then,[by Definition 8], $int_{\tau_1^{sp}}^{sp}(U) \cup int_{\tau_2^{sp}}^{sp}(U)$ is a pairwise spherical fuzzy open set in $\left(S, \tau_1^{sp}, \tau_2^{sp}\right)$. Thus, U is a pairwise spherical fuzzy open set.

Corollary 3 *Let* $\left(S, \tau_1^{sp}, \tau_2^{sp}\right)$ *be a spherical fuzzy bitopological space. Then,*

$$int_p^{sp}(U) = int_{\tau_1^{sp}}^{sp}(U) \cup int_{\tau_2^{sp}}^{sp}(U).$$

Definition 13 *An operator* $\pi : SF(S) \to SF(S)$ *is called a spherical fuzzy supra interior operator if it satisfies the following conditions for all* U, $V \in SF(S)$.

1. $\pi\left(0_S\right) = 0_S$,

2. $\pi\left(U\right) \subseteq U$,

3. $\pi(U \cap V) \subseteq \pi(U) \cap \pi(V)$

4. $\pi\left(\pi\left(U\right)\right) = \pi(U)$.

Theorem 10 *Let* $\left(S, \tau_1^{sp}, \tau_2^{sp}\right)$ *be a spherical fuzzy bitopological space. Then, the operator* $int_p^{sp} : SF(S) \to SF(S)$ *which defined by*

$$int_p^{sp}\left(U\right) = int_{\tau_1^{sp}}^{sp}\left(U\right) \cup int_{\tau_2^{sp}}^{sp}\left(U\right)$$

is spherical fuzzy supra interior operator and it is induced, a unique spherical fuzzy supra topology given by $\left\{U \in SF(S) : int_p^{sp}\left(U\right) = U\right\}$ which is precisely $\tau_{1,2}^{sp}$.

Proof. Straightforward.

Theorem 11 *Let* $\left(S, \tau_1^{sp}, \tau_2^{sp}\right)$ *be a spherical fuzzy bitopological space and* $U \in SF(S)$. *Then,*

1. $int_p^{sp}\left(U\right) = \left(cl_p^{sp}(U^c)\right)^c$.

2. $cl_p^{sp}(U) = \left(int_p^{sp}(U^c)\right)^c$.

Proof. Starightforward.

Definition 14 *Let* $\left(S, \tau_1^{sp}, \tau_2^{sp}\right)$ *be a spherical fuzzy bitopological space,* $U \in SF(S)$ *and* $s_{\theta,\pi,\rho} \in SF(S)$. *Then* U *is said to be a pairwise spherical fuzzy neighborhood of* $s_{\theta,\pi,\rho}$, *if there exists a pairwise spherical fuzzy open set* U *such that* $s_{\theta,\pi,\rho} \in U \subseteq U$. *The family of pairwise spherical fuzzy neighborhood of spherical fuzzy point* $s_{\theta,\pi,\rho}$ *denoted by* $U_{\tau_{1,2}^{sp}}\left(s_{\theta,\pi,\rho}\right)$.

Theorem 12 *Let* $\left(S, \tau_1^{sp}, \tau_2^{sp}\right)$ *be a spherical fuzzy bitopological space and* $U \in SF(S)$. *Then* U *is pairwise spherical fuzzy open set iff* U *is a pairwise spherical fuzzy neighborhood of its spherical fuzzy points.*

Proof. Let U be a pairwise spherical fuzzy open set and $s_{\theta,\pi,\rho} \in U$. Then $s_{\theta,\pi,\rho} \in U \subseteq U$. Therefore U is a pairwise spherical fuzzy neighborhood of $s_{\theta,\pi,\rho}$ for each $s_{\theta,\pi,\rho} \in U$.

Conversely, suppose that U is a pairwise spherical fuzzy neighborhood of its spherical fuzzy points and $s_{\theta,\pi,\rho} \in U$. Then there exists a pairwise spherical fuzzy open set U such that $s_{\theta,\pi,\rho} \in U \subseteq U$. Since

$$U = \bigcup_{s_{\theta,\pi,\rho} \in U} \{s_{\theta,\pi,\rho}\} \subseteq \bigcup_{s_{\theta,\pi,\rho} \in U} U \bigcup_{s_{\theta,\pi,\rho} \in U} U = U$$

it follows that U is an union of pairwise spherical fuzzy open sets. Hence, U is a pairwise spherical fuzzy open set.

Proposition 1 *Let* $\left(S, \tau_1^{sp}, \tau_2^{sp}\right)$ *be a spherical fuzzy bitopological space and*

$\left\{U_{\tau_{1,2}^{sp}}\left(s_{\theta,\pi,\rho}\right) : s_{\theta,\pi,\rho} \in SF(S)\right\}$ be a system of pairwise spherical fuzzy neighborhoods. Then,

1. For every $U \in U_{\tau_{1,2}^{sp}}\left(s_{\theta,\pi,\rho}\right)$, $s_{\theta,\pi,\rho} \in U$;

2. $U \in U_{\tau_{1,2}^{sp}}\left(s_{\theta,\pi,\rho}\right)$ and $U \subseteq V \Rightarrow V \in U_{\tau_{1,2}^{sp}}\left(s_{\theta,\pi,\rho}\right)$;

3. $U \in U_{\tau_{1,2}^{sp}}\left(s_{\theta,\pi,\rho}\right) \Rightarrow \exists V \in U_{\tau_{1,2}^{sp}}\left(s_{\theta,\pi,\rho}\right)$ such that $V \subseteq U$ and $V \in U_{\tau_{1,2}^{sp}}\left(y_{\theta',\pi',\rho'}\right)$, for every $y_{\theta',\pi',\rho'} \in V$.

Proof. Proofs of 1 and 2 are straightforward.

3. Let U be a pairwise spherical fuzzy neighborhood of $s_{\theta,\pi,\rho}$, then there exists a pairwise spherical fuzzy open set $V \in \tau_{1,2}^{sp}$ such that $s_{\theta,\pi,\rho} \in V \subseteq U$. Since $s_{\theta,\pi,\rho} \in V \subseteq V$ can be written, then $V \in U_{\tau_{1,2}^{sp}}\left(s_{\theta,\pi,\rho}\right)$. From the Theorem 12, if V is pairwise spherical fuzzy open set then U is a pairwise spherical fuzzy neighborhood of its spherical fuzzy points, i.e., $V \in U_{\tau_{1,2}^{sp}}\left(y_{\theta',\pi',\rho'}\right)$, for every $y_{\theta',\pi',\rho'} \in V$.

Remark 2 *Generally,* $U,V \in U_{\tau_{1,2}^{sp}}\left(s_{\theta,\pi,\rho}\right) \Rightarrow U \cap V \notin U_{\tau_{1,2}^{sp}}\left(s_{\theta,\pi,\rho}\right)$. *Actually, if* $U,V \in U_{\tau_{1,2}^{sp}}\left(s_{\theta,\pi,\rho}\right)$, *there exist* $U_1,U_2 \in \tau_{1,2}^{sp}$ *such that* $s_{\theta,\pi,\rho} \in U_1 \subseteq U$ *and* $s_{\theta,\pi,\rho} \in U_2 \subseteq V$. *But* $U_1 \cap U_2$ *need not be a pairwise spherical fuzzy open set*. *Therefore,* $U \cap V$ *need not be a pairwise spherical fuzzy neighborhood of* $s_{\theta,\pi,\rho}$.

Theorem 13 *Let* $\left(S,\tau_1^{sp},\tau_2^{sp}\right)$ *be a spherical fuzzy bitopological space. Then*

$$U_{\tau_{1,2}^{sp}}\left(s_{\theta,\pi,\rho}\right) = U_{\tau_1^{sp}}\left(s_{\theta,\pi,\rho}\right) \cup U_{\tau_2^{sp}}\left(s_{\theta,\pi,\rho}\right)$$

for each $s_{\theta,\pi,\rho} \in SF(S)$.

Proof. Let $s_{\theta,\pi,\rho} \in SF(S)$ be any spherical fuzzy point and $U \in U_{\tau_{1,2}^{sp}}\left(s_{\theta,\pi,\rho}\right)$. Then there exists a pairwise spherical fuzzy open set $V \in \tau_{1,2}^{sp}$ such that $s_{\theta,\pi,\rho} \in V \subseteq U$. If $V \in \tau_{1,2}^{sp}$, there exist $V_1 \in \tau_1^{sp}$ and $V_2 \in \tau_2^{sp}$ such that $V = V_1 \cup V_2$. Since $s_{\theta,\pi,\rho} \in V = V_1 \cup V_2$, then $s_{\theta,\pi,\rho} \in V_1$ or $s_{\theta,\pi,\rho} \in V_2$. So, $s_{\theta,\pi,\rho} \in V_1 \subseteq V \subseteq U$ or $s_{\theta,\pi,\rho} \in V_2 \subseteq V \subseteq U$. In this case, $U \in U_{\tau_1^{sp}}\left(s_{\theta,\pi,\rho}\right)$ or $U \in U_{\tau_2^{sp}}\left(s_{\theta,\pi,\rho}\right)$, i.e., $U \in U_{\tau_1^{sp}}\left(s_{\theta,\pi,\rho}\right) \cup U_{\tau_2^{sp}}\left(s_{\theta,\pi,\rho}\right)$.

Conversely, suppose that $U \in U_{\tau_1^{sp}}\left(s_{\theta,\pi,\rho}\right) \cup U_{\tau_2^{sp}}\left(s_{\theta,\pi,\rho}\right)$. Then $U \in U_{\tau_1^{sp}}\left(s_{\theta,\pi,\rho}\right)$ or $U \in U_{\tau_2^{sp}}\left(s_{\theta,\pi,\rho}\right)$. Hence, there exists $s_{\theta,\pi,\rho} \in V_1 \in \tau_1^{sp}$ or $s_{\theta,\pi,\rho} \in V_2 \in \tau_2^{sp}$ such that $s_{\theta,\pi,\rho} \in V_1 \subseteq U$ and $s_{\theta,\pi,\rho} \in V_2 \subseteq U$. As a result, $s_{\theta,\pi,\rho} \in V_1 \cup V_2 = V \subseteq U$ such that $V \in \tau_{1,2}^{sp}$ i.e., $U \in U_{\tau_{1,2}^{sp}}\left(s_{\theta,\pi,\rho}\right)$.

Definition 15 *An operator* $\nu : SF(S) \to SF(S)$ *is called a spherical fuzzy supra neighborhood operator if it satisfies the following conditions for all* U, $V \in SF(S)$.

1. $\forall U \in \nu\left(s_{\theta,\pi,\rho}\right)$, $s_{\theta,\pi,\rho} \in U$;

2. $U \in \nu\left(s_{\theta,\pi,\rho}\right)$ and $U \subseteq V \Rightarrow V \in \nu\left(s_{\theta,\pi,\rho}\right)$;

3. $U \in \nu\left(s_{\theta,\pi,\rho}\right) \Rightarrow \exists V \in \nu\left(s_{\theta,\pi,\rho}\right)$ such that $U \subseteq V$ and $V \in \nu\left(y_{\theta,\pi,\rho}\right)$, $y_{\theta,\pi,\rho} \in V$.

Theorem 14 *Let* $\left(S,\tau_1^{sp},\tau_2^{sp}\right)$ *be a spherical fuzzy bitopological space. Then, the operator* $U_{\tau_{1,2}^{sp}}:SF(S)\to SF(S)$ *which defined by*

$$U_{\tau_{1,2}^{sp}}\left(s_{\theta,\pi,\rho}\right)=U_{\tau_1^{sp}}\left(s_{\theta,\pi,\rho}\right)\cup U_{\tau_2^{sp}}\left(s_{\theta,\pi,\rho}\right)$$

is spherical fuzzy supra neighboorhod operator and it is induced, a unique spherical fuzzy supra topology given by $\left\{U\in SF(S):\forall s_{\theta,\pi,\rho}\in U\text{for}U\in U_{\tau_{1,2}^{sp}}\left(s_{\theta,\pi,\rho}\right)\right\}$ which is precisely $\tau_{1,2}^{sp}$.

Conclusion

In this paper, spherical fuzzy bitopological spaces are presented. By defining open(closed) sets, interior, closure and neighbourhood systems, fundamentals theorems for spherical fuzzy bitopological spaces are proved and some examples on the subject are given. We hope that, the results of this study may help in the investigation of separation axioms on the spherical fuzzy bitopological spaces and many researchers.

References

[1] Ashraf, Shahzaib; Abdullah, Saleem; Mahmood, Tahir; Ghani, Fazal; Mahmood, Tariq (2018). Spherical fuzzy sets and their applications in multi-attribute decision making problems. Journal of Intelligent & Fuzzy Systems, (), 1–16. doi:10.3233/JIFS-172009

[2] Atanassov, K.T. Intuitionistic fuzzy sets. Fuzzy Sets Syst. 1986, 20, 87–96.

[3] Atanassov, K.T. Intuitionistic Fuzzy Sets. In Studies in Fuzziness and Soft Computing, Physica; Springer: Berlin/Heidelberg, Germany. 1999; Volume 35, pp. 1–137.

[4] Atanassov, K.T.; Stoeva, S. Intuitionistic fuzzy sets. In Polish Symposium on Interval and Fuzzy Mathematics, Poznan; 1983; pp. 23–26

[5] Black, M. Vagueness: An Exercise in Logical Analysis. Philos. Sci. 1973, 4, 427–455. Reprinted in Int. J. Gen. Syst. 2022, 17, 107–128

[6] Cuong, B.C.; Kreinovich, V. Picture fuzzy sets. J. Comput. Sci. Cybern. 2014, 30, 409–420

[7] Deveci, M.; Pamucar, D.; Gokasar, I.; Köppen, M.; Gupta, B.B. Personal Mobility in Metaverse With Autonomous Vehicles Using Q-Rung Orthopair Fuzzy Sets Based OPA-RAFSI Model. IEEE Trans. Intell. Transp. Syst. 2022

[8] Feng, F.; Zheng, Y.; Sun, B.; Akram, M. Novel score functions of generalized orthopair fuzzy membership grades with application to multiple attribute decision making. Granul. Comput. 2022, 7, 95–111.

[9] H. Garg, F. Perveen P A, S. J.John, L. Perez-Dominguez, "Spherical Fuzzy Soft Topology and Its Application in Group Decision-Making Problems", Mathematical Problems in Engineering, vol. 2022, Article ID 1007133, 19 pages, 2022. https://doi.org/10.1155/2022/1007133

[10] Gündoğdu FK, Kahraman C (2019) Spherical fuzzy sets and spherical fuzzy TOPSIS method. J Intell Fuzzy Syst 36(1):337–352

[11] Mahmood, T.; Ullah, K.; Khan, Q.; Jan, N. An Approach towards decision making and medical diagnosis problems using the concept of spherical fuzzy sets. Neural Comput. Appl. 2019, 31, 7041–7053.

[12] Molodtsov, D. Soft set theory-first results. Comput. Math. Appl. 1999, 37, 19–31.

[13] Ozturk, T. Y., & Yolcu, A. (2020). Some structures on Pythagorean fuzzy topological spaces. Journal of New Theory, (33), 15-25.

[14] Öztürk, T. Y., Karataş, E., & Yolcu, A. (2021). On neutrosophic soft continuous mappings. Turkish Journal of Mathematics, 45(1), 81-95.

[15] Ozturk, T. Y., & Yolcu, A. (2021). On neutrosophic hypersoft topological spaces. Theory and Application of Hypersoft Set, 215.

[16] Princy R, Mohana K, (2019) An Introduction to Spherical Fuzzy Topological Spaces, International Journal of Innovative Research in Technology 6(5) 110–112.

[17] Riaz, M.; Jamil, N.; Zararsiz, Z. Distance and similarity measures for bipolar fuzzy soft sets with application to pharmaceutical logistics and supply chain management. J. Intell. Fuzzy Syst. 2022, 42, 3169–3188.

[18] Smarandache, F. A Unifying Field in Logics: Neutrosophy: Neutrosophic Probability, Set and Logic; American Research Press: Rehoboth, DE, USA, 1999; pp. 1–141

[19] Smarandache, F. Extension of soft set to hypersoft set, and then to plithogenic hypersoft set. Neutrosophic Sets Syst. 2018, 22, 168-170.

[20] Yager, R.R.; Abbasov, A.M. Pythagorean membership grades, complex numbers, and decision making. Int. J. Intell. Syst. 2013, 28, 436–452.

[21] Yager, R.R. Generalized orthopair fuzzy sets. IEEE Trans. Fuzzy Syst. 2016, 25, 1222–1230

[22] Yolcu, A. (2022). Bipolar Spherical Fuzzy Soft Topology with Applications to Multi-Criteria Group Decision-Making in Buildings Risk Assessment. Symmetry, 14(11), 2362.

[23] Yolcu, A. (2023). Intuitionistic fuzzy hypersoft topology and ıts applications to multi-criteria decision-making. Sigma Journal of Mathematics, 41(1), 106-118.

[24] Yolcu, A., Benek, A., & Öztürk, T. Y. (2023). A new approach to neutrosophic soft rough sets. Knowledge and Information Systems, 1-18.

[25] Yolcu, A., & Büşra, A. K. A. (2023). On Neutrosophic Soft Multisets and Neutrosophic Soft Multi Topological Spaces. Erzincan University Journal of Science and Technology, 16(1), 89-109.

[26] Yolcu, A., Smarandache, F., & Öztürk, T. Y. (2021). Intuitionistic fuzzy hypersoft sets. Communications Faculty of Sciences University of Ankara Series A1 Mathematics and Statistics, 70(1), 443-455.

[27] Yolcu, A., & Ozturk, T. Y. (2021). Fuzzy hypersoft sets and it's application to decision-making. Theory and application of hypersoft set, 50.

[28] Yolcu, A., Karatas, E., & Ozturk, T. Y. (2021). A new approach to neutrosophic soft mappings and application in decision making. Neutrosophic Operational Research: Methods and Applications, 291-313.

[29] Zadeh, L.A. Fuzzy sets. Inform. Control. 1965, 8,338–353.

Recent Advances In Sustainable Geotechnics: A Review On The Use Of Geosynthetics

Yesim TUSKAN[1]

Introduction

Geosynthetics have become an essential part of modern geotechnical engineering due to numerous advantages, including durability, high strength, and flexibility. Moreover, there is a growing demand for biodegradable alternatives that prioritize environmental sustainability. Consequently, geosynthetics with only minimal variations in long-lasting functionality are typically favored. The aim of the study is to provide an overview of the existing sustainable practices in geotechnical engineering, as well as to identify the gaps in the literature and the potential avenues for future research. The study identifies several sustainable practices that have been successfully implemented in geotechnical engineering, such as the use of recycled materials, geosynthetics, and ground improvement techniques. The use of these practices has been shown to reduce the environmental impact of infrastructures, as well as to improve the durability and safety of the structures. The study also concludes that sustainable approaches are essential for the future of geotechnical engineering in the transportation and environmental practices. The use of recycled materials, geosynthetics, and ground improvement techniques can significantly reduce the environmental impact of construction, while also improving the performance of the structures. However, the review also highlights the need for further research to identify other sustainable practices and to better understand their long-term performance with a valuable summary of the current state of sustainable geotechnical engineering practices

In the last few decades, the use of geosynthetics (e.g. geogrids, geotextiles, and geomembranes) has become increasingly prevalent in geotechnical engineering applications, owing to their unique properties and benefits. In geotechnical engineering, geosynthetics are employed for a variety of purposes, such as reinforcement, drainage, erosion control, and soil stabilization. As a result, they have become an essential component in the design and construction of many infrastructure projects. Geosynthetics are used to reinforce soil, such as in retaining walls, slopes, and embankments, to increase their load-carrying capacity and reduce deformation under stress. The use of geosynthetics can also lead to significant cost savings by minimizing the amount of earthwork required to construct the geotechnical system. Another function that geosynthetics serve in geotechnical engineering is drainage. Geosynthetics can be employed to improve the drainage conditions of the soil by acting as a filter and facilitating the flow of water through the soil. Such applications include drainage systems for roadways, railway tracks, and landfills. Additionally, geosynthetics can be utilized for erosion control purposes, such as in the construction of coastal structures, riverbank protection, and shorelines. A further function of geosynthetics is soil stabilization. Geosynthetics are used to stabilize the soil by confining the soil particles, thereby reducing their movement, and increasing the shear strength of the soil. This allows for improved load distribution, reduced deformation, and improved overall stability of the geotechnical system. The numerous benefits of geosynthetics in geotechnical engineering, such as reinforcement, drainage, erosion control, and soil stabilization, make them an essential part of modern infrastructure construction. The versatility

[1] Dr., Manisa Celal Bayar University, Faculty of Engineering, Civil Engineering Department

and effectiveness of these materials have led to widespread adoption of geosynthetics in various applications, and they continue to play a crucial role in the future of geotechnical engineering.

Furthermore, the implementation of geosynthetics have a significant impact on the overall energy consumption of a project. Since such materials are often sourced from renewable sources, they can reduce the need for non-renewable energy consumption, thus contributing to a more sustainable project. In terms of CO^2 emissions, the use of geosynthetics can lead to a pronounced reduction when compared to conventional geotechnical solutions. Geosynthetics often require less construction material, resulting in less transportation of construction materials and reducing associated emissions. Moreover, the manufacturing process of many geosynthetics produces less emissions than that of traditional geotechnical solutions with a significant reduction in CO^2 emissions and other environmental impacts, making them an essential tool for sustainable development of geotechnical engineering. This study discusses the sustainable approaches in geotechnical engineering, transportation geotechnics and environmental geotechnics considering recent developments.

Recent Advances and Sustainable Approaches in Geosynthetics

Banerjee et. al (2023) investigated the geocell stabilization through laboratory tests, and the results indicates that the use of geocell reinforcement significantly improves the performance of the sub-ballast layer (Figure 1). The maximum stress and strain values were reduced by 50% and 40%, respectively, while the resilient modulus increased by 200%.

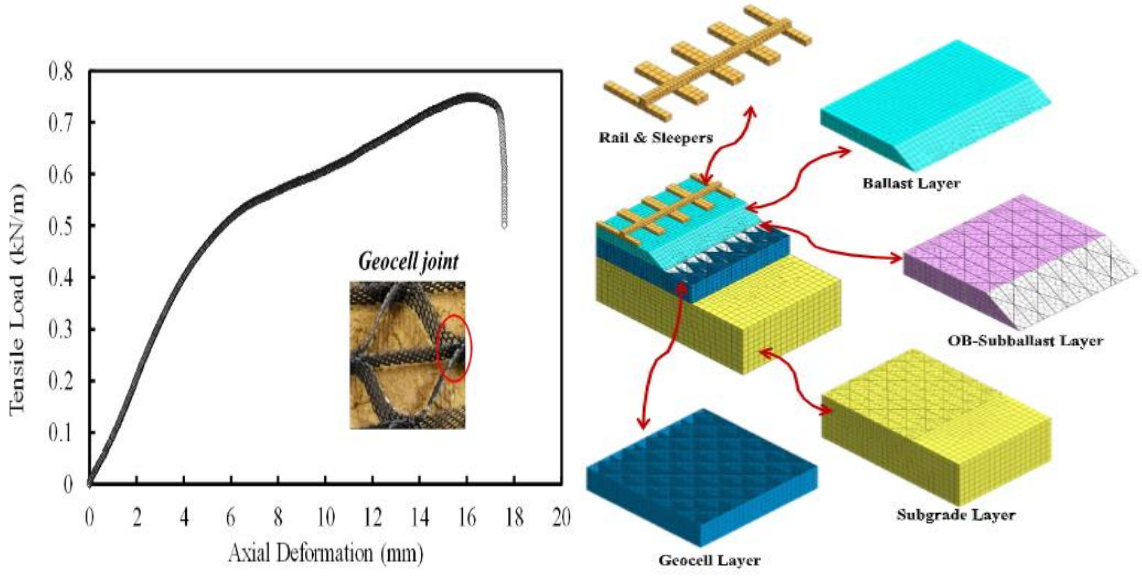

(a) *(b)*

Figure 1. (a) Experimental investigation of geocell joint, (b) FEM modelling of the rail, ballast layer, geocell layer elements (Banerjee et. al, 2023)

Bathurst and Naftchali (2023) investigated the influence of uncertainty in geosynthetic stiffness on the analysis of three reinforced soil problems. They founded that incorporating uncertainty into the analysis had a significant impact on the results and that the use of probabilistic methods could provide more realistic predictions of the performance of geosynthetic-reinforced soil structures.

Chenari and Bathurst (2023) investigated the impact of geosynthetic over undrained soft clay supported on thin reinforced granular layers using numerical modeling. The varying stiffness values of geosynthetics commonly used in geotechnical engineering practice were

considered for the analysis. The conducted analysis demonstrates that the stiffness of the geosynthetic has a significant influence on the bearing capacity of strip footings seated on thin reinforced granular layers over undrained soft clay. The study reveals that the bearing capacity of the strip footing increased by up to 70% by incorporating a stiffer non-woven geotextile with high tensile strength.

Hassan et al. (2023) conducted an experimental investigation to assess the soil-geosynthetic interface shear strength, pullout resistance, and tensile strength of the geosynthetics. The results indicated that geosynthetics can significantly enhance the soil's bearing capacity and contribute to its stability. However, the study also revealed that the effectiveness of geosynthetics varied with soil plasticity index. The authors suggested that the incorporation of geosynthetics in soil engineering should consider soil plasticity index as a significant factor.

Jamshidi Chenari and Bathurst (2023) founded that the addition of geosynthetic reinforcements to granular layers improved the bearing capacity of strip footings seated on soft clay deposits. They found that the increase in bearing capacity ranged from 14% to 47% depending on the type of reinforcement and the spacing between the reinforcement layers.

Vadavadagi and Chawla (2023) explored geosynthetic reinforced mechanically stabilized earth (MSE) walls using a combination of experimental and numerical methods considering the impact of axle load. The full-scale experiments were conducted under varying axle loads on railway, while the numerical simulations were performed. The findings indicate that increasing the rail axle load results in greater deformation of the MSE walls, with the largest deformation occurring at the base of the walls with a reduction of 58% compared to the conventional geogrid.

Becker (2022) focused on the design of geosynthetic reinforcement for subgrade support, and accurate predictions of the pavement response. Mechanistic-based analysis procedures have been developed to design geosynthetic reinforcement in pavement systems.

Bhandari et. al (2022) investigated Mechanically Stabilized Earth (MSE) walls which are commonly used in transportation infrastructure projects. In this study, the use of recycled plastic pins (RPP) was explored as a potential solution for controlling the base movement of MSE walls (Figure 2(a)). The pins were placed beneath the base of the wall and anchored into the subgrade. The performance of the wall was evaluated through laboratory testing and numerical modeling. Results showed significant improvements in the stability and base movement control of the MSE wall with the use of recycled plastic pins.

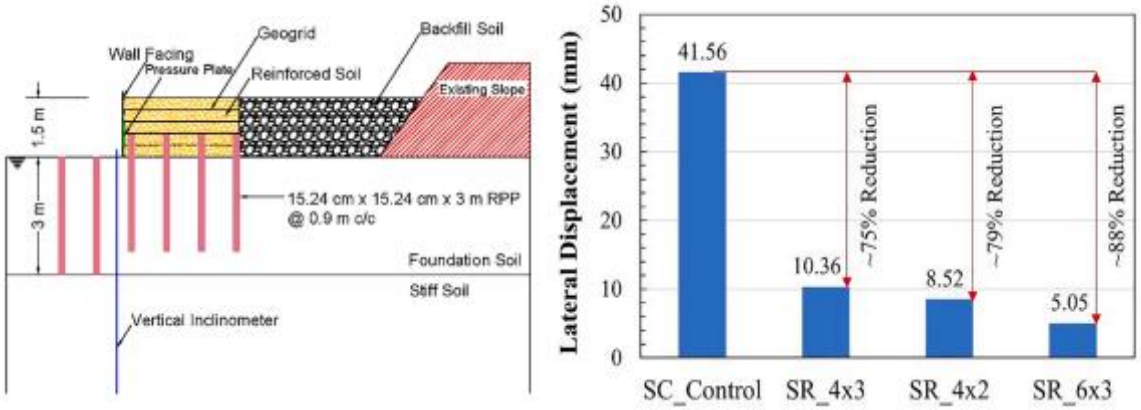

(a) *(b)*

Figure 2. (a) Mechanically Stabilized Earth (MSE) wall, (b) Lateral displacement for different RPP layouts (Bhandari et.al, 2022)

The testing and numerical modeling revealed that the use of recycled plastic pins decreased the maximum horizontal displacement of the MSE wall base by up to 75%-88% compared to the control wall without pins (Figure 2(b)). The maximum tensile strain was also reduced by up to 60% with the plastic pin treatment. The use of these pins resulted in significant improvements in wall stability and reduced the maximum horizontal displacement and tensile strain. The results suggest that the use of recycled plastic pins can be a viable and sustainable alternative to traditional methods for stabilizing and controlling the base movement of MSE walls in transportation infrastructure projects.

Hasthi et. al (2022) presented an experimental and intelligent modeling study on geocell-reinforced soil with footing under vibratory load. The results showed that the amplitude of the footing was reduced by up to 50% when geocells were used. The intelligent modeling approach was able to accurately predict the amplitude of the footing with an error of 2%. To design geo-structures that can support vibration loads, reliable estimation of displacement amplitude is essential. However, traditional approaches have limited knowledge in this area. The study proposes a novel hybrid paradigm with dragonfly optimizer (DFO) integrated artificial neural network (ANN).

Pramanik et. al (2022) presented a study using multivariate adaptive regression splines (MARS) (Figure 3). The study found that MARS is an effective tool for predicting maximum wall facing displacement, with a high degree of accuracy for both deterministic and probabilistic prediction. The results showed that the mean absolute error for deterministic prediction was 0.04 mm, and the coefficient of determination (R^2) was 0.99.

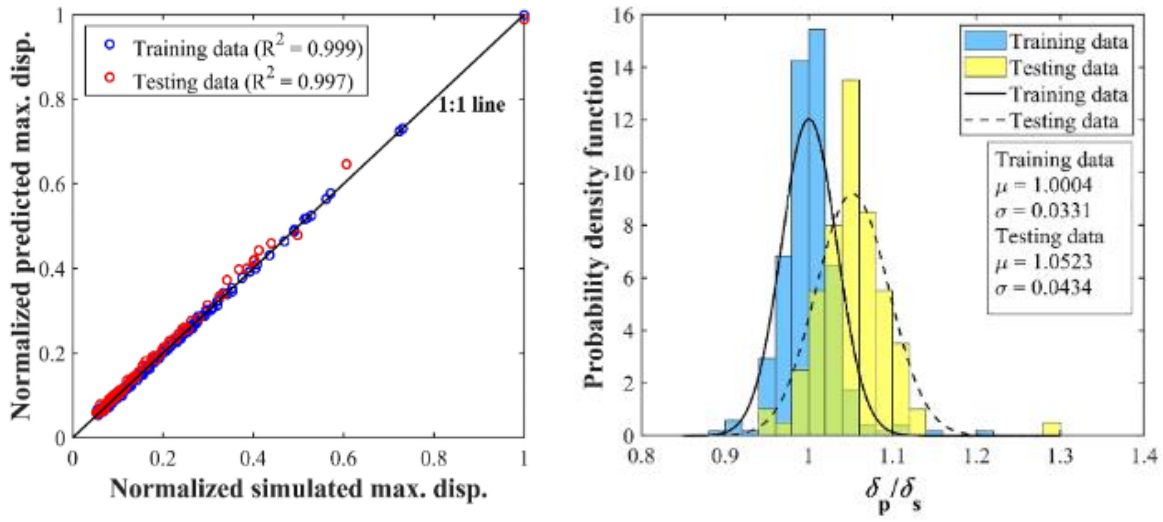

(a) *(b)*

Figure 3. (a) The prediction on the maximum wall displacement using MARS model (b) Probability density function - δ_p/δ_s or both testing and training datasets (Pramanik et. al, 2022)

Al-Atroush and Sebaey (2021) reviewed the use of hydrophobic polyurethane foam in stabilizing expansive soil. The authors discuss the properties of the foam and its application techniques, as well as the various factors that can affect its effectiveness on load-bearing capacity. They also highlight the importance of proper testing and monitoring to ensure the long-term success of soil stabilization projects.

Baadiga et. al (2021) investigated the optimal values of these factors to improve the performance of granular bases. The results show that increasing the tensile strength of the geogrid and subgrade modulus can significantly improve the layer coefficients of the granular base. The study concludes that the tensile strength of the geogrid and subgrade modulus are critical factors that influence the layer coefficients of granular bases. Increasing these factors

can significantly improve the performance of the granular base. The study recommends that a minimum tensile strength of 50 kN/m and subgrade modulus of 30 MPa should be used in the design of granular bases to achieve.

Namjoo et al. (2021) investigated the effects of moisture on the mechanical behavior of sand-geogrid using laboratory experiments. The study focused on the effect of moisture content, confining pressure, and loading rate on the behavior of sand-geogrid mixtures. The results showed that the moisture content significantly influenced the mechanical behavior of the mixtures. The shear strength increased with the moisture content up to a certain level and then decreased. The confining pressure and loading rate also affected the behavior of the mixtures.

Valipour et. al (2021) investigated the use of recycled tire polymer fibers and glass fibers for clay reinforcement. The study used laboratory testing to analyze the effect of adding recycled tire polymer fibers and glass fibers to clay soil. The addition of these fibers leads to a significant increase in the unconfined compressive strength of the soil and a reduction in the deformation characteristics. The study recommends the use of 1.5% recycled tire polymer fibers and 2% glass fibers in the design of reinforced clay soil. Overall, the study provides a sustainable solution to improve deformation characteristics of clays.

Di Battista and Rowe (2020) investigated the diffusion behavior of trichloroethylene (TCE) and tetrachloroethylene (PCE) through five different geomembranes, including two that were coextruded with an ethylene vinyl alcohol (EVOH) layer. The results showed that the presence of an EVOH layer significantly improved the barrier properties of the geomembranes, reducing the diffusion coefficients of both TCE and PCE by up to 90% compared to the non-coextruded geomembranes. The mass flux values also decreased significantly in the presence of the EVOH layer, indicating a greater ability to prevent the migration of organic contaminants.

Jayawardane et al. (2020) performed laboratory experiments using different geotextile types, soil types, fly ash content, and curing periods. The results showed that the geotextile reinforcement significantly improved the strength and ductility of the stabilized soil. The strength enhancement was more significant for the grid type geotextile compared to the woven type. Increasing the fly ash content and curing period improved the strength of the stabilized soil.

Khadka et.al (2020) focused on improving the characteristics and properties of the soil, thereby reducing the negative effects of the high sulfate content. The experimental investigation involved the use of varying amounts of geopolymer, metakaolin, and lime, as well as different curing periods. The results show that the geopolymer modified with lime and gypsum is effective in stabilizing the soil, reducing the soil's plasticity index, and improving its compressive strength.

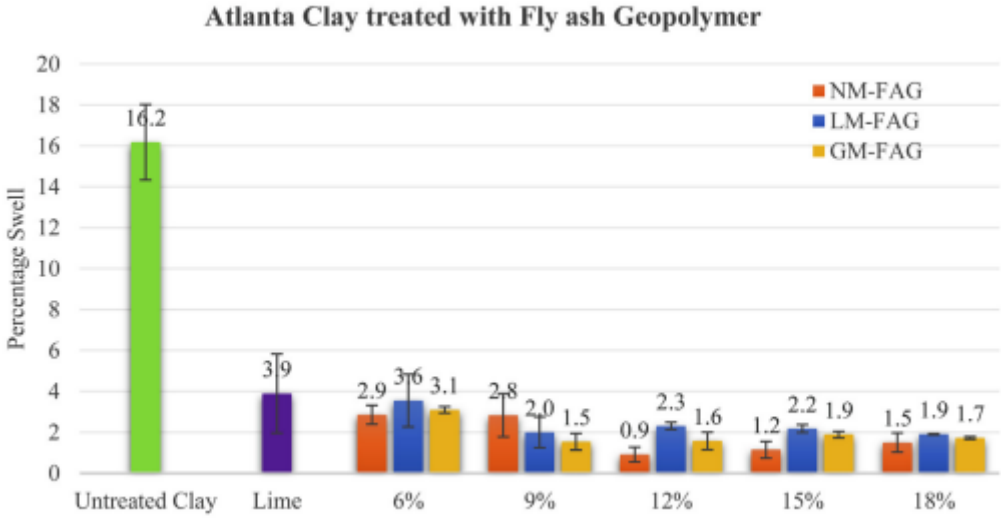

Figure 4. Metakaolin geopolymer reinforced Atlanta clay (Khadka et.al, 2020)

It was noted in Figure 4. that Atlanta Clay treated with NM-MKG at percentages of 6, 12, and 15% exhibited greater swelling compared to untreated clay. The optimum curing period for the stabilized soil was found to be 28 days. The addition of the geopolymer modified with lime and gypsum improved the soil's compressive strength and reduced its plasticity index. The study provides evidence that the geopolymer modification technique is a viable means of stabilizing highly expansive soils containing sulfate.

Leal et. al (2020) evaluated the environmental impacts of two slope repair techniques: conventional riprap and soil bioengineering using coconut fiber matting. The study found that the soil bioengineering technique had lower impacts in most of the impact categories Soil bioengineering had a 13% lower global warming potential than conventional riprap Soil bioengineering had a 61% lower non-renewable energy demand than conventional riprap Soil bioengineering had a 69% lower land use impact than conventional riprap The study shows that soil bioengineering using coconut fiber matting is a more environmentally sustainable slope repair technique compared to conventional riprap, although site-specific factors should be considered before making a final decision.

Rowe (2020) reviewed the perceptions and misconceptions about geosynthetic clay liners (GCLs). misconceptions such as the belief that GCLs are impervious were addressed and corrected. The authors emphasized the importance of proper installation and quality control to ensure optimal performance of GCLs.

Singh et al. (2020) in their study founded that the CBR value increased with increasing reinforcement layers and thickness. The maximum CBR value was found to be 16.6% for a 3-layer reinforcement system with a thickness of 0.6 m. The dynamic cone penetration resistance also increased with increasing reinforcement layers and thickness. The maximum dynamic cone penetration resistance was found to be 276 mm/blow for a 3-layer reinforcement system with a thickness of 0.6 m.

Vieira et. al (2020) investigated the pullout behavior of geosynthetics embedded in a recycled construction and demolition material (CDM) under cyclic loading. The laboratory study showed that the cyclic loading caused a decrease in the peak pullout force and an increase in the residual interface friction angle. The results also demonstrated that the degree of degradation of the recycled CDM material had a significant impact on the pullout behavior of the geosynthetics. The study provides valuable insights into the performance of geosynthetics in recycled materials, which can inform the design of sustainable transportation infrastructure.

Alkhorshid et al. (2019) conducted test setup on a geosynthetic reinforced column to explore its effectiveness in improving the soil's bearing capacity. The authors used a full-scale test setup to assess the load-bearing capacity. The tests indicated that the geosynthetic encasement improved the soil's bearing capacity by up to 4000% for woven geotextiles made of polypropylene (G-2). The study concluded that geosynthetic reinforced columns could be a practical solution for strengthening weak soils and structures founded on them (Figure 5).

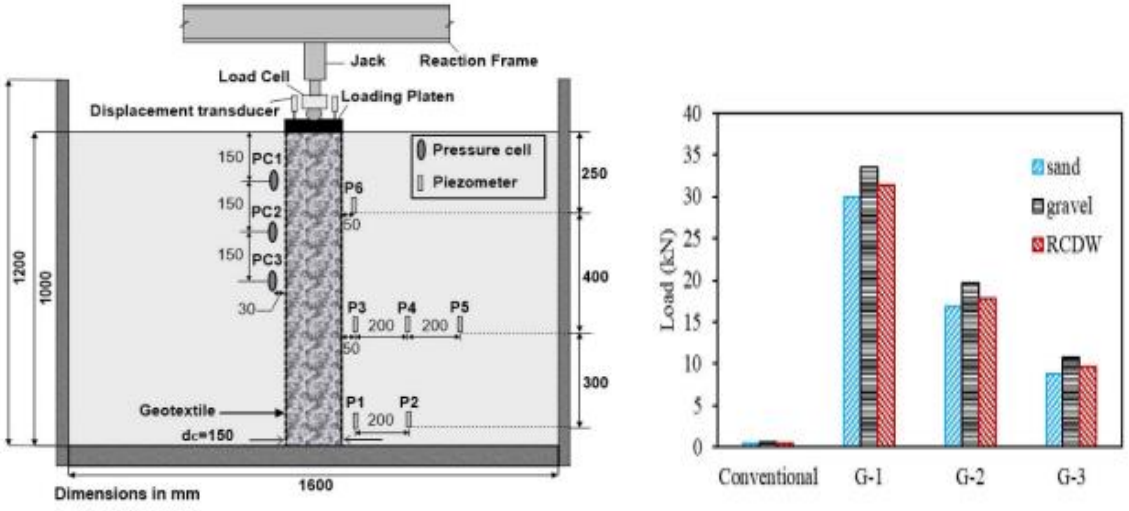

(a) *(b)*

Figure 5. (a) Test box of geosynthetic reinforced column, (b) Bearing capacity of geotextile reinforcement (Alkhorshid et al., 2019)

Francois et al. (2019) evaluated the impact of different types of stabilized bases on the overall performance of flexible pavements. The study found that stabilization with cement and calcium chloride improved the performance of flexible pavements and reduced the rutting and cracking by increasing the stiffness of the pavement.

Mamatha et al. (2019) evaluated the flexural behavior of geosynthetic-reinforced unbound granular material beams. The study found that the use of geosynthetics improved the flexural behavior of the pavements.

Orekanti and Dommaraju (2019) studied the load-settlement response of geotextile encased laterally reinforced granular piles in expansive soil under compression. The maximum bearing capacity was found to be 420 kPa for a pile with a diameter of 50 mm and length of 1.5 m.

Rowe et al. (2019) studied the chemical interaction and hydraulic performance of GCLs in a silty sand subgrade. The authors founded that the chemical interaction between GCLs and silty sand had minimal effect on the hydraulic conductivity of the liners. The hydraulic conductivity of the GCLs decreased as the moisture content increased.

Mittal and Gill (2018) investigated the sustainable application of waste tire chips and geogrid in improving the load carrying capacity of granular soils. The authors conducted laboratory tests to evaluate the effect of varying tire chip content and geogrid reinforcement on the soil's shear strength. The authors recommended the use of waste tire chips and geogrid as an environmentally friendly solution for improving the shear strength of granular soils.

Muzammil et al. (2018) investigated the behavior of geosynthetic encased stone columns under an oil storage tank using numerical simulation. They found that the maximum vertical displacement decreased as the diameter and length of the columns increased.

Benmebarek and Djabri (2017) applied numerical analysis with different ratios of overlapping reinforcements to assess the stability of the embankment. Therefore, the design of these embankments should consider the use of overlapping reinforcement, which can lead to a safer, more stable, and more durable structure (Figure 6).

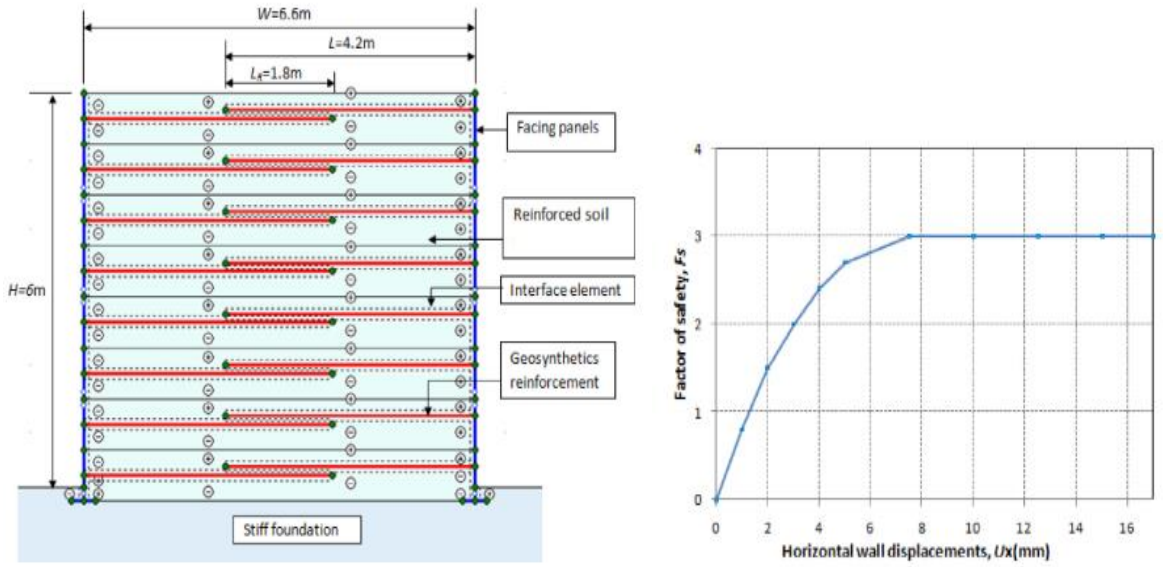

(a) *(b)*

Figure 6. (a) Finite element baseline model (b) Horizontal wall displacement-factor of safety for L_R/H = 0.3 (Benmebarek and Djabri, 2017)

Cuelho and Perkins (2017) aimed to calibrate the design method for geosynthetic stabilization of subgrade soils based on their field testing. They conducted a series of plate load tests on untreated and stabilized subgrades on a test site in Brazil. The calibration of the design method shows that it can accurately predict the performance of geosynthetic stabilization in the field. Plate load tests on untreated subgrade showed an average modulus of 17 MPa. Plate load tests on stabilized subgrade showed an average modulus of 43 MPa. the design method can accurately predict the performance of geosynthetic stabilization in the field.

Nanda et al. (2017) investigated the use of geosynthetic liners as a foundation isolation method for seismic protection. The results show that the use of geosynthetic liners can reduce the seismic response of a structure by up to 70%.

Zornberg et. al (2017) discussed the use of geosynthetics with enhanced lateral drainage capabilities in roadway systems to improve their performance and durability. The authors present case studies from various locations around the world where these techniques have been implemented and discuss the benefits in terms of reduced maintenance costs and increased safety for road users. The authors conclude that geosynthetics with enhanced lateral drainage capabilities offer an effective solution for addressing poor drainage conditions in roadway systems. The study showed a 60% reduction in maintenance costs for a roadway system with geosynthetics compared to traditional drainage methods.

Choudhary and Krishna (2016) discussed the experimental investigation of interface behavior between different types of granular soil and geosynthetics. Results show that the interface shear strength of clayey soil with geotextile was found to be higher than that of sandy soil with geotextile.

Das (2016) presented a case study on the use of geotextile bags for riverbank protection in India. A total of 80,000 geotextile bags were used to construct a 2.5 km long embankment along the Jia Bharali River. The performance of the embankment was monitored for a period of 2 years, during which time it withstood several floods. The study found that the geotextile bags provided effective protection against erosion, and the use of this technique was cost-effective compared to other traditional methods.

Indraratna (2016) provided an overview of the factors affecting the performance of ballast and substructure layers, as well as the methods used to improve their performance. The study

highlights that the performance of ballast and substructure layers is influenced by a combination of factors such as the drainage conditions, and the load distribution characteristics of the rail track. The use of modern technologies such as geosynthetics, geocomposites and recycled materials can significantly improve the performance of these layers by enhancing their strength, stiffness, and drainage characteristics. The paper sheds light on the critical factors affecting the performance of railways, specifically ballast and substructure layers.

Madhavi Latha and Manju (2016) focused on geocell reinforced retaining walls through experimental process under the seismic conditions. Results show that the geocell retaining walls have higher displacement capacity and energy dissipation than conventional retaining walls. The maximum horizontal displacement observed was approximately 10 cm.

Nimbalkar and Indraratna (2016) studied the performance of ballasted rail track using geosynthetics and rubber. The authors conducted laboratory tests to investigate the effects of geosynthetics and rubber on the track's stiffness and settlement. Geosynthetics reduced the track's settlement by up to 50% and increased the stiffness by up to 60%. The authors recommended the use of geosynthetics and rubber as a practical solution for improving the performance of ballasted rail track.

Suku et. al (2016) investigated the effectiveness of using geocell reinforcement in improving the bearing capacity, settlement, and deformation characteristics of granular bases. The study used numerical modeling to analyze the behavior of geocell-reinforced granular base under repeated loading (Figure 7(b)). The study also reveals that the effectiveness of the reinforcement depends on several factors such as the size and shape of the geocell, the soil properties, and the loading conditions. The study concludes that the use of geocell reinforcement can effectively improve the performance of granular base under repeated loading. The study also emphasizes the importance of considering the appropriate size and shape of geocell for the specific soil properties and loading conditions encountered in the project to maximize the effectiveness of the reinforcement.

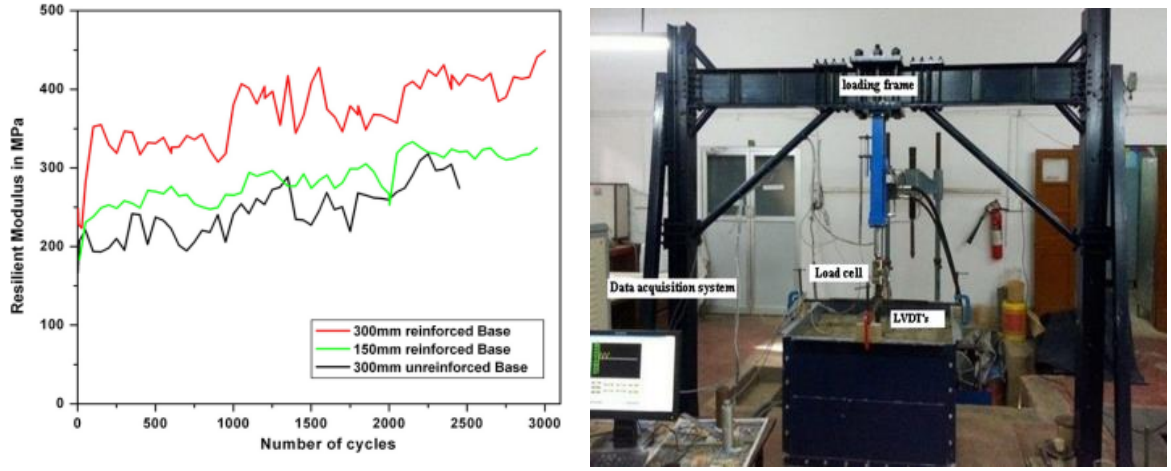

(a) *(b)*

Figure 7. (a) Resilient deformation of unreinforced and geocell-reinforced granular base (b) Plate load experimental setup (Suku et. al, 2016)

The study provides valuable insight into the behavior of geocell-reinforced granular base and highlights the potential benefits of geosynthetics. The reinforced specimen showed up to 93% resilience and up to 62% stiffness improvement compared to the unreinforced specimen. The resilient modulus improved from 160 MPa to 310 MPa for the reinforced specimen The stiffness improvement factor ranged from 1.07 to 1.62 for reinforced specimen The maximum deviator stress increased from 210 kPa to 300 kPa for reinforced specimen. Geocell reinforcement can significantly improve the resilience and stiffness of granular base under

repeated loading (Figure 7(a)). The improved properties can lead to better pavement performance and longer service life.

Vahedifard et. al (2016) investigated the role of suction stress on the service state behavior of geosynthetic-reinforced soil structures through a series of testing. The effects of matric suction and degree of saturation were evaluated on the pullout behavior of geosynthetics. The pullout resistance decreased from 68.9 kN/m at 100% saturation to 22.5 kN/m at 0% saturation.

Yazdani and Hatami (2016) provided an overview of the state of development of sensor-enabled geogrids used for stabilization and performance monitoring of earth structures. The study includes a review of the literature on the topic, as well as a discussion of the current state of technology and future directions for research. The paper presents several case studies of sensor-enabled geogrids in various applications, such as dams, slopes, and retaining walls. The results demonstrate that these systems can provide valuable information on the performance of earth structures and can be used to optimize their design and maintenance.

Kazi et al. (2015) investigated submerged test samples of different depths. Submergence depth of 0.3m resulted in a settlement of 6.9 mm and a bearing capacity of 4.38MN/m2. Submergence depth of 0.6m resulted in a settlement of 8.8 mm and a bearing capacity of 3.55MN/m2.Results showed that submergence had a significant effect on both settlement and bearing capacity, with deeper submergence resulting in greater settlement and lower bearing capacity.

Pinho-Lopes et al. (2015) investigated the use of geosynthetics in reinforcing fine soil for building walls of salt pans. Flume tests were conducted on samples with varying amounts and types of geosynthetics. Without geosynthetics, the maximum strength achieved was 80 kPa. With the addition of geotextile reinforcement, the maximum strength increased to 151 kPa. The use of a geogrid reinforcement resulted in a maximum strength of 270 kPa, almost 3.5 times the strength of the soil without any reinforcement. Results showed that the addition of geosynthetics significantly improved the strength and stability of the soil, with the highest strength achieved with the use of a geogrid reinforcement.

Pinho-Lopes and Lopes (2015) aimed to investigate the effects of mechanical damage and abrasion damage on the hydraulic behavior of geosynthetics. The results showed that mechanical damage had a more significant impact on the mechanical properties, while abrasion damage had a more remarkable influence on the hydraulic properties. The combined damage had a synergistic effect, causing a more significant reduction in the mechanical and hydraulic properties. The combined damage has a synergistic effect, leading to a reduction in both the mechanical and hydraulic properties.

Vieira and Pereira (2015) investigated the short-term tensile behavior of two geosynthetics subjected to tensile tests after being exposed to various levels of waste content for 28 days. It was concluded that the tensile strength decreased from 19.3 kN/m at 0% waste content to 10.4 kN/m at 20% waste content. The study can lead to damage and reduce their tensile strength, which may have implications for their long-term performance.

Arulrajah et. al (2013) studied the physical and mechanical properties of the recycled materials evaluated through a series of laboratory. The CBR values ranged from 30% to 120% depending on the type of material and the compaction level. The UCS values varied from 2 MPa to 25 MPa for different materials. The water permeability rate was also measured and found to be within acceptable limits. In terms of environmental properties, leachate tests were performed to assess the potential leaching of contaminants from the materials into the environment. The results showed that the leachate pH, electrical conductivity, and heavy metal concentrations were all below the regulatory limits. The recycled materials tested in this study demonstrated suitable physical, mechanical, and environmental properties for use in pavement subbase applications. The results showed that these materials can provide similar or better performance compared to natural aggregates while also reducing the demand for virgin materials and landfill space for waste material.

Flutcher and Wu (2013) conducted a study on low-volume asphalt roadway pavements and geosynthetics. The study found that the use of geosynthetics improved the structural integrity, reduced rutting, and extended the life of the pavement.

Santos et al. (2013) investigated the behavior of a geogrid reinforced wall made of recycled construction and demolition waste (CDW) backfill. The results showed that the geogrid reinforced wall made with recycled CDW backfill exhibited acceptable behavior on a foundation prone to collapse. The peak bearing capacity of the reinforced wall was 33 kN/m with a displacement of 31 mm. The deformation of the backfill material was also observed to be smaller compared to the control wall and had nearly constant behavior under compression.

REFERENCES

Alkhorshid, N. R., Araujo, G. L., Palmeira, E. M., & Zornberg, J. G. (2019). Large-scale load capacity tests on a geosynthetic encased column. *Geotextiles and Geomembranes*, *47*(5), 632-641.

Arulrajah, A., Piratheepan, J., Disfani, M. M., & Bo, M. W. (2013). Geotechnical and geoenvironmental properties of recycled construction and demolition materials in pavement subbase applications. *Journal of Materials in Civil Engineering*, 25(8), 1077-1088.

Banerjee, L., Chawla, S., & Dash, S. K. (2023). Investigations on cyclic loading behavior of geocell stabilized tracks with coal overburden refuse recycled as subballast material. *Transportation Geotechnics*, 40, 100969.

Bathurst, R. J., & Naftchali, F. M. (2023). Influence of uncertainty in geosynthetic stiffness on deterministic and probabilistic analyses using analytical solutions for three reinforced soil problems. *Geotextiles and Geomembranes*, 51(1), 117-130.

Becker, P. (2022). A Mechanistic-Based Analysis Procedure for Designing Geosynthetic Reinforcement in Pavement Systems. In *Advances in Transportation Geotechnics IV: Proceedings of the 4th International Conference on Transportation Geotechnics Volume 1* (pp. 87-100). Springer International Publishing.

Benmebarek, S., & Djabri, M. (2017). FEM to investigate the effect of overlapping-reinforcement on the performance of back-to-back embankment bridge approaches under self-weight. *Transportation Geotechnics*, 11, 17-26.

Bhandari, P., Hossain, M. S., Islam, M. A., & Badhon, F. F. (2022). Controlling base movement of MSE walls using recycled plastic pins. *Transportation Geotechnics*, *32*, 100707.

Chenari, R. J., & Bathurst, R. J. (2023). Influence of geosynthetic stiffness on bearing capacity of strip footings seated on thin reinforced granular layers over undrained soft clay. *Geotextiles and Geomembranes*, 51(1), 43-55.

Choudhary, A. K., & Krishna, A. M. (2016). Experimental investigation of interface behaviour of different types of granular soil/geosynthetics. *International Journal of Geosynthetics and Ground Engineering*, 2, 1-11.

Cuelho, E. V., & Perkins, S. W. (2017). Geosynthetic subgrade stabilization–Field testing and design method calibration. *Transportation Geotechnics*, 10, 22-34.

Das, U. K. (2016). A case study on performance of Jia Bharali River Bank protection measure using geotextile bags. *International Journal of Geosynthetics and Ground Engineering*, 2, 1-9.

Di Battista, V., & Rowe, R. K. (2020). TCE and PCE diffusion through five geomembranes including two coextruded with an EVOH layer. *Geotextiles and Geomembranes*, 48(5), 655-666.

Flutcher, S., & Wu, J. T. (2013). A state-of-the-art review on geosynthetics in low-volume asphalt roadway pavements. *International Journal of Geotechnical Engineering*, 7(4), 411-419.

Francois, A., Ali, A., & Mehta, Y. (2019). Evaluating the impact of different types of stabilised bases on the overall performance of flexible pavements. *International Journal of Pavement Engineering*, *20*(8), 938-946.

Hassan, W., Farooq, K., Mujtaba, H., Alshameri, B., Shahzad, A., Nawaz, M. N., & Azab, M. (2023). Experimental Investigation of Mechanical Behavior of Geosynthetics in Different Soil Plasticity Indexes. *Transportation Geotechnics*, 100935.

Hasthi, V., Raja, M. N. A., Hegde, A., & Shukla, S. K. (2022). Experimental and intelligent modelling for predicting the amplitude of footing resting on geocell-reinforced soil bed under vibratory load. *Transportation Geotechnics*, 35, 100783.

Indraratna, B. (2016). 1st Proctor Lecture of ISSMGE:: Railroad performance with special reference to ballast and substructure characteristics. Transportation Geotechnics, 7, 74-114.

Jamshidi Chenari, R., & Bathurst, R. J. (2023). Bearing Capacity of Strip Footings Seated on Unreinforced and Geosynthetic-Reinforced Granular Layers over Spatially Variable Soft Clay Deposits. *Journal of Geotechnical and Geoenvironmental Engineering*, 149(6), 04023034.

Jayawardane, V. S., Anggraini, V., Li-Shen, A. T., Paul, S. C., & Nimbalkar, S. (2020). Strength enhancement of geotextile-reinforced fly-ash-based geopolymer stabilized residual soil. *International Journal of Geosynthetics and Ground Engineering*, 6, 1-15.

Kazi, M., Shukla, S. K., & Habibi, D. (2015). Effect of submergence on settlement and bearing capacity of surface strip footing on geotextile-reinforced sand bed. *International Journal of Geosynthetics and Ground Engineering*, 1, 1-11.

Khadka, S. D., Jayawickrama, P. W., Senadheera, S., & Segvic, B. (2020). Stabilization of highly expansive soils containing sulfate using metakaolin and fly ash based geopolymer modified with lime and gypsum. *Transportation Geotechnics*, 23, 100327.

Leal, D., Winter, M. G., Seddon, R., & Nettleton, I. M. (2020). A comparative life cycle assessment of innovative highway slope repair techniques. *Transportation Geotechnics*, 22, 100322.

Madhavi Latha, G., & Manju, G. S. (2016). Seismic response of geocell retaining walls through shaking table tests. *International Journal of Geosynthetics and Ground Engineering*, 2, 1-15.

Mamatha, K. H., Dinesh, S. V., & Dattatreya, J. K. (2019). Evaluation of flexural behaviour of geosynthetic-reinforced unbound granular material beams. *Road Materials and Pavement Design*, *20*(4), 859-876.

Mittal, R. K., & Gill, G. (2018). Sustainable application of waste tire chips and geogrid for improving load carrying capacity of granular soils. *Journal of Cleaner Production*, *200*, 542-551.

Muzammil, S. P., Varghese, R. M., & Joseph, J. (2018). Numerical simulation of the response of geosynthetic encased stone columns under oil storage tank. *International Journal of Geosynthetics and Ground Engineering*, 4, 1-12.

Nanda, R. P., Dutta, S., Das, A., & Khan, H. A. (2017). Geosynthetic liner as foundation isolation for seismic protection. International Journal of Geosynthetics and Ground Engineering, 3, 1-7.

Nimbalkar, S., & Indraratna, B. (2016). Improved performance of ballasted rail track using geosynthetics and rubber shockmat. *Journal of Geotechnical and Geoenvironmental Engineering*, *142*(8), 04016031.

Orekanti, E. R., & Dommaraju, G. V. (2019). Load-settlement response of geotextile encased laterally reinforced granular piles in expansive soil under compression. *International Journal of Geosynthetics and Ground Engineering*, 5(3), 17.

Pinho-Lopes, M., & Lopes, M. L. (2015). Synergisms between laboratory mechanical and abrasion damage on mechanical and hydraulic properties of geosynthetics. *Transportation Geotechnics*, 4, 50-63.

Pinho-Lopes, M., Carlos, D. M., & Lopes, M. L. (2015). Flume tests on fine soil reinforced with geosynthetics: walls of the salt pans (Aveiro Lagoon, Portugal). *International Journal of Geosynthetics and Ground Engineering*, 1, 1-11.

Pramanik, R., Mukherjee, S., & Babu, G. S. (2022). Deterministic and probabilistic prediction of maximum wall facing displacement of geosynthetic-reinforced soil segmental walls using multivariate adaptive regression splines. *Transportation Geotechnics*, 36, 100816.

Rowe, R. K. (2020). Geosynthetic clay liners: perceptions and misconceptions. *Geotextiles and Geomembranes*, 48(2), 137-156.

Rowe, R. K., Garcia, J. D. D., Brachman, R. W. I., & Hosney, M. S. (2019). Chemical interaction and hydraulic performance of geosynthetic clay liners isothermally hydrated from silty sand subgrade. *Geotextiles and Geomembranes*, 47(6), 740-754.

Santos, E. C., Palmeira, E. M., & Bathurst, R. J. (2013). Behaviour of a geogrid reinforced wall built with recycled construction and demolition waste backfill on a collapsible foundation. *Geotextiles and Geomembranes*, 39, 9-19.

Singh, M., Trivedi, A., & Shukla, S. K. (2020). Influence of geosynthetic reinforcement on unpaved roads based on CBR, and static and dynamic cone penetration tests. *International Journal of Geosynthetics and Ground Engineering*, 6(2), 13.

Suku, L., Prabhu, S. S., Ramesh, P., & Babu, G. S. (2016). Behavior of geocell-reinforced granular base under repeated loading. *Transportation Geotechnics*, 9, 17-30.

Vadavadagi, S. S., & Chawla, S. (2023). Effect of rail axle load on geosynthetic reinforced back-to-back mechanically stabilized earth walls: Experimental and numerical studies. *Transportation Geotechnics*, 38, 100907.

Vahedifard, F., Mortezaei, K., Leshchinsky, B. A., Leshchinsky, D., & Lu, N. (2016). Role of suction stress on service state behavior of geosynthetic-reinforced soil structures. *Transportation Geotechnics*, 8, 45-56.

Vieira, C. S., Ferreira, F. B., Pereira, P. M., & de Lurdes Lopes, M. (2020). Pullout behaviour of geosynthetics in a recycled construction and demolition material–Effects of cyclic loading. *Transportation Geotechnics*, 23, 100346.

Vieira, C. S., & Pereira, P. M. (2015). Damage induced by recycled construction and demolition wastes on the short-term tensile behaviour of two geosynthetics. *Transportation Geotechnics*, 4, 64-75.

Yazdani, H., & Hatami, K. (2016). Sensor-enabled geogrids for stabilization and performance monitoring of earth structures: state of development. *International Journal of Geosynthetics and Ground Engineering*, 2, 1-7.

Zornberg, J. G., Azevedo, M., Sikkema, M., & Odgers, B. (2017). Geosynthetics with enhanced lateral drainage capabilities in roadway systems. *Transportation Geotechnics*, 12, 85-100.

Comparison of OLS, M And R Regression Estimators When The Error Distribution Is Skew Family Distributions

Barış ERGÜL[1]
Arzu ALTIN YAVUZ[2]

Introduction

Regression analysis is one of the most commonly used techniques to determine the functional relationship between the dependent and independent variables (David, 1981). The basis of regression analysis is to determine the functional structure of an observed event. While performing regression analysis, the observation values and the affected events must be expressed with a mathematical representation or function. This established model is called the "Regression Model".

There are some assumptions to making parameter estimation using the least-squares technique, a commonly used technique in regression analysis. These assumptions are generally related to the error terms. Error terms have a normal distribution with ε_i independent and identical, zero mean, and variance. In the case of rejection of these assumptions, lose their significance and the regression equation that is obtained cannot be used for inferential purposes (Mosteller & Tukey, 1977).

When error terms do not have normal distribution or when outliers are present in, the data set, alternative regression methods may substitute least squares. Robust regression techniques are those that lessen the effect of outliers and violation of assumptions (Öztürk, 2003). The factor that violates the normality assumption of the observed values is outliers which are regarded as a big error term. Outliers harm the statistical technique and the constructed regression model. Moreover, outliers are least likely to be values that explain the model. If the model is altered, the effect of the outlier decreases considerably. Robust regression techniques first update the observation value with outliers; then, carry out the analysis with this updated value (Mutan & Şenoğlu, 2009).

Regarding the robust regression analysis, M regression is quite popular. However, M estimators are robust estimators designed for long-tailed and symmetric data sets. When the data have an asymmetric distribution, their effect diminishes. R regression is a robust technique that is based on rank values. R regression studies started with Hodges and Lehman's (1963) studies. Later, many studies were done on the sequential prediction of parameters in linear regression models. Among these are studied by Adichie (1967), Sen (1969), Jureckova (1971), Koul (1971), Jaeckel (1972), and Heiler and Willers (1988). As for right-censored and left-truncated data on the dependent variable, Lai and Ying (1991) demonstrated that rank regression methods asymptotically have a normal distribution. Gutenbrunner et al. (1993) emphasized that R estimators resemble M estimators in linear regression models; however, different from M estimators, R estimators stressed the importance of sign rank. In their studies, Jureckova and Sen (1996), Hajek, Naranjo, and McKean (1997), and Sidak ve Sen (1999) stated that rank-based estimators are preferred rather than other estimators due to robustness and

[1] Araş. Gör. Dr., Eskişehir Osmangazi Üniversitesi Fen Fakültesi İstatistik Bölümü
[2] Prof. Dr., Eskişehir Osmangazi Üniversitesi Fen Fakültesi İstatistik Bölümü

effectiveness in regression when appropriate score function is used. Mukherjee and Bai (2000) developed a score function for R estimators in autoregressive models. Andrews et al. (2006) stated that Jaeckel's (1972) R-estimators are more robust compared to LAD (Least Absolute Deviations) and maximum likelihood estimators. Mukherjee (2007) used R-estimators in the heteroscedasticity problem. Rashid (2012) implemented R-estimators on a data set obtained as a result of clinical studies. Jureckova et al. (2016) researched the effects of R-estimators' effectiveness regression with measurement error.

When relevant literature is reviewed, studies that compare least squares, M-regression and R regression techniques altogether are very few. Therefore, in the linear regression model of this study, the error term has Skew-Normal and Skew-t distributions have been considered. For the regression model, these estimation methods were compared with the Monte Carlo simulation. The performance of estimators was evaluated based on the MSE criterion. In the second phase of the study, Skew-Normal and Skew-t distributions were introduced. Later in the third phase, the least-squares, M-regression and R-regression methods in linear regression technique were given. In the fourth phase, the effectiveness of these estimators based on various location, shape and skewness parameter values of these distributions were compared with simulation studies for different sample sizes and given a real-life example.

Skew Distribution Family

Skew-Normal Distribution

The skew-normal distribution is due to its mathematical flexibility and inclusion of the standard normal distribution. Azzalini (1986), Chiogna (1998) and Henze (1986) discussed the basic mathematical and probabilistic properties of the SN(α) distribution. Azzalini and Dalla Valle (1996), Azzalini and Capitanio (2003), Arnold et al. (1993), Arnold and Beaver (2002), Gupta et al. (2002) and Branco and Dey (2001) showed the theoretical developments and multivariate generalizations of the skew-normal distribution. Applications in reliability were discussed by Gupta and Brown (2001).

While the normal distribution has location and scale parameters, the skew-normal distribution has an additional skewness parameter. This is a very desirable property, where in many real-life situations, some skewness is always present in the data. The skew-normal distribution is often used in recent years due to reasons such as simplicity of mathematical operation, the content of normal distribution and more flexible structure for data modelling. Skew-normal distribution is a good alternative to a normal distribution. It is a skew-normal distribution, which is also a model of extreme values in the distribution because it is skew and heavy-tailed at the same time.

A random variable (RV) X has a skew-normal distribution with skewness parameter α denoted by X~SN(α) if its probability density function (pdf) is given by $f(x,\alpha)=2\Phi(\alpha x)\phi(x)$, where Φ is the standard normal cumulative distribution function (CDF) and ϕ is the standard normal pdf, respectively α and x are real numbers (Azzalini, 1985).

Some basic properties of the $SN(\alpha)$ distribution are given below: (Azzalini, 1985)

1. $SN(0) = \mathrm{N}(0,1)$

2. If $\mathrm{X}\sim SN(\alpha)$ then $-\mathrm{X}\sim SN(-\alpha)$

3. If $\mathrm{X}\sim SN(\alpha)$ then $\mathrm{X}^2\sim\chi_1^2$

4. If α increases, the skewness of the distribution also increases.

The mean and variance of the skew-normal distribution are given by

$E(\mathrm{X}) = \sqrt{\frac{2}{\pi}}\frac{\alpha}{\sqrt{1+\alpha^2}}$ and $Var(\mathrm{X}) = 1 - \frac{2\alpha^2}{\pi(1+\alpha^2)}$ (Dey, 2010).

Skew-t Distribution

The skew t distribution is denoted by St(μ,σ,α,τ) and was introduced by Branco and Dey (2001) and Azzalini and Capitanio (2003). As the skewness parameter α and the degrees of freedom τ, this model can accommodate both skewness and heavy tails. Thus, it provides considerable flexibility for fitting data that exhibit deviations from normality.

Arellano-Valle and Genton (2005) discussed skew-t distribution in the multivariate case. Huang and Chen (2006) showed generalized skew-t distributions and used them in data analysis. Hasan (2013) introduced a new approach to defining the non-central skew-t distribution. Shafiei and Doostparast (2014) presented the Balakrishnan skew-t distribution. Azzalini and Capitanio (2014) discussed the skew-normal distribution and related families in detail and showed its moments and properties.

The skew-t distribution with location parameter μ, scale parameter σ, skewness parameter α and degrees of freedom τ, has a probability density function (pdf),

$f(x,\mu,\sigma,\alpha,\tau) = 2\sigma^{-1}t(y,\tau)T(\alpha y\gamma,\tau+1), \quad -\infty < x < \infty$

where $y = (x-\mu)/\sigma$ and $\gamma = \sqrt{(\tau+1)/(y^2+\tau)}$.

Also,

$t(y,\tau) = \frac{\Gamma((\tau+1)/2)}{(\pi\tau)^{1/2}\Gamma(\tau/2)}(1+y^2/\tau)^{-(\tau+1)/2}, \quad -\infty < y < \infty$ is the pdf of the student t distribution with τ degrees of freedom.

$T(y,\tau) = \int_{-\infty}^{y} t(u,\tau)du$ is the CDF of the student t distribution with τ degrees of freedom.

Some basic properties of the skew-t distribution are given below: (Basalamah, 2017)
Let $X \sim St(\mu,\sigma,\alpha,\tau)$ then
1. If $\alpha = 0$, $X \sim t_\tau(\mu,\sigma)$.
2. As $\tau \to \pm\infty$ then $X \sim SN(\mu,\sigma,\alpha)$.
3. If $\alpha \to \pm\infty$, $X \sim |t_\tau|$.
4. The skew-t is unimodal.

The mean and variance of the skew-t distribution are given by

$E(X) = \mu + \sigma a_\tau \delta, if\ \tau > 1$ and $Var(X) = \sigma^2[\frac{\tau}{\tau-2} - (a_\tau\delta)^2], if\ \tau > 2.$

where $a_\tau = \frac{\sqrt{\tau}\Gamma(\frac{\tau-1}{2})}{\sqrt{\pi}\Gamma(\frac{\tau}{2})}, if\ \tau > 1$ and $\delta = \frac{\alpha}{\sqrt{1+\alpha^2}}$, $\delta \in (-1,1)$.

Methodology

The definition of linear regression in matrix form is as follows:

$Y = (Y_1, Y_2, \dots, Y_n)^T = \boldsymbol{X\beta} + \boldsymbol{\varepsilon}$
(1)

Here; $\boldsymbol{X} = (X_1^T, X_2^T, \dots, X_n^T)^T$, $n \times p$ shows a dimensional matrix of independent variables, $\boldsymbol{\beta} = (\beta_1, \beta_2, \dots, \beta_p)^T$, displays unknown regression parameters and ε_i demonstrates a random variable that is defined as independent and identical but referred to as an error term whose distribution function is unknown. The first column of $\boldsymbol{X}$ is comprised of $(1,1, \dots,1)^T$ (Greene, 2007).

Least Squares Technique

The presentation of multiple linear regression in matrix form with *p* number of independent variables $X_1, X_2, , , X_p$ is as in Equation 2:

$$Y = \begin{bmatrix} y_1 \\ y_2 \\ . \\ . \\ . \\ y_n \end{bmatrix} X = \begin{bmatrix} 1 x_{11} x_{12} \dots x_{1p} \\ 1 x_{21} x_{22} \dots x_{2p} \\ . \quad . \quad . \quad \dots \quad . \\ . \quad . \quad . \quad \dots \quad . \\ . \quad . \quad . \quad \dots \quad . \\ 1 x_{n1} x_{n2} \dots x_{np} \end{bmatrix} b = \begin{bmatrix} \beta_1 \\ \beta_2 \\ . \\ . \\ . \\ \beta_p \end{bmatrix} \varepsilon = \begin{bmatrix} \varepsilon_1 \\ \varepsilon_2 \\ . \\ . \\ . \\ \varepsilon_n \end{bmatrix} \quad (2)$$

Y: dependent variable vector; $X_1, X_2, , , X_p$: independent variables and X data matrix; β_i $(0 \leq i \leq p)$ regression coefficient; ε random error vector.

In the least-squares technique, the aim is to minimize the sum of squares of error terms. In the simple linear regression model given in Equation 3, the least-squares estimators of parameters β_0 and β_1 are as follows:

$$\hat{\beta}_0 = \overline{y} - \hat{\beta}_1 \overline{x}$$

$$\hat{\beta}_1 = \frac{\sum_{i=1}^{n} (x_i - \overline{x})(y_i - \overline{y})}{\sum_{i=1}^{n} (x_i - \overline{x})^2}$$

(3)

R Regression Technique

Hodges and Lehman (1963) defined R-estimation first. In the R-regression technique, the rank of error terms is also considered for parameter estimation.

Error term vector of linear rank order statistics can be defined as follows:

$$S_n(\boldsymbol{\beta}) = (S_{n1}(\beta), \dots, S_{np}(\beta))^T \quad (4)$$

More precisely.

$$S_{nj}(\beta) = \sum_{i=1}^{n} \left(c_{ij} - \overline{c_{nj}}\right) a_n\left(R_{ni}(\beta)\right), \quad j = 1, \dots, p \quad (5)$$

is written and the rank of the error term $R_{ni}(\boldsymbol{\beta})$,

$$\delta_i(\boldsymbol{\beta}) = Y_i - x_i^T \boldsymbol{\beta}$$

is obtained. Here; $\delta_i(\boldsymbol{\beta})$, symbolizes the ordered vector of error terms and $\boldsymbol{a_n}$, stands for obtained scores ranked in ascending order, $\bar{c}_{nj}$, is the mean score obtained from the score function.
In this technique the purpose is,

$$min \sum_{j=1}^{p} \left| S_{nj}(\beta) \right| \tag{6}$$

or

$$min \sum_{i=1}^{n} \left\{ a_n\left(R_{ni}(\boldsymbol{\beta})\right) - \overline{a_n} \right\} \delta_i(\boldsymbol{\beta}) \tag{7}$$

to minimize the function. R-estimators minimize the function that has a different sign rank. In (7) and (8), the calculation of objective functions is quite difficult. To calculate these functions iterative procedures are necessary. In general, three procedures are stated. The first of these is assigning initial values to β coefficient that is obtained by using error terms based on rank order statistics. This method is also known as the selection of parameter values from a close interval. Second is the Newton-Raphson method which is frequently used in minimization problems. The third is the one-step regression method used in large samples (Jureckova et al., 2013). If values in Equation (6) and Equation (7) are reorganized for a simple linear R-regression model to eliminate computational complexity, Equation (8) is obtained. Parameter predictors that minimize Equation (8) are called R-estimators.

$$\min_{\hat{\beta}} \sum_{i=1}^{n} a_n(R_i)\varepsilon_i \tag{8}$$

Here, R_i, ε_i stands for the rank of the error term, $a_n(i)$ which, on the other hand, means a monotonous score function of the equation $\sum_{i=1}^{n} a_n(i) = 0$ (Zhou, 1992).

1) In the first step, values for an independent variable are listed. Error term values are found by including corresponding dependent variable values that relate to these values in the calculation.
2) Then, the obtained ε_i values are listed and R_i values are obtained. $a_n(R_i)$ values are calculated with the help of one of the score functions given in Table 1.
3) For various values of the $\hat{\beta}_1$ parameter, a total of terms $a_n(R_i)\varepsilon_i \ (i = 1,2,..., n)$ is calculated. The parameter value where this total value is minimum is regarded as the initial value.
4) In the next step, the first step is repeated for $\hat{\beta}_1$ values that comprise $\hat{\beta}_1$ values obtained in the first step and selected from a smaller interval; this is continued until $\hat{\beta}_1$ the value approach each other.
5) In the last step, the value $\hat{\beta}_0 = med\left\{ y_i - \hat{\beta}_1 x_i \right\}$ is found (Heikkila, 2006; Zhou, 1992).

Table 1. Score Functions

Score Function	$a_n(i)$
Wilcoxon	$i-\frac{n+1}{2}$
Van Der Waerden	$\Phi^{-1}\left(\frac{i}{n+1}\right)$ (Φ^{-1} opposite of cumulative normal distribution function
Median	$\text{sgn}\left(i-\frac{n+1}{2}\right)$

M-Regression Technique

When the normality assumption is violated for the distribution of error terms in regression analysis, it is not appropriate to use the least-squares technique and use the obtained model for estimation., M-Regression is developed to be used for the case of errors having more long-tailed symmetric distribution than normal when this assumption is not met. This approach is a mediator between the robustness of L1 estimators and the effectiveness of least squares. M-estimation is known as the generalized form of maximum likelihood predictors. M-estimation is defined below in Equation (9) based on the minimization of one of the functions of errors:

$$\sum_{i=1}^{n}\rho(\widehat{e_i}), \quad i=1,2,\dots,n \tag{9}$$

Here, ρ(.) is a continuous, non-negative and symmetric function also referred to as an objective function whose only minimum is zero?. M-estimation is the robust predictor that minimizes ρ(.) the function is given in Equation (9). In the literature, many objective functions (Huber, Andrews, Tukey) exist with these characteristics (Birkes & Dodge, 1993). The most widely used objective function is the one suggested by Huber. Huber's suggested objective function is given in Equation (10).

$$\rho(\widehat{e_i})=\begin{cases}\widehat{e_i^2/2}, & |\widehat{e_i}|\le k\\ k|\widehat{e_i}|-\frac{k^2}{2}, & |\widehat{e_i}|\ge k\end{cases} \tag{10}$$

Here, k is selected from values that are called constant and have high efficiency in the normal distribution. The value of k=1.345 is used for the Huber predictor.

To estimate parameters in the regression model, the derivative of Equation (10) is calculated, and its minimum value is found by vanishing.

$$\sum_{i=1}^{n}\psi(\widehat{e_i})x_i=0, \quad i=1,2,\dots,n \tag{11}$$

Here, ψ(.) is known as the score function and is a derivative of ρ(.). Analysis of Equation (12) is referred to as M-estimation. The result is not a standardized outcome. First, standardization of error terms must be done.

$$\sum_{i=1}^{n}\psi(\widehat{e_i}/s)x_i=0, \quad i=1,2,\dots,n \tag{12}$$

Here, s is a simultaneously predicted scale factor. As for the predictor of s, median absolute deviation (MAD) is used and defined as below:

$$s = \frac{MAD}{0.6745} \tag{13}$$

Here, $MAD\ (residual) = median\{|\hat{e}_i - median\{\hat{e}_i\}|\}, i = 1,2,\dots,n$. Increasing residual magnitudes are substituted by appropriate weight values. Equation (12) can be rewritten as follows by using $w_i = w(\hat{e}_i) = \frac{\psi(\hat{e}_i)}{\hat{e}_i}, i = 1,2,\dots,n$

$$\sum_{i=1}^{n} w_i(\hat{e}_i/s)x_i = 0\,, \quad i = 1,2,\dots,n \tag{14}$$

In practice, M-estimation may not be calculated directly from data because their weight values are dependent on residuals. For that reason, to obtain M-estimation iteratively reweighted least squares algorithm is used.

Results

In simulation studies, N=100000/n was executed, error terms for n=10,20,30,50 unit of samples, various skewness parameters from Skew-normal distribution as (α) (0.0,2.0,10.0), location and scale parameters were obtained. Similarly, various skewness parameters from skew-t distribution were found in simulation studies.

For values of β_0=0 and β_1=1 simulation mean and standard error and MSE values were calculated. These values are given in Table 2-9. 1 outlier was generated and for this 1 outlier simulation mean, standard error and MSE values were calculated. Simulation values are shown in Table 10-17. Also, 2 outliers were generated and for these 2 outlier simulation mean, standard error and MSE values were calculated. Simulation values are shown in Table 18-25.

Based on MSE results without outliers, when least squares, M and R regression results are analyzed with a sample size of n=10; given the error terms distribution is the skew-normal distribution (α= 0.0,2.0,5.0,10.0) to estimate β_0 parameter, it is observed that the R-Wilcoxon technique provides more effective results compared with least squares and Huber-M techniques. In all other sample sizes, it is observed that the R-Median technique provides more effective results compared to the least squares and Huber-M techniques. When error terms are Skew-normal distribution, the Huber-M technique performed the worst for β_1.

Based on MSE results with 1 and 2 outliers, when least squares, M and R regression results are analyzed with a sample size of n=10; given the error terms distribution is a skew-normal distribution with all skewness parameter to estimate β_0 parameter, it is observed that the R-Median technique displays more effective results compared with least squares and Huber-M techniques. It also gives similar results for the estimation of β_1 parameter. In all other sample sizes, it is observed that the R-Median technique provides more effective results compared to the least squares and Huber-M techniques. When error terms are Skew-normal distribution, the least-squares technique performed the worst for β_1.

Based on MSE results without outliers, when least squares, M and R regression results are analyzed with a sample size of n=10; given the error terms distribution is the skew-t distribution (α= 0.5,1.0) to estimate β_0 parameter, it is observed that the R-Median technique provides more effective results compared with least squares and Huber-M techniques. In all other sample sizes, it is observed that the R-Median technique provides more effective results compared to the least

squares and Huber-M techniques. When error terms are Skew-t distribution, the least-squares technique performed the worst for β_1.

Based on MSE results with 1 and 2 outliers, when least squares, M and R regression results are analyzed with a sample size of n=10; given the error terms distribution is a skew-t distribution with all skewness parameter to estimate β_0 parameter, it is observed that R-Median and R-Wilcoxon (only α=0.5) technique displays more effective results compared with the least-squares and Huber-M techniques. It also gives similar results for the estimation of β_1 parameter. In all other sample sizes, it is observed that the R-Median technique provides more effective results compared to the least squares and Huber-M techniques. When error terms are Skew-t distribution, the least-squares technique performed the worst for β_1.

Table 2. Means, Variances and MSE's for the estimators $\widehat{\beta_0}$ and $\widehat{\beta_1}$, $n = 10$ when error term is the skew-normal distribution

$\mu = 0{,}0;\ \sigma = 1{,}0;\ \alpha = 0{,}0$						
	β_0			β_1		
	Mean	Variance	MSE	Mean	Variance	MSE
OLS	0,0065592	0,4947116	0,494754593	0,991596	1,5102659	1,5103366
Huber-M	0,002435	0,5147066	0,514712573	0,999672	1,5749945	1,5749946
R-Wilcoxon	0,174505	0,1855457	0,215997656	0,65463	0,1777443	0,2970248
R-VDW	0,1864488	0,1874446	0,222207767	0,630435	0,1919702	0,3285484
R-Median	0,175181	0,1857028	0,216391234	0,65372	0,1771684	0,2970782
$\mu = 0{,}0;\ \sigma = 1{,}0;\ \alpha = 2{,}0$						
	β_0			β_1		
	Mean	Variance	MSE	Mean	Variance	MSE
OLS	0,0068271	0,4934989	0,493545524	0,9893832	1,5086984	1,5088111
Huber-M	0,0108312	0,5150975	0,515214814	0,983648	1,5854452	1,5857126
R-Wilcoxon	0,1778571	0,1872812	0,21891435	0,64665	0,1793747	0,3040309
R-VDW	0,1892728	0,1939011	0,229725256	0,62407	0,193258	0,3345813
R-Median	0,1777498	0,187414	0,21900901	0,647265	0,1796567	0,3042787
$\mu = 0{,}0;\ \sigma = 1{,}0;\ \alpha = 10{,}0$						
	β_0			β_1		
	Mean	Variance	MSE	Mean	Variance	MSE
OLS	0,0075248	0,4934889	0,493545523	0,9892756	1,5086961	1,5088111
Huber-M	0,0114408	0,5150839	0,515214812	0,9836727	1,585446	1,5857126
R-Wilcoxon	0,1785151	0,1872866	0,219154287	0,64662	0,1794545	0,3041319
R-VDW	0,1899507	0,1938433	0,229924576	0,62398	0,1932393	0,3346303
R-Median	0,178415	0,1873648	0,219196707	0,647205	0,1797084	0,3041727

Table 3. Means, Variances and MSE's for the estimators $\widehat{\beta_0}$ and $\widehat{\beta_1}$, $n = 20$ when error term is the skew-normal distribution

$\mu = 0{,}0;\ \sigma = 1{,}0;\ \alpha = 0{,}0$						
	β_0			β_1		
	Mean	Variance	MSE	Mean	Variance	MSE
OLS	0,0034868	0,2200992	0,2201114	1,0034662	0,6555614	0,6555734
Huber-M	0,0045697	0,231211	0,2312319	1,0043023	0,6911478	0,6911663
R-Wilcoxon	0,1455754	0,1112242	0,1324164	0,71794	0,1378517	0,2174096
R-VDW	0,164512	0,1151616	0,1422259	0,68271	0,1594584	0,2601314
R-Median	0,1455195	0,1106607	0,1318366	0,71875	0,1368223	0,2159239
$\mu = 0{,}0;\ \sigma = 1{,}0;\ \alpha = 2{,}0$						
	β_0			β_1		
	Mean	Variance	MSE	Mean	Variance	MSE
OLS	-0,0037789	0,2166143	0,2166286	1,0007303	0,6630648	0,6630653
Huber-M	-0,0033861	0,2277801	0,2277916	1,0020541	0,7030399	0,7030441
R-Wilcoxon	0,143704	0,1102658	0,1309167	0,71234	0,1401097	0,222858
R-VDW	0,1567712	0,1150548	0,139632	0,687	0,1610662	0,2590352
R-Median	0,1420966	0,1097974	0,1299888	0,71573	0,1376896	0,218499
$\mu = 0{,}0;\ \sigma = 1{,}0;\ \alpha = 10{,}0$						

	β_0			β_1		
	Mean	Variance	MSE	Mean	Variance	MSE
OLS	-0,0106333	0,2150588	0,2151719	1,0194712	0,6488153	0,6491944
Huber-M	-0,0121778	0,2229367	0,223085	1,0199636	0,6751069	0,6755055
R-Wilcoxon	0,133867	0,1063494	0,1242697	0,72834	0,135562	0,2093611
R-VDW	0,1482099	0,1108915	0,1328577	0,69883	0,1535048	0,2442082
R-Median	0,133643	0,106214	0,1240745	0,72915	0,1344737	0,2078334

Table 4. Means, Variances and MSE's for the estimators $\widehat{\beta_0}$ and $\widehat{\beta_1}$, $n = 30$ when error term is the skew-normal distribution

$\mu = 0{,}0;\ \sigma = 1{,}0;\ \alpha = 0{,}0$						
	β_0			β_1		
	Mean	Variance	MSE	Mean	Variance	MSE
OLS	0,0039485	0,1418012	0,1418167	0,9970203	0,4233502	0,4233591
Huber-M	0,0048709	0,1491346	0,1491583	0,9950751	0,444405	0,4444292
R-Wilcoxon	0,1237081	0,0812382	0,0965419	0,7528653	0,1147975	0,175873
R-VDW	0,1358578	0,0870613	0,1055187	0,7279778	0,1334059	0,207402
R-Median	0,1242393	0,0810768	0,0965122	0,7517852	0,1140522	0,1756628
$\mu = 0{,}0;\ \sigma = 1{,}0;\ \alpha = 2{,}0$						
	β_0			β_1		
	Mean	Variance	MSE	Mean	Variance	MSE
OLS	-0,014504	0,1448421	0,1450525	1,0237683	0,4416897	0,4422546
Huber-M	-0,0143902	0,1519103	0,1521174	1,0243107	0,4593997	0,4599907
R-Wilcoxon	0,1168321	0,0796834	0,0933331	0,7607261	0,1108611	0,1681131
R-VDW	0,1309635	0,0867384	0,1038898	0,7322832	0,1325319	0,2042042
R-Median	0,1160563	0,0792886	0,0927576	0,7619862	0,1101407	0,1667912
$\mu = 0{,}0;\ \sigma = 1{,}0;\ \alpha = 10{,}0$						
	β_0			β_1		
	Mean	Variance	MSE	Mean	Variance	MSE
OLS	-0,0036429	0,1434538	0,143467	1,0026662	0,4268226	0,4268297
Huber-M	-0,0034227	0,1493936	0,1494053	1,0025521	0,446553	0,4465595
R-Wilcoxon	0,1213169	0,0786737	0,0933914	0,7566157	0,1137115	0,1729474
R-VDW	0,1402156	0,0845782	0,1042386	0,7187519	0,1368346	0,2159351
R-Median	0,1205417	0,0775976	0,0921279	0,7585659	0,110382	0,1686725

Table 5. Means, Variances and MSE's for the estimators $\widehat{\beta_0}$ and $\widehat{\beta_1}$, $n = 50$ when error term is the skew-normal distribution

$\mu = 0{,}0;\ \sigma = 1{,}0;\ \alpha = 0{,}0$						
	β_0			β_1		
	Mean	Variance	MSE	Mean	Variance	MSE
OLS	0,0008653	0,0810214	0,0810222	1,0099739	0,2371179	0,2372174
Huber-M	-0,0005349	0,0862583	0,0862585	1,0118089	0,2520127	0,2521522
R-Wilcoxon	0,1007147	0,0509802	0,0611236	0,8073	0,0772854	0,1144186
R-VDW	0,1179802	0,0578003	0,0717196	0,772625	0,1017552	0,1534546
R-Median	0,0994761	0,0502351	0,0601306	0,81055	0,0747436	0,1106349
$\mu = 0{,}0;\ \sigma = 1{,}0;\ \alpha = 2{,}0$						
	β_0			β_1		
	Mean	Variance	MSE	Mean	Variance	MSE
OLS	-0,0045148	0,0852887	0,0853091	1,0083589	0,2601809	0,2602508
Huber-M	-0,0019205	0,0888514	0,0888551	1,0061992	0,2700356	0,270074
R-Wilcoxon	0,1020795	0,0525305	0,0629507	0,80435	0,0796059	0,1178848
R-VDW	0,1166527	0,056767	0,0703748	0,776075	0,0986182	0,1487606
R-Median	0,1018308	0,0525162	0,0628857	0,805075	0,0786873	0,1166831
$\mu = 0{,}0;\ \sigma = 1{,}0;\ \alpha = 10{,}0$						
	β_0			β_1		
	Mean	Variance	MSE	Mean	Variance	MSE
OLS	0,0034785	0,086165	0,0861771	0,9952277	0,2645837	0,2646065
Huber-M	0,0030215	0,089729	0,0897381	0,9946623	0,2792803	0,2793088
R-Wilcoxon	0,1053903	0,050941	0,0620481	0,79085	0,0866446	0,1303883
R-VDW	0,1218421	0,056048	0,0708935	0,756175	0,1082047	0,1676554
R-Median	0,1028882	0,0502002	0,0607861	0,795975	0,0836219	0,1252481

Table 6. Means, Variances and MSE's for the estimators $\widehat{\beta_0}$ and $\widehat{\beta_1}$, $n = 10$ when error term is the skew-t distribution

$\tau = 3{,}0; \alpha = 0{,}5$						
	β_0			β_1		
	Mean	Variance	MSE	Mean	Variance	MSE
OLS	-0,0061725	0,4534962	0,4535343	1,0198166	1,4826292	1,4830219
Huber-M	-0,0823701	0,288825	0,2956099	1,0076287	0,8499986	0,8500568
R-Wilcoxon	-0,0256577	0,1047346	0,1053929	0,72941	0,1331234	0,2063423
R-VDW	-0,0103997	0,110111	0,1102191	0,69944	0,1499432	0,2402795
R-Median	-0,0247713	0,1047034	0,105317	0,72787	0,1328931	0,2062478
$\tau = 5{,}0; \alpha = 0{,}5$						
	β_0			β_1		
	Mean	Variance	MSE	Mean	Variance	MSE
OLS	-0,0006238	0,483817	0,4838174	1,0067945	1,4910072	1,4910534
Huber-M	-0,0625961	0,4143519	0,4182702	1,0077184	1,2574709	1,2575305
R-Wilcoxon	0,0070375	0,150881	0,1509305	0,68755	0,1583878	0,2560128
R-VDW	0,0228945	0,1567976	0,1573217	0,65665	0,1755373	0,2934266
R-Median	0,0062966	0,149943	0,1499826	0,68874	0,1570574	0,2539402
$\tau = 10{,}0; \alpha = 0{,}5$						
	β_0			β_1		
	Mean	Variance	MSE	Mean	Variance	MSE
OLS	-0,0101067	0,4931452	0,4932473	1,0168598	1,5265635	1,5268477
Huber-M	-0,0561444	0,4725356	0,4756878	1,0161373	1,4376317	1,4378921
R-Wilcoxon	0,0269492	0,1738524	0,1745787	0,67548	0,1679556	0,2732688
R-VDW	0,0422929	0,179208	0,1809967	0,646305	0,1833739	0,3084741
R-Median	0,0260655	0,1738258	0,1745052	0,6774	0,167103	0,2711737
$\tau = 3{,}0; \alpha = 1{,}0$						
	β_0			β_1		
	Mean	Variance	MSE	Mean	Variance	MSE
OLS	0,0038793	0,4696608	0,4696759	0,9806388	1,4364216	1,4367964
Huber-M	-0,0994969	0,2456472	0,2555469	0,9878815	0,6960049	0,6961518
R-Wilcoxon	-0,0887061	0,0970653	0,1049341	0,75427	0,1166814	0,1770647
R-VDW	-0,0641723	0,1061249	0,110243	0,707935	0,1425945	0,2278965
R-Median	-0,090603	0,0962734	0,1044823	0,757805	0,1147043	0,1733627
$\tau = 5{,}0; \alpha = 1{,}0$						
	β_0			β_1		
	Mean	Variance	MSE	Mean	Variance	MSE
OLS	-0,0095601	0,4901633	0,4902547	1,0177725	1,4685951	1,468911
Huber-M	-0,0970605	0,3739991	0,3834198	1,0232264	1,0964935	1,097033
R-Wilcoxon	-0,0681601	0,1464048	0,1510506	0,72239	0,1415058	0,2185732
R-VDW	-0,0443572	0,1547204	0,1566879	0,6776	0,1694222	0,2733639
R-Median	-0,0700263	0,1460657	0,1509694	0,726485	0,1385782	0,2133886
$\tau = 10{,}0; \alpha = 1{,}0$						
	β_0			β_1		
	Mean	Variance	MSE	Mean	Variance	MSE
OLS	0,0062424	0,4916677	0,4917067	0,99635	1,4909351	1,4909484
Huber-M	-0,0580333	0,4484609	0,4518288	0,9967931	1,3241711	1,3241814
R-Wilcoxon	-0,0267072	0,1818706	0,1825839	0,68674	0,158606	0,2567379
R-VDW	-0,0041232	0,186324	0,186341	0,64387	0,1824542	0,3092827
R-Median	-0,0301633	0,1814328	0,1823427	0,69356	0,1552566	0,249162

Table 7. Means, Variances and MSE's for the estimators $\widehat{\beta_0}$ and $\widehat{\beta_1}$, $n = 20$ when error term is the skew-t distribution

$\tau = 3{,}0; \alpha = 0{,}5$						
	β_0			β_1		
	Mean	Variance	MSE	Mean	Variance	MSE
OLS	-0,0036937	0,1988273	0,1988409	1,0049902	0,6301603	0,6301852
Huber-M	-0,1010066	0,1101164	0,1203187	1,0016782	0,3253026	0,3253054
R-Wilcoxon	-0,0736424	0,0576199	0,0630431	0,79404	0,0847854	0,127205
R-VDW	-0,0554916	0,0656352	0,0687145	0,76043	0,1058829	0,1632767
R-Median	-0,0741927	0,0568369	0,0623414	0,7949	0,0845839	0,1266499
$\tau = 5{,}0; \alpha = 0{,}5$						
	β_0			β_1		
	Mean	Variance	MSE	Mean	Variance	MSE
OLS	-0,0034742	0,2209661	0,2209782	0,9980777	0,6785346	0,6785383
Huber-M	-0,0834775	0,1768622	0,1838307	0,995549	0,5150677	0,5150875
R-Wilcoxon	-0,0434096	0,0899539	0,0918383	0,74924	0,1159986	0,1788792
R-VDW	-0,0256671	0,097754	0,0984128	0,71575	0,1389042	0,2197023
R-Median	-0,0459577	0,0888236	0,0909357	0,75366	0,1142735	0,1749569
$\tau = 10{,}0; \alpha = 0{,}5$						
	β_0			β_1		
	Mean	Variance	MSE	Mean	Variance	MSE
OLS	0,0157777	0,2231431	0,2233921	0,9791112	0,6716264	0,6720628
Huber-M	-0,049535	0,2066925	0,2091462	0,9833516	0,6131128	0,61339
R-Wilcoxon	-0,0030701	0,1053391	0,1053486	0,72674	0,1284087	0,2030797
R-VDW	0,0170343	0,11318	0,1134702	0,68818	0,1554184	0,2526501
R-Median	-0,0042747	0,1037865	0,1038048	0,72882	0,1260186	0,1995572
$\tau = 3{,}0; \alpha = 1{,}0$						
	β_0			β_1		
	Mean	Variance	MSE	Mean	Variance	MSE
OLS	0,000969	0,2163671	0,216368	0,9987781	0,6141261	0,6141276
Huber-M	-0,1262429	0,0937731	0,1097103	1,0035787	0,2632667	0,2632795
R-Wilcoxon	-0,1488338	0,0494409	0,0715924	0,83148	0,065154	0,093553
R-VDW	-0,1192309	0,0606923	0,0749083	0,77779	0,0973287	0,146706
R-Median	-0,1544315	0,0473336	0,0711827	0,84125	0,0599199	0,0851215
$\tau = 5{,}0; \alpha = 1{,}0$						
	β_0			β_1		
	Mean	Variance	MSE	Mean	Variance	MSE
OLS	-0,0033036	0,2108264	0,2108374	1,0115894	0,6482407	0,648375
Huber-M	-0,107936	0,154725	0,1663752	1,0056725	0,4437783	0,4438105
R-Wilcoxon	-0,1216998	0,0839743	0,0987851	0,77864	0,1001358	0,149136
R-VDW	-0,0937449	0,0926278	0,1014159	0,72428	0,1341293	0,2101508
R-Median	-0,127555	0,0818182	0,0980884	0,78968	0,0931171	0,1373516
$\tau = 10{,}0; \alpha = 1{,}0$						
	β_0			β_1		
	Mean	Variance	MSE	Mean	Variance	MSE
OLS	-0,0074	0,2235996	0,2236544	1,0100917	0,6689307	0,6690325
Huber-M	-0,0943679	0,1941404	0,2030458	1,0054635	0,5562977	0,5563276
R-Wilcoxon	-0,0887763	0,1053046	0,1131858	0,7545	0,1159229	0,1761932
R-VDW	-0,0593189	0,1157347	0,1192534	0,69918	0,1505504	0,2410431
R-Median	-0,0955663	0,1030236	0,1121565	0,76735	0,1083311	0,1624572

Table 8. Means, Variances and MSE's for the estimators $\widehat{\beta_0}$ and $\widehat{\beta_1}$, $n = 30$ when error term is the skew-t distribution

$\tau = 3{,}0; \alpha = 0{,}5$						
	β_0			β_1		
	Mean	Variance	MSE	Mean	Variance	MSE
OLS	-0,0050786	0,1287127	0,1287385	1,008601	0,4140497	0,4141237
Huber-M	-0,1032428	0,0698817	0,0805408	0,9976446	0,1980085	0,198014
R-Wilcoxon	-0,0974572	0,0395634	0,0490613	0,8325833	0,0604386	0,088467
R-VDW	-0,0788914	0,0465763	0,0528001	0,7968197	0,0820112	0,1232934
R-Median	-0,0979947	0,0390234	0,0486264	0,8333933	0,0601165	0,0878743
$\tau = 5{,}0; \alpha = 0{,}5$						
	β_0			β_1		
	Mean	Variance	MSE	Mean	Variance	MSE
OLS	0,0108088	0,1472156	0,1473324	0,9810558	0,4267481	0,4271069
Huber-M	-0,0753061	0,1172765	0,1229475	0,9841427	0,3277293	0,3279808
R-Wilcoxon	-0,0600815	0,0654156	0,0690254	0,7820282	0,0915467	0,1390584
R-VDW	-0,0393608	0,0736611	0,0752103	0,7418542	0,1191301	0,1857693
R-Median	-0,0617957	0,0646799	0,0684986	0,7850285	0,0893091	0,1355218
$\tau = 10{,}0; \alpha = 0{,}5$						
	β_0			β_1		
	Mean	Variance	MSE	Mean	Variance	MSE
OLS	0,0071504	0,1451358	0,1451869	0,9873608	0,435852	0,4360118
Huber-M	-0,0674149	0,1324151	0,1369598	0,9981306	0,3879904	0,3879939
R-Wilcoxon	-0,0389445	0,0750296	0,0765463	0,770477	0,1026155	0,1552963
R-VDW	-0,0181109	0,0843973	0,0847253	0,730048	0,1303956	0,2032697
R-Median	-0,0406841	0,0737836	0,0754388	0,7738524	0,0993604	0,1505031
$\tau = 3{,}0; \alpha = 1{,}0$						
	β_0			β_1		
	Mean	Variance	MSE	Mean	Variance	MSE
OLS	-0,0010045	0,1295868	0,1295878	0,9973626	0,3983909	0,3983979
Huber-M	-0,1349045	0,055781	0,0739802	0,9973648	0,1566782	0,1566851
R-Wilcoxon	-0,1698396	0,0332005	0,062046	0,8622262	0,0436417	0,0626234
R-VDW	-0,1420012	0,044227	0,0643914	0,810096	0,0748958	0,1109593
R-Median	-0,1752223	0,0316019	0,0623047	0,8721722	0,0387309	0,0550709
$\tau = 5{,}0; \alpha = 1{,}0$						
	β_0			β_1		
	Mean	Variance	MSE	Mean	Variance	MSE
OLS	0,0035104	0,1382058	0,1382181	0,9919609	0,4113401	0,4114047
Huber-M	-0,1088473	0,0981024	0,1099501	0,9892964	0,2785452	0,2786597
R-Wilcoxon	-0,1441756	0,0580459	0,0788325	0,810171	0,073525	0,10956
R-VDW	-0,1103656	0,0693843	0,0815649	0,7458896	0,1110785	0,1756506
R-Median	-0,1529118	0,0551924	0,0785744	0,8264026	0,0645473	0,0946833
$\tau = 10{,}0; \alpha = 1{,}0$						
	β_0			β_1		
	Mean	Variance	MSE	Mean	Variance	MSE
OLS	0,0064782	0,1404967	0,1405386	0,9817147	0,4223091	0,4226435
Huber-M	-0,0838951	0,1208992	0,1279376	0,9797639	0,3419607	0,3423702
R-Wilcoxon	-0,1127386	0,0745993	0,0873093	0,7864386	0,0899181	0,1355265
R-VDW	-0,0814064	0,0858044	0,0924314	0,7289379	0,1282327	0,2017074
R-Median	-0,1218057	0,0716444	0,086481	0,8029403	0,0803665	0,119199

Table 9. Means, Variances and MSE's for the estimators $\widehat{\beta_0}$ and $\widehat{\beta_1}$, $n = 50$ when error term is the skew-t distribution

$\tau = 3{,}0; \alpha = 0{,}5$						
	β_0			β_1		
	Mean	Variance	MSE	Mean	Variance	MSE
OLS	-0,0141637	0,0718177	0,0720183	1,012901	0,2232733	0,2234397
Huber-M	-0,1165269	0,0399102	0,0534887	1,0046311	0,1102292	0,1102507
R-Wilcoxon	-0,1250864	0,0233056	0,0389522	0,8734	0,0360505	0,052078
R-VDW	-0,1103179	0,0280016	0,0401717	0,8453	0,0517363	0,0756684
R-Median	-0,1253151	0,0231198	0,0388236	0,8741	0,0353819	0,0512327
$\tau = 5{,}0; \alpha = 0{,}5$						
	β_0			β_1		
	Mean	Variance	MSE	Mean	Variance	MSE
OLS	-0,0104148	0,0763076	0,0764161	1,0177805	0,2363283	0,2366444
Huber-M	-0,0994358	0,0585193	0,0684068	1,0155929	0,1746839	0,174927
R-Wilcoxon	-0,1004568	0,0372678	0,0473594	0,84585	0,05451	0,0782723
R-VDW	-0,0840636	0,0421091	0,0491758	0,81485	0,0744992	0,1087797
R-Median	-0,1006198	0,0366814	0,0468057	0,8467	0,0528305	0,0763314
$\tau = 10{,}0; \alpha = 0{,}5$						
	β_0			β_1		
	Mean	Variance	MSE	Mean	Variance	MSE
OLS	0,0083255	0,0789866	0,079056	0,9900183	0,2378188	0,2379185
Huber-M	-0,0642926	0,073421	0,0775545	0,991726	0,2097755	0,209844
R-Wilcoxon	-0,0625402	0,0493658	0,0532771	0,82015	0,0670725	0,0994185
R-VDW	-0,0430039	0,0574671	0,0593164	0,781325	0,092939	0,1407577
R-Median	-0,0643941	0,0479259	0,0520725	0,8234	0,0636493	0,0948368
$\tau = 3{,}0; \alpha = 1{,}0$						
	β_0			β_1		
	Mean	Variance	MSE	Mean	Variance	MSE
OLS	0,0024021	0,0787416	0,0787474	0,988195	0,2325964	0,2327357
Huber-M	-0,1355935	0,0328116	0,0511971	0,9948584	0,089808	0,0898344
R-Wilcoxon	-0,1918789	0,0186378	0,0554553	0,89455	0,0258282	0,0369479
R-VDW	-0,1681331	0,0250219	0,0532906	0,8491	0,0472678	0,0700386
R-Median	-0,1976211	0,0171679	0,054222	0,90535	0,0208268	0,0297854
$\tau = 5{,}0; \alpha = 1{,}0$						
	β_0			β_1		
	Mean	Variance	MSE	Mean	Variance	MSE
OLS	-0,0002607	0,0857645	0,0857646	1,0011165	0,247682	0,2476832
Huber-M	-0,1197445	0,0570687	0,0714074	0,9979023	0,1532504	0,1532548
R-Wilcoxon	-0,172879	0,0366844	0,0665716	0,85795	0,0473905	0,0675687
R-VDW	-0,1458106	0,0455079	0,0667686	0,804425	0,0797666	0,1180161
R-Median	-0,1809474	0,0341413	0,0664832	0,87295	0,0392379	0,0553796
$\tau = 10{,}0; \alpha = 1{,}0$						
	β_0			β_1		
	Mean	Variance	MSE	Mean	Variance	MSE
OLS	0,0134084	0,0831189	0,0832987	0,9995322	0,2442858	0,244286
Huber-M	-0,0860063	0,0679504	0,0753475	1,0007656	0,1893661	0,1893667
R-Wilcoxon	-0,1338902	0,0458369	0,0637635	0,84185	0,0565218	0,0815333
R-VDW	-0,1026868	0,0559688	0,0665134	0,78225	0,094102	0,1415171
R-Median	-0,1430214	0,0426898	0,0631449	0,859375	0,0462465	0,0660219

Table 10. Means, Variances and MSE's for the estimators $\widehat{\beta_0}$ and $\widehat{\beta_1}$, $n = 10$ when error term is the skew-normal distribution with 1 outlier

$\mu = 0{,}0;\ \sigma = 1{,}0;\ \alpha = 0{,}0$						
	β_0			β_1		
	Mean	Variance	MSE	Mean	Variance	MSE
OLS	-0,3350845	0,8591991	0,9714807	2,0325439	4,6266889	5,6928357
Huber-M	-0,1971727	0,6782788	0,7171559	1,6059709	2,9928534	3,3600541
R-Wilcoxon	0,1786782	0,1796031	0,211529	0,75041	0,1563755	0,2186706
R-VDW	0,2028242	0,1866907	0,2278284	0,69732	0,1784662	0,2700813
R-Median	0,1760738	0,1791692	0,2101712	0,75585	0,1544237	0,2140329
$\mu = 0{,}0;\ \sigma = 1{,}0;\ \alpha = 2{,}0$						
	β_0			β_1		
	Mean	Variance	MSE	Mean	Variance	MSE
OLS	-0,3350845	0,8591991	0,9714807	2,0325439	4,6266889	5,6928357
Huber-M	-0,1971727	0,6782788	0,7171559	1,6059709	2,9928534	3,3600541
R-Wilcoxon	0,1786782	0,1796031	0,211529	0,75041	0,1563755	0,2186706
R-VDW	0,2028242	0,1866907	0,2278284	0,69732	0,1784662	0,2700813
R-Median	0,1760738	0,1701692	0,2001712	0,75585	0,1444237	0,2040329
$\mu = 0{,}0;\ \sigma = 1{,}0;\ \alpha = 10{,}0$						
	β_0			β_1		
	Mean	Variance	MSE	Mean	Variance	MSE
OLS	-0,3223171	0,8521598	0,9560481	2,0227445	4,6018932	5,6478996
Huber-M	-0,1900599	0,6763701	0,7124928	1,6075006	3,0152415	3,3842984
R-Wilcoxon	0,1857231	0,1757083	0,2102014	0,74702	0,1581609	0,2221598
R-VDW	0,2068296	0,1845786	0,2273571	0,70027	0,1789408	0,2687789
R-Median	0,1837396	0,1701562	0,2000164	0,75163	0,1448625	0,2035502

Table 11. Means, Variances and MSE's for the estimators $\widehat{\beta_0}$ and $\widehat{\beta_1}$, $n = 20$ when error term is the skew-normal distribution with 1 outlier

$\mu = 0{,}0;\ \sigma = 1{,}0;\ \alpha = 0{,}0$						
	β_0			β_1		
	Mean	Variance	MSE	Mean	Variance	MSE
OLS	-0,1874133	0,2200992	0,2201114	1,0034662	0,6555614	0,6555734
Huber-M	0,0045697	0,231211	0,2312319	1,0043023	0,6911478	0,6911663
R-Wilcoxon	0,1455754	0,1112242	0,1324164	0,71794	0,1378517	0,2174096
R-VDW	0,164512	0,1151616	0,1422259	0,68271	0,1594584	0,2601314
R-Median	0,1455195	0,1106607	0,1318366	0,71875	0,1368223	0,2159239
$\mu = 0{,}0;\ \sigma = 1{,}0;\ \alpha = 2{,}0$						
	β_0			β_1		
	Mean	Variance	MSE	Mean	Variance	MSE
OLS	-0,1873844	0,308706	0,3438189	1,5746106	1,449962	1,7801394
Huber-M	-0,0885889	0,2600638	0,2679117	1,2719744	0,9466382	1,0206083
R-Wilcoxon	0,1391801	0,1026986	0,1220697	0,77928	0,1231793	0,1718966
R-VDW	0,1632911	0,1103118	0,1369758	0,73077	0,1476562	0,220141
R-Median	0,134598	0,1010775	0,1191941	0,78819	0,119679	0,1645424
$\mu = 0{,}0;\ \sigma = 1{,}0;\ \alpha = 10{,}0$						
	β_0			β_1		
	Mean	Variance	MSE	Mean	Variance	MSE
OLS	-0,1767169	0,3079694	0,3391983	1,5312176	1,4199885	1,7021806
Huber-M	-0,0857497	0,2639736	0,2713267	1,2504634	0,9501346	1,0128665
R-Wilcoxon	0,1296723	0,1041382	0,1209531	0,77588	0,1259074	0,1761372
R-VDW	0,1524737	0,1127661	0,1360143	0,7286	0,1503671	0,2240251
R-Median	0,12573	0,1034004	0,1192085	0,78436	0,1237821	0,1602828

Table 12. Means, Variances and MSE's for the estimators $\widehat{\beta_0}$ and $\widehat{\beta_1}$, $n = 30$ when error term is the skew-normal distribution with 1 outlier

$\mu = 0{,}0;\ \sigma = 1{,}0;\ \alpha = 0{,}0$						
	β_0			β_1		
	Mean	Variance	MSE	Mean	Variance	MSE
OLS	-0,1297335	0,1765649	0,1933957	1,39431	0,7505041	0,9059844
Huber-M	-0,0563986	0,1584787	0,1616595	1,1708539	0,5430384	0,5722295
R-Wilcoxon	0,1169746	0,0720393	0,0857224	0,8071407	0,1004292	0,1376239
R-VDW	0,141722	0,0803324	0,1004176	0,7565557	0,1285112	0,1877763
R-Median	0,1111749	0,0701678	0,0825276	0,8190219	0,0952143	0,1375674
$\mu = 0{,}0;\ \sigma = 1{,}0;\ \alpha = 2{,}0$						
	β_0			β_1		
	Mean	Variance	MSE	Mean	Variance	MSE
OLS	-0,129515	0,1795324	0,1963066	1,3863634	0,7591971	0,9084738
Huber-M	-0,0649329	0,159901	0,1641172	1,1862929	0,5493525	0,5840576
R-Wilcoxon	0,1185466	0,0718549	0,0859082	0,8045005	0,0995176	0,1377376
R-VDW	0,1421431	0,0793706	0,0995752	0,7585059	0,1258978	0,1842172
R-Median	0,1140811	0,0706413	0,0836558	0,8128263	0,0966339	0,1316679
$\mu = 0{,}0;\ \sigma = 1{,}0;\ \alpha = 10{,}0$						
	β_0			β_1		
	Mean	Variance	MSE	Mean	Variance	MSE
OLS	-0,1299136	0,1833001	0,2001776	1,3918238	0,7766215	0,9301475
Huber-M	-0,0574096	0,1606128	0,1639086	1,1707764	0,5522162	0,5813808
R-Wilcoxon	0,11525	0,0730954	0,086378	0,8027903	0,1013458	0,1402374
R-VDW	0,1420612	0,0805011	0,1006825	0,7485449	0,1294059	0,1926356
R-Median	0,1096273	0,0719917	0,0840098	0,8145665	0,0971399	0,1315255

Table 13. Means, Variances and MSE's for the estimators $\widehat{\beta_0}$ and $\widehat{\beta_1}$, $n = 50$ when error term is the skew-normal distribution with 1 outlier

$\mu = 0{,}0;\ \sigma = 1{,}0;\ \alpha = 0{,}0$						
	β_0			β_1		
	Mean	Variance	MSE	Mean	Variance	MSE
OLS	-0,071399	0,0976085	0,1027063	1,2236908	0,3861924	0,43623
Huber-M	-0,0244762	0,0889263	0,0895254	1,080454	0,2923728	0,2988456
R-Wilcoxon	0,0974283	0,0467479	0,0562401	0,82895	0,0745842	0,1038423
R-VDW	0,1204984	0,0539455	0,0684654	0,7821	0,1024858	0,1499662
R-Median	0,0942415	0,045973	0,0548545	0,8357	0,0706383	0,0976328
$\mu = 0{,}0;\ \sigma = 1{,}0;\ \alpha = 2{,}0$						
	β_0			β_1		
	Mean	Variance	MSE	Mean	Variance	MSE
OLS	-0,0905211	0,0989881	0,1071822	1,2614479	0,3736958	0,4420508
Huber-M	-0,0463367	0,0950079	0,097155	1,1264202	0,3048829	0,3208649
R-Wilcoxon	0,0869955	0,0477644	0,0553326	0,84095	0,0696729	0,0949698
R-VDW	0,107988	0,0541952	0,0658566	0,797775	0,0946011	0,1354961
R-Median	0,0823913	0,0463819	0,0531703	0,850125	0,0659067	0,0883692
$\mu = 0{,}0;\ \sigma = 1{,}0;\ \alpha = 10{,}0$						
	β_0			β_1		
	Mean	Variance	MSE	Mean	Variance	MSE
OLS	-0,0856582	0,0941799	0,1015172	1,2428291	0,3512176	0,4101835
Huber-M	-0,0409891	0,0874789	0,089159	1,105552	0,283254	0,2943952
R-Wilcoxon	0,0855954	0,0463968	0,0537234	0,84135	0,0669987	0,0921685
R-VDW	0,1094415	0,0541592	0,0661367	0,79365	0,0927761	0,1353564
R-Median	0,0809387	0,0456974	0,0522484	0,850725	0,0637076	0,0859906

Table 14. Means, Variances and MSE's for the estimators $\widehat{\beta_0}$ and $\widehat{\beta_1}$, $n = 10$ when error term is the skew-t distribution with 1 outlier

$\tau = 3{,}0; \alpha = 0{,}5$						
	β_0			β_1		
	Mean	Variance	MSE	Mean	Variance	MSE
OLS	-0,3304962	0,8305979	0,9398256	2,0372033	4,575063	5,6508537
Huber-M	-0,2402508	0,3494516	0,4071721	1,5415839	1,5138237	1,8071368
R-Wilcoxon	-0,020845	0,0986174	0,0990519	0,8262	0,1022518	0,1324582
R-VDW	0,0032382	0,1088844	0,1088949	0,77709	0,1302277	0,1799165
R-Median	-0,022511	0,0976542	0,0981609	0,829245	0,1008771	0,1300343
$\tau = 5{,}0; \alpha = 0{,}5$						
	β_0			β_1		
	Mean	Variance	MSE	Mean	Variance	MSE
OLS	-0,3240066	0,8714533	0,9764336	2,0292492	4,6155195	5,6748734
Huber-M	-0,2144285	0,501167	0,5471465	1,5275259	2,129383	2,4076666
R-Wilcoxon	0,0195632	0,1496501	0,1500328	0,77225	0,1368126	0,1886827
R-VDW	0,0428817	0,1594002	0,1612391	0,72478	0,1614516	0,2371976
R-Median	0,0177018	0,1490388	0,1493522	0,77671	0,1349096	0,184768
$\tau = 10{,}0; \alpha = 0{,}5$						
	β_0			β_1		
	Mean	Variance	MSE	Mean	Variance	MSE
OLS	-0,3376984	0,9073034	1,0213436	2,0539827	4,8329239	5,9438036
Huber-M	-0,2019062	0,5953914	0,6361575	1,5220783	2,5381949	2,8107607
R-Wilcoxon	0,0501023	0,1717834	0,1742936	0,7479	0,1532749	0,2168293
R-VDW	0,0717621	0,1820162	0,187166	0,70251	0,1759628	0,2644631
R-Median	0,0480582	0,1702832	0,1725928	0,752375	0,1516008	0,2129189
$\tau = 3{,}0; \alpha = 1{,}0$						
	β_0			β_1		
	Mean	Variance	MSE	Mean	Variance	MSE
OLS	-0,3368006	0,7644285	0,8778632	2,0382432	4,0759172	5,153866
Huber-M	-0,2558123	0,2754578	0,3408977	1,5279862	1,1482368	1,4270063
R-Wilcoxon	-0,0848202	0,093734	0,1009284	0,86193	0,0788916	0,0979549
R-VDW	-0,0567744	0,1041041	0,1073274	0,80545	0,1142597	0,1521094
R-Median	-0,0874195	0,0929099	0,1005521	0,86688	0,0761227	0,0938436
$\tau = 5{,}0; \alpha = 1{,}0$						
	β_0			β_1		
	Mean	Variance	MSE	Mean	Variance	MSE
OLS	-0,3394077	0,8798155	0,905013	2,058839	4,127054	5,1794708
Huber-M	-0,2352977	0,4532679	0,5086329	1,5227737	1,9108827	2,184175
R-Wilcoxon	-0,0460973	0,146082	0,1482069	0,7844	0,1255572	0,1720406
R-VDW	-0,0147883	0,1595045	0,1597232	0,72209	0,1611711	0,2384051
R-Median	-0,049668	0,1445366	0,1470035	0,79164	0,1217043	0,1651182
$\tau = 10{,}0; \alpha = 1{,}0$						
	β_0			β_1		
	Mean	Variance	MSE	Mean	Variance	MSE
OLS	-0,3332956	0,8663223	0,9774082	2,0455058	4,624532	5,7176144
Huber-M	-0,2192648	0,5391135	0,5871906	1,5203111	2,2959436	2,5666672
R-Wilcoxon	-0,0153623	0,177308	0,177544	0,7582	0,142819	0,2012863
R-VDW	0,0115261	0,1871195	0,1872523	0,70232	0,1723183	0,2609317
R-Median	-0,0172861	0,1759169	0,1762157	0,76227	0,14029	0,1968055

Table 15. Means, Variances and MSE's for the estimators $\widehat{\beta_0}$ and $\widehat{\beta_1}$, $n = 20$ when error term is the skew-t distribution with 1 outlier

$\tau = 3{,}0; \alpha = 0{,}5$						
	β_0			β_1		
	Mean	Variance	MSE	Mean	Variance	MSE
OLS	-0,1802585	0,2772227	0,3097158	1,5506937	1,275379	1,5786425
Huber-M	-0,1693466	0,1169161	0,1455944	1,239451	0,4115575	0,4688943
R-Wilcoxon	-0,0819281	0,0507347	0,0574469	0,86688	0,0636358	0,0813567
R-VDW	-0,06011	0,058771	0,0623842	0,82333	0,0878208	0,1190331
R-Median	-0,0837133	0,0498088	0,0568167	0,86989	0,0623454	0,079274
$\tau = 5{,}0; \alpha = 0{,}5$						
	β_0			β_1		
	Mean	Variance	MSE	Mean	Variance	MSE
OLS	-0,1735528	0,305138	0,3352586	1,5518097	1,3796724	1,6841664
Huber-M	-0,149154	0,1856846	0,2079315	1,2424816	0,6749314	0,7337287
R-Wilcoxon	-0,0445762	0,0817264	0,0837134	0,81532	0,0946722	0,1287789
R-VDW	-0,0179246	0,0911862	0,0915075	0,76355	0,1268763	0,1827849
R-Median	-0,0485253	0,0808152	0,0831699	0,82295	0,0920822	0,1234289
$\tau = 10{,}0; \alpha = 0{,}5$						
	β_0			β_1		
	Mean	Variance	MSE	Mean	Variance	MSE
OLS	-0,1888185	0,3167278	0,3523802	1,5776197	1,4597124	1,7933569
Huber-M	-0,1366879	0,2285358	0,2472193	1,2450215	0,81048	0,8705155
R-Wilcoxon	-0,0177534	0,0992217	0,0995369	0,793	0,1134577	0,1563067
R-VDW	0,0083319	0,1091109	0,1091803	0,74019	0,1433499	0,2108512
R-Median	-0,0215139	0,0976082	0,0980711	0,80076	0,1101685	0,149865
$\tau = 3{,}0; \alpha = 1{,}0$						
	β_0			β_1		
	Mean	Variance	MSE	Mean	Variance	MSE
OLS	-0,1798005	0,2835907	0,3159189	1,5565393	1,2395852	1,5493211
Huber-M	-0,1925988	0,0940818	0,1311761	1,2306479	0,3105124	0,3637108
R-Wilcoxon	-0,153365	0,0434198	0,0669406	0,89914	0,0411615	0,0513342
R-VDW	-0,1223999	0,0540459	0,0690276	0,83914	0,0759973	0,1018732
R-Median	-0,1595912	0,0409868	0,0664561	0,911	0,034999	0,04292
$\tau = 5{,}0; \alpha = 1{,}0$						
	β_0			β_1		
	Mean	Variance	MSE	Mean	Variance	MSE
OLS	-0,1887673	0,3018905	0,3375236	1,5714286	1,2983691	1,6248998
Huber-M	-0,1792402	0,1613787	0,1935058	1,237955	0,5680536	0,6246762
R-Wilcoxon	-0,1280872	0,0758049	0,0922112	0,83612	0,0827039	0,1095605
R-VDW	-0,0946865	0,087913	0,0968786	0,77059	0,1240224	0,1766513
R-Median	-0,1345092	0,0730729	0,0911657	0,84857	0,0742823	0,0972134
$\tau = 10{,}0; \alpha = 1{,}0$						
	β_0			β_1		
	Mean	Variance	MSE	Mean	Variance	MSE
OLS	-0,1840506	0,2951502	0,3290249	1,5527227	1,4027306	1,708233
Huber-M	-0,1547696	0,1944359	0,2183895	1,2186736	0,6865202	0,7343383
R-Wilcoxon	-0,095148	0,0961604	0,1052135	0,80716	0,0982764	0,1354637
R-VDW	-0,061778	0,1083063	0,1121228	0,74127	0,1402683	0,2072096
R-Median	-0,1014715	0,0935239	0,1038203	0,82001	0,0909503	0,1233467

Table 16. Means, Variances and MSE's for the estimators $\widehat{\beta_0}$ and $\widehat{\beta_1}$, $n = 30$ when error term is the skew-t distribution with 1 outlier

$\tau = 3{,}0; \alpha = 0{,}5$						
	β_0			β_1		
	Mean	Variance	MSE	Mean	Variance	MSE
OLS	-0,1159923	0,5765477	0,590002	1,3728902	1,3088751	1,4479222
Huber-M	-0,1516798	0,0734196	0,0964264	1,1587597	0,2363023	0,2615069
R-Wilcoxon	-0,1054208	0,0353912	0,0465048	0,8885389	0,0451927	0,0576163
R-VDW	-0,0851502	0,0431139	0,0503645	0,8489049	0,0683294	0,0911591
R-Median	-0,1066857	0,0347491	0,0461309	0,8908641	0,044338	0,0562487
$\tau = 5{,}0; \alpha = 0{,}5$						
	β_0			β_1		
	Mean	Variance	MSE	Mean	Variance	MSE
OLS	-0,1237546	0,1813468	0,196662	1,3684867	0,7589809	0,8947633
Huber-M	-0,1325469	0,1194578	0,1370265	1,1432997	0,3895598	0,4100946
R-Wilcoxon	-0,0722726	0,0595441	0,0647674	0,8316532	0,079481	0,1078216
R-VDW	-0,0502919	0,065608	0,0681372	0,7873987	0,1022796	0,1474789
R-Median	-0,0750151	0,0584276	0,0640549	0,8365887	0,0777643	0,1044675
$\tau = 10{,}0; \alpha = 0{,}5$						
	β_0			β_1		
	Mean	Variance	MSE	Mean	Variance	MSE
OLS	-0,1378811	0,1866038	0,205615	1,4101017	0,8034411	0,9716245
Huber-M	-0,1242053	0,1412366	0,1566635	1,1680171	0,4706147	0,4988445
R-Wilcoxon	-0,047621	0,0671713	0,069439	0,8236724	0,0852588	0,1163502
R-VDW	-0,0222177	0,0761996	0,0766932	0,7735974	0,1158018	0,1670599
R-Median	-0,0514543	0,0653704	0,0680179	0,8311581	0,0819783	0,1104859
$\tau = 3{,}0; \alpha = 1{,}0$						
	β_0			β_1		
	Mean	Variance	MSE	Mean	Variance	MSE
OLS	-0,1178231	0,1990392	0,2129215	1,3647222	0,7348398	0,8678621
Huber-M	-0,1754219	0,0586615	0,0894344	1,144577	0,1787692	0,1996717
R-Wilcoxon	-0,1755971	0,0287307	0,059565	0,9123612	0,0309336	0,0386141
R-VDW	-0,1481779	0,0373014	0,0592581	0,8621062	0,0573496	0,0763643
R-Median	-0,1806785	0,0274528	0,0591975	0,9220372	0,0262272	0,0323053
$\tau = 5{,}0; \alpha = 1{,}0$						
	β_0			β_1		
	Mean	Variance	MSE	Mean	Variance	MSE
OLS	-0,1292812	0,173879	0,1905926	1,3821407	0,7602005	0,906232
Huber-M	-0,1559985	0,095853	0,1201886	1,1401493	0,3118817	0,3315235
R-Wilcoxon	-0,1534781	0,052513	0,0760686	0,8570057	0,0612572	0,0817045
R-VDW	-0,1200636	0,0651483	0,0795635	0,7941044	0,1020023	0,1443953
R-Median	-0,1618892	0,0497574	0,0759655	0,8727573	0,0520997	0,0682905
$\tau = 10{,}0; \alpha = 1{,}0$						
	β_0			β_1		
	Mean	Variance	MSE	Mean	Variance	MSE
OLS	-0,1253425	0,1759383	0,191649	1,3752077	0,7432782	0,884059
Huber-M	-0,1377677	0,1224115	0,1413914	1,143553	0,3985251	0,4191326
R-Wilcoxon	-0,1246027	0,0654019	0,0809278	0,8351335	0,0751188	0,1022998
R-VDW	-0,0917015	0,0759489	0,0843581	0,7728623	0,1143901	0,1659817
R-Median	-0,1325999	0,0622855	0,0798683	0,8505551	0,0655992	0,087933

Table 17. Means, Variances and MSE's for the estimators $\widehat{\beta_0}$ and $\widehat{\beta_1}$, $n = 50$ when error term is the skew-t distribution with 1 outlier

$\tau = 3{,}0; \alpha = 0{,}5$						
	β_0			β_1		
	Mean	Variance	MSE	Mean	Variance	MSE
OLS	-0,081564	0,0849749	0,0916275	1,2394034	0,3221625	0,3794765
Huber-M	-0,1417446	0,0408913	0,0609828	1,0976893	0,1251761	0,1347193
R-Wilcoxon	-0,1302166	0,0209892	0,0379455	0,90815	0,0272522	0,0356886
R-VDW	-0,1131755	0,026598	0,0394067	0,8757	0,0437139	0,0591644
R-Median	-0,1321585	0,020389	0,0378549	0,912225	0,0257147	0,0334191
$\tau = 5{,}0; \alpha = 0{,}5$						
	β_0			β_1		
	Mean	Variance	MSE	Mean	Variance	MSE
OLS	-0,0702028	0,0914282	0,0963566	1,2221968	0,3437829	0,3931543
Huber-M	-0,1153415	0,0647358	0,0780394	1,0855052	0,194012	0,2013232
R-Wilcoxon	-0,1012564	0,036962	0,0472149	0,8683	0,0485794	0,0659243
R-VDW	-0,0801428	0,04311	0,0495329	0,82505	0,0718384	0,1024459
R-Median	-0,10407	0,0362462	0,0470767	0,873425	0,0466759	0,0626971
$\tau = 10{,}0; \alpha = 0{,}5$						
	β_0			β_1		
	Mean	Variance	MSE	Mean	Variance	MSE
OLS	-0,0791694	0,0984087	0,1046765	1,2273621	0,3782004	0,4298939
Huber-M	-0,0995059	0,0780146	0,087916	1,0786877	0,2471605	0,2533523
R-Wilcoxon	-0,074101	0,0460319	0,0515228	0,84555	0,0622213	0,0860761
R-VDW	-0,0493567	0,0540707	0,0565068	0,795325	0,0911725	0,1330643
R-Median	-0,078206	0,0445024	0,0506185	0,853225	0,0580074	0,0795503
$\tau = 3{,}0; \alpha = 1{,}0$						
	β_0			β_1		
	Mean	Variance	MSE	Mean	Variance	MSE
OLS	-0,073852	0,0855892	0,0910433	1,2210517	0,3122373	0,3611012
Huber-M	-0,1614323	0,0313098	0,0573702	1,0877049	0,0900231	0,0977152
R-Wilcoxon	-0,1947493	0,017024	0,0549513	0,93115	0,0173634	0,0221037
R-VDW	-0,1719899	0,0231969	0,0527774	0,886725	0,0366383	0,0494696
R-Median	-0,2007034	0,015683	0,0549509	0,941775	0,0129526	0,0163427
$\tau = 5{,}0; \alpha = 1{,}0$						
	β_0			β_1		
	Mean	Variance	MSE	Mean	Variance	MSE
OLS	-0,0818277	0,1007408	0,1074366	1,242143	0,3873871	0,4460203
Huber-M	-0,1499503	0,0573865	0,0798716	1,0974463	0,1759295	0,1854253
R-Wilcoxon	-0,1815814	0,0330369	0,0660087	0,89295	0,0360933	0,047553
R-VDW	-0,1524047	0,0423892	0,0656164	0,836975	0,0679531	0,0945302
R-Median	-0,188364	0,0308913	0,0654723	0,907225	0,0285958	0,037203
$\tau = 10{,}0; \alpha = 1{,}0$						
	β_0			β_1		
	Mean	Variance	MSE	Mean	Variance	MSE
OLS	-0,0702772	0,0960034	0,1009423	1,2309748	0,3754532	0,4288026
Huber-M	-0,1151202	0,0713331	0,0845858	1,0797737	0,2227979	0,2291618
R-Wilcoxon	-0,1411657	0,0411442	0,061072	0,8613	0,0543495	0,0735872
R-VDW	-0,1094638	0,0512217	0,063204	0,802175	0,0909395	0,1300742
R-Median	-0,1510183	0,0379863	0,0607928	0,8806	0,0440732	0,0583295

Table 18. Means, Variances and MSE's for the estimators $\widehat{\beta_0}$ and $\widehat{\beta_1}$, $n = 10$ when error term is the skew-normal distribution with 2 outliers

$\mu = 0{,}0;\ \sigma = 1{,}0;\ \alpha = 0{,}0$						
	β_0			β_1		
	Mean	Variance	MSE	Mean	Variance	MSE
OLS	-0,5590822	1,0778499	1,3904228	2,8063356	6,5672373	9,8300855
Huber-M	-0,4280158	0,9481236	1,1313211	2,3713339	5,4565386	7,3370954
R-Wilcoxon	0,2222593	0,1863899	0,2357891	0,79105	0,1427052	0,1863653
R-VDW	0,2418845	0,1946405	0,2531486	0,74844	0,1656761	0,2289586
R-Median	0,2196816	0,1857358	0,2339958	0,79703	0,1396751	0,180872
$\mu = 0{,}0;\ \sigma = 1{,}0;\ \alpha = 2{,}0$						
	β_0			β_1		
	Mean	Variance	MSE	Mean	Variance	MSE
OLS	-0,5500794	1,014153	1,3167403	2,7977556	6,1408886	9,3728139
Huber-M	-0,4142045	0,9013704	1,0729358	2,3515112	5,182014	7,0085966
R-Wilcoxon	0,2163888	0,1863965	0,2332206	0,79571	0,1395506	0,181285
R-VDW	0,2365983	0,1968555	0,2528343	0,750015	0,1629755	0,225468
R-Median	0,2142856	0,1860679	0,2319863	0,80034	0,1380687	0,1779328
$\mu = 0{,}0;\ \sigma = 1{,}0;\ \alpha = 10{,}0$						
	β_0			β_1		
	Mean	Variance	MSE	Mean	Variance	MSE
OLS	-0,5290699	1,0439986	1,3239136	2,7616331	6,3945843	9,4979354
Huber-M	-0,4073706	0,92841	1,0943608	2,356659	5,3759485	7,2164721
R-Wilcoxon	0,2225031	0,18604	0,2355477	0,79714	0,1388937	0,1800459
R-VDW	0,2431057	0,1923498	0,2514502	0,75224	0,1624202	0,2238052
R-Median	0,2213955	0,185073	0,2340889	0,800005	0,1376265	0,1776245

Table 19. Means, Variances and MSE's for the estimators $\widehat{\beta_0}$ and $\widehat{\beta_1}$, $n = 20$ when error term is the skew-normal distribution with 2 outliers

$\mu = 0{,}0;\ \sigma = 1{,}0;\ \alpha = 0{,}0$						
	β_0			β_1		
	Mean	Variance	MSE	Mean	Variance	MSE
OLS	-0,3358178	0,3701955	0,4829691	2,0557183	2,0764621	3,1910032
Huber-M	-0,1839921	0,2921274	0,3259805	1,5852832	1,3256202	1,6681766
R-Wilcoxon	0,1454818	0,0941356	0,1153006	0,82678	0,1066822	0,1366873
R-VDW	0,1732301	0,1021057	0,1321143	0,76804	0,137382	0,1911875
R-Median	0,1416404	0,0931036	0,1131657	0,83482	0,1063222	0,1366067
$\mu = 0{,}0;\ \sigma = 1{,}0;\ \alpha = 2{,}0$						
	β_0			β_1		
	Mean	Variance	MSE	Mean	Variance	MSE
OLS	-0,3230704	0,3711195	0,475494	2,0082036	1,9994356	3,0159101
Huber-M	-0,1821703	0,3006348	0,3338208	1,5632057	1,3088615	1,6260621
R-Wilcoxon	0,1360044	0,100473	0,1189702	0,82144	0,1092182	0,1411018
R-VDW	0,1609246	0,1092968	0,1351936	0,76857	0,136935	0,1904949
R-Median	0,1324943	0,0996783	0,1172331	0,82917	0,1063229	0,1355058
$\mu = 0{,}0;\ \sigma = 1{,}0;\ \alpha = 10{,}0$						
	β_0			β_1		
	Mean	Variance	MSE	Mean	Variance	MSE
OLS	-0,3318885	0,3605402	0,4706902	2,0470909	2,0132638	3,1096632
Huber-M	-0,1854856	0,2902921	0,324697	1,5853671	1,320693	1,6633476
R-Wilcoxon	0,1457812	0,0987096	0,1199617	0,8227	0,1070921	0,1385274
R-VDW	0,1709013	0,1075211	0,1367284	0,76891	0,1386346	0,1920372
R-Median	0,1413075	0,0979756	0,1179434	0,83287	0,1029857	0,1309181

Table 20. Means, Variances and MSE's for the estimators $\widehat{\beta_0}$ and $\widehat{\beta_1}$, $n = 30$ when error term is the skew-normal distribution with 2 outliers

$\mu = 0{,}0;\ \sigma = 1{,}0;\ \alpha = 0{,}0$						
	β_0			β_1		
	Mean	Variance	MSE	Mean	Variance	MSE
OLS	-0,2364178	0,2082658	0,2641592	1,7274205	1,0353139	1,5644545
Huber-M	-0,1231539	0,1725584	0,1877253	1,3728025	0,6733877	0,8123694
R-Wilcoxon	0,118794	0,0679221	0,0820341	0,8425443	0,0859806	0,1107729
R-VDW	0,1449184	0,0760809	0,0970823	0,7906391	0,1147488	0,1585808
R-Median	0,1132764	0,0663455	0,079177	0,8540204	0,0809187	0,1022287
$\mu = 0{,}0;\ \sigma = 1{,}0;\ \alpha = 2{,}0$						
	β_0			β_1		
	Mean	Variance	MSE	Mean	Variance	MSE
OLS	-0,2221987	0,2097091	0,2590814	1,7095767	1,0603648	1,5638639
Huber-M	-0,1017927	0,1685968	0,1789586	1,3365556	0,6609698	0,7742395
R-Wilcoxon	0,1243968	0,0716911	0,0871656	0,8380138	0,087267	0,1135065
R-VDW	0,1504341	0,0806662	0,1032967	0,7826883	0,117853	0,1650774
R-Median	0,1196724	0,0707956	0,0851171	0,8474047	0,0808581	0,1011434
$\mu = 0{,}0;\ \sigma = 1{,}0;\ \alpha = 10{,}0$						
	β_0			β_1		
	Mean	Variance	MSE	Mean	Variance	MSE
OLS	-0,232868	0,2090911	0,2633186	1,7311007	1,0356598	1,570168
Huber-M	-0,1113465	0,1696953	0,1820933	1,3552054	0,6489928	0,7751637
R-Wilcoxon	0,1167079	0,0725439	0,0861646	0,840114	0,0870248	0,1125884
R-VDW	0,1382432	0,0797735	0,0988847	0,7946295	0,1133295	0,1555065
R-Median	0,1118041	0,0709348	0,0834349	0,850195	0,0801841	0,1006256

Table 21. Means, Variances and MSE's for the estimators $\widehat{\beta_0}$ and $\widehat{\beta_1}$, $n = 50$ when error term is the skew-normal distribution with 2 outliers

$\mu = 0{,}0;\ \sigma = 1{,}0;\ \alpha = 0{,}0$						
	β_0			β_1		
	Mean	Variance	MSE	Mean	Variance	MSE
OLS	-0,1449514	0,1100562	0,1310671	1,443167	0,4944995	0,6908965
Huber-M	-0,0635595	0,0969802	0,10102	1,1979501	0,3462468	0,385431
R-Wilcoxon	0,0925629	0,047437	0,0560049	0,8592	0,0670589	0,0868835
R-VDW	0,1168866	0,0537141	0,0673766	0,809175	0,0925709	0,128985
R-Median	0,086085	0,0462159	0,0536265	0,87125	0,0630024	0,079579
$\mu = 0{,}0;\ \sigma = 1{,}0;\ \alpha = 2{,}0$						
	β_0			β_1		
	Mean	Variance	MSE	Mean	Variance	MSE
OLS	-0,1626904	0,1088	0,1352681	1,4709067	0,4956625	0,7174156
Huber-M	-0,0841828	0,0921991	0,0992858	1,2311572	0,3310067	0,3844404
R-Wilcoxon	0,082276	0,0447096	0,0514789	0,8719	0,0602605	0,0766701
R-VDW	0,1077533	0,0511452	0,062756	0,820075	0,0857786	0,1181516
R-Median	0,0775809	0,0437241	0,0497429	0,8824	0,0556306	0,0694603
$\mu = 0{,}0;\ \sigma = 1{,}0;\ \alpha = 10{,}0$						
	β_0			β_1		
	Mean	Variance	MSE	Mean	Variance	MSE
OLS	-0,1464398	0,1024171	0,1238617	1,4565143	0,4487086	0,6571138
Huber-M	-0,0635636	0,0911972	0,0952375	1,2006953	0,3084756	0,3487542
R-Wilcoxon	0,0906553	0,0437387	0,051957	0,86645	0,0594391	0,0772747
R-VDW	0,1140663	0,0522431	0,0652542	0,8178	0,0885149	0,1217118
R-Median	0,0837438	0,0420267	0,0490397	0,88035	0,0538908	0,0682069

Table 22. Means, Variances and MSE's for the estimators $\widehat{\beta_0}$ and $\widehat{\beta_1}$, $n = 10$ when error term is the skew-t distribution with 2 outliers

$\tau = 3{,}0; \alpha = 0{,}5$						
	β_0			β_1		
	Mean	Variance	MSE	Mean	Variance	MSE
OLS	-0,5348908	0,9831581	1,2692663	2,7816079	6,2113498	9,3854764
Huber-M	-0,417772	0,4923398	0,6668732	2,1845437	2,7851544	4,1882981
R-Wilcoxon	0,0160969	0,1039257	0,1041849	0,88513	0,0748854	0,0879805
R-VDW	0,035293	0,1108244	0,11207	0,8445	0,1010954	0,1252756
R-Median	0,0156915	0,1040298	0,104276	0,886365	0,0750538	0,0880668
$\tau = 5{,}0; \alpha = 0{,}5$						
	β_0			β_1		
	Mean	Variance	MSE	Mean	Variance	MSE
OLS	-0,5434336	1,0943368	1,3896569	2,8006659	6,7210422	9,9634398
Huber-M	-0,3965739	0,7123206	0,8695915	2,1798649	4,099987	5,4920682
R-Wilcoxon	0,0551967	0,159118	0,1621646	0,81563	0,1224069	0,1563992
R-VDW	0,0728329	0,1659901	0,1712947	0,77954	0,14161	0,1902127
R-Median	0,0539907	0,1579608	0,1608758	0,817655	0,1206876	0,1539373
$\tau = 10{,}0; \alpha = 0{,}5$						
	β_0			β_1		
	Mean	Variance	MSE	Mean	Variance	MSE
OLS	-0,5459876	1,084569	1,3826715	2,8003494	6,6996061	9,9408641
Huber-M	-0,3822138	0,8237347	0,969822	2,1673502	4,7969901	6,1596966
R-Wilcoxon	0,0870394	0,187207	0,1947829	0,7872	0,1393221	0,1846059
R-VDW	0,1077611	0,1979955	0,2096079	0,7455	0,162738	0,2275083
R-Median	0,0852018	0,1863211	0,1935804	0,79109	0,1373433	0,1809867
$\tau = 3{,}0; \alpha = 1{,}0$						
	β_0			β_1		
	Mean	Variance	MSE	Mean	Variance	MSE
OLS	-0,5411755	0,9967612	1,2896321	2,7795089	6,0815725	9,2482242
Huber-M	-0,4242229	0,3829346	0,5628997	2,1344897	2,1540115	3,4410783
R-Wilcoxon	-0,0510828	0,0932909	0,0959004	0,91818	0,0505445	0,0572391
R-VDW	-0,0284327	0,1024251	0,1032335	0,87064	0,0829018	0,0996358
R-Median	-0,0528796	0,0926628	0,0954591	0,92099	0,0487783	0,0550209
$\tau = 5{,}0; \alpha = 1{,}0$						
	β_0			β_1		
	Mean	Variance	MSE	Mean	Variance	MSE
OLS	-0,5372796	1,0788532	1,3675226	2,7836641	6,6341777	9,8156354
Huber-M	-0,3840709	0,6074135	0,7549239	2,0774333	3,4798284	4,640691
R-Wilcoxon	-0,0104391	0,1573184	0,1574274	0,8239	0,1112439	0,1422551
R-VDW	0,0119997	0,1661818	0,1663257	0,777665	0,1415391	0,1909719
R-Median	-0,0117297	0,1566012	0,1567388	0,82665	0,1088032	0,1388534
$\tau = 10{,}0; \alpha = 1{,}0$						
	β_0			β_1		
	Mean	Variance	MSE	Mean	Variance	MSE
OLS	-0,5566571	1,0894897	1,3993569	2,8015731	6,4399791	9,6856447
Huber-M	-0,3921742	0,7885171	0,9423177	2,1052953	4,3144966	5,5361744
R-Wilcoxon	0,0183737	0,1895333	0,1898709	0,78939	0,1345639	0,1789205
R-VDW	0,0393045	0,200124	0,2016689	0,74389	0,1617738	0,2273662
R-Median	0,0160077	0,1889466	0,1892028	0,793845	0,1315955	0,1740954

Table 23. Means, Variances and MSE's for the estimators $\widehat{\beta_0}$ and $\widehat{\beta_1}$, $n = 20$ when error term is the skew-t distribution with 2 outliers

$\tau = 3{,}0; \alpha = 0{,}5$						
	β_0			β_1		
	Mean	Variance	MSE	Mean	Variance	MSE
OLS	-0,3352048	0,3628589	0,4752211	2,0703682	1,9636771	3,1093653
Huber-M	-0,2602577	0,1304942	0,1982283	1,5497492	0,5726456	0,8748698
R-Wilcoxon	-0,0741466	0,0471581	0,0526558	0,91338	0,0457561	0,0532592
R-VDW	-0,0529567	0,0547507	0,0575551	0,87082	0,072292	0,0889795
R-Median	-0,0753792	0,0466079	0,05229	0,91572	0,0446938	0,0517969
$\tau = 5{,}0; \alpha = 0{,}5$						
	β_0			β_1		
	Mean	Variance	MSE	Mean	Variance	MSE
OLS	-0,3407379	0,3776418	0,4937441	2,0506486	2,0288174	3,1326799
Huber-M	-0,2377723	0,2084852	0,2650209	1,5097872	0,9097909	1,1696739
R-Wilcoxon	-0,0439821	0,0813123	0,0832467	0,8518	0,0850418	0,107005
R-VDW	-0,0217636	0,0903595	0,0908331	0,80527	0,1137695	0,1516893
R-Median	-0,0475938	0,0799979	0,0822631	0,85872	0,0821554	0,1021154
$\tau = 10{,}0; \alpha = 0{,}5$						
	β_0			β_1		
	Mean	Variance	MSE	Mean	Variance	MSE
OLS	-0,330821	0,3764084	0,4858509	2,0413647	2,0911202	3,1755606
Huber-M	-0,2175003	0,2483368	0,2956432	1,5162923	1,0857076	1,3522653
R-Wilcoxon	-0,0072376	0,0958334	0,0958857	0,8335	0,0969791	0,1247014
R-VDW	0,0181683	0,1051802	0,1055103	0,78144	0,127416	0,1751845
R-Median	-0,0097093	0,0949739	0,0950682	0,83792	0,0956072	0,1218771
$\tau = 3{,}0; \alpha = 1{,}0$						
	β_0			β_1		
	Mean	Variance	MSE	Mean	Variance	MSE
OLS	-0,3339727	0,3293991	0,4409368	2,0293993	1,7738518	2,8335147
Huber-M	-0,2767604	0,1010312	0,1776275	1,5069401	0,4212467	0,6782349
R-Wilcoxon	-0,1496102	0,0385256	0,0609088	0,94164	0,0256032	0,0290091
R-VDW	-0,1250385	0,0470803	0,0627149	0,89163	0,0558836	0,0676277
R-Median	-0,1525597	0,0376174	0,0608919	0,94777	0,022159	0,0248869
$\tau = 5{,}0; \alpha = 1{,}0$						
	β_0			β_1		
	Mean	Variance	MSE	Mean	Variance	MSE
OLS	-0,3144718	0,3625043	0,4613968	2,0060597	2,0050551	3,0172113
Huber-M	-0,2351782	0,182129	0,2374378	1,4622282	0,7821917	0,9958466
R-Wilcoxon	-0,10999	0,0764374	0,0885352	0,86566	0,0708489	0,0888962
R-VDW	-0,0793829	0,0867744	0,093076	0,80406	0,1094344	0,1478269
R-Median	-0,1152	0,0745875	0,0878585	0,8758	0,0641372	0,0795628
$\tau = 10{,}0; \alpha = 1{,}0$						
	β_0			β_1		
	Mean	Variance	MSE	Mean	Variance	MSE
OLS	-0,3301173	0,3676008	0,4765782	2,0429839	2,0355065	3,1233218
Huber-M	-0,2250652	0,2244828	0,2751371	1,4894112	1,0007087	1,240232
R-Wilcoxon	-0,0785312	0,0957813	0,1019484	0,84332	0,0870128	0,1115614
R-VDW	-0,0464144	0,1061487	0,108303	0,7784	0,127849	0,1769556
R-Median	-0,082304	0,0942456	0,1010196	0,85118	0,0815959	0,1037433

Table 24. Means, Variances and MSE's for the estimators $\widehat{\beta_0}$ and $\widehat{\beta_1}$, $n = 30$ when error term is the skew-t distribution with 2 outliers

$\tau = 3{,}0; \alpha = 0{,}5$						
	β_0			β_1		
	Mean	Variance	MSE	Mean	Variance	MSE
OLS	-0,2306971	0,205178	0,2583991	1,7296355	1,0109911	1,5433591
Huber-M	-0,1987781	0,0769578	0,1164705	1,3162692	0,2807643	0,3807905
R-Wilcoxon	-0,1047333	0,0316032	0,0426723	0,9168617	0,0337552	0,0406672
R-VDW	-0,0846354	0,0388566	0,0460197	0,8775728	0,0553305	0,0703189
R-Median	-0,1075803	0,0310619	0,0425354	0,9226373	0,0320842	0,0380692
$\tau = 5{,}0; \alpha = 0{,}5$						
	β_0			β_1		
	Mean	Variance	MSE	Mean	Variance	MSE
OLS	-0,2390898	0,2154512	0,2726151	1,7499937	1,0481855	1,610676
Huber-M	-0,1870973	0,1224762	0,1574816	1,3374031	0,4557024	0,5695433
R-Wilcoxon	-0,0730298	0,0550478	0,0603812	0,879658	0,0590399	0,0735221
R-VDW	-0,0494304	0,0623515	0,0647948	0,8316382	0,0881681	0,1165139
R-Median	-0,0762602	0,0538416	0,0596572	0,8858986	0,0561261	0,0691453
$\tau = 10{,}0; \alpha = 0{,}5$						
	β_0			β_1		
	Mean	Variance	MSE	Mean	Variance	MSE
OLS	-0,2190999	0,2098243	0,257829	1,6923577	1,0280283	1,5073875
Huber-M	-0,155339	0,1469777	0,1711079	1,2961897	0,5474519	0,6351802
R-Wilcoxon	-0,0435489	0,0682636	0,0701601	0,8461446	0,0806191	0,1042906
R-VDW	-0,0169435	0,0776465	0,0779336	0,7930693	0,1118802	0,1547005
R-Median	-0,0468564	0,0671086	0,0693041	0,8526553	0,0771276	0,098838
$\tau = 3{,}0; \alpha = 1{,}0$						
	β_0			β_1		
	Mean	Variance	MSE	Mean	Variance	MSE
OLS	-0,2282309	0,1904322	0,2425215	1,7100827	0,9432793	1,4474968
Huber-M	-0,2238028	0,057589	0,1076767	1,3158593	0,2055201	0,3052872
R-Wilcoxon	-0,1733584	0,0261796	0,0562328	0,9474347	0,0184726	0,0212357
R-VDW	-0,1531879	0,0323241	0,0557907	0,9071557	0,0391407	0,0477608
R-Median	-0,1769147	0,0248713	0,0561701	0,9542604	0,0147493	0,0168414
$\tau = 5{,}0; \alpha = 1{,}0$						
	β_0			β_1		
	Mean	Variance	MSE	Mean	Variance	MSE
OLS	-0,2364643	0,2081159	0,2640313	1,7335018	1,0498869	1,5879118
Huber-M	-0,1986211	0,1005244	0,1399748	1,2936693	0,3693868	0,4556285
R-Wilcoxon	-0,1483279	0,0506649	0,0726661	0,890309	0,0487686	0,0608007
R-VDW	-0,1151293	0,0621295	0,0753843	0,8247225	0,0907362	0,1214584
R-Median	-0,1555606	0,0482701	0,0724692	0,9045605	0,040671	0,0497797
$\tau = 10{,}0; \alpha = 1{,}0$						
	β_0			β_1		
	Mean	Variance	MSE	Mean	Variance	MSE
OLS	-0,2273774	0,2095002	0,2612007	1,7066201	1,0508541	1,550166
Huber-M	-0,1703986	0,1293341	0,1583697	1,2754807	0,4741423	0,550032
R-Wilcoxon	-0,1145451	0,0678237	0,0809443	0,8583858	0,068967	0,0890216
R-VDW	-0,0803798	0,0803852	0,0868461	0,789994	0,113415	0,1575175
R-Median	-0,1212579	0,0648741	0,0795776	0,8722172	0,0597516	0,0760800

Table 25. Means, Variances and MSE's for the estimators $\widehat{\beta_0}$ and $\widehat{\beta_1}$, $n = 50$ when error term is the skew-t distribution with 2 outliers

$\tau = 3{,}0; \alpha = 0{,}5$						
	β_0			β_1		
	Mean	Variance	MSE	Mean	Variance	MSE
OLS	-0,1414687	0,1083671	0,1283805	1,441613	0,4802511	0,6752731
Huber-M	-0,161083	0,0386277	0,0645754	1,1755672	0,132873	0,1636969
R-Wilcoxon	-0,1319809	0,0187776	0,0361966	0,9306	0,0218746	0,0266909
R-VDW	-0,1134942	0,023405	0,0362859	0,8939	0,0387622	0,0500194
R-Median	-0,1340294	0,0181631	0,036127	0,93475	0,0200425	0,0243
$\tau = 5{,}0; \alpha = 0{,}5$						
	β_0			β_1		
	Mean	Variance	MSE	Mean	Variance	MSE
OLS	-0,140929	0,1076376	0,1274986	1,4332316	0,4660702	0,6537599
Huber-M	-0,1391923	0,0653884	0,0847629	1,1664468	0,2158073	0,2435118
R-Wilcoxon	-0,0977766	0,0327148	0,042275	0,89255	0,0422206	0,0537661
R-VDW	-0,0762656	0,0396862	0,0455026	0,8485	0,0667736	0,0897259
R-Median	-0,0998424	0,0319402	0,0419087	0,89775	0,040185	0,0506401
$\tau = 10{,}0; \alpha = 0{,}5$						
	β_0			β_1		
	Mean	Variance	MSE	Mean	Variance	MSE
OLS	-0,1490162	0,1049668	0,1271726	1,4510105	0,4713867	0,6747972
Huber-M	-0,1309429	0,0792237	0,0963697	1,1825693	0,2669637	0,3002952
R-Wilcoxon	-0,0790558	0,0438207	0,0500705	0,88125	0,0512591	0,0653606
R-VDW	-0,0533564	0,0521407	0,0549876	0,829675	0,0808911	0,1099017
R-Median	-0,0840553	0,0422077	0,049273	0,890875	0,0468589	0,0587672
$\tau = 3{,}0; \alpha = 1{,}0$						
	β_0			β_1		
	Mean	Variance	MSE	Mean	Variance	MSE
OLS	-0,1427556	0,1167166	0,1370958	1,4464374	0,4659977	0,665304
Huber-M	-0,1886697	0,0312227	0,066819	1,1816924	0,0954459	0,128458
R-Wilcoxon	-0,1945222	0,0148154	0,0533543	0,9542	0,0115882	0,0136858
R-VDW	-0,1747286	0,0203117	0,0538418	0,91545	0,0280278	0,0351765
R-Median	-0,1984727	0,0140355	0,052727	0,962225	0,0084135	0,0098405
$\tau = 5{,}0; \alpha = 1{,}0$						
	β_0			β_1		
	Mean	Variance	MSE	Mean	Variance	MSE
OLS	-0,1516095	0,103233	0,1262184	1,4541433	0,460642	0,6668882
Huber-M	-0,1708809	0,0559943	0,0851946	1,1706907	0,1824834	0,2116188
R-Wilcoxon	-0,1776467	0,03142	0,0633783	0,9111	0,0319828	0,039886
R-VDW	-0,1495106	0,0401549	0,0635084	0,8559	0,0641147	0,0848796
R-Median	-0,1850545	0,0296265	0,0628717	0,9252	0,0251575	0,0307526
$\tau = 10{,}0; \alpha = 1{,}0$						
	β_0			β_1		
	Mean	Variance	MSE	Mean	Variance	MSE
OLS	-0,1454604	0,1066802	0,1278389	1,4485578	0,4697572	0,6709613
Huber-M	-0,1452055	0,0731024	0,094187	1,168242	0,2410109	0,2693163
R-Wilcoxon	-0,1423531	0,041445	0,0617094	0,8867	0,0473468	0,0601837
R-VDW	-0,111249	0,0510928	0,0634691	0,8241	0,0836985	0,1146393
R-Median	-0,1491565	0,0391276	0,0613753	0,9009	0,0384884	0,0483092

A Real Life Example

In this section, it is thought that the work should be supported by the application experiment. Altındağ (2003) used data obtained from a concrete experiment. In this study of Altındağ (2003), he tried to relate the amount of energy released and the pulse value. The impact value is measured by a variable called brittleness. The energy released is called the specific energy (MJ/m3). In the study, the specific energy is considered the dependent variable and the brittleness is allowed as the independent variable.

The regression model results with the OLS technique between specific energy and brittleness are given in Table 26 and the regression equation is given in Equation (15).

Table 26. Regression Analysis Result with OLS for Concrete Experiment

Model		Coefficients		t	Sig.
		b	Std. Error		
	(Constant)	14,872	3,490	4,262	,001
	B_3	,037	,005	7,050	,001
	R^2			0,684	
	F			49,709	,001

The regression equation is,

$$\widehat{SE} = 14{,}872 + 0{,}037 * B_3 \quad (15)$$

Accordingly, the model and regression coefficients established by the OLS method are statistically significant at the 95% significance level. To use this obtained equation for inference purposes, as mentioned before, the error term should have a normal distribution and not contain an outlier value.

When the Q-Q plot and the correlation between the theoretical quantiles and quantiles of input sample (r=0,991) values for the error term are examined, it is seen that the Skew-t distribution is suitable with parameters $\tau = 3{,}0$; $\alpha = 0{,}5$. The Q-Q plot is shown in Figure 1.

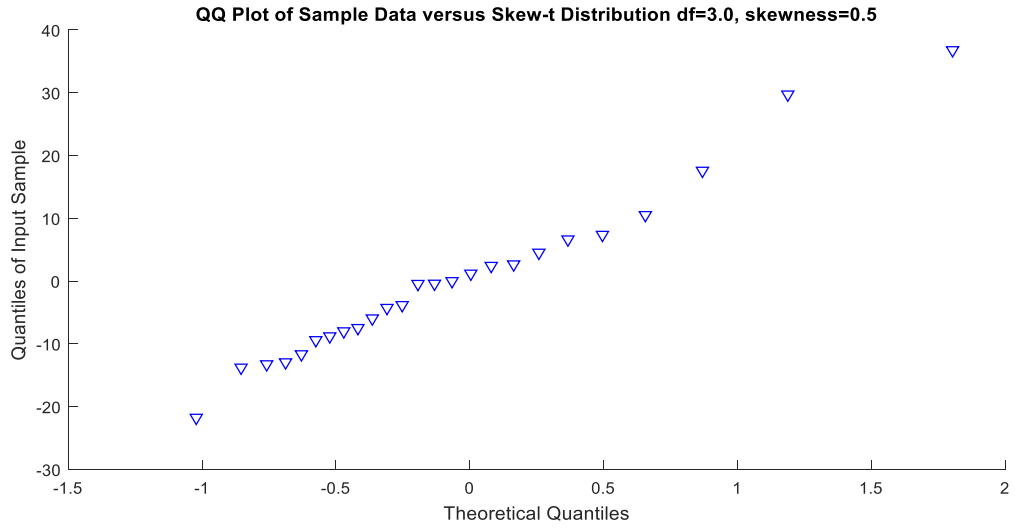

Figure 1. Q-Q Plot for Error Term

The techniques in the simulation study have been applied to concrete experiment data. The results are given in Table 27. The R-Median technique showed the lowest AIC value. Therefore, it can be said that the best technique is the R-Median technique.

Table 27. Regression Analysis Results for Concrete Experiment

Technique	$\widehat{b_0}$	$\widehat{b_1}$	**AIC**
OLS	14,872	0,037	137,993
Huber-M	13,074	0,038	138,293
R-Wilcoxon	14,381	0,038	138,020
R-VDW	14,403	0,038	138,019
R-Median	14,902	0,037	137,983

Conclusion

The OLS estimate process offers good solutions when the error terms have a normal distribution. In this study, the efficiency and robustness properties of some robust estimators have been evaluated simulation when the error terms come from skew-normal and skew-t distributions. The methods giving the smallest MSE for various skewness, scale parameters, and sample models were defined for different sample sizes.

In the cases of MSE results without outliers and with 1 and 2 outliers; R-Median and R-Wilcoxon, two of the R regression techniques, must be used in all skewness parameters that have error terms in skew-normal and skew-t distributions, and small sample sizes.

REFERENCES

Adichie, J. N. (1967) Estimates of regression parameters based on rank tests. *Ann. Math. Statist., 38*, 894-904.

Altındağ, R. (2003) Correlation of specific energy with rock brittleness concepts on cutting. *The Journal of the South African Institute of Mining and Metallurgy, 15*, 163-171.

Andrews, B. Davis, R. & Breidt, J. (2006) *Rank-Based Estimation for All-Pass Time Series Models*. NFS and EPA STAR.

Arellano-Valle, R. B. & Genton, M. G. (2005) On fundamental skew distributions. *Journal of Multivariate Analysis, 96* (1), 93–116.

Arnold, B. & Beaver, R. (2002) Skewed multivariate models related to hidden truncation and/or selective reporting (with discussion). *Test, 11*, 7-54.

Arnold, B. Beaver, R. Groeneveld, R. & Meeker, W. (1993) The nontruncated marginal of a truncated bivariate normal distribution. *Psychometrika, 58*, 471-488.

Azzalini, A. (1985) A class of distributions which includes the normal ones. *Scandinavian Journal of Statistics, 12*, 171-178.

Azzalini, A. (1986) Further results on the class of distributions which includes the normal ones. *Statistica, 46*, 199-208.

Azzalini, A. & Dalla Valle, A. (1996) The multivariate skew-normal distribution. *Biometrika, 83*, 715-726.

Azzalini, A. & Capitanio, A. (2003) Distributions generated by perturbation of symmetry with emphasis on a multivariate skew t distribution. *Journal of the Royal Statistical Society, Series B, 65*, 367-389.

Azzalini, A. & Capitanio, A. (2014) *The Skew-Normal and Related Families*. Cambridge University Press.

Basalamah, D. (2017) *Statistical Inference for A New Class Of Skew t Distribution And Its Related Properties*. PhD thesis, Bowling Green State University.

Birkes, D. & Dodge, Y. (1993) *Alternative Methods of Regression*. NY: Wiley.

Branco, M. D. & Dey, D. K. (2001) A general class of multivariate skew-elliptical distributions. *Journal of Multivariate Analysis, 79*, 99-113.

Chiogna, M. (1998) Some results on the scalar skew-normal distribution. *Journal of the Italian Statistical Society, 1*, 1-13.

David, A. (1981) *Introduction to Statistics*. St. Paul: West Publishing Company.

Dey, D. (2010) *Estimation of the Parameters of Skew Normal Distribution by Approximating the Ratio of the Normal Density and Distribution Functions*. PhD. Thesis.

Ergül, B. (2006) *Robust Regression ve Uygulamaları*. Eskişehir Osmangazi Üniversitesi, Yüksek Lisans Tezi, Eskişehir.

Evans, M. Hastings, N. & Peacock, B. (1993) *Statical Distributions*. Second Edition. A Wiley -Interscience Publication: John Wiley & Sons, Inc. New York, Chichester, Brisbane, Toronto, Singapore. Printed in the United States of America.

Fox, J. (2002) *Robust Regression*. Appendix to An R and S-PLUS Companion to Applied Regression. S-PLUS Software.

Greene, W. H. (2007) *Econometric Analysis*. Prentice Hall: New Jersey.

Gupta, A. K. Chang, F. C. & Huang, W. J. (2002) Some skew-symmetric models. *Random Operators and Stochastic Equations, 10*, 133-140.

Gupta, R. C. & Brown, N. (2001) Reliability studies of the skew-normal distribution and its application to a strength-stress model. *Communications in Statistics: Theory and Methods, 30*, 2427-2445.

Gutenbrunner, C. Jureckova, J. Koenker, R. & Portnoy, S. (1993) Tests of Linear Hypotheses Based on Regression Rank Scores. *Journal of Nonparametric Statistics, 2* (4), 307-331.

Hajek, J. Sidak, Z. & Sen, P. K. (1999) *Theory of Rank Tests*. Academic Press, San Diego.

Hasan, A. M. (2013) *A Study of Non-Central Skew t Distributions and Their Applications in Data Analysis and Change Point Detection*. PhD thesis, Bowling Green State University.

Heikkila, J. (2006) *Graduate course on Advanced statistical signal processing.* Web address: http://www.ee.oulu.fi/~jth/robust.pdf. (Retrieved Date: 02.04.2021)

Heiler, S. & Willers, R. (1988) Asymptotic normality of R-Estimates in the linear model. *Statistics, 19*, 173-184.

Henze, N. (1986) A probabilistic representation of the skew-normal distribution. *Scandinavian Journal of Statistics, 13*, 271-275.

Hodges, J. & Lehmann, E. (1963) Estimates of location based on rank tests. *Ann. Math. Stat., 34*, 598-611.

Huang, W. J. & Chen, Y.H. (2006) Quadratic forms of multivariate skew normal-symmetric distributions. *Statistics & Probability Letters, 76* (9), 871–879.

Jaeckel, L. A. (1972) Estimating regression coefficients by minimizing the dispersion of the residuals. *Ann. Math. Statist., 43*, 1449-1458.

Jureckova, J. (1971) Nonparametric estimates of regression coefficients. *Ann. Math. Statist., 42*, 1328-1338.

Jureckova, J. & Sen, P. K. (1996) *Methodology In Robust and NonParametric Statistics*. Taylor and Francis Group, NW.

Jureckova, J. Sen, P. K. & Picek, J. (2013) *Robust Statistical Procedures: Asymptotics and Interrelations*. Wiley, New York.

Jureckova, J. Koul, H. Navratil, R. & Picek, J. (2016) Behavior of R-estimators under measurement errors. *Bernoulli, 22* (2), 1093-1112.

Koul, H. L. (1971) Asymptotic behavior of a class of confidence region based on rank in regression. *Ann. Math. Statist., 42*, 466-476.

Lai, T. L. & Ying, Z. (1991) Rank Regression Methods For Left-Truncated and Right-Censored Data. *The Annals Of Statistics, 19* (2), 531-556.

Mosteller, F. & Tukey, J. W. (1977) *Data Analysis and Regression*. Philippines: Addison-Wesley Publishing Company.

Mukherjee, K. & Bai, Z.D. (2007) *R-estimation in autoregression with square-integrable score function*. The National University of Singapore.

Mukherjee, K. (2007) Generalized R-estimators under Conditional Heteroscedasticity. *Journal Of Econometrics, 141* (2), 383-415.

Mutan, O. C. & Şenoğlu, B. (2009) A Monte Carlo Comparison of Regression Estimators When the Error Distribution is Long-Tailed Symmetric. *Journal of Modern Applied Statistical Methods, 8* (1), 161-172.

Naranjo, J. D. & McKean, J. W. (1997) Rank Regression with estimated scores. *Statistics and Probability Letters, 33*, 209-216.

Öztürk, L. (2003) *Doğrusal Regresyonda Sağlam Kestirim Yöntemleri ve Karşılaştırılmaları*. Mimar Sinan Üniversitesi, Doktora Tezi, İstanbul.

Rashid, M. (2012) R Estimates and Associated Inferences for Mixed Models with Covariates in a Multi-Center Clinical Trial. *Statistics in Biopharmaceutical Research, 4*, 37-49.

Sen, P. K. (1987) On a class of rank order tests for the parallelism of several regression line. *Ann. Math. Statist., 40*, 1668-1683.

Shafiei, S. & Doostparast, M. (2014) Balakrishnan skew-t distribution and associated statistical characteristics. *Communications in Statistics-Theory and Methods, 43* (19), 4109–4122.

Wiens, D. & Zhou, J. (1994) Bounded-Influence rank estimation in the linear model. *The Canadian Journal of Statistics, 22* (2), 233-245.

Zhou, J. (1992) *Bounded-Influence R-Estimators in the Linear Model*. University of Alberta, A Thesis of Master of Science, Canada.

Comparison Of OLS, M, MM And S Regression Estimators When The Error Distribution Is Lindley-Exponential Distribution

Barış ERGÜL[1]
Arzu ALTIN YAVUZ[2]

Introduction

Regression analysis is one of the widely used techniques to determine the functional relationship between the dependent and independent variables (David, 1981). The basis of regression analysis is to determine the functional structure of an observed event. In performing regression analysis, the observed values and the events involved must be expressed by a mathematical representation or function. This created model is called a "Regression Model".

There are some assumptions for parameter estimation using the ordinary least squares (OLS) technique, a commonly used technique in regression analysis. These assumptions relate to the error terms. The error terms have the normal distribution with ε_i independent and identical, zero mean, variance σ^2. If these assumptions are rejected, they lose their significance and the obtained regression equation cannot be used for inference (Mosteller & Tukey, 1977).

When error terms are not normally distributed or when outliers are present in the data set, alternative regression methods can replace OLS. Robust regression techniques are those that reduce the effects of outliers and violations of assumptions (Öztürk, 2003). The factor that violates the normality assumption of the observed values is outliers, which are considered as a large error term. Outliers affect the statistical technique and the constructed regression model. In addition, outliers are unlikely to be values that explain the model. When the model is changed, the effect of outliers is significantly reduced. Robust regression techniques first update the observed value with outliers and analyze this updated value (Mutan & Şenoğlu, 2009).

As for robust regression analysis, M regression is quite popular. However, M estimators are robust estimators designed for long-tailed and symmetric data sets. When the data have an asymmetric distribution, their effect decreases. M, MM, and S regression are robust methods based on a special type of M regression.

Alma (2011) discussed the definition of the behavior of outliers in linear regression and compared some robust regression methods (LTS, M, MM, and S regression) using a simulation study. Yu & Yao (2017) proposed to review and describe some available and popular robust methods (OLS, LTS, LMS, MM, and S), including some recently developed methods, and compare them in terms of breakdown point and efficiency. Almetwally & Almongy (2018) discuss estimation methods compared to achieve the best estimate: the Humpel estimation method, Bisquare estimation method, Huber estimation method, S estimation method, and MM estimation method in the robust regression to determine a regression model.

[1] Araş. Gör. Dr., Eskişehir Osmangazi Üniversitesi Fen Fakültesi İstatistik Bölümü
[2] Prof. Dr., Eskişehir Osmangazi Üniversitesi Fen Fakültesi İstatistik Bölümü

Reviewing the relevant literature, there are very few studies comparing the OLS, M, MM and S regression methods. Therefore, the error terms with Lindley-exponential distribution were considered in the linear regression model of this study. These estimation methods were compared with Monte Carlo simulation for the regression model. The performance of the estimation methods was evaluated using the MSE criterion. In the second phase of the study, the Lindley-exponential distribution was introduced. Later, in the third phase, the OLS, M, MM, and S regression methods were introduced in the linear regression technique. In the fourth phase, the effectiveness of these estimation methods based on different shape parameters of the Lindley-exponential distribution was compared with a simulation study for different sample sizes.

The Lindley-Exponential Distribution

The Lindley distribution has attracted the attention of researchers because of its use in modelling lifetime data, and several papers have found that this distribution has produced excellent results. The Lindley distribution was originally proposed by Lindley (1958).

Many authors have proposed various extensions of the distribution, and some of these recent studies on the generalization of the exponential distribution include the Lindley-exponential distribution by Oguntunde et al. (2016), the Lomax-exponential distribution by Ieren & Kuhe (2018), the odd generalized exponential-exponential distribution by Maiti & Pramanik (2015) and, the Weibull-exponential distribution by Oguntunde et al. (2015). Lindley-exponential distribution is positively skewed and performs better than some existing distributions such as the conventional Lindley and exponential distributions (Oguntunde et al., 2016).

The probability density function (pdf) of Lindley-exponential distribution is defined by: (Bhati & Malik, 2016).

$$f(x,\theta,\lambda) = \frac{\theta^2\lambda\exp(-\lambda x)(1-\exp(-\lambda x))^{\theta-1})(1-\log(1-\exp(-\lambda x)))}{1+\theta}, \quad x>0, \theta, \lambda > 0$$

where θ and λ are the shape parameters.

The mean and variance of the Lindley-exponential distribution are given by Bhati & Malik (2016). The PDF plot for different values of λ and θ is shown in Figure 1.

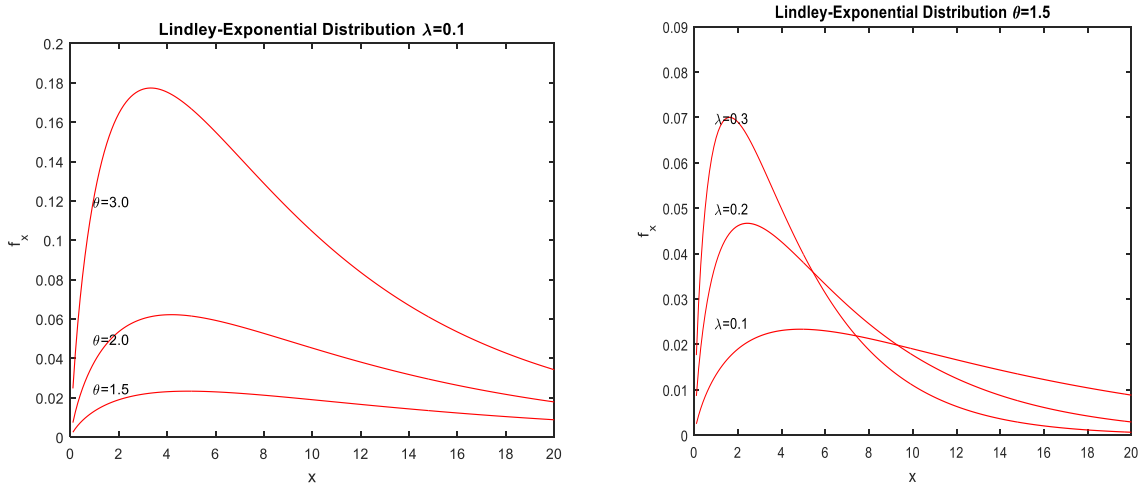

Figure 1. Lindley-Exponential PDF plot for various values of λ and θ

Methodology

The definition of linear regression in matrix form is as follows:

$$Y = (Y_1, Y_2, \dots, Y_n)^T = \boldsymbol{X\beta} + \boldsymbol{\varepsilon} \quad (1)$$

Here; $\boldsymbol{X} = (X_1^T, X_2^T, \dots, X_n^T)^T$, $n \times p$ shows a dimensional matrix of independent variables, $\boldsymbol{\beta} = (\beta_1, \beta_2, \dots, \beta_p)^T$, displays unknown regression parameters and ε_i demonstrates a random variable that is defined as independent and identical but referred to as an error term whose distribution function is unknown. The first column of $\boldsymbol{X}$ is comprised of $(1,1, \dots,1)^T$ (Greene, 2007).

Least Squares Technique

The presentation of multiple linear regression in matrix form with *p* number of independent variables $X_1, X_2, , , X_p$ is as in Equation 2:

$$Y = \begin{bmatrix} y_1 \\ y_2 \\ . \\ . \\ y_n \end{bmatrix} X = \begin{bmatrix} 1 x_{11} x_{12} \dots x_{1p} \\ 1 x_{21} x_{22} \dots x_{2p} \\ . \quad . \quad . \quad \dots \quad . \\ . \quad . \quad . \quad \dots \quad . \\ . \quad . \quad . \quad \dots \quad . \\ 1 x_{n1} x_{n2} \dots x_{np} \end{bmatrix} b = \begin{bmatrix} \beta_1 \\ \beta_2 \\ . \\ . \\ . \\ \beta_p \end{bmatrix} \varepsilon = \begin{bmatrix} \varepsilon_1 \\ \varepsilon_2 \\ . \\ . \\ . \\ \varepsilon_n \end{bmatrix} \quad (2)$$

$\boldsymbol{Y}$: dependent variable vector; $X_1, X_2, , , X_p$: independent variables and *X* data matrix; β_i ($0 \leq i \leq p$) regression coefficient; ε random error vector.

In the least-squares technique, the aim is to minimize the sum of squares of error terms. In the simple linear regression model given in Equation 3, the least-squares estimators of parameters β_0 and β_1 are as follows:

$$\hat{\beta}_0 = \bar{y} - \hat{\beta}_1 \bar{x}$$

$$\hat{\beta}_1 = \frac{\sum_{i=1}^{n} (x_i - \bar{x})(y_i - \bar{y})}{\sum_{i=1}^{n} (x_i - \bar{x})^2} \quad (3)$$

M-Regression Technique

When the normality assumption is violated for the distribution of error terms in regression analysis, it is not appropriate to use the least-squares technique and use the obtained model for estimation., M-Regression is developed to be used for the case of errors having more long-tailed symmetric distribution than normal when this assumption is not met. This approach is a mediator between the robustness of L1 estimators and the effectiveness of least squares. M-estimation is known as the generalized form of maximum likelihood predictors. M-estimation is defined below in Equation (4) based on the minimization of one of the functions of errors:

$$\sum_{i=1}^{n} \rho(\hat{e_i}), \quad i = 1,2, \dots, n \quad (4)$$

Here, ρ(.) is a continuous, non-negative and symmetric function also referred to as an objective function whose only minimum is zero?. M-estimation is the robust predictor that minimizes ρ(.) the function is given in Equation (4). In the literature, many objective functions (Huber, Andrews, Tukey) exist with these characteristics (Birkes & Dodge, 1993). The most widely used objective function is the one suggested by Huber. Huber's suggested objective function is given in Equation (5).

$$\rho(\hat{e_i}) = \begin{cases} \widehat{e_i^2/2}, & |\hat{e_i}| \leq k \\ k|\hat{e_i}| - \frac{k^2}{2}, & |\hat{e_i}| \geq k \end{cases} \quad (5)$$

Here, k is selected from values that are called constant and have high efficiency in the normal distribution. The value of k=1.345 is used for the Huber predictor.

To estimate parameters in the regression model, the derivative of Equation (5) is calculated, and its minimum value is found by vanishing.

$$\sum_{i=1}^{n} \psi(\hat{e_i}) x_i = 0\,, \quad i = 1,2,\dots,n \quad (6)$$

Here, ψ(.) is known as the score function and is a derivative of ρ(.). Analysis of Equation (7) is referred to as M-estimation. The result is not a standardized outcome. First, standardization of error terms must be done.

$$\sum_{i=1}^{n} \psi(\hat{e_i}/s) x_i = 0\,, \quad i = 1,2,\dots,n \quad (7)$$

Here, s is a simultaneously predicted scale factor. As for the predictor of s, median absolute deviation (MAD) is used and defined as below:

$$s = \frac{MAD}{0.6745} \quad (8)$$

Here, $MAD\ (residual) = median\{|\hat{e_i} - median\{\hat{e_i}\}|\}, i = 1,2,\dots,n$. Increasing residual magnitudes are substituted by appropriate weight values. Equation (12) can be rewritten as follows by using $w_i = w(\hat{e_i}) = \frac{\psi(\hat{e_i})}{\hat{e_i}}, i = 1,2,\dots,n$

$$\sum_{i=1}^{n} w_i(\hat{e_i}/s) x_i = 0\,, \quad i = 1,2,\dots,n \quad (9)$$

In practice, M-estimation may not be calculated directly from data because their weight values are dependent on residuals. For that reason, to obtain M-estimation iteratively reweighted least squares algorithm is used.

S Regression

S-regression is an estimation method defined by Rousseuw & Yohai (1984), which is a regression estimation associated with M-regression. S-regression is based on scaling the error terms by M- regression. M-regression is the weakness of the estimation method that does not take the median value by weighting function and considering the data distribution. S-regression is found by minimizing the following function:

$$\min \sum_{i=1}^{n} \rho\left(\frac{y_i - \hat{y}_i}{\widehat{\sigma_s}}\right) \quad (10)$$

where $\widehat{\sigma_s} = \sqrt{\frac{1}{nK}\sum_{i=1}^{n} w_i e_i^2}$, $K = 0.199$ and w_i, is the weight function.

$$w_i = \begin{cases} [1 - (\frac{u_i}{c})^2]^2, & |u_i| \le c \\ 0, & |u_i| > c \end{cases} \quad (11)$$

where $c = 1.547$ and $u_i = \frac{e_i}{\widehat{\sigma_s}}$.

The ψ function is used to find weights and calculated as follows:

$$\rho(u_i) = \begin{cases} u_i \left[1 - \left(\frac{u_i}{c}\right)^2\right]^2, & |u_i| \le c \\ 0, & |u_i| > c \end{cases} \quad (12)$$

It is calculated using the following algorithm: (Susanti et al., 2014)

1. Calculate the regression coefficients with OLS.
2. Test the regression model assumptions.
3. Diagnose the outliers.
4. Set $\hat{\beta}^0$ with OLS.
5. Determine the error term.
6. Calculate $\widehat{\sigma_i} = \begin{cases} \frac{median|e_i - median(e_i)|}{0{,}6745}, & iteration = 1 \\ \sqrt{\frac{1}{nK}\sum_{i=1}^{n} w_i e_i^2}, & iteration > 1 \end{cases}$.
7.Calculate $u_i = \frac{e_i}{\widehat{\sigma_i}}$.
8. Calculate $w_i = \begin{cases} \begin{cases} [1 - (\frac{u_i}{1{,}547})^2]^2, & |u_i| \le 1{,}547 \\ 0, & |u_i| > 1{,}547 \end{cases}, iterasyon = 1 \\ \frac{\rho(u)}{u^2}, \ iterasyon > 1 \end{cases}$
9. Using the weight values, calculate $\hat{\beta}^s$ with weighted OLS.
10. Apply between steps 5-8 until the parameter values get closer.
11. Test the parameter significance for $\hat{\beta}^s$.

MM Regression

MM-regression is an estimation method that is a high and high degradation statistical activity method (assuming that the error terms are normally distributed). Proposed by Yohai (1987). MM-regression is obtained by applying the estimation method to the error terms obtained by the S-regression.

It is obtained by solving the following function:

$$\sum_{i=1}^{n} \rho\left(\frac{y_i - \sum_{j=0}^{k} X_{ij}\widehat{\beta_j}}{s_{MM}}\right) X_{ij} = 0 \quad (13)$$

where s_{MM} is the standard deviation of error terms using the S Regression and ρ is the weight function of Tukey.

It is calculated using the following algorithm: (Almetwally & Almongy, 2018)

1. Calculate the regression coefficients with OLS.
2. Test the regression model assumptions.
3. Diagnose the outliers.
4. Set $\hat{\beta}^0$ with S Regression.
5. Determine the error term using S Regression.
6. Calculate $\widehat{\sigma_i} = \widehat{\sigma_{sn}}$

7.Calculate $u_i = \frac{e_i}{\hat{\sigma}_i}$.

8. Calculate $w_i = \begin{cases} [1 - (\frac{u_i}{4{,}685})^2]^2, & |u_i| \leq 4{,}685 \\ 0, & |u_i| > 4{,}685 \end{cases}$

9. Using the weight values, calculate $\hat{\beta}^{MM}$ with weighted OLS.

10. Apply between steps 5-8 until the parameter values get closer.

11. Test the parameter significance for $\hat{\beta}^{MM}$.

Results

In the simulation studies, N=100000/n was performed, and error terms for $n = 10{,}20{,}30{,}50$ sample sizes and error terms with different shape and scale parameters from Lindley-exponential distribution were obtained. The simulation means, variances, and MSE were calculated for the values of $\beta_0 = 0$ and $\beta_1 = 1$. These values are given in Table 1-4. 1 outlier was generated and for this 1 outlier, the simulation means, variances and MSE values were calculated. The simulation values are shown in Tables 5-8. Also, 2 outliers were generated and the simulation means, variances and MSE values were calculated for these 2 outlier simulation. The simulation values are listed in Tables 9-12.

Based on the MSE results without outliers, when analyzing the OLS, M, MM, and S regression results with a sample size of n=10; given the error terms distribution is the Lindley-exponential distribution ($\theta = 1.5$; $\lambda = 0.5{,}1.0{,}1.5$) to estimate the $\hat{\beta}_0$ parameter, the S-regression technique is found to produce more effective results compared to OLS, M, and MM-regression techniques. For all other sample sizes, it is observed that the S regression technique provides more effective results compared to the OLS, M and MM techniques. Since the distribution of error terms is the Lindley-exponential distribution, the OLS technique performs the worst for $\hat{\beta}_1$.

Based on the MSE results with 1 and 2 outliers, when analyzing the OLS, M and MM-regression results with a sample size of n=10 and given the error terms distribution is the Lindley-Exponential distribution with all parameters to estimate the parameter $\hat{\beta}_0$, it is found that the S-regression technique provides more effective results compared to the OLS, M, and MM-regression techniques. It also provides similar results for the estimation of the $\hat{\beta}_1$ parameter. For all other sample sizes, it is observed that the S regression technique provides more effective results compared to the OLS, M, and MM-regression techniques. For error terms in the Lindley-exponential distribution, the OLS technique performs the worst for $\hat{\beta}_1$.

When θ is held constant and λ increases, the MSE decreases. As n increases, the bias decreases and the MSE decreases. As the number of outliers increases, the MSE for OLS increases. As the number of outliers increases, the MSE for M, MM, and S-regression decreases.

Table 1. Means, Variances and MSE's for the estimators $\widehat{\beta_0}$ and $\widehat{\beta_1}$, $n = 10$ when the error term is the Lindley-Exponential distribution

$\theta = 1.5;\ \lambda = 0.5$						
	β_0			β_1		
	Mean	Variance	MSE	Mean	Variance	MSE
OLS	1.9810	1.7987	5.7231	0.9653	5.4789	5.4801
M Regression	1.3573	1.7265	3.9688	0.9816	5.0493	5.0496
MM Regression	1.3545	1.5291	3.2995	0.9811	4.1542	4.1545
S Regression	1.3524	1.5285	3.2917	0.9808	4.1527	4.1530
$\theta = 1.5;\ \lambda = 1.0$						
	β_0			β_1		
	Mean	Variance	MSE	Mean	Variance	MSE
OLS	0.9915	0.4497	1.4308	0.9827	1.3697	1.3700
M Regression	0.6787	0.4316	0.9922	0.9908	1.3123	1.3124
MM Regression	0.6316	0.3821	0.9915	0.9907	1.0381	1.0382
S Regression	0.6321	0.3823	0.9918	0.9909	1.0385	1.0386
$\theta = 1.5;\ \lambda = 1.5$						
	β_0			β_1		
	Mean	Variance	MSE	Mean	Variance	MSE
OLS	0.6603	0.1999	0.6359	0.9884	0.6088	0.6089
M Regression	0.4524	0.1363	0.4410	0.9919	0.5721	0.5722
MM Regression	0.4518	0.1299	0.3777	0.9940	0.4616	0.4617
S Regression	0.4510	0.1298	0.3770	0.9942	0.4614	0.4615

Table 2. Means, Variances and MSE's for the estimators $\widehat{\beta_0}$ and $\widehat{\beta_1}$, $n = 20$ when the error term is the Lindley-Exponential distribution

$\theta = 1.5;\ \lambda = 0.5$						
	β_0			β_1		
	Mean	Variance	MSE	Mean	Variance	MSE
OLS	1.9802	0.8175	4.7426	0.9931	2.4620	2.4621
M Regression	1.1356	0.7189	2.0085	0.9959	2.0422	2.0423
MM Regression	1.0724	0.5585	2.0009	0.9963	1.4443	1.4444
S Regression	1.0719	0.5581	2.0002	0.9967	1.4430	1.4431
$\theta = 1.5;\ \lambda = 1.0$						
	β_0			β_1		
	Mean	Variance	MSE	Mean	Variance	MSE
OLS	0.9906	0.2044	1.1856	0.9965	0.6155	0.6156
M Regression	0.5978	0.1797	0.5021	0.9979	0.5106	0.5107
MM Regression	0.5855	0.1395	0.5011	0.9980	0.3607	0.3609
S Regression	0.5862	0.1396	0.5015	0.9982	0.3611	0.3614
$\theta = 1.5;\ \lambda = 1.5$						
	β_0			β_1		
	Mean	Variance	MSE	Mean	Variance	MSE
OLS	0.6602	0.0908	0.5270	0.9977	0.2735	0.2736
M Regression	0.3785	0.0799	0.2232	0.9986	0.2269	0.2270
MM Regression	0.3241	0.0620	0.2218	0.9988	0.1604	0.1605
S Regression	0.3233	0.0620	0.2218	0.9989	0.1603	0.1604

Table 3. Means, Variances and MSE's for the estimators $\widehat{\beta_0}$ and $\widehat{\beta_1}$, $n = 30$ when the error term is the Lindley-Exponential distribution

$\theta = 1.5;\ \lambda = 0.5$						
	β_0			β_1		
	Mean	Variance	MSE	Mean	Variance	MSE
OLS	1.9649	0.5161	4.3771	1.0091	1.5657	1.5658
M Regression	1.0487	0.4044	1.5042	1.0078	1.1560	1.1561
MM Regression	1.0391	0.3434	1.4121	0.9983	0.8738	0.8739
S Regression	1.0354	0.3426	1.4114	0.9987	0.8727	0.8728
$\theta = 1.5;\ \lambda = 1.0$						
	β_0			β_1		
	Mean	Variance	MSE	Mean	Variance	MSE
OLS	0.9825	0.1290	1.0943	1.0045	0.3914	0.3915
M Regression	0.5244	0.1011	0.3760	1.0039	0.2890	0.2891
MM Regression	0.5195	0.0868	0.3480	0.9989	0.2185	0.2186
S Regression	0.5187	0.0861	0.3473	0.9991	0.2182	0.2183
$\theta = 1.5;\ \lambda = 1.5$						
	β_0			β_1		
	Mean	Variance	MSE	Mean	Variance	MSE
OLS	0.6550	0.0573	0.4863	1.0030	0.1740	0.1741
M Regression	0.3496	0.0449	0.1671	1.0026	0.1284	0.1285
MM Regression	0.3430	0.0381	0.1613	0.9991	0.0971	0.0972
S Regression	0.3431	0.0380	0.1611	0.9992	0.0969	0.0970

Table 4. Means, Variances and MSE's for the estimators $\widehat{\beta_0}$ and $\widehat{\beta_1}$, $n = 50$ when the error term is the Lindley-Exponential distribution

$\theta = 1.5;\ \lambda = 0.5$						
	β_0			β_1		
	Mean	Variance	MSE	Mean	Variance	MSE
OLS	1.9608	0.2984	4.1827	1.0005	1.5657	0.8961
M Regression	0.9922	0.1977	1.1822	0.9986	0.5523	0.5524
MM Regression	0.9911	0.1944	1.1141	0.9988	0.4856	0.4857
S Regression	0.9901	0.1941	1.1114	0.9991	0.4849	0.4850
$\theta = 1.5;\ \lambda = 1.0$						
	β_0			β_1		
	Mean	Variance	MSE	Mean	Variance	MSE
OLS	0.9814	0.0746	1.0457	1.0002	0.2240	0.2241
M Regression	0.4960	0.0494	0.2955	0.9991	0.1380	0.1381
MM Regression	0.4955	0.0486	0.2921	0.9993	0.1214	0.1215
S Regression	0.4901	0.0485	0.2912	0.9995	0.1212	0.1213
$\theta = 1.5;\ \lambda = 1.5$						
	β_0			β_1		
	Mean	Variance	MSE	Mean	Variance	MSE
OLS	0.6539	0.0332	0.4647	1.0001	0.0995	0.0996
M Regression	0.3307	0.0219	0.1314	0.9994	0.0614	0.0615
MM Regression	0.3266	0.0216	0.1282	0.9995	0.0540	0.0541
S Regression	0.3243	0.0213	0.1274	0.9995	0.0538	0.0540

Table 5. Means, Variances and MSE's for the estimators $\widehat{\beta_0}$ and $\widehat{\beta_1}$, $n = 10$ when the error term is the Lindley-Exponential distribution with 1 outlier

$\theta = 1.5;\ \lambda = 0.5$						
	β_0			β_1		
	Mean	Variance	MSE	Mean	Variance	MSE
OLS	2.1905	2.5131	7.3113	1.0392	7.8560	7.8584
M Regression	1.2907	1.1581	3.7918	1.0289	4.5019	5.0020
MM Regression	1.2884	1.1417	3.0408	1.0228	4.1053	4.1055
S Regression	1.2781	1.1398	3.0392	1.0209	4.1022	4.1023
$\theta = 1.5;\ \lambda = 1.0$						
	β_0			β_1		
	Mean	Variance	MSE	Mean	Variance	MSE
OLS	1.0960	0.6479	1.8492	1.0376	2.0676	2.0722
M Regression	0.6399	0.4132	0.9907	1.0087	1.3096	1.3097
MM Regression	0.6204	0.3653	0.9903	1.0083	1.0187	1.0189
S Regression	0.6123	0.3647	0.9894	1.0029	1.0176	1.0177
$\theta = 1.5;\ \lambda = 1.5$						
	β_0			β_1		
	Mean	Variance	MSE	Mean	Variance	MSE
OLS	0.7312	0.1985	0.6532	1.0307	0.6751	0.9811
M Regression	0.4011	0.1242	0.4051	1.0013	0.5648	0.5650
MM Regression	0.3957	0.1228	0.3466	1.0008	0.4522	0.4523
S Regression	0.3937	0.1216	0.3426	1.0004	0.4518	0.4519

Table 6. Means, Variances and MSE's for the estimators $\widehat{\beta_0}$ and $\widehat{\beta_1}$, $n = 20$ when the error term is the Lindley-Exponential distribution with 1 outlier

$\theta = 1.5;\ \lambda = 0.5$						
	β_0			β_1		
	Mean	Variance	MSE	Mean	Variance	MSE
OLS	2.0851	0.9850	5.3329	1.0343	3.0257	3.0268
M Regression	1.1238	0.7074	1.9951	1.0238	2.0238	2.0245
MM Regression	1.0655	0.5382	1.9908	1.0188	1.4183	1.4186
S Regression	1.0645	0.5368	1.9902	1.0119	1.4122	1.4123
$\theta = 1.5;\ \lambda = 1.0$						
	β_0			β_1		
	Mean	Variance	MSE	Mean	Variance	MSE
OLS	1.0927	0.2504	1.3376	1.0326	0.7803	0.7820
M Regression	0.5399	0.1632	0.4107	1.0074	0.4697	0.4699
MM Regression	0.5204	0.1253	0.4096	1.0063	0.3387	0.3388
S Regression	0.5123	0.1246	0.4090	1.0012	0.3374	0.3375
$\theta = 1.5;\ \lambda = 1.5$						
	β_0			β_1		
	Mean	Variance	MSE	Mean	Variance	MSE
OLS	0.6952	0.1135	0.5968	1.0310	0.3597	0.3616
M Regression	0.3511	0.0642	0.2111	1.0003	0.1948	0.1949
MM Regression	0.3148	0.0519	0.2106	1.0002	0.1522	0.1523
S Regression	0.3134	0.0516	0.2102	1.0001	0.1518	0.1519

Table 7. Means, Variances and MSE's for the estimators $\widehat{\beta_0}$ and $\widehat{\beta_1}$, $n = 30$ when the error term is the Lindley-Exponential distribution with 1 outlier

$\theta = 1.5;\ \lambda = 0.5$						
	β_0			β_1		
	Mean	Variance	MSE	Mean	Variance	MSE
OLS	2.0347	0.5927	4.7328	1.0346	1.8165	1.8177
M Regression	1.0704	0.4196	1.5654	1.0227	1.2103	1.2108
MM Regression	1.0286	0.3213	1.2215	1.0174	0.8640	0.8644
S Regression	1.0221	0.3206	1.2208	1.0106	0.8627	0.8629
$\theta = 1.5;\ \lambda = 1.0$						
	β_0			β_1		
	Mean	Variance	MSE	Mean	Variance	MSE
OLS	1.0174	0.1499	1.1849	1.0338	0.4642	0.4654
M Regression	0.5196	0.1004	0.3465	1.0046	0.2437	0.2438
MM Regression	0.5174	0.0808	0.3410	0.9991	0.2057	0.2058
S Regression	0.5166	0.0801	0.3407	0.9993	0.2048	0.2049
$\theta = 1.5;\ \lambda = 1.5$						
	β_0			β_1		
	Mean	Variance	MSE	Mean	Variance	MSE
OLS	0.6783	0.0675	0.5275	1.0335	0.2119	0.2130
M Regression	0.3219	0.0369	0.1579	1.0016	0.1178	0.1179
MM Regression	0.3210	0.0324	0.1517	0.9995	0.0891	0.0892
S Regression	0.3204	0.0312	0.1509	0.9997	0.0889	0.0890

Table 8. Means, Variances and MSE's for the estimators $\widehat{\beta_0}$ and $\widehat{\beta_1}$, $n = 50$ when the error term is the Lindley-Exponential distribution with 1 outlier

$\theta = 1.5;\ \lambda = 0.5$						
	β_0			β_1		
	Mean	Variance	MSE	Mean	Variance	MSE
OLS	2.0111	0.3264	4.1737	1.0159	0.9942	0.9946
M Regression	0.9812	0.1917	1.1760	1.0069	0.5493	0.5495
MM Regression	0.9806	0.1914	1.1642	0.9990	0.5266	0.5267
S Regression	0.9801	0.1911	1.1616	0.9994	0.5259	0.5260
$\theta = 1.5;\ \lambda = 1.0$						
	β_0			β_1		
	Mean	Variance	MSE	Mean	Variance	MSE
OLS	1.0055	0.0722	1.0333	1.0138	0.2224	0.2225
M Regression	0.4837	0.0455	0.2835	1.0012	0.1316	0.1317
MM Regression	0.4825	0.0443	0.2827	0.9993	0.1184	0.1185
S Regression	0.4817	0.0441	0.2822	0.9995	0.1178	0.1179
$\theta = 1.5;\ \lambda = 1.5$						
	β_0			β_1		
	Mean	Variance	MSE	Mean	Variance	MSE
OLS	0.6404	0.0319	0.4563	1.0127	0.1042	0.1046
M Regression	0.3287	0.0208	0.1259	0.9996	0.0533	0.0535
MM Regression	0.3215	0.0207	0.1222	0.9997	0.0525	0.0527
S Regression	0.3208	0.0206	0.1219	0.9998	0.0521	0.0522

Table 9. Means, Variances and MSE's for the estimators $\widehat{\beta_0}$ and $\widehat{\beta_1}$, $n = 10$ when the error term is the Lindley-Exponential distribution with 2 outliers

$\theta = 1.5;\ \lambda = 0.5$						
	β_0			β_1		
	Mean	Variance	MSE	Mean	Variance	MSE
OLS	2.3978	3.2117	8.9613	1.1131	10.1479	10.1607
M Regression	1.2577	2.1564	2.4913	1.0169	3.7289	3.7302
MM Regression	1.2465	1.1419	2.1404	1.0118	3.6144	3.6156
S Regression	1.2443	1.1373	2.1343	1.0107	3.6072	3.6080
$\theta = 1.5;\ \lambda = 1.0$						
	β_0			β_1		
	Mean	Variance	MSE	Mean	Variance	MSE
OLS	1.2004	0.8372	2.2781	1.1028	2.7229	2.7422
M Regression	0.7083	0.5103	0.9847	1.0053	1.2494	1.2522
MM Regression	0.6107	0.3393	0.9816	1.0022	1.0062	1.0066
S Regression	0.6093	0.3364	0.9782	1.0013	1.0044	1.0047
$\theta = 1.5;\ \lambda = 1.5$						
	β_0			β_1		
	Mean	Variance	MSE	Mean	Variance	MSE
OLS	0.8013	0.3905	1.0324	1.1006	1.3089	1.3365
M Regression	0.3674	0.1228	0.3424	1.0038	1.1548	1.1550
MM Regression	0.3556	0.1209	0.3402	1.0016	1.0026	1.0027
S Regression	0.3542	0.1186	0.3374	1.0002	1.0011	1.0012

Table 10. Means, Variances and MSE's for the estimators $\widehat{\beta_0}$ and $\widehat{\beta_1}$, $n = 20$ when the error term is the Lindley-Exponential distribution with 2 outliers

$\theta = 1.5;\ \lambda = 0.5$						
	β_0			β_1		
	Mean	Variance	MSE	Mean	Variance	MSE
OLS	2.1854	1.1484	5.9243	1.0834	3.5680	3.5749
M Regression	1.1180	0.6378	1.9342	1.0186	2.0046	2.0114
MM Regression	1.0572	0.5144	1.9317	1.0114	1.3543	1.3623
S Regression	1.0553	0.5129	1.9309	1.0111	1.3521	1.3592
$\theta = 1.5;\ \lambda = 1.0$						
	β_0			β_1		
	Mean	Variance	MSE	Mean	Variance	MSE
OLS	1.0929	0.2949	1.4893	1.0911	0.9369	0.9452
M Regression	0.5206	0.1579	0.4029	1.0116	0.3627	0.3633
MM Regression	0.5136	0.1189	0.3856	1.0093	0.3281	0.3284
S Regression	0.5017	0.1148	0.3848	1.0085	0.3266	0.3268
$\theta = 1.5;\ \lambda = 1.5$						
	β_0			β_1		
	Mean	Variance	MSE	Mean	Variance	MSE
OLS	0.7288	0.1352	0.6663	1.0735	0.4407	0.4495
M Regression	0.3287	0.0584	0.2072	1.0028	0.1545	0.1548
MM Regression	0.3031	0.0479	0.1993	1.0012	0.1488	0.1489
S Regression	0.3024	0.0462	0.1988	1.0009	0.1478	0.1479

Table 11. Means, Variances and MSE's for the estimators $\widehat{\beta_0}$ and $\widehat{\beta_1}$, $n = 30$ when the error term is the Lindley-Exponential distribution with 2 outliers

$\theta = 1.5;\ \lambda = 0.5$						
	β_0			β_1		
	Mean	Variance	MSE	Mean	Variance	MSE
OLS	2.0982	0.6645	5.0668	1.0719	2.0588	2.0640
M Regression	1.0660	0.3988	1.5443	1.0156	1.1935	1.1946
MM Regression	1.0122	0.3073	1.2077	1.0124	0.8352	0.8359
S Regression	1.0101	0.3054	1.2068	1.0100	0.8312	0.8316
$\theta = 1.5;\ \lambda = 1.0$						
	β_0			β_1		
	Mean	Variance	MSE	Mean	Variance	MSE
OLS	1.0491	0.1696	1.2702	1.0692	0.5350	0.5398
M Regression	0.5069	0.0993	0.3235	1.0126	0.2378	0.2380
MM Regression	0.5054	0.0738	0.3168	0.9993	0.1926	0.1927
S Regression	0.5046	0.0733	0.3157	0.9995	0.1919	0.1920
$\theta = 1.5;\ \lambda = 1.5$						
	β_0			β_1		
	Mean	Variance	MSE	Mean	Variance	MSE
OLS	0.6994	0.0772	0.5663	1.0684	0.2487	0.2530
M Regression	0.2756	0.0309	0.1411	1.0014	0.1018	0.1019
MM Regression	0.2626	0.0263	0.1387	0.9996	0.0721	0.0722
S Regression	0.2613	0.0258	0.1379	0.9998	0.0717	0.0718

Table 12. Means, Variances and MSE's for the estimators $\widehat{\beta_0}$ and $\widehat{\beta_1}$, $n = 50$ when the error term is the Lindley-Exponential distribution with 2 outliers

$\theta = 1.5;\ \lambda = 0.5$						
	β_0			β_1		
	Mean	Variance	MSE	Mean	Variance	MSE
OLS	2.0492	0.3492	4.5483	1.0413	1.0750	1.0766
M Regression	0.9614	0.1537	1.1649	1.0063	0.5403	0.5405
MM Regression	0.9536	0.1494	1.1523	0.9992	0.5212	0.5213
S Regression	0.9531	0.1488	1.1512	0.9995	0.5205	0.5206
$\theta = 1.5;\ \lambda = 1.0$						
	β_0			β_1		
	Mean	Variance	MSE	Mean	Variance	MSE
OLS	1.0245	0.0885	1.1381	1.0408	0.2761	0.2776
M Regression	0.4639	0.0331	0.2742	1.0042	0.1117	0.1118
MM Regression	0.4563	0.0325	0.2726	0.9994	0.1072	0.1073
S Regression	0.4552	0.0317	0.2721	0.9997	0.1069	0.1070
$\theta = 1.5;\ \lambda = 1.5$						
	β_0			β_1		
	Mean	Variance	MSE	Mean	Variance	MSE
OLS	0.6825	0.0399	0.5063	1.0406	0.1266	0.1273
M Regression	0.3049	0.0184	0.1017	0.9996	0.0364	0.0365
MM Regression	0.3028	0.0179	0.1002	0.9998	0.0347	0.0348
S Regression	0.3013	0.0174	0.0998	0.9999	0.0339	0.0340

A Real Life Example

In this section, it is thought that the work should be supported by the application experiment. Altındağ (2003) used data obtained from a concrete experiment. In this study of Altındağ (2003), he tried to relate the amount of energy released and the pulse value. The impact value is measured by a variable called brittleness. The energy released is called the specific

energy (MJ/m3). In the study, the specific energy is considered the dependent variable and the brittleness is allowed as the independent variable.

The regression model results with the OLS technique between specific energy and brittleness are given in Table 13 and the regression equation is given in Equation (14).

Table 13. Regression Analysis Result with OLS for Concrete Experiment

Model		Coefficients		t	Sig.
		b	Std. Error		
	(Constant)	14,872	3,490	4,262	,001
	B_3	,037	,005	7,050	,001
	R^2			0,684	
	F			49,709	,001

The regression equation is,

$$\widehat{SE} = 14{,}872 + 0{,}037 * B_3 \quad (14)$$

Accordingly, the model and regression coefficients established by the OLS method are statistically significant at the 95% significance level. To use this obtained equation for inference purposes, as mentioned before, the error term should have a normal distribution and not contain an outlier value.

When the Q-Q plot and the correlation between the theoretical quantiles and quantiles of input sample (r=0,9815) values for the error term are examined, it is seen that the Lindley-exponential distribution is suitable with parameters θ = 2.0; λ = 1.5. The Q-Q plot is shown in Figure 2.

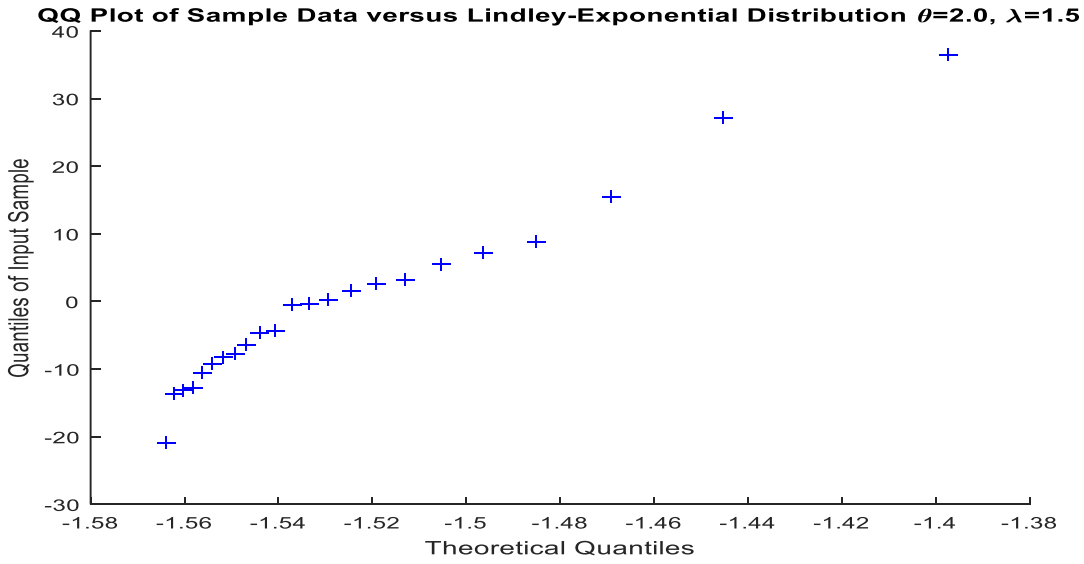

Figure 2. Q-Q Plot for Error Term

The techniques in the simulation study have been applied to concrete experiment data. The results are given in Table 14. The S Regression technique showed the lowest AIC value and highest R^2. Therefore, it can be said that the best technique is the S Regression technique.

Table 14. Regression Analysis Results for Concrete Experiment

Technique	$\widehat{b_0}$	$\widehat{b_1}$	**AIC**	$\mathbf{R^2}$
OLS	14.87229	0.03723	210.93741	0.68371
M	12.58289	0.02999	148.72123	0.83764
MM	12.54671	0.02987	148.70148	0.83982
S	12.45514	0.02967	147.06554	0.84273

Conclusion

The OLS estimation procedure provides good solutions when the error terms have a normal distribution. In this study, the efficiency and robustness properties of some robust estimators were evaluated by simulations when the error terms are from the Lindley-exponential distribution. The methods yielded the smallest MSE for different shape parameters and were defined for different sample sizes. For the MSE results without outliers and with 1 and 2 outliers, the OLS, M, MM, and S-regression methods must be used for all shape parameters with error terms from the Lindley-exponential distribution and small sample sizes. For all other sample sizes, it is observed that the S-regression technique gives more effective results compared to the OLS, M and MM techniques.

According to the results, the error terms originate from the Lindley-exponential distribution, and when θ is held constant and λ increases, the MSE decreases. As n increases, the bias decreases and the MSE decreases. As the number of outliers increases, the MSE for OLS increases. As the number of outliers increases, the MSE for M, MM and S-regression decreases.

REFERENCES

Almetwally, E. M. & Almongy, H. M. (2018) Comparison Between M-Estimation, S-Estimation, and MM Estimation Methods Of Robust Estimation With Application and Simulation. *International Journal of Mathematical Archive*, 9 (11), 55-63.

Alma, Ö. G. (2011) Comparison of Robust Regression Methods in Linear Regression. *Int. J. Contemp. Math. Sciences*, 6 (9), 409 – 421.

Bhati, D. & Malik, A. M. (2016) On Lindley-Exponential Distribution: Properties and Application. *arXiv: 1406.3106v1 [stat.AP]*, 1-17.

Birkes, D. & Dodge, Y. (1993) *Alternative Methods of Regression*. NY: Wiley.

David, A. (1981) *Introduction to Statistics*. St. Paul: West Publishing Company.

Greene, W. H. (2007) *Econometric Analysis*. Prentice Hall: New Jersey.

Ieren, T. G. & Kuhe, A. D. (2018) On the properties and applications of Lomax-exponential distribution. *Asian J. Prob. Stat*., 1 (4), 1-13.

Lindley, D. V. (1958) Fiducial distributions and Bayes theorem. *J. R. Stat. Soc. Series: B*, 20 (1), 102–107.

Maiti, S. S. & Pramanik, S. (2015) Odds generalized exponential-exponential distribution. *J. of Data Sci.,* 13, 733-754.

Mosteller, F. & Tukey, J. W. (1977) *Data Analysis and Regression*. Philippines: Addison-Wesley Publishing Company.

Mutan, O. C. & Şenoğlu, B. (2009) A Monte Carlo Comparison of Regression Estimators When the Error Distribution is Long-Tailed Symmetric. *Journal of Modern Applied Statistical Methods*, 8 (1), 161-172.

Oguntunde, P. E., Adejumo, A. O., Okagbue, H. I. & Rastogi, M.K. (2016) Statistical properties and applications of a new Lindley exponential distribution. *Gazi University Journal of Science*, 29 (4), 831-838.

Oguntunde, P. E., Balogun, O. S., Okagbue, H. I. & Bishop, S. A. (2015) The Weibull-exponential distribution: Its properties and applications. *J. Appl. Sci*., 15 (11), 1305-1311.

Öztürk, L. (2003) *Doğrusal Regresyonda Sağlam Kestirim Yöntemleri ve Karşılaştırılmaları*. Mimar Sinan Üniversitesi, Doktora Tezi, İstanbul.

Rousseeuw, P. J. & Yohai, V. J. (1984) *Robust regression using S-estimators. In W. H. J. Franke and D. Martin (Editors.), Robust and Nonlinear Time Series Analysis*. Springer-Verlag, New York.

Susanti, Y., Pratiwi, H., Sulistijowati, S. H. & Liana, T. (2014) M-Estimation, S-Estimation, and MM- Estimation in Robust Regression. *International Journal of Pure and Applied Mathematics*, 91 (3), 349-360.

Yohai, V. J. (1987) High breakdown-point and high-efficiency robust estimates for regression. *The Annals of Statistics*, 15, 642-656.

Yu, C. & Yao, W. (2017) Robust Linear Regression: A Review and Comparison. *Communications in Statistics - Simulation and Computation*, 46 (8), 1-27.

Reinforcement Of Bituminous Mixtures Using Natural Fibers

Dilay YILDIRIM UNCU[1]
Adem OZER[2]

Introduction

Due to the traffic growth, loads of vehicles, weather conditions and environmental effects, deformations may occur on the road before the expected service life for the roads paved with bituminous mixtures. Reduction in the durability and strength of the road can lead to settlement cracks, fatigue cracks, and reflection cracks. This type of deformations reduces the service life of the pavement. Studies on the use of various additives are carried out to minimize deformations by improving the performance of the mixture. A good quality asphalt mixture is expected to have qualities such as being strong, resistant to fatigue, permanent deformation, and environmental conditions, economical, and having high durability (Kar, 2012). Due to the increasing traffic loads and maintenance costs, there is a need for the development of roads that are better, more durable, more efficient, and that prevent or minimize problems with asphalt pavement (Kumar & Ravitheja, 2019).

Layers formed by multi-phase complex bituminous mixtures is sensitive to loads and temperature. The use of fibrous materials as an additive to enhance mixture properties against problems caused by this sensitivity become increasingly common. The modern development of modification using fiber began in the early 1950s. Initially, studies were carried out the use of mesh to prevent reflection cracks in bituminous pavements. Afterward, asbestos fibers were used until their deleterious effects were determined. The main function of fibers as a modification material is to provide additional tensile strength to the resulting composite structure. This enhances the amount of absorption of energy during the fatigue and fracture of the composite (Ramalingam, Murugasan & Nagabhushana, 2017). Fibers have a higher tensile strength than bitumen. When they are used in hot bituminous mixtures as additives, the strength value of the composite mixture increases. Using fibers enhances the properties of the mixture against cracks and deformation (Guzel, 2020). Fibers modify the viscoelasticity of bituminous mixtures by improving their flexibility and tensile strength. They are also considered as additives that can enhance friction resistance, rutting resistance, and stability for roads with high traffic density and heavy vehicle axle loads (Harne et al. 2020; Serin et al., 2018).

Fibers are added in relatively small amounts to bituminous mixtures. It is generally observed that stability and viscosity increase by adding fiber to the mixture because of increasing strength. Fibers, by absorbing the bitumen, cause an increase in the air voids within it (Kumar & Sunitha, 2016). Improving moisture sensitivity, providing higher rutting resistance, anti-cracking at low temperatures, reducing the number of reflection cracks, increasing fatigue life, getting higher durability, and getting strong viscoelasticity that prevents binder segregation

[1] Asst. Prof. Dr., Manisa Celal Bayar University
[2] Res. Asst., Manisa Celal Bayar University

are also advantages of fiber modification (Herráiz et al., 2016; Serin et al., 2012). These positive effects enhance the performance of pavement by extending its service life. Fibers also have an important role in terms of their impact on the Marshall properties. The use of fibers in dense bituminous mixtures is known to provide increased stability, reduced rutting, and resistance to cracking (NCHRP, 2015, Pandey & Majumdar 1990). However, the fact that the fiber content is too high does not mean that it will always contribute positively to the Marshall values. Thus, increasing the fiber added to the mixture should be limited to a certain extent (Kumar & Sunitha, 2016). Fibers are also used as stabilizing additives in Stone Mastic Asphalt (SMA) as an alternative to polymers. Research and experience have shown that fibers tend to outperform polymers at reducing bitumen leaching (Raju & Rao, 2013).

Fibers for modification of mixture are obtained artificially and naturally. Many researchers have shown that fibers, whether synthetic or natural, enhance the tensile strength and cohesion of hot bituminous mixtures (Sani, 2011). Despite providing many advantages, the artificial fibers supplied as standard can quite expensive. They increase the cost of the mixture. For this reason, researchers have turned their attention to exploring the potential of utilizing naturally occurring fibrous materials (Herráiz, 2016). This tendency has brought natural fibers into consideration for use in asphalt mixtures. Due to various advantages, natural fibers are preferred as modification material compared to traditional man-made synthetic fibers in terms of their use as strengtheners (Ramalingam, Murugasan & Nagabhushana, 2017). Natural fibers are cheaper and available locally in many countries. The use of natural fibers as a structural material to enhance the properties of composites is highly cost-effective compared to the overall cost of composites (Ali et al., 2012; Hadiwardoyo, 2013). Some of the other important advantages of natural fibers include their low density, less wear during processing, and low energy consumption during extraction (Ramalingam, Murugasan & Nagabhushana, 2017).

Natural Fibers and Their Effects on Asphalt Mix Performance

The fibers increase the resistance, dynamic modulus and ductility of the layers against friction, freeze-thaw, rutting, weathering; It is used to provide the desired performance from the coating by reducing the most common types of deformation, especially thermal, fatigue cracking (Serin et al., 2018). In addition, the fibers change the viscoelasticity of the mixture, reducing the amount of reflective cracks in the coatings. Composite materials obtained as a result of adding fibers with higher tensile strength than bitumen to conventional bituminous hot mixtures have high fracture energy absorption and tensile strength; the binder, aggregate, fiber bond acts as a barrier preventing crack formation and propagation of cracks in the asphalt mixture (Callomamani, 2020).

The conditions for adding additives during the mixing phase with bituminous binders and mixtures are of paramount importance. Changes in the mixture conditions result in different effects on the binder and mixture properties. Therefore, the optimum mixing parameters and methods need to be determined. When reviewing the related studies, it is observed that natural fibers are generally added to the mixture in low percentages. The impact of using fibers with different lengths on the mixture properties is also being studied.

When analyzing the performance of the produced asphalt mixture, it is observed that the most influential parameters are the mixing rate and dimensions of fibers. Fibers can be added to the asphalt mixture in different rates and sizes. According to the studies in the literature, fibers are generally mixed in rates ranging from a minimum of 0.05% to a maximum of 0.8% of the mixture weight. In terms of fiber length values, it has been determined that different length values are used in the related studies, with fiber length ranging from a minimum of 5 mm to a maximum of 35 mm. Some fibers with different lengths are shown at Figure 1.

a) Sisal Fiber (Panda, 2010)

b) Basalt Fiber (Hanafi et al., 2020)

c) Coconut Fiber (Ting et al., 2015)

d) Hemp Fiber (Serin et al., 2018)

Figure 1. Fiber Additive Samples in Different Sizes

Regarding the performance of the mixture, it is observed that the fiber content ratio and dimensions have an impact on the results. Specifically, an increase in the fiber content rates challenges in achieving a homogeneous distribution of fibers, resulting in a non-uniform mixture (Figure 2). The increased fiber content tends to absorb the bitumen within the mixture, thereby changing the optimal bitumen content and adversely affecting workability. This situation also hinders the compaction of the sample and leads to an increase in void volume within the mixture. As a result, there is a decrease in stability values, which causes a negative impact on the overall performance of the mixture (Morova, 2013; Kumar & Sunitha, 2016).

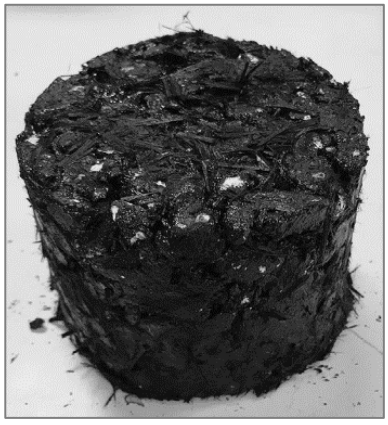

Figure 2. An Asphalt Sample with a Heterogeneous Structure Due to Its High Fiber Content (Cetin et al., 2021)

Considering these inferences, the importance of parameters related to mixing emerges once again while preparing asphalt samples. Mixing methods and their effects are detailed in the "Methods of Sample Preparation" section.

Methods of Sample Preparation

A procedure for adding fibers to the asphalt mix has not been specified by ASTM, and this is of great importance in terms of mix properties (Abtahi, et al. 2010). There are two methods in the literature: wet and dry methods (Abtahi et al. 2010; Abiola et al. 2014; Ting et al. 2015).

In the wet method, the fibers are added into the bituminous binder using a high shear mixer and then the mixture is combined with aggregates to create fiber reinforced asphalt. In the dry

method, the fiber and aggregate are mixed before the bituminous binder added into the mixture (Abiola et al. 2014; Ting et al., 2015). Abtahi et al. stated that there is no difference in the Marshall properties as stability and flow between the wet and dry methods according to the values obtained from the test results (Abtahi et al., 2008). In addition, since the fibers do not melt in the asphalt mixture, the wet method does not contribute to it. For this reason, the dry method was preferred more in the experimental studies (Hejazi, 2007). According to researchers, the dry method is considered more favorable than the wet method due to its simplicity, as it doesn't require a high shear mixer. Moreover, the dry method results in significantly lower fiber agglomeration compared to the wet method, which minimizes the formation of weak zones within the asphalt mixture (Abtahi et al., 2010; Chen et al., 2009; Dehghan & Modarres, 2017).

In this section, the application of wet and dry methods explained and the effects of these methods on the mixture performance are discussed. There are three different natural fiber types, and the most frequently used additives are plant fibers among them. The other types of fibers are mineral and animal fibers. Different fiber types and their effects on asphalt mixture performance are discussed in the "Types of Natural Fibers" section.

Types of Natural Fibers

In recent years, it has been observed that fiber additives are widely used to enhance the performance of asphalt mixtures. Fiber additives are used with the aim of enhancing the friction resistance, freeze-thaw resistance, rutting resistance, resistance to aging, as well as the dynamic modulus and ductility of asphalt mixtures. Moreover, these fibers are effective in reducing common types of deformation such as thermal and fatigue cracking (Huang & White, 1996; Putman & Amirkhanian, 2004; Chen et al., 2004; Wu et al., 2007; Tapkın, 2008; Serin et al., 2018). Numerous experimental studies have been conducted on the use of fiber additives, providing their reinforcing effect on asphalt mixtures. In this field, researchers have also conducted studies on the potential use of natural fibers obtained from natural sources in asphalt mixtures.

It is observed that the use of natural fibers in asphalt mixture design has various advantages. These advantages include easy availability, low density, specific characteristics, high energy savings, and biodegradability (Abiola, 2014). The comparative analyses reveal that fibers obtained from natural resources are more efficient and environmentally friendly than those derived from artificial materials. Moreover, obtaining natural fibers is much more cost-effective (Bindu &Beena, 2015).

Studies related to natural fibers focus on both stone mastic asphalt and hot mix asphalt, but their application is predominantly observed in SMA. According to the literature, the natural fibers which are used as an additive are categorized into three main groups based on their origins, as presented in Figure 3.

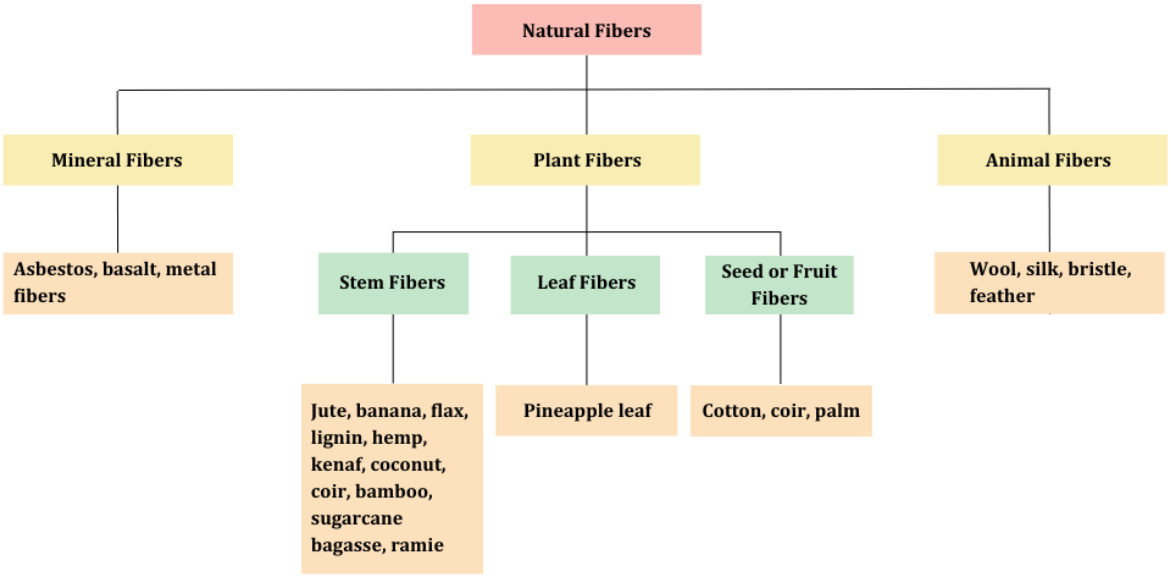

Figure 3. Types of Natural Fibers

Plant fibers classified into three categories upon the part from where it is extracted; stem fibers (jute, banana etc.), leaf fibers (sisal, pineapple etc.) and fruit fibers (cotton, coir, palm etc.). In addition, when the studies are examined, it is seen that the use of plant-based fiber is quite diverse.

Plant-Based Fibers

In some countries, plants are commonly available and generate tons of waste annually. It is also necessary to find a solution for the disposal of plant wastes. For this reason, there are many studies in the literature on the use of plant fibers in construction materials. In this section, some plant fiber types that are frequently used are discussed, and the plant fibers found in the literature but less frequently used are mentioned in the other plant fibers section.

Banana Fibers

Banana fibers, regarded as a form of agricultural waste resulting from banana cultivation, are abundantly found across the globe. These fibers are primarily derived from the remnants left to undergo natural decomposition, consequently releasing significant quantities of carbon dioxide and methane gases (Mostafa & Uddin, 2016). When the studies carried out, it is seen that the banana fibers added to the mixture in low percentages, as discussed in the "Natural Fibers and Their Effects on Asphalt Mix Performance" section.

Khajuria & Chopra (2019) modified the base bitumen with the addition of banana fiber and zeolite in their study. The banana fiber additive ratio varies between 0-0.3% with 0.05% increments. When the Marshall stability results were examined, it was observed that the stability values increased with the increase in the additive ratio but decreased after the 0.15% additive ratio. The flow value, on the other hand, remained within the limit values in all additive ratios and reached its highest value at 0.1% additive ratio.

Parimita (2020) focused on the utilization of natural fibers obtained from the banana stem and the discarded portions of fully ripe coconuts. These fibers were examined due to their robust intermolecular forces and the exceptional linear structure of cellulose molecules, which impart a crystalline nature to fibers sourced from abundant natural reservoirs. In the study, Banana and coir fiber have been used as additives in the SMA mixture. Both two additives were added at

the rate of 3%. According to the results, 0.3% of banana fiber can bring adequate improvement in Marshall characteristics.

Coconut or Coir Fibers

Coconut or coir fiber is a product which is extracted from the outer shell of the coconut fruit. Coir fiber, which is derived from the husk of coconuts, is entirely natural and sourced from the seedpod of the coconut palm. The nation's pollution problem is exacerbated by the significant contribution of coconut shells, which are among the primary sources of pollution (Ting et al., 2015). Annually, approximately 3.18 million tons of solid waste in the form of shells are generated (Gunasekaran et al., 2012). As coconuts reach maturity, a deposition of lignin occurs within the cellulose walls of the fiber, resulting in a darkened appearance. Unlike fibers such as flax or cotton, matured coir fibers possess a higher proportion of lignin-a complex woody chemical-and a lower amount of cellulose. As a result, coir exhibits enhanced strength while being comparatively less flexible. In terms of water resistance, coir fiber stands out as it possesses a relatively high degree of waterproofing and is the sole natural fiber capable of withstanding damage caused by saltwater (Abiola et al., 2014). Coconut shell (CS) and coconut fiber (CF) are new waste materials that used in highway construction. Besides, it has no economic value, and its dispose process is costly and will cause environmental problem (Nagarajan et al., 2014).

Hadiwardoyo (2013) investigated the effects of the short coconut fibers on the asphalt mixture performance. The coconut fibers were used with lengths of 5-12.5 mm and 0.5%, 0.75%, 1%, 1.25%, and 1.50% ratios in the study. The addition of 0.75%-and 5 mm fibers by weight of the asphalt was increased the value of the Marshall stability by 10-15% and produced a lower penetration grade bitumen. According to the test results increase in fiber length caused difficulties in the mixing process. The sample with 0.75% coconut fiber showed the best performance and performed better than the sample with base bitumen. The test results showed that the 0.75% coconut fiber content provided the best performance of the contents studied. Additionally, the 0.75% CFA performed better than fiber-free asphalt mixture sample.

Panda et al. (2013) studied SMA containing ripe coconut fibers with 0.3%, 0.5%, and 0.7% ratios and 3-5 mm lengths. The coconut fibers were added directly to the aggregate sample and thoroughly mixed before adding required quantity of bitumen. In general addition of coconut fiber increased the Marshall stability and unit weight value and reduced the flow values and air voids. It is evident that a marginal 0.3% fiber addition yielded significant enhancements in Marshall characteristics by meeting all the Marshall criteria. The inclusion of coconut fibers had led to a considerable increase in the resilient modulus, irrespective of the type of bitumen used.

Subramani (2012) determined the fiber content as 0.3, 0.5, 0.7% and the fiber length as 10, 15 and 20 mm in the study about coir fiber reinforced bituminous mixes. It is found that the addition of coir fiber to the bituminous mix contributed significant improvement on the performance of the mix according to the Marshall test results. The optimum bitumen content, fiber content and fiber length were obtained as respectively 5%, 0.46% and 17.25 mm after analysis. The stability value has increased by 1.3 times when compared to the reference sample making the mix more stable for the traffic loads. However, flow value has showed an increment of about 1.8 times on comparison with the reference sample.

Raju & Rao (2015) studied the use of a naturally and locally available material called coir fiber as stabilizer in SMA. The fiber content varied from 0.2 %, 0.3% and 0.4%, the fiber length

varied from 10 mm and 15 mm. The addition of 0.3% fiber was found as the optimum fiber content in SMA samples. The Marshall stability value of SMA with optimum fiber content was found as 16.237 KN, which is higher than the prescribed value of 6.20 KN and the percentage increase in stability value has been found as 22% according to the conventional mix. The flow value of SMA with 0.3% content and 10 mm length fiber was found as 4.32 mm whereas the flow value for conventional mix is 5.96 mm. The drain-down test results indicated that coir fiber can retard the drain-down of the bitumen, the 10 mm length and 0.3% fiber gave the best results compared to conventional mix. The indirect tensile strength and the tensile strength ratio indicated that 10 mm and 0.3% of coir fiber mixes was found to be respectively higher by 2.56% and 4% than conventional mix.

Kenaf Fibers

Kenaf, a natural plant, has garnered increasing interest as a bio composite material due to its rapid growth characteristics, enabling it to provide a substantial quantity of raw material within a brief timeframe (Hainin et al., 2018). Kenaf typically reaches a height of 5 meters, exhibiting a cylindrical shape with or without branches. Its stem comprises two types of fibers, namely bast and core. Bast fibers, found in the bark, are notably longer than the core fibers, which are generated within the interior of the stem. The leaves of kenaf are either entirely heart-shaped or feature lobes that radiate outward. It is primarily grown in India and Pakistan but also grows in Africa, South East Asia, Cuba, Indonesia, Mexico, Russia, the Philippines, and the United States (Abi, 2010). The global cultivation of kenaf has witnessed a significant surge, particularly in subtropical and tropical regions, owing to its extensive industrial applications and the multitude of advantages it offers.

Sani et al. (2011) aimed to evaluate the performance of HMA added with coir fiber and kenaf fiber. In the study kenaf fiber was used in different weight range from 1 g to 5 g ang length 10 mm to 30 mm. The optimum weight of kenaf fiber was determined as 4.4 g from the graphics of the Marshall procedure. It was noticed that the sample containing optimum kenaf fiber had the lowest density and lowest VMA among the HMA, coir fiber modified asphalt samples, besides had highest Marshall stability value. The coir fiber and kenaf fiber increased the Marshall stability according to ordinary HMA by 3.2% and 9.7% respectively. Coir fiber and kenaf fiber asphalt modified samples were considered more durable and stronger than ordinary HMA samples according to the Cantabro abrasion loss.

Pirmohammad et al. (2022) investigated the fracture strength of asphalt mixtures containing kenaf and goat wool. Both the kenaf and goat wool fibers were used with three different lengths as 4 mm, 8 mm and 12 mm and contents as 0.1%, 0.2% and 0.3% by weight of total asphalt mixture. In the study, also mixing methods as wet, dry and combination of them as the third method were evaluated. The third method was selected for mixing because of having the least agglomeration of fibers in the samples. To provide additional clarification regarding the third method employed in this study, it should be emphasized that a thorough blending of aggregates and bitumen is conducted for approximately three minutes to guarantee complete coating of all aggregates by the bitumen. The fracture experiments were conducted under various mode mixites using semi-circular bend specimen at a low temperature of -15°C. Both the kenaf and goat wool fibers were improved the fracture strength of asphalt mixture significantly according to the test results. The amount of improvement was dependent on the length and ratio of the fibers used in the asphalt mixture. The asphalt mixture was reinforced by 0.3% kenaf fibers with 8 mm length demonstrated the best results compared to other mixtures containing kenaf fibers. Findings of this research indicated that the kenaf and goat wool fibers were promising materials for manufacturing asphalt pavements.

Sisal Fibers

Sisal fibers, natural fibers obtained from the leaves of the sisal plant, are native to Southern Mexico and can now be found in many tropical and subtropical countries (Guo et al., 2023). Utilizing sisal fiber enhances the strength and durability of the material while effectively preventing drainage or settling of the mixture (Sandeep, 2017).

Suraj et al. (2019) used sisal fiber as stabilizer in SMA and as an additive in BC in their study. The bitumen content has been varied from 4% to 7% and fiber content varied as 0%, 0.3% and 0.5% of total mix. The optimum fiber content for both BC and SMA mixes was found to be 0.3% according to Marshall procedure. Incorporating sisal fiber into both HMA and SMA mixes leads to improved mixture properties, including enhanced Marshall stability, reduced drain-down characteristics, and increased indirect tensile strength. Furthermore, it was noted that SMA exhibits superior performance compared to HMA in terms of indirect tensile strength and creep characteristics.

Kundal & Goel (2019) used sisal fibers varied to 0%-0.8% of total aggregates and stone dust as a filler with the various percentages of bitumen varied to 4%-6% in their study. The optimum bitumen and fiber contents were obtained as 5% and %0.4 respectively. The Sisal fiber size was taken to be length 6 mm to 18 mm with diameter 0.2 mm to 0.6 mm. Based on research experience, it has been demonstrated that sisal fiber outperforms other fibers and polymers in effectively reducing the drain down of the mixture (Kumar, 2016). The graphs of stability showed increase until adding up to fiber length 10 mm and content 0.4%. The addition of Sisal fiber to the mix, with a fiber content of 0.4%, fiber length of 10 mm, and bitumen content of 5%, resulted in an increase in mix stability. However, further increases in fiber content beyond 0.4% led to a decrease in stability. It was observed that as the fiber content and length increased up to a certain threshold, there was a reduction in air voids and flow value. Consequently, the consistency of the asphalt changed, becoming harder. Furthermore, the use of emulsion coated fiber improved resistance against moisture-induced damage, while also reducing binder drain down. These findings highlight favorable characteristics of the bitumen.

In a study conducted by Kar (2012), sisal fibers were utilized in SMA with lengths ranging from 15-20 mm and diameters between 0.2-0.6 mm. The fiber content varied from 0.3 to 0.5%. The addition of fibers resulted in an increase in the stability values of the samples. However, it was observed that stability values began to decrease with further fiber additions due to improper distribution of excess fibers within the asphalt. In terms of flow value, it decreased in samples with lower fiber contents but increased with higher fiber content. Comparing the asphalt sample with 0.3% fiber to the one with 0.4% fiber, the former exhibited increased stability while the bitumen content decreased. It was concluded that sisal fiber-modified SMA showed excellent performance in various tests such as drainage, indirect tensile strength, and static creep, making it a viable option for flexible pavement applications.

Other Plant-Based Fibers

Nowadays, the consumed parts of various plants, trees and fruits are taken, and their fibrous parts are left to nature as waste material. While these waste materials can be used, different materials are used instead of them, increasing the cost and decreasing natural resources. From this point of view, there are also studies to investigate the properties of different types of fiber-containing asphalt mixtures, which are rarely used in the literature.

Serin et al. (2018) carried out a study about the usability of natural hemp fiber, a woody annual plant native to Asia and belonging to the Cannabinaceae family. It holds industrial

significance for fiber production. The optimum bitumen content was determined as 4.2% and used natural hemp fiber at varying rates of 0.05%, 0.075%, 0.1%, 0.125%, and 0.25%. Based on literature research, a fiber length of 12 mm was chosen. The Marshall stability test was conducted on fiber-reinforced samples to assess the performance of asphalt concrete mixtures. The results indicated that as the fiber content increased, flow values initially showed an increment up to a certain point, followed by a decrease. Comparing the Marshall stability values, the sample without fiber had a stability value of 1276.8 kg, while the addition of fiber led to an increase in stability. The highest stability value of 1789 kg was achieved with a 0.1% fiber-added mixture. Despite the observed decline in stability values for the mixtures containing 0.125% and 0.25% fiber content, it is noteworthy that these compositions exhibited results surpassing the specification limits.

Herraiz et al. (2016) used Posidonia oceanica fiber in their study for o improving the mechanical properties of asphalt mixtures. Posidonia oceanica is an algae fiber type comes from the beaches by the Mediterranean Sea. The investigation of the combination of SMA with algae fiber was carried out by comparing the outcomes of various fiber-reinforced SMA mixtures with hemp and polyester fibers. The algae fibers were added by 0.3, 0.5, 1, 1.5, 2, 3, 4 and 5% ratios and other fibers were added by 0.3%. The asphalt samples containing fibers were examined about water absorption, thermostability and binder drain-down properties. Moreover, the optimum bitumen amount, plastic deformation, bearing capacity and the fatigue life were studied. When the algae fibers were analyzed alone, the results showed that they presented poor properties to achieve the desired effects. When they were added into the asphalt mixture, interesting results were obtained. Especially, algae fiber-reinforced mixtures present proper results with content of fiber less or equal to 2 wt%. A higher value of the optimum bitumen content was obtained than the cellulose fiber-reinforced mixtures with similar binder drainage with these percentages. Moreover, higher stiffness values were obtained and at the same time the fatigue life was increased. Additionally, the stiffness variation in water existence and the rutting resistance were improved with algae fiber compared to the one used in the control mixture.

Satyavathi et al. (2016) investigated the use of coir and pineapple fibers in SMA samples at rates of 0.1, 0.2, 0.3 and 0.4% and the fibers were used in two different gradations (grade I and grade II). They stated that the problem about SMA mixes was drain-down during transportation and laying. Therefore, this research was to check the usability of these fibers as stabilizing additives by analyzing the flow and stability values obtained from the Marshall Stability test. In this study, the fibers used for reducing the drain-down of SMA. Drain-down test was initially performed to find the optimum fiber content and then to find the optimum bitumen content. The test results for mixes with two gradations reduced the drain-down value by the use of fibers and maximum stability value for both gradations was obtained for coir fiber when compared with pineapple fiber. The optimum coir fiber and pineapple fiber content obtained as 0.3% and 0.1% respectively according to the test results. The optimum bitumen content was found as 6.6% & 6.7% for coir fiber and 6.25% & 5.75% for pineapple fiber for the mixes grade I and grade II respectively. The coir fibers showed better than pineapple fibers in both mixes. It was concluded that coir and pineapple fibers reduced the drain-down and increased the stability of the samples for grade I and grade II mixes.

Ahmed et al. (2022) investigated the performance of bamboo fiber (BF) and sugarcane bagasse fiber (SCF) on the mechanical properties of HMA samples. Marshall test, and performance tests such indirect tensile strength test and rutting test were conducted to evaluate the performance of HMA samples containing bamboo and sugarcane bagasse fibers. The fibers were used in the range from 0.2% to 0.5% of the total weight of the sample. The optimum bitumen content and both fiber contents were obtained at 5.2% and 0.3% respectively. The fibers improved the performance of asphalt pavements to resist external loads. Both fibers at

0.3% content improved the Marshall stability, ITS of HMA, and rutting resistance. The HMA-0.3%BF and HMA-0.3% SCFs mixtures had a low bulk density, high air void, high void in mineral aggregate, high flow, and higher stability than the control mixture. Comparing the two fiber types, the test results showed that BF had better performance based on stability, indirect tensile strength, Marshall stiffness and rutting resistance performance.

Mineral-Based Fibers

Asbestos Fibers

Asbestos, found in fibrous reins of serpentine or amphibole rock, is the only mineral substance used as a textile fiber (Majoryl, 1986). The earlier application of asbestos can be found in the patents published by Warren Brothers Company of Boston in 1917 and 1918, where asbestos fibers were used in sheet asphalts to prevent asphalt bleeding at high temperatures, and in cold-laid asphalt pavements, a small amount of asbestos fibers can reduce the segregation of aggregates during the placement procedure (Kietzman, 1960). In asphalt mixtures, the addition of asbestos fibers, according to Kietzman's findings, led to an enhancement in the plastic strength (Kietzman, 1960). Due to concerns regarding health and the environment, this application persisted only until the 1960s (Busching et al., 1970).

Most studies typically compared the effects of utilizing asbestos fibers in asphalt mixtures with those of other fiber types. In their study, Chen et al. (2009) conducted an evaluation of four different types of fibers (polyester, polyacrylonitrile, lignin, and asbestos fibers). All these fibers demonstrated the capability to increase the optimum asphalt content, air void content, void content in mineral aggregate, and Marshall stability, while reducing the bulk specific gravity. Polymer fiber-reinforced asphalt mixtures exhibited enhanced stability attributed to the formation of a network structure. On the other hand, the inclusion of lignin and asbestos fibers resulted in higher optimal asphalt content and VFA (voids filled with asphalt) due to their superior absorption properties. Characterized by their softness, flexibility, and exceptional resistance to heat, electricity, and chemical corrosion, asbestos fibers possess versatile properties. Moreover, their compatibility extends to various materials such as cement, paper, textiles, and more, effectively reinforcing and enhancing their strength (Bijwe, 1997).

Basalt Fibers

Basalt fiber produced from basalt rock fibers is very similar to carbon and glass fiber and has superior physical mechanical properties. The reason why basalt fiber is produced using new technology is that its cost is similar or lower than other fibers (Singha, 2012).

Morova (2013) investigated the usability of basalt fibers in hot mix asphalt in his study. Marshall mixtures were prepared with different basalt fiber contents and different bitumen ratios. Five different fiber ratios as 0.25%, 0.75%, 1.0%, 1.5%, 2% were used for samples. The highest Marshall Stability value obtained from 5% bitumen content and 0.50% basalt fiber addition as 1310 kg. After these values, stability has decreased. The stability values have decreased due to increasing amounts of fiber ratio. In summary, the study revealed that incorporating basalt fibers in hot-mix asphalt concrete had a beneficial effect on its stability. However, to prevent potential damage to vehicle tires, it is advisable to limit the use of basalt fibers to the binder course only. While there may be additional expenses associated with adding basalt fibers to the asphalt mixtures, considering their long-term advantages, it is deemed viable to employ basalt fiber asphalt concrete in the binder course.

Cetin et al. (2021) investigated the effects of basalt fiber on the performance of SMA mixtures. The basalt fibers were used with 0.1% to 0.8% ratios by dry weight aggregate. Furthermore, the inclusion of 0.4% basalt fibers in the mixture demonstrated the highest level

of resistance to permanent deformation, as evidenced by the outcomes of the static uniaxial creep test conducted at 40°C. It should be noted that basalt fibers do not exhibit any beneficial effects when the decrease in bitumen viscosity surpasses the bitumen softening point during repeated uniaxial tests. Conversely, the results of the bitumen drain down and water damage tests remained within acceptable thresholds. The addition of basalt fiber to the SMA mixtures seriously improved the rigidity and resistance against deformation of the SMA samples.

Metal Fibers

It is seen that steel fiber additives are used most under this heading. In the studies examined about steel fibers, it is stated that the most important advantage of the steel fiber mixtures is that the coatings can be repaired by heating in-situ by providing the coatings with self-healing properties due to their electrical conductivity; in addition, it has been determined that the mechanical properties are affected by compression energy, mixture gradation, mixture temperature, fiber size and amount (Guzel, 2020).

Guzel (2020) has used steel fibers with 0.15%, 0.2% ratios and 10 mm, 1 mm diameters. As a result, while the highest Marshall stability and conditioned indirect tensile strength are obtained in 0.10% steel fiber binder mixtures compared to those without additives; In the wear mixture tests with additives, results close to or lower than those without additives were obtained. Marshall stability of the wear course did not provide significant increases in conditioned indirect tensile strength values compared to the base samples. Bitumen and steel fiber fibers added to the binder mixtures at the rate of 0.10% of the total weight of the aggregate increased the first and second Marshall stability, conditioned indirect tensile strength values by 18% on average compared to those without additives.

Serin et al. (2018) were used steel fibers in asphalt concrete mixtures in different ratios as 0.25, 0.50, 0.75, 1.0, 1.5, 2.0 and 2.5%. The highest Marshall Stability value as 1109.5 kg obtained from 5.5% bitumen content and 0.75% fiber addition. After this fiber amount value, it was seen a decrease for stability values. Marshall stability values are lower than other steel fiber blends and even control samples at 2.0% and 2.5% fiber ratios. As a conclusion, it was observed that the use of steel fiber additions in hot-mix asphalt concrete had a positive impact for stability. But it may be considered by adding them only to binder course in order to avoid the negative effects as come up to the top of the surface and damage the tires and comfort of drivers, due to steel fibers that can be damage for vehicle tires. Although additional costs may be required adding steel fibers to the asphalt mixtures, when its overall long-term contributions are taken into account, it is still considered that steel fiber asphalt concrete can be utilized in the binder course.

Animal-Based Fibers

Natural materials obtained from animals such as wool, silk, bristle and feather can be used as animal fibers. However, when the studies in the literature are examined, it is seen that the use of animal fibers are not as common as plant fibers.

Pirmohammad, Shokorlou & Amani (2020) used goat wool as animal fiber in their study. They have added goat wool fibers with five lengths as 4, 8, 12, 16 and 20 mm and five contents as 0.1, 0.2, 0.3, 0.4 and 0.5% to the asphalt mixture. Agglomeration problems have experienced for some samples which have long lengths (16 and 20 mm) and high contents (0.4 and 0.5%). The goat wool fibers have improved the fracture strength of asphalt mixtures significantly according to the test results. It has been observed that the level of improvement of mixture performance depends on the length and content of the fibers used. The sample 0.3% goat wool fibers with 4 mm length have showed the best results compared to the other mixtures examined

in this study. The findings of the study showed that goat wool fibers are promising materials for asphalt pavement production.

Dalhat et al. (2020) have achieved fibers like wool from chicken feathers. They have used fibers 0.15, 0.3 and 0.45% weight of aggregate. Based on the test results, it is seen that the fibers improved moisture resistance and rutting of asphalt mixture. But the chicken feather fibers consumed more bitumen according to a standard asphalt mixture. However, they stated that due to potential biodegradation in extremely humid conditions, the chicken feather fibers should be used carefully (Dalhat et al., 2020).

The difficulties experienced in the use of animal fibers in terms of collection, recycling, reuse, quality control and high temperature stability have led to limited studies on the use of animal fibers in asphalt mixtures (Wu, Haji &Adkins, 2022).

Conclusions

In the field of pavement engineering, current studies are increasingly centered around investigating eco-conscious methodologies and materials. This includes the utilization of fibers within paving materials. Employing natural fibers presents a viable sustainable option owing to their advantages such as reduced energy consumption and cost, renewability, and biodegradability. Additionally, fibers derived from waste materials or by-products hold significant potential for recycling purposes, further enhancing their value. Therefore, studies in this field gain importance.

The fibers used in asphalt mixtures are basically additives used to change the viscoelasticity of asphalt, increase the dynamic modulus, moisture sensitivity, friction resistance, rutting resistance and freeze-thaw resistance. Many experimental studies have been carried out on fiber additives related to increasing the performance of asphalt mixtures and it has been proven that fibers have a strengthening effect on asphalt mixture performance. The utilization of natural fibers as reinforcement yields several benefits, including improved fatigue life, heightened stability, and the potential to enhance the structural resistance of flexible pavement against distress resulting from traffic loads.

When the test results of the studies are examined, it is revealed that the mixing ratio and length of the fibers are quite effective on the values. Consensus among natural fiber researchers is that achieving a uniform distribution, appropriate fiber length, optimal percentage, and correct orientation are crucial factors for enhancing mixture performance. Obtaining a homogeneous mixture becomes difficult if the fiber content added to asphalt mixtures increases excessively or is longer than necessary. As a result, the compaction process is affected and ultimately the void volume increases. The increased void volume value in the samples also affects the Marshall stability values negatively, causing a decrease in the values. On the other hand, it is observed that the fibers added to the mixture absorb the bitumen in the mixture and affect the bitumen content of the mixture, thus negatively affecting the workability. For this reason, special attention should be paid to this issue in asphalt mixtures containing fiber.

When the results of studies in the literature are examined, it is seen that natural fibers can replace synthetic fibers in SMA mixtures due to their good adhesion with asphalt and can be used as a reinforcing material in bituminous mixtures in terms of performance properties.

REFERENCES

Abi Zaid, A.L. (2010). The laboratory evaluation of hot mix asphalt and kenaf fibre modified asphalt mixes. *Thesis, Department of Civil Engineering, Faculty of Engineering, National Defence University of Malaysia.*

Abiola, O.S., Kupolati, W.K., Sadiku, E.R., & Ndambuki, J.M. (2014). Utilisation of natural fiber as modifier in bituminous mixes: A review. *Construction and Building Materials, 54*, 305-312. Doi: 10.1016/j.conbuildmat.2013.12.037

Abtahi, S., Hejazi, S. M., Sheikhzadeh, M., & Semnani, D. (2008). An investigation on the use of textile materials to mechanical reinforcement of asphalt-concrete (AC) structures and analysis of results by an artificial neural network (ANN). *4th National Congress on Civil Engineering*, Tehran (Iran).

Ahmed, K.U., Geremew, A., & Jemal, A. (2022). The comparative study on the performance of bamboo fiber and sugarcane bagasse fiber as modifiers in asphalt concrete production. *Heliyon, 8* (7), e09842. Doi: 10.1016/j.heliyon.2022.e09842

Ali, M., Liu, A., Sou, H., & Chouw N. (2012). Mechanical and dynamic properties of coconut fiber reinforced concrete. *Construction Building Materials, 30*, 814-825. Doi: 10.1016/j.conbuildmat.2011.12.068

Bijwe, J. (1997). Composites as friction materials: recent developments in nonasbestos fiber reinforced friction materials. *Polymer Composites, 18* (3). 378–396.

Bindu, S. & Beena, S. (2015). Shear strength characteristics of coir fiber stabilised stone matrix asphalt mixtures. *International Journal of Sustainable Construction Engineering and Technology, 6* (2), 26–36.

Busching, H.W., Elliott, E.H., & Reyneveld, N.G. (1970). A state-of-the-art survey of reinforced asphalt paving. *Association of Asphalt Paving Technologists Proc, 39*, 766-798.

Callomamani, L., (2020). Laboratory investigation of the performance of fiber modified asphalt mixes in cold regions. *Master Thesis of Civil and Environmental Engineering in University of Alberta*.

Cetin, A., Evirgen, B., Karslioglu, A., & Tuncan, A. (2021). The effect of basalt fiber on the performance of stone mastic asphalt. *Periodica Polytechnica Civil Engineering, 65* (1), 299–308. Doi: 10.3311/PPci.14190

Chen, H., Li, N., Hu, C., & Zhang, Z. (2004). Mechanical performance of fibers-reinforced asphalt mixture. *J Chan Univ (Nat Sci Ed), 24* (2), 1–5.

Chen, H., Xu, Q., Chen, S., & Zhang, Z. (2009). Evaluation and design of fiber-reinforced asphalt mixtures. *Materials & Design, 30,* 2595–2603. Doi: 10.1016/j.matdes.2008.09.030

Dalhat, M. A., Osman, S. A., Alhuraish, A. A., Almarshad, F. K., Oarwan, S. A., & Adesina, A. Y. (2020). Chicken feather fiber modified hot mix asphalt concrete: rutting performance, durability, mechanical and volumetric properties. *Construction and Building Materials, 239*, Article 117849. Doi: 10.1016/j.conbuildmat.2019.117849

Dehghan, Z. & Modarres, A. (2017). Evaluating the fatigue properties of hot mix asphalt reinforced by recycled PET fibers using 4-point bending test, *Construction and Building Materials, 139*, 384–393. Doi: 10.1016/j.conbuildmat.2017.02.082

Gunasekaran, K., Annadurai, R., & Kumar, P.S. (2012). Long term study on compressive and bond strength of coconut shell aggregate concrete. *Construction and Building Materials, 28* (1), 208-215. Doi: 10.1016/j.conbuildmat.2011.08.072

Guo, Y., Tataranni, P., & Sangiorgi, C. (2023). The use of fibres in asphalt mixtures: A state of the art review. *Construction and Building Materials, 390*, 131754. Doi: 10.1016/j.conbuildmat.2023.131754

Guzel, I. (2020). Çelik fiberli asfalt betonu karışımların marshall stabilitesi ve indirekt çekme mukavemetinin incelenmesi. *Engineering Sciences, 4* (15), 209-217.

Hadiwardoyo, S.P. (2013). Evaluation of the addition of short coconut fibers on the characteristics of asphalt mixtures. *Civil and Environmental Research, 3* (4), 63-73.

Hainin, M.R., Idham, M.K., Yaro, N.S.A., Hussein, S.O.A.E., Warid, M.N.M., Mohamed, A., Naqibah, S.N., & Ramadhansyah, P.J. (2018). Performance of hot mix asphalt mixture incorporating kenaf fibre. *IOP Conference Series: Earth and Environmental Science, 140*, 012092. Doi :10.1088/1755-1315/140/1/012092

Hanafi, M., Aydin, E., & Ekinci, A. (2020). Engineering properties of basalt fiber-reinforced bottom ash cement paste composites. *Materials, 13* (8), 1952. Doi :10.3390/ma13081952

Harne, V., Sharma, A.K., Tallapragada, K.R., & Mewara, S. (2020). Effect of polypropylene fiber on engineering properties of bitumen and bituminous mix. *Helix, 10* (1), 116-120. Doi: 10.29042/2020-10-1-116-120

Hejazi, S.M. (2007). Mechanical reinforcement of hot mix asphalt using textile materials. MSc thesis, *Department of Textile Engineering, Isfahan University of Technology*.

Herraiz, T.R., Herriaz, J.I.R., Domingo, L.M., & Domingo, F.C. (2016). Posidonia oceanica used as a new natural fiber to enhance the performance of asphalt mixtures. *Construction and Building Materials, 102* (2016) 601–612. Doi: 10.1016/j.conbuildmat.2015.10.193

Huang, H., & White, T. D. (1996). Dynamic properties of fiber-modified overlay mixture. *Transportation Research Record, 1545*(1), 98–104. Doi: 10.1177/0361198196154500113

Joseph, M. L. (1986*). Introductory textile science* (5th edit). Holt, Rinehart, and Winston.

Kar, D. (2012). A laboratory study of bituminous mixes using a natural fiber. *Master of Technology Degree in Civil Engineering at National Institute of Technology.*

Khajuria, N. & Chopra, A. (2019). Effect of using banana fibre and zeolite as an additive on the engineering properties of bituminous concrete. *International Journal of Civil Engineering and Technology, 10* (4), 367-372.

Kietzman, J.H. (1960) Effect of short asbestos fibers on basic physical properties of asphalt pavement mixes. *Highway Research Board Bulletin, 270*, 1-19.

Kumar, N. & Sunitha, V. (2016). Experimental investigation of stone mastic asphalt with sisal fiber. *International Journal of Engineering Research & Technology (IJERT), 11* (5), 546-550.

Kumar N.L.N.K. & Ravitheja, A. (2019). Characteristics of stone matrix asphalt by using natural fibers as additives. *Materials Today: Proceedings*, *19*, 397–402. Doi: 10.1016/j.matpr.2019.07.624

McDaniel, Rebecca S., (2015). *NCHRP Synthesis of Highway Practice: Fiber additives in asphalt mixtures, 475,* Washington, D.C. (USA): Transportation Research Board

Morova, N. (2013). Investigation of usability of basalt fibers in hot mix asphalt concrete, *Construction and Building Materials, 47*, 175-180. Doi: 10.1016/j.conbuildmat.2013.04.048

Mostafa, M. & Uddin, N. (2016). Experimental analysis of Compressed Earth Block (CEB) with banana fibers resisting flexural and compression forces. *Case Studies in Construction Materials, 5*, 53-63. Doi: 10.1016/j.cscm.2016.07.001

Nagarajan, V.K., Aruna Devi, S.A., Manohari, S.P., & Santha, M.M. (2014). Experimental study on partial replacement of cement with coconut shell ash in concrete. *International Journal of Science and Research (IJSR), 3* (3), 651-661.

Panda, M., Suchismita, A. & Giri, J. P. (2013). Utilization of ripe coconut fiber in stone matrix asphalt mixes, *International Journal of Transportation Science and Technology, 2* (4), 289-302. Doi: 10.1260/2046-0430.2.4.289

Pandey, S.N. & Majumdar, A.K. (1990). Jute and applied fibers as non-woven Geo-Jute and their application in civil engineering. *International reinforced soil conference,* Glasgow (UK).

Parimita, P. (2020). Influence of natural fibers as additive on characteristics of stone mastic asphalt. *IOP Conference Series: Materials Science and Engineering, 970*, 012021. Doi:10.1088/1757-899X/970/1/012021

Pirmohammad, S., Shokorlou, Y.M., & Amani, B. (2020). Influence of natural fibers (kenaf and goat wool) on mixed mode I/II fracture strength of asphalt mixtures. *Construction and Building Materials, 293*, Article 117849. Doi: 10.1016/j.conbuildmat.2019.117850

Putman B.J. & Amirkhanian S.N. (2004) Utilization of waste fibers in stone matrix asphalt mixtures. *Resources, Conservation and Recycling, 42* (3), 265–274. Doi: 10.1016/j.resconrec.2004.04.005

Raju, B.G. & Rao, K.N.S. (2015). Characterization of fibre reinforced bituminous mixes. *International Journal of Science and Research, 4* (12), 802-806.

Ramalingam, S., Murugasan, R., & Nagabhushana, M.N. (2017). Laboratory performance evaluation of environmentally sustainable sisal fiber reinforced bituminous mixes. *Construction and Building Materials, 148*, 22–29. Doi: 10.1016/j.conbuildmat.2017.05.006

Sani, M.A.,Abd Latib, A.Z., Ng, C.P., Yusof, M.A., Ahmad, N., & Mat Rani, M.A. (2011). Properties of coir fiber and kenaf fiber modified asphalt mixes. *Journal of the Eastern Asia Society for Transportation Studies, 9*, 1274-1285. Doi: 10.11175/easts.9.1274.

Sandeep, G., & Reddy, M. S. (2017). Experimental study of bituminous mixes using natural fibre. *International Journal of Advance Engineering and Research Development, 4* (2).

Satyavathi, M., Rao, B.S., & Rao, G.V. (2016). Experimental study of Stone Matrix Asphalt with coir fiber and pineapple fiber. *International Journal of Engineering Sciences & Research Technology, 5* (11), 378-377.

Serin, S., Macit, M., Çinar, E., & Çelik, S., (2018) Doğal kenevir lifi kullanımının asfalt beton karışımlara etkisi. *Düzce Üniversitesi Bilim ve Teknoloji Dergisi, 6*, 2-7.

Serin, S., Morova, N., Saltan, M. & Terzi, S. (2012). Investigation of usability of steel fibers in asphalt concrete mixtures. *Construction and Building Materials, 36*, 238–244. Doi: 10.1016/j.conbuildmat.2012.04.113

Singha, K. (2012). A Short Review on Basalt Fiber, *International Journal of Textile Science, 1*, 1-10. Doi: 10.5923/j.textile.20120104.02

Tapkın, S. (2008). The effect of polypropylene fibers on asphalt performance. *Building and Environment, 43*, 1065–1071. Doi: 10.1016/j.buildenv.2007.02.011

Ting, T.L., Jaya, R.P., Hassan, N.A., Yaacob, H., & Jayanti, D.S. (2015). A review of utilization of coconut shell and coconut fiber in road construction. Jurnal Teknologi (Sciences & Engineering), 76 (14), 121-125.

Wu, S., Haji, A., & Adkins, I. (2022). State of art review on the incorporation of fibers in asphalt pavements. *Road Materials and Pavement Design, 24* (6), 1559-1594. Doi: 10.1080/14680629.2022.2092022

Wu, S., Ye, Q., Li, N., & Yue, H. (2007). Effects of fibers on the dynamic properties of asphalt mixtures. *The Journal of Wuhan University of Technology-Mater. Sci. Ed., 22*, 733–736. Doi: 10.1007/s11595-006-4733-3

Stackıng Ensemble Approach For Predıctıon Of Heart Dıseases

Erkan AKKUR[1]

Introduction

Heart disease (HD) is defined as the general name for a series of diseases that impair the proper functioning of the heart. Rheumatic, congenital and coronary heart diseases, peripheral artery disease and cerebrovascular diseases and other conditions constitute the types of this disease. The factors such as smoking and alcohol use, high cholesterol, lack of physical activity, hypertension are the main risk factors for this disease. This disease is one of the most threatening diseases to human health today and causes the death of 18 million people every year (Ahmad et al. 2022). Thus, early diagnosis and treatment of HD is critical for human health.

It is possible to carry out studies for the early diagnosis of the disease with the help of machine learning (ML) algorithms by using information such as age, gender, diabetes collected from people with and without HD. ML algorithms are a sub-branch of artificial intelligence that can make predictions on data and model systems that increase their accuracy over time (Azmi et al., 2022). Many researchers have used different ML algorithms to predict HD. Since each technique has advantages and disadvantages associated with classification, using a single technique may not always provide high accuracy. The ensemble learning is used to increase the strength of individual classifiers and reduce their weaknesses. It aims to achieve a higher classification rate in a shorter time by combining multiple classifiers under a certain combination rule (Islam et al., 2022). This study aims to predict heart diseases by using different ML algorithms on a known dataset. The stacking ensemble learning method is used to detect HD with the highest accuracy. In this study, the stacking ensemble method is applied for the prediction of HD and the performance is compared with the basic machine learning methods used in this field.

Related Works

The studies using ML algorithms for the prediction of HD are carried out in the literature. Riyaz et al. applied different classification algorithms for the detection of this disease in their studies and artificial neural networks achieved the highest success rate with 86.91% accuracy. Kannan et al. utilized four different classification algorithms for the prediction of HD and the logistic regression (LR) algorithm achieved the highest success rate with 87% accuracy. Pouriyeh et al. tried to detect heart diseases with the Naive Bayes algorithm using 13 features and achieved an accuracy rate of 83.49%. Dwivedi (2018) suggested a model comparing various ML techniques to predict HDs. LR outperformed with 85% of accuracy. Khateeb and Usman (2017) suggested K-nearest neighbor (K-NN)-based model to predict of HD with 80% accuracy. Bhat et al. suggested an efficient classification approach for the prediction of this disease using ML algorithms. Multiplayer perception algorithm achieved the highest performance with 87.28. Gürfidan et al. (2021) studied heart disease prediction by applying the six most commonly used ML methods. When the algorithms are compared, the most successful method for the related problem has been support vector machines (SVM) with an accuracy rate

[1] Dr., Turkish Medicines and Medical Devices Agency, Ankara, Turkey,

of 83%. Shorewala (2021) suggested a stacking approach for prediction of this disease and the suggested approach achieved 75.1% of accuracy. Ouf and ElSeddawy (2021) suggested a novel model includes repeated random with random forest (RF) algorithms and the model achieved 89.01% of accuracy.

Materials and Methods

The suggested methodology is explained in this section. The suggested methodology is illustrated in Figure 1. In the first step of the suggested method, the HD dataset is passed through a series of data pre-processing. Then, the feature selection method is utilized to select the relevant of the attributes. After feature selection process, six ML algorithms are employed for classification. Finally, stacking ensemble learning algorithm is used to maximize the classification performance.

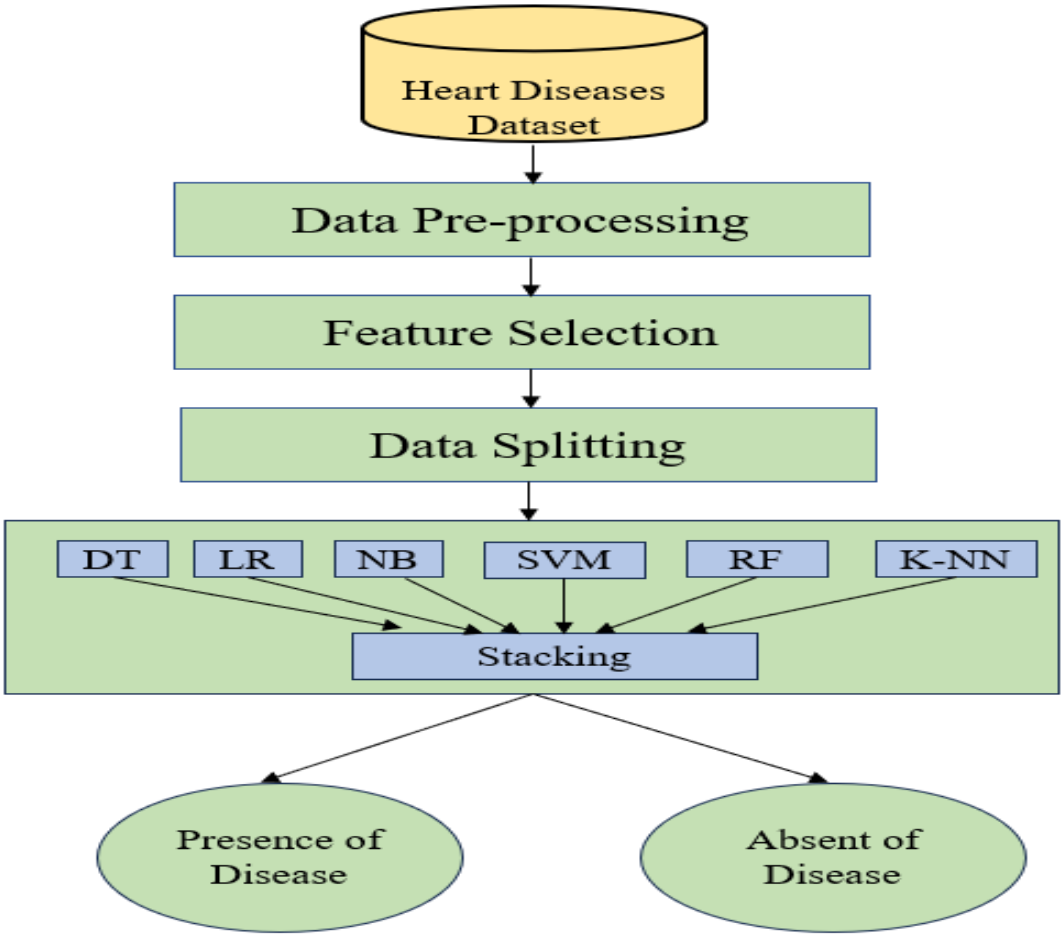

Figure 35: The flow diagram of the suggested model for heart disease prediction

Dataset Description

The Kaggle repository's cardiovascular disease dataset is utilized for prediction of heart diseases. This dataset was created by combining five different datasets which are Cleveland, Hungarian, Switzerland, Long Beach VA, StatLog. It has 1190 samples with 11 attributes which are age, sex, chest pain type (cpt), resting bp s, cholesterol, fasting blood sugar (fbs), resting ecg, max heart rate (mhrt), exercise angina (ea), oldpeak, ST slope. The presence and absence of HD is illustrated as 1 and 0, respectively. The heart diseases status is identified as

the target variable in the dataset. While 629 people in the dataset have heart disease, 561 people do not have heart disease (Siddhartha, 2020). The number of individuals with and without HD in the dataset is shown in Figure 2.

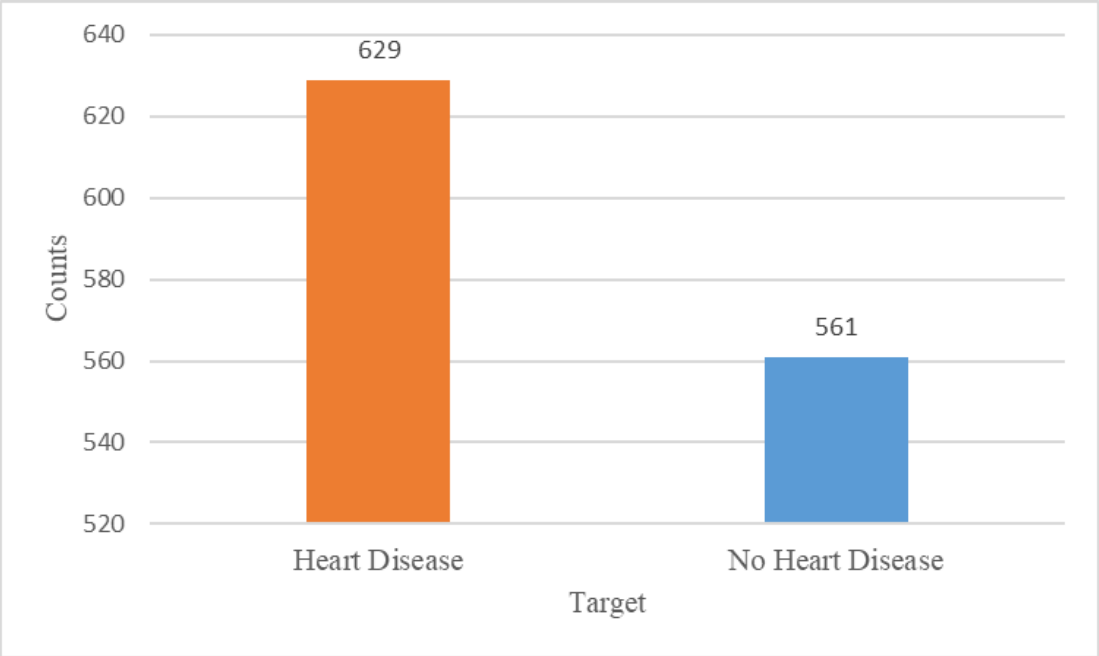

Figure 36: Count plot of target attribute

Data Pre-processing

Data preprocessing is the process of making data analyzable. The datasets are preprocessed before being used directly. These steps correct errors and omissions in the data, remove redundant information and ultimately optimize the data for better results. Data pre-processing plays a significant role in ML applications. If the data pre-processing process are not used, the results of ML algorithms maybe inaccurate or misleading. The first stage of data preprocessing is data cleaning. Data cleaning consists of identifying and correcting errors or inconsistences in data such as missing values, outliers and duplicates. When the data is analyzed, missing data in the data set is checked and no missing records are found. During the outlier detection process, outliers at several cholesterol levels are observed during box plotting and these values are deleted using the z-score criteria. The second stage of data preprocessing is the feature scaling. It provides to standardize the features found in the data in a fixed range. In this study, Min-max scaling technique is utilized for data normalization (Fan et al., 2021).

Feature Selection

Feature selection (FS) is a crucial step in the data mining process that aims to minimize the number of features in a dataset by selecting the most useful ones. These techniques can increase the performances of classification algorithms and are very useful in reducing the learning process of classification algorithms (Kumar & Minz, 2014). In this study, a two-stage feature selection method is applied. In the first stage, the correlation of the independent features in the data set with the target attribute is examined. In the second stage, the Recursive Feature Elimination method is used to select the most useful features in the data set.

Each data set contains different stories within itself. One of the ways to uncover these hidden stories is to examine the relationships between the variables. The statistical relationship between two random variables is called correlation. The correlation is one of the most important

and fundamental steps of exploratory data analysis. While building a model for ML, correlation plays an important role in determining the variables to be used in the model. The correlation analysis is a statistical analysis to determine whether there is a relationship between two or more variables, and if there is, its strength and direction. A heat map can be used to perform correlation analysis. It is kind of chart that visualizes the strength relationship between numerical attributes (Haarman et al., 2014).

The heat map of the dataset is presented in Figure 3. Using this heatmap, it is possible to examine the correlation between the target attribute and other variables. When the correlation heat map is examined, it can be observed that there is a very weak correlation between the target attribute and heart rate (-0.41), cholesterol (-0.12) and resting bps (0.12). Therefore, these attributes are eliminated from the dataset.

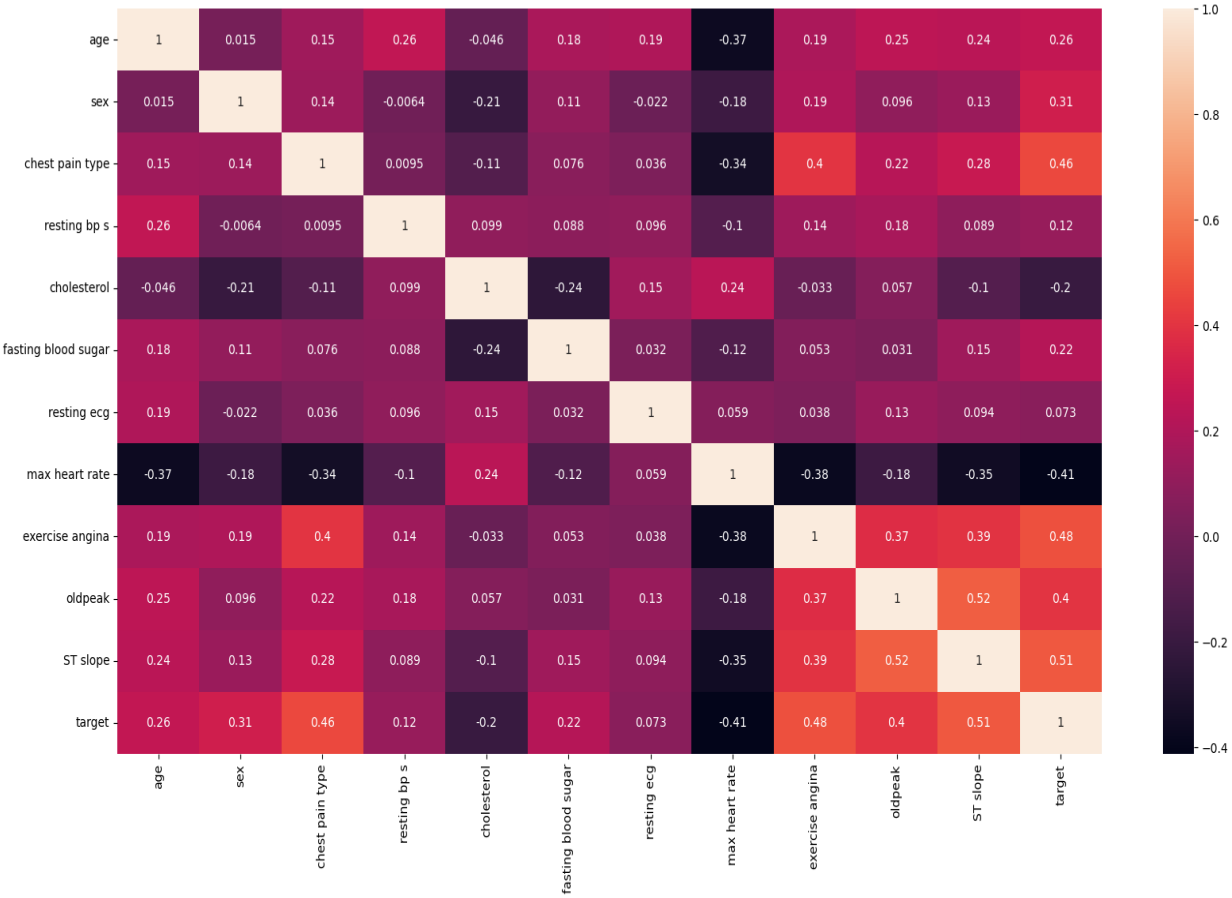

Figure 37: Correlation heatmap

In the second step of feature selection, RFE technique is preferred. The main point of this technique is to determine the key attributes of the dataset. The process in this technique is to rank the attributes in the dataset from the largest to the smallest according to their effect on success. After the features are ranked according to their effect on success, the most successful ones are selected and the FS is made. When the ranking attributes, a classification algorithm is used. In this study, SVM is preferred as a classification algorithm (Sanz et al., 2018). The working steps of the RFE algorithm are as follows.

- By choosing a classification algorithm, the importance of all the features in the data set is ranked.
- The least important attribute in the data set is eliminated.

- A model is created with the remaining attributes.
- The previous steps are repeated until the desired number of attributes is reached.

Machine Learning Algorithms

ML algorithms in daily life without realizing it used in many applications. It is a collection of methodology that enables a system to build a model using a data set, using past experience, and make predictions about future situations. Today, the current studies are carried out utilizing these algorithms in order to help diagnose many diseases. In this study, different ML methods such as logistic regression (LR), decision tree (DT), support vector machine (SVM), K-nearest neighbor (K-NN), random forest (RF), Naive Bayes (NB) and stacking ensemble learning have been used to predict HD.

LR is used to estimate the probabilities of these attributes when a series of descriptive independent attributes are encountered. This method can be preferred if the target attribute is known as a dependent variable with categorical values. DT is generally used for regression and classification purposes. This algorithm aims to divide the features in the data set into subsets until they have the same class label with a clustering method. SVM aims to find a hyperplane curve that divides a data into best classes. The hyperplane curve is farthest from both classes. With the finding of the hyperplane using the training data, the test data is assigned to the class on whichever side of the hyperplane it is located (Ahmad, 2022). NB calculates the probability of an item falling into a certain category based on the conditional probability rule. The algorithm assumes that the effect of the value of an attribute in a class is independent of other attributes. This assumption process is defined as the conditional probability rule. The conditional probability rule is calculated using Bayes' Theorem (Pattekari & Parveen, 2012). K-NN aims to classify a new sample according to the similarity between the samples in the training set. RF algorithm makes a prediction by combining the predictions of the multiple DT models. This process begins with training multiple decision trees on a random subset of the data. A final outcome is made by averaging the predictions of all trees in the model (Ahmad, 2022). Stacking is an ensemble learning algorithm used to build a new model and improve model performance. The algorithm tries to do this by predicting more than one node. This technique allows to train multiple models to solve similar problems and allows to create a new model with better performance based on their combined results. A stacking model example is presented in Figure 4. Stacking generally takes weak learners into account. It learns them in a parallel form and then combine them using a meta learner in order to obtain output that depends on the predictions of the weak learners. The meta learner utilizes the feature as inputs and the main aim here is the basic real values of the data. The algorithm goes through a learning process to find the best combination of input predictions and aims to make a better output prediction. In this study, SVM is preferred as meta learner (Hu et al., 2021).

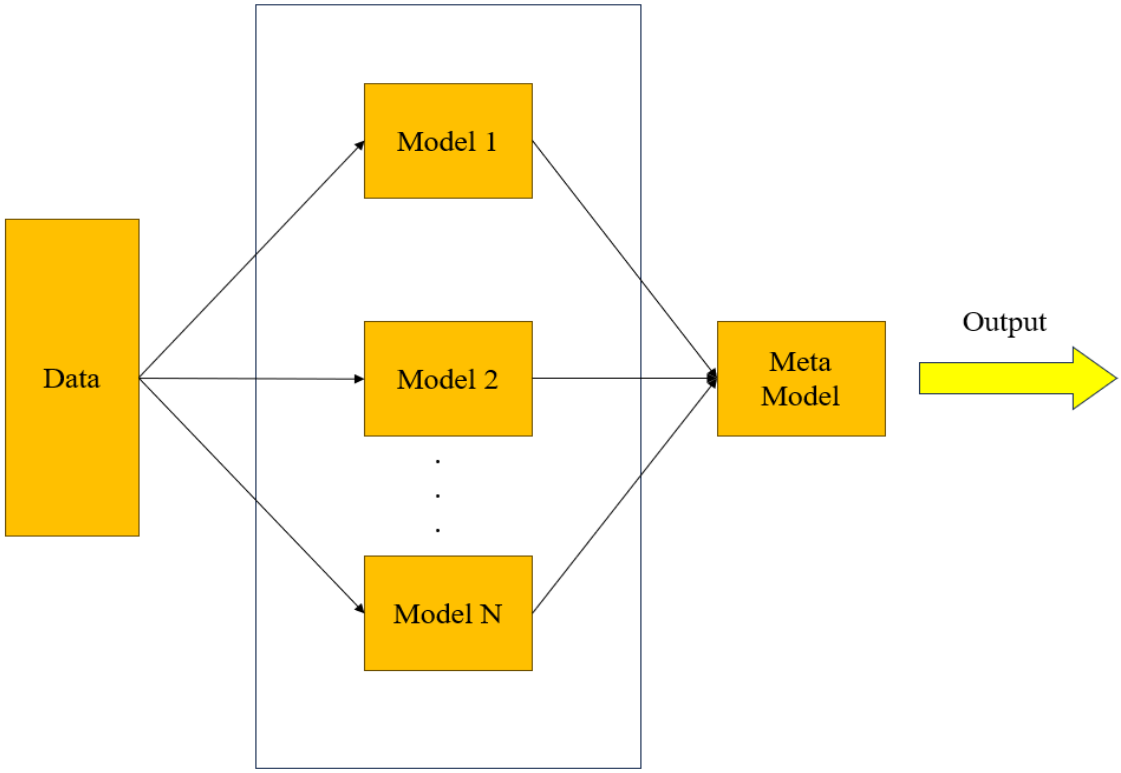

Figure 38: A stacked ensemble model example

Experimental Results and Discussion

The experiments are employed using the Pyhton programming on Jupyter Notebook Platform. All the ML algorithms are made up of 80% training and 20% testing data. The classification performance of ML algorithms is evaluated utilizing a set of performance metrics. To measure each of ML algorithm, accuracy, precision, recall and F1-measure performance metrics are utilized.

In this study, a two-stage feature selection method is applied. First of all, the correlation between the target attribute and other attributes in the data set is examined. The correlation analysis is shown in Figure 3 with the heat map. As a result of this process, max. heart rate, cholesterol and resting bp s are excluded from the data set because they have very little correlations with the target. Thus, eight attributes are obtained by subtracting three variables from eleven variables. In the next step, the RFE method is applied to select the useful attributes in the data set. After the phase of determining the most effective features with the suggested RFE-FS method, the five most effective features are selected among eight features. According to the scores of RFE-FS, sex, chest pain type, fasting blood sugar, exercise angina and ST slope are selected.

The different ML algorithms such as LR, NB, RF, K-NN, DT, SVM and Stacked EL are employed for HD prediction after the FS process. The results of ML algorithms are presented in Table 1. The results depict that stacked EL obtained the highest classification results with accuracy of 87.39%, precision of 86.24%, recall of 86.24% and F1-measure of 86.24%. The second most successful ML algorithm is RF with accuracy of 86.55%, precision of 84.40%, recall of 85.98% and F1-measure 85.19%.

Table 1. The results of ML algorithms

Algorithms	Accuracy (%)	Precision (%)	Recall(%)	F1-Measure (%)
LR	79.83	77.98	77.98	77.98
NB	85.29	85.32	83.04	84.16
K-NN	83.61	84.40	80.70	82.51
DT	82.77	79.82	82.08	80.93
SVM	84.45	79.82	85.29	82.46
RF	86.55	84.40	85.98	85.19
Stacked EL	87.39	86.24	86.24	86.24

The performance of an ML algorithm can also be represented graphically by the AUC-ROC curve. The ROC curve represents a probability curve and AUC represents the measure of separability that shows the power of the model to separate the classes. The higher the AUC, the better the algorithm is at distinguishing between people with and without the disease. Figure 5 illustrates the AUC-ROC of ML algorithms. As shown in Figure 5, the Stacked EL algorithm has a high AUC of 0.87 compared to other algorithms.

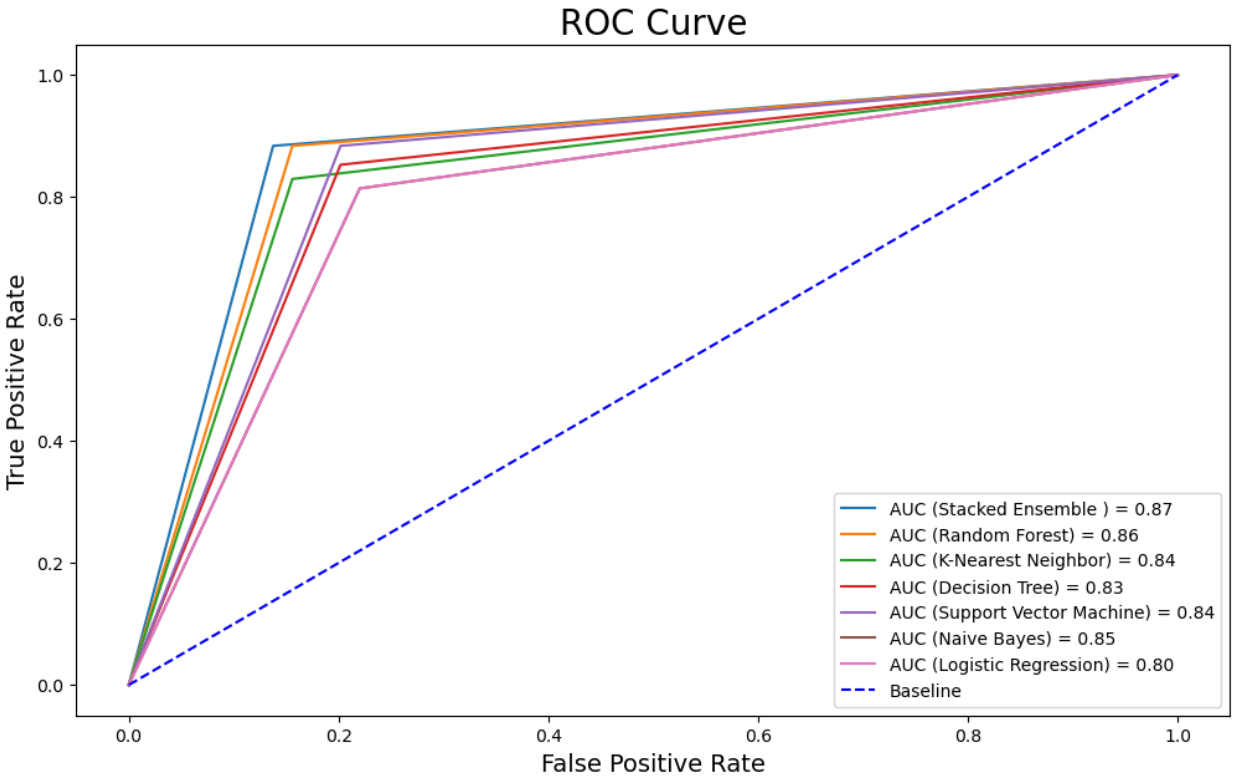

Figure 39: The AUC-ROC Curve of each ML algorithm

The clinical decisions made according to the results obtained with ML algorithms in the field of health are very important for the lives of patients. It is beneficial for such applications to be both accurate and include interpretable prediction models. For the purpose of interpreting a model, the Shapley additive explanations (SHAP) technique can be used to explore the effect of attributes on the result obtained. Figure 6 presents the importance of each attribute for HD prediction, and the contribution of each attribute to performance of model. This figure depicts

the SHAP values for the Stacked EL algorithm with the highest prediction rate. The higher the SHAP value of an attribute, the more useful that attribute is to the heart disease prediction model. When the SHAP values in the Figure 6 are examined, it can be said that the ST slope feature is the most important risk factor for a person with heart disease.

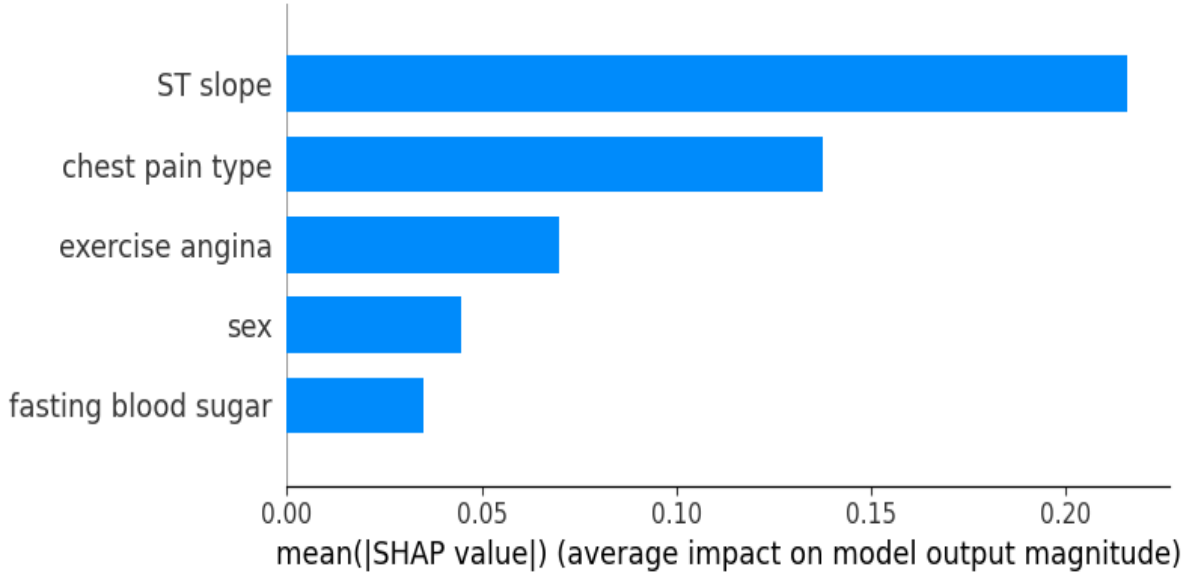

Figure 40: SHAP values of the stacked EL algorithm

Conclusion

Early detection of HD and timely intervention are critical to prevent the disease from causing further problems. Recently, ML algorithm-based models have taken a place in the prediction of HD. In this study, the prediction is performed on a HD dataset using different ML algorithms. In order to increase the classification rates of these algorithms, feature selection method is employed. By using the FS algorithm, 11 attributes are reduced to 5. When the classification performances of ML algorithms are compared, the stacked EL algorithms achieves a better result for the prediction of HD. As ensemble learning methods generally use more than one classifier, they are expected to outperform a single classifier. According to the results obtained as a result of this study, the stacked EL algorithm meets this expectation. With the help of SHAP analysis, the most important risk factor affecting heart disease is tried to be determined with this study. According to the results of the SHAP analysis, it can be said that the ST slope parameter is the most important risk factor in the determination of heart disease.

In conclusion; it is thought that the development of HD prediction studies with such ML methods will make an important contribution to the field of health, in order to assist healthcare professionals by providing a second opinion.

References

Ahmad, G. N., Fatima, H., Abbas, M., Rahman, O., & Alqahtani, M. S. (2022). Mixed machine learning approach for efficient prediction of human heart disease by identifying the numerical and categorical features. *Applied Sciences*, 12(15), 7449.

Azmi, J., Arif, M., Nafis, M. T., Alam, M. A., Tanweer, S., & Wang, G. (2022). A systematic review on machine learning approaches for cardiovascular disease prediction using medical big data. *Medical Engineering & Physics*, 103825. https://doi.org/10.1016/j.medengphy.2022.103825

Bhatt, C. M., Patel, P., Ghetia, T., & Mazzeo, P. L. (2023). Effective heart disease prediction using machine learning techniques. *Algorithms*, 16(2), 88.

Dwivedi, A. K. (2018). Performance evaluation of different machine learning techniques for prediction of heart disease. *Neural Computing and Applications*, 29(10), 685-693.

Fan, C., Chen, M., Wang, X., Wang, J., & Huang, B. (2021). A review on data preprocessing techniques toward efficient and reliable knowledge discovery from building operational data. *Frontiers in Energy Research*, 9, 652801. https://doi.org/10.3389/fenrg.2021.652801.

Gurfidan, R. and Ersoy, M. (2021). Classification of death related to heart failure by machine learning algorithms. *Advances in Artificial Intelligence Research*, 1(1), 13-18.

Haarman, B. C. B., Riemersma-Van der Lek, R. F., Nolen, W. A., Mendes, R., Drexhage, H. A., & Burger, H. (2015). Feature-expression heat maps–A new visual method to explore complex associations between two variable sets. *Journal of biomedical informatics*, 53, 156-161.

Hu, X., Mei, H., Zhang, H., Li, Y., & Li, M. (2021). Performance evaluation of ensemble learning techniques for landslide susceptibility mapping at the Jinping country, Southwest China. *Nat Hazards* 105, 1663–1689. https://doi.org/10.1007/s11069-020-04371-4

Islam, M.M., Tania, T.N., Akter, S., Shakib, K.H. (2023). An Improved Heart Disease Prediction Using Stacked Ensemble Method. In: Satu, M.S., Moni, M.A., Kaiser, M.S., Arefin, M.S. (eds) Machine Intelligence and Emerging Technologies. *MIET 2022. Lecture Notes of the Institute for Computer Sciences, Social Informatics and Telecommunications Engineering*, vol 490. Springer, Cham. https://doi.org/10.1007/978-3-031-34619-4_

Kannan R. & Vasanthi V. (2019), Machine learning algorithms with ROC curve for predicting and diagnosing the heart disease. *In: Soft Computing and Medical Bioinformatics. SpringerBriefs in Applied Sciences and Technology().* Springer, Singapore. https://doi.org/10.1007/978-981-13-0059-2_8.

Khateeb, N., & Usman, M. (2017). Efficient heart disease prediction system using K-nearest neighbor classification technique. *In proceedings of the International Conference on Big Data and Internet of Thing*, December, pp. 21-26. https://doi.org/10.1145/3175684.3175703.

Kumar, V., & Minz, S. (2014). Feature selection: a literature review. *SmartCR*, 4(3), 211-229.

Ouf, S., ElSeddawy, A.I.B. (2021). A proposed paradigm for intelligent heart disease prediction system using data mining techniques. *J. Southwest Jiaotong Univ*. 56, 220–240.

Pattekari, S. A., & Parveen, A. (2012). Prediction system for heart disease using Naïve Bayes. International Journal of Advanced Computer and Mathematical Sciences, 3(3), 290-294.

Pouriyeh S., Vahid, G. Sannino, G. De Pietro, H. Arabnia, and J. Gutierrez, A comprehensive investigation and comparison of machine learning techniques in the domain of heart disease, (2017). *IEEE Symposium on Computers and Communications (ISCC)* , 03-06 June, Heraklion, Greece, pp. 204–207.

Riyaz, L., Butt, M. A., Zaman, M., & Ayob, O. (2022). Heart disease prediction using machine learning techniques: a quantitative review. *In International Conference on Innovative Computing and Communications: Proceedings of ICICC 2021*, Volume 3, Springer Singapore, pp. 81-94. https://doi.org/10.1007/978-981-16-3071-2_8

Sanz, H., Valim, C., Vegas, E., Oller, J. M., & Reverter, F. (2018). SVM-RFE: selection and visualization of the most relevant features through non-linear kernels. *BMC bioinformatics*, 19(1), 1-18.

Shorewala, V. (2021). Early detection of coronary heart disease using ensemble techniques. *Inform. Med. Unlocked*. 26, 100655. https://doi.org/10.1016/j.imu.2021.10065.

Siddhartha M., (November 5, 2020). Heart Disease Dataset (Comprehensive). *IEEE Dataport*, https://www.kaggle.com/datasets/sid321axn/heart-statlog-cleveland-hungary-final/ Accessed 09 May, 2023.

Pumıce Fılled Polymer Composıtes And Theır Applıcatıons

F. Fulya TAKTAK [1]

Introduction

Pumice is a type of extrusive rock formed by the outflow of lava with a very high water and gas content from a volcano. It has the structure of a light sponge with a hard texture because it contains numerous pores from the macro to the micro level, which were formed by the sudden escape of gases in the body during its formation and the sudden cooling (Hossain, 2004). Pumice is usually light in color but can also be brown or black. This is due to the chemical structure of pumice. In general, pumice is composed of about 40-70% SiO_2 and may contain mainly Na_2O-K_2O (7-8%) and Al_2O_3 (13-17%). Small amounts of MnO, MgO and other oxides such as CaO, TiO_2 and Fe_2O_3 may also be present (Benlikaya & Kahrıman, 2022). Light colored pumice is acidic and the most common type of pumice. Basic pumice can range in color from brown to black. SiO_2 content is lower in basic pumice and contains higher proportions of Al_2O_3 and Fe_2O_3 than in acidic pumice. In general, a SiO_2 content of 40-52 wt% corresponds to basic pumice, also known as scoria, while 63-75% SiO_2 corresponds to acidic pumice (Xue-min et al., 2018).

The presence of unconnected pore spaces makes pumice suitable for thermal and acoustic insulation (Soyaslan, 2020). Therefore, it is one of the oldest materials used by man. Today, pumice is used in more than 50 different sectors, mainly in the construction, textile, agriculture, and chemical industries, for various purposes such as fillers, abrasives, and filtration. In addition to the numerous superior technological advantages offered by pumice, the fact that it is very cheap and can be used without pretreatment is an important economic advantage in the sectors concerned.

We know that the total reserves of pumice in Turkey, which has been extensively quarried since 2010, is approximately $3Tm^3$ (Bideci & et al., 2014). A large part of the world's reserves is located in America, and Turkey is the second largest supplier of reserves in the world. Bitlis province has 50% of the available reserves, while the Kayseri-Nevsehir region is another important reserve region. Table 1 shows some physical properties and SiO_2 contents of pumice samples from different regions of Turkey. Judging by the SiO_2 content, it appears that both acidic and basic pumice are present in Turkey.

[1] Doç. Dr., Uşak University

Tablo 1. Chemical composition and physical properties of pumice samples from Turkey

Reference	Source	Specific gravity (g/cm^3)	Surface area (m^2/g)	SiO_2 content (%)
Gencel & et al., 2016	Erzincan	2.50	3.697	58.44
Saridemir & Bulut, 2021	Aksaray	2.87	3.165	51.16
Guneyisi & et al., 2014	Hatay	2.84	4.548	49.5
Sariisik & Sariisik, 2012	Nevşehir	2.26	-	70.06
Pinarci & Kocak, 2022	Isparta	2.70	0.265	56.32
Karaaslan & et al., 2022	Ağrı	2.67	0.498	67.49
Kanarya & et al., 2021	Kayseri	-	-	53.50
Balun & Karatas, 2021	Bitlis-Tatvan	2.33	0.292	63.60
Durgun, 2020	Kahramanmaraş	3.09	-	43.58
Kabay & et al., 2021	Nevşehir	2.40	-	77.52
Felekoglu, 2012	Nevşehir	2.09	-	74.10
Ozturk & Yildirim, 2007	Kayseri	0.73	3.8	57.00
Durgun et al., 2017	Adana	2.91	0.371	47.63
Binici et al., 2012	Osmaniye	2.88	0.300	53.80
Aydın & Baradan, 2007	İzmir	2.03	-	75.51
Demirel & Kelestemur, 2010	Elazığ	2.80	-	49.52
Karakoc, 2011	Van	2.20	-	69.78

The use of pumice as an adsorbent in the treatment of waste-water

The presence of many organic and inorganic pollutants, especially dyes and heavy metals, in industrial wastewater can cause major problems for wastewater treatment plants. Today, industry has to do its own pre-treatment to remove such contaminants before entering wastewater treatment facilities. Adsorptive processes for wastewater treatment have gained popularity because they are inexpensive, simple and highly efficient (Ighalo & et al., 2002; Rathi & Kumar, 2001). The adsorbents are the most important part of this process.

Among potential adsorbents, volcanic materials have attracted considerable attention in recent years for the removal of pollutants from wastewater. This is due to their large surface area, strength, low cost and local availability in large quantities. Pumice is one of the most economical and widely used adsorbents of interest to researchers for the removal of many

pollutants from aqueous solutions. Pumice, a volcanic rock, has a high specific surface area due to its microporous structure (Wacey & et al., 2013). Pumice has been used for the removal of various pollutants, including heavy metals (Wang & et al., 2014; Wand & et al., 2015), various dyes (Gupta & et al., 2015; Norouzbeigi & et al., 2016), phenol (Morad i& et al., 2018), fluoride (Salifu & et al., 2013; Jin & et al., 2021) and phosphate (Jin & et al., 2023).

Chemical activation with acids, alkalis, surfactants and oxidising agents as well as thermal activation are often used to increase the adsorption capacity of mineral adsorbents in wastewater treatment. Parian et al. (2023) used raw pumice and pumice modified with five different acids (sulphuric, nitric, acetic, phosphoric and hydrochloric) to remove the dye Remazol Black B from an aqueous solution. The results showed that H_2SO_4 was the most effective acid and could increase the removal efficiency of Remazol Black B (q_m = 10.00 mg/g) twofold compared to raw pumice (q_m = 5.26 mg/g). Scanning electron microscope (SEM) analysis showed that the morphology of raw pumice and pumice modified with different acids was different. While the raw pumice had a flatter morphological appearance, the morphology of the acid-modified pumice samples changed and became fissured-roughened and porous. This study showed that acid activation can increase the surface area of pumice. In another study, the potential of NaOH-modified pumice and raw pumice for adsorption of the hardness-causing cations Ca^{2+} and Mg^{2+} was investigated. The maximum adsorption capacities were found to be 57.27 and 62.34 mg/g for Ca^{2+} and 44.53 and 56.11 mg/g for Mg^{2+} in the raw and modified pumice, respectively. The specific surface areas of the adsorbents were 36.30 and 2.34 m^2/g for natural and modified pumice, respectively, as measured by Brunauer-Emmett-Teller (BET) analysis. It was reported that the impurities in the pores of pumice could be removed after alkali modification, which significantly increased the surface area (Zarrabi & et al, 2013).

On the other hand, the zeta potential of pumice is negative. The formation of cationic charges on the pumice by surface modification is particularly desirable for interaction with cationic pollutants. To this end, cationic surfactants such as cetyltrimethylammonium bromide (CTAB) have been modified, and their ability to adsorb anionic pollutants through electrostatic interactions has been greatly enhanced. Shayesteh et al. investigated the potential of natural pumice (NP) and pumice modified with CTAB (SMP) to remove Congo red, an anionic dye, from aqueous solutions. The measured maximum adsorption capacities, calculated using the linear Langmuir isotherm equation, were 3.87 mg/g for NP and 27.32 mg/g for SMP at 25 °C, respectively (Shayesteh & et al., 2016).

Dehghani et al. (2017) modified natural pumice with $FeCl_3.6H_2O$-modified pumice (FEMP) and hexadecyltrimethylammonium bromide (HDTM.Br), which has a positive effect on the surface area for adsorption of fluoride anions in water. The specific surface area (m^2/g), average pore diameter (nm) and total pore volume (cm^3/g) obtained with BET for raw pumice (NP), $FeCl_3.6H_2O$ modified pumice (FEMP) and hexadecyltrimethylammonium bromide (HMP) were (9.51, 18.39, 0.0437), (24.50, 7.11, 0.0435) and (31.51, 2.23, 0.0432), respectively. The significantly improved specific surface area after modification was attributed to the separation of the constituents in the pores of the raw pumice. On the other hand, it was found that the pore diameters decreased. This change can be explained by the coating of the outer surface of the pumice with HDTMA and $FeCl_3$. The maximum adsorption capacity was calculated to be 1.17, 21.74 and 25 mg/g for NP, FEMP and HMP, respectively. The modification of pumice with $FeCl_3.6H_2O$ and HDTM.Br resulted in the formation of a positive charge on the pumice surface and the fluoride anion was adsorbed better than the raw pumice. In general, it was found that the specific surface area, pore structure and chemical functional groups of the adsorbent surface changed with the modification of the adsorbent, and the adsorption capacities increased significantly compared with the raw pumice. In addition, the incorporation of inorganic materials into various polymer matrices can lead to a significant increase in adsorption capacity as the final adsorbent contains more functional groups.

Pumice/polymer composites are nowadays appreciated for their high adsorption capacity, fast equilibrium and improved thermal and mechanical properties. The homogeneous dispersion of inorganic particles in a polymer matrix also prevents the agglomeration of inorganic particles that would be used alone as adsorbents.

Pumice/polymer composites

Polymeric materials are often preferred for the removal of pollutant components from wastewater. The presence of various functional groups can provide for the establishment of suitable interactions with pollutants. In particular, polymeric hydrogels can adsorb a considerable amount of water in their structures. On the other hand, the mechanical and thermal stability of polymers during adsorption processes may be insufficient. A suitable way to modify polymers is to reinforce the polymer matrix structures with inorganic fillers.

Inorganic fillers such as bentonite, zeolite, and montmorillonite are combined with various polymers by researchers because they are inexpensive and widely available. Inorganic materials have advantages such as high chemical, thermal and mechanical strength, but their disadvantages such as generally lower specific surface area and limited water adsorption prevent their efficient use in the adsorption process alone. Polymer composites reinforced with inorganic fillers have the potential to be good adsorbents due to the favorable properties of both components. The literature contains numerous studies in which natural inorganic materials such as zeolite, bentonite and montmorillonite have been incorporated with various polymers. In contrast, the number of polymer composites filled with pumice is very limited.

The pumice-polymer composites described in the literature are listed in Table 2 with their composition, developed properties, and adsorption applications and capacities. As can be seen, the number of pumice-filled polymer composites produced is small. They were generally used for adsorption applications. It has been reported that pumice provides thermal stability and improves the mechanical properties of the fabricated composite structures. It is believed that the improved mechanical and thermal properties are due to the strong interfacial interactions between pumice and the polymer matrix.

Table 2. Literature review of various pumice/polymer composites and their improved properties and adsorption applications

Reference	Composition	Enhanced properties by pumice	Applications	Adsorption capacity
Ramesan& et al, 2016	poly (vinyl alcohol)/cashew tree gum/pumice composite	DSC studies have shown an increase in melting and glass transition temperatures (Tg) with increasing pumice content.		
Gök & Göde, 2018	poly(2-chloroaniline) (P2ClAn)/pumice (Pmc), poly(o-toluidine) (POT)/Pmc composites		Removal of Cr (VI) ions	0.19 mmol/g (POT/Pmc) 4.96 (P2ClAn/Pmc)
Sahan & et al, 2019	N-[Tris (hydroxymethyl)methyl]acrylamide grafted pumice (PTHAM@PMC)		Removal of methylene blue dye	69.00 (mg/g)

Gök & et al, 2006	polyaniline/pumice (PAn/Pmc)	Thermal analysis has shown an increase in thermal stability of PAn/Pmc composite compared to PAn.		
Taşdelen & et al, 2017	N-isopropylacrylamide/ itaconic acid/pumice	Compression strength tests have shown improved mechanical properties and the adsorption capability with pumice addition.	Removal of methylene blue dye	22.62 (mg/g)
Akkaya, 2013	polyhydroxyethylmethacrylate-pumice composite		Removal of UO22+ and Th4+	
Sharma & et al, 2007	polyacrylonitrile/pumice composite		Removal of Cu2+, Cr3+	3.37 mg/g (Cu2+), 13.94 mg/g (Cr3+)
Taktak & Ilbay, 2015)	poly[2-(dimethylamino) ethyl methacrylate]/ pumice		Removal of humic acid	86.27 mg/g
Soyaslan, 2021	pumice/polyurethane composite	The sound absorption, sound transmission loss and thermal conductivity tests have shown that composites have higher thermal and sound insulation properties compared to polyurethane.		

REFERENCES

Akkaya, R. (2013). Uranium and thorium adsorption from aqueous solution using a novel polyhydroxyethylmethacrylate-pumice composite. *Journal of environmental radioactivity*, *120*, 58-63. https://doi.org/10.1016/j.jenvrad.2012.11.015.

Aydın, S. & Baradan, B. (2007). Effect of pumice and fly ash incorporation on high temperature resistance of cement based mortars. *Cement and concrete research*, *37*(6), 988-995. https://doi.org/10.1016/j.cemconres.2007.02.005.

Balun, B. & Karataş, M. (2021). Influence of curing conditions on pumice-based alkali activated composites incorporating Portland cement. *Journal of Building Engineering*, *43*, 102605.https://doi.org/10.1016/j.jobe.2021.102605.

Benlikaya, R. & Kahrıman, M. (2022). Chemical Inferences Drawn From Basalt Volcanic Pumice. *Celal Bayar University Journal of Science*, *18*(2), 225-231. Doi: 10.18466/cbayarfbe.993131.

Bideci, Ö. S., Bideci, A., Gültekin, A. H., Oymael, S. & Yildirim, H. (2014). Polymer coated pumice aggregates and their properties. *Composites Part B: Engineering*, *67*, 239-243. https://doi.org/10.1016/j.compositesb.2013.10.009.

Binici, H., Kapur, S., Arocena, J. & Kaplan, H. (2012). The sulphate resistance of cements containing red brick dust and ground basaltic pumice with sub-microscopic evidence of intra-pore gypsum and ettringite as strengtheners. *Cement and Concrete Composites*, *34*(2), 279-287. https://doi.org/10.1016/j.cemconcomp.2011.10.001.

Brasier, M. D., Matthewman, R., McMahon, S., Kilburn, M. R. & Wacey, D. (2013). Pumice from the∼ 3460 Ma Apex Basalt, Western Australia: A natural laboratory for the early biosphere. *Precambrian Research*, *224*, 1-10. https://doi.org/10.1016/j.precamres.2012.09.008.

Dehghani, M. H., Faraji, M., Mohammadi, A. & Kamani, H. (2017). Optimization of fluoride adsorption onto natural and modified pumice using response surface methodology: isotherm, kinetic and thermodynamic studies. *Korean Journal of Chemical Engineering*, *34*, 454-462. https://doi.org/10.1007/s11814-016-0274-4.

Demirel, B. & Keleştemur, O. (2010). Effect of elevated temperature on the mechanical properties of concrete produced with finely ground pumice and silica fume. *Fire Safety Journal*, *45*(6-8), 385-391. https://doi.org/10.1016/j.firesaf.2010.08.002.

Durgun, M. Y. (2020). Effect of wetting-drying cycles on gypsum plasters containing ground basaltic pumice and polypropylene fibers. *Journal of Building Engineering*, *32*, 101801. https://doi.org/10.1016/j.jobe.2020.101801.

Felekoğlu, B. (2012). A method for improving the early strength of pumice concrete blocks by using alkyl alkoxy silane (AAS). *Construction and Building Materials*, *28*(1), 305-310.https://doi.org/10.1016/j.conbuildmat.2011.07.026.

Gök, A., Göde, F. & Türkaslan, B. E. (2006). Synthesis and characterization of polyaniline/pumice (PAn/Pmc) composite. *Materials Science and Engineering: B*, *133*(1-3), 20-25. https://doi.org/10.1016/j.mseb.2006.04.040.

Gök, A. U. & Göde, F. (2008). Composites of poly (2-chloroaniline) and poly (o-toluidine) with pumice and their application in the removal of chromium (VI) ions from aqueous solutions. *Journal of applied polymer science*, *107*(4), 2295-2303. https://doi.org/10.1002/app.27251.

Güneyisi, E., Gesoğlu, M., Al-Rawi, S. & Mermerdaş, K. (2014). Effect of volcanic pumice powder on the fresh properties of self-compacting concretes with and without silica fume. *Materials and structures*, *47*, 1857-1865. https://doi.org/10.1617/s11527-013-0155-9.

Heibati, B., Rodriguez-Couto, S., Turan, N. G., Ozgonenel, O., Albadarin, A. B., Asif, M. & Gupta, V. K. (2015). Removal of noxious dye-Acid Orange 7 from aqueous solution using

natural pumice and Fe-coated pumice stone. *Journal of Industrial and Engineering Chemistry*, *31*, 124-131. https://doi.org/10.1016/j.jiec.2015.06.016.

Heydari, M., Karimyan, K., Darvishmotevalli, M., Karami, A., Vasseghian, Y., Azizi, N., Ghayebzadeh, M. & Moradi, M. (2018). Data for efficiency comparison of raw pumice and manganese-modified pumice for removal phenol from aqueous environments-application of response surface methodology. *Data in brief*, *20*, 1942-1954. https://doi.org/10.1016/j.dib.2018.09.027.

Hossain, K. M. A. (2004). Properties of volcanic pumice based cement and lightweight concrete. *Cement and concrete research*, *34*(2), 283-291. https://doi.org/10.1016/j.cemconres.2003.08.004.

Ighalo, J. O., Omoarukhe, F. O., Ojukwu, V. E., Iwuozor, K. O. & Igwegbe, C. A. (2022). Cost of adsorbent preparation and usage in wastewater treatment: A review. *Cleaner Chemical Engineering*, 100042. https://doi.org/10.1016/j.clce.2022.100042.

Kabay, N., Miyan, N., & Özkan, H. (2021). Utilization of pumice powder and glass microspheres in cement mortar using paste replacement methodology. *Construction and Building Materials*, *282*, 122691. https://doi.org/10.1016/j.conbuildmat.2021.122691.

Karaaslan, C., Yener, E., Bağatur, T., Polat, R., Gül, R., & Alma, M. H. (2022). Synergic effect of fly ash and calcium aluminate cement on the properties of pumice-based geopolymer mortar. *Construction and Building Materials*, *345*, 128397. https://doi.org/10.1016/j.conbuildmat.2022.128397.

Karakoç, M. B., Demirboğa, R., Türkmen, İ., & Can, I. (2011). Modeling with ANN and effect of pumice aggregate and air entrainment on the freeze–thaw durabilities of HSC. *Construction and Building Materials*, *25*(11), 4241-4249. https://doi.org/10.1016/j.conbuildmat.2011.04.068

Kocak, Y., & Pinarci, İ. Hydration Mechanisms and Mechanical Properties of Pumice Substituted Cementitious Binder. *Available at SSRN 4064368*. https://doi.org/10.1016/j.conbuildmat.2022.127528

Lemougna, P. N., Wang, K. T., Tang, Q., Nzeukou, A. N., Billong, N., Melo, U. C., & Cui, X. M. (2018). Review on the use of volcanic ashes for engineering applications. *Resources, Conservation and Recycling*, *137*, 177-190. https://doi.org/10.1016/j.resconrec.2018.05.031.

Liu, T., Wang, Z. L., Yan, X., & Zhang, B. (2014). Removal of mercury (II) and chromium (VI) from wastewater using a new and effective composite: Pumice-supported nanoscale zero-valent iron. *Chemical Engineering Journal*, *245*, 34-40. https://doi.org/10.1016/j.cej.2014.02.011.

Liu, T., Wang, Z. L., & Sun, Y. (2015). Manipulating the morphology of nanoscale zero-valent iron on pumice for removal of heavy metals from wastewater. *Chemical Engineering Journal*, *263*, 55-61. https://doi.org/10.1016/j.cej.2014.11.046.

Ozturk, B., & Yildirim, Y. (2008). Investigation of sorption capacity of pumice for SO2 capture. *Process Safety and Environmental Protection*, *86*(1), 31-36.https://doi.org/10.1016/j.psep.2007.10.010.

Ramesan, M. T., Jose, C., Jayakrishnan, P., & Anilkumar, T. (2018). Multifunctional ternary composites of poly (vinyl alcohol)/cashew tree gum/pumice particles. *Polymer Composites*, *39*(1), 38-45. https://doi.org/10.1002/pc.23899.

Rathi, B. S., & Kumar, P. S. (2021). Application of adsorption process for effective removal of emerging contaminants from water and wastewater. *Environmental Pollution*, *280*, 116995. https://doi.org/10.1016/j.envpol.2021.116995.

Salifu, A., Petrusevski, B., Ghebremichael, K., Modestus, L., Buamah, R., Aubry, C., & Amy, G. L. (2013). Aluminum (hydr) oxide coated pumice for fluoride removal from drinking water: Synthesis, equilibrium, kinetics and mechanism. *Chemical Engineering Journal*, *228*, 63-74. https://doi.org/10.1016/j.cej.2013.04.075.

Sarıdemir, M., & Bulut, M. (2021). Effects of ground basaltic pumice and high temperatures on the properties of HSMs. *Journal of Building Engineering*, *41*, 102772. https://doi.org/10.1016/j.jobe.2021.102772.

Sariisik, A., & Sariisik, G. (2012). New production process for insulation blocks composed of EPS and lightweight concrete containing pumice aggregate. *Materials and structures*, *45*, 1345-1357. https://doi.org/10.1617/s11527-012-9836-z.

Sepehr, M. N., Zarrabi, M., Kazemian, H., Amrane, A., Yaghmaian, K., & Ghaffari, H. R. (2013). Removal of hardness agents, calcium and magnesium, by natural and alkaline modified pumice stones in single and binary systems. *Applied Surface Science*, *274*, 295-305. https://doi.org/10.1016/j.apsusc.2013.03.042.

Sevinc, A. H., Durgun, M. Y., & Eken, M. (2017). A Taguchi approach for investigating the engineering properties of concretes incorporating barite, colemanite, basaltic pumice and ground blast furnace slag. *Construction and Building Materials*, *135*, 343- 351. https://doi.org/10.1016/j.conbuildmat.2016.12.209

Shayesteh, H., Rahbar-Kelishami, A., & Norouzbeigi, R. (2016). Evaluation of natural and cationic surfactant modified pumice for congo red removal in batch mode: Kinetic, equilibrium, and thermodynamic studies. *Journal of Molecular Liquids*, *221*, 1-11. https://doi.org/10.1016/j.molliq.2016.05.053.

Soleimani, H., Sharafi, K., Parian, J. A., Jaafari, J., & Ebrahimzadeh, G. (2023). Acidic modification of natural stone for Remazol Black B dye adsorption from aqueous solution-central composite design (CCD) and response surface methodology (RSM). *Heliyon*, *9*(4). https://doi.org/10.1016/j.heliyon.2023.e14743.

Soyaslan, İ. İ. (2020). Thermal and sound insulation properties of pumice/polyurethane composite material. *Emerging Materials Research*, *9*(3), 859-867. , https://doi.org/10.1680/jemmr.20.0016

Taktak, F., & İlbay, Z. (2015). Synthesis of novel poly [2-(dimethylamino) ethyl methacrylate]/pumice stone hydrogel composite for the rapid adsorption of humic acid in aqueous solution. *Journal of Macromolecular Science, Part A*, *52*(4), 307-315. https://doi.org/10.1080/10601325.2015.1007277

Taşdelen, B., Çifçi, D. İ., & Meriç, S. (2017). Preparation of N-isopropylacrylamide/itaconic acid/Pumice highly swollen composite hydrogels to explore their removal capacity of methylene blue. *Colloids and Surfaces A: Physicochemical and Engineering Aspects*, *519*, 245-253. https://doi.org/10.1016/j.colsurfa.2016.11.003.

Ulusu, H., Aruntas, H. Y., & Gencel, O. (2016). Investigation on characteristics of blended cements containing pumice. *Construction and Building Materials*, *118*, 11-19. https://doi.org/10.1016/j.conbuildmat.2016.05.030

Uzun, O., Gokalp, Z., Irik, H. A., Varol, I. S., & Kanarya, F. O. (2021). Zeolite and pumice-amended mixtures to improve phosphorus removal efficiency of substrate materials from wastewaters. *Journal of Cleaner Production*, *317*, 128444. https://doi.org/10.1016/j.jclepro.2021.128444.

Yavuz, M., Gode, F., Pehlivan, E., Ozmert, S., & Sharma, Y. C. (2008). An economic removal of Cu2+ and Cr3+ on the new adsorbents: Pumice and polyacrylonitrile/pumice composite. *Chemical Engineering Journal*, *137*(3), 453-461. https://doi.org/10.1016/j.cej.2007.04.030.

Yılmaz, Ş., Zengin, A., Ecer, Ü., & Şahan, T. (2019). Conversion from a natural mineral to a novel effective adsorbent: utilization of pumice grafted with polymer brush for methylene blue decolorization from aqueous environments. *Colloids and Surfaces A: Physicochemical and Engineering Aspects*, *583*, 123961. https://doi.org/10.1016/j.colsurfa.2019.123961.

Zhang, Y., Xu, G. S., Xu, M. D., Wang, D. C., Wang, H., Zhan, Y., & Jin, Z. (2021). Preparation of MgO porous nanoplates modified pumice and its adsorption performance on

fluoride removal. *Journal of Alloys and Compounds*, *884*, 160953. https://doi.org/10.1016/j.jallcom.2021.160953.

Zhang, Y., Xiao, Y. F., Xu, G. S., Wang, D. C., Li, J., Huang, J., & Jin, Z. (2023). Preparation of Fe2O3 Porous Microspheres Modified Pumice and Its Adsorption Performance on Phosphate Removal. *Journal of Environmental Chemical Engineering*, 109995. https://doi.org/10.1016/j.jece.2023.109995.

The Evolutıon Of Deterıoratıon In Hıstorıcal Buıldıngs After Restoratıon: The Example Of Hagıa Elenı Church (Konya-Turkey)

Mehmet Can BALCI[1]
İsmail İNCE[2]
M. Ergün HATIR[3]

Introduction

Restoration works are extremely important when attempting to preserve the structural integrity of cultural heritage. While the achievement of these studies can securely transfer the heritage to future generations, the opposite situation can accelerate the development of deterioration and lead to critical mistakes that can impact the static status of the monuments (Hatır, İnce & Bozkurt, 2022). Therefore, it is vital to develop scientific approaches to achieve the solution of problems in restoration works with the multidisciplinary cooperation of experts (architects, geological engineers, civil engineers, chemists, biologists, etc.). The first stages of these studies are to determine the types and origins of deterioration and the determination of the material properties utilized in the monument. The aim is to determine the mineralogical composition, petrographic, durability, and index-strength properties of the materials employed in the historic structure and also their relationship with the deterioration development, which will form the basis of the restoration methods to be implemented. One or more of the appropriate restoration treatments (consolidation, filling, cleaning, etc.) will be chosen according to the level of deterioration obtained from this stage. In cases that cannot be saved with restoration treatments or where part of the monument is destroyed, completion works will be required. In these cases, completion works that are not compatible with the original material of the historical structure will accelerate the deterioration processes as well as damaging the visual aesthetics of the monument (Hatır, İnce & Bozkurt, 2022).

This study investigated the process of deterioration that occurred after the restoration works, in the case of Hagia Eleni Church (Konya-Turkey). During the restoration work, it was observed that the completion work was not suitable for the original mortar and therefore increased the deterioration process in the building stones. For this purpose, the types of deterioration in the monument were analysed and their origin was investigated. In addition, the index-engineering properties of the original building stones were determined by laboratory studies and their relationship with the deterioration processes was discussed.

Study Area

Eleni Church is located in the Sille region, about 8 km from Konya city center. The church, which has rooms carved into the rock in its courtyard, has three naves (Figure 1). The middle nave of the monument is held up by four piers and covered with a dome. There are

[1] Assistant Professor, Batman University
[2] Associate Professor, Konya Technical University
[3] Associate Professor, Necmettin Erbakan University

friezes of Jesus Christ, Mary and the apostles on both the piers and transition elements of the dome. The apse and the main space of the church are separated by a wooden sermon pulpit which is subsequently decorated with plaster. The church, which is unique in the region due to the frescoes and planning scheme, has undergone many repairs throughout history. The monument, whose inscription claims that it was last repaired in 1833, was restored in 2012.

Figure 1. General View of Hagia Eleni Church

Materials And Method

ln this study, Sille stone, which is widely employed in the construction of cultural stone heritage in the Konya region was investigated. This type of stone was also used in the construction of the church of St. Elena, and was extracted from ancient quarries excavated in volcanic rocks located 8 km northwest of Konya. For the experimental phase of this study, 30x30x30 cm uniform rock samples were collected from the ancient quarries. Dry density ($\square_d$) and porosity (n) values of the index properties of Sille stone were determined according to the methods recommended in TS EN-1936 (2010), although the P-wave velocity (Vp) value was occurred according to the methods in ASTM E494 (2010). After the P-wave velocity, measurement of the rock was taken three times and then the mean value was obtained as the P-wave velocity value. The capillary water absorption value of the samples was determined in accordance with the methods specified in TS EN-1925 (2000). Uniaxial compression strength (UCS), one of the strength parameters of Sille stone, was determined according to TS EN-1926 (2007). UCS tests were carried out on cube samples with a side length of 7 cm. In the test, the loading rate was implemented within the limits of 0.5-1.0 MPa/s. The test was then carried out on 5 samples and the mean value of these tests was determined based on the UCS value of Sille stone. The Schmidt hammer hardness (SHR) values of the rock were determined according to the method recommended in ASTM D5873 (2014) which was implemented with the use of an L-type hammer. While determining the SHR value of Sille stone, measurements were performed at 10 different points of the sample and then the mean measurement was calculated. To determine the SHR value, the deviations of more than seven units from the average were subtracted.

The remaining measurements were again given a mean value and this value was therefore used as the SHR value of Sille stone. In order to determine the mineralogical composition and textural properties of Sille stone, thin sections were prepared according to the recommended method in TS EN-12407 (2019) and then examined under a polarizing microscope. The types

of deterioration in Hagia Eleni Church were identified based on the definitions in the ICOMOS (2008) dictionary.2012.

Results And Discussions

Petrographic Properties of The Samples

Macro examination of Sille stone displays plagioclase, biotite and quartz phenocrysts floating in a light-dark pink-coloured paste (Figure 2). The mineralogical composition of the rock includes 32% plagioclase, 16% biotite, 16% plagioclase microlites, 10% quartz, 3% opaque minerals and 23% volcanic glass. Due to the mineralogical composition, this can be defined as "plagiodacite" according to Streckeisen (1979). It was determined that Sille stone has a hypo crystalline porphyritic texture in thin sections. In addition, Hatır (2020) defined the rock as dacite based on the anaoxide values.

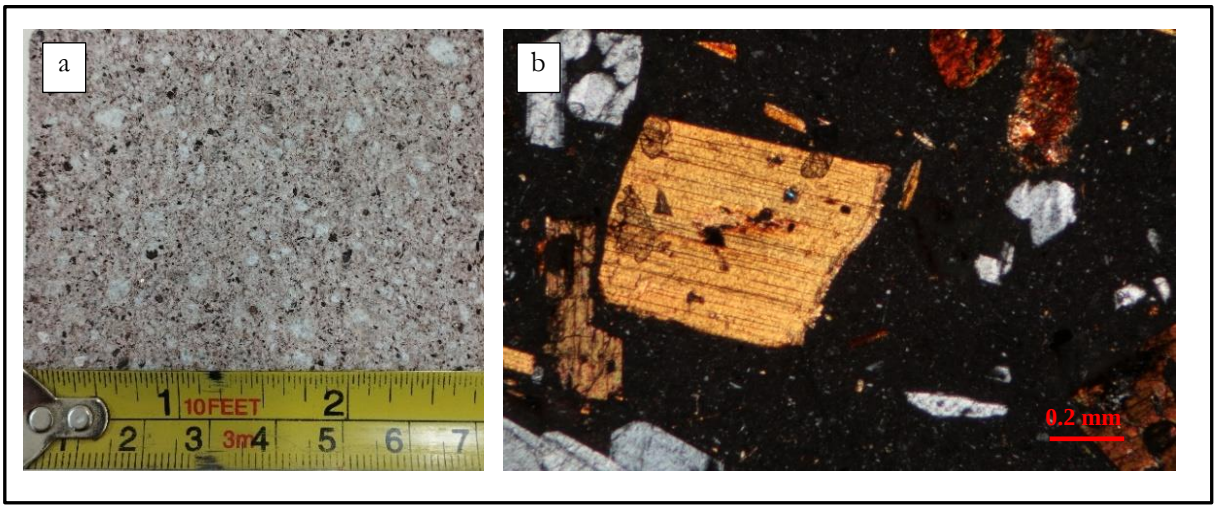

Figure 2. The appearance of Sille stone (a) macroscopic image, (b) microscope image (Crossed polars)

Indexes-Strength and Weathering Properties of The Samples

The index-strength and weathering properties of Sille stone are presented in Table 1. Among the index properties, porosity, dry density and P-wave velocity values are 5.55%, 2.35 g/cm^3 and 3.75 km/s, respectively. According to NBG (1985) porosity classification, Sille stone is classified as high porosity rock. The capillary water absorption value of Sille stone is 5.41 g/m^{2}s$^{0.5}$ and is in the lower absorption rock group according to the classification of capillary water absorption value of rocks in Snethlage (2005). SHR and HL values of the surface hardness are 37.30 and 651.57 respectively. The UCS value of the rock was determined as 58.30 MPa.

The variation of Sille stone against freeze-thaw (F-T) and salt crystallization (SC) processes from atmospheric events have been studied by a variety of different researchers (Zedef & et al., 2007; İnce, 2013; Fener & İnce, 2015; Saydan, Keskin & Kansun, 2020). The dry weight loss (DWL) value of Sille stone, which is widely preferred to determine the alteration in rocks after rapid degradation tests, was determined as 0.144% for the F-T test and 35.77% for the SC test (Zedef & et al., 2007; İnce, 2013). Considering the DWL values, it can be suggested that the SC process is more influential in the deterioration of Sille stone.

Table 1. Index-Strength and DWL Values of Sille Stone

	index				strength			weathering	
Sample	n	C	ρ_d	Vp	SHR	HL*	UCS	F-T_{DWL}**	SC_{DWL}***
	%	$g/m^2s^{0,5}$	g/cm^3	km/s			MPa	%	%
Sille Stone	5.55	5.41	2.35	3.75	37.30	651.57	58.30	0.144	35.77

* Obtained from İnce & Bozdağ, 2021 ** İnce, 2013 *** Zedef & et al., 2007

Types of Deterioration Observed in The Monument

Restoration implementations of historical buildings are significant for the maintenance of the monuments. However, in cases where the implementations are not based on scientific grounds, the deterioration processes in monuments may accelerate and their structural integrity may be at risk to larger threat. In this study, the deterioration observed in the monument after the restoration works carried out in the church of Hagia Eleni in the Sille region of Konya in the year 2012 is evaluated. After the restoration of the monument, a moist area was examined due to capillarity (Figure 3a). This occurred because the drainage lines were not designed and implemented during the restoration works.

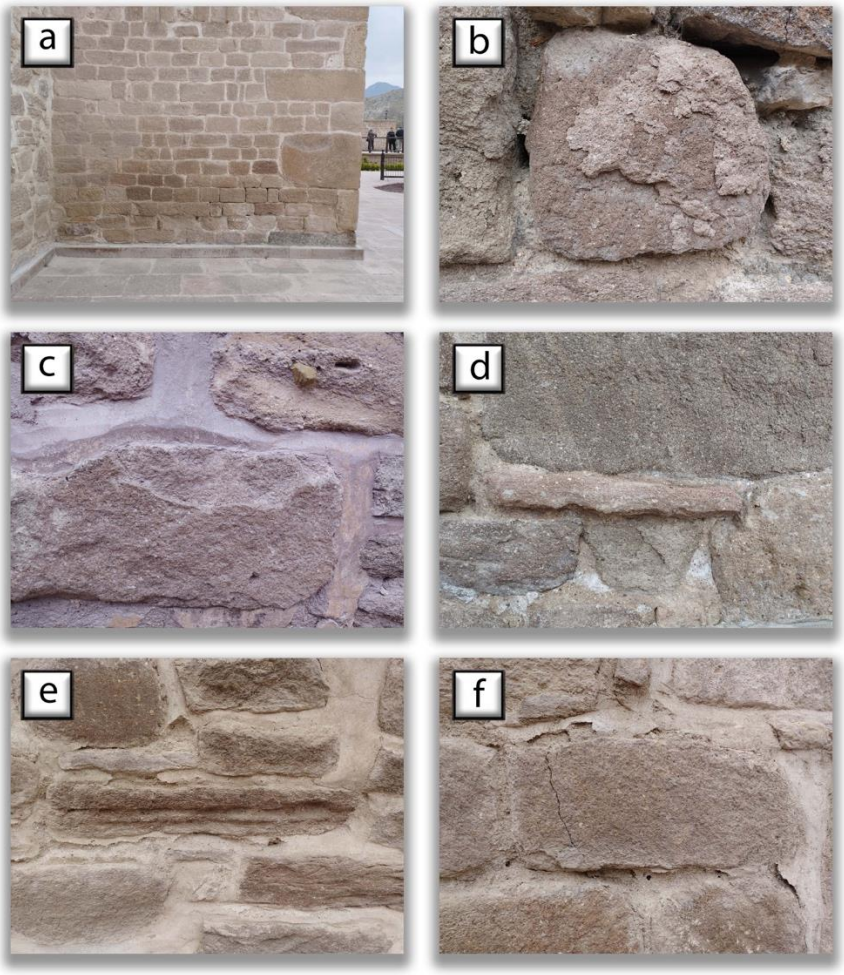

Figure 3. Types Of Deterioration Observed on The Building Stones of Hagia Eleni Church; a) Moist Area, b) Flaking, c) Contour Scaling, d) Efflorescence, e) Differential Erosion, f) Crack

Moist area development caused widespread flaking (Figure 3b), contour scaling (Figures 3b and 3c) and efflorescence deterioration (Figure 3d) in the capillary zone. The sensitivity of the rock to freeze-thaw, wetting-drying and salt crystallization processes were the main factors in the development of these processes. In other parts of the church, differential erosion (Figure 3e) type developed concerning the textural characteristics of Sille stone. As a result of the deterioration processes of the monument, cracks (Figure 3f) were observed in the building stones whose strength properties were weakened as a result. In addition, the metal railings of the building's windows have been corroded over time and have caused subsequently staining type on the building stones.

The fact that the mortar used in the restoration of the monument was incompatible with the original material was a factor in the acceleration of the deterioration process. In this process, the chemical additives in the mortar dissolved with the effect of capillary water. In the next stage, the increase in temperature caused the intensification of efflorescence development around the mortars in the capillary region. In the following stage of this cycle, the mortars gradually lost their binding properties and in places disintegrated (Figure 4). As a result of the increase in the contact surfaces of the water with the building blocks in the missing joint areas, the degradation mechanisms became more influential and increased the development of deterioration.

Figure 4. Mortar losses in monument joints

Conclusion

While restoration work should contribute to the conservation of monuments, in some cases the implementation of incorrect procedures can accelerate the deterioration process. This study examined this process in the case of Hagia Eleni Church and the findings are provided below.

• Failure to examine the fundamental causes of deterioration processes in historical buildings before restoration reduces the success rate of the implementations. Failure to design the drainage infrastructure in Hagia Eleni Church resulted in a moist area throughout the monument.

• Not utilizing the original building materials of the monument in restoration implementations may accelerate the deterioration processes. The mortar used without determining the original properties of the structure caused deterioration starting from the joint areas of the monument.

REFERNCES

ASTM D5873. (2014). Standard test method for determination of rock hardness by rebound Hammer method. Annual book of ASTM standards. American Society for Testing and Materials, West Conshohocken, pp 1–6

ASTM E494. (2010). Standard practice for measuring ultrasonic velocity in materials. Annual Book of ASTM Standards, American Society for Testing and Materials, West Conshohocken, pp. West Conshohocken pp 1-14

Fener, M., İnce, İ. (2015). Effects of the freeze–thaw (F–T) cycle on the andesitic rocks (Sille-Konya/Turkey) used in construction building. *Journal of African Earth Sciences*, 109, 96-106. Doi: 10.1016/j.jafrearsci.2015.05.006

Hatır, M. E. (2020). Determining the weathering classification of stone cultural heritage via the analytic hierarchy process and fuzzy inference system. *Journal of Cultural Heritage*, 44, 120-134. Doi: 10.1016/j.culher.2020.02.011

Hatır, M. E., İnce, İ., Bozkurt, F. (2022). Investigation of the effect of microclimatic environment in historical buildings via infrared thermography. *Journal of Building Engineering*, 57, 104916. Doi: 10.1016/j.jobe.2022.104916

ICOMOS-ISCS. (2008). Illustrated Glossary on Stone Deterioration Patterns, Champigny/Marne, France.

İnce, İ., 2013. Effect of freezing-thawing cycle on engineering parameters of rock. S.Ü. Graduate School of Natural Sciences. Ph.D. Thesis Konya, 197 (in Turkish)

İnce, İ., Bozdağ, A. (2021). An investigation on sample size in Leeb hardness test and prediction of some index properties of magmatic rocks. *Arabian Journal of Geosciences*, 14, 1-13. Doi:10.1007/s12517-021-06478-9

NBG (1985) Engineering Geology and Rock Engineering, Norwegian Group of Rock Mechanics, Fornebu, Norway.

Saydan, M., Keskin, Ü. S., & Kansun, G. (2020). The effects of petrographic differences on the geomechanical properties and freeze-thawing (FT) processes of building stones used in Aya Helena Church (Sille/Konya/Turkey). *Scientific Herald of the Voronezh State University of Architecture & Civil Engineering*, 45(1).

Streickeisen, A. (1979). Classification and nomenclature of volcanic rock lomprophyres, corbanatites and millitic rocks. *Geology*, 7, 331-335.

Snethlage, R. (2005). Leitfaden Steinkonservierung. *Fraunhofer IRB, Stuttgart*, 289, 1-10.

TS EN-1925. (2000). Natural Stone Test Methods - Determination of Water Absorption Coefficient by Capillarity. Turkish Standards Institution Ankara, Turkey (in Turkish)

TS EN-1926. (2007). Natural stone test methods - Determination of uniaxial compressive strength. Turkish Standards Institution, Ankara, Turkey (in Turkish)

TS EN-1936. (2010). Natural stone test methods - Determination of real density and apparent density and of total and open porosity. Turkish Standards Institution, Turkey (in Turkish)

TS EN-12407. (2019). Natural Stone Test Methods - Petrographic Examination, Turkish Standards Institution, Ankara, Turkey (in Turkish).

Zedef, V., Kocak, K., Doyen, A., Ozsen, H., Kekec, B. (2007). Effect of salt crystallization on stones of historical buildings and monuments, Konya, Central Turkey. *Building and environment*, 42(3), 1453-1457. Doi: 10.1016/j.buildenv.2005.12.010

Hybrid Adhesive Bonding Techniques

Nergizhan ANAÇ[1]

Introduction

Materials can be joined by using a variety of methods. Until recently the main used methods; mechanical fastening, welding, brazing, soft soldering or adhesive bonding. The joining processes have several limitations, including stress concentration, the need for extensive surface preparation, additional weight, variations in material metallurgy, and the emission of harmful environmental pollutants.

Each joining process has its own advantages. However, hybrid joining processes have emerged to eliminate the deficiencies where traditional methods are insufficient in complex applications. The essence of hybrid joining techniques lies in the combination of two or more coupling methods (Maggiore et al., 2021). In addition to traditional methods, a wide range of hybrid methods that involve the use of adhesives are extensively utilized in the industry for bonding mechanical components.

The adhesive bonding process is used almost one of the part of every industrial product. With the improved features in the recent years, the adhesive materials usage areas has increased considerably compared to the past. Therefore, it is important to know the concept of bonding. Adhesive bonding is a process of joining two or more solid parts (dissimilar or similar) with an adhesive substance.

Structural adhesive is considered an engineering material, and adhesive bonding techniques are widely accepted as integral parts of production engineering. The bonding strength of joints that are subjected to specified loads is influenced by various factors. Generally, the strength of adhesive bonding is associated with factors such as the size, thickness, geometry, and elastic modulus of the bonded parts, the length of the bond area, the cleanliness of the bonding surfaces, the conditions under which the bonding is sustained, the adhesive material used, and the care taken during the adhesive bonding process. Additionally, the surface roughness of the bonded parts also affects the bonding strength. The adhesive bonding process involves various joint geometries and different loads. The different joint geometries and the loads applied to adhesive joints are depicted in Figure 1 and Figure 2, respectively.

[1] Mechanical Engineering Department, Zonguldak Bulent Ecevit University, Orcid: 0000-0001-6738-9741

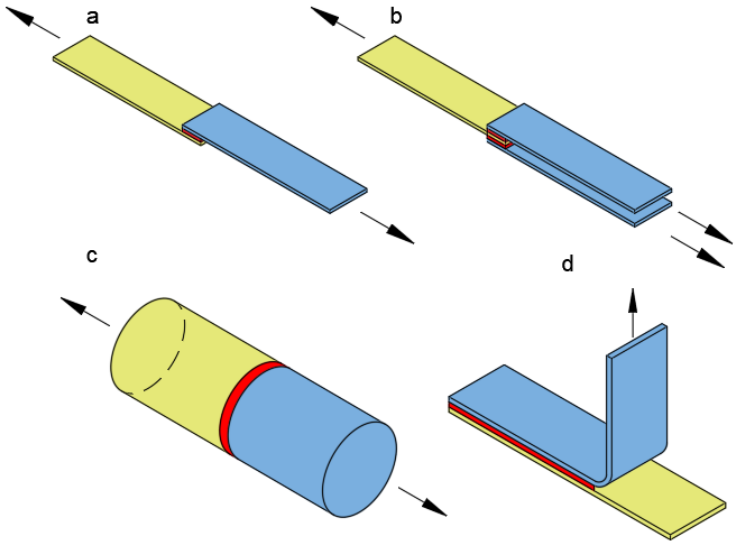

Figure 1. Types of adhesive joints (a) Single lap, (b) double lap, (c) cylindrical butt (d) 90°peel.

In the adhesive bonding studies, it is known that mostly single lap joints are using due to simplicity of production and convenience of calculation.

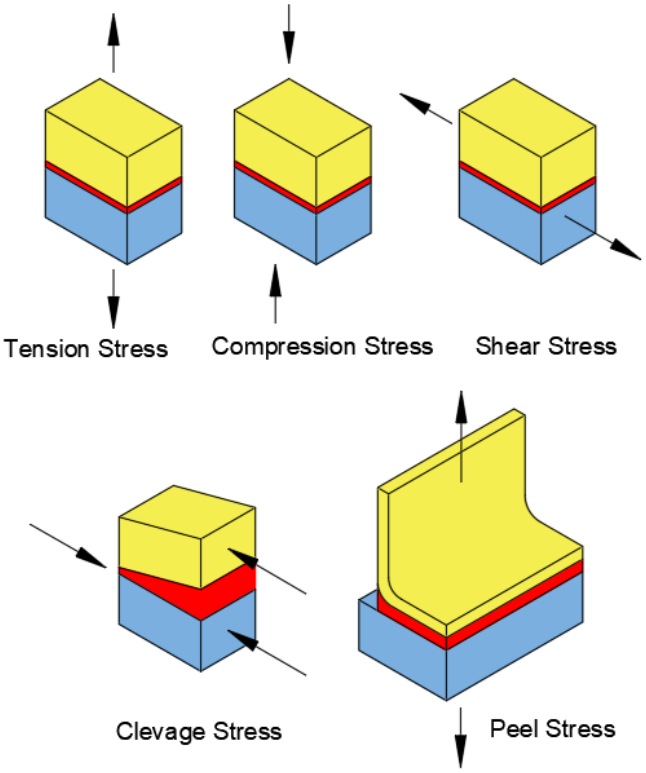

Figure 2. Typical forces in adhesive joints.

Adhesives and adhesive techniques are widely used in aviation, aerospace, and automotive industries and offering quick and cost-effective solutions *(Yacobi et al., 2002).*

Adhesives that are an engineering materials is favored for its ability to provide tightness, electrical resistivity, vibration isolation, and uniform load distribution. However, the strength of adhesives is constrained, and their operational performance is subject to limitations.

The adhesives are chemical compounds. The adhesives have limited ability to work at high temperatures. In adhesive bonding process, the cleaning the surface is more important than in other classical joining methods. Various physical and chemical factors, such as moisture and ultraviolet light, can impact the long-term strength of adhesive bonding (Brockmann et al., 2008).

Combining adhesives with other joining methods is one way to enhance the strength of adhesive joints. When creating joints using bolts and rivets (mechanical fastening), it is necessary to drill holes in the parts being joined. However, this approach can introduce challenges such as increased weight, issues with sealing, and potential corrosion. Welded joints, on the other hand, may require high temperatures and precise control of heat during the welding process, posing significant disadvantages when working with different materials.

The combination of the best features from two different processes into a one method is known as a hybrid method. Hybrid methods have found extensive application in various technologies. This is because hybrid joints generally exhibit superior characteristics compared to classical joining methods such as adhesive bonding, welding, or mechanical fastening. In addition, the more special methods would be necessary for joining of different materials unlike the joining of same kinds of materials.

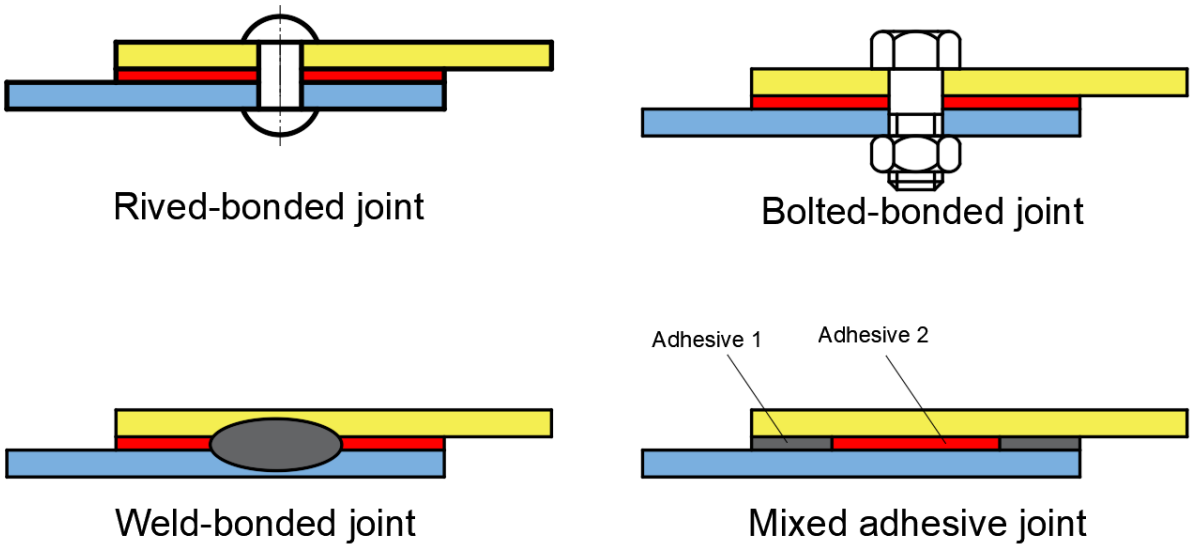

Figure 3. Hybrid joints.

Figure 3 illustrates adhesive hybrid joints, which possess distinct characteristics and may present certain challenges during application. Hybrid methods are employed to address problems that cannot be effectively solved using classical methods *(Da Silva & Öchsner, 2008)*.

This chapter describes some hybrid bonding methods (weld-bonding, mixed adhesive bonding, adhesive-soft soldered joint etc.) as an alternative to currently used classical methods.

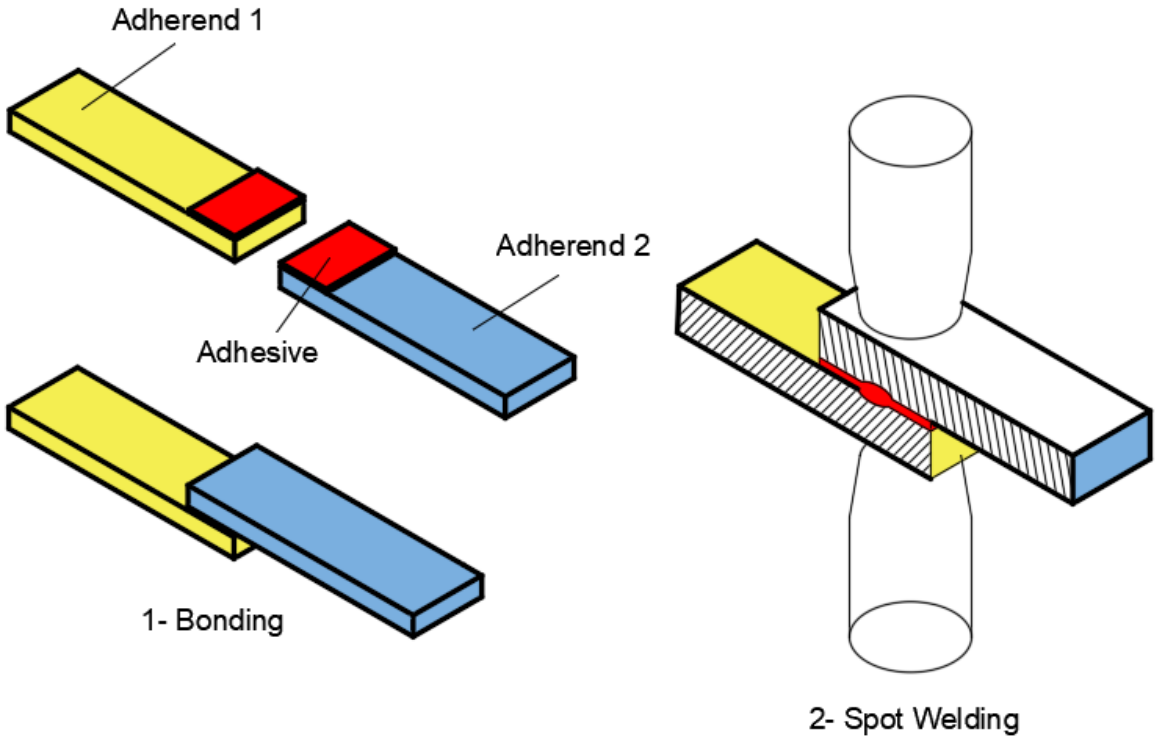

Figure 4. Schematic outline of the weld bonding process.

Weld-bonding *technique*

The welding is one the classical methods that is widely used in manufacturing industry and has many types (Santos et al., 2004). Therefore, this basic method is used to obtain hybrid methods by combined with other basic methods. Spot welding, one of the weld methods (Figure 4), is performed in short processing time and pieces to be joined do not need any additional materials.

The pieces to be welded are firstly compressed by pressure and passing the electric current through these parts by the help of electrodes is provided. The connection is formed in junction area with a high energy concentration. It is used to make all kinds of steel, non-ferrous metals and different material joints.

The basis of weld-bonding method used first in USSR (Darwish & Ghanya, 2000) are formed by the using of this resistance spot welding and adhesive bonding together. It was developed in the 1950s and is today continues to be a subject of many studies (Chang et al., 1999).

In Figure 5, the different techniques of weld-bonding method are shown basically. Weld-bonding method shown in Figure 5 schematically is performed with two different ways as "flow-in" and "weld-through" [8]. In the flow-in technique, firstly pieces are welded and gap at joint area is filled with adhesive by the help of capillary effect. Then, the process is finished with heat applying for curing of adhesive at joint area.

In weld-through technique, firstly pieces bonded with adhesive. This is classical and basic adhesive bonding process. Then spot welding process is applied. The critical point here is necessity of that adhesive is less heated just before the spot welding process application. Because, adhesive is not conductive material and complicates the welding process. The heat should be sufficient to not disrupt the bonding characteristics of the adhesive. Finally, the joints

bonded with weld-bonding method are heated again for curing the adhesive. The joints will be reinforced.

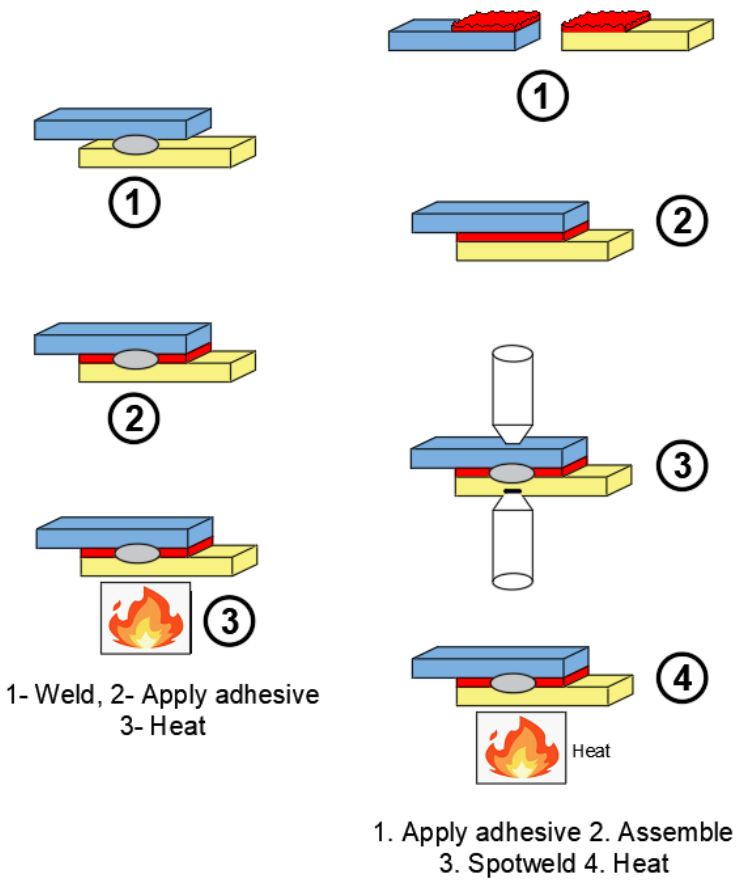

Figure 5. Weld bonding: (a) the flow-in technique, (b) the weld-through technique.

Compared to the weld-through technique, the flow-in weld-bond technique is easier to implement. From an economic standpoint, the flow-in weld-bond technology is also more cost-effective compared to the weld-through technology.

Weld-bonded aluminum sheets tensile-shear strength were tested and reported in S.M. Darwish study (Darwish, 2003). Significant increase in tensile-shear strength have been observed in weld-bonded aluminum sheets compared to corresponding spot-welded joints.

Mixed adhesive joints

The method, which is about 40-year history, is examined in detail with practical and theoretical application by researchers (Da Silva & Adams, 2007a, 2007b; Da Silva & Lopes, 2009; Fitton & Broughton, 2005; Kavak, 2013; Kong et al., 2008; Pires et al., 2003). Mixed modulus joints are obtained by application of the adhesive having a different elasticity modulus from each other in different amounts on adhesion region. The stress intensity at the adhesive joints is higher near the edges of the adhesion region.

While the low elasticity modulus adhesive is applied to these edge regions where the stress intensity is higher, stiff and brittle adhesive is applied into the middle of adhesion region. The simple view of the method is shown in the Figure 6. The main purpose of the using mixed modulus adhesive in bonding is to improve the joint strength.

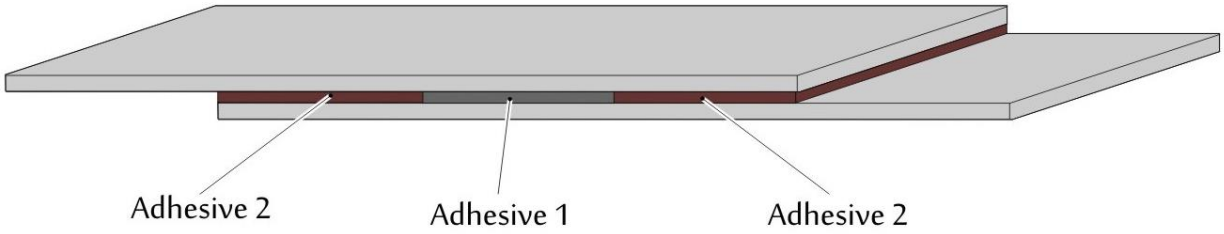

Figure 6. Single lap joint, showing of the two adhesives (the adhesive 1 and adhesive 2).

The process seems easy in theory, contains some issues to be considered during the application. Each adhesive curing temperature, curing time and performance (bond strength) on the pieces to be bonded are different from each other. Therefore, in the mixed modulus adhesive bonding method the adhesive curing temperature and time must be considered very careful. Deciding the process parameters on the information given by the manufacturer is useful to avoid the not to be curing or the deterioration of adhesive at improper temperature.

The mixing of adhesive to other one is one of the difficulties encountered while bonding with this method.

Pires and colleagues (Pires et al., 2003) studied on mixed modulus joints with DP490 and ESP110 adhesives. In the study, it is mentioned that the pressure applied to joints caused the adhesive mixing and it can't be avoided.

According to the other study (Pires et al., 2003), studies on mixed adhesive joints utilizing DP490 and ESP110 adhesives have demonstrated a substantial increase in strength, up to 22%, when compared to the strengths obtained from joints made using the two adhesives separately.

Da Silva and Lopes (Da Silva & Lopes, 2009), used 1 mm thickness and 5 mm in width silicon strips on adhesion region. First silicon strip had been placed on the material to be bonded, then adhesives were applied. In this way separation of the different adhesives was provided.

In addition, according to the Da Silva and Lopes's opinion (Da Silva & Lopes, 2009), the absence of a separator between adhesives can contribute to an increase in joint strength. The mixed adhesive process can also be used in bonding the dissimilar materials such as composite and metal.

Da Silva and Adams obtained similar (titanium/titanium) and dissimilar (titanium/composite) adherents as double lap joints using mixed adhesive method in their study (Da Silva & Adams, 2007a). They used stiff- brittle Redux 326 (Hexcel Composites) and ductile-less stiff Supreme 10HT (Master Bond) in these bonding. It is shown that indicated that when dealing with a joint consisting of dissimilar adherends, the combination of two adhesives provides better performance, particularly in terms of increased load capacity, across a wider temperature range compared to using a high-temperature adhesive alone.

Adhesive-soft soldered joints

Reinforcing adhesive joints can be accomplished by incorporating organic or inorganic particles into adhesive materials (Gerson et al., 2010; Kahraman et al., 2008; Kilik & Davies, 1989; Sancaktar & Kumar, 2000; Wetzel et al., 2006; Zhai et al., 2006; Zhai et al., 2008). There are many kind of materials added into adhesives as additives. Thus, it is well-established that adhesive properties, including strength, electrical conductivity, and thermal conductivity, undergo variations (Kilik & Davies, 1989; Novák & Krupa, 2004; Xian et al., 2006; Zhang et al., 2007). While all powder keeps their powder form in adhesive, recent studies have brought a new perspective to this topic.

This section introduces a novel hybrid bonding technique as a viable alternative to the conventional adhesive-soft soldered joints. This method (Kavak & Altan, 2014) has been in the literature for the last 10 years and is open to improvement.

Unlike traditional adhesive bonding, in this method a certain amount of solder powder is added into adhesive. In the adhesive-soft soldering method, the joint area is subjected to heat from an external source. This heat serves two purposes: it cures the adhesive and melts the soft soldering powders within the adhesive. Once the process is complete, a hybrid joint is formed, combining both adhesive and soft soldering elements.

The application of the dispersion of solder in the adhesive can be done in different ways. In Figure 7, the dispersion of solder powder in adhesive is shown. The first case is achieved by homogeneous distribution of the solder additive in the adhesive. Solder particles are located all over the bonding region.

The second case is similar to the operation principle of the conductive adhesive. The solder powder in the adhesive create joint by contacting to both each other and material to be bonded. Thus, both the joint strength is increased and the electrical conductivity is increased. For both conditions the application of the method is as described above. Already this method has emerged with to be inspired by the way of work of the conductive adhesive.

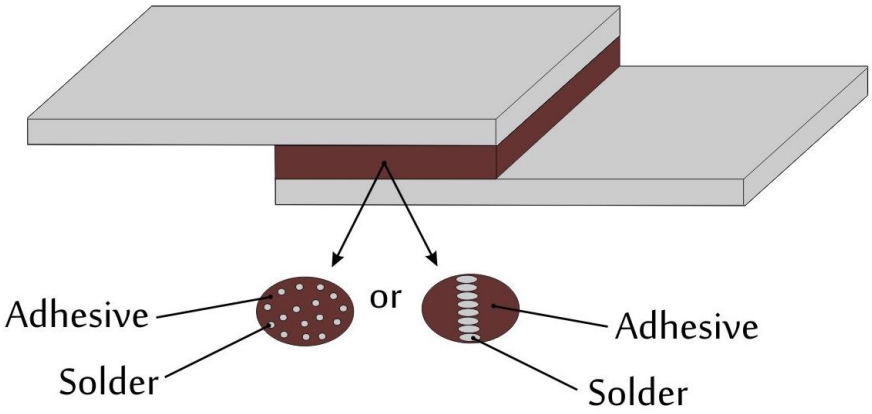

Figure 7. The dispersion of solder in the adhesive-soft soldered joints

Soldering used mostly in electronics and military industry is joining method which process temperature not exceeded 450 °C. While melting of pieces to be joined is not observed, a metallurgical joint is provided by melting the additional metal (Darwish et al., 2000; Strauss, 1998). Despite the use of lead solder as an additive metal material mostly, the use of lead-free solder is increasing because of such as environmental and health reasons. In Figure 8, traditional soldering iron and leaded soldering powder are shown.

Unlike traditional adhesive methods, the adhesive-soft soldering process offers an increase in strength by utilizing both adhesive and soldering techniques. The inclusion of melted soft solder powder in this new hybrid method enhances the mechanical strength of the joint.

While the strength decreases on the joint prepared with 50 wt.% of solder powder, that the joint strength gives best results with the %5 solder powder addition has emerged by experiments (Kavak & Altan, 2014).

In adhesive-soft soldering method, the preparation steps of the samples surface and mechanical tests were performed just same as in adhesive bonding processes. The solder material sizes and type (leaded/free lead) used in the adhesive-soft soldering method are unlimited. Nevertheless, there is an important point to be considered in the adhesive-soft soldering method. The melting temperature of solder powder additive used in this method must be less than adhesive curing temperature.

The adhesive-soft soldered joint method offers several advantages, including:

- The curing temperature of the adhesive used is higher than the melting temperature of the additive powder. This ensures that the bonding strength remains unaffected by variations in curing temperatures during processing, as the curing temperature is kept constant.
- There is no limitation on the thickness of the materials (adherends) that can be connected using this method.
- The adhesive-soft soldered joints eliminate the need for additional connection elements such as fasteners and extra processes like drilling.
- These joints are lightweight and possess sealing properties, providing additional benefits in various applications.

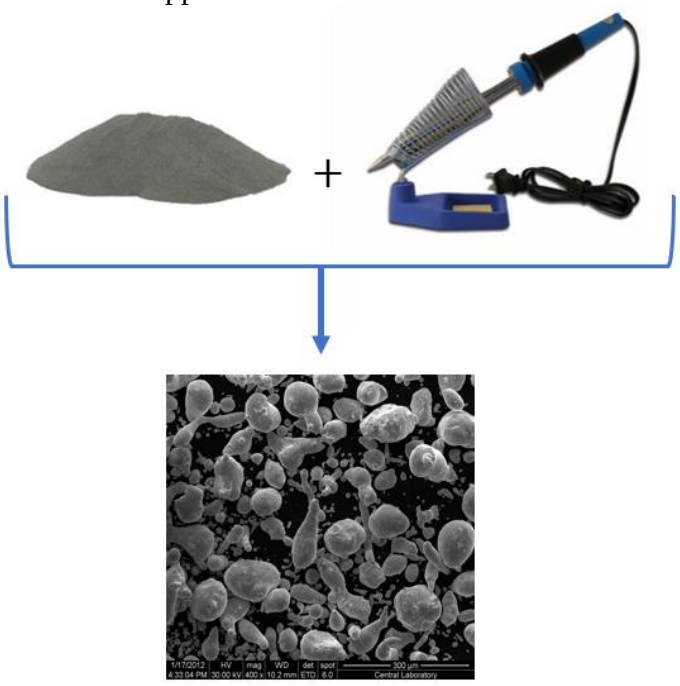

Figure 8. Solder alloy and traditional soldering iron

In the adhesive-soft soldered method, there is a reversal of the typical scenario where the melting temperature of the added powders is higher than the adhesive cure temperature. Instead, the adhesive in this method needs to withstand the melting temperature of the solder alloy. As a result, it is currently not feasible to create adhesive-soft soldered joints using adhesive materials that cure at room temperature and have a service life lower than the soldering temperature.

Ongoing research is focused on developing new nano-solder alloys to lower the temperature requirements in traditional soft soldering processes (Pfahl & McElroy, 2005; Wallner et al., 2010).

Once these advancements are successfully implemented, soldering at lower temperatures will become feasible. This development will expand the applicability of the proposed hybrid method due to the wider range of solder powder materials available. Moreover, utilizing smaller-sized solder powders and bonding diverse metallic materials can lead to improved outcomes using this hybrid method.

Bolted-bonded joint or rived-bonded joining

Adhesive bonded joints are used for their light weight and simplicity of application, whereas bolted and riveted joints are preferred for their strength and ease of maintenance and durability. Stress distribution in adhesive bonded joints is uniform and force distribution occurs

over the entire surface. There are non-uniform stress distribution and spot force transmission in rivets and fasteners. In some studies, it has been observed that higher joint strength is obtained by combining the two methods instead of using bonded or bolted joint alone (Dindar et al., 2022). In this hybrid methods (the hybrid bolted-bonded joining method or rived-bonded joining), it is possible for the bolts or rivets to carry the load in case the adhesive fails.
In adhesive bonding processes, the adhesive material is affected by environmental factors such as temperature and humidity. In hybrid joints, it is important to ensure sealing between the layers joined by bolts and rivets and to prevent moisture diffusion through the holes (Delzendehrooy et al., 2022).

Conclusions

The variety of industrial materials and joining of these materials has always been a subject of interest. Joining of components is usually accomplished by mechanical fastening, welding, or adhesive bonding. The economy, lightness and joining different materials issues have gained more importance with the development of the technology. Hybrid methods can be applied when dissimilar materials need to be joined or superior mechanical properties are desired. Therefore, hybrid methods are offered. Various hybrid joints have been investigated analytically and verified numerically in the literature. In this chapter, some of adhesive hybrid bonding are explained. The problems encountered in adhesive hybrid bonding will disappear with the development of the adhesive properties of the material. Future studies will promote the use of these hybrid methods and will help to emerge in many different methods.

References

Brockmann, W., Geiß, P. L., Klingen, J., & Schröder, K. B. (2008). *Adhesive bonding: materials, applications and technology*. John Wiley & Sons.

Chang, B., Shi, Y., & Dong, S. (1999). Comparative studies on stresses in weld-bonded, spot-welded and adhesive-bonded joints. *Journal of Materials Processing Technology*, *87*(1-3), 230-236.

Da Silva, L. F., & Adams, R. (2007a). Adhesive joints at high and low temperatures using similar and dissimilar adherends and dual adhesives. *International journal of adhesion and adhesives*, *27*(3), 216-226.

Da Silva, L. F., & Adams, R. (2007b). Techniques to reduce the peel stresses in adhesive joints with composites. *International journal of adhesion and adhesives*, *27*(3), 227-235.

Da Silva, L. F., & Lopes, M. J. C. (2009). Joint strength optimization by the mixed-adhesive technique. *International journal of adhesion and adhesives*, *29*(5), 509-514.

Da Silva, L. F. M., & Öchsner, A. (2008). *Modeling of adhesively bonded joints*. Springer.

Darwish, S. (2003). Characteristics of weld-bonded commercial aluminum sheets (BS 1050). *International journal of adhesion and adhesives*, *23*(3), 169-176.

Darwish, S., Al-Habdan, S., & Al-Tamimi, A. (2000). A knowledge-base for electronics soldering. *Journal of Materials Processing Technology*, *97*(1-3), 1-9.

Darwish, S., & Ghanya, A. (2000). Critical assessment of weld-bonded technologies. *Journal of Materials Processing Technology*, *105*(3), 221-229.

Delzendehrooy, F., Akhavan-Safar, A., Barbosa, A., Carbas, R., Marques, E., & da Silva, L. (2022). Investigation of the mechanical performance of hybrid bolted-bonded joints subjected to different ageing conditions: Effect of geometrical parameters and bolt size. *Journal of Advanced Joining Processes*, *5*, 100098.

Dindar, B., Ağır, İ., & Çallıoğlu, H. (2022). Experimental investigation of single-lap bolted and bolted/bonded (hybrid) joints of polymeric plates. *Open Chemistry*, *20*(1), 1612-1621.

Fitton, M. D., & Broughton, J. (2005). Variable modulus adhesives: an approach to optimised joint performance. *International journal of adhesion and adhesives*, *25*(4), 329-336.

Gerson, A. L., Bruck, H. A., Hopkins, A. R., & Segal, K. N. (2010). Curing effects of single-wall carbon nanotube reinforcement on mechanical properties of filled epoxy adhesives. *Composites Part A: Applied Science and Manufacturing*, *41*(6), 729-736.

Kahraman, R., Sunar, M., & Yilbas, B. (2008). Influence of adhesive thickness and filler content on the mechanical performance of aluminum single-lap joints bonded with aluminum powder filled epoxy adhesive. *Journal of Materials Processing Technology*, *205*(1-3), 183-189.

Kavak, N. The Application of The Mixed-Adhesive Technique with Metal Powder Filled Adhesive Karışık Yapıştırma Tekniğinde Metal Toz Katkılı Yapıştırıcı Uygulaması. 7 th International Advanced Technologies Symposium,

Kavak, N., & Altan, E. (2014). A new hybrid bonding technique: Adhesive-soft soldered joints. *Proceedings of the Institution of Mechanical Engineers, Part L: Journal of Materials: Design and Applications*, *228*(2), 137-143.

Kilik, R., & Davies, R. (1989). Mechanical properties of adhesive filled with metal powders. *International journal of adhesion and adhesives*, *9*(4), 224-228.

Kong, F.-R., You, M., & Zheng, X.-L. (2008). Three-dimensional finite element analysis of the stress distribution in bi-adhesive bonded joints. *The Journal of Adhesion*, *84*(2), 105-124.

Maggiore, S., Banea, M. D., Stagnaro, P., & Luciano, G. (2021). A review of structural adhesive joints in hybrid joining processes. *Polymers*, *13*(22), 3961.

Novák, I., & Krupa, I. (2004). Electro-conductive resins filled with graphite for casting applications. *European Polymer Journal*, *40*(7), 1417-1422.

Pfahl, R., & McElroy, J. (2005). The 2004 international electronics manufacturing initiative (iNEMI) technology roadmaps. 2005 Conference on High Density Microsystem Design and Packaging and Component Failure Analysis,

Pires, I., Quintino, L., Durodola, J., & Beevers, A. (2003). Performance of bi-adhesive bonded aluminium lap joints. *International journal of adhesion and adhesives*, *23*(3), 215-223.

Sancaktar, E., & Kumar, S. (2000). Selective use of rubber toughening to optimize lap-joint strength. *Journal of Adhesion Science and Technology*, *14*(10), 1265-1296.

Santos, I., Zhang, W., Goncalves, V., Bay, N., & Martins, P. (2004). Weld bonding of stainless steel. *International Journal of Machine Tools and Manufacture*, *44*(14), 1431-1439.

Strauss, R. (1998). *SMT soldering handbook*. Elsevier.

Wallner, E., Myers, B., Sarma, D., Shah, S., Chengalva, S., Eesley, G., Dykstra, C., Parker, R., & Ihms, D. (2010). Nanotechnology applications in future automobiles. *SAE Int*.

Wetzel, B., Rosso, P., Haupert, F., & Friedrich, K. (2006). Epoxy nanocomposites–fracture and toughening mechanisms. *Engineering fracture mechanics*, *73*(16), 2375-2398.

Xian, G., Walter, R., & Haupert, F. (2006). Friction and wear of epoxy/TiO2 nanocomposites: Influence of additional short carbon fibers, Aramid and PTFE particles. *Composites science and technology*, *66*(16), 3199-3209.

Yacobi, B., Martin, S., Davis, K., Hudson, A., & Hubert, M. (2002). Adhesive bonding in microelectronics and photonics. *Journal of applied physics*, *91*(10), 6227-6262.

Zhai, L., Ling, G., Li, J., & Wang, Y. (2006). The effect of nanoparticles on the adhesion of epoxy adhesive. *Materials letters*, *60*(25-26), 3031-3033.

Zhai, L., Ling, G., & Wang, Y. (2008). Effect of nano-Al2O3 on adhesion strength of epoxy adhesive and steel. *International journal of adhesion and adhesives*, *28*(1-2), 23-28.

Zhang, H., Zhang, Z., & Friedrich, K. (2007). Effect of fiber length on the wear resistance of short carbon fiber reinforced epoxy composites. *Composites science and technology*, *67*(2), 222-230.

The Complex-Type Padovan *p*-Cırculant Sequences

Özgür ERDAĞ[1]
Ömür DEVECİ[2]

Introduction and Preliminaries

The Padovan p-numbers $\{Pap(n)\}$ for any given $p(p=2,3,4,\ldots)$ is defined (Deveci & Karaduman, 2017) by the following homogeneous linear recurrence relation:

$$Pap(n+p+2)=Pap(n+p)+Pap(n) \tag{1}$$

for $n\geq 1$, with initial conditions $Pap(1)=Pap(2)=\cdots=Pap(p)=0$, $Pap(p+1)=1$ and $Pap(p+2)=0$. When $p=1$ in (1), the Padovan p-numbers $\{Pap(n)\}$ is reduced to the usual Padovan sequence $\{P(n)\}$.

The complex Fibonacci sequence $\{F_n^*\}$ is defined (Horadam, 1961) by a two-order recurrence equation:

$$F_n^* = F_n + iF_{n+1}$$

for $n\geq 0$, where $i=\sqrt{-1}$ and F_n is the n^{th} Fibonacci number (cf. (Berzsenyi, 1975; Horadam, 1963)).

The complex-type Padovan- p sequence $\{Pa_p^{(i)}(n)\}$ for any given $p(p=3,5,7,\ldots)$ and $n\geq 1$ is defined (Erdag, Halıcı & Deveci, 2022) by the following homogeneous linear recurrence relation:

$$Pa_p^{(i)}(n+p+2)=i^2\cdot Pa_p^{(i)}(n+p)+i^{p+2}\cdot Pa_p^{(i)}(n)$$

with the initial conditions $Pa_p^{(i)}(1)=\cdots=Pa_p^{(i)}(p)=0$, $Pa_p^{(i)}(p+1)=1$ and $Pa_p^{(i)}(p+2)=0$.

It is easy to see that the characteristic polynomial of the complex-type Padovan- p sequence is $f(x)=x^{p+2}+x^p-i^{p+2}$.

In (Davis, 1979), Davis defined the circulant matrix $C_n=\left[c_{ij}\right]_{n\times n}$ associated with the numbers $c_0,c_1,\ldots,c_{n-1}$ as follows:

[1] Arş. Gör. Dr., Kafkas Universitym
[2] Prof. Dr., Kafkas University

$$C_n=\begin{bmatrix} c_0 & c_{n-1} & \cdots & c_2 & c_1 \\ c_1 & c_0 & \cdots & c_3 & c_2 \\ \vdots & \vdots & \ddots & \vdots & \vdots \\ c_{n-2} & c_{n-3} & \cdots & c_0 & c_{n-1} \\ c_{n-1} & c_{n-2} & \cdots & c_1 & c_0 \end{bmatrix}.$$

The $(n-1)$ th degree polynomial $P(x)=c_0+c_1x+\cdots+c_{n-1}x^{n-1}$ is called the associated polynomial of the circulant matrix C_n.

For more information on the circulant matrix C_n; see, (Bozkurt & Tin-Yau, 2012; Ingleton, 1956; Muir, 1911; Pan, & Jiang, 2015; Stephen, 1990).

Kalman (Kalman, 1982) mentioned that these sequences are special cases of a sequence which is defined recursively as a linear combination of the preceding k terms:

$$a_{n+k}=c_0a_n+c_1a_{n+1}+\cdots+c_{k-1}a_{n+k-1},$$

where $c_0,c_1,\ldots,c_{k-1}$ are real constants. In (Kalman, 1982), Kalman derived a number of closed-form formulas for the generalized sequence by the companion matrix method as follows:

$$A_k=\begin{bmatrix} 0 & 1 & 0 & \cdots & 0 & 0 \\ 0 & 0 & 1 & \cdots & 0 & 0 \\ 0 & 0 & 0 & \cdots & 0 & 0 \\ \vdots & \vdots & \vdots & \ddots & \vdots & \vdots \\ 0 & 0 & 0 & \cdots & 0 & 1 \\ c_0 & c_1 & c_2 & \cdots & c_{k-2} & c_{k-1} \end{bmatrix}.$$

Then by an inductive argument he obtained that

$$A_k^n\begin{bmatrix} a_0 \\ a_1 \\ \vdots \\ a_{k-1} \end{bmatrix}=\begin{bmatrix} a_n \\ a_{n+1} \\ \vdots \\ a_{n+k-1} \end{bmatrix}.$$

Recurrence sequences are widely utilized to solve some problems in various scientific fields, or different problems in different scientific disciplines are directly created by taking the structural aspects of these sequences into account. In the literature, many interesting properties and applications of the recurrence sequences relevant to this paper have been studied by many authors; see, for example, (Akuzum, 2020; Akuzum, Deveci & Shannon, 2017; Akuzum, Deveci & Artun, 2019; Deveci, Adiguzel & Akuzum, 2020; Deveci, Akuzum & Karaduman, 2015; Horadam & Shannon, 1976; Kilic, 2008; Kilic & Tasci, 2006; Kilic & Tasci, 2007; Ozgur, 2005; Shannon, 1974a; Shannon, 1974b; Shannon, 1976; Stakhov & Rozin, 2006a; Stakhov & Rozin, 2006b; Tasci & Firengiz, 2010). Especially, in (Akuzum, 2023a; Akuzum, 2023b; Deveci & Shannon, 2018; Deveci & Shannon, 2021), the authors defined the new sequences using the quaternions and complex numbers and then they gave miscellaneous properties and many applications of the sequences defined. Now we give new sequences which are called the complex-type Padovan p-circulant sequences. These sequences are defined by using the circulant matrix which is obtained from the characteristic polynomials of the complex-type Padovan p-circulant sequences. Also, we obtain generating matrices of the complex-type Padovan p-circulant sequences. Finally, we give various properties of the complex-type

Padovan p-circulant numbers such as the combinatorial, permanental, determinantal and exponential representations, and the finite sums by matrix methods.

The Main Results

Now we define new sequences that we call the complex-type Padovan p-circulant sequences $\left\{C_p^{(Pa,i)}(n)\right\}$ as follows:

$$C_p^{(Pa,i)}(n+p+3) = -i^{p+2}\cdot C_p^{(Pa,i)}(n+p+2) + C_p^{(Pa,i)}(n+2) + C_p^{(Pa,i)}(n) \qquad (2)$$

for any given $p(p=3,5,7,\ldots)$, $n\geq 0$ and $i=\sqrt{-1}$, with the initial conditions $C_p^{(Pa,i)}(n)=\cdots=C_p^{(Pa,i)}(p+1)=0$, $C_p^{(Pa,i)}(p+2)=1$.

From the equation (2), we can write the following companion matrix:

$$A_p = \left[a_{jk}^{(p)}\right]_{(p+3)\times(p+3)} = \begin{bmatrix} -i^{p+2} & 0 & \cdots & 0 & 1 & 0 & 1 \\ 1 & 0 & \cdots & 0 & 0 & 0 & 0 \\ 0 & 1 & \cdots & 0 & 0 & 0 & 0 \\ \vdots & \ddots & \ddots & \ddots & \vdots & \vdots & \vdots \\ 0 & \cdots & 0 & 1 & 0 & 0 & 0 \\ 0 & \cdots & 0 & 0 & 1 & 0 & 0 \\ 0 & \cdots & 0 & 0 & 0 & 1 & 0 \end{bmatrix}.$$

The matrix A_p is said to be the complex-type Padovan p-circulant matrix. Then we can write the following matrix relation:

$$\begin{bmatrix} C_p^{(Pa,i)}(n+p+3) \\ C_p^{(Pa,i)}(n+p+2) \\ \vdots \\ C_p^{(Pa,i)}(n+2) \\ C_p^{(Pa,i)}(n+1) \end{bmatrix} = A_p \cdot \begin{bmatrix} C_p^{(Pa,i)}(n+p+2) \\ C_p^{(Pa,i)}(n+p+1) \\ \vdots \\ C_p^{(Pa,i)}(n+1) \\ C_p^{(Pa,i)}(n) \end{bmatrix}.$$

It can be readily established by mathematical induction that for $n\geq 2$,

$$\left(A_p\right)^n = \begin{bmatrix} C_p^{(Pa,i)}(n+p+2) & C_p^{(Pa,i)}(n+p+3)-i^p\cdot C_p^{(Pa,i)}(n+p+2) & C_p^{(Pa,i)}(n+p+4)-i^p\cdot C_p^{(Pa,i)}(n+p+3) & \cdots \\ C_p^{(Pa,i)}(n+p+1) & C_p^{(Pa,i)}(n+p+2)-i^p\cdot C_p^{(Pa,i)}(n+p+1) & C_p^{(Pa,i)}(n+p+3)-i^p\cdot C_p^{(Pa,i)}(n+p+2) & \cdots \\ C_p^{(Pa,i)}(n+p) & C_p^{(Pa,i)}(n+p+1)-i^p\cdot C_p^{(Pa,i)}(n+p) & C_p^{(Pa,i)}(n+p+2)-i^p\cdot C_p^{(Pa,i)}(n+p+1) & \cdots \\ \vdots & \vdots & \vdots & \\ C_p^{(Pa,i)}(n+1) & C_p^{(Pa,i)}(n+2)-i^p\cdot C_p^{(Pa,i)}(n+1) & C_p^{(Pa,i)}(n+3)-i^p\cdot C_p^{(Pa,i)}(n+2) & \cdots \\ C_p^{(Pa,i)}(n) & C_p^{(Pa,i)}(n+1)-i^p\cdot C_p^{(Pa,i)}(n) & C_p^{(Pa,i)}(n+2)-i^p\cdot C_p^{(Pa,i)}(n+1) & \cdots \end{bmatrix}$$

$$\begin{bmatrix} C_p^{(Pa,i)}(n+2p+2)-i^p\cdot C_p^{(Pa,i)}(n+2p+1) & C_p^{(Pa,i)}(n+p) & C_p^{(Pa,i)}(n+p+1) \\ C_p^{(Pa,i)}(n+2p+1)-i^p\cdot C_p^{(Pa,i)}(n+2p) & C_p^{(Pa,i)}(n+p-1) & C_p^{(Pa,i)}(n+p) \\ C_p^{(Pa,i)}(n+2p)-i^p\cdot C_p^{(Pa,i)}(n+2p-1) & C_p^{(Pa,i)}(n+p-2) & C_p^{(Pa,i)}(n+p-1) \\ \vdots & \vdots & \vdots \\ C_p^{(Pa,i)}(n+p+1)-i^p\cdot C_p^{(Pa,i)}(n+p) & C_p^{(Pa,i)}(n-1) & C_p^{(Pa,i)}(n) \\ C_p^{(Pa,i)}(n+p)-i^p\cdot C_p^{(Pa,i)}(n+p-1) & C_p^{(Pa,i)}(n-2) & C_p^{(Pa,i)}(n-1) \end{bmatrix}$$

For more information on the companion matrices; see, (Lancaster & Tismenetsky, 1985; Lidl & Niederreiter, 1994).

Let $C(c_1, c_2, \ldots, c_v)$ be a $v \times v$ companion matrix as follows:

$$C(c_1, c_2, \ldots, c_v) = \begin{bmatrix} c_1 & c_2 & \cdots & c_v \\ 1 & 0 & \cdots & 0 \\ \vdots & \ddots & \ddots & \vdots \\ 0 & \cdots & 1 & 0 \end{bmatrix}.$$

Theorem 4 (Chen & Louck, 1996) The (i, j) entry $c_{i,j}^{(n)}(c_1, c_2, \ldots, c_v)$ in the matrix $C^n(c_1, c_2, \ldots, c_v)$ is given by the following formula:

$$c_{i,j}^{(n)}(c_1, c_2, \ldots, c_v) = \sum_{(t_1, t_2, \ldots, t_v)} \frac{t_j + t_{j+1} + \cdots + t_v}{t_1 + t_2 + \cdots + t_v} \times \binom{t_1 + \cdots + t_v}{t_1, \ldots, t_v} c_1^{t_1} \cdots c_v^{t_v} \tag{3}$$

where the summation is over nonnegative integers satisfying $t_1 + 2t_2 + \cdots + vt_v = n - i + j$, $\binom{t_1 + \cdots + t_v}{t_1, \ldots, t_v} = \frac{(t_1 + \cdots + t_v)!}{t_1! \cdots t_v!}$ is a multinomial coefficient, and the coefficients in (3) are defined to be 1 if $n = i - j$.

Here we investigate combinatorial representations for the complex-type Padovan p-circulant numbers by the following Corollary.

Corollary 5 *i.* For $n \geq 2$,

$$C_p^{(Pa,i)}(n) = \sum_{(t_1, t_2, \ldots, t_{p+3})} \binom{t_1 + t_2 + \cdots + t_{p+3}}{t_1, t_2, \ldots, t_{p+3}} \left(-i^{p+2}\right)^{t_1}$$

where the summation is over nonnegative integers satisfying $t_1 + 2t_2 + \cdots + (p+3)t_{p+3} = n - p - 2$.

ii. For $n \geq 2$,

$$C_p^{(Pa,i)}(n) = \sum_{(t_1, t_2, \ldots, t_{p+3})} \frac{t_{p+2} + t_{p+3}}{t_1 + t_2 + \cdots + t_{p+3}} \times \binom{t_1 + t_2 + \cdots + t_{p+3}}{t_1, t_2, \ldots, t_{p+3}} \left(-i^{p+2}\right)^{t_1}$$

and

$$C_p^{(Pa,i)}(n) = \sum_{(t_1, t_2, \ldots, t_{p+3})} \frac{t_{p+3}}{t_1 + t_2 + \cdots + t_{p+3}} \times \binom{t_1 + t_2 + \cdots + t_{p+3}}{t_1, t_2, \ldots, t_{p+3}} \left(-i^{p+2}\right)^{t_1}$$

where the summation is over nonnegative integers satisfying $t_1 + 2t_2 + \cdots + (p+3)t_{p+3} = n + 1$.

Proof. In Theorem 4, if we take $i = p + 3$ and $j = 1$ for the case i. and, $i = \varepsilon - 1$ and $j = \varepsilon$ such that $p + 2 \leq \varepsilon \leq p + 3$ for the case ii., then we can directly see the conclusions from $\left(A_p\right)^n$.

Now we consider the permanental representations of the complex-type Padovan p-circulant numbers.

Definition 6 A $u \times v$ real matrix $M = \left[m_{i,j}\right]$ is called a contractible matrix in the k^{th} column

(resp. row.) if the k^{th} column (resp. row.) contains exactly two non-zero entries.

Suppose that $x_1, x_2, \ldots, x_u$ are row vectors of the matrix M. If M is contractible in the k^{th} column such that $m_{i,k} \neq 0, m_{j,k} \neq 0$ and $i \neq j$, then the $(u-1)\times(v-1)$ matrix $M_{ij:k}$ obtained from M by replacing the i^{th} row with $m_{i,k}x_j + m_{j,k}x_i$ and deleting the j^{th} row. The k^{th} column is called the contraction in the k^{th} column relative to the i^{th} row and the j^{th} row.

In (Brualdi & Gibson, 1977), Brualdi and Gibson obtained that $per(M) = per(N)$ if M is a real matrix of order $\alpha > 1$ and N is a contraction of M.

Now we concentrate on finding relationships among the complex-type Padovan p-circulant numbers and the permanents of certain matrices that are obtained by using the generating matrix of the complex-type Padovan p-circulant numbers. Let p be a positive odd integer such that $p \geq 3$ and let $U_m^{(p,i)} = \left[u_{j,k}^{(p,i,m)} \right]$ be the $m \times m$ super-diagonal matrix, defined by

$$u_{j,k}^{(p,i,m)} = \begin{cases} i^p & \text{if } j = \eta \text{ and } k = \eta \text{ for } 1 \leq \eta \leq m, \\ & \text{if } j = \eta \text{ and } k = \eta + p \text{ for } 1 \leq \eta \leq m - p, \\ 1 & j = \eta \text{ and } k = \eta + p + 2 \text{ for } 1 \leq \eta \leq m - p - 2 \\ & \text{and} \\ & j = \eta + 1 \text{ and } k = \eta \text{ for } 1 \leq \eta \leq m - 1, \\ 0 & \text{otherwise.} \end{cases}, \text{ for } m \geq p + 3.$$

Then we have the following Theorem.

Theorem 7 Let p be a positive odd integer such that $p \geq 3$,

$$perU_m^{(p,i)} = C_p^{(Pa,i)}(m + p + 2)$$

for $m \geq p + 3$.

Proof. Let us consider the matrix $U_m^{(p,i)}$ and let the equation be hold for $m \geq p + 3$. We prove by induction on m. Then we show that the equation holds for $m+1$. If we expand the $U_m^{(p,i)}$ by the Laplace expansion of permanent with respect to the first row, then we obtain

$$perU_{m+1}^{(p,i)} = -i^{p+2} \cdot perU_m^{(p,i)} + perU_{m-p}^{(p,i)} + perU_{m-p-2}^{(p,i)}.$$

Since $perU_m^{(p,i)} = C_p^{(Pa,i)}(m + p + 2)$, $perU_{m-p}^{(p,i)} = C_p^{(Pa,i)}(m + 2)$ and $perU_{m-p-2}^{(p,i)} = C_p^{(Pa,i)}(m)$, it is clear that $perU_{m+1}^{(p,i)} = C_p^{(Pa,i)}(m + p + 3)$. So the proof is complete.

Let p be a positive odd integer such that $p \geq 3$ and let $V_m^{(p,i)} = \left[v_{j,k}^{(p,i,m)} \right]$ be the $m \times m$ diagonal matrix, defined by

$$v_{j,k}^{(p,i,m)} = \begin{cases} i^p & \text{if } j=\eta \text{ and } k=\eta \text{ for } 1\le\eta\le p+2, \\ & \text{if } j=\eta \text{ and } k=\eta+p \text{ for } 1\le\eta\le m-p-1, \\ 1 & j=\eta \text{ and } k=\eta+p+2 \text{ for } 1\le\eta\le m-p-2 \\ & \text{and} \\ & j=\eta+1 \text{ and } k=\eta \text{ for } 1\le\eta\le m-1, \\ 0 & \text{otherwise.} \end{cases}, \text{ for } m\ge p+3.$$

Then we have the following Theorem.

Theorem 8 Let p be a positive odd integer such that $p\ge 3$,

$$perV_m^{(p,i)} = C_p^{(Pa,i)}(m-1)$$

for $m\ge p+3$.

Proof. Let us consider the matrix $V_m^{(p,i)}$ and let the equation be hold for $m\ge p+3$. We prove by induction on m. Then we show that the equation holds for $m+1$. If we expand the $V_m^{(p,i)}$ by the Laplace expansion of permanent with respect to the first row, then we obtain

$$perV_{m+1}^{(p,i)} = -i^{p+2}\cdot perV_m^{(p,i)} + perV_{m-p}^{(p,i)} + perV_{m-p-2}^{(p,i)}.$$

Since $perV_m^{(p,i)} = C_p^{(Pa,i)}(m-1)$, $perV_{m-p}^{(p,i)} = C_p^{(Pa,i)}(m-p-1)$ and $perV_{m-p-2}^{(p,i)} = C_p^{(Pa,i)}(m-p-3)$, it is clear that $perV_{m+1}^{(p,i)} = C_p^{(Pa,i)}(m)$. So the proof is complete.

Assume next that $W_m^{(p,i)} = \left[w_{j,k}^{(p,i,m)} \right]$ be the $m\times m$ matrix, defined by

$$W_m^{(p,i)} = \begin{bmatrix} 1 & \cdots & 1 & 0 & \cdots & 0 \\ 1 & & & & & \\ 0 & & & & & \\ \vdots & & & V_{m-1}^{(p,i)} & & \\ 0 & & & & & \\ 0 & & & & & \end{bmatrix}, \text{ for } m> p+3,$$

($(m-p-3)$th column)

then we have the following results:

Theorem 8 Let p be a positive odd integer such that $p\ge 3$,

$$perW_m^{(p,i)} = \sum_{t=0}^{m-2} C_p^{(Pa,i)}(t)$$

for $m> p+3$.

Proof. If we extend $perW_m^{(p,i)}$ with respect to the first row, we write

$$perW_m^{(p,i)} = perW_{m-1}^{(p,i)} + perV_{m-1}^{(p,i)}.$$

Thus, by the results and an inductive argument, the proof is easily seen.

A matrix M is called convertible if there is an $n\times n$ $(1,-1)$-matrix K such that $perM = \det(M\circ K)$, where $M\circ K$ denotes the Hadamard product of M and K.

Now we give relationships among the complex-type Padovan p-circulant numbers and the determinants of certain matrices which are obtained by using the matrix $U_m^{(p,i)}$, $V_m^{(p,i)}$ and $W_m^{(p,i)}$.

Let $m > p+3$ and let H be the $m \times m$ matrix, defined by

$$H = \begin{bmatrix} 1 & 1 & 1 & \cdots & 1 & 1 \\ -1 & 1 & 1 & \cdots & 1 & 1 \\ 1 & -1 & 1 & \cdots & 1 & 1 \\ \vdots & \ddots & \ddots & \ddots & \ddots & \vdots \\ 1 & \cdots & 1 & -1 & 1 & 1 \\ 1 & \cdots & 1 & 1 & -1 & 1 \end{bmatrix}.$$

Corollary 9 Let p be a positive odd integer such that $p \geq 3$,

$$\det\left(U_m^{(p,i)} \circ H\right) = C_p^{(Pa,i)}(m+p+2),$$
$$\det\left(V_m^{(p,i)} \circ H\right) = C_p^{(Pa,i)}(m-1)$$

and

$$\det\left(W_m^{(p,i)} \circ H\right) = \sum_{t=0}^{m-2} C_p^{(Pa,i)}(t)$$

for $m > p+3$.

Proof. Since $perU_m^{(p,i)} = \det\left(U_m^{(p,i)} \circ H\right)$, $perV_m^{(p,i)} = \det\left(V_m^{(p,i)} \circ H\right)$ and $perW_m^{(p,i)} = \det\left(W_m^{(p,i)} \circ H\right)$ for $m > p+3$, by Theorem 6, Theorem 7 and Theorem 8, we have the conclusion.

It is easy to see that the generating function of the complex-type Padovan p-circulant sequence $\left\{C_p^{(Pa,i)}(n)\right\}$ is as follows:

$$g(x) = \frac{x^{p+2}}{1 + i^{p+2} \cdot x - x^{p+1} - x^{p+3}},$$

where p is a positive odd integer such that $p \geq 3$.

Now we are concerned about the exponential representation of the complex-type Padovan *p*-circulant numbers by the aid of the generating function with the following Theorem.

Theorem 10 The complex-type Padovan *p* -circulant sequence $\left\{C_p^{(Pa,i)}(n)\right\}$ have the following exponential representation:

$$g(x) = x^{p+2} \exp\left(\sum_{a=1}^{\infty} \frac{(x)^a}{a}\left(-i^{p+2} + x^p + x^{p+2}\right)^a\right),$$

where p is a positive odd integer such that $p \geq 3$.

Proof. Since

$$\ln g(x)=\ln\frac{x^{p+2}}{1+i^{p+2}\cdot x-x^{p+1}-x^{p+3}}=\ln x^{p+2}-\ln\left(1+i^{p+2}\cdot x-x^{p+1}-x^{p+3}\right)$$

and

$$\begin{aligned}-\ln\left(1+i^{p+2}\cdot x-x^{p+1}-x^{p+3}\right)=-[&-x\left(-i^{p+2}+x^{p}+x^{p+2}\right)-\\&-\frac{1}{2}x^{2}\left(-i^{p+2}+x^{p}+x^{p+2}\right)^{2}-\cdots-\\&-\frac{1}{a}x^{a}\left(-i^{p+2}+x^{p}+x^{p+2}\right)^{a}-\cdots]\end{aligned}$$

it is clear that

$$\ln\frac{g(x)}{x^{p+2}}=\sum_{a=1}^{\infty}\frac{(x)^{a}}{a}\left(-i^{p+2}+x^{p}+x^{p+2}\right)^{a}$$

Thus the conclusion is obtained.

Now we give the sums of the complex-type Padovan p-circulant numbers. Let

$$S_n=\sum_{k=1}^{n}C_p^{(p_k,i)}(k)$$

for $n\geq 2$ and p is a positive odd integer such that $p\geq 3$, and suppose that Z_p is the $(p+4)\times(p+4)$ matrix such that

$$Z_p=\begin{bmatrix}1&0&\cdots&0\\1&&&\\0&&A_p&\\\vdots&&&\\0&&&\end{bmatrix}.$$

If we use induction on n, then we obtain

$$\left(Z_p\right)^{n}=\begin{bmatrix}1&0&\cdots&0\\S_{n+p+1}&&&\\S_{n+p}&&\left(A_p\right)^{n}&\\\vdots&&&\\S_{n-1}&&&\end{bmatrix}.$$

Conclusions

In this paper, we have defined the complex-type Padovan p-circulant sequences by using the circulant matrix which is obtained from the characteristic polynomials of the complex-type Padovan p-circulant sequences. Also, we have provided a new combinatorial representation of the complex-type Padovan p-circulant numbers by the aid of the nth power of the generating matrix of the complex-type Padovan p-circulant sequences. In addition, we have derived various properties of the complex-type Padovan p-circulant numbers such as the permanental, determinantal and exponential representations and the finite sums by matrix methods.

REFERENCES

Akuzum, Y. (2023a). The Complex-type Narayana-Fibonacci Numbers. *Journal of the Institute of Science and Technology*, 13(1), 563-571.

Akuzum, Y. (2023b). The Complex-Type *k*-Pell Numbers and Their Applications. J. Math., 2023, Article ID 6631659.

Akuzum, Y. (2020). The Hadamard-type Padovan-*p* Sequences. *Turkish Journal of Science*, 5(2), 102-109.

Akuzum, Y., Deveci, O. & Shannon, A. G. (2017). On the Pell *p*-circulant sequences. *Notes on Number Theory and Discrete Mathematics*, 23(2), 91-103.

Akuzum, Y., Deveci, O. & Artun, G. (2019). The Adjacency-Pell-circulant sequences. *Util. Math.*, 110, 49-61.

Berzsenyi, G. (1975). Sums of products of generalized Fibonacci numbers. *Fibonacci Quart.*, 13(4), 343-344.

Bozkurt, D. & Tin-Yau, T. (2012). Determinants and inverses of circulant matrices with Jacobsthal and Jacobsthal-Lucas numbers. *Applied Mathematics and Computation*, 219(2), 544-551.

Brualdi, R. A. & Gibson, P. M. (1977). Convex polyhedra of doubly stochastic matrices I. Applications of permanent function. *J. Combin. Theory, Series A*, 22(2), 194-230.

Chen, W. Y. C. & Louck, J. D. (1996). The combinatorial power of the companion matrix. *Linear Algebra Appl.*, 232, 261-278.

Davis, P. J. (1979). *Circulant Matrices*. John Wiley, New York.

Deveci, O., Adiguzel, Z. & Akuzum, Y. (2020). On the Jacobsthal-circulant-Hurwitz numbers. *Maejo International Journal of Science and Technology*, 14(1), 56-67.

Deveci, O., Akuzum, Y. & Karaduman, E. (2015). The Pell-Padovan *p*-sequences and its applications. *Util. Math.*, 98, 327-347.

Deveci, O. & Karaduman, E. (2017). On the Padovan *p*-numbers. *Hacettepe J. Math. Stat.*, 46(4), 579-592.

Deveci, O. & Shannon, A. G. (2021). The complex-type *k*-Fibonacci sequences and their applications. *Comm. Algebra*, 49(3), 1352-1367.

Deveci, O. & Shannon, A. G. (2018). The quaternion-Pell sequence. *Comm. Algebra*, 46(12), 5403-5409.

Erdag, O., Halıcı, S. & Deveci, O. (2022). The complex-type Padovan-*p* sequences. Mathematica Moravica, 26(1), 77-88.

Horadam, A. F. (1961). A generalized Fibonacci sequence. *American Math. Monthly*, 68(5), 455-459.

Horadam, A. F. (1963). Complex Fibonacci numbers and Fibonacci quaternions. *American Math. Monthly*, 70(3), 289-291.

Horadam, A. F. & Shannon, A. G. (1976). Ward's Staudt-Clausen problem. *Mathematica Scandinavica*, 39(2), 239-250.

Ingleton, A. W. (1956). The rank of circulant matrices. *J. London Math. Soc.*, 1-31(4), 445-460.

Kalman, D. (1982). Generalized Fibonacci numbers by matrix methods. *Fibonacci Quart.*, 20(1), 73-76.

Kilic, E. (2008). The Binet formula, sums and representations of generalized Fibonacci *p*-numbers. *European J. Combin.*, 29(3), 701-711.

Kilic, E. & Tasci, D. (2006). On the generalized order-*k* Fibonacci and Lucas numbers. *Rocky Mountain J. Math.*, 36(6), 1915-1926.

Kilic, E. & Tasci, D. (2007). On the permanents of some tridiagonal matrices with applications to the Fibonacci and Lucas numbers. *Rocky Mountain J. Math.*, 37(6), 1953-1969.

Lancaster, P. & Tismenetsky, M. (1985). *The theory of matrices: with applications*. Elsevier.

Lidl, R. & Niederreiter, H. (1994). *Introduction to finite fields and their applications*. Cambridge U.P.

Muir, T. (1911). *The Theory of Determinants in Historical Order of Development*. Volume 4, Macmillan, London.

Ozgur, N. Y. (2005) On the sequences related to Fibonacci and Lucas numbers. *J. Korean Math. Soc.*, 42(1), 135-151.

Pan, H. & Jiang, Z. (2015). VanderLaan circulant type matrices. *Abstract and Applied Analysis*, Vol.2015, Article ID 329329, http://dx.doi.org/10.1155/2015/329329.

Shannon, A. G. (1974a). Explicit expressions for powers of arbitrary order linear recursive sequences. *Fibonacci Quart.*, 12(3), 281-287.

Shannon, A. G. (1974b). Some properties of a fundamental recursive sequence of arbitrary order. *Fibonacci Quart.*, 12(4), 327-335.

Shannon, A. G. (1976). Ordered partitions and arbitrary order linear recurrence relations. *Math. Student*, 43(3), 110-117.

Stakhov, A. P. & Rozin, B. (2006a). Theory of Binet formulas for Fibonacci and Lucas *p*-numbers. *Chaos, Solitons Fractals*, 27(5), 1162-1177.

Stakhov, A. & Rozin, B. (2006b). The continuous functions for the Fibonacci and Lucas *p*-numbers. *Chaos, Solitons Fractals*, 28(4), 1014-1025.

Stephen, B. (1990). *Matrices Methods and Applications*. Oxford University Press, New York.

Tasci, D. & Firengiz, M. C. (2010). Incomplete Fibonacci and Lucas *p*-numbers. *Math. Comput. Modell.*, 52(9-10), 1763-1770.

The Narayana-Fibonacci Sequence in Finite Groups

Yeşim AKÜZÜM [1]
Ömür DEVECİ [2]

Introduction

The study of recurrence sequences in algebraic structures began with the earlier work of Wall (Wall, 1960), where the ordinary Fibonacci sequences in cyclic groups were investigated. In the mid-eighties, Wilcox extended the concept to abelian groups (Wilcox, 1986). Lü and Wang contributed to study of Wall numbers for *k*-step Fibonacci sequence (Lü & Wang, 2006). Algebraic structures associated with the Fibonacci sequence were also explored by DeCarli (DeCarli, 1970) and Shannon (Shannon, 1979) in the seventies. The theory had been expanded to some finite simple groups by Campbell et al. (Campbell, Doostie & Robertson, 1990). There, they examined the periods of Fibonacci sequence in two-generator groups. In (Knox, 1992), Knox defined the *k*-nacci sequence considering the *k*-step Fibonacci sequence in a group and then he investigated the *k*-nacci sequence in a finite group in detail. In next process, the theory extended to the generalized order-*k* Pell sequence by Deveci and Karaduman(Deveci & Karaduman, 2015). Recently, some special linear recurrence sequences defined by the aid of group elements have been studied by many authors; for example, (Aydin & Dikici, 1998; Campbell & Campbell, 2004; Deveci et. al., 2015; Deveci, Erdag & Gungoz, 2023; Deveci & Shannon, 2018; Deveci & Shannon, 2021; Deveci, Karaduman & Campbell, 2011; Doostie & Hashemi, 2006; Erdag & Deveci, 2018; Erdag & Deveci, 2020; Erdag & Deveci, 2022; Erdag, Deveci & Karaduman, 2022; Hashemi & Mehraban, 2021; Karaduman & Aydin, 2003; Karaduman & Aydin, 2009; Mehraban & Hashemi, 2021; Ozkan, 2003; Ozkan, 2014). In this study, we extend the Naraya-Fibonacci sequence to groups and we redefine the Naraya-Fibonacci sequence by means of the elements of groups which is called the Naraya-Fibonacci orbit. Also, obtain the periods of the Naraya-Fibonacci orbit of the semi dihedral groups SD_{2^m} as applications of the results obtained.

Preliminaries

Akuzum and Deveci (Akuzum & Deveci, 2022) defined the Narayana-Fibonacci sequence by the following homogeneous linear recurrence relation for $k \geq 0$

$$n_{k+5}^{f} = 2n_{k+4}^{f} - n_{k+1}^{f} - n_{k}^{f}$$

in which $n_0^f = n_1^f = n_2^f = n_3^f = 0$ and $n_4^f = 1$.

Also in (Akuzum & Deveci, 2022), they gave Narayana-Fibonacci matrix as shown:

[1] Asst. Prof. Dr., Kafkas University
[2] Prof. Dr, Kafkas University,

$$N^F=\begin{bmatrix}2&0&0&-1&-1\\1&0&0&0&0\\0&1&0&0&0\\0&0&1&0&0\\0&0&0&1&0\end{bmatrix}_{5\times5}$$

Then, for $\alpha\geq4$, they obtained that

$$\left(N^F\right)^{\alpha}=\begin{bmatrix}n_{\alpha+4}^f & -n_{\alpha+1}^f-n_{\alpha}^f & -n_{\alpha+2}^f-n_{\alpha+1}^f & -n_{\alpha+3}^f-n_{\alpha+2}^f & -n_{\alpha+3}^f\\ n_{\alpha+3}^f & -n_{\alpha}^f-n_{\alpha-1}^f & -n_{\alpha+1}^f-n_{\alpha}^f & -n_{\alpha+2}^f-n_{\alpha+1}^f & -n_{\alpha+2}^f\\ n_{\alpha+2}^f & -n_{\alpha-1}^f-n_{\alpha-2}^f & -n_{\alpha}^f-n_{\alpha-1}^f & -n_{\alpha+1}^f-n_{\alpha}^f & -n_{\alpha+1}^f\\ n_{\alpha+1}^f & -n_{\alpha-2}^f-n_{\alpha-3}^f & -n_{\alpha-1}^f-n_{\alpha-2}^f & -n_{\alpha}^f-n_{\alpha-1}^f & -n_{\alpha}^f\\ n_{\alpha}^f & -n_{\alpha-3}^f-n_{\alpha-4}^f & -n_{\alpha-2}^f-n_{\alpha-3}^f & -n_{\alpha-1}^f-n_{\alpha-2}^f & -n_{\alpha-1}^f\end{bmatrix}.$$

It is important to note that $\det N^F=-1$.

Definition 1. The semidihedral group SD_{2^m}, ($m\geq4$) is defined by the presentation

$$SD_{2^m}=\left\langle x,\ y:\ x^{2^{m-1}}=y^2=e,\ yxy=x^{2^{m-2}-1}\right\rangle$$

Note that $\left|SD_{2^m}\right|=2^m$, $\left|x\right|=2^{m-1}$ and $\left|y\right|=2$.

Definition 2. A sequence is periodic if, after a certain point, it consists only of repetitions of a fixed subsequence. The number of elements in the shortest repeating subsequence is called the period of the sequence. In particular, if the first n elements in the sequence form a repeating subsequence, then this sequence is simply periodic and its period is n.

MAIN RESULTS

Let G be a finite j-generator group and let

$$X=\left\{\left(x_0,x_1,\ldots,x_{j-1}\right)\in\underbrace{G\times G\times\cdots\times G}_{j}\ \middle|\ \left\langle\left\{x_0,x_1,\ldots,x_{j-1}\right\}\right\rangle=G\right\}.$$

We call $\left(x_0,x_1,\ldots,x_{j-1}\right)$ a generating j-tuple for G.

Definition 3. For a generating j-tuple $\left(x_0,x_1,\ldots,x_{j-1}\right)\in X$, we define the Narayana-Fibonacci orbit $a_N^f\left(G:x_0,x_1,\ldots,x_{j-1}\right)$ as shown::

$$a_N^f(k+5)=\left(a_N^f(k)\right)^{-1}\left(a_N^f(k+1)\right)^{-1}\left(a_N^f(k+4)\right)^2$$

for $k\geq0$, with initial conditions

$$\begin{cases}a_N^f(0)=x_0,a_N^f(1)=x_1,\ldots,a_N^f(j-1)=x_{j-1},a_N^f(j)=e,\ldots,a_N^f(4)=e & \text{if } j<4,\\ a_N^f(0)=x_0,a_N^f(1)=x_1,a_N^f(2)=x_2,a_N^f(3)=x_3,a_N^f(4)=x_4 & \text{if } j=4.\end{cases}$$

Theorem 1. If G is a finite group, then a Narayana-Fibonacci orbit of the group G is simply periodic.

Proof. Let s be the order of the group G, then it is clear that there are s^5 distinct 5-tuples of elements of G. Then, it is easy to see that at least one of the 5-tuples appears twice in the Narayana-Fibonacci orbit. Because of the repeating, the Narayana-Fibonacci orbit of the group G is periodic. Since the orbit $a_N^f\left(G: x_0, x_1, \ldots, x_{j-1}\right)$ is periodic, there exist natural number u and v with $u \equiv v \pmod 5$, such that

$$a_N^f(u) = a_N^f(v), a_N^f(u+1) = a_N^f(v+1), \ldots, a_N^f(u+4) = x_p^F(v+4).$$

By the definition of the Narayana-Fibonacci orbit $a_N^f\left(G: x_0, x_1, \ldots, x_{j-1}\right)$, it is clear that

$$a_N^f(k) = \left(a_N^f(k+1)\right)^{-1}\left(a_N^f(k+4)\right)^2\left(a_N^f(k+5)\right)^{-1}.$$

Therefore, we obtain $a_N^f(u) = a_N^f(v)$, and hence

$$a_N^f(u-v) = a_N^f(0), a_N^f(u-v+1) = a_N^f(1), \ldots, a_N^f(u-v+4) = a_N^f(4),$$

which implies that the Narayana-Fibonacci orbit is simply periodic.

We denote the length of the period of Narayana-Fibonacci orbit $a_N^f\left(G: x_0, x_1, \ldots, x_{j-1}\right)$ by $La_N^f\left(G: x_0, x_1, \ldots, x_{j-1}\right)$.

In (Deveci & Akuzum, 2022), Deveci and Akuzum denoted the period of the sequence $\left\{n_k^{f,m}\right\}$ by $hn^{f,m}$.

Now we give the lengths of the periods of the Narayana-Fibonacci orbit of the semidihedral group SD_{2^m} as applications of the results obtained.

Theorem 2. The length of the period of the Narayana-Fibonacci orbit of the semidihedral group SD_{2^m} is $2^{m-2} \cdot hn^{f,2}$.

Proof. We consider the length of the period of the Narayana-Fibonacci orbit in the semidihedral group by the aid of the period $hn^{f,2} = 21$. The orbit $a_N^f\left(SD_{2^m} : x, y\right)$ is

$$\begin{aligned}
&x, y, e, e, e, x^{-1}y, yx^{2^{m-2}}, e, e, yx, x^{2^{m-2}-1}, yx^{2\left(2^{m-3}-1\right)}, e, yx^{2^{m-2}+1},\\
&yx^{2^{m-2}+2}, yx^{2^{m-2}-3}, yx^{-2}, yx, x^{2^{m-2}+1}, x^{2^{m-2}-3}, x^{(-1)^{m-1}\left(2^{m-3}-1\right)}, x^{2^{m-2}+9},\\
&yx^2, x^2, x^{(m-2)\left(2^{m-3}\right)}, x^4, yx^3, yx^{2^{m-2}}, x^2, x^4, xy, x^{-3}, yx^{2^{2m-6}}, x^{-6},\\
&yx^7, yx^{2^{m-2}+2}, yx^5, yx^{-2}, yx^{2^{m-2}+1}, x^{(m-2)\left(2^{m-3}\right)-1}, x^9, x^{2^{m-2}-1}, x,\\
&yx^8, x^{(m-2)\left(2^{m-3}\right)}, x^{\left(2^{m-2}\right)}, x^{\left(2^{m-2}\right)}, \ldots,
\end{aligned}$$

and so the orbit becomes:

$$a_N^f(0)=x,\ a_N^f(1)=y,\ a_N^f(2)=e,\ a_N^f(3)=e,\ a_N^f(4)=e,\ldots,$$
$$a_N^f\left(2\cdot hn^{f,2}\lambda\right)=x^{4\lambda\alpha_1+1},\ a_N^f\left(2\cdot hn^{f,2}\lambda+1\right)=yx^{4\lambda\alpha_2},\ a_N^f\left(2\cdot hn^{f,2}\lambda+2\right)=x^{4\lambda\alpha_3},$$
$$a_N^f\left(2\cdot hn^{f,2}\lambda+3\right)=x^{4\lambda\alpha_4},\ a_N^f\left(2\cdot hn^{f,2}\lambda+4\right)=x^{4\lambda\alpha_5},\ldots.$$

Where $\alpha_1,\alpha_2,\alpha_3,\alpha_4$ and α_5 are positive integers such that $\gcd(\alpha_1,\alpha_2,\alpha_3,\alpha_4,\alpha_5)=1$. Thus, for $\delta\in\mathcal{N}$, we need the smallest integer λ such that $4\lambda=2^{m-1}\cdot\delta$. If we choose $\lambda=2^{m-3}$, we get

$$a_N^f\left(2^{m-2}\cdot hn^{f,2}\right)=x,\ a_N^f\left(2^{m-2}\cdot hn^{f,2}+1\right)=y,\ a_N^f\left(2^{m-2}\cdot hn^{f,2}+2\right)=e,$$
$$a_N^f\left(2^{m-2}\cdot hn^{f,2}+3\right)=e,\ a_N^f\left(2^{m-2}\cdot hn^{f,2}+4\right)=e,\ldots.$$

Since the elements succeeding $a_N^f\left(2^{m-2}\cdot hn^{f,2}\right)$, $a_N^f\left(2^{m-2}\cdot hn^{f,2}+1\right)$, $a_N^f\left(2^{m-2}\cdot hn^{f,2}+2\right)$, $a_N^f\left(2^{m-2}\cdot hn^{f,2}+3\right)$ and $a_N^f\left(2^{m-2}\cdot hn^{f,2}+4\right)$ depend on x, y, e for their values, the cycle begins again with the $a_N^f\left(2^{m-2}\cdot hn^{f,2}\right)$nd element. Thus it is verified that the length of the period of the Narayana-Fibonacci orbit is SD_{2^m} is $2^{m-2}\cdot hn^{f,2}$.

Example 1. The orbit $a_N^f\left(SD_{16}:x,\ y\right)$ is

$$x,\ y,e,e,e,x^{-1}y,\ yx^4,e,e,\ yx,x^3,\ yx^2,e,\ yx^5,\ yx^6,$$
$$yx,\ yx^{-2},\ yx,x^5,x,x^{-1},x^5,\ yx^2,x^2,x^4,x^4,\ yx^3,$$
$$yx^4,x^2,x^4,xy,x^{-3},\ yx^4,x^{-6},\ yx^7,\ yx^6,\ yx^5,\ yx^{-2},$$
$$yx^5,x^3,x,x^3,x,\ y,x^4,x^4,x^4,\ yx^5,\ y,e,e,\ yx^5,x^{-1},$$
$$yx^{-2},e,\ yx,\ yx^{-2},\ yx,\ yx^2,\ yx^5,x,x,x^3,x^5,\ yx^2,x^{-2},$$
$$e,e,\ yx^3,\ y,x^2,x^4,\ yx^{-1},x,\ y,e,\ yx^3,\ yx^{-2},\ yx^5,\ yx^2,$$
$$yx,x^{-1},x,x^{-1},x,\ y,e,e,e,\ldots.$$

So we obtain that $La_N^f\left(SD_{16}:x,\ y\right)=84$.

Conclusion

In this study, we move the Naraya-Fibonacci sequence to groups. In this sense, we redefine the Naraya-Fibonacci sequence by means of the elements of groups and call the Naraya-Fibonacci orbit to this relation redefined. Then, We show that this orbit is simply periodic. Also, we examine the Naraya-Fibonacci orbit in the semi dihedral groups SD_{2^m}. We obtain the periods of this orbit of the semi dihedral groups SD_{2^m} as applications of the results obtained.

REFERENCES

Akuzum, Y. & Deveci, O. (2022). The Narayana-Fibonacci Sequence and its Binet Formulas. *6th International Congress on Life, Social, and Health Sciences in a Changing World*, 2-3 July 2022, Turkey, (pp. 303-307).

Aydin, H. & Dikici, R. (1998). General Fibonacci sequences in finite groups. *Fibonacci Quarterly*, 36(3), 216–221.

Campbell, C. M. & Campbell, P. P. (2004). On the Fibonacci length of powers of dihedral groups. (In: Howard, F. T., ed., pp. 69-85). Applications of Fibonacci Numbers, Vol. 9. Dordrecht, Kluwer Academic Publisher.

Campbell, C. M., Doostie, H. & Robertson, E. F. (1990). Fibonacci length of generating pairs in groups. (In: Bergum, G. E., ed., pp. 27-35). Applications of Fibonacci Numbers, Vol. 3. Dordrecht: Kluwer Academic Publishers/Springer.

DeCarli, D. J. (1970). A generalized Fibonacci sequence over an arbitrary ring. *Fibonacci Quarterly*, 8(2), 182-184.

Deveci, O., & Akuzum, Y. (2022). The Narayana-Fibonacci Sequence modulo m. *6th International Congress on Life, Social, and Health Sciences in a Changing World*, 2-3 July 2022, Turkey, (pp. 308-311).

Deveci, O., Akuzum, Y., Karaduman, E. & Erdag, O. (2015). The Cyclic Groups via Bezout Matrices. *Journal of Mathematics Research, 7*(2), 34-41.

Deveci, O., Erdag, O. & Gungoz, U. (2023). The complex-type cyclic-Fibonacci sequence and its applications. *Journal of Mahani Mathematical Research*, 12(2), 235-246.

Deveci, O. & Shannon, A. G. (2018). The quaternion-Pell sequence. *Communications* in *Algebra*, 46(12), 5403-5409.

Deveci, O. & Shannon, A. G. (2021). The complex-type k-Fibonacci sequences and their applications. *Communications* in *Algebra*, 49(3), 1352-1367.

Deveci, O. & Karaduman, E. (2015). The Pell sequences in finite groups. *Utilitas mathematica*, 96, 263-276.

Deveci, O., Karaduman, E. & Campbell, C. M. (2011). On the k-nacci sequences in finite binary polyhedral groups. *Algebra Colloquium*, 18(1), 945-954.

Doostie, H. & Hashemi, M. (2006). Fibonacci lengths involving the Wall number k(n). *Journal of Applied Mathematics and Computing*, 20(1), 171-180.

Erdag O., & Deveci, O. (2018). The arrowhead-Pell-random-type sequences in finite groups. *AIP Conference Proceedings*. Vol. 1991. No. 1. AIP Publishing LLC.

Erdag O., & Deveci, O. (2020). The Pell-Fibonacci Sequence in Finite Groups. *3rd International Conference On Mathematical and Related Sciences: Current Trends and Developments*, 20-22 November 2020, Turkey, (pp. 136-139).

Erdag O., & Deveci, O. (2022). The Complex-Type Cyclic-Jacobsthal Sequence and its Applications. Elif Orhan & Elanur Seven (Ed.), *Teoriden Uygulamaya Fizik Ve Matematik Alanında Akademik Çalışmalar II* içinde (s. 197-212), Ankara, Iksad Publications House.

Erdag O., Deveci, O. & Karaduman, E. (2022). The Complex-type Cyclic-Pell Sequence and its Applications. *Turkish Journal of Science*, 7(3), 202-210.

Hashemi, M. & Mehraban, E. (2021). The generalized order k-Pell sequences in some special groups of nilpotency class 2. *Communications* in *Algebra*, 50(4), 1768-1784.

Karaduman, E. & Aydin, H. (2003). General 2-step Fibonacci sequences in nilpotent groups of exponent *p* and nilpotency class 4 *Applied mathematics and computation*, 141(2–3), 491-497.

Karaduman, E. & Aydin, H. (2009). *k*-nacci sequences in some special groups of finite order. *Mathematical and computer modelling*, 50(1–2), 53-58.

Knox, S. W. (1992). Fibonacci sequences in finite groups. . *Fibonacci Quarterly*, 30(2), 116-120.

Lu, K. & Wang, J. (2006). *k*-step Fibonacci sequence modulo *m*. *Utilitas mathematica*, 71, 169-177.

Mehraban, E. & Hashemi, M. (2021). Fibonacci length and the generalized order *k*-Pell sequences of the 2-generator *p*-groups of nilpotency class 2. *Journal of Algebra and Its Applications*, Doi:10.1142/S0219498823500615.

Ozkan, E. (2003). 3-step Fibonacci sequences in nilpotent groups. *Applied mathematics and computation*, 144(2–3), 517-527.

Ozkan, E. (2014). Truncated Lucas sequences and its period. *Applied Mathematics and Computation*, 232, 285-291.

Shannon, A. G. (1979). Generalized Fibonacci numbers as elements of ideals. *Fibonacci Quarterly*, 17(4), 347-349.

Wall, D. D. (1960). Fibonacci series modulo *m*. *The American Mathematical Monthly*, 67(6), 525-532.

Wilcox, H. J. (1986). Fibonacci sequences of period *n* in Groups. *Fibonacci Quarterly*, 24(4), 356-361.

On Some Properties of Poloids and Mappings

Hasan KELEŞ[1]

Introduction

This section is about the poloid created by introducing the new property to the monoid. The concept of monoid, which has a great place in algebraic theory, is the important categorical expression. The expression of monoids in a cryptic manner is made meaningful to new properties. This cryptic categorical structure is made even more evident with the concept of poloid. In particular, the monoid is extended to the poloid with the condition (P4). The poloid structure is gained even more meaning. The new results presented on poloid provide additional contributions to algebraic structures such as goup, ring, and field. Better expression of these structures allows for a better understanding of categorical structures. Obtaining partial transformation systems gives us the opportunity to recognize similar structures. Jonsson gave partial property of the poloid structure in 2018. The structure is made even more prominent in 2022.

The (P4) feature covers the definition given by Jonsson.

Definition 1. Let $(G,*)$ be group. $(G,*)$ is called a poloid such that for every $x \in G$ there is a unique $x^{-1} \in G$ such that $x * x^{-1}$ and $x^{-1} * x$ are defined and units.

Definition 2. A group is a set P equipped with a binary operation $*: P \times P \to P$ that associates an element $a * b \in P$ to every pair of elements $a, b \in P$, and having the following properties: $*$ is associative, has an identity element $e \in P$, and every element in P is invertible More explicitly, this means that the following equations hold for all $a, b, c, d \in P$:

$P1.\ a * (b * c) = (a * b) * c$, (associativity).

$P2.\ a * e = e * a$, (identity).

$P3.$ For every $a \in P$, there is some $a^{-1} \in P$ such that $a * a^{-1} = a^{-1} * a = e$ (inverse).

$P4.$ For every $a \in P \setminus \{e\}$, there are some $b, c, d \in P \setminus \{e\}$ such that $b * c = c * d = a$ with $b \neq d$ (escort).

A set P together with an operation $*: P \times P \to P$ and satisfying only conditions (P1), (P2), (P3) and (P4) is called a poloid. It is denoted by $(P,*)$.

[1] Lecturer, Karadeniz Technical University,

Properties of Poloids and Mappings

In this chapter, besides the operational properties of some matrices, the subject of mappings is covered.

The following lemma explains this situation.

Lemma 1. If $(P,*)$ is a poloid then for every $x \in P$ there is a unique $x^{-1} \in P$ such that $x * x^{-1}$ and $x^{-1} * x$ are defined.

Proof. If $(P,*)$ is a poloid then for every $a \in P \setminus \{e\}$, there are some $b,c,d \in P \setminus \{e\}$ such that $b*c = c*d = a$ with $b \neq d$.

$$(b*c)*x = (c*d)*x = a*x = e \text{, where } x \in P$$

$b*c = c*d = a$ by (P3).

$$b*c = c*d = a \Rightarrow x = (b*c)^{-1} = c^{-1} * b^{-1}$$

$$x = (c*d)^{-1} = d^{-1} * c^{-1},$$

And

$$x := a^{-1}.$$

a^{-1} element is also uniqe since $b,c,d \in P \setminus \{e\}$ are uniqe elements.

Note: Each element of the unit different poloid is obtained from the elements one common and one different of group.

Property 2. Let $(P,*)$ be a poloid. If all $x \in P \setminus \{e\}$ $x = x_2 * x_1 = x_1 * x_3$ then

$$x^{-1} = x_1^{-1} * x_2^{-1} = x_3^{-1} * x_1^{-1}.$$

Proof. For all $x \in P \setminus \{e\}$ $x = x_2 * x_1 = x_1 * x_3$,

$$x * x^{-1} = x_2 * x_1 * x^{-1} = e$$

$$x^{-1} = x_1^{-1} * x_2^{-1},$$

And

$$x * x^{-1} = x_1 * x_3 * x^{-1} = e$$

$$x^{-1} = x_3^{-1} * x_1^{-1},$$

$$x^{-1} = x_1^{-1} * x_2^{-1} = x_3^{-1} * x_1^{-1}, \text{ where } x_2^{-1} \neq x_3^{-1}.$$

Let $f : P \to P$ be a mapping satisfying the following properties

i. For every $y \in P$ there exist $x \in P$ such taht $y = f(x)$.

ii. If every two elements $x_1, x_2 \in P$ there exist $y_1, y_2 \in P$ such that $y_1 = f(x_1), y_2 = (x_2)$ then $y_1 = y_2$.

iii. For any two $x_1, x_2 \in P$ $f(x_1 * x_2) = f(x_1) * f(x_2)$.

$$f : P \to P$$

$$x \to y = f(x).$$

The f transform that satisfies the three conditions above is called the poloid mapping.

If $f(P) = \{x | f(x) = x, x \in P\}$, then $(f(P), *)$ is a poloid. It is clearly.

Lemma 3. Let f be a poloid mapping. The following situations hold.

i. For every $x \in P$ there exist $x_1, x_2 \in P \setminus \{e\}$ such taht $f(x) = f(x_1) * f(x_2)$.

ii. For every two $x_1, x_2 \in P \setminus \{e\}$ there exist $x_3 \in P \setminus \{e\}$ such taht $f(x_2) * f(x_1) = f(x_1) * f(x_3)$, where $f(x_2) \neq f(x_3)$.

iii. For every $x \in P$ there exist $x_1, x_2 \in P \setminus \{e\}$ such taht $f^{-1}(x) = f^{-1}(x_2) * f^{-1}(x_1)$.

iv. $f(x^{-1}) = f^{-1}(x)$ for every $x \in P$.

v. $f(e) = e$

Proof. Let $(P, *)$ be a poloid and f a poloid mapping.

i. For every $x \in P$ there exist $x_1, x_2 \in P \setminus \{e\}$ such taht $x = x_1 * x_2$ by (P4).

If a mapping f then

$$f(x) = f(x_1 * x_2) = f(x_1) * f(x_2).$$

ii. For every $x \in P$ there exist $x_1, x_2, x_3 \in P \setminus \{e\}$ such taht $x = x_2 * x_1 = x_1 * x_3$ by (P4).

$$f(x_2) * f(x_1) = f(x_1) * f(x_3)$$

$f(x_2) \neq f(x_3)$ because $x_2 \neq x_3$.

iii. For every $x \in P$ there exist $x_1, x_2 \in P \setminus \{e\}$ such taht $f(x) = f(x_1) * f(x_2)$,

$$\begin{aligned} e = y * y^{-1} &= f(x) * f^{-1}(x) \\ &= f(x_1) * f(x_2) * f(x_2^{-1}) * f(x_1^{-1}) \\ &= f(x_1) * f(x_2) * f^{-1}(x_2) * f^{-1}(x_1) \end{aligned}$$

$$y^{-1} = f^{-1}(x) = f^{-1}(x_2) * f^{-1}(x_1).$$

iv. If $x \in P$ then

$$e = f(x) * f^{-1}(x) = f(x) * f(x^{-1}).$$

v.

$$\begin{aligned} e &= f(x) * f^{-1}(x) \\ &= f(x) * f(x^{-1}) \\ f(e) &= f(x * x^{-1}) = e. \end{aligned}$$

Lemma 4. Let f be a poloid mapping. The following situations hold.

i. For every $x \in P$ there exist $x_1, x_2 \in P \setminus \{e\}$ such taht

$$(f \circ f)(x) = (f \circ f)(x_1) * (f \circ f)(x_2).$$

ii. If $x = e$ then

$$\left(\underbrace{f \circ f \circ \cdots \circ f}_{n-times} \right)(e) = e.$$

Proof. Let $(P, *)$ be a poloid and f a poloid mapping.

i. It is clearly.

ii. If $x = e$ then

$$\begin{aligned} \left(\underbrace{f \circ f \circ \cdots \circ f}_{n-times} \right)(e) &= \left(\underbrace{f \circ f \circ \cdots \circ f}_{(n-1)-times} \right)(f(e)) \\ &= \left(\underbrace{f \circ f \circ \cdots \circ f}_{(n-1)-times} \right)(e) \\ &\vdots \\ &= f(e) = e. \end{aligned}$$

Definition 5. Let $(P,*)$ be a poloid and $x, x_1 \in P$. x_1 is called divides x if $x = x_1 * x_2$, where $x_2 \in P$. They are denoted $x_1 | x$ and $x_2 = \frac{x}{x_1}$. Each of the two elements of the poloid divides the other. x_1 is called not divide x if $x \neq x_1 * x_2$. It is denoted $x_1 \nmid x$.

Note. The set of regular matrices is given as the example of poloid in our previous studies. The set of all regular matrices of order $n \in \mathbb{Z}^+$ over a field F is denoted by

$$M_n(F) = \left\{ \left[a_{ij} \right]_n \middle| a_{ij} \in F, n \in \mathbb{Z}^+ \right\}$$

The transpose of $A \in M_n(F)$ is denoted by A^T.

If $M_n(\mathbb{Z})$ and considering the elementary operations in the matrices $M_n(\mathbb{Z})$, the following property is given without proof.

Example 6. If $A = \begin{bmatrix} 1 & 5 \\ 2 & 4 \end{bmatrix}, B = \begin{bmatrix} 3 & 2 \\ 1 & 4 \end{bmatrix}$, then

$$AC = \begin{bmatrix} 1 & 5 \\ 2 & 4 \end{bmatrix} \begin{bmatrix} 0 & \frac{6}{5} \\ \frac{1}{2} & \frac{7}{10} \end{bmatrix} = \begin{bmatrix} 3 & 2 \\ 1 & 4 \end{bmatrix} = B.$$

Thus, $A | B$.

Example 7. If $A = \begin{bmatrix} 1 & 5 \\ 2 & 4 \end{bmatrix}, B = \begin{bmatrix} 4 & 2 \\ 1 & 6 \end{bmatrix}$, then

$$AC = \begin{bmatrix} 1 & 5 \\ 2 & 4 \end{bmatrix} \begin{bmatrix} 2 & 3 \\ 5 & 1 \end{bmatrix} = \begin{bmatrix} 27 & 8 \\ 24 & 10 \end{bmatrix},$$

$A \nmid B$ that $AC \neq B$.

Property 8. For all $A, B, C \in M_n(\mathbb{Z})$ the followings hold.

i. If $A, B \in M_n(\mathbb{Z})$ then $A | B$, $C = \frac{B}{A}$ and $B | A$, $C = \frac{A}{B}$.

ii. If $A | B$ then $A = \left(\frac{B^T}{C^T} \right)^T$.

iii. If $A \nmid B$ then $B = AC + D, C = \frac{B - D}{A}$.

Lemma 9. For any $A,B \in M_n(\square)$ If $A \not| B$, then there exist $D_1 \in M_n(\square)$ such that $B = A(C + D_1)$.

Proof. For any $A,B \in M_n(\square)$ If $A \not| B$, then

$$B = AC + D,$$

$$A|D \text{ and } D = AD_1, \text{ where } D_1 \in M_n(\square),$$

$$B = AC + AD_1,$$

$$B = A(C + D_1).$$

Corollary. If $A \not| B$ then there exist two unique $C, D_1 \in M_n(\square)$ such that $A = \left(\frac{B^T}{(C + D_1)^T} \right)^T$.

Property 10. Let $(P,*)$ be a poloid. There are infinite divisors every element different from unit.

Proof. Let $(P,*)$ be a poloid. For every $a \in P \setminus \{e\}$, there are some $b,c,d \in P \setminus \{e\}$ such that $a = b * c$. There are $b_1, s_1 \in P \setminus \{e\}$ such that $b = b_1 * s_1$ for $b \in P \setminus \{e\}$.

$$a = b * c$$

$$a = b_n * (s_n * c), \text{ where } n \in \square^+.$$

$$b_n | a.$$

Lemma 11. Let $(P,*)$ be a poloid and f a poloid mapping.

i. If $x, x_1, x_2 \in P$ then

$$f(x_1) | f(x).$$

ii. $f^{-1}(x) = \frac{e}{f(x)}$.

Proof. Let $(P,*)$ be a poloid and f a poloid mapping.

i. If $x, x_1, x_2 \in P$ then

$$x = x_1 * x_2$$

$$f(x) = f(x_1) * f(x_2)$$

$$f(x_1) \mid f(x).$$

ii. For all $x \in P \setminus \{e\}$, $e = f(x) f^{-1}(x)$,

$$f^{-1}(x) = \frac{e}{f(x)}.$$

Lemma 12. Let $f : P \to P$ be a poloid mapping on poloid $(P,*)$. $(f(P),*)$ is a poloid, where $f(P) = \{ f(x) \mid x \in P \}$.

Proof. Let $(P,*)$ be a poloid. For any $a \in P$ there exist $b,c,d \in P$ that $a = b*c = c*d$, where $b \neq d$. The property (P4) of $(f(P),*)$ is given by

$$f(a) = f(b*c) = f(b) * f(c),$$

$$= f(c*d) = f(c) * f(d)$$

$$f(a) = f(b) * f(c) = f(c) * f(d), \text{ where } f(b) \neq f(d).$$

$(f(P),*)$ is a poloid.

For any $z \in f(P)$ there exist $a,b,\cdots,u,v \in P$ that $z = f(a) * f(b) = \cdots = f(u) * f(v)$, where $f(a) \neq f(u), \cdots, f(b) \neq f(v)$.

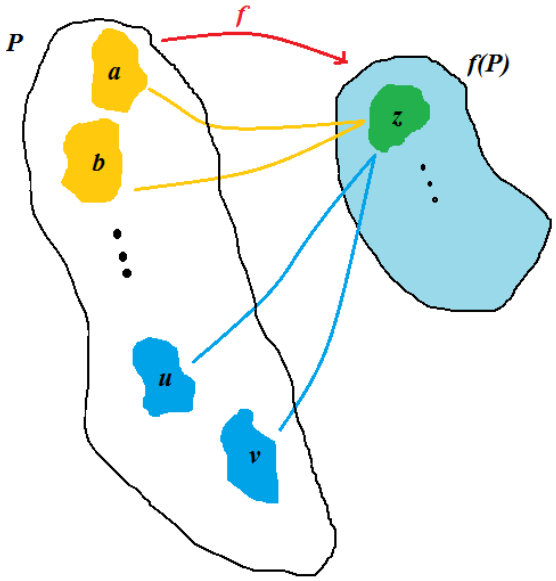

Example 13. If $M_n(\square)$ and the mapping f on poloid $(M_n(\square),.)$ is defined as

$$f : M_n(\square) \to M_n(\square)$$

$$X \to f(X) = X^k \text{, where } k \in \square^+$$

For $A, B \in M_n(\square)$

Then

$$f(AB) = (AB)^k = A^k B^k = f(A) f(B), \quad f(A) \mid f(AB) .$$

The mapping f is the poloid mapping.

Example 14. If $M_n(\square)$ and the mapping g on poloid $(M_n(\square), .)$ is defined as

$$g : M_n(\square) \to M_n(\square)$$

$$X \to g(X) = e^X$$

For any $A, B \in M_n(\square)$

Then

$$g(AB) = e^{AB} = (e^A)^B ,$$

$$g(AB) \neq g(A) g(B) .$$

The mapping g is not the poloid mapping.

Discussion and Conclusion

There are very studies about dividing matrices. The explanation was given about non-divisible matrices with this study. In addition, the study provided a new perspective for elements not associated with division. The transformation that relates to a poloid is given for the first time. New gains are expected for future transformations.

References

Jonsson D., (2018). Poloids From The Points of View of Partial Transformatıons and Category Theory , arXiv : 1710.04634v4.

Rafael B,, Maria T. G., Isabel G. and José A. S., (2015). The Hadamard Product of a Nonsingular General H-Matrix and Its Inverse Transpose Is Diagonally Dominant, Hindawi Publishing Corporation Journal of Applied Mathematics Volume, Article ID 264680, 6 pages.

Keles, H**., (2022).** Poloids and Matrices, The Aligarh Bulletin of Mathematics**,** Volume 41, Number 1, 41-52.

Duggal**,**B. P**., (**2008). Upper Triangular Operator Matrices, SVEP and Browder, Weyl Theorems, Integr. equ. oper. theory 63, 17–28. https://doi.org/10.1007/s00020-008-1648-8.

Keleş, H., (2015). Introduction to Linear Algebra-I-, Bordo publications**, Trabzon, Turkiye.**

Keleş, H., (2015). Different Approaches on the Matrix Division and Generalization of Cramer's Rule, Journal of Scientific and Engineering Research, 2017, 4(3):105-108.

Keleş, H., (2022). On The Relationship Between Transpose and Division, 8. International İstanbul scıentific Research Congress March 12-13, pages 719-722, İstanbul, Turkiye.

Keleş, H., (2022). On Results Divisibility and Multipliers of Regular Matrices of Order *nth,* 8. International İstanbul Scientific Research Congress March 12-13, pages 712-718, İstanbul, Türkiye.

Volodymyr, P. S., (2020). A Greatest Common Divisor and a Least Common Multiple of Solutions of A Linear Matrix Equation, Pidstryhach Institute for Applied Problems of Mechanics and Mathematics, National Academy of Sciences of Ukraine, 16 October,. MATH. GM.

Porter, D. A., (1976). Solvability of the Matric Equation $AX = B$, Linear Algebra and Its Applzcatzons, 13, 177-164.

A Student Follow-Up And Famıly Informatıon System For Students' Attendance Problems

Erkan DÖLEK[1]
Mehmet Cabir AKKOYUNLU[2]

Introduction

School attendance is mandatory. Parents and school management are responsible for ensuring that their students attend school. Pursuant to Article 26 of the Basic Law of National Education, school administrators, directors of national education and local civil administrations take the necessary measures regarding the enrollment and attendance of students. (Ministry of National Education Regulation on Secondary Education Institutions-Article-36(1)). The problem of absenteeism at all levels of education affects the success of students. (Yıldız, 2011;Girgin, 2016). Especially in compulsory education levels, students may be inclined to be absent when they feel the supervision of their families is insufficient. As a result of this absenteeism, students' success levels decrease. (Dalkılıç, F., & Aydın, Ö. (2016). The fact that students' absenteeism information is followed seriously by their families reduces the courage of students to be absent, thus increasing their success grades after their attendance levels.

The aim of this study is to analyze in detail the studies carried out in cooperation with the Parent-School on the establishment of a control over the student's attendance, going and returning to school, and to reveal the similarities and differences of the studies conducted on this subject(Anonymus 1-7).

It is seen that one of the factors besides individual intelligence and environment on student success is the student's attendance at school. It is of great importance for the student's success that the project contributes positively to the student's success by carrying out an audit task in order to increase the student's attendance at the school, thus increasing the satisfaction of the students with the school and increasing their academic success (Dalkılıç, F., & Aydın, Ö. (2016).

Conceptual Framework and Related Studies

Reasons for absenteeism and dropout: A meta-synthesis study was conducted by Ünver (2022). In the study; With the education system extended from eight years to 12 years with the 4+4+4 application, activities have been put forward to ensure that students continue to school, to eliminate the factors that cause school dropout, and to connect them to school.

In the study conducted by Sönmez (2019); The reasons for absenteeism of vocational and technical secondary school students were examined (Kastamonu province example). In the study; It was seen that research was conducted on 864 vocational high school students, the data for the research were taken with the Absenteeism Data Form, and the reasons for absenteeism

[1] MSc, Karamanoğlu Mehmetbey Universty
[2] PhD,,Karamanoglu Mehmetbey University

were tried to be understood with this method, and the highest reason for absenteeism was health problems and the lowest reason for absenteeism was due to friends.

Face Detection And Recognition Based Automatic Class Attendance Management System has been reviewed Tanrıverdi (2017). In the study; A real-time polling system with a face detection and recognition based system has been developed by using the existing technological infrastructure without the cost of extra equipment, and the system has been developed by Ankara University Engineering It has been revealed that it was applied on students and positive results were obtained.

In the study conducted by Karabulut (2010); Fingerprint Recognition Based Real Time Student Attendance System Automation has been examined. In the study; It is aimed to monitor the attendance of the students by taking the attendance of the lessons with the sensor terminal placed in each classroom via the fingerprint Biometric identifier, and to eliminate the problem of time and attendance confusion.

The reasons for absenteeism of secondary school students were examined by Girgin (2016). In the study; The research population consisted of 3103 teachers and 6,689 students in 33 secondary education institutions in the city center of Balıkesir, 1243 students and 429 teachers were studied with the random sampling method for the sample, and the Student Reasons for Absenteeism Scale was applied separately for students and teachers. It was also emphasized that male students were more absent than female students.

In the study conducted by Öztekin (2013); The reasons for absenteeism of high school students were examined. In the study; In the research, the Causes of Absenteeism Form and the Student Interview Form were used in the research, where the screening model was used to determine the reasons for absenteeism, the phenomenological approach, one of the qualitative research designs, and two separate sample groups were used to examine the absenteeism problems of students with significant absenteeism, and the first group consisted of 1037 high school students and the second sample group consisted of 18 high school students As a result of the research, it was revealed that the highest reason for absenteeism was due to health problems, the lowest reason for absenteeism was family-related, and also the behavior of absenteeism was not due to a single factor, but to many factors.

In the study conducted by Yıldız(2011); Investigation of the reasons for absenteeism of primary school students was carried out. In the study; The Student Absenteeism Questionnaire was applied to 2600 students out of 12080 students studying in the 7th and 8th grades of 58 primary schools affiliated to Elazığ Provincial MEM by stratified sampling method; In addition, in the Teachers' Opinion Questionnaire on Student Absenteeism, it was applied to 178 teachers selected by simple random sampling method from 2459 primary school teachers working in the city center of Elazığ Provincial MEM, and as a result of the evaluations, the reason for the absenteeism of primary school students; In the first place, it has been revealed that another reason for health problems is the SBS exam.

In the study conducted by Akrin (2009); Student tracking system was examined with fingerprint. In the study; The fingerprints of the students, whose fingerprints were transferred to the fingerprint reader devices before, are stored on the devices by reading the fingerprints of the students at the lesson entrance or lesson exit, and this data is transferred to the interface program installed on the computer after a certain period of time and converted into absenteeism information with the algorithm on the software, and thus the system is made available to the students. It has been seen that the report, which includes the information, is aimed to be presented to the lecturers.

In the study conducted by Pehlivan (2006); Student absenteeism in public high schools and related school management policies (Ankara Province example) were examined. In the study; A total of 568 (56 administrators, 61 counsellors, counsellors) in 28 schools with the multi-stage stratified sampling method, which was conducted in two dimensions, with the scanning model in the first dimension, the research universe consisted of 263 administrators,

230 guidance teachers and 4780 branch teachers working in 75 high schools in the central districts of Ankara. It was emphasized that the data were obtained by applying the Continuous Student Absenteeism in High Schools and School Management Policies Questionnaire for This, which was conducted with the participants (451 branch teachers), and based on these data, it was emphasized that the reasons for absenteeism were family reasons, educational reasons, and student-based reasons. In the second dimension, information was obtained from the students who were at the school that day and agreed to be interviewed at the schools that were chosen impartially from the absent students through interviews, and 35 absentee students were interviewed in a total of 4 schools. The most important result obtained from the research findings is that teachers and students think differently from each other about absenteeism, Students consider school and teachers as the reason for absenteeism, teachers consider the family of the student as the reason for absenteeism. concluded that it was.

In accordance with the Article 26 of the Basic Law of National Education in the 1st paragraph of Article 36 of the Regulation on Secondary Education Institutions of the Ministry of National Education, school administrators, directors of national education and local civil administrators take the necessary measures regarding the enrollment and attendance of students. Parents and school management are responsible for ensuring that their students attend school.

Göçen and Kaya(2019) emphasized that absenteeism has many psychological, physical and social factors, and that absenteeism is a behavior that negatively affects the success of the student who cannot attend the classes and the education process and is not accepted by the society.

Sezdi and Tüysüz (2018) was emphasized that student attendance, which should be held regularly, is also a waste of time and that sometimes the attendance lists cannot be found, problems arise due to these reasons, this can be prevented with secure electronic attendance systems in the classrooms, and the attendance process is made transparent by reducing the loss of time and recording received in the electronic environment.

In the research article by Dalkılıç and Aydın (2016); There are many factors in increasing the academic success of students and one of these important factors is the undesirable behavior of absenteeism, that the underlying reason may be the school environment, family problems, bad weather conditions, transportation, health and personal inadequacies, and special precautions should be taken for these reasons. should be emphasized.

In compulsory education, with the effect of social and friend circles, the desire to attend school decreases day by day, and as a result, absenteeism increases and as a result, the student either fails in the class or the progress of the course success in the desired direction is negatively affected. Especially in metropolitan cities, if a parent who sends his/her student to school does not enter the school on time, if he/she does not enter, his/her absenteeism increases and he/she stays in the class after a certain value or the decrease in the course success in the courses that he/she does not attend causes anxiety in the student's parents.

Presented Student Information System

It has been determined how functional it is on the students of Gülnar Hatun Vocational and Technical Anatolian High School in Gülnar District of Mersin. In the table below, the number of absentee students and the rates of students attending school for the months of January, February, March and April 2023, the decrease in the tendency of student absenteeism and the system's feedback from the parents can be seen.

Table 1. Attendance rates of January, February, March and April 2023

Total number of students:78	*2023*			
Month	*January*	*February*	*March*	*April*
5 day absentee	*10 students*	*8 students*	*7 students*	*5 students*
Rate of attendance (%)	*87,17*	*89,74*	*91,02*	*93,58*

Working Principle of the System

The student who enters the school or will leave the school reads the student identification card on the barcode reader on the system. Upon reading, an Information message is sent to the student's parent via SMS. The parent will have information about the student's condition.

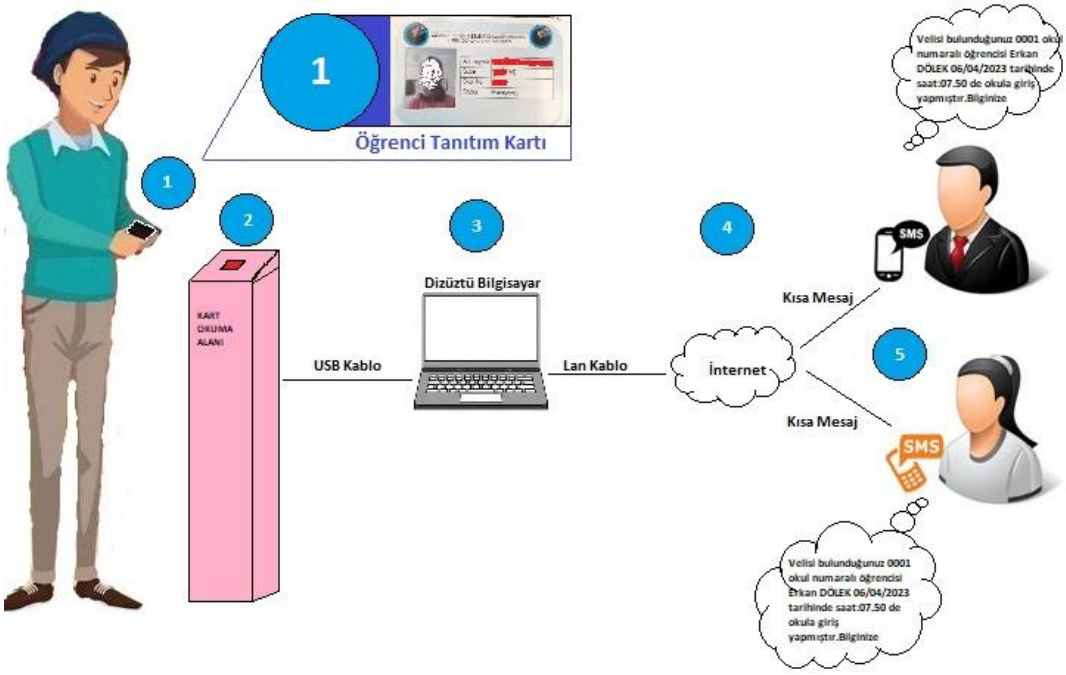

Figure 1. Working Principle

Process Steps

When the Working Principle diagram (Figure 1) is examined;

- Step 1: The student prepares the student identification card defined for himself/herself for reading.
- Step 2: The student brings the student identification card closer to the appropriate area in the card reading block. The barcode reader should hear the reading sound.
- Step 3: The data received from the barcode reader is transferred to the software in the computer environment for processing.
- Step 4: After the data is processed, an internet connection is required to send a text message to the parent. The correctness of the Internet connection should be checked.
- Step 5: The student's attendance information is sent as a message to the parent registered in the system.

System Requirements

- Any of the Win7 and above operating systems must be installed,
- Must have at least 6GB Ram,
- There must be 46.81MB of free space on the hard disk drive (D:\\, E:\\ etc.) to be installed, other than the C:\\ drive,
- Microsoft Office 2007 must be installed (Access 2007 was used for the database), those with Microsoft Office 2010 installed Microsoft Access Database Engine 2010 etc.
- Microsoft.Net Framework 4.5 must be installed,
- The barcode reader must be in continuous reading mode.

As soon as the student identification cards are read to the barcode reader according to the transaction type selected in the Data Entry panel, an Information message is sent to the parents in a short time as seen in Figure 3. The content of the sent message is arranged as an example.

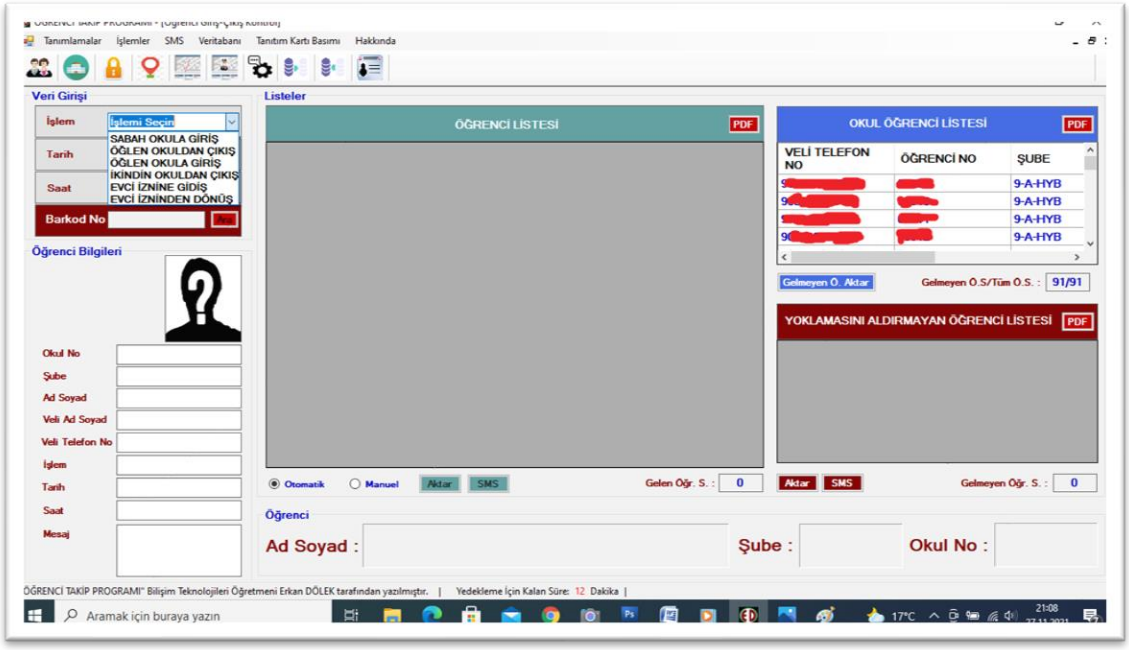

Figure 2. Screenshot of the homepage

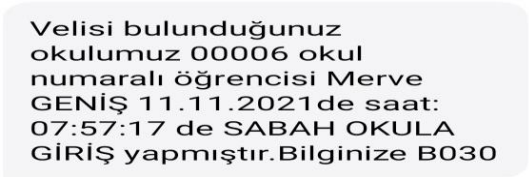

Figure 3. Example of an SMS

Student card (front)	Student card(back)
	

Sample student card


Figure 4. Sample student card

Findings

When we look at the studies carried out with the Student Tracking and Family Information System for Students' Absenteeism Problems, it has been determined that the student tracking system with fingerprints (Akrin, 2009) was carried out in the National Thesis Center. When the studies are compared and the fingerprint student tracking system in the National Thesis Center is examined (Akrin, 2009);

As an advantage; It was seen that the subject studied was reduced to the grade level. Its usefulness is that absenteeism can be taken every hour. Having a fingerprint is a correct practice for a student to take attendance using the card on behalf of his friend, that is, for system reliability.

As a disadvantage; To be costly. It will be costly as there should be separate fingerprint reading devices for each class. This system is difficult to implement if adequate financial support is not provided.

When the Student Tracking and Family Information System for Students' Absenteeism Problems is examined;

As an advantage; Even schools without a budget can easily acquire this system, as it is economical, consists of a barcode reader, a few stationery items and a computer.

As a disadvantage; It can be said that it can be used at the time of entering and leaving the school, but not at intermediate times.

In addition, the fingerprint student tracking system in the National Thesis Center (Akrin, 2009) will be really functional if it can be integrated into the e-school. In this way, the Assistant Director of Student Affairs will not waste time with daily absentee entries. Only the Ministry of National Education does not give access to the .api files and source codes of e-okul, except for its own software developers. If the purpose is to inform the parents about the student's attendance at school, the Student Tracking and Family Information System for Students' Absenteeism Problems offers the necessary solution.

Conclusion

In order for our student who continues in compulsory education not to fail in the classroom due to absenteeism and not to negatively affect the course success, our system will inform the student's attendance at school with an instant message to the parents by reading the student identification card, which is embezzled by the cooperation of the school and family, and the identification card, which is read to the barcode reader during the daily entrance and return to school. acts as a supervisor. With this practice, the absenteeism rate in our school Gülnar Hatun Vocational and Technical Anatolian High School was reduced to 6.42%, excluding the students who are constantly absent. Advantages of the system When similar systems used in the market are examined, the biggest advantage of our system over other systems is its cost. Other advantages are; its usefulness is that the software is suitable for all types of schools. The cons are that the system SMS infrastructure is suitable for Türk Telekom SMS package service. In the software content, separate source code should be developed for companies providing other SMS package services, or SMS API source codes of other companies providing SMS package service should be requested and integrated into the software.

Fingerprint reader can be used instead of barcode reader. Fingerprint reader apparatus can be attached separately for each class and each lesson and the received data can be collected in a center. It is possible to improve the software used by the system. The software can be developed web-based, not Windows-based.

In schools using the system, it reflects positively on school management and parent relations. There is an increase in the trust of the parents in the school. The school administration shares the responsibility with the parents, and from the parents' point of view, the use of the system is important since they receive feedback about whether their child arrives at school on time. In this way, although it is a deterrent on the student who is trying to be absent, an increase in the direction of the student's attendance and, as a result, an increase in the student's success in the course will be observed and the school-parent-student communication balance will be established.

REFERENCES

Akrin, İ. (2009). Parmak izi ile öğrenci öğrenci takip sistemi. Yüksek Lisans Tezi, Marmara Üniversitesi, İstanbul, Türkiye.

Anonymus 1: Çözümarge.”Kartlı Geçiş Sistemleri”,erişim:28/03/2023, https://www.cozumarge.com.tr/kartli-gecis-sistemleri/

Anonymus 2: Sppedtrackgps.”RFID, ERP ve Biyometrik Okul Sistemi”,erişim:01/04/2023, https://sppedtrackgps.in/school-attendance-management-system/

Anonymus 3: Perkotek.”Öğrenci Takip Sistemi”,erişim:07/04/2023, https://www.cozumarge.com.tr/kartli-gecis-sistemleri/

Anonymus 4: SchoolPass.” Attendance Automation”,erişim:07/04/2023, https://schoolpass.com/solutions/attendance-automation/

Anonymus 5:QuickSchools.” Student Attendance Management System”,erişim:07/04/2023, https://www.quickschools.com/quickschools/features/attendance

Anonymus 6:RG.” Student Tracking System”,erişim:07/04/2023, https://www.rginfotechs.com/RFID-Student-Tracking-System.php

Anonymus 7:BBSPL.” Student Tracking System”,erişim:07/04/2023, https://bestbarcodeworld.com/student-tracking-system/

Dalkılıç, F., & Aydın, Ö. (2016). Öğrenci Devamsızlıklarının Akademik Başarı Üzerindeki Etkisi: Dokuz Eylül Üniversitesi, İktisadi ve İdari Bilimler Fakültesi Örneği. 3rd international Eurasian Educational Research Congress. 31 May-3 June 2016. Muğla, Turkey.

GİRGİN, S. (2016). Ortaöğretim öğrencilerinin devamsızlık nedenleri.Yüksek Lisans Tezi, Okan Üniversitesi, İstanbul, Türkiye.

GÖÇEN, A. KAYA, A. (2019). Öğrenci Devamsızlığının Azaltılmasına Yönelik Uluslararası Stratejiler Ve Uygulama Örnekleri, Milli Eğitim, 48(1), 353-370. https://dergipark.org.tr/en/download/article-file/928912 adresinden 28 Mart 2023 tarihinde edinilmiştir.

KARABULUT, M. M.(2010). Parmak İzi Tanıma Temelli Gerçek Zamanlı Öğrenci Yoklama Sistemi Otomasyonu. Yüksek Lisans Tezi, Fırat Üniversitesi, Elazığ, Türkiye.

Milli Eğitim Bakanlığı Ortaöğretim Kurumaları Yönetmeliği, T.C. Resmi Gazete, 32014, 15/11/2022

ÖZTEKİN, Ö.(2013). Lise öğrencilerinin devamsızlık nedenlerinin incelenmesi. Yüksek Lisans Tezi, Eskişehir Osman Gazi Üniversitesi, Eskişehir, Türkiye.

PEHLİVAN, Z.(2006). Resmi genel liselerde öğrenci devamsızlığı ve buna dönük okul yönetimi politikaları (Ankara İli örneği). Doktora Tezi, Ankara Üniversitesi, Ankara, Türkiye.

SEZDİ, E. TÜYSÜZ, B. (2018). Elektronik Bilgi Sistemleri Tabanlı Öğrenci Yoklama Kontrol Sistemi,Bilgi yönetimi Dergisi,1(1), https://dergipark.org.tr/en/download/article-file/482374 adresinden 07 Nisan 2023 tarihinde edinilmiştir.

SÖNMEZ, A.(2019). Mesleki ve teknik ortaöğretim okulu öğrencilerinin devamsızlık nedenlerinin incelenmesi (Kastamonu ili örneği) . Yüksek Lisans Tezi, Kastamonu Üniversitesi, Kastamonu, Türkiye.

TANRIVERDİ, M.(2017). Yüz Bulma Ve Tanıma Tabanlı Otomatik Sınıf Yoklama Yönetim Sistemi. Yüksek Lisans Tezi, Ankara Üniversitesi, Ankara, Türkiye.

ÜNVER, G.(2022). Okula devamsızlık ve okul terki nedenleri: Bir meta-sentez incelemesi. Yüksek Lisans Tezi, İstanbul Medeniyet Üniversitesi, İstanbul, Türkiye.

YILDIZ, M. (2011). İlköğretim okulu öğrencilerinin devamsızlık sebeplerinin araştırılması. Yüksek Lisans Tezi, Ahi Evran Üniversitesi, Kırşehir, Türkiye.

Determination of Some Polyphenols in the Water Extracts of the Herbal Teas Widely Consumed in Turkey Using HPLC-DAD

Hatice ÇAĞLAR YILMAZ
Serkan BAŞGEL
Sema ERDEMOĞLU

Introduction

Herbal teas have been widely consumed in many countries for centuries due to they have health benefits. However herbal teas differ from traditional teas in some ways because they not only the leaves, but also the flowers, seeds, leafs, bark, stems, roots of the plant and are mostly prepared by drying and brewing in hot water. Since they contain different parts of the plant, the polyphenol content of herbal teas is richer and more diverse. Tea polyphenols are also the most important functional components that affect the taste characteristics of herbal teas as well as their benefits on human health and are classified as flavonoids, phenolic acids, lignins and stilbenes (Samanidou & et al., 2015; Sun & et al., 2022). As it is known, herbal teas due to their rich and varied polyphenol content have antioxidant, antimicrobial, anti-inflammatory, anti-carcinogenic, anti-atherogenic, anti-aging, anti-diabetic, cardio-protective, chemo-preventive, hepato-protective and neuro-protective activities properties. Free radicals, which are occur as a result of metabolic processes in the human body or due to some external factors (such as cigarettes, x-rays, chemicals), mostly cause oxidative stress, thus many diseases such as cancer and cardiovascular disorders. In these processes, polyphenols act as antioxidants by preventing the formation of free radicals in vivo. Catechins which are found in green tea is called epigallocatechin-3-gallate (EGCG), epicatechin gallate (ECG), epicatechin (EC) and epigallocatechin (EgC) and help to prevent cell damage and provide other beneficial effects. Consuming green tea is also known to aid weight loss and play preventive role in hyperglycaemia (McAlpine & Ward, 2016; Pandit 2019). Herbal teas also contribute to the intake of some trace elements necessary for daily nutrition, such as Na, Mg, Mn. Therefore, it is often consumed in the form of tea as natural remedies to prevent or cure many ailments such as cough, influenza, respiratory disorders, colds, diarrhea, dysentery and fever (Vuong & et al., 2022; Loh & et al., 2018). Given all these benefits, it is not surprising that the nutraceutical industry is investing in the production and commercialization of the herbal teas (Loh & et al., 2018).

An herbal tea can be easily prepared for daily consumption without the need for any equipment. in a glass beaker (or ceramic pot) with boiling water, and allowing them to steep for an optimal time period. But, it is difficult to preserve the polyphenol content in fresh herbal teas. Polyphenols are also easily degraded when the plant is damaged, so they are mostly sold dried or frozen and packaged to preserve and ensure the integrity of the polyphenols in herbal teas. Undoubtedly, the total antioxidant effects of herbal teas due to polyphenols will vary depending on the geographical origin of the teas, drying methods (oven-drying, freeze-drying, microwave-drying, and ambient air drying) brewing temperature/time, particle sizes of the teas, and consumer habits (such as consuming with lemon, honey, sugar) (Cleverdon & et al., 2018).

However, it shows that the minerals in the water and the pH affect the polyphenol components in the brew and change the quality and aroma of the brew. The presence of high mineral ions in tap water, especially Ca and Mg ions and hydrogen carbonate ions, inhibit the extraction process of polyphenols and reduce their concentration in the brew and thus their antioxidant properties. Green tea, black tea, mint leaves, chamomile tea, sage and lavender flowers extracted with pure water had higher polyphenol content and thus antioxidant capacity. In addition, pH is a very important factor, especially low pH values prevent the oxidation of polyphenols, so they form chelates with metal ions and eliminate their harmful effects. Catechins in brew are more stable in an acidic environment, but they are unstable because they are easily degraded in an alkaline environment (Wyrostek & Kowalski, 2021). The EGCG is water soluble and is not affected much by high temperature conditions such as boiling water. However, EGCG may show low bioavailability due to poor membrane and intestinal transit. Therefore, there is a need to increase its bioavailability when taken orally (Pandit & et al., 2019).

Extraction steps from plants are very important in the analysis of polyphenols. Methanol, ethanol, acetone, or different combinations thereof with water, ethyl acetate are used. Optimum extraction conditions depend on the type of plant and the parameters applied. Conventional extraction can be done by extraction at 80-100^{o}C for a few hours or soaking with the extraction solution for one day at room temperature. However, some new extraction techniques such as ultrasonic extraction and microwave extraction are also applied for the isolation of flavonoids. High temperature and prolonged extraction time can lead to degradation of target compounds (Sun & et al., 2022; Samanidou & et al., 2012). Campanella & et al., 2013 found that after 5 minutes of extraction of green or any herbal tea with hot water, polyphenols and antioxidants were transferred to the brew at the maximum rate, but after 5 minutes, their antioxidants either precipitated or formed micelles, which is favoured by gradual cooling of the solution, This, in turn, reduces both the antioxidant capacity and polyphenol content of the solution extract.

However, all these benefits of herbal teas, there are also reports of unexpected toxicity of high concentrations of green tea polyphenols. In 2003, an anti-obesity product containing 25% catechin was introduced to the Spanish and French markets, and toxicity was reported in 13 cases as a result of increased liver enzyme activity. A total of 79 cases of liver-related disease taking green tea extract were reported in PubMed from January 1966 to June 2007. This has received considerable attention in some countries and it has become clear that scientific research is needed on the toxicity of green tea catechins. In 2008, 218 reports on green tea extracts (including 34 on liver damage) were analyzed by US Pharmacopeia. It was concluded that consuming highly concentrated green tea extracts on an empty stomach was more likely to cause side effects (Chen & Lin, 2015).

The total polyphenol content, the determination individual of polyphenol is very important in terms of both the quality of the tea and the determination of the active species in antioxidant capacity. This will also provide very significant information in terms of the commercialization of herbal teas. Therefore, the analysis of polyphenols in herbal teas with easy to apply and accurate analytical methods is very important for the promotion of standardization and commercialization of teas. There are many methods to determine polyphenols in different samples; such as near infrared reflectance spectroscopy micellar electrokinetic chromatography, Capillary electrophoretic techniques, spectrophotometry and high-pressure column liquid chromatography-HPLC (Zou & et al., 2002).

HPLC-UV/DAD) is a suitable method for the individual analysis of polyphenols, especially in herbal teas containing high concentrations of catechins. Although mass spectrometry demonstrates high a sensitivity and low detection limit compared to UV/DAD detectors, the high polyphenol concentration into herbal tea infusions easily causes severe matrix effects on the ESI ion source. UHPLC-MS/MS is also a very successful analysis technique in terms of selectivity and sensitivity for the qualitative and quantitative analysis of

low concentrations of polyphenols in tea extracts, matrix problems need to be resolved in the analysis process. HRMS technologies, such as Q-TOF and Q-Orbitrap, are increasingly used in the analysis of tea metabolomics because of their fast acquisition speed, high full-scan sensitivity, and high mass resolution (Sun & et al., 2022).

In this work, it was evaluated the phenolic content of several selected simple single herbal teas and tisanes from Turkey market. Turkey is among the richest countries in the world in terms of flora diversity and there are about 3000 endemic plant species. For this reason, herbal teas are widely consumed as food and beverage in daily life. Herbal teas especially black or green tea is prepared from fresh or dried herbs and traditionally consumed up to 10-15 cups. Tea plants are collected in the summer, dried and stored for the winter. Alternatively, it is sold in local spice shops (aktar) or markets. Although black tea is the most consumed herbal tea in Turkey, especially in winter, linden, rosehip and sage are also consumed quite a lot (Dalar & Konczak, 2013). There are many studies in the literature on the benefits of herbal teas in Turkey their polyphenolic contents, determination of their antioxidant capacity. Since antioxidant and antimicrobial activity studies regarding the endemic Turkish herbs are relatively few in number (Yildirim & et al., 2000; Karaman & et al., 2001; Candan & et al., 2003; Oktay & et al., 2003; Vardar-Unlu & et al., 2003; Elmastas & et al., 2004; Sokmen & et al. 2004; Apak & et al., 2006) these herbs (used here as infusions) are worthy of investigation for their antioxidant activity.

Therefore, the objective of this present study is to establish the levels of polyphenols such as gallic acid, epicatechin gallate, epigallocatechin, epigallocatechin gallate, and epicatechin in the infusions of the herbs widely and habitually consumed for medical purposes in Turkey. The polyphenol contents of the most consumed herbal teas (Table 1) such as chamomile (*Matricaria chammomile L.*), fennel (*Foeniculum vulgare*), linden (*Tilia vulgaris*), nettle (*Urtica dioical*), rosehip (*Fr.Rosa caninae*), sage (*Salvia officinalis*) and senna tea (*Cassia anqustifolia*) were determined by HPLC-DAD, taking into account the traditional consumption pattern.

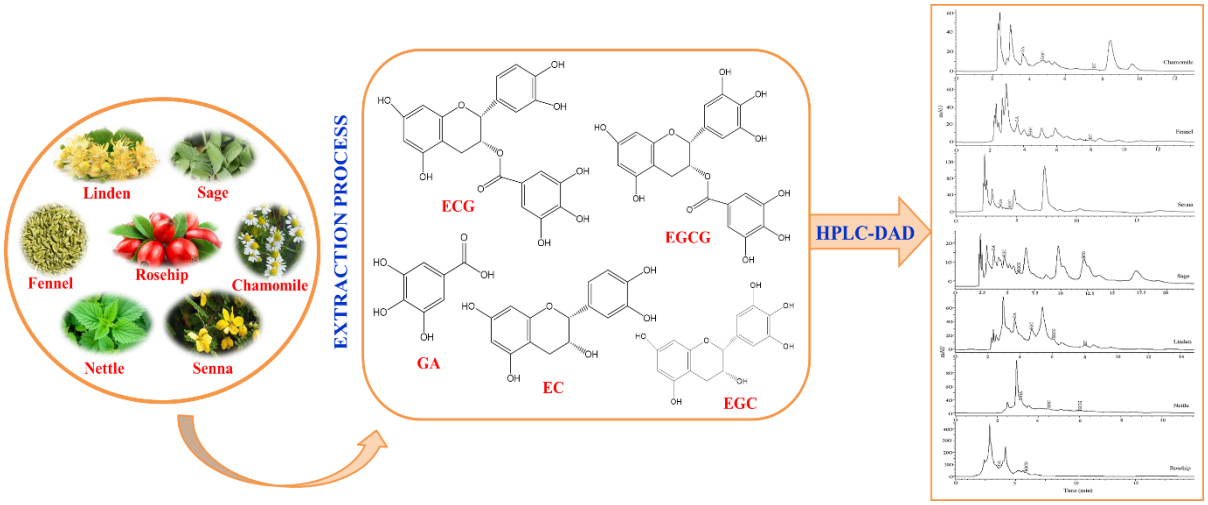

Figure 1. The general scheme of the experimental study

Table 1. Major herbs consumed as tea for medical purposes in Turkey.

Herb (Scientific name)	Indications
Chamomile (*Matricaria chammomile L.*)	Anti-inflammatory, spasmolytic, vulnerary, antimicrobial, mild sedative, carminative, antiseptic, anticatarrhal
Fennel (*Foeniculum vulgare*)	Analgesic, antidepressive, anti-inflammatory, digestive disorders, spasmolytic
Linden (*Tilia vulgaris*)	Diuretic, antidepressive, a cold
Nettle (*Urtica dioical*)	Disturbances in metabolism against a shortage of microelements, inflammation of urine, tracts in gastrics and colits, against to cancer
Rosehip (*Fr.Rosa caninae*)	Rich of vitamin C, a cold
Sage (*Salvia officinalis*)	Refresh body, Fights virus and bacteria antiinflammatory, dental caries
Senna tea (*Cassia anqustifolia*)	Relieving occasional constipation

These teas are easy to prepare, do not contain alcohol and caffeine, and are allowed to be consumed in certain quantities by children and pregnant women. In particular, chamomile and fennel are extensively used for babies especially for spasmolytic and antiseptic purposes. After proposing a suitable sample preparation procedure for polyphenols analysis, a simple, rapid, and precise gradient HPLC method with an economical mobile phase was utilized for simultaneous separation, identification and quantification of individual polyphenols. Thus, it is aimed to contribute to the commercialization of traditionally grown herbal teas by developing an easily applicable simple analysis method to determine the polyphenol content.

Material and Methods

Materials

Samples of linden, sage, rosehip, chamomile, fennel, nettle and senna tea were supplied as tea bags from local herbalists and markets in Turkey. The most widely accepted, the most frequently consumed and commercially available several brand names (Doğadan, Tema and Arifoğlu) of each herbal product were selected. Each herbal tea bag of different varieties was separately ground in a stainless steel mixer mill. One portion of the ground samples was blended for homogenization using an agate pestle. They were one by one mixed and placed individually in polyethylene containers and the samples were dried at 70°C for 24 h.

Reagents

Gallic acid (GA), (-)-Epicatechin gallate (ECG), (-)-Epigallocatechin (EGC), (-)-Epigallocatechin gallate (EGCG), (-)-Epicatechin(EC), were purchased from Sigma Chemical Co.(St.Louis, MO, USA), with purities greather than 98%. The methanol and glacial acetic acid (HPLC grade) were obtained from Merck (Darmstadt, Germany). Double deionized water (Milli-Q, Millipore with 18.2 MΩ/cm resistance) was used for preparation of solutions and infusions.

Preparation of standard solutions

The main stock solutions were 1000 mg/l of EGCG, ECG, GA, EC and EGC. The main stock solutions were prepared individually from 0.25 g of the respective compound dissolved in 250 ml deionized water using ultrasonic bath. Operating standards for calibration were prepared with concentrations of 1, 5, 10, 20, 30, 40 and 50 mg/l.

Sample preparation

Two different extraction methods were applied on samples: a normal tea brew with boiling water and methanolic extract of ground herbal tea. For preparation of tea brews, 0.500 g of the ground herbal tea was extracted with 25 ml of boiling water at 95°C and incubating at 70°C for 4 hour including shaking at 150 rpm and then cooled. For preparation of methanolic extract, 0.500 g ground herbal tea was extracted two times with 20 ml 80% methanol containing 0.15% HCl for 3 h and then two extracts were combined.

The extracts obtained via both of the way were filtered through cotton to get rid of rough particles. The solution was further filtered through 0.45 µm of Nylon membrane filter and the filtrates were injected onto HPLC. Since catechins were photo sensitive, preparation of the samples and standard solutions was carried out under a dim lighting-working environment.

HPLC analysis

HPLC analysis were conducted on Agilent 1100 Series liquid chromatography equipped with Agilent 1100 G 1322A model degasser, Agilent 1100 G 1311A dual solvent pump, injection valve, and Agilent 1100 DAD G 1315B photodiode array detector. SGE C_{18} reversed-phase packing column (4.6 x 250 mm, 5 mµ) was used for separation. The DAD acquisition wavelength was set in the range of 200-400 nm, analogue output channel A at wavelength 280 nm with bandwidth 10 nm. A gradient elution was performed by varying the proportion of solvent A (deionized water) to solvent B (methanol containing 1% acetic acid) with a flow rate of 1 ml/min. Mobile phase was degassed before injection onto HPLC. The gradient elution profile started with A-B (90:10), B was increased to 20% at from 3 to 14 min. and back to the initial conditions A-B (90:10) after from 15 min. The column was than re-equilibrated with the initial conditions for 3 min before the next injection. The injection volume was 20 µl.

Results and Discussion

Effect of sample extraction on separations

The critical step in the quantification of catechins phenolic acids in herbal teas is sample extraction. The extraction method must enable complete extraction of the compounds of interest and must avoid chemical modification three different extraction methods, (1) a normal tea brew with boiling water, (2) an acetonitrile or methanolic extract of ground tea and (3) Official German Method for determination of soluble solids (1h boiling under the reflux) were used in previous studies. The Official German Method, leads to decomposition of catechins while

acetonitrile and methanolic extracts gave the highest yields. Thus, a single extraction with acetonitrile or methanol has been widely used in quantitative analysis of tea polyphenols. However, the experimental results of Zuo & et al. have shown that large amounts of polyphenols and caffeine remained in the tea residues after a single methanolic extraction. The authors carried out a two times extraction with 80% aqueous methanol containing 0.15% HCl on linden and sage samples. Figure 2 gives a chromatogram of linden and sage in methanolic extracts. However, our experimental results have shown that resolution in chromatograms of polyphenols extracted with methanol was very bad than water extract. Severe peak splitting and tailing can occur, if methanolic extracts are directly injected onto an HPLC system. As can be seen, a good resolution was obtained using water extracts, relative to methanolic extract. Therefore, normal tea brew that was prepared with boiling water of ground herbal teas was injected onto HPLC.

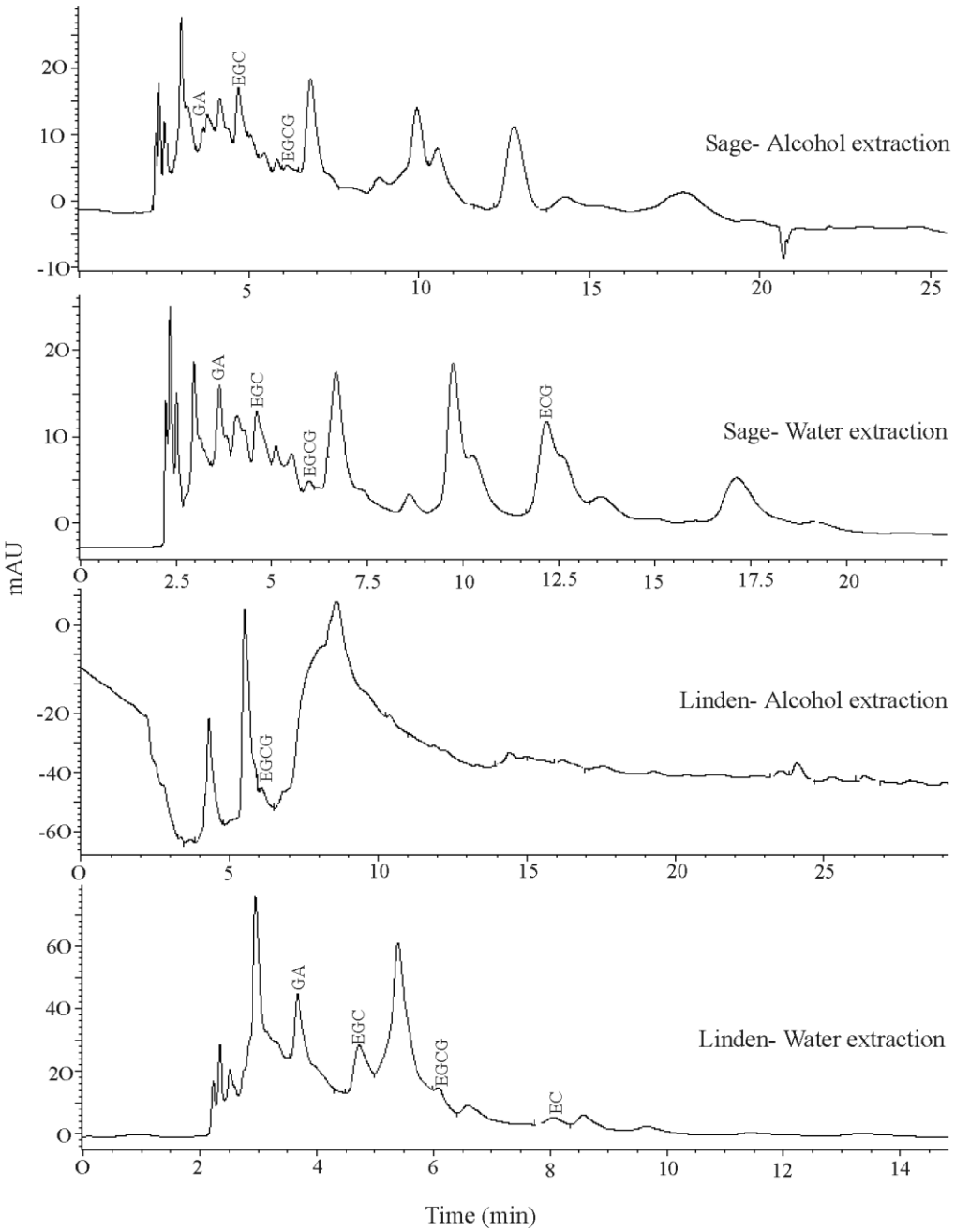

Figure 2. Chromatograms for linden and sage in water and methanolic extracts.

Optimisation of chromatographic separations

A gradient elution program using methanol, acetic acid and water as solvent was chosen. Figure 3 shows an HPLC chromatogram of a standard mixture of five polyphenols, containing 20 mg/l of GA, 10 mg/l of EGC, 20 mg/l of EGCG, 10 mg/l of EC and 20 mg/l of ECG at 280 nm. The compounds were successfully separated within 14 min. A series of experiments were carried out to compare the effect of acetic acid concentration. It was proved that there was little effect on the separation, when the concentration of acetic acid in the mobile phase was between 0.1-1%. The retention time decreased a little, when the acetic acid concentration was increased. The suitable proportion of water-methanol-acetic acid was found as to be 70-29-1. In addition, when methanol concentration was increased to higher values than 29%, the signal for polyphenols was inhibited greatly and peak width was increased.

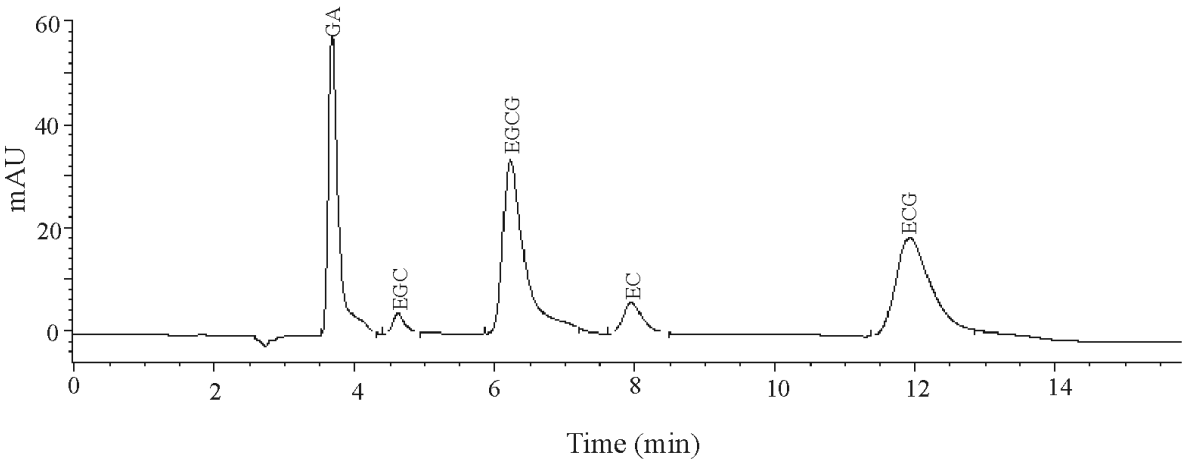

Figure 3. HPLC chromatogram of a standard mixture of five polyphenols, containing 20 mg/l of GA, 10 mg/l of EGC, 20 mg/l of EGCG, 10 mg/l of EC and 20 mg/l of ECG

Analysis of the samples

Under the optimized HPLC conditions described in section 3.2, good separation of herbal extract was obtained within 14 min with DAD detector scanning at 400-250 nm. Considering the levels of polyphenol in herbal tea infusions, 280 nm as a good detection wavelength was selected for these chemicals. Calibration curves were obtained by the external standard for five polyphenol, a series of standard solutions over the concentration range from 1-50 mg/l. All calibration curves were linear over the concentration ranges tested, with correlation coefficients ≥ 0.99. The calibration graphs for all the studied compounds showed good correlation between the peak areas and phenolic concentrations, with regression coefficients 0.99 in all cases. Five separate water extract of each herbal tea was prepared, each extract was separately injected to HPLC three times and arithmetic mean of three measurements was collected as result.

Figure 4 illustrated the representative separations of each polyphenol in the water extract of the herbal teas. A total seven herbal teas were analysed for the content of some polyphenol by using the proposed method. The results are presented in Table 2. Linden and sage are rich in polyphenols as compared to the other herbs. GA was found in all herbs in the range of 0.35-2.28 mg/g, but the highest GA level corresponded to linden, followed by chamomile and rosehip. ECG was determined only in sage, with 0.58 mg/g. EGC was found in all herbs, except rosehip, in the range of 1.45-7.02 mg/g, with the highest level of linden. EGCG which was not detected in chamomile, fennel and sage is present at low concentrations in the other herbs with 0.18-0.56 mg/g. EC was determined only in linden, chamomile and fennel at 0.32-0.86 mg/g concentrations. GA and EGC were presented in all samples at high concentrations.

Table 2. The concentrations of individual polyphenols in water extracts of the herbal teas

	Concentrationα mg polyphenol / g herbal tea				
Herbal tea	GA	EGC	EGCG	EC	ECG
Linden	2.28 ± 0.40	7.02 ± 0.41	0.36 ± 0.09	0.86 ± 0.09	nd
Nettle	0.63 ± 0.01	3.44 ± 0.04	0.38 ± 0.05	nd	nd
Rosehip	1.17 ± 0.08	nd	0.56 ± 0.06	nd	nd
Chamomile	1.19 ± 0.04	1.69 ± 0.33	nd	0.32 ± 0.04	nd
Fennel	0.60 ± 0.03	1.50 ± 0.14	nd	0.39 ± 0.04	nd
Sage	0.50 ± 0.03	1.83 ± 0.02	0.18 ± 0.03	nd	0.58 ± 0.03
Senna	0.35 ± 0.02	1.45 ± 0.07	nd	nd	nd

α Mean ± standard deviation (n=5)
nd: not detected

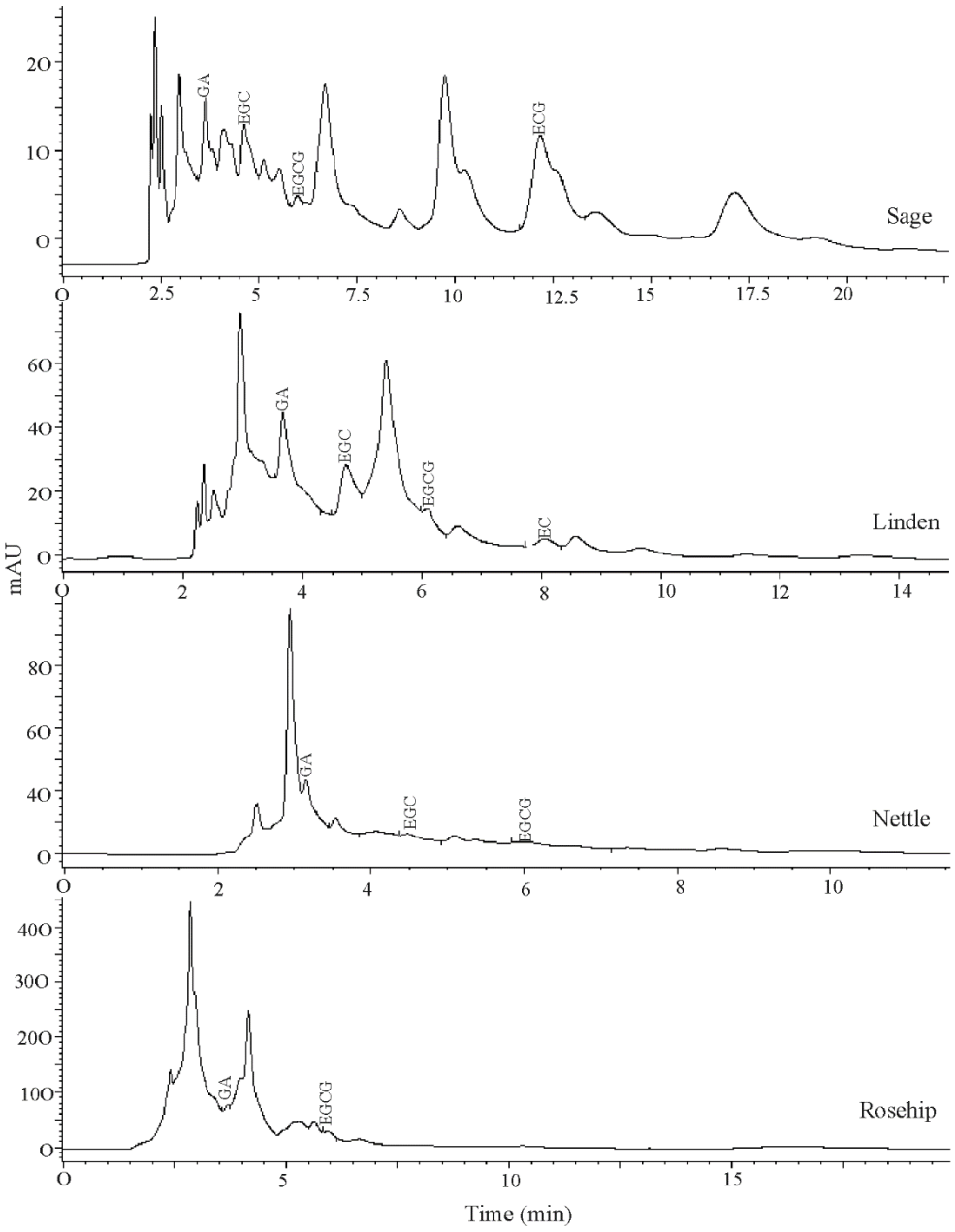

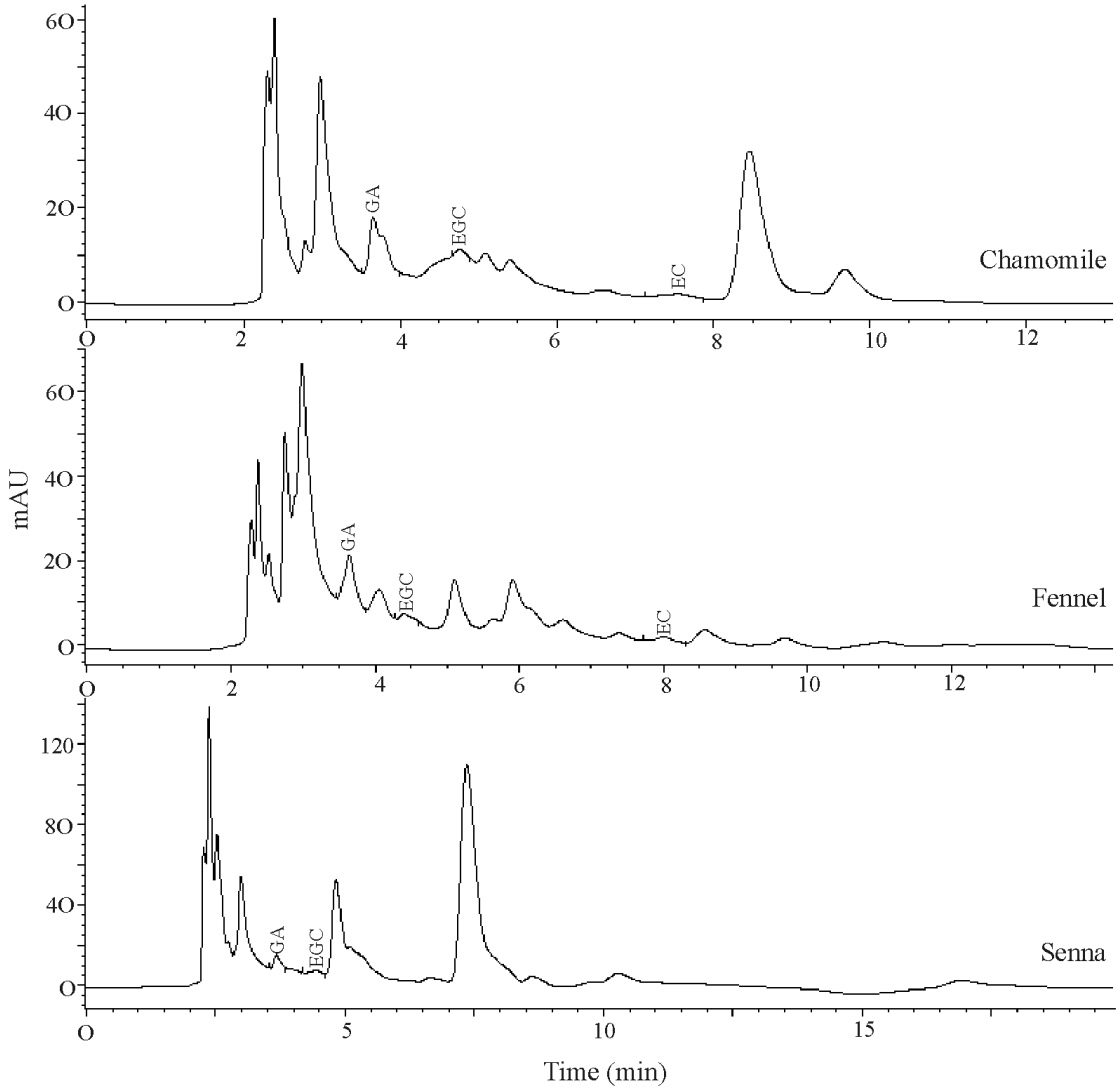

Figure 4. HPLC chromatograms for polyphenol in the water extract of the herbal teas

Concentration levels of polyphenols either in green tea or in black tea are high as compared to the herbal teas investigated in this study. In the analysis performed by Zuo & et al. in eight different green and black tea samples, all the other polyphenols, except GA, was determined at higher concentrations than the samples at the present study. In addition, green tea contains all of the polyphenols mentioned. In this study were used herbal teas directly from drying and steaming the fresh tealeaves and thus no fermentation (i.e.oxidation) occurs as green tea. During the fermentation, tea catechins are oxidized or condensed to other large polyphenolic molecules such as theaflavins and thearubigins. The health effect of these oxidized products is not well understood yet. The presence of polyphenols in plant foods is large factors and environmental conditions. Other factors, such as germination, degree of ripening, variety processing and storage also plant phenolics. Besides polyphenols, there is also stimulating caffeine in green tea and black tea, whereas the herbal teas not. Therefore, no side effects were observed especially in babies fed by linden, chamomile or fennel tea. Consequently the herbal teas investigated in this study contain significant amounts of polyphenols, however their concentrations are not as high as green tea.

Conclusions

The present study demonstrates the polyphenols content widely consumed in Turkey. The method applied on herbal tea samples allows rapid and is more precise for data collection. It

provides useful information for the polyphenol content in the herbal teas. The major polyphenols found in the all-herbal tea infusions are epicatechin gallate, epigallocatechin, epigallocatechin gallate, and epicatechin whereas gallic acid is the main phenolic acid.

References

Apak, R., Güçlü, K., Özyürek, M., Karademir, S.E. & Erçağ, E. (2006). The cupric ion reducing antioxidant capacity and polyphenolic content of some herbal teas. *International Journal of Food Sciences and Nutrition, 57(5/6),* 292-304. https://doi.org/10.1080/09637480600798132.

Başgel, S. & Erdemoğlu, S. (2006). Determination of mineral and trace elements in some medicinal herbs and their infusions consumed in Turkey. *Science of the Total Environment, 359,* 82-89. https://doi.org/10.1016/j.scitotenv.2005.04.016.

Campanella, L., Bonanni, A. & Tomassetti, M. (2003). Determination of the antioxidant capacity of samples of different types of tea, or of beverages based on tea or other herbal products, using a superoxide dismutase biosensor. *J Pharm Biomed Anal, 327,* 725-736. https://doi.org/10.1016/S0731-7085(03)00180-8.

Candan, F., Unlu, M., Tepe, B., Daferera, D., Polissiou, M., Sokmen, A. & Akpulat, H.A. (2003). Antioxidant and antimicrobial activity of the essential oil and methanol extracts of Achillea millefolium subsp. Millefolium Afan. (Asteraceae). *J. Ethnopharmacol, 87,* 215-220. https://doi.org/10.1016/S0378-8741(03)00149-1.

Chen, Z.M. & Lin, Z. (2015). Tea and human health: biomedical functions of tea active components and current issues, *Journal of Zhejiang University-Science B (Biomedicine & Biotechnology) 16(2),* 87-102. https://doi.org/10.1631/jzus.B1500001.

Cleverdon, R., Elhalaby, Y., McAlpine, M.D., Gittings, W. & Ward, W.E. (2018). Total Polyphenol Content and Antioxidant Capacity of Tea Bags: Comparison of Black, Green, Red Rooibos, Chamomile and Peppermint over Different Steep Times, *Beverages, 4,* 15 https://doi:10.3390/beverages4010015

Dalar, A. & Konczak, I. (2013). Phenolic contents, antioxidant capacities and inhibitory activities against key metabolic syndrome relevant enzymes of herbal teas from Eastern Anatolia, *Industrial Crops and Products, 44,* 383-390. https://doi.org/10.1016/j.indcrop.2012.11.037.

Elmastas, M., Ozturk, L., Gokce, I., Erenler, R. & Aboul-Enein, H.Y. (2004). Determination of antioxidant activity of marshmallow flower (Althaea officinalis L.). *Anal Lett, 37,* 1859-1869. https://doi.org/10.1081/AL-120039431.

Karaman, S., Digrak, M., Ravid, U. & Ilcim, A. (2001). Antibacterial and antifungal activity of the essential oils of Thymus revolutus Celak from Turkey. *J Ethnopharmacol ,76,* 183-186. https://doi.org/10.1016/S0378-8741(01)00238-0.

Loh, H.Z., Oh, H.K.F., Lim, Y.Y. (2018). Relationship between polyphenol oxidase activity and phenolics degradation on ambient air-drying of herbal plants, *J Food Process Preserv.* e13672. https://doi: 42:e13672.

McAlpine, M.D. & Ward, W.E. (2016). Influence of Steep Time on Polyphenol Content and Antioxidant Capacity of Black, Green, Rooibos, and Herbal Teas. *Beverages 2,* 17-21. https://doi:10.3390/beverages2030017.

Oktay, M., Gulcin, I. & Kufrevioglu, O.I. (2003). Determination of in vitro antioxidant activity of fennel (foeniculum vulgare) seed extracts. *Lebensm-Wiss Technol, 36,* 263-271. https://doi.org/10.1016/S0023-6438(02)00226-8.

Pandit, A.P., Joshi, S.R., Dalal, P.S. & Patole, V.C. (2019). Curcumin as a permeability enhancer enhanced the antihyperlipidemic activity of dietary green tea extract, *BMC Complementary and Alternative Medicine, 19,* 129. https://doi.org/10.1186/s12906-019-2545-1.

Samanidou, V., Tsagiannidis, A., Sarakatsianos, I. (2015). Simultaneous determination of polyphenolsand major purine alkaloids in Greek Sideritis species, herbal extracts, green tea, black tea,and coffee by high-performance liquid chromatography-diode array detection, *Sep. Sci.,35,* 608–615.

Sökmen, A., Gulluce, M., Akpulat, H.A., Daferera, D., Tepe, B., Polissiou, M., Sökmen, M. & Sahin, F. (2004). The in vitro antimicrobial and antioxidant activities of the essential oils and methanol extracts of endemic Thymus spathulifolius. *Food Control, 15*, 627-634.

Sun, M.F., Jiang, C.L., Kong, Y.S., Luo, J.L., Yin, P., Guo, G.Y. (2022). Recent Advances in Analytical Methods for Determination of Polyphenols in Tea: A Comprehensive Review, *Foods, 11(10),* 1425, https://doi.org/10.3390/foods11101425.

Wyrostek, J. & Kowalski, R. (2021). The Effect of water mineralization on the extraction of active compounds from selected herbs and on the antioxidant properties of the obtained brews. *Foods*, *10*, 1227. https://doi.org/10.3390/foods10061227.

Vardar-Unlu, G., Candan, F., Sokmen, A., Daferera, D., Polissiou, M., Sokmen, M., Donmez, E. & Tepe, B. (2003). Antimicrobial and antioxidant activity of the essential oil and methanol extracts of Thymus pectinatus Fisch. Et Mey. Var. pectinatus (Lamiaceae). *J Agric Food Chem 51*, 63-67. https://doi.org/10.1021/jf025753e.

Vuong, Q.V., Pham, H.N.T. & Negus, C. (2022). From Herbal Teabag to Infusion-Impact of Brewing on Polyphenols and Antioxidant Capacity, Beverages, 8(4), 81. https://doi.org/10.3390/beverages8040081.

Yildirim, A., Mavi, A., Oktay, M., Kara, A.A., Algur, O.F. & Bilaloglu, V. (2000). Comparison of antioxidant and antimicrobial activities of tilia (Tilia argentea Desf ex DC), sage (Salvia triloba L.) and black tea (Camelia sinensis) extracts. *J Agric Food Chem, 48*, 5030-5034.

Zuo, Y., Chen, H. & Deng, Y. (2002). Simultaneous determination of catechins, caffeine and gallic acids in green, Oolong, black and pu-erh teas using HPLC with a photodiode array detector. *Talanta, 57*, 307-316. https://doi.org/10.1016/S0039-9140(02)00030-9.

Current Debates on Natural and Engineering Sciences

9